Murujuga Rock Art Monitoring Program:

Monitoring Studies Report 2025

Technical Report on Monitoring Studies completed from April 2024 to March 2025.

Prepared for
Murujuga Aboriginal Corporation
and
Department of Water and Environmental Regulation, Western Australia.

Preferred citation:

Curtin University (2025) *Murujuga Rock Art Monitoring Program: Monitoring Studies Report 2025*. Submitted to the Murujuga Aboriginal Corporation and the Department of Water and Environmental Regulation, Government of Western Australia. DWER Technical report COPP21065-REP-G-109, revision 0.

Doc No	Current Rev	Revision Date	Checked By	Approved By
COPP21065-REP-G-109	0	20/04/2026	B. Mullins	N. Armstrong

Revision history

Revision	Date	Revision Reason
A	18/07/2025	Preliminary for review
B	13/08/2025	Issued to DWER for peer review
C	5/01/2026	Updated following peer review
0	20/04/2026	Issued for use following close-out review

Authors and contributors

Nicola Armstrong, Glen Aubrey, David Belton, Kasziem Bin-Sali, Katelyn Boase, Arne Bredin, Edward Campbell, Marco Coolen, Noel Cressie, Thomas Di Loreto, Katy Evans, Ronald Fellows-Smith, Kliti Grice, Karl Gruber, Monica Gumulya, Toni Hannelly, Stephanie Hogg, Alex Holman, Peter Hopper, Melanie Johnston-Hollitt, Andrew King, Pete Kinny, Katherine Landwehr, Zhen Li, David Lynch, Dan Marrable, Alex Martin, Ryan Mead-Hunter, Abraj Mohomed, Benjamin Mullins, Rebecca O'Leary, Calvin Pang, Anuradha Patel, Chloe Ramirez, Will Rickard, Robert Ryan, Bettina Schaefer, Robyn Schofield, Sebastian Stanley, Amy Stevens, Andrew Thorn, Victoria Wade, Candace Willison, Arun Veluchamy.

Acknowledgements

This work was supported by resources provided by the Pawsey Supercomputing Research Centre's Setonix Supercomputer (CFD and Spatial and Bioinformatics Modelling, https://doi.org/10.48569/18sb-8s43) and Nimbus Research Cloud (AQM data storage and processing, https://doi.org/10.48569/v0j3-qd51), with funding from the Australian Government and the Government of Western Australia.

The authors also gratefully acknowledge: (1) Emeritus Distinguished Professor Adrian Baddeley for his work on the study design, Year 1 and 2 reports and associated methods and wish him a long and happy retirement. (2) The West Australian Biogeochemistry Centre (UWA) and Dr Greg Skryzpek for provision of rainwater *pH* data, (3) A/Prof John Holdsworth, Dr Liam Sutton and colleagues at U. Newcastle for provision of their LiDAR, (4) DWER Air Quality branch for provision of their LiDAR and (4) Prof. Jo McDonald and Dr Mick O'Leary (UWA) for useful discussions.

The data associated with this report is available on request from the Department of Water and Environmental Regulation.

The information contained in this report is copyright © 2021–2025 the Department of Water and Environmental Regulation (DWER) WA, except for prior art (background IP) of Curtin University and subcontractors. No part of the report may be reproduced or transmitted in any form by any means including, without limitation, electronic, photocopying, recording, or otherwise, without the prior written permission of DWER. No information embodied in the report which is not already in the public domain shall be communicated in any manner whatsoever to any third party without the prior written consent of DWER. While Curtin University and subcontractors consider that the information and opinions given in this work are sound, all parties must rely upon their own skill and judgement when making use of it. Curtin University and subcontractors do not make any representation or warranty, expressed or implied, as to the accuracy or completeness of the information contained in this report and assumes no responsibility for the accuracy or completeness of such information. Curtin University and subcontractors will not assume any liability to anyone for any loss or damage arising out of the provision of this report.

Executive summary

The Murujuga Rock Art Monitoring Program (**MRAMP**) is currently the world's largest scientific study examining the impact of industrial air emissions on rock art engravings of Murujuga, an area covering the Burrup Peninsula and Dampier Archipelago in Western Australia. Most importantly, the region was recently inscribed as Australia's 21st UNESCO (United Nations Educational, Scientific and Cultural Organization) World Heritage site, second cultural landscape, and first Indigenous-led Australian nomination. MRAMP reporting and ongoing monitoring, led by the Ngarda Ngarli, have been written into the inscription conditions of the Heritage site.

This technical report presents and discusses the results from the first three years of work, involving research being undertaken to establish acceptable and unacceptable levels of air pollution affecting the Murujuga rock art. The focus of this report is to expand and confirm the results presented in the Monitoring Studies Report 2024 (Curtin University, 2024c). In future, more extensive data fusion and analyses of new data streams will be provided in the final report (due mid 2026), before the program transitions to ongoing monitoring following peer review and publication.

The extensive monitoring program and the high spatial resolution of the data collected, combined with the rigorous laboratory and statistical framework, enabled the research team to identify important spatial patterns in rock porosity and microbiome composition that are linked with (historic) patterns of air quality in the Monitoring Studies Report 2024 (Curtin University, 2024c). The evidence backing these patterns and associations would have been unlikely to have any statistically significance if a smaller number of study sites had been selected. Furthermore, the findings related to porosity have been verified in this report using a second set of rock samples, collected with cultural approval following the Monitoring Studies Report 2024 (Curtin University, 2024c) findings.

Research undertaken over the past three years has been based on the peer-reviewed *Murujuga Rock Art Monitoring Program: Monitoring Studies Data Collection and Analysis Plan* (**MSDCA Plan**) (Curtin University, 2022). This current report builds on the progress reported in the Monitoring Studies Report 2024 (Curtin University, 2024c), released in May 2025. The present report is not intended to be a stand-alone document; rather it is intended to be read in conjunction with the suite of published Murujuga Rock Art Strategy documents, including the:

- *Murujuga Rock Art Strategy* (DWER, 2020),
- *Murujuga Rock Art Monitoring Program: Conceptual Model* (DWER, 2021),
- *Murujuga Rock Art Monitoring Program: Monitoring Studies Data Collection and Analysis Plan* (Curtin University, 2022).

MRAMP will ultimately develop Environmental Quality Criteria (**EQC**) as part of an Environmental Quality Management Framework (**EQMF**) for the ongoing management of the **Murujuga region**, with a focus on air quality and atmospheric deposition on or near the rock art. The EQC will consist of guideline (early warning) and standard (limit) levels for all key air pollutants (DWER, 2020). This management and monitoring approach will form a foundation for the long-term protection of the rock art from anthropogenic emissions. The first Interim EQC (Curtin University, 2024a) were published in conjunction with the Monitoring Studies Report 2024 (Curtin University, 2024c), and an Interim EQC Update is being developed to incorporate new knowledge from this report. One further study report is planned following completion of research studies, at which point a Final EQC

document will be issued for use as the project transitions to ongoing monitoring against EQC. It is however likely that some ongoing research may be recommended to resolve any remaining research questions.

So far, three fieldwork campaigns have been completed during the third year of work, between April 2024 and March 2025 inclusive, with ten campaigns in total since the start of the project. The third year of fieldwork lasted 40 weeks in total and included the continued monitoring of 54 rock art panels across the five rock types found in the study area. All fieldwork on Murujuga, including rock sample collection, is approved by the Murujuga Aboriginal Corporation (**MAC**) Elders. To date, over 186,200 spectral/colour measurements of rock art condition have been recorded, along with over 5,500 surface electrochemical measurements (*pH*, *Eh*, Cl^-). Surface elemental measurements using x-ray fluorescence (**pXRF**) were discontinued for this study year, as the previous analysis found that this approach was not useful for monitoring change over time.

The 64 sample rocks and additional microbial samples collected in 2022, as well as a further 23 rock samples collected in 2023 have been analysed for their microstructure and inorganic geochemistry. The bulk of these analyses are nearing completion at the end of the third year of studies. This report presents further results from geological and geochemical analyses. More extensive data synthesis of the inorganic geochemistry, microbial, and air quality studies is ongoing and will be presented in the final monitoring studies report, at which time the ongoing monitoring plan will be finalised and implemented. Also presented here is an extensive statistical data synthesis.

Air quality

As part of this project, 18 solar/passive air quality and weather monitoring stations and four mains-powered air quality monitors (**AQM**s) have been established and are currently running. A further 12 months of monitoring data from all these instruments has been analysed in this report. The results presented here show that the concentrations and spatial patterns of air quality data are broadly consistent between the datasets from the second and third year of research studies.

On average, air quality at Murujuga remains below relevant health guideline limits and the (lower) interim EQC concentrations set previously for three chemical species: ammonia (NH_3), sulfur dioxide (SO_2), and nitrogen dioxide (NO_2). The only exception to this is particulate matter (dust, PM_{10}), which appears to exceed health guidelines at times, however no EQC values have been established to date. For NH_3, data collected show that it is consistently highest at monitoring stations AQA1 and AQ11, which are located in a direct line between the fertiliser plant(s) and the Port of Dampier export terminal. SO_2 is highest at AQ11, a location that overlooks port facilities and King Bay, and on locations from the outer islands (e.g., AQ18), depending on the prevailing winds. SO_2 levels appear to be dominated by shipping activities; however some contribution may come from gas combustion or flaring. NO_2 and nitric acid levels (HNO_3, a secondary air pollutant) are highest in the region spanning Dampier (EX02), Mt Wongama (EX09) and Katrin's Hill (AQ07/08), which overlooks the airport. Ozone (O_3), has less spatial variability due to the time scales and organic species required for formation. The peak in ozone levels seen in 2023 occurred at location EX09 and the peak in 2024 at location AQ18. As discussed in the Monitoring Studies Report 2024 (Curtin University, 2024c), moderate levels of formaldehyde (CH_2O) have also been observed, which is an intermediate product in the decomposition of methane (CH_4). CH_2O is a weak but non-trivial contributor to O_3 formation when combined with NO_2. There is no suggestion at this stage that organic air pollutant species are significant with respect to rock art, however, sufficiently

high concentrations of CH_2O or O_3 at ground level could be expected to impact the microbiome via established biocidal effects (at high concentrations) or accelerate oxidation reaction rates on the rock surface.

Relatively high levels of black carbon (soot) were observed in Monitoring Studies Report 2024 (Curtin University, 2024c). Additional data are not presented in this report due to equipment electronic issues, however additional physical samples were collected using both the Aethalometer and a High Volume sampler and will be analysed and included in the final report. There are suggestions in the literature that black carbon (from both natural and anthropogenic sources) may contribute to delamination of rock surfaces (Dorn, 2020).

pH and rainfall measurements

Measurements of *pH* from inert surfaces such as the AQM deposition samplers and rainfall samplers clearly show that average wet and dry deposition over the past three years continues to be neutral or slightly alkaline. *pH* measurements undertaken on fresh rock cubes installed in AQMs were found to be close to neutral and differentiated by rock type. The average rainfall *pH* is 7.4 and the deposition sampler dry *pH* is 6.7 for all measurements (years 1-3) presented in this report. This contrasts to previous measurements in 2005-2009 by CSIRO 2010 which show mean and median rainfall pH <5.6 for this period. The Murujuga region is the most cyclone prone part of Australia (https://www.dfes.wa.gov.au/hazard-information/cyclone) and in early 2025 it experienced Tropical Cyclone Sean, which saw an all-time record of 274 mm of rainfall in the Karratha Aero (Bureau of Meteorology) station over a period of 24 hours, and 303 mm of rainfall was measured at two MRAMP stations. This event saw a lower rainfall *pH* of 5.6-7, which is closer to global average values.

The results of this project also showed that *pH* measurements on ‘live’ or patinated rock surfaces tend to be slightly acidic. However, these data are more complex to interpret. The lower *pH* appears to be primarily due to microbial activity. Measurements on the surface of bushfire-exposed rocks in the second year of studies showed a clear alkaline signal (as high as pH 8.9), which reverted back to (slightly acidic) baseline levels over 9-12 months following the exposure. Another important consideration in rock *pH* measurements is the contribution of clay minerals (e.g., dust), which are expected to be alkaline, as well as sea spray, which could range between acid and alkaline. Additional data collected appear to confirm previous observations of microbial responses to rainfall or dust deposition, which may result in the production of organic acids by the microbiome.

Porosity and patina formation

In the second year of research studies, the porosity of the weathered rind (subsurface layer) of granophyre rock was higher in a region centered around King Bay, extending to south of Dampier town, north to encompass the industrial precincts and lower elsewhere. As all natural causes have been ruled out, this pattern may represent historical anthropogenic impact, most likely due to higher emission levels in the past, and may also be associated with historical ground-level concentrations of chemical species. The porosity significance analysis plotted in the Monitoring Studies Report 2024 (Curtin University, 2024c) was calculated at 99.5% instead of the more typical 95%. This has been identified and corrected which results in an apparent increase in the region of statistical significance for rock porosity. However, it should be noted that this does not represent an increase since the year two data. The spatial porosity pattern determined from the original rock samples

collected in 2022 and a second validation set collected in 2024 produce comparable results when analysed using appropriate statistical techniques developed for the project.

Chamber-accelerated weathering studies and Interim EQC

The chamber studies have demonstrated a mechanism by which exposure to air pollutants can increase porosity under either predominantly dry or wet conditions. This observation has been confirmed chemically, through analysis of leachate, and physically, through high-resolution imaging of minerals before and after exposure. Interim EQC were developed following the second year of studies for NH_3, NO_2 and SO_2. The latter two chemical species were linked, as results were from combustion experiments producing both species as well as a range of carbon compounds.

In order to differentiate individual responses, geochemical weathering studies switched to single gas exposures, and microbial culture exposures commenced. Some possible issues with sample rock reuse and experiment sequencing were identified and additional experiments have been undertaken to address this. Most importantly, the experiments have found no response to NO_2, apart from a likely response at the highest possible dose obtainable under the revised/improved experimental protocol. Other weathering literature has suggested this is due to Henry's law, which relates to the solubility and reactivity of weak gas mixtures. Henry's law suggests that SO_2 is approximately 110 times more effective in promoting weathering than NO_2, and NH_3 approximately 5,000 times more important (compared to NO_2). For this reason, SO_2 has always been the major contributor to acid rain globally. In agreement with this theory, a clear dose-response relationship has been found for SO_2 using both the original and revised experimental protocol. It is expected that a combined weathering index can be developed for future EQC, which will account for varying concentrations and species of air pollutants.

Microbiome chamber studies are progressing on schedule. However, they are not yet at a stage where they can contribute to EQC development. Preliminary results appear to agree with the relative importance of NO_2 vs SO_2 found in the abiotic experiments.

Field rock art spectrometry and photogrammetry

Spectral imaging of rock art is now producing high-quality results after considerable work to optimise the methodology, with initial analyses and the real-time error detection taking place in the field in real time. Novel software with a graphical user interface has been developed for this purpose, to validate measurements at the time of data collection.

In this report, all analyses of field colour data were restricted to four sites, (AQ03_GPH, AQ04_GPH, AQ11_GPH and EX06_GPH), measured by both instruments during campaigns 7–10. The final MRAMP monitoring studies report will include analysis of all sites.

There was no temporal change in rock surface colour over the three-year study period (campaigns 1 to 10) for four sites using the JAZ instrument.

The (older) JAZ instrument was found to be more variable than the (newer) HDX instrument. This is most likely explained by the HDX taking only about 5 seconds to record all 100 replicates, whereas the JAZ measurements may take several minutes. Both the longer measurement interval and smaller number of replicates appear to be a source of variability or error in the JAZ data.

For campaigns 7 to 10, there was no difference in trends between the two instruments. Thus the

spectral rock surface colour measurements are similar between JAZ and HDX instruments.

The current (HDX) approach and associated method for rock art condition monitoring over time appears to be producing reproducible measurements for the long-term monitoring of rock surface colour. However, given the HDX operational problems during the summer (Garrbarn) months, it is recommended that future colour monitoring should only be conducted in the cooler months (Muthu).

Additionally, a simplified photogrammetry approach has been developed and validated. This complementary approach is reliably able to detect changes in rock art panels at the sub-millimetre scale.

Further work

Remaining components of the MSDCA Plan (Curtin University, 2022) and subsequent MSDCA Plan Amendment 2024b to further interrogate rock surface porosity findings continue to be progressed as planned.

Also, many opportunities remain for increased integration and analyses of combined datasets. These opportunities will be explored further in the final reporting period. It was hoped that some of these could be undertaken during the current reporting period, however the large volume of data and analyses precluded this. The project remains on track to achieve the outcomes of delivering an EQC and embedded ongoing monitoring strategy.

Contents

Executive Summary **ii**

1 Introduction **1**
1.1 Background . . . 1
1.2 Objectives of the MRAMP monitoring studies . . . 3
1.3 Scope of this report . . . 3
1.3.1 Inclusions . . . 4
1.4 Abbreviations and definitions . . . 5
1.4.1 Abbreviations . . . 5
1.4.2 Chemical notation . . . 9
1.4.3 Glossary . . . 10
1.4.4 Site and sample numbering nomenclature . . . 17

2 Study methodologies, verification of competency, and quality assurance **19**
2.1 Elaboration of methodologies described in the MSDCA plan . . . 19
2.2 Personnel and verification of competency . . . 19
2.3 Quality assurance . . . 20
2.3.1 Air quality monitoring . . . 20
2.3.2 Fieldwork . . . 21
2.3.3 Laboratory analysis . . . 21
2.4 Review of Literature . . . 22
2.4.1 Weathering studies and estimates for other sites . . . 22
2.4.2 Weathering studies using Murujuga rock samples . . . 22

3 Monitoring studies undertaken in the field **25**
3.1 Field monitoring generally . . . 25
3.1.1 Location of field monitoring sites . . . 25
3.1.2 Summary of field campaigns in the first three years of studies . . . 25
3.2 Inorganic geochemistry fieldwork . . . 26
3.2.1 Objectives . . . 26
3.2.2 Methodology . . . 27
3.2.3 Modifications to fieldwork methodology . . . 27
3.2.4 Fieldwork activities . . . 28
3.3 Surface change analysis (spectroscopy) fieldwork . . . 43
3.3.1 Objectives . . . 43
3.3.2 Methodology . . . 43
3.4 Microbiome collection fieldwork . . . 44

4 Laboratory analysis of field samples **45**
4.1 Organic geochemistry laboratory analysis . . . 45
4.1.1 Objectives . . . 45
4.1.2 Methodology . . . 45
4.1.3 Summary of previous work . . . 45

4.1.4 Gas chromatography - Mass Spectrometry (GC-MS) analysis 46
4.1.5 Pyrolysis-Gas chromatography - Mass Spectrometry (GC-MS) analysis 49
4.1.6 Gas chromatography - isotope ratio mass spectrometry (GC-irMS) analysis 52
4.2 Geology and inorganic geochemistry laboratory analysis 53
4.2.1 Objectives 53
4.2.2 Methodology: Inorganic geochemistry 54
4.2.3 Activities undertaken 56
4.2.4 Mineralogical and textural characterisation of sample rocks 56
4.2.5 Discussion 92
4.3 Microbiome laboratory analysis 114
4.3.1 Objectives 114
4.3.2 Methodology 114
4.3.3 Work to date 115
4.3.4 cDNA Bacterial and Fungal community profiles 116
4.3.5 Rock Cube Sampling 117
4.3.6 Group D sampling and analysis 118
4.3.7 Fungi isolates from Murujuga sample rocks 119
4.4 Chamber exposure (accelerated degradation) testing 122
4.4.1 Objectives 122
4.4.2 Physico-chemical weathering 122
4.4.3 Microbiome 124

5 Air quality monitoring network operation 127
5.1 Objectives 127
5.2 Methodology 127
5.3 Solar/passive sites 127
5.3.1 AQM rock cube samplers 129
5.3.2 Solar/passive AQM network changes in the third year of studies . . . 129
5.4 Powered air quality monitoring sites 130
5.4.1 Powered AQM site changes in the third year of studies 131
5.5 Environmental challenges for AQM equipment operations 132
5.6 Monitoring equipment calibration 133
5.7 Lidar campaign 133
5.8 AQM network data analysis 134

6 Spatial mapping and surface modelling 137
6.1 Objectives 137
6.2 Spatial mapping 137
6.3 Computational fluid dynamics (**CFD**) modelling 137
6.3.1 Objectives 137
6.3.2 Methodology 137

7 Statistical analysis of data from each component study 139
7.1 Chamber studies 140
7.1.1 Introduction 140

7.1.2 Experiments presented in the Monitoring Studies Report 2024 141
7.1.3 Domestic gas exposure 143
7.1.4 NH_3 exposure 143
7.1.5 Vegetation combustion exposure 147
7.1.6 SO_2 gas exposure 150
7.1.7 NO_2 gas exposure 153
7.1.8 NO_2 gas exposure with freshly cut granophyre rocks 156
7.1.9 SO_2 gas exposure with freshly cut granophyre rocks 157
7.1.10 Henry's law 157
7.1.11 Summary of key findings to guide future experiments 159
7.2 Field colour measurements 161
7.2.1 Summary of JAZ and HDX instruments for campaigns 7 to 10 161
7.2.2 Statistical methodology for analysing percent reflectance 163
7.2.3 Results of analyses 165
7.2.4 Conclusion of field colour measurements 171
7.3 Industry air quality monitoring data 173
7.4 Inorganic geochemistry – *pH*, *Eh*, Cl^- 177
7.4.1 Background 177
7.4.2 *pH* observations 178
7.4.3 Chloride ion (Cl^-) observations 183
7.4.4 Oxidation-reduction potential (*ORP*) observations 186
7.4.5 Multivariate association between *pH*, *ORP* and Cl^- 189
7.4.6 AQM rock cube observations 191
7.5 Inorganic geochemistry – pXRF 197
7.5.1 Background 197
7.5.2 Multivariate analysis 197
7.5.3 Ratios of pairs of elements 201
7.5.4 pXRF measurements on rock cube samples 204
7.6 Inorganic geochemistry – porosity 207
7.6.1 Locations of sample rocks 207
7.6.2 Porosity analysis 209
7.6.3 Spatial analysis 211
7.6.4 Statistical significance — correction to Monitoring Studies Report 2024 215
7.6.5 Statistical significance — updated analysis with this year's data included 217
7.6.6 Conclusion of porosity 221
7.7 Inorganic geochemistry – permeameter 223
7.7.1 Background 223
7.7.2 Permeability observations on rock surface 223
7.7.3 Permeability observations on rock cubes 227
7.8 Microbiome 229
7.9 Organic geochemistry 231
7.9.1 Background 231
7.9.2 Exploratory data analysis 232
7.10 Deposition sampler data 245
7.10.1 Background 245

7.10.2 Exploratory analysis of 3-buckets . . . 245
7.10.3 Exploratory analysis of *pH* dry deposition sampler data . . . 246
7.10.4 Exploratory analysis of chemical species concentrations from the dry deposition sampler data . . . 250
7.10.5 Analysis of co-located AQM sites . . . 257
7.10.6 Spatial smoothing of deposition sampler data . . . 261
7.10.7 Rainfall *pH* . . . 273
7.11 Total (flask) deposition sample . . . 277
7.11.1 Background . . . 277
7.11.2 Exploratory analysis of *pH* total (flask) deposition sampler data . . . 277
7.11.3 Exploratory analysis of chemical species concentrations from the total (flask) deposition sampler data . . . 279
7.11.4 Analysis of co-located AQM sites . . . 286
7.11.5 Spatial smoothing of total (flask) deposition sampler data . . . 290
7.12 Passive samplers . . . 303
7.12.1 Introduction . . . 303
7.12.2 Exploratory data analysis of passive sampler values . . . 304
7.12.3 Correlations between gases . . . 320
7.12.4 Residual variability . . . 321
7.12.5 Short scale variability . . . 327
7.12.6 Spatial patterns of gas concentration . . . 336
7.13 Real-time powered sites . . . 349
7.13.1 Gaseous species . . . 349
7.13.2 Particulates . . . 367
7.13.3 Other instruments . . . 373
7.14 Low powered sensors . . . 395
7.14.1 NO . . . 395
7.14.2 NO_2 . . . 398
7.14.3 NH_3 . . . 401
7.14.4 CO_2 . . . 401
7.14.5 Particulates . . . 404
7.14.6 Summary measures of gas species . . . 410
7.14.7 Summary measures of particulates . . . 411
7.15 Weather: AQM and BoM stations . . . 413
7.16 Key findings from statistical analysis . . . 419
7.16.1 Chamber studies . . . 419
7.16.2 Field measurement of colour . . . 419
7.16.3 Industry data . . . 420
7.16.4 Inorganic geochemistry — *pH*, *Eh*, Cl^- . . . 420
7.16.5 Inorganic chemistry — pXRF . . . 420
7.16.6 Inorganic geochemistry — porosity . . . 421
7.16.7 Inorganic geochemistry – permeameter . . . 421
7.16.8 Microbiome . . . 421
7.16.9 Deposition sampler data . . . 422
7.16.10 Total (flask) deposition sample . . . 422

7.16.11 Organic geochemistry . . . 422
7.16.12 Passive samplers . . . 423
7.16.13 Real-time powered sites . . . 424
7.16.14 Low powered sensors . . . 424
7.16.15 Weather: AQM and BoM stations . . . 425

8 Associations between variables 427
8.1 Deposition versus passive samplers . . . 427
8.1.1 Background . . . 427
8.2 Bucket deposition versus total flask deposition . . . 433
8.3 Validation against satellite observations . . . 435
8.4 Low-power versus real-time powered instruments . . . 437
8.4.1 Background . . . 437
8.4.2 Gaseous species . . . 437
8.4.3 Particulates . . . 440
8.4.4 Comparison of temperature versus gaseous species. . . . 441
8.4.5 Comparison of humidity versus gaseous species . . . 442
8.5 Exploration of relationships between datasets . . . 444
8.6 Key findings from statistical comparative analysis . . . 447
8.6.1 Deposition samplers vs passive samplers . . . 447
8.6.2 Bucket deposition versus total flask deposition . . . 447
8.6.3 Validation against satellite observations . . . 447
8.6.4 Low power versus real time powered instruments . . . 447
8.6.5 Exploration of relationships between datasets . . . 448

9 General summary 449
9.1 Summary . . . 449
9.2 Conclusion . . . 452

REFERENCES 455

APPENDICES 464

***A* Organic geochemistry – additional tables and figures 464**

B Photogrammetry 471

***C* Amended estimation of major historic emissions (Dampier power station) to account for historic Iron Pellet Plant 537**

***D* Statistical analysis: additional results 543**
D.1 Introduction . . . 543
D.2 Field colour . . . 543
D.2.1 Faulty field colour data . . . 543
D.2.2 Comparison of trends between campaigns 1 to 10 for JAZ instrument 543
D.3 Industry gas measurements: further results and diagnostics . . . 547
D.4 Organic geochemistry . . . 549

D.5 IVL Passive sampler: further results and diagnostics 551
D.5.1 Exploratory analysis 551
D.5.2 Temporal analysis 554
D.5.3 Correlations between gases 561
D.5.4 Residual variability 563
D.5.5 Short scale comparison further analysis 568
D.5.6 Spatial Analysis 588
D.6 Low powered sensors 599
D.6.1 NH_3 long term and week plots 599
D.6.2 Further low powered gas and particulate matter summaries 602

List of Figures

Figure *1.1-1*: (a) Murujuga Region showing approximate locations of major industrial activity. (b) Map of field (rock art) monitoring sites and co-located rock art and air quality monitoring sites (labelled). (c) Locations of sample rocks collected in Years One (Group A) and Three (Group B), respectively. "NA" indicates locations of samples that did not provide usable data. Group A sample locations are within the corresponding AQ/EX/AS study squares. 2

Figure *3.2-1*: Comparison of repeated measurements using the WP90 and new Ranger equipment for: (a) *pH*; (b) ORP; (c) Electrical conductivity (EC). Measurements made during weeks 3 and 4 of campaign 10. Each pair of measurements sampled the same solution and the measurements took place within five minutes of each other. 34

Figure *3.2-2*: Permeameter in operation in the field. January 2025. 37

Figure *3.2-3*: Aerial photograph showing collection locations of Group D samples. The purple line shows the area accessed and assessed for sample collection. Samples were collected from within the red square. Image from Google Maps. 42

Figure *3.2-4*: Photo of the five rock cubes. Microbiome, *pH*, and pXRF data were collected from the rock cubes prior to campaign 9. 42

Figure *4.1-1*: a) GC-MS total ion chromatogram (TIC) of the derivatised polar fraction from rock surface sample AQ05_DOL B, representative of samples analysed. The pie chart illustrates the relative proportion of compound groups detected, b) is the highlighted section from a) expanded by a factor of five. Observed ions ranged from m/z 50 to m/z 550. 48

Figure *4.1-2*: Flash Pyrolysis GC-MS total ion chromatogram (TIC) of rock surface sample AQ05_DOL B, representative of samples analysed. Pie chart illustrates the relative proportion of 12 product groups. Main peaks in chromatogram are labelled for products, including some single compounds. Observed ions ranged from m/z 50 to m/z 550. 51

Figure *4.2-1*: Schematic illustration of adapted workflow applied to the Group B, C, and D samples. 55

Figure *4.2-2*: BSE-SEM images showing the variable nature of the transition from the fresher rock to the weathered rind in granophyre sample D001_GPH. Voids are shown in black, as is the region above the upper surface of the rock. (a) Area showing large sub-surface voids. The upper red box delineates the area shown at higher magnification in the lower red box; (b) Voids ranging from a few micrometres to 100 micrometres in size; (c) Image showing large quartz grains (dark grey mineral) surrounded by voids; (c) Unpatinated part of the surface showing a fracture, over 1 mm long, that penetrates the weathered rind. 58

Figure *4.2-3*: A comparison of photomicrographs of Group A thin-section of sample AQ03_GPH (upper) and the Group C billet of the same sample (lower image). Upper image shows darker central area that is less well polished than the upper left and lower right areas. Lower image shows a more homogeneous polish. Both images RFL PPL. Abbreviations: RFL: reflected light; PPL: Plane polarised light. 59
Figure *4.2-4*: Examples of radial textures. (a) D001_GPH TL PPL; (b) D001_GPH TL XPL; (c) EN01_GPH TL PPL; (d) EN01_GPH TL XPL. The pale green mineral is chlorite, which is widespread in the matrix and forms coronae around intergrown felsic minerals. Abbreviations: TL: Transmitted light; PPL: Plane polarised light; XPL: cross-polarised light. 61
Figure *4.2-5*: Examples of acicular textures. (a) EL01_GPH Granophyre TL PPL; (b) EL01_GPH Granophyre TL XPL; (c) EN01_GPH TL PPL; (d) EN01_GPH TL XPL. Pale green chlorite is widespread throughout the matrix. Abbreviations: TL: Transmitted light; PPL: Plane polarised light; XPL: cross-polarised light. 62
Figure *4.2-6*: Green chlorite surrounds quartz (clear) and plagioclase (altered to brown aggregates). Sample BU01_GPH. TL. PPL. Abbreviations: TL: Transmitted light; PPL: Plane polarised light. 63
Figure *4.2-7*: Sericite alteration of plagioclase and K-feldspar. Fresher rock. Sample GI03_GPH. TL. XPL. Abbreviations: TL: Transmitted light; XPL: cross-polarised light. 64
Figure *4.2-8*: (a) BU02_GPH showing quartz vein (TL, PPL). (b) Same as (a) TL, XPL. (c) Fracture filled with quartz in sample GI01_GPH (TL, PPL) (d) Same as (c) TL XPL. Abbreviations: TL: Transmitted light; PPL: Plane polarised light; XPL: cross-polarised light. 66
Figure *4.2-9*: Photomicrographs of railway cutting samples showing fractures and veins. (a, b) RT02_GPH. Fractures filled with iron oxides (dark and orange lines) or quartz (colourless fracture in (b)); (c) RT04_GPH showing opaque minerals withn the sinuous fracture; (d) MB02_GPH showing a fracture that does not contain minerals. All transmitted plane polarised light. . . 67
Figure *4.2-10*: Plane polarized (a, c) and crossed polarised (b, d) photomicrographs of dolerite WL01_DOl in transmitted light. (a, b) Patina and weathered rind; the patina is the very thin layer indicated by the arrow in (a). (c, d) Fresher rock of sample RI01_DOL (c, d). The large crystal in (c) and (d) is clinopyroxene. 70
Figure *4.2-11*: BSE-SEM image of the transition from fresher rock to patina to weathered rind for (a) EN01_DOL Zoning in clinopyroxene and marginal Fe-Ti oxides shown by yellow arrows. (b) EI01_DOL. Loss of clinopyroxene has formed porosity within the weathered rind. The brighter particles are Fe-Ti oxides. 71
Figure *4.2-12*: BSE-SEM images of the transition from fresher rock to the weathered rind and patina. (a) WL01_DOL; (b) EI01_DOL. Loss of clinopyroxene has formed porosity within the weathered rind. The bright rim indicated by a yellow arrow shows the location of Fe-oxide minerals. 72

Figure *4.2-13*: Plane polarized (a, c) and crossed polarized (b, d) photomicrographs of granite sample D003_GRT in transmitted light. (a, b) show the fresher rock. The large quartz grain shows extensive inclusion trails. Albite and microcline are not individually recognisable on this relatively low magnification image. (c and d) show the weathered rind and patina. Feldspar grains within the weathered rind show extensive sericite alteration and clay formation and it is unclear whether they originally formed as K-feldspar or plagioclase. 73

Figure *4.2-14*: Plane polarized (a, c) and crossed polarised (b, d) photomicrographs of gabbro sample D002_GBR in transmitted light. Clinopyroxene grains show second-order birefringence. Clinopyroxene and plagioclase are replaced by chlorite and epidote. 74

Figure *4.2-15*: SEM-BSE images of granite sample D003_GRT. K-feldspar shows the highest BSE signal (palest grey). Quartz and albite show a similar BSE signal (darker grey than K-feldspar) but albite is typically more porous, altered, shows a slightly higher BSE signal, and is typically less well polished than quartz. (a) intergrown quartz and albite (darker grey) and K-feldspar (lighter grey). (b) weathered rind characterized by formation of voids within albite (darker grey) and K-feldspar (lighter grey). (c, d) voids formed within albite (darker grey) and K-feldspar (lighter grey) create extensive microporosity. 80

Figure *4.2-16*: BSE-SEM image of gabbro sample D002_GBR. (a) Panorama image showing fresher rock, weathered rind, and patina. (b) Area shown by the red box in (a) showing extensive void space within the weathered rind. (c) Skeletal structures after clinopyroxene within the weathered rind. The clinopyroxene and plagioclase exhibit exsolution lamellae. (d) Variable development of voids, ranging from micrometre-sized pits along planes of exsolution to complete grain loss. 82

Figure *4.2-17*: Plane polarised transmitted light photmicrographs comparing granophyre samples that show: (a) well-developed patina and weathered rind (Group B sample EI03_GPH) and (b) no weathered rind and thin discontinuous orange patina (Group D railway cutting sample RT03_GPH). 84

Figure *4.2-18*: Preliminary unprocessed micro-CT data from Group B granophyre BU02_GPH, showing (a) two-dimensional representation of reconstructed volume; (b) x-z slice; (c) x-y slice; (d) y-z slice. 86

Figure *4.2-19*: Preliminary unprocessed micro-CT data from Group B granophyre EL02_GPH, showing (a) two-dimensional representation of reconstructed volume; (b) x-z slice; (c) x-y slice; (d) y-z slice. In panels (b) to (d), individual grains are revealed by changes in the grey scale of the image. 87

Figure *4.2-20*: Preliminary unprocessed micro-CT data from Group B gabbro D002_GBR, showing (a) two dimensional representation of reconstructed volume; (b) x-z slice; (c) x-y slice; (d) y-z slice. Data were cropped to remove the holder. In panels (b) to (d), individual grains are revealed by changes in the grey scale of the image. 88

Figure *4.2-21*: Preliminary unprocessed micro-CT data from Group B granite D003_GRT, showing (a) two-dimensional representation of reconstructed volume; (b) x-z slice; (c) x-y slice; (d) y-z slice. Image cropped to remove holder. In panels (b) to (d), individual grains are revealed by changes in the grey scale of the image. 89

Figure *4.2-22*: Preliminary unprocessed micro-CT data from Group B granite EI01_DOL, showing (a) two dimensional representation of reconstructed volume; (b) x-z slice; (c) x-y slice; (d) y-z slice. Image cropped to remove holder. In panels (b) to (d), individual grains are not visible, possibly because the sample consisted of a single grain. 90

Figure *4.2-23*: Chalky orange patina forming on fractures in granophyre in the field near Cowrie Cove. 93

Figure *4.2-24*: Comparison of TIMA maps for the Group A thin section of sample AQ03_GPH and the Group C polished billet of sample AQ03_GPH. Group A analysis performed with pulse-TOR detector and mineral characterisation library optimised for this detector. Group C analysis performed with EDAX detector and mineral characterisation library optimised for this detector. The striking change in colour, from blue at the top to purple at the bottom, reflects a difference in the calculated modes of quartz and alkali feldspar. 95

Figure *4.2-25*: Variations in mode of individual major minerals between the four rock sample groups estimated by TIMA for the fresher rock of granophyre samples from Groups A, B, C, and D. 96

Figure *4.2-26*: Variations in mode of individual major minerals between the four rock sample groups estimated by TIMA for the weathered rind and patina of granophyre samples from Groups A, B, C, and D. 97

Figure *4.2-27*: Variations in mode of individual minor minerals between the four rock sample groups estimated by TIMA for the fresher rock of granophyre samples from Groups A, B, C, and D. 98

Figure *4.2-28*: Variations in mode of individual minor minerals between the four rock sample groups estimated by TIMA for the weathered rind and patina of granophyre samples from Groups A, B, C, and D. 99

Figure *4.2-29*: Comparison of the average mineral modes, measured by TIMA, for all of the Group A and C samples. FR: fresher rock. WR: weathered rind. Differences may relate to changes in analytical techniques or preparation artefacts. Scales were selected to show the mineral modes of the specific rock as clearly as possible. If the dots are close or superimposed than the two different sample preparation methods provide near-identical results. If they are far apart then some kind of analytical or preparation-related artefact is inferred. 100

Figure *4.2-30*: Comparison of optical photomicrograph (transmitted plane polarised light) (left) with SEM-BSE image (right) of sample BM03 (Group D). The two views are of the same area of the same thin section without repolishing or other treatment between the time of acquisition of the two images. The circled area on the left of each image is green in the plane polarised light image (left panel) and consists of chlorite. However, in the SEM-BSE image (right panel), this area appears black and would be identified, incorrectly, as porosity by the porosity measurement algorithm. The circled area on the right hand side of each image is colourless in plane polarised light and black in cross polarised light (not shown). This area does not contain a mineral. It appears black in the SEM-BSE image (right hand panel) and would be identified correctly as porosity. 101

Figure *4.2-31*: Comparison of the average mineral modes, measured by TIMA, for Group A thin section and Group C billet of samples AQ03_GPH, AQ10_GPH, and RS03_GPH. These samples show polishing artefacts. FR: fresher rock. WR: weathered rind. Differences may relate to changes in analytical techniques or preparation artefacts. Scales were selected to show the mineral modes of the specific rock as clearly as possible. If the dots are close or superimposed than the two different sample preparation methods provide near-identical results. If they are far apart then some kind of analytical or preparation-related artefact is inferred. 103

Figure *4.2-32*: Comparison of mineral modes measured by TIMA for sample AQ06_GPH from Group A and Group C, which does not show polishing artefacts. FR: Fresher rock; WR+P Weathered rind plus patina. Differences may relate to changes in analytical techniques or preparation artefacts. Scales were selected to show the mineral modes of the specific rock as clearly as possible. If the dots are close or superimposed than the two different sample preparation methods provide near-identical results. If they are far apart then some kind of analytical or preparation-related artefact is inferred. 104

Figure *4.2-33*: Comparison of mineral modes measured by TIMA for sample EX07_GPH from Group A and Group C, which does not show polishing artefacts. FR: Fresher rock; WR+P Weathered rind plus patina. Differences may relate to changes in analytical techniques or preparation artefacts. Scales were selected to show the mineral modes of the specific rock as clearly as possible. If the dots are close or superimposed than the two different sample preparation methods provide near-identical results. If they are far apart then some kind of analytical or preparation-related artefact is inferred. 105

Figure *4.2-34*: Comparison of mineral modes measured by TIMA for sample AQ03_GPH from Group A, which shows polishing artefacts, and Group C, which does not show polishing artefacts. FR: Fresher rock; WR+P Weathered rind plus patina. Scales were selected to show the mineral modes of the specific rock as clearly as possible. If the dots are close or superimposed than the two different sample preparation methods provide near-identical results. If they are far apart then some kind of analytical or preparation-related artefact is inferred. 106
Figure *4.2-35*: Comparison of mineral modes measured by TIMA for sample AQ10_GPH from Group A, which shows polishing artefacts, and Group C, which does not show polishing artefacts. FR: Fresher rock; WR+P Weathered rind plus patina. Scales were selected to show the mineral modes of the specific rock as clearly as possible. If the dots are close or superimposed than the two different sample preparation methods provide near-identical results. If they are far apart then some kind of analytical or preparation-related artefact is inferred. 107
Figure *4.2-36*: Locations of Group A samples that clearly show polishing artefacts are indicated by red squares. These samples are located proximal and distal to industrial emission sources. 108
Figure *4.2-37*: Porosity values for the Group A granophyre samples from Monitoring Studies Report 2024 (Curtin University, 2024c). The names of samples that clearly show polishing artefacts are shown in bold and a dashed line highlights the porosity values for these samples. The different symbols are used to provide a visual separation between the different values. There is no systematic relationship between the presence or absence of a polishing artefact and the absolute average porosity value. 109
Figure *4.2-38*: (a) Flaking on non-rock art panels on the Dampier Salt Lease. (b) Flaking on rock art panel on the Dampier Salt Lease. Site of photographs is 650 m from the ocean and 1.8 km from the nearest salt pond. The darker-appearing patches inside the flakes are not obviously biological and the darker appearance relates to a change in relief within the flaked patch. Flaking is also seen commonly elsewhere on Murujuga. Images taken 4^{th} July 2024. 113
Figure *4.3-1*: Bacterial and Fungal microbial profile of both cDNA and DNA sequencing data, averaged on Genus level and season. A) Bacterial 16S rRNA gene data. B) Fungal ITS data. 117
Figure *4.3-2*: Relative abundance of the bacterial communities of the Group D rock surface samples (orange) and the original sample rock samples (blue) at Phylum, Family and Genus levels. Any respective level that had an abundance of less than 2% were grouped into the “Other” category. . . 120
Figure *4.3-3*: Relative abundance of the fungal communities of the Group D rock surface samples (orange) and the original sample rock samples (blue) at Phylum, Family and Genus levels. Any respective level that had an abundance of less than 2% were grouped into the “Other” category. . . 121
Figure *4.4-1*: Diagram of the microbiology exposure chamber. 125

Figure *5.3-1*: Passive AQM AQ14, showing the range of instruments deployed in each passive/solar AQM. Visible are the anemometer (top left of mast crossbar), rain water collector (front left of cage), rain gauge (visible behind the collector), control box (white box to the rear left) and bucket (deposition) sampler (on central concrete block). 128

Figure *5.3-2*: 3-bucket deposition sampler in dry position, with AS/NZS 3580.10.1 total deposition flask in lower right of image. (Note image is tilted slightly, samplers are mounted flat) 129

Figure *5.4-1*: Powered AQM EX09, as installed on Mount Wongama. Visible on the are the mast (1), with anemometer on the crossbar (2). Visible on the roof are the Max-DOAS (3), the Radon detector inlet (4), the main sample inlet (5) and the FIDAS inlet (6). At the front of the station, above the door, the rock samplers can be seen (7). 131

Figure *5.7-1*: Photo of the MiniMPL lidar on right and Windcube 200S on left, facing in the general measurement direction $\pm 90°$. 134

Figure *5.7-2*: Photo of the MiniMPL lidar operating at night. Photo Credit: Heather Osborne 135

Figure *5.7-3*: Photo of the University of Newcastle lidar. 136

Figure *7.1-1*: Copy of Figure 7.1-6 from Monitoring Studies Report 2024 (Curtin University, 2024c). Boxplots of cumulative response (concentration after exposure minus concentration before exposure) against average dose NO_x plus SO_2, (a) broken down by rock type, and (b) for all rock types combined. The blue curve is the smoothed conditional mean; grey shading is the pointwise 95% confidence interval. The cumulative response represents the sum of concentrations of Ca, K, Mg, and Na measured in mg/L . . 142

Figure *7.1-2*: (a) Boxplots of the change in Ca + Mg + Na + K concentrations after exposure to a domestic gas/diesel mix, broken down by rock type; and (b) histogram showing the frequency distribution of these changes. The average dose of NO_x and SO_2 are 161.509 $\mu g/m^3$ and 16.783 $\mu g/m^3$, respectively. 143

Figure *7.1-3*: Boxplots of cumulative response (concentration after exposure minus concentration before exposure) against the average dose concentration of NH_3. Blue curve: smoothed mean response. Grey shading: pointwise 95% confidence intervals. 144

Figure *7.1-4*: Boxplots of cumulative response (concentration after exposure minus concentration before exposure) against the exposure days for NH_3 exposures. Blue curve: smoothed mean response. Grey shading: pointwise 95% confidence intervals. 145

Figure *7.1-5*: Boxplots of cumulative response (concentration after exposure minus concentration before exposure) against the batch number for NH_3 exposures. Blue curve: smoothed mean response. Grey shading: pointwise 95% confidence intervals. 146

Figure *7.1-6*: Boxplots of cumulative response (concentration after exposure minus concentration before exposure) against the average dose of NO_x from vegetation combustion. Blue curve: smoothed mean response. Grey shading: pointwise 95% confidence intervals. 147

Figure *7.1-7*: Boxplots of cumulative response (concentration after exposure minus concentration before exposure) against the exposure days (for NO_x) vegetation combustion exposures. Blue curve: smoothed mean response. Grey shading: pointwise 95% confidence intervals. 148

Figure *7.1-8*: Boxplots of cumulative response (concentration after exposure minus concentration before exposure) against the batch number for NO_x from vegetation combustion exposures. Blue curve: smoothed mean response. Grey shading: pointwise 95% confidence intervals. 149

Figure *7.1-9*: Boxplots of cumulative response (concentration after exposure minus concentration before exposure) against the average dose of SO_2 (as a single source gas). Blue curve: smoothed mean response. Grey shading: pointwise 95% confidence intervals. 150

Figure *7.1-10*: Boxplots of cumulative response (concentration after exposure minus concentration before exposure) against the exposure days for dose SO_2 (as a single-source gas). Blue curve: smoothed mean response. Grey shading: pointwise 95% confidence intervals. 151

Figure *7.1-11*: Boxplots of cumulative response (concentration after exposure minus concentration before exposure) against the batch number for SO_2 exposures (as a single-source gas. Blue curve: smoothed mean response. Grey shading: pointwise 95% confidence intervals. 152

Figure *7.1-12*: Boxplots of cumulative response (concentration after exposure minus concentration before exposure) against the average dose of NO_2 (from a single-source gas). Blue curve: smoothed mean response. Grey shading: pointwise 95% confidence intervals. 153

Figure *7.1-13*: Boxplots of cumulative response (concentration after exposure minus concentration before exposure) against the exposure days for NO_2 (from a single-source gas). Blue curve: smoothed mean response. Grey shading: pointwise 95% confidence intervals. 154

Figure *7.1-14*: Boxplots of cumulative response (concentration after exposure minus concentration before exposure) against the batch number for NO_2 exposures (from a single-source gas). Blue curve: smoothed mean response. Grey shading: pointwise 95% confidence intervals. 155

Figure *7.1-15*: Boxplots of cumulative response (concentration after exposure minus concentration before exposure) against the average dose of NO_2 (from a single-source gas), with freshly cut granophyre rocks. Blue curve: smoothed mean response. Grey shading: pointwise 95% confidence intervals. 156

Figure *7.1-16*: Boxplots of cumulative response (concentration after exposure minus concentration before exposure) against the average dose of SO_2 (from a single-source gas), with freshly cut granophyre rocks. Blue curve: smoothed mean response. Grey shading: pointwise 95% confidence intervals. 157
Figure *7.1-17*: Henry's Law constants for relevant gas species. 158
Figure *7.2-1*: Estimated percent reflectance vs wavelength (nm) for (a) AQ03_GPH, (b) AQ04_GPH, (c) AQ11_GPH and (d) EX06_GPH for campaigns 1 to 10.166
Figure *7.2-2*: Mean difference curves. For each wavelength, the mean % reflectance across all reps was computed for each site × campaign × target × instrument combination. The mean difference is then the JAZ mean subtracted from the HDX mean, so negative values indicate wavelengths where the HDX recorded higher % reflectance, and positive values indicate wavelengths where the JAZ recorded higher % reflectance. Panels: (a) AQ03_GPH, (b) AQ04_GPH, (c) AQ11_GPH and (d) EX06_GPH. Within each site, each mean difference curve corresponds to one target for each campaign. 167
Figure *7.3-1*: Boxplots of gas concentration measurements from IVL and Radiello samplers at all Woodside stations from September 2021 to November 2022. Each panel presents boxplots for one gas species: (a) NO_2, (b) NH_3, (c) SO_2, and (d) HNO_3. The vertical axes in panels (c) and (d) use logarithmic scales due to the wide range of concentrations. 174
Figure *7.3-2*: Scatterplots of gas concentration measurements by Radiello samplers versus IVL samplers at Woodside monitoring stations for corresponding sampling periods between September 2021 and November 2022. Each panel represents one gas species: (a) NO_2, (b) NH_3, (c) SO_2, and (d) HNO_3. 175
Figure *7.4-1*: Boxplots of *pH* by campaign. The green dashed line represents the neutral pH value. 178
Figure *7.4-2*: Boxplots of *pH* by rock type for each campaign. The green dashed line represents the neutral *pH* value. 179
Figure *7.4-3*: Boxplots of observed *pH* minus campaign median *pH*, by rock type for each campaign. 180
Figure *7.4-4*: Spatially smoothed *pH* values of campaigns 1 to 10 (C1-C10). 181
Figure *7.4-5*: Spatially smoothed observed *pH* minus campaign median *pH* of campaigns 1 to 10 (C1-C10). 182
Figure *7.4-6*: Boxplots of Cl^- concentration by campaign. Note logarithmic scale. ISA (Ionic Strength Adjuster). 184
Figure *7.4-7*: Boxplots of Cl^- concentration by rock type for different campaigns. Note logarithmic scale. ISA (Ionic Strength Adjuster). 184
Figure *7.4-8*: Spatially smoothed chloride ion (Cl^-) concentration of campaigns 2 to 10 (C2-C10). 185
Figure *7.4-9*: Boxplots of *ORP* by campaign. 186
Figure *7.4-10*: Boxplots of *ORP* by rock type for different campaigns. 187
Figure *7.4-11*: Spatially smoothed *ORP* from data from campaigns 2 to 10 (C2-C10). . 188

Figure *7.4-12*: Campaign 8 pairwise scatterplots between *pH*, *ORP* and logarithm of chloride concentration. The panels above the diagonal show the correlation between two variables; panels on the diagonal show the histogram of each variable; panels below the diagonal show a scatterplot between two variables. 189
Figure *7.4-13*: Campaign 9 pairwise scatterplots between *pH*, *ORP* and logarithm of chloride concentration. The panels above the diagonal show the correlation between two variables; panels on the diagonal show the histogram of each variable; panels below the diagonal show a scatterplot between two variables. 190
Figure *7.4-14*: Campaign 10 pairwise scatterplots between *pH*, *ORP* and logarithm of chloride concentration. The panels above the diagonal show the correlation between two variables; panels on the diagonal show the histogram of each variable; panels below the diagonal show a scatterplot between two variables. 191
Figure *7.4-15*: Rock cube *pH* for all AQM sites for each rock type. 192
Figure *7.4-16*: Rock cube *pH* for all rock types for each AQM site. 193
Figure *7.4-17*: Rock cube *pH* for each rock type by each AQM site. 195
Figure *7.5-1*: RDA biplot showing the relationship between chemical elements from the pXRF and rock types in campaign 8. Percentage in parentheses is the percentage of total variation explained by the RDA. 199
Figure *7.5-2*: RDA biplot showing the relationship between pXRF chemical elements, rock types, and the field campaigns 1 to 8. 200
Figure *7.5-3*: Boxplots of SiO_2:Ti by campaign, coloured by rock type. Note logarithmic scale. 202
Figure *7.5-4*: Boxplots of SiO_2:Ti ratio by campaign after winsorization, coloured by rock type. Note logarithmic scale. 202
Figure *7.5-5*: Spatial smoothing of SiO_2:Ti ratio in granophyre (GPH) of campaigns 1 (a) to 9 (i), respectively. The white colour polygons are the islands with no granophyre samples. 203
Figure *7.5-6*: Boxplots of SiO_2:Ti measured on rock cube samples coloured by rock type. Note logarithmic scale. 204
Figure *7.5-7*: Boxplots of SiO_2:Ti measured on rock cube samples after winsorization, coloured by rock type. Note logarithmic scale. 205
Figure *7.5-8*: RDA biplot showing the relationship between chemical elements from the pXRF and rock types in rock cube samples. Percentage in parentheses is the percentage of total variation explained by the RDA. 206
Figure *7.6-1*: Locations of sample rocks collected in Years One (Group A) and Three (Group B), respectively. “NA” indicates locations of samples that did not provide usable data. Black circles indicate location of Dampier and Karratha town centres. 208
Figure *7.6-2*: Values of average porosity index for each Group B rock sample collected (excluding Eaglehawk Island). Perspective view with dot height equal to porosity index value. The scale is identical to that in the next Figure *7.6-3*. 209

Figure *7.6-3*: Values of average porosity index for the full Group A and B rock-sample collection (excluding Eaglehawk Island). Perspective view with dot height equal to porosity index value. The scale is identical to that in the previous Figure *7.6-2*. 210
Figure *7.6-4*: Sitewise mean of average porosity index for the combined Group A and B rock sample collection. Perspective view with dot height proportional to the mean of the porosity-index values at each location. Note the scale is different from that in Figures *7.6-2* and *7.6-3*. 212
Figure *7.6-5*: Spatially smoothed (Nadaraya-Watson) average porosity index based on data from the combined Group A and B rock samples. A Gaussian kernel with bandwidth 1.5 km was used. Pink circles indicate the locations of Dampier and Karratha town centres. 213
Figure *7.6-6*: Spatially weighted median of average porosity index based on data from the combined Group A and B rock samples. Gaussian kernel with bandwidth 2.5 km. 214
Figure *7.6-7*: Copy of Figure 7.6-9 of the Monitoring Studies Report 2024 (Curtin University, 2024c). Monte Carlo test of the null hypothesis of constant mean porosity against the alternative of locally elevated porosity, based on the data from Group A sample rocks only. (a) p-value of the pointwise Monte Carlo test; (b) orange colour identifies the region where the pointwise test is statistically significant at level α=0.005 (erroneously stated as α=0.05 in the Monitoring Studies Report 2024). 216
Figure *7.6-8*: Corrected version of Figure 7.6-9 of the Monitoring Studies Report 2024 (Curtin University, 2024c). Monte Carlo test of the null hypothesis of constant mean porosity against the alternative of locally elevated porosity, based on the data from Group A sample rocks only. (a) p-value of the pointwise Monte Carlo test; (b) orange colour identifies the region where the pointwise test is statistically significant at level α=0.05. Blue cross-hair symbol indicates the location of Karratha town centre. 216
Figure *7.6-9*: p-value of the pointwise Monte Carlo test of the null hypothesis of constant mean porosity against the alternative of locally elevated porosity, based on the pooled data from Group A and B samples. Blue cross-hair symbols indicate town centres of Dampier and Karratha. 218
Figure *7.6-10*: Pointwise statistical significance outcome for elevated rock surface porosity including Year Three data: either significant (SIGNIF) or non-significant (NONSIG) at level 0.05. Industry from Figure *1.1-1* (a) overlaid for context. 219
Figure *7.6-11*: Pointwise statistical significance outcome for elevated rock surface porosity including Year Three data: either significant (SIGNIF) or non-significant (NONSIG) at level a) 0.005, b) 0.01, c) 0.05 and d) 0.1. 220
Figure *7.7-1*: Permeability measurements for all sites and the dolerite standard for each rock type. Note logarithmic scale. 223
Figure *7.7-2*: Permeability measurements for all sites and the dolerite standard after winsorization. Note logarithmic scale. 224
Figure *7.7-3*: Spatial plots of winsorized permeability for campaigns 7 (a) to 10 (d), respectively. 225

Figure *7.7-4*: Spatial smoothing of winsorised permeability in granophyre (GPH) for campaigns 7 (a) to 10 (d), respectively. The grey-colour polygons are the islands with no granophyre samples. 226
Figure *7.7-5*: Boxplots of the winsorised unpatinated rock cube permeability measurements for each rock type, over all AQM sites. 227
Figure *7.7-6*: Boxplots of the winsorised unpatinated rock cube permeability measurements for each AQM site, coloured by each rock type. 228
Figure *7.9-1*: Boxplots of organic chemical ratios for a) Alkylbenzenes (BAB) relative to n-C_{17} and n-C_{18}, Note logarithmic scale; b) Methylphenanthrene relative to phenanthrene (MP/P) ratio plus methylphenanthrene index (MPI-1); c) Gymnosperm biomarkers (Gymno) relative to n-C_{17} and n-C_{18}, Note logarithmic scale ; d) fluoranthene/ (fluoranthene + pyrene). 232
Figure *7.9-2*: Discrete point plot of Alkylbenzenes (BAB) relative to n-C_{17} and n-C_{18} against sampling sites. Note logarithmic scale. Points were jittered to avoid overlap. 233
Figure *7.9-3*: Discrete point plot of Methylphenanthrene relative to phenanthrene ratio (MP/P). 234
Figure *7.9-4*: Discrete point plot of methylphenanthrene index (MPI-1). 234
Figure *7.9-5*: Discrete point plot of Gymnosperm biomarkers relative to n-C_{17} and n-C_{18}. Note logarithmic scale. Points were jittered to avoid overlap. 235
Figure *7.9-6*: Discrete point plot of fluoranthene/(fluoranthene + pyrene) ratio. 236
Figure *7.9-7*: Spatial plot of Alkylbenzenes (BAB) relative to n-C_{17}. 237
Figure *7.9-8*: Spatial plot of Alkylbenzenes (BAB) relative to n-C_{18}. 238
Figure *7.9-9*: Spatial plot of Methylphenanthrene relative to phenanthrene (MP/P). . 239
Figure *7.9-10*: Spatial plot of methylphenanthrene index (MPI-1). 240
Figure *7.9-11*: Spatial plot of Gymnosperm biomarkers relative to n-C_{17}. 241
Figure *7.9-12*: Spatial plot of Gymnosperm biomarkers relative to n-C_{18}. 242
Figure *7.9-13*: Spatial plot of fluoranthene / (fluoranthene + pyrene). 243
Figure *7.10-1*: Boxplots of *pH* for dry, wet, and mist deposition samples (H_2O is deionised water), across all sites and all sampling periods (from May 2023 to March 2025). The green dashed line represents the neutral pH value. 246
Figure *7.10-2*: Boxplots of *pH* for the dry deposition samples by sampling periods, across all sites. The green dashed line represents the neutral pH value. 247
Figure *7.10-3*: Boxplots of *pH* for the dry deposition samples by sampling sites, over all sampling periods. The green dashed line represents the neutral pH value. 247
Figure *7.10-4*: Boxplots of *pH* for dry deposition samples from all AQMs, co-located AQ07 and AQ08, and AQMs with bare/weathering, and AQMs without bare/weathering (other AQMs). Data from May 2023 to March 2025. . . 249
Figure *7.10-5*: Boxplots of Ca^{2+}, K^{+}, and Mg^{2+} deposition rates across all sites for the dry deposition samples by sampling period. Note logarithmic scale. . . 251
Figure *7.10-6*: Boxplots of Ca^{2+}, K^{+}, and Mg^{2+} deposition rates across for the dry deposition samples by site, from May 2023 to March 2025. Note logarithmic scale. 251
Figure *7.10-7*: Boxplots of Na^{+},Cl^{-}, and $SO_4{}^{2-}$ deposition rates for the dry deposition samples across all sites by sampling period. Note logarithmic scale. . . 252

Figure *7.10-8*: Boxplots of Na^+, Cl^-, and SO_4^{2-} deposition rates by site, from May 2023 to March 2025. Note logarithmic scale. 253
Figure *7.10-9*: Boxplots of NH_4^+, NO_3^-, and P deposition rates for the dry deposition samples across all sites by sampling period. Note logarithmic scale. . . 253
Figure *7.10-10*: Boxplots of NH_4^+, NO_3^-, and P deposition rates for the dry deposition samples by site, from May 2023 to March 2025. Note logarithmic scale. 254
Figure *7.10-11*: Average *pH* and deposition rates by AQM. Data represent approximately 24 months of observation (8/02/2023 to 12/03/2025) except for EX02, EX09, and AQ01 (indicated by grey dots), where less than 18 months of data are available. 255
Figure *7.10-12*: Median *pH* and deposition rates by AQM. Data represent approximately 24 months of observation (8/02/2023 to 12/03/2025) except for EX02, EX09, and AQ01 (indicated by grey dots), where less than 18 months of data are available. 256
Figure *7.10-13*: Boxplots of deposition rates of chemical species from dry deposition samples of co-located AQ07 and AQ08 sites, from May 2023 to March 2025. Note logarithmic scale. 257
Figure *7.10-14*: Scatterplots of the AQ07 vs AQ08 deposition rates for each chemical species from dry deposition samples. The black line ($y = x$) indicates the same deposition rate at both monitoring stations. 258
Figure *7.10-15*: Time series plots of deposition rates of chemical species, from dry deposition samples at co-located AQ07 (circles) and AQ08 (triangles) sites, against collection date. Note logarithmic scale. Points were jittered to avoid overlap. 260
Figure *7.10-16*: Spatially smoothed average *pH* for the dry deposition samples by sampling period. 263
Figure *7.10-17*: Spatially smoothed average Ca^{2+} deposition rate for the dry deposition samples by sampling period. 264
Figure *7.10-18*: Spatially smoothed average Mg^{2+} deposition rate for the dry deposition samples by sampling period. 265
Figure *7.10-19*: Spatially smoothed average K^+ deposition rate for the dry deposition samples by sampling period. 266
Figure *7.10-20*: Spatially smoothed average Na^+ deposition rate for the dry deposition samples by different sampling period. 267
Figure *7.10-21*: Spatially smoothed average Cl^- deposition rate for the dry deposition samples by sampling period. 268
Figure *7.10-22*: Spatially smoothed average SO_4^{2-} deposition rate for the dry deposition samples by sampling period. 269
Figure *7.10-23*: Spatially smoothed average NH_4^+ deposition rate for the dry deposition samples by sampling period. 270
Figure *7.10-24*: Spatially smoothed average NO_3^- deposition rate for the dry deposition samples by sampling periods. 271
Figure *7.10-25*: Spatially smoothed average P deposition rate for the dry deposition samples by sampling period. 272

Figure *7.10-26*: Historical and MRAMP measurements of rainfall *pH* plotted against the year of observation. The red dots are digitised from Bednarik (2007). 2004-2005, 2007-2008, and 2008-2009 data are from CSIRO monitoring studies report 2010. 2023 onwards are samples collected by MRAMP and analysed by Greg Skrypek, UWA. AQ01-AC denotes an air conditioner condensate sample during dry conditions. JH denotes samples collected by Professor Jo McDonald in Dampier during Tropical Cyclone Sean in January 2025. 274
Figure *7.10-27*: Rainfall *pH* measured during MRAMP studies plotted against month of observation. The green dashed line represents the neutral pH value. . 275
Figure *7.11-1*: Boxplots of *pH* for the total (flask) deposition samples by sampling period. The green dashed line represents the neutral *pH* value. 278
Figure *7.11-2*: Boxplots of *pH* for the total (flask) deposition samples by sampling site. The green dashed line represents the neutral *pH* value. 278
Figure *7.11-3*: Boxplots of Ca^{2+}, K^{+}, and Mg^{2+} deposition rates for the total deposition samples by sampling period. Note logarithmic scale. 280
Figure *7.11-4*: Boxplots of Ca^{2+}, K^{+}, and Mg^{2+} deposition rates for the total deposition samples by site. Note logarithmic scale. 280
Figure *7.11-5*: Boxplots of Na^{+},Cl^{-}, and $SO_4{}^{2-}$ deposition rates for the total deposition samples by sampling period. Note logarithmic scale. 281
Figure *7.11-6*: Boxplots of Na^{+}, Cl^{-}, and $SO_4{}^{2-}$ deposition rates for the total deposition samples by site. Note logarithmic scale. 282
Figure *7.11-7*: Boxplots of $NH_4{}^{+}$, $NO_3{}^{-}$, and P deposition rates for the total deposition samples by sampling period. Note logarithmic scale. 282
Figure *7.11-8*: Boxplots of $NH_4{}^{+}$, $NO_3{}^{-}$, and P deposition rates for the total deposition samples by site. Note logarithmic scale. 283
Figure *7.11-9*: Average *pH* and total deposition rates by AQM. Data represent approximately 19 months of observation (September 2023 to March 2025). 284
Figure *7.11-10*: Median *pH* and total deposition rates by AQM. Data represent approximately 19 months of observation (September 2023 to March 2025). 285
Figure *7.11-11*: Boxplots of *pH* for total deposition samples from all AQMs, co-located AQ07 and AQ08 from September 2023 to March 2025. 286
Figure *7.11-12*: Boxplots of total (flask) deposition rates of chemical species from total deposition samples of co-located AQ07 and AQ08 sites; September 2023 to March 2025. Note logarithmic scale. 287
Figure *7.11-13*: Scatterplots of the AQ07 vs AQ08 total (flask) deposition rates for each chemical species, September 2023 to March 2025. The black line (y $=$ x) indicates the same deposition rate at both monitoring stations. 288
Figure *7.11-14*: Time series plots of deposition rates of chemical species, from total deposition samples at co-located AQ07 (circles) and AQ08 (triangles) sites, against collection date. Note logarithmic scale. Points were jittered to avoid overlap. 292
Figure *7.11-15*: Spatially smoothed average *pH* for the total deposition samples by sampling period. 293

Figure *7.11-16*: Spatially smoothed average Ca^{2+} deposition rate for the total deposition samples by sampling period. 294
Figure *7.11-17*: Spatially smoothed average Mg^{2+} deposition rate for the total deposition samples by sampling period. 295
Figure *7.11-18*: Spatially smoothed average K^{+} deposition rate for the total deposition samples by sampling period. 296
Figure *7.11-19*: Spatially smoothed average Na^{+} deposition rate for the total deposition samples by sampling period. 297
Figure *7.11-20*: Spatially smoothed average Cl^{-} deposition rate for the total deposition samples by sampling period. 298
Figure *7.11-21*: Spatially smoothed average SO_4^{2-} deposition rate for the total deposition samples by sampling period. 299
Figure *7.11-22*: Spatially smoothed average NH_4^{+} deposition rate for the total deposition samples by sampling period. 300
Figure *7.11-23*: Spatially smoothed average NO_3^{-} deposition rate for the total deposition samples by sampling period. 301
Figure *7.11-24*: Spatially smoothed average P deposition rate for the total deposition samples by sampling period. 302
Figure *7.12-1*: Histograms (colour bars) and density estimates (black curves) of IVL sampler gas concentration measurements from all stations and all months. Each panel displays one gas species: (a) NO_2, (b) NH_3, (c) O_3, (d) SO_2, and (e) HNO_3. Panels (d) and (e) use a logarithmic scale on the horizontal axis. 305
Figure *7.12-2*: Histograms and density estimates of IVL sampler VOC concentration measurements for (a) benzene, (b) toluene, (c) n-octane, (d) ethylbenzene, (e) m-p-xylene, (f) o-xylene, and (g) n-nonane. Panels (c) – (f) use a logarithmic scale on horizontal axis. 306
Figure *7.12-3*: Plots of individual IVL sampler gas concentration estimates against air quality station identifier, coloured by Murujuga season. Separate gases are shown for each panel: (a) NO_2, (b) NH_3, (c) O_3, (d) SO_2, and (e) HNO_3. Panels (d) and (e) use logarithmic scale on the vertical axis. . . 308
Figure *7.12-4*: Boxplots of IVL sampler gas concentration observations for each gas species by Murujuga season across all stations. Separate gases are shown for each panel: (a) NO_2, (b) NH_3, (c) O_3, (d) SO_2 and (e) HNO_3. Panels (d) and (e) use logarithmic scale on the vertical axis. 311
Figure *7.12-5*: Histograms of IVL sampler gas concentration observations for each gas species by Murujuga season across all stations. Separate gases are shown for each panel: (a) NO_2, (b) NH_3, (c) O_3, (d) SO_2, and (e) HNO_3. Panels (d) and (e) use logarithmic scale on the horizontal axis. 312
Figure *7.12-6*: Boxplots of IVL sampler gas concentration observations for each month of observation: (a) NO_2, (b) NH_3, (c) O_3, (d) SO_2 and (e) HNO_3. Panels (d) and (e) use logarithmic scale on the vertical axis. 313

Figure *7.12-7*: Plots of IVL sampler VOC measurements against air quality station for each VOC species, coloured by Murujuga season. AQM stations are ordered by increasing average NO_2 concentration. Panels: (a) benzene, (b) toluene, (c) n-octane, (d) ethylbenzene, (e) m-p-xylene, (f) o-xylene, and (g) n-nonane. Panels (c) — (f) use logarithmic scale on the vertical axis. 316

Figure *7.12-8*: Boxplots of VOC IVL sampler gas concentration estimates for each month across all stations. Separate gases are shown for each panel: (a) benzene, (b) toluene, (c) n-octane, (d) ethylbenzene, (e) m-p-xylene, (f) o-xylene, and (g) n-nonane. Panels (c) — (f) use logarithmic scale on the vertical axis. 318

Figure *7.12-9*: Boxplots of IVL sampler measurements for each VOC species by Murujuga season across all stations. Panels: (a) benzene, (b) toluene, (c) n-octane, (d) ethylbenzene, (e) m-p-xylene, (f) o-xylene, and (g) n-nonane. Panels (c) — (g) use logarithmic scale on the vertical axis. 319

Figure *7.12-10*: Diagnostic plots for the variance-mean relationship. Scatterplots of individual estimates of variance (S^2, "paired variance") versus individual estimates of mean value ($\overline{X}$, "paired mean") calculated from duplicate pairs of passive sampler measurements for each gas species: (a) NO_2, (b) NH_3, (c) O_3, and (d) HNO_3. Plots show paired measurements for measurements over 2023 and 2024. All axes use logarithmic scale. . 323

Figure *7.12-11*: Diagnostic plots for the variance-mean relationship for SO_2 data. Top row shows a scatterplot of individual estimates of variance (S^2, "paired variance") versus individual estimates of mean value ($\overline{X}$, "paired mean") calculated from duplicate pairs of passive sampler measurements for SO_2. Left scatterplot is coloured according to calendar month; right scatterplot is coloured according to air quality station. Logarithmic scale is used for both variables. Bottom row shows individual estimates of variance plotted against calendar month (left) and against air quality station (right). Plots show paired measurements collected over 2023 and 2024. The legend on the bottom left hand side show the stations by colour while the legend on the bottom right hand side show the months by colour. The axis labels `1e-03` and `1e+01` (for example) are computer notation for 10^{-3} and 10^{1} respectively, that is, 0.001 and 10 respectively. 324

Figure *7.12-12*: Scatter plots of pairwise variance by pairwise mean for VOC species (a) benzene, (b) toluene, (c) n-octane, and (d) ethylbenzene. Plots show paired measurements for sample data collected over 2023 and 2024. Both axes use logarithmic scale. 325

Figure *7.12-13*: Scatter plots of residual variance versus mean for VOCs species (a) m-p-xylene, (b) o-xylene, and (c) n-nonane. Plots show paired measurements for sample data collected over 2023 and 2024. Both axes use logarithmic scale. 326

Figure *7.12-14*: Boxplots of passive sampler gas concentration measurements for stations AQ07 and AQ08 for gas species (a) NO_2, (b) NH_3, (c) O_3, (d) SO_2 and (e) HNO_3. For each species, only data for which corresponding observations are available for both AQ07 and AQ08 have been used. The mean value is diamond shape. Panels (d) and (e) use logarithmic scale on the vertical axis. 328
Figure *7.12-15*: Boxplots IVL passive sampler for the combined AQ07 and AQ08, other stations (all stations except for AQ07 and AQ08) and all stations for (a) NO_2, (b) NH_3, (c) O_3, (d) SO_2 and (e) HNO_3. Panels (d) and (e) use logarithmic scale on the vertical axis. 329
Figure *7.12-16*: Scatterplots of passive sampler gas concentration measurements for station AQ07 versus station AQ08 for gas species: (a) NO_2, (b) NH_3, (c) O_3, (d) SO_2 and (e) HNO_3. For each species, only data for which corresponding observations are available for both AQ07 and AQ08 have been used. The 1:1 line corresponds to equal relation between AQ07 and AQ08. A small amount of jitter has been used in these plots so that all points can be seen. 330
Figure *7.12-17*: Boxplots of passive sampler gas concentration measurements for stations AQ07 and AQ08 for VOC species: (a) benzene, (b) toluene, (c) n-octane, (d) ethylbenzene, (e) m-p-xylene, (f) o-xylene, and (g) n-nonane. For each species, only data for which corresponding observations are available for both AQ07 and AQ08 have been used. The mean value is diamond shape. Panels (b) to (g) (inclusive) use logarithmic scale on the vertical axis. 331
Figure *7.12-18*: Scatterplots of passive sampler gas concentration measurements for station AQ07 versus station AQ08 for gas species (a) benzene, (b) toluene, (c) n-octane, (d) ethylbenzene, (e) m-p-xylene, (f) o-xylene, and (g) n-nonane. For each VOC, only data for which corresponding observations are available for both AQ07 and AQ08 have been used. The 1:1 line corresponds to equal relation between AQ07 and AQ08. A small amount of jitter has been used in these plots so that all points can be seen. 332
Figure *7.12-19*: Spatially smoothed average concentration of NO_2 by meteorological seasons aggregated across all passive sampler data. Common colour map based on percentiles. 338
Figure *7.12-20*: Assessment of concordance between spatial patterns of NO_2 concentration across all sampler periods, estimated from spatially smoothed passive sampler data. (a) consensus ranks; (b) disagreement (standard deviation).339
Figure *7.12-21*: Spatially smoothed average concentration of NH_3 by meteorological season. Common colour map based on percentiles. 340
Figure *7.12-22*: Assessment of concordance between spatial patterns of NH_3 concentration across all sampler periods, estimated from spatially smoothed passive sampler data. (a) consensus ranks; (b) disagreement (standard deviation).341
Figure *7.12-23*: Spatially smoothed average concentration of O_3 by meteorological season. Common colour map based on percentiles. 342

Figure *7.12-24*: Assessment of concordance between spatial patterns of O_3 concentration across all sampler periods, estimated from spatially smoothed passive sampler data. (a) consensus ranks; (b) disagreement (standard deviation).343
Figure *7.12-25*: Spatially smoothed average concentration of SO_2 by meteorological season. Common colour map based on percentiles. 344
Figure *7.12-26*: Assessment of concordance between spatial patterns of SO_2 concentration across all sampler periods, estimated from spatially smoothed passive sampler data. (a) consensus ranks; (b) disagreement (standard deviation).345
Figure *7.12-27*: Spatially smoothed average concentration of HNO_3 by meteorological season. Common colour map based on percentiles. 346
Figure *7.12-28*: Assessment of concordance between spatial patterns of HNO_3 concentration in over all sampling periods, estimated from spatially smoothed passive sampler data. (a) consensus ranks; (b) disagreement (standard deviation).347
Figure *7.13-1*: Time series plots for SO_2 concentration to date, for sites (a) AQ01, (b) EX02, (c) EX07 and (d) EX09. Gaps in the data correspond to times where the instruments were offline, or where the data have been excluded due to concerns about the validity. 352
Figure *7.13-2*: Time series plots for NO to date, where (a) AQ01, (b) EX02, (c) EX07 and (d) EX09. Gaps in the data correspond to times where the instruments were offline, or where the data have been excluded due to concerns about the validity. 353
Figure *7.13-3*: Time series plots for NO over one week in November 2024, where (a) AQ01, (b) EX02, (c) EX07 and (d) EX09. The data shown in blue corresponds to nighttime (defined as sunset to sunrise) measurements, and data shown in orange correspond to daytime (defined as sunrise to sunset). The red up-pointing triangles are midday, and black down-pointing triangles are midnight. Data have been excluded where the validity is in question. 355
Figure *7.13-4*: Boxplot of NO, NO_2, NH_3, O_3 and SO_2 for the four powered sites (AQ01, EX02, EX07, EX09) combined according to the meteorological and Murujuga seasons Garrbarn (hot) and Muthu (cold). Note the vertical axis is logarithmic scale for all panels. 356
Figure *7.13-5*: Time series data for NO_2, where (a) AQ01, (b) EX02, (c) EX07 and (d) EX09. Gaps in the data correspond to times where the instruments were offline, or where the data have been excluded due to concerns about the validity. 360
Figure *7.13-6*: Time series plots for NO_2 over one week in November 2024, where (a) AQ01, (b) EX02, (c) EX07 and (d) EX09. The data shown in blue corresponds to nighttime (defined as sunset to sunrise) measurements, and data shown in orange correspond to daytime (defined as sunrise to sunset). The red up-pointing triangles are midday, and black down-pointing triangles are midnight. Data have been excluded where the validity is in question. 361

Figure *7.13-7*: Time series data for NH_3 for (a) AQ01, (b) EX02 (c) EX07 and (d) EX09. Gaps in the data correspond to times where the instruments were offline, or where the data have been excluded due to concerns about the validity. 362

Figure *7.13-8*: Time series plots for O_3 at (a) AQ01, (b) EX02, (c) EX07 and (d) EX09. Gaps in the data correspond to times where the instruments were offline, or where data have been excluded due to concerns about validity. . . . 363

Figure *7.13-9*: Time series plots for O_3 over one week in November 2024, where (a) AQ01, (b) EX02, (c) EX07, and (d) EX09. The data shown in blue corresponds to nighttime (defined as sunset to sunrise) measurements, and data shown in orange corresponds to daytime (defined as sunrise to sunset). The red up-pointing triangles are midday, and black down-pointing triangles are midnight. Data have been excluded where the validity is in question. 364

Figure *7.13-10*: Time series plots for NO/NO_2 over one week in November 2024, where (a) AQ01, (b) EX02, (c) EX07, and (d) EX09. The data shown in blue corresponds to nighttime (defined as sunset to sunrise) measurements, and data shown in orange corresponds to daytime (defined as sunrise to sunset). The red up-pointing triangles are midday, and black down-pointing triangles are midnight. Data have been excluded where the validity is in question. 365

Figure *7.13-11*: Time series plots for NO_2/NOx over one week in November 2024, where (a) AQ01, (b) EX02, (c) EX07, and (d) EX09. The data shown in blue corresponds to nighttime (defined as sunset to sunrise) measurements, and data shown in orange corresponds to daytime (defined as sunrise to sunset). The red up-pointing triangles are midday and black down-pointing triangles are midnight. Data have been excluded where the validity is in question. 366

Figure *7.13-12*: Time series plots for $PM_{2.5}$ at (a) AQ01, (b) EX02, (c) EX07 and (d) EX09. Gaps in the data correspond to times where the instruments were offline, or where the data have been excluded due to concerns about the validity. 368

Figure *7.13-13*: Time series plots for $PM_{2.5}$ over one week in November 2024, where (a) AQ01, (b) EX07, and (c) EX09. The data shown in blue corresponds to nighttime measurements, and data shown in orange corresponds to daytime. Data have been excluded where the validity is in question. Note EX02 had no data available in November 2024. 369

Figure *7.13-14*: Time series plot for PM_{10} at (a) AQ01, (b) EX02, (c) EX07 and (d) EX09. Gaps in the data correspond to times where the instruments were offline, or where the data have been excluded due to concerns about the validity. 370

Figure *7.13-15*: Time series plots for PM_{10} over one week in November 2024, where (a) AQ01, (b) EX07, and (c) EX09. The data shown in blue corresponds to nighttime measurements, and data shown in orange corresponds to daytime. Data have been excluded where the validity is in question. Note EX02 had no data available in November 2024. 371

Figure *7.13-16*: Time series plot of total suspended particulates (TSP) at (a) AQ01, (b) EX02, (c) EX07, and (d) EX09. Gaps in the data correspond to times where the instruments were offline, or where the data have been excluded due to concerns about the validity. 372

Figure *7.13-17*: Time series plot of CO_2 from the Picarro instrument at EX09. Gaps in the data correspond to times where the instrument was offline, or where data have been excluded due to concerns about validity. 374

Figure *7.13-18*: Time series plot of CO_2 from the Picarro instrument at EX09 over a week in December 2024. The data shown in blue corresponds to nighttime (defined as sunset to sunrise) measurements, and the data shown in orange corresponds to daytime (defined as sunrise to sunset). The red up-pointing triangles are midday, and black down-pointing triangles are midnight. Note that there was no data available for 11 to 14 November 2024, the period used for visualisation of daily peaks for other real time instruments. 375

Figure *7.13-19*: Time series plot of CH_4 from the Picarro instrument at EX09. Gaps in the data correspond to times where the instrument was offline, or where data have been excluded due to concerns about validity. 376

Figure *7.13-20*: Time series plot of C_2H_6 from the Picarro instrument at EX09. Gaps in the data correspond to times where the instrument was offline, or where data have been excluded due to concerns about validity. 377

Figure *7.13-21*: Time series plot of the ratio between C_2H_6 and CH_4 from the Picarro data. Gaps in the data correspond to times where the instrument was offline, or where data have been excluded due to concerns about validity. . . . 378

Figure *7.13-22*: Time series plots for NO_2 and CH_2O from MAxDOAS at 1° elevation, raw data product from spectral fitting, trace gas concentration integrated over the atmospheric light path. Note that the NO_2 and CH_2O have been divided by 10^{15} (one hundred quadrillion) to simplify the tick marks on the y-axis. 380

Figure *7.13-23*: Time series plots for NO_2 and CH_2O from MAxDOAS at 10° elevation, raw data product from spectral fitting, trace gas concentration integrated over the atmospheric light path. Note that the NO_2 and CH_2O have been divided by 10^{15} (one hundred quadrillion) to simplify the tick marks on the y-axis. 381

Figure *7.13-24*: Time series plots for NO_2 and CH_2O from MAxDOAS at 30° elevation, raw data product from spectral fitting, trace gas concentration integrated over the atmospheric light path. Note that the NO_2 and CH_2O have been divided by 10^{15} (one hundred quadrillion) to simplify the tick marks on the y-axis. 382

Figure *7.13-25*: Time series plots for NO_2 and CH_2O from MAxDOAS at 5° elevation, near surface concentrations estimated from the raw data. Note that the NO_2 and CH_2O have been divided by 10^{10} (one hundred quadrillion) to simplify the tick marks on the y-axis. 383

Figure *7.13-26*: Time series plots for NO_2 and CH_2O from MAxDOAS at 30° elevation, vertical column density estimate for the trace gas. Note that the NO_2 and CH_2O have been divided by 10^{15} (one hundred quadrillion) to simplify the tick marks on the y-axis. 384
Figure *7.13-27*: NO_2 from MAxDOAS for first two weeks in February 2025 at 0° (W), 180° (E) and 90° (N), points are coloured by elevation angle. NO_2 is the raw data product from spectral fitting, trace gas concentration integrated over the atmospheric light path.Note that the NO_2 has been divided by 10^{15} (one hundred quadrillion) to simplify the tick marks on the y-axis. 385
Figure *7.13-28*: NO_2 from MAxDOAS for first two weeks in February 2025 at 0° (W), 90° (N) and 180° (E). NO_2 is the near surface concentration estimated from raw data. Note that the NO_2 has been divided by 10^{10} (one hundred quadrillion) to simplify the tick marks on the y-axis. 386
Figure *7.13-29*: NO_2 from MAxDOAS for first two weeks in February 2025 at 0° (W), 90° (N) and 180° (E). NO_2 is vertical column density estimate for the trace gas. Note that the NO_2 has been divided by 10^{15} (one hundred quadrillion) to simplify the tick marks on the y-axis. 387
Figure *7.13-30*: CH_2O from MAxDOAS for first two weeks in February 2025 at 0° (W), 90° (N) and 180° (E), raw data product from spectral fitting. Note that the CH_2O has been divided by 10^{15} (one hundred quadrillion) to simplify the tick marks on the y-axis. 388
Figure *7.13-31*: Scatterplot of NO_2 from T201 and MAxDOAS instruments. NO_2 from the MAxDOAS is the near surface concentrations estimated from the raw data. Note that the NO_2 from the MAxDOAS has been divided by 10^{15} (one hundred quadrillion) to simplify the tick marks on the y-axis. 389
Figure *7.13-32*: Scatterplot of NO_2 from T201 and MAxDOAS instruments. NO_2 from the MAxDOAS is the vertical column density estimate for the trace gas. Note that the NO_2 from the MAxDOAS has been divided by 10^{15} (one hundred quadrillion) to simplify the tick marks on the y-axis. 390
Figure *7.13-33*: Time series plot of radon at EX09. 392
Figure *7.13-34*: Time series plot of radon at EX09 over one week in November 2024. Daytime is defined as 8 am to 6 pm, associated with convective atmospheric mixing rather than daylight hours, and nighttime is the rest of each day. 393
Figure *7.14-1*: Time series plots for NO measurements from low powered sensors from January 2024 to February 2025 (inclusive), at locations (a) AQ01, (b) EX02, and (c) EX09, (d) AQ04, (e) AQ11, (f) AQ18. Where each point is the daily mean of NO. 396
Figure *7.14-2*: Time series plots for NO measurements from low powered sensors over one week in November 2024, at locations (a) AQ01, (b) EX02, and (c) EX09, (d) AQ04, (e) AQ11, (f) AQ18. The data shown in blue corresponds to nighttime (defined as sunset to sunrise) measurements, and data shown in orange correspond to daytime (defined as sunrise to sunset). The red up-pointing triangles are midday and black down-pointing triangles are midnight. 397

Figure *7.14-3*: Time series plots for NO_2 measurements from low powered sensors from January 2024 to April 2025 (inclusive), at locations (a) AQ01, (b) EX02, and (c) EX09, (d) AQ04, (e) AQ11, (f) AQ18. Where each point is the daily mean of NO_2. 399

Figure *7.14-4*: Time series plots for NO_2 measurements from low powered sensors over one week in November 2024, at locations (a) AQ01, (b) EX02, and (c) EX09. The data shown in blue corresponds to nighttime (defined as sunset to sunrise) measurements, and data shown in orange correspond to daytime (defined as sunrise to sunset). The red up-pointing triangles are midday and black down-pointing triangles are midnight. Data have been excluded where the validity is in question. 400

Figure *7.14-5*: Time series plots for CO_2 measurements from low powered sensors from January 2024 to February 2025 (inclusive), at locations (a) AQ01, (b) EX02, (c) EX09, (d) AQ04, (e) AQ11, and (f) AQ18. Where each point is the daily mean of CO_2. 402

Figure *7.14-6*: Time series plots for CO_2 measurements from low powered sensors over one week in November 2024, at locations (a) AQ01, (b) EX02, (c) EX09, (d) AQ04, (e) AQ11, and (f) AQ18. The data shown in blue corresponds to nighttime (defined as sunset to sunrise) measurements, and data shown in orange correspond to daytime (defined as sunrise to sunset). The red up-pointing triangles are midday and black down-pointing triangles are midnight. 403

Figure *7.14-7*: Time series plots for $PM_{2.5}$ measurements from low powered sensors from January 2024 to April 2025 (inclusive), at locations (a) AQ01, (b) EX02, and (c) EX09, (d) AQ04, (e) AQ11, and (f) AQ18. Each point is the daily mean of $PM_{2.5}$. 405

Figure *7.14-8*: Time series plots for $PM_{2.5}$ measurements from low powered sensors over one week in November 2024, at locations (a) AQ01, (b) EX02, (c) EX09, (d) AQ04, (e) AQ11, and (f) AQ18. The data shown in blue corresponds to nighttime (defined as sunset to sunrise) measurements, and data shown in orange correspond to daytime (defined as sunrise to sunset). The red up-pointing triangles are midday, and black down-pointing triangles are midnight. 406

Figure *7.14-9*: Time series plots for PM_{10} measurements from low powered sensors from January 2024 to April 2025 (inclusive), at locations (a) AQ01, (b) EX02, and (c) EX09, (d) AQ04, (e) AQ11, and (f) AQ18. Each point is the daily mean of PM_{10} 408

Figure *7.14-10*: Time series plots for PM_{10} measurements from low powered sensors over one week in November 2024, at locations (a) AQ01, (b) EX02, (c) EX09, (d) AQ04, (e) AQ11, and (f) AQ18. The data shown in blue corresponds to nighttime (defined as sunset to sunrise) measurements, and data shown in orange correspond to daytime (defined as sunrise to sunset). The red up-pointing triangles are midday and black down-pointing triangles are midnight. Data have been excluded where the validity is in question. . 409

Figure *7.14-11*: Scatterplots for mean gas concentration measurements from low powered sensors across all low powered sites and indicating Murujuga season for (a) NO_2, (b) NO, (c) NH_3, and (d) CO_2. Stations are ordered separately for each gas from highest to lowest: this allows us see how individual gases vary across sites. Means are across passive sampling periods in 2024 to allow comparison to passive sampling measures. 410

Figure *7.14-12*: Boxplots of gas concentration measurements from low powered sensors across all sites by Murujuga season for (a) NO_2, (b) NO, (c) NH_3, and (d) CO_2. Means are across passive sampling periods in 2024 to allow comparison to passive sampling measures. 411

Figure *7.14-13*: Scatterplots for mean particulate matter measurements from low powered sensors across all low powered sites and indicating Murujuga season for $PM_{2.5}$ and PM_{PM10}. Means are across passive sampling periods in 2024 to allow comparison to passive sampling measures. 412

Figure *7.14-14*: Boxplots of mean particulate matter measurements from low powered sensors across all sites by Murujuga season for $PM_{2.5}$. Means are across passive sampling periods in 2024 to allow comparison to passive sampling measures. 412

Figure *7.15-1*: The daily temperature (first column) and daily relative humidity (second column) during campaigns 7 (26 February - 21 March 2024), 8 (01 July - 26 July 2024), and 9 (14 October - 07 November 2024) recorded at the AQM (red) and BoM (black) stations. The dots are the minimum daily values and the stars are the maximum daily values. 416

Figure *7.15-2*: Time series plot for relative humidity over the first week of campaign 10. The data shown in blue correspond to the nighttime (defined as sunset to sunrise) measurements, and data shown in orange correspond to the daytime (defined as sunrise to sunset). The red up-pointing triangles are midday and black down-pointing triangles are midnight. 417

Figure *7.15-3*: Rainfall during campaigns 7 and 10 recorded at the AQM (red) and BoM (black) stations. There is one red dot for each AQM station and one black dot for each BoM station. 418

Figure *8.1-1*: Simplified 2D boxplots of dry bucket SO_4^{2-} and passive sampler SO_2 from each AQ and EX site. The points are the median SO_4^{2-} and the median SO_2, and the horizontal and vertical lines are the inter-quartile ranges. Note the logarithmic scale in both axes. Data between May 2023 and January 2025. 429

Figure *8.1-2*: Simplified 2D boxplots of dry bucket NO_3^- and passive sampler NO_2 from each AQ and EX site. The points are the median NO_3^- and the median NO_2, and the horizontal and vertical lines are the inter-quartile ranges. Note the logarithmic scale in both axes. Data between May 2023 and January 2025. 430

Figure *8.1-3*: Simplified 2D boxplot of dry bucket NH_4^+ and passive sampler NH_3 from each AQ and EX site. The points are the median NH_4^+ and the median NH_3, and the horizontal and vertical lines are the inter-quartile ranges. Note the logarithmic scale in both axes. Data between May 2023 and January 2025. 431
Figure *8.2-1*: Scatterplots of 3-bucket deposition sampler (dry, wet, mist) and total flask deposition data. Combined data from September 2023 and March 2025. 434
Figure *8.3-1*: Boxplots comparing IVL passive samplers with satellite observations (generated using Copernicus Atmosphere Monitoring Service (CAMS)). Note the vertical axis is logarithmic scale. 436
Figure *8.4-1*: Scatterplots of low power (“L”) versus powered (“P”) sensors for NO (first row) and NO_2 (second row) at AQ01 (first column), EX02 (second column) and EX09 (third column) over one week in November 2024. Data have been excluded where the validity is in question. 438
Figure *8.4-2*: Scatterplots of low-power (“L”) versus powered (“P”) sensors for CO_2 at EX09 over one week in December 2024. Data have been excluded where the validity is in question. 439
Figure *8.4-3*: Scatterplots of low power (“L”) versus powered (“P”) sensors for $PM_{2.5}$ (first row) at AQ01 (first column) and EX09 (second column) over one week in November 2024. Data have been excluded where the validity is in question. 441
Figure *8.4-4*: Scatterplots of low power (“L”) versus temperature (°C) for NO (first row) and NO_2 (second row) at AQ01 (first column), EX02 (second column) and EX09 (third column) over one week in November 2024. Data have been excluded where the validity is in question. 442
Figure *8.4-5*: Scatterplots of low power (“L”) versus relative humidity for NO (first row) and NO_2 (second row) at AQ01 (first column), EX02 (second column) and EX09 (third column) over one week in November 2024. Data have been excluded where the validity is in question. 443
Figure *8.5-1*: RDA of instruments T100, T201, T400, Radon and wind direction. Where the data has been summarised into daily means 445
Figure *8.5-2*: RDA of low cost, powered, temperature, relative humidity, wind direction. Where the data has been summarised into daily means. 446
Figure *A-1*: GC-MS total ion chromatograms. a) overlaid chromatograms of rock surface sample AQ05_DOL B, procedure blank and reagent blank, b) AQ05_DOL B, c) procedure blank, d) reagent blank. Observed ions ranged from 50 to m/z 550. 464
Figure *A-2*: GC-MS total ion chromatogram (TIC) of the derivatised polar fraction from rock surface sample AS02_DOL and corresponding fresh rock sample FR_AS02_DOL. The shift in the retention time between the samples is due to time difference in the time of analysis. Retention time has been adjusted in the magnified section. Observed ion ranged from m/z 50 to m/z 550. 465

Figure *A-3*: Flash Pyrolysis GC-MS total ion chromatogram (TIC) of rock surface sample RS16_GBR extracted and not extracted for comparison. Observed ions ranged from 50 to m/z 550. 466

Figure *A-4*: Flash Pyrolysis GC-MS total ion chromatogram (TIC) of rock surface sample RS16_GBR extracted and fresh rock sample extracted for comparison. Observed ions ranged from 50 to m/z 550. 466

Figure *C*.1-1: Timeline of the Dampier power plant complex, categorised according to fuel type, including the Parker Point iron pellet plant. 538

Figure *C*.1-2: Estimated annual emission rates of NOx out of the Dampier power plant site, including the iron pellet plant. 539

Figure *C*.1-3: Estimated annual emission rates of SO_2 out of the Dampier power plant site, including the iron pellet plant. 540

Figure *C*.1-4: maximum values of the NOx emission rate using the 100% utilisation and growth models (mean values are indicated by black horizontal lines), compared against the Ramboll 2014 and 2030 models. 541

Figure *C*.1-5: maximum values of the SO_2 emission rate using the 100% utilisation and growth models (mean values are indicated by black horizontal lines), compared against the Ramboll 2014 and 2030 models. 542

Figure *D.3-1*: Histograms (colour bars) and density estimates (black curves) of IVL and Radiello sampler gas concentration measurements from all Woodside stations from September 2021 to November 2022. Each panel shows histogram for one gas species: (a) NO_2, (b) NH_3, (c) SO_2, and (d) HNO_3. 548

Figure *D.4-1*: Spatial plot of Dibenzothiophene/phenanthrene (DBT/P). 549

Figure *D.4-2*: Spatial plot of methyldibenzothiophene/methylphenanthrene (MDBT/MP).550

Figure *D.5-1*: Plots of individual IVL sampler VOC concentration estimates against air quality station identifier, labelled by meteorological season (colour) and month (shape). Each panel shows results for one gas species: (a) NO_2, (b) NH_3, (c) O_3, (d) SO_2, and (e) HNO_3. Panels (d) and (e) use logarithmic scale on the vertical axis. 552

Figure *D.5-2*: Scatterplots of IVL sampler gas concentration estimates against air quality station identifier, coloured by meteorological season (colour). Separate gases are shown for each panel: (a) benzene, (b) toluene, (c) n-octane, (d) ethylbenzene, (e) m-p-xylene, (f) o-xylene, and (g) n-nonane. Panels (c) — (f) use logarithmic scale on vertical axis. 553

Figure *D.5-3*: Boxplots of IVL sampler gas concentration observations for each gas species by meteorological season across all stations. Separate gases are shown for each panel: (a) NO_2, (b) NH_3, (c) O_3, (d) SO_2, and (e) HNO_3. Panels (d) and (e) use logarithmic scale on the vertical axis. . . 555

Figure *D.5-4*: Histograms of IVL sampler gas concentration observations for each Gas species by meteorological season across all stations. Separate gases are shown for each panel: (a) NO_2, (b) NH_3, (c) O_3, (d) SO_2, and (e) HNO_3. Panels (d) and (e) use logarithmic scale on the horizontal axis. 556

Figure *D.5-5*: Boxplots of IVL sampler VOC measurements for each VOC species by meteorological season across all stations. Panels: (a) benzene, (b) toluene, (c) n-octane, (d) ethylbenzene, (e) m-p-xylene, (f) o-xylene, and (g) n-nonane. Panels (c) – (g) use logarithmic scale on vertical axis. . . 558

Figure *D.5-6*: Histograms of IVL sampler VOC measurements for each VOC species by meteorological season across all stations. Panels: (a) benzene, (b) toluene, (c) n-octane, (d) ethylbenzene, (e) m-p-xylene, (f) o-xylene, and (g) n-nonane. Panels (c) – (g) use logarithmic scale on horizontal axis. 559

Figure *D.5-7*: Histograms of IVL sampler VOC measurements for each VOC species by Murujuga season across all stations. Panels: (a) benzene, (b) toluene, (c) n-octane, (d) ethylbenzene, (e) m-p-xylene, (f) o-xylene, and (g) n-nonane. Panels (c) — (g) use logarithmic scale on the horizontal axis. 560

Figure *D.5-8*: RDA biplot showing the relationship between gas measurements (NO_2, NH_3,O_3, SO_2, and HNO_3) and time of year (month sin and month cos). 562

Figure *D.5-9*: RDA biplot showing the relationship between gas measurements (NO_2, NH_3, O_3, SO_2 and HNO_3) and Northing and Easting. 563

Figure *D.5-10*: Diagnostic plots for the variance-mean relationship for NO_2 data. Top row shows a scatterplot of individual estimates of variance (S^2, "paired variance") versus individual estimates of mean value ($\overline{X}$, "paired mean") calculated from duplicate pairs of passive sampler measurements for NO_2. Left scatterplot is coloured according to calendar month; right scatterplot is coloured according to air quality station. Logarithmic scale is used for both variables. Bottom row shows individual estimates of variance plotted against calendar month (left) and against air quality station (right). Plots show paired measurements collected over 2023 and 2024. The legend on the bottom left hand side show the stations by colour while the legend on the bottom right hand side show the months by colour. The axis labels `1e-03` and `1e+01` (for example) are computer notation for 10^{-3} and 10^{1} respectively, that is, 0.001 and 10 respectively. 564

Figure *D.5-11*: Diagnostic plots for the variance-mean relationship for NH_3 data. Top row shows a scatterplot of individual estimates of variance (S^2, "paired variance") versus individual estimates of mean value ($\overline{X}$, "paired mean") calculated from duplicate pairs of passive sampler measurements for NH_3. Left scatterplot is coloured according to calendar month; right scatterplot is coloured according to air quality station. Logarithmic scale is used for both variables. Bottom row shows individual estimates of variance plotted against calendar month (left) and against air quality station (right). Plots show paired measurements collected over 2023 and 2024. The legend on the bottom left hand side show the stations by colour while the legend on the bottom right hand side show the months by colour. The axis labels `1e-03` and `1e+01` (for example) are computer notation for 10^{-3} and 10^{1} respectively, that is, 0.001 and 10 respectively. 565

Figure *D.5-12*: Diagnostic plots for the variance-mean relationship for O_3 data. Top row shows a scatterplot of individual estimates of variance (S^2, "paired variance") versus individual estimates of mean value ($\overline{X}$, "paired mean") calculated from duplicate pairs of passive sampler measurements for O_3. Left scatterplot is coloured according to calendar month; right scatterplot is coloured according to air quality station. Logarithmic scale is used for both variables. Bottom row shows individual estimates of variance plotted against calendar month (left) and against air quality station (right). Plots show paired measurements collected over 2023 and 2024. The legend on the bottom left hand side show the stations by colour while the legend on the bottom right hand side show the months by colour. The vertical axis labels `1e-03` and `1e+01` (for example) are computer notation for 10^{-3} and 10^{1} respectively, that is, 0.001 and 10 respectively. 566

Figure *D.5-13*: Diagnostic plots for the variance-mean relationship for HNO_3 data. Top row shows a scatterplot of individual estimates of variance (S^2, "paired variance") versus individual estimates of mean value ($\overline{X}$, "paired mean") calculated from duplicate pairs of passive sampler measurements for HNO_3. Left scatterplot is coloured according to calendar month; right scatterplot is coloured according to air quality station. Logarithmic scale is used for both variables. Bottom row shows individual estimates of variance plotted against calendar month (left) and against air quality station (right). Plots show paired measurements collected over 2023 and 2024. The legend on the bottom left hand side show the stations by colour while the legend on the bottom right hand side show the months by colour. The vertical axis labels `1e-03` and `1e+01` (for example) are computer notation for 10^{-3} and 10^{1} respectively, that is, 0.001 and 10 respectively. 567

Figure *D.5-14*: Histograms (coloured bars) and probability density estimates (coloured curves) of passive sampler gas concentration measurements for stations AQ07 and AQ08 for gas species (a) NO_2, (b) NH_3, (c) O_3, (d) SO_2, and (e) HNO_3. Panels (d) and (e) use logarithmic scale on the horizontal axis. 569

Figure *D.5-15*: Histograms and density estimates of passive sampler VOC concentration measurements for stations AQ07 and AQ08 for VOC species (a) benzene, (b) toluene, (c) n-octane, (d) ethylbenzene, (e) m-p-xylene, (f) o-xylene, and (g) n-nonane. Panels (b) to (g) (inclusive) use logarithmic scale on the horizontal axis. 570

Figure *D.5-16*: Boxplots of passive sampler gas concentration measurements by meteorological season across both stations AQ07 and AQ08 for gas species (a) NO_2, (b) NH_3, (c) O_3, (d) SO_2 and (e) HNO_3. Panels (d) and (e) use logarithmic scale on vertical axis. 574

Figure *D.5-17*: Boxplots of passive sampler gas concentration measurements by Murujuga season across both stations AQ07 and AQ08 for gas species (a) NO_2, (b) NH_3, (c) O_3, (d) SO_2 and (e) HNO_3. Panels (d) and (e) use logarithmic scale on vertical axis. 575

Figure *D.5-18*: Boxplots of passive sampler gas concentration measurements by meteorological season across both stations AQ07 and AQ08 for VOC species: (a) benzene, (b) toluene, (c) n-octane, (d) ethylbenzene, (e) m-p-xylene, (f) o-xylene, and (g) n-nonane. Panels (b) to (g) (inclusive) use logarithmic scale on vertical axis. 576

Figure *D.5-19*: Boxplots of passive sampler gas concentration measurements by Murujuga season across both stations AQ07 and AQ08 for VOC species: (a) benzene, (b) toluene, (c) n-octane, (d) ethylbenzene, (e) m-p-xylene, (f) o-xylene, and (g) n-nonane. Panels (b) to (g) (inclusive) use logarithmic scale on vertical axis. 577

Figure *D.5-20*: Boxplots of passive sampler gas concentration measurements by station and Murujuga seasons for gas species (a) NO_2, (b) NH_3, (c) O_3, (d) SO_2, and (e) HNO_3. Boxplots for Garrbarn (hot) are in red and boxplots for Muthu (cold) are in blue. Logarithmic scale is used on the vertical axes for SO (d) and HNO_3 (e). 579

Figure *D.5-21*: Boxplots of passive sampler gas concentration measurements by station and Murujuga season for VOC species (a) benzene, (b) toluene, (c) n-octane, (d) ethylbenzene, (e) m-p-xylene, (f) o-xylene, and (g) n-nonane. 582

Figure *D.5-22*: Boxplots of passive sampler gas concentration measurements by station and meteorological season for gases species (a) NO_2, (b) NH_3, (c) O_3, (d) SO_2 and (e) HNO_3. Panels (d) and (e) use logarithmic scale on horizontal axis. 586

Figure *D.5-23*: Boxplots of passive sampler gas concentration measurements by station and meteorological season for VOC species (a) benzene, (b) toluene, (c) n-octane, (d) ethylbenzene, (e) m-p-xylene, (f) o-xylene, and (g) n-nonane. All panels use logarithmic scale on vertical axis. 587

Figure *D.5-24*: Spatially smoothed monthly average concentration of NO_2 by majority month for 2024. Common colour map based on percentiles. 589

Figure *D.5-25*: Spatially smoothed monthly average concentration of NH_3 by majority month for 2024. Common colour map based on percentiles. 590

Figure *D.5-26*: Spatially smoothed monthly average concentration of O_3 by majority month for 2024. Common colour map based on percentiles. 591

Figure *D.5-27*: Spatially smoothed monthly average concentration of SO_2 by majority month for 2024. Common colour map based on percentiles. 592

Figure *D.5-28*: Spatially smoothed monthly average concentration of HNO_3 by majority month for 2024. Common colour map based on percentiles. 593

Figure *D.5-29*: Assessment of concordance between spatial patterns of NO_2 concentration in different seasons, estimated from spatially smoothed passive sampler data. 594

Figure *D.5-30*: Assessment of concordance between spatial patterns of NH_3 concentration in different seasons, estimated from spatially smoothed passive sampler data. 595

Figure *D.5-31*: Assessment of concordance between spatial patterns of O_3 concentration in different seasons, estimated from spatially smoothed passive sampler data. 596

Figure *D.5-32*: Assessment of concordance between spatial patterns of SO_2 concentration in different seasons, estimated from spatially smoothed passive sampler data. 597

Figure *D.5-33*: Assessment of concordance between spatial patterns of HNO_3 concentration in different seasons, estimated from spatially smoothed passive sampler data. 598

Figure *D.6-1*: Time series plots for NH_3 measurements from low powered sensors from January 2024 to February 2025 (inclusive), at locations (a) AQ01, (b) EX02, (c) EX09, (d) AQ04, (e) AQ11, and (f) AQ18. Where each point is the daily mean of NH_3. 600

Figure *D.6-2*: Time series plots for NH_3 measurements from low powered sensors over one week in November 2024, at locations (a) AQ01, (b) EX02, (c) EX09, (d) AQ04, (e) AQ11, and (f) AQ18. The data shown in blue corresponds to nighttime (defined as sunset to sunrise) measurements, and data shown in orange correspond to daytime (defined as sunrise to sunset). The red up-pointing triangles are midday and black down-pointing triangles are midnight. 601

Figure *D.6-3*: Boxplots of mean gas concentration measurements from low powered sensors by month for all low powered sites for (a) NO, (b) NO_2, (c) NH_3, and (d) CO_2. Means are across passive sampling periods in 2024 to allow comparison to passive sampling measures. Boxplot colours indicate the particulate matter type: NO is sea green, NO_2 is forest (or dark) green, NH_3 is medium green, and CO_2 is slate blue. A log scale is used for the vertical axis. 603

Figure *D.6-4*: Scatterplots for mean gas concentration measurements from low powered sensors across all low powered sites and indicating meteorological season for (a) NO_2, (b) NO, (c) NH_3, and (d) CO_2. Means are across passive sampling periods in 2024 to allow comparison to passive sampling measures. Seasons are shown by colour where red points indicate summer, purple points indicate autumn, blue points indicate winter, and green points indicate spring. The stations for all plots are ordered by NO_2 levels from highest to lowest: this allows us to compare gas concentrations to NO_2. The vertical axis uses a log scale in all plots. . 604

Figure *D.6-5*: Boxplots of gas concentration measurements from low powered sensors across all low powered sites by meteorological season for (a) NO_2, (b) NO, (c) NH_3, and (d) CO_2. Means are across passive sampling periods in 2024 to allow comparison to passive sampling measures. Seasons are shown by colour where red points indicate summer, purple points indicate autumn, blue points indicate winter, and green points indicate spring. 605

Figure *D.6-6*: Histograms of gas concentration measurements from low-power sensors across all low-power sites by Murujuga season for (a) NO_2, (b) NO, (c) NH_3, and (d) CO_2. Means are across passive sampling periods in 2024 to allow comparison to passive sampling measures. Seasons are shown by colour where red points indicate Garrbarn (hot) and blue points indicate Muthu (cold) season. The horizontal axis uses a logarithmic scale. . . . 606
Figure *D.6-7*: Boxplots of mean particulate matter measurements from low powered sensors by month for all low powered sites for (a) $PM_{2.5}$ and (b) PM_{10}. Means are across passive sampling periods in 2024 to allow comparison to passive sampling measures. Boxplot colours indicate the particulate matter type: light blue is $PM_{2.5}$ and dark blue is PM_{10}. A log scale is used for the vertical axis. 607
Figure *D.6-8*: Scatterplots for mean particulate matter measurements from low powered sensors across all low powered sites and indicating meteorological season for (a) $PM_{2.5}$ and (b) PM_{10}. Means are across passive sampling periods in 2024 to allow comparison to passive sampling measures. Seasons are shown by colour where red points indicate summer, purple points indicate autumn, blue points indicate winter, and green points indicate spring. The stations for both plots are ordered by $PM_{2.5}$ levels from highest to lowest. 608
Figure *D.6-9*: Boxplots of particulate matter measurements from low powered sensors across all low powered sites by meteorological season for (a) $PM_{2.5}$ and (b) PM_{10}. (Means are across passive sampling periods in 2024 to allow comparison to passive sampling measures. Seasons are shown by colour where red points indicate summer, purple points indicate autumn, blue points indicate winter, and green points indicate spring. The stations for both plots are ordered by $PM_{2.5}$ levels from highest to lowest. . . . 609
Figure *D.6-10*: Histograms of mean particulate matter measurements from low-power sensors across all sites by Murujuga season for (a) $PM_{2.5}$ and (b) PM_{10}. Means are across passive sampling periods in 2024 to allow comparison to passive sampling measures. Seasons are shown by colour where red points indicate Garrbarn (hot) and blue points indicate Muthu (cold) season. The horizontal axis uses a log scale. Plot (a) uses exponential notation, where e indicates "times ten to the power of". The numbers after e is the exponent. For example 1e+02 is 1×10^{2}=1 $\times$100=100, while 1e-02 is 1×10^{-2}=1 $\times$0.01=0.01 610

List of Tables

Table *1.4-1*: Analytical abbreviations and definitions. 5
Table *1.4-2*: Chemical terms. 10
Table *1.4-3*: Glossary. 10
Table *1.4-4*: Study site nomenclature. 18
Table *1.4-5*: Abbreviation codes for sample rock types. 18
Table *3.1-1*: Summary of field monitoring campaigns undertaken in the first three years of monitoring studies. 26
Table *3.2-1*: Number of *pH*, *Eh*, Cl^- and pXRF measurements on rock art panels taken for each campaign by site type. 29
Table *3.2-2*: Number of *pH*, *Eh*, Cl^- and pXRF measurements on sample rocks taken for each campaign by site type. 30
Table *3.2-3*: Number of *pH*, *Eh*, Cl^- and pXRF measurements taken on rock art panels for each campaign by rock type. Note: * indicates a repeat measurement on one rock art panel. 31
Table *3.2-4*: Number of *pH*, *Eh*, Cl^- and pXRF measurements taken on sample rocks for each campaign by rock type. 32
Table *3.2-5*: *pH* measurements made during opportunistic post-rain sampling on January 24^{th}, 2025. 38
Table *3.2-6*: Location of Group B samples. * indicates samples used for micro-CT analysis. 40
Table *3.2-7*: Collection locations of Group D samples, all samples were granophyre. 41
Table *4.1-1*: Status of analyses in the rock surface and fresher rock samples. 46
Table *4.2-1*: Summary of mineral modes for Group D dolerite samples estimated by TIMA. The zone referred to as weathered rind + patina may include some of the fresher rock. The fresher rock is the area below the weathered rind plus patina. “Holes” refers to areas identified by the TIMA as free of rock material, and may differ from the measured porosity. Estimated modes of less than 0.01% are omitted. 68
Table *4.2-2*: Summary of mineral modes for granite sample D003_GRT estimated by TIMA. The zone referred to as weathered rind + patina may include some of the fresher rock. The fresher rock is the area below the weathered rind plus patina. “Holes” refers to areas identified by the TIMA as free of rock material, and may differ from the measured porosity. Estimated modes of less than 0.01% are omitted. 69
Table *4.2-3*: Mineral modes for gabbro sample DO02_GBR estimated by TIMA. The zone referred to as weathered rind + patina may include some of the fresher rock. The fresher rock is the area below the weathered rind plus patina. “Holes” refers to areas identified by the TIMA as free of rock material, and may differ from the measured porosity. Estimated modes of less than 0.01% are omitted. 75

Table *4.2-4*: Summary of mineral modes for Group B granophyre samples estimated by TIMA. The zone referred to as weathered rind + patina may include some of the fresher rock. The fresher rock is the area below the weathered rind plus patina. “Holes” refers to areas identified by the TIMA as free of rock material, and may differ from the measured porosity. Estimated modes of less than 0.01% are omitted. 76

Table *4.2-5*: Summary of mineral modes for Group C granophyre samples estimated by TIMA. The zone referred to as weathered rind + patina may include some of the fresher rock. The fresher rock is the area below the weathered rind plus patina. “Holes” refers to areas identified by the TIMA as free of rock material, and may differ from the measured porosity. Estimated modes of less than 0.01% are omitted. 77

Table *4.2-6*: Summary of mineral modes for Group A granophyre samples estimated by TIMA. The zone referred to as weathered rind + patina may include some of the fresher rock. The fresher rock is the area below the weathered rind plus patina. “Holes” refers to areas identified by the TIMA as free of rock material, and may differ from the measured porosity. Estimated modes of less than 0.01% are omitted. 78

Table *4.2-7*: Summary of mineral modes for Group D granophyre samples estimated by TIMA. These samples do not show a weathered rind and patina so only the fresher rock is provided. “Holes” refers to areas identified by the TIMA as free of rock material, and may differ from the measured porosity. Estimated modes of less than 0.01% are omitted. 85

Table *4.2-8*: Summary of microCT measurements. 86

Table *4.2-9*: Results of oxalate and formate analyses obtained by ion chromatorgraphy 91

Table *4.3-1*: Microbiome laboratory analysis work to date. 115

Table *4.4-1*: Summary of physicochemical weathering exposures completed to date. 123

Table *7.2-1*: Summary of rock art panel measurements using the JAZ and HDX instruments in campaigns 8 to 10. 162

Table *7.2-2*: Summary of data validity from JAZ and HDX measurements for four rock art panels over all field campaigns, 1 to 10. Yes “Y” indicates all measurements were valid. “Partial (Fx)” indicates at least some measurements were valid and the number indicates the data fault type experienced. “Fx” indicates faulty data and the corresponding data fault. See above for definitions of the fault types. 163

Table *7.2-3*: For each site, campaign and target combinations are the mean and maximum absolute deviation from the median curve for the JAZ and HDX instruments. Additionally, p-values from the functional Levene’s test that compares the variability (absolute deviations from the median curve) between the two instruments. Bold p-values indicate statistically significant at the <0.05 level. 168

Table *7.2-4*: Comparison of mean trends (mean reflectance curves) between two instruments. Bold p-values indicate statistically significant at the 0.05 level.170

Table *7.3-1*: Spearman correlation estimates for IVL versus Radiello measurements of gas concentrations measured by Woodside monitoring stations by species for corresponding observations only. 176

Table *7.4-1*: Overall campaign data: start and end dates, days since last rain (before start of campaign), rain recorded during campaign, and median *pH*. . . 177

Table *7.6-1*: Number of SEM images of thin-sections, and number of distinct spatial locations, in sample Groups A and B for the porosity study. “NA” indicates locations where sample images were unusable. 208

Table *7.10-1*: p-values of the Wilcoxon rank-sum test, and Spearman correlation coefficient between samples at AQ07 and AQ08. 259

Table *7.11-1*: p-values of the Wilcoxon rank-sum test (p-value), and Spearman correlation coefficient between samples at AQ07 and AQ08. 289

Table *7.12-1*: Overall summary statistics for passive sampler data. Mean, variance, standard deviation (SD), and ratio of standard deviation to mean, for assayed concentration of each analyte in μg$/m^3$, using data from all AQM stations and sampling months. 307

Table *7.12-2*: Spearman rank correlations between gases for spatial data. For each spatial measurement location, the average gas value was determined across all sampling periods for each gas from all available IVL passive sampler assay results. Each table entry shows the correlation between gases for these average spatial values. Statistically significant correlations are shown in bold type and annotated with one, two or three asterisks representing statistical significance at the 0.05, 0.01, and 0.001 level respectively. 320

Table *7.12-3*: Spearman rank correlations between gas species for spatial temporal data. For each spatial measurement location and each month, the average gas measure was determined. Gas measures were assigned to the month in which the majority of the sampling period took place. Each table entry shows the correlation between gases for these average spatial monthly values. Values marked with one, two or three asterisks indicate results that are statistically significant at the levels 0.05, 0.01, and 0.001 respectively. 321

Table *7.12-4*: Summary statistics for duplicate measurements from passive samplers for sampling periods for 2023 and 2024. For each analyte (gas species and VOCs) is the overall mean (mean of means), estimate of residual variance, estimate of residual standard deviation (SD), residual standard deviation divided by the overall mean, and proportion of residual variability. Mean measures are in μg$/m^3$. 322

Table *7.12-5*: Calculation of raw estimates of the short-range mean square difference τ^2 between true values of gas concentrations at the sites AQ07 and AQ08. Columns give the number n of months for which paired data were available, the estimate of $\sigma^2 + \tau^2$, and the resulting estimate of τ^2 plus the ratio. 333

Table *7.12-6*: Results for the Kruskal-Wallis analysis of gas concentration by sites (AQ07 and AQ08) for matched data only. The column “total observations” gives the number of observations for a gas species across both sites, while the column ”used observations” gives the number of observations in the matched dataset across the two sites. The column Kruskal-Wallis p-value shows the strength of supporting evidence for differences between gas concentration measurements using the Kruskal-Wallis test. p-values of less than 0.05 indicate there is evidence of significant difference in values between the two stations, these values are in bold. 334

Table *7.12-7*: Results of two-way ANOVA analysis of gas concentrations by sites (AQ07 and AQ08) and meteorological seasons for matched and ranked data only. The column “total observations” gives the number of observations for a gas species across both sites, while the column ”used observations” gives the number of observations in the matched dataset across the two sites. The last three columns shows the p-value for station, meteorological seasons and the interaction between station and season. p-values less than 0.05 indicate a significant difference in values, these values are in bold. 335

Table *7.12-8*: Results of two-way ANOVA analysis of gas concentrations by sites (AQ07 and AQ08) and Murujuga seasons for matched and ranked data only. The column “total observations” gives the number of observations for a gas species across both sites, while the column ”used observations” gives the number of observations in the matched dataset across the two sites. The last three columns shows the p-value for station, Murujuga seasons and the interaction between station and season. p-values less than 0.05 indicate a significant difference in values, these values are in bold. . . . 336

Table *7.13-1*: Percentage of valid data (i.e. excluding time each powered instrument was inoperable or removed for repair at each of the powered AQM sites). 350

Table *7.13-2*: Mean NO/NO_2 and NO_2/NOx for each powered AQM site and distance to the LNG (km). Where LNG is defined as the closest of either the main Pluto or Karratha Gas Plant flare towers. 355

Table *7.15-1*: Summary of weather data for campaigns 5 to 10 (dates in brackets) from the AQM weather stations. Columns show the minimum, mean, and maximum over all AQM weather stations, for daily temperature (temp.; °C), daily relative humidity (RM; %), and daily total rainfall (mm). 413

Table *7.15-2*: Summary of BoM weather data for campaigns 1 to 10 (dates in brackets) at Dampier Port (DP), Dampier Salt (DS), and Karratha Aero (KA). Columns show the minimum and maximum temperature (temp.; °C) over all three stations, minimum and maximum relative humidity (RH; %) over all three stations, and total rainfall (mm) at each of Dampier Port (DP), Dampier Salt (DS), and Karratha Aero (KA). 415

Table *8.1-1*: Spearman rank correlation coefficients between corresponding measurements from the “dry” deposition samplers and passive samplers. Statistically significant correlations are shown in bold type, and annotated with one asterisk for $p < 0.05$, two asterisks for $p < 0.01$, and three asterisks for $p < 0.001$. 428

Table *A-1*: Compound-specific carbon isotope ratio $^{13}C/^{12}C$ ($\delta^{13}C$) for specific *n*-alkanes on the rock surface. Carbon isotope data are reported relative to the Pee Dee Belemnite (PDB) standard. 467

Table *D.2-1*: Comparison of mean trends (mean reflectance curves) between two campaigns. Bold p-values indicate statistically significant at the 0.05 level. 543

Table *D.5-1*: Results of ANOVA analysis of gas concentrations by sites (AQ07 and AQ08). The column total observations gives the number of observations for a gas species across both sites, while the column used observations gives the number observations used by a specific analysis across the two sites. The column ANOVA p-value:station shows the strength of supporting evidence for differences between gas concentration measurements. For a significance level of 0.05, p-values less than 0.05 indicate there is evidence of a significant difference in values. The constant variance and normal distribution columns indicate if key assumptions about the data for the ANOVA analysis are met or not. The Levine-Walsh test is an alternative test to ANOVA that does not assume constant variance; while the Kruskal-Wallis test is an alternative test to ANOVA that does not assume a specific distribution of the data. As before, p-values of less than 0.05 indicate there is evidence of significant difference in values between stations, these values are in bold. 572

Table *D.5-2*: ANOVA results for gas concentrations by sites (AQ07 and AQ08) and Murujuga seasons. The column total observations gives the number of observations for a gas species across both sites, while the column used observations gives the number of observations used by a specific analysis across the two sites. The three columns starting p-value show the strength of supporting evidence for differences in observations for a given factor, where p-values less than 0.05 indicate a significant difference in values, these values are in bold. The three factors are station, season, and station for each season. The final two columns indicate if two key assumptions about the data for the ANOVA analysis are met or not. 578

Table *D.5-3*: Results of ANOVA analysis of gas concentrations by sites (AQ07 and AQ08) and meteorological seasons. The column total observations gives the number of observations for a gas species across both sites, while the column used observations gives the number of observations used by a specific analysis across the two sites. The three columns starting ANOVA p-value shows the strength of supporting evidence for differences in observations for a given factor, where p-values less than 0.05 indicate a significant difference in values. The three factors are station, season, and station for each season. The final two columns indicate if two key assumptions about the data for the ANOVA analysis are met or not. . . 583

Table *D.5-4*: Results of ANOVA analysis of VOC concentrations by sites (AQ07 and AQ08) and meteorological seasons. The column total observations gives the number of observations for a gas species across both sites, while the column used observations gives the number of observations used by a specific analysis across the two sites. The three columns starting ANOVA p-value shows the strength of supporting evidence for differences in observations for a given factor, where p-values less than 0.05 indicate a significant difference in values. The three factors are station, season, and station for each season. The final two columns indicate if two key assumptions about the data for the ANOVA analysis are met or not. . . 584

1 Introduction

1.1 Background

The Murujuga Rock Art Monitoring Program (**MRAMP**) will develop Environmental Quality Criteria (**EQC**), with a focus on air quality and atmospheric deposition on or near the rock art. These EQC will be incorporated into an Environmental Quality Management Framework (**EQMF**) for the ongoing management of the Murujuga region.

This report presents a summary of the activities conducted during the third year of the program, including field work, laboratory studies, data collection and analyses. The work presented here covers the time period since the approval of the Program's *Monitoring Studies Data Collection and Analysis Plan* (**MSDCA Plan**) in March 2022, the formal start of the first fieldwork campaign. This report builds on the findings presented in the two technical reports published to date for the MRAMP research studies:

- The *Murujuga Rock Art Monitoring Program: Monitoring studies report 2023* (Curtin University, 2023), published in December 2023 following peer review.
- The *Murujuga Rock Art Monitoring Program: Monitoring studies report 2024* (Curtin University, 2024c), published in May 2025 following peer review.

This report is not intended to be a stand-alone document, rather it is intended to be read in conjunction with the *Murujuga Rock Art Monitoring Program: Conceptual Model*, MSDCA Plan, MSDCA Plan Amendment 2024b, Curtin University (2025a), and detailed methodology statements for component studies as referenced throughout.

The MSDCA Plan comprises a five-year scientific research program, and as such some components remain in progress with results not yet available. Likewise, statistical data analyses and the integration of datasets is ongoing. Section 1.3 summarises the work completed to date, and included or excluded in this report. For context, Figure *1.1-1* shows the local context including major industrial activities, study sites and (rock) sample collection sites.

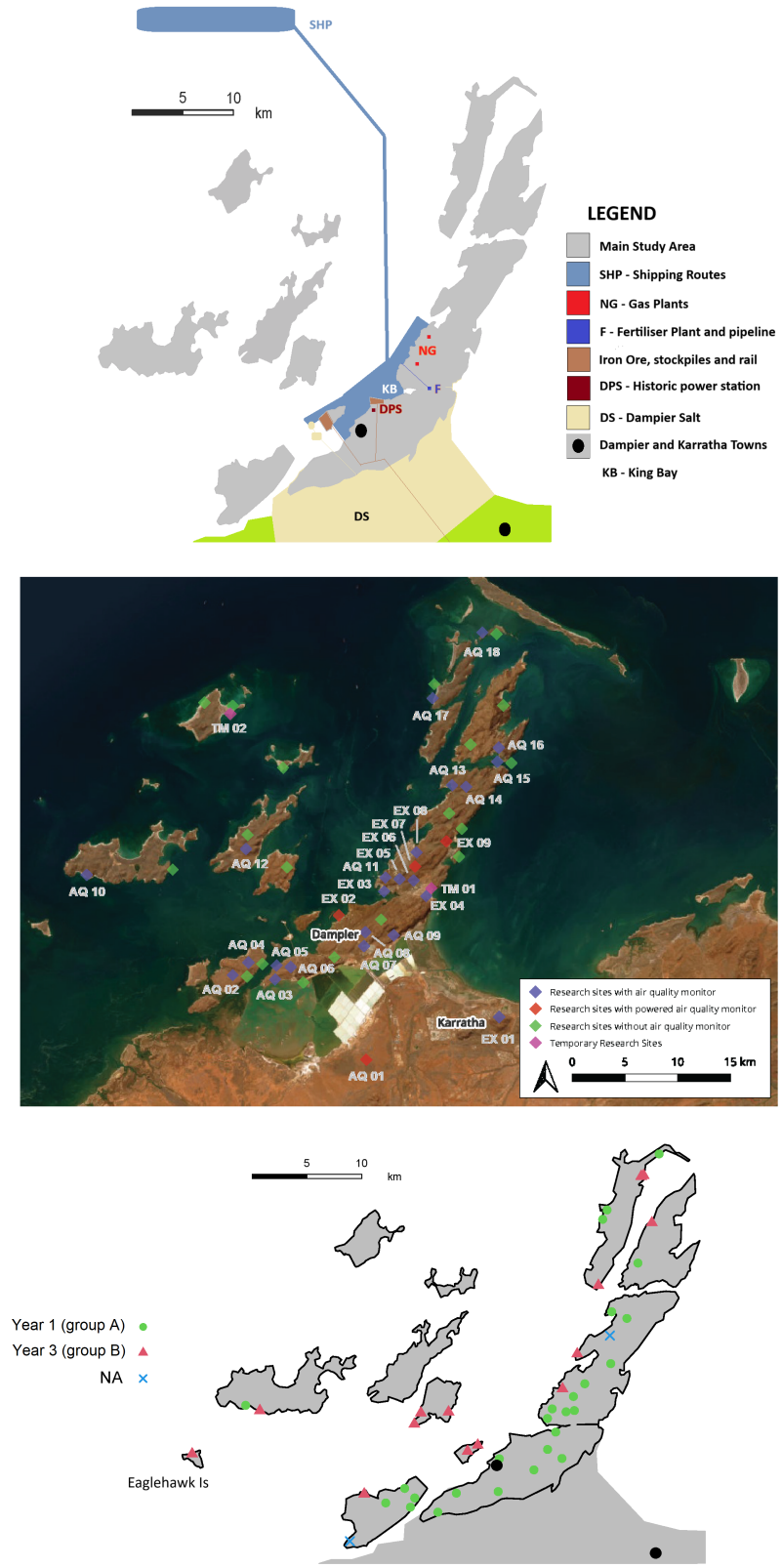

Figure 1.1-1: (a) Murujuga Region showing approximate locations of major industrial activity. (b) Map of field (rock art) monitoring sites and co-located rock art and air quality monitoring sites (labelled). (c) Locations of sample rocks collected in Years One (Group A) and Three (Group B), respectively. "NA" indicates locations of samples that did not provide usable data. Group A sample locations are within the corresponding AQ/EX/AS study squares.

1.2 Objectives of the MRAMP monitoring studies

From Section 1.3 of the MSDCA Plan (Curtin University, 2022), the main research goals of the MRAMP studies are to:

1. Measure accurately the colour and surface texture of rocks across the Murujuga region, establish baseline values for a long-term monitoring program, identify important differences in colour or surface texture that may be associated with accelerated (anthropogenic) weathering, and develop criteria for assessing weathering rates.
2. Identify and characterise the minerals, inorganic and organic chemicals, and microbes present on the rock surface and in the sub-layers, which are relevant to the appearance and integrity of the petroglyphs or may be involved in accelerating or preventing the degradation of the petroglyphs.
3. Determine which atmospheric pollutants are present in industrial (e.g., port, shipping, and local industry) and natural emissions (e.g., marine aerosols, emissions from bushfires) on Murujuga, and which are capable of causing degradation of, or change in, the petroglyphs and undertake accurate measurements of same at appropriate spatial and temporal scales.
4. Measure the effect of a known amount of pollutant chemical on the constituents of the rock surface and sub-layers. This task will be conducted under controlled laboratory conditions, using small samples of rocks (“Chamber studies”).
5. Identify the weather conditions, environmental conditions, and industrial output conditions that are most likely to pose the greatest risk of degradation to petroglyphs.
6. Calculate the timescales over which changes are predicted to occur, and thresholds of pollutants giving rise to accelerated change.
7. Identify sentinel variables (“canary in the coal mine”), which can be observed in the field and which can serve as indicators (EQC) of increased risk of degradation.
8. Determine if soil monitoring can inform about some of the processes or measurements found on the rock surface.
9. Utilise world-leading statistical design, methodology, and analysis techniques.
10. Link all the evidence obtained throughout this project to reach rigorous scientific conclusions and provide a rigorous evidence base for the Conceptual Model, the EQMF, and the Monitoring Program as a whole.

The studies conducted during this Program involve measuring and studying many aspects that will not be part of the final monitoring phase, but which must be understood in order to demonstrate links between the environmental variables and their impacts on the petroglyphs.

1.3 Scope of this report

This report summarises the outputs of all the work completed during the third year of the monitoring studies, from April 2024 to March 2025. Works still in progress are reported as such, and results will be forthcoming in the final study report.

1.3.1 Inclusions

Activities undertaken during the first three years of studies and reported here are described in the following sections.

Fieldwork

- Ten fieldwork campaigns (three in the current year, three in the second year, and four in the first year) have been undertaken, totalling approximately 40 weeks. Fieldwork involved monitoring 54 rock art panels and 64 sample rocks across the five rock types found in the study area. Sample rocks comprise the original 64 samples collected in 2022 as approved in the MSDCA Plan, and an additional 22 sample rocks collected in 2024 following endorsement of the MSDCA Amendment 2024 as well as four additional sample rocks collected from a railway cutting in 2024. These 22 rocks were selected to include any islands containing granophyre or gabbro which had not previously been sampled, adding Eaglehawk, Angel and East Intercourse to the list of sample sites as well as other locations on islands or island groups previously visited.
- All available results from this work are presented in this document.

Spectrometry:

- Over 186,200 spectral/colour measurements of rock art condition are reported on and analysed in detail.

Field X-ray fluorescence:

- Over 1,600 valid surface elemental measurements using portable X-ray fluorescence (**pXRF**) were collected and analysed.

Electrochemical measurements:

- Over 5,500 surface electrochemical measurements (*pH*, *Eh*, Cl^-) were taken, analysed in detail and examined for any correlation with air quality estimates.

AQM operation:

- Operation of the 18 solar/passive and four mains-powered air quality monitoring stations (**AQM**s) in the MRAMP network remained ongoing throughout the third year of studies. Available results and data synthesis are presented here.

Laboratory analysis

- Detailed organic chemical characterisation of patina has been completed, and the results are presented here. Detailed characterisation of some fractions of the current samples remain outstanding.
- Extensive investigation of the inorganic geochemistry of the original 64 rock samples has been undertaken. In addition, the inorganic geochemistry of the 22 additional sample rocks collected in 2024 and the four sample rocks collected from a railway cutting in 2024 has also been investigated. Key findings on the composition of the patina and weathered rind are presented in this report. The porosity findings and historical weathering has formed the basis for the determination of some of the most sensitive response variables for the chamber studies.

- The chamber studies for both geochemical weathering and microbial toxicology tests have been completed.

1.4 Abbreviations and definitions

1.4.1 Abbreviations

The abbreviations listed in Table *1.4-1* are used throughout this report.

Table 1.4-1: Analytical abbreviations and definitions.

Abbreviations	Definition
2D	Two-dimensional
3D	Three-dimensional
AGRF	Australian Genome Research Facility
AHD	Australian Height Datum
ANOSIM	Analysis of similarity
ANOVA	Analysis of variance
APT	Atom probe tomography
AQI	Air quality index
AQM	Air quality monitoring / air quality monitoring station
ASV	Amplicon sequence variants
AUSPOS	Online GPS processing service
BDL	Below detection limit
BSE	Backscattered electron
BSE-SEM	Backscattered electron scanning electron microscopy
BSFTA	O-Bis(trimethylsilyl)trifluoroacetamide
CASA	Civil Aviation Safety Authority
cDNA	Complementary DNA
CFD	Computational fluid dynamics
CIE	Commission Internationale de l'Éclairage (International Commission on Illumination)
CIELAB	The $L^*a^*b^*$ colour space defined by CIE. (Also CIELab or CIE $L^*a^*b^*$).
CSIRO	Commonwealth Scientific and Industrial Research Organisation
DBCA	Department of Biodiversity, Conservation and Attractions (Western Australia)
DEM	Digital elevation model
DBT	Dibenzothiophene
DI	De-ionised

Abbreviations	Definition
DNA	Deoxyribonucleic acid
DSM	Digital surface model
DWER	Department of Water and Environmental Regulation (Western Australia)
EA	Elemental analyser
EBSD	Electron backscatter diffraction
EC	Electrical conductivity
EDS	Energy dispersive X-ray spectroscopy
Eh	Oxidation reduction potential (see also *ORP*) relative to the potential of a Standard Hydrogen Electrode (SHE)
EMP	Electron microprobe
EQC	Environmental quality criteria
EQMF	Environmental quality management framework
F	Faraday Constant (96,500 Coulombs)
fANOVA	Functional Analysis of Variance
FR	Fresher rock, which is the rock that does not show weathering alteration.
HAADF	High-angle-annular dark-field
HDX	Ocean HDX-UV-VIS spectrometer (Ocean Insight, Orlando, 2893 Florida, United States of America), MRAMP portable spectrometer introduced for year two field observations.
HFO	Heavy fuel oil
ISA	Ionic strength adjuster
GC-irMS	Gas chromatography – isotope ratio mass spectrometry
GCxGC-TOFMS	Two dimensional gas chromatography - time of flight mass spectrometry
GC-MS	Gas chromatography – mass spectrometry
GC-TQ	Gas chromatography triple quadrupole
GNSS	Global navigation satellite systems
GSD	Ground sampling distance
CSIA	Compound specific isotopic analysis
ICP-AES	Inductively coupled plasma-atomic emission spectroscopy
IQR	Interquartile range
ISO	International Organization for Standardization
ITS	Internal transcribed spacer (genomic marker)
IVL	Stiftelsen Institutet för Vatten- och Luftvårdsforskning (Swedish Institute for Water and Air Pollution Research)

Abbreviations	Definition
JAZ	Portable spectrophotometer (Ocean Insight, Orlando, 2893 Florida, United States of America). This instrument will continue to be used for the remainder of the study programme, in order to establish adequate cross validation between the JAZ and HDX instruments, and to serve as a backup instrument in the field. However the use of the JAZ instrument will be discontinued at the conclusion of the study when the ongoing Monitoring Program is established.
JdLC	John de Laeter Centre, Curtin University. High-resolution X-ray micro-CT analysis was performed at the X-Ray Computed Tomography Facility in the JdLC.
LAM-EDS	Large area map-EDS
LOD	Limit of detection
LOEC	Lowest observed effect concentration (LOEC)
MAC	Murujuga Aboriginal Corporation
MAG	Metagenome assembled genome
MAx-DOAS	Multi AXis Differential Optical Absorption Spectrometer
MDBT	Methylated dibenzothiophenes
MP	Methylphenanthrene
MPI-1	Methylphenanthrene index
MicroCT	Micro-computed tomography
MGA2020	Map Grid of Australia 2020
MRAMP (the Program)	Murujuga Rock Art Monitoring Program
MSDCA Plan	Monitoring Studies Data Collection and Analysis Plan
NATA	National Association of Testing Authorities
NMDS	Non-metric multidimensional scaling
NOTAM	Notices To Air Missions (aviation safety alert document system)
NOEC	No observed effect concentration (NOEC)
OH, HO or OH/HO Radical	Hydroxyl radical – short lived, highly reactive chemical species formed through a reaction between UV and H_2O.
ORP	Oxidation reduction potential (mV)
P	Phenanthrene
PAHs	Polycyclic aromatic hydrocarbons
pe	Negative logarithm to base 10 of electron activity (dimensionless) $pe = F\ Eh / 2.3\ R\ T$
pH	Negative logarithm to base 10 of the hydrogen ion activity (dimensionless)
PL	Plane polarised light

Abbreviations	Definition
PM	Particulate matter
$PM_{2.5}$, PM_{10}	Particulate matter $<$ 2.5 and $<$ 10 microns (µm) aerodynamic diameter, respectively.
PCoA	Principal coordinates analysis
pXRF	Portable X-ray fluorescence
PY-GC-MS	Pyrolysis gas chromatography-mass spectrometry
QA/QC	Quality assurance and quality control
QTZ	Quartz fibre filter
R	Universal gas constant 8.314 J mol^{-1} K^{-1}
RDA	Redundancy analysis
RNA	Ribonucleic Acid
rRNA	Ribosomal RNA
RTK	Real time kinematic (processing)
SAB	Sabouraud agar
SD	Standard Deviation
SEM	Scanning electron microscope / scanning electron microscopy
SE-SEM	Secondary electron SEM images
SEM-EDS	Scanning electron microscopy with energy dispersive X-ray spectroscopy
SI	Saturation index
SOA	Secondary organic aerosol
SSM	Standard survey marks
STEM	Scanning transmission electron microscopy
STEM-EDS	Scanning transmission electron microscopy with energy dispersive X-ray spectroscopy
T	Absolute temperature in Kelvin
TDS	Total dissolved solids
TE	Tris-EDTA buffer
TEM	Transmission electron microscopy
TIC	Total ion chromatograms
TIMA	Tescan Integrated Mineral Analyser
TL	Transmitted light
TLE	Total lipid extract (mg)
TOC	Total organic carbon
ToF-SIMS	Time-of-flight-secondary ion mass spectrometry

Abbreviations	Definition
TSA	Trypton soy agar
TSP	Total suspended particulates
UAV	Unmanned aerial vehicle
UCM	Unresolved complex mixture
UNESCO	United Nations Educational, Scientific and Cultural Organization
USA	United States of America
UV	Ultraviolet light
UWA	University of Western Australia
VLOS	Visual line of sight
VOC	Volatile organic compound
vol.%	Percentage by volume of mineral, often estimated using percentage by area on a thin section
WR	Weathered rock
wt%	Percentage by weight
XPL	Cross-polarised light
XRD	X-ray diffraction
XRF	X-ray fluorescence

1.4.2 Chemical notation

The following standard chemical notation has been used in this report.

Table 1.4-2: Chemical terms.

Term	Name	Term	Name
Al	Aluminium	Mn	Manganese
As	Arsenic	Ni	Nickel
Ba	Barium	Na	Sodium
Bi	Bismuth	NO	Nitric oxide
C	Carbon	NO_2	Nitrogen dioxide
Ca	Calcium	NO_x	Oxides of nitrogen (NO + NO_2)
Ce	Cerium	N_2O_5	Dinitrogen pentoxide
CH_2O	Formaldehyde	NH_3	Ammonia
Cl	Chlorine	O	Oxygen
Cl^-	Chloride ion	O_3	Ozone
Co	Cobalt	OH^-	Hydroxide
CO	Carbon monoxide	Os	Osmium
CO_2	Carbon dioxide	P	Phosphorus
Cr	Chromium	Pb	Lead
Cs	Caesium	Pt	Platinum
Cu	Copper	Pu	Plutonium
DCM:MeOH	Dichloromethane : methanol	Rb	Rubidium
Eu	Europium	Ru	Ruthenium
Fe	Iron	S	Sulfur
Ga	Gallium	Sc	Scandium
Fe_3O_4	Magnetite	Si	Silicon
Fe_2O_3	Hematite	SiO_2	Silica
H	Hydrogen	SO_2	Sulfur dioxide
Hg	Mercury	SO_x	Oxides of Sulfur (SO_2 + SO_3)
H_2O	Water	Sr	Strontium
In	Indium	Th	Thorium
K	Potassium	Ti	Titanium
La	Lanthanum	U	Uranium
Li	Lithium	V	Vanadium
Mg	Magnesium	Y	Yttrium
N	Nitrogen	Zn	Zinc

1.4.3 Glossary

Table 1.4-3: Glossary.

Term	Definition
Airshed	A geographical region with a common flow of air or over which air pollutants are dispersed.

Term	Definition
Anthropogenic	From human activity. In the context of this research anthropogenic includes human impact, including industrial, transport, tourism, site management, and all other impact that can be attributed to human activity. It can also be considered to include distal or global human activity, which may impact the natural environment through changes in climate.
Analysis of Variance (ANOVA)	A statistical method for partitioning variance into components attributable to different sources. Estimates of these variance components can be used to test hypotheses of interest. For example, to test the hypothesis that two or more sensors have the same mean response. The key assumptions are that the data are independent, normally distributed and that each population has the same variance. Normality is typically assessed using a Shapiro-Wilk. Common population variances can be assessed using Levene's test.
Barcoding gene	A gene that is shared by a group of organisms but differs in the genetic code between species because of evolutionary changes. Sequencing analysis of these genes in environmental samples can reveal evolutionary differences between the organisms within the group. This makes it possible to classify organisms that cannot be distinguished based on morphological features.
Biofilm	A biofilm growing on a surface typically comprises a syntrophic (feeding together) consortium of microbial cells that are embedded in a slimy extracellular matrix that is composed of extracellular polymeric substances (EPS). The organisms that live close together can "communicate" with each other (share nutrients, exchange genes to make them immune to antibiotics etc.). In some cases a biofilm can comprise a single species of microbial cells, however it is not common in environmental contexts.
Biomarkers	Organic compounds produced from natural degradation of biochemicals produced by living organisms. The structure of a biomarker can sometimes be linked to a biochemical produced by a specific organism or group of organisms, while others are more general.
Bioweathering	The degradation of mineral/rock surfaces through biological mechanisms. Some examples include organic/inorganic acid production, physical alterations from hyphae growing into rock surfaces and metabolic processes resulting in the release of metals from the rock, and/or formation of new minerals.
Boxplot	The middle line (inside the box) is the median (50% of the data); the lower bound of the box is the lower quartile (first 25% of the data) and upper bound of the box is the third (75% of the data) quartile; "whiskers"(values at which the horizontal lines stop) are approximately 95% confidence interval; data points greater or lesser than the termination of the whiskers are outliers. For further details see https: //en.wikipedia.org/wiki/Box_plot
CAMx	Comprehensive air quality model, specially a multi-scale photochemical modelling system for gas and particulate air pollution.
Chemolithoautotrophic	Organisms that are able to utilise atmospheric carbon dioxide as a carbon source and utilise inorganic compounds as an energy source.

Term	Definition
Culturally Important Place / Culturally Important Site	A location that has been identified as having cultural significance to Traditional Owners and Custodians. This may be due to the existence of archaeological, ethnographic, historic, natural or social values. Such values may or may not be tied to a specific feature or geographic point in the landscape. They may include tangible or intangible features that may be tied to specific points in the landscape or may apply to a broader area or landform unit.
Cumulative campaign	Cumulative values of a parameter during a MRAMP field measurement campaign, commencing on the first day of measurements until the final day of continuous (weekdays) measurement. Typically, 35 week duration.
Cumulative monthly	Cumulative values of a parameter during a calendar month.
Data cleaning	The process of correcting or removing incorrect, corrupted, incorrectly formatted, incorrectly duplicated, incomplete or spurious data values within a dataset.
Density	A density line, often referred to as a Kernel Density Estimate (KDE) plot, provides a smoothed curve that approximates how the data are distributed. It is a non-parametric way to estimate the probability density function (PDF) of a continuous random variable based on a finite set of observed data. The KDE is constructed by placing a smooth, symmetric function (called a kernel) on each data point and then summing these individual curves. The result is a continuous curve where the area under the curve equals one. For further details see https://en.wikipedia.org/wiki/Kernel_density_estimation
Dispersion	The spreading out of emissions from a localised source (e.g. industry stack, wildfire) over a wide area due to the effect of wind.
Eh-pH	A parameter that indicates the stability of mineral or chemical systems based on the activity of hydrogen ions (*pH*) and electrons (*Eh*). These are often compared using an *Eh-pH* diagram (Pourbaix diagram).
End member	A pure chemical compound/mineral component entering into solid solution with other pure chemical compounds to form a series of minerals.
Endolithic lichens	Lichens that grow in rocks. Lichens were originally thought to occur through a symbiotic relationship of fungi and photosynthetic algae or cyanobacteria. It is currently understood that yeast and other bacterial species can also be present in the lichen consortium.
Environmental Quality Criteria (EQC)	EQC include both “Standard” and “Guideline” EQC (Environmental Protection Authority, 2016, 2017). The former represents limits above which sufficient evidence exists that impacts are likely to occur (to appropriate levels of confidence), whereas the latter represents EQC, which are set to a level where effects could theoretically occur, so as to ensure appropriate early warning such that emissions can be reduced before standards are reached. Both types of EQC may be “Interim” (preliminary), however, it is expected that EQC will be finalised in 2025/2026 (subject to periodic review). EQC may monitor dose (e.g., air pollutants) or response (rock/art) parameters.
Environmental Quality Management Framework (EQMF)	A framework to guide the assessment and management of activities related to a particular environmental value.

Term	Definition
Environmental Quality Objective	A specific management goal for a designated part of the environment that signals the level of environmental quality needed to protect the environmental value of an EQMF.
Environmental value	A beneficial use or an ecosystem health condition which requires protection from the effects of emissions or environmental harm.
Eukarya	Members of the domain Eukarya–calledeukaryotes–have membrane-bound organelles (including a nucleus containing genetic material) and are represented by five kingdoms: Plantae, Protista, Animalia, Chromista, and Fungi.
Extracellular polymeric substances (EPS)	A variety of macromolecules that are secreted by microorganisms in the environment to make biofilms.
Fermentation	The microbial enzymatic degradation of organic matter (e.g., carbohydrates) into short-chain fatty acids (notably acetic, propionic, and butyric acids) that can lower the *pH* of the patina.
Fresher rock	Rock that does not show weathering alteration.
Gene transcription	The active expression of a gene that produces an RNA copy. This can be a structural component, such as ribosomal RNA that makes up the ribosomes. Functional gene products are messenger RNA, which are translated into proteins within the ribosomes. Transcripts are indicative that the cell was alive and possibly active at the time of sampling, since RNA is much more unstable and prone to degradation than DNA. DNA survives much longer in the environment.
Heterotrophs	Heterotrophic bacteria and fungi that derive energy from organic compounds.
Histogram	A histogram is a graphical representation of continuous data used to show the distribution of values. The individual observations are grouped into intervals called bins. There are several rules for choosing bin sizes, which can influence the appearance of the histogram. Each bin is shown as a vertical bar, with the height of the bar indicating how many observations fall within that range. This helps visualize the density and shape of the data. See the definition of 'density' for further information. For further information on histograms see https://en.wikipedia.org/wiki/Histogram
Hypolithic	Microbial communities that colonise and grow below the rock surface, where they are protected against UV damage and desiccation.
Interquartile range (IQR)	Is a measure of the spread of a distribution. It is the difference between the 75th percentile (3rd quartile) and 25th percentile (1st quartile). (see also the Glossary term Quartile). It is also the width of the box in a boxplot (see above).
Levene's Test	A test for equality of variance in two or more groups. A typical example is testing for common population means using Analysis of Variance (ANOVA, see Glossary item). Levene's test is less sensitive to lack of normality than other tests.
Metagenome Assembled Genomes (MAGs)	This technique combines short environmental DNA sequences (metagenomes) to build genomes of key species present in the microbiome. Expressed genes (metatranscriptome) that are sequenced in parallel can be mapped against the assembled genomes to link these processes with the key species involved in patina formation and/or degradation.

Term	Definition
Metabolic pathways	A linked series of chemical reactions occurring within a cell. The reactants, products, and intermediates of an enzymatic reaction are known as metabolites, which are modified by a sequence of chemical reactions catalysed by enzymes. The genes involved in the individual enzymatic processes as part of the metabolic pathways and the active expression of these genes will be identified through respectively metagenomics and metatranscriptomics, as defined below.
Metagenomics	The study of sequenced genetic material in environmental samples. Depending on sequence depth, this can reveal a holistic overview of the relative abundance of all microbial genes present. In our study, this refers to microbial genes that encode for enzymes involved in processes leading to patina formation and/or degradation.
Metatranscriptomics	The study of microbial gene expression in environmental samples. Depending on sequence depth, this can reveal a holistic overview of the relative abundance of all actively expressed microbial genes present. In the MRAMP research, this refers to actively expressed microbial genes that encode for enzymes involved in processes leading to patina formation and/or degradation. Owing to the short-lived survival of gene transcripts in the environment, their presence is indicative of an active role in these processes.
Meteorological seasons	The temperate meteorological seasons for the southern hemisphere are spring (September, October, and November), summer (December, January, February), autumn (March, April, May), and winter (June, July, and August).
Microbial metabolites	A wide range of chemical compounds produced by metabolic processes of microorganisms. Primary metabolites typically include metabolites that are essential for growth (sugars and amino acids) and secondary metabolites are used for other functions such as ecological signalling and defence functions (antibiotics).
Microbiome	An integrated community of micro-organisms (bacteria, archaea, unicellular eukaryotes, and fungi) occupying a particular habitat.
Microcolonial fungi	A specific group of Fungi that are growing in microcolonial form and typically have thick cell walls and dark pigmentation. They are highly resistant against desiccation and ultraviolet damage.
Mineral assemblages	Presence and abundance of mineral species in a given spatial region (either across the rock surface or from the rock surface to the “fresh(er)” rock below the outer weathered rind).
Mode	Also referred to as ’mineral mode’. Volume percentage of a mineral within a rock. Equivalent to area percentage measured on a thin section except where the rock shows a strong anisotropic fabric (e.g., flow-orientated igneous rock, banded rock)
Murujuga	Traditional name for Burrup Peninsula and the surrounding islands of the Dampier Archipelago.
Murujuga Rock Art Monitoring Program (MRAMP)	The overall program of work to be conducted up to 2026. The program includes initial studies to inform the design of the ongoing monitoring framework, as well as the development of EQC and the EQMF.

Term	Definition
Murujuga seasons	Ngarda-Ngarli categorise seasons into two key periods – Muthu (the cold time, dry season) and Garrbarn (Yindjibarndi) / Garrwarn (Ngarluma) (the hot time, wet season) (Department of Biodiversity, Conservation and Attractions (DBCA), 2021). These seasons roughly correspond to the months of September to March for Garrbarn/Garrwarn and April to October for Muthu.
Ongoing monitoring	The ongoing monitoring refers to the longer-term monitoring program to be jointly run by MAC and DWER once the current program of works is complete (expected to commence from 2026). Also referred to as “long-term monitoring”.
Ordination	A group of statistical techniques for visualising and analysing multivariate data, which involve projecting high-dimensional data onto a two-dimensional graph so that similar data points are projected to similar positions in the graph.
Organic geochemistry	The study of organic compounds in the environment, including in rocks, sediments, soils, petroleum, aquatic environments, and the atmosphere. Organic geochemistry studies the origin of organic compounds, their transportation processes, and the alteration they undergo in the environment, over time scales ranging from the present day to hundreds of millions of years ago.
Patina	In the Murujuga context, the texture and colour of the rock surface is referred to as a patina. This is a deliberately broad definition, which encompasses the full spectrum of rock surface characterisation, including rock varnish or desert varnish. It also includes any other exposed, highly weathered rock surface and biota that may be present on the surface. The patina has been shown to form over a depletion zone, referred to as the crust or weathered rind. Weathered rind generally has a lighter appearance than both the patina and the underlying rock. An engraving is formed by breaking through the naturally formed patina to expose the lighter crust beneath. There may be cases where the engraving is deep enough to expose the underlying rock, which in this case may result in a darker engraved channel. There are many examples where a fully developed patina/varnish layer has regrown in engraved grooves. These examples are generally considered among the oldest petroglyphs for this reason.
Petroglyph	Literally “rock mark”, the term describes any cultural marking engraved on rock surfaces. The marks can be produced by a range of techniques, including pecking, pounding, incising, scratching or abrading, or a combination of two or more techniques. Techniques such as scratching can be very shallow (< 1 mm), while pecking can be from 1 mm to more than 100 mm deep. All petroglyphs at Murujuga are Culturally Important.
Photoautotrophs	Photoautotrophs are organisms that can make their own energy using light and carbon dioxide via the process of photosynthesis. Examples are cyanobacteria and green algae, known to colonise rock surfaces. Photoautotrophs are considered primary producers since their biomass can be consumed by heterotrophs (defined above) as a source of carbon and energy.
Photolysis	The process by which molecules are broken into small fragments by exposure to sunlight (typically UV radiation).

Term	Definition
Photospectrometry	An instrumental technique for measuring the chromatic reflectance of a surface by scanning at frequencies that cover the visible spectrum and beyond. Photospectrometry provides both a single value colour designation and spectral data that can indicate non-chromatic change. The technique has been applied to both the measurement of change and the characterisation of unknown minerals and compounds.
Primary producers	See definition of “photoautotrophs”.
p-value	A statistical measure used in evaluating the strength of evidence for a hypothesis. First a “null hypothesis” is formulated. The p-value is defined as the probability of obtaining data at least as extreme as the data that were obtained, where this probability is calculated under the assumption that the null hypothesis is true. A small p-value is interpreted as evidence against the null hypothesis, because if the p-value is very small, then “either something very unlikely has happened, or the null hypothesis is false”. In this report, following standard conventions, a p-value < 0.05 is deemed ‘statistically significant’ evidence against the null hypothesis.
Quartile	The quartiles are three numbers which divide a sorted set of data values into four equal segments. The first quartile is the value which has one-quarter of the data below it and three-quarters lies above it. The second quartile is also the median, lying above half the values and below the other half. The third quartile lies above three-quarters of the values and below one-quarter.
Secondary organic aerosol (SOA)	Solid or liquid organic molecules produced in the atmosphere by the reaction of smaller, gaseous organic molecules with oxygen (and often ozone and UV / OH radicals).
Shapiro-Wilk test	A test used to assess if data are normally distributed or not. A typical example is testing if the data in each group is normally distributed before using Analysis of Variance (ANOVA, see Glossary item).
Stable isotopes	Atoms of the same element which contain a different number of neutrons in the nucleus. Most elements consist of more than one stable isotope, the ratios of which can be measured using specialised instrumentation. Stable isotope ratios in organic compounds are affected by the processes of formation and alteration, hence their measurement gives information on source and alteration history.
Weathered rind	The portion of the rock between the surface (patina) layer and the fresher inner rock. This layer is sufficiently close to the surface to have interacted with oxygen or other environmental conditions. The weathered rind is significantly thicker than the surface patina layer and has a different colouration to the underlying fresher rock (core).

Term	Definition
Weathering	In the Murujuga context, the concepts of weathering are differentiated as natural weathering and accelerated/anthropogenic weathering, which may be termed “degradation” to distinguish it from natural weathering. However, these effects may be difficult to decouple. • Natural Weathering: the alteration of a rock surface through natural agents such as the impacts of temperature cycles, microbial activity, and interactions with water and aerosols/gases released by the surrounding (natural) terrestrial and marine environments. Weathering may be subtractive (erosion) or additive (mineral formation or accretion). • Accelerated weathering: degradation due to anthropogenic activity over and above the rate of natural weathering.

1.4.4 Site and sample numbering nomenclature

Study sites

Study sites are generally identified with an alphanumeric code in the format:

AABB

where:

- AA is a two letter code indicating the type of study site, as described in Table *1.4-4*.
- BB is a two digit sequential number derived from the study design outputs (MSDCA Plan Appendix I and Appendix II).

The exception to this standard nomenclature is study site “AQA1”, which was added to the Program during the course of the first year of scientific studies and designates the MAC Office AQM.

Sample rocks

Sample rocks are identified with an alphanumeric code in the format:

AABB_CCC

where:

- AA is a two letter code indicating the type of study site as described in Table *1.4-5*.
- BB is a two digit sequential number derived from the study design outputs (MSDCA Plan Appendix I and Appendix II).
- CCC is the rock type as defined in Table *1.4-5*.

Rock art panels

Rock art panels are referred to in the same manner as the host rock. Where a study square includes more than one rock art panel on the same rock type, a numeral will be added after the rock type to differentiate between the art panels (e.g., RS10_GPH1).

Table 1.4-4: Study site nomenclature.

Site code	Numbering	Count	Name	Descriptor
AQ	01 to 18	18	Air quality	Study squares where new MRAMP air quality monitors are installed. AQ01 is a mains powered station.
AQA	1	1	Air quality additional	Designation given to the location of the initial field prototype AQM installed at the MAC Office.
AS	01 to 02	2	Additional sample	Study squares providing targeted samples of rare rock types.
EX	01 to 09	9	Existing (AQM)	Study squares with existing industry or government air quality monitors, both solar or passive and mains powered. EX02 was a decommissioned mains powered monitoring station which has been replaced by MRAMP, EX07 is a mains powered industry monitoring station which contains additional equipment owned by MRAMP and operated on our behalf by an independent contractor, EX09 contains an industry solar or passive station and an MRAMP powered station.
RS	01 to 18	18	Representative sample	Study squares without AQMs, where field observations and sample collection occur to form a rigorous representative sample of the entire Murujuga region.
TM	01 to 02	2	Temporary AQM	1) the north end of Hearson's Cove and 2) Rosemary Island.
Total		**50**		

Table 1.4-5: Abbreviation codes for sample rock types.

Rock type code	Descriptor
BAS	Basalt
DOL	Dolerite
GBR	Gabbro
GBP	Polished gabbro
GPH	Granophyre
GPHC	Granophyre coarse crystal size
GPHF	Granophyre fine crystal size
GPHP	Polished granophyre
GRT	Granite

2 Study methodologies, verification of competency, and quality assurance

2.1 Elaboration of methodologies described in the MSDCA plan

Full methods have been prepared as separate documents and provided to DWER. For the current report, the following methodology documents are applicable:

- COPP21065-PRO-G-102 Murujuga Rock Art Monitoring Program: Passive Air Quality Monitoring (AQM) Installation and Commissioning [unchanged from previous study years]
- COPP21065-PRO-G-103 Murujuga Rock Art Monitoring Program: Passive AQM Sample Collection, Maintenance, and Context Observations [unchanged from previous study years]
- COPP21065-PRO-G-104 Murujuga Rock Art Monitoring Program: Powered Air Quality Monitor Installation and Commissioning [unchanged from previous study years]
- COPP21065-PRO-G-105 Murujuga Rock Art Monitoring Program: Unmanned Aerial Vehicle and Spatial Mapping [unchanged from previous study years]
- COPP21065-PRO-G-106 Murujuga Rock Art Monitoring Program: Inorganic Monitoring (pH and Portable X-Ray Fluorescence) [unchanged from previous study years]
- COPP21065-PRO-G-107 Murujuga Rock Art Monitoring Program: Microbiome Field Sample [unchanged from previous study years]
- COPP21065-PRO-G-110 Murujuga Rock Art Monitoring Program: Photospectrometric Colour Change Measurement [unchanged from previous study years]
- COPP21065-PRO-G-111 Murujuga Rock Art Monitoring Program: Field Permeameter [unchanged from previous study years]
- COPP21065-PRO-G-113 Murujuga Rock Art Monitoring Program: Organic Geochemistry of Rock Surfaces, Dust and Particulates [updated during the current study year]
- COPP21065-PRO-G-114 Murujuga Rock Art Monitoring Program: Inorganic Geochemistry Laboratory Analysis [unchanged from previous study years]
- COPP21065-PRO-G-117 Murujuga Rock Art Monitoring Program: Chamber Exposure Studies [unchanged from previous study years]
- COPP21065-PRO-G-118 Murujuga Rock Art Monitoring Program: Powered AQM Operations, Procedures and Observations [unchanged from previous study years]

2.2 Personnel and verification of competency

All personnel are appropriately trained and/or supervised in all methods relevant to their work prior to start of any task or activity.

In most cases, this training, supervision, and certification is undertaken by the lead researcher in each discipline or by the relevant facility/laboratory/instrument manager. Training for each discipline or activity is detailed in the relevant methods documents.

A key component of this project is to train the MAC Rangers in all relevant skills and methods required to undertake ongoing monitoring under the EQMF, and a series of five "Curtin Credentials" have been created for this purpose. These are modelled on other Curtin University Credentials developed for Indigenous ranger training. Credentials represent a body of work approximately 1/5th of a typical university unit (subject) of study, therefore all five are the equivalent of one university level unit or 1/24th of a typical Bachelor level degree. The Credentials developed for MRAMP are:

- Passive Air Quality Monitoring
- Introduction to Workplace Health and Safety
- Real time Air Quality Monitoring
- Geology and Geochemistry for Rock Art Monitoring (in progress).
- Rock Art Surface Monitoring (under development).

Rangers have completed qualifications in the first three credentials, with fourth in progress by the rangers (at the time of writing) and the fifth due for release before mid 2026.

2.3 Quality assurance

Extensive calibration, validation, and quality assurance controls have been developed for all measurements and study components. These are detailed in the respective methodologies.

Some of the key protocols are summarised below.

2.3.1 Air quality monitoring

Passive sampler deployment occurs in duplicate at each AQM and utilises multiple field blanks as per best practice. Samples are analysed by IVL (Sweden) under International Organization for Standardization (**ISO**) certification (EN ISO IEC 17025:2017 *General Requirements for the Competence of Testing and Calibration Laboratories*) equivalent to the Australian National Association of Testing Authorities (**NATA**) certification standard.

Deposition samples are analysed by the NATA-accredited ChemCentre (who hold NATA accredited ISO/IEC 17025 (2017) certification for most analyses) following their chain of custody, documented blank, calibration, and validation protocols for each method. Type 1 ultrapure water used in the methods has been obtained from the ChemCentre. Blank samples of ultrapure water are returned with each set of measurements.

Powered AQMs use a suite of real-time instruments meeting the requirements of relevant Australian Standard AS3580: *2023 Methods of Sampling and Analysis of Ambient Air* and United States Environmental Protection (USEPA) standards for ambient air monitoring. These instruments are subject to zero and span calibrations at a minimum of four-weekly intervals, to ensure reliable results for research purposes. The data collected from these instruments together with the data from the co-located passive samplers will be used by the statistical team to develop robust region- and climate-specific calibrations for the low power samplers in the passive AQMs.

2.3.2 Fieldwork

Spectrometry methods utilise thin films with known properties to undertake instrument calibrations at least once per rock art panel. The statisticians working on this project have developed a set of rigorous protocols and criteria for quality assurance and quality control (**QA/QC**) checking of data. These protocols have been automated and applied in the field in real-time.

The pXRF instrument used for geological fieldwork contains an internal calibration standard and is calibrated each time it powers on. In addition, standard reference materials are measured twice per day, and the results are recorded.

The equipment used for *pH*/*Eh*/Cl^- measurements is calibrated at least twice per day using known reference solutions. Ultrapure water is supplied by the ChemCentre and is the same water used for AQM sample processing. Field blanks are tested twice per day, and additional blanks are sent back to the ChemCentre each month for *pH* testing.

2.3.3 Laboratory analysis

All laboratory measurements utilise blanks and reference standards as per best practice. All instruments and equipment are serviced and calibrated according to manufacturer's protocols.

2.3.3.1 Quality assurance of SEM microanalysis data

Scanning electron microscopy (**SEM**) is an analytical technique used to obtain high-resolution images and elemental analyses of a sample's surface. QA/QC is an essential aspect of the analysis of SEM microanalysis data to ensure that the data obtained are reliable and accurate.

The protocol for the QA/QC of SEM microanalysis data involves:

- Instrument calibration
  The SEM instrument is calibrated regularly to ensure the accuracy of the data. Calibration includes the electron beam energy, beam current, and magnification. Instrumentation used in this study is regularly calibrated and analysis conditions are standardised.
- Sample preparation
  Proper sample preparation is crucial for obtaining accurate and reliable data. Samples are cleaned using ultrapure compressed air or water, as appropriate, to remove any surface contamination. They are also handled with care to avoid any alteration. If appropriate, samples are prepared and fixed in resin to ensure their integrity during the analysis process.
- Reproducibility
  To ensure the reproducibility of the data, multiple measurements of the same sample or replicate measurements of different samples are taken under the same experimental conditions.
- Data analysis
  The SEM microanalysis data are analysed using appropriate statistical methods to identify significant differences between the samples. Data are also validated using complementary techniques such as Time-of-flight secondary ion mass spectrometry (**ToF-SIMS**), X-ray diffraction or XRF.
- Quality control

To ensure the quality of the data, the SEM microanalysis data are checked for outliers, systematic errors, and other sources of variability. Data are reviewed by experts in the field to identify any potential issues or limitations.

2.4 Review of Literature

This section presents a limited review of relevant literature published since the completion of the Monitoring Studies Report 2024 (Curtin University, 2024c) or discovered through additional literature searches in response to previous findings.

2.4.1 Weathering studies and estimates for other sites

Previous literature searches have generally been limited to studies conducted at Murujuga or other comparable petroglyph sites, and relevant technical literature (e.g., rock *pH* measurement methods (Aho and Weaver, 2006)). However, literature searches have since been broadened to examine other recently published literature, in addition to continuing to review new research relevant to Murujuga petroglyphs or rock types.

Broomandi et al. (2022) and Spezzano (2021) have recently published comparative weathering rate studies for heritage sites around the world, which develop site specific cumulative weathering rates for rock/stone, concrete and metals based on combined air quality, rainfall and climate data.

Many of the global sites examined by Broomandi et al. (2022) and Spezzano (2021) have higher levels of air pollutants compared to those measured by MRAMP at Murujuga. Particularly NO_2, with some cites reported by Broomandi et al. (2022) and Spezzano (2021) having average levels up to 100 times higher. The works have developed combined/additive relationships for gas species and other air pollutants based on Henry's law (Hites and Raff, 2012), which relates to the solubility and reactivity of weak gas mixtures. This has primarily considered their solubility in water and influence on rainfall *pH* (Singh et al., 2016), however an adaptation or variation of this approach may be appropriate to permit determination of combined weathering rates at Murujuga under both wet and dry conditions. The benefit of this approach is that it permits the impact of multiple air pollutant species combined into a single weathering parameter. The application of Henry's Law as a basis also appears to be supported by single species chamber studies presented in this report.

2.4.2 Weathering studies using Murujuga rock samples

Dr Neuman and his Masters and Doctoral supervisor Prof Geisler have done some high quality weathering studies over a number of years on rock samples from Murujuga (Neumann et al., 2022). The most recent output from this group is discussed below ((Neumann, 2025)). The insights from the research are useful and many of the methods are complementary to MRAMP. In particular, the Raman patina mineralogy studies (see Figures 3.8 - 3.11), however some caution should be used based on the small sample sizes and the reliance on the Raman technique only for mineral identification.

Sample sizes are grossly underpowered to draw any meaningful conclusions regarding 'comparison with older [single] varnish sample from 1994'. For comparative purposes, MRAMP data from a

single site/sample (e.g., AQ11) has Mn levels which span the whole range presented by Neumann (2025).

The chamber/accelerated weathering studies in the work also utilised a relatively small sample size and a *pH* value of 5.0 with a control of *pH* 7.0. This simulated "acid rain" (*pH* 5.0) may be a reasonable representation of 2005-2009 conditions at Murujuga, based on the CSIRO 2010 measurements, however does not appear to be relevant to current conditions. The findings for weathering rates at *pH* 5.0 are however consistent with Broomandi et al. (2022); Spezzano (2021) and further add to the evidence of historic accelerated weathering under lower *pH* conditions which are no longer present.

Interestingly, some samples became darker (Neumann (2025), p153) during weathering experiments, which was attributed to removal of an overlying Fe-rich layer, however may also have been due to microbial activity after the addition of water to the system.

Microbial studies were also undertaken, however were limited to one gabbro rock and one granophyre rock, sampled three times over a year with the 16S amplified (Neumann, 2025). It is unclear if triplicate extractions were conducted - or sequenced in triplicate. Either way, the sample size and statistical power are insufficient for meaningful conclusions, particularly with respect to weathering effects.

The overall microbial profile is similar to MRAMP data - Rubrobacter and Geodermatophlius being the most abundant genera. There is, however a lack of cyanobacteria in Neumann's (2025) samples. The research shows almost no change in the microbiome over the year in granophyre between acidic and neutral conditions. Gabbro on the other hand does show a change in microbiome between acidic and neutral conditions - however the beta diversity indicates the acidic microbiome is closely related to the day zero samples over the neutral samples. Gabbro sees an increase in relative abundance of Rubrobacter and Geodermatophilus in the acidic samples - however they were already quite high, and other than Deinococcus, other genera are not apparent. Explanations for the microbiome results are very brief and unsupported by literature citations. The claim that "The stability observed on the granophyre may be linked to its more stable mineralogical properties, which could provide a consistent microhabitat for microbial colonization.", is not explained nor supported by evidence (Neumann, 2025). The work states that "Pairwise comparisons indicated that acidic treatments of gabbro samples differed significantly from neutral and day zero samples, further emphasizing the impact of pH on microbial community structure." however information on the statistical analysis is not provided and from the principal coordinates analysis (**PCoA**) a significant difference between zero and acidic day five would be surprising. Furthermore Neumann (2025) did not report on the significance of the difference between the day zero and neutral samples.

MRAMP data does not show a significant difference in microbiome composition between rock types, based on a sample size almost two orders of magnitude larger, which further emphasises the methodological flaw in using only one sample each of two rock types.

If any valid conclusions can be drawn from this component of the Neumann (2025) study, it would appear to indicate that *pH* 5.0 is not impacting the microbiome significantly. However, again the caveat of insufficient sample size must be applied to any interpretation. It may also be possible, given MRAMP observations of rock surface *pH*, that this lies in the range of *pH* preferred by the microbiome, given the higher *pH* of (current) wet and dry deposition.

The accelerated geochemical weathering argued by Neumann (2025) at *pH* 5.0 is however plausible based on the research discussed in Section 2.4.1. However, it should be noted that, as shown in Section 7.10.7, *pH* 5.6 is the lowest recorded in rainfall samplers over the past 3 years at Murujuga, with intermittent values lower than this recorded in deposition samplers, possibly due to natural phenomena.

3 Monitoring studies undertaken in the field

This section reports on the monitoring studies that were undertaken in the field in the third year of MRAMP research.

- Section 3.1 provides general information about the field monitoring work.
- Section 3.2 covers the inorganic chemistry fieldwork.
- Section 3.3 reports on the colorimetry fieldwork.
- Section 3.4 summarises the microbiological field sample collection work completed.

3.1 Field monitoring generally

3.1.1 Location of field monitoring sites

Figure *1.1-1*b) shows the location of field monitoring sites arising from the site selection process undertaken previously during development of the MSDCA Plan (Curtin University, 2022). All sites and artifacts included in the Program were approved by the Murujuga Aboriginal Corporation's Circle of Elders prior to commencement of the monitoring studies.

3.1.2 Summary of field campaigns in the first three years of studies

Table *3.1-1* outlines the ten fieldwork campaigns included in the first three years of monitoring studies.

Fieldwork campaign dates were selected to correspond with wet, dry, and shoulder seasons, to create an understanding of the effect of seasonal changes. Historically, long-term peak rainfall occurred during February and the lowest rainfall levels were recorded during October. A secondary rainfall peak occurs frequently during May-July and may be the dominant peak when cyclone-driven rain does not occur during January-March.

For the purposes of the project field works, the February-April campaigns are referred to as wet season campaigns, the June-July campaigns as dry season, and the October-November campaigns as shoulder season. Note that this naming convention is purely for convenience, and any analysis considers actual temperature and rainfall.

Table *3.1-1* does not include:

- Collection of additional sample rocks undertaken in 2024. This information is provided as part of the inorganic geochemistry discussion in Section 3.2.
- Microbial sampling from the additional railway cutting sample rocks. This information is provided as part of the microbiological sample collection discussion in Section 3.4.
- Inorganic and microbiological sampling of AQM rock cubes. This information is provided as part of the discussion in Section 3.2 and 3.4, respectively.
- Sample collection from the MRAMP AQM network. This information is provided as part of the air quality monitoring discussion in Section 5.

Table 3.1-1: Summary of field monitoring campaigns undertaken in the first three years of monitoring studies.

Campaign no.	Date	Inorganic geo-chemistry	Colour monitoring	Organic/Microbiome	Vegetation collection	Spatial mapping	Ad hoc (fire)
1	08 Mar - 08 Apr 2022	Y	Y	Y	Y	-	-
2	20 Jun - 29 Jul 2022	Y	Y	Y	Y	Y	-
3	10 Oct - 04 Nov 2022	Y	Y	-	-	Y	-
4	27 Feb - 24 Mar 2023	Y	Y	-	-	-	-
5	03 Jul - 21 Jul 2023	Y	Y	-	-	-	Y
6	23 Oct - 17 Nov 2023	Y	Y	-	-	-	-
7	26 Feb - 21 Mar 2024	Y	Y	-	-	-	-
8	01 Jul - 26 Jul 2024	Y	Y	-	-	-	-
9	14 Oct - 07 Nov 2024	Y	Y	-	-	-	-
10	24 Feb - 21 Mar 2025	Y	Y	-	-	-	-

Note that some of the campaign dates listed in Tables 3.1-1 in Monitoring Studies Report 2024 (Curtin University, 2024c) were wrong due to typographical errors. These dates have now been corrected.

3.2 Inorganic geochemistry fieldwork

3.2.1 Objectives

The objectives of the inorganic geochemistry fieldwork that took place between April 2024 and March 2025 were to:

1. Continue to monitor visual characteristics (approximate colour, roughness, lustre, patina thickness) and electrochemical parameters (*Eh*, *pH*, chloride ion concentration) on all rock art panels listed in Table *1.4-4*.

2. Optimise field protocols to effectively measure the condition and characteristics of the rock art panels included in the study (see Table *1.4-4*).

3. Collect additional sample rocks for laboratory testing to confirm previous findings on spatial variation in rock surface porosity.

4. Assess whether it was possible to develop a non-destructive field measurement that correlated to the rock surface porosity measurements observed in (destructive) laboratory testing.

3.2.2 Methodology

Inorganic geochemistry fieldwork in the third year of studies involved:

1. Additional sample rock collection for laboratory analysis (see Section 3.2.4.6).
2. Elemental surface analysis of the rock art panels using a portable X-ray fluorescence (**pXRF**) device (field campaign 8).
3. Measurements of *Eh*, *pH*, and chloride ion concentrations on the surface of the selected rock art panels (campaigns 8, 9, and 10).
4. Field permeability measurements (campaigns 8, 9, and 10, see Section 3.2.4.3).
5. Measurement of the permeability, *pH*, and elemental composition of the surfaces of rock cubes located within the AQMs (see Section 3.2.4.7).

Section 3.2.4 of the MSDCA Plan (Curtin University, 2022) provides details of the inorganic geochemistry field methodologies employed. Further detail is provided in the following component study methodology statements:

- COPP21065-PRO-G-106 Murujuga Rock Art Monitoring Program: Inorganic Monitoring (pH and Portable X-Ray Fluorescence)
- COPP21065-PRO-G-115 Murujuga Rock Art Monitoring Program: Sample Rock Collection
- COPP21065-PRO-G-111 Murujuga Rock Art Monitoring Program: Field Permeameter

3.2.3 Modifications to fieldwork methodology

Some modifications to fieldwork techniques and protocols were made to optimise the value of the data collected. These modifications included:

1. Changes to electrochemistry protocols - The electrochemistry protocols were modified to use an ionic strength adjuster (**ISA**) for analysis of *pH* and chloride ion concentration. The *pH* and chloride ion probes respond slowly in very diluted solutions, such as those produced by current methods, and the addition of an ISA increases the speed and precision of the response. Updates to the method are incorporated into COPP21065-PRO-G-106.
2. Discontinuation of pXRF - Monitoring by pXRF was discontinued after the end of campaign 9. Analysis of the uncertainties of these results indicated that the magnitude of a signal expected from changes in the rock patina composition is likely to be indistinguishable from analytical error (Section 7.5).
3. Introduction of new measurements - Permeability measurements were introduced to corroborate and test the finding of spatially variable rock porosity reported in the Monitoring Studies Report 2024 (Section 7.7, of Curtin University, 2025). Permeability is related to porosity, although the two parameters are not identical. Permeability was measured using a TinyPerm permeameter. The permeameter was initially deployed, tested, and methods developed during campaign 8. This methodology was applied during campaigns 9 and 10.
4. Collection of new samples - Water samples were collected for oxalate and formate analysis to establish whether these solutes can be detected in solutions collected from rock surfaces.

Ten millilitre samples were collected using the electrochemistry protocols described in COPP21065-PRO-G-106, slightly modified to use 25 mm (diameter) collection tubes. Samples were equilibrated with the rock for two minutes to maintain consistency with other field measurement protocols.

5. Testing of new equipment - A new model of the field monitoring equipment, the TPS Ranger, was tested against the current model (TPS WP90) during campaign 10. After three years and ten field campaigns, much of the electrochemistry field monitoring equipment is reaching the end of life.

3.2.4 Fieldwork activities

The reporting time period used here includes:

- Campaign 8 (2 – 26 July 2024);
- Campaign 9 (14 October – 7 November 2024);
- Campaign 10 (24 February – 24 March 2025).

3.2.4.1 Surface analysis by portable X-ray fluorescence spectrometer

A total of 75 and 109 measurements by pXRF were taken during campaigns 8 and 9, respectively (Tables *3.2-1* and *3.2-3*). Monitoring by pXRF was discontinued for campaign 10 after data analyses indicated that the magnitude of a signal expected from changes in the rock patina composition is likely to be indistinguishable from analytical error (Section 7.5).

Table 3.2-1: Number of pH, Eh, Cl^- and pXRF measurements on rock art panels taken for each campaign by site type.

Campaign no.	Site type	Number of measurements on rock art			
		pH	***ORP* (*Eh*)**	**Chloride**	**pXRF**
1	AQ	69	0	36	66
	AS	6	0	6	12
	EX	27	0	21	30
	RS	53	12	35	62
2	AQ	66	66	66	66
	AS	9	9	9	9
	EX	27	27	27	27
	RS	60	60	60	60
3	AQ	66	66	66	66
	AS	9	9	9	9
	EX	27	27	27	27
	RS	60	60	60	60
4	AQ	69	69	69	69
	AS	9	9	9	9
	EX	27	27	27	27
	RS	60	60	60	60
5	AQ	66	66	66	66
	AS	9	9	9	9
	EX	27	27	27	27
	RS	21	21	21	21
6	AQ	66	66	66	66
	AS	9	9	9	9
	EX	27	27	27	27
	RS	18	18	18	18
7	AQ	66	66	66	66
	AS	9	9	9	9
	EX	27	27	27	27
	RS	21	21	21	21

Campaign no.	Site type	Number of measurements on rock art			
		pH	***ORP* (*Eh*)**	**Chloride**	**pXRF**
8	AQ	66	60	60	30
	AS	9	9	9	9
	EX	27	27	27	15
	RS	24	18	18	21
9	AQ	66	66	41	66
	AS	9	9	2	9
	EX	27	27	6	27
	RS	21	21	12	21
10	AQ	66	66	64	0
	AS	9	9	9	0
	EX	27	26	23	0
	RS	30	30	30	0

Table 3.2-2: Number of pH, Eh, Cl^- and pXRF measurements on sample rocks taken for each campaign by site type.

Campaign no.	Site type	Number of measurements on sample rocks			
		pH	***ORP* (*Eh*)**	**Chloride**	**pXRF**
1	AQ	66	2	36	63
	AS	6	0	6	12
	EX	24	0	24	30
	RS	81	10	49	87
2	AQ	63	63	63	63
	AS	9	9	9	9
	EX	27	27	27	27
	RS	87	87	87	87

*Table 3.2-3: Number of pH, Eh, Cl^- and pXRF measurements taken on rock art panels for each campaign by rock type. Note: * indicates a repeat measurement on one rock art panel.*

Campaign no.	Site type	Number of measurements on rock art			
		pH	***ORP* (*Eh*)**	**Chloride**	**pXRF**
1	BAS	11	2	9	12
	DOL	15	0	12	15
	GBR	39	3	20	36
	GPH	87	7	54	98
	GRT	3	0	3	9
2	BAS	12	12	12	12
	DOL	15	15	15	15
	GBR	39	39	39	39
	GPH	90	90	90	90
	GRT	6	6	6	6
3	BAS	12	12	12	12
	DOL	15	15	15	15
	GBR	39	39	39	39
	GPH	90	90	90	90
	GRT	6	6	6	6
4	BAS	12	12	12	12
	DOL	15	15	15	15
	GBR	39	39	39	39
	GPH*	93	93	93	93
	GRT	6	6	6	6
5	BAS	6	6	6	6
	DOL	12	12	12	12
	GBR	27	27	27	27
	GPH	72	72	72	72
	GRT	6	6	6	6
6	BAS	6	6	6	6
	DOL	12	12	12	12
	GBR	24	24	24	24
	GPH	72	72	72	72
	GRT	6	6	6	6
7	BAS	6	6	6	6
	DOL	9	9	9	9
	GBR	30	30	30	30
	GPH	72	72	72	72
	GRT	6	6	6	6

Campaign no.	Site type	Number of measurements on rock art			
		pH	***ORP* (*Eh*)**	**Chloride**	**pXRF**
8	BAS	9	6	6	9
	DOL	15	12	12	12
	GBR	27	27	27	12
	GPH	69	63	63	39
	GRT	6	6	6	3
9	BAS	3	3	3	3
	DOL	9	9	4	9
	GBR	27	27	17	27
	GPH	78	78	33	78
	GRT	6	6	4	6
10	BAS	6	6	6	0
	DOL	9	9	9	0
	GBR	36	36	35	0
	GPH	75	74	70	0
	GRT	6	6	6	0

Table 3.2-4: Number of pH, Eh, Cl^- and pXRF measurements taken on sample rocks for each campaign by rock type.

Campaign no.	Site type	Number of measurements on sample rocks			
		pH	***ORP* (*Eh*)**	**Chloride**	**pXRF**
1	BAS	18	1	10	18
	DOL	21	0	21	21
	GBR	36	3	18	36
	GPH	87	8	60	93
	GRT	15	0	6	21
2	BAS	18	18	18	18
	DOL	24	24	24	24
	GBR	33	33	33	33
	GPH	93	93	93	93
	GRT	18	18	18	18

3.2.4.2 Electrochemistry measurements (*pH*, *Eh*, electrical conductivity, and chloride ion concentrations)

A large number of *pH*, *Eh*, and chloride ion concentration measurements were obtained during campaigns 8, 9, and 10, to complement those measured in earlier campaigns (Tables *3.2-1* to *3.2-4*). Measurement were taken on the rock art panels and on the rock cubes that are mounted within the AQMs. Spatial and temporal variability in these measurements are discussed in Section 7.4. The rock cube data are discussed in Section 7.4.6.

The latest generation of field monitoring equipment, the Ranger from TPS (https://tps.com.au/pro

ducts/ranger), has a number of advantages relative to the WP90 model used for campaigns one to nine that motivated it's evaluation as a candidate for long-term MRAMP monitoring:

- The Ranger is a waterproof ruggedised instrument. The WP90 is also supposed to be waterproof but suffered on accidental immersion.
- Relative to the WP90, the Ranger yields better response times for low ionic strength solutions, has a simpler set-up protocol and is easier to use in the field, because three probes can be connected and read simultaneously. This approach saves time and reduces the possibility of errors related to connecting and disconnecting the probes continuously. It also reduces wear and tear of the probes related to frequent connection and disconnection (cable breakage at the connection point is one of the most common faults experienced with the current equipment).
- Each of the Ranger probes has an integrated temperature sensor, reducing temperature uncertainties. The WP90 uses a separate temperature sensor.
- Charging and data transfer are simpler with the Ranger, compared with the WP90, so the instrument is suitable for use by field personnel with a wide range of skills and experience.

The Ranger was tested against the existing TPS WP90 and associated probes between the 8th and 21st March during campaign 10 (Figure *3.2-1*). For *pH*, 26 measurements were repeated. The measurements included the three *pH* samples taken from each rock surface at sites AQ17 (GPH), AQ12 (BAS), AQ04 (GPH), and AQ02 (GPH), surface water samples from sites AQ09 and AQ12, and mixtures of deionised water plus the ionic strength adjuster. Fifteen measurements were repeated for *ORP*. For each repetition, the sample was collected as usual and measured with either the WP90 or the Ranger equipment. Within a few minutes of the measurement, the same sample was measured with the second instrument, using the same methods to cover duration of measurement, addition of ionic strength adjuster, and other details as described in COPP21065-PRO-G-106.

Comparison of the chloride ion (Cl^-_{aq}) concentration is complicated by non-availability of a chloride ion selective electrode for the Ranger instrument. Electrical conductivity (**EC**) electrodes are available instead. Electrical conductivity increases with chloride ion concentration but the two measurements are not equivalent. The ion selective electrode for chloride measures the concentration of chloride ions directly via a selective membrane. In contrast, the *EC* electrode measures the conductivity of the aqueous sample solution, and this value is converted into a total dissolved solid (**TDS**) measurement by algorithms that form part of the Ranger internal software. The comparison shown in (Figure *3.2-1*) is based on the assumption that sodium and chloride ions dominate the budget of positive and negative ions, respectively, in solutions collected on Murujuga. This assumption is considered reasonable because salt aerosols are formed naturally by the ocean, and by release of seawater used for cooling by Yara from the cooling towers.

The average of the difference between *pH* measurements is -0.43 (n = 26), with a standard deviation of 0.63, which is within error of zero, but highlights the relatively low precision on measurements of these dilute solutions. The maximum absolute difference is 2.01 *pH* units and the minimum absolute difference is 0.03 *pH* units (Figure *3.2-1*a).

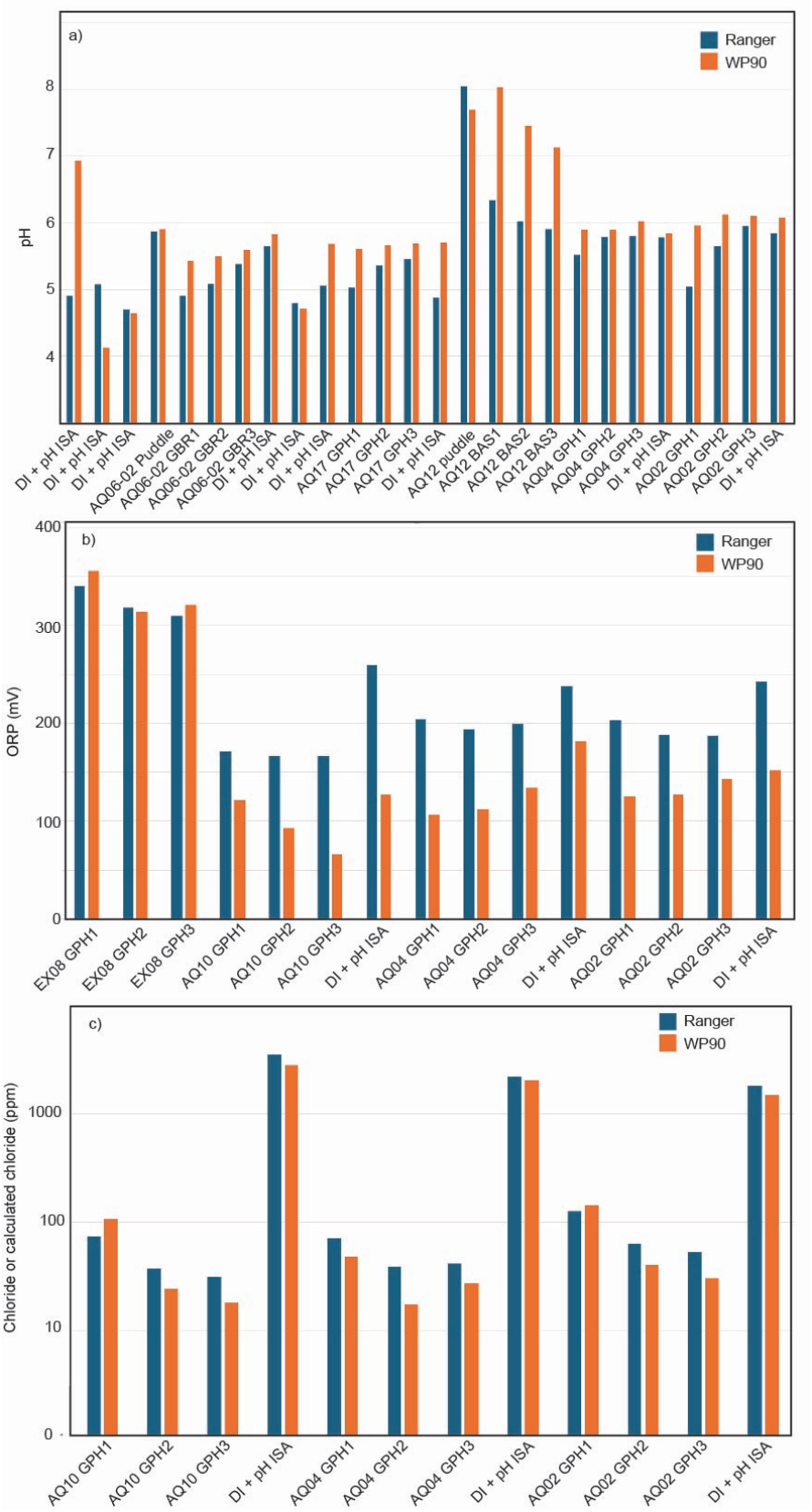

Figure 3.2-1: Comparison of repeated measurements using the WP90 and new Ranger equipment for: (a) pH; (b) ORP; (c) Electrical conductivity (EC). Measurements made during weeks 3 and 4 of campaign 10. Each pair of measurements sampled the same solution and the measurements took place within five minutes of each other.

The largest differences that relate systematically to the observations are those of AQ12 BAS, which follow opportunistic measurements of standing water within a creek bed with carbonate precipitates. The high *pH* of the puddle measurement (8.04 Ranger, 7.69 WP90) is expected, given that carbonate precipitates buffer *pH* to such values. Following the puddle measurement, measurements by the WP90 *pH* electrode remain high and decrease over the following three measurements, consistent with manifestation of a memory effect, which means that the previous measurement affects subsequant measurements. Memory effects in very dilute solutions are well known (Buck et al., 2002). Measurements acquired with the Ranger *pH* electrode show a small but still noticeable memory effect, offering an improvement on previous analytical capabilities. It is worth noting that memory effects are unlikely to be a problem when the solutions are similar in ionic strength, so the memory effects for sequences of measurements of dilute solutions obtained from the rock surfaces, where *pH* and ionic strength values are similar, are not expected to be large. However, care must be taken when field *pH* measurements follow calibration measurements of higher ionic strength solutions.

The average of the differences between *ORP* measurements is 61 mV and the standard deviation is 42 mV (Figure *3.2-1*b). The minimum and maximum absolute differences are 5 and 133 mV, respectively. These differences are relatively high and highlight the difficulty of *ORP* measurements in dilute solutions where the concentration of redox sensitive ions such as $Fe^{2}+$ are low (Nordstrom and Wilde, 2005). The variability of Ranger values measured at a single locality is consistently less than that of WP90 values, indicating better precision.

The average of the differences between chloride ion and calculated chloride ion based on *EC* measurements is 118 ppm with a standard deviation of 240 ppm. The minimum and maximum absolute differences are 13 and 796 ppm, respectively. These values show good agreement within the precision of the technique.

While the performance of the Ranger is generally as good, or superior, to that of the WO90, some features of the Ranger instrument require adaptation of the MRAMP field methodologies:

- As discussed above, electrodes available for the Ranger measure *EC* rather than the concentration of chloride ions, which has been measured up to now using the WP90 instrument via an ion-specific electrode. For this reason, *EC* measurements need to be converted for direct comparison with the Cl^{-} measurements obtained from the WP90 instrument and probes, or vice versa.
- The Ranger probes are not available with flat bottoms, so it was necessary to use 2 mL of solution, rather than the 1 mL achievable with the WP90 flat-bottomed probes. Further, addition of ISA affects the *EC* value because it increases the ionic strength, and thereby the conductivity, of the solution. For this reason, ISA was used for *pH* but not for *EC*.

3.2.4.3 TinyPerm permeameter

The findings of elevated porosity proximal to industrial sites on Murujuga motivated the development of field porosity monitoring protocols. However, porosity is difficult to measure non-destructively in the field. Permeability, which measures the capacity of a substance to allow gases or liquids to flow through it, was measured using the TinyPerm permeameter on the rock art panels (Figure *3.2-2*) and on rock cubes.

The permeameter is relatively straightforward to use. Permeability measurements were made on the same spots as those used for electrochemical measurements, but prior to the rock surface being wetted with deionised water. A total of 277, 322, and 319 measurements were made in campaigns 8, 9, and 10, respectively. The permeability measurements are shown and interpreted in Section 7.7. The spatial distribution of permeability measurements is consistent amongst campaigns, and shows a similar spatial pattern to the laboratory porosity measurements (Section 7.6).

Regular measurements of the reference material show a drop in permeability between campaigns 9 and 10. The reference material, a cut slab of dolerite from site AS02, was analysed three times each morning of the field campaign at the field accommodation. The total number of measurements for each campaign ranges from 42 to 51. The average and standard deviations of these measurements made during campaigns 8, 9, and 10 are 7.3 $\pm$ 1.1, 6.2 $\pm$ 1.3, and 1.7 $\pm$ 0.6 millidarcies (mD). Consistent results within a campaign indicate that the permeability values are meaningful. The drop between campaigns 9 and 10 accompanied a commensurate decrease in field measurements, indicating that the cause does not relate only to the reference material. The manufacturers were consulted and, after some basic checks, responded that they are not aware of any hardware-related issues were could have caused the issue. Initially, it was thought that high temperatures and humidities may have affected the values, but preliminary analyses made in the Curtin laboratories prior to campaign 11, and three months after campaign 10, yielded similar low values (0.9 $\pm$ 0.2 mD, n = 15). The temperature and humidity under laboratory conditions are not high, so it seems unlikely that these factors were the primary cause of the change in observed values. Further, work on sandstones indicates that changes in relative humidity may account for changes in permeability of a factor of two (Meng, 1992), much lower than the factor of five observed between campaigns 8 and 10. However, the addition of the campaign 11 data, which provides a full year of permeability monitoring, will confirm or refute this hypothesis. The full data set will be discussed in the final report. Until this issue is resolved, comparisons of measurements between field campaigns for which the reference material values differ should be undertaken with caution.

Figure 3.2-2: Permeameter in operation in the field. January 2025.

3.2.4.4 Wet weather opportunistic sampling January 2025

Murujuga received what appears to be record amounts of rainfall during the Tropical Cyclone Sean (T.C. Sean), a Category 1 system that impacted the study region on 19 and 20 January 2025. An official record of 274 mm of rain was recorded in 24 hours at Karratha Aero Bureau of Meteorology station, and 303 mm was recorded at two MRAMP stations in and around Dampier. Curtin researchers undertook opportunistic sampling in the field on the 24 January to assess the effect of heavy rain on the *pH* of rock surfaces. The main purpose of this sampling was to test competing hypotheses proposed to explain the relatively low *pH* values (typically less than 6), of the patinated rock surfaces at Murujuga:

1. If low *pH* values are caused by acidic deposition, as suggested by Black et al. (2017) and subsequent researchers, then washing of the rock surfaces and infiltration of the rock substrate by rain will remove acidic salts from the rock surface and underlying porosity. If soluble acidic salts were present before rain and removed by the rain then the *pH* is likely to increase.

2. If low *pH* values are related to metabolites produced by the microbiome, as suggested by MacLeod (2005), then rain may increase microbial activity with a concomitant decrease in *pH*.

Table 3.2-5: pH measurements made during opportunistic post-rain sampling on January 24th, 2025.

Site	Rock type	*pH*	Temperature (°C)
AQ13	GPH	4.6	34.6
AQ13	GPH	5.8	40.4
AQ13	GPH	5.8	41.4
AQ14	GPH	4.6	40.7
AQ14	GPH	4.5	42.8
AQ14	GPH	4.9	43.3
EX02	GPH	4.2	39.9
EX02	GPH	5.2	43.2
EX02	GPH	4.8	44.6
EX09	GPH	4.9	39.3
EX09	GPH	5.2	38.3
EX09	GPH	5.3	38.1

Twelve measurements were taken at four localities. The *pH* values obtained ranged from 4.24 to 5.82, with an average, standard deviation, and median of 5.0, 0.5, and 4.9, respectively (see Table *3.2-5*). These values are similar to those measured during other field campaigns and show no evidence of increases expected for hypothesis (1). See Section 7.10.7 for figures and data.

3.2.4.5 Oxalate and formate sample collection during campaign 10

Oxalate and formate are organic metabolites produced by biological activity. To further test hypotheses (1) and (2) above, a 10 mL sample was collected from gabbro and granophyre rock surfaces at 13 localities during campaign 10 and analysed at the ChemCentre (Table *4.2-9*). Sample collection methods were the same as those used for *pH* sample collection and described in COPP21065-PRO-G-106, with the exception that larger tubes were used to collect the larger samples. Samples were analysed using a Dionex ICS 5000 high pressure ion chromatography system. For both oxalate and formate, results were determined with reference to a calibration curve resulting from the analysis of standards prepared at concentrations of 0.2, 0.5, 1, 2, 5 and 10 mg/L of the target analyte. The results are discussed in Section 4.2.4.6.

3.2.4.6 New sample collection

The findings of high porosity proximal to industrial sites motivated the collection of additional rock samples to add additional statistical power to the analyses. Samples were collected and prepared using the same protocols used to collect the initial sample suite, which is referred to as Group A (COPP21065-PRO-G-115 Sample Rock Collection). Three additional suites of samples were collected. The four suites of samples are referred to as Groups A to D, and are described briefly below:

- Group A: thin sections of the original 64 sample rocks collected in 2022 and described in the Monitoring Studies Report 2024 (Curtin University, 2024c).

- Group B: thin sections of 22 new samples, including all five rock types that host rock art, collected in August 2024 and described in Section 3.2.4.6.
- Group C: polished billets of 11 granophyre samples from the original sample suite (Section 3.2.4.6).
- Group D samples. Four samples were collected in 2024 from the railway cutting outside Karratha (Figure *3.2-3*) to provide examples of rocks with short weathering histories (Section 3.2.4.6).

Group B samples

Twenty-two rock samples were collected from four lithologies in August 2024. Sites were selected to increase sampling density in more sparsely sampled areas of Murujuga. These samples include:

- 16 granophyre samples;
- three dolerite samples;
- one gabbro sample;
- one granite sample;
- one sample with unclear contact relations which is either a coarse-grained sample from a dolerite dyke or from a fine-grained zone within the gabbro.

The collection locations of these samples are listed in Table *3.2-6*.

Group C samples

The Group C samples are prepared from the same rocks that yielded the Group A samples. The Group A samples are thin sections, which are thin slices of rock, 30 micrometres thick, attached to glass slides. Thin sections are prepared from rock billets, which are tabular pieces of rock, approximately 47 mm long x 25 mm wide x 12 mm thick. The 47 x 25 mm dimension is attached to the glass slide using adhesive, and most of the billet is cut off to produce the thin section plus a remnant billet that is very similar to the rock prepared as the thin section. Eleven of these billets were polished to form Group C. These billets provide effective replicates of their corresponding Group A samples that can be used to test the reproducibility of the mineralogical and porosity results.

Group D samples

Four additional granophyre samples were collected on 13 November 2024, from a railway cutting close to Dampier (Figure *3.2-3*, Table *3.2-7*). These samples were selected because the railway cutting was created relatively recently, in 1965/66, so rocks exposed on the walls of the cutting since construction of the cutting have only been weathered over the last few decades. These timescales are short relative to the thousands, tens of thousands, or even hundreds of thousands of years of weathering experienced by natural rock exposures on Murujuga. This short weathering history means that exposure to industrial emissions occurred over a high proportion of these rocks' weathering history, so they may offer an opportunity to distinguish between natural weathering processes over extended periods of time and potentially anthropogenically enhanced weathering processes on shorter timescales. These samples were split into two and two thin sections were made from each sample.

*Table 3.2-6: Location of Group B samples. * indicates samples used for micro-CT analysis.*

Location	Sample	Rock type	Latitude	Longitude	Orientation of patinated surface
Burrup Peninsula	BU01	granophyre	20°34’23.8”	116°46’46.1”	090/63°S
Burrup Peninsula	BU02*	granophyre	20°36’07.4”	116°45’59.6”	024/32°W
Angel Island	AN01	granophyre	20°31’00.5”	116°47’53.0”	176/56°E
East Lewis Island	EL01	granophyre	20°37’15.3”	116°40’00.2”	176/82°W
East Lewis Island	EL02*	granophyre	20°37’51.4”	116°38’12.3”	155/52°W
East Lewis Island	EL03	granophyre	20°37’18.1”	116°38’32.9”	155/25°W
West Lewis Island	WL01	dolerite	20°33’59.4”	116°39’56.2”	Not collected
East Intercourse Island	EI01*	dolerite dyke	20°38’55.1”	116°41’33.5”	160/55°W
East Intercourse Island	EI02	granophyre	20°38’54.0”	116°41’32.3”	030/85°NW
East Intercourse Is	EI03	granophyre	20°39’12.1”	116°41’00.1”	098/32°N
West Intercourse Is	WI01	granophyre	20°41’18.2”	116°35’33.9”	153/70°W
West Intercourse Is	WI02	granophyre	20°43’38.3”	116°34’47.9”	060/10°N
Enderby Island	EN01	granophyre	20°37’09.9”	116°30’05.4”	014/18°W
Enderby Island	EN02	dolerite	20°34’25.1”	116°33’10.5”	146/70°W
Rosemary Island	RI01	dolerite	20°28’05.4”	116°35’29.2”	173/12°W
Dolphin Island	DO01	granophyre	20°27’54.8”	116°50’41.8”	135/20°S
Dolphin Island	DO02*	gabbro	20°27’53.0”	116°50’56.3”	143/46°NE
Dolphin Island	DO03*	granite	20°27’48.7”	116°50’51.3”	080/vertical
Gidley Island	GI01	granophyre	20°25’37.2”	116°50’08.3”	034/15°W
Gidley Island	GI02	granophyre	20°25’34.9”	116°50’12.5”	142/12°SW
Gidley Island	GI03	granophyre	20°25’34.3”	116°50’16.1”	060/62°NW
Eaglehawk Island	EA01	granophyre	20°39’17.7”	116°26’31.6”	070/34°N

Table 3.2-7: Collection locations of Group D samples, all samples were granophyre.

Sample	Latitude	Longitude	Orientation of patinated surface
RT01_GPH and MB01_GPH	S 20°39'46.7"	E 116°43'10.7"	155/58° E
RT02_GPH and MB02_GPH	S 20°39'46.3"	E 116°43'10.9"	065/74° E
RT03_GPH and MB02_GPH	S 20°39'45.3"	E 116°43'10.9"	040/80° E
RT04_GPH and MB04_GPH	S 20°39'44.4"	E 116°43'11.1"	030/70° E

Samples were taken from 0.5 to 1.0 m above ground level. The samples were split into two, and organic geochemistry and microbiome sampling were completed on one of the sub-samples (MB prefix). The other sub-sample was reserved for geological analysis (RT prefix). Epoxy-impregnated rock billets and thin sections were made from both sub-samples of each of the four samples, to provide duplicates.

3.2.4.7 Rock cube measurements of *pH*, permeability, and rock surface composition

Five rock cubes are located within each AQM. Each of the five rock cubes is made of one of the five main lithologies that host rock art at Murujuga (granophyre, gabbro, dolerite, basalt, granite) (Figure *3.2-4*). The *pH*, permeability, and rock surface composition of the rock cubes located within the AQMs were measured between 1 October 2024 and 4 October 2024. Permeability was measured using the TinyPerm permeameter as described above (Section 3.2.3). Rock surface composition was measured using the portable X-ray fluorescence analyser (pXRF) instrument, and *pH* was measured using the flat bottomed probe and the TPS WP90 instrumentation. The results are shown and discussed in Section 7.4 to Section 7.7.

Figure 3.2-3: Aerial photograph showing collection locations of Group D samples. The purple line shows the area accessed and assessed for sample collection. Samples were collected from within the red square. Image from Google Maps.

Figure 3.2-4: Photo of the five rock cubes. Microbiome, pH, and pXRF data were collected from the rock cubes prior to campaign 9.

3.3 Surface change analysis (spectroscopy) fieldwork

3.3.1 Objectives

From Section 1.7 of the MSDCA Plan (Curtin University, 2022), the objectives of the spectroscopy investigations are to:

1. Accurately measure the colour, texture, and elemental composition of selected rock surfaces across Murujuga.
2. Study the secondary reflectance characteristics to monitor chemical change, anticipating future colour change.
3. Capture the broad surface elemental distribution to understand colour change across whole surfaces to correlate with and inform spot measurements.
4. Establish baseline values for a long-term monitoring program.
5. Identify important differences or changes in colour, surface texture, and elemental composition which may be associated with degradation of appearance or condition.
6. Develop a deeper understanding of variation in elemental composition across the rock surface and its relationship to colour and texture.
7. Develop criteria for assessing degradation of appearance or condition.
8. Ensure that the study data provide the information required by other component studies (such as the precise spatial location of each observation).

3.3.2 Methodology

Spectroscopy fieldwork in the field campaigns involved:

1. Spectroscopic measurement of ten targets on each rock panel.
2. In-field management of spectral files.
3. Gathering of environmental and condition data at each site, including a comprehensive photographic record of the site and its context.

Further information on spectroscopy field methodologies can be found in Section 3.2.3 of the MSDCA Plan (Curtin University, 2022) and the component study methodology statement:

- COPP21065-PRO-G-110 Murujuga Rock Art Monitoring Program: Photospectrometric Colour Change Measurement

Variations from planned methodology

The extensive revisions and improvements made to equipment and methods to optimise the spectroscopy field measurements are described in Section 7.2.2 and Section 7.2.3 of the Monitoring Studies Report 2024 (Curtin University, 2024c) for the JAZ and HDX instruments, respectively.

The original study design assumed that the representative sample (RS) sites would only be visited in year one. However, the variability in the spectrometry, *pH*, and other inorganics measurements

required RS sites to remain in the study for a longer period. The statistical team decided that the RS sites would be stratified across campaigns so that each RS site would be measured at least once per year, and DWER accepted this recommendation.

3.4 Microbiome collection fieldwork

The purpose of the microbiome fieldwork is to acquire material for use in laboratory microbiome testing.

Microbiome fieldwork took place in the first two field campaigns and involved collecting microbiome samples for later laboratory analysis.

Further information on microbiome field methodologies can be found in Section 3.3.3 of the MSDCA Plan (Curtin University, 2022) and the component study methodology statement:

- COPP21065-PRO-G-107 Murujuga Rock Art Monitoring Program: Microbiome Field Sample

As mentioned in Section 3.2.4.6 four granophyre samples were collected on 13 November 2024 from the (original 1966) rail cutting near Dampier (Group D). The four granohpyre rocks were sampled in triplicate using a sterile dremel and sterile water to make a paste of the surface of the rock. The paste was collected with sterile swabs and submerged in DNA/RNA Shield (Zymo Research), frozen and transported to Curtin University for DNA extractions.

As mentioned in Section 3.2.4.7, five rock cubes are located within each AQM, 29 stations in total. Microbial samples were collected from these rock cubes between 1 October 2024 and 4 October 2024. Samples were taken by extensively swabbing a randomly selected side of the rock cube, and the swab submerged in DNA/RNA Shield (Zymo Research), frozen and transported to Curtin University for DNA extractions.

4 Laboratory analysis of field samples

This Section reports on laboratory analysis of samples collected in the field, and accelerated weathering (chamber) experiments.

- Section 4.1 covers organic geochemistry.
- Section 4.2 covers geology and inorganic chemistry.
- Section 4.3 covers analysis of the microbiome.
- Section 4.4 reports on the chamber experiments.

4.1 Organic geochemistry laboratory analysis

4.1.1 Objectives

From Section 1.4 of the MSDCA Plan (Curtin University, 2022), the objectives of the organic geochemistry investigations are to:

1. Measure the molecular and stable isotopic composition of organics from all sources, including natural emissions (terrestrial vegetation, fire), anthropogenic emissions (shipping, traffic, industry). In addition, organics present in the host rocks (including rock dust from iron ore transport), will also be measured. Furthermore, this objective includes determining the occurrence and magnitude of seasonal variations in emissions. This approach will produce a detailed and comprehensive characterisation of organic emissions in the Murujuga region.
2. Measure the molecular and stable isotope composition of organics deposited on rock surfaces and in soils, to link organics on rock surfaces to the various emission sources. This approach will determine which sources contribute the highest quantity of organics to the surface deposition.
3. Identify any organics that are likely to affect weathering of rock art. For example, organics that affect the growth of microorganisms (in conjunction with microbiome expert(s)) or interaction with specific minerals (in conjunction with inorganic geochemist(s)).
4. Understand confounding factors introduced by (reported) changed fire management regimes approximately coinciding with the commencement of industrial activity on the Burrup.

4.1.2 Methodology

Organic geochemistry laboratory methodologies are described in Section 3.3.3 of the MSDCA Plan (Curtin University, 2022) and the component study methodology statement:

- COPP21065-PRO-G-113 Murujuga Rock Art Monitoring Program: Organic Geochemistry of Rock Surfaces, Dust and Particulates

4.1.3 Summary of previous work

The data analyses of rock surface and fresher rock samples that commenced in year two of the MRAMP are almost complete (Table *4.1-1*). Comprehensive two-dimensional Gas Chromatography

– Time-of-Flight Mass Spectrometry (**GC×GC-TOFMS**) analyses are in progress and are expected to be completed by September 2025.

Table 4.1-1: Status of analyses in the rock surface and fresher rock samples.

Instrumentation	**Rock Surface Samples**			
		Fraction		
	Bulk	**Saturated**	**Aromatic**	**Polar**
GC-MS	NA	✓	✓	✓
GCxGC-TOF	NA	in progress	in progress	NA
GC-TQ	NA	✓	NA	NA
GC-irMS (carbon)	NA	✓	NA	NA
PY GC-MS	✓	NA	NA	NA
EA - δ^{13}C(‰)	✓	NA	NA	NA
TOC	✓	NA	NA	NA
	Fresher Rock Samples			
		Fraction		
	Bulk	**Saturated**	**Aromatic**	**Polar**
GC-MS	NA	✓	✓	✓
GCxGC-TOF	NA	NA	NA	NA
GC-TQ	NA	NA	NA	NA
GC-irMS (carbon)	NA	NA	NA	NA
PY GC-MS	✓	NA	NA	NA
EA - δ^{13}C(‰)	NA	NA	NA	NA
TOC (wt%)	✓	NA	NA	NA

Note: NA denotes not applicable.

4.1.4 Gas chromatography - Mass Spectrometry (GC-MS) analysis

The GC-MS analysis of the saturated and aromatic hydrocarbon fractions was reported in the Monitoring Studies Report 2024 (Curtin University, 2024c). The analysis of the polar fractions has been completed in the last year and is detailed in this report.

Polar fraction

Compounds in the polar fraction, such as fatty acids and alcohols, must be chemically modified (derivatised) to make them more amenable to GC-MS analysis. The samples were derivatised using N, O-Bis(trimethylsilyl)trifluoroacetamide (BSFTA), and pyridine (see COPP21065-PRO-G-113). Reagent blanks and full procedural blanks were analysed alongside the samples to identify compounds present at low abundances in the derivatisation reagents. Appendix Figure *A-1* shows the chromatogram of a rock surface sample, a procedural blank, and a reagent blank for comparison.

Peaks are reported when their relative peak area exceeds 0.1% of the largest peak and are identified based on the National Institute of Standards and Technology mass spectral library (NIST17).

Abundances are expressed as a percentage of the total area of all reported peaks. These data do not represent absolute abundances but instead, provide a profile of organic compounds present on the rock surface. Identified peaks are grouped into the following major compound classes: saturated fatty acids, unsaturated fatty acids, hydroxy fatty acids, saturated alcohols, glycerol, sugars, sterols, hydroxy-benzaldehyde, unidentified compounds, and reagent-derived compounds.

4.1.4.1 Rock surface samples

The most abundant compounds found in all rock sampled are typically saturated and unsaturated fatty acids. These compounds are ubiquitous and serve as fundamental building blocks in many biological processes. The relative abundances of fatty acids with different carbon numbers and chemical configurations can provide insight into their potential sources. Microorganisms, for example, produce a diverse array of fatty acids, among which the most common are saturated $C_{16}H_{32}O_2$ palmitic acid, designated as '16:0' where 16 refers to the carbon chain length and 0 refers to the number of double bonds, and two unsaturated acids: palmitoleic (16:1, cis-9) and vaccenic (18:1, cis-11) acids (Volkman et al., 1998; Cronan and Thomas, 2009). Some bacteria also produce branched chain fatty acids and 3-hydroxyaryl acids (Kaneda, 1991; Cronan and Thomas, 2009). Cyanobacteria predominantly synthesise saturated fatty acids with a carbon chain length from C_{14} (14:0) to C_{18} (18:0) and unsaturated fatty acids with one to four double bonds (e.g., 18:1, 18:2) (Los and Mironov, 2015). Specific fatty acid profiles can vary among cyanobacterial species (Los and Mironov, 2015; Montero-Lobato et al., 2020). In contrast, most plants primarily produce unsaturated fatty acids such as oleic (18:1), linoleic (18:2), and α-linolenic (18:3) acids (He et al., 2020).

As a representative example, the chromatogram in Figure *4.1-1* shows the derivatised polar fraction of rock surface sample AQ05_DOL B, displaying a distribution of polar compounds typical of that observed across most samples. The chromatogram of sample AQ05_DOL B shows that the major components are saturated and unsaturated fatty acids, comprising approximately $\sim$36% and $\sim$40% of the total peak area, respectively. The saturated fatty acids are predominantly long chain acids (C_{13} to $C_{21)}$, accounting for around 85%, with minor contributions from very long chain (>C_{22}, $\sim$10%) and mid-chain acids (C_6 to C_{12}, $\sim$5%). The unsaturated fatty acids are almost entirely present as long chain acids, which make up approximately 98% of that group.

The saturated long chain fatty acids consist predominantly of palmitic (16:0) and stearic acid (18:0), comprising approximately 59% and 33% of the group, respectively. The unsaturated fatty acids are mainly present as oleic acid (18:1) with multiple isomers collectively accounting for around 95%, and minor traces of linoleic acid (18:2, $\sim$3%). Palmitoleic acid (16:1) is present in trace amounts, contributing less than 1%.

Glycerol-related compounds, which constitute approximately 7% of the total peak area, are synthesised through the reaction of palmitic or stearic acid with glycerol. These compounds are known metabolites of algae and plants but are also commonly found in emulsifiers (Xue et al., 2017; Gull and Pasek, 2021). Sugars are ubiquitous compounds in nature and were detected in the samples in form of mono- disaccharides and anhydro-saccharides (< 2%). The presence of levoglucosan, a product of thermal decomposition of cellulose and hemicellulose can be used as a tracer for biomass burning (Marynowski and Simoneit, 2022). Other biologically relevant compounds (Volkman, 2005; Zhang et al., 2024), such as hydroxy fatty acids and sterols, are

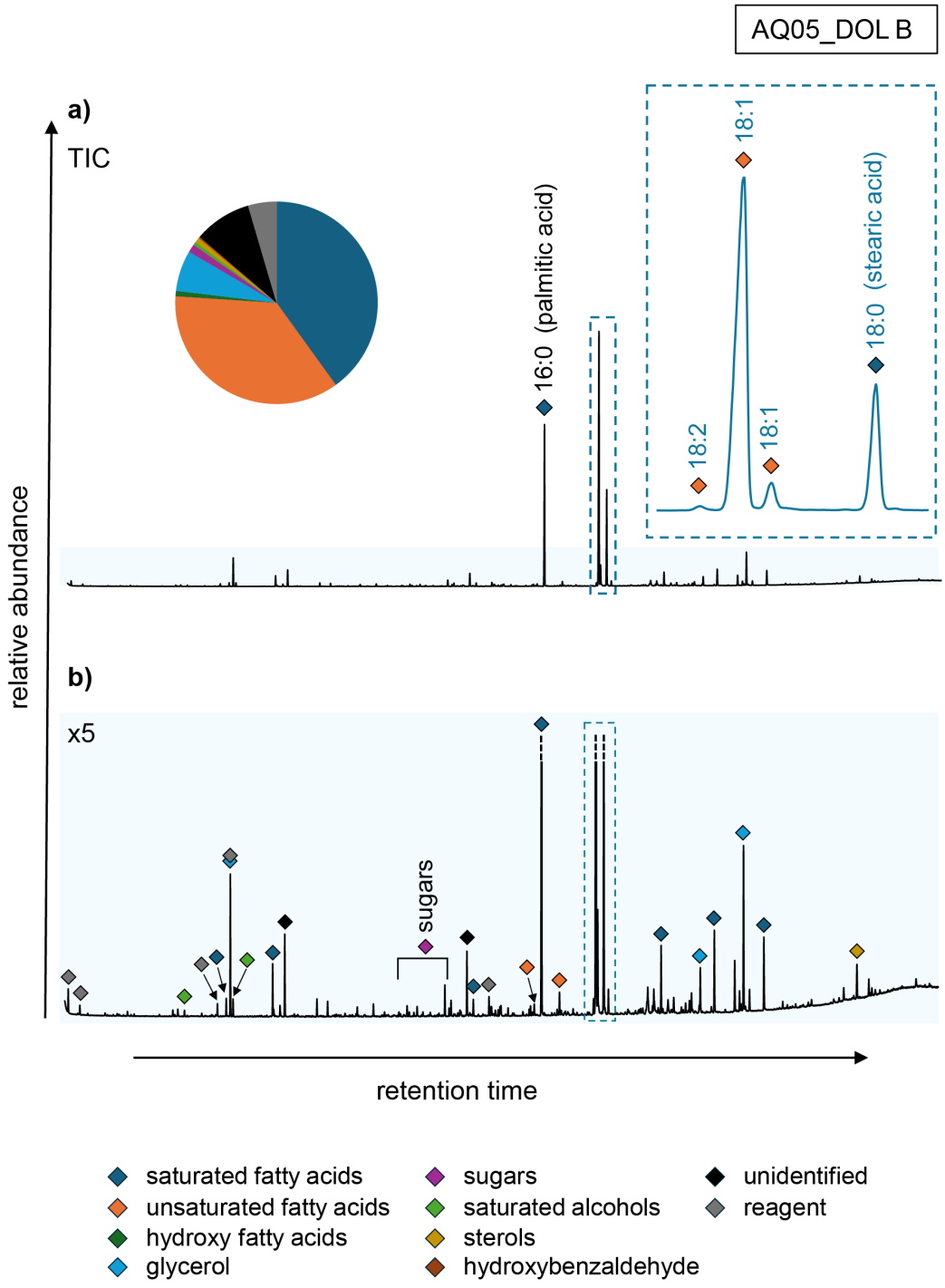

Figure 4.1-1: a) GC-MS total ion chromatogram (TIC) of the derivatised polar fraction from rock surface sample AQ05_DOL B, representative of samples analysed. The pie chart illustrates the relative proportion of compound groups detected, b) is the highlighted section from a) expanded by a factor of five. Observed ions ranged from m/z 50 to m/z 550.

present in low abundances (∼1%). Unidentified peaks account for about 9% of the total signal, while derivatisation reagent-related compounds represent about 5%.

Some samples have other biotic and abiotic constituents e.g. phenolic compounds such as hydroxybenzoic acids originating from plant sources, microbial and chemical synthesis (e.g. Khadem and Marles, 2010; Haman et al., 2015; Holman et al., 2024) as well as abiotic phenolic substances e.g. Bisphenol A related to the production of polycarbonate plastics and epoxy resin (Michałowicz, 2014, and references therein).

The polar constituents on the rock surfaces reveals a composition consistent with compounds derived from bacteria, cyanobacteria, and plants. Minor unidentified peaks may originate from yet unknown sources.

4.1.4.2 Fresher surface samples

GC-MS analyses of the derivatised polar fractions of fresher rock samples show no compounds above detection limits, except for palmitic (16:0) and stearic acids (18:0), which are present in negligible abundances compared to the rock surface (Appendix Figure *A-2*). Based on these findings, any contribution from the interior of the rock to the surface is considered negligible. As with the rock surface samples, peaks consistent with derivatisation reagents were also present in the chromatograms of the fresher rock samples.

4.1.5 Pyrolysis-Gas chromatography - Mass Spectrometry (GC-MS) analysis

Pyrolysis Gas Chromatography (PY-GC-MS) is used to analyse large, insoluble organic matter (macromolecules) that cannot be recovered through traditional solvent extraction. Pyrolysis thermally decomposes intact molecules or fragments of larger molecules, which are then separated and analysed by GC-MS (White et al., 2004). Solvent extracted samples are preferred for PY-GC-MS analysis, as free unbound components could potentially interfere with analytical data. The products formed during pyrolysis were identified based on mass spectral library data (NIST17). The results provide insights into the molecular compounds on the rock surface.

The PY-GC-MS analysis of both the extracted rock surface samples and the fresh rock samples has been completed. Additionally, the six rock surface samples that were not solvent extracted (due to an insufficient amount of material, less than 3 g of surface rock, collected) have also been analysed by PY-GC-MS. A comparison of PY-GC-MS chromatograms from the extracted and non-extracted rock surfaces of the same sample revealed no significant differences (Appendix Figure *A-3*). Therefore, the PY-GC-MS results from the non-solvent-extracted rock surfaces can be directly compared to those from the remaining samples that were solvent extracted.

Peaks are reported when the relative peak area exceeds 0.1% of the largest peak. The organic compounds produced are then expressed as percentages of the total sample peak areas. These data do not represent absolute abundances but rather provide a profile of organic compounds present on the rock surface. The identified compounds were grouped based on their origin, such as gases, nitrogen compounds, polysaccharides, and aromatic compounds.

4.1.5.1 Rock surface samples

In general, the pyrolysis chromatograms of all samples are dominated by low- molecular-weight gaseous products, with carbon dioxide (CO_2) being by far the most abundant. These gases are artifacts of the pyrolysis process, resulting from the thermal cracking of organic macromolecules at high temperatures. For most samples, nitrogen-containing products represent the largest fraction after CO_2. These products are formed through pyrolysis of amino acids, nucleic acids, proteins, and microbial cells (Tsuge and Matsubara, 1985; Leng et al., 2020). Acetonitrile (aliphatic nitrile) is the most abundant product, followed by pyrrole.

In the samples, higher plant contribution is reflected in pyrolysis compounds derived from polysaccha -rides, which are predominantly present as furans and related compounds (van Der Kaaden et al., 1983; Pouwels et al., 1987; Vancampenhout et al., 2009; Lockhart et al., 2013). Furfural is related to the pyrolysis of carbohydrates, lignocellulosic materials, proteins, and other aliphatic organic compounds (Zhou et al., 2023). Some samples also show a low abundance of acetic acid, formed by the pyrolysis of lipids, fats and waxes, carbohydrates, and lignocellulose material (Bracewell and Robertson, 1984; Sarchami et al., 2021).

Aldehyde and ketones in the samples originate from the pyrolysis of cellulose and hemicellulose but are also byproducts of the pyrolysis process (Luo et al., 2004). Phenol and phenolic compounds were detected in all samples. These phenolic products can derive from lignocellulose structures and amino acids (Hatcher et al., 1988; Chiavari and Galletti, 1992; Hu et al., 2022). Organic sulfur products, identified as methanethiol and thiophenes, were found in low abundance. Possible sources of these compounds include humic substances and kerogen (Saiz-Jimenez, 1995).

Aromatic products are present primarily in the form of benzene, toluene, ethylbenzene, and xylenes (BTEX e.g., Vitzthum von Eckstaedt et al. (2012) and are mainly derived from the condensed aromatic structures of humified organic matter (Hatcher and Clifford, 1994). Polycyclic aromatic hydrocarbons (**PAHs**), e.g., (Grice et al. (2005)) are present in low relative abundance, mostly present as naphthalene. These aromatic products can also indicate the presence of various plastics, such as polyvinylchloride (PVC), polyethylene (PE), polystyrene (PS) and others (Picó and Barceló (2020) and references therein).

As a representative example, the chromatogram in Figure *4.1-2* shows rock surface sample AQ05_DOL B, exhibiting a typical distribution of pyrolysis products observed in most samples. An exception is sample RS15_BAS, where sulfur dioxide and hydrochloric acid were detected in relatively high abundance. RS15_BAS also displayed differences in bacterial phyla compared to most of the samples with a high abundance of *Halobacterota* (66%) and a very low percentage of *Actinobacteria* and *Proteobacteria* (Curtin University (2024c), Section 7.8.3).

In the sample, A05_DOL B, the combined proportions of carbon dioxide and other low molecular weight hydrocarbons account for approximately 42%. A dominance of biological sources is reflected in the significant abundance of acetonitrile and other nitrogen products ($\sim$24%). A prominent plant signature is indicated by the presence of polysaccharides ($\sim$10%) and lignocellulose/cellulose products ($\sim$8%). Aromatic products contribute around 6% and are considered to have a mixed origin. Other product groups are present only in trace amounts (0.5 to 1.9%), while unidentified peaks account for about 5%.

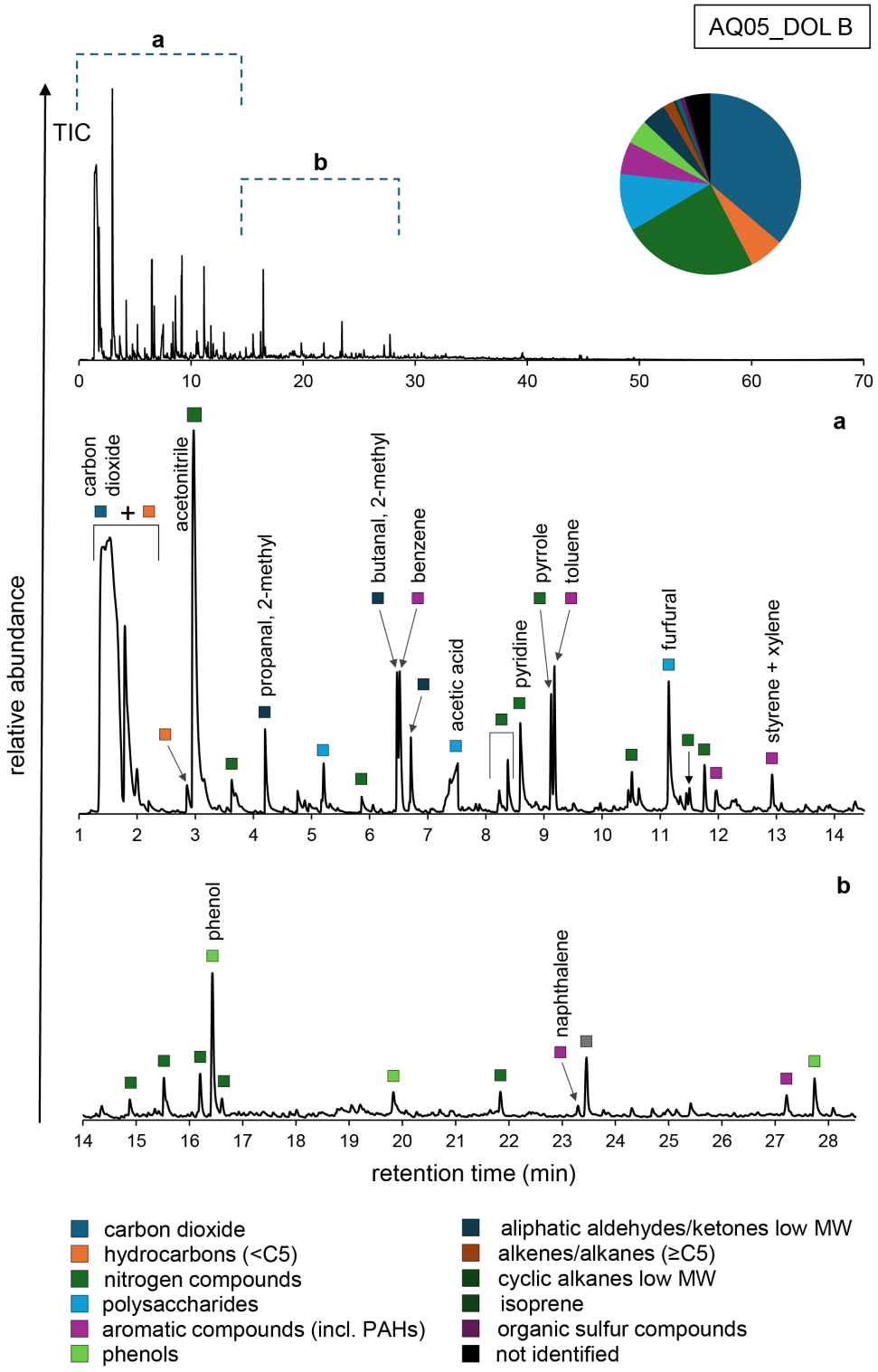

Figure 4.1-2: Flash Pyrolysis GC-MS total ion chromatogram (TIC) of rock surface sample AQ05_DOL B, representative of samples analysed. Pie chart illustrates the relative proportion of 12 product groups. Main peaks in chromatogram are labelled for products, including some single compounds. Observed ions ranged from m/z 50 to m/z 550.

4.1.5.2 Fresher surface samples

The pyrolysis products of the fresher rock samples did not exhibit any compounds above the detection limit, except for carbon dioxide produced during pyrolysis (Appendix Figure *A-4*). Therefore, any contribution from the fresher rock to the rock surface can be disregarded.

4.1.6 Gas chromatography - isotope ratio mass spectrometry (GC-irMS) analysis

Natural samples, such as the Murujuga rock surfaces, often contain organic compounds from multiple distinct sources that cannot be determined by bulk isotope measurements. Compound specific isotopic analysis (**CSIA**) measures the isotopic values of individual compounds in a complex mixture, providing details on the origin of each compound (Grice and Brocks, 2011). CSIA was used to measure the stable carbon isotopic composition ($\delta^{13}C$) of straight-chain alkanes (*n*-alkanes) from the rock surface extracts. For accurate measurements, CSIA requires each compound to be present in sufficiently high abundance. Hence, due to the low amounts of organics in many samples only 38 of the rock surface samples could be analysed. $\delta^{13}C$ values were determined for the short-chain *n*-alkanes *n*-C_{15} and *n*-C_{17}, and the long-chain *n*-alkanes *n*-C_{27}, *n*-C_{29}, *n*-C_{31} and *n*-C_{33}.

The isotopic signatures for short chain *n*-alkanes *n*-C_{15} and *n*-C_{17} ranged from -27.8‰ to -24.9‰ and -29.4‰ to -22.1‰, respectively (Appendix Table *A-1*), indicating an origin such as algae and cyanobacteria (Grice et al., 2001; Pancost and Pagani, 2006; Grice and Brocks, 2011; Chikaraishi, 2014). The presence of *n*-alkanes > C_{25} with a predominance of odd carbon numbers, indicates a strong contribution from the leaf waxes of land plants (Grice et al., 2001; Bush and McInerney, 2013; Diefendorf and Freimuth, 2017). The carbon isotope composition of land plant *n*-alkanes is primarily influenced by the mechanism of photosynthesis used by the plant, with C3 plants (trees) typically within the range of -35‰ to -30‰ and C4 plants (grasses) within the range of -20‰ to -15‰ (Collister et al., 1994; Grice and Brocks, 2011; Chikaraishi, 2014; Diefendorf and Freimuth, 2017). In the rock surface samples, the long-chain n-alkanes showed a range of -32.6‰ to -23.5‰ for n-C_{25}, -33.6‰ to -18.3‰ for n-C_{27}, -32.3‰ to -21.6‰ for n-C_{31}, and -31.4 ‰ to -23.2‰ for *n*-C_{33} (Appendix Table *A-1*). Most of these values indicate a mixed signal with contributions from both C3 and C4 plant types.

4.2 Geology and inorganic geochemistry laboratory analysis

4.2.1 Objectives

Section 1.5 of the MSDCA Plan (Curtin University, 2022), states that the objectives of the inorganic geochemistry investigations are to:

1. Characterise the mineralogy and mineral compositions of the fresher rock, weathered rind, and patina for the granophyre, gabbro, dolerite, granite, and basalt rock types. Samples have been sourced from a range of settings including high and low exposure to industry emissions and differences in exposure to rain and wind.

2. Determine the mineralogy of the samples mentioned in Objective 1 at thermodynamic equilibrium. Thermodynamic calculations and best-practice approaches have been used to estimate the timescales of change based upon measured reaction rates, reaction mechanisms, and the results of other component studies (organic, microbiome, field observations, weathering experiments).

3. Compare the expected versus observed mineralogy for sites with different exposure to anthropogenic emissions. Here, the goal was to obtain proof-of-concept for the thermodynamic calculations and investigate the presence of statistically significant differences among the sites, potentially linking to industry emissions.

4. Use the observations and calculations to identify components of the mineralogy that are most sensitive to industrial emissions and that can act as early indicators of change (potential EQC parameters) and devise a monitoring strategy that will form part of the EQMF and ongoing monitoring Program.

Objectives [1] to [3] were addressed in Monitoring Studies Report 2024 (Curtin University, 2024c). The findings reveal elevated porosity of the uppermost layers of granophyre rocks that increases towards sites of industrial emissions. Therefore, a primary objective for the current year of studies was to test and corroborate those findings by a comparison of the mineralogical and porosity analysis of the three additional sample suites described in section 3.2.4.6.

In addition, a sub-group of five samples from Group B (two granophyres, one dolerite, one gabbro, and a granite), were prepared for micro-computed tomography (**micro-CT**) analysis. Micro-CT provides a three-dimensional (**3D**) representation of the mineral phases and porosity within a small cylindrical sample. The purpose of this analysis was to compare 3D representations of porosity obtained by micro-CT with the two-dimensional (**2D**) representations obtained by thin section analysis.

Finally, the results of the oxalate and formate analyses are reported here (see Section 3.2.4.5 for description of sample collection). Oxalate and formate are organic compounds. Natural occurrences of these compounds are generally interpreted as metabolites produced by biological activity, so their presence is a record of that activity on the rock surfaces.

4.2.2 Methodology: Inorganic geochemistry

4.2.2.1 Workflow

The workflow for analyses in this report is an adapted version of the workflow presented in Figure 3-8 of the MSDCA Plan (Curtin University, 2022). The revised workflow focuses on the characteristics of rocks related to the mineralogy and porosity.

Methods for thin section preparation, optical microscopy (including whole-thin section imaging using the Axio Imager), automated mineralogy by TIMA (Tescan Integrated Mineral Analysis), and scanning electron microscopy (SEM) have been described previously in Section 3.3.2 of the MSDCA Plan (Curtin University, 2022) and the Murujuga Rock Art Monitoring Program: Inorganic Geochemistry Laboratory Analysis methodology (COPP21065-PRO-G-114). The TIMA imaging undertaken this year used the mineral classification libraries developed for the Murujuga rocks as part of the second year of studies, so results for the two years should be directly comparable.

4.2.2.2 Micro-computed tomography analysis

Cylinders of rock, 2–3 mm in diameter and 3–5 mm in height were drilled out of epoxy-impregnated billets for Group B samples (BU02, EL02, EI01, D002, D003, see Table *3.2-6* for sample locations). High-resolution X-ray micro-CT analysis was performed on these cylinders at the X-Ray Computed Tomography Facility in the John de Laeter Centre (**JdLC**) at Curtin University, Western Australia, using a Thermo Fisher Scientific HeliSCAN Micro CT Mk2 system. The cylinder-shaped drill-cores of Murujuga sample rocks were glued to a cylindrical stand which was then screwed onto the sample stage to minimise any drift artefacts during tomography data acquisition. The samples were scanned in space-filling trajectory at a tube voltage of 80 kV and a tube current of 72 μA, with a 2 mm aluminium filter plate attached to the detector to reduce beam hardening artifacts. This acquisition trajectory allowed for continuous, geometrically accurate 3D imaging of tall samples without potential stitching artefacts to yield sharp images (Kingston et al., 2018; Latham et al., 2018). A total of 2129 to 2768 projections were taken from each sample during the measurements, which were then reconstructed on a graphics processing unit (GPU) cluster using an iterative method provided by Thermo Fisher Scientific. The voxel sizes (the 3D volume resolution) of the reconstructed 3D images varied from 2.5 μm^3 to 4.2 μm^3 according to the size and geometry of samples and the specified image resolution. The data were reconstructed and analysed using the free academic license for the commercial Dragonfly software.

4.2.2.3 Oxalate and formate analysis

Oxalate and formate were determined using ion chromatography on aqueous solutions produced by the same techniques used to produce samples for *pH* measurement (Section 3.2.4.5). This method involves chromatographic separation of the anions present in the sample, followed by determination of concentrations using conductivity detection. Data are quantified by reference to standards prepared from sodium oxalate and sodium formate respectively.

Figure 4.2-1: Schematic illustration of adapted workflow applied to the Group B, C, and D samples.

4.2.3 Activities undertaken

The following work was completed for laboratory sample analysis covered in this report:

- Thin section preparation for 22 samples from Group B and eight samples from Group D;
- Billet preparation for 11 samples from Group C;
- Whole thin section imaging using reflected and transmitted light in plane and cross-polarised light for the 22 samples from Group B and eight samples from Group D;
- Whole billet imaging using reflected light in plane and cross-polarised light for the 11 samples from Group C;
- Detailed optical microscopy observations of representative thin sections or billets from Group B and D samples;
- Automated mineralogy scanning and data processing to obtain mineral distribution maps and modes for all samples from Groups B, C, and D;
- Detailed SEM observations for selected representative thin sections or billets from all groups and lithologies.

Taken together, the results of these activities provide an integrated mineralogical and textural characterisation of the rock samples in Groups B, C and D. In addition, micro-CT was performed on five samples, and oxalate and formate analysis was performed on 18 samples. These results are provided and discussed separately below.

4.2.4 Mineralogical and textural characterisation of sample rocks

4.2.4.1 General comments

Samples from Groups B and C are mineralogically and texturally comparable to the Group A samples described in the MSDCA Plan (Curtin University, 2022) and Monitoring Studies Report 2024 (Curtin University, 2024c), but are summarised briefly here. All of the sampled lithologies from Groups A to C show a three-layered structure. Using the terminology adopted previously (MSDCA Plan (Curtin University, 2022), Monitoring Studies Report 2024 (Curtin University, 2024c)), this comprises, from the outside in: patina, weathered rind, and fresher rock.

The patina is a dark thin external coating less than a millimetre thick. The weathered rind is a pale, orange or brown zone that forms the transition between the patina and the underlying fresher rock.

The fresher rock of the Group D (railway cutting) samples is indistinguishable to that of granophyre samples from Groups A to C. However, the Group D samples lack weathered rind and generally lack patina, with only a discontinuous chalky orange friable coating on parts of some surfaces.

The TIMA uses a mineral characterisation library to estimate the modes of the different minerals within each sample, based on the elemental composition of each analysed pixel. Many mineral groups, such as plagioclase and chlorite, show variable compositions and these can be split, or grouped, by the user. For this report, stoichiometric chlorite, amphibole, and clinopyroxene of all compositions are grouped and referred to as chlorite, amphibole, and clinopyroxene, respectively. An exception is K-altered chlorite, which refers to mineral that is most consistent with chlorite, but shows a non-zero K content, consistent with the presence of micrometre-scale illite alteration below

the spatial resolution of the TIMA. Plagioclase is split into a sodic end-member referred to as albite, and a group referred to as plagioclase that includes all of the more calcic compositions (andesine, labradorite). The clay minerals are commonly fine-grained and show highly variable compositions, so a number of classifications were set up to capture Fe-rich clays, which are common in the patina but may also occur within the weathered rind (Fe-Clay/Patina). Iron-poor clays, which are present in the patina, are classified as Fe poor_Patina. Similarly, Mn-Patina and Fe-Ca-K_Clay classifications were set up to capture Mn-rich material within the patina and Fe-, Ca-, and K-bearing clays. In some samples, a P and Al association is sufficiently common that a classification for "Al-P_clay" was set up to capture this material, which may relate to interaction between the patina and weathered rind, and bird excrement. These clay and patina classifications do not refer to a single mineral, but rather to a range of composition that characterises different regions within the patina and the highly altered parts of the weathered rind.

The TIMA results for the fresher rock samples from Groups B, C, and D are broadly consistent with those of previous reports, although the Group D samples lack features characteristic of the weathered rind and patina. Generally, features observed within the SEM images of samples from Groups B, C, and D are consistent with those observed in the Group A samples and documented in the Monitoring Studies Report 2024 (Curtin University, 2024c). In all lithologies, the detailed SEM images reveal abundant porosity within many of the samples (e.g., Figure *4.2-2*). The porosity increases towards the surface. The absence of weathered rind and near-absence of patina on the Group D samples is confirmed at the micrometre-scale by the SEM images. Given these similarities, the EMP, XRD, TOF-SIMS analytical results presented for the Group A samples in the Monitoring Studies Report 2024 (Curtin University, 2024c) are considered to represent the characteristics of fresher rock, weathered rind, and patina from Groups B and C, and of the fresher rock from Group D.

4.2.4.2 Fresher rock

Granophyre

Sixteen Group B, 11 Group C, and eight Group D granophyre samples were investigated by optical microscopy. The Group B samples, which were prepared as thin sections, show similar characteristics to the Group A samples documented in the Monitoring Studies Report 2024 (Curtin University, 2024c).

The Group C samples, prepared as billets, are mineralogically similar to their Group A equivalents, so their mineralogy is not described in detail here. However, the Group C billets show a better polish than the Group A samples of the same rocks. This difference in polish manifests as plucking, damage, or dissolution of chlorite in some of the thin section samples from Group A (Figure *4.2-3*). This feature is discussed further below (Section 4.2.5.1). The Group D samples show similar characteristics to the fresher rock of granophyre samples from Groups A to C, but lack weathered rind and almost completely lack patina.

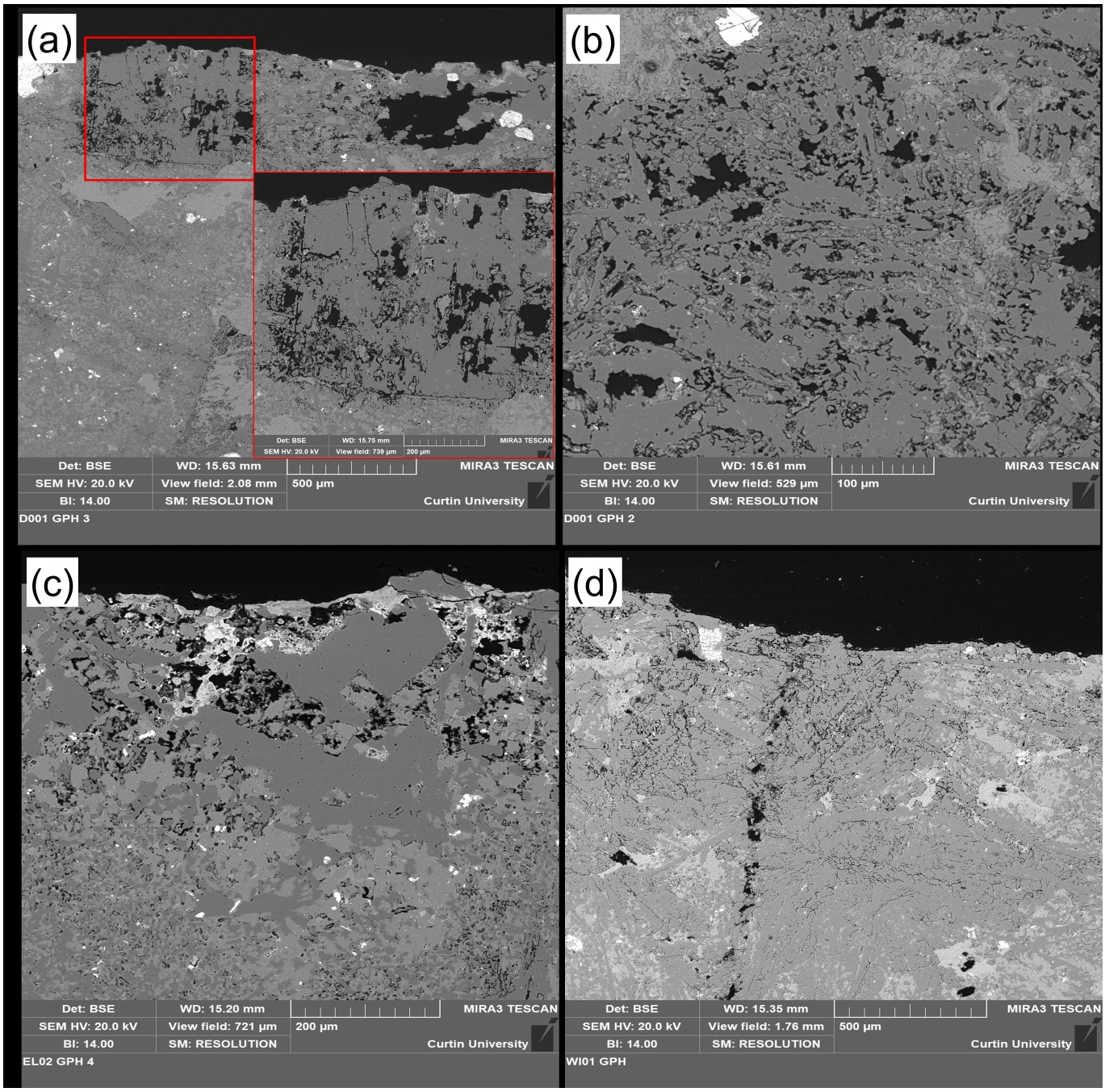

Figure 4.2-2: BSE-SEM images showing the variable nature of the transition from the fresher rock to the weathered rind in granophyre sample D001_GPH. Voids are shown in black, as is the region above the upper surface of the rock. (a) Area showing large sub-surface voids. The upper red box delineates the area shown at higher magnification in the lower red box; (b) Voids ranging from a few micrometres to 100 micrometres in size; (c) Image showing large quartz grains (dark grey mineral) surrounded by voids; (c) Unpatinated part of the surface showing a fracture, over 1 mm long, that penetrates the weathered rind.

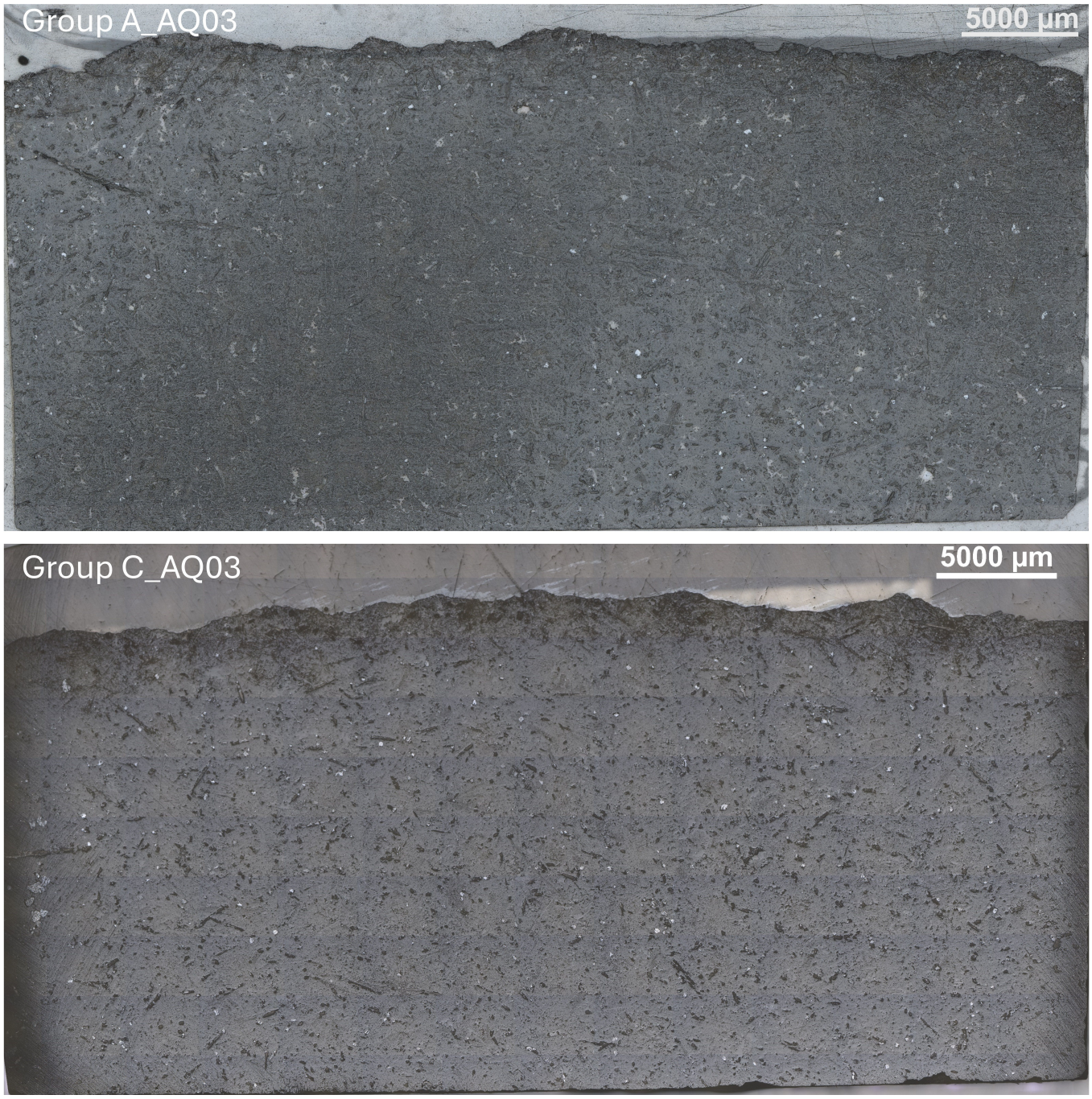

Figure 4.2-3: A comparison of photomicrographs of Group A thin-section of sample AQ03_GPH (upper) and the Group C billet of the same sample (lower image). Upper image shows darker central area that is less well polished than the upper left and lower right areas. Lower image shows a more homogeneous polish. Both images RFL PPL. Abbreviations: RFL: reflected light; PPL: Plane polarised light.

The mineralogy, mineral compositions, and microstructures of the Murujuga granophyre have been described in detail by Curtin University (2023) and the Monitoring Studies Report 2024 (Curtin University, 2024c). The findings of those reports, which are also applicable to the Group B and C samples are summarised briefly here.

The fresher rock ranges in colour from dark-grey to purple-brown. Within the fresher rock, the major minerals, with modes greater than 20% by area, are quartz, albite, and microcline. Minor minerals, with modes between 5% and 20% by area, include Mg-rich chlorite, Al-rich epidote, stilpnomelane, plagioclase of a labradorite composition, and amphibole. Accessory minerals, with modes less than 5% by area, include hematite, magnetite, ilmenite, titanite, apatite, and rare calcite. Of the major rock-forming minerals, quartz is considered primary in that it would have formed from the magma during crystallisation. Feldspars would have formed from the magma but their composition and morphology was variably altered by the hydrothermal alteration. Chlorite, stilpnomelane, epidote, and, in most cases, the amphiboles, would have formed during hydrothermal alteration and are considered to be secondary.

The rock texture ranges from equigranular to porphyritic with a highly variable microstructure within the fine-grained groundmass. (i.e. porphyritic rocks have a fine-grained groundmass, whereas equigranular rocks do not. The fresher rock of the granophyres shows either acicular or radiating textures. Radiating textures are shown by samples AN01, BU02, D001, EI03, EL01, GI02, WI02 from Group B (Figure *4.2-4*). Consistent with images in the Monitoring Studies Report 2024 (Curtin University, 2024c), the radiating texture is defined by micro-aggregates of acicular quartz, albite, and microcline that project into the surrounding groundmass. Locally, bright orange stilpnomelane forms radiating clusters (Figure *4.2-4*a). The groundmass consists of equant to sub-equant grains of the same minerals, plus the minor and accessory minerals listed above. The radiating aggregates are frequently surrounded by coronae of chlorite and/or epidote. The distribution of mineral aggregates gives the rock a patchy appearance. These fine radiating mineral intergrowths are common and characteristic within granophyres and are interpreted as quench devitrification features that formed after rapid magma cooling.

The acicular texture is seen in samples BU01, EA01, EL03, EN01, WI01 from Group B and all samples from Group D (Figure *4.2-5*). This texture is characterised by elongated prisms of quartz and tabular chlorite grains within a groundmass rich in alkali feldspar (Figure *4.2-5*a). Based on their acicular morphology, the elongate quartz grains may be pseudomorphs after tridymite, a high temperature polymorph of quartz, that inverted to lower-temperature quartz when the magma that formed the granophyre cooled.

Granophyre samples commonly show porphyritic textures defined by subhedral to anhedral albite phenocrysts $<$500 µm in size, within a finer-grained matrix (Figure *4.2-6*). Many of the minerals are altered. Plagioclase and K-feldspar are sericitised and chlorite is interpreted as after biotite (Figures *4.2-6* and *4.2-7*). For example, large euhedral grains of plagioclase in samples GI03_GPH and EL02-2_GPH show brownish sericite alteration. Pale green chlorite associated with epidote fills fractures. Alteration is also associated with an increase in the modes of the opaque minerals. While the effects of hydrothermal alteration are pervasive, the extent is variable. The glassy matrix of fine-grained rocks is more strongly affected by hydrothermal alteration than the phenocrysts. In some samples, only the fine-grained or glassy matrix is altered, while in others, even large phenocrysts are strongly modified. In some cases, this hydrothermal alteration is difficult to

distinguish from the characteristic weathering-related alteration textures of the weathered rind.

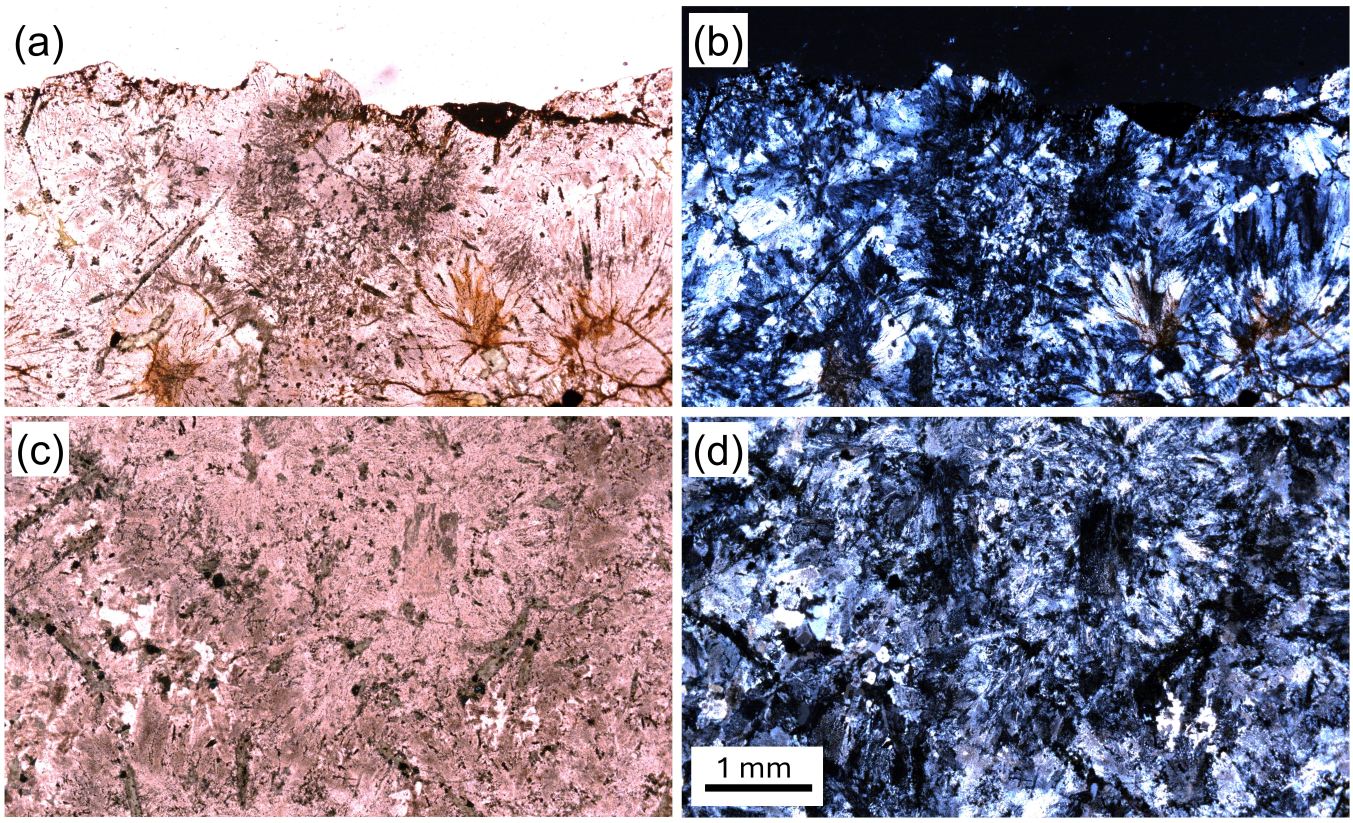

Figure 4.2-4: Examples of radial textures. (a) D001_GPH TL PPL; (b) D001_GPH TL XPL; (c) EN01_GPH TL PPL; (d) EN01_GPH TL XPL. The pale green mineral is chlorite, which is widespread in the matrix and forms coronae around intergrown felsic minerals. Abbreviations: TL: Transmitted light; PPL: Plane polarised light; XPL: cross-polarised light.

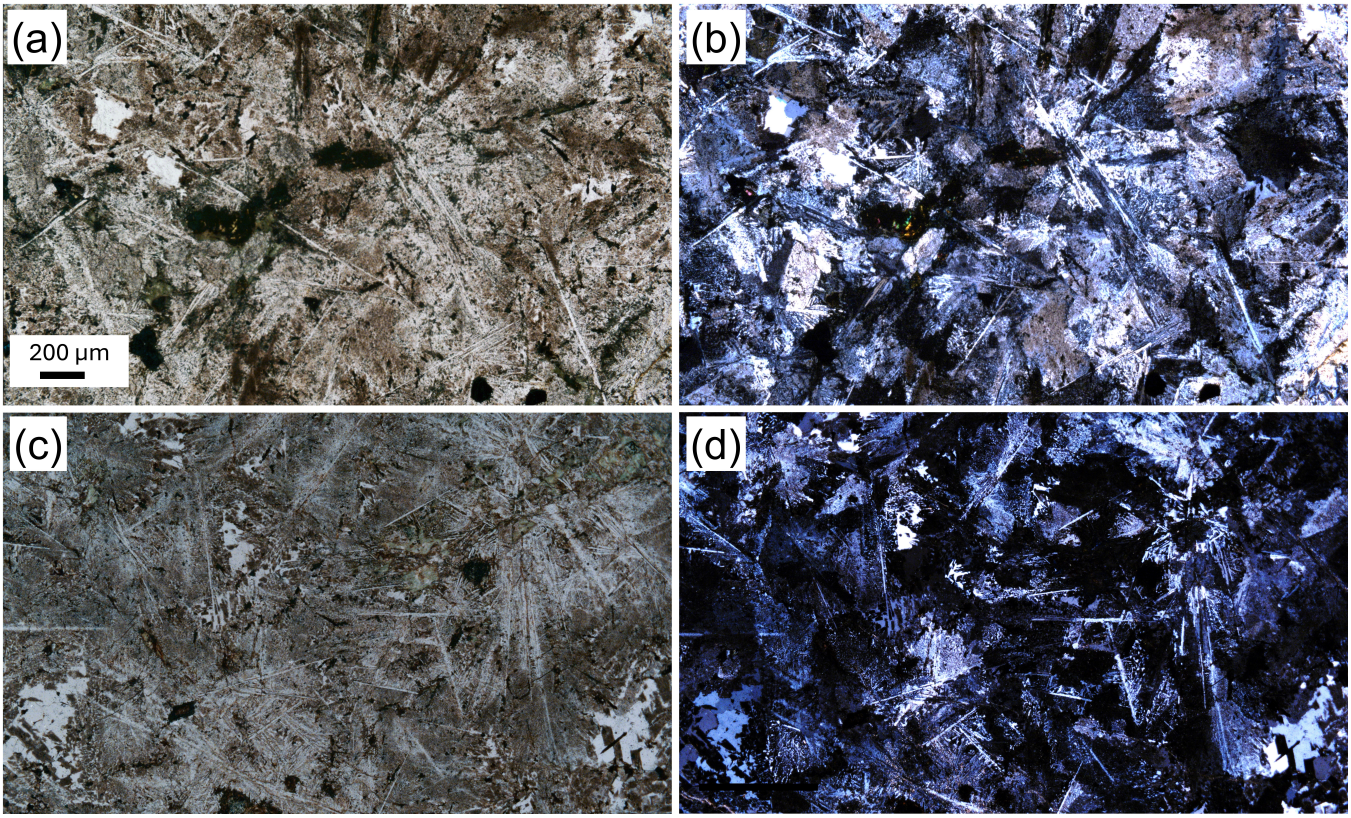

Figure 4.2-5: Examples of acicular textures. (a) EL01_GPH Granophyre TL PPL; (b) EL01_GPH Granophyre TL XPL; (c) EN01_GPH TL PPL; (d) EN01_GPH TL XPL. Pale green chlorite is widespread throughout the matrix. Abbreviations: TL: Transmitted light; PPL: Plane polarised light; XPL: cross-polarised light.

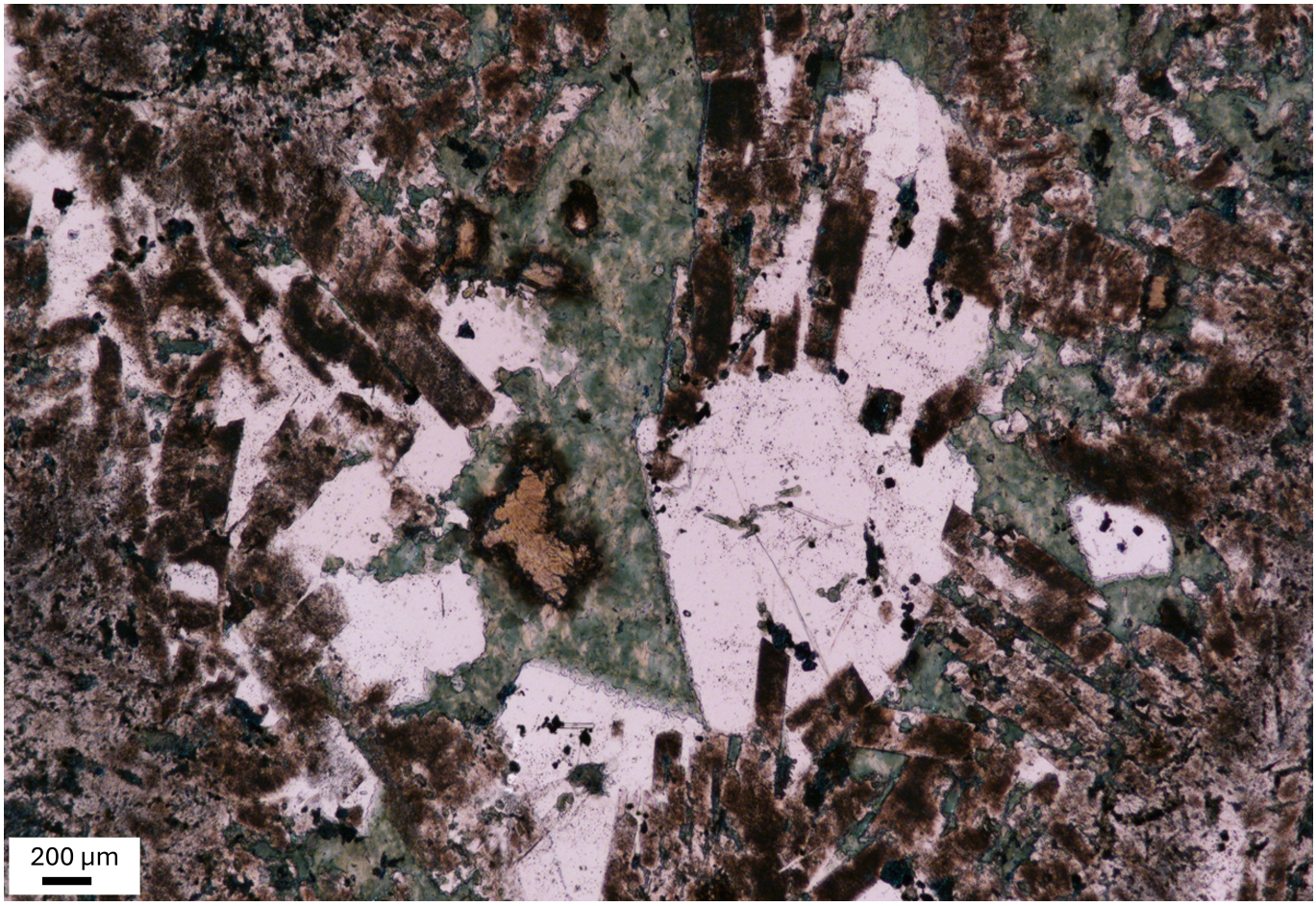

Figure 4.2-6: Green chlorite surrounds quartz (clear) and plagioclase (altered to brown aggregates). Sample BU01_GPH. TL. PPL. Abbreviations: TL: Transmitted light; PPL: Plane polarised light.

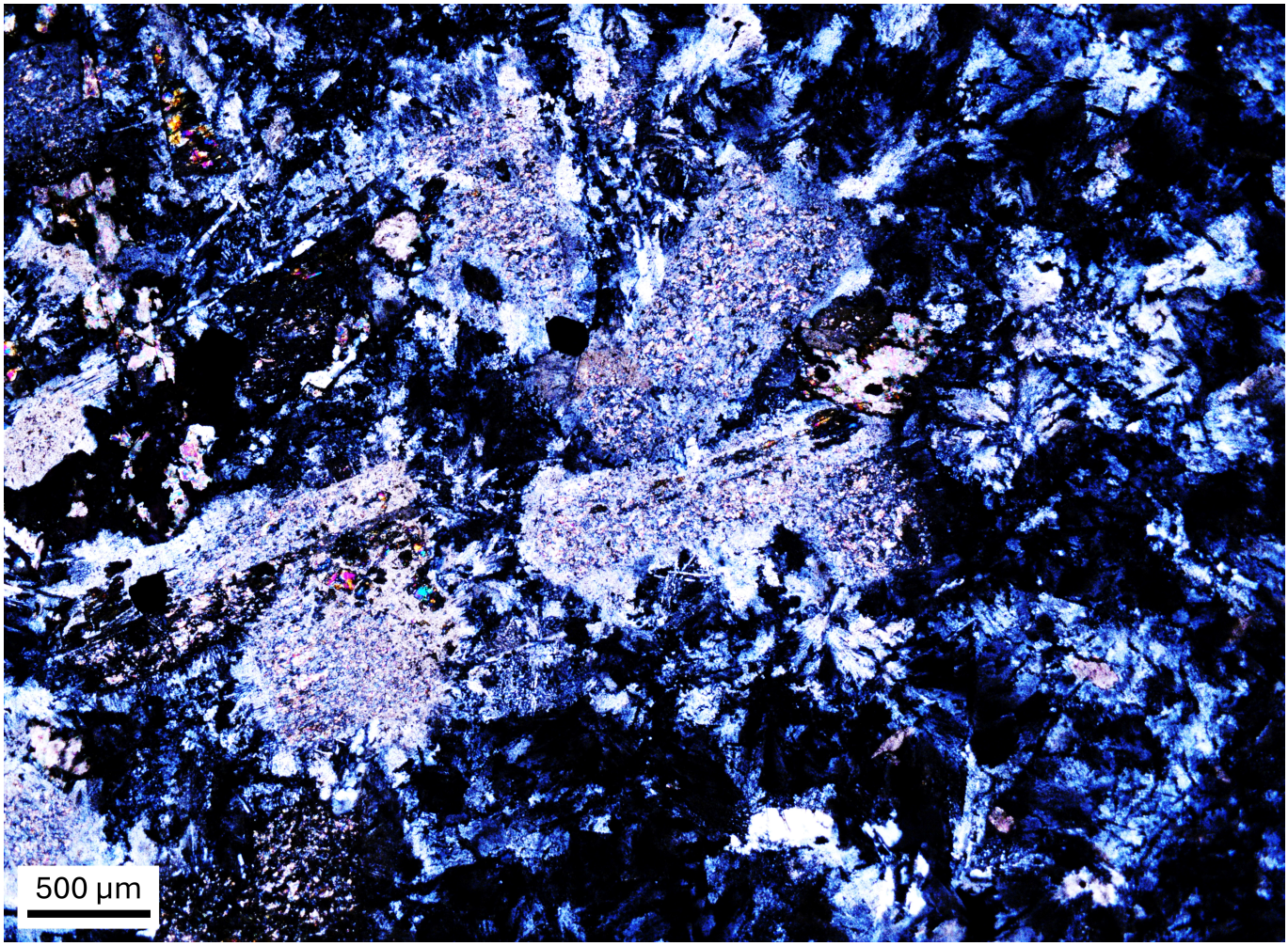

Figure 4.2-7: Sericite alteration of plagioclase and K-feldspar. Fresher rock. Sample GI03_GPH. TL. XPL. Abbreviations: TL: Transmitted light; XPL: cross-polarised light.

Quartz is the least altered mineral. For example, in sample EA01_GPH, a cluster of quartz grains, up to 2 mm across, which are much larger than those found in typical fresher granophyre, weathered rind, or patina, occur at the surface of sample. These quartz grains penetrate the matrix, are unstrained, and show abundant fluid inclusion trails. Below the rock surface, the grain boundaries are relatively planar. Based on these characteristics, the cluster of quartz grains is interpreted as part of a quartz vein that intersects the current sample surface or as an microxenolith of granite. Such features would have formed prior to weathering. Embayments within the grain margins at or close to the surface of the rock are attributed to the effects of weathering, but these effects are much less than the pervasive weathering-related alteration that affects other minerals.

Other samples are cut by veins. Samples BU02_GPH and GI01_GPH host micro-fractures that cut the section from fresher rock to patina (Figure *4.2-8*). These fractures are filled by quartz and are separated from the fresher rock by a selvage of chlorite (Figure *4.2-8*). Some of the Group D samples contain micro-fractures that cut the sections from patina to fresher rock (Figure *4.2-9*). These fractures are filled with chlorite in sample MB02_GPH. These veins are interpreted to have formed during hydrothermal alteration. Other fractures do not contain minerals and are thought to have formed by mechanical stresses during blasting to form the railway cutting, or during sample preparation.

Dolerite

Four dolerite samples from Group B were collected, prepared, and examined by optical microscopy, TIMA, and SEM (EI01_DOL, EN02_DOL, RI01_DOL and WL01_DOL). Mineral compositions obtained by electron probe microanalysis (EPMA) for similar samples from Group A are provided the in Monitoring Studies Report 2024 (Curtin University, 2024c). Mineral modes are provided in Table *4.2-1*. The results were similar to those for the Group A samples and are summarised briefly here. The most abundant minerals detected were amphibole, ortho- and clinopyroxene, plagioclase, and chlorite. Minor phases include epidote, quartz, clay minerals, muscovite, and minor microcline. Accessory minerals include titanite, ilmenite, magnetite, hematite, apatite, calcite, and pyrite. The Fe-Ti oxides are distributed throughout the matrix.

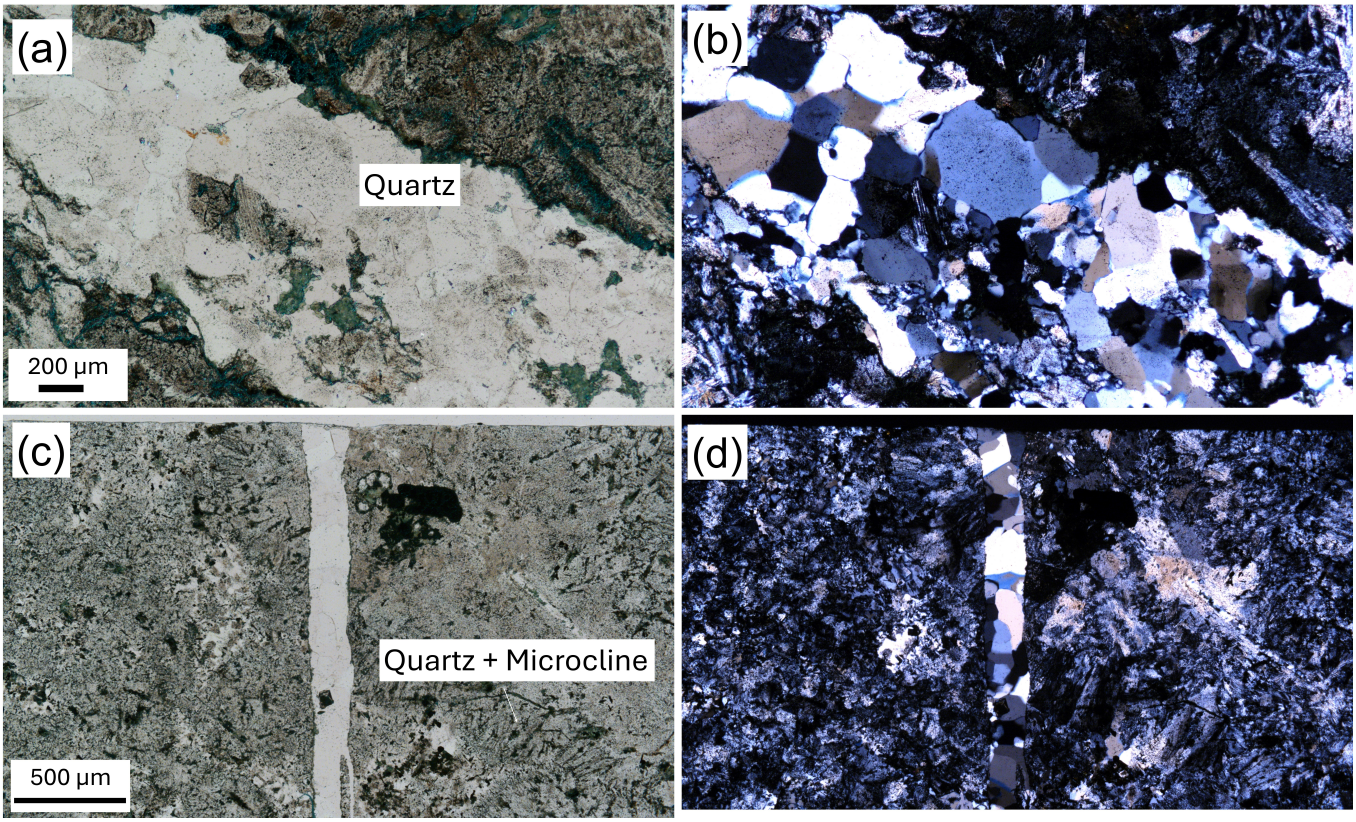

Figure 4.2-8: (a) BU02_GPH showing quartz vein (TL, PPL). (b) Same as (a) TL, XPL. (c) Fracture filled with quartz in sample GI01_GPH (TL, PPL) (d) Same as (c) TL XPL. Abbreviations: TL: Transmitted light; PPL: Plane polarised light; XPL: cross-polarised light.

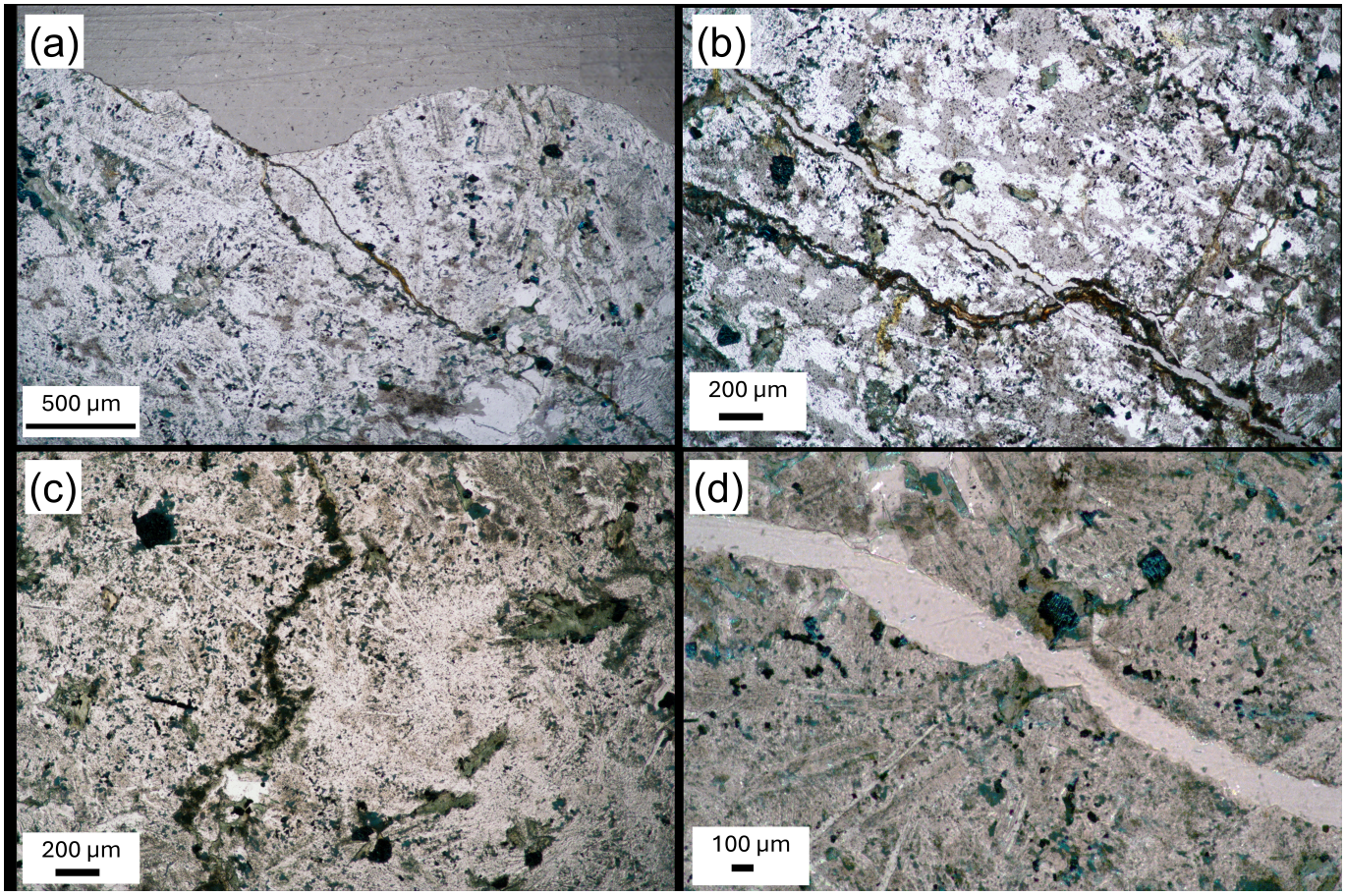

Figure 4.2-9: Photomicrographs of railway cutting samples showing fractures and veins. (a, b) RT02_GPH. Fractures filled with iron oxides (dark and orange lines) or quartz (colourless fracture in (b)); (c) RT04_GPH showing opaque minerals withn the sinuous fracture; (d) MB02_GPH showing a fracture that does not contain minerals. All transmitted plane polarised light.

Table 4.2-1: Summary of mineral modes for Group D dolerite samples estimated by TIMA. The zone referred to as weathered rind + patina may include some of the fresher rock. The fresher rock is the area below the weathered rind plus patina. "Holes" refers to areas identified by the TIMA as free of rock material, and may differ from the measured porosity. Estimated modes of less than 0.01% are omitted.

Group B: N = 4	**Fresher rock**		**Weathered Rind + Patina**	
Primary phases vol %	**AVG**	**STDV**	**AVG**	**STDV**
Amphibole	23.59	4.8	23.72	5.0
Albite	15.71	5.4	16.57	8.4
Clinopyroxene	17.01	5.7	12.32	4.0
Epidote	10.87	3.2	11.58	3.8
Chlorite	11.55	5.6	10.60	2.8
Plagioclase	8.68	3.3	9.80	2.7
Quartz	6.11	1.4	5.79	2.3
Fe-Clay/Patina	3.15	1.5	3.99	1.8
Alkali Feldspar	1.47	1.4	1.40	1.3
Titanite	0.63	0.1	0.65	0.1
Muscovite/Illite	0.36	0.6	0.38	0.6
Hematite/Magnetite	0.01	0.0	0.31	0.5
Ilmenite	0.10	0.1	0.12	0.1
Apatite	0.05	0.1	0.05	0.1
Pyrite	0.02	0.0	0.00	0.0
Calcite	0.02	0.0	0.00	0.0
Unclassified	0.63	0.1	0.74	0.2
Holes	0.01	0.0	1.97	0.5
Total	100.00		100.00	

Of the major and minor minerals, the pyroxenes formed from the magma and are considered primary igneous minerals. Some of the pyroxenes were altered to amphiboles during hydrothermal alteration, which is also likely to have modified the morphology and composition of the feldspars (Figure *4.2-11*). Chlorite and epidote are attributed to hydrothermal alteration and are considered to be secondary.

Clinopyroxene is augitic and forms subhedral to anhedral grains that are widely distributed throughout the fresher rock (Figure *4.2-10*c, d). Zoning is observed within some clinopyroxene. Systematic changes in the composition of a phase, referred to as zonation, are a common feature in pyroxene phenocrysts in dolerite and basalt. These features are considered as a primary igneous growth feature. The concentric zones form as temperature and or pressure decrease as the magma cools and the composition of the pyroxene alters to maintain equilibrium with the co-existing magma. Narrow reaction rims that show sharper changes in composition than the gradational changes associated with the zoning may form as a consequence of chemical disequilibrium between the clinopyroxene phenocryst and a fluid under sub-solidus conditions during hydrothermal alteration. These narrow rims may also form during low-temperature weathering as pyroxene breaks down. The Fe-Ti oxides that occur proximal to the clinopyroxene form from Fe and Ti that is lost by

the clinopyroxene as its composition changes, and the type and composition of Fe-Ti oxides can provide information on the environmental conditions during pyroxene alteration.

Chlorite, amphibole, and some clay minerals after clinopyroxene show a complex distribution (Figure *4.2-11*). Clinopyroxene adjacent to chlorite shows chemical zonation, revealed by bright rims on some grains, which are enriched in Fe, Ca, Mn, Ti, and Mn and depleted in Mg and Si (Figure *4.2-12*). These features are also documented in the Monitoring Studies Report 2024 (Curtin University, 2024c).

Granite

Only one new sample of granite, D003_GRT from Group B, was collected for analysis in the third year of studies. This sample was prepared and observed by optical microscopy and analysed by TIMA. Mineral modes for the fresher rock are provided in Table *4.2-2*. The mineralogy of the sample is consistent with that of the granite samples documented in the Monitoring Studies Report 2024 (Curtin University, 2024c). The most abundant phases are albite, plagioclase, quartz, and K-feldspar, with minor amounts of epidote, Mg-rich chlorite, muscovite, stilpnomelane, and rare amphibole. The K-feldspar shows cross-hatched twinning characteristic of the microcline polymorph. Large anhedral quartz grains are surrounded by smaller grains of albite and microcline (Figure *4.2-13*). Quartz grains are commonly fractured.

Table 4.2-2: Summary of mineral modes for granite sample D003_GRT estimated by TIMA. The zone referred to as weathered rind + patina may include some of the fresher rock. The fresher rock is the area below the weathered rind plus patina. "Holes" refers to areas identified by the TIMA as free of rock material, and may differ from the measured porosity. Estimated modes of less than 0.01% are omitted.

Primary phases vol %: N=1	Fresher rock	Weathered Rind + Patina
Plagioclase (Albite)	41.19	41.12
Quartz	37.50	35.20
Alkali Feldspar	13.54	14.87
Muscovite/Illite	3.88	4.51
Chlorite	1.61	1.53
K-alt-Chlorite	0.56	0.57
Titanite	0.39	0.46
Plagioclase	0.27	0.21
Fe-Clay/Patina	0.11	0.15
Amphibole	0.10	0.10
Apatite	0.04	0.05
Epidote	0.04	0.03
Mn-Patina	0.02	0.01
Unclassified	0.57	0.62
Holes	0.19	0.56
Total	100.00	100.00

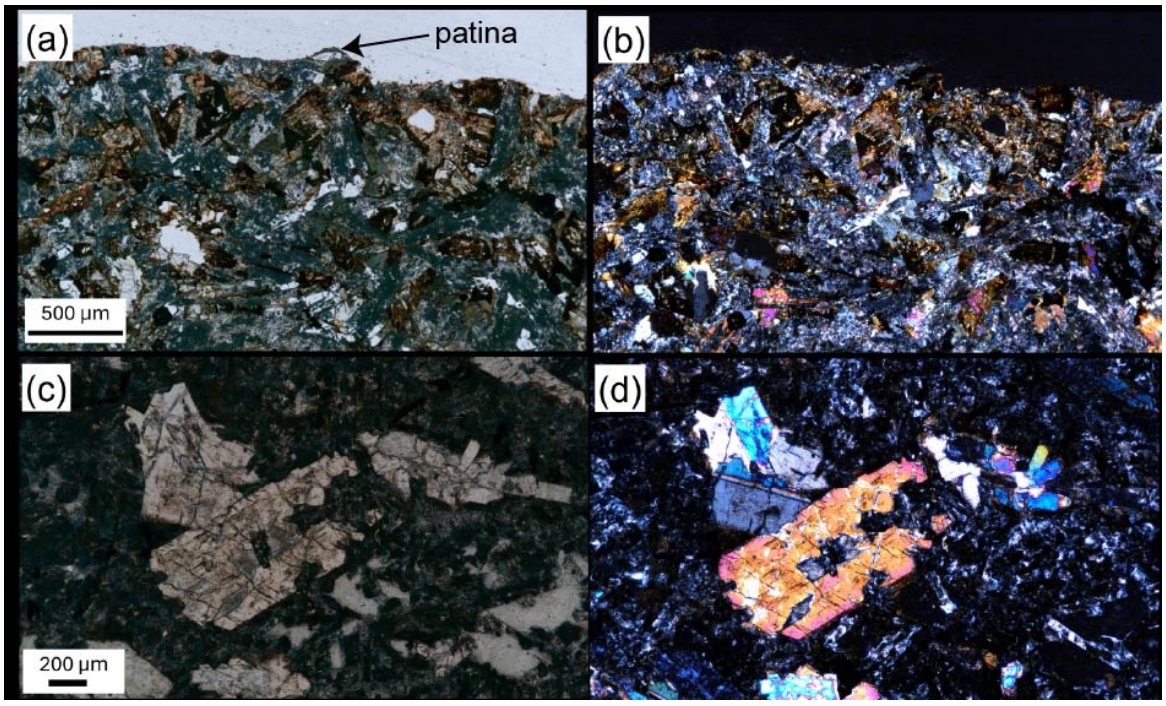

Figure 4.2-10: Plane polarized (a, c) and crossed polarised (b, d) photomicrographs of dolerite WL01_DOI in transmitted light. (a, b) Patina and weathered rind; the patina is the very thin layer indicated by the arrow in (a). (c, d) Fresher rock of sample RI01_DOL (c, d). The large crystal in (c) and (d) is clinopyroxene.

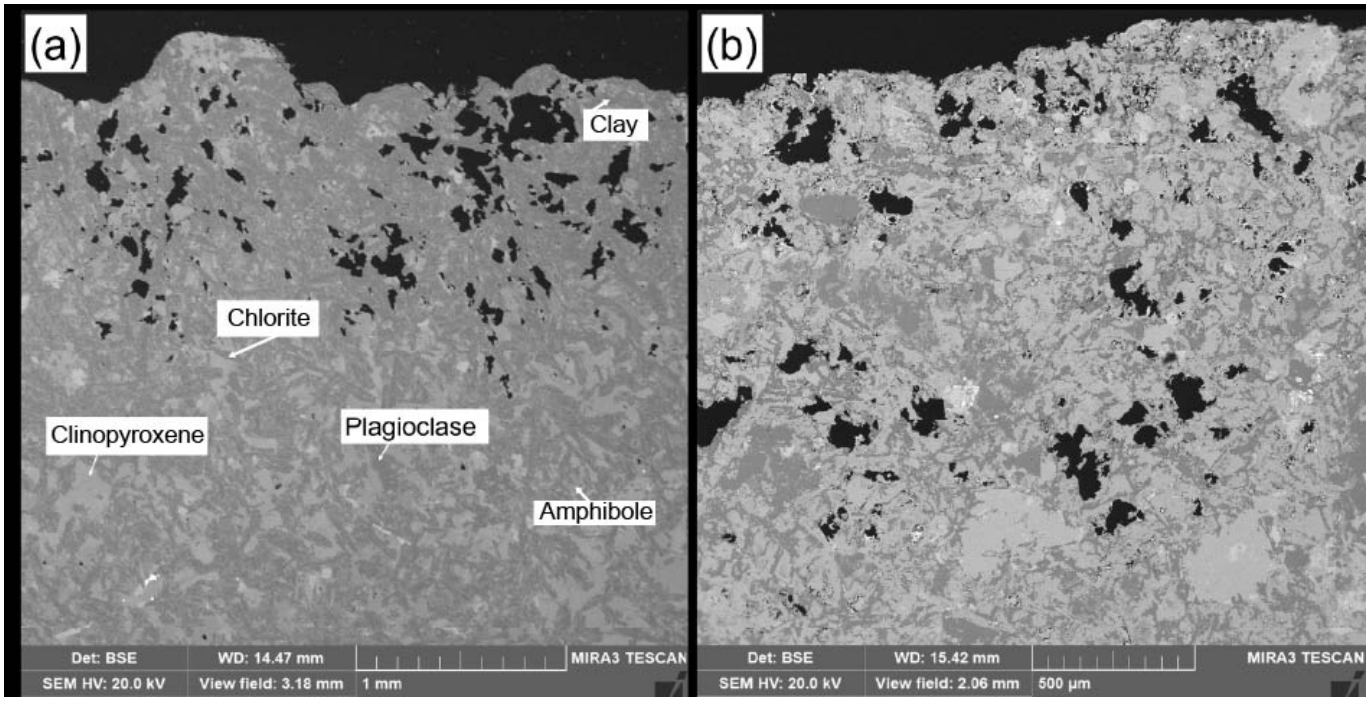

Figure 4.2-11: BSE-SEM image of the transition from fresher rock to patina to weathered rind for (a) EN01_DOL Zoning in clinopyroxene and marginal Fe-Ti oxides shown by yellow arrows. (b) EI01_DOL. Loss of clinopyroxene has formed porosity within the weathered rind. The brighter particles are Fe-Ti oxides.

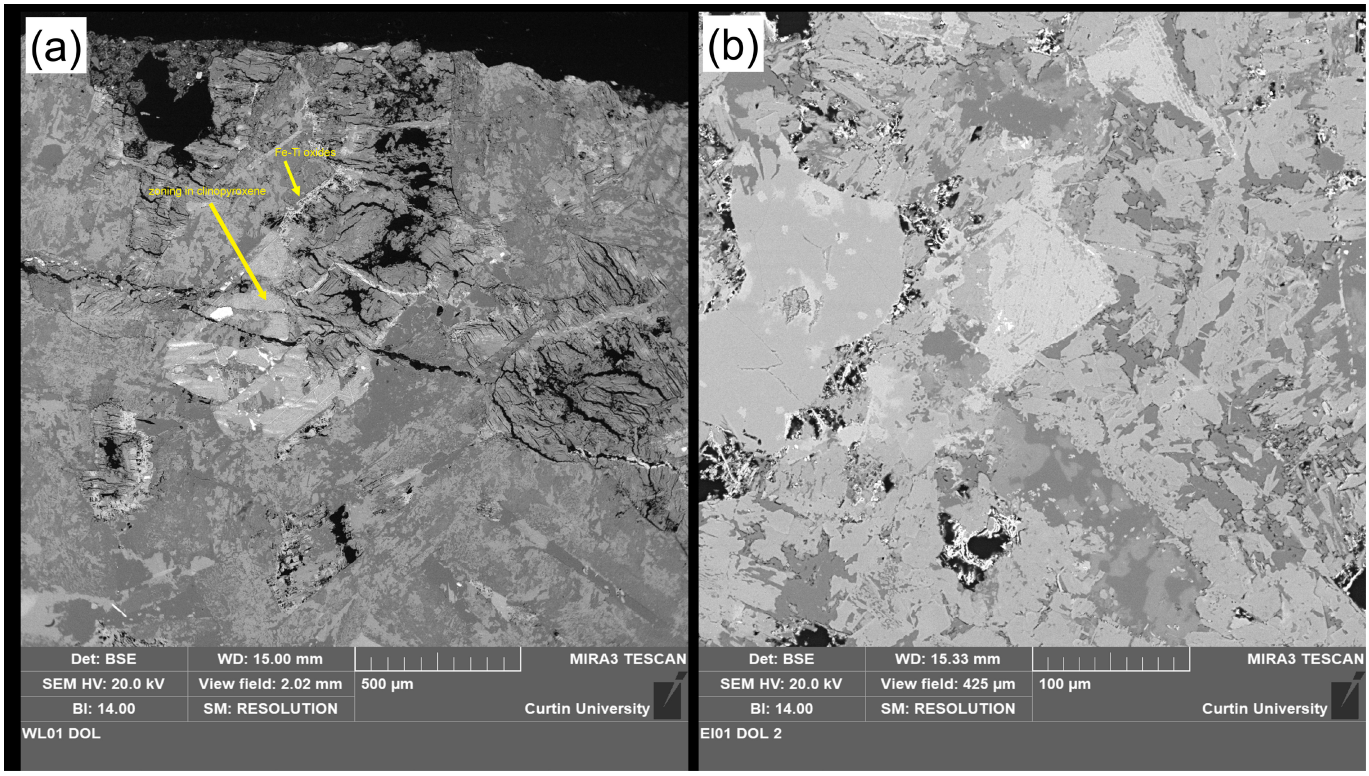

Figure 4.2-12: BSE-SEM images of the transition from fresher rock to the weathered rind and patina. (a) WL01_DOL; (b) EI01_DOL. Loss of clinopyroxene has formed porosity within the weathered rind. The bright rim indicated by a yellow arrow shows the location of Fe-oxide minerals.

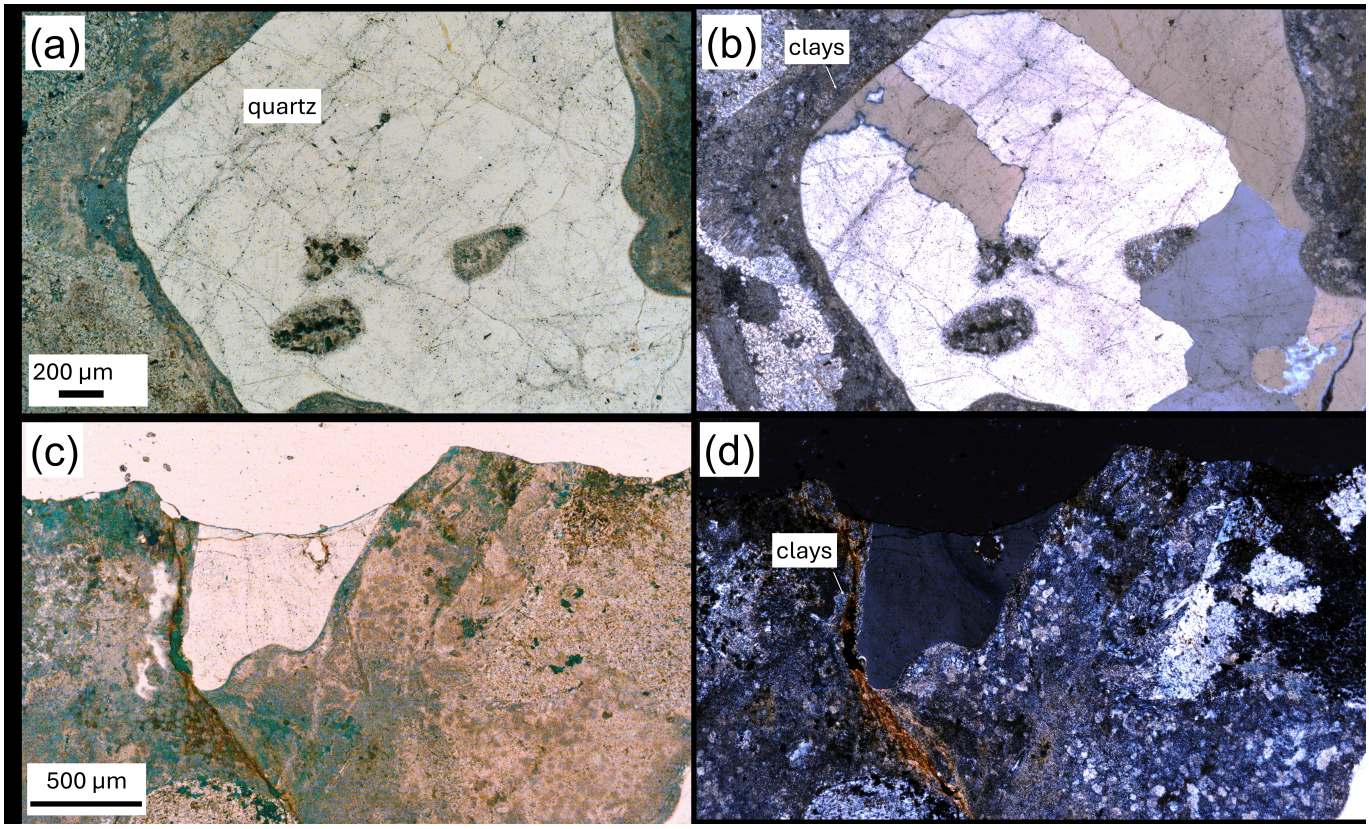

Figure 4.2-13: Plane polarized (a, c) and crossed polarized (b, d) photomicrographs of granite sample D003_GRT in transmitted light. (a, b) show the fresher rock. The large quartz grain shows extensive inclusion trails. Albite and microcline are not individually recognisable on this relatively low magnification image. (c and d) show the weathered rind and patina. Feldspar grains within the weathered rind show extensive sericite alteration and clay formation and it is unclear whether they originally formed as K-feldspar or plagioclase.

Of the major and minor minerals, most of the quartz formed from the magma and is considered as a primary igneous phase. Hydrothermal alteration likely modified the morphology and composition of the feldspars. Chlorite, epidote, and stilpnomelane are attributed to hydrothermal alteration and are considered to be secondary.

Gabbro

Only one of the new samples collected in the third study year, from Group B, is a gabbro (DO02_GBR). This sample was investigated by optical microscopy and TIMA. The mineralogy and characteristic features are similar to those described for other Murujuga gabbro samples in the Monitoring Studies Report 2024 (Curtin University, 2024c). Mineral modes are reported in Table *4.2-3*. Sample DO02_GBR is coarse-grained, mafic, and phaneritic. Abundant minerals within the fresher rock include clinopyroxene, with a mode of 57%, and chlorite (Figure *4.2-14*). Quartz is a minor mineral within the gabbro.

Of the major and minor minerals, the pyroxenes formed from the magma and are considered primary igneous minerals. Some of the pyroxenes were altered to amphiboles during hydrothermal alteration, which is also likely to have modified the morphology and composition of the feldspars.

Chlorite and epidote are attributed to hydrothermal alteration and are referred to as secondary.

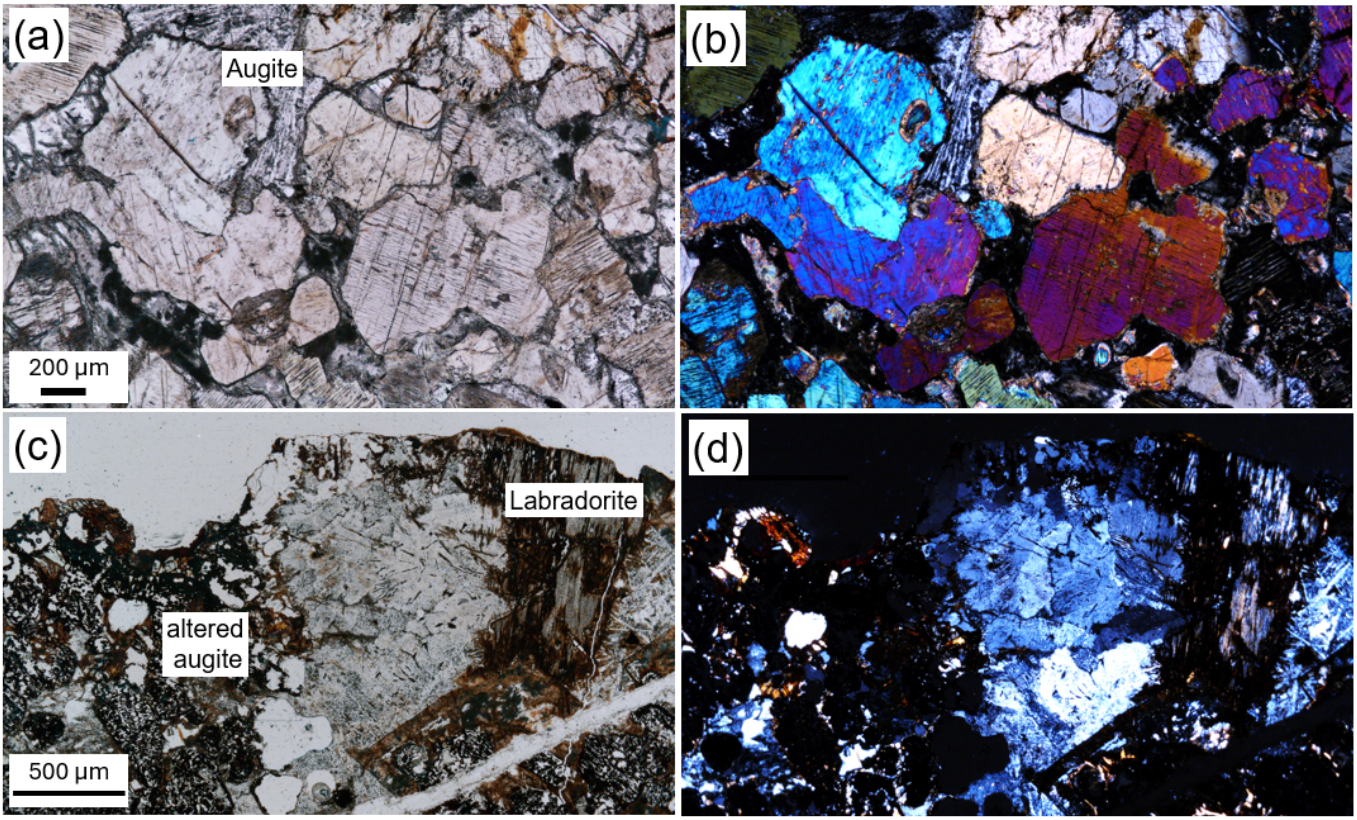

Figure 4.2-14: Plane polarized (a, c) and crossed polarised (b, d) photomicrographs of gabbro sample D002_GBR in transmitted light. Clinopyroxene grains show second-order birefringence. Clinopyroxene and plagioclase are replaced by chlorite and epidote.

4.2.4.3 Weathered rind

The weathered rind extends from the base of the patina to depths of up to few millimetres. This zone is pale orange to reddish/dark brown in colour and shows highly variable textures and mineralogy. The weathered rind is present in all the Group B and C samples but is absent from the Group D samples. Differences in colour amongst the samples are attributed to different degrees of iron oxidation, different Fe- and Mn-bearing minerals, and variable alteration of feldspar minerals to clays (Figure *4.2-4*). For example, altered albite and microcline are cream to pale orange or yellow in colour, whereas altered chlorite and epidote show green to brown colours. Some grain boundaries show more intense colours, highlighting the highly heterogeneous nature of the fresher rock to clay transition.

Table 4.2-3: Mineral modes for gabbro sample DO02_GBR estimated by TIMA. The zone referred to as weathered rind + patina may include some of the fresher rock. The fresher rock is the area below the weathered rind plus patina. "Holes" refers to areas identified by the TIMA as free of rock material, and may differ from the measured porosity. Estimated modes of less than 0.01% are omitted.

Primary phases vol %: N = 1	Fresher rock	Weathered Rind + Patina
Clinopyroxene	57.22	26.50
Chlorite	17.57	23.21
Quartz	9.69	14.54
Albite	3.23	4.53
Epidote	4.06	3.30
Plagioclase	2.95	2.01
Fe-Clay/Patina	0.04	4.21
Muscovite/Illite	1.87	2.13
Hematite/Magnetite	0.02	3.83
Orthopyroxene	1.54	1.43
Amphibole	0.35	0.77
Mn-Patina	0.26	0.68
Ilmenite	0.24	0.42
Alkali Feldspar	0.13	0.16
Titanite	0.23	0.06
Apatite	0.03	0.02
Rutile	0.00	0.01
Unclassified	0.33	0.87
Holes	0.25	11.30
Total	100.00	100.00

Granophyre

In Group B and C samples, the proportion of clay minerals is higher within the patina and weathered rind than in the fresher rock (Tables *4.2-4* and *4.2-5*). Albite and chlorite, including weathering-altered chlorite, are the most common minerals within the weathered rind. The term weathering-altered chlorite, or altered chlorite, refers to chlorite that has partially altered to clay minerals during weathering. Altered chlorite shows a grain shape that is still typical of chlorite, and some areas show the characteristic anomalous birefringence. However, the composition is non-stoichometric, reflecting weathering-related changes in chlorite composition. The modes of albite and chlorite decrease from the fresher rock to the weathered rind, whereas the mode of quartz increases from the fresher rock to the weathered rind (Tables *4.2-4* and *4.2-5*). The mode of Fe-oxides, represented in the TIMA analysis by hematite and magnetite, increase through the weathered rind, towards the patina.

Within the granophyre, the weathered rind is characterised by voids previously occupied by matrix albite and K-feldspar, as documented in the Monitoring Studies Report 2024 (Curtin University, 2024c). Quartz, which is relatively unaffected by weathering, forms skeletal grains that surround

voids originally filled by the feldspars. These structures preserve the original morphology of the granophyric intergrowths that are common within the fresher rock (Curtin University, 2024c). These features are well represented within the Group B samples (Figure *4.2-2*).

Table 4.2-4: Summary of mineral modes for Group B granophyre samples estimated by TIMA. The zone referred to as weathered rind + patina may include some of the fresher rock. The fresher rock is the area below the weathered rind plus patina. "Holes" refers to areas identified by the TIMA as free of rock material, and may differ from the measured porosity. Estimated modes of less than 0.01% are omitted.

Group B: N = 16	**Fresher rock**		**Weathered Rind + Patina**	
Primary phases vol %	**AVG**	**STDV**	**AVG**	**STDV**
Plagioclase (Albite)	52.56	7.8	48.60	7.7
Quartz	20.67	5.0	20.81	4.6
Alkali Feldspar	16.15	6.1	16.20	5.7
Chlorite	4.10	1.2	4.02	1.5
K-alt-Chlorite	2.04	0.5	3.21	1.1
Epidote	1.11	1.0	0.69	0.7
Plagioclase	1.02	0.4	0.73	0.3
Hematite/Magnetite	0.63	0.2	0.75	0.4
Fe-Clay/Patina	0.13	0.1	0.61	0.4
Titanite	0.17	0.1	0.20	0.1
Ilmenite	0.18	0.1	0.17	0.1
Amphibole	0.18	0.0	0.06	0.0
Mn-Patina	0.00	0.0	0.22	0.4
Stilpnomelane	0.07	0.0	0.10	0.1
Calcite	0.10	0.2	0.02	0.0
Muscovite/Illite	0.01	0.0	0.06	0.1
Apatite	0.03	0.0	0.02	0.0
Kaolinite	0.00	0.0	0.04	0.1
P-Al concretions	0.00	0.0	0.01	0.0
Rutile	0.00	0.0	0.01	0.0
Ankerite	0.01	0.0	0.00	0.0
Unclassified	0.61	0.1	0.75	0.3
Holes	0.20	0.2	2.74	1.6
Total	100.00		100.00	

Table 4.2-5: Summary of mineral modes for Group C granophyre samples estimated by TIMA. The zone referred to as weathered rind + patina may include some of the fresher rock. The fresher rock is the area below the weathered rind plus patina. "Holes" refers to areas identified by the TIMA as free of rock material, and may differ from the measured porosity. Estimated modes of less than 0.01% are omitted.

Group C: N = 11	**Fresher rock**		**Weathered Rind + Patina**	
Primary phases vol %	**AVG**	**STDV**	**AVG**	**STDV**
Plagioclase (Albite)	36.46	7.9	23.17	6.2
Quartz	27.49	5.0	31.44	3.6
Alkali Feldspar	19.43	5.3	19.13	5.1
K-alt-Chlorite	7.85	1.9	12.35	4.1
Chlorite	2.09	1.3	1.51	1.0
Plagioclase	1.18	0.4	1.43	0.6
Epidote	1.41	1.6	0.97	1.2
Hematite/Magnetite	0.79	0.7	0.79	0.7
Fe-Clay/Patina	0.39	0.2	0.73	0.5
Ilmenite	0.34	0.3	0.52	0.3
Stilpnomelane	0.30	0.4	0.22	0.2
Amphibole	0.40	0.3	0.08	0.1
Mn-Patina	0.00	0.0	0.25	0.5
Titanite	0.10	0.1	0.03	0.0
Fe-Ca-K_Clay	0.04	0.0	0.05	0.0
Calcite	0.05	0.1	0.01	0.0
Apatite	0.02	0.0	0.01	0.0
Clinopyroxene	0.02	0.0	0.00	0.0
P-Al concretions	0.00	0.0	0.02	0.0
Kaolinite	0.00	0.0	0.01	0.0
Muscovite/Illite	0.00	0.0	0.01	0.0
Rutile	0.00	0.0	0.01	0.0
Unclassified	1.13	0.3	1.44	0.5
Holes	0.49	0.5	5.80	4.2
Total	100.00		100.00	

Table 4.2-6: Summary of mineral modes for Group A granophyre samples estimated by TIMA. The zone referred to as weathered rind + patina may include some of the fresher rock. The fresher rock is the area below the weathered rind plus patina. "Holes" refers to areas identified by the TIMA as free of rock material, and may differ from the measured porosity. Estimated modes of less than 0.01% are omitted.

Group A: N = 31	**Fresher rock**		**Weathered Rind + Patina**	
Primary phases vol %	**AVG**	**STDV**	**AVG**	**STDV**
Quartz	35.47	6.3	36.08	5.7
Albite	33.08	9.9	26.81	10.9
Alkali Feldspar	15.21	5.3	14.97	5.3
K-alt-Chlorite	1.56	0.6	2.76	1.4
Plagioclase	1.98	1.2	1.64	1.1
Epidote	1.70	1.5	1.39	1.2
Chlorite	1.95	1.3	1.06	1.2
Hematite/Magnetite	0.72	0.5	0.74	0.7
Muscovite/Illite	0.17	0.3	0.83	1.3
Fe-Clay/Patina	0.31	0.5	0.61	1.0
Amphibole	0.39	0.4	0.16	0.3
Stilpnomelane	0.33	0.5	0.20	0.2
Ilmenite	0.23	0.2	0.24	0.2
Mn-Patina	0.00	0.0	0.15	0.3
Titanite	0.13	0.1	0.04	0.1
Pyrophyllite	0.01	0.1	0.09	0.3
Fe-Ca-K_Clay	0.03	0.0	0.06	0.1
Kaolinite	0.00	0.0	0.05	0.1
Calcite	0.06	0.1	0.01	0.0
Clinopyroxene	0.03	0.1	0.01	0.0
P-Al Concretions	0.00	0.0	0.04	0.1
Apatite	0.02	0.0	0.01	0.0
Fe poor_Patina	0.00	0.0	0.02	0.1
Rutile	0.00	0.0	0.01	0.0
Unclassified	5.73	4.1	7.12	5.1
Holes	0.85	1.2	4.87	2.5
Total	100.00	0.0	100.00	0.0

Dolerite

The weathered rind shows slightly higher modes of amphibole, plagioclase, epidote, Fe-clay/patina, titanite, muscovite/illite, hematite/magnetite, and ilmenite than the fresher rock. Decreases in mode are observed for clinopyroxene (4%), chlorite (1%), and quartz (Table *4.2-1*). Clinopyroxene within the weathered rind is fractured and anhedral. Irregular margins on clinopyroxene may reflect resorption under magmatic conditions, alteration during hydrothermal alteration, or modification by weathering. Clinopyroxene within the fresher rock is commonly subhedral to anhedral, consistent with some pre-weathering modification. However, clinopyroxene within the weathered rind is substantially more embayed and irregular in shape than that within the fresher rock, consistent with substantial weathering-related grain shape modification. Locally, SEM-bright rims on clinopyroxene grains within the weathered rind record the presence of clay minerals and Fe-oxides. In addition, clinopyroxene exhibits a characteristic skeletal structure that mimics the original distribution of exsolution lamellae and cleavage. Plagioclase is altered to form clay minerals, and voids with the same shape as the plagioclase grains indicate that plagioclase has been lost locally to form voids. The proportion of voids decreases from the rim to the core of grains. The voids have created well-developed porosity within the weathered rind.

Granite

Like the granite samples described in the Monitoring Studies Report 2024 (Curtin University, 2024c), granite sample D003_GRT has a thinner weathered rind and patina than granophyre and gabbro samples, except for the Group D samples from the railway cutting where the weathering is absent. Alteration increases from the base of the weathered rind towards the surface (e.g., Figure *4.2-13*). Within the weathered rind, protolith feldspar grains are altered to illite and other clay minerals, which gives the altered feldspar grains a dark brown colour (Figure *4.2-13*). Voids are present, particularly where the feldspars and quartz form fine-grained intergrowths (Figure *4.2-15*), but voids are less common and less extensive than in samples from other lithologies in Groups A to C. The clay minerals are mostly K-rich (e.g., illite), or Mg-rich, and form massive replacive aggregates or pseudomorphic replacement of matrix minerals, phenocrysts, and secondary hydrothermal minerals.

The TIMA results show a decrease in the modes of plagioclase, chlorite, and quartz within the weathered rind relative to the fresher rock (Table *4.2-2*). In contrast, the modes of clay minerals, illite, and K-feldspar increase from the base of the weathered rind towards the surface. The decreases in chlorite mode towards the surface are consistent with potassic alteration of chlorite during weathering, as reported in the Monitoring Studies Report 2024 (Curtin University, 2024c).

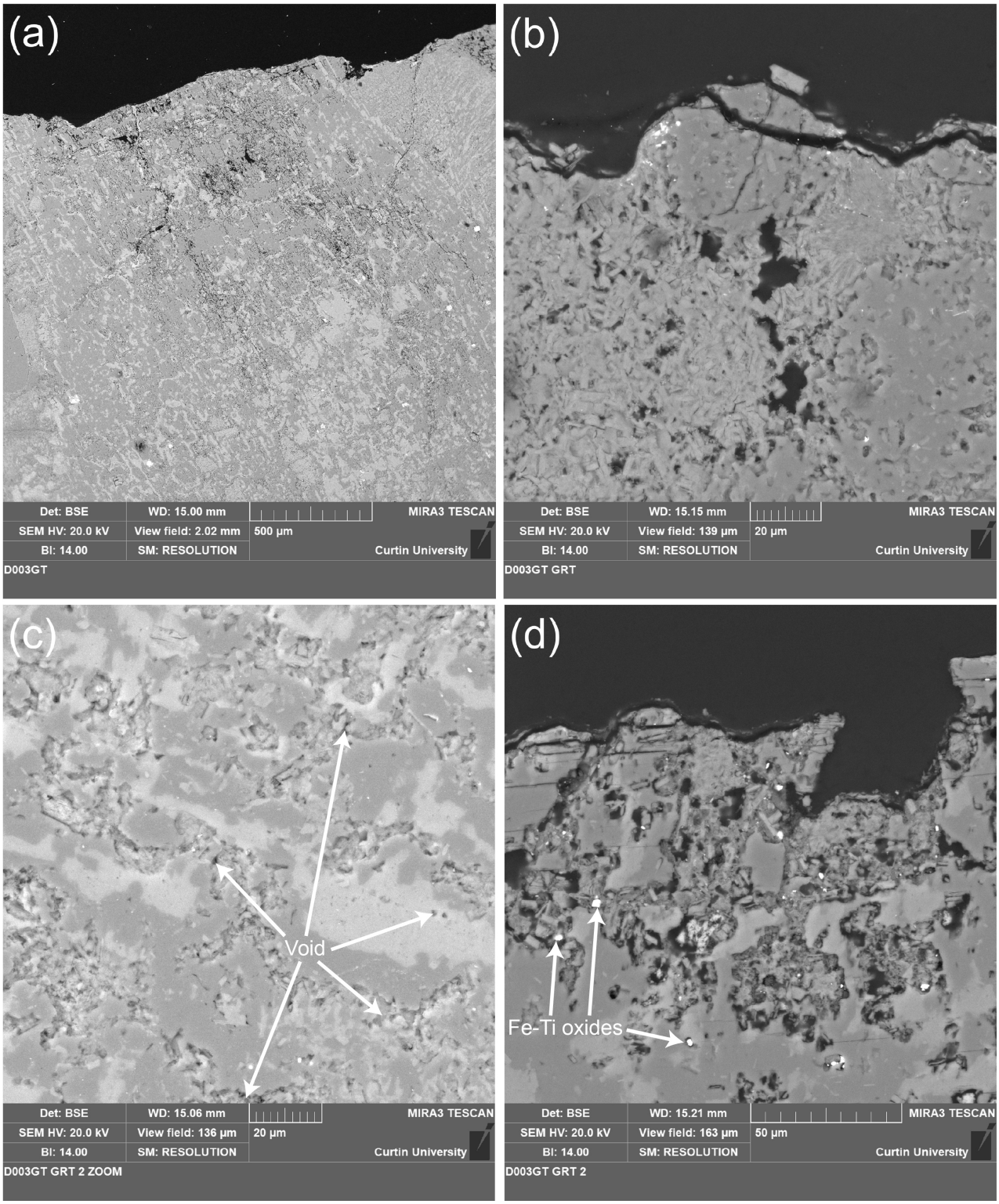

Figure 4.2-15: SEM-BSE images of granite sample D003_GRT. K-feldspar shows the highest BSE signal (palest grey). Quartz and albite show a similar BSE signal (darker grey than K-feldspar) but albite is typically more porous, altered, shows a slightly higher BSE signal, and is typically less well polished than quartz. (a) intergrown quartz and albite (darker grey) and K-feldspar (lighter grey). (b) weathered rind characterized by formation of voids within albite (darker grey) and K-feldspar (lighter grey). (c, d) voids formed within albite (darker grey) and K-feldspar (lighter grey) create extensive microporosity.

Gabbro

The weathered rind of sample DO02_GBR, where cut by the plane of the thin section, shows a strong relief. In this context, relief refers to differences in the height of the crests and troughs that define the surface of the patina on the thin section. The relief of the weathered rind is stronger than the relief shown by the finer-grained granophyres. In addition, the weathered rind of the gabbro shows a distinct colour contrast against fresher gabbro (Figure *4.2-14*). The weathered rind is brown to orange in colour. Within the weathered rind, clinopyroxene is altered and locally absent, leaving voids.

The TIMA analysis shows decreases of up to 30% by area in the mode of clinopyroxene relative to the clinopyroxene mode within the fresher rock. The decrease in clinopyroxene mode is coupled with an increase in the modes of clay minerals, by up to 8% by area, of Fe-clay, and Fe- and Ti-oxide minerals. In addition, the mode of chlorite, which may include other Mg-bearing clays, increases within the weathered rind relative to the fresher rock by up to 10% by area (Table *4.2-3*). These losses are coupled with increases in the modes of chlorite, albite, muscovite/illite and Fe-oxide minerals (Table *4.2-3*).

Relict clinopyroxene within the weathered rind is heavily altered. Alteration manifests as the removal of material along original exsolution lamellae and cleavage planes to form skeletal clinopyroxene grains, similar to those described in the Monitoring Studies Report 2024 (Curtin University, 2024c). Incipient alteration is evident in the presence of pits within the exsolution lamellae (Figure *4.2-16*a). As weathering progresses, the pits expand and coalesce to form large cavities that are occupied, in some cases, by Mg- and K-bearing clay minerals (e.g., illite). The remaining skeletons of clinopyroxene grains are commonly decorated by Fe-oxides. Plagioclase also shows evidence of alteration to form K-bearing clay minerals. Voids are surrounded by bright rims of Fe- and Mn-oxide minerals similar to those that make up the patina (Figure *4.2-16*b). The exsolution lamellae in clinopyroxene are commonly altered and, like other skeletal components of the clinopyroxene, host tiny grains of bright Fe oxides (Figure *4.2-16*d).

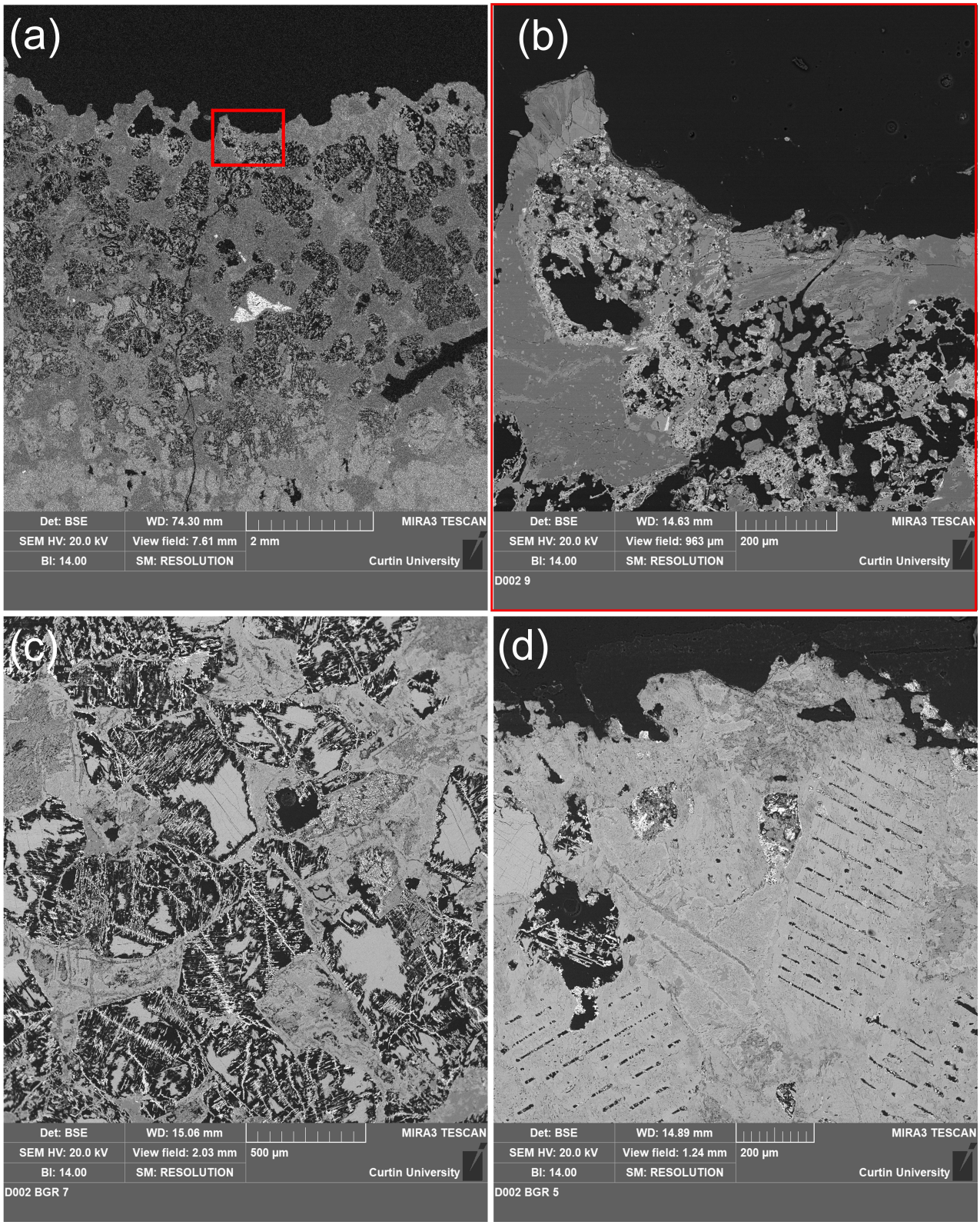

Figure 4.2-16: BSE-SEM image of gabbro sample D002_GBR. (a) Panorama image showing fresher rock, weathered rind, and patina. (b) Area shown by the red box in (a) showing extensive void space within the weathered rind. (c) Skeletal structures after clinopyroxene within the weathered rind. The clinopyroxene and plagioclase exhibit exsolution lamellae. (d) Variable development of voids, ranging from micrometre-sized pits along planes of exsolution to complete grain loss.

4.2.4.4 Patina

Patina refers to a thin, distinctly coloured, layer that forms on the surface of a rock over time. Generally, the patina is so fine-grained that individual minerals cannot be resolved by optical microscopy. Oxide minerals are observed by transmitted optical microscopy as large or small black specks. The patina ranges from orange to red to brown to black or grey in colour. Based on pXRF results presented previously in the Monitoring Studies Report 2024 (Curtin University, 2024c), and existing mineral descriptions (Neumann, 2025), the colour variation is interpreted to reflect differences in the amounts and oxidation state of redox-sensitive elements such as Mn and Fe in the patina, and differences in the extent of hydration of Fe- and Mn-oxides and hydroxides. For example, iron hydroxides tend to be red-orange or pale-orange whereas hematite, which is anhydrous, is commonly red-purple or black in colour. In addition, Mn-rich patinas are typically brown or black whereas Fe-rich patina are mostly dominated by orange and red minerals. In some cases, the black patinas are enriched in Ti.

Granophyre

Patina is well-developed in eight of the 16 granophyre samples in Group B (AN01, BU01, BU02, DOO1, EI03, EL02-1, EL02, GI03). The patina is Fe- and Mn-rich and the modes of Fe-clay, Fe-patina, Mn-patina, and Mn-clay are relatively high. This is as expected, given that these phases were defined in the TIMA mineral library to represent the fine-grained mixed material that makes up the patina. Titanite is the most common accessory mineral in the patina of granophyre (Tables *4.2-6* to *4.2-7*).

Only one of the Group D samples shows any patina on the rock surface exposed to the atmosphere (RT04_GPH, Figure *4.2-9*), and this patina is thin and discontinuous. However, during sample preparation, the billet for MB02_GPH fractured, and a thin discontinuous orange patina was observed on the fracture surface.

Dolerite

On the dolerite, patina is thin or is locally absent. A detailed description of patina on dolerite is provided in the Monitoring Studies Report 2024 (Curtin University, 2024c).

Granite

Patina on the granite is thin or absent. A detailed description of patina on granite is provided in the Monitoring Studies Report 2024 (Curtin University, 2024c).

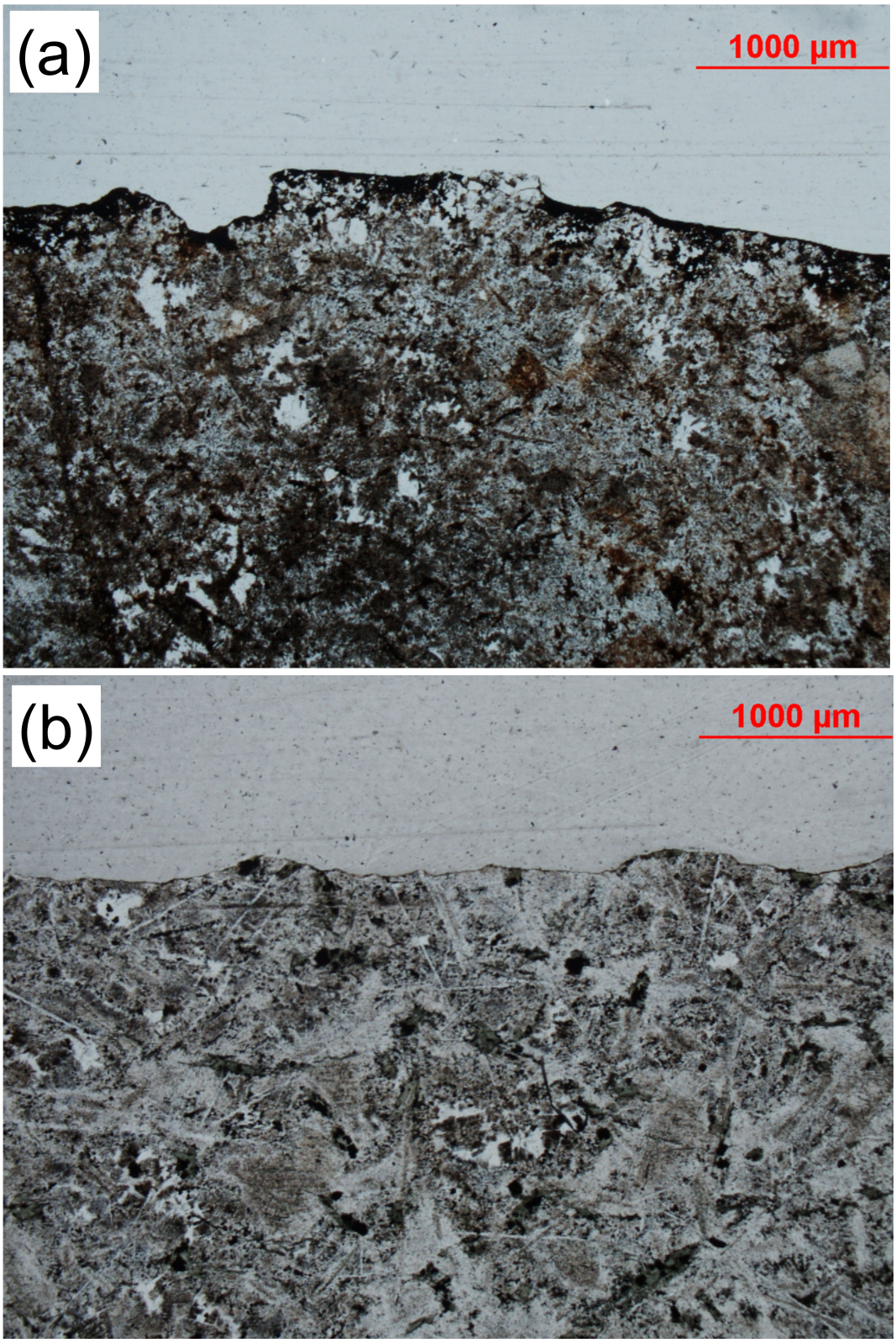

Figure 4.2-17: Plane polarised transmitted light photmicrographs comparing granophyre samples that show: (a) well-developed patina and weathered rind (Group B sample EI03_GPH) and (b) no weathered rind and thin discontinuous orange patina (Group D railway cutting sample RT03_GPH).

Table 4.2-7: Summary of mineral modes for Group D granophyre samples estimated by TIMA. These samples do not show a weathered rind and patina so only the fresher rock is provided. "Holes" refers to areas identified by the TIMA as free of rock material, and may differ from the measured porosity. Estimated modes of less than 0.01% are omitted.

Group D: N = 8	**Fresher rock**	
Phase	**AVG (vol %)**	**STDV (vol %)**
Plagioclase (Albite)	56.10	3.0
Alkali Feldspar	16.73	3.3
Quartz	15.12	0.9
Chlorite/Clinochlore	3.96	1.1
K-alt-Chlorite	3.05	0.4
Hematite/Magnetite	1.00	0.1
Plagioclase (Labradorite)	0.70	0.1
Amphibole	0.49	0.1
Epidote	0.30	0.1
Titanite	0.27	0.0
Calcite	0.22	0.1
Ilmenite	0.15	0.1
Stilpnomelane	0.08	0.0
Fe-Clay/Patina	0.07	0.0
Ankerite	0.01	0.0
Apatite	0.01	0.0
Fe-Ca-K_Clay	0.01	0.0
Unclassified	0.71	0.1
Holes	1.03	0.6
Total	100.00	

4.2.4.5 Micro-CT Analyses

Five samples from Group B were scanned by micro-CT. These included two granophyre samples, one dolerite, one gabbro, and one granite (BU02_GPH, EL02_GPH, EI01_DOL, D002_GBR, D003_GRT). Locations of these samples are provided in Table *3.2-6*. Voxel edge length and number of pixels in the analysis are provided in Table *4.2-8*. Preliminary images are provided in Figures *4.2-18* to *4.2-22*. These preliminary results are promising; the images show the differences in grain size in the different rock types, with finer grains within the granophyres, coarser grains within the gabbro, and potentially a single grain within the granite. Analysis of the micro-CT scans is ongoing and will be presented in the final monitoring studies report.

Table 4.2-8: Summary of microCT measurements.

Sample Code	Rock Type	Dataset ID	Voxel Size (μm)	Pixels X	Pixels Y	Pixels Z	Total Volume (μm^3)
BU02_GPH	Granophyre	BU02_03-FFS-SF	2.50	2438	2438	2082	1.91×10^{11}
EI01_DOL	Dolerite	EI01_01-FFS-SF	4.20	2430	2430	1160	4.15×10^{11}
EL02_GPH	Granophyre	EL02_01-FFS-SF	2.50	2438	2438	1203	1.10×10^{11}
D002_GBR	Gabbro	D002_02-FFS-SF	3.80	2430	2430	1280	4.15×10^{11}
D003_GRT	Granite	D003_01-FFS-SF	4.20	2444	2444	1269	5.60×10^{11}

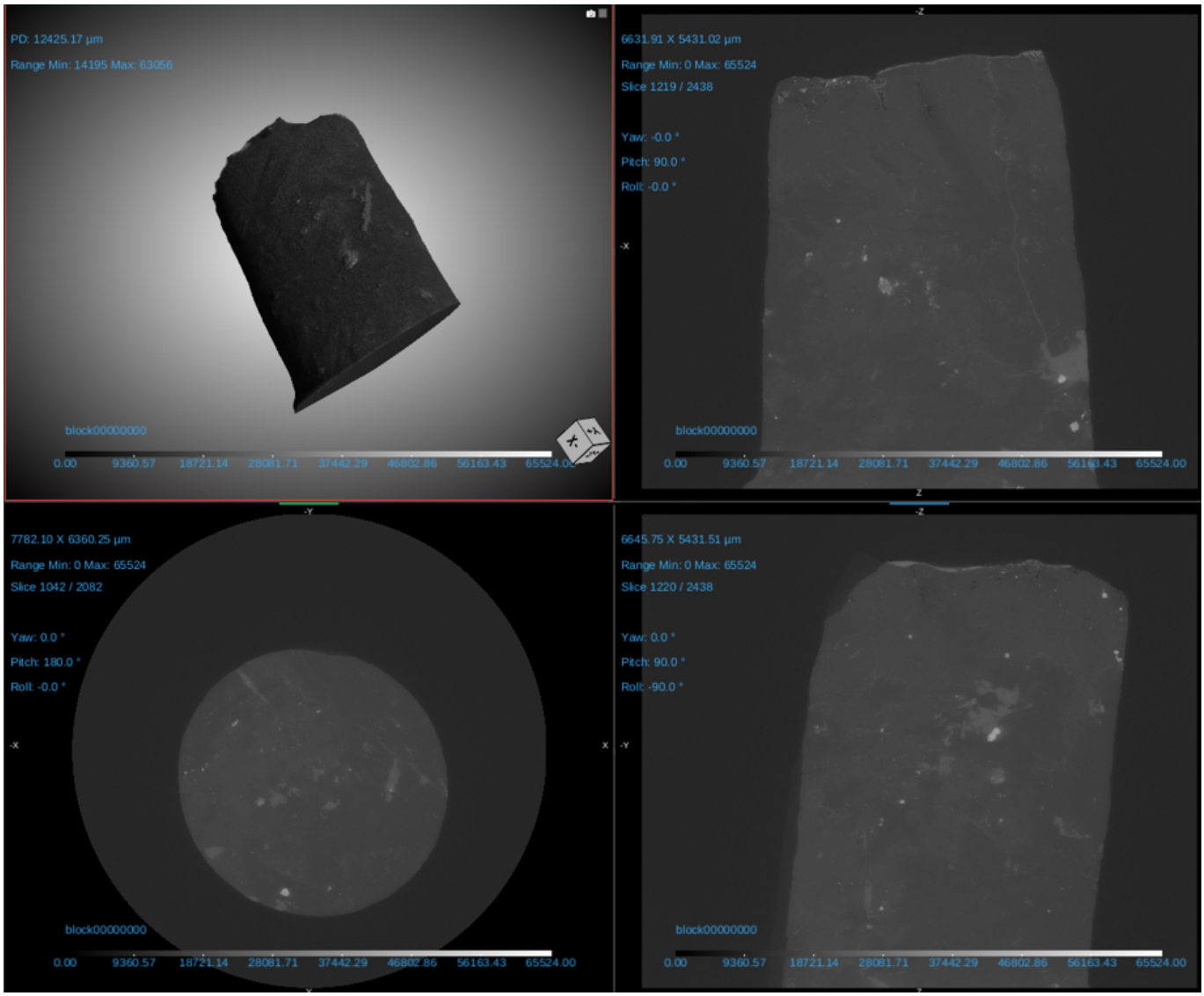

Figure 4.2-18: Preliminary unprocessed micro-CT data from Group B granophyre BU02_GPH, showing (a) two-dimensional representation of reconstructed volume; (b) x-z slice; (c) x-y slice; (d) y-z slice.

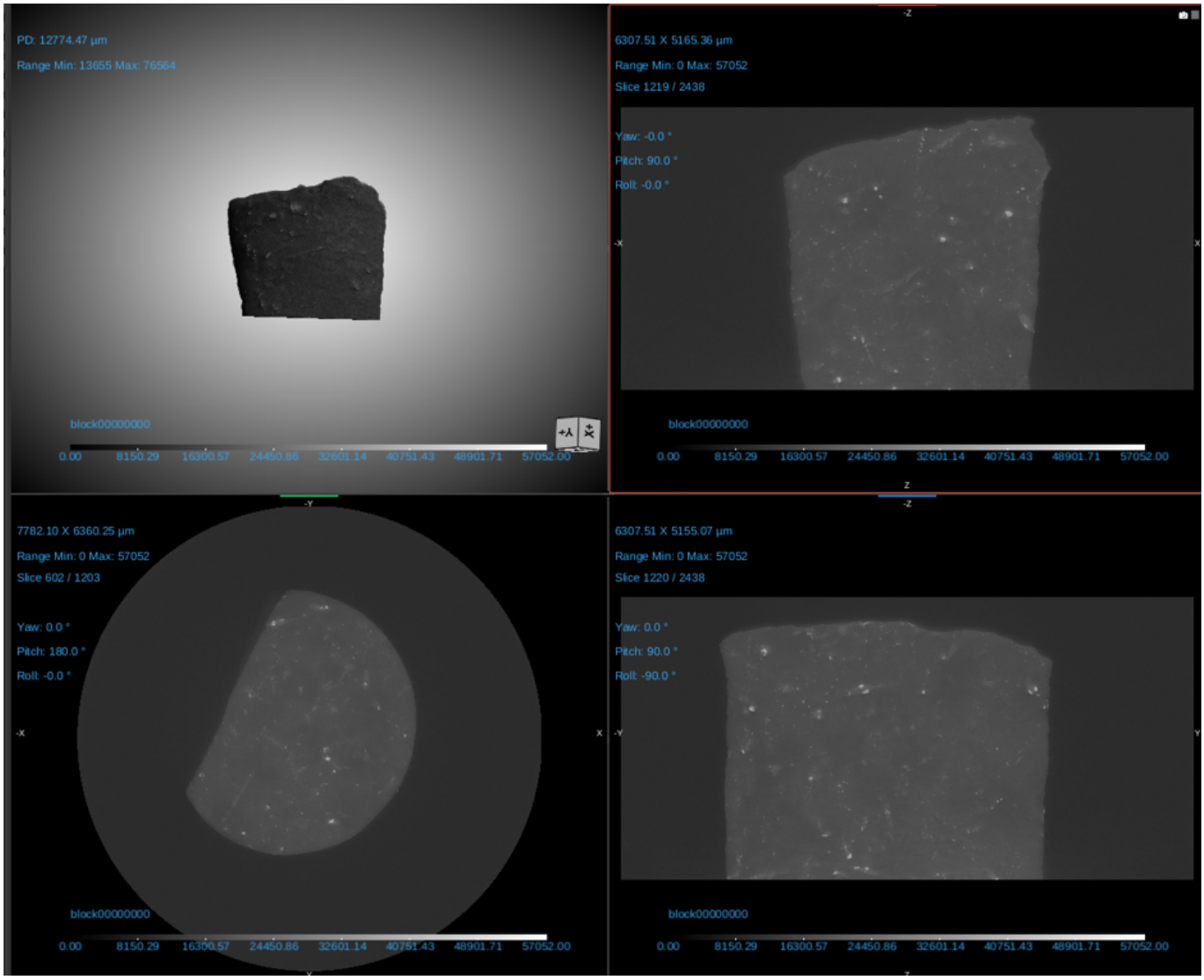

Figure 4.2-19: Preliminary unprocessed micro-CT data from Group B granophyre EL02_GPH, showing (a) two-dimensional representation of reconstructed volume; (b) x-z slice; (c) x-y slice; (d) y-z slice. In panels (b) to (d), individual grains are revealed by changes in the grey scale of the image.

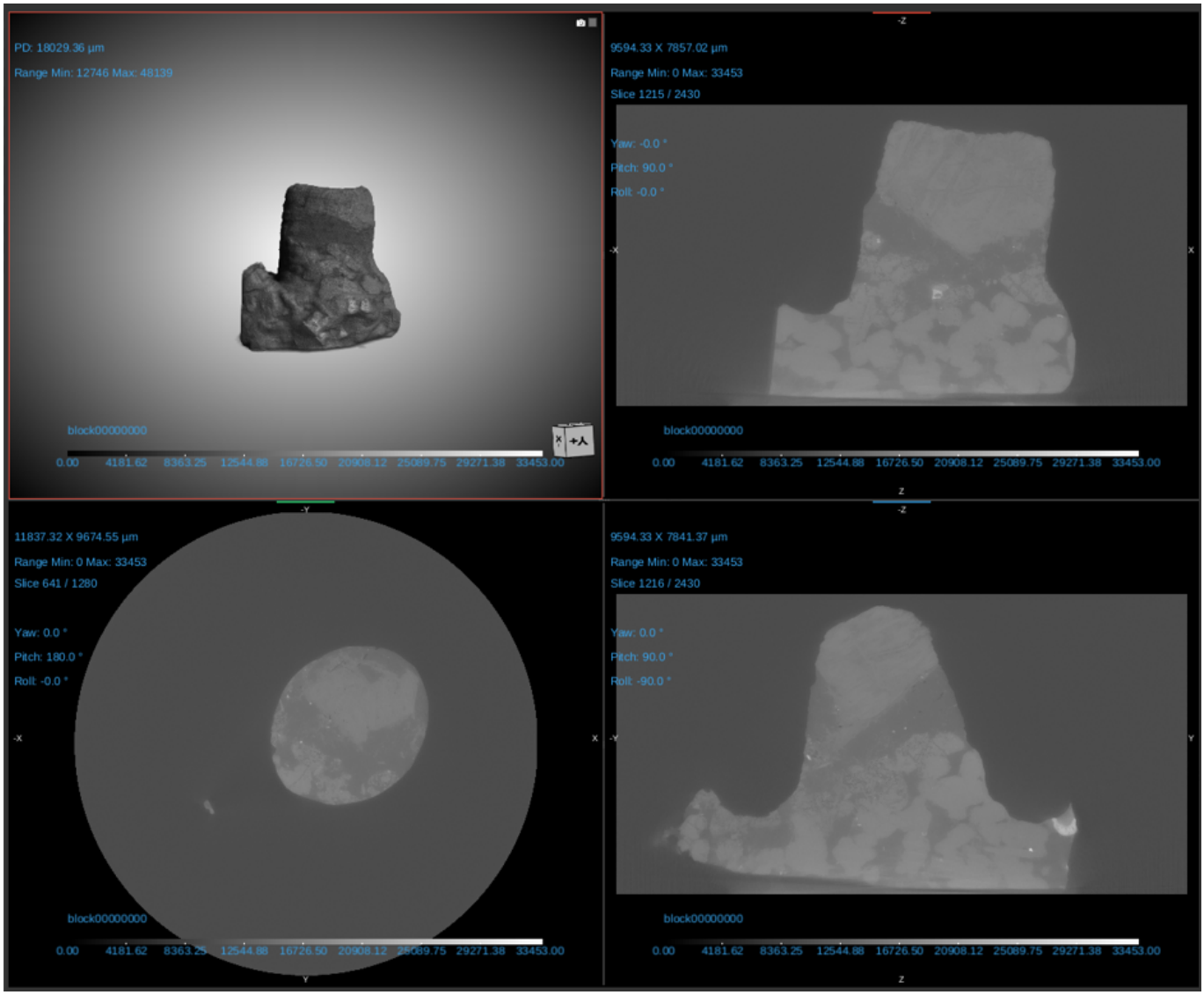

Figure 4.2-20: Preliminary unprocessed micro-CT data from Group B gabbro D002_GBR, showing (a) two dimensional representation of reconstructed volume; (b) x-z slice; (c) x-y slice; (d) y-z slice. Data were cropped to remove the holder. In panels (b) to (d), individual grains are revealed by changes in the grey scale of the image.

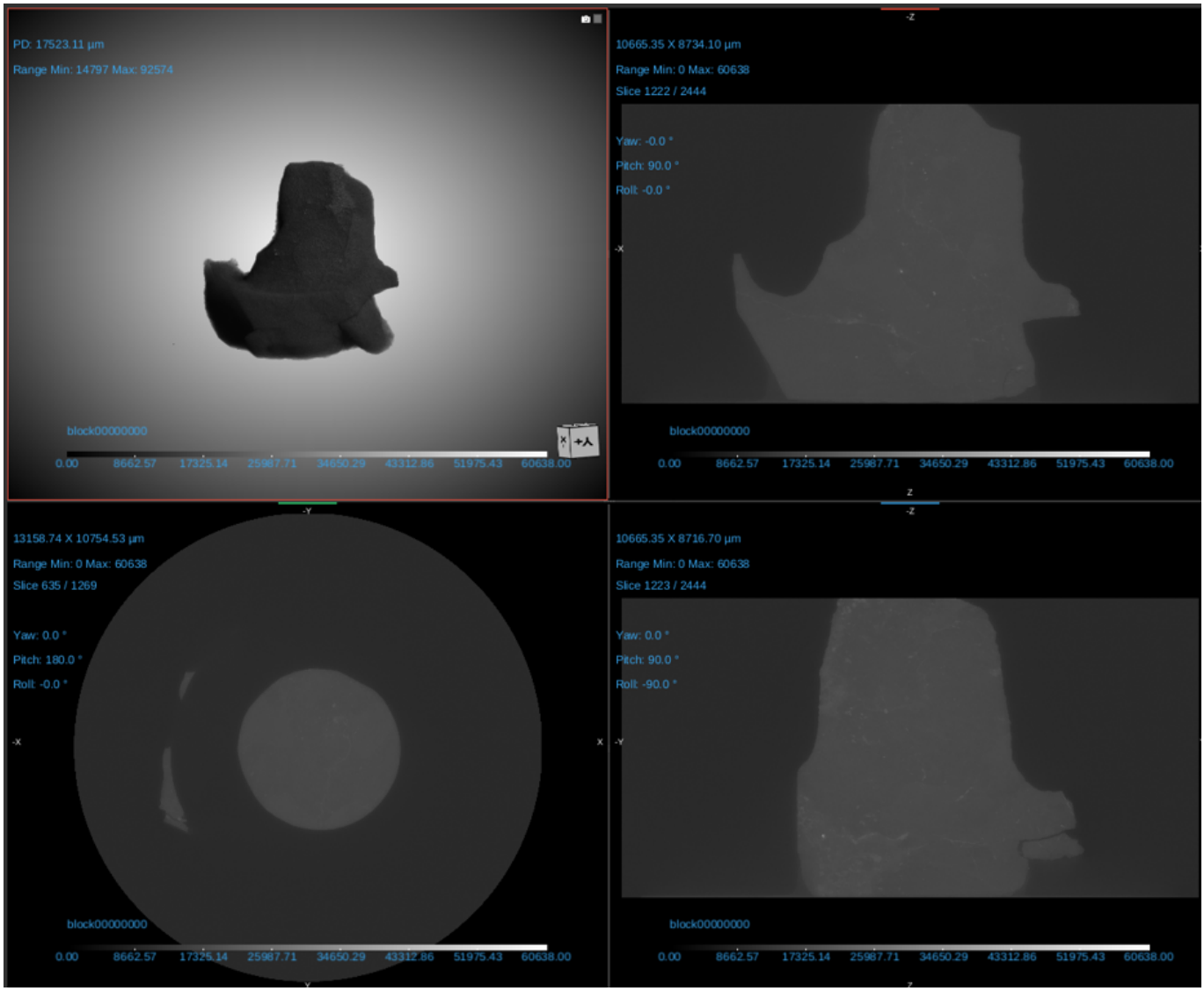

Figure 4.2-21: Preliminary unprocessed micro-CT data from Group B granite D003_GRT, showing (a) two-dimensional representation of reconstructed volume; (b) x-z slice; (c) x-y slice; (d) y-z slice. Image cropped to remove holder. In panels (b) to (d), individual grains are revealed by changes in the grey scale of the image.

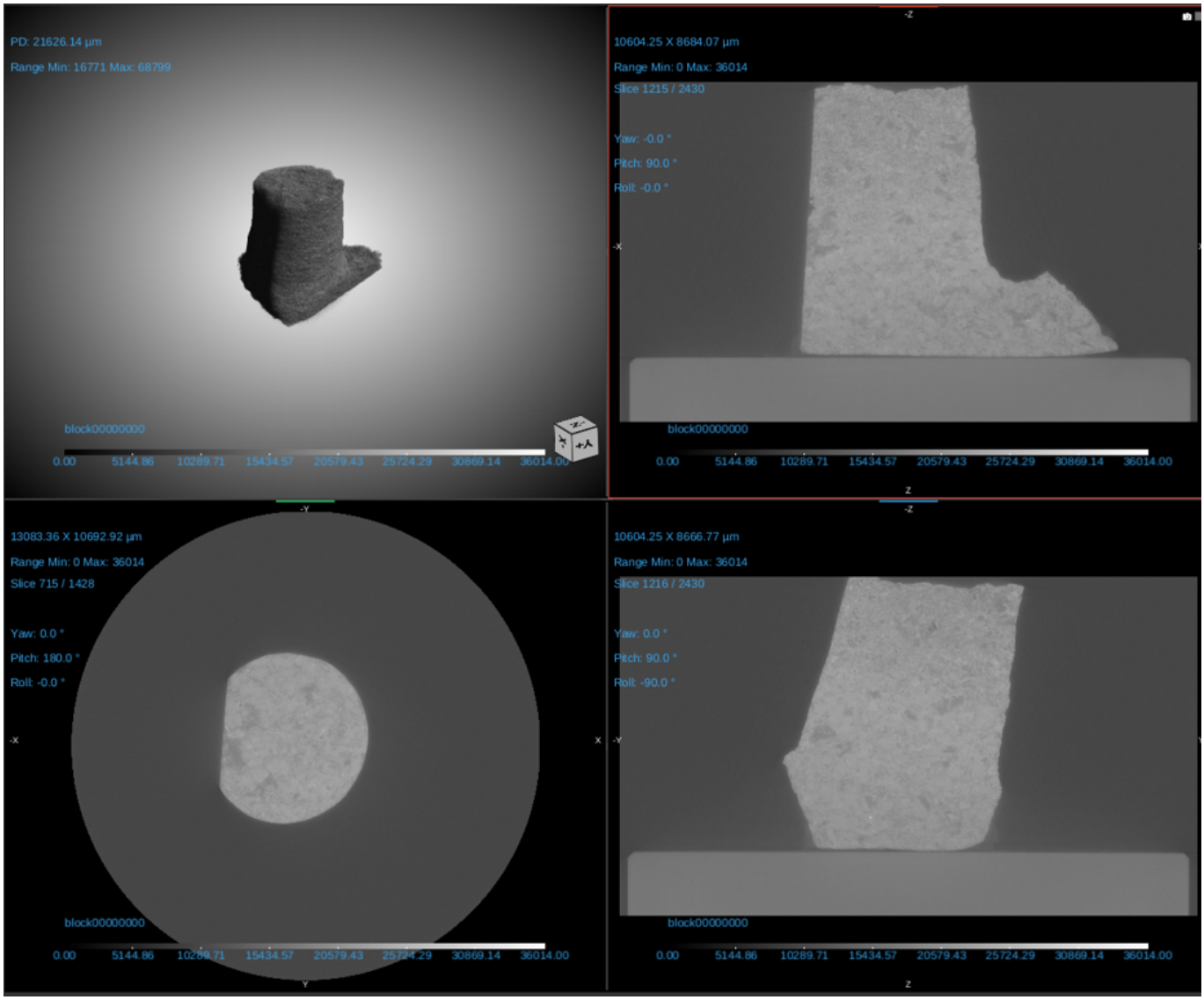

Figure 4.2-22: Preliminary unprocessed micro-CT data from Group B granite EI01_DOL, showing (a) two dimensional representation of reconstructed volume; (b) x-z slice; (c) x-y slice; (d) y-z slice. Image cropped to remove holder. In panels (b) to (d), individual grains are not visible, possibly because the sample consisted of a single grain.

4.2.4.6 Oxalate and formate analysis

Eighteen samples were collected for oxalate and formate analysis, nine from gabbro and nine from granophyre, as described in Section 3.2.4.5. Three of the 18 samples were above the detection limit of 0.1 mg L^{-1} for formate (Table *4.2-9*). Seven of the 18 samples were above the detection limit of 0.1 mg L^{-1} for oxalate. The maximum concentrations of formate and oxalate were 0.1 and 0.2 mg L^{-1} respectively. Formate values above the detection limit were observed on different samples to those with oxalate concentrations above the detection limit. Two of the three samples above the detection limit for formate, and four of the seven samples above the detection limit for oxalate were taken from patina on gabbro.

Oxalate and formate are products of microbiome activity, so their presence indicates that the techniques are sufficiently sensitive to detect these products, and that the microbiome is active. There is some indication that concentrations are higher on gabbro patina but further work is necessary to confirm this finding. Such work is beyond the scope of planned activities for year 4, but is recommended as part of the ongoing research program.

Table 4.2-9: Results of oxalate and formate analyses obtained by ion chromatorgraphy

Rock Panel	Date Sampled	Cl (mg/L)	Formate (mg/L)	Oxalate (mg/L)
Detection limits **Units**		**1** **mg/L**	**0.1** **mg/L**	**0.1** **mg/L**
AQ03-2 GBR	5/3/2025	5	0.1	<0.1
AQ09-02 GPH	5/3/2025	4	0.1	<0.1
AQ11 GPH	4/3/2025	6	<0.1	<0.1
AQ13 GPH	24/2/2025	3	<0.1	<0.1
AQ13 GPH	24/2/2025	10	<0.1	<0.1
AQ16 GBR	25/2/2025	6	0.1	<0.1
AQ16 GBR	25/2/2025	4	<0.1	0.1
AQ18 GPH	27/2/2025	144	<0.1	0.1
EX03 GPH	4/3/2025	9	<0.1	<0.1
EX07 GPH	4/3/2025	7	<0.1	0.2
RS02 GBR	26/2/2025	31	<0.1	0.2
RS02 GBR	26/2/2025	19	<0.1	0.2
RS04 GBR	26/2/2025	4	<0.1	0.1
RS04 GBR	26/2/2025	5	<0.1	<0.1
RS13 GBR	25/2/2025	11	<0.1	<0.1
RS13 GBR	25/2/2025	11	<0.1	<0.1
RS17 GPH	27/2/2025	8	<0.1	0.1
RS18 GPH	27/2/2025	27	<0.1	<0.1

4.2.5 Discussion

A comprehensive analysis of the results documented here, and the integration of the findings with those of the other components of MRAMP, will be provided in the final report. However, some aspects of the results are discussed here because they are relevant for the activities planned over the next eight months.

4.2.5.1 New insights

Most of the observations corroborate and support the findings of the previous Monitoring Studies Report 2024 (Curtin University, 2024c). However, some new insights have been derived from the additional sample characterisation presented here. These new insights are presented in the context of the conceptual model described previously (Curtin University, 2024c), where fresher rock is the least altered rock and records the processes that initially formed and modified the rock prior to its exposure on Earth's surface. The weathered rind and patina formed during weathering at, or close, to the surface of Earth, and record the interactions between the rock and the surface environment over the rock's weathering history.

Patina formation and thickness

Two key observations provide insights into the first-order processes that affect patina formation and thickness.

1. During sample preparation, the billet for MB02_GPH fractured, and a thin chalky discontinuous orange patina was observed on the fracture surface. Thus, it is likely that the patina begins to form within incipient fractures very early in the weathering process. This observation is supported by field observations, where a similar chalky orange patina is observed on fractured surfaces (Figure *4.2-23*). This finding is consistent with models for patina formation described by Dorn (2024), where chalky orange patina forms underground or in other settings without direct exposure to airborne dust.
2. Dolerite, granite, and basalt typically show thin or absent patina, whereas gabbro and granophyre typically show well-developed patina. Patina is thought to be formed from externally derived material at rates that are not thought, currently, to be rock type dependent (Dorn, 2024). If formation rates do not depend on the rock type then differences in patina thickness record differences in the frequency of flaking, spalling, or other patina-loss that relate to the characteristics of the underlying material. Such characteristics may include, but are not limited to: the rate of dissolution of minerals in the underlying rock; lithology-dependent strength or thermal property differences between the weathered rind, patina, and fresher rock; grain size or morphological differences; lithology-dependent changes in volume as weathered rind forms from fresher rock; microbial community-dependent differences in weathering rind formation; and pre-existing joint and fissure intensity and geometry. Further work is necessary to better understand the relative importance of these factors.

Figure 4.2-23: Chalky orange patina forming on fractures in granophyre in the field near Cowrie Cove.

Comparison of granophyre samples between Groups A, B, C, and D

This comparison focuses on granophyre samples because they are the most numerous and widespread type of sample available. Similar analyses could be performed for the other rock types. In most cases, the mineral assemblages and textures of the patina are comparable to the fresher rock and weathered rind plus patina for all four groups, with some variation that is consistent with natural variation amongst granophyre samples within a single group (Figures *4.2-24* to *4.2-28*, Tables *4.2-6* to *4.2-7*).

Any differences between Group A and Group C are expected to be minor, because 11 of the Group C samples are also present within Group A. These differences were investigated in more detail by plots of the average modes of the major and minor minerals within the two sample suites (Figure *4.2-29*).

This comparison of TIMA mineral modes between the different groups revealed differences (Figures *4.2-24* to *4.2-29*). For example, sample AQ03 from Group A shows a predominantly blue colour in the TIMA map (Figure *4.2-24*, upper panel), whereas sample AQ03 from Group C shows a predominantly pink/purple colour in the TIMA map (Figure *4.2-24*, lower panel). Blue and pink/purple represent quartz and K-feldspar, respectively, so the images imply differences in the mineral modes that is implausible given that the polished thin section (Group A) and polished billet (Group C) were made from the same rock. Causes of the difference were investigated and two possible causes were identified.

1. At some point in 2023, the detectors used for element analysis on the TIMA instrument (pulse-TOR brand) reached end-of-life and were replaced with newer models (EDAX brand). As a result of this change, peak shapes changed slightly, requiring changes to the mineral characterisation libraries that manifest as changes in the way that mixed analyses (e.g., quartz and albite) are interpreted. After considerable effort to reconcile data from the two detectors, it became clear that the best option was to re-analyse all of the TIMA data, including re-acquisition where necessary, and this process is under way.
2. The modes of some minerals, such as K-altered chlorite and illite/muscovite, are higher in the Group C billets than in the equivalent Group A thin sections. Re-analysis of the Group A billets using the new detector showed that these differences do not relate to the detector or mineral characterisation library. These differences motivated a close comparison of the Group A and C samples using optical and SEM-BSE imaging. Dark areas on the SEM-BSE images were located and examined using optical microscopy. The Group C billets were polished using a different technique to the thin sections used for the other groups. The comparison revealed that the sheet silicates in six of the 55 Group A thin sections, and some of the Group D railway cutting samples, were poorly polished and would not have produced a good signal during the TIMA analysis (Figure *4.2-30*). Without a good signal, the modes of these minerals in the thin sections would have been underestimated, and poorly polished minerals may have been classified as porosity by the porosity measurement workflow (Curtin University, 2024c).

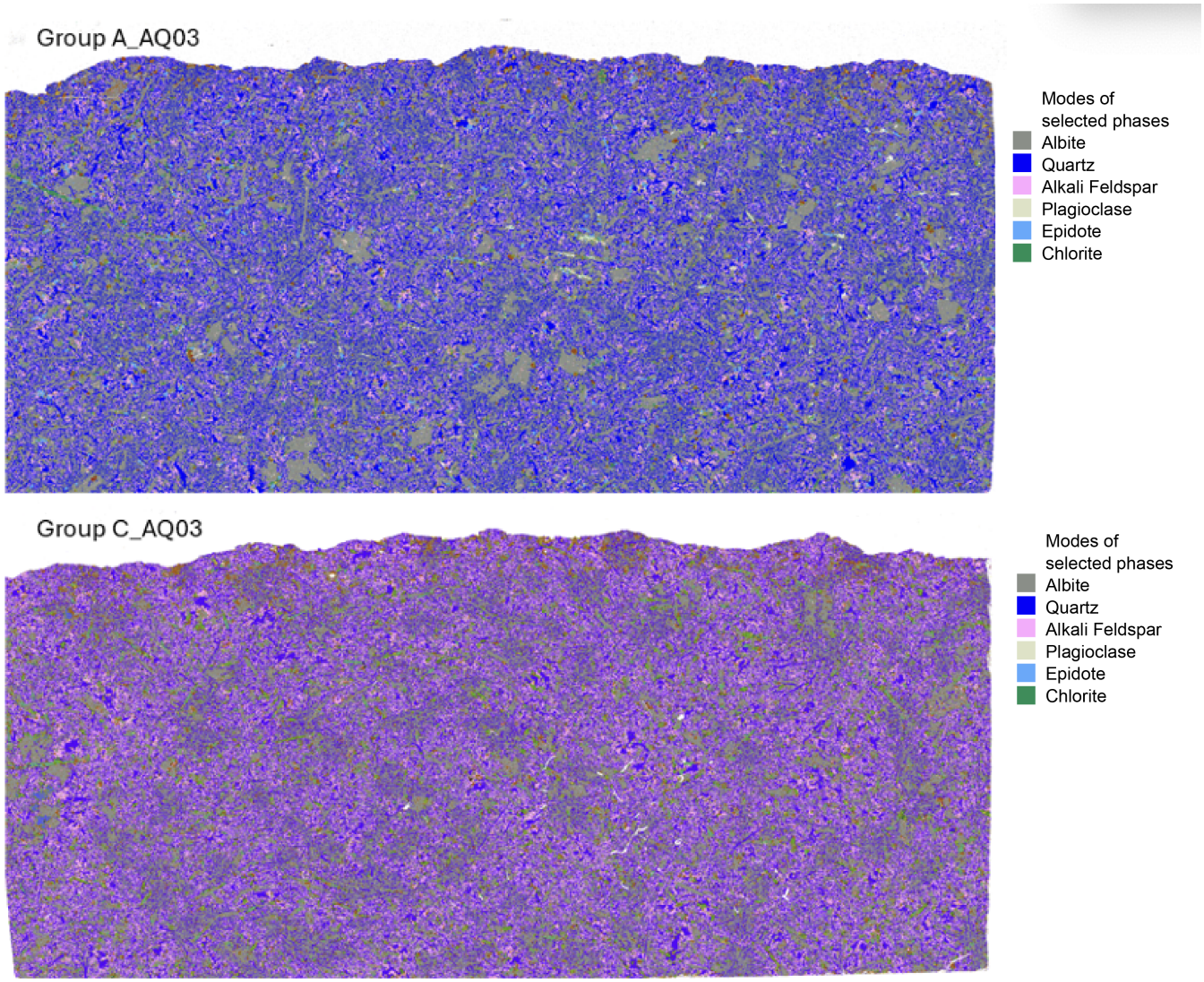

Figure 4.2-24: Comparison of TIMA maps for the Group A thin section of sample AQ03_GPH and the Group C polished billet of sample AQ03_GPH. Group A analysis performed with pulse-TOR detector and mineral characterisation library optimised for this detector. Group C analysis performed with EDAX detector and mineral characterisation library optimised for this detector. The striking change in colour, from blue at the top to purple at the bottom, reflects a difference in the calculated modes of quartz and alkali feldspar.

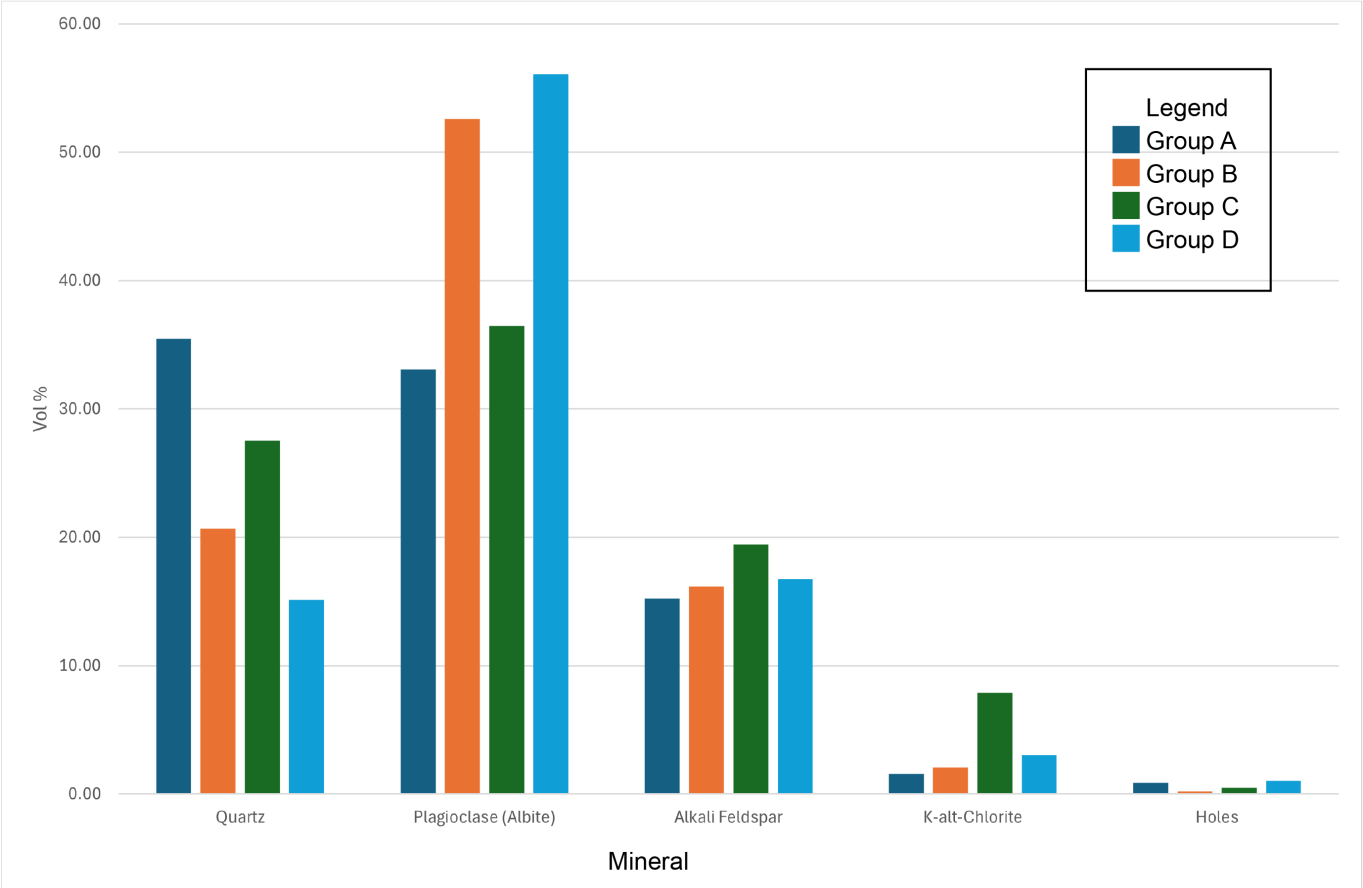

Figure 4.2-25: Variations in mode of individual major minerals between the four rock sample groups estimated by TIMA for the fresher rock of granophyre samples from Groups A, B, C, and D.

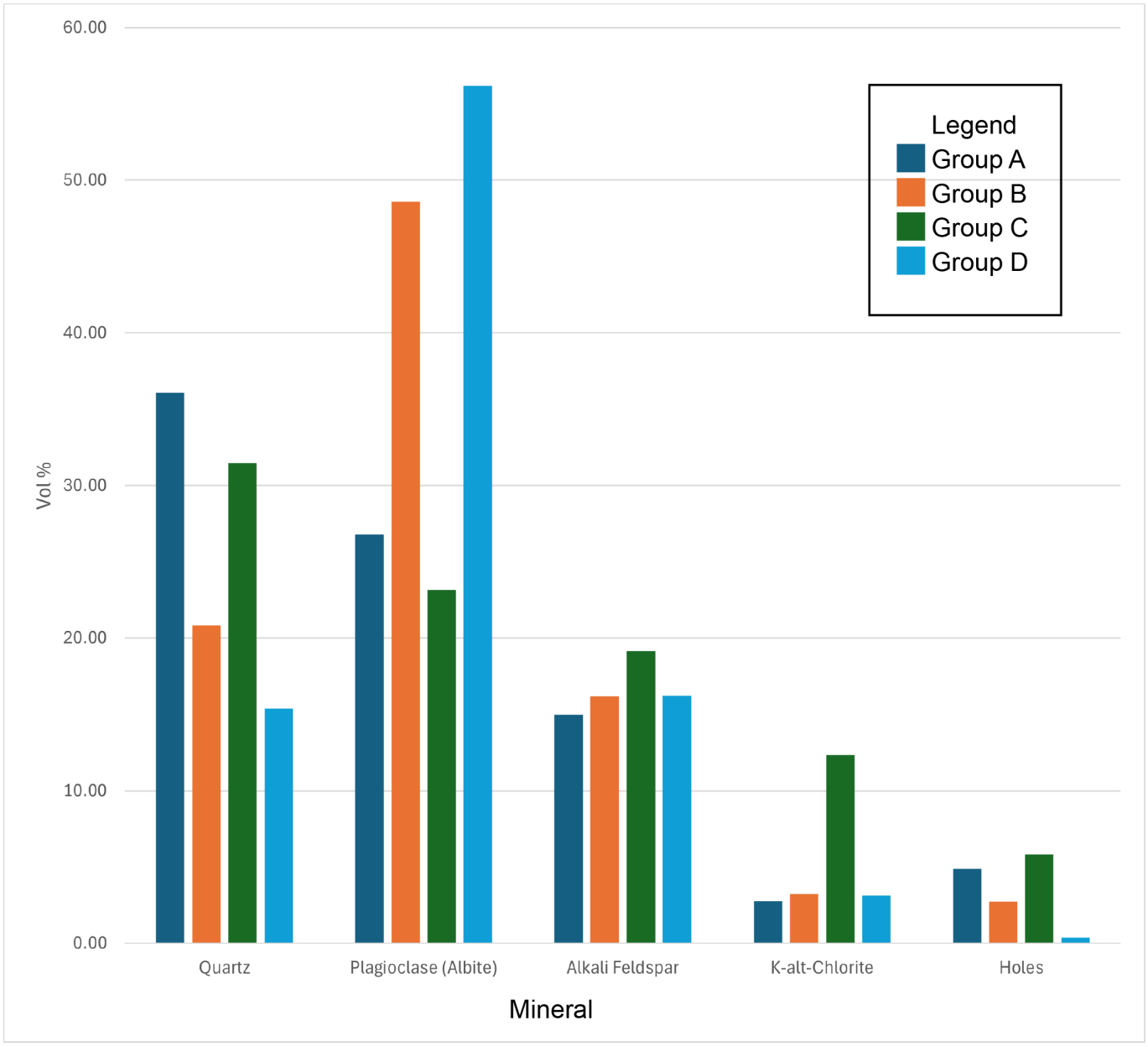

Figure 4.2-26: Variations in mode of individual major minerals between the four rock sample groups estimated by TIMA for the weathered rind and patina of granophyre samples from Groups A, B, C, and D.

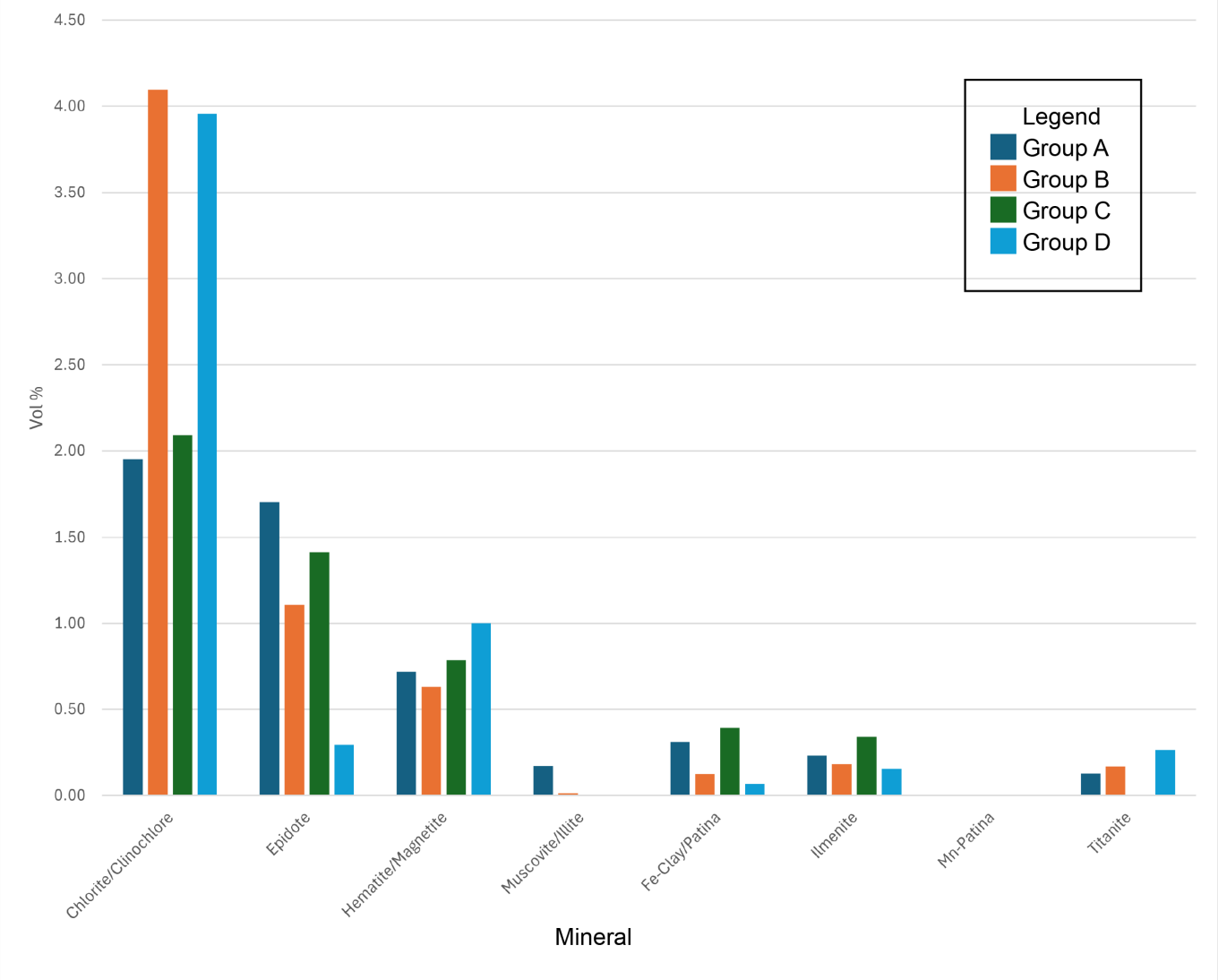

Figure 4.2-27: Variations in mode of individual minor minerals between the four rock sample groups estimated by TIMA for the fresher rock of granophyre samples from Groups A, B, C, and D.

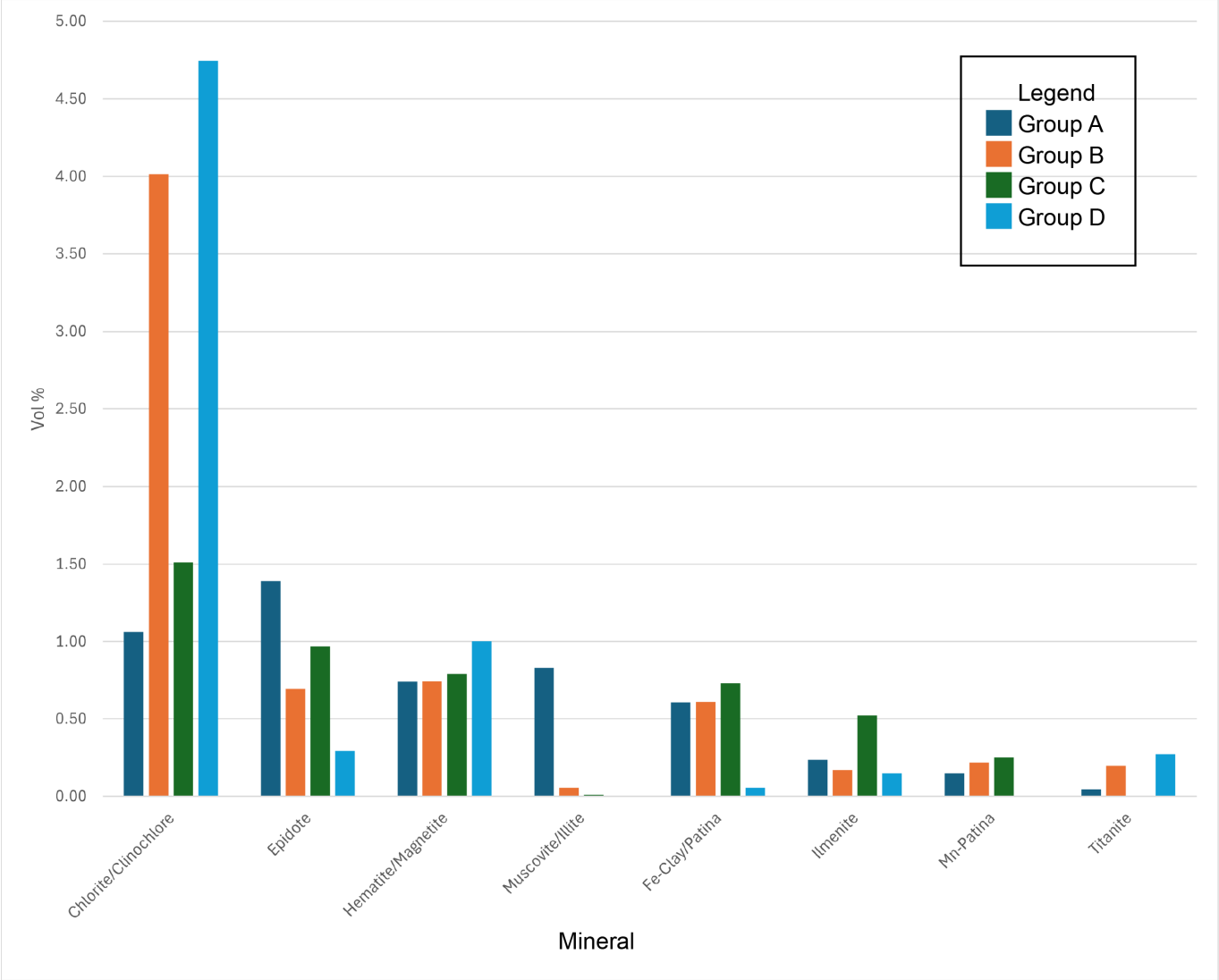

Figure 4.2-28: Variations in mode of individual minor minerals between the four rock sample groups estimated by TIMA for the weathered rind and patina of granophyre samples from Groups A, B, C, and D.

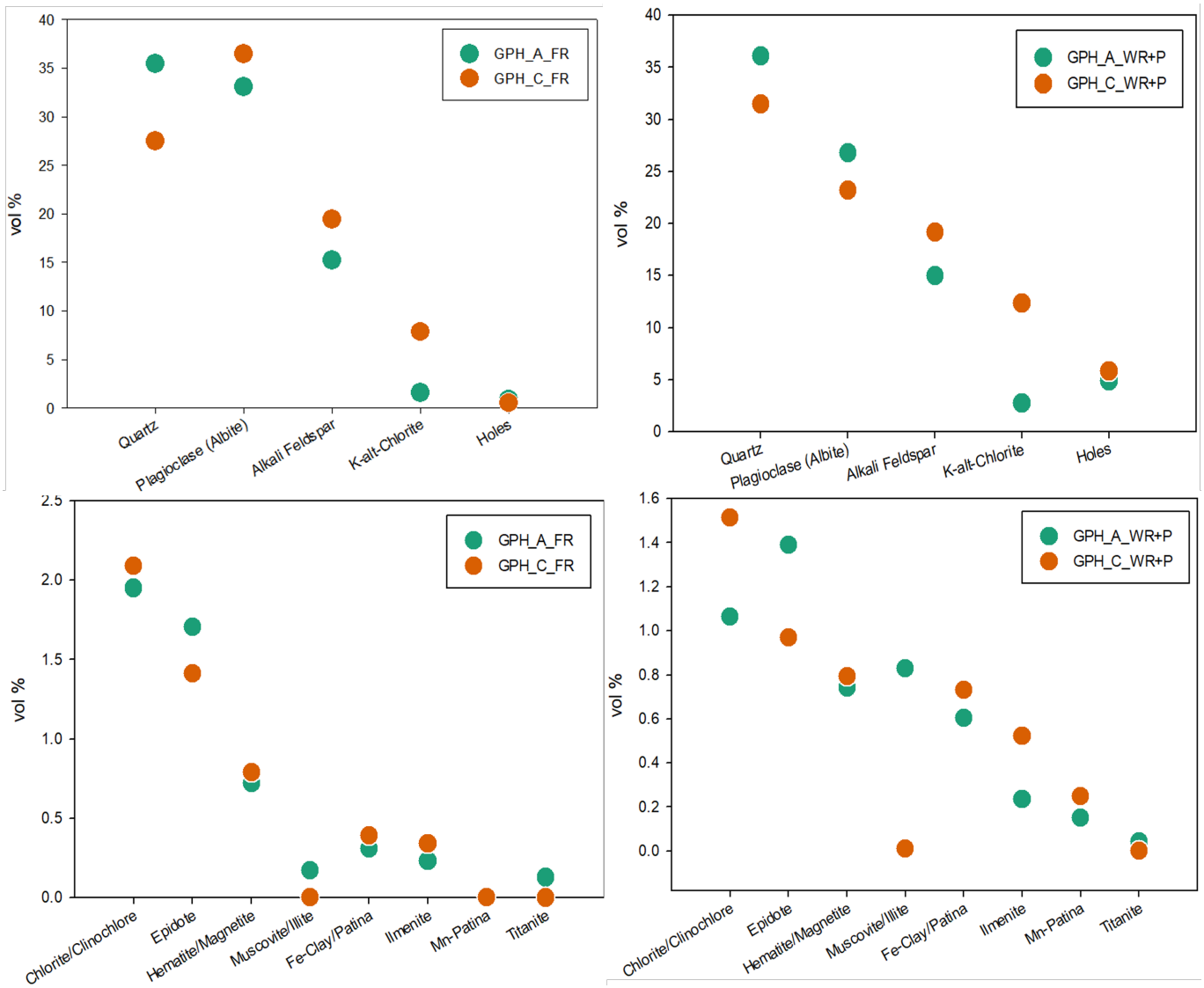

Figure 4.2-29: Comparison of the average mineral modes, measured by TIMA, for all of the Group A and C samples. FR: fresher rock. WR: weathered rind. Differences may relate to changes in analytical techniques or preparation artefacts. Scales were selected to show the mineral modes of the specific rock as clearly as possible. If the dots are close or superimposed than the two different sample preparation methods provide near-identical results. If they are far apart then some kind of analytical or preparation-related artefact is inferred.

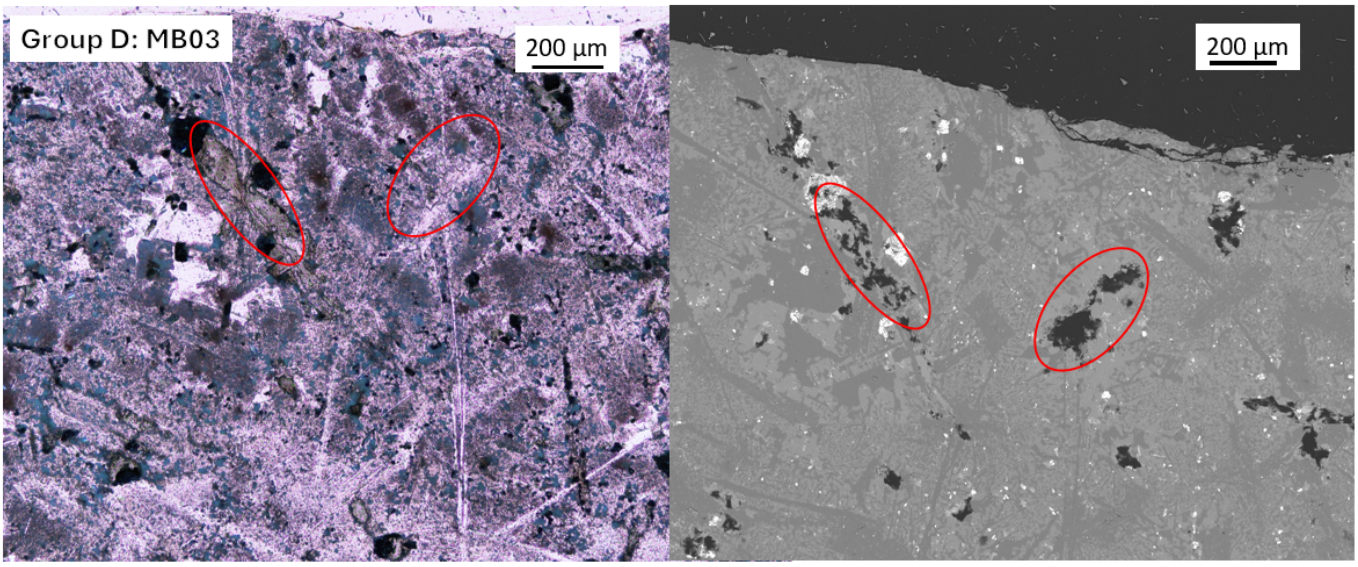

Figure 4.2-30: Comparison of optical photomicrograph (transmitted plane polarised light) (left) with SEM-BSE image (right) of sample BM03 (Group D). The two views are of the same area of the same thin section without repolishing or other treatment between the time of acquisition of the two images. The circled area on the left of each image is green in the plane polarised light image (left panel) and consists of chlorite. However, in the SEM-BSE image (right panel), this area appears black and would be identified, incorrectly, as porosity by the porosity measurement algorithm. The circled area on the right hand side of each image is colourless in plane polarised light and black in cross polarised light (not shown). This area does not contain a mineral. It appears black in the SEM-BSE image (right hand panel) and would be identified correctly as porosity.

Importantly, these findings do not affect any interpretations based on within-section variations in mineral mode, such as changes from fresher rock to weathered rind. Further, the BSE-SEM images, which are used for the porosity analysis, are obtained with a back-scattered detector, not the element detectors used for modal analysis, so findings related to porosity are unaffected by the change in TIMA detector. The possibility of systematically distributed polishing artefacts and their implications for interpretations of rock art longevity are discussed below (Section 4.2.5.1).

Extent and implications of polishing issues

In the following discussion, the term ‘porosity’ is used to refer to voids in the rock that existed prior to sampling and sample preparation. The term ‘artefacts’ is used to refer to voids or apparent voids in the rock that exist only as a consequence of sample preparation.

Further to this finding, the average modes of three samples that showed poor polish on the sheet silicates (samples AQ03_GPH, AQ10_GPH, and RS03_GPH) were compared (Figure *4.2-31*). The largest differences are observed for the sheet silicates, particularly chlorite and K-altered chlorite, confirming the findings of optical and SEM–BSE microscopy.

The average mineral modes were also plotted against each other for two samples that do not show clear polishing artefacts (sample AQ06_GPH and EX07_GPH) (Figure *4.2-32* and Figure *4.2-33*), and for two samples that do show clear polishing artefacts (AQ03_GPH, AQ10_GPH) (Figure *4.2-34* and Figure *4.2-35*).

In addition, the porosity calculated for individual Group A samples using the methods described in the Monitoring Studies Report 2024 (Curtin University, 2024c) was compared with the porosity calculated for the corresponding Group C billets.

The findings described above are relatively recent and their implications have not yet been fully explored. However, it seems likely that the measured porosity values presented in the Monitoring Studies Report 2024 (Curtin University, 2024c) include some artefacts produced by polishing and sample preparation. Hence, it is necessary to consider the implications of these findings for the interpretations of porosity variation in future reports.

Based on these findings, the porosity shown spatially in the Monitoring Studies Report 2024 (Curtin University, 2024c) consists of porosity plus artefacts. The order of Group A thin-section preparations did not relate in any way to sample location, so it is difficult to envisage a mechanism that would link the extent of preparation artefacts to the spatial location of samples at Murujuga. In this case, the preparation artefacts do not have a spatial bias, so any spatial trend observed relates to porosity only. As discussed in the Monitoring Studies Report 2024 (Curtin University, 2024c), this trend may be linked to environmental field-related factors, such as industrial emissions.

This finding is supported by the location of Group A samples that show porosity artefacts (Figure *4.2-36*), and a comparison of the porosities measured for the Group A samples that show artefacts (marked with a star) and those that do not show obvious artefacts (Figure *4.2-37*). In these plots, neither the location of the artefact-affected samples nor the magnitudes of the porosity values show systematic spatial trends that could have produced the elevated porosity values observed near industrial development sites.

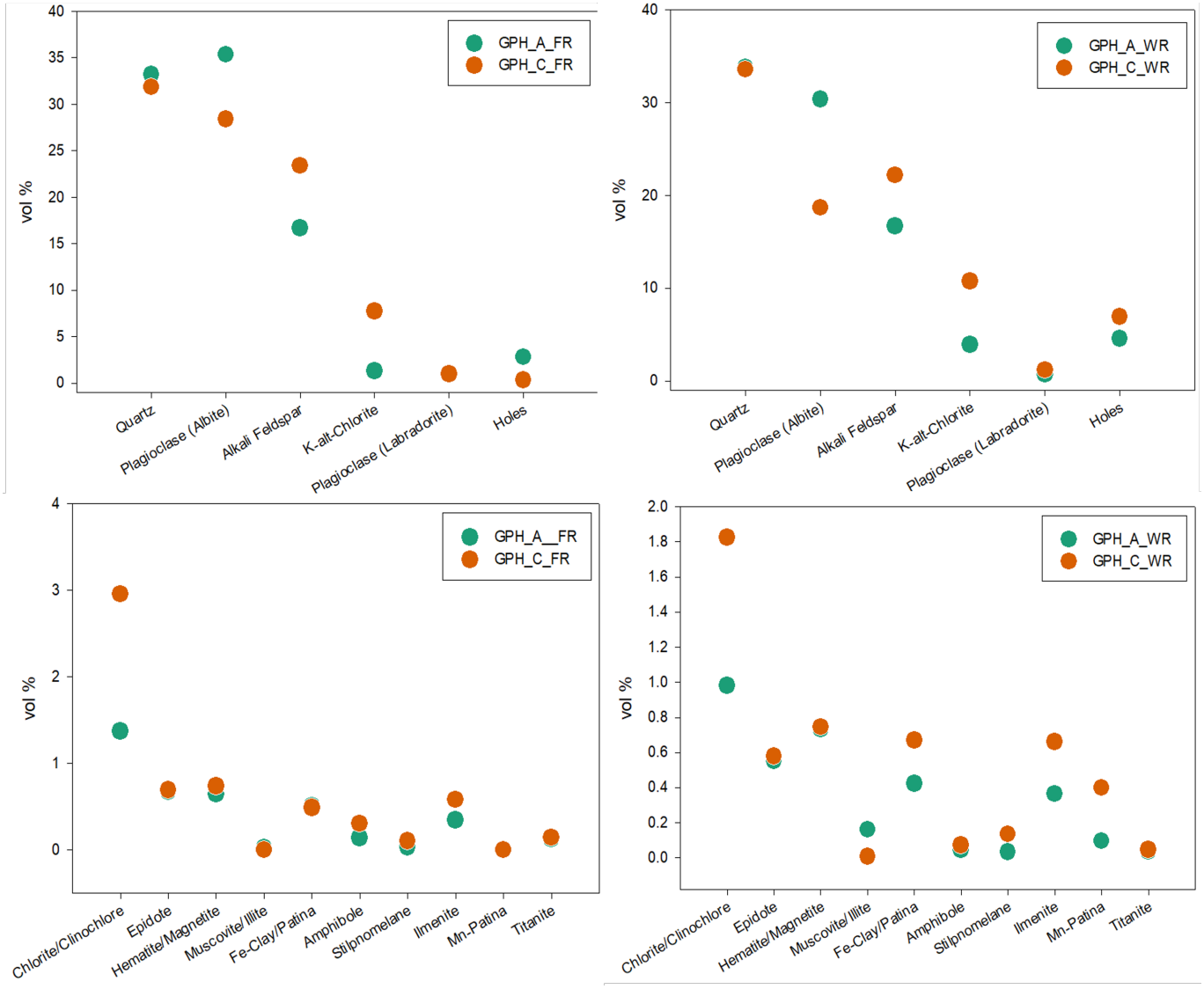

Figure 4.2-31: Comparison of the average mineral modes, measured by TIMA, for Group A thin section and Group C billet of samples AQ03_GPH, AQ10_GPH, and RS03_GPH. These samples show polishing artefacts. FR: fresher rock. WR: weathered rind. Differences may relate to changes in analytical techniques or preparation artefacts. Scales were selected to show the mineral modes of the specific rock as clearly as possible. If the dots are close or superimposed than the two different sample preparation methods provide near-identical results. If they are far apart then some kind of analytical or preparation-related artefact is inferred.

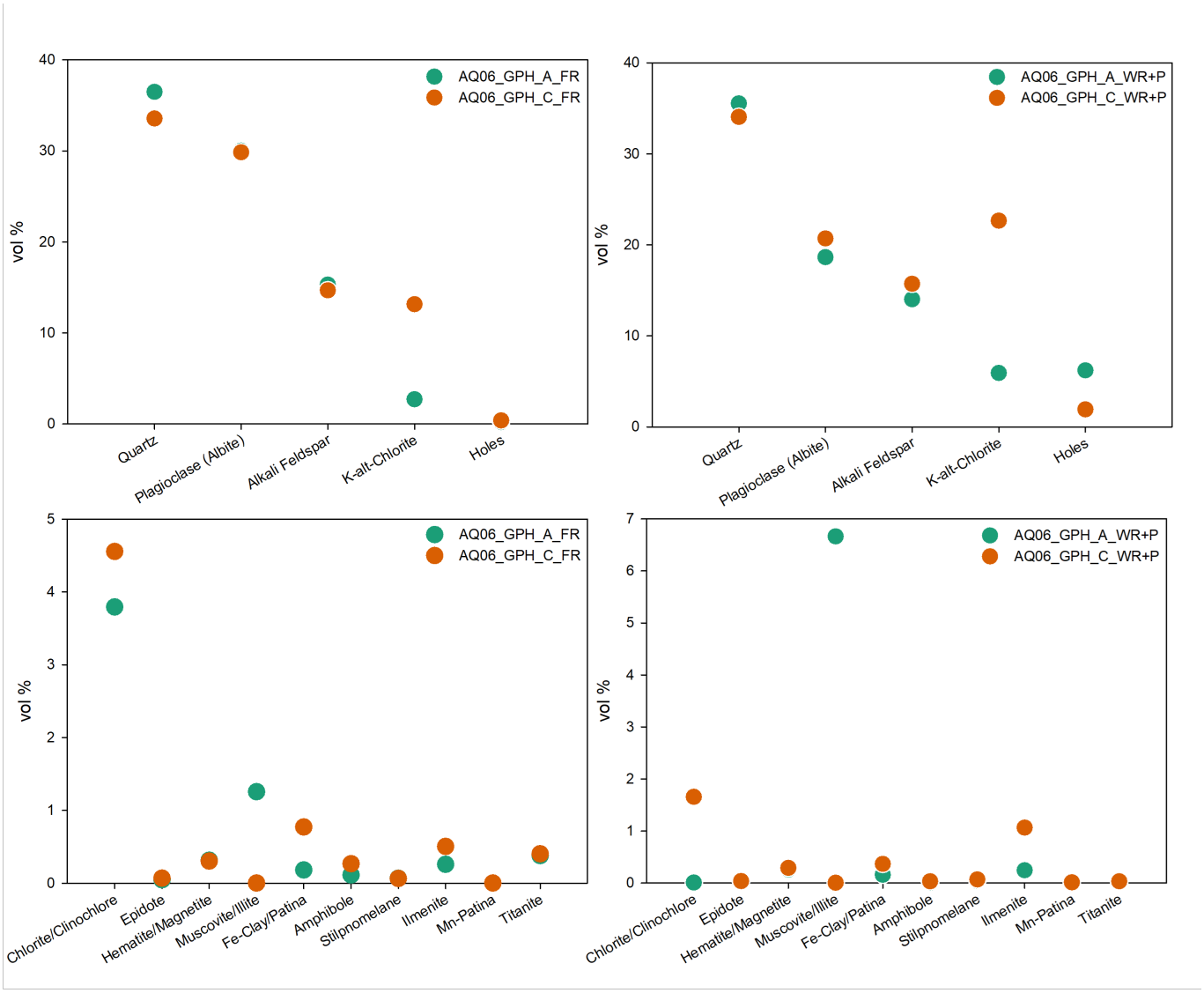

Figure 4.2-32: Comparison of mineral modes measured by TIMA for sample AQ06_GPH from Group A and Group C, which does not show polishing artefacts. FR: Fresher rock; WR+P Weathered rind plus patina. Differences may relate to changes in analytical techniques or preparation artefacts. Scales were selected to show the mineral modes of the specific rock as clearly as possible. If the dots are close or superimposed than the two different sample preparation methods provide near-identical results. If they are far apart then some kind of analytical or preparation-related artefact is inferred.

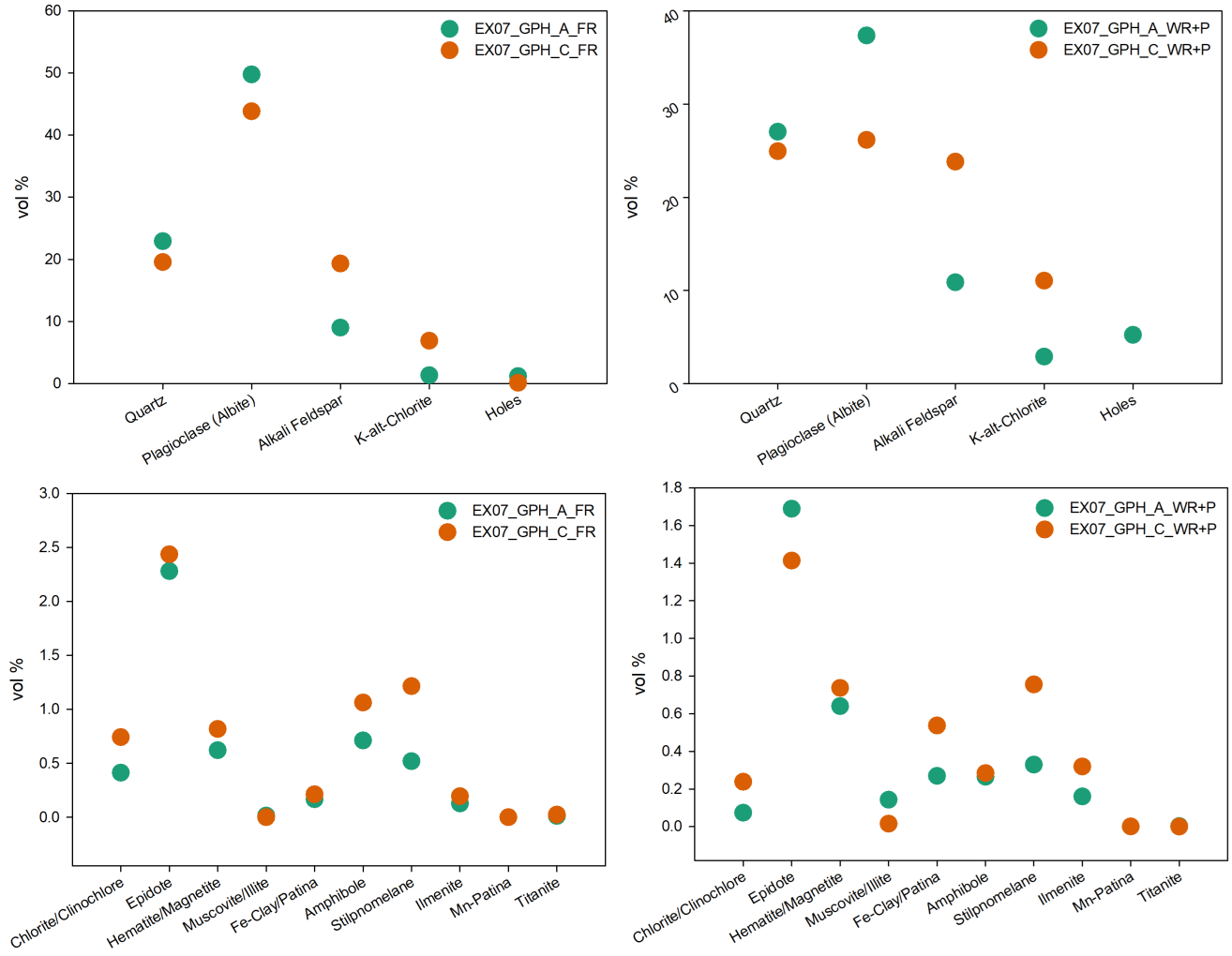

Figure 4.2-33: Comparison of mineral modes measured by TIMA for sample EX07_GPH from Group A and Group C, which does not show polishing artefacts. FR: Fresher rock; WR+P Weathered rind plus patina. Differences may relate to changes in analytical techniques or preparation artefacts. Scales were selected to show the mineral modes of the specific rock as clearly as possible. If the dots are close or superimposed than the two different sample preparation methods provide near-identical results. If they are far apart then some kind of analytical or preparation-related artefact is inferred.

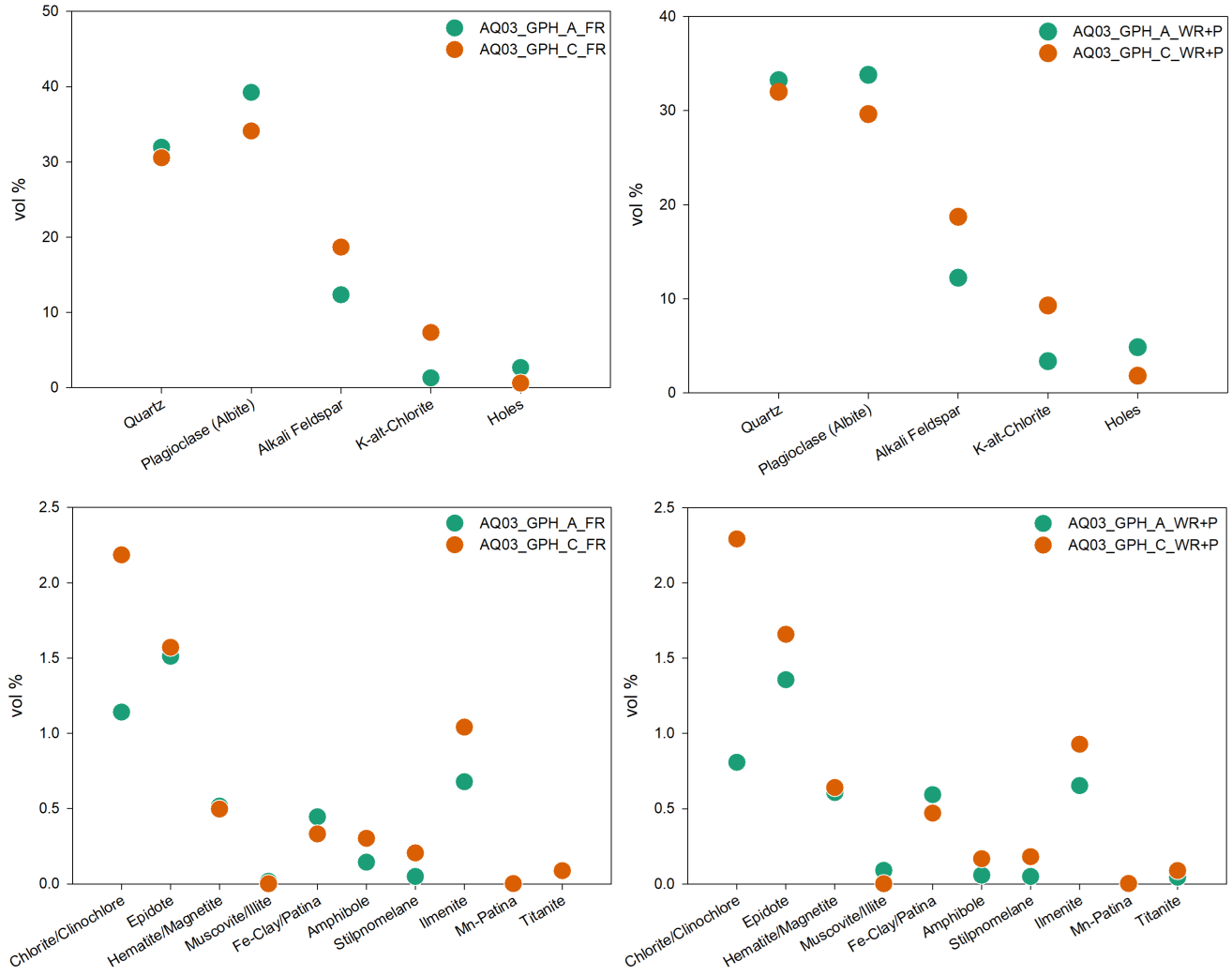

Figure 4.2-34: Comparison of mineral modes measured by TIMA for sample AQ03_GPH from Group A, which shows polishing artefacts, and Group C, which does not show polishing artefacts. FR: Fresher rock; WR+P Weathered rind plus patina. Scales were selected to show the mineral modes of the specific rock as clearly as possible. If the dots are close or superimposed than the two different sample preparation methods provide near-identical results. If they are far apart then some kind of analytical or preparation-related artefact is inferred.

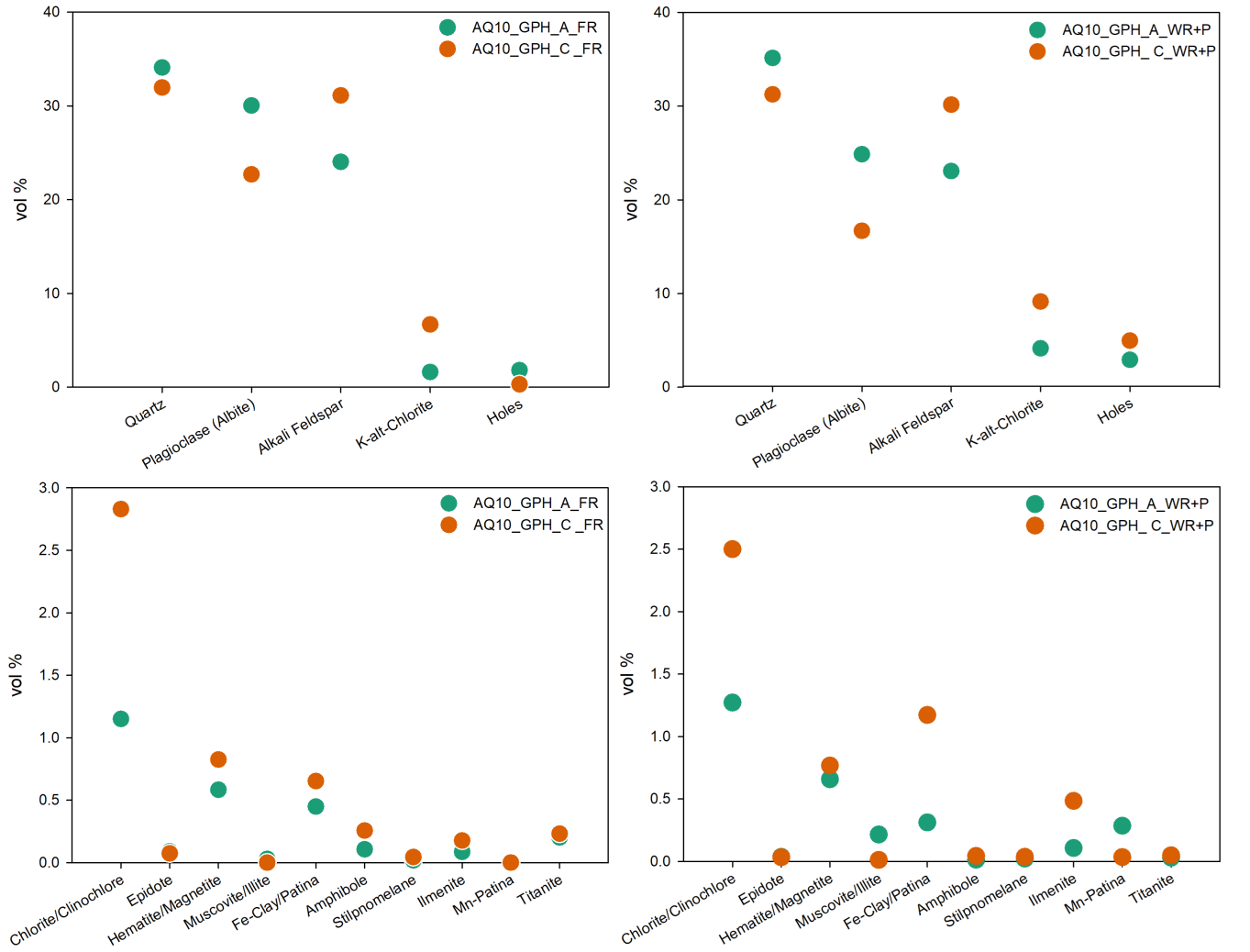

Figure 4.2-35: Comparison of mineral modes measured by TIMA for sample AQ10_GPH from Group A, which shows polishing artefacts, and Group C, which does not show polishing artefacts. FR: Fresher rock; WR+P Weathered rind plus patina. Scales were selected to show the mineral modes of the specific rock as clearly as possible. If the dots are close or superimposed than the two different sample preparation methods provide near-identical results. If they are far apart then some kind of analytical or preparation-related artefact is inferred.

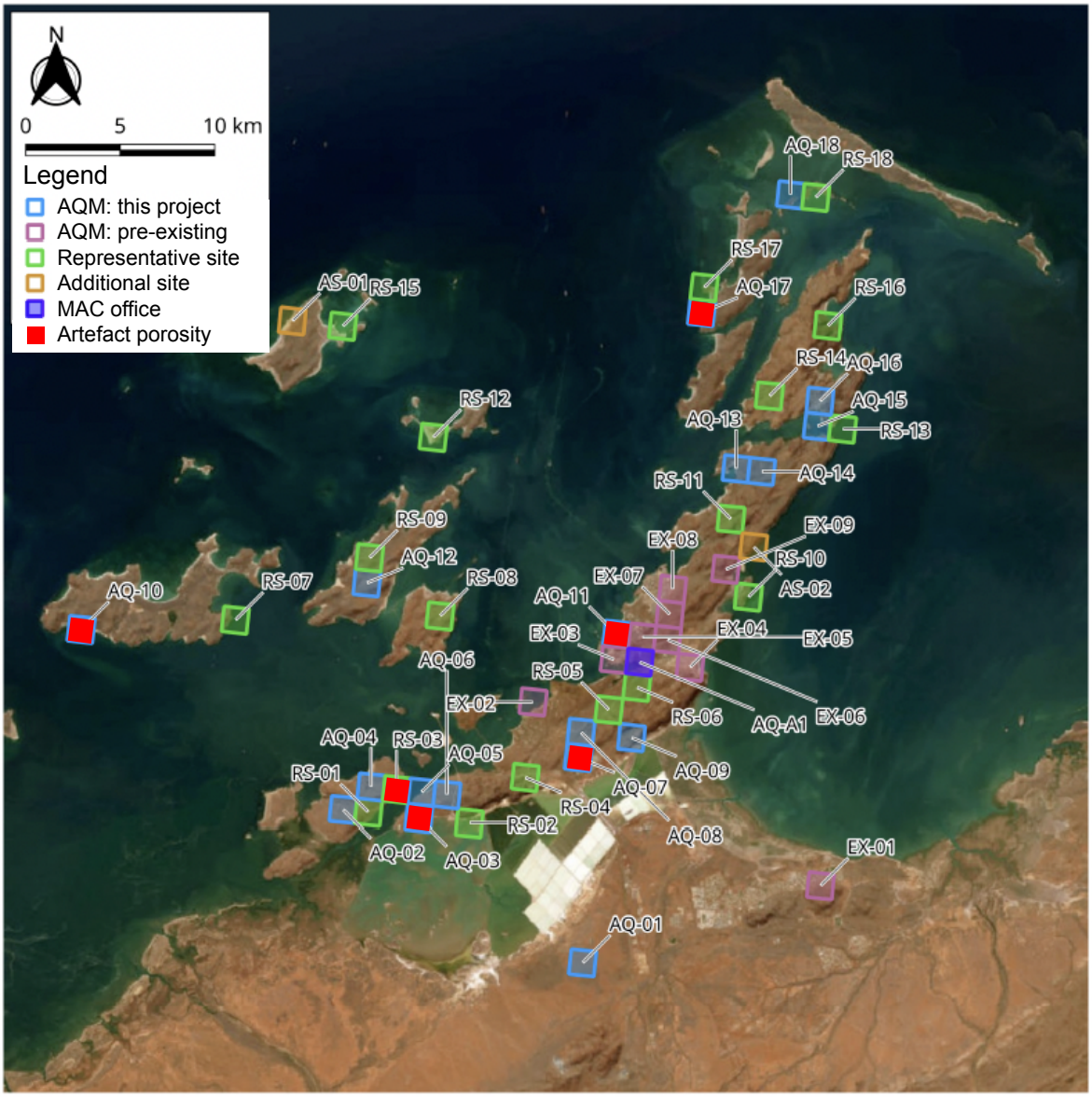

Figure 4.2-36: Locations of Group A samples that clearly show polishing artefacts are indicated by red squares. These samples are located proximal and distal to industrial emission sources.

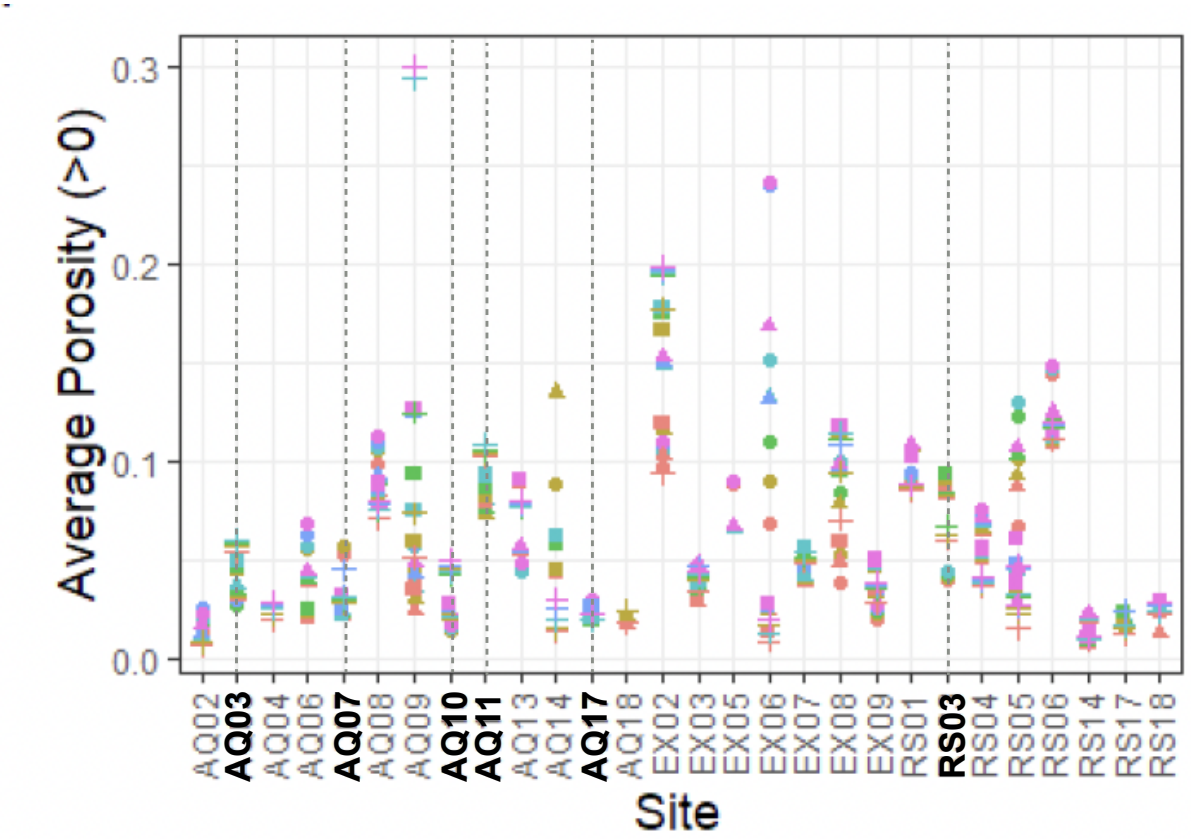

Figure 4.2-37: Porosity values for the Group A granophyre samples from Monitoring Studies Report 2024 (Curtin University, 2024c). The names of samples that clearly show polishing artefacts are shown in bold and a dashed line highlights the porosity values for these samples. The different symbols are used to provide a visual separation between the different values. There is no systematic relationship between the presence or absence of a polishing artefact and the absolute average porosity value.

Although the fundamental findings of the Monitoring Studies Report 2024 (Curtin University, 2024c) are not affected by the presence of polishing artefacts, these artefacts are a source of random error that is superimposed on any non-random spatial pattern defined by porosity unrelated to sample preparation. Any increase in the random error increases the magnitude of a non-random signal required to draw statistically robust conclusions. For this reason, it is desirable to reduce the incidence of polishing artefacts as much as possible. To achieve this reduction, several strategies will be tested and the results described in the final report. These include:

- Repetition of TIMA analysis and data interpretation to check whether operator-related factors contributed to the difference between Group A and Group C samples;
- Development of polishing protocols that minimise damage to sheet silicates such as chlorite and softer minerals, which may also be plucked or damaged by polishing;
- Further comparisons of billets with their corresponding thin sections;
- Testing multi-image workflows (e.g., optical, micro-CT, BSE-SEM) to distinguish between preparation- or polishing-related induced artefacts and porosity present prior to sample preparation.

Insights from the opportunistic *pH* measurements and oxalate and formate analyses

The main purpose of the opportunistic *pH* sampling on 24 January 2025 (Section 3.2.4.4), and the oxalate and formate analyses (Sections 3.2.4.5 and 4.2.4.6) was to test the competing hypotheses proposed to explain the relatively low *pH* values detected for the patinated rock surfaces at Murujuga, as outlined in Section 3.2.4.4. In summary, an increase in *pH* after rain is likely to follow removal of soluble acidic salts from the rock surface and underlying porosity, while a decrease in *pH* after heavy rain may be interpreted as an increase in microbial activity.

The analyses showed that the *pH* values neither increase nor decrease after rain, so measurements presented in this report (Sections 3.2.4.4, 3.2.4.5, and 4.2.4.6) do not unequivocally support either hypothesis. The lack of a *pH* increase is considered strong evidence that acidic salts deposited on the surface and precipitated within the rock subsurface are not the main cause of *pH* values less than 6. However, the lack of a *pH* decrease is not strong evidence for an absence of microbial activity. Indeed, the results of the oxalate and formate analyses indicate that microbiome produces organic acids within the rocks. It is possible that the response time for acid production by microbial activity after rain is different to the time-gap between rain and sampling, or that near-detection values of oxalate and formate, and the lack of a time-series for oxalate and formate sampling, limited the information available from these measurements such that microbial activity was present but not detected.

Evidence of oxalate-bearing minerals or oxalate-mediated mineral dissolution would help to constrain the role of oxalate and other organic compounds in mineral dissolution. However, oxalate minerals were not observed, and it is not possible to recognise oxalate-mediated mineral dissolution unambiguously in the field.

Further work, potentially with improved sampling protocols (e.g., longer equilibration times, greater rock:water surface areas), is necessary to better support links between *pH* and microbial activity. Such work is beyond the scope of planned activities for year 4, but it is recommended to form part of the ongoing research program.

Plan for ongoing monitoring of porosity

The finding of elevated porosity within the weathered rind of granophyre samples close to industrial sites indicates that porosity is sensitive to industrial emissions. This finding is supported and corroborated by the data presented in this report.

Porosity within the weathered rind reduces the strength of the bond between the patina, the underlying weathered rind, and fresher rock. Weakening of the weathered rind increases the probability that patina, with or without underlying weathered rind, will flake or spall from the rock surface (Figure *4.2-38*). If flaking or spalling occurs on the patina that hosts rock art then the rock art will be visibly damaged. The timescales that link the initiation of porosity increases to eventual flaking and spalling are not yet well understood, but could range from decades to thousands of years.

Therefore, longer-term monitoring of porosity may be a useful component of a future monitoring program, once the initial phases of the Murujuga Rock Art Monitoring Program are complete. The field permeameter instrument has provided useful corroboration of the lab-derived porosity results. However, the uncertainties on the permeameter readings are relatively large and this instrument is not considered sufficiently sensitive to recognise changes in rock permeability on shorter timescales of less than ten years.

An alternative is to repeat the porosity measurements described here, but it is not financially, logistically, or culturally desirable to collect new sample rocks regularly for porosity monitoring. A viable alternative is to mount patinated rock billets, approximately 50 x 50 x 5 mm in size, within the air quality monitors. These billets could be collected annually, shipped to Perth, and the mineral and porosity distributions could be measured using optical microscopy, BSE–SEM, and TIMA imaging using the protocols developed and optimised over the first three years of MRAMP.

After completing the analyses to detect any year-on-year changes, the billets could be remounted within the air quality monitoring stations for another year of exposure to weathering. If samples of gabbro and granophyre were placed in each AQM then 42 samples, 21 of each lithology, would be required, providing a sample set large enough to provide effective statistical power. There are a number of advantages to this approach:

- The same samples are characterised annually, so uncertainties related to inter-sample variation are reduced;
- The field work can be accomplished by the Murujuga Rangers;
- Analyses of the samples follow a well-developed workflow;
- There is no additional preparation of the samples for analysis once the billets have been prepared initially, minimising the additional formation of preparation-related artefacts and reducing preparation-induced uncertainty;
- The use of gabbro as well as granophyre provides a way to monitor this rock type, which hosts significant rock art but is difficult to monitor using field exposure alone because of its relatively restricted distribution.

Progress relative to the objectives

In summary, the objectives of the inorganic geochemistry team for year three of the Murujuga Rock

Art Monitoring Project have been completed:

- Monitoring of field-based proxies and indicators of rock art conditions has continued, augmented by some additional measurements to better constrain processes that control parameters such as *pH* (Section 3.2);
- An extended suite of samples has been collected and analysed. The results generally support the findings in the Monitoring Studies Report 2024 (Curtin University, 2024c), particularly with respect to spatial trends in porosity across Murujuga;
- Preparation-related artefacts that increase the uncertainties of porosity measurements have been identified, and additional work is required to develop sample preparation techniques that minimise these uncertainties.

Figure 4.2-38: (a) Flaking on non-rock art panels on the Dampier Salt Lease. (b) Flaking on rock art panel on the Dampier Salt Lease. Site of photographs is 650 m from the ocean and 1.8 km from the nearest salt pond. The darker-appearing patches inside the flakes are not obviously biological and the darker appearance relates to a change in relief within the flaked patch. Flaking is also seen commonly elsewhere on Murujuga. Images taken 4th July 2024.

4.3 Microbiome laboratory analysis

4.3.1 Objectives

From Section 1.6 of the MSDCA Plan (Curtin University, 2022), the objectives of the microbiome investigations are to:

1. Use advanced molecular biology approaches to characterise:

    a) Microbial community composition associated with rock patina and the underlying weathered rind;

    b) Diversity and relative abundance of functional genes involved in microbial processes and pathways that may contribute to stabilising or bio-deteriorating (bio-weathering) the rock patina: This answers the question “what are they potentially doing?”;

    c) Which of these functional genes are expressed transcripts that can potentially be translated into functional proteins/enzymes that carry out these processes?

2. Use advanced bioinformatics tools to:

    a) Build metagenome assembled genomes (**MAGs**) from the shotgun metagenome dataset of objective 1b and map the functional gene transcripts from objective 1c to the MAGs. This will reveal all sequenced genes belonging to the same species that were expressed at the time of sampling;

    b) Determine the number of mutations that occurred post-mortem in the assembled metagenomic bins (from objective 2a) to distinguish between microbial taxa that have been preserved in the patina as ancient DNA vs. those that represent modern taxa represent. Since this DNA damage increases with time it may be possible to determine the order in which these taxa died;

    c) Estimate the growth rate of the patina associated microbial communities by measuring genome replication rates from shotgun metagenomic bins without the need for cultivation;

3. Use live representative bacterial and fungal pure cultures in chamber studies to understand the effects of pollutants on these microbes.

4.3.2 Methodology

Microbiome laboratory methodologies are described in Section 3.3.3 of the MSDCA Plan (Curtin University, 2022) and the component study methodology statement:

- COPP21065-PRO-G-112 Murujuga Rock Art Monitoring Program: Microbiome Laboratory Analysis.

Variations to the planned methodology have been previously described in the Monitoring Studies Report 2024 (Curtin University, 2024c).

4.3.3 Work to date

The status of work completed to date is summarised in Table *4.3-1*. DNA and RNA extractions of all the patina samples were completed in the second year of studies. For the DNA extractions of the patina samples, the following tasks have been completed:

- The 16S rRNA gene (V3-V4) and ITS1 region has been amplified and sequenced. The relative abundance, taxonomy, and diversity of the bacteria, archaea, and fungal communities present in the patina were presented in the Monitoring Studies Report 2024 (Curtin University, 2024c). A similar analysis was also presented for soil and lichen samples in the same report;
- High quality DNA samples were analysed using shotgun metagenomic sequencing and the bioinformatic analyses of these sequencing data is ongoing. Currently, 68 samples have been assembled, binned, annotated, and taxonomically assigned. Multiple databases are currently being used to understand potential metabolic processes linked to the MAGs we have generated. This data will be presented in the final report.

Table 4.3-1: Microbiome laboratory analysis work to date.

Analysis	Description	Status
DNA extractions	DNA extractions of all patina, soil and lichen samples from the sample rocks	Completed
RNA extractions	RNA extractions of all patina, soil and lichen samples from the sample rocks	Completed
16S PCR and sequencing of DNA	All DNA samples for PCR amplication of the 16S rRNA amplicon and sent to AGRF for microbial diversity sequencing	Completed
ITS PCR and sequencing of DNA	All DNA samples for PCR amplication of the ITS fungal amplicon and sent to AGRF for microbial diversity sequencing	Completed
Sampling from bacterial and fungal isolates	Sub-sampling 200 SAB and TSA plates for colonies that grew on respective plates innoculated from the sample rocks on site	Completed
PCR and amplicon submission to AGRF of the colony isolates	All samples from the colony plates to be amplified with 16S and ITS primers and sent to AGRF for sequencing to identify what microbes were grown from the sample rocks	In progress
DNA depletion and cDNA synthesis of RNA samples	All patina, soil and lichen RNA samples to be DNase treated and subsequently subject to cDNA synthesis	Completed
16S and ITS PCR and sequencing of cDNA samples	All cDNA samples to be amplified with 16S rRNA primers and ITS primers and sent to AGRF for sequencing to determine the microbial diversity of active microbes at time of sampling	Completed
DNA cleanup for metagenome sequencing	DNA samples that failed quality control for metagenome sequencing at AGRF to be concentrated and cleaned	Completed
Meta-transcriptome sequencing	RNA samples need to be submitted to AGRF for meta-transcriptomic sequencing	Completed

For the RNA samples the following tasks have been completed:

- DNA depletion and cDNA synthesis of the RNA samples as well as the amplification and sequencing of the 16S rRNA and ITS genes. These data will help us understand the relative

abundance of the active microbial communities at the time of sampling. This work has now been completed and results will be presented in the final MRAMP study report.

- High quality patina RNA samples have been sequenced for meta-transcriptome sequencing and analysis of this data is ongoing. This data will be mapped to corresponding MAGs to understand what specific genes from the MAGs were being transcribed at the time of sampling and will also be analysed in isolation using the nf-core/metatdenovo pipeline. These results will be presented in the final report.

4.3.4 cDNA Bacterial and Fungal community profiles

Complementary DNA (cDNA) microbial profiling is used to understand the active microbial community of a given sample. It involves converting extracted RNA (which has a much shorter half-life to DNA, thus, represents the active community) into cDNA, followed by amplification and sequencing using typical microbial profiling methods.

The rock surfaces in the Burrup peninsula harbour specialised microbial communities that are adapted to cope with the environmental challenges present. As presented in Monitoring Studies Report 2024 (Curtin University, 2024c), the dominant bacterial and fungal species present in the patinated Group A samples are known to be able to manage extremes in UV radiation, temperature fluctuations and dessication. The goal of the cDNA microbial profiling is to build on our understanding of the previous results and identify which bacterial and fungal species are most active between the wet and dry seasons.

Methodology

RNA was extracted from the patinated Group A samples using the ZymoBIOMICS DNA/RNA Miniprep Kit. RNA samples were treated with DNase I and PCR'd using the 16S rRNA V3-V4 gene primers to ensure no amplification of contaminant DNA occurred. Once validation of no DNA contamination was successful, the RNA was reverse transcripted into cDNA using a reverse transcriptase. The cDNA was amplified for both the 16S rRNA gene (V3-V4) and the ITS1 region and the amplicons were submitted to the Australian Genome Research Facility (AGRF) for sequencing. Sequence quality was assessed with FastQC and MultiQC. Sequences were filtered, trimmed, denoised, merged, chimera removed and taxonomy assigned (Silva non redundant v138.1 for bacteria and UNITE v04.04.2024 for fungi) using tools from the DADA2 R package (version 1.34.0) (Callahan et al. (2016)).

Results

The cDNA microbial profiling of bacteria as compared to the original DNA microbial profiling revealed Cyanobacteriales, *Rubrobacter* and *Craurococcus-Caldovatus* as the most abundant bacteria in the active community. There is little difference in the relative abundance of the microbial communities between the wet and dry seasons. ANOSIM was used to test the difference between the wet and dry season communities which resulted in a R value of 0.05 and p-value of 0.079, supporting there is no difference in seasonal communities. *Craucoccus-Caldovatus* abundance drops in the dry season whereas Chroococcidiopsaceae and *Rubrobacter* relative abundance increases in the dry season. As for the Fungal cDNA profiling data, Ascomycota reads that could not be taxonomically classified past phylum level and *Spissiomyces* were the most abundant in the active

fungal community. Ascomycota had a slightly higher abundance in the wet season over the dry season, and the opposite was true for *Spissiomyces*.

These results indicate that the abundant microbial communities presented in the Monitoring Studies Report 2024 (Curtin University, 2024c) are also reflected as the abundant active communities. The microbial communities remain stable between the two sampling time points in the wet and dry seasons.

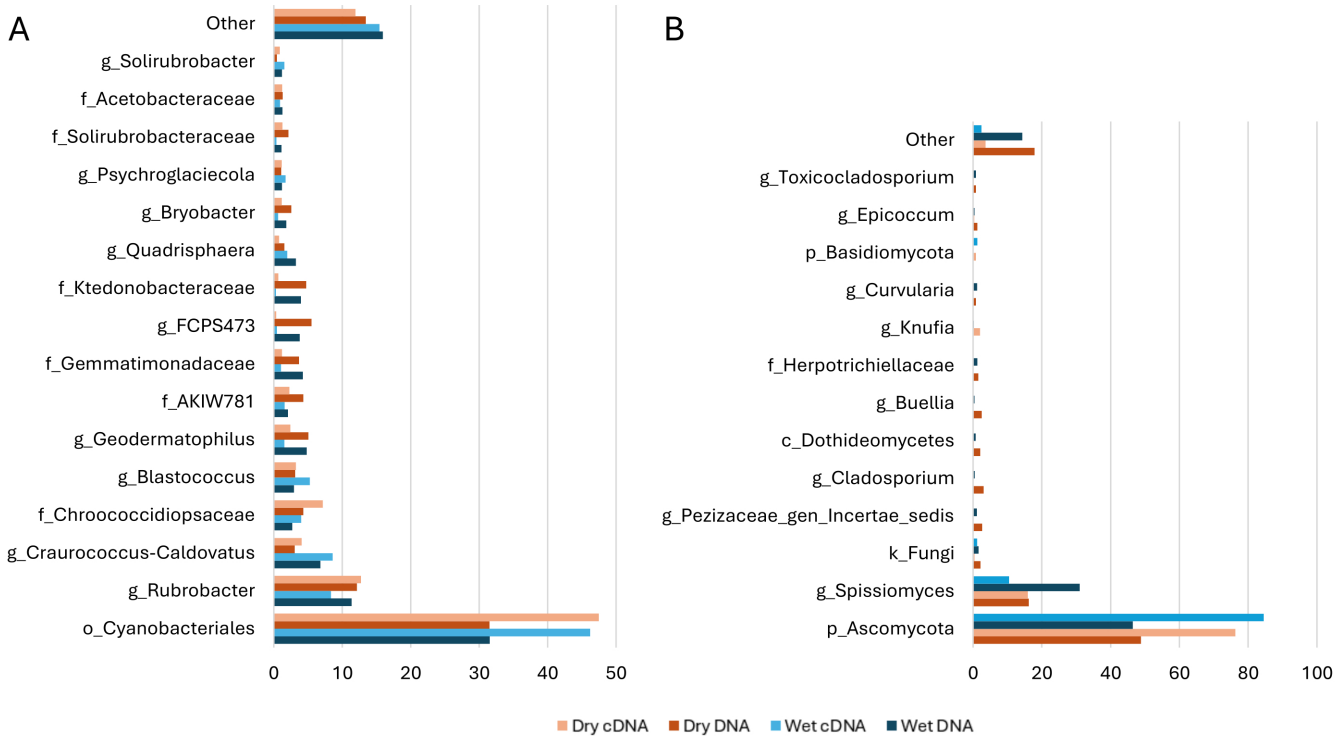

Figure 4.3-1: Bacterial and Fungal microbial profile of both cDNA and DNA sequencing data, averaged on Genus level and season. A) Bacterial 16S rRNA gene data. B) Fungal ITS data.

4.3.5 Rock Cube Sampling

Sterilised fresh rock cubes were mounted onto the AQMs across the Burrup Peninsula in November 2023 as part of the second year studies. Five rock cubes, one of each rock type (granophyre, gabbro, granite, basalt and dolerite), were sterilised by submerging the rock cube into 80% ethanol and flamed. They were then mounted onto a bracket and fixed to the AQM cages. This included all industry AQMs (EX01, EX03-EX09), comprising 29 total study sites (noting The industry (solar/passive) EX09 and MRAMP powered EX09 are separate but co-located and both have rock cubes fitted).

These fresh rock cubes will allow the monitoring of changes in pH, porosity, microbial communities and the identification of patina production over a long time period. This will allow us to develop an understanding of what microbial communities are responsible for rock colonisation, how these communities change over time, and how that relates to the rocks weathering.

In late September 2024, after the rock cubes were exposed to the elements for 10 months, samples were taken for genomic analysis. Sterile swabs were submerged in sterile molecular grade water and one face of each rock cube (randomly pre-selected by the statisticians) was vigorously swabbed. The swab was then submerged into 1 mL of DNA / RNA shield, and put on ice for initial field storage transport.

DNA and RNA extractions were completed when the samples were taken back to Curtin University. DNA and RNA extractions of these samples were unsuccessful. No samples had detectable concentrations of DNA or RNA to warrant further extraction or PCR amplification. Visually, the rock cubes had no signs of patina production. Some rocks had small specks of browning rust, but these were very localised. These results do not rule out colonisation of the rock samples by microbes. Further sampling of these rock cubes in the future may lead to successful DNA extractions due to increasing microbial abundance: as the rock weathers there is more surface area and protective micro-niches for the slow-growing microbes to colonise and thrive.

4.3.6 Group D sampling and analysis

The Group D samples include four granophyre samples that were obtained from the railway cutting outside of Karratha (as described in Table *3.2-7*). These samples are similar to the rock cubes discussed above; however, there are fewer of them and they have been exposed to the atmosphere for the last 60 years, as opposed to 10 months. These samples are useful to understand how their microbiome compare to the sample rock panels that have a distinct patina established. They will help in understanding the differences between patinated rock and non-patinated rock microbiomes, and what this might mean for the 'health' of the patinated rocks with petroglyphs. By understanding the key microbes that lead to patina production and maintenance, future monitoring will be more informative.

Methodology

Two sampling methodologies were used on these samples, one following the swabbing protocol described above, and the other using a Dremel to penetrate the surface of the rock (followed by swabbing and storing the swab in temperature controlled DNA/RNA shield). DNA extractions of these samples were completed with the Zymobiomics DNA mini kit.

Sufficient DNA concentrations were obtained from the Dremel samples for further analysis. Following sample preparation at Curtin University, amplicon sequencing of the 16S rRNA gene (V3-V4) and the ITS region was completed by the AGRF. Sequence quality was assessed with FastQC and MultiQC. Sequences were filtered, trimmed, denoised, merged, chimeras removed and taxonomy assigned using tools from the DADA2 R package (version 1.34.0) (Callahan et al. (2016)).

Results

Actinobacteriota, Proteobacteria and Chloroflexi were the dominant bacterial phyla identified in the Group D rock surfaces (Figure *4.3-2*). These phyla are also dominant in the original (Group A) patinated rocks collected in 2023, however Cyanobacteria are considerably less abundant in the Group D samples. The Group D samples additionally had the highest percentage of amplicon sequence variants (**ASVs**) that had low abundances, indicating a more diverse microbial community. *Geodermatophilus*, *Rubrobacter*, *Blastococcus* and *Craurococcus-caldovatus* were the abundant

genera in both patinated and unpatinated sample types. Again, at Genus level it is clear that the Group D samples lack any Cyanobacterial ASVs that are abundant in the patinated samples. As discussed in the previous MRAMP study report (Curtin University 2025), the genera identified are commonly found in rock surface microbiome studies. Cyanobacteria are currently hypothesized to be the key phyla contributing to the sequestration of manganese in the patina. Further analysis of Cyanobacterial MAGs that have been generated in the metagenome data will allow us to confirm genomically. The harsh conditions existing on the rock surfaces make these microbial communities extremely slow growing. It is unclear at this point if a lack of Cyanobacteria on the rock surfaces of the Group D samples is a production of a (relatively) short atmospheric exposure time period or other environmental factors.

Based on average relative abundances, the fungal communities are similar between the unpatinated Group D railway cutting samples and the original Group A patinated rock samples, with the Ascomycota Phyla being the most abundant in both sample types (Figure *4.3-3*). The *Spissomycetes* genus is more abundant in the patinated samples as opposed to the Group D samples. *Toxicocladosporium* and *Nigrospora* are more abundant in the Group D samples.

4.3.7 Fungi isolates from Murujuga sample rocks

Due to constraints on importing international laboratory isolates, additional sampling was performed to obtain fungi isolates from Murujuga rock surfaces for characterisation and use in the chamber experiments. Swabs from the rock surface were inoculated onto Sabouraud agar (**SAB**) plates and incubated for a week at room temperature. Single colonies were subsequently plated out onto separate SAB plates. This protocol led to the successful isolation of two fungal isolates. Once sufficient growth was achieved, fungal colonies were cut out of the SAB plates. DNA was extracted using the Zymobiomics DNA mini kit and the ITS1 region was sequenced. Taxonomic assignment of the sequences revealed isolate 1 and 5 to be *Toxicocladosporium* and *Myrmaecium* respectively.

The *Toxicocladosporium* genus is a cladospoium-like fungi with dark thick-walled conidial and conidiophore septa Crous et al. (2007). Most *Toxicocladosporium* species have been isolated from plant hosts and have been characterised as endophytic, however several have also been isolated from non-plant associated environments (Bezerra et al. (2017); Cruywagen et al. (2015); Fotedar et al. (2019); Che et al. (2024); Bakhshi et al. (2022); Hashimoto et al. (2021)). Blast analysis revealed that the *Toxicocladosporium* isolate had the highest identity to *T. irritans* (100% identity and coverage) which has been identified in air conditioners and causing biodeterioration on paintings (Hashimoto et al. (2021); Sterflinger (2010)). *Toxicocladosporium* sp. have been identified in sequencing data on rock surfaces, such as biofilms on Basalt sculptures in China and Limestone monuments in Portugal (Wang et al. (2021); Paiva et al. (2022)). ASVs belonging to the *Toxicocladosporium* genus were present in the original Group A patinated rock samples (0-26%) and the unpatinated Group D samples (0.5-15%).

The *Myrmaecium* isolate had 100% identity and coverage to *M. rubricosum* (synonyms *Hypoxylon rubricosum, Melogramma rubricosum* and *Valsaria rubricosa*). *Myrmaecium* species have been commonly identified as plant pathogens (Gutiérrez-Flores et al. (2020); Wang et al. (2023); Jaklitsch et al. (2015)). Very little literature has been published on this genus. Reads belonging to the *Myrmaecium* genus were not present in the Group A samples nor the Group D samples.

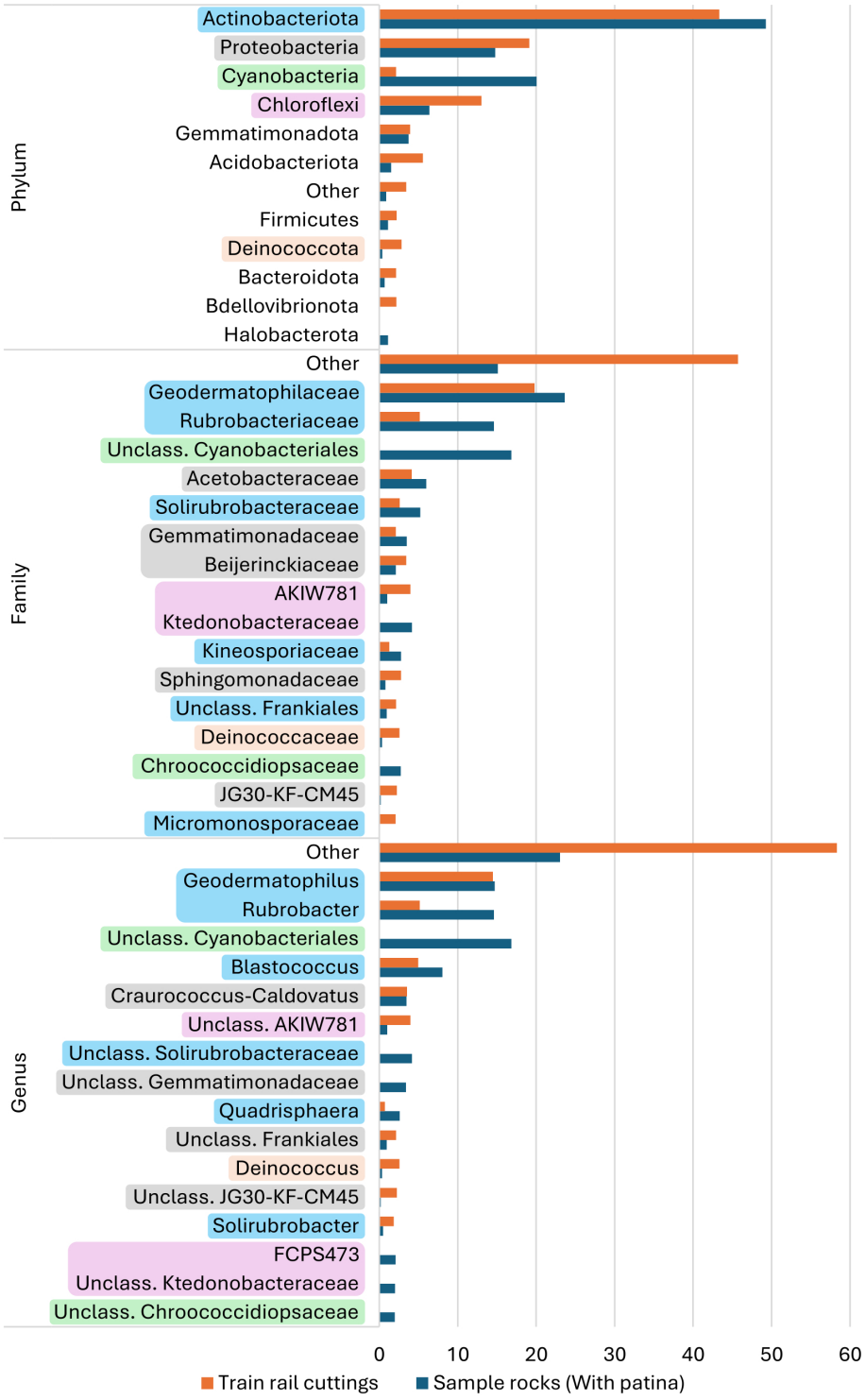

Figure 4.3-2: Relative abundance of the bacterial communities of the Group D rock surface samples (orange) and the original sample rock samples (blue) at Phylum, Family and Genus levels. Any respective level that had an abundance of less than 2% were grouped into the "Other" category.

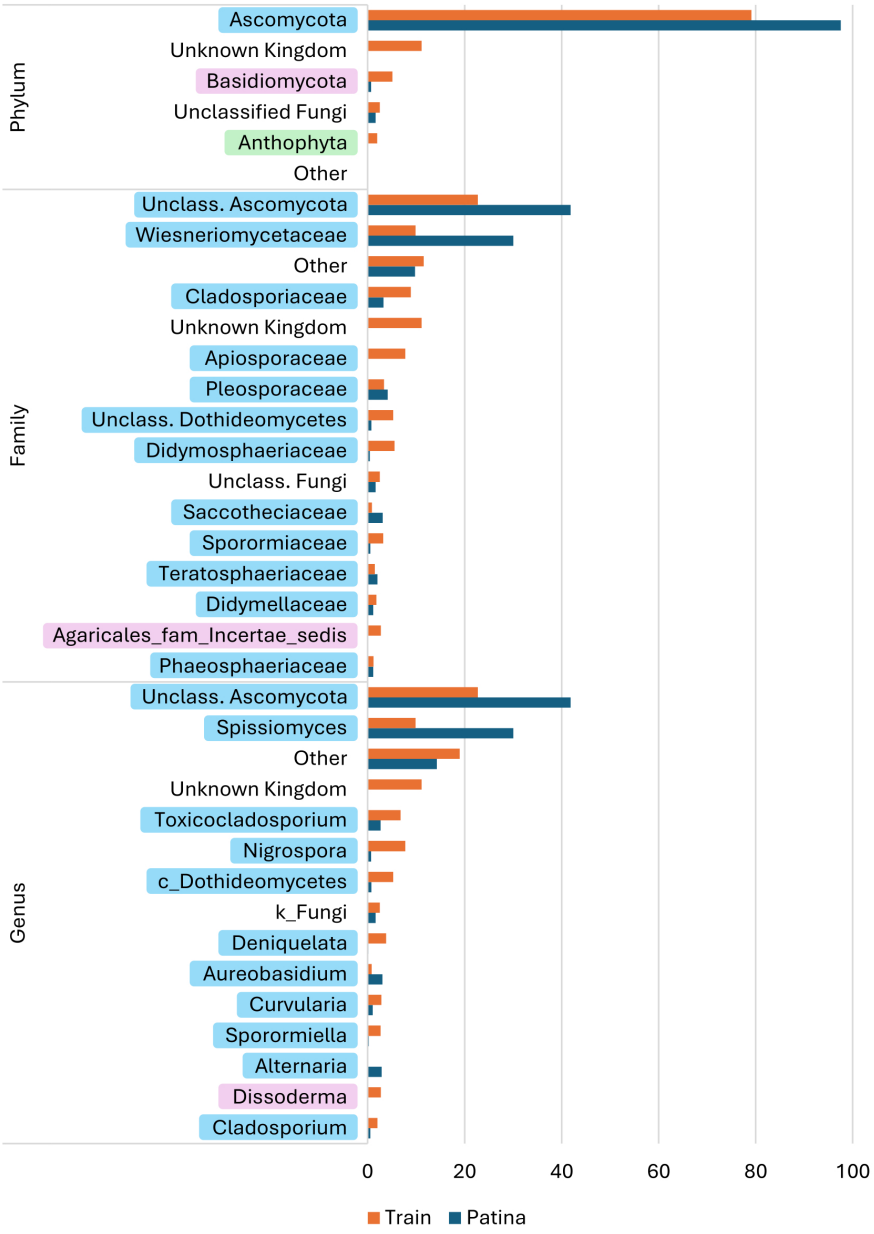

Figure 4.3-3: Relative abundance of the fungal communities of the Group D rock surface samples (orange) and the original sample rock samples (blue) at Phylum, Family and Genus levels. Any respective level that had an abundance of less than 2% were grouped into the "Other" category.

As mentioned previously, these fungal isolates are currently being utilised in the chamber studies where we will be able to determine if these fungal species are able to grow on a rock substrate, and how they respond to different industrial pollutants.

4.4 Chamber exposure (accelerated degradation) testing

4.4.1 Objectives

From Section 2.2.6 and 3.4 of the MSDCA Plan (Curtin University, 2022), the objective of the chamber exposure testing is to ensure that a dose-response relationship for (elevated) air pollutant concentrations can be established. It remains possible that the current level of anthropogenic emissions at Murujuga may not have a measurable impact on the rock art, or may have an effect below the level of measurement accuracy and precision inherent in field work. If that is the case, no field study of any size will result in a statistically significant outcome. For this reason, chamber studies are vital to give the project certainty in its ability to establish EQC levels. The chamber studies will consider as broad a range of parameters as possible, however will be focused on

a) physicochemical weathering of the rock and measurement of any by-products or results of such weathering and

b) exposure concentrations which may reduce the “health” or growth rates of the most abundant components of the microbiome.

The studies in point (b) will include analysis of the same inorganic geochemical weathering products as in (a), in order to account for biotic/abiotic interactions (e.g. additional weathering due to organic acids).

4.4.2 Physico-chemical weathering

4.4.2.1 Methodology

Information on the chamber exposure methodologies can be found in Section 3.4 of the MSDCA Plan (Curtin University, 2022). Whilst the aims of the experimental program remain the same, the methodology has been significantly revised in response to the inorganic geochemistry findings (specifically porosity), and the need for more controlled microbial experiments. The revised methods are detailed in the associated methods document:

- COPP21065-PRO-G-117 Murujuga Rock Art Monitoring Program: Chamber Exposure Studies.

Section 4.4.2 of Monitoring Studies Report 2024 (Curtin University, 2024c) details the design and methodologies of the chamber experiments.

Notably, the protocol has been revised and improved further to utilise freshly cut rock cubes for each exposure, rather than reuse previously cut samples.

4.4.2.2 Work to date

A comprehensive suite of abiotic geochemical weathering dose-response tests has been conducted using a blend of diesel and natural gas condensate. Table *4.4-1* summarises the physicochemical weathering exposures completed to date.

Analysis of the chamber studies results is discussed in Section 7.1.

Table 4.4-1: Summary of physicochemical weathering exposures completed to date.

Batch ID	Exposure	Pollutant	Average concentration of pollutant (µg/m3)	Active exposure duration (days)	Experiment date
1	Diesel/Condensate	NO_x & SO_2	27098 & 1876	5	12 December 2023
2	Diesel/Condensate	NO_x & SO_2	24506 & 1620	4	21 December 2023
3	Diesel/Condensate	NO_x & SO_2	15227 & 933	3	28 December 2023
4	Diesel/Condensate	failed	-	-	04 January 2024
5	Diesel/Condensate	NO_x & SO_2	334 & 261	1	12 January 2024
6,7,8	Diesel/Condensate	failed	-	-	19 January 2024 – 19 February 2024
9	Heavy Fuel Oil	NO_x & SO_2	7175 & 1900	2	04 April 2024
10	NH_3	NH_3	315	5	11 April 2024
11	Domestic gas/diesel	NO_x & SO_2	162 & 17	1	25 June 2024
12	NH_3	NH_3	2030	4	16 July 2024
13	NH_3	NH_3	483	1	05 August 2024
14	NH_3	NH_3	3600	5	27 August 2024
15	NH_3	NH_3	1925	3	04 September 2024
16	NH_3	NH_3	1350	2	11 September 2024
17	NH_3	NH_3	4100	6	24 September 2024
18	Vegetation	NOx	730	4	29 October 2024
19	Vegetation	NO_x	543	3	06 November 2024
20	Vegetation	NO_x	577	2	13 November 2024
21	Vegetation	NO_x	300	1	21 November 2024
22	Vegetation	NO_x	836	5	02 December 2024
23	SO_2	SO_2	36690	4	04 February 2025
24	SO_2	SO_2	19650	3	11 February 2025
25	SO_2	SO_2	13645	2	18 February 2025
26	SO_2	SO_2	6865	1	28 February 2025
27	SO_2	SO_2	30380	5	28 February 2025
28	blank test	-	-	-	18 March 2025
29	NO_2	NO_2	3175	1	01 April 2025
30	NO_2	NO_2	6555	2	08 April 2025
31	NO_2	NO_2	11150	3	29 April 2025
32	NO_2	NO_2	15500	4	05 May 2025
33	NO_2	NO_2	17055	5	12 May 2025
34	NO_2 (fresh rocks)	NO_2	3579	1	22 May 2025
35	NO_2 (fresh rocks)	NO_2	7641	2	28 May 2025
36	NO_2 (fresh rocks)	NO_2	12398	3	03 June 2025
37	NO_2 (fresh rocks)	NO_2	13790	4	09 June 2025
38	NO_2 (fresh rocks)	NO_2	17856	5	16 June 2025
39	NO_2 (fresh rocks)	NO_2	35436 (double dose)	5	16 June 2025
40	SO_2 (fresh rocks)	SO_2	7450	1	09 July 2025
41	SO_2 (fresh rocks)	SO_2	14408	2	16 July 2025
42	SO_2 (fresh rocks)	SO_2	21845	3	22 July 2025
43	SO_2 (fresh rocks)	SO_2	27843	4	29 July 2025

4.4.3 Microbiome

The microbiome chamber study follows the same rationale explained above, albeit with a focus on the dose response curve between the pollutants and the viability of bacteria and fungi. Utilising microbes that have been directly isolated from Murujuga rocks, and representative microbes obtained from cultured collections, we hope to gain insight on the response of microbes to pollutants. Currently, range finding exposures are being conducted to understand the limits of measurable changes. The bacteria and fungi being used include:

- *Rubrobacter spartanus*^{T} DSM 102139, obtained from DSMZ German Collection of Microorganisms and Cell Cultures. *Rubrobacter* had an average abundance of 15% across the patina samples reported in the Monitoring Studies Report 2024 (Curtin University, 2024c).
- *Chroococcidiopsis cubana*^{T} DSM 107010, obtained from DSMZ German Collection of Microorganisms and Cell Cultures. Although the vast majority of the 16S rRNA gene cyanobacterial reads could not be classified past order level, the Chroococcidiopsaceae family was the most abundant cyanobacterial family.
- Unknown fungal isolate 1 (FS1), a black filamentous fungi was isolated from the Murujuga rocks on SAB agar and will be used in the chamber study. This isolate has been submitted for sequencing of the ITS region for taxonomic assignment so we will be able to understand if this isolate is common to the sample rocks and to what extent.
- Unknown fungal isolate 2 (FS2), another filamentous fungi which forms irregular edged, slightly raised, brown-coloured colonies. This isolate was also obtained from a Murujuga sample rock on SAB agar and is similarly being sequenced for taxonomical classification.

4.4.3.1 Methodology

R. spartanus and *C. cubana* are grown in liquid culture under optimal conditions to the log phase. Liquid cultures are centrifuged, supernatant removed and washed with Tris-EDTA (**TE**) buffer. The washed cultures are centrifuged and diluted in TE buffer and inoculated onto the surface of a rock cube. The fungi are grown on SAB agar and inoculated on the rock surface directly. Inoculated rock cubes are transferred to the chamber (Figure *4.4-1*) and subjected to the designated pollutant at a given concentration. Appropriate exposure durations are currently being determined through range finding experiments (see Section 4.4.3.2 following). After exposure, the rock cube surface is dyed with 6 µM SYTO nine stain and 30 µM propidium iodide, then incubated in the dark for 15 minutes. The rock surface is then rinsed with TE buffer and imaged using the Nikon A1 confocal laser scanning microscope with the 40x objective. Ten images are taken across the rock surface, and the syto9 and propridium iodide intensity sum is measured using the Imaris viewer. Control samples follow the same protocol however are not exposed to the pollutants. Post imaging, the same protocol will be used as the inorganic methodology to assess the extent of mineral leaching and pH changes.

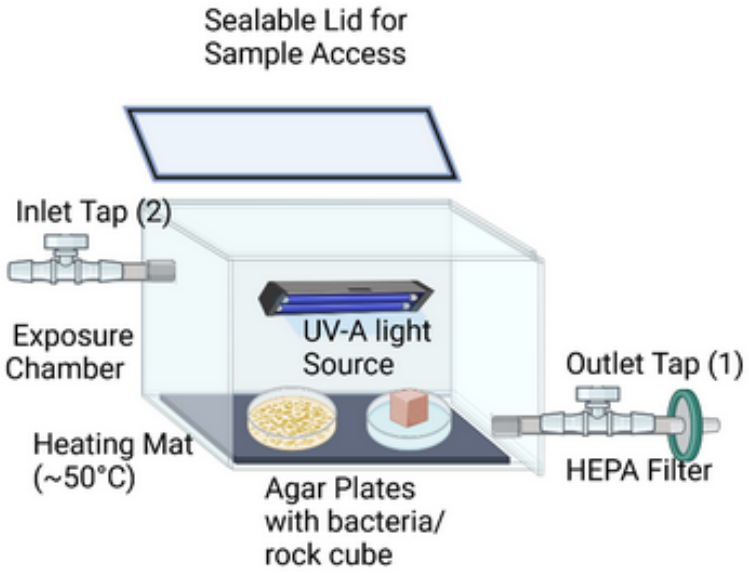

Figure 4.4-1: Diagram of the microbiology exposure chamber.

4.4.3.2 Work to date

Range finding exposures are currently being undertaken to determine the upper and lower limits of measurable change in the microbial viability at different pollutant concentrations and exposure times. Similar to the inorganic chamber studies, SO_2 appears to be producing a stronger response compared to NO_2.

This page is intentionally blank.

5 Air quality monitoring network operation

5.1 Objectives

As described in Section 1.8 of the MSDCA Plan (Curtin University, 2022), the objectives of the air quality monitoring (**AQM**) network are to deploy and maintain a range of air quality monitoring equipment at appropriate spatial locations such that the air quality across all of the Murujuga region can be determined.

5.2 Methodology

The AQM network includes both passive monitors (with low voltage solar power), and mains powered AQMs to provide accurate real time monitoring data where existing power infrastructure was available. The passive AQMs are contained within a specifically designed cage, whereas the powered AQMs are built in (and on), modified 20’ (6.1 m) insulated shipping containers.

In order to meet all relevant National Code of Construction standards, the enclosures housing the equipment and relevant components were designed and/or certified following AS4100; AS1170; AS3600; AS1554; AS1252; AS2923 and the relevant sections of AS3580.

The following documents provide further information on the methodologies relevant to AQM installation, deployment, and operation:

- COPP21065-PRO-G-102 Murujuga Rock Art Monitoring Program: Passive Air Quality Monitoring (AQM) Installation and Commissioning
- COPP21065-PRO-G-103 Murujuga Rock Art Monitoring Program: Passive Air Quality Monitoring (AQM) Sample Collection, Maintenance and Context Observations
- COPP21065-PRO-G-104 Murujuga Rock Art Monitoring Program: Powered Air Quality Monitor Installation and Commissioning
- COPP21065-SPE-G-100 Murujuga Rock Art Monitoring Program: Air Quality Monitoring Station Control Functional Specification.

5.3 Solar/passive sites

The solar/passive AQMs (as shown in Figure *5.3-1*) have now been in operation for over three years since the first operational installation. Each of these stations consists of:

- a complete weather station;
- a suite of passive gas samplers;
- a three-bucket deposition sampler;
- a total (flask) deposition sampler;
- rock cube samplers;
- a set of ‘low power’ gas analysers;
- supporting power (solar) and communications infrastructure.

Figure 5.3-1: Passive AQM AQ14, showing the range of instruments deployed in each passive/solar AQM. Visible are the anemometer (top left of mast crossbar), rain water collector (front left of cage), rain gauge (visible behind the collector), control box (white box to the rear left) and bucket (deposition) sampler (on central concrete block).

All passive samplers (IVL, total flask and three-bucket deposition samplers) are changed over at nominal four-weekly intervals. During these AQM site visits, instruments and infrastructure are inspected and maintained. Note that this excludes the rock cubes, which are expected to be sampled at 6-12 month intervals.

Weather station data and data from the ‘low power’ analysers are live-streamed to Perth for storage and analysis. These are available on a dashboard for viewing in real time.

Figure 5.3-2: 3-bucket deposition sampler in dry position, with AS/NZS 3580.10.1 total deposition flask in lower right of image. (Note image is tilted slightly, samplers are mounted flat)

5.3.1 AQM rock cube samplers

Rock cube samplers were deployed at all AQM locations (including existing Industry monitoring sites) previously in November 2023. These consist of five rock cubes (one of each rock type) that have freshly exposed and sterilised surfaces, to allow us to monitor the establishment of the microbiome on the rocks as well as *pH* and permeability. These were sampled for the first time in the third year of studies, in October 2024.

5.3.2 Solar/passive AQM network changes in the third year of studies

Two additional (limited) air quality monitoring sites were added in 2024 and additional samplers were added to an existing industry AQM. These were added to fill any possible gaps in the network and ensure interpolations and spatial smoothing of data is accurate in these regions. These additions are:

1. TM01, a new temporary AQM located near the north end of Hearson's Cove, fitted with NO_2 and NH_3 IVL samplers only;
2. TM02, a new temporary AQM located on Rosemary Island, fitted with NO_2 and SO_2 IVL samplers only;
3. EX04, an existing industry AQM at the southern end of Hearson's Cove where IVL NO_2 and NH_3 samplers were added.

The selection of IVL passive samplers at these locations was based on the main chemical species expected to be present as primary air pollutants. NO_2 is generally the most abundant gas species at all sites. NH_3 was expected to be elevated near the fertiliser plant and/or port area. Likewise SO_2 has been found to be elevated on the outer islands at certain times of the year and this may extend to the TM02 site on Rosemary Island.

It is expected these samplers will be discontinued after 12 months of data has been collected.

5.4 Powered air quality monitoring sites

There are four mains-powered AQMs operating to provide real time monitoring of NO, NO_2, NH_3, SO_2, O_3 and dust (see Figure *5.4-1*). Powered sites were installed at locations where there was existing power infrastructure. Three of these sites were installed and are operated by the MRAMP researchers, with the fourth being an existing Woodside monitoring station operated by ACOEM/Ecotech. This site (designated EX07) has additional MRAMP owned equipment installed to ensure the above suite of pollutants are all measured. EX07 has a real time optical particle counter (Palas FIDAS 200), like the three stations operated by the MRAMP researchers, however it features different makes/models of gas analysers, chosen for ease of integration into the existing equipment onsite.

In addition to the species listed above the three MRAMP operated powered AQMs (AQ01, EX02, EX09) feature additional monitoring equipment. These stations include the same monitoring equipment installed at the passive AQMs:

- a complete weather station;
- a suite of passive gas samplers;
- a three-bucket deposition sampler;
- a total (flask) deposition sampler;
- rock cube samplers;
- a set of 'low power' gas analysers;
- communications infrastructure.

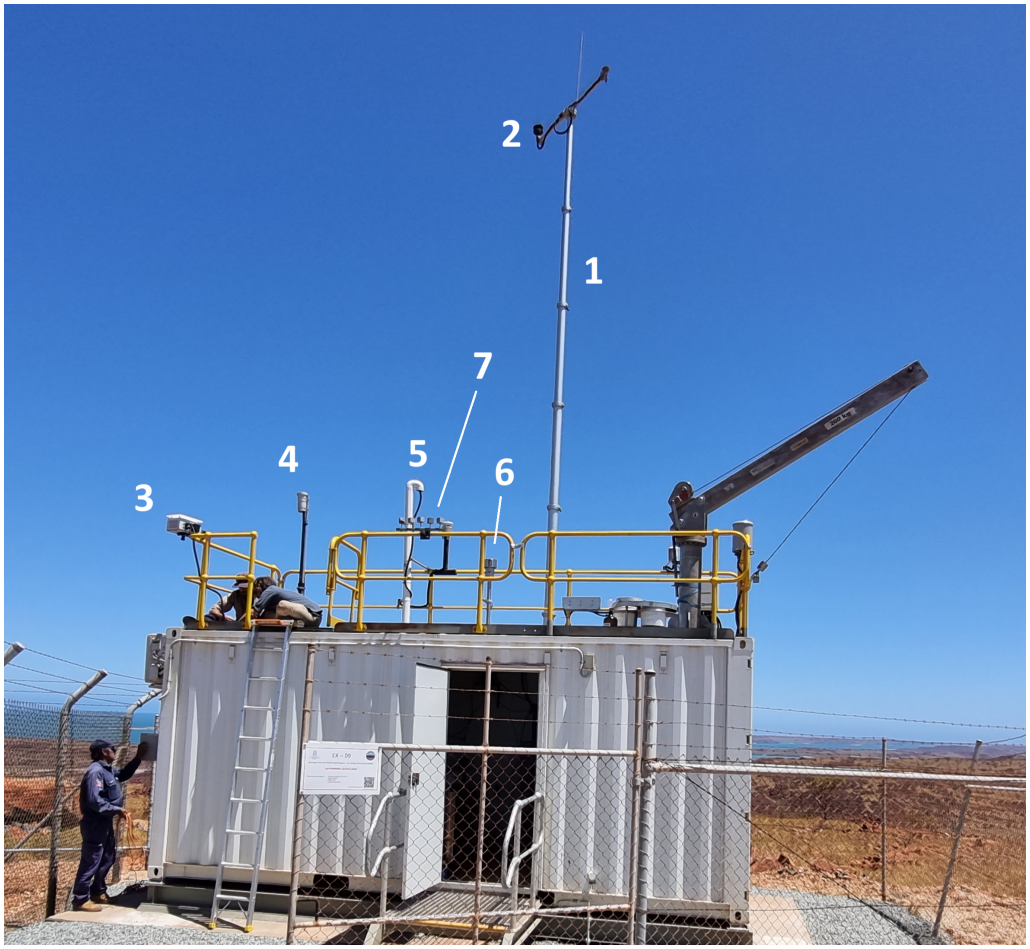

Figure 5.4-1: Powered AQM EX09, as installed on Mount Wongama. Visible on the are the mast (1), with anemometer on the crossbar (2). Visible on the roof are the Max-DOAS (3), the Radon detector inlet (4), the main sample inlet (5) and the FIDAS inlet (6). At the front of the station, above the door, the rock samplers can be seen (7).

A methane and non-methane hydrocarbon detector has also been installed with the suite of reference grade gas analysers. AQM EX09 has additional instrumentation, including an aethalometer (black carbon monitor), radon detector, Max-DOAS (2D scanning), and an isotopic methane analyser (Picarro). The sites are routinely visited for maintenance, inspection, and calibration purposes.

5.4.1 Powered AQM site changes in the third year of studies

The inlet air handling of the Aethelometer at EX09 was upgraded to better exclude moisture during high humidity periods, however the instrument nevertheless sustained water ingress during Tropical Cyclone Sean. The Radon detector at EX09 also experienced issues with humidity accumulation inside the instrument and required repair. As the MAx-DOAS instrument appeared to be highly useful for monitoring NO_2 and other species of interest, in November 2024 the MAxDOAS Compact unit from EX09 was relocated to EX02 and a new MAxDOAS 2D unit was installed at EX09. The 2D unit permits measurement at multiple locations in a horizontal plane without manual repositioning. As these instruments can each measure over a distance of 15+ km horizontally, they can span the

majority of the regional airshed when both are operational.

All real time instruments are internally networked to an onboard PC. This contains a suite of software to handle data logging and transfer as well as remote access to each of the instruments.

5.5 Environmental challenges for AQM equipment operations

Given the nature of the environment there has been the need for some repair and maintenance work to be conducted on the AQMs. Much of this was expected and planned for, with the AQMs located on islands particularly susceptible to corrosion and salt deposition/build-up. Impacts were:

- A small amount of wildlife damage has occurred, likely due to native rodents or birds. In all bar one case this impacted outer protective cable covers only with no loss of data;
- AQ13 and AQ14 were within the boundary of 2024 prescribed/cultural burns. Both experienced no impact of burns in the immediate vicinity;
- Many of the pneumatic, telescopic masts have developed leaks from the base seal. These are presently locked in the extended position pending seal replacement prior to the 2025/2026 cyclone season;
- Salt/sea spray exposure requires ongoing maintenance and lubrication to all moving parts such as hinges, locks and deposition sampler mechanisms. A program of refurbishment of deposition samplers has commenced;
- Some faults with system components have occurred with the replacement of batteries, solar panels and charge controllers required at a number of sites, repairs to deposition samplers being required, and replacement of faulty data-loggers, sensors and Raspberry Pi computers;
- High ambient temperatures and extreme levels of ultraviolet (UV) radiation result in high weathering and deterioration rates for any plastic, rubber or painted components.

As mentioned above, some impact was experienced by the powered stations (particularly some instruments at EX09) during Tropical Cyclone Sean, which deposited all time record rainfall for the region over a 24 hour period. All pneumatic AQM masts were lowered during the cyclone due to wind speed. Successive lowering and reinflation during the cyclone while solar charging was ineffective and led to multiple flat or defective batteries. This resulted in a revision to the AQM operating system software to only permit mast reinflation during charging (measured based on time of day and UV level). AQ03 experienced over 30 cm of flooding which resulted in the air compressor being flooded but no other damage.

During the same period, controlled burns were undertaken at AQ13 and AQ14 with no operational impact.

Overall, the performance of the AQMs has been reliable, with a schedule of planned maintenance being developed based on our experiences in the field. Most faults can be detected remotely through diagnostic telemetry, which allows repairs/replacements to be planned and conducted as part of the regular sample changeovers or dedicated maintenance missions. Occasional, temporary communications outages occur in the region, related to the 4G mobile network, however, the stations are able to automatically reconnect to the network and resume data transfer, once the network is back online. No data are lost as data are stored locally until successfully transmitted.

In summary, the design of the stations is reliable and fit for purpose. Minor revisions to the design have been incorporated to increase reliability and streamline maintenance and repair processes.

5.6 Monitoring equipment calibration

Total deposition samplers following with AS/NZS 3580.10.1 (4L flask and 150 mm diameter glass funnel) have been deployed at all AQMs for over 12 months at this point. Samplers at AQ04, AQ10, AQ17, AQ18 are installed at an AS/NZS 3580.10.1 compliant inlet funnel height of 2.0±0.2 m, those at AQ01, EX02, EX09 are installed at approximately 3 m and all remaining samplers at approximately 1.2 m. This was due to the need to co-locate with the 3-bucket deposition samplers for comparison purposes.

The results of the total deposition samplers are presented Section 7.11. Data from the MRAMP novel 3-bucket deposition samplers are presented in Section 7.10. Plus Section 8.2 compares the two samplers.

Powered instruments are calibrated as part of the scheduled fieldwork. For the gas analyser suite this involves both a zero, using zero air generators on site and a calibration using the appropriate calibration gas. Specific calibration gases are obtained from our supplier, with NATA certified certificates of analysis. Each analyser is zeroed with zero air and observed to ensure stability. Calibrations are the performed, typically at a concentration of 200 ppb, though sometimes as low as 100 ppb (this is usually for SO_2, where measured concentrations are between 0 and 9 ppb). The new slope and offset following these procedures are recorded and compared to both the previous values and the ranges specified by the instrument manufacturer. Any instrument alerts are investigated and troubleshot where required, the aim being to resolve any issues while on site. Other key parameters are noted (e.g. sample flow rates, and in the case of the T201 the molybdenum converter temperature). Multipoint calibrations are periodically performed to check linearity. We have observed very little drift in the instrument measurements overtime, though there have been instrument faults that have required either on-site repair or a return to the vendor. In these cases, the data have been omitted. This is noted in Section 7.13.1.

The FIDAS dust analysers undergo a calibration check using the vendor supplied calibration dust. The Radon detector at EX09 is subject to calibration using a gas which does not contain radon. This is typically nitrogen, though in earlier calibrations was helium.

5.7 Lidar campaign

Three complementary lidar systems were deployed on Mt Wongama between September 2024 and early March 2025 to measure dust and other aerosols. The systems deployed were:

- a Windcube 200S (Vaisala, Finland) provided by DWER (Figure *5.7-1*);
- a MiniMPL (Droplet Measurement Technologies (USA)), provided by the University of Melbourne (Figure *5.7-2*);
- a novel lidar provided by the University of Newcastle and was operational from 29 October 2024 to 24 February 2025.(Figure *5.7-3*).

The deployment period included the significant weather event, Trocial Cyclone Sean, in January

Figure 5.7-1: Photo of the MiniMPL lidar on right and Windcube 200S on left, facing in the general measurement direction ±90°.

2025, and the Windcube and MiniMPL captured data throughout this event. These two units also captured data during a second tropical cyclone (T.C Zelia) that crossed the Pilbara coast east of Port Hedland in February 2025 with minimal impact on the Murujuga region.

It has not been possible to sufficiently analyse the many terabytes of data collected from the lidar campaign in time for this report, and this will be presented in the final MRAMP study report.

5.8 AQM network data analysis

Analysis of data collected from the AQM network is presented in Section 7 of this report as follows:

- Section 7.10 deposition sampler data;
- Section 7.11 total deposition flask data;
- Section 7.12 passive IVL gas sampler data;
- Section 7.13 powered real time analyser data;
- Section 7.14 low powered gas sensor data;
- Section 7.15 weather station data.

Figure 5.7-2: Photo of the MiniMPL lidar operating at night. Photo Credit: Heather Osborne

Figure 5.7-3: Photo of the University of Newcastle lidar.

6 Spatial mapping and surface modelling

6.1 Objectives

It is important to understand how environmental and air quality parameters measured at the AQMs relate to the exposures at the rock (art) surfaces being studied. For all sites containing both air quality monitors and rock art or sample rocks included in the study design (i.e., all AQ and EX sites except for AQ01 and EX01), work has been completed in previous years to:

1. Map the topography of the sites, incorporating a region around each sample rock and rock art panel, and the AQM location.
2. Triangulate and fill in the mapping between each of (1) and include any nearby features likely to be major airflow paths.

Following the field mapping, processed topographies were provided to the computational fluid dynamics (CFD) team to develop meso-scale models of airflow in the regions above the study targets. This will provide improved determination of pollutant exposures at the rock surface.

6.2 Spatial mapping

No additional spatial mapping data was collected or processed in the current year of research. Please refer to Appendix D of the Monitoring Studies Report 2024 (Curtin University, 2024c) for mapping summaries of the MRAMP AQM localities.

6.3 Computational fluid dynamics (CFD) modelling

6.3.1 Objectives

Section 4.5 of the MSDCA Plan (Curtin University, 2022) states the objective of the computational fluid dynamics (CFD) modelling as assisting interpretation of the field-based air quality monitoring studies.

The focus of this work was originally meso-scale air pollutant and atmospheric dynamics as reported previously (Curtin University, 2024c). However in year three the focus has switched to micro-scale (pore/rock surface) simulations to better understand moisture retention within rock structures and diffusive interactions between rock pores and gas species.

6.3.2 Methodology

The CFD process creates a virtual model of a region of Murujuga, with complete control over the inputs, and with fine spatial resolution. The four main stages in the modelling are:

- defining the inputs (including geometry, emissions, meteorology, etc.),
- creating the model (meshing the domain, setting the boundary conditions),
- running the model (flow, and species transport),
- post-processing (extracting results).

Current micro-scale simulation work is utilising 3D geometric datasets from the micro-CT scanning reported in the inorganic geochemistry laboratory work (Section 4.2.4). For the MRAMP project OpenFOAM v10 (Greenshields, 2022) has been used for the modelling thus far, and this version will be used for future CFD simulations.

Micro-scale simulation work remains ongoing and will be presented in the final study report.

7 Statistical analysis of data from each component study

This section reports the analysis of data collected in each of the component studies, focusing on one component study at a time. Relationships between the variables measured in different component studies are investigated in Section 8.

The key findings from the statistical analyses in this section are summarised in Section 7.16.

The cut-off dates for each individual dataset (presented in each section) vary depending on the order of data collation, data analysis and complexity. In general, the cut-off dates were March–May 2025.

The plan of the section is as follows:

- Section 7.1 concerns the chamber experiments in which sample rocks were subjected to high concentrations of pollutants.
- Section 7.2 concerns the measurements of rock surface colour in the field.
- Section 7.3 compares the Woodside IVL and Radiello passive sampler data.
- Section 7.4 concerns the measurement of *pH*, *Eh* and Cl^- ion concentration on rock surfaces, and *pH* on rock cubes.
- Section 7.5 concerns the measurements of rock composition using the pXRF instrument.
- Section 7.6 concerns rock porosity, as determined from microscope images of thin sections of rock samples.
- Section 7.7 reports initial analysis of data from the permeameter instrument, which was deployed in the field in response to the findings about rock porosity.
- Section 7.8 summaries that there are no new results on the microbiome in the patina, soil, and lichen samples.
- Section 7.9 concerns organic geochemistry.
- Section 7.10 concerns the data from the three bucket deposition samplers on the *pH* of deposited material and the deposition rate of various chemical species.
- Section 7.11 reports the data from the total deposition flasks (traceable to an Australian Standard) on *pH* and the deposition rate of various chemical species.
- Section 7.12 concerns the data from the IVL passive sampler tubes on the atmospheric concentrations of various gases.
- Section 7.13 concerns the data from the real-time air quality monitoring stations.
- Section 7.14 reports the data from the ‘low power’ sensors that measurement CO_2, NO, NO_2, NH_3, $PM_{2.5}$ and PM_{10}.
- Section 7.15 summarises the temperature, relative humidity and rainfall data from the air quality monitoring stations and Bureau of Meteorology.
- Key findings from this section are summarised in Section 7.16.

7.1 Chamber studies

7.1.1 Introduction

The Monitoring Studies Report 2024 (Curtin University, 2024c) chamber studies predominantly utilised a methodology which exposed rock cubes to cooled, diluted combustion gases, consisting of air (N_2 and O_2), CO_2, CO, NO, NO_2, SO_2, H_2O, VOCs, trace gases and soot particulates. The method also utilised a UV lamp to assist with NO to NO_2 conversion (oxidation) and generate O_3 through reaction between NO_2 and VOCs. Additionally, the water vapour, temperature and UV would have been expected to induce reactions to convert many of the gases to their respective acids. The exposure of rock cubes to this cocktail of gases, droplets and particles produced an apparent exposure effect. This effect was measured as leached elements post exposure, which could be attributed to weathering of minerals within the rock. The magnitude of this effect was determined, for NOx ($NO+NO_2$) + SO_2 as these are the dominant gaseous air pollutants at Murujuga and were believed to be the most reactive and relevant exposure species at the time.

Preliminary year two chamber studies explored the effect of reusing rock cubes over multiple exposures and determined this method was acceptable (and preferred as it was the most efficient use of rock samples, reducing the need to collect additional samples, which is culturally undesirable). The experiments also utilised all rock types, which reduced the number of replicates of each rock type per experiment.

The Monitoring Studies Report 2025 (Curtin University, 2025b) chamber studies planned to differentiate the effects of NO_2, SO_2 and other air pollutants through direct exposure to individual (bottled) gas species. NO_2 was selected as the first exposure as it is the most abundant gaseous air pollutant at Murujuga and has received the most attention in previous literature. However, both our own work and literature cited in this report has now identified that NO_2 likely has only a very weak effect on rock weathering. Commencing single gas exposure experiments with NO_2 highlighted methodological deficiencies in the chamber studies, namely, rock cube reuse, the number of replicates per rock type and exposure scheduling, which have now been addressed and overcome. This has resulted in a decrease in the measured effect of determined for NO_2 and to a lesser extent SO_2.

Detailed background information on the chamber studies is provided in the Monitoring Studies Report 2024 (Curtin University, 2024c). In brief, rock cube exposures are conducted for a six-day incubation period, with air pollution (either from hydrocarbon combustion or bottled gases) actively introduced at the commencement of the exposure on day one for one hour and then (if repeated) at 24-hour intervals for up to six days. After the active exposure period, the concentration inside the chamber is progressively reduced over the subsequent 23 hours, due to chemical reaction or diffusion in the chamber. For all exposure scenarios, incubation and UV light exposure are continued for six days to permit secondary reactions to occur. Rock cubes are rinsed in a defined quantity of ultra-pure water, then given a “bath” in ultra-pure water for 30 minutes both pre- and post-exposure. Pre- and post-exposure samples and blanks are analysed by the ChemCentre using Inductively Coupled Plasma-Atomic Emission Spectroscopy (ICP-AES) to determine the concentrations of leached elements. For further details, see Section 7.1 in the Monitoring Studies Report 2024 (Curtin University, 2024c).

The experiments presented in last year’s report (Curtin University, 2024c) comprised ten exposure

rounds (batches). The dose-response relationship between the chemical elements Calcium (Ca), Potassium (K), Magnesium (Mg), and Sodium (Na) when exposed to different doses of a 50/50 diesel/natural gas condensate mix were explored. Experiments using diesel, heavy fuel oil (**HFO**), and ammonia (NH_3) were also undertaken.

In the third year of studies, additional chamber studies data are available from exposure rounds 11 to 43. Table *4.4-1* provides full details of the physicochemical weathering exposures. These exposures are:

- 50/50 (by volume) combination of natural gas condensate and diesel, exposure rounds 1 to 8.
- HFO exposure round 9.
- Domestic gas diesel mix exposure round 11.
- NH_3 exposure round 10 and rounds 12 to 17.
- Vegetation combustion exposure rounds 18 to 22.
- SO_2 gas exposure rounds 23 to 27
- Blank exposure round 28
- NO_2 gas exposure rounds 29 to 33
- NO_2 gas exposure with freshly cut independent granophyre rocks, exposure rounds 34 to 39.
- SO_2 gas exposure with freshly cut independent granophyre rocks, exposure rounds 40 to 43.

From last year's report (Curtin University, 2024c), multivariate analysis indicated a strong positive correlation between the concentrations of Ca, K, Mg, and Na, all in units of mg/L. For simplicity, the sum of these concentrations was modelled. The preferred measure of the response is therefore defined as the difference in the sum total of the assayed concentrations of Ca, K, Mg, and Na, expressed in mg/L.

A summary of the data and figures for each element is provided below. In each case, plots of concentration response against average dose, duration of exposure, and order of exposure given by batch number, are shown. Brief observations are provided in each case, then key findings arising are summarised to guide future experiments.

7.1.2 Experiments presented in the Monitoring Studies Report 2024

For the 50/50 diesel/natural gas condensate mix, there were eight experimental exposures/batches, with exposure durations ranging from one to six days. However, some exposures failed, and others lacked dose data. See Table *4.4-1* for full details of the physicochemical weathering exposures. Data from four exposures were used to calculate the dose-response curve. Figure *7.1-1* shows the NO_x plus SO_2 dose-response curve from the Monitoring Studies Report 2024 (Curtin University, 2024c). A clear dose-response relationship is evident.

HFO was a single-dose exposure experiment. The HFO data was not used in the (NO_2 and SO_2) dose-response relationship as the results were sufficiently different to make their inclusion problematic. Results of the hydrocarbon exposure experiments are provided in the Monitoring Studies Report 2024 (Curtin University, 2024c).

a)

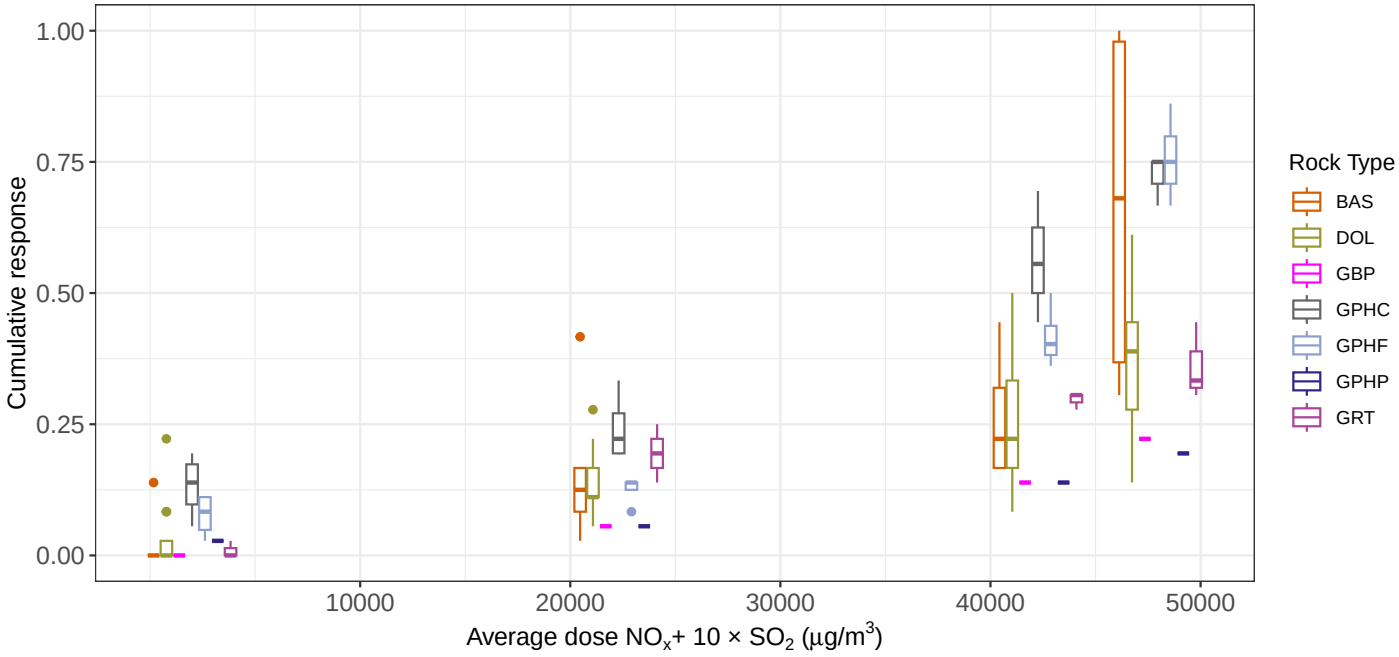

b)

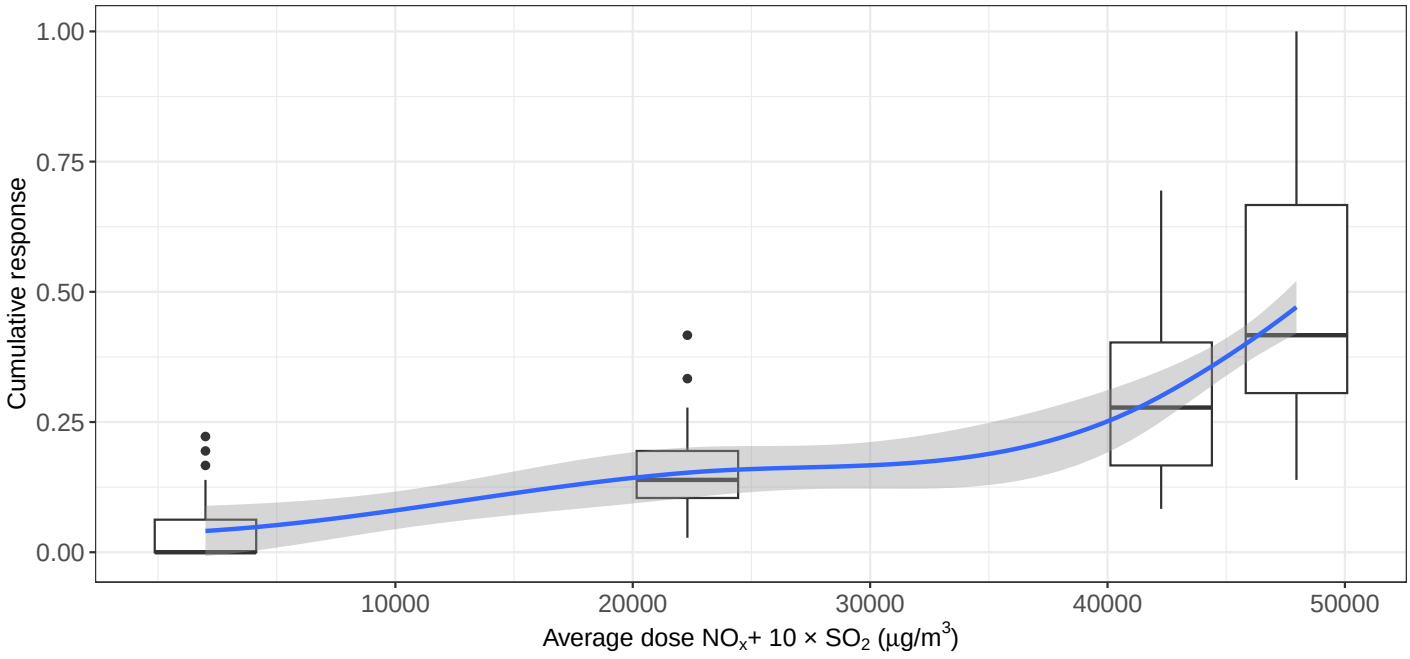

Figure 7.1-1: Copy of Figure 7.1-6 from Monitoring Studies Report 2024 (Curtin University, 2024c). Boxplots of cumulative response (concentration after exposure minus concentration before exposure) against average dose NO_x plus SO_2, (a) broken down by rock type, and (b) for all rock types combined. The blue curve is the smoothed conditional mean; grey shading is the pointwise 95% confidence interval. The cumulative response represents the sum of concentrations of Ca, K, Mg, and Na measured in mg/L

.

7.1.3 Domestic gas exposure

Exposure round 11 is a single trial experiment using a methane (CH_4) based gas mixture known as domestic gas, as it is supplied to the Dampier-Bunbury domestic gas pipeline, co-combusted with diesel. As further experiments and supply of sufficient gas were problematic, it was not used in further dose-response studies, and the decision was made at this point to switch to single-gas exposure studies for NO_2, SO_2, NH_3 as well as bushfire/wildfire-smoke exposure studies.

Figure *7.1-2* shows boxplots of the response (change in Ca+Mg+Na+K concentration) recorded for the domestic gas/diesel exposure.

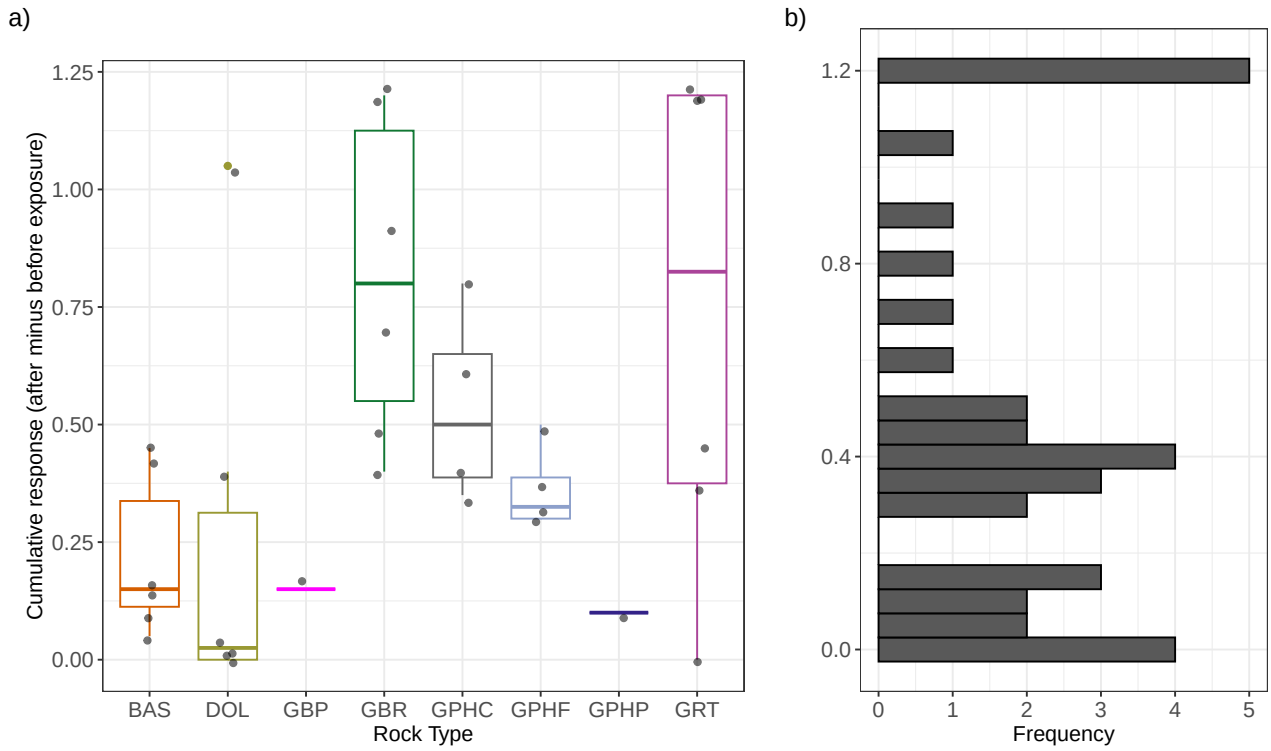

Figure 7.1-2: (a) Boxplots of the change in Ca + Mg + Na + K concentrations after exposure to a domestic gas/diesel mix, broken down by rock type; and (b) histogram showing the frequency distribution of these changes. The average dose of NO_x and SO_2 are 161.509 $\mu g/m^3$ and 16.783 $\mu g/m^3$, respectively.

7.1.4 NH_3 exposure

Figures *7.1-3* to *7.1-5* show the boxplots of the cumulative response against dose, days, and batch, respectively. It can be seen in these figures that the observed dose-response is non-monotonic, which is unexpected. This is reflected also in the plot of response against duration. Also note that greater responses were observed in the earlier batches, indicating that rock surfaces may be more responsive when they are fresh and unused (batches 12 and 13). Their responsiveness appears to decline when reused. See the summary of key findings (Section 7.1.11) for further discussion on this point.

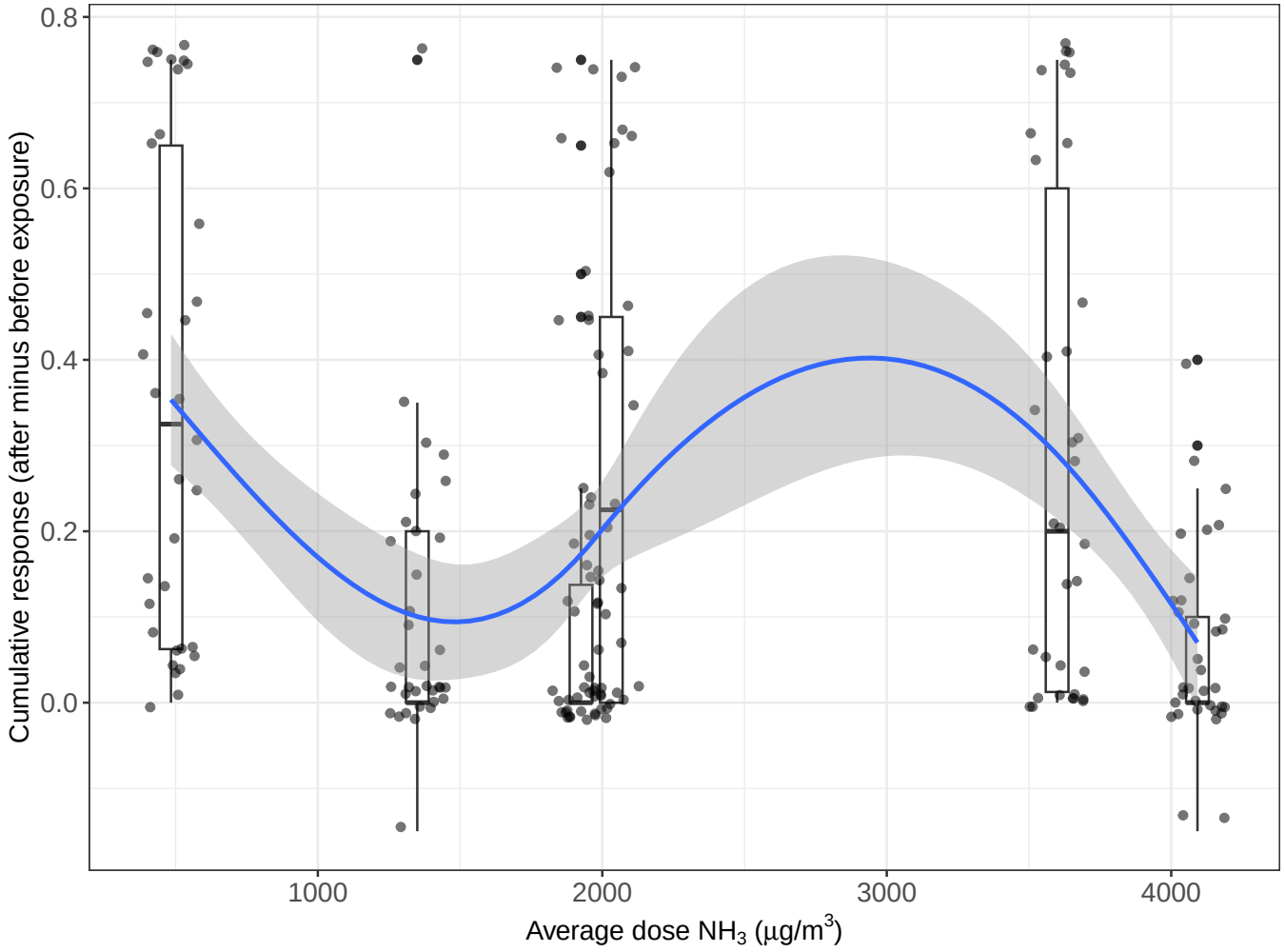

Figure 7.1-3: Boxplots of cumulative response (concentration after exposure minus concentration before exposure) against the average dose concentration of NH_3. Blue curve: smoothed mean response. Grey shading: pointwise 95% confidence intervals.

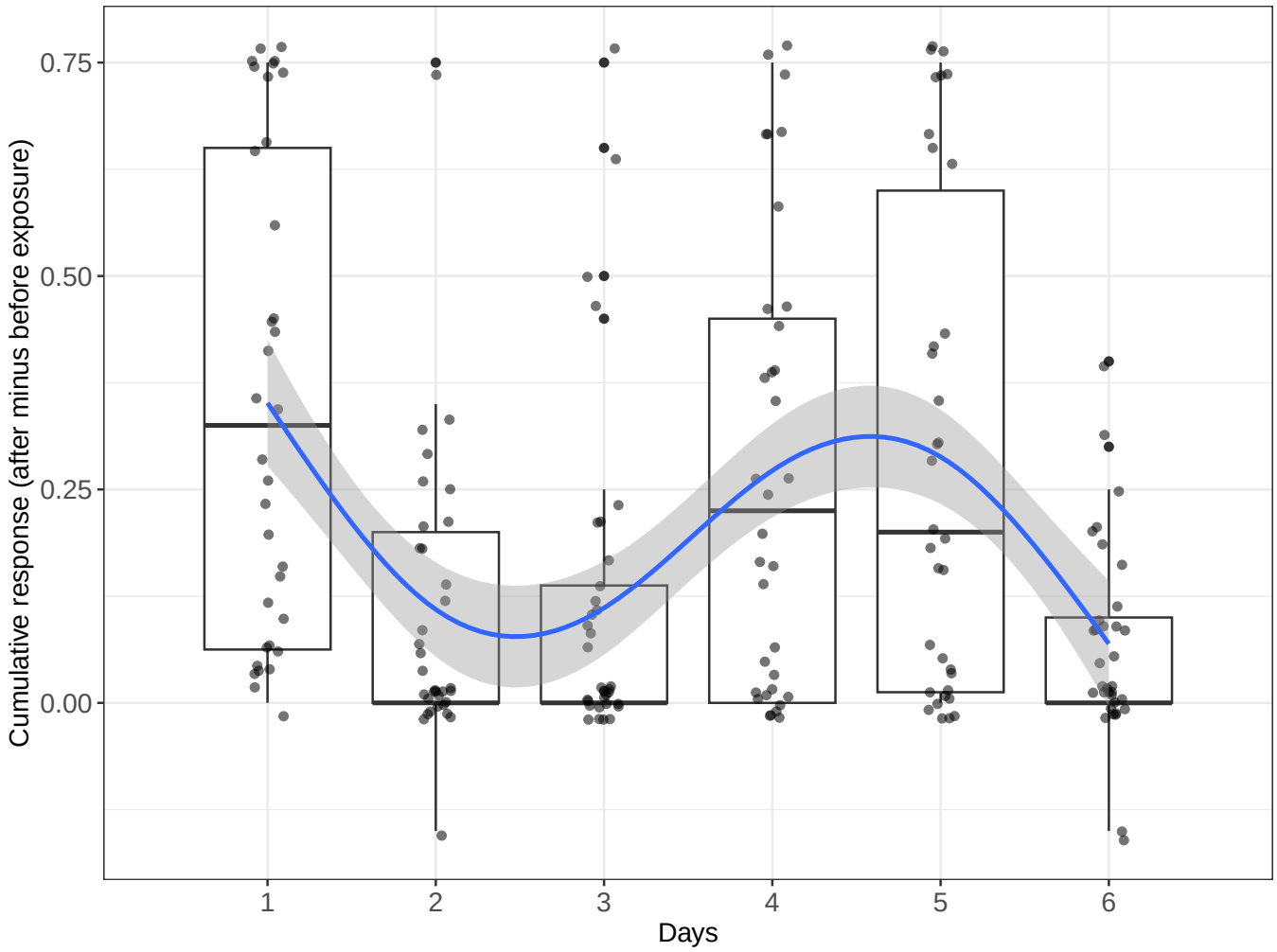

Figure 7.1-4: Boxplots of cumulative response (concentration after exposure minus concentration before exposure) against the exposure days for NH_3 exposures. Blue curve: smoothed mean response. Grey shading: pointwise 95% confidence intervals.

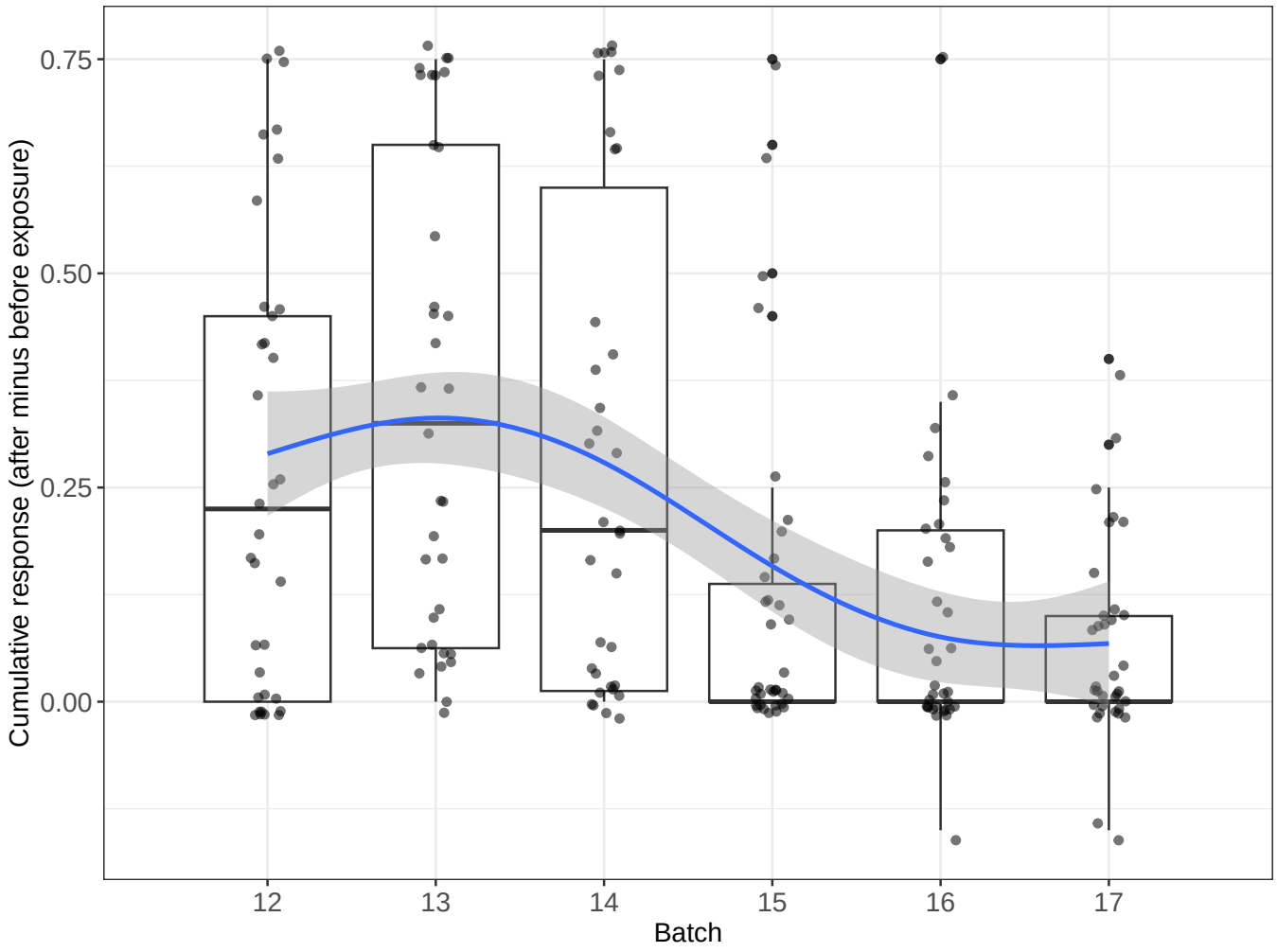

Figure 7.1-5: Boxplots of cumulative response (concentration after exposure minus concentration before exposure) against the batch number for NH_3 exposures. Blue curve: smoothed mean response. Grey shading: pointwise 95% confidence intervals.

7.1.5 Vegetation combustion exposure

During the previous year, several cultural/prescribed burns were undertaken at Murujuga. Additionally, a large wildfire occurred on Dolphin Island that was believed to have been started by a dry lightning strike, burning a significant portion of the island. Therefore, bushfire smoke is an important potential impact which must be considered. The following details bushfire smoke exposure studies utilising samples collected with appropriate permits and approvals from Murujuga. NOx is used as an indicator for the complex mix of all air pollutants generated, which were generally proportional to NOx level. However, given the findings with respect to gaseous SO_2 exposure presented in this section, the results may be better expressed in terms of this species.

Figures *7.1-6* to *7.1-8* demonstrate a non-monotonic dose-response relationship for vegetation-combustion exposures. The response against exposure duration increases up to four days of exposure, and much of the five-day exposure data was below detection. The final figure shows a declining response against batch number (i.e., in successive experiments), very similar to what was observed for NH_3.

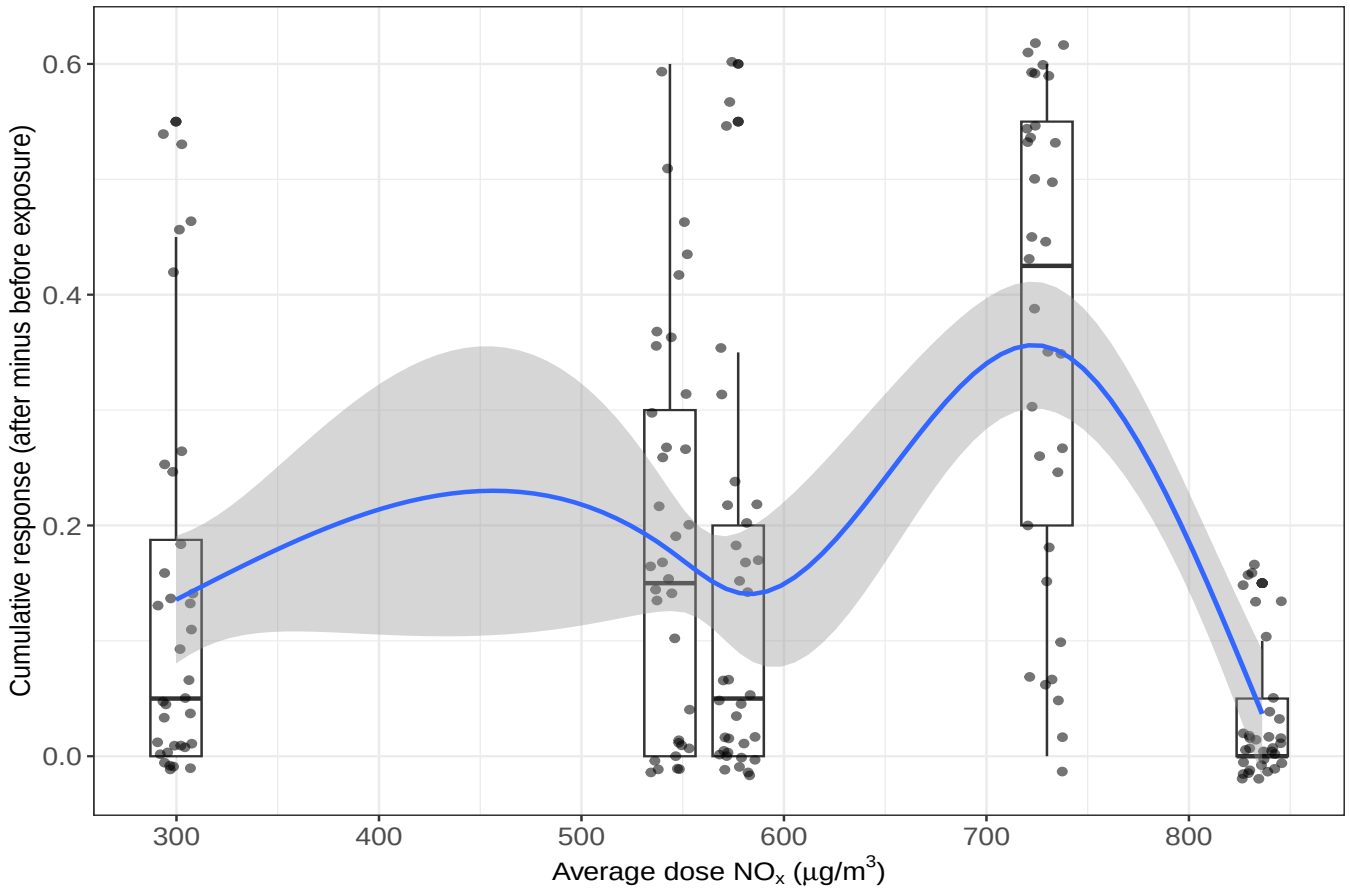

Figure 7.1-6: Boxplots of cumulative response (concentration after exposure minus concentration before exposure) against the average dose of NO_x from vegetation combustion. Blue curve: smoothed mean response. Grey shading: pointwise 95% confidence intervals.

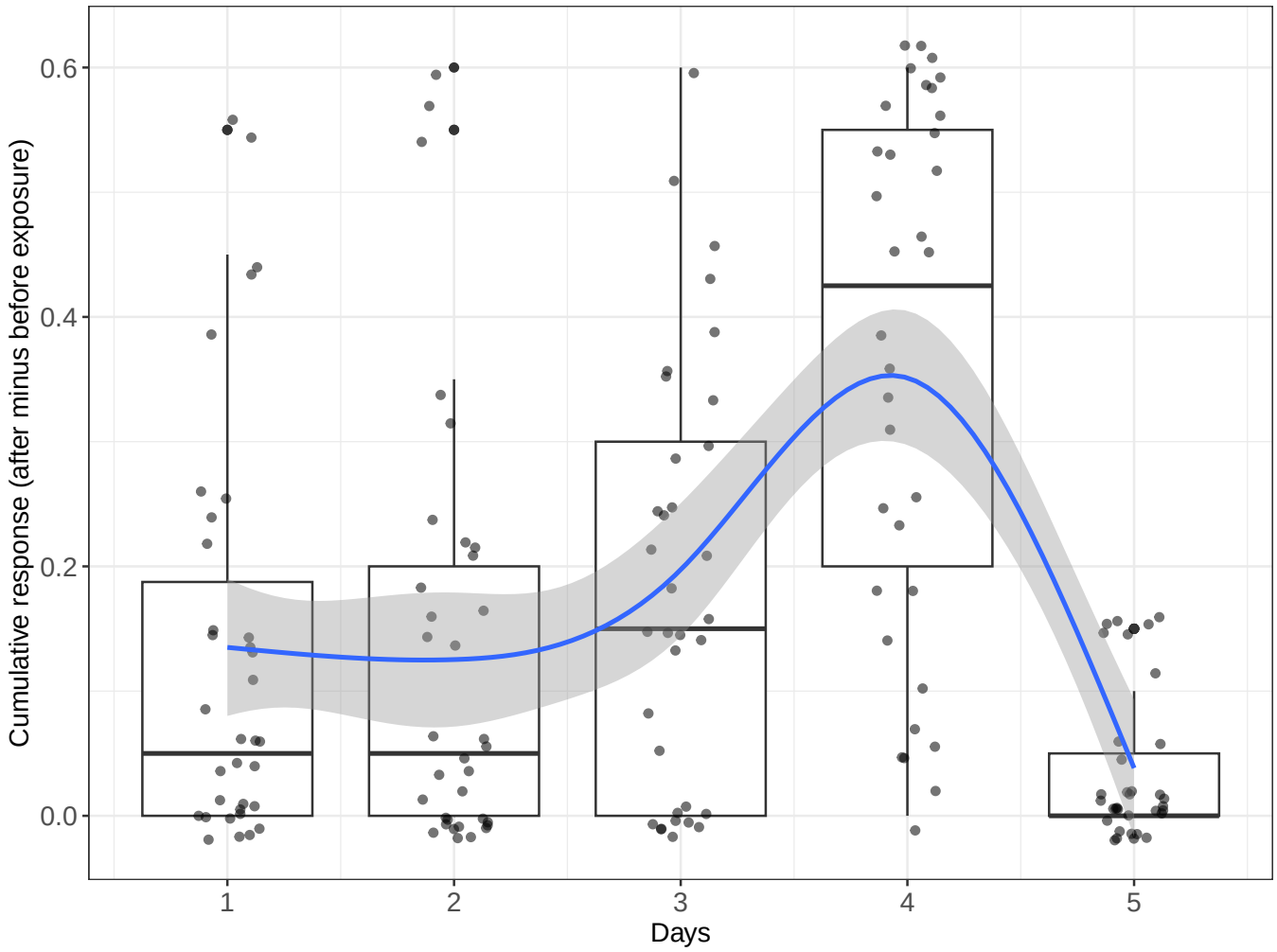

Figure 7.1-7: Boxplots of cumulative response (concentration after exposure minus concentration before exposure) against the exposure days (for NO_x) vegetation combustion exposures. Blue curve: smoothed mean response. Grey shading: pointwise 95% confidence intervals.

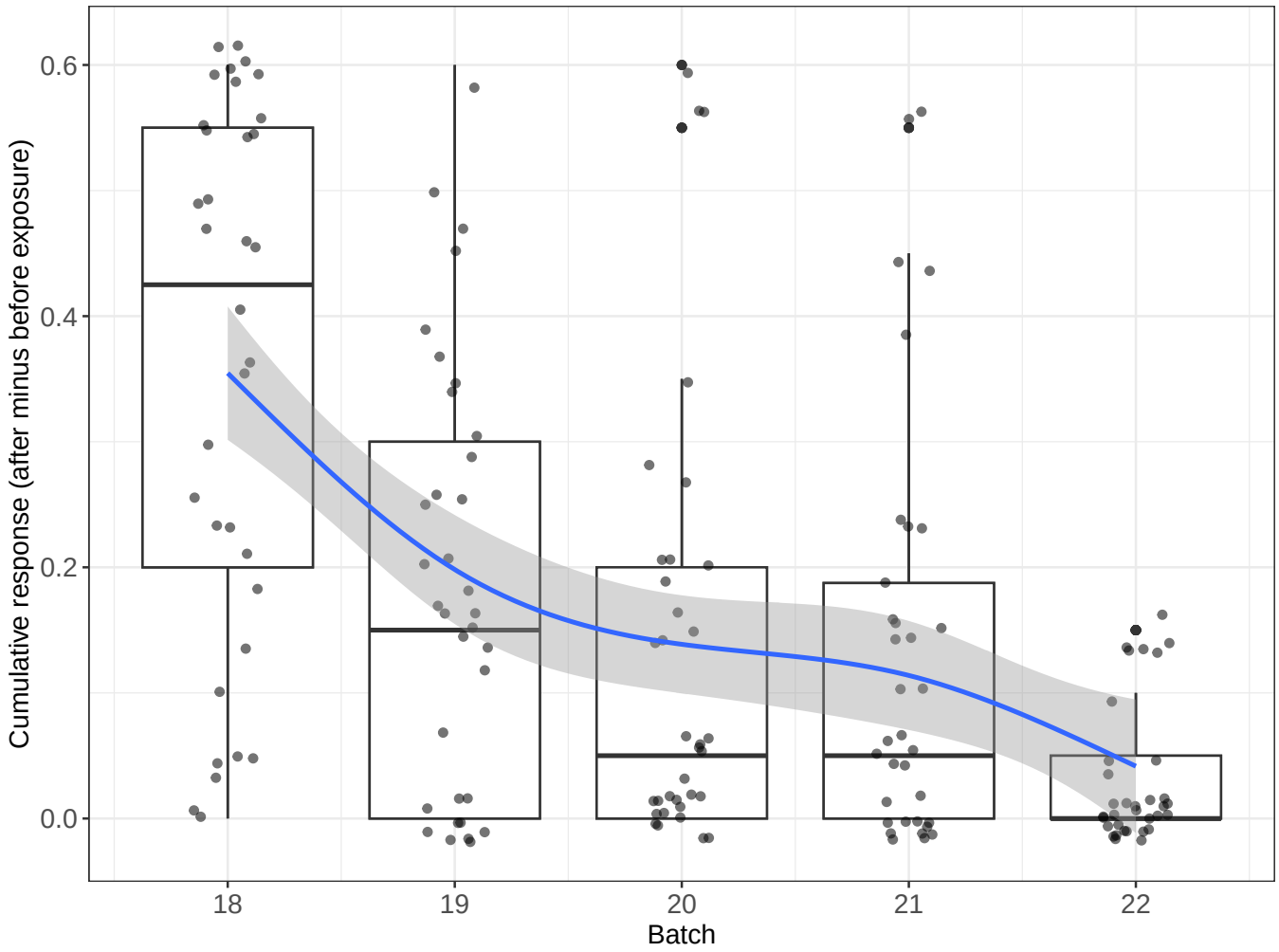

Figure 7.1-8: Boxplots of cumulative response (concentration after exposure minus concentration before exposure) against the batch number for NO_x from vegetation combustion exposures. Blue curve: smoothed mean response. Grey shading: pointwise 95% confidence intervals.

Given the findings relating to rock cube reuse below, these experiments may be repeated using fresh rock cubes for each experiment.

7.1.6 SO_2 gas exposure

Chamber experiment batches 23 to 27 were single-gas SO_2 exposures. These exposures aimed to further differentiate the response contribution from the combined (NO_2 and SO_2) exposures in experiment batches 1 to 11.

Figures *7.1-9* to *7.1-11* show an increasing dose response which then plateaus, which is the most typical form of dose-response curve. Note though that most of the data from rounds 23 to 27 are below the detection limit for both before and after exposure measurements (Ca, K, Mg, and Na). It is therefore difficult to draw definitive conclusions about the dose-response relationship from the SO_2 exposure rounds. There is no clear relationship with the batch number in this case.

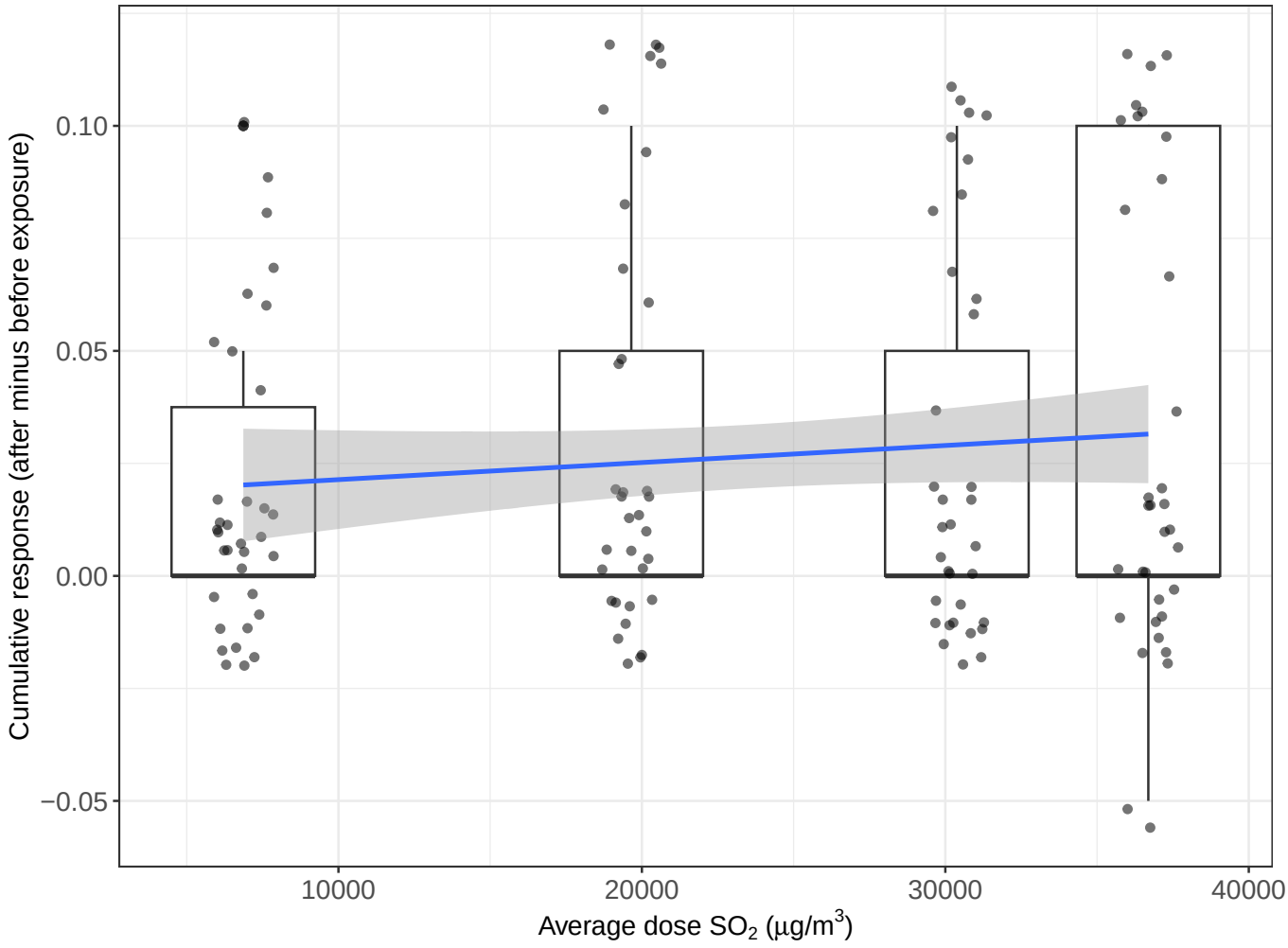

Figure 7.1-9: Boxplots of cumulative response (concentration after exposure minus concentration before exposure) against the average dose of SO_2 (as a single source gas). Blue curve: smoothed mean response. Grey shading: pointwise 95% confidence intervals.

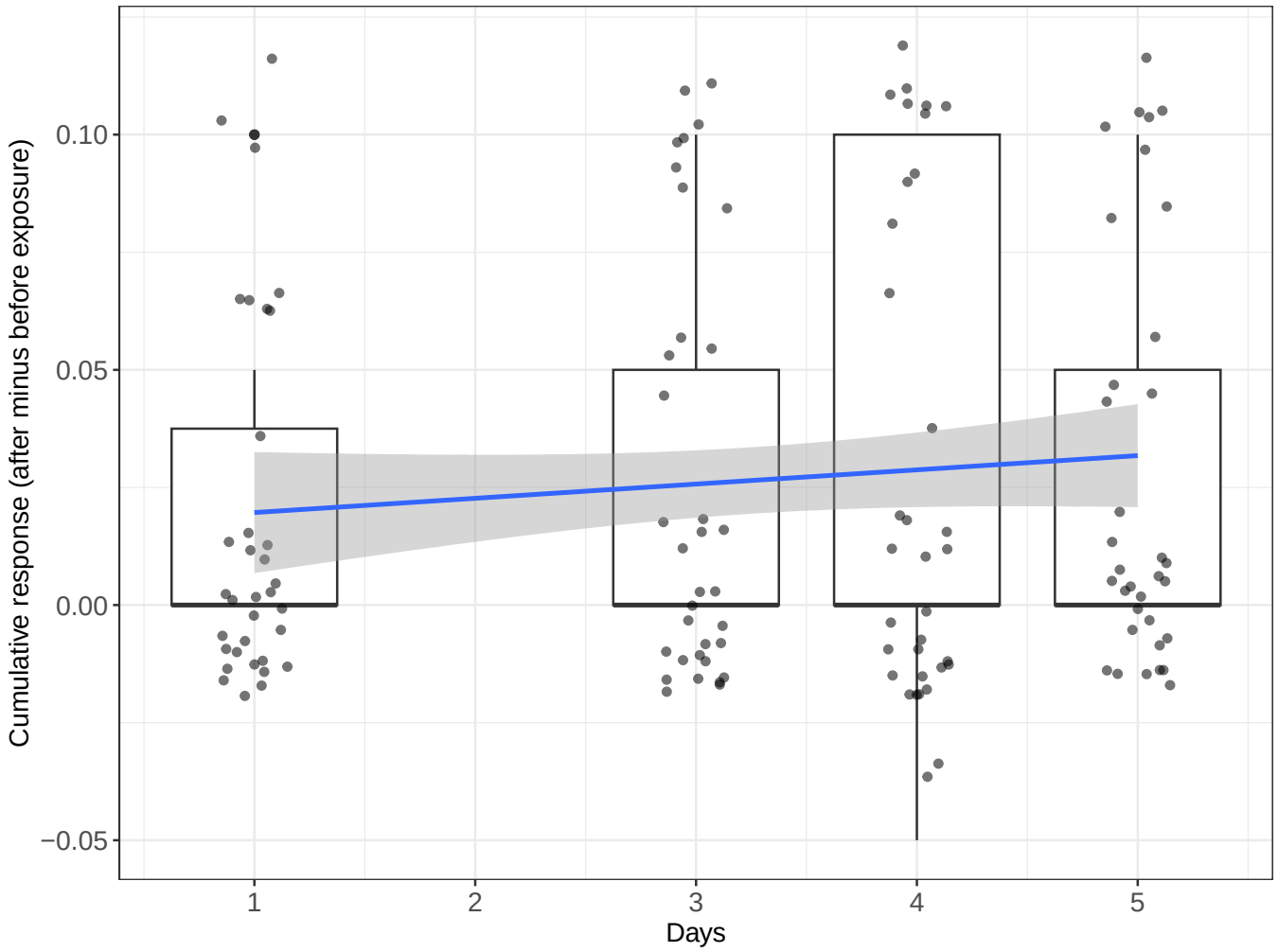

Figure 7.1-10: Boxplots of cumulative response (concentration after exposure minus concentration before exposure) against the exposure days for dose SO_2 (as a single-source gas). Blue curve: smoothed mean response. Grey shading: pointwise 95% confidence intervals.

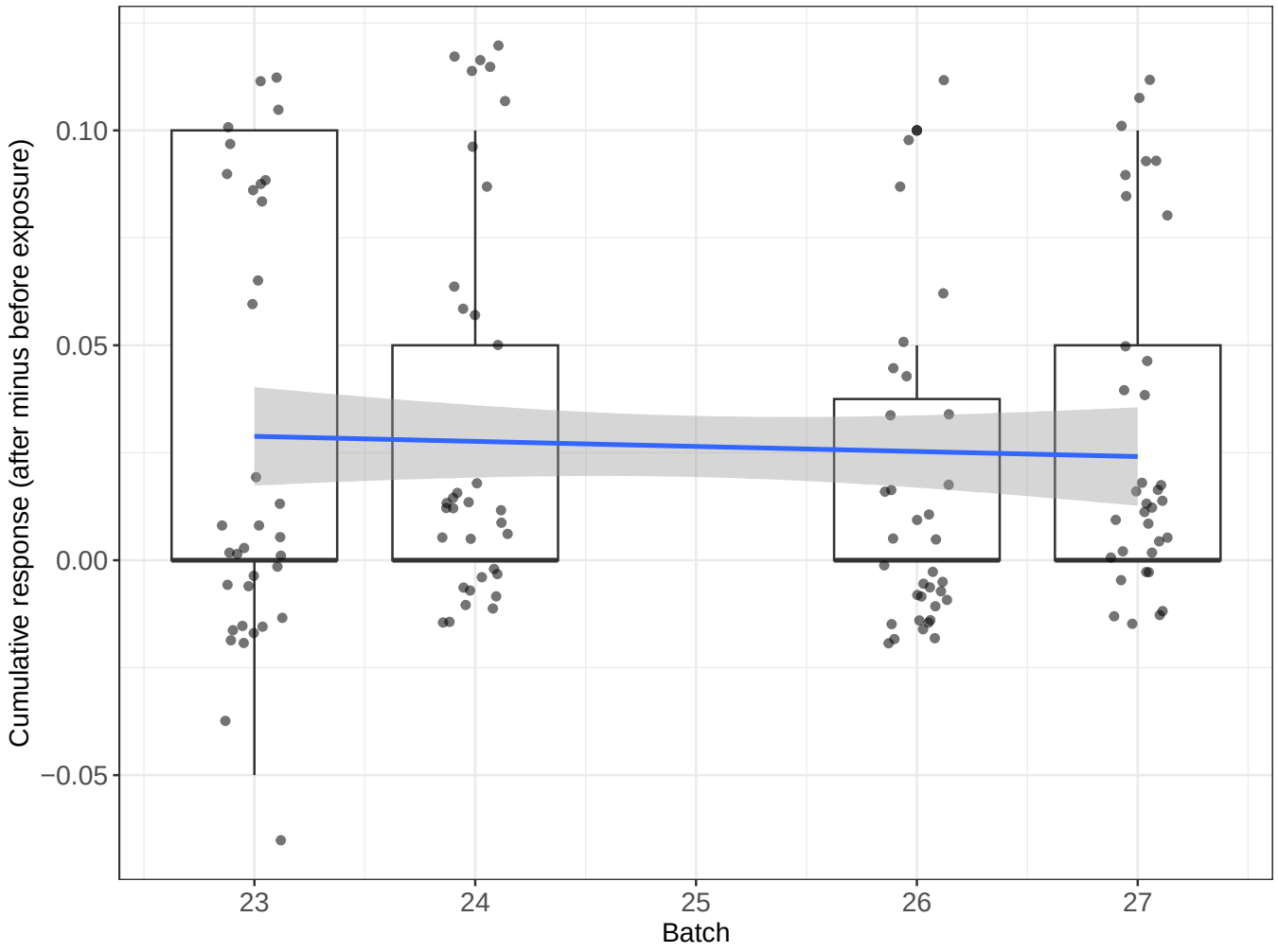

Figure 7.1-11: Boxplots of cumulative response (concentration after exposure minus concentration before exposure) against the batch number for SO_2 exposures (as a single-source gas. Blue curve: smoothed mean response. Grey shading: pointwise 95% confidence intervals.

7.1.7 NO_2 gas exposure

As for the SO_2 exposures discussed in the previous section, chamber experiment batches 29 to 33 were single-gas NO_2 exposures. These exposures aimed to further differentiate the response contribution from the combined (NO_2 and SO_2) exposures in experiment batches 1 to 11.

Figures *7.1-12* to *7.1-14* show there is no clear dose-response evident, and the strongest response was for batch 29, the first batch. This is consistent with concerns previously noted regarding a decrease in response with the reuse of rock samples.

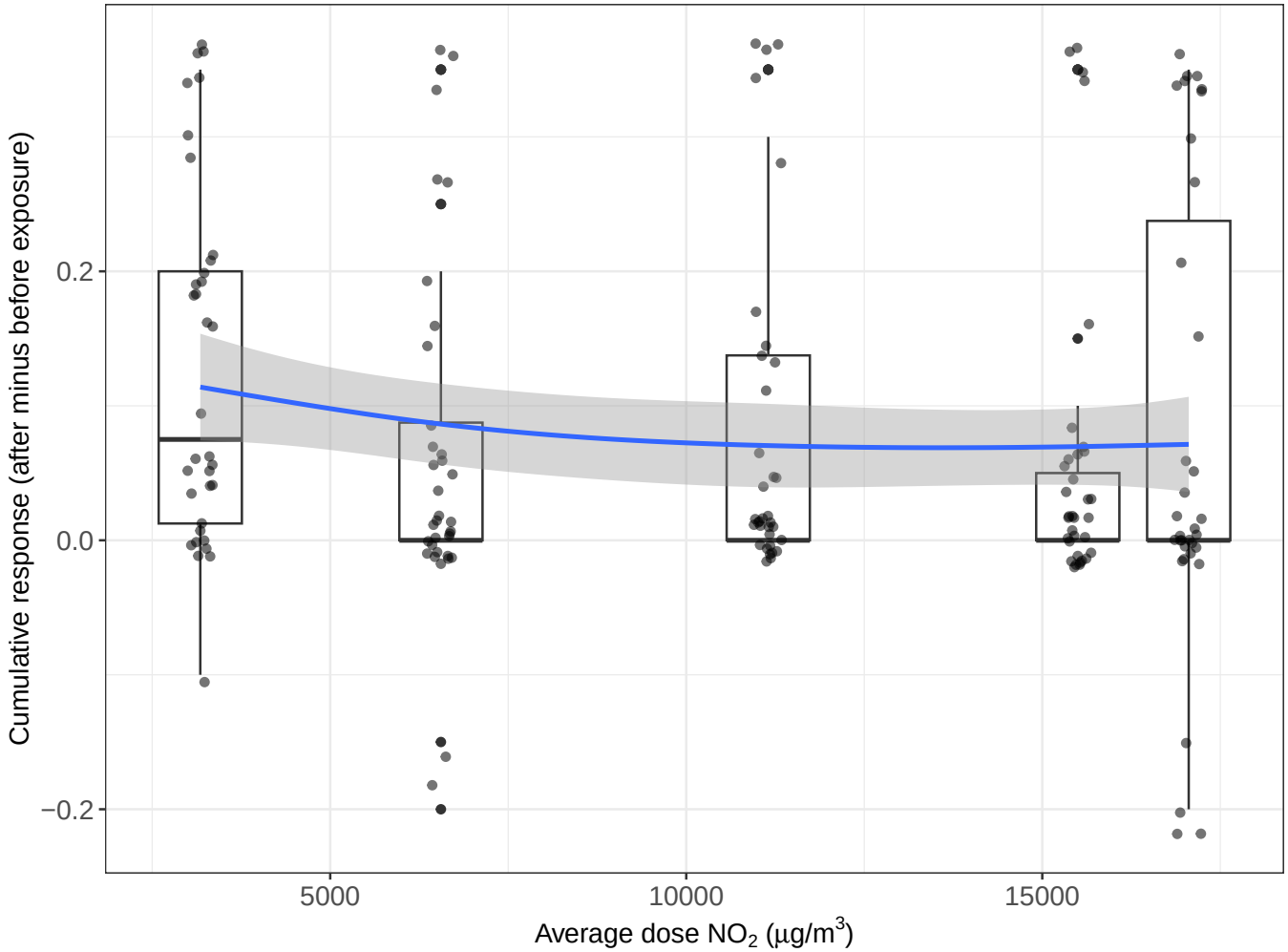

Figure 7.1-12: Boxplots of cumulative response (concentration after exposure minus concentration before exposure) against the average dose of NO_2 (from a single-source gas). Blue curve: smoothed mean response. Grey shading: pointwise 95% confidence intervals.

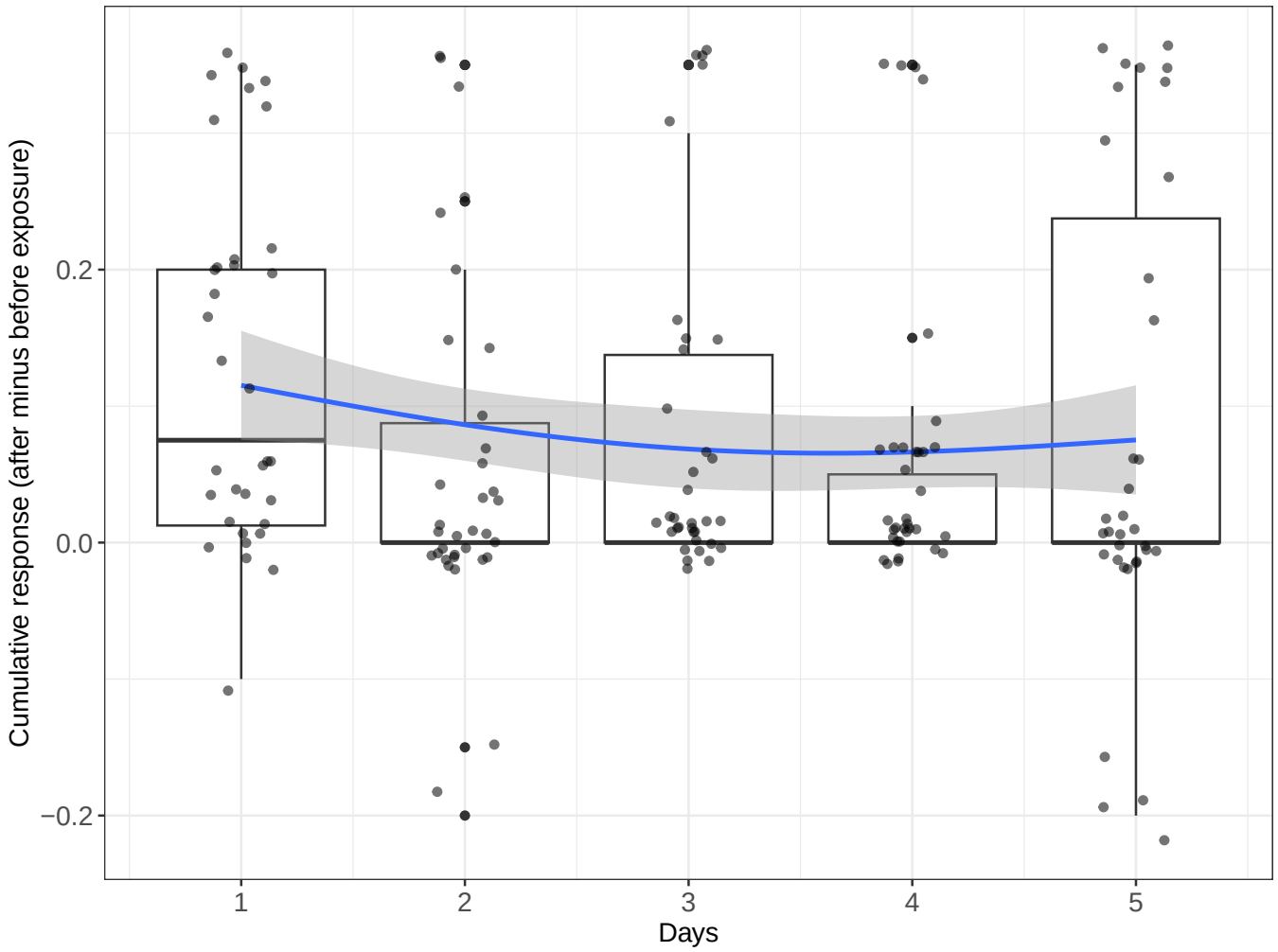

Figure 7.1-13: Boxplots of cumulative response (concentration after exposure minus concentration before exposure) against the exposure days for NO_2 (from a single-source gas). Blue curve: smoothed mean response. Grey shading: pointwise 95% confidence intervals.

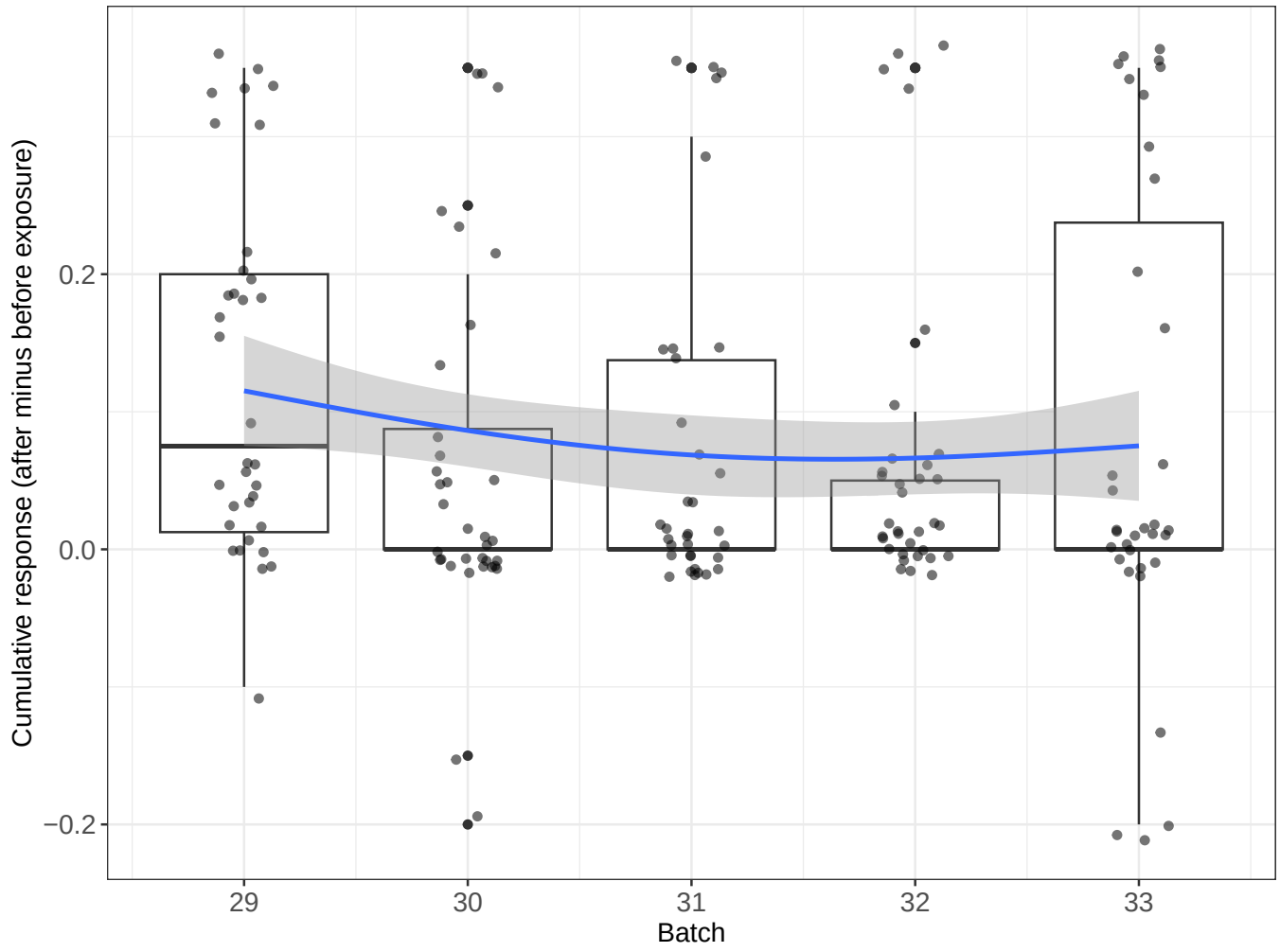

Figure 7.1-14: Boxplots of cumulative response (concentration after exposure minus concentration before exposure) against the batch number for NO_2 exposures (from a single-source gas). Blue curve: smoothed mean response. Grey shading: pointwise 95% confidence intervals.

7.1.8 NO_2 gas exposure with freshly cut granophyre rocks

The statistical science team recommended conducting an additional NO_2 gas chamber exposure experiment, using ten freshly cut granophyre rocks per batch, with a total of six batches. This was done and, for each batch, the samples were randomly assigned within the chamber.

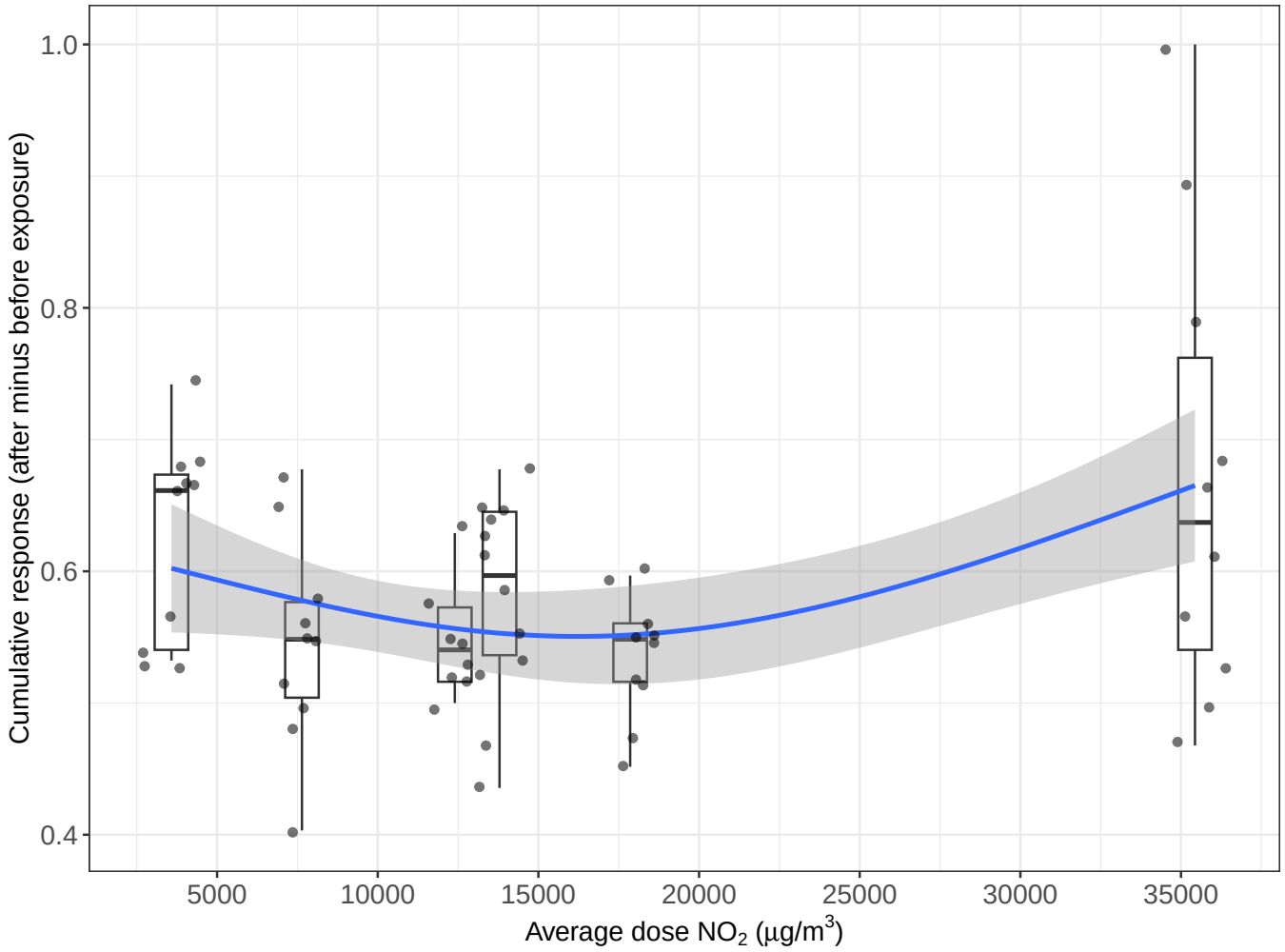

Figure 7.1-15: Boxplots of cumulative response (concentration after exposure minus concentration before exposure) against the average dose of NO_2 (from a single-source gas), with freshly cut granophyre rocks. Blue curve: smoothed mean response. Grey shading: pointwise 95% confidence intervals.

Figure *7.1-15* shows there is no clear dose-response evident in the freshly cut granophyre samples. The highest dose test may represent the onset of a response. The highest median value was observed in the first (single exposure) test, however the second-highest response and highest peak values were observed in the highest dose test (batch 39). This test received ten doses in total, instead of six doses as used as the highest dose case in all previous tests. One dose in the morning and one in the afternoon over five days.

7.1.9 SO_2 gas exposure with freshly cut granophyre rocks

Figure *7.1-16* shows recently completed tests exposing freshly cut granophyre rocks to SO_2. The figure shows the 1-4 days exposure cases, with the remaining two exposures currently being undertaken at the time of writing. Unlike the equivalent NO_2 experiments, these SO_2 experiments appear to show a clear dose-response relationship, which will be likely be confirmed once the remaining tests are analysed.

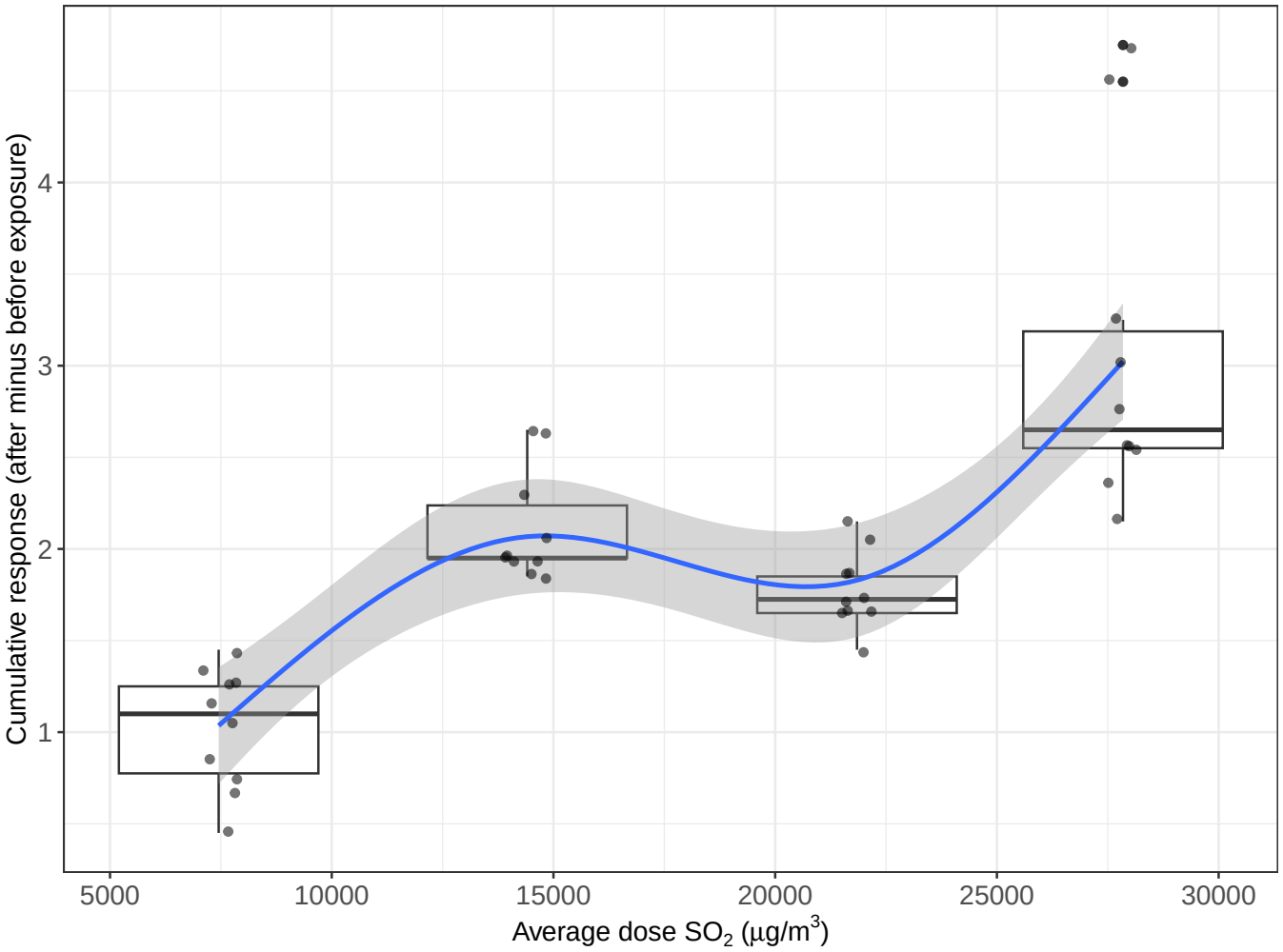

Figure 7.1-16: Boxplots of cumulative response (concentration after exposure minus concentration before exposure) against the average dose of SO_2 (from a single-source gas), with freshly cut granophyre rocks. Blue curve: smoothed mean response. Grey shading: pointwise 95% confidence intervals.

7.1.10 Henry's law

Separate to any artefacts discussed above from rock cube reuse or experiment sequencing, the year two chamber studies largely utilised hydrocarbon combustion experiments which resulted in co-exposures of NO, NO_2, SO_2, CO, CO_2, and other species including soot/particulates. The latter

was considered an explanation for the differing HFO response. As such, the differential effect, or even any effect at all, of each gas species (or particulates) could not be determined and was not guaranteed.

Other weathering literature (Broomandi et al., 2022; Spezzano, 2021) has established differential gas-species weathering relationships based on Henry's law (Hites and Raff, 2012), which relates to the solubility and reactivity of weak gas mixtures, for example when in contact with water (Singh et al., 2016), which may be present in sufficient quantities on rock surfaces without rainfall. Figure *7.1-17* shows Henry's law (Hites and Raff, 2012) for relevant gas species (see https://henrys-law.org/ and citations therein).

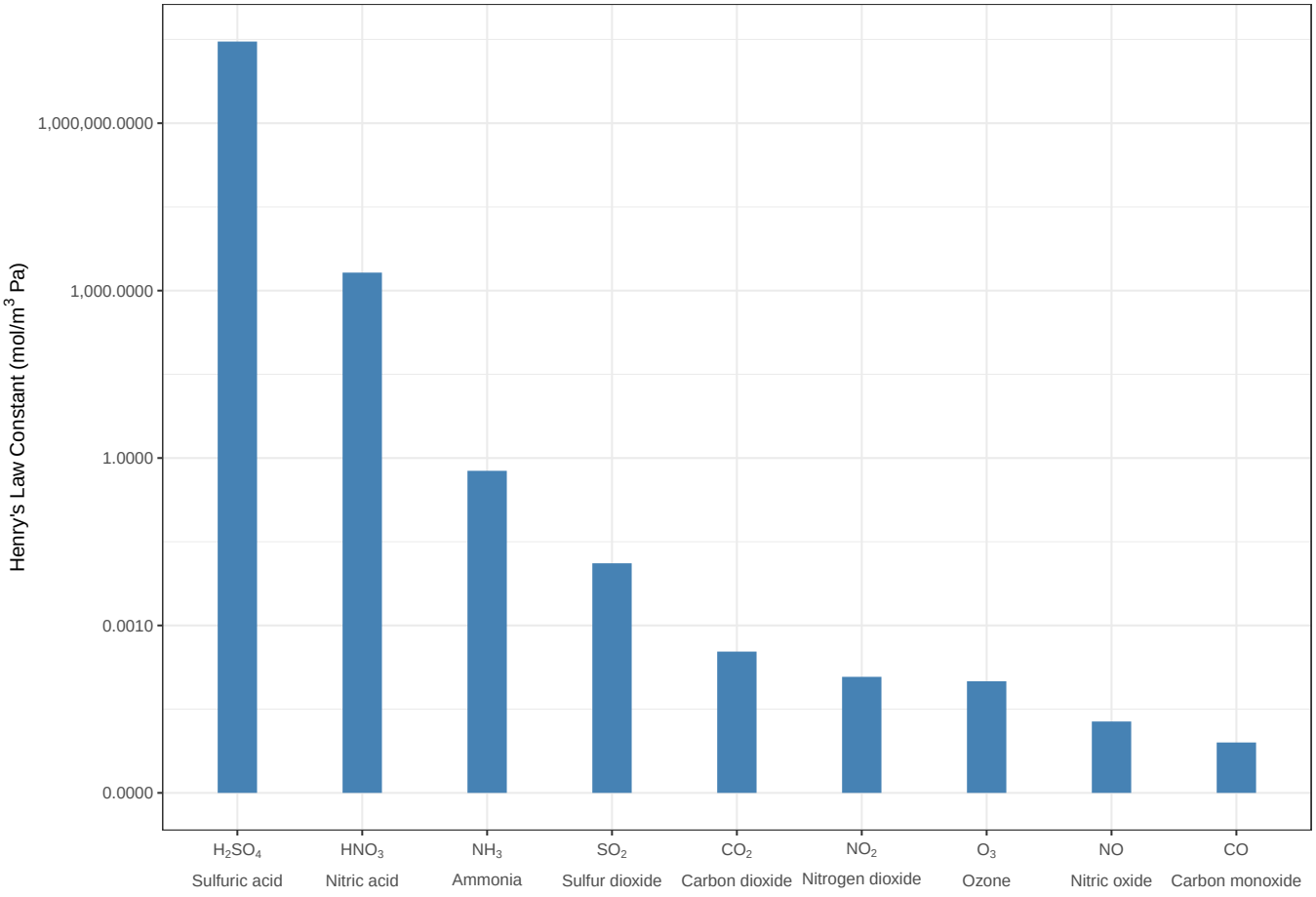

Figure 7.1-17: Henry's Law constants for relevant gas species.

Henry's law suggests that SO_2 is approximately 110 times more important to weathering than NO_2, and NH_3 is approximately 5,000 times more important than NO_2. For this reason, SO_2 has always been the major contributor to acid rain globally. Likewise, for the conjugate acids, H_2SO_4 has a Henry's law constant 14,000 times that of HNO_3.

When this is considered, it is not unexpected that chamber studies using NO_2 have produced no consistent response, whereas experiments using SO_2 have produced relatively clear dose-response curves, both for the experiments where rock cubes were reused and more apparent for *7.1-16* with

'fresh' rock cubes for each test. Indeed, the studies mentioned above appear to have discounted any significant effect of NO_2, even at levels orders of magnitude above those found at Murujuga. The onset of a possible response to NO_2 in *7.1-15* for the highest dose, versus the response to SO_2 in *7.1-16* would appear to be proportional to the relative relationships given by Henry's law.

7.1.11 Summary of key findings to guide future experiments

The key finding from these studies is that the dose-response utilising re-used rock cubes is typically non-monotonic. While a range of dose-response curves are reported in the literature (linear-no-threshold response, threshold response, hormetic or J-shaped response, saturation curve, sigmoid curve, and U-shaped (continuous) curve), we would in this case expect either a linear response or a logarithmic/saturation response. In these experiments there is no physicochemical explanation for greater exposure leading to a lower response. The SO_2 experiments above, most closely resemble the expected response (saturation/logarithmic response).

The order in which the experiments were conducted is highly indicative of an explanation for the unusual response found here. We observe a strong response when using fresh-cut rock, and the evidence suggests that the response declines on re-use. A similar suggestion is mentioned in a different context (Malmström et al., 2000; Drever and Clow, 1995). This effect was less apparent in the Monitoring Studies Report 2024 (Curtin University, 2024c) data given the overall stronger effect from simultaneous exposure to multiple chemical species from hydrocarbon combustion processes.

From an experimental-design perspective, to extract strong evidence from the chamber studies requires that the rock samples be statistically independent. The evidence is that re-use renders the samples dependent on previous use, a clear violation of this assumption.

The use of freshly cut independent granophyre rocks has been implemented with good results and will now be utilised for all further chamber studies. Findings from these tests will be reconfirmed with patinated rocks to determine if they are more or less sensitive, as well as incorporating microbiome response effects. The results to-date appear to show (as supported by literature) that NO_2 has a very weak effect on abiotic rock weathering. The effect of SO_2 has also been revised upwards.

Furthermore, given the complex mix of interactions and reactions discussed in the introduction to this section, experiments exploring the impact of moisture to promote acidification reactions and the impact multispecies exposures will be explored.

Preliminary microbiome chamber studies and some relevant literature, e.g. (Wang et al., 2021) appear to show a differential response of key microbial groups to relevant air pollutants. This will be a key focus of the remaining chamber studies, as well as exploring combined (synergistic) effects from combustion emissions.

This page is intentionally blank.

7.2 Field colour measurements

This section reports on the measurement of rock surface colour in the field campaigns and the statistical analysis of the data obtained.

Section 7.2 of the Monitoring Studies Report 2024 (Curtin University, 2024c) details the background information of the rock surface colour measurements in the field campaigns, including a description of the two instruments used: the original JAZ and the new HDX (Ocean Insight) spectrophotometers. The Monitoring Studies Report 2024 (Curtin University, 2024c) also describes the interactive software developed to assist in taking valid measurements with both instruments and to test for any faults in the field whilst taking measurements of the rock art panels. This software has continued to be used in the current year of studies, for field campaigns 8 to 10.

7.2.1 Summary of JAZ and HDX instruments for campaigns 7 to 10

Table *7.2-1* shows the total number of rock art panels measured using the JAZ and HDX instruments for campaigns 8 to 10. In addition, this table shows the percent of measurements for which no data collection faults occurred and the percent of measurements that returned partially valid data (measurements from one or more targets on the rock art panel that were deemed not faulty). Faulty measurements occur when all ten targets are deemed faulty.

During campaigns 8 to 10, a total of 12 rock art panels were measured using the JAZ instrument and 119 were measured using the HDX instrument (Table *7.2-1*).

During the ten campaigns completed to date, a total of 346 targets on rock art panels have been measured by the JAZ instrument and 128 were measured by the HDX instrument (Table *7.2-1* and Table 7.2-1 in Monitoring Studies Report 2024 (Curtin University, 2024c)).

In campaigns 8 to 10, 100% of the rock art panel measurements using the JAZ instrument were valid or partially valid. However, between 82.93% to 97.44% of rock art panel measurements using the HDX instrument were valid, with campaign 10 (the 2025 wet season) having the lowest percentage of valid measurements.

Section 7.2.7 of Monitoring Studies Report 2024 (Curtin University, 2024c) details problems encountered during campaign 7. Campaign 7 was conducted late February to late March 2024 (Table *3.1-1*), which is summer and the wet season in Murujuga. Campaign 10 was conducted over similar dates in 2025, and the HDX instrument had similar problems for this campaign. During campaign 10:

- On most days the temperature was 35°C or greater (see Section 7.15).
- Rain occurred on six days during the campaign, with a total rainfall of 35.38 mm (see Section 7.4 and 7.15). One rock art panel could not be measured after one of the rainfall events because there was too much water flowing over the rock for the HDX instrument to take a measurement. This location was subsequently re-visited and measured later in the campaign.
- A battery fault caused the field laptop to lose charge, resulting in multiple percent reflectance curves. The interactive HDX software picked up a fault, the expert spectroscopist (Mr Andrew Thorn) was then able to identify and resolve the battery problem.

For further details on the weather during the field campaigns see Section 7.15.

Table 7.2-1: Summary of rock art panel measurements using the JAZ and HDX instruments in campaigns 8 to 10.

	Campaign 8 JAZ	Campaign 8 HDX	Campaign 9 JAZ	Campaign 9 HDX	Campaign 10 JAZ	Campaign 10 HDX
Total measured	4	39	3	39	5	41
% rock art panels - no data faults	100%	92.31%	0%	97.44%	80%	82.93%
% rock art panels - partially valid data	0%	7.69%	100%	2.56%	20%	4.88%

The HDX instrument was delivered to the MAC office during campaign 7 (the last field campaign in the second year of studies) and was used to measure eight rock art panels in this campaign. During campaigns 8 to 10, both the JAZ and HDX instruments were used to measure a number of rock art panels to allow results from the two instruments to be compared. The following sites were measured with both instruments:

- AQ03_GPH
- AQ04_GPH
- AQ11_GPH
- EX06_GPH

Table *7.2-2* summarises the data validity achieved for measurements of these four rock art panels.

There were six types of faults that occurred when measuring these four rock art panels using either instrument over the ten campaigns. These were:

- F1 = High peak in % reflectance <= 450 nm, due to % reference being too low before 450 nm.
- F2 = After about 650nm the % reflectance was >100%.
- F3 = After about 700 nm the % reflectance was < 0%.
- F4 = S (sample sensed photon count) values were zero.
- F5 = Dark current not flat.
- F6 = Calculated % reflectance was extremely large and/or small with values being less than -500% and/or greater than 500%.

See Appendix G.3 in the Monitoring Studies Report 2024 (Curtin University, 2024c) for full details of the fault descriptions, and Appendix *D*.2 for a summary of new faults identified.

For campaigns 1 to 6, the measurements from the JAZ were either partially or totally faulty for all four of the rock art panels listed above. The most common fault was “F3” (where wavelengths after about 700 nm had percent reflectance < 0%).

During the initial HDX trials and familiarisation in campaign 7, only AQ03_GPH was measured by both instruments, and partial faults were identified in the measurements returned from both instruments.

During campaign 8, due to time constraints, only AQ04_GPH was measured by both instruments, and the measurements of all ten targets from both instruments were valid (Table *7.2-2*).

During campaign 9, all rock art panels, except for AQ04_GPH, were measured by both instruments. Due to time constraints, AQ04_GPH was only measured using the HDX instrument (Table *7.2-2*).

During campaign 10, both instruments measured all four rock art panels, with AQ11_GPH and EX06_GPH having valid measurements from both instruments. However, HDX AQ04_GPH measurements were faulty (after about 650 nm wavelength the reflectance was >100%) (Table *7.2-2*).

Table 7.2-2: Summary of data validity from JAZ and HDX measurements for four rock art panels over all field campaigns, 1 to 10. Yes "Y" indicates all measurements were valid. "Partial (Fx)" indicates at least some measurements were valid and the number indicates the data fault type experienced. "Fx" indicates faulty data and the corresponding data fault. See above for definitions of the fault types.

Campaign	Instrument	AQ03_GPH	AQ04_GPH	AQ11_GPH	EX06_GPH
1	JAZ	F3	F2	Partial (F5)	F6
2	JAZ	Partial (F3)	Partial (F3)	F3	Partial (F3)
3	JAZ	Partial (F3)	F3	Partial (F3)	Partial (F3)
4	JAZ	Partial (F3)	Partial (F3)	Partial (F3)	Partial (F3)
5	JAZ	Partial (F3 & F4)	Partial (F3)	Partial (F3)	F3
6	JAZ	Partial (F1)	Partial (F3)	Partial (F3)	Partial (F3)
7	JAZ	Partial (F1)	Partial (F3)	Not measured	Y
7	HDX	Partial (F4)	Not measured	Y	Not measured
8	JAZ	Not measured	Y	Not measured	Not measured
8	HDX	Y	Y	Y	Y
9	JAZ	Partial (F3)	Not measured	F3	Partial (F3)
9	HDX	Y	Y	Y	Partial (F4)
10	JAZ	Partial (F3)	Partial (F1)	Y	Y
10	HDX	Y	F2	Y	Y

7.2.2 Statistical methodology for analysing percent reflectance

In this report, all analyses of the field colour data were restricted to four sites (AQ03_GPH, AQ04_GPH, AQ11_GPH and EX06_GPH), as they were the only ones measured by both instruments during campaigns 7–10. The final MRAMP monitoring studies report will include analysis of all sites.

To evaluate the potential similarities/differences between the JAZ and HDX instruments, a functional data analysis (FDA) framework was applied to campaigns 7 to 10. FDA is a statistical methodology used to analyse data sets that consist of functions or curves rather than traditional scalar or vector

observations (Zhang, 2013). The analysis consisted of three stages: (1) exploratory analysis using mean difference curves; (2) smoothing and functional representation of each spectrum; and (3) testing differences between the two instruments in both variability and mean functional behaviour.

7.2.2.1 Mean difference curves

The mean difference curves were calculated for the four sites (AQ03_GPH, AQ04_GPH, AQ11_GPH and EX06_GPH) and campaigns 7 to 10. For each wavelength, the mean % reflectance across all replicates was computed for each target × campaign × site × instrument combination. The mean difference was calculated by subtracting the JAZ mean from the HDX mean. Thus, negative values indicate wavelengths where the HDX recorded higher % reflectance, and positive values indicate wavelengths where the JAZ recorded higher % reflectance.

7.2.2.2 Curve smoothing and construction of functional observations

Raw reflectance spectra were first converted into smooth functional curves. Specifically, for each replicate measured by each instrument, a generalised additive model (**GAM**) was fitted, with wavelength (300 to 800 nm) as the continuous predictor and percent reflectance as the response. A spline-based smooth term was applied to wavelength, with the basis dimension set to k = 20 to allow sufficient flexibility while avoiding over-fitting. The GAM provides a flexible, non-parametric way to model spectral curves, ensuring that the smooth fitted functions reflect the underlying trend across wavelengths rather than interpreting noisy point-to-point lines. The resulting smooth curves (trends) form the functional data objects used in the next stage.

7.2.2.3 Compare instruments performance

Two types of functional analyses were applied to assess instrument performance:

1. Functional Levene's test for instrument variability
2. Comparing the trend between instruments

1. Functional Levene's test for instrument variability

To test whether the variability in measurements differs between the two instruments across the wavelength range, a functional extension of the Levene's test was applied. Specifically, this tests whether the variation between the replicates for one instrument is greater than that for the other instrument.

First, for each instrument, the "central" curve (functional median) across all replicate measurements was calculated. This represents the typical measurement at each wavelength. Next, for every replicate curve, the absolute difference from its group's median curve at each wavelength was computed. These deviations reflect the variability of each replicate around the group's central tendency. A one-way functional analysis of variance (**ANOVA**) was applied to test the absolute deviation curves from both instruments, using the fanova.onefactor function from fda.usc package in R. This tests whether the variability (deviation) differed between the instruments across the wavelength domain. To account for multiple comparisons, p-values were adjusted using the false discovery rate (FDR) procedure (Benjamini and Hochberg, 1995). A significant result indicates that

one instrument shows systematically larger deviations than the other, that is, one instrument had greater variability compared to the other. A non-significant result suggests that the variability is similar between two instruments.

2. Comparing the trend between instruments

To test the trend (mean reflectance curves) between the two instruments, a one-way functional ANOVA was performed using fanova.onefactor function in R, which evaluates whether the mean functions differ between the HDX and JAZ instruments. Similarly to the above analysis, the p-values were adjusted using FDR. A significant result indicates that the mean reflectance curves differ between the two instruments across the wavelength range (i.e., differences in spectral shape, magnitude, or both). Whilst a non-significant outcome suggests that the two instruments measured comparable trends.

7.2.2.4 Comparing trends between campaigns for just JAZ instrument

To test if there were any differences in rock surface colour across campaigns 1 to 10 for the JAZ instrument, a one-way functional ANOVA was performed. For each site, pairwise comparisons were conducted between campaigns, to test if the mean reflectance curves differ between two campaigns across the wavelength range (i.e., differences in spectral shape, magnitude, or both). Similarly to the above analysis, the p-values were adjusted using FDR.

7.2.3 Results of analyses

7.2.3.1 Comparison of trends between campaigns 1 to 10 for JAZ instrument

For each of the four sites, a one-way functional ANOVA was performed to compare the trends (mean reflectance curves) between campaigns for the JAZ instrument. For all sites, there were no statistically significant differences between campaigns (see Appendix *D*.2).

Figure *7.2-1* shows the GAM estimated percent reflectance for the four rock art panels measured by the JAZ instrument across campaigns 1 to 10.

7.2.3.2 Results of analysis comparing the JAZ and HDX instruments

Figure *7.2-2* shows the mean difference curves between two instruments for AQ03_GPH, AQ04_GPH, AQ11_GPH and EX06_GPH. There are only difference curves when both instruments had no faults or partial faults. For example, for AQ04_GPH, only campaign 8 had valid data for both instruments.

All four sites and campaigns 7 to 10: For wavelengths less than 550 nm, the mean difference between the two instruments was typically less than 10 % reflectance. However, after 550 nm there is a larger mean difference between the two instruments.

Instrument variability

Table *7.2-3* summarises the results of the functional Levene's test, which compared measurement variability between the JAZ and HDX instruments. This table shows the mean and maximum deviation across all wavelengths for both instruments and the functional Levene's test p-values. A p-value less than 0.05 indicates there is evidence of higher variability in one instrument compared

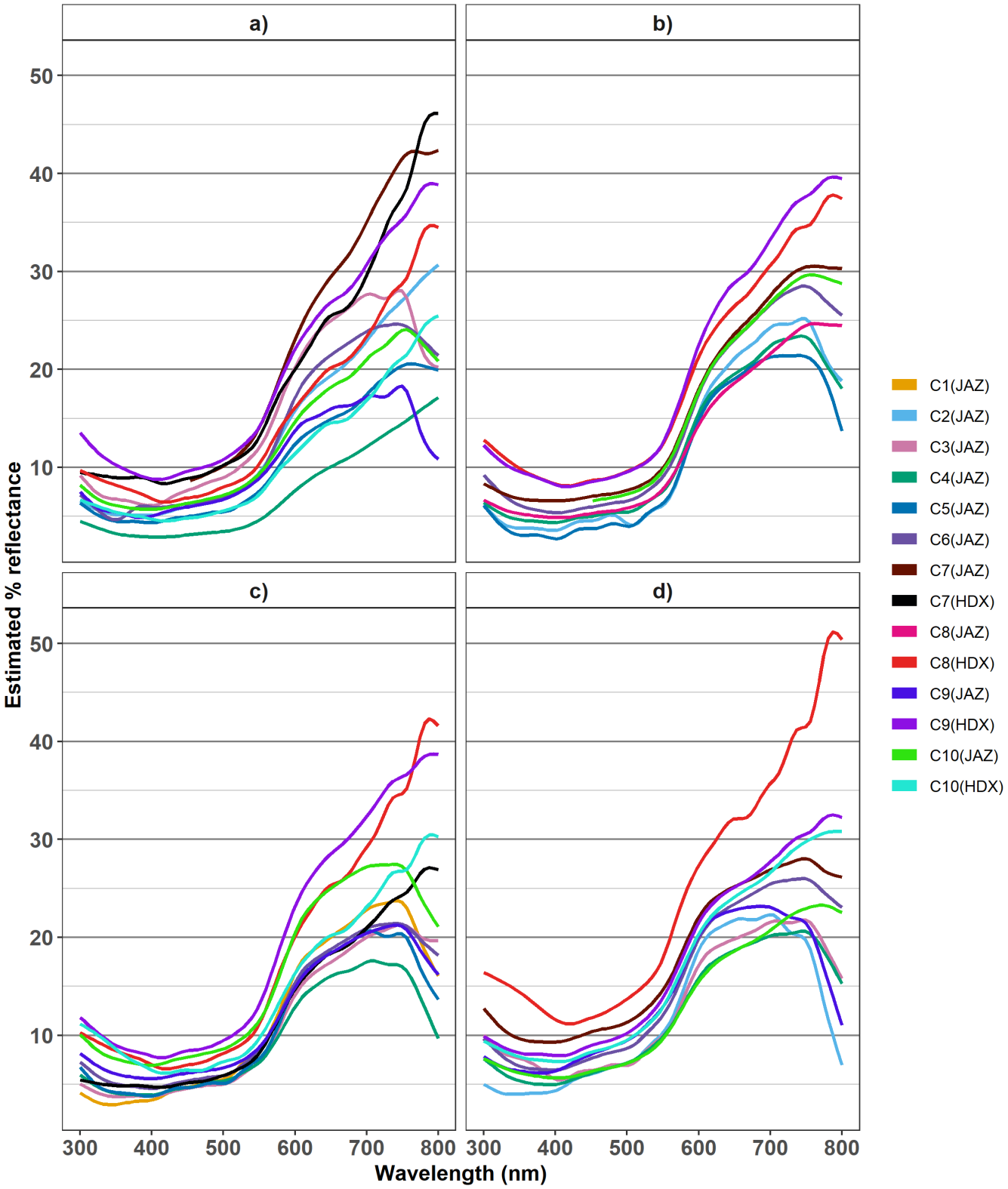

Figure 7.2-1: Estimated percent reflectance vs wavelength (nm) for (a) AQ03_GPH, (b) AQ04_GPH, (c) AQ11_GPH and (d) EX06_GPH for campaigns 1 to 10.

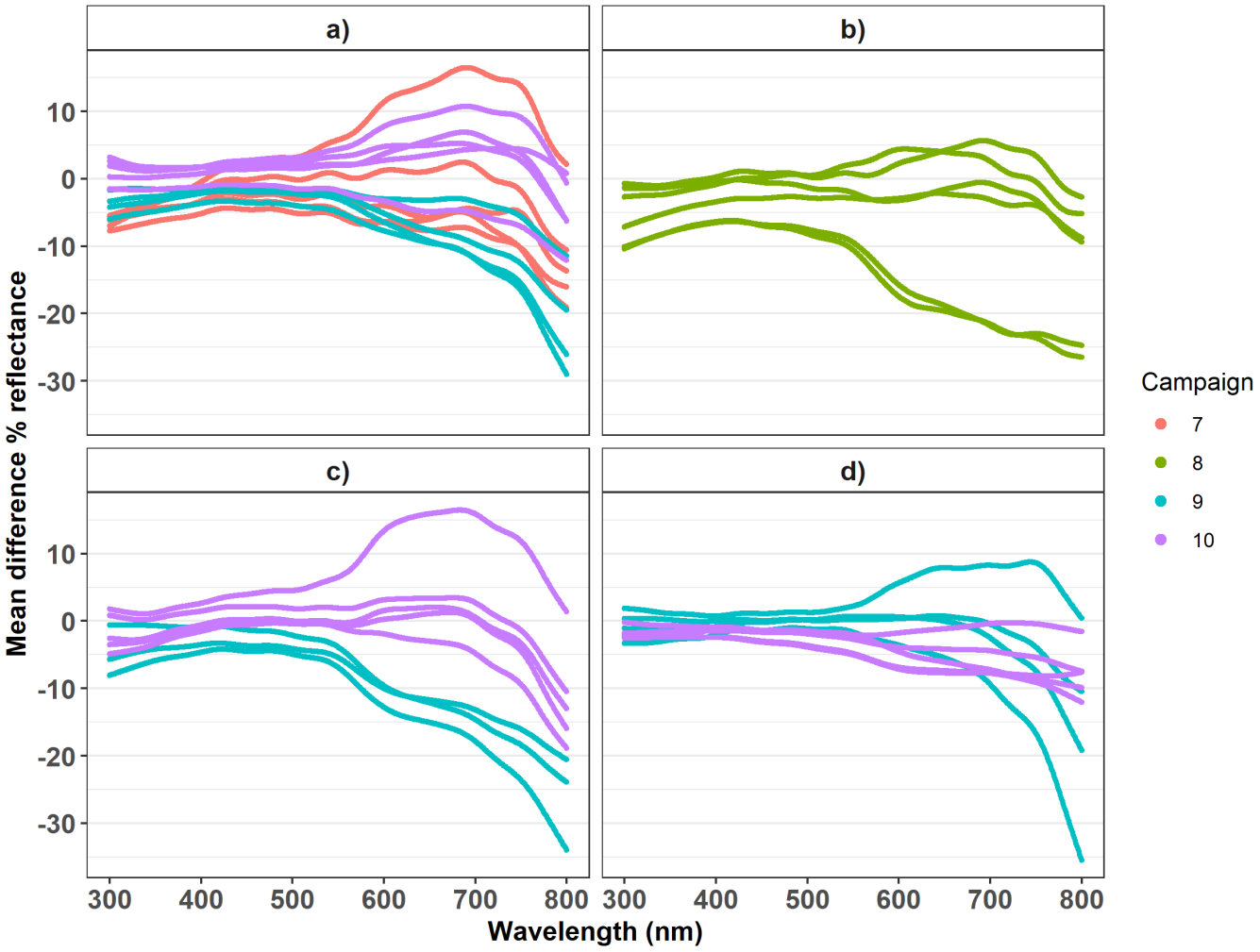

Figure 7.2-2: Mean difference curves. For each wavelength, the mean % reflectance across all reps was computed for each site × campaign × target × instrument combination. The mean difference is then the JAZ mean subtracted from the HDX mean, so negative values indicate wavelengths where the HDX recorded higher % reflectance, and positive values indicate wavelengths where the JAZ recorded higher % reflectance. Panels: (a) AQ03_GPH, (b) AQ04_GPH, (c) AQ11_GPH and (d) EX06_GPH. Within each site, each mean difference curve corresponds to one target for each campaign.

to the other. The instrument with the larger deviation indicates which instrument had the higher variability. The maximum absolute deviation corresponds to the replicate curve that was furthest from the median curve. For some targets, the maximum absolute deviation was much larger than other targets within a campaign. Typically the largest deviation occurs at the end of the visible spectrum (near 800 nm). For example, AQ03_GPH during campaign 7 at target 3, the deviation for JAZ was 9.094 and that for HDX was 11.002, both of these deviations occurred near 800 nm wavelength.

Across all site × campaign × target combinations, 60% showed a significant difference in variability between the two instruments (Table *7.2-3*). Among these significant cases, the JAZ instrument

had greater variability than the HDX in 80% of the cases. This is understandable, as the HDX measurements takes only about 5 seconds to record all 100 replicates, whereas the JAZ measurements take several minutes. During this longer measurement time, the JAZ instrument is more likely to have been moved slightly, which could result in greater variation in the recorded colour measurements.

Therefore, from the analysis given above, it can be concluded that the JAZ instrument is more variable than the HDX instrument.

Table 7.2-3: For each site, campaign and target combinations are the mean and maximum absolute deviation from the median curve for the JAZ and HDX instruments. Additionally, p-values from the functional Levene's test that compares the variability (absolute deviations from the median curve) between the two instruments. Bold p-values indicate statistically significant at the <0.05 level.

Site	Campaign	Target	Mean dev JAZ	Max dev JAZ	Mean dev HDX	Max dev HDX	adj p-value
AQ03	7	1	8.282	49.767	0.469	4.008	**< 0.001**
AQ03	7	2	1.135	7.276	0.151	2.180	**< 0.001**
AQ03	7	3	1.015	9.094	1.410	11.002	0.340
AQ03	7	4	3.084	22.631	0.554	4.310	**0.021**
AQ03	7	8	0.919	4.886	0.181	2.642	**< 0.001**
AQ03	7	9	1.030	4.851	0.187	2.347	**< 0.001**
AQ03	7	10	0.731	5.931	0.220	2.979	**< 0.001**
AQ03	9	4	3.467	13.367	0.988	7.204	**< 0.001**
AQ03	9	6	1.242	8.290	0.328	3.108	**< 0.001**
AQ03	9	8	0.878	4.474	0.596	4.157	0.127
AQ03	9	9	1.017	12.336	0.086	1.359	0.050
AQ03	9	10	1.845	9.723	1.192	6.815	**0.021**
AQ03	10	1	1.212	5.397	0.153	2.556	**< 0.001**
AQ03	10	3	0.953	6.146	0.190	2.780	**0.021**
AQ03	10	4	1.089	8.063	0.408	3.018	0.076
AQ03	10	5	1.055	6.557	0.150	3.647	0.050
AQ03	10	6	1.775	17.150	0.143	2.936	0.064
AQ03	10	7	1.718	6.695	0.123	2.252	**0.038**
AQ03	10	9	1.541	8.645	0.140	2.428	**< 0.001**
AQ03	10	10	0.234	3.692	0.144	1.647	0.118
AQ04	8	1	0.953	10.009	0.294	1.474	0.159
AQ04	8	2	0.125	2.691	0.095	1.317	**0.021**

Site	Campaign	Target	Mean dev JAZ	Max dev JAZ	Mean dev HDX	Max dev HDX	adj p-value
AQ04	8	3	0.209	4.134	0.259	1.697	**< 0.001**
AQ04	8	4	0.368	3.226	0.209	3.912	0.076
AQ04	8	5	2.265	15.624	0.120	1.049	**< 0.001**
AQ04	8	10	0.420	1.959	0.091	1.514	**< 0.001**
AQ11	9	1	0.572	5.138	2.366	8.599	**< 0.001**
AQ11	9	2	0.443	11.006	0.337	2.532	0.150
AQ11	9	8	0.393	3.490	0.158	1.389	0.127
AQ11	9	9	0.343	5.116	0.883	6.046	**< 0.001**
AQ11	9	10	0.998	6.688	0.296	2.141	0.021
AQ11	10	1	2.742	19.069	0.271	4.090	0.139
AQ11	10	2	0.126	1.771	0.300	5.931	**< 0.001**
AQ11	10	3	0.797	6.272	0.272	4.269	0.064
AQ11	10	4	0.341	1.768	0.266	3.961	0.166
AQ11	10	5	0.353	5.921	0.304	3.996	0.505
AQ11	10	6	0.420	5.672	0.238	5.284	0.400
AQ11	10	7	0.239	1.692	0.280	4.386	0.314
AQ11	10	8	0.218	2.566	0.643	5.377	**< 0.001**
AQ11	10	9	0.136	1.740	0.280	3.740	**< 0.001**
AQ11	10	10	0.648	5.114	0.273	4.654	0.333
EX06	9	1	1.146	6.275	0.929	6.514	0.423
EX06	9	3	2.161	9.975	0.366	2.225	**< 0.001**
EX06	9	4	1.152	5.569	0.206	2.090	**< 0.001**
EX06	9	5	0.795	8.031	0.221	1.246	**< 0.001**
EX06	9	7	1.438	7.583	0.419	2.714	0.274
EX06	9	8	0.648	11.575	0.084	0.991	0.050
EX06	9	9	1.165	9.482	0.472	4.185	0.050
EX06	10	1	0.383	2.798	0.117	1.895	**< 0.001**
EX06	10	2	0.372	2.307	0.671	8.848	**0.021**
EX06	10	3	1.443	8.577	0.112	1.517	**< 0.001**
EX06	10	4	1.235	6.634	0.255	3.520	**< 0.001**
EX06	10	5	1.325	9.613	0.111	1.541	**< 0.001**
EX06	10	6	1.680	7.638	0.089	1.359	**< 0.001**

Site	Campaign	Target	Mean dev JAZ	Max dev JAZ	Mean dev HDX	Max dev HDX	adj p-value
EX06	10	7	1.159	8.580	0.108	1.049	**0.038**
EX06	10	8	1.904	8.990	0.205	1.792	**< 0.001**
EX06	10	9	0.359	2.279	0.113	1.593	**0.038**
EX06	10	10	0.921	6.200	0.326	2.730	0.076

Comparison of trends between instruments

Figure *7.2-1* shows the estimated percent reflectance (from GAM) versus wavelength for the four rock art panels measured by both instruments during campaigns 4 to 10.

Since the JAZ instrument has larger variability than the HDX, the average curve across all replicates was calculated. Then the one-way functional ANOVA was applied to compare the average curves between the two instruments. Specifically, for each site x campaign combination, the analysis compared the average curves for the ten targets between two instruments.

Table *7.2-4* summarises the results of the comparison of trends (mean reflectance curves) between the two instruments, showing the one-way functional ANOVA p-values for each site and campaign combination. Only in AQ11_GPH in campaign 9 were the mean reflectance curves between the JAZ and HDX significantly different. Figure *7.2-1* shows that the HDX had a higher estimated mean percentage reflectance than the JAZ, particularly after 600 nm.

The rest of the p-values in Table *7.2-4* were greater than 0.05, indicating that there is no difference in the mean reflectance curves between the two instruments. Therefore, although JAZ is more variable, both instruments appear to be measuring the same spectral colour of the rock art panels.

Table 7.2-4: Comparison of mean trends (mean reflectance curves) between two instruments. Bold p-values indicate statistically significant at the 0.05 level.

Site	Campaign	Adjusted p-values
AQ03_GPH	7	0.487
AQ03_GPH	9	0.157
AQ03_GPH	10	0.418
AQ04_GPH	8	0.157
AQ11_GPH	9	**0.047**
AQ11_GPH	10	0.367
EX06_GPH	9	0.157
EX06_GPH	10	0.157

7.2.4 Conclusion of field colour measurements

In summary:

- There was no temporal change in rock surface colour over the three-year study period (campaigns 1 to 10) for AQ03_GPH, AQ04_GPH, AQ11_GPH and EX06_GPH using the JAZ instrument.
- The JAZ instrument is more variable than the HDX instrument.
- For campaigns 7 to 10, there was no difference in trends (mean reflectance curves) between the two instruments. Thus the spectral rock surface colour measurements are similar between JAZ and HDX.

In conclusion, the HDX is reproducible and suitable instrument for the long-term monitoring of rock surface colour. However, given the HDX operational problems during the summer (Garrbarn) months, it is recommended that future colour monitoring should only be conducted in the cooler months (Muthu).

This page is intentionally blank.

7.3 Industry air quality monitoring data

Woodside measures pollutant gases at five sites that are situated close to the Woodside properties. IVL passive samplers (previously Fermi) were used to measure pollutant gases from September 2021 to November 2022 while Radiello passive samplers were used from December 2002 to the present. That is, both sampler types were deployed by Woodside between September 2021 and November 2022. The Monitoring Studies Report 2024 (Curtin University, 2024c) showed a scatterplot of the Woodside IVL passive sample data for five sites. In the final study report, a detailed analysis that will potentially include the air quality monitoring data from industry will be presented. In order to ascertain if the industry data (Radiello) is comparable to the MRAMP data (IVL), an exploration of the correspondence between the IVL and Radiello industry data are presented here.

The most recent Radiello data available to the statistics team is from August 2023. Radiello data was collected with duplicate samplers at all Woodside stations, while IVL samplers were only duplicated for 3 months (September to December 2021). Boxplots (see the *boxplot* in Glossary Table *1.4-3*) are used to show the spread and central tendency of gas-concentration measurements. Figure *7.3-1* shows the boxplots of gas concentrations measured by the two sampler types from all observations collected across all Woodside stations from September 2021 to December 2022. For all gas types, there is considerable overlap in the range of gas concentrations measured by the IVL and Radiello sampler types.

For NO_2 concentrations in Figure *7.3-1*(a), the interquartile range (**IQR**) (difference between the 25th and 75th percentiles) of the IVL measurements completely overlaps the wider IQR for the Radiello. The median IVL NO_2 measurement is slightly lower than the Radiello median. Neither IVL or Radiello NO_2 measurements include outliers and the histograms are fairly symmetrical suggesting a normal distribution.

For NH_3 in Figure *7.3-1*(b), the IQR for IVL and Radiello largely overlap and have similar median values. Both instruments have upper outliers (the points above the lines extending from the IQR box), which suggests that an underlying distribution is skewed.

SO_2 in Figure *7.3-1*(c) and HNO_3 in Figure *7.3-1*(d) use a logarithmic scale for the vertical axis due to highly skewed ranges. The IQR for the Radiello measurements of SO_2 and HNO_3 are wider than the IQR for the IVL measurements, but the IVL median measurements are higher than the Radiello median measurements. These differences may be due to the innate random variability of measurements or to more systematic differences between these instruments.

Figure *7.3-2* shows scatterplots of gas measurements for IVL versus the Radiello samplers for corresponding sampling periods and stations. Where measurements were duplicated for a sampling period and station, the average of the two measurements was used. Table *7.3-1* shows the estimated Spearman correlation between IVL and Radiello samplers. Spearman correlation was applied because the distributions of most gases were highly skewed and did not follow a normal distribution.

Figure *7.3-2*(a) shows a very distinct linear, increasing relationship between IVL and Radiello measurements of NO_2 concentrations. This is confirmed by the strong Spearman correlation between IVL and Radiello for NO_2 concentrations in Table *7.3-1*, with a p value indicating statistical significance at the 0.05 level.

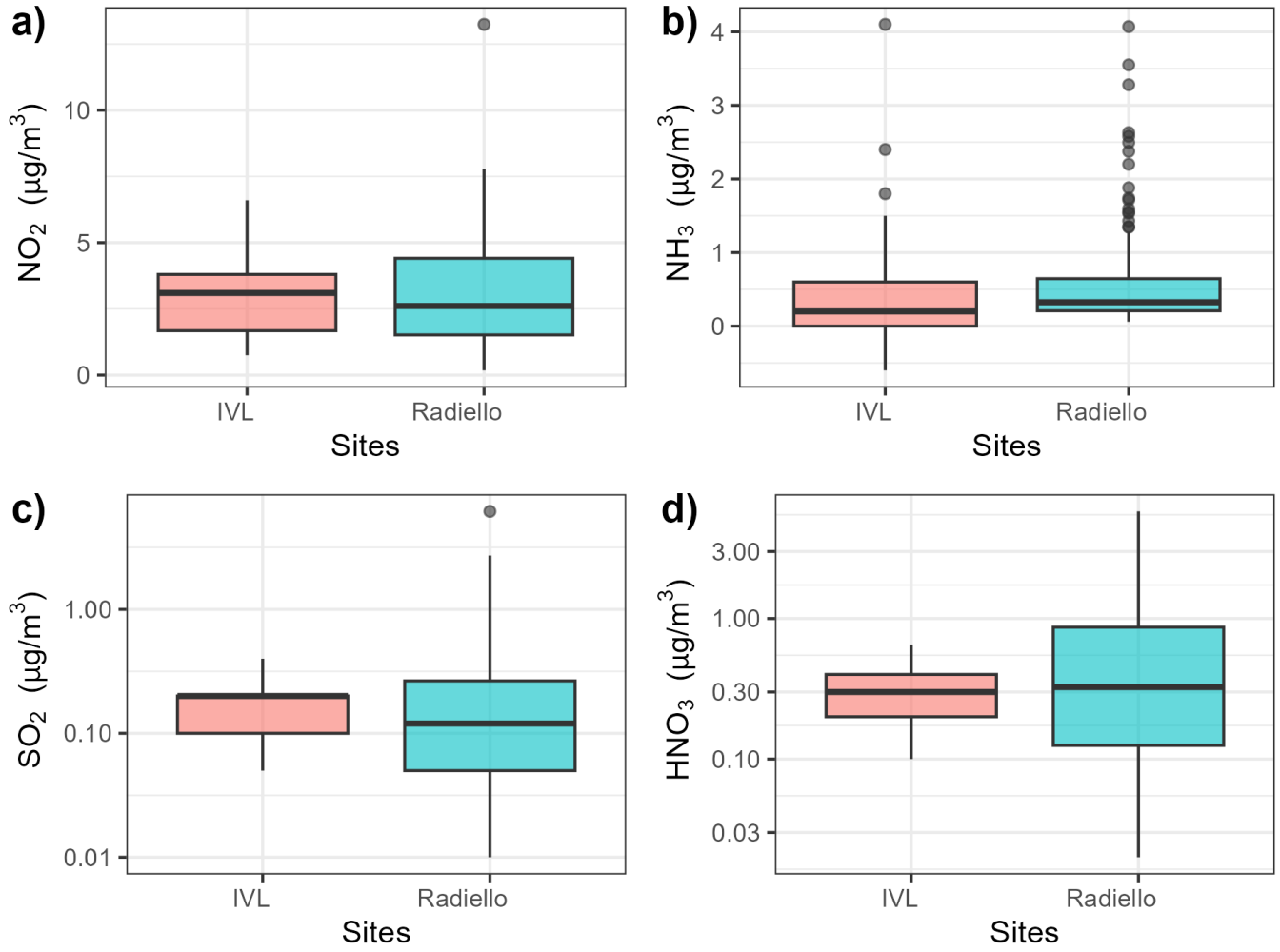

Figure 7.3-1: Boxplots of gas concentration measurements from IVL and Radiello samplers at all Woodside stations from September 2021 to November 2022. Each panel presents boxplots for one gas species: (a) NO_2, (b) NH_3, (c) SO_2, and (d) HNO_3. The vertical axes in panels (c) and (d) use logarithmic scales due to the wide range of concentrations.

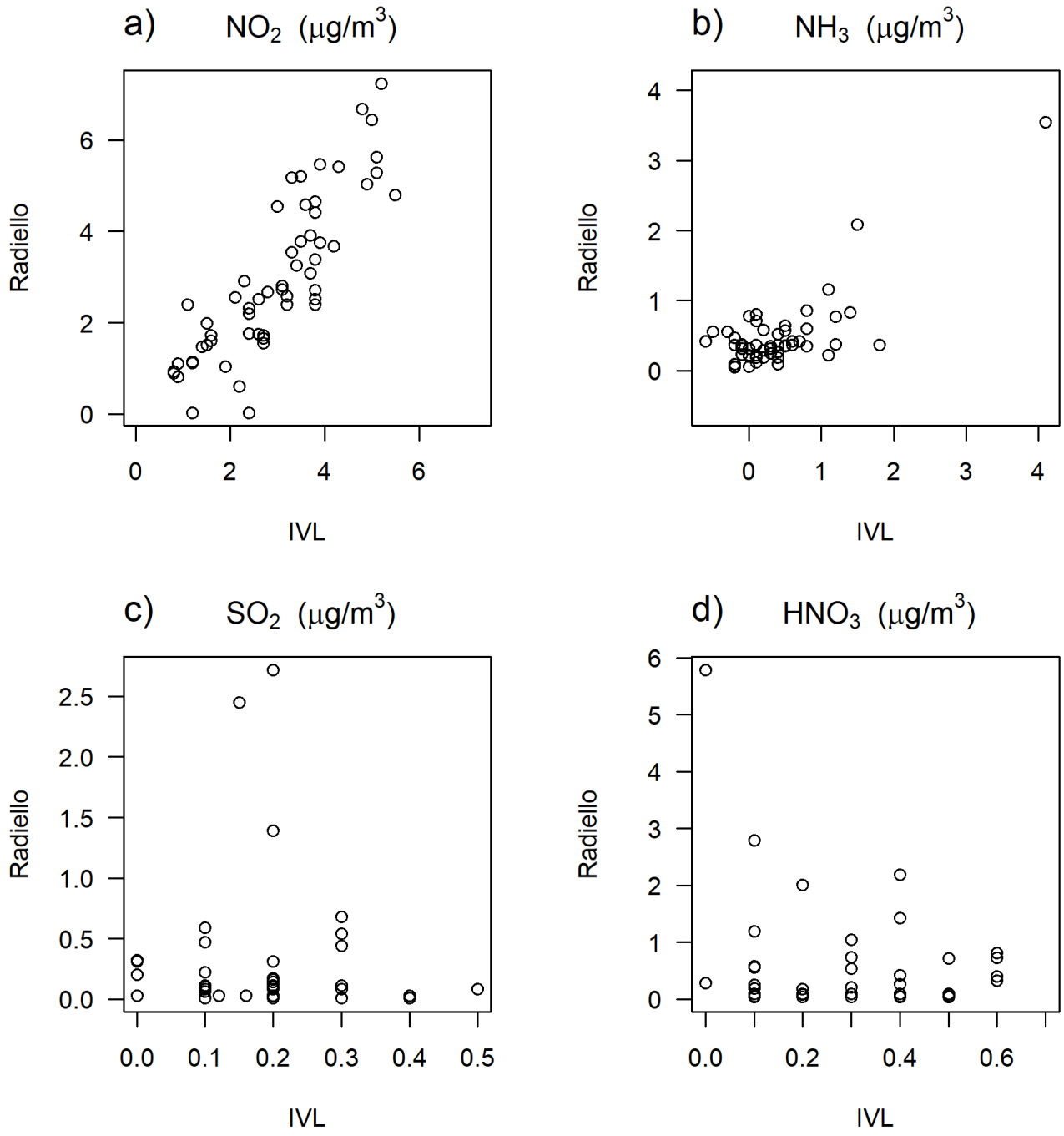

Figure 7.3-2: Scatterplots of gas concentration measurements by Radiello samplers versus IVL samplers at Woodside monitoring stations for corresponding sampling periods between September 2021 and November 2022. Each panel represents one gas species: (a) NO_2, (b) NH_3, (c) SO_2, and (d) HNO_3.

Figure *7.3-2*(b) shows an apparent increasing relationship between IVL and Radiello measurements of NH_3 concentrations, although observations are clustered at lower values. The increasing relationship is confirmed by the moderate Spearman correlation between the IVL and Radiello NH_3 measurements in Table *7.3-1*, with a p value showing evidence of correlation for significance level 0.05.

However, measurements of SO_2 in Figure *7.3-2*(c) and HNO_3 in Figure *7.3-2*(d) do not show a clear relationship between the two measuring instruments. Table *7.3-1* shows a very small Spearman correlation estimates for measurements of these two gases and are not significant at level 0.05.

Based on this analysis, it appears that the Radiello data for NO_2 and NH_3 can be used in the advanced analysis as the correspondence with IVL measurements is reasonable. However, further analysis of the relationship between the Radiello and IVL samplers for SO_2 and HNO_3 must be undertaken in the final MRAMP monitoring studies report before these data can be included.

Table 7.3-1: Spearman correlation estimates for IVL versus Radiello measurements of gas concentrations measured by Woodside monitoring stations by species for corresponding observations only.

Gas	Estimated correlation	p value
NO_2	0.890	<0.001
NH_3	0.422	0.005
SO_2	-0.043	0.802
HNO_3	-0.031	0.856

7.4 Inorganic geochemistry – *pH*, *Eh*, Cl^-

7.4.1 Background

The acidity of rock surfaces has been an important topic of previous research on rock art. Our study design involves measuring *pH*, oxidation-reduction potential (*Eh*, equivalent *ORP*) and chloride ion concentration (Cl^-) on selected rock surfaces during each field campaign.

The Monitoring Studies Report 2023 (Curtin University, 2023) dealt with the observations of *pH*, *Eh*, and concentration of Cl^- from the first four field campaigns. Monitoring Studies Report 2024 (Curtin University, 2024c) expanded this analysis with campaigns 5 to 7.

Campaign 1 yielded results that were quite different in some respects from those obtained in the subsequent campaigns 2 through 7. This discrepancy could have been explained either by startup effects (such as operator learning curves), revisions of technique, and deterioration of reagents.

A further three field campaigns (8 through 10) were completed in the third year of studies and the results have been added to the observations from previous campaigns.

A few rainy days were also reported during campaigns 1, 4, 7, and 10; with campaign 7 and 10 having more than 10 mm of rain. Table *7.4-1* shows the campaign dates, the number of days since the most recent rain before the start of the campaign, any occurrence of rain during the campaign, rain beyond a 10 mm threshold, and the median *pH* recorded. Bureau of Meteorology defines "heavy precipitation days" as those with daily precipitation of 10 mm or more (http://www.bom.gov.au/climate/change/about/extremes.shtml).

As mentioned in Section 3.2.3, since campaign 5 an ionic strength adjuster (ISA) has been used when making *pH* and chloride ion measurements.

Table 7.4-1: Overall campaign data: start and end dates, days since last rain (before start of campaign), rain recorded during campaign, and median pH.

Campaign	Start date	End date	Days since last rain				Rain during		Median *pH*
			Any rain	>10 mm	>20 mm	>40 mm	Any rain	>10 mm	
1	08/03/2022	08/04/2022	23	32	288	313	**Y**	N	6.63
2	20/06/2022	29/07/2022	9	19	19	21	N	N	4.78
3	10/10/2022	04/11/2022	37	37	131	133	N	N	4.50
4	27/02/2023	24/03/2023	4	7	271	273	**Y**	N	4.44
5	03/07/2023	21/07/2023	12	13	13	13	N	N	4.46
6	23/10/2023	17/11/2023	124	125	125	125	N	N	5.81
7	26/02/2024	21/03/2024	3	251	251	251	**Y**	**Y**	6.03
8	01/07/2024	26/07/2024	3	3	29	81	N	N	6.05
9	14/10/2024	07/11/2024	4	72	73	186	N	N	4.52
10	24/02/2025	21/03/2025	8	35	35	35	**Y**	**Y**	5.33

The next section reports a combined analysis of the results from all campaigns 1 through 10.

7.4.2 *pH* observations

Figure *7.4-1* shows boxplots and individual values of *pH* recorded in each campaign. The striking difference between campaign 1 and campaigns 2–4 was noted in the Monitoring Studies Report 2023 (Curtin University, 2023): the median *pH* in campaign 1 is close to 7 (neutral), while the median in each of campaigns 2–4 is close to 4.5. With the additional data from campaigns 5–10, we note that the median *pH* recorded in campaign 5 is again close to 4.5, while in campaigns 6–8 the median is close to 6, while in campaign 9 the median dropped to close to 4.5 again before rising slightly in campaign 10. Also, two unusually high pH values were noted in campaign 9 (11.69) and 10 (13.5), which are most likely due to an unknown operator error.

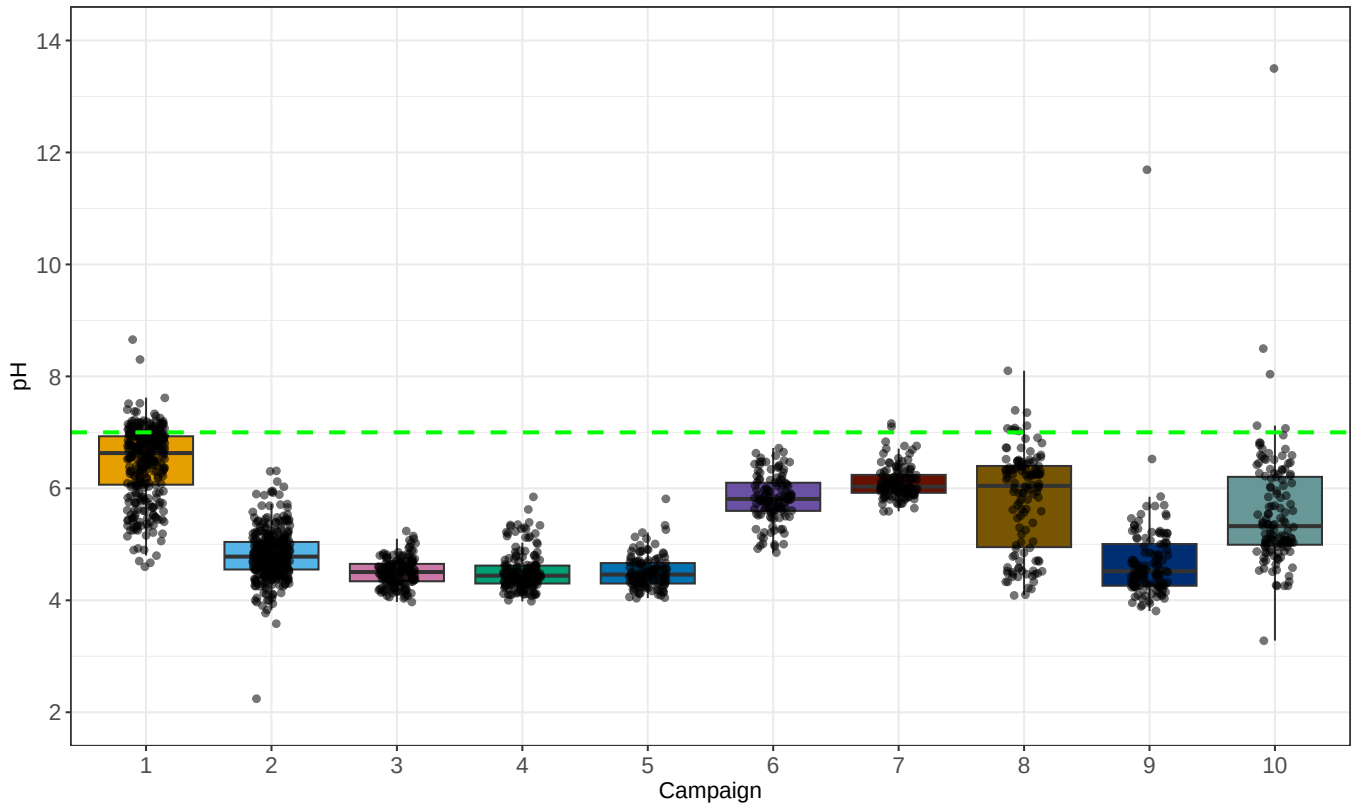

Figure 7.4-1: Boxplots of pH by campaign. The green dashed line represents the neutral pH value.

Figure *7.4-2* shows boxplots of *pH* broken down by rock type, within each campaign. Differences between campaigns are much greater than differences between rock types within a campaign. There seems to be no evidence for systematic differences between rock types.

Possible explanations for the large differences between campaigns include the following:

- Data may reflect real fluctuations in rock surface *pH* (e.g., seasonal effects related to temperature, rainfall, and other environmental factors).
- Lower *pH* for campaigns 2 to 5 and 9 may reflect biotic or other activity associated with rainfall.
- Campaigns 1, 6, 7 and 8 may have higher *pH* because of methodological factors (trial effects and equipment failure in campaign 1, introduction of ionic strength adjuster (ISA) in campaign 6).

Evidence for a seasonal effect (i.e., periodic variation with a period of one year) is inconclusive. The campaigns conducted in March were 1, 4, 7 and 10. If campaign 1 is excluded (as noted above), campaign 4 recorded the lowest *pH* values, campaign 7 the highest and campaign 10 had values that fell between those observed in campaigns 4 and 7. Even though the *pH* data from campaigns 2 and 5 (both conducted in July) were quite similar, campaign 8 - also conducted in July - were much higher. The October–November campaigns were 3, 6 and 9: campaigns 3 and 9 had low *pH* values but campaign 6 had substantially high values.

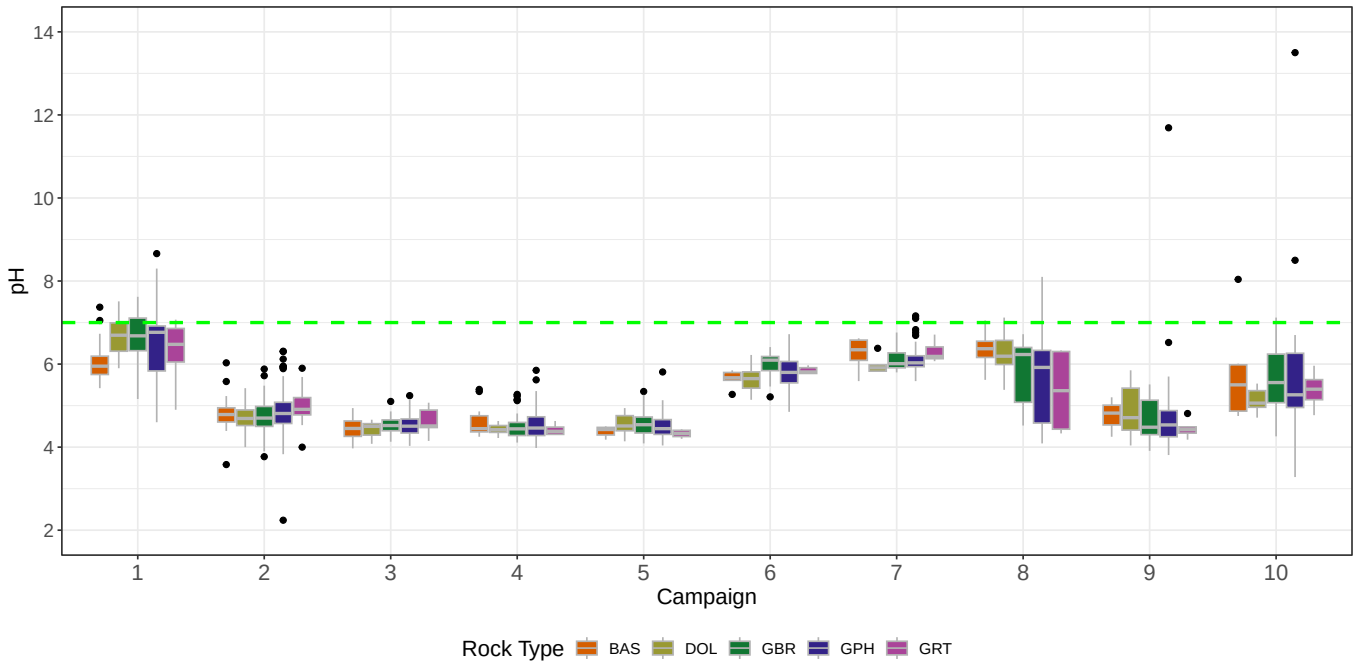

Figure 7.4-2: Boxplots of pH by rock type for each campaign. The green dashed line represents the neutral pH value.

Recent rainfall appears to be highly influential. Campaigns 1 and 6 were preceded by long dry periods, whereas campaigns 2–4 and 10 were preceded by, or took place during, rain. Water in equilibrium with atmospheric CO_2 is expected to have a *pH* around 5.6; this is consistent with the observed *pH* values in campaign 6 and 10. If this explanation is valid, it would indicate that rock surface chemistry is dynamic, and that *pH* fluctuates on timescales longer than a year, which would make *pH* a poor choice for an Environmental Quality Criterion.

Evidence for consistent differences in *pH* between different rock types (a rock type "effect") is mixed. Figure *7.4-3* shows boxplots of *pH* after subtracting the median *pH* for the relevant campaign. Data from campaigns 1, 6, and 7 suggest that there may be a rock effect. However, data from the other campaigns 2–5 and 8–10 did not support this. For example, in campaign 2, the median *pH* for granite (GRT) is higher than for other rock types, but in campaign 5, the median *pH* for granite is lower than for other rock types. The possibility of an interaction between rock type and seasonal/weather effects (i.e., different seasonal effects on different rock types) should still be considered.

It is important to assess evidence for any spatial trend in electrochemistry, because such trends could be associated with the gradient in exposure to industrial output. Figure *7.4-4* shows spatially

smoothed *pH* surfaces for each campaign obtained by the Nadaraya-Watson smoothing technique (see Appendix F,Monitoring Studies Report 2024 (Curtin University, 2024c)). The standard colour map for *pH* values is used in all panels, despite the very different values of *pH* obtained in the different campaigns. Spatial variations in *pH* are generally much smaller than the differences between campaigns. The exceptions are campaigns 1, 8 and 10 whose higher-variability boxplots seem to be related to spatial location.

The spatial smoothing plots in Figure *7.4-4* show that, although pH values vary considerably between campaigns, spatial variability within each campaign is generally much smaller. Figure *7.4-5* removes overall temporal/campaign differences, highlighting spatial patterns likely driven by geological or site-specific factors. For most campaigns, adjusted pH values range between –1 and 1, indicating relatively minor deviations from the campaign median. Only Campaigns 1, 8, and 10 show higher deviations. Hence, temporal/seasonal differences are the dominant factor in the variation of pH between campaigns.

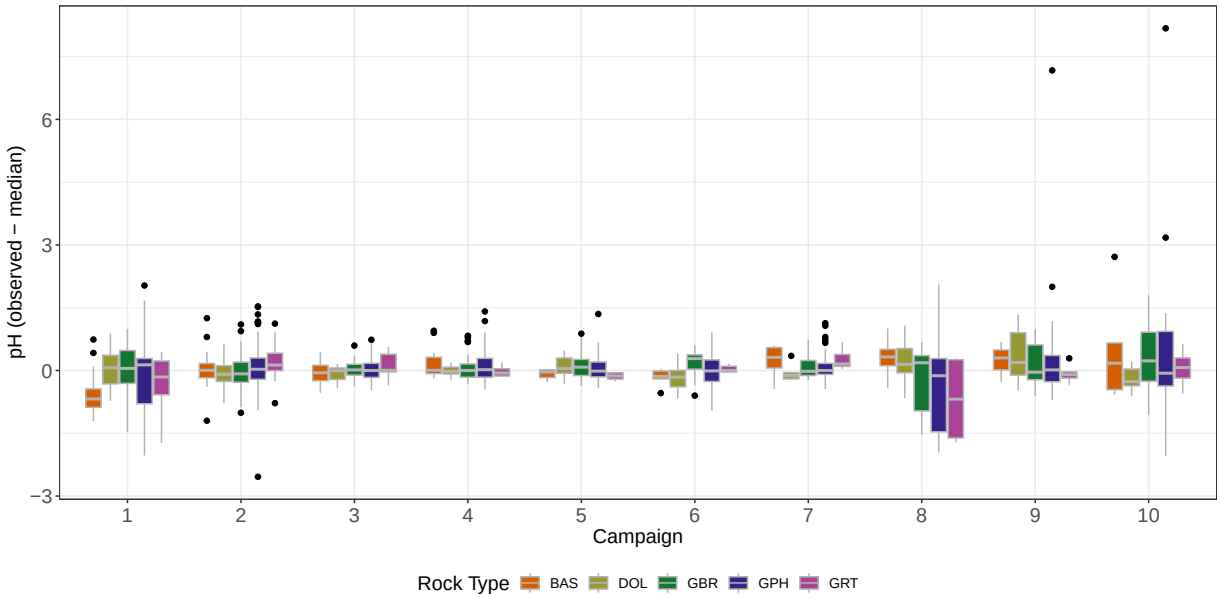

Figure 7.4-3: Boxplots of observed pH minus campaign median pH, by rock type for each campaign.

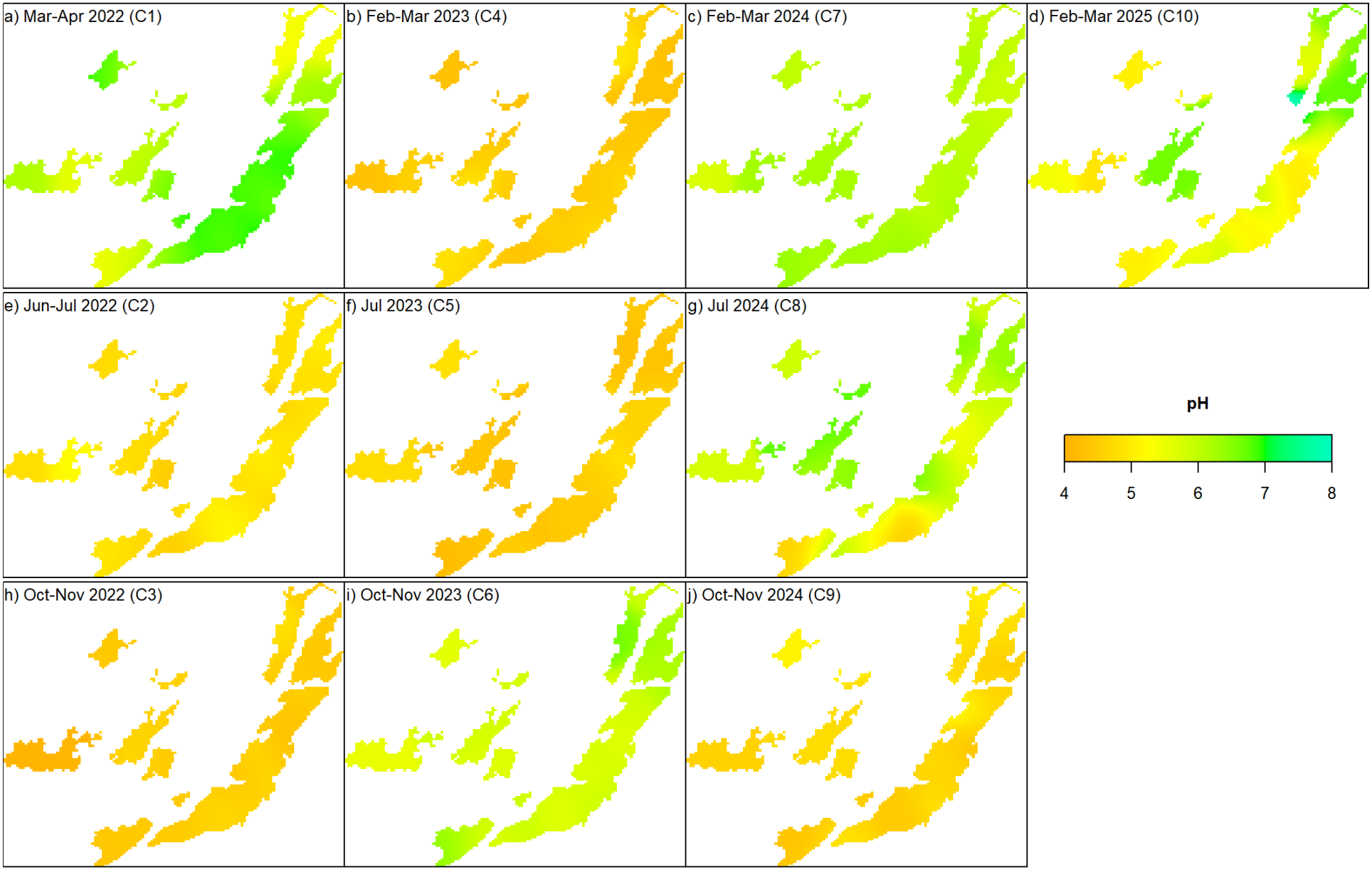

Figure 7.4-4: Spatially smoothed pH values of campaigns 1 to 10 (C1-C10).

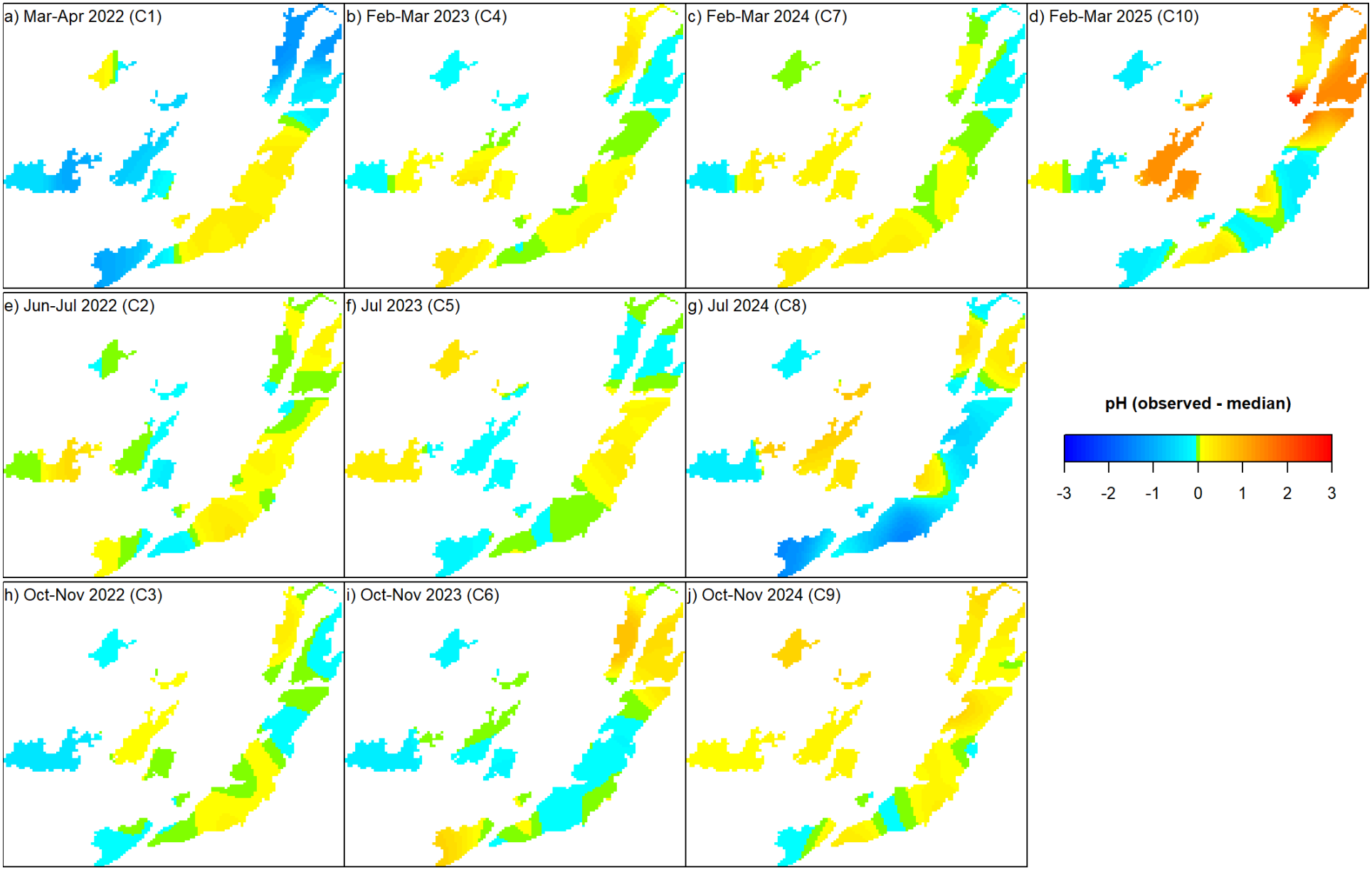

Figure 7.4-5: Spatially smoothed observed pH minus campaign median pH of campaigns 1 to 10 (C1-C10).

7.4.3 Chloride ion (Cl^-) observations

Chloride ion Cl^- concentration (in parts per million) was measured three times at each sample rock in each campaign, starting from campaign 2 (because of a device breakdown in campaign 1).

The recorded values of Cl^- concentration vary over several orders of magnitude, and are strongly skewed to the right. Accordingly, a logarithmic transformation was used to analyse these data.

Figure *7.4-6* shows boxplots, on a logarithmic scale, of Cl^- concentration for each campaign. For campaign 5, there are separate boxplots for the results with and without ISA.

There are substantial differences in Cl^- concentration between campaigns:

- The median chloride concentration in each campaign is very high for campaign 5 (with and without ISA), and for campaign 10.
- Cl^- concentration is very low in campaigns 2 and 3 which give similar results.
- It is moderate in campaigns 4, 6–8, which give similar results.
- It is high for campaign 9.

There are also substantial differences in variability within each campaign. Figure *7.4-7* shows boxplots, again on a logarithmic scale, of Cl^- concentration for each rock type in each campaign. There does not appear to be a systematic effect associated with rock type. There are numerous extreme values, particularly in campaign 10, indicating a possible malfunctioning instrument (servicing by the vendor following the campaign confirmed the instrument was nearing end of life).

Figure *7.4-8* shows spatially smoothed Cl^- concentration for each campaign. A common colour key has been used, shown at the bottom right. The upper ribbon shows the colour key over the entire range of values from zero to 450 ppm, while the lower key is a magnified display for the range from zero to 50 ppm. The use of a common colour key allows immediate recognition of the systematic differences between campaigns. There does not appear to be a consistent spatial trend in Cl^- values.

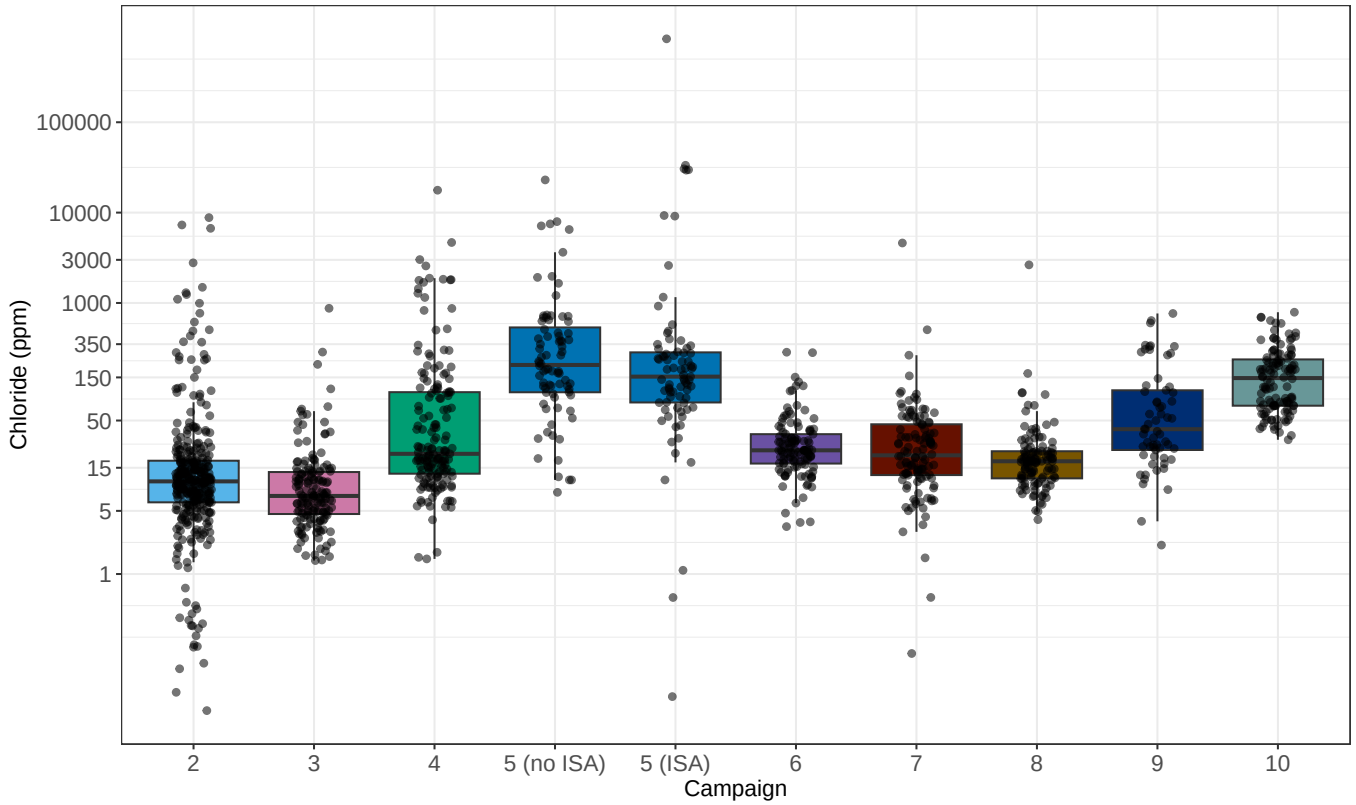

Figure 7.4-6: Boxplots of Cl^- concentration by campaign. Note logarithmic scale. ISA (Ionic Strength Adjuster).

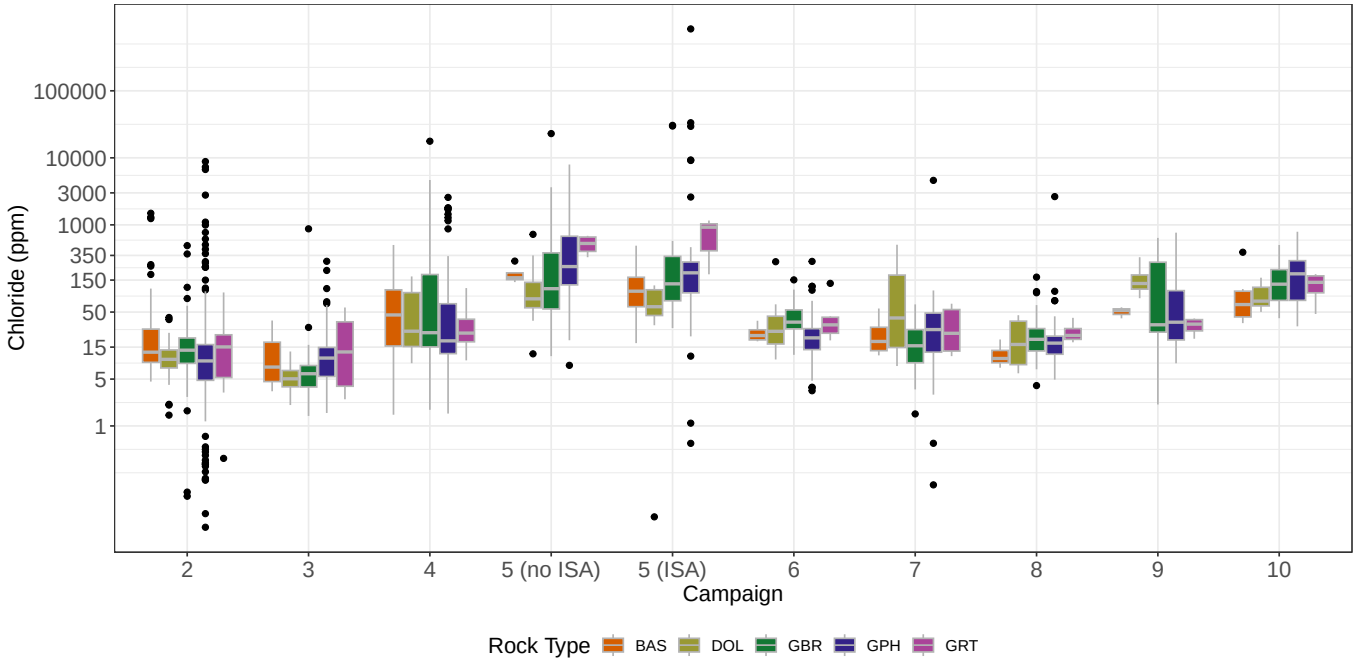

Figure 7.4-7: Boxplots of Cl^- concentration by rock type for different campaigns. Note logarithmic scale. ISA (Ionic Strength Adjuster).

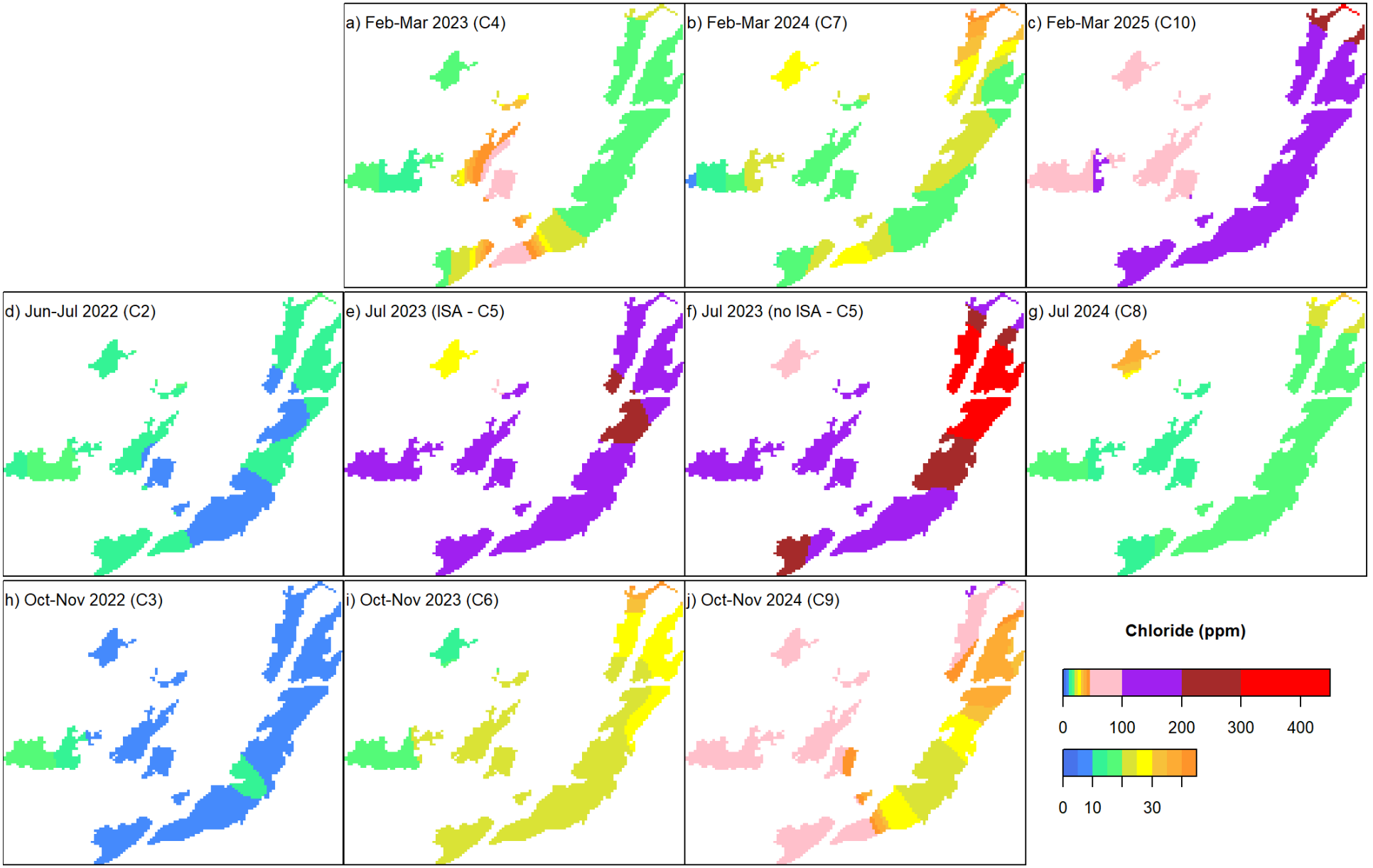

Figure 7.4-8: Spatially smoothed chloride ion (Cl^-) concentration of campaigns 2 to 10 (C2-C10).

7.4.4 Oxidation-reduction potential (*ORP*) observations

Figure *7.4-9* shows boxplots of rock surface *ORP* measurements (i.e., *Eh*) in millivolts (mV) for each campaign, starting from campaign 2. Values range between 80-400 mV with quartiles at about 200, 250 and 300 mV. Boxplots and histograms suggest good approximation by a normal distribution for exploratory purposes. There are slight differences between campaigns of medians and variability.

Figure *7.4-10* shows boxplots of *ORP* for each rock type in each campaign. Since the variability is relatively large, there is no discernible effect of rock type.

Figure *7.4-11* shows spatially smoothed *ORP* surfaces for each campaign. Estimates of the spatial trend are similar in panels (a)–(c), obtained from campaigns 2–4 respectively, and are similar in panels (d)–(f), obtained from campaigns 5–7. In panels (g)–(i), obtained from campaigns 8–10, the spatial trends show features of the earlier panels but no pattern of spatial trends emerges. In the next section, the multivariate association of *pH*, Cl^-, and *ORP* will be investigated for the ten campaigns.

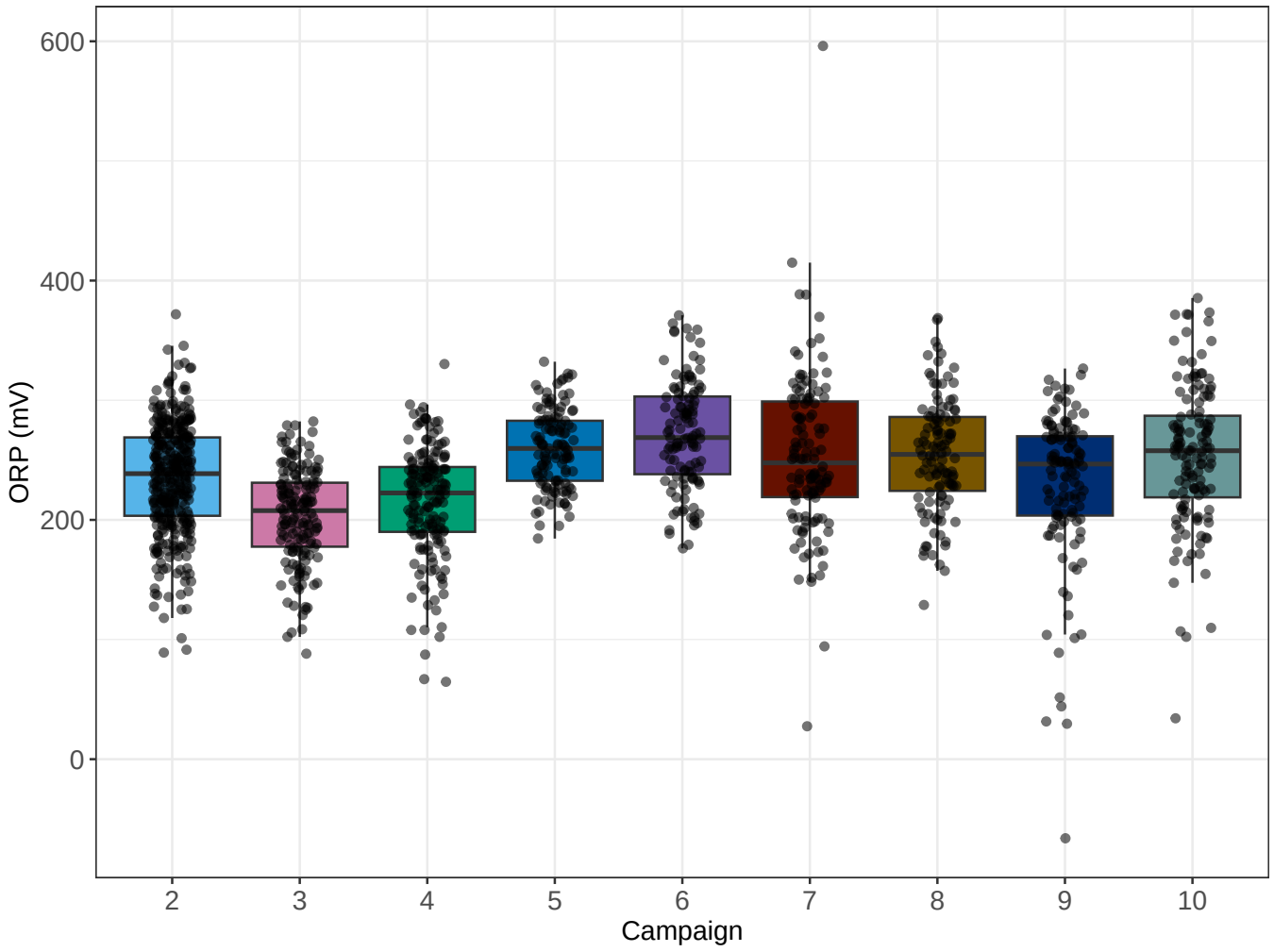

Figure 7.4-9: Boxplots of ORP by campaign.

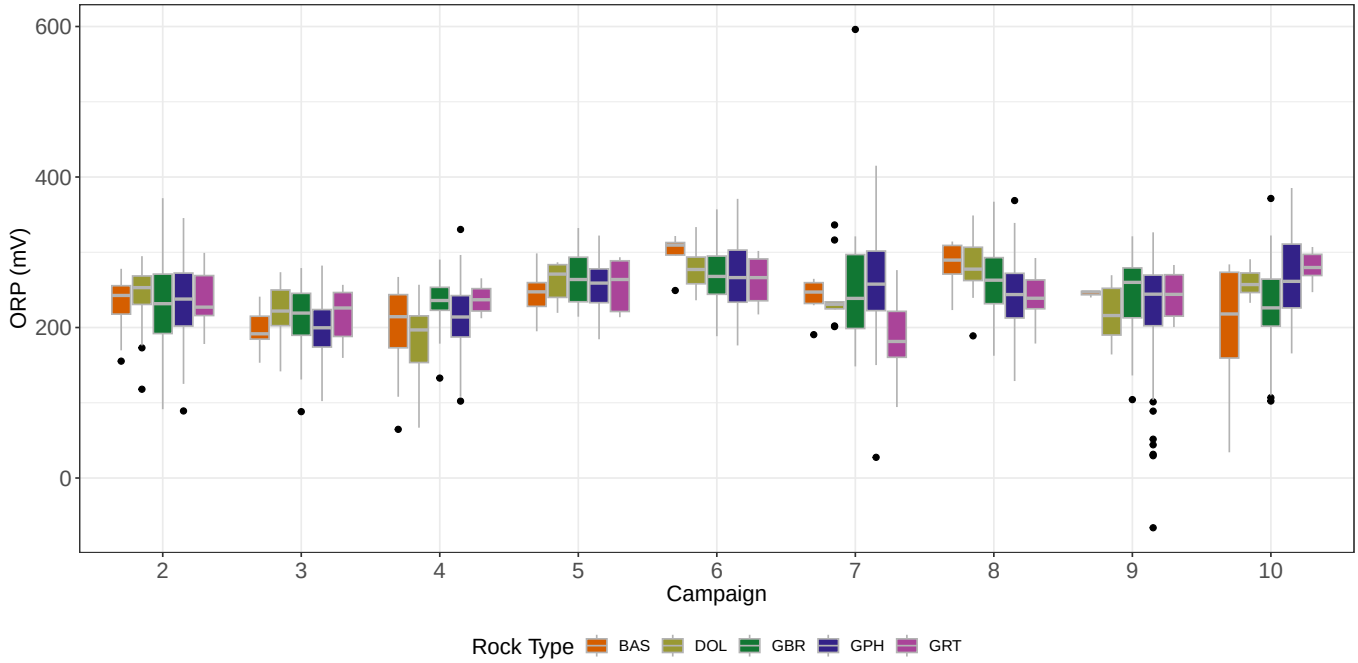

Figure 7.4-10: Boxplots of ORP by rock type for different campaigns.

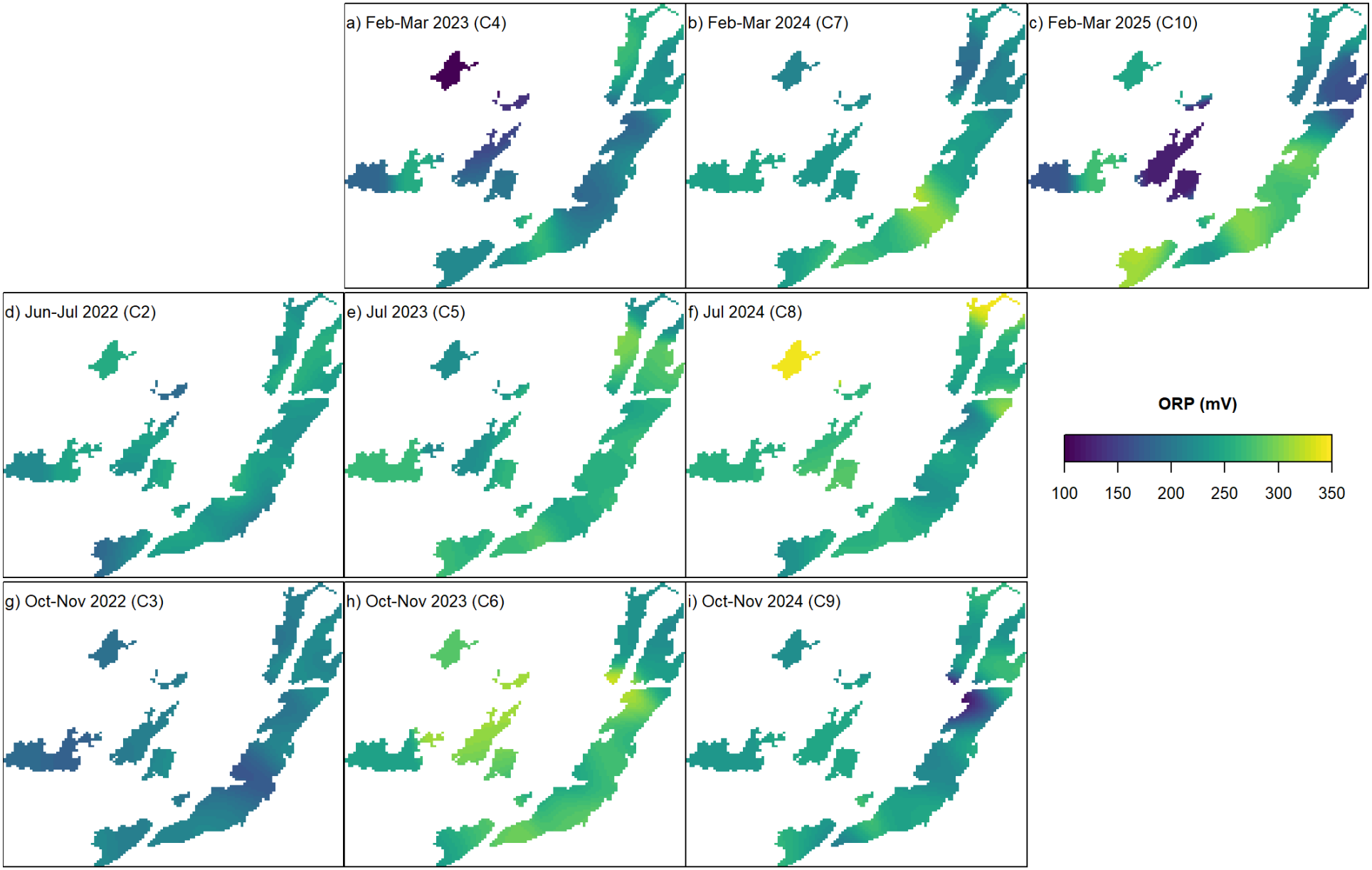

Figure 7.4-11: Spatially smoothed ORP from data from campaigns 2 to 10 (C2-C10).

7.4.5 Multivariate association between *pH*, *ORP* and Cl^-

Figures *7.4-12–7.4-14* each show a scatterplot matrix for investigating relationships between *pH*, *ORP* and the decimal logarithm of Cl^- concentration for campaigns 8 to 10. The upper right panels in these figures show the corresponding Spearman correlation coefficient. Note that the corresponding scatterplot matrix for campaigns 2 to 7 can be found in the Monitoring Studies Report 2024 (Curtin University, 2024c).

Spearman correlation coefficients are denoted by stars based on their significance levels. The lower panels show scatterplots with loess curves that visually display the relationship between variables (positive, negative, or no relationship).

- No stars (zero stars): The correlation coefficient is not statistically significant.
- One star (*): The correlation coefficient is significant at the 0.05 level (two-tailed test).
- Two stars (**): The correlation coefficient is significant at the 0.01 level (two-tailed test).
- Three stars (***): The correlation coefficient is significant at the 0.001 level (two-tailed test).

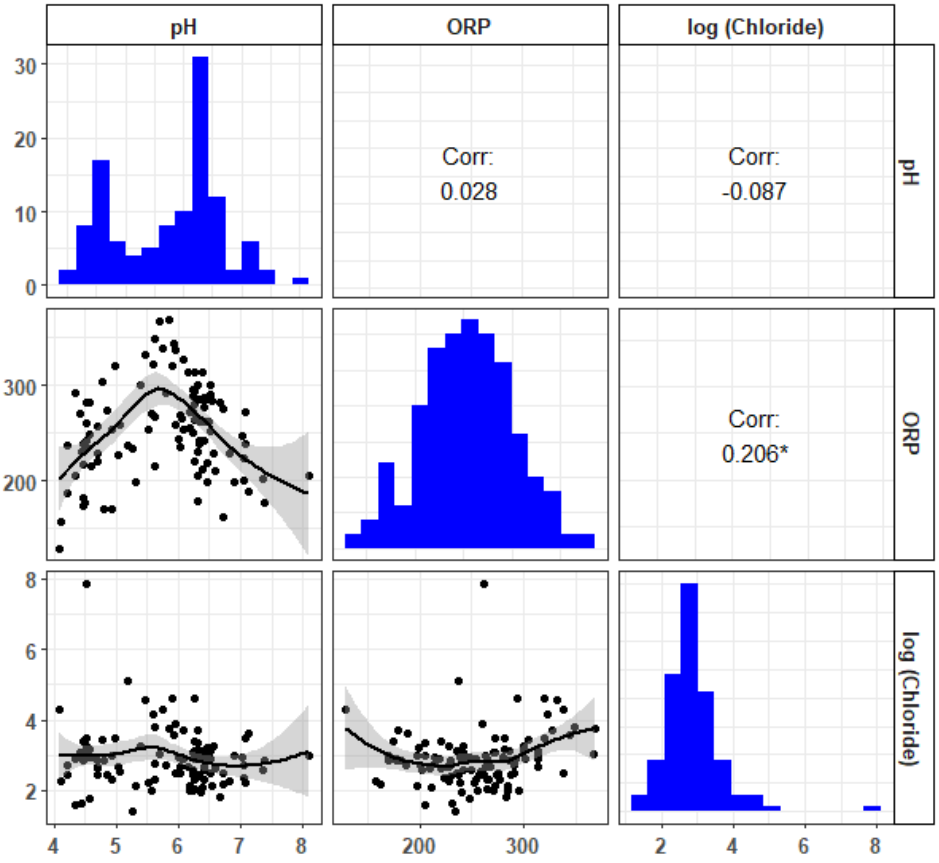

Figure 7.4-12: Campaign 8 pairwise scatterplots between pH, ORP and logarithm of chloride concentration. The panels above the diagonal show the correlation between two variables; panels on the diagonal show the histogram of each variable; panels below the diagonal show a scatterplot between two variables.

In summary, pairwise associations between *pH*, *ORP* and logarithm of Cl^- concentration were either statistically non significant at the 0.05 level or were weak as measured by the linear (Spearman) sample correlation. Further multivariate analysis of these data will be undertaken in the context of the overall study design, but this preliminary analysis suggests no strong association between these variables.

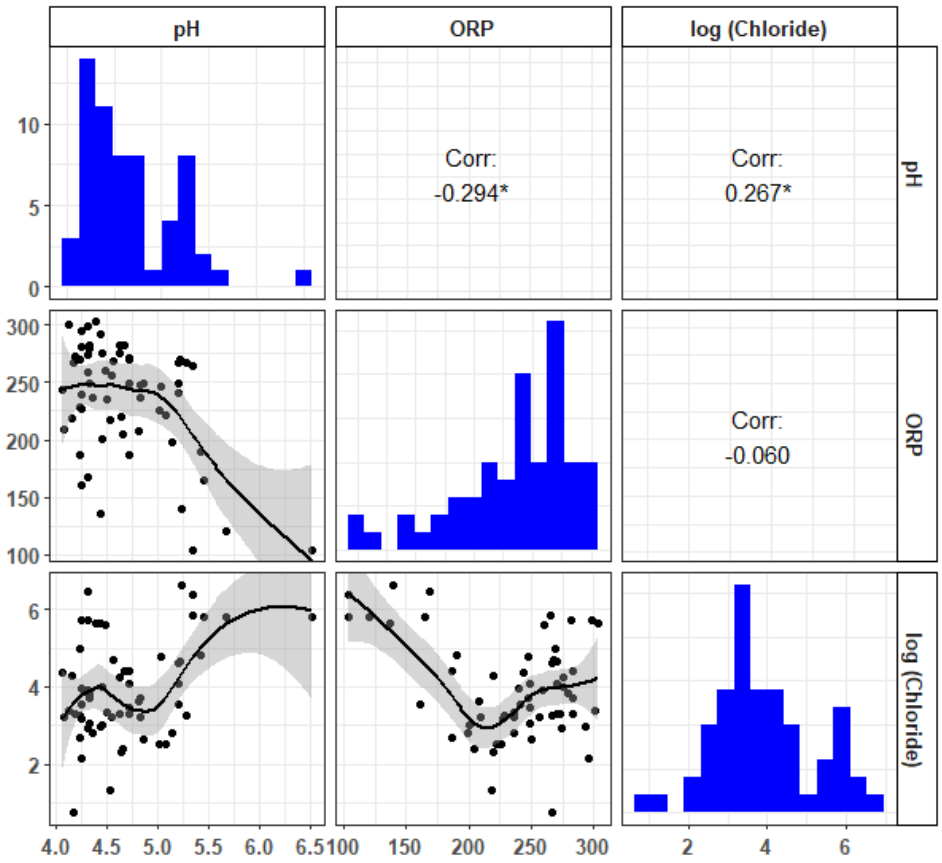

Figure 7.4-13: Campaign 9 pairwise scatterplots between pH, ORP and logarithm of chloride concentration. The panels above the diagonal show the correlation between two variables; panels on the diagonal show the histogram of each variable; panels below the diagonal show a scatterplot between two variables.

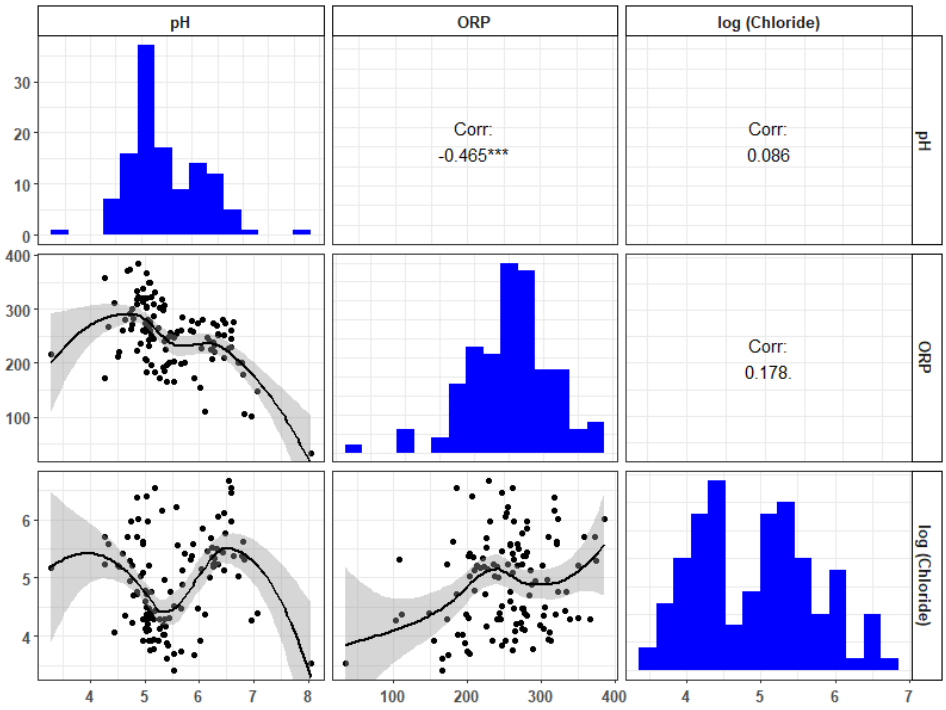

Figure 7.4-14: Campaign 10 pairwise scatterplots between pH, ORP and logarithm of chloride concentration. The panels above the diagonal show the correlation between two variables; panels on the diagonal show the histogram of each variable; panels below the diagonal show a scatterplot between two variables.

7.4.6 AQM rock cube observations

Each of 29 industry and MRAMP AQMs have had unpatinated rock cubes installed, consisting of a 50 x 50 x 50 mm (approximately) cube of each of the five rock types being studied. As the cubes were installed primarily to understand microbial colonisation, they were rendered abiotic prior to installation using ethanol and flame.

In addition, *pH* was measured on the rock cubes as part of campaign 9 to enable a comparison amongst patinated and unpatinated rocks.

Values of *pH* ranged from 5.17 to 6.69 (Figure *7.4-15* and *7.4-16*). The vast majority of the 145 measurements (131 out of 145) were greater than 5.6, which is the value of pure water equilibrated with atmospheric concentrations of carbon dioxide. Of the lower values, four were from AQ17 (Gidley Island), four were from AQ18 (Collier Rocks), and three were from EX06 (near Dampier) (Figure *7.4-16*). The vast majority of values were higher than those measured on the patinated rock art panels during campaign 9, which were generally below 5 (Figure *7.4-2*).

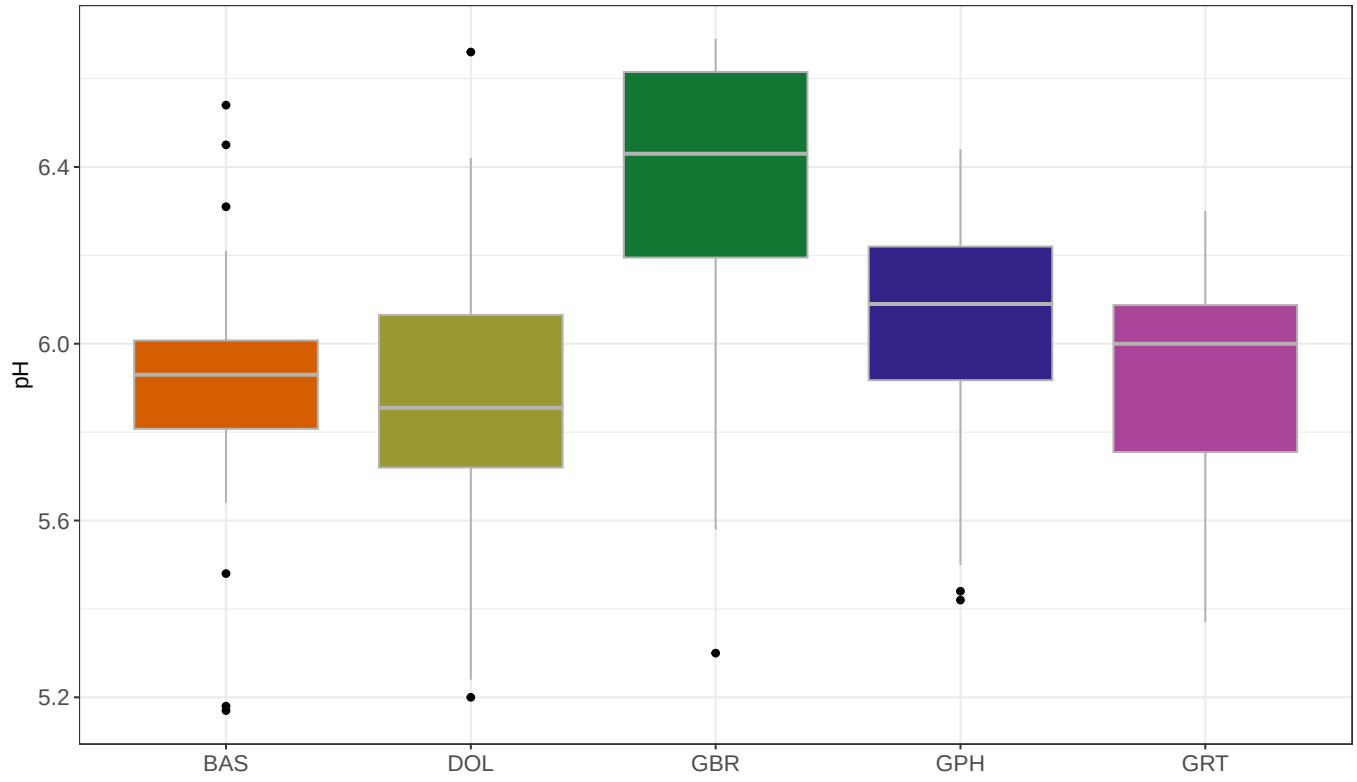

Figure 7.4-15: Rock cube pH for all AQM sites for each rock type.

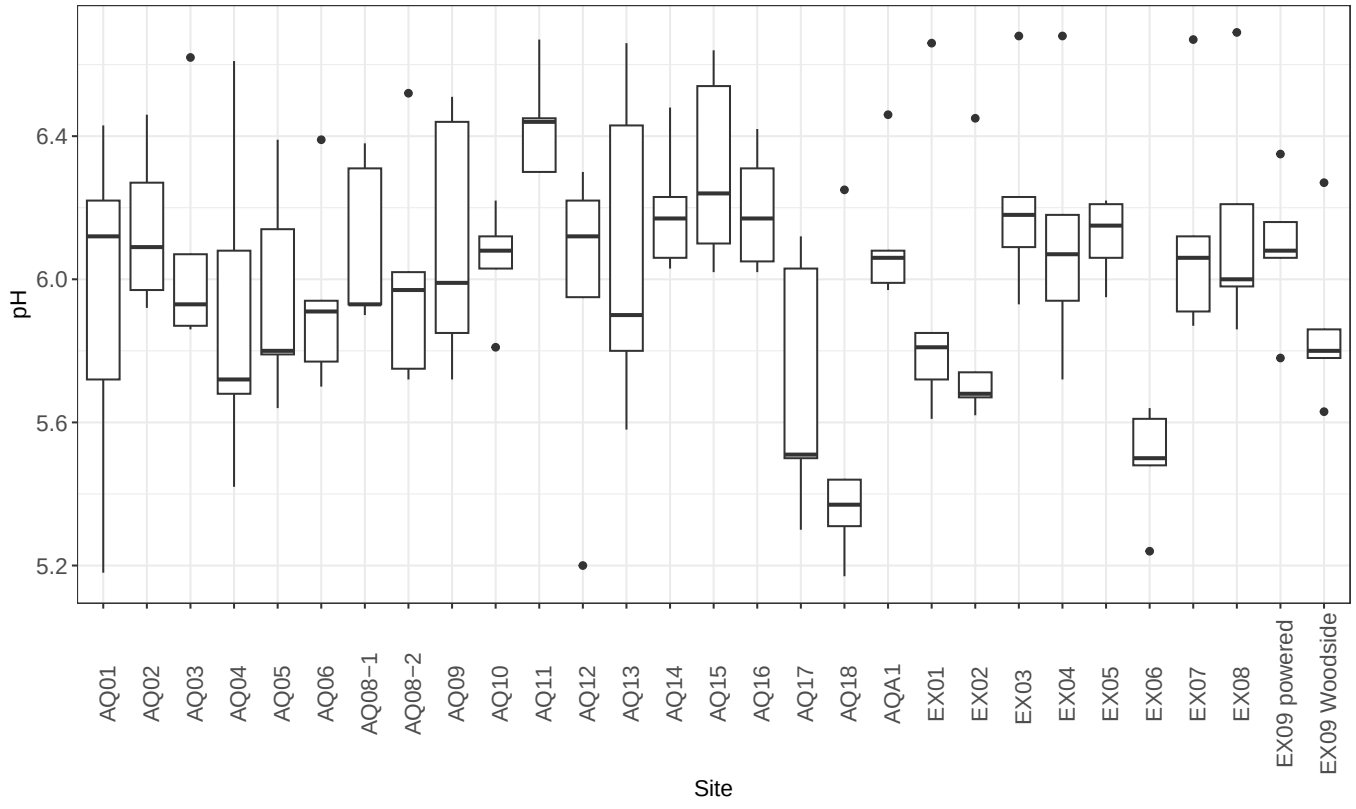

Figure 7.4-16: Rock cube pH for all rock types for each AQM site.

There was some evidence of variation in *pH* as a function of rock type (Figure *7.4-15*). Values for gabbro were higher than those for the other lithologies, with an average value of around 6.3 $\pm$ 0.3 (one standard deviation), whereas the average *pH* for the other lithologies ranged from 5.9 to 6, with similar standard deviations (Figure *7.4-15*). However, these results are close to within error of each other so individual measurements would be difficult to attribute unambiguously to a rock type effect.

A plausible explanation for the higher *pH* values on unpatinated rock cubes relative to equivalent but patinated rock surfaces is that the low *pH* values relate to properties of the surfaces rather than environmental factors common to both patinated and unpatinated surfaces, such as atmospheric chemistry. The *pH* of the patinated surfaces is likely to be affected by microbial activity (MacLeod, 2005) and partial equilibria between water and the patina minerals, which include iron and manganese oxides and hydroxides. The *pH* of unpatinated surfaces, which host little microbiome (Section 7.8), is likely to be controlled by partial equilibrium between water and minerals of the weathered rind. These minerals are mostly silicate and are likely to impose a higher *pH* than the iron and manganese oxides and hydroxides of the weathered rind.

The lowest *pH* values are observed at localities AQ17, AQ18, and EX06 (Figure *7.4-16*), so it is relevant to consider the proximity of these sites to the sources of industrial emissions. Sites AQ17 and AQ18 are located on Gidley Island and Collier Rocks, respectively. These sites may be exposed to elevated SO_2 from shipping but are not amongst the sites exposed to the higher NO_2 levels (Curtin University, 2024c). Site EX06 is proximal to industry, but the lower *pH* values observed there are not replicated at the adjacent sites at EX05 and EX07, which are likely to be exposed to similar emission levels. Based on the available data, there is little evidence of a systematic relationship between rock cube *pH* and industrial emissions, although links between shipping emissions and *pH* may warrant further investigation.

In the context of the expected *pH* values related to mineral dissolution, it is useful to consider whether the elevated *pH* values measured on the gabbro samples relate to systematic differences in the mineral assemblage and dissolution rates amongst the rock type. The mafic rock types (GBR, BAS, DOL) are rich in minerals such as clinopyroxene that more susceptible to chemical decomposition during long periods of weathering than the minerals found within the felsic rock types (GPH, GRT). Rock dissolution consumes protons, increasing *pH*, and dissolution of the minerals found in mafic rocks consumes more protons than dissolution of the minerals found in felsic rocks. However, if mineral dissolution were the first-order control on the *pH* of the rock cubes, then the highest values would be expected on the fine-grained basalts, which are expected to dissolve faster than the gabbros, based on grain-size–effective surface area relationships. This is not observed.

An alternative possibility is that early colonisation by the microbiome was more effective on the coarser-grained gabbro, where mineral dissolution forms a network of interconnected voids, and that release of organic acids reduced *pH*. The relatively faster decomposition of the mafic rock types may create porosity to form a more hospitable environment for the microbiome than the quartz-rich granophyre. However, no DNA or RNA was recovered by microbiome sampling of any of the rock cubes (Section 4.3.5), so there is no evidence to support this suggestion. It is possible that some colonisation had occurred but at levels that were undetectable after only one year. The rock cubes will be sampled again during campaign 11 to investigate this hypothesis further.

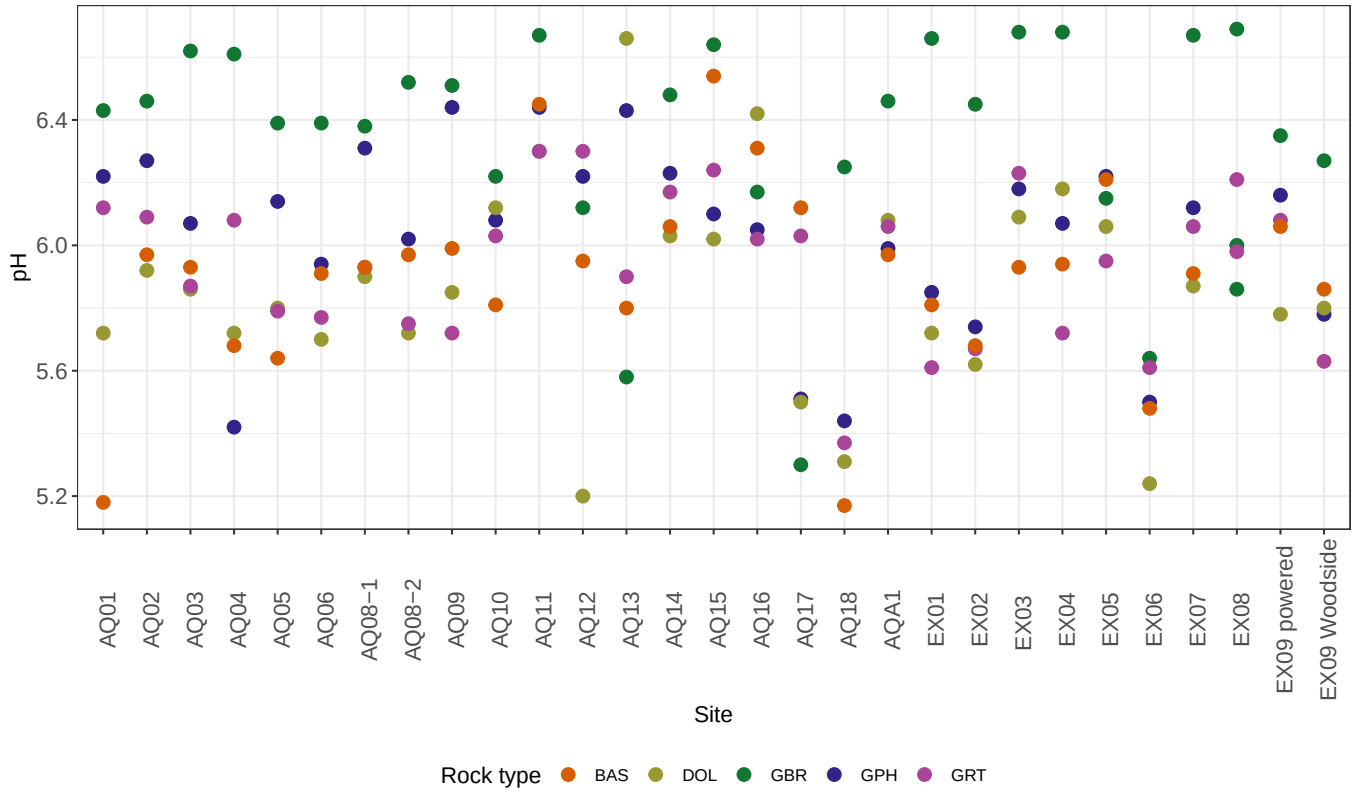

Figure 7.4-17: Rock cube pH for each rock type by each AQM site.

This page is intentionally blank.

7.5 Inorganic geochemistry – pXRF

7.5.1 Background

Section 7.3 of the Monitoring Studies Report 2023 (Curtin University, 2023) and Section 7.5 of the Monitoring Studies Report 2024 (Curtin University, 2024c) details the background information on the portable X-Ray Fluorescence (pXRF) instrument. The Monitoring Studies Report 2023 (Curtin University, 2023) presented analysis of pXRF readings for campaigns 1 to 4. The Monitoring Studies Report 2024 (Curtin University, 2024c) expanded this analysis of pXRF readings for campaigns 1 to 7.

pXRF readings were taken in the first nine field campaigns on the same rock surfaces in each campaign. pXRF measurements were discontinued for campaign 10 as the prior campaigns yielded pXRF data which were consistent between campaigns and had insufficient signal-to-noise ratio to enable detection of trends over short periods of time.

This section presents analysis of the pXRF readings for campaigns 8 and 9.

7.5.2 Multivariate analysis

In the Monitoring Studies Report 2024 (Curtin University, 2024c), redundancy analysis (**RDA**) was applied to investigate the relationship between the chemical elements from the pXRF and the rock types. RDA helps determine the extent to which the chemical elements explain the differences between the rock types. This exploratory analysis is reasonable because rock types are defined partially by their geochemistry, so that one would expect to see strong associations between particular rock types and particular elements. In last year's report (Curtin University, 2024c), RDA was applied to campaigns 1 to 7. In this section, RDA was applied only to campaign 8. There were an insufficient number of pXRF samples in campaign 9 to perform an RDA (see Table *3.2-3*). Specifically, some rock types were under-represented - only one BAS site and two GRT sites were measured in campaign 9 using the pXRF.

Figure *7.5-1* shows the RDA for campaign 8, and Figure *7.5-2* shows the RDA for all eight campaigns. In these figures, the blue arrows represent pXRF elements and red labels indicate rock types. Arrow length reflects the strength of correlation with rock types, while the angle between arrows shows how elements relate to each other. The position and direction of rock type labels relative to arrows illustrate their association with specific elements, with closer or aligned labels indicating stronger or positive correlations. The "RDA1" (x-axis of the RDA biplot) is the direction that explains the most variation in pXRF data and rock types. The "RDA2" (y-axis) is the next-most important direction of explained variation, perpendicular to RDA1. The point at (0,0), i.e., the starting point for all arrows, represents no deviation along either gradient.

Similar to campaigns 1 to 7, GPH was positively correlated with Thorium (Th) for campaign 8. GBR is positively correlated with magnesium oxide (MgO) in campaigns 1 to 3, 5, 6, 7, and 8. For the majority of the campaigns, including campaign 8, BAS and GRT are close to the origin (almost zero values of RDA1 and/or RDA2). This indicates that the average chemical element composition of BAS and GRT can be considered as the "average" of the analysed rock types captured by the model, such that BAS and GRT accounts for little of the data variability. Therefore, the RDA for campaign 8 is similar to the RDA plots for campaigns 1 to 7.

Minor differences between the campaigns may be related to variation in the mineralogy at the specific spots selected for measurement, which change from one campaign to another. Additional differences may arise from changes in the composition of the surface layers, associated with the formation or dissolution of minerals within the weathered rind and patina. Variation in the effectiveness of contact between the pXRF instrument and rock surface may also contribute to these differences. In particular, undulating rock surfaces generally give lower elemental concentrations than flat rock surfaces, with lighter elements such as Si and Mg being more affected than heavier elements such as Fe. Changes in the modes of rock-forming minerals within the fresher rock are unlikely to be detected. If changes in mineral assemblages within the weathered rind and patina could be related reliably to pXRF data then this technique would provide a valuable monitor of rock surface condition. However, the other uncertainties preclude useful results from this technique as an annual monitoring technique.

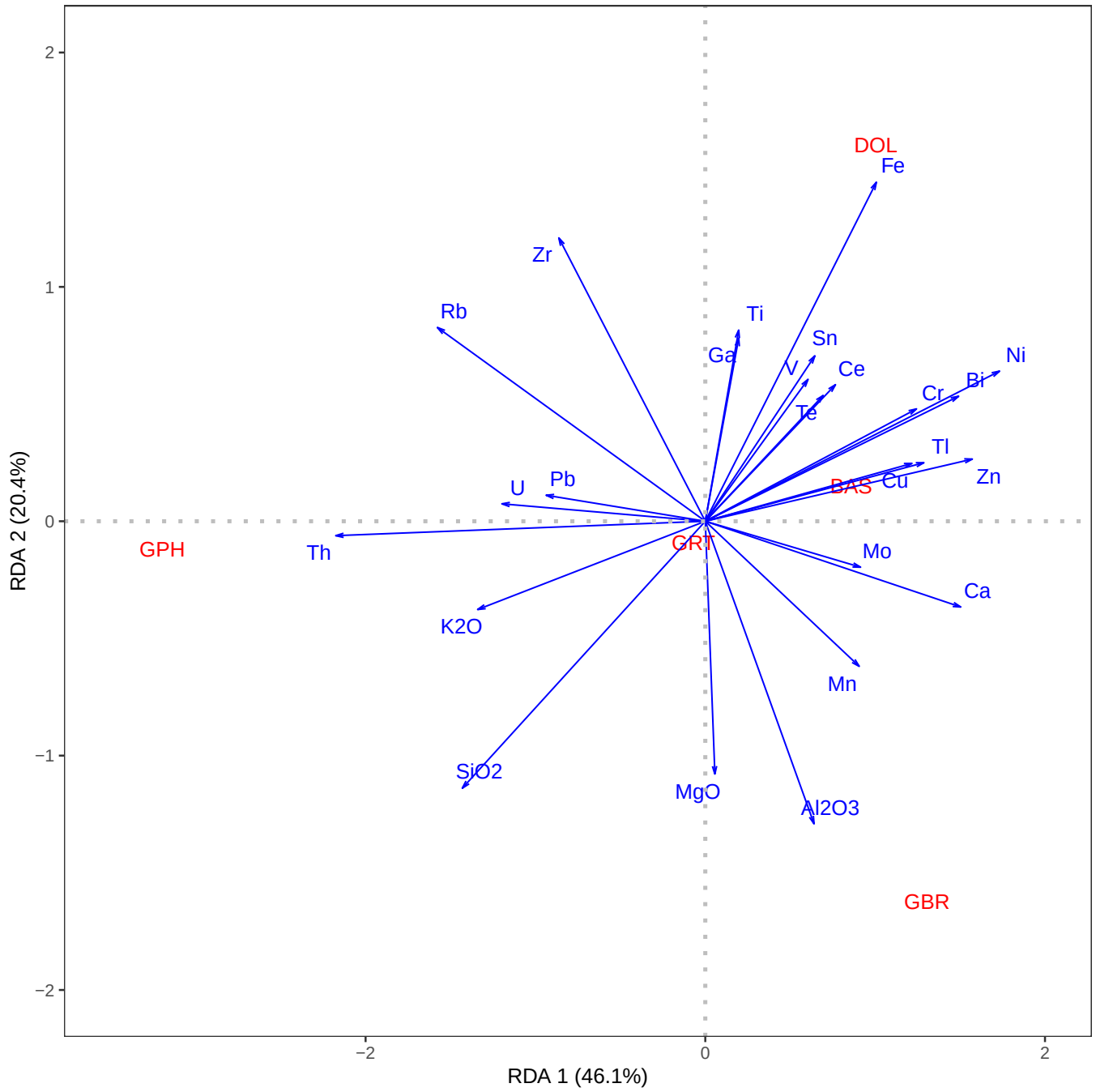

Figure 7.5-1: RDA biplot showing the relationship between chemical elements from the pXRF and rock types in campaign 8. Percentage in parentheses is the percentage of total variation explained by the RDA.

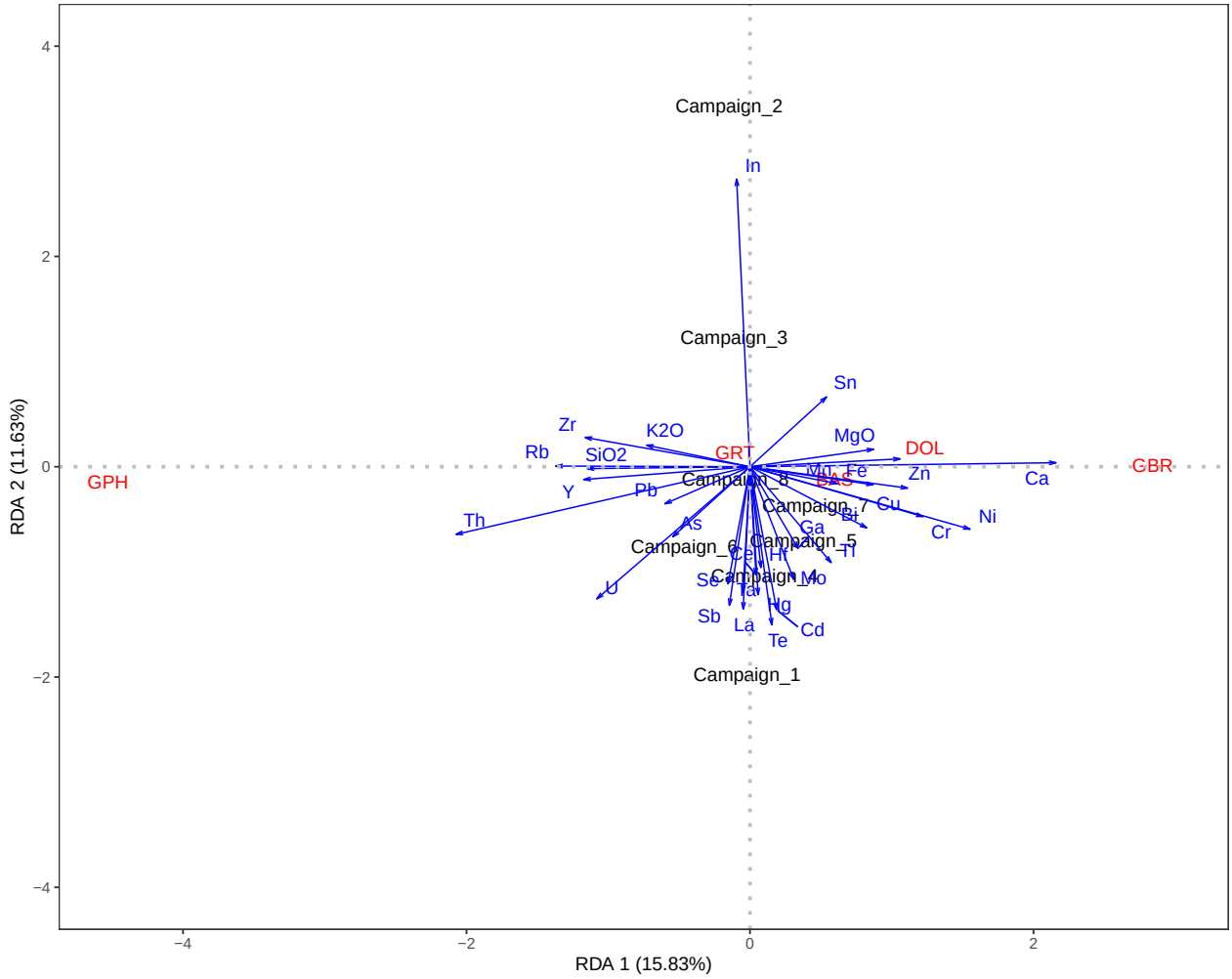

Figure 7.5-2: RDA biplot showing the relationship between pXRF chemical elements, rock types, and the field campaigns 1 to 8.

Figure *7.5-2* shows a biplot for the pooled pXRF data from all eight campaigns in which pXRF measurements were taken, where the campaign number is included as an explanatory variable. There is only $\sim 27\%$ total variation explained by this RDA, which is a lot lower than for each individual campaign RDA. This RDA shows that campaigns 1, 4 to 8 are positively correlated, thus suggesting that these campaigns are similar in pXRF chemical elements. Campaigns 2 and 3 are positively correlated, this suggests these two campaigns are similar. Campaigns 1, 4 to 8 are negatively correlated with campaign 2 and 3, thus suggesting there are some differences in chemical element composition between these two groups.

7.5.3 Ratios of pairs of elements

In Monitoring Studies Report 2023 (Curtin University, 2023) and Monitoring Studies Report 2024 (Curtin University, 2024c), ratios of pairs of elements were used to assess the utility of pXRF as a way to monitor patina composition and thickness. In last year's report (Curtin University, 2024c) boxplots of SiO_2/Ti by campaign were presented both with and without winsorization, for campaigns 1 to 7. In addition, last year's report (Curtin University, 2024c) displayed the spatial smoothing of SiO_2:Ti ratio in granophyre (GPH) for campaigns 1 to 7. In this section, the boxplots and spatial smoothing of SiO_2:Ti ratio have been updated to also include campaigns 8 and 9.

Figure *7.5-3* shows the boxplots of SiO_2 to Ti ratio by campaign and coloured by rock type. There were a few extremely high values amongst these ratios. The technique of winsorization described in Appendix F Monitoring Studies Report 2024 (Curtin University, 2024c), increases robustness and resistance to outliers by reducing extreme values without removing them.

Figure *7.5-4* shows the boxplots of the SiO_2 to Ti ratio after winsorization. These boxplots show that dolerite has the lowest median ratio, while granite has the highest median ratio among all other rock types. Gabbro has a higher median ratio compared to granophyre and basalt.

Similar to last year's report (Curtin University, 2024c), the SiO_2:Ti values vary systematically with rock type (Figure *7.5-4*), so the different rock types were separated in the spatial-smoothing analysis.

Figure *7.5-5* shows spatially smoothed SiO_2:Ti values for rocks classified as granophyre only, based on pXRF data from campaigns 1 to 9. Assayed values of SiO_2 and Ti lower than 50 ppm, and missing values, were reset to 50 ppm. The individual ratios exhibited considerable variation and a strongly skewed distribution, so the smoothing was performed on a logarithmic scale.

Figure *7.5-5* panels for campaigns 5 and 8 show substantially higher values of SiO_2:Ti in the north (Gidley and Dolphin Islands). Also, campaign 7 has the highest ratio in the northern part of the peninsula. Campaign 3 has the lowest ratio over the entire region. There is no apparent spatial trend in element-composition ratios within a particular rock type. The same analysis was done for some other major element ratios, including the ratios of manganese to silica, sulfur to silica, chlorine to silica, and vanadium to silica. No systematic trends in these ratios were observed.

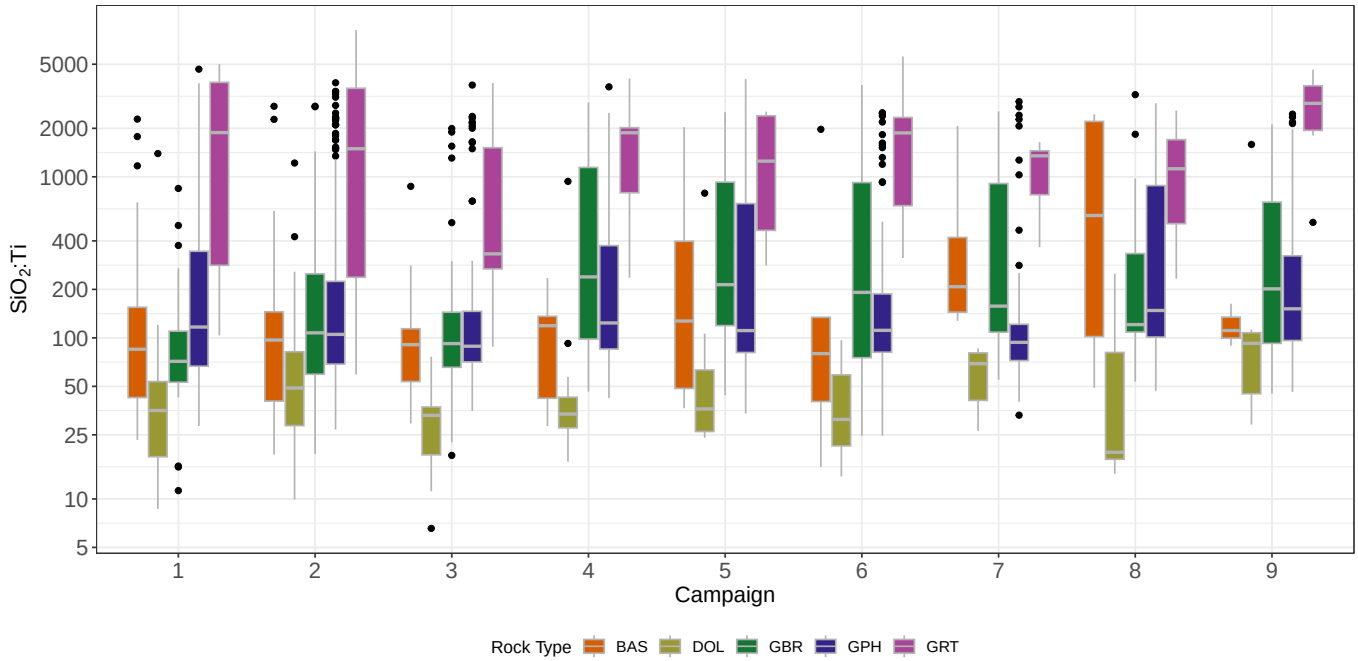

Figure 7.5-3: Boxplots of SiO_2:Ti by campaign, coloured by rock type. Note logarithmic scale.

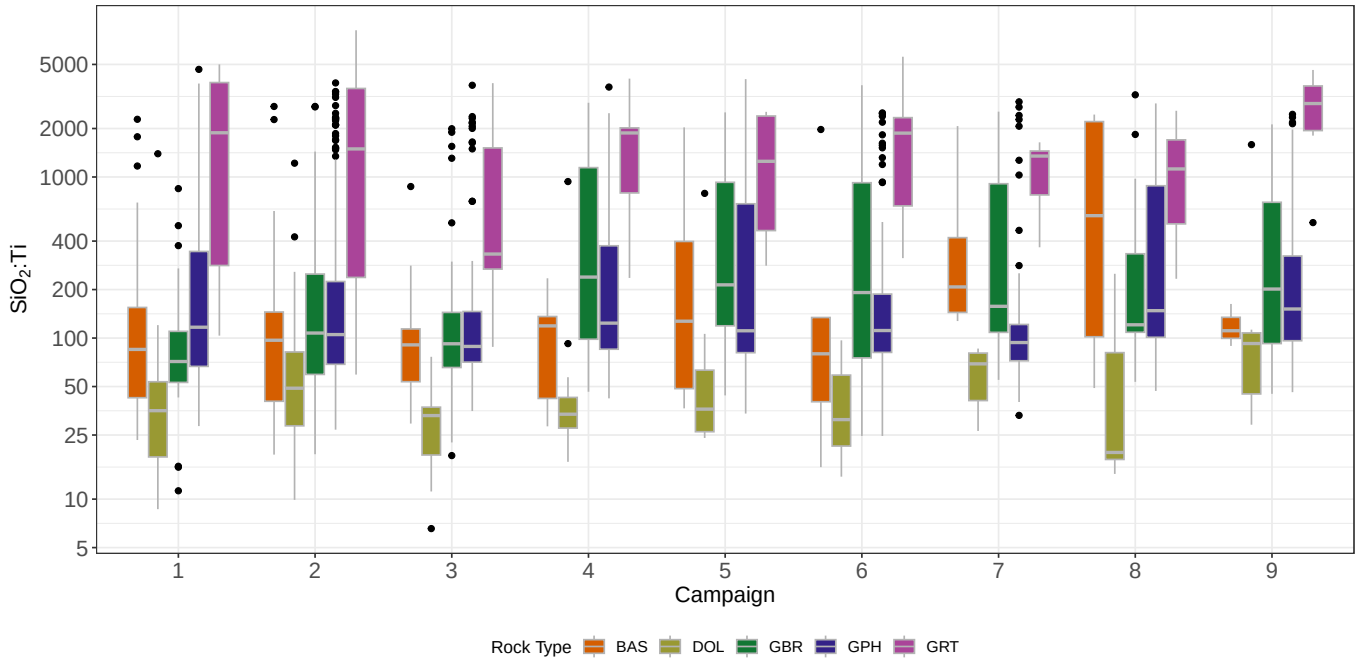

Figure 7.5-4: Boxplots of SiO_2:Ti ratio by campaign after winsorization, coloured by rock type. Note logarithmic scale.

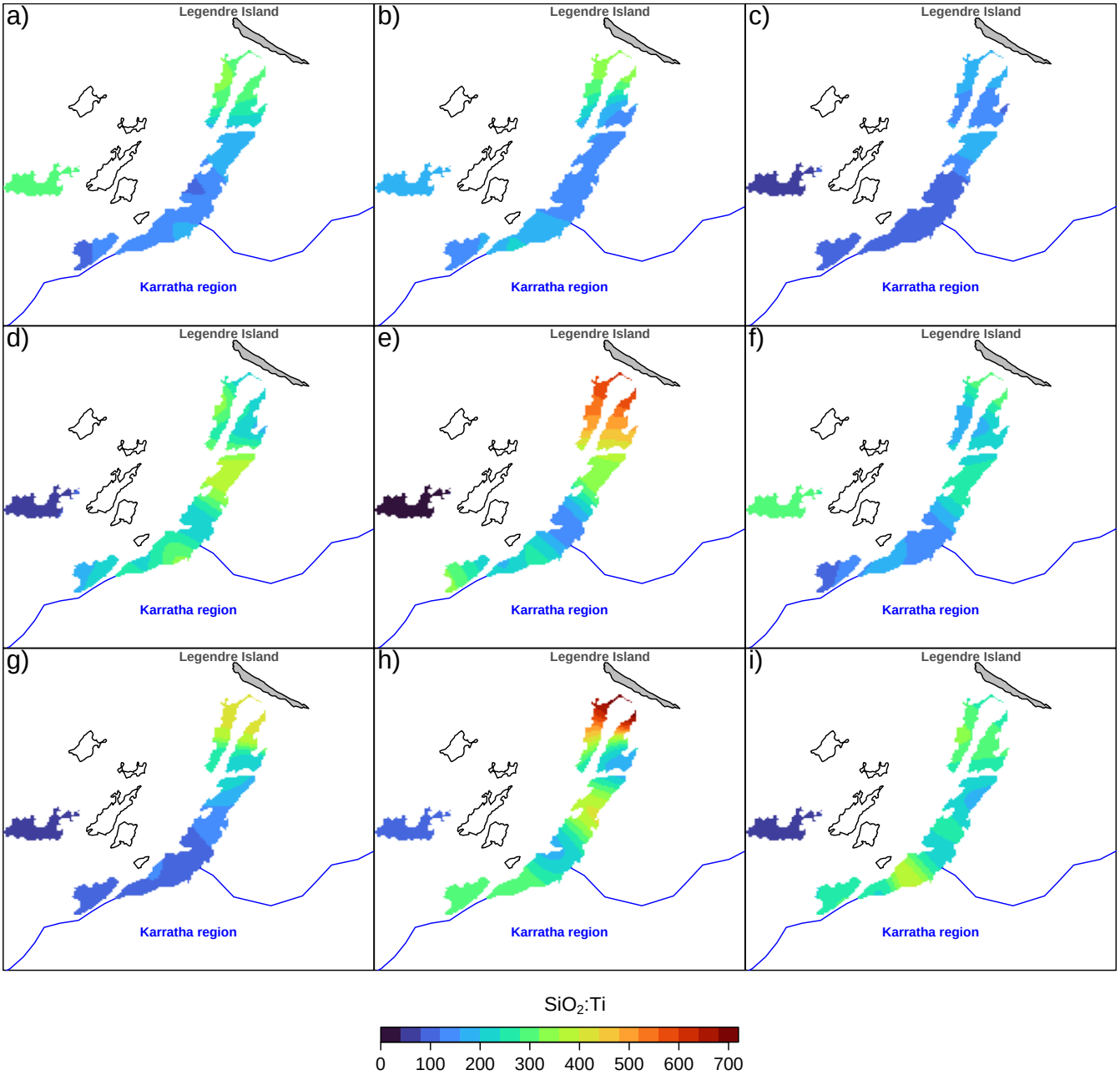

Figure 7.5-5: Spatial smoothing of SiO_2:Ti ratio in granophyre (GPH) of campaigns 1 (a) to 9 (i), respectively. The white colour polygons are the islands with no granophyre samples.

7.5.4 pXRF measurements on rock cube samples

Section 7.4.6 describes the unpatinated rock cubes installed at the industry and MRAMP AQMs. During campaign 9, pXRF was measured on the rock cubes to enable a comparison amongst patinated and unpatinated rocks, and to serve as a baseline for changes in composition of the unpatinated rocks after exposure within the AQMs.

Figure *7.5-6* shows the boxplots of SiO_2:Ti by rock type measured on rock cube samples. Figure *7.5-7* shows the boxplots of the SiO_2:Ti by rock type after winsorization. Both boxplots show that granite has the highest SiO_2:Ti ratio and dolerite and basalt has the lowest SiO_2:Ti ratio. This is similar to the patinated rocks.

Figure *7.5-8* shows the RDA biplot for rock cube pXRF and rock type data. Similar to the patinated rocks, the unpatinated granophyre (GPH) was positively correlated with Thorium (Th) and positively correlated with Rubidium (Rb). The unpatinated dolerite (DOL) was positively correlated with Titanium (Ti). Dolerite and basalt (BAS) were positively correlated for the unpatinated rocks, which also occurred in the RDA biplots for campaign 3, 4, 6, 7, 8 and 9 in the patinated rocks.

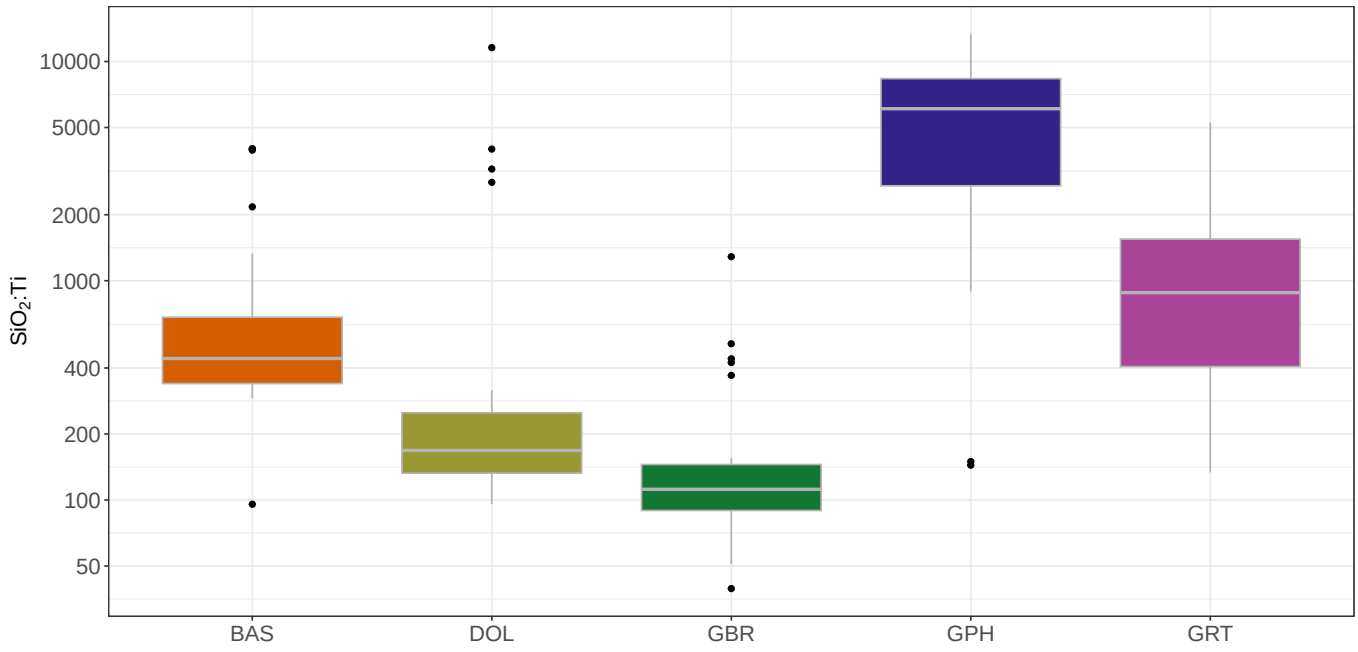

Figure 7.5-6: Boxplots of SiO_2:Ti measured on rock cube samples coloured by rock type. Note logarithmic scale.

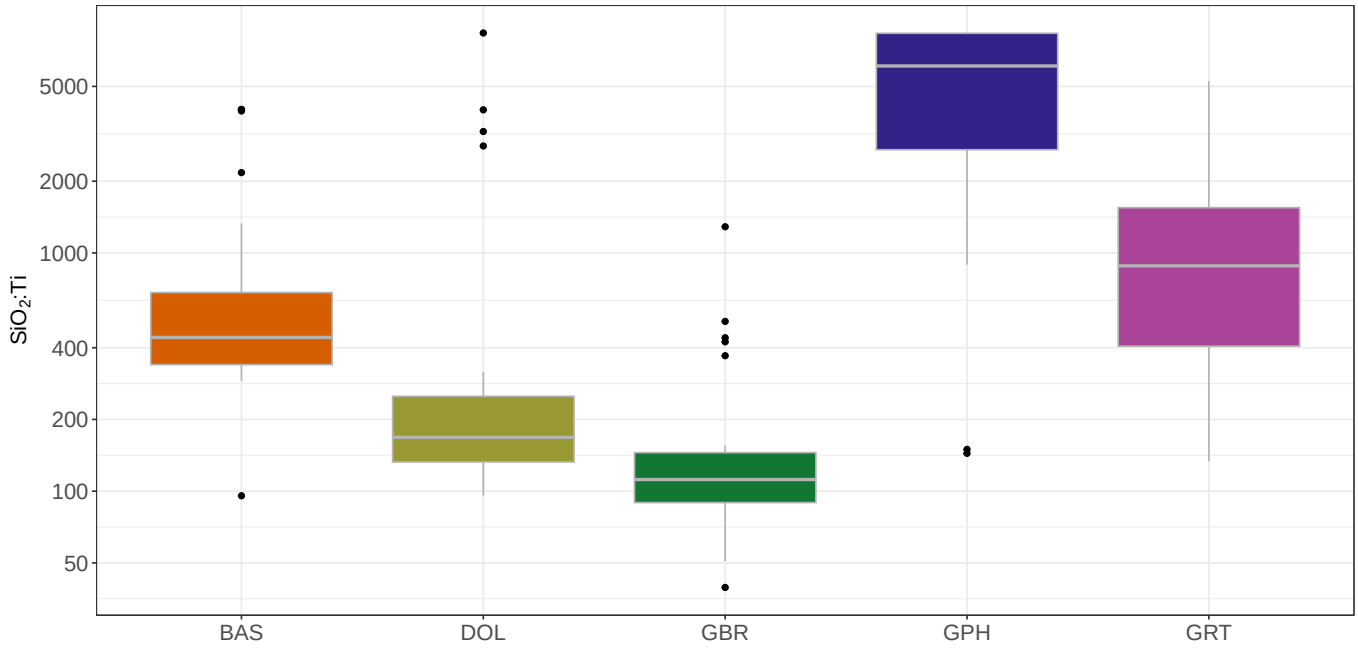

Figure 7.5-7: Boxplots of SiO_2:Ti measured on rock cube samples after winsorization, coloured by rock type. Note logarithmic scale.

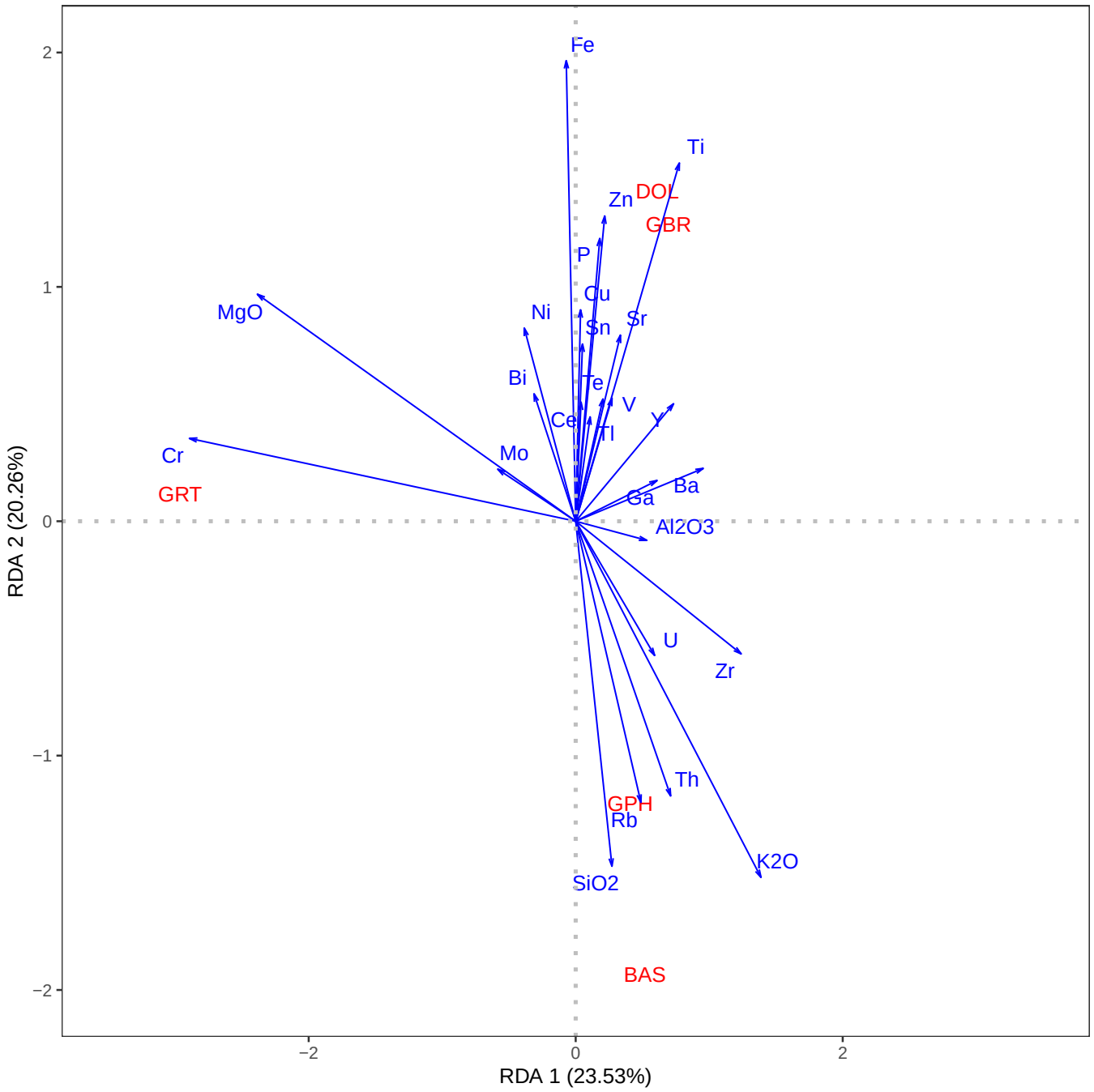

Figure 7.5-8: RDA biplot showing the relationship between chemical elements from the pXRF and rock types in rock cube samples. Percentage in parentheses is the percentage of total variation explained by the RDA.

7.6 Inorganic geochemistry – porosity

Microscope images of thin sections of sample rocks from Murujuga show that the rock is porous (i.e., holes are present) in the shallow layer within a few millimetres of the rock surface. Section 7.6 of the Monitoring Studies Report 2024 (Curtin University, 2024c) noted that granophyre rocks taken from different locations across Murujuga had quite substantial differences in porosity. The investigation concluded that there is statistically significant evidence of elevated porosity in a region close to Dampier and King Bay. The most plausible explanation is that chronic exposure to industrial emissions has caused porosity to increase in this region, by a mechanism that remains to be established.

In order to scrutinise and validate this finding, it was recommended that:

(1) additional sample rocks be collected for porosity analysis;
(2) measurements of rock *permeability* be obtained at many sites across Murujuga.

The purpose of (1) is to increase the sample size of the porosity dataset and to reduce any gaps in spatial coverage, thereby increasing statistical power and allowing more searching scrutiny of the findings. However, it is not feasible to collect many sample rocks for porosity analysis, because the procedure for measuring porosity is costly, time-consuming, and destructive (the sample rock is physically removed from its original location and cut into thin sections).

The purpose of (2) is to obtain complementary information with much greater sample size, by using the cheaper and non-destructive measurement of permeability as a surrogate for porosity (Section 3.2.4.3).

This section reports on the analysis of rock porosity using the expanded dataset obtained from the original 64 sample rocks and 20 additional samples collected in the current study year (see Section 3.2.4.6). Section 7.7 presents the analysis of the field measurements of permeability.

7.6.1 Locations of sample rocks

Figure *7.6-1* shows the spatial locations where sample rocks were obtained originally in year one and in the supplementary year three collection. This map, and all the analysis reported in this section, relates to the sample rocks that were classified as granophyre. Although a few sample rocks belonging to other rock types were collected, the analysis in this section is restricted to the granophyre samples, which allowed a valid comparison between results from different locations.

Originally, sample rocks were obtained from AQ, EX and RS sites, at locations that had been carefully selected according to the original protocol described in the Monitoring Studies Data Collection and Analysis Plan (Curtin University, 2022) and the Monitoring Studies Report 2023 (Curtin University, 2023). These sample rocks have subsequently been designated as Group A. In 2025, using improved knowledge of the distribution of granophyre, 16 sample rocks were collected to reduce any gaps in the spatial coverage. These have been designated as Group B. A further four sample rocks were collected from a railway cutting that was constructed around the same time that industrialisation of the Burrup Peninsula commenced. These are designated as Group D samples. Analysis of the Group D samples will be included in the final MRAMP report.

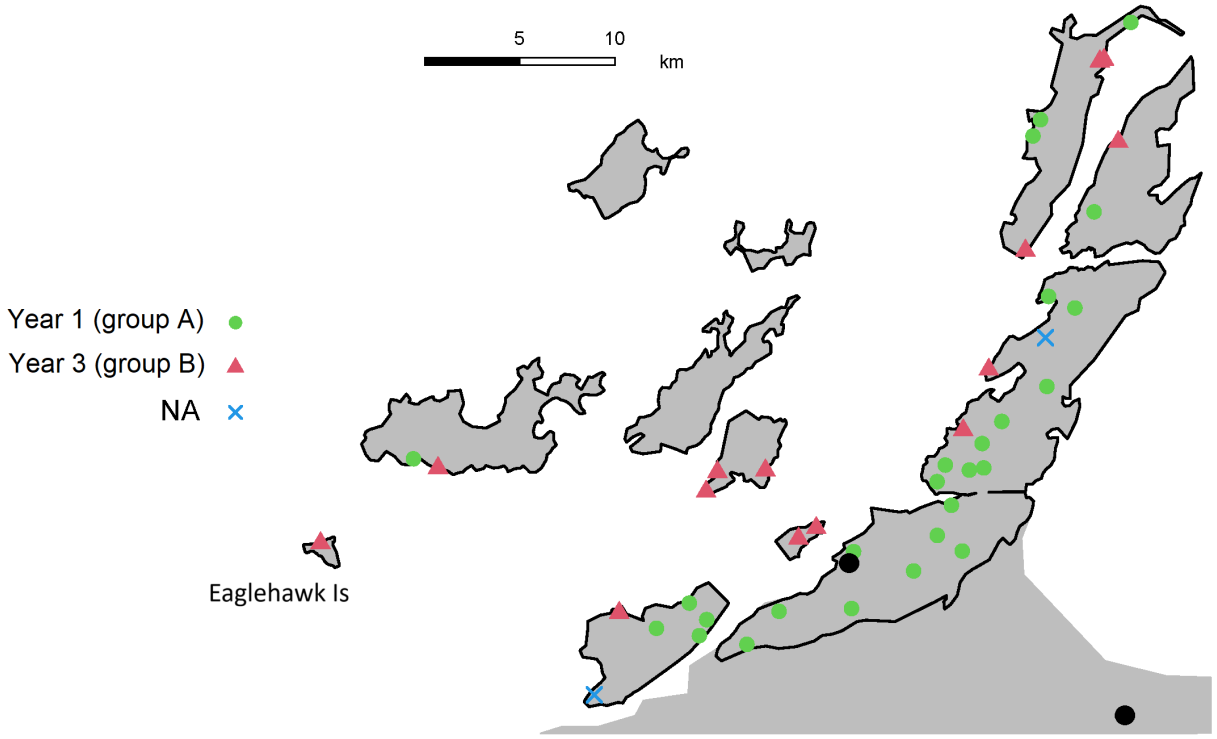

Figure 7.6-1: Locations of sample rocks collected in Years One (Group A) and Three (Group B), respectively. "NA" indicates locations of samples that did not provide usable data. Black circles indicate location of Dampier and Karratha town centres.

Table 7.6-1: Number of SEM images of thin-sections, and number of distinct spatial locations, in sample Groups A and B for the porosity study. "NA" indicates locations where sample images were unusable.

Sample Group	Images	Locations
A	99	26
B	55	14
NA	0	2
TOTAL	154	42

Table *7.6-1* shows the number of distinct spatial locations and the number of Scanning Electron Microscope (SEM) thin-section images obtained in each sample Group.

Two locations are labelled NA in Figure *7.6-1* and Table *7.6-1*, indicating that no data were produced from these locations because there were technical problems with the thin-section image. The sample rocks from these locations will be re-cut and analysed in subsequent work.

Eaglehawk Island, the small island at the extreme south-west of the map in Figure *7.6-1*, is excluded from the subsequent analysis, in order to avoid technical problems with the spatial smoothing technique. This decision is unlikely to have had a material effect on the analysis.

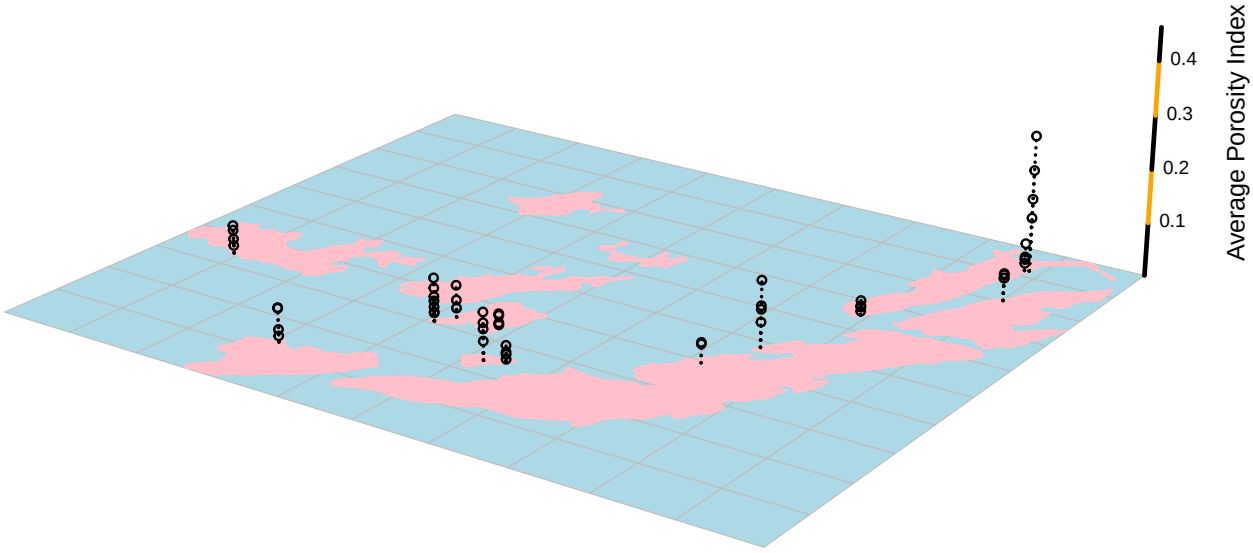

Figure 7.6-2: Values of average porosity index for each Group B rock sample collected (excluding Eaglehawk Island). Perspective view with dot height equal to porosity index value. The scale is identical to that in the next Figure 7.6-3.

7.6.2 Porosity analysis

Section 7.6 and Appendix F.2 of the last year's report (Curtin University, 2024c)described techniques for inferring the porosity of rock, and especially for inferring the variation in porosity as a function of depth below the rock surface. This is done from microscope images of thin sections of sample rocks. In last year's report (Curtin University, 2024c), these techniques were applied to 99 images of thin sections of granophyre. For this report, the same techniques were applied to the additional granophyre samples.

Figure *7.6-2* shows (in perspective view) the resulting values of the average porosity index (averaged from depth 0 to depth 3.1 mm) for the 52 thin-section images of rock samples collected in Year Three, plotted at the corresponding spatial locations of the sample rocks. Individual porosity index values in Group B range from 0.003 to 0.254 (porosity 0.3% to 25.4%).

Figure *7.6-3* shows the pooled dataset of average porosity index values from sample Groups A and B combined. Individual porosity index values in the pooled sample range from 0.003 to 0.461 (porosity 0.3% to 46.1%).

The porosity index values depicted in Figure *7.6-3* show variability between replicates, as well as a suggestion of a spatial trend. Variability between replicates is expected to be present in data obtained using stereological methods (Baddeley and Jensen, 2005, chap. 13). There are several

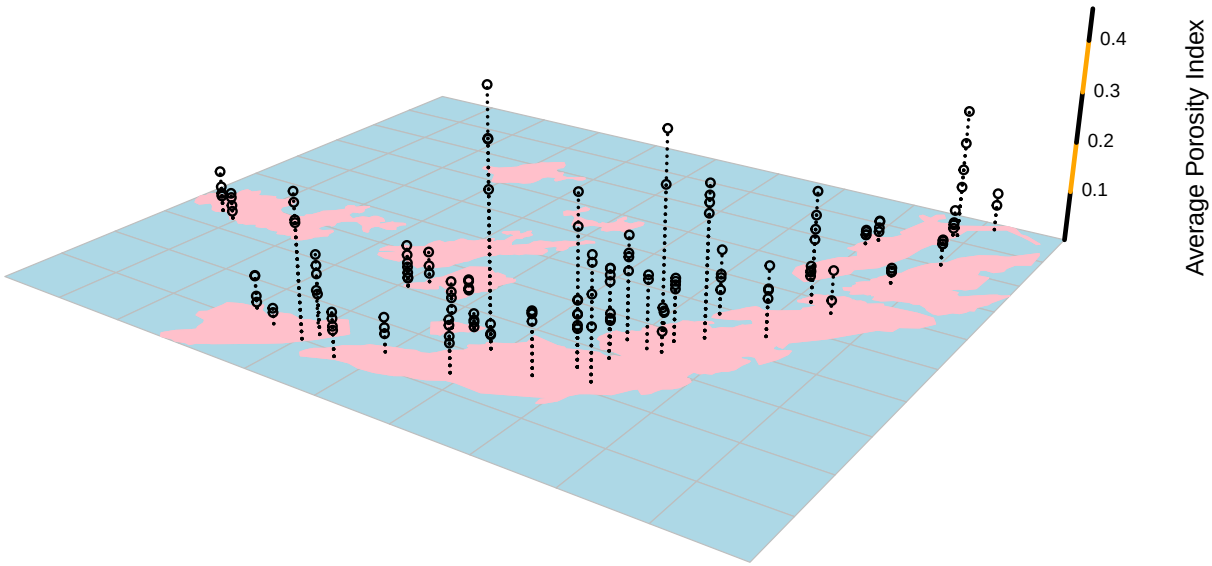

Figure 7.6-3: Values of average porosity index for the full Group A and B rock-sample collection (excluding Eaglehawk Island). Perspective view with dot height equal to porosity index value. The scale is identical to that in the previous Figure 7.6-2.

sources of such variability. Porosity index values obtained from different thin sections of the same rock are subject to sampling variability. Differences between individual rocks and between different surfaces of the same rock, are also expected to occur naturally. The variability apparent in the raw data from each spatial location incorporates all such sources of variability.

7.6.3 Spatial analysis

A visual impression of a spatial trend in porosity is evident to some degree in Figure *7.6-3*. This impression is strengthened in Figure *7.6-4*, which shows the “sitewise mean” porosity values. That is, for each spatial location where rock samples were obtained, the mean of the porosity index values for the samples from that location was calculated. The figure shows a single spike at each location, with height equal to the mean porosity at that location. The sitewise mean porosity values range from 0.017 to 0.253 (porosity 1.7% to 25.3%).

In Section 7.6 of the Monitoring Studies Report 2024 (Curtin University, 2024c), spatial trends in porosity were investigated by spatially smoothing the porosity index values. Figure *7.6-5* shows the same smoothing technique applied to the pooled data from the Group A and B samples. The input data were the average porosity index values from sample Groups A and B, with each value attributed to the original spatial location of the samples of rock. Nadaraya-Watson spatial smoothing (explained in Appendix F.1 of the Monitoring Studies Report 2024 (Curtin University, 2024c)was applied using an isotropic Gaussian kernel with an initial bandwidth of 2 km. The Nadaraya-Watson smoother uses least-squares validation which semi-automates the bandwidth. The bandwidth value is based on the most practical value. The value and hence the colour of the image at any spatial location is determined by a weighted average of the porosity index values observed at sites close to that location; the closer the site, the larger the weight. The smoothed porosity values range between 0.007 and 0.218 (porosity 0.7% to 21.8%). A porosity value of 0.2 is substantial (indicating that 20% of the volume is occupied by voids). Figure *7.6-4* shows there are differences in porosity values for different spatial locations, which result in substantial variations in the spatially smoothed porosity estimates seen in Figure *7.6-5*.

Grey shading in Figure *7.6-5* indicates land areas that were not considered in the analysis, including islands where no data was collected, and regions outside the study area.

Figure *7.6-6* shows the spatially-weighted *median* of the same porosity data. The median values range between 0.015 and 0.370 (porosity 1.5% to 37%), again indicating that the spatial component of variation is substantial.

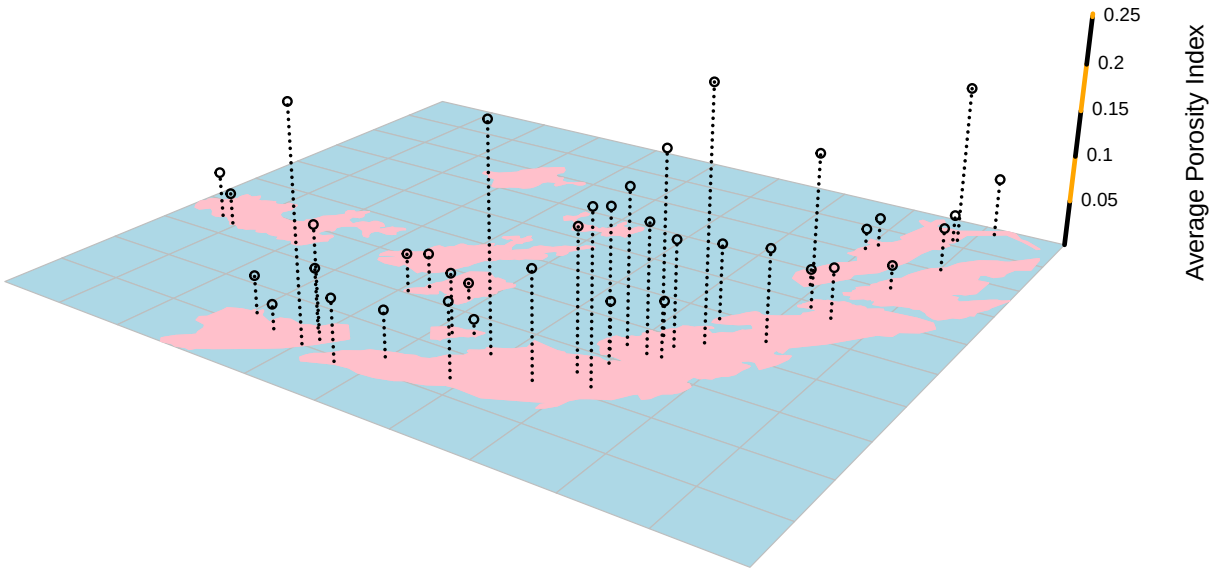

Figure 7.6-4: Sitewise mean of average porosity index for the combined Group A and B rock sample collection. Perspective view with dot height proportional to the mean of the porosity-index values at each location. Note the scale is different from that in Figures 7.6-2 and 7.6-3.

Figure 7.6-5: Spatially smoothed (Nadaraya-Watson) average porosity index based on data from the combined Group A and B rock samples. A Gaussian kernel with bandwidth 1.5 km was used. Pink circles indicate the locations of Dampier and Karratha town centres.

Figure 7.6-6: Spatially weighted median of average porosity index based on data from the combined Group A and B rock samples. Gaussian kernel with bandwidth 2.5 km.

7.6.4 Statistical significance — correction to Monitoring Studies Report 2024

In Section 7.6 of the Monitoring Studies Report 2024 (Curtin University, 2024c), a Monte Carlo test yielded statistically significant evidence that porosity is elevated, relative to the overall average porosity, in an area of Murujuga close to Dampier and King Bay. Figure *7.6-7* is a copy of Figure 7.6-9 from the Year Two report.

Due to a coding error, the analysis in the Year Two report unintentionally applied the significance threshold α=0.005 instead of the conventional standard α=0.05. That is, the analysis inadvertently applied a much stricter standard of statistical significance than the customary standard.

Consequently in Figure *7.6-7*, panel (a) showing the pointwise p-value is correct, but in panel (b), the orange-coloured area is incorrect, and it is in fact the region where the pointwise p value is less than or equal to 0.005, instead of 0.05 as intended. The result is that the orange region originally shown in Figure 7.6-9 of the Monitoring Studies Report 2024 (Curtin University, 2024c) and reproduced in Figure *7.6-7*:

- is an underestimate of the area where there is statistically significant evidence of elevated porosity (according to the conventional standard α=0.05);
- can be interpreted as a region where there is extremely strong evidence of elevated porosity (according to the much stricter standard α=0.005).

Figure *7.6-8* shows a corrected version of Figure 7.6-9 of the Monitoring Studies Report 2024, using the intended, conventional significance level α=0.05.

The correction to the computer code has the effect that the region labelled orange (SIGNIF) has grown from 44 km^2 to 75 km^2. In the previous report, the orange area was described as being "centred on Dampier and King Bay". The orange area shown in the corrected Figure *7.6-8* could be more accurately described as an area centred on King Bay and ranging from Dampier town and Rio Tinto's 2-Mile Rail Maintenance Yard in the south to Withnell Bay and Cowrie Cove in the north.

A "global" p-value was also reported in the Monitoring Studies Report 2024 (Curtin University, 2024c). This is a single measure of the strength of evidence. The originally reported global p-value was 0.001; this was incorrect due to the coding error. The correct global p-value obtained is 0.002. The overall conclusion from the previous data analysis remains: there is statistically significant evidence of elevated porosity in the region centred around King Bay relative to the remainder of the monitored study area.

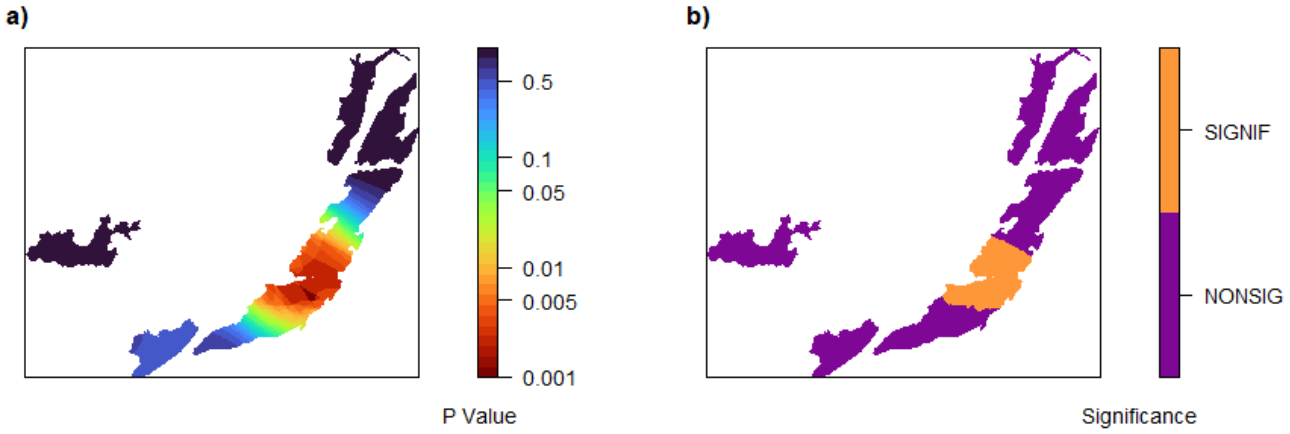

Figure 7.6-7: Copy of Figure 7.6-9 of the Monitoring Studies Report 2024 (Curtin University, 2024c). Monte Carlo test of the null hypothesis of constant mean porosity against the alternative of locally elevated porosity, based on the data from Group A sample rocks only. (a) p-value of the pointwise Monte Carlo test; (b) orange colour identifies the region where the pointwise test is statistically significant at level α=0.005 (erroneously stated as α=0.05 in the Monitoring Studies Report 2024).

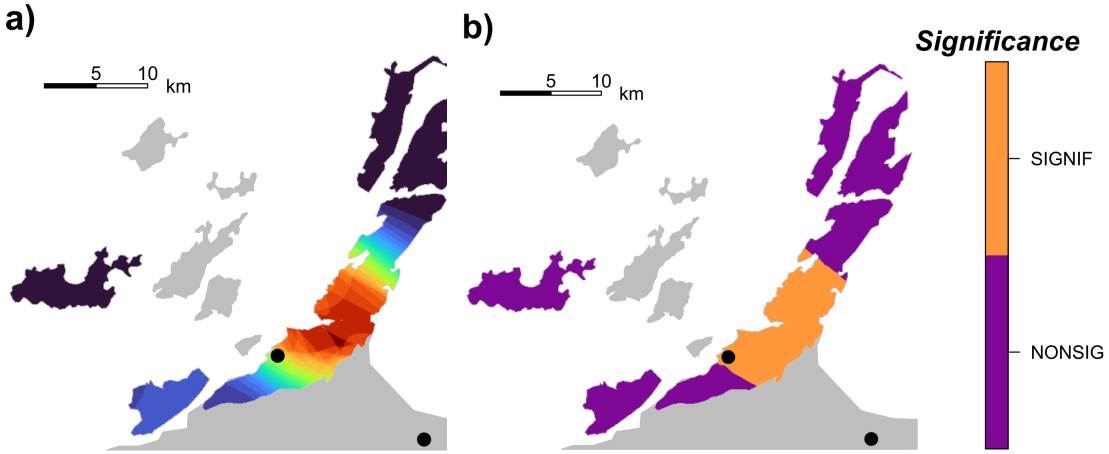

Figure 7.6-8: Corrected version of Figure 7.6-9 of the Monitoring Studies Report 2024 (Curtin University, 2024c). Monte Carlo test of the null hypothesis of constant mean porosity against the alternative of locally elevated porosity, based on the data from Group A sample rocks only. (a) p-value of the pointwise Monte Carlo test; (b) orange colour identifies the region where the pointwise test is statistically significant at level α=0.05. Blue cross-hair symbol indicates the location of Karratha town centre.

7.6.5 Statistical significance — updated analysis with this year's data included

Figures *7.6-9* and *7.6-10* show the results of the statistical significance analysis applied to the granophyre porosity data from the combined Group A and B samples.

Figure *7.6-9* shows the p-value of the pointwise Monte Carlo test of the null hypothesis of constant mean porosity against the alternative hypothesis of locally elevated porosity. The test involved m=999 random permutations of the porosity data. Smaller values of p indicate stronger evidence against the null hypothesis in favour of the alternative. Details of the Monte Carlo test technique are given in Appendix F of the Monitoring Studies Report 2024 (Curtin University, 2024c).

Note that in Figure *7.6-9*, there are fewer areas coloured grey than there are in Figure *7.6-8*, because data has now been collected from East Lewis Island and East Intercourse Island.

In Figure *7.6-10*, the locations coloured orange are those locations where the pointwise Monte Carlo test is statistically significant according to the conventional standard of evidence, namely, these are the locations where the pointwise p-value is less than or equal to 0.05. In brief, at each location coloured orange in the figure, there is statistically significant evidence that the porosity of rocks in the vicinity of this location is elevated, relative to the overall average porosity. In the analysis presented here (after correction of coding errors), the orange-coloured region has increased in area by about 7%, from 74.97 km^2 to 80.48 km^2. The interpretation of these figures is similar to the results of Section 7.6 in the Monitoring Studies Report 2024 (Curtin University, 2024c).

Figure *7.6-11* shows the effect of changing the pointwise significance level (0.005, 0.01, 0.05 and 0.1) for the outcome of the Monte Carlo test shown in Figure *7.6-10*. The area considered significant increases as the significance level increases. The changes in the area considered significant at different levels are relatively small but remain centred around King Bay. Figure *7.6-11* a) shows the pointwise significance area at level 0.005, which is equivalent to the significance level used in the previous study report (Curtin University, 2024c). Here the area of significance has increased slightly compared to the previous study report (Curtin University, 2024c) with the additional samples from Group B included.

In order to avoid the technical problem of multiple hypothesis testing, a "global" test of significance is required. The distinction between "pointwise" and "global" tests was explained in Section 7.6 of the previous study report (Curtin University, 2024c). Following the procedure outlined there, and using the pooled data from Group A and B samples, the global hypothesis test yielded a p-value of 0.001, indicating very strong evidence that there is an area of Murujuga where porosity is elevated relative to the overall average.

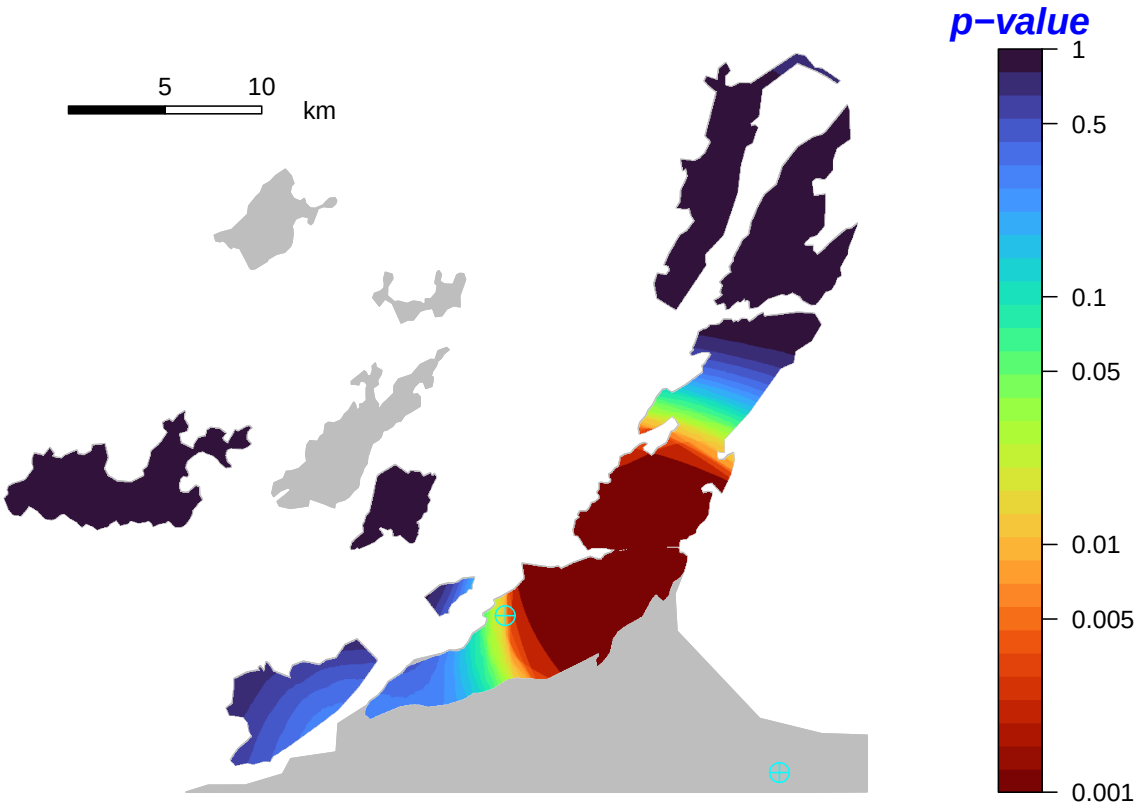

Figure 7.6-9: p-value of the pointwise Monte Carlo test of the null hypothesis of constant mean porosity against the alternative of locally elevated porosity, based on the pooled data from Group A and B samples. Blue cross-hair symbols indicate town centres of Dampier and Karratha.

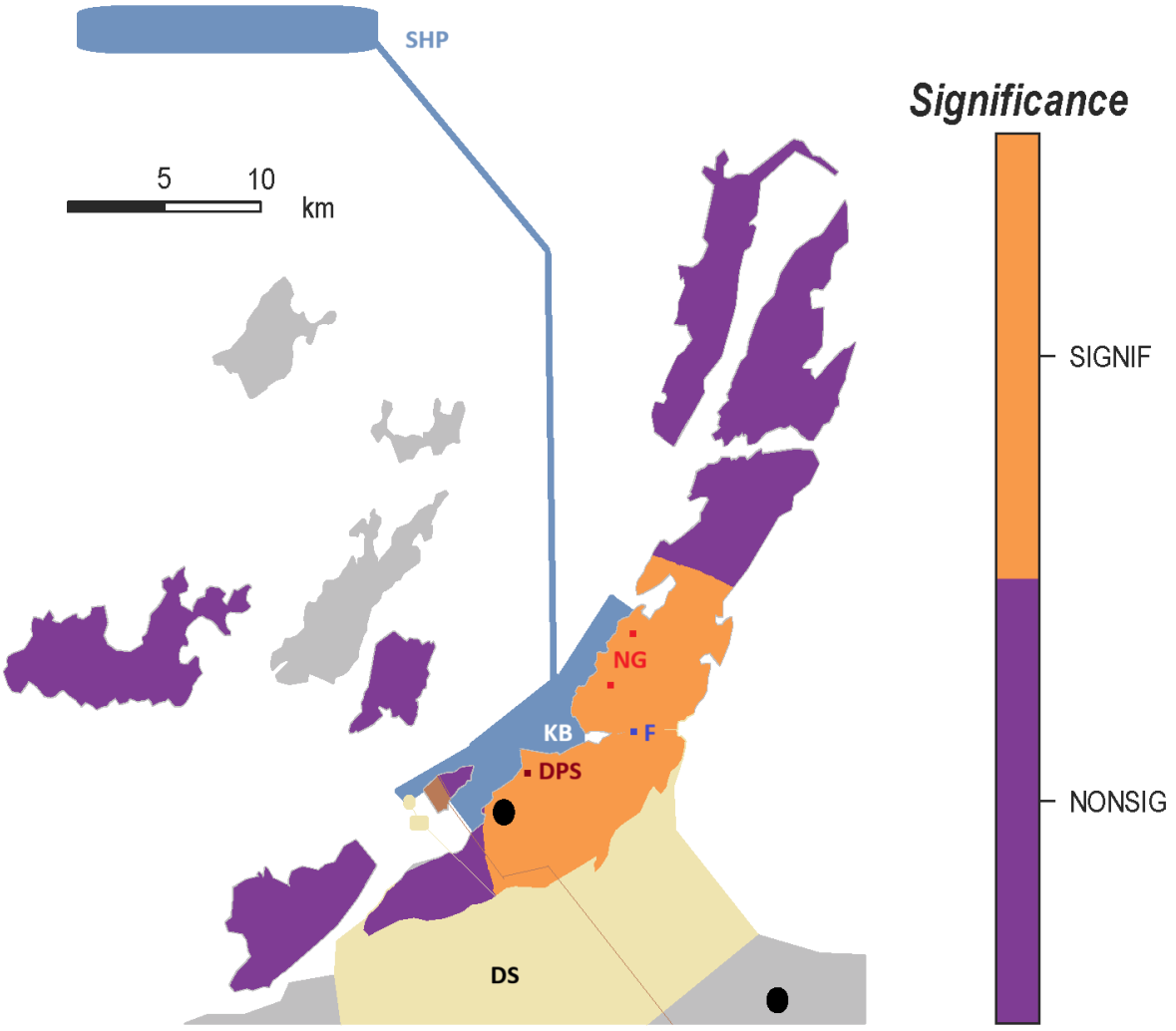

Figure 7.6-10: Pointwise statistical significance outcome for elevated rock surface porosity including Year Three data: either significant (SIGNIF) or non-significant (NONSIG) at level 0.05. Industry from Figure 1.1-1 (a) overlaid for context.

Figure 7.6-11: Pointwise statistical significance outcome for elevated rock surface porosity including Year Three data: either significant (SIGNIF) or non-significant (NONSIG) at level a) 0.005, b) 0.01, c) 0.05 and d) 0.1.

7.6.6 Conclusion of porosity

The overall conclusion of porosity is that:

1. There is very strong statistically significant evidence ($p <= 0.001$) that an area of Murujuga has elevated porosity;
2. The best estimate of the area of elevated porosity is the area coloured orange in Figure *7.6-10*, which is an area of 80 km^2, centred on King Bay and ranging from Dampier town and Rio Tinto's 2-Mile Rail Maintenance Yard in the south to Withnell Bay and Cowrie Cove in the north.

This page is intentionally blank.

7.7 Inorganic geochemistry – permeameter

7.7.1 Background

Section 7.7 of the Monitoring Studies Report 2024 (Curtin University, 2024c) details the background information and validation of the portable handheld device (TinyPerm 3) which measures the *permeability* ("air permeability") of the rock surface. During campaign 7, this instrument measured the permeability of 29 of the 41 visited rock art panels.

In year three, this instrument measured the permeability of all rock art panels visited during campaigns 8 to 10. Section 7.7.2 presents boxplots, spatial plots, and spatial smoothing of the permeability measurements from campaigns 7 to 10.

Section 7.4.6 describes the unpatinated rock cubes installed at the industry and MRAMP AQMs. During campaign 9, permeability was measured on the rock cubes to enable a comparison between patinated and unpatinated rocks. Section 7.7.3 presents boxplots and scatterplots of the permeability.

7.7.2 Permeability observations on rock surface

Figure *7.7-1* displays the boxplots (on a logarithmic scale) of the full set of permeameter measurements obtained in campaigns 7 to 10 by rock type.

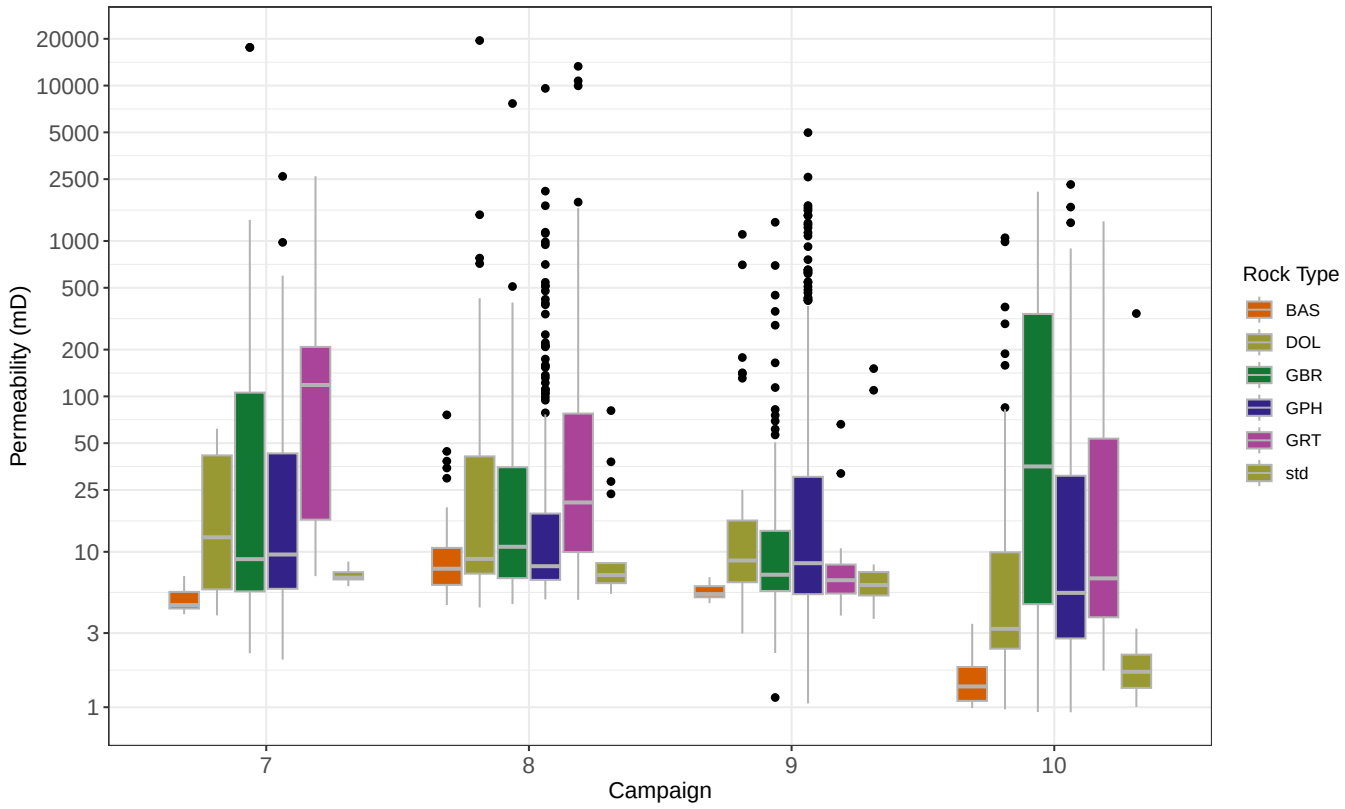

Figure 7.7-1: Permeability measurements for all sites and the dolerite standard for each rock type. Note logarithmic scale.

The data mostly ranged between 1 and 1000 mD, and there were some very large values recorded. For instance, there were many such values in campaign 8 due to an imperfect seal issue. Winsorization (Appendix F), Monitoring Studies Report 2024 (Curtin University, 2024c) was applied to reduce the impact of possible spurious outliers on subsequent analysis by limiting extreme values in the observed data without deleting extremes altogether. Figure *7.7-2* shows the boxplots of permeability after winsorization.

Granite shows the highest median permeability in campaigns 7 and 8, while basalt consistently has the lowest across all campaigns. Gabbro stands out in campaign 10 with the highest median permeability among all rock types. During campaigns 7 to 9, dolerite, granophyre, and gabbro generally exhibited similar median permeability values with moderate variability.

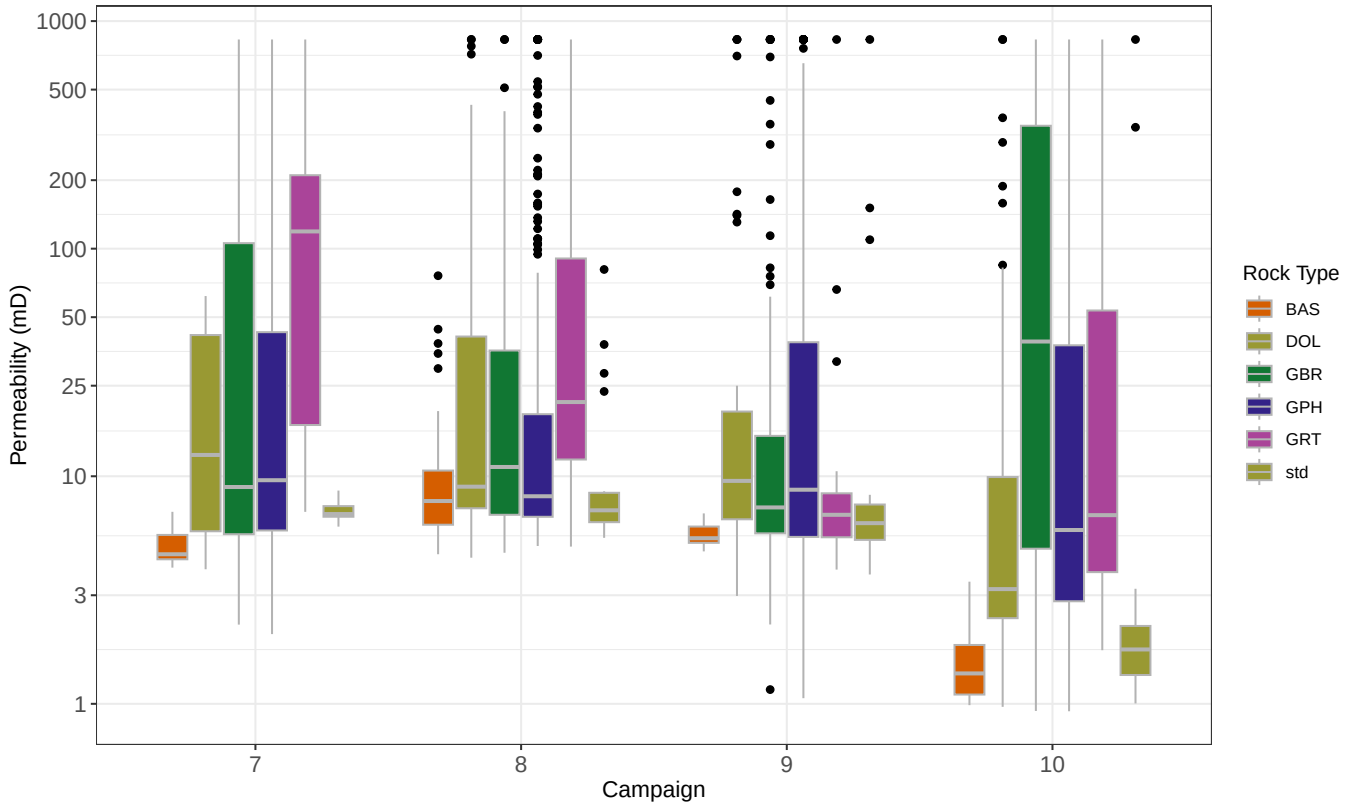

Figure 7.7-2: Permeability measurements for all sites and the dolerite standard after winsorization. Note logarithmic scale.

Figure *7.7-3* shows spatial point data, and Figure *7.7-4* shows spatial smoothing plots of the winsorized permeability measurements for granophyre only. The spatial trend is consistent between campaigns. In addition, the pattern of spatial variation in permeability appears broadly similar to that observed for the porosity data. The presence of extreme values in the permeability data was an additional challenge that was not present in the porosity data. Further investigation and observation is required; however this appears to be a promising approach for field monitoring.

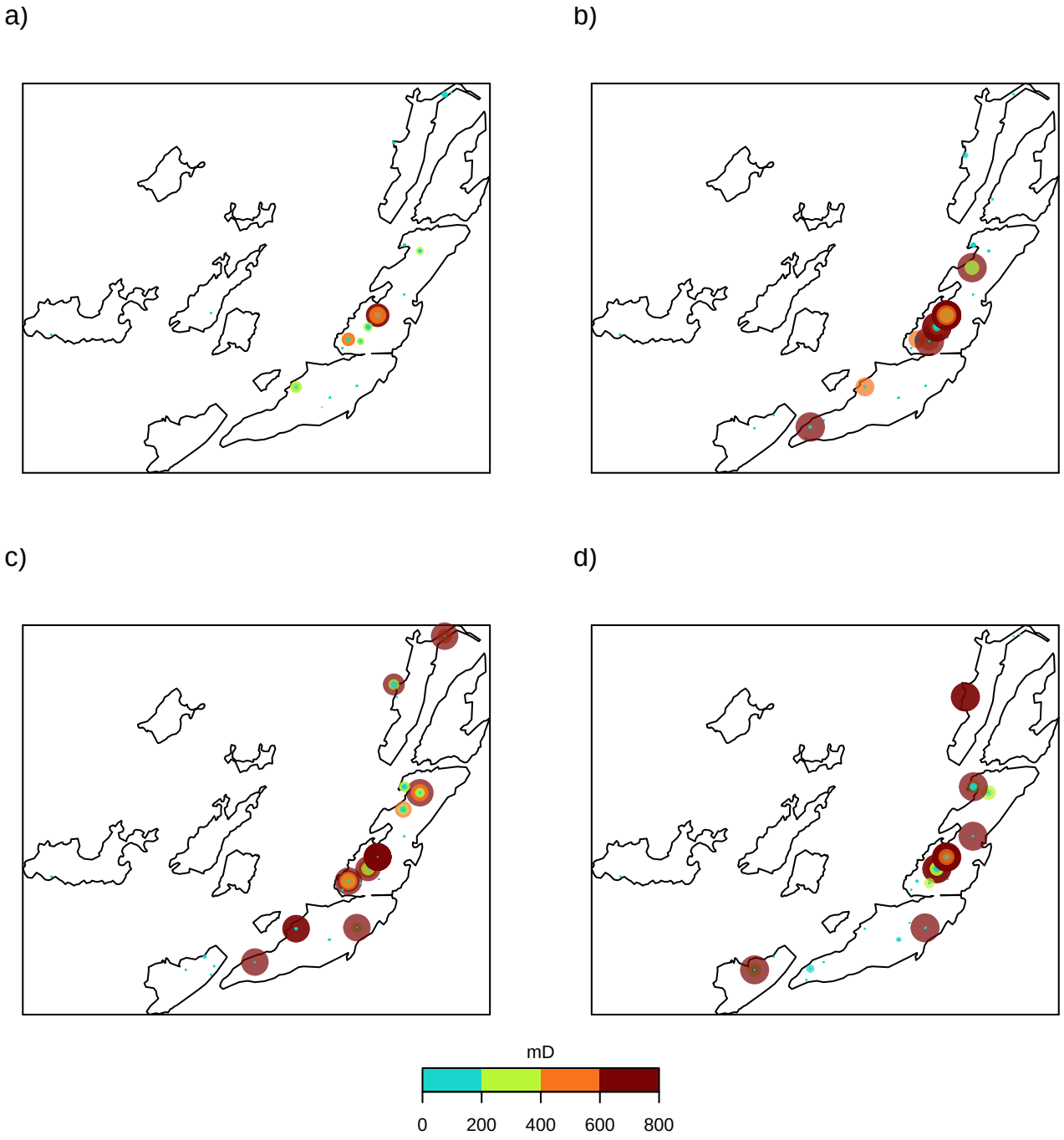

Figure 7.7-3: Spatial plots of winsorized permeability for campaigns 7 (a) to 10 (d), respectively.

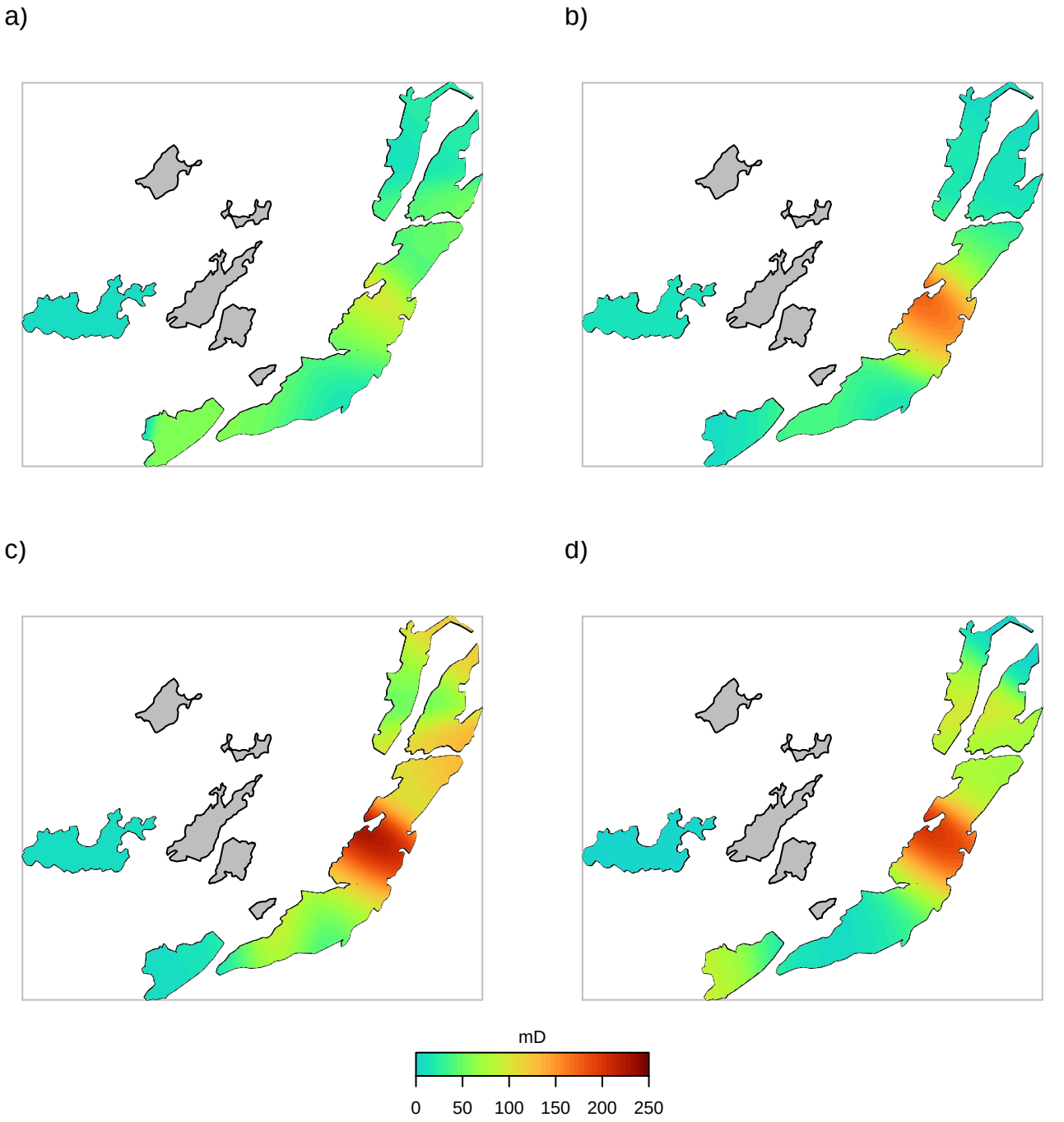

Figure 7.7-4: Spatial smoothing of winsorised permeability in granophyre (GPH) for campaigns 7 (a) to 10 (d), respectively. The grey-colour polygons are the islands with no granophyre samples.

7.7.3 Permeability observations on rock cubes

During campaign 9, the permeability of the unpatinated rock cubes were measured (see Section 7.4.6 for further details of the rock cubes). The objective of these measurements is to provide a baseline for any subsequent monitoring of these rock cubes.

Figure *7.7-5* displays the boxplots of the rock cube permeability measurements by rock type. Granite (GRT) had the highest permeability values for the unpatinated rock cubes. This was quite consistent with the patinated rock art panels, where granite typically had the highest permeability values over campaigns 7 and 8. Similar to campaign 10 in the patinated rocks, gabbro (GBR) had a high permeability values in the unpatinated rock cubes. In the patinated rock art panels, basalt had the lowest permeability values over campaigns 7 to 10. However, in the unpatinated rock cubes, basalt had the second highest median permeability value.

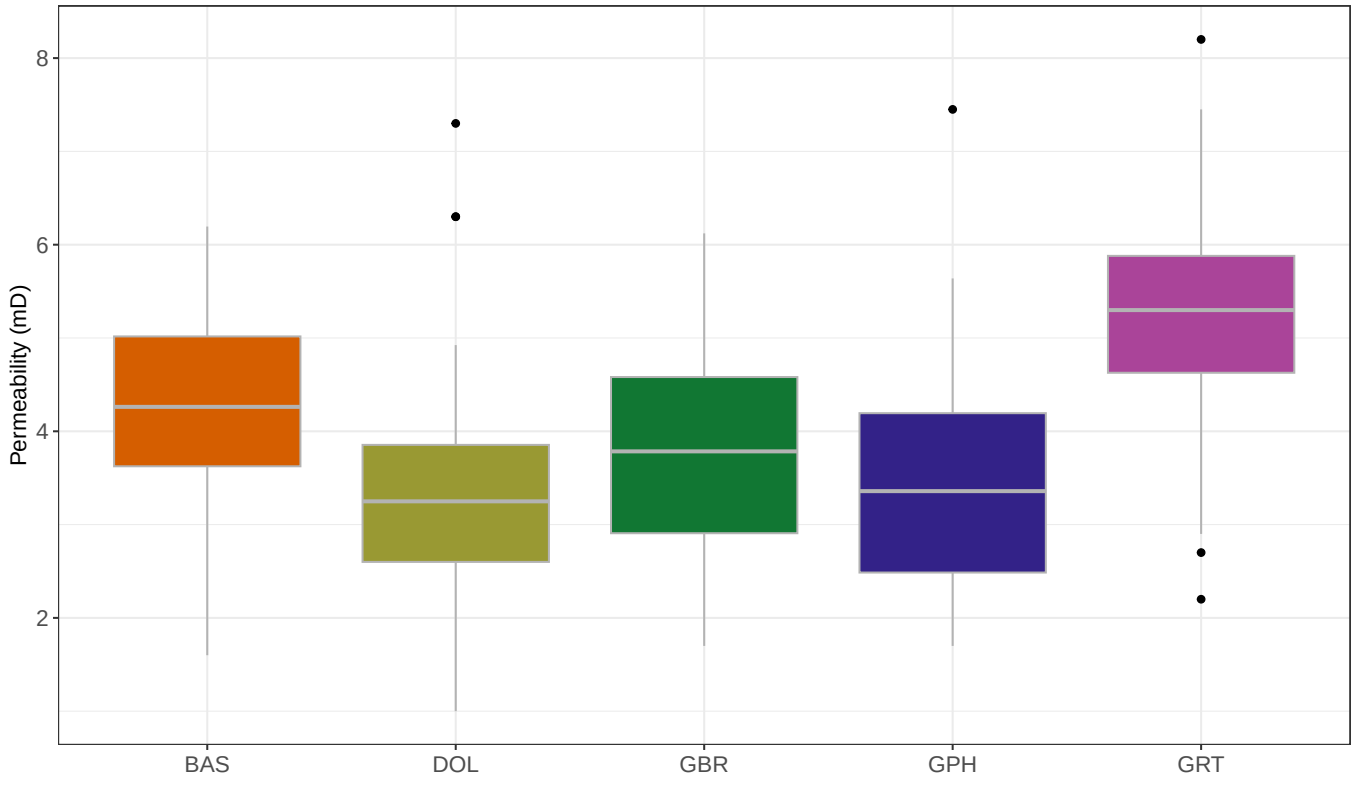

Figure 7.7-5: Boxplots of the winsorised unpatinated rock cube permeability measurements for each rock type, over all AQM sites.

Figure *7.7-6* shows the boxplots of rock cube permeability measurements by AQM site, in campaign 9, with the different rock types indicated also. The AQM sites that had the highest permeability measurements were AQ01, AQ03, AQ11, EX06, and EX09 powered station. Whereas the AQM sites with the lowest permeability measurements were AQ02, AQ10, and EX02. Each site displays a wide range of permeability, reflecting local heterogeneity in rock properties. Some patterns emerge — for example, GRT tends to cluster at higher permeability values, whereas GBR and BAS tend to cluster at the second highest permeability values in the majority of sites. No clear

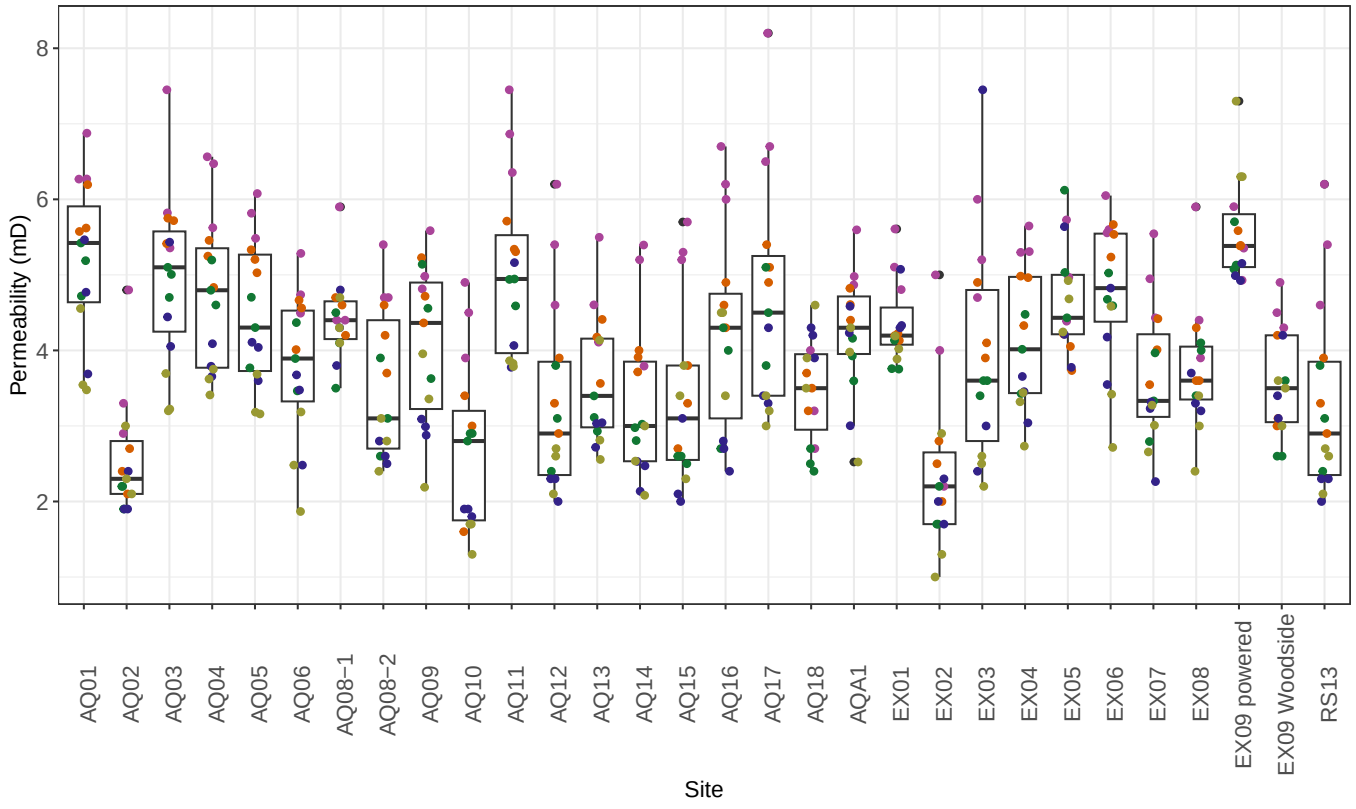

Figure 7.7-6: Boxplots of the winsorised unpatinated rock cube permeability measurements for each AQM site, coloured by each rock type.

overall trend in rock cube permeability variation across sites is evident; some sites (e.g., AQ08-1) show more consistent permeability, while others (e.g., EX03) display greater variability.

7.8 Microbiome

The Monitoring Studies Data Collection and Analysis Plan (Curtin University, 2022) specified that samples of material would be collected from the patina, the weathered rind, lichen patches, and soil, for the purpose of analysing the microbiome (the collection of all microbes). Section 7.8 of the Monitoring Studies Report 2024 (Curtin University, 2024c) presented an exploratory analysis of the microbiome data that had been collected during the first two years of studies.

In accordance with the study design, large-scale microbiome sampling was not performed during year 3.

During campaign 9 (October 2024), microbial sampling was undertaken on the (initially abiotic) rock cubes in the AQMs using a swabbing technique. This yielded no recoverable DNA/RNA.

Further field sampling was undertaken on 13 November, 2024 for the railway cutting (group D) samples, including swabbing and the original Dremel collection method described in the Monitoring Studies Report 2024 (Curtin University, 2024c). The swabbing again returned no recoverable material, however the Dremel method led to recovering enough material for successful DNA extractions.

A second round of microbial sampling is planned for the AQM rock cubes in the final year of studies and this will utilise the Dremel method.

It is intended to present a formal statistical analysis of all available microbiome data in the final study report.

This page is intentionally blank.

7.9 Organic geochemistry

7.9.1 Background

Although most of the rock extracts sampled from Murujuga could be adequately analysed by traditional Gas Chromatography – Mass Spectrometry (**GC-MS**), about a quarter of the extracts were highly complex and were therefore further analysed by comprehensive two-dimensional Gas Chromatography – Time-of-Flight Mass Spectrometry (GC×GC-TOFMS), which provides enhanced chromatographic resolution (Phillips and Beens, 1999). Used in combination, these analytical techniques identified additional compounds to those previously reported. Many of these compounds are associated with the geological origins of the rocks. Some of the identified compounds may provide useful information pertaining to the surface chemistry of the rocks or contamination from anthropogenic sources such as industrial emissions.

In some samples, a suite of abietane-type compounds was observed that are usually associated with an origin from gymnosperm plants i.e., the Coniferophyta, Cycadophyta, Gingkophyta, and Gnetophyta (Biswas and Johri, 2014). However, abietic acids are also produced by cyanobacteria (Costa et al., 2016), many species of which are known to occur on the surface of Murujuga rocks and may play a key role in surface chemistry (Monitoring Studies Report 2024 (Curtin University, 2024c)). Some species of cyanobacteria also produce the straight chain alkane n-C_{17} in greater abundance than n-C_{18}, which has multiple sources (Schirmer et al., 2010). Plots of ratios of gymnosperm biomarkers to n-C_{17} and n-C_{18} are provided here, but a more in-depth analysis of individual gymnosperm biomarkers and the presence of cyanobacteria species may be informative with regard to the production of abietic acid type compounds and rock surface chemistry.

Medium to long chain alkylbenzenes (one aromatic ring hydrocarbons) were observed to be present in several rock extracts. Alkylbenzenes are ubiquitous environmental contaminants (Booth et al., 2007; Scarlett et al., 2008) that occur naturally in crude oils and their products, and are also industrially synthesised for widespread applications. Similarly, polycyclic aromatic hydrocarbons (PAHs), e.g., the 3-ring compounds phenanthrene (**P**) and methylphenanthrene (**MP**), observed in several rock extracts, can be derived from petroleum products, but are also commonly found in rock samples due to natural processes. The methylphenanthrene index (**MPI-1**) is often used in biogeochemistry to provide maturity information i.e., the heat and pressure that samples have been subjected to over time (Boreham et al., 1988). Together with the ratio of methylphenanthrene/phenanthrene (**MP/P**), MPI-1 can also provide information on biodegradation as methylphenanthrenes, especially specific isomers, are more resistant to microbial attack (Huang et al., 2019).

Fluoranthene is a 4-ring PAH that is likely to derive from partial combustion of hydrocarbons i.e., pyrogenic sources such as bushfires and atmospheric pollution. Another 4-ring PAH, pyrene, is more likely to originate from a petrogenic source (Wang et al., 1999). Hence the ratio of fluoranthene/(fluoranthene + pyrene) provides an indication of input from industrial emissions and/or bushfires. A ratio less than 0.4 indicates a petrogenic source, whereas rocks with ratios greater than 0.5 are more likely to have an input from pyrogenic sources.

Very high molecular weight PAHs (5-ring or greater) that are also mostly associated with pyrogenic sources (Wang et al., 1999) were typically below detection limits. Dibenzothiophene (**DBT**) is likely derived from land plants whereas the major sources of methylated dibenzothiophenes (**MDBT**) are

reported to be algae and bacteria (Niu et al., 2022). Ratios of DBT/P and MDBT/MP are commonly applied to provide information on the depositional environment in which the rocks were formed but in the context of the Murujuga rocks, they may highlight input to the rock surface from other sources.

As this study did not set out to quantify specific organic geochemical compounds, ratios were used to aid comparison between sites.

7.9.2 Exploratory data analysis

Figure *7.9-1* shows the boxplots of organic chemical ratios on sample rock surfaces. The data displayed in these boxplots were derived from all sample sites based on GC-MS data cross-checked with two dimensional gas chromatography - time of flight mass spectrometry (**GCxGC-TOFMS**) data.

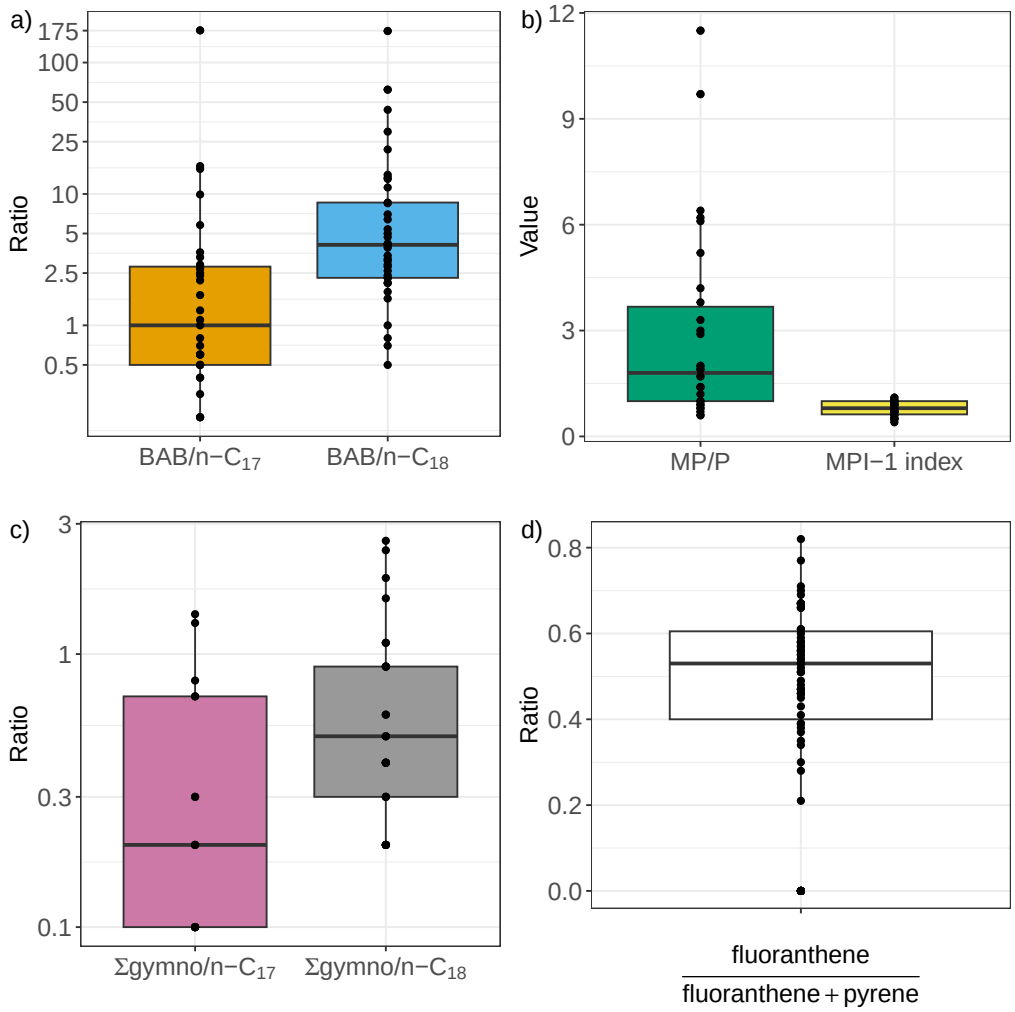

Figure 7.9-1: Boxplots of organic chemical ratios for a) Alkylbenzenes (BAB) relative to n-C_{17} and n-C_{18}, Note logarithmic scale; b) Methylphenanthrene relative to phenanthrene (MP/P) ratio plus methylphenanthrene index (MPI-1); c) Gymnosperm biomarkers (Gymno) relative to n-C_{17} and n-C_{18}, Note logarithmic scale ; d) fluoranthene/ (fluoranthene + pyrene).

The BAB/n-C_{18} ratio is higher than the BAB/n-C_{17} ratio. The gymnosperm biomarker relative to n-C_{18} ratio is higher than the gymnosperm biomarker relative to n-C_{17} ratio. A logarithmic transformation is used for all ratios except fluoranthene/(fluoranthene + pyrene) because it shows a symmetric distribution, while the other ratios are heavily skewed.

There is another ratio considered, dibenzothiophene/phenanthrene, plus methyldibenzothiophene /methylphenan-threne, for which most of the values are below the detection limit; plots are included in Appendix *D*.4. Also, BDLs were removed for further analysis.

Figures *7.9-2* to *7.9-6* show discrete point plots of each ratio, differentiated by rock type and site.

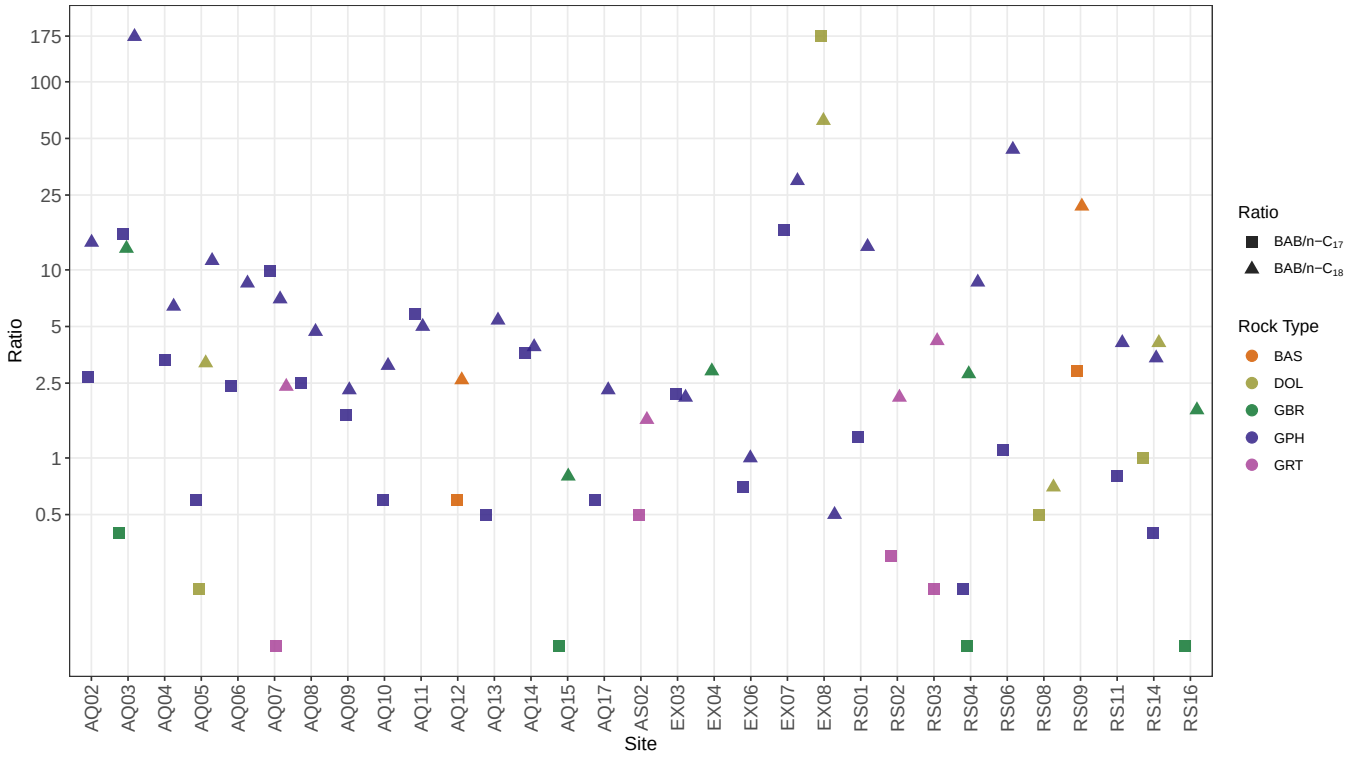

Figure 7.9-2: Discrete point plot of Alkylbenzenes (BAB) relative to n-C_{17} and n-C_{18} against sampling sites. Note logarithmic scale. Points were jittered to avoid overlap.

In general, both the BAB/n-C_{17} and BAB/n-C_{18} ratios include some values below the detection limit ($\sim$0). The highest BAB/n-C_{17} ratio occurs at EX08 dolerite ($\sim$175), while the highest BAB/n-C_{18} ratio is observed at AQ03 granophyre ($\sim$175). EX08 dolerite also shows a high BAB/n-C_{18} ratio ($\sim$60). Other elevated ratios include those at EX07 and RS06 granophyre ($\sim$30). Most ratios fall between 0.5 and 10. EX07 and EX08 are located near industrial areas, and RS06 is also relatively close to industry. However, the highest ratio at AQ03 warrants further investigation, as it is located far from industrial areas.

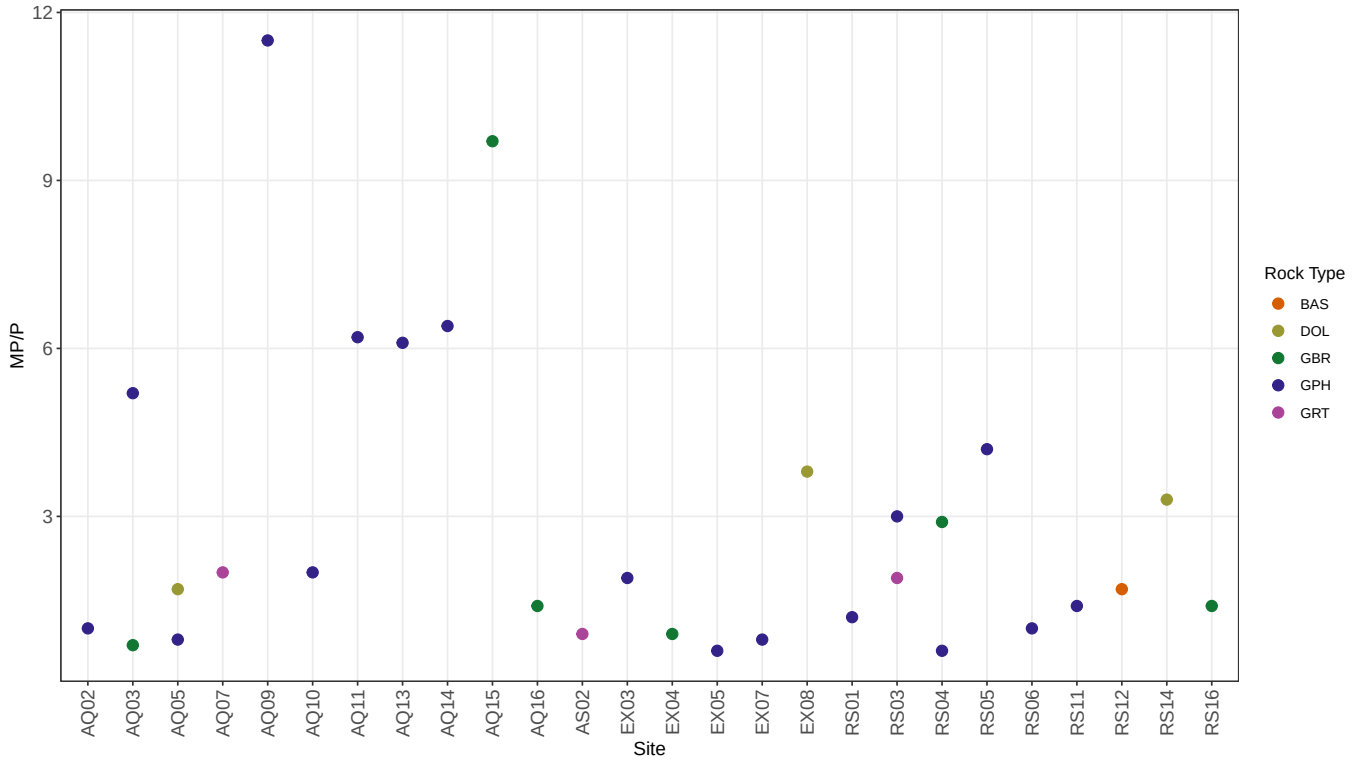

Figure 7.9-3: Discrete point plot of Methylphenanthrene relative to phenanthrene ratio (MP/P).

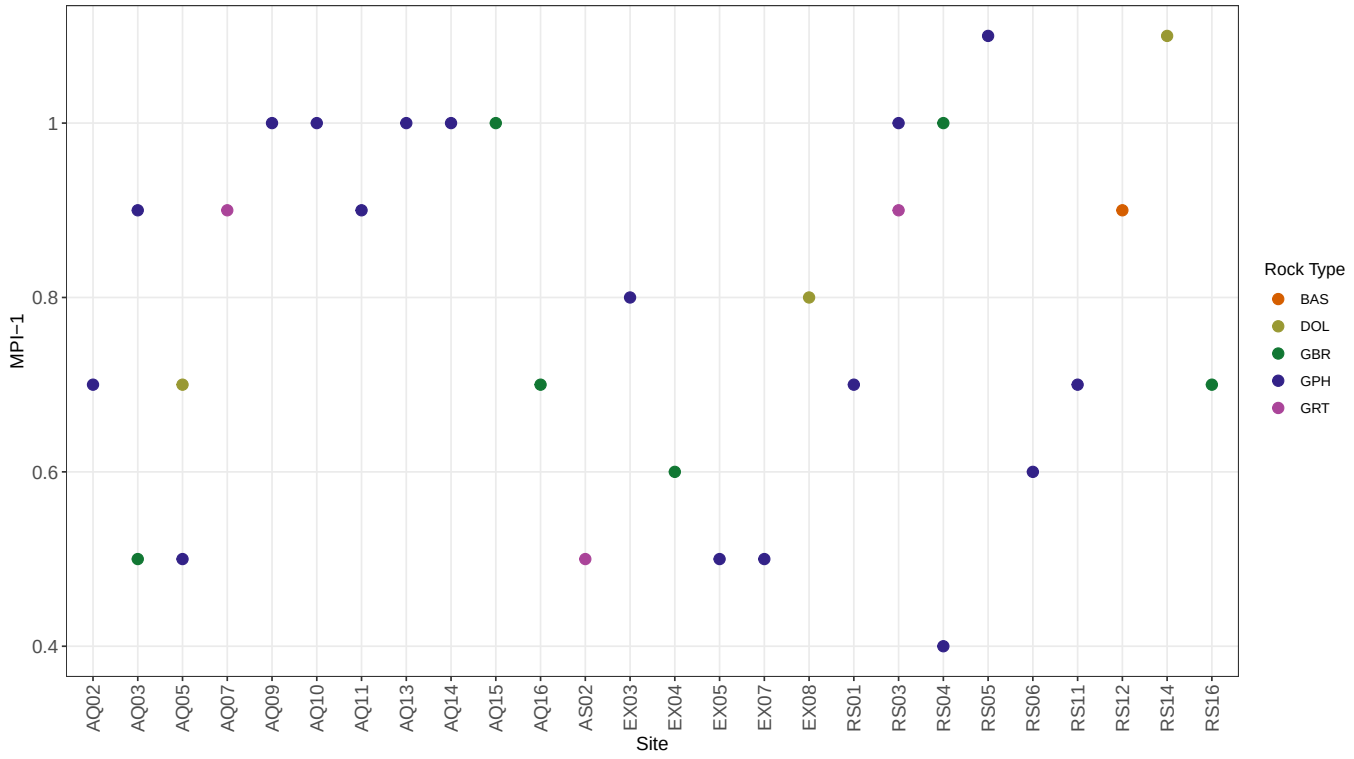

Figure 7.9-4: Discrete point plot of methylphenanthrene index (MPI-1).

The highest MP/P ratios occur in AQ09 granophyre and AQ15 gabbro (∼10), while the highest MPI-1 index values are found in RS05 granophyre and RS14 dolerite (∼1.5). Additionally, some MP/P ratios exceed 1.5, with values greater than five observed on granophyre samples from AQ03, AQ09, AQ11, AQ13, and AQ14, making these notable sites where biodegradation may have had a stronger influence on the rock surfaces. RS05, AQ09, and AQ11 are located close to industrial areas. However, the high ratios at AQ03, AQ13, AQ14, and AQ15 warrant further investigation, as these sites are located far from industry.

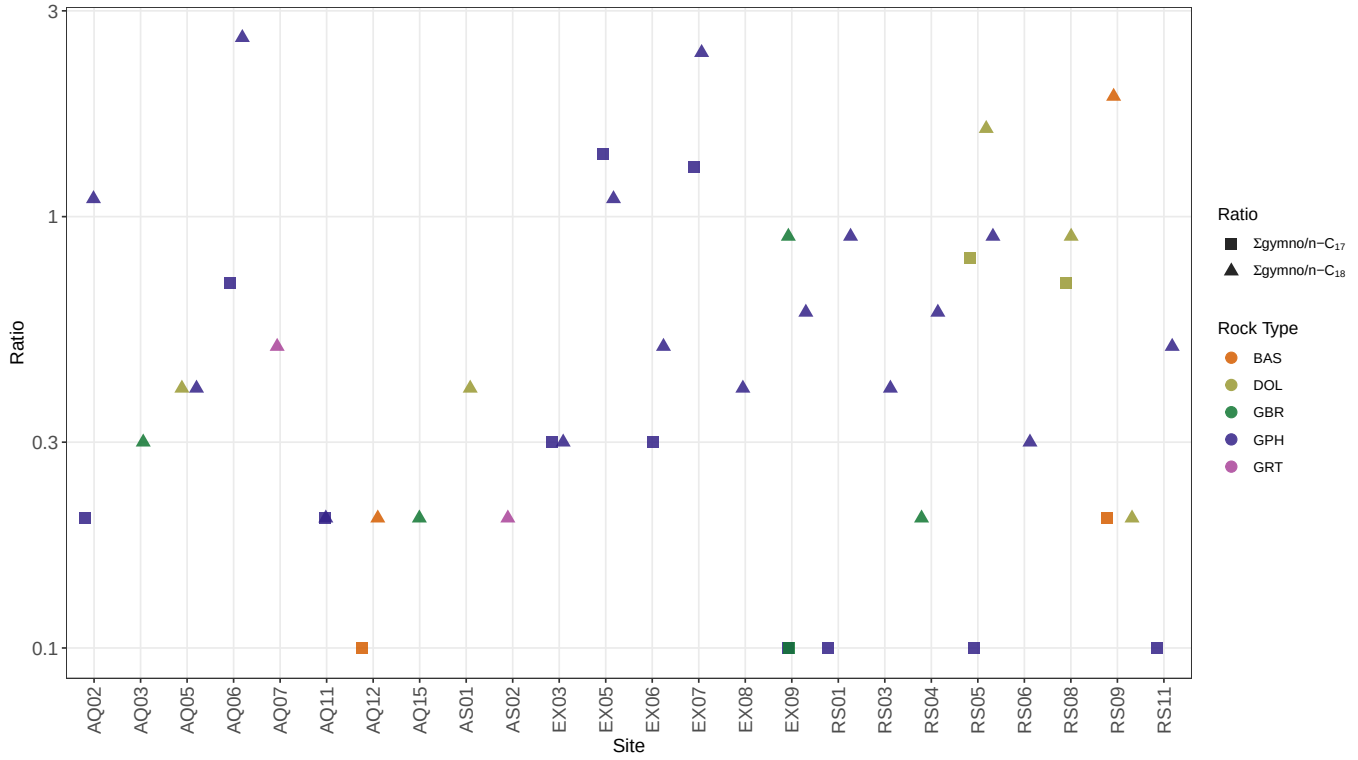

Figure 7.9-5: Discrete point plot of Gymnosperm biomarkers relative to n-C_{17} and n-C_{18}. Note logarithmic scale. Points were jittered to avoid overlap.

The gymnosperm biomarkers relative to n-C_{18} are high in the granophyres at AQ06 and EX07 (∼3), RS05 dolerite (∼2), and RS09 basalt (∼2.5). Biomarkers relative to n-C_{17} are relatively higher in the granophyres at EX05 and EX07 (∼1.5), and many of these ratios are below 1. EX05, EX07, and RS05 are located close to industrial areas. However, the highest ratios observed at AQ06 and RS09 warrant further investigation, as these sites are located somewhat farther from industry.

As it seems unlikely that these compounds would be derived from gymnosperms at the time the rock for formed, it is possible that they originate from cyanobacteria. Further study would be required to investigate if these mono- and diaromatic diterpenoids are associated with cyanobacteria species currently present on the rocks. Rather than the hydrocarbons, the cyanobacteria would be producing dehydroabietic and abietic acids, but these were not prevalent in the polar fraction of the samples. It is therefore unlikely that these acids are currently playing a major role in the surface chemistry of the rocks.

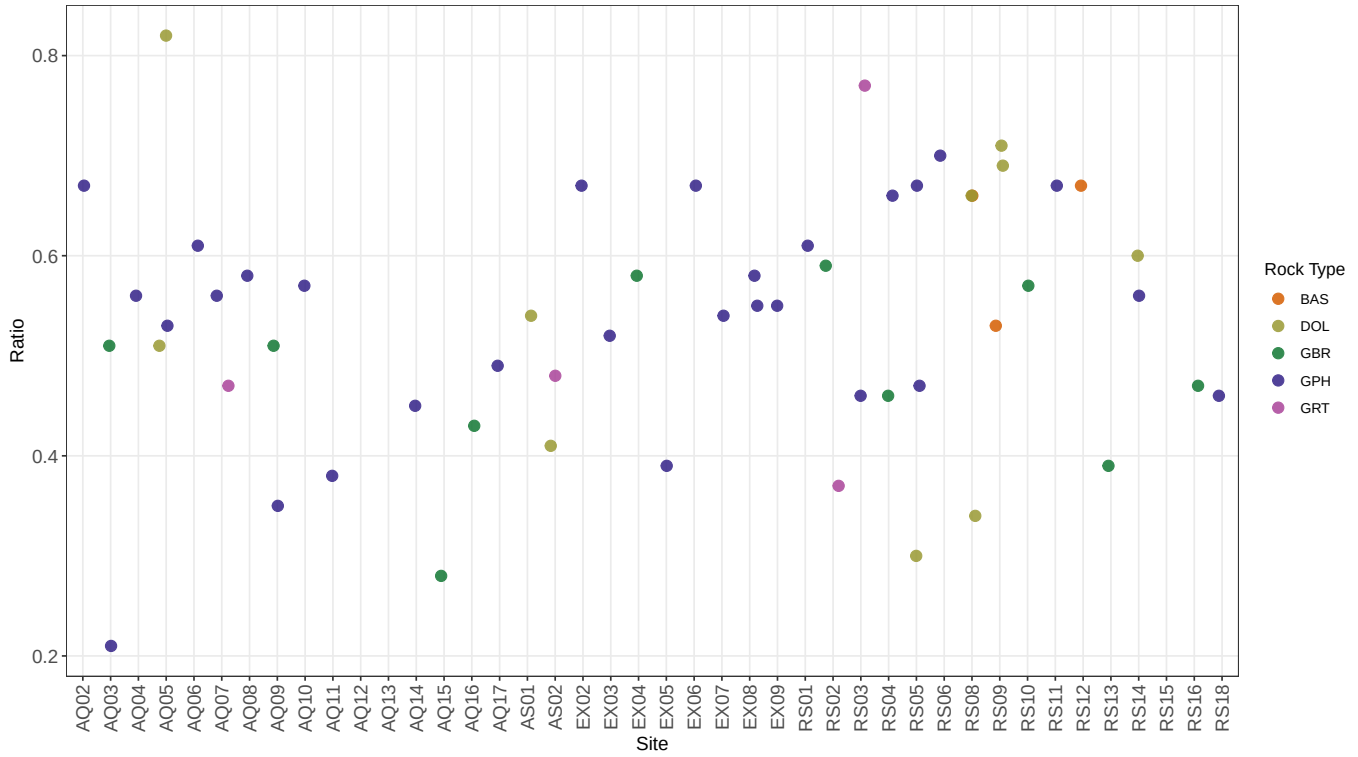

Figure 7.9-6: Discrete point plot of fluoranthene/(fluoranthene + pyrene) ratio.

The fluoranthene/(fluoranthene + pyrene) ratio is high at AQ05 dolerite (∼0.9) and RS03 granite (∼0.75). It is also somewhat elevated in RS06 granophyre and RS09 dolerite (∼0.65). Nearly half of the samples had fluoranthene/(fluoranthene + pyrene) ratios greater than 0.5, indicating input from pyrogenic sources, which could include emissions from industry or bushfires. Of these sites, only some are located near industry, suggesting that in the context of the organics analyses the industrial emissions are not a significant factor influencing rock art degradation processes.

Overall, EX07, EX08, RS05, RS06, AQ09, and AQ11 show elevated organic geochemical ratios such as BAB/n-C_{17}, BAB/n-C_{18}, and MP/P, industry may be affecting these ratios. EX08 dolerite has the highest BAB/n-C_{17} ratio (∼175) and a high BAB/n-C_{18} ratio (∼60), while RS05 and AQ09 exhibit high MP/P ratios. However, some sites with high ratios, including AQ03, AQ13, AQ14, AQ15, AQ06, and RS09, are located farther from industry and require further investigation to understand the causes. Fluoranthene/(fluoranthene + pyrene) ratios are mostly consistent with input from pyrogenic sources, i.e., greater than 0.5, but many are not located near industry, suggesting that other sources are affecting the ratios. Hence, proximity to industrial areas correlates with higher organic geochemical ratios at several sites, potentially contributing to rock art degradation.

Figures *7.9-7* to *7.9-13* present spatial point plots of each ratio, differentiated by rock type and site. These plots may help to identify whether certain ratios cluster in specific locations, particularly around or near industrial areas.

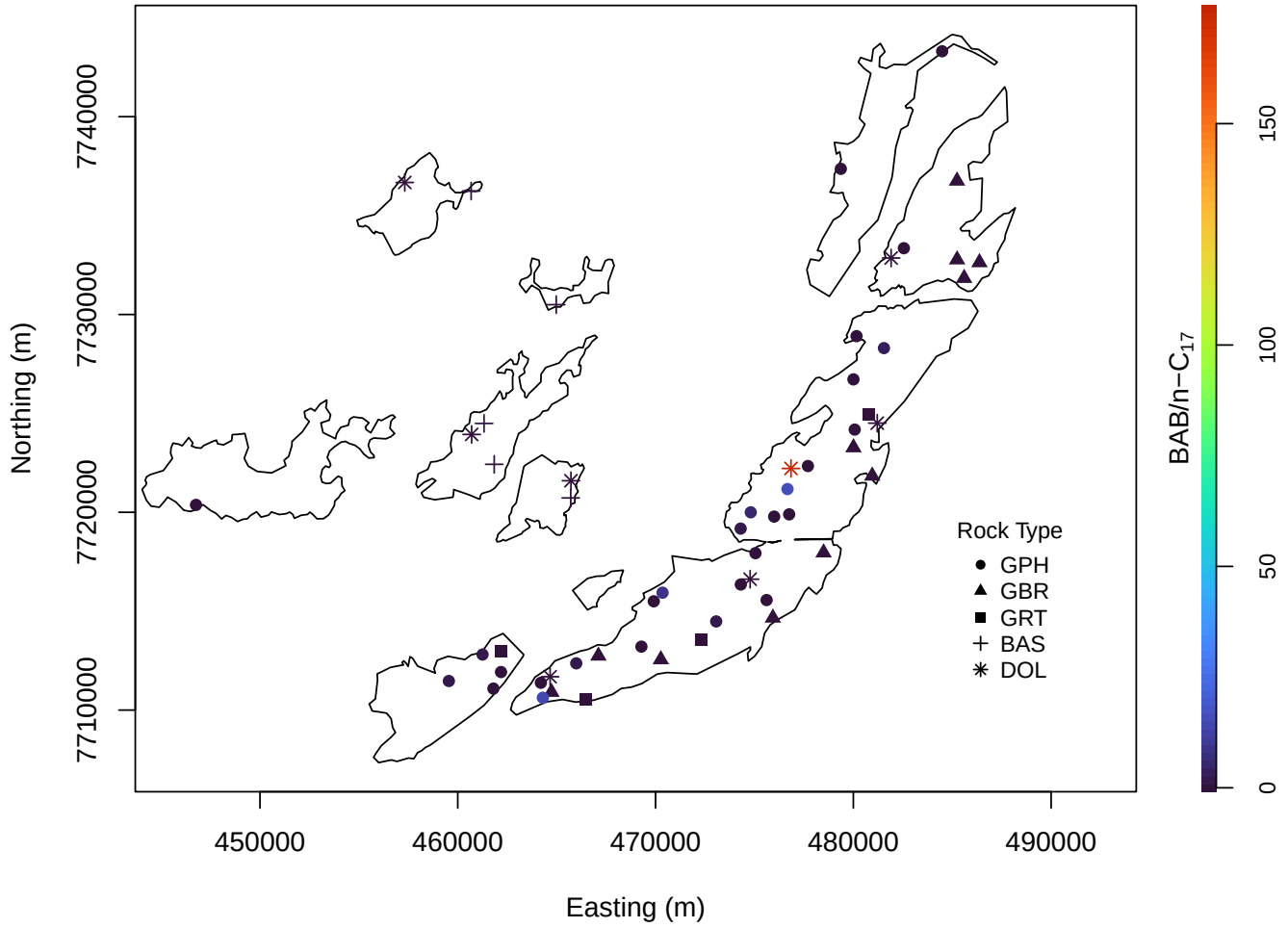

Figure 7.9-7: Spatial plot of Alkylbenzenes (BAB) relative to n-C_{17}.

Only one high BAB/n-C_{17} value is observed in dolerite near industry (red asterisk), with a somewhat elevated value in granophyre near industry (blue circle). All other values near industrial areas are very low.

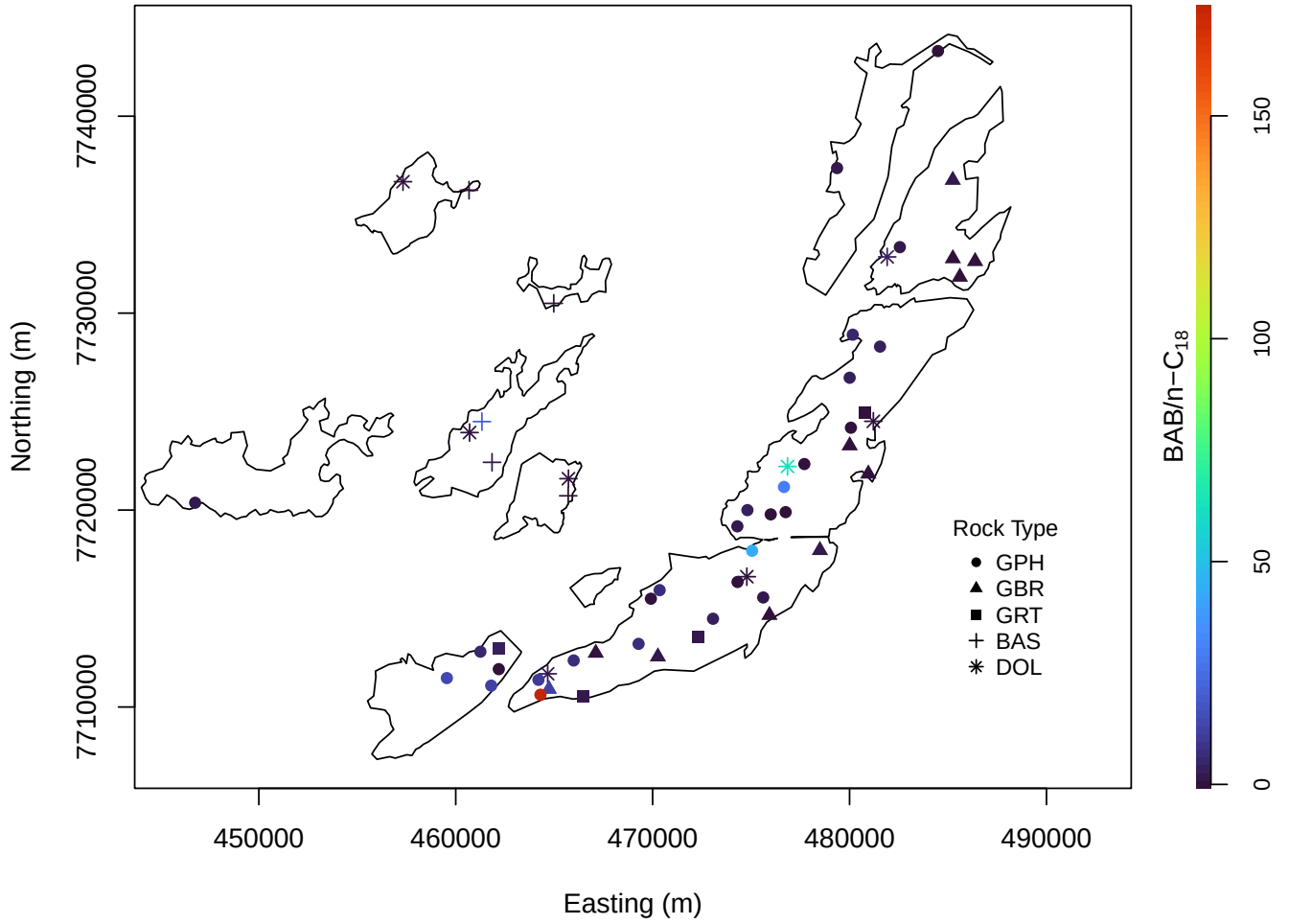

Figure 7.9-8: Spatial plot of Alkylbenzenes (BAB) relative to n-C_{18}.

The highest BAB/n-C_{18} value is observed in granophyre located far from industrial areas (red circle). Somewhat elevated values near industry are found in dolerite (light green asterisk) and granophyre (light blue circle). All other values near industrial areas are very low.

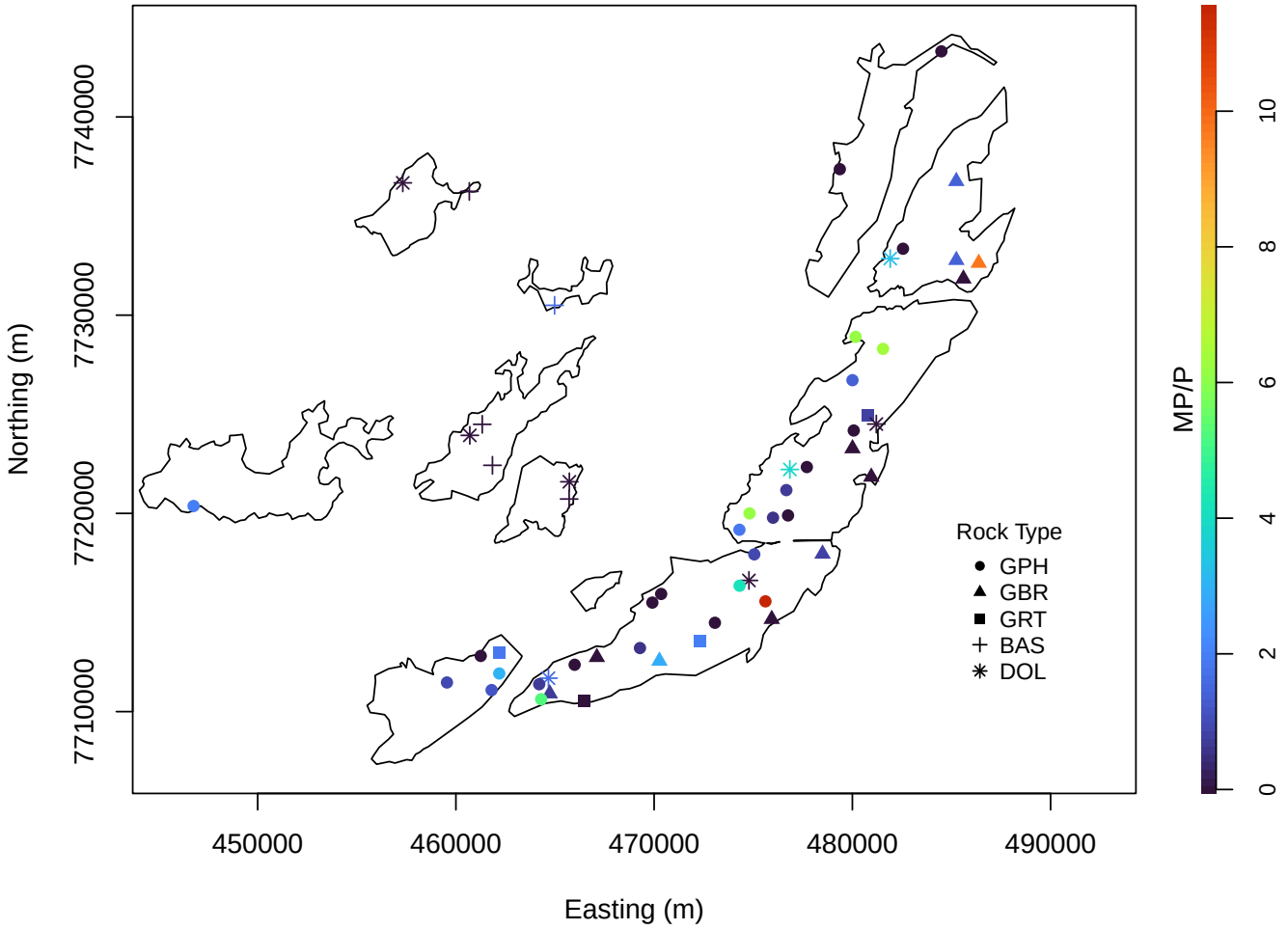

Figure 7.9-9: Spatial plot of Methylphenanthrene relative to phenanthrene (MP/P).

The highest MP/P value is observed in granophyre located near an industrial area (red circle). Somewhat elevated values near industry are also found in granophyre (light green to blue circles), with a few higher values present in gabbro and granite samples. However, some values near industrial areas remain very low.

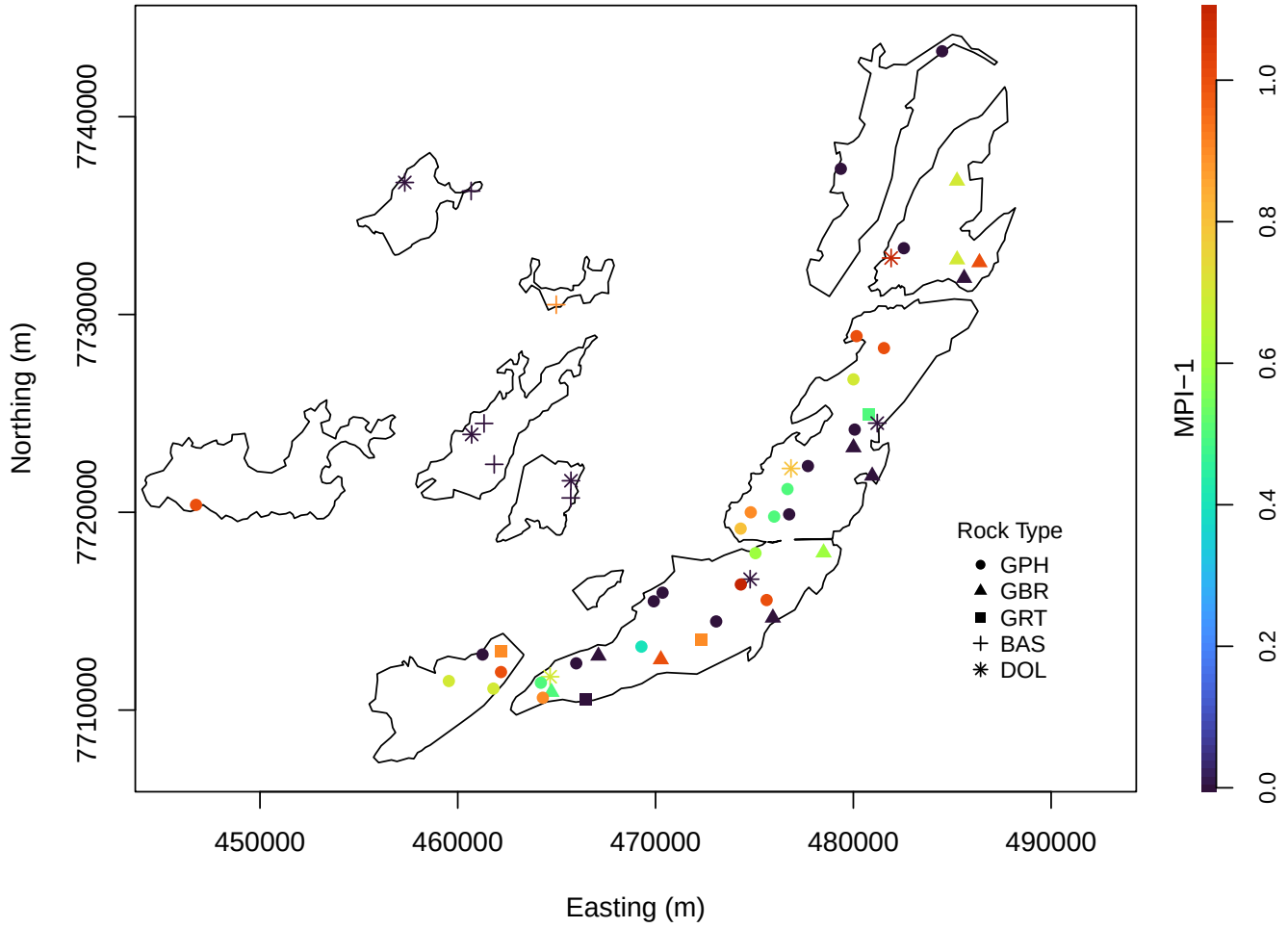

Figure 7.9-10: Spatial plot of methylphenanthrene index (MPI-1).

The MPI-1 index has higher values across the Burrup Peninsula, without a specific cluster of elevated values. Therefore, this index does not appear to be particularly high near industrial areas.

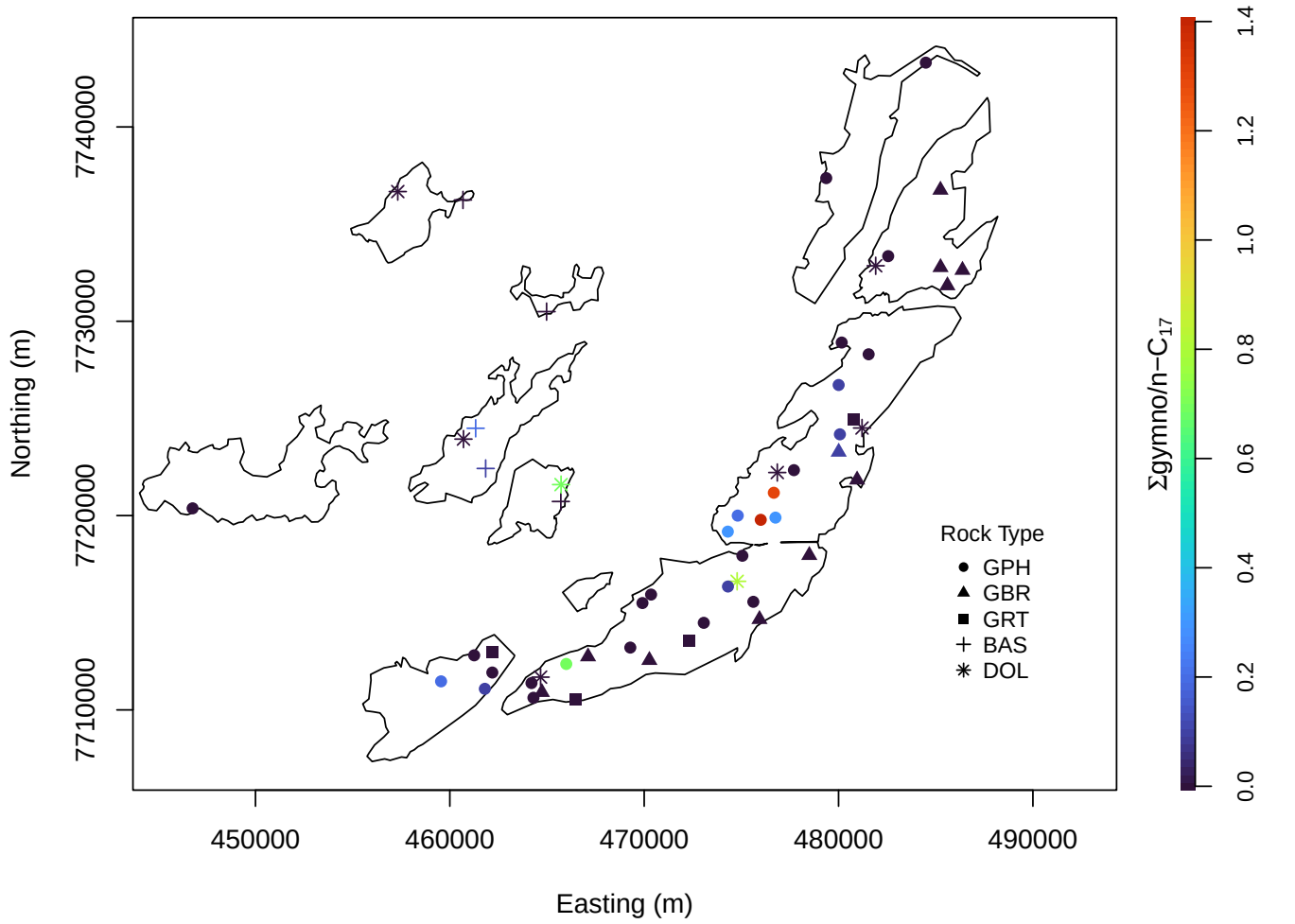

Figure 7.9-11: Spatial plot of Gymnosperm biomarkers relative to n-C_{17}.

The highest gymnosperm biomarker value relative to n-C_{17} is observed in granophyre located near an industrial area (red circles). Somewhat elevated values near industry are also found in granophyre (light blue circles) and dolerite (light green asterisk). However, some values near industrial areas remain very low.

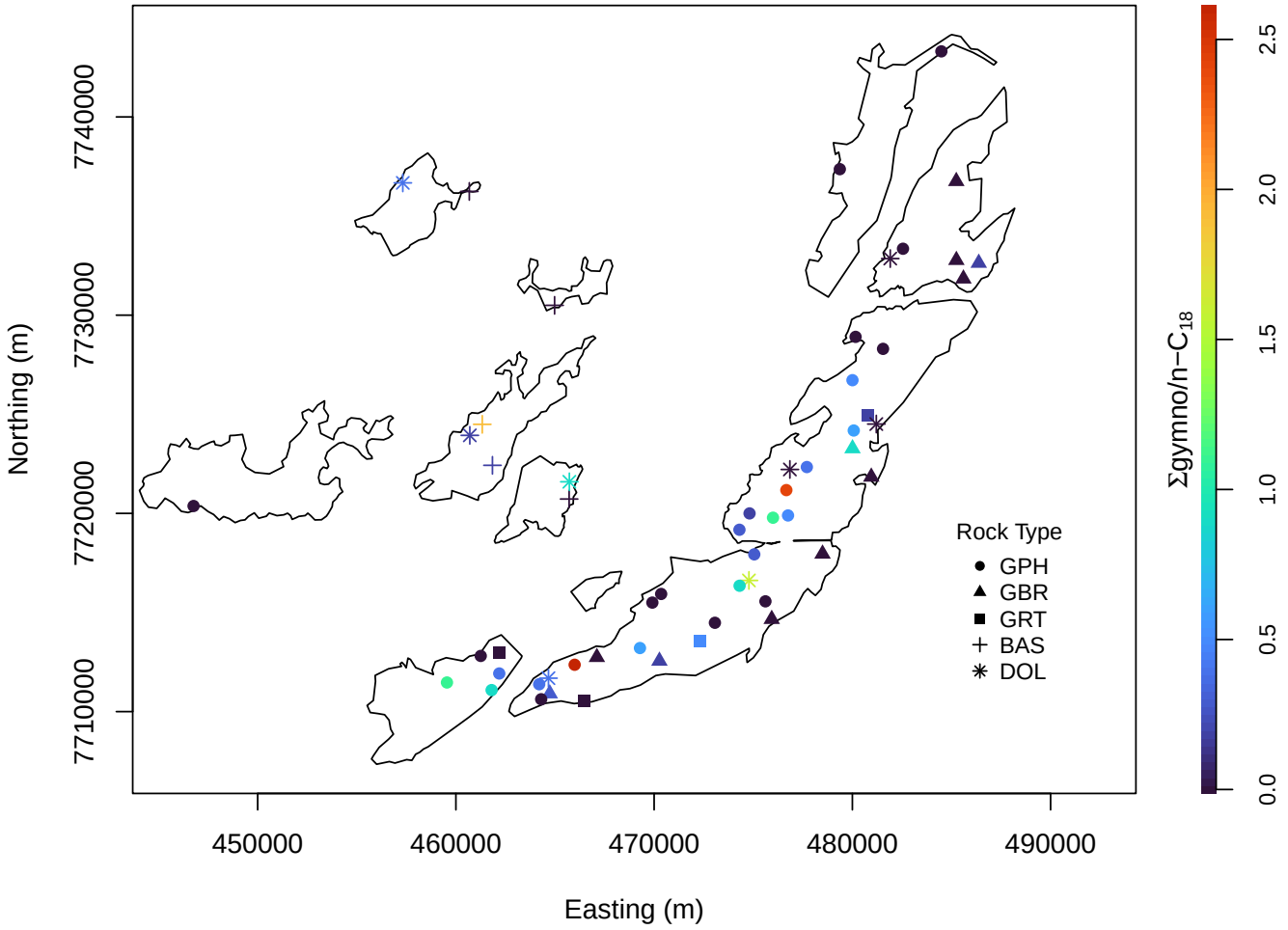

Figure 7.9-12: Spatial plot of Gymnosperm biomarkers relative to n-C_{18}.

The highest gymnosperm biomarker value relative to n-C_{18} is observed in granophyre located near an industrial area (red circle). Somewhat elevated values near industry are also found in granophyre (light blue circles) and dolerite (light green asterisk). However, a few values near industrial areas remain very low.

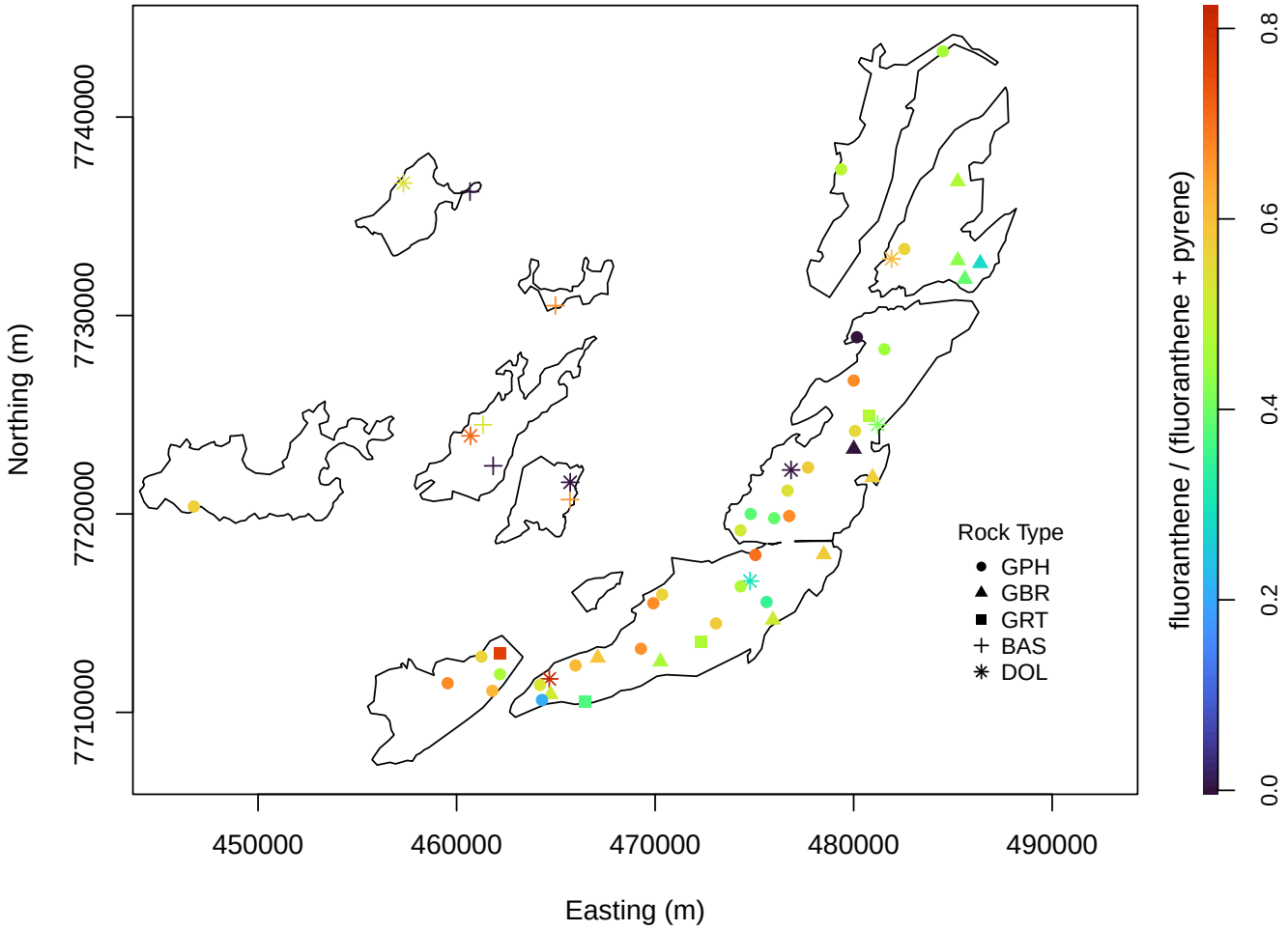

Figure 7.9-13: Spatial plot of fluoranthene / (fluoranthene + pyrene).

The fluoranthene/(fluoranthene + pyrene) ratio is symmetrically distributed across the peninsula, with no specific clusters of higher values observed, particularly near industrial areas.

Spatial plots of organic geochemical ratios reveal limited clustering near industrial areas. Only a few high values, such as BAB/n-C_{17} in dolerite and gymnosperm biomarkers (n-C_{17} and n-C_{18}) in granophyre, are found near industry. MP/P ratios show several elevated values near industrial sites, but MPI-1 values are broadly distributed without clustering. BAB/n-C_{18} shows its highest value far from industry, and fluoranthene/(fluoranthene + pyrene) ratios are symmetrically distributed, lacking any spatial pattern.

Overall, most ratios near industrial areas are low, with few exceptions. These findings suggest that while some organic geochemical ratios may be influenced by proximity to industrial areas, no consistent spatial clustering is observed. Therefore, only selected ratios, particularly MP/P and certain gymnosperm biomarker values may be useful indicators for potential rock art degradation processes, thus further investigation will be included in the final MRAMP monitoring studies report.

This page is intentionally blank.

7.10 Deposition sampler data

7.10.1 Background

Section 7.10 of the Monitoring Studies Report 2024 (Curtin University, 2024c) details the 3-bucket deposition sampler developed for this project and is also detailed in the following documents:

- COPP21065-PRO-G-102 Passive Air Quality Monitoring (AQM) Installation and Commissioning;
- COPP21065-PRO-G-103 Passive Air Quality Monitoring (AQM) Sample Collection, Maintenance and Context Observations; and
- COPP21065-SPE-G-100 Air Quality Monitoring Station Control Functional Specification.

Figure *5.3-2* displays a photo of the 3-bucket deposition sampler.

As mentioned earlier, passive samplers, including total and three-bucket deposition samplers are changed at nominal 28$\pm$4 day intervals.

In the previous study report (Curtin University, 2024c), the deposition sampler data was summarised from May 2023 to March 2024, this included boxpots, scatterplots and spatial smoothing. In this section, these figures have been updated to include all available data from May 2023 to March 2025.

Similar to Monitoring Studies Report 2024 (Curtin University, 2024c), Section 7.10.2 shows an update of the *pH* boxplots of the dry, wet and mist deposition sampler data. In addition, Section 7.10.3 shows the updated figures for *pH* dry deposition samples. Section 7.10.4 shows the updated figures for the chemical species concentrations provided by ChemCentre, which includes Ca^{2+}, K^{+}, Mg^{2+}, Cl^{-}, Na^{+}, $SO_4{}^{2-}$, $NH_4{}^{+}$, $NO_3{}^{-}$, P, and $NO_2{}^{-}$. Section 7.10.5 displays the updated analyses for the co-located sites. Section 7.10.6 presents the spatial smoothing of *pH* and assayed concentrations from the dry deposition samples.

7.10.2 Exploratory analysis of 3-buckets

Figure *7.10-1* shows the boxplots of *pH* for the dry, wet and mist deposition sampler data. There was no notable difference in *pH* among dry, wet, and mist deposition samples. Note that there has been a minor procedural change in processing the bucket samples prior to laboratory analysis. 50 mL of deionised water was added to the sample from March 2023 to June 2023, and this changed to 60 mL of water from July 2023.

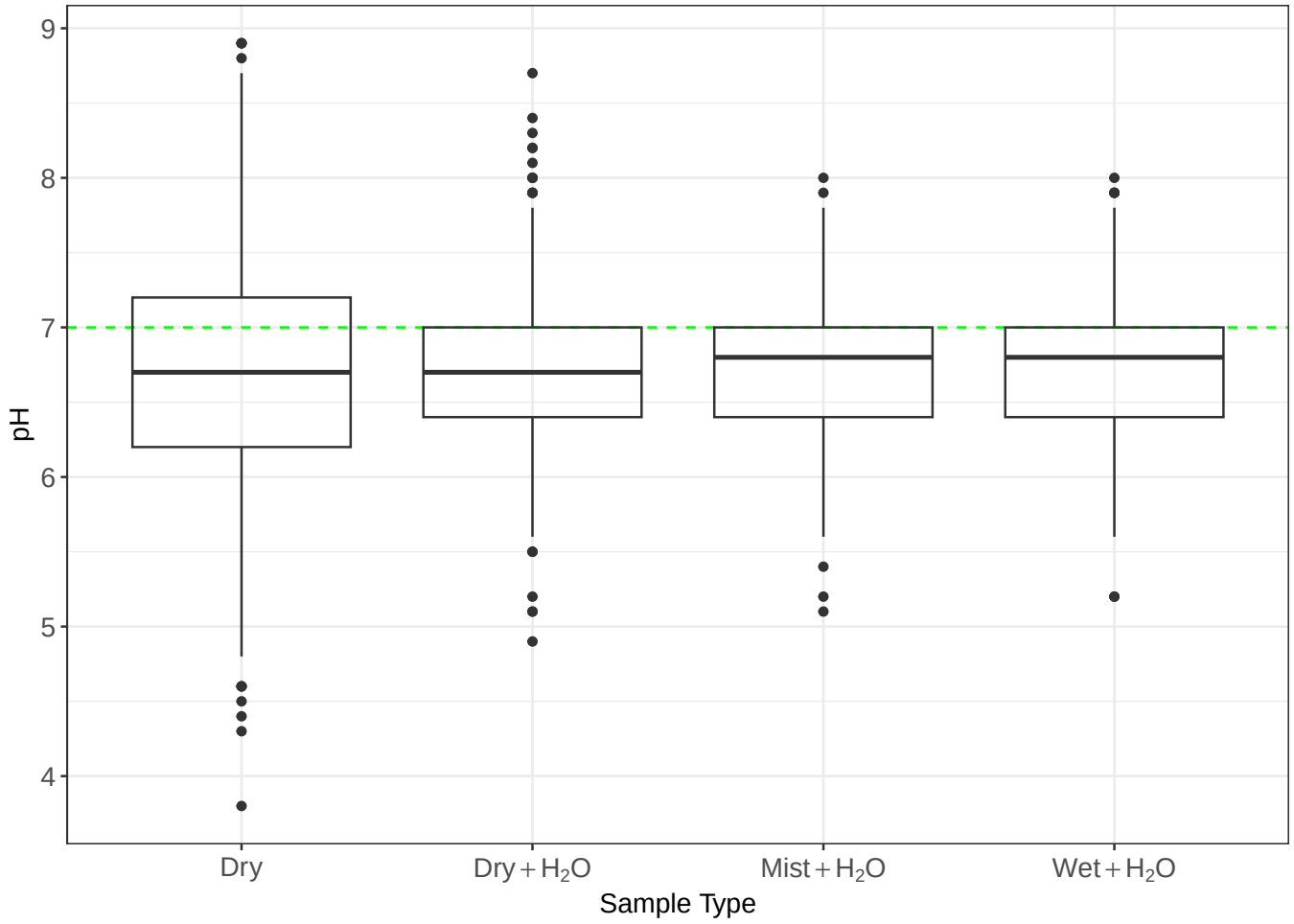

Figure 7.10-1: Boxplots of pH for dry, wet, and mist deposition samples (H_2O is deionised water), across all sites and all sampling periods (from May 2023 to March 2025). The green dashed line represents the neutral pH value.

7.10.3 Exploratory analysis of *pH* dry deposition sampler data

Figure *7.10-2* shows boxplots of *pH* values of dry deposition samples collected between May 2023 and March 2025, broken down by the date of sample collection. In the previous study report (Curtin University, 2024c), the *pH* was recorded from May 2023 to March 2024, varying between 5.5 and 8, with the majority of samples above 6.5. The relatively high *pH* is most likely attributable to geogenic dust/clay mineral deposition and possibly salt/sea spray deposition (although this can at times be acidic). Particularly notable is that the dry buckets from June 23 2023, show comparatively low *pH* (with a median of 6), which coincides with a period of low dust/deposition as the likely cause.

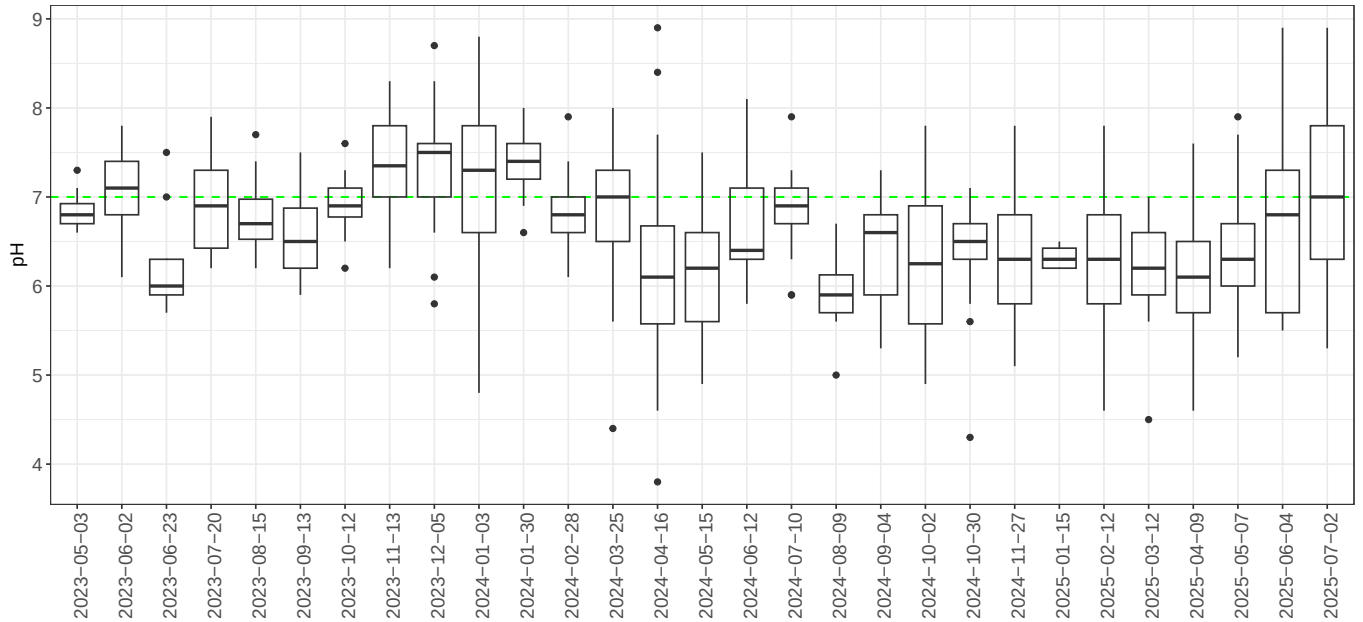

Figure 7.10-2: Boxplots of pH for the dry deposition samples by sampling periods, across all sites. The green dashed line represents the neutral pH value.

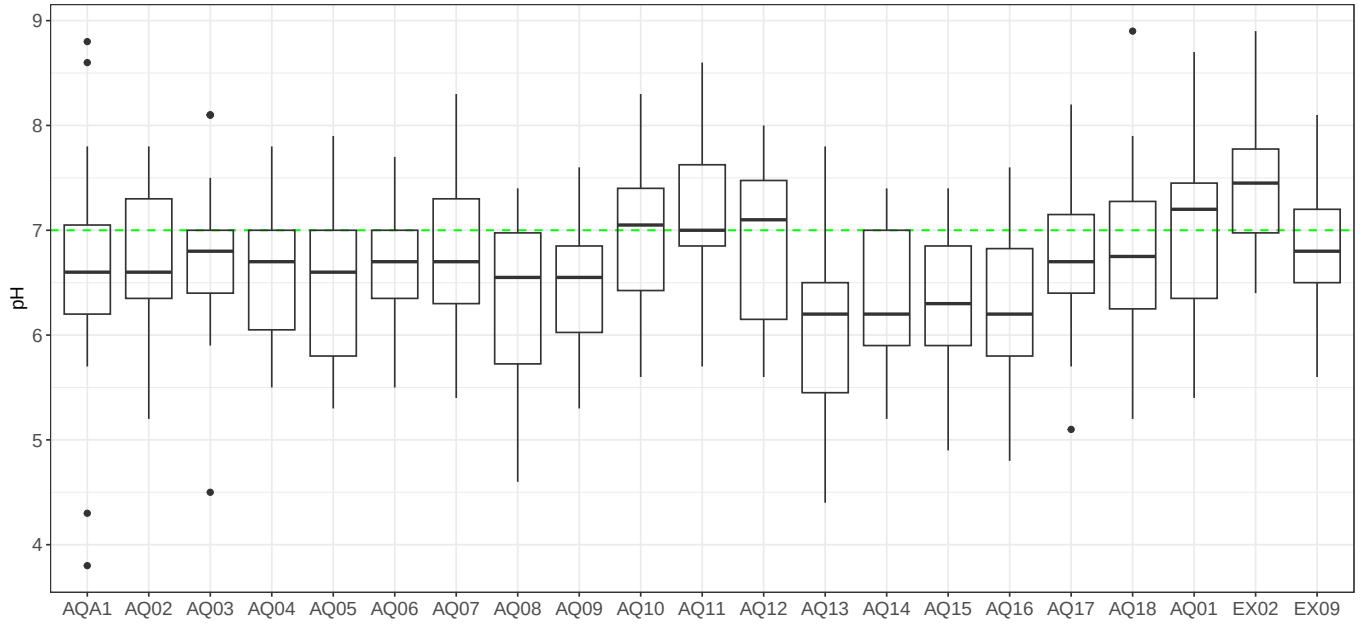

Figure 7.10-3: Boxplots of pH for the dry deposition samples by sampling sites, over all sampling periods. The green dashed line represents the neutral pH value.

However, this year's data shows that the *pH* measured from May 2023 to March 2025 largely lies between 5.5 and 7. Hence, there is a slight drop in the *pH* of the dry deposition samples,

suggesting less influence from natural dust or other alkaline deposition sources.

Figure *7.10-3* shows boxplots of the same *pH* data (May 2023 to March 2025), broken down by site. In the Monitoring Studies Report 2024 (Curtin University, 2024c):

- AQ01 shows by far the highest median *pH* of $\sim$8. This may be due to its location in a dusty flood plain and/or the site's very different geology compared to the Dampier archipelago.
- AQ11, AQ12, EX02, and EX09 have the next highest median *pH* values of about 7.5.
- Other sites have a median *pH* between 6.5 and 7.5.
- The lowest median *pH* values were at AQ18 and AQ17 with values 6.6 and 6.7, respectively. It can be seen from the passive sampler results that these latter two sites generally have the highest SO_2, however, they also have low deposition rates of dust/clay minerals.

However, analysis for this report (Figure *7.10-3*), inclusive of data collected up to March 2025 shows a different outcome:

- EX02 has the highest median *pH* of approximately 7.5
- AQ01 has the second highest median *pH*, with a value of around 7.2.
- AQ10, AQ11, and AQ12 have the next highest median *pH* values, each around 7.
- The lowest median *pH* values are observed at AQ13, AQ14, AQ15, and AQ16, with values near 6.2.
- The remaining sites have median *pH* values between 6.3 and 7.

Thus, Figures *7.10-2* and *7.10-3* show some variation in *pH* after the inclusion of recent samples.

Dry deposition samples generally showed an approximately neutral *pH*, which is very similar to the *pH* measured on the rock surfaces in campaigns 6 and 7 (October–November 2023, February–March 2024).

Dry deposition samples had a median *pH* of approximately 6.5 in June–July 2024, which is slightly higher than the median *pH* measured on rock surfaces during campaign 8 (June–July 2024). In October–November 2024, the median *pH* of dry deposition samples was about 6.3, noticeably higher than that of rock surfaces *pH* in campaign 9. Similarly, in February–March 2025, dry deposition samples showed a median *pH* of around 6.2, which is somewhat higher than the rock surface *pH* in campaign 10.

As mentioned in Monitoring Studies Report 2023 (Curtin University, 2023), the AQMs were designed to blend-in to their surroundings if they were located in publicly visible areas. Seven cages (AQA1, AQ02, AQ11-14, AQ16) located in proximity to patinated rocks were made from Weathering (CorTen) steel and left unpainted. However some components (e.g. the mesh) was unavailable in weathering steel and mild steel was substituted. Over time, these components have been observed to release rust flakes which under high winds may deposit in deposition samplers. Particularly the dry bucket of the three-bucket samplers. This would be expected to lower the pH when the sample are analysed. The same effect would not be expected (nor has it been observed) in the other AQMs which are either galvanised steel or galvanised and painted. The spatial distribution of the seven bare steel AQMs is similar to the galvanised/painted AQMs, apart from the former being located further from the coast.

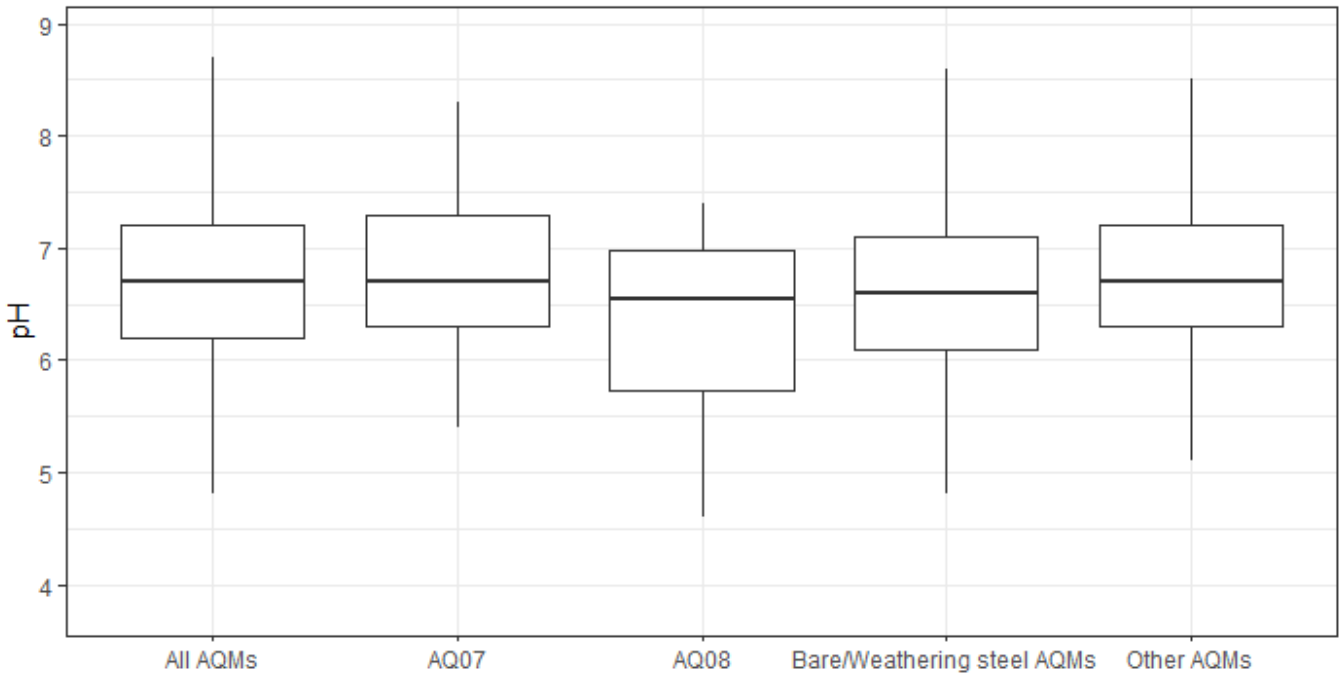

Figure 7.10-4: Boxplots of pH for dry deposition samples from all AQMs, co-located AQ07 and AQ08, and AQMs with bare/weathering, and AQMs without bare/weathering (other AQMs). Data from May 2023 to March 2025.

Figure *7.10-4* displays the boxplots of dry deposition *pH* for all 21 AQMs combined, the seven bare/weathering steel AQMs and the other 14 AQMs. The bare/weathering steel cages can be seen to have a slightly lower median *pH* compared to all AQMs and the other cages. The IQR for the cages without bare/weathering steel were slightly higher than the bare/weathering steel cages. All values below a *pH* of 5 are observed in the bare/weathering steel group, apart from AQ08 in the other group. Further investigation is warranted, especially since AQ08 and AQ07 are co-located. Another source of low *pH* in dry deposition samplers is scats/guano or other biological matter. Some AQMs provide a source of significant structure and are frequented by local birds and other wildlife. Preliminary observations on rock cubes appear to show that heavy guano deposits can provide approximately 0.5 reduction in *pH*. Figure *7.11-11* shows a similar trend for the *pH* of total flask samples at AQ07 and AQ08, albeit less pronounced and with AQ07 lower than AQ08.

Another source of the low *pH* at AQ08 could be due to the fact that the site is adjacent to the airport and under the flight path of rotary wing aircraft servicing the oil/gas industry. The Karratha Airport is reported to be the second busiest in Western Australia based on annual passenger numbers on commercial flights. Likely not including specialist aviation servicing the local industry. Aviation fuels are currently permitted to contain 300 times the sulfur levels of domestic (land) transport fuels (Exxon Mobil, 2025) and aviation engine technology does not have exhaust after treatment technology that many land and marine combustion processes have. Marine shipping fuels may potentially contain higher sulfur levels again, however many ships servicing Dampier ports appear

to be operating on natural gas rather than heavier marine fuels.

In Section 7.12, Figure *7.12-15* shows boxplots of the IVL passive sampler for the combined AQ07 and AQ08, other stations excluding AQ07 and AQ08 and all stations for NO_2, NH_3, O_3, SO_2 and HNO_3. It can be seen that NO_2 and HNO_3 are consistently above average at these two sites and SO_2 may be slightly elevated.

7.10.4 Exploratory analysis of chemical species concentrations from the dry deposition sampler data

Chemical analysis of the bucket samples also provided assayed concentrations of Ca^{2+}, K^+, Mg^{2+}, Cl^-, Na^+, SO_4^{2-}, NH_4^+, NO_3^-, P and NO_2^-. The concentrations that were below the detection limit were removed.

The sample assay values provided by the ChemCentre give the concentration (mg/L) of chemical species in the original 60 mL of water added during sample processing. This 60 mL value is somewhat arbitrary and does not account for differing water quantity (e.g., rainfall in wet buckets), or different open area of the collector (e.g., the AS/NZS 3580.10.1 samplers use a 150 mm funnel as a collector). For these reasons, and to account for slight differences in time between sample collection, samples were standardised to a deposition rate measured in milligrams per square metre per day (mg/m^2/day).

In the following analysis we have converted the assayed concentrations in the dry bucket samplers to deposition rates in mg/m^2/day.

Figures *7.10-5* and *7.10-6* show boxplots of the calculated deposition rates of Ca^{2+}, K^+, and Mg^{2+} broken down by sampling date and by location, respectively.

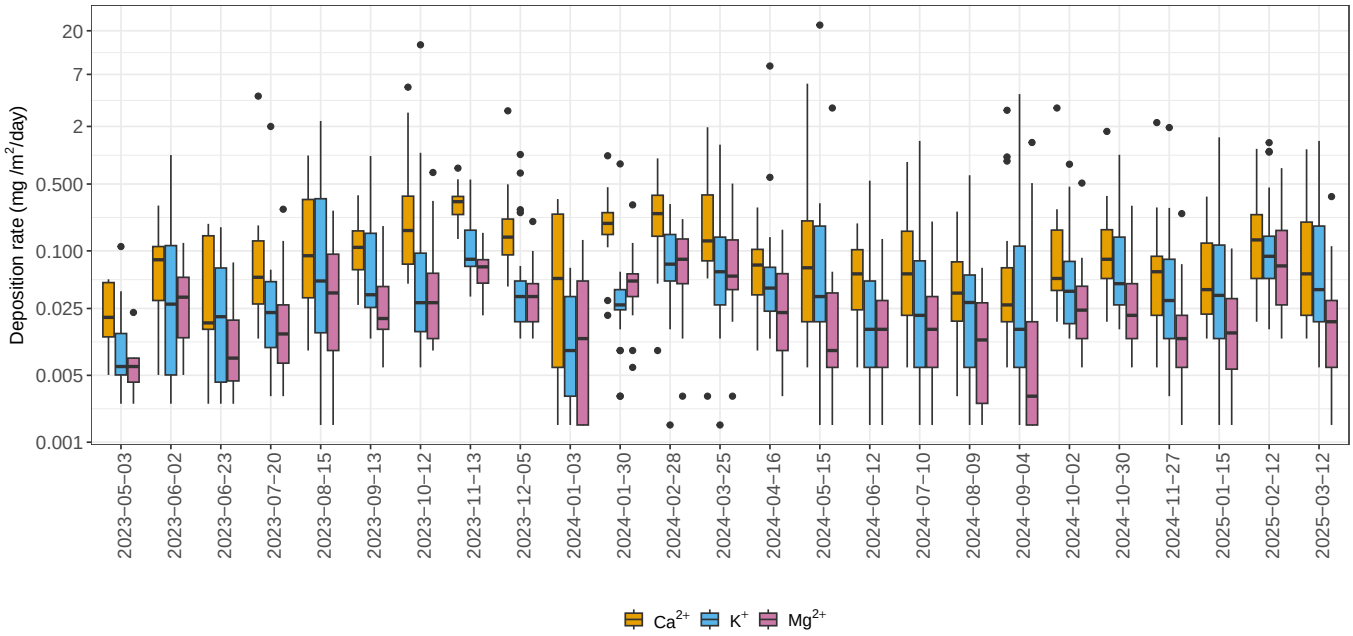

Figure 7.10-5: Boxplots of Ca^{2+}, K^{+}, and Mg^{2+} deposition rates across all sites for the dry deposition samples by sampling period. Note logarithmic scale.

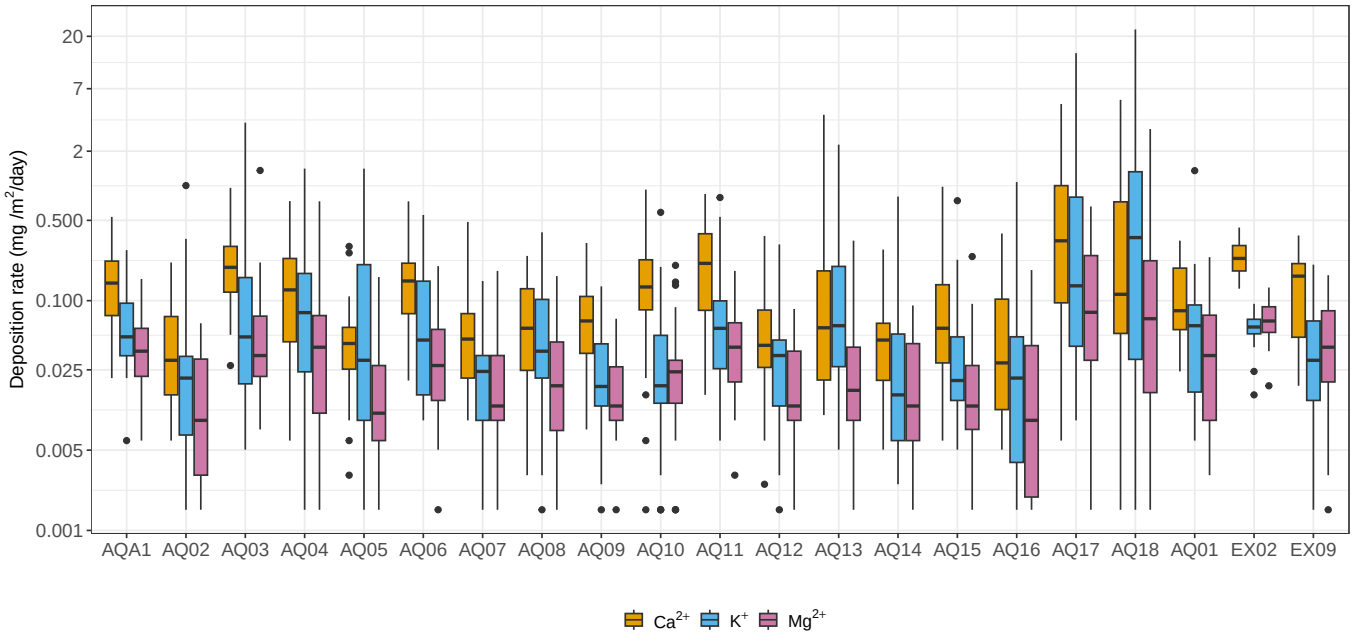

Figure 7.10-6: Boxplots of Ca^{2+}, K^{+}, and Mg^{2+} deposition rates across for the dry deposition samples by site, from May 2023 to March 2025. Note logarithmic scale.

Ca^{2+}, K^{+} and Mg^{2+} are all likely to arise mainly from geogenic sources and to be indicators of dust and clay mineral deposition, although other sources such as combustion/bushfires remain possible.

The ratio of these three species appears to be roughly constant, with some variation between sites. Further data analysis will be undertaken. A possible explanation for systematic differences between sites is a composition/size relationship due to differences in dust transport distances. This may need investigation.

Figures *7.10-7* and *7.10-8* show boxplots of Cl^-, Na^+, and SO_4^{2-} deposition rates by sampling date and site, respectively. In contrast to the previous species, these three species may originate from geogenic dust, sea salt/sea spray (including anthropogenically generated NaCl from cooling towers) and (in the case of sulfates and SO_4^{2-}) may arise from combustion or biomass sources. Again the ratios at each location appear consistent. These data and subsequent deposition data will undergo more detailed investigation in the final reporting period.

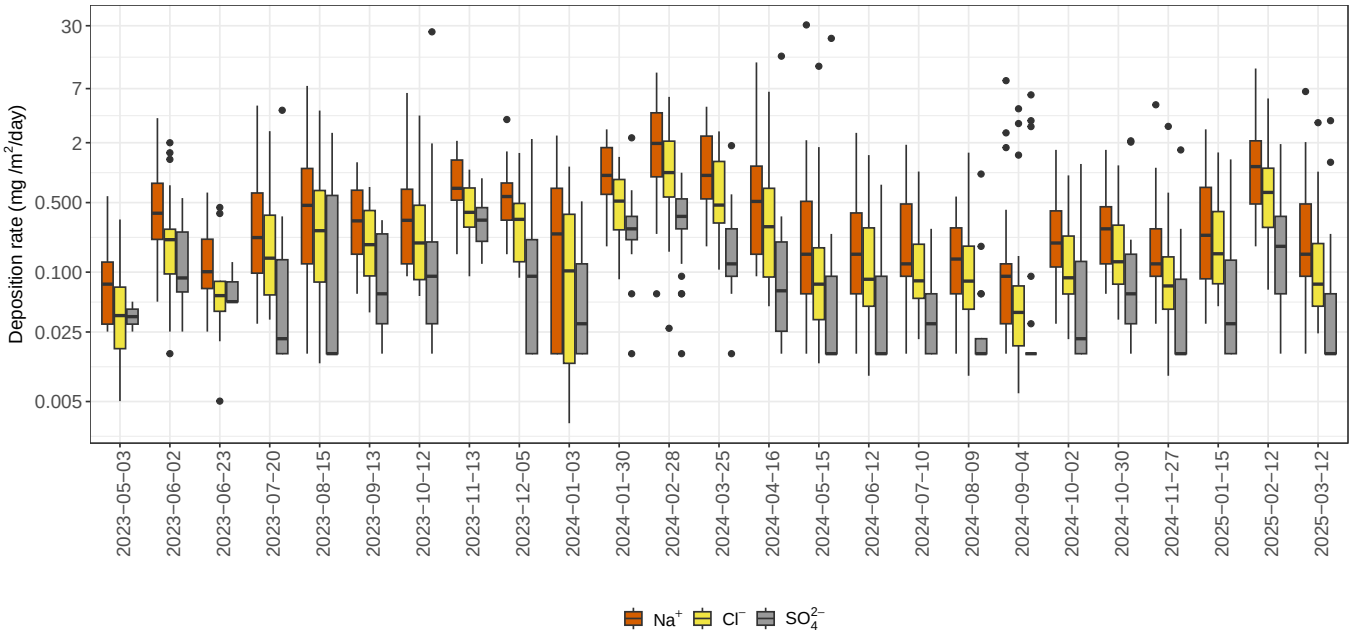

Figure 7.10-7: Boxplots of Na^+,Cl^-, and SO_4^{2-} deposition rates for the dry deposition samples across all sites by sampling period. Note logarithmic scale.

Boxplots of NH_4^+, NO_3^-, and P deposition rates for each sampling date and location are shown in Figures *7.10-9* and *7.10-10*. These species may also arise from a range of natural, anthropogenic, marine, and terrestrial sources. The results show high temporal or seasonal variability, with NH_4^+ and P frequently showing values BDL. More analysis of the causes of these fluctuations would be desirable. Some results may be able to be explained due to TC Sean.

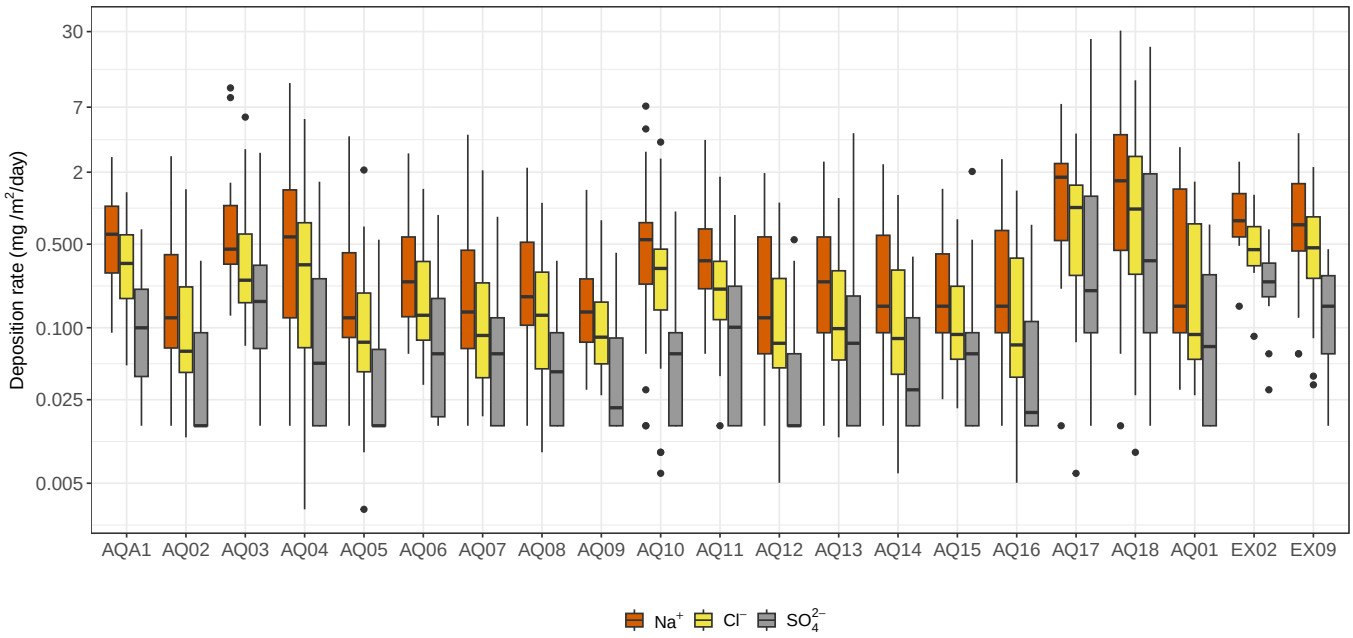

Figure 7.10-8: Boxplots of Na^+, Cl^-, and SO_4^{2-} deposition rates by site, from May 2023 to March 2025. Note logarithmic scale.

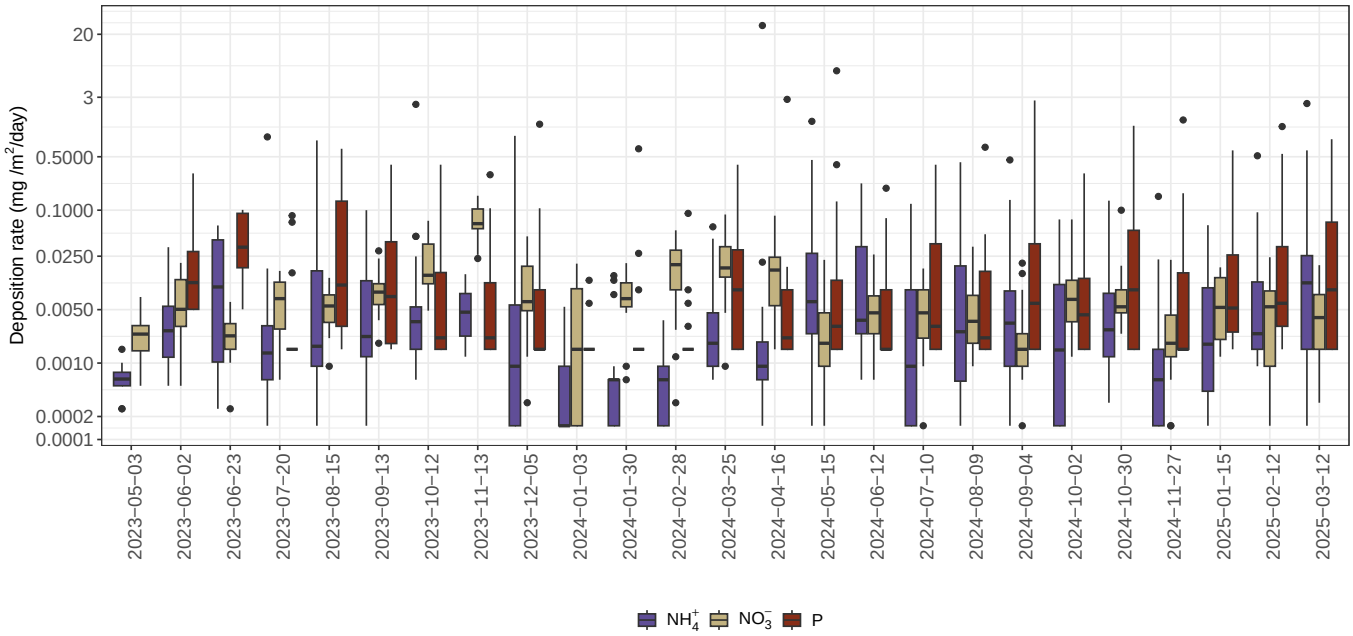

Figure 7.10-9: Boxplots of NH_4^+, NO_3^-, and P deposition rates for the dry deposition samples across all sites by sampling period. Note logarithmic scale.

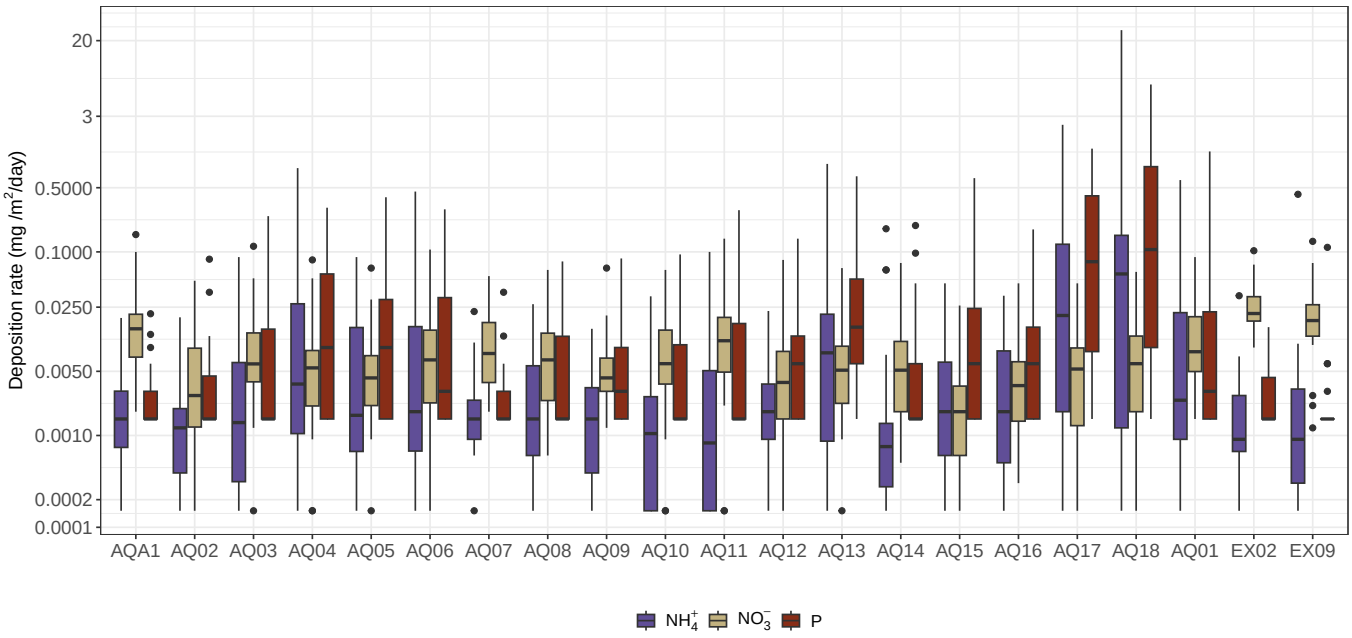

Figure 7.10-10: Boxplots of NH_4^+, NO_3^-, and P deposition rates for the dry deposition samples by site, from May 2023 to March 2025. Note logarithmic scale.

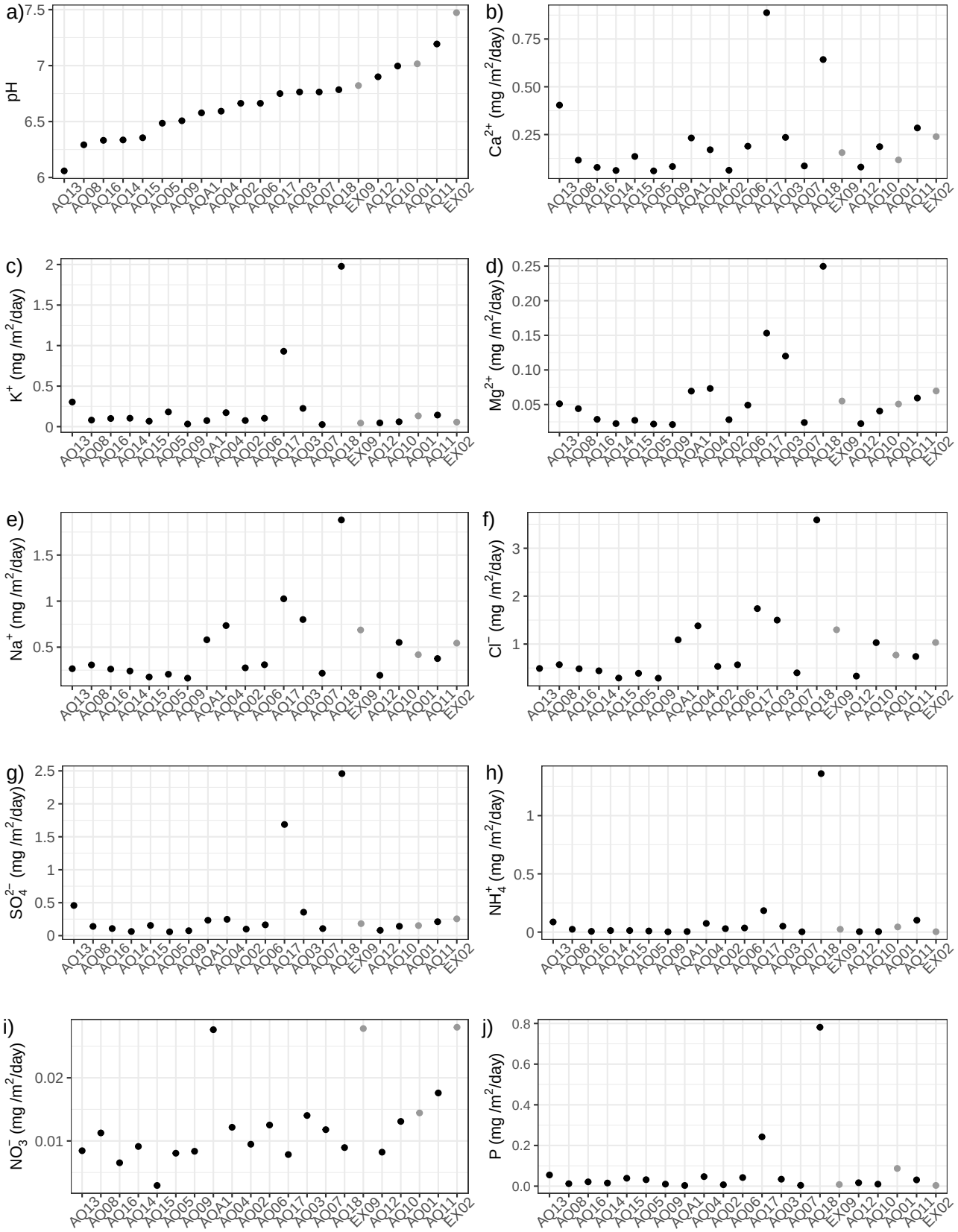

Figure 7.10-11: Average pH and deposition rates by AQM. Data represent approximately 24 months of observation (8/02/2023 to 12/03/2025) except for EX02, EX09, and AQ01 (indicated by grey dots), where less than 18 months of data are available.

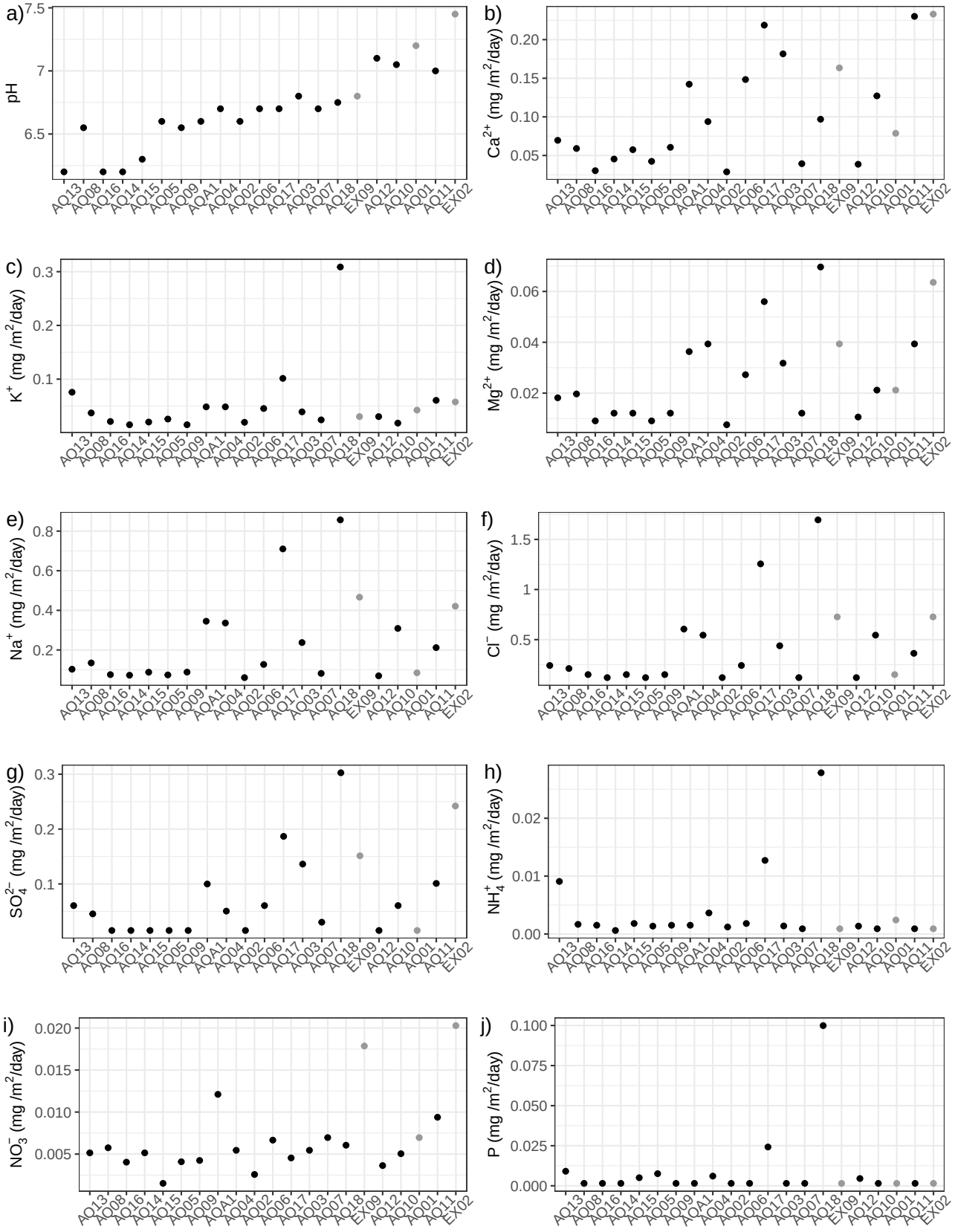

Figure 7.10-12: Median pH and deposition rates by AQM. Data represent approximately 24 months of observation (8/02/2023 to 12/03/2025) except for EX02, EX09, and AQ01 (indicated by grey dots), where less than 18 months of data are available.

Figure *7.10-11* shows the average *pH* and deposition rates of chemical species at each AQM site, and *7.10-12* shows the median *pH* and deposition rates of chemical species at each AQM site. In each plot panel, the sites are ordered according to increasing average pH. It can be seen that EX02 has the highest *pH* in both cases, whereas AQ17 and AQ18 have the highest mean values for many chemical species, largely due to a small number of high measurements (extreme outliers). Overall, however, some clear trends are appearing across the sites, which require more comprehensive investigation in conjunction with other datasets.

7.10.5 Analysis of co-located AQM sites

Section 7.10.3 of the Monitoring Studies Report 2024 (Curtin University, 2024c) details the co-located air quality monitors used to assess variability over small spatial scales. These sites are AQ07 and AQ08, which are located approximately 20 metres apart. Similar to above, this section updates the analyses presented in last year's report (Curtin University, 2024c), here presenting the dry deposition data from May 2023 to March 2025 for AQ07 and AQ08.

Figure *7.10-13* shows boxplots of deposition rates for different chemical species at AQ07 and AQ08.

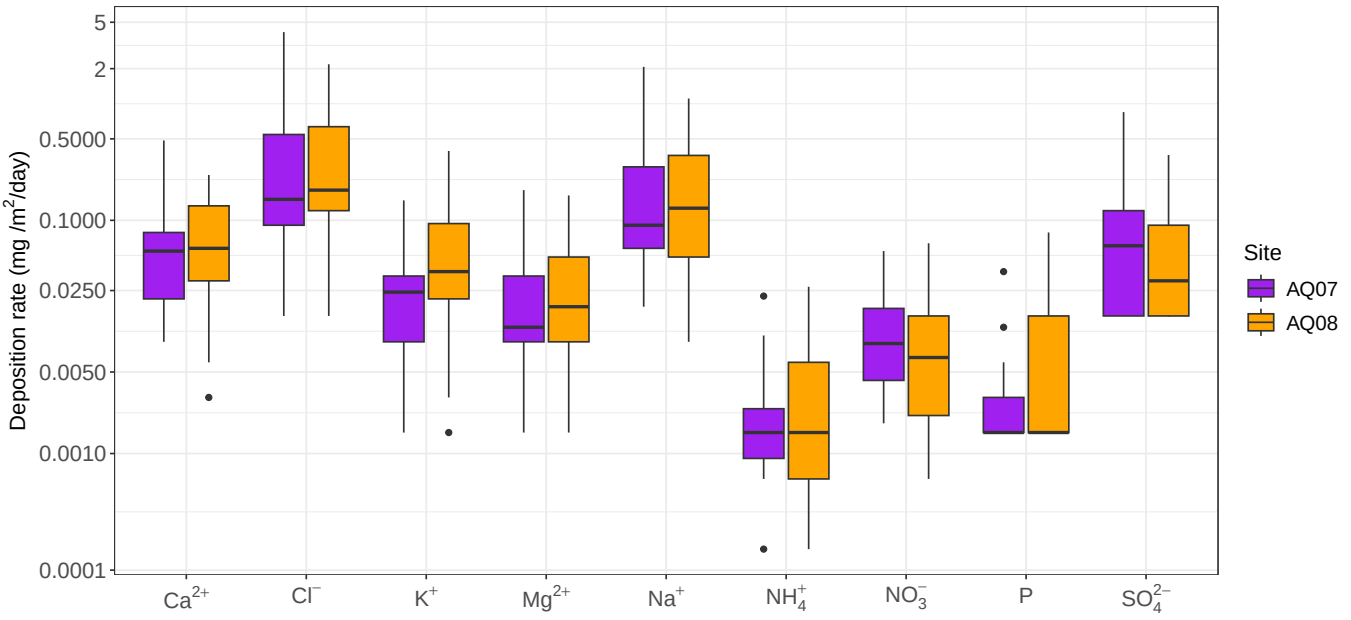

Figure 7.10-13: Boxplots of deposition rates of chemical species from dry deposition samples of co-located AQ07 and AQ08 sites, from May 2023 to March 2025. Note logarithmic scale.

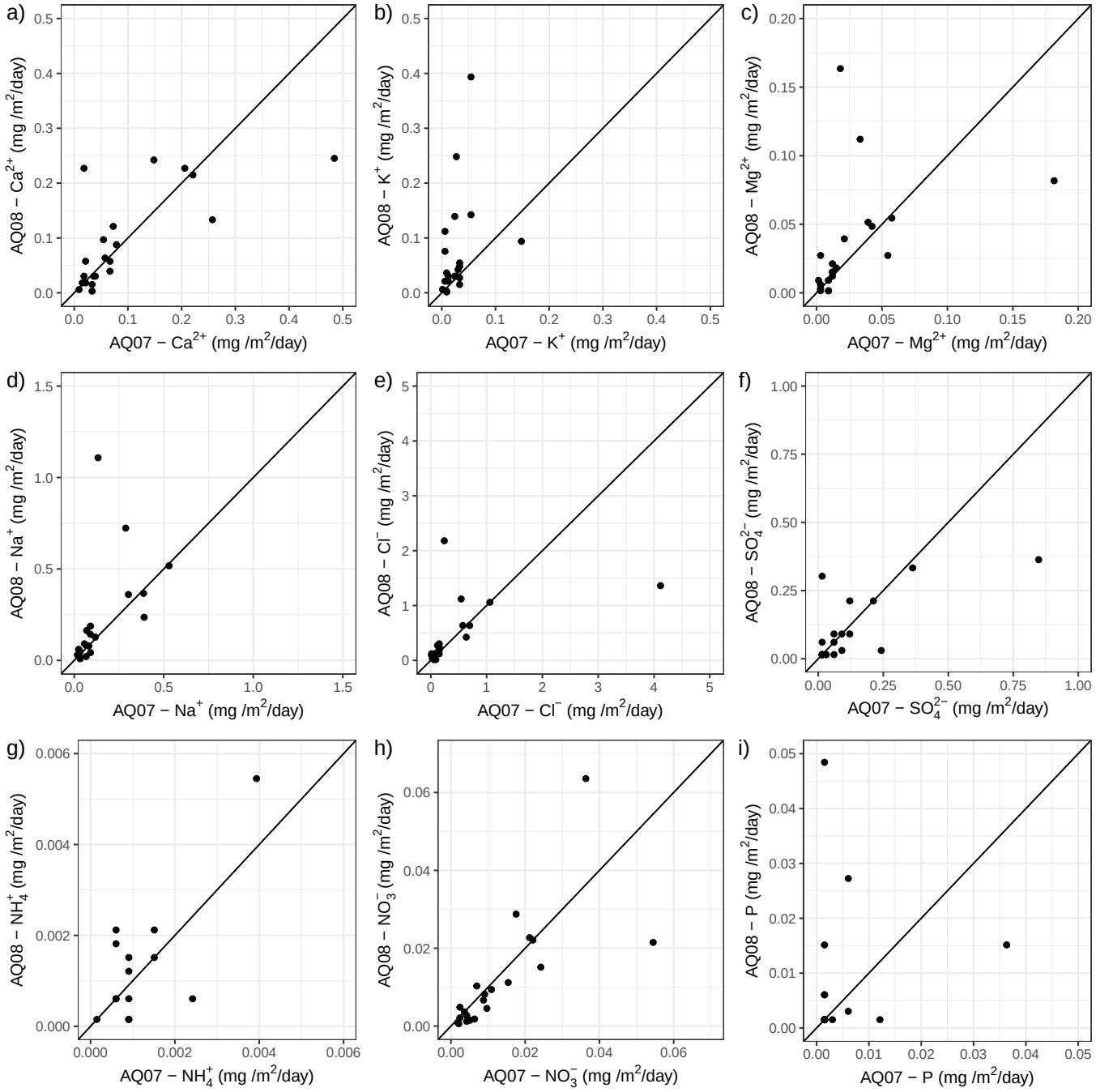

Figure 7.10-14: Scatterplots of the AQ07 vs AQ08 deposition rates for each chemical species from dry deposition samples. The black line (y = x) indicates the same deposition rate at both monitoring stations.

Figure *7.10-14* shows scatterplots of the deposition rates observed at AQ07 and AQ08, separately for each chemical species. Observations at the two sites generally agree well, except for NH_4^+ and P, which had many values below detection limits.

Differences between the observations at the two sites may be attributed to short-scale variability

(including intrinsic variability of the sampler and assay technique), provided that there is no evidence of systematic difference. For each chemical species, we performed a Wilcoxon rank sum test (Mann-Whitney test) comparing the distributions of the deposition rates at the two sites. Table *7.10-1* suggests that there is no evidence of a systematic discrepancy between the two sites (p-values > 0.05, i.e., no significant difference in distributions at the 5% significance level). Additionally, a strong positive relationship exists between samples at AQ07 and AQ08, except for K^+, NH_4^+ and P, which show a moderate relationship.

Table 7.10-1: p-values of the Wilcoxon rank-sum test, and Spearman correlation coefficient between samples at AQ07 and AQ08.

Sample	Number of observations (AQ07 and AQ08)	Wilcoxon Rank-Sum Test (p-value)	Spearman correlation coefficient
Ca^{2+}	22	0.888	0.733
Cl^-	22	0.420	0.864
K^+	22	0.051	0.443
Mg^{2+}	22	0.505	0.814
Na^+	22	0.678	0.850
NH_4^+	22	0.920	0.502
NO_3^-	22	0.435	0.880
P	22	0.192	0.306
SO_4^{2-}	22	0.675	0.703

Figure *7.10-15* shows a multiple time series plot of dry bucket sample deposition rates against collection date, with a different colour for each chemical species. Circles represent AQ07 and triangles represent AQ08. The overall impression is that colours cluster together, indicating that the differences between AQ07 and AQ08 are generally much smaller than the variability over time.

- Ca^{2+}, Cl^-, Na^+, Mg^{2+}, and SO_4^{2-} deposition rates increase from July 2023 to March 2024, then slightly drop in March and April 2024, with a large drop in May 2024. Levels then slowly increase to February 2025.
- K^+ levels remain fairly flat between August 2023 and January 2024, followed by a slight increase during February and April 2024. Levels then drop in May 2024, show a slight increase in August 2024, and remain relatively stable thereafter.
- NO_3^- is low in July and August 2023, and high in October-December 2023 and March 2025. It was also very low in May and June 2024.
- NH_4^+ and P did not show notable variation with time compared to the scale of variability for the other species.

Together, the above results indicate that the measurement process is consistent and reliable.

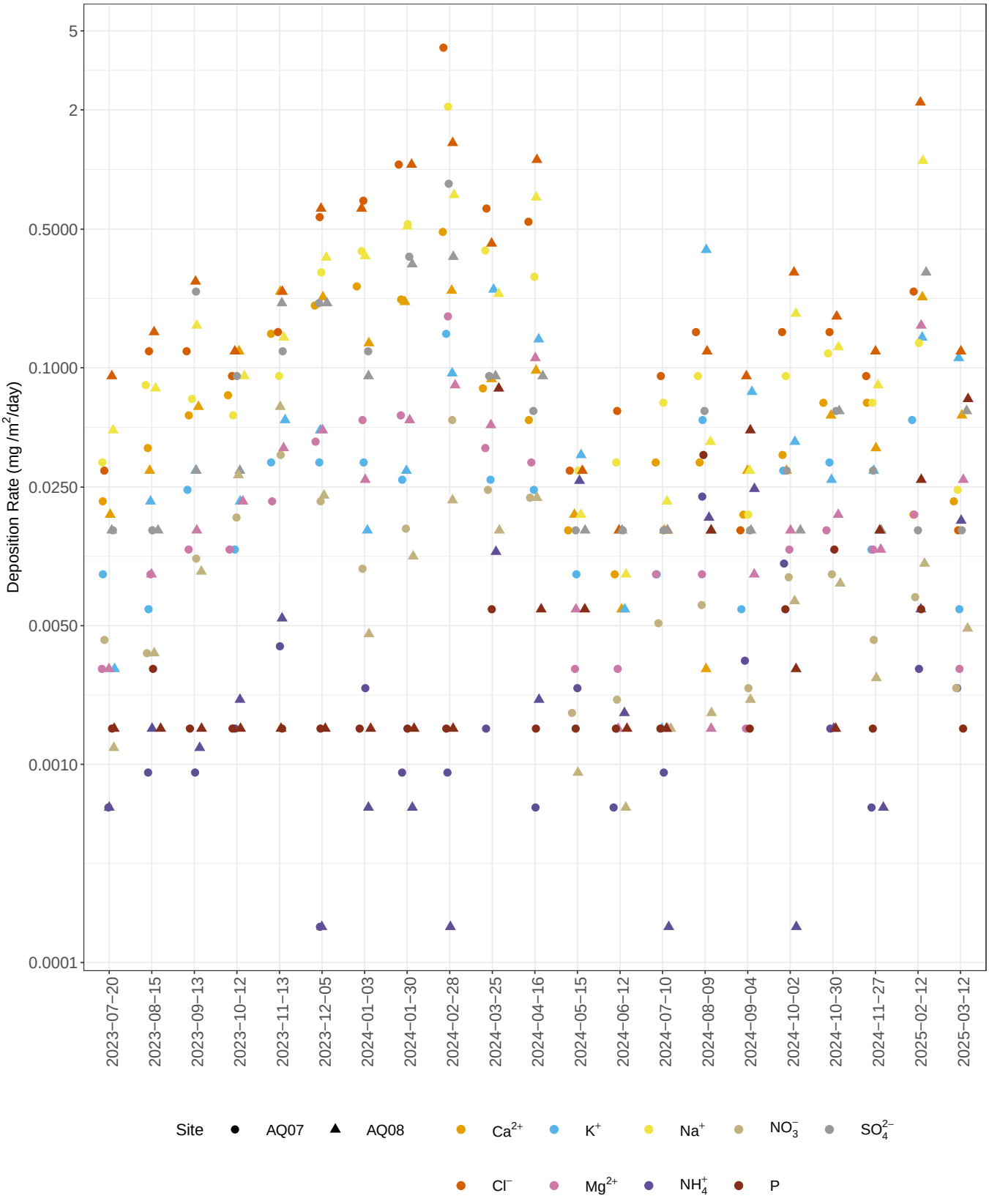

Figure 7.10-15: Time series plots of deposition rates of chemical species, from dry deposition samples at co-located AQ07 (circles) and AQ08 (triangles) sites, against collection date. Note logarithmic scale. Points were jittered to avoid overlap.

7.10.6 Spatial smoothing of deposition sampler data

Figure *7.10-16* shows the result of Nadaraya-Watson spatial smoothing of the dry bucket sample *pH* for each collection date. All *pH* smoothed values are between 6.5 and 7.5, and there is relatively little spatial variation.

Figures *7.10-17* to *7.10-25* show the Nadaraya-Watson spatial smoothed surfaces for dry bucket deposition rates for each of the species Ca^{2+}, K^{+}, Mg^{2+}, Cl^{-}, Na^{+}, $SO_4{}^{2-}$, $NH_4{}^{+}$, $NO_3{}^{-}$, and P.

Ca^{2+} and Mg^{2+} deposition rates show quite similar spatial patterns of variation.

- In the north (Dolphin and Gidley Islands), there are high deposition rates of Ca^{2+} and Mg^{2+} in August 2023, October 2023, May 2024, September-November 2024 and February–March 2025.
- There is a high deposition rate of Ca^{2+} and Mg^{2+} in February–April 2024 to the west (Enderby Island).
- Ca^{2+} and Mg^{2+} deposition rates were somewhat higher near the Dampier and Burrup regions from September 2023 to March 2024. In June–July 2023 and April 2024 to March 2025, there is little spatial variation in Ca^{2+} and Mg^{2+} near the Dampier and Burrup regions, except that Mg^{2+} deposition rates are quite high in February 2025.
- February 2024 showed the highest and some extreme Ca^{2+} and Mg^{2+} deposition rates in the northwest of the Dampier Archipelago. However, this seems to be due to some unknown error in the data (such as a wrong bucket position issue) that needs further investigation.
- The spatial variation in K^{+} deposition rate is almost similar to Ca^{2+} and Mg^{2+} in most months, but there are some differences.
- August, October, and December 2023 have high deposition rates of K^{+} in the north (Dolphin and Gidley Islands).
- The highest K^{+} deposition rate was observed near West and East Lewis islands in February 2024.
- There are also somewhat higher K^{+} deposition rates in February and March 2025 to the north of the Burrup.
- In other months, there is little spatial variation in the K^{+} deposition rate across sites.

Spatial variation in Na^{+} and Cl^{-} deposition rates is very similar. Generally, Na^{+} and Cl^{-} deposition rates over the Murujuga region are higher from July 2023 to April 2024 and lower from May 2024 to March 2025, except for higher values in February 2025. However, there are some regions with notably higher deposition rates.

- In February 2024, very high Na^{+} and Cl^{-} deposition rates were observed in Dampier, southern Burrup, east and west Lewis Islands, and West Intercourse Island. This seems to be due to some unknown error in the data, such as a wrong bucket position issue, that needs further investigation.
- Dolphin and Gidley Islands also had higher Na^{+} and Cl^{-} deposition rates in August 2023, April 2024, May 2024, and February–March 2025.
- Slightly higher Na^{+} and Cl^{-} deposition rates were observed in the Burrup and Dampier regions in January 2024, March 2024, and February 2025.

The following observations have been made on SO_4^{2-} deposition:

- The deposition rates of SO_4^{2-} in February 2024 are extremely high around Dampier, the southern Burrup, East and West Lewis Islands, and West Intercourse Island. This is very similar to Ca^{2+}, Mg^{2+}, Na^{+}, and Cl^{-}, suggesting that there may be some issue with the February 2024 samples.
- Higher SO_4^{2-} deposition rates were also observed near Dampier and the southern Burrup in November 2023 and January 2024.
- Dolphin and Gidley Islands showed very high SO_4^{2-} deposition rates in August 2023.
- There were higher rates in the west in March 2024.
- Somewhat higher SO_4^{2-} deposition rates were observed near the Dolphin and Gidley Islands from April 2024 to March 2025, except in July–August 2025.
- Data collected from March 2024 to March 2025 showed SO_4^{2-} deposition rates around Dampier and Burrup were generally quite low.

Spatial smoothing showed high levels of K^{+}, Na^{+}, Cl^{-} and SO_4^{2-} on Rosemary Island. However, as no monitoring stations exist on this island such interpolations must be treated with caution.

In general, NH_4^{+} deposition rates are higher in all months except January–February 2024, April 2024, and November 2024 compared to other months.

- In particular, high deposition rates of NH_4^{+} were observed in the north (Dolphin and Gidley Islands) during August 2023, October 2023, early December 2024, and May 2024 to March 2025 (except for August 2024).
- From July to December 2023, May to June 2024, October 2024, and March 2025, NH_4^{+} deposition rates were noticeably higher near the Burrup region.

P deposition rates are generally low near the Dampier and the Burrup regions. However, they are consistently higher on Dolphin and Gidley Islands in many months.

Across Murujuga, samples collected on 13 November 2023 showed relatively high NO_3^{-} deposition rates.

For cross-checking purposes, the analysis was repeated after applying winsorization to all deposition rate data to moderate the effects of extreme values. After winsorization, NO_3^{-} ranged between 0 and 0.02 ng/m^2/day, except on 13/11/2023, when NO_3^{-} ranged between 0.023 and 0.036 ng/m^2/day. We concluded that the spatial smoothing results appear to be resistant to extremes, and the extreme NO_3^{-} observed on 13^{th} November 2023 may require further analysis or comparison with other component studies.

Apart from this date, NO_3^{-} levels were very high in Dampier (near industrial installations) in October 2023, December 2023, and from February to April 2024. In general, NO_3^{-} was somewhat higher in the Dampier and southern Burrup regions in September 2023 and October 2024.

Conversely, NO_3^{-} was very low over Murujuga from May to August 2023, May to September 2024, and November 2024 to March 2025.

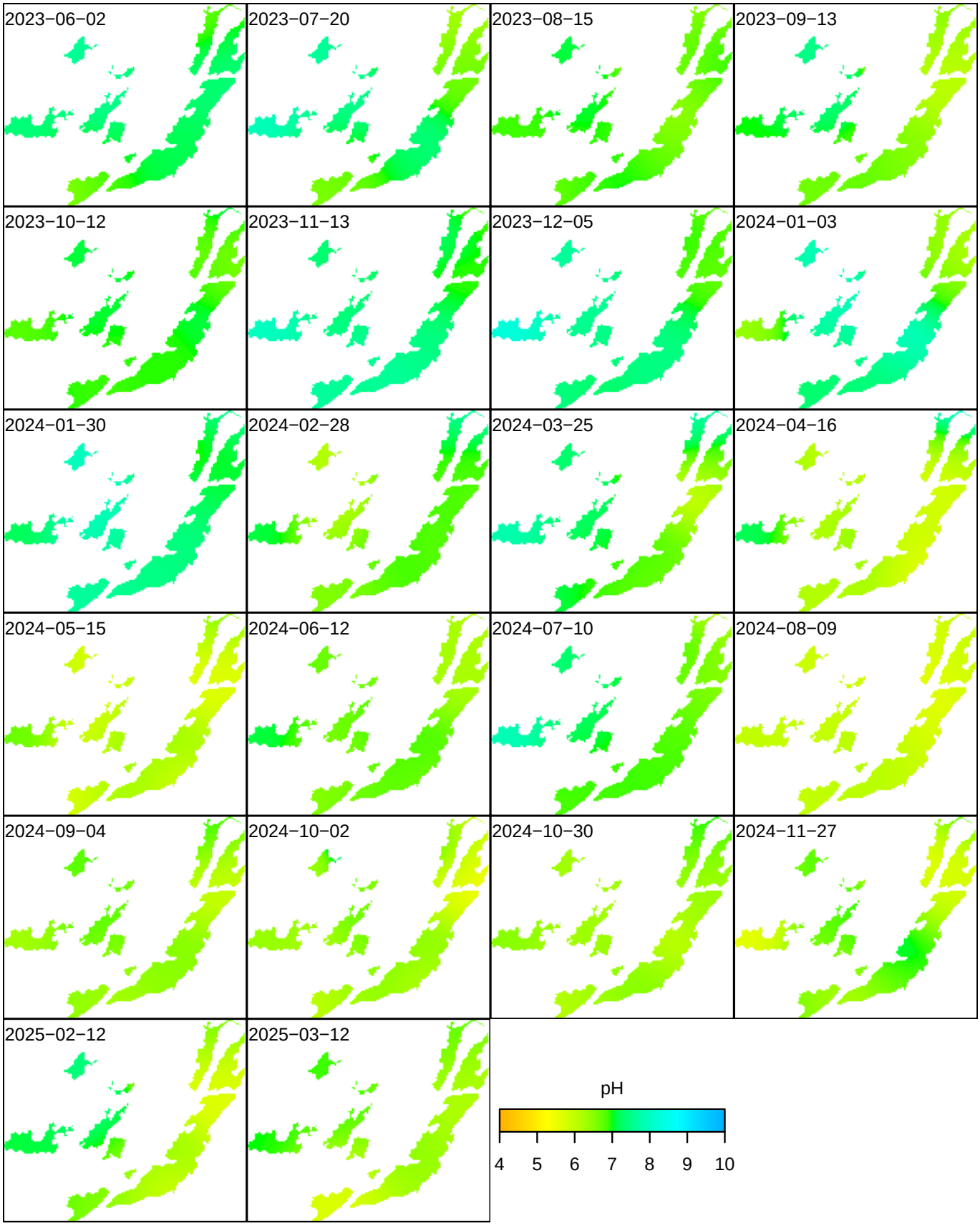

Figure 7.10-16: Spatially smoothed average pH for the dry deposition samples by sampling period.

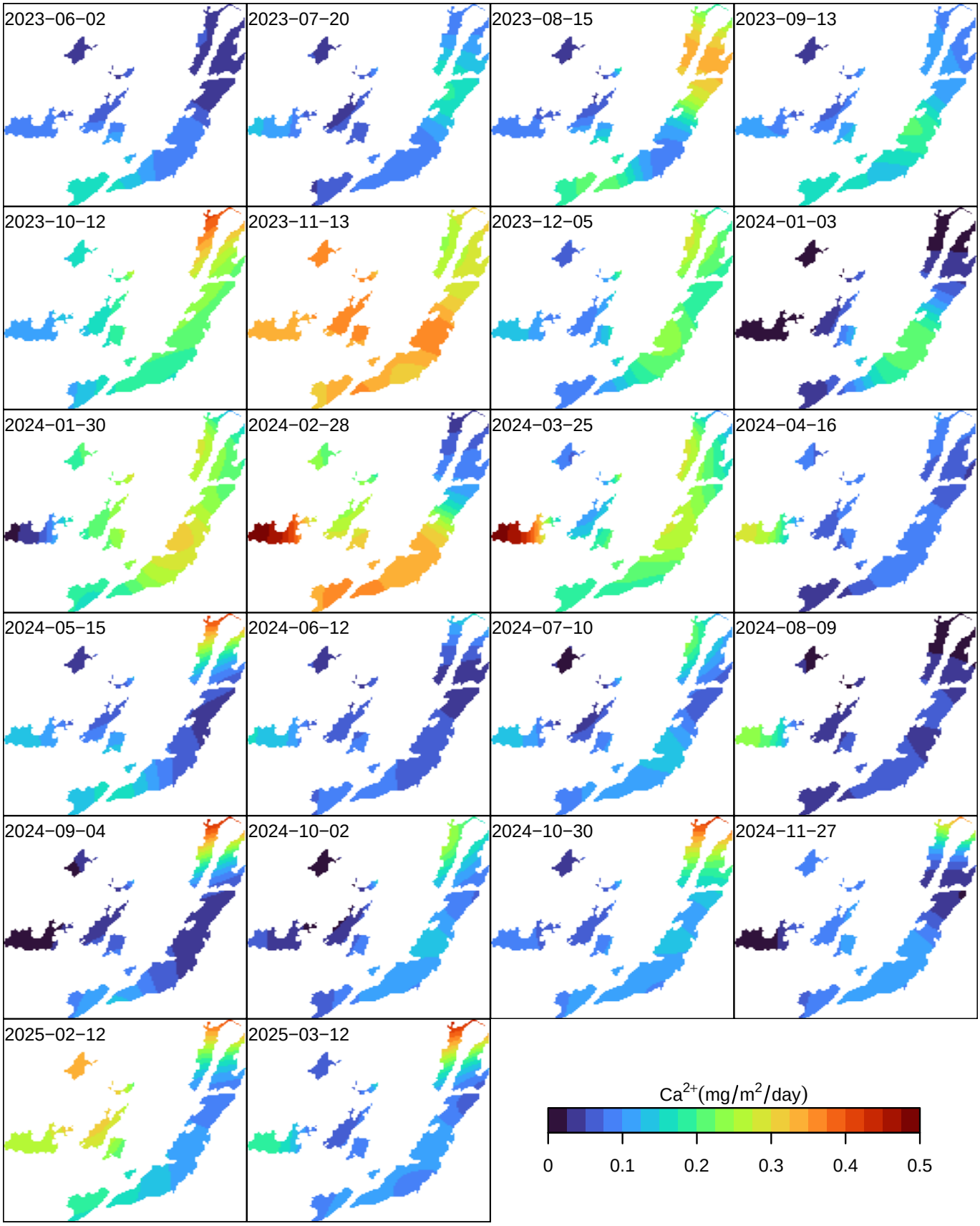

Figure 7.10-17: Spatially smoothed average Ca^{2+} deposition rate for the dry deposition samples by sampling period.

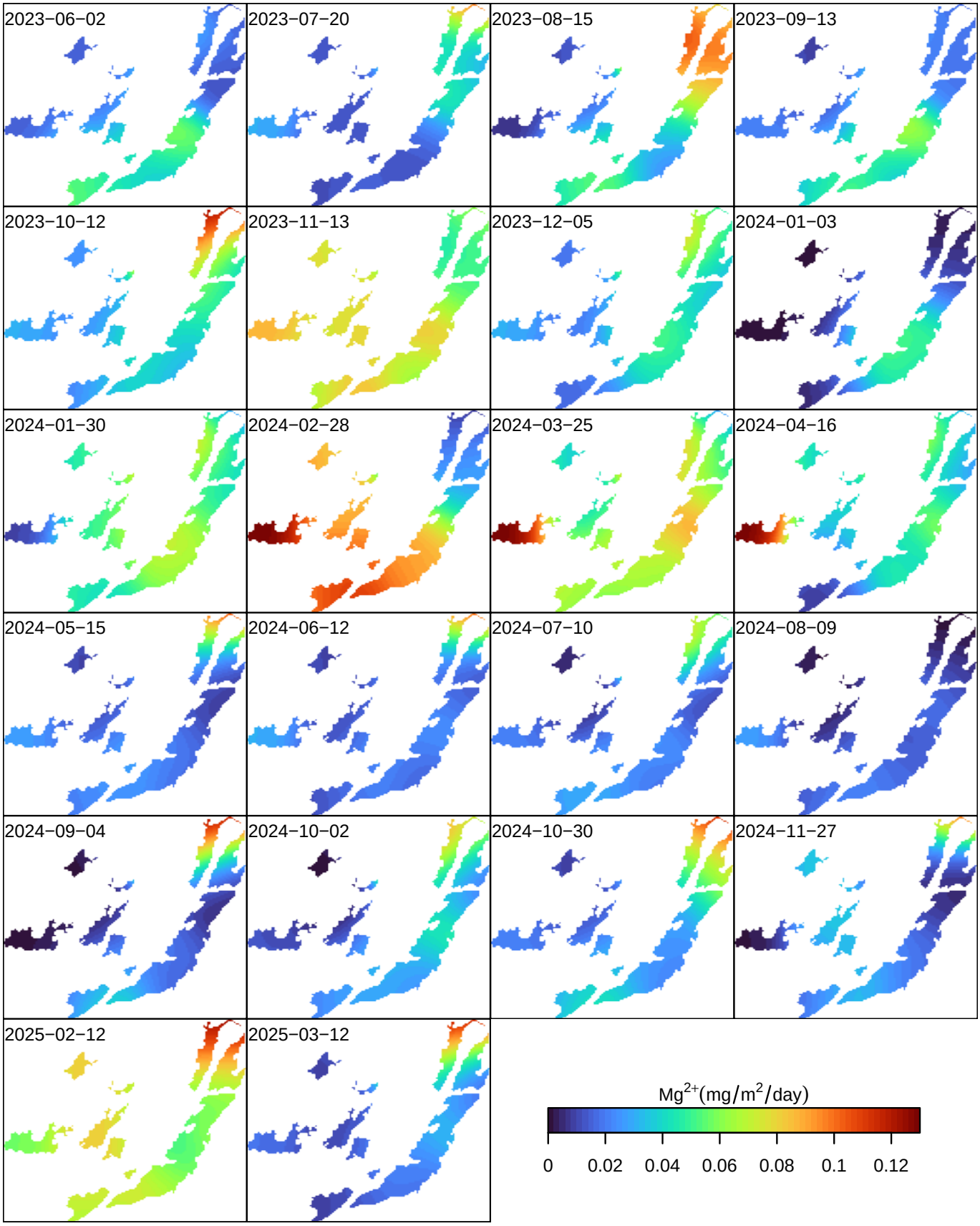

Figure 7.10-18: Spatially smoothed average Mg^{2+} deposition rate for the dry deposition samples by sampling period.

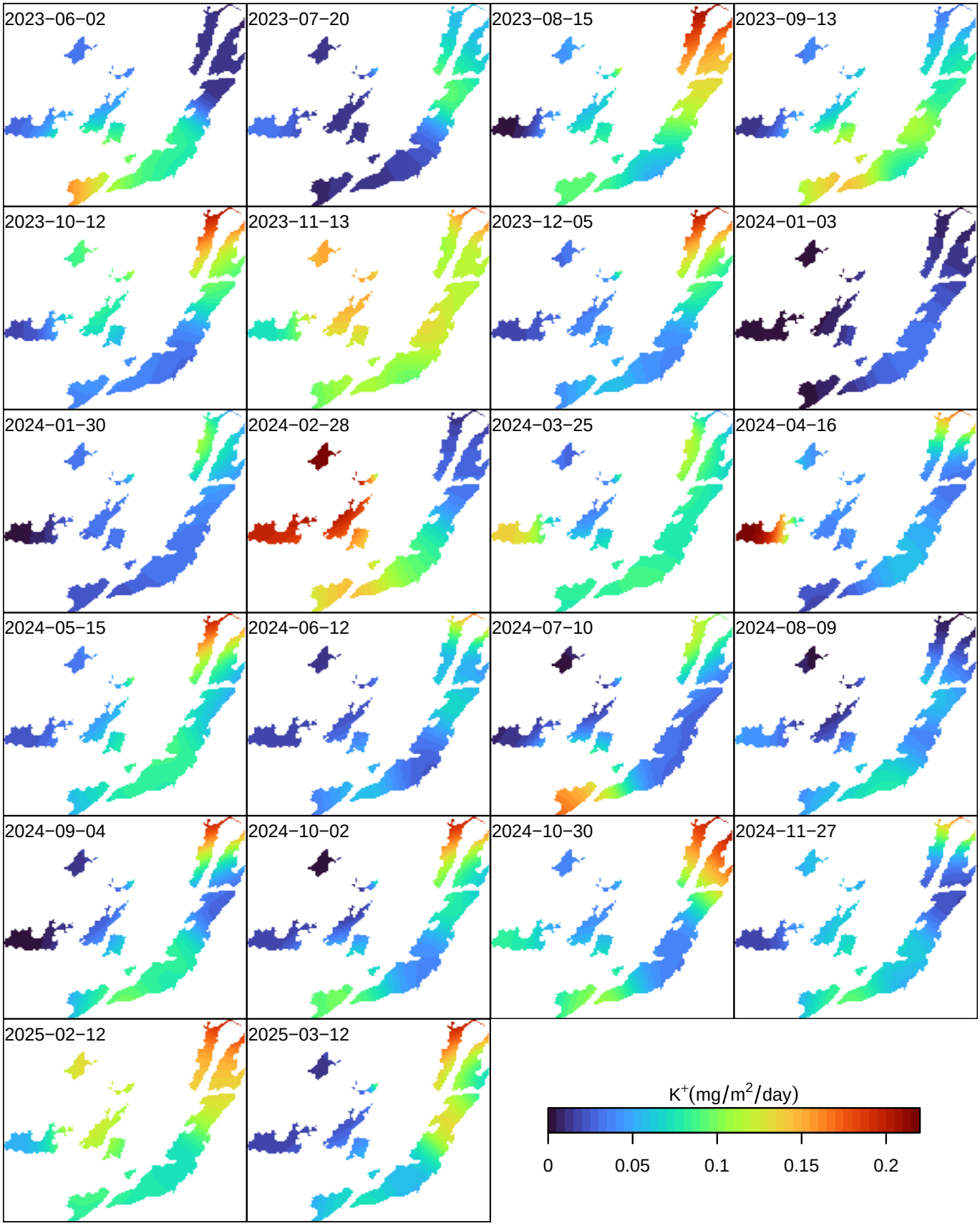

Figure 7.10-19: Spatially smoothed average K^+ deposition rate for the dry deposition samples by sampling period.

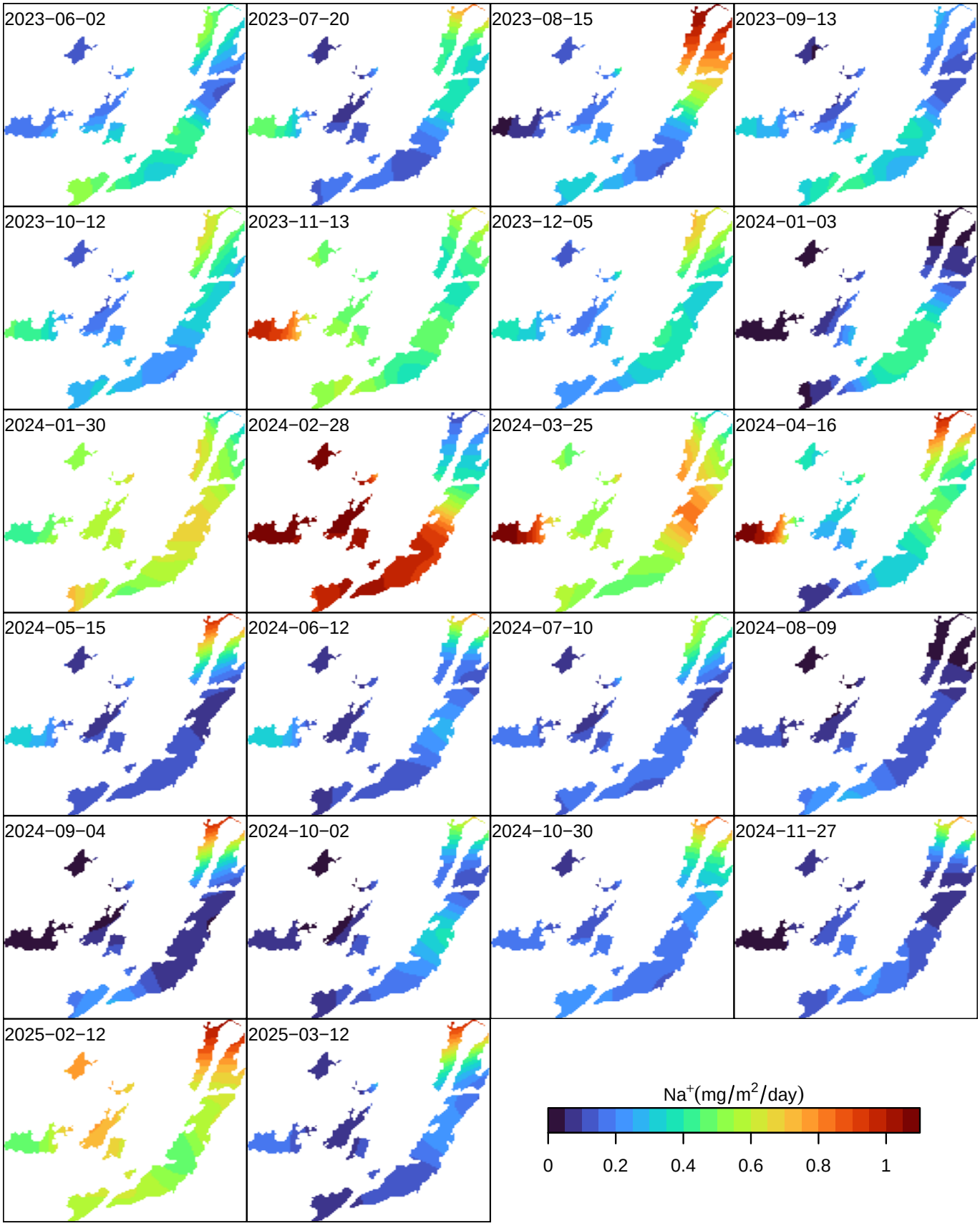

Figure 7.10-20: Spatially smoothed average Na^+ deposition rate for the dry deposition samples by different sampling period.

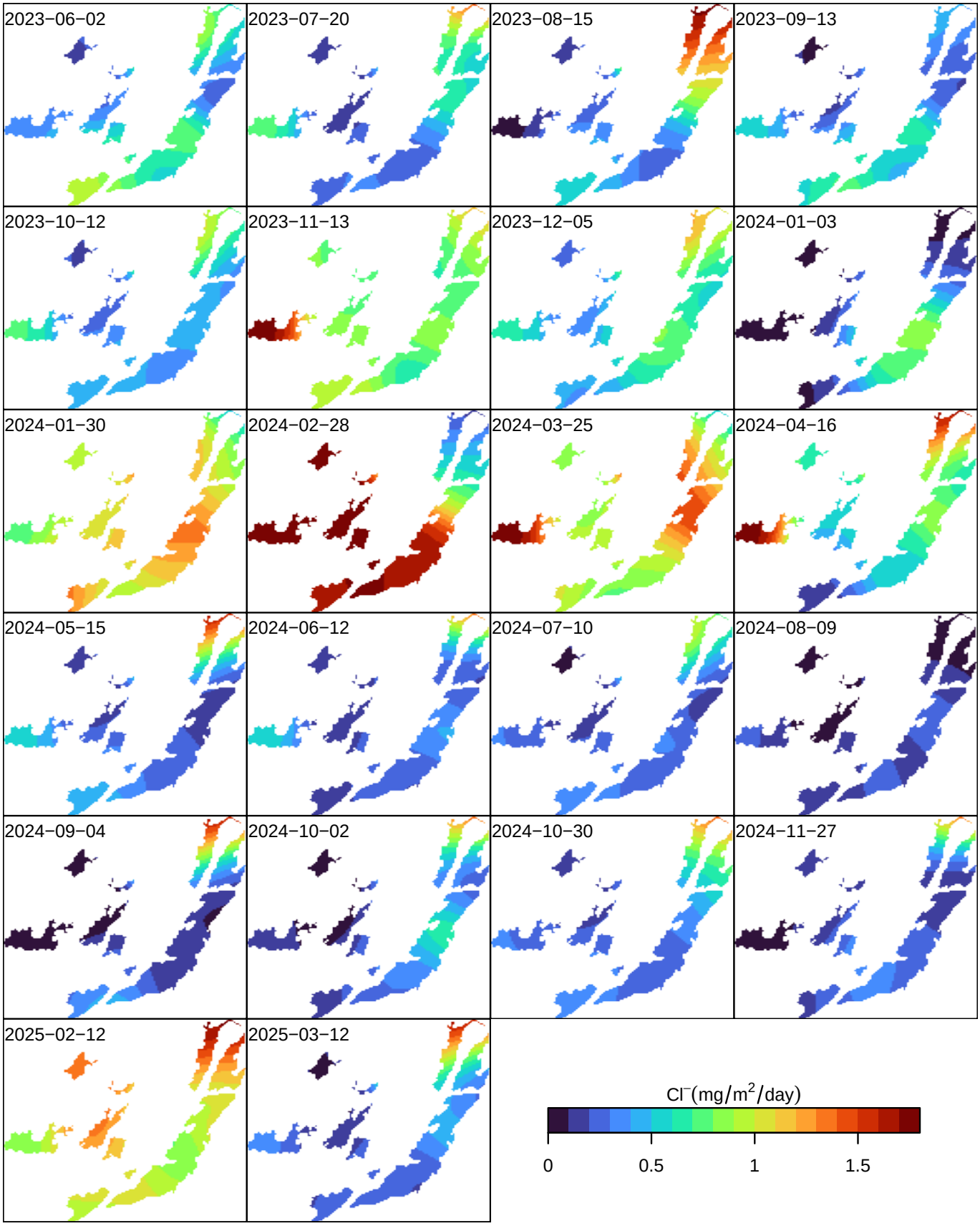

Figure 7.10-21: Spatially smoothed average Cl^- deposition rate for the dry deposition samples by sampling period.

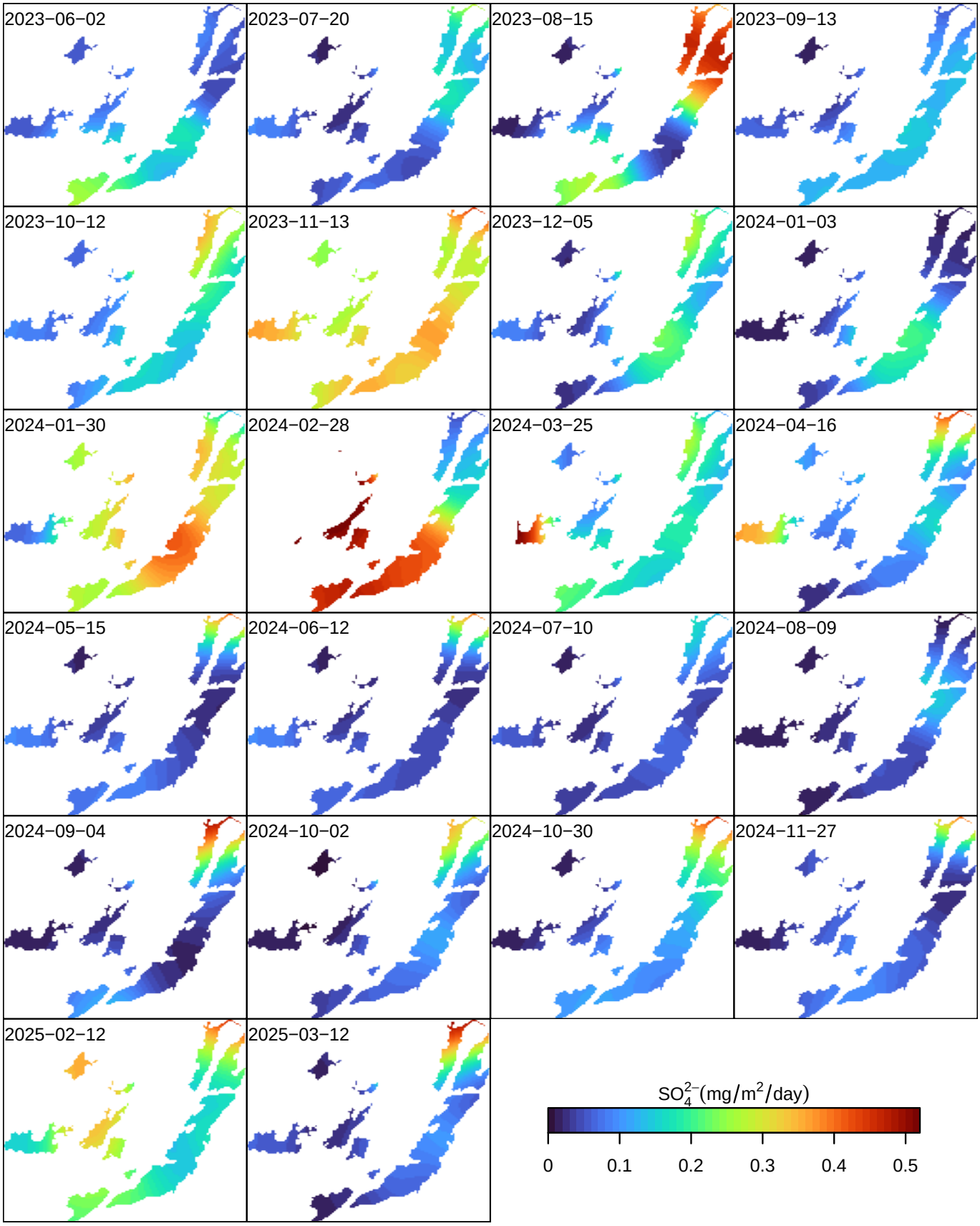

Figure 7.10-22: Spatially smoothed average SO_4^{2-} deposition rate for the dry deposition samples by sampling period.

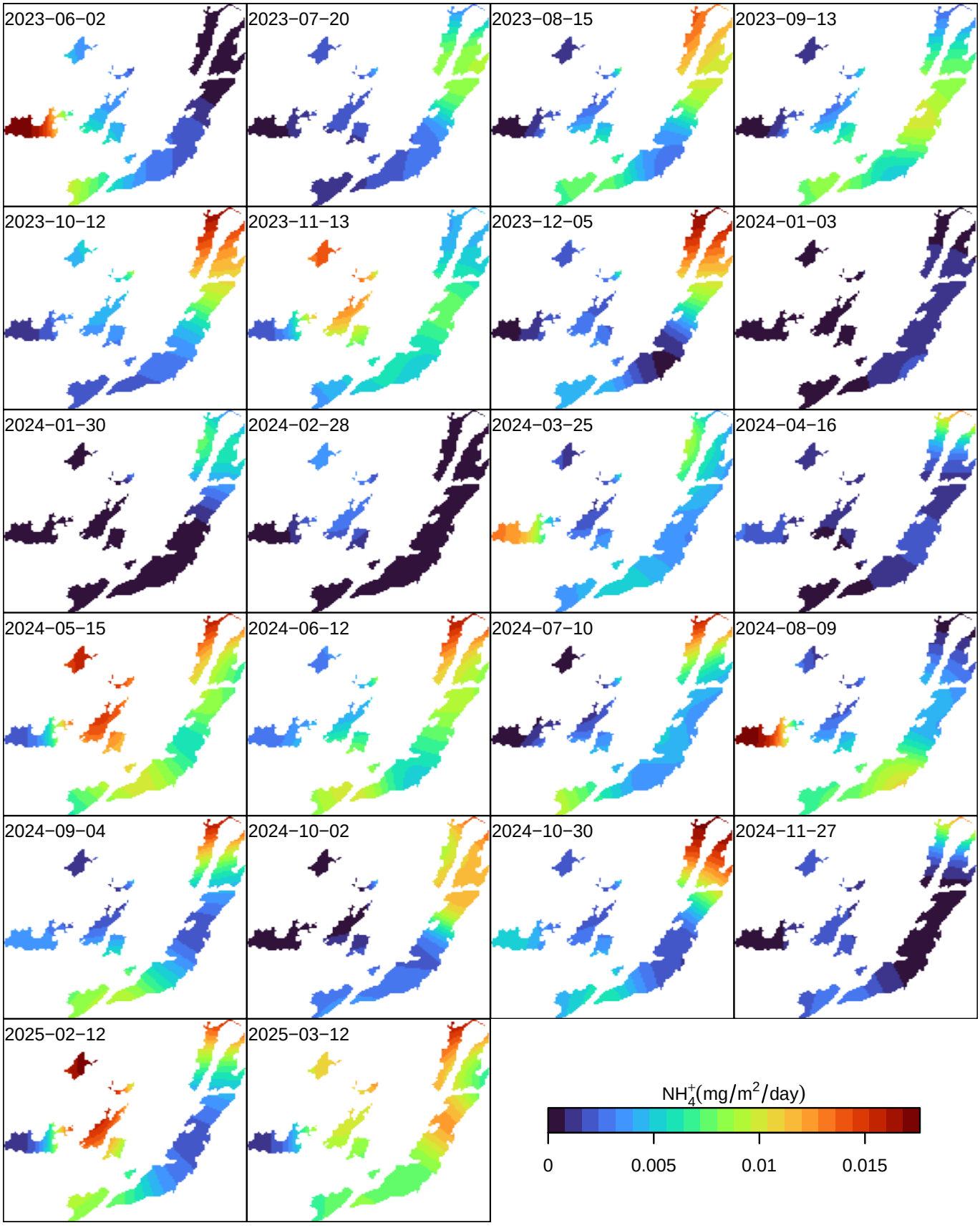

Figure 7.10-23: Spatially smoothed average NH_4^+ deposition rate for the dry deposition samples by sampling period.

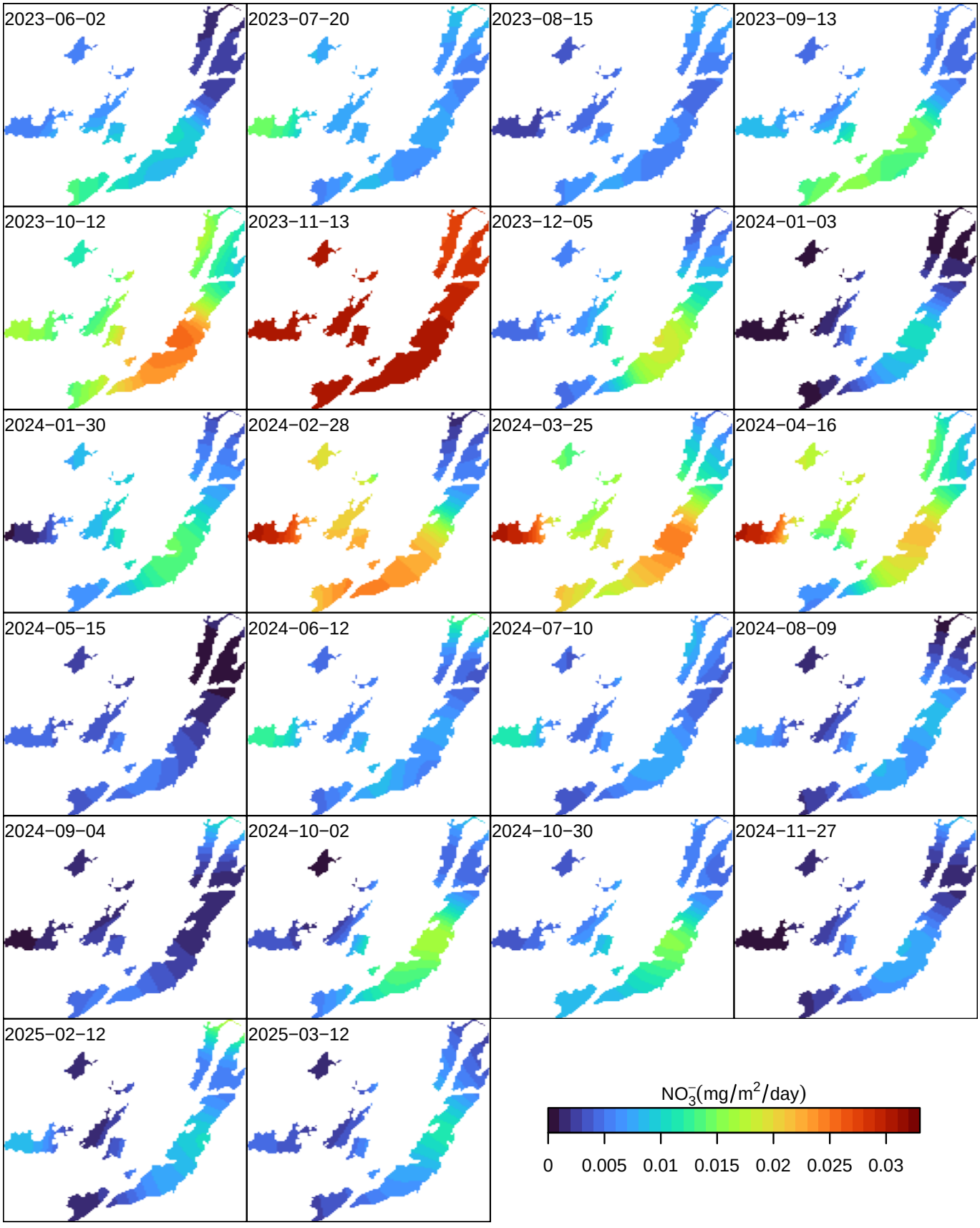

Figure 7.10-24: Spatially smoothed average NO_3^- deposition rate for the dry deposition samples by sampling periods.

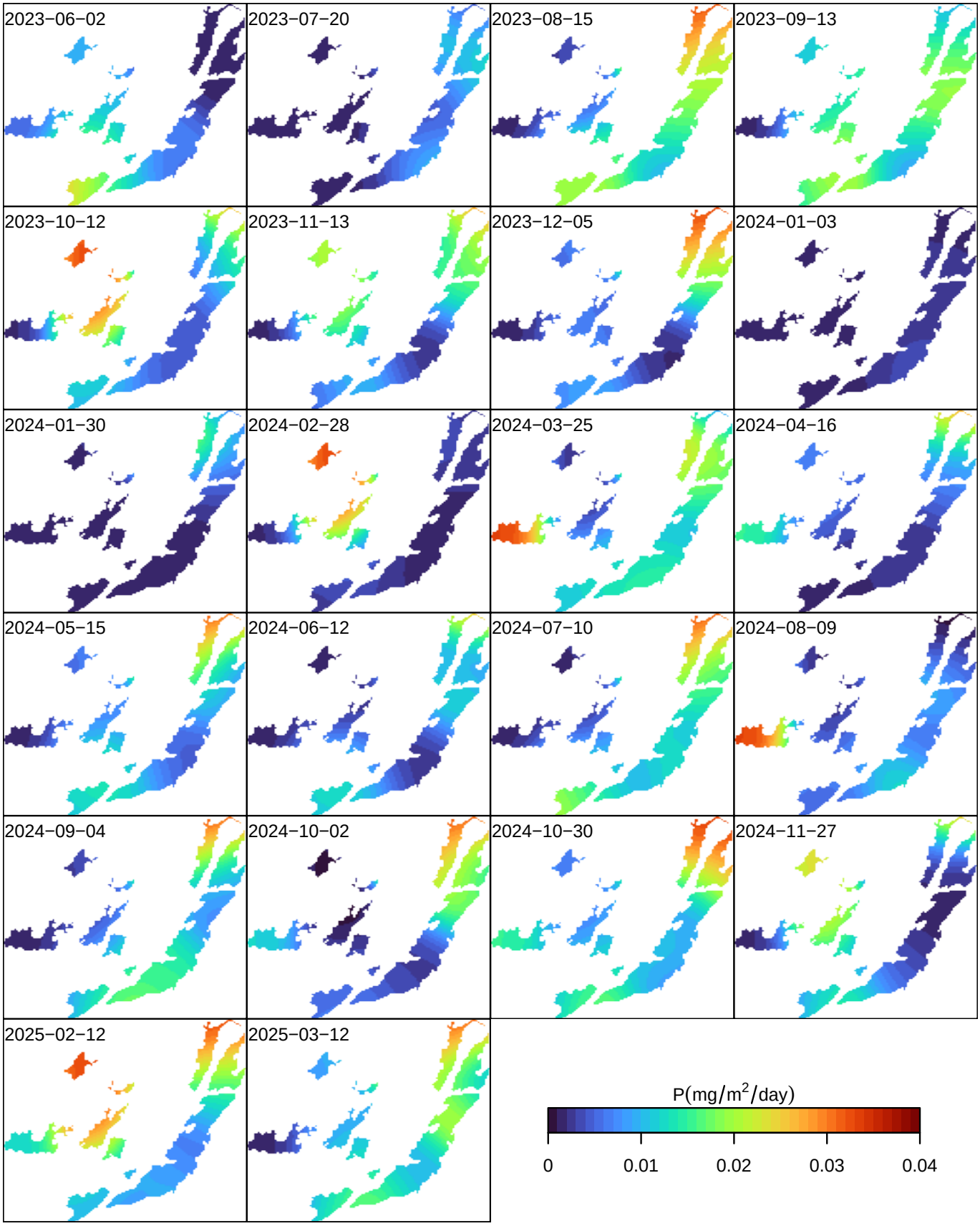

Figure 7.10-25: Spatially smoothed average P deposition rate for the dry deposition samples by sampling period.

7.10.7 Rainfall *pH*

Section 7.10.5 of the Monitoring Studies Report 2024 (Curtin University, 2024c) discusses a dominant narrative in previous studies and commentary by others that there has been increasing acidification at Murujuga (i.e., increasingly acidic rainfall). This section updates Figure 7.10-25 in the previous study report (Curtin University, 2024c).

Figure *7.10-26* shows historic and recent rainfall data from Murujuga. The red dots represent *pH* measurements reported by Bednarik (2007), which have been digitally extracted from the published material. Personal communication has established that the horizontal bars published in the original paper represent single points at the centroid of the bar and have been extracted as such, however since the Monitoring Studies Report 2024 (Curtin University, 2024c) was published, the 2005 data point has since been found to refer to the mean data value from CSIRO monitoring studies report 2006. The complete 2005/2006 data are now included from the CSIRO study. These data show a mean of approximately 5.0 and a median of 4.8 for measurements during 2005 (Bednarik's paper shows a (mean) value of 4.6). CSIRO report 20 individual measuments. While two measurements are within the range of MRAMP data, 14 are *pH* 5.0 or below and two are *pH* 4.6 or below. CSIRO 2010 reports an additional two years of rainfall *pH*data (2007/2008 and 2008/2009), which shows a similar, but possibly a slightly increasing trend compared to 2005. Notably, the fertiliser plant is reported to have commenced initial operation in 2006.

Whether we accept the general definition of the onset of acid rain as $\leq$*pH* 4.5, or the definition of $\leq$*pH* 5.0 given in (Neumann, 2025), there are multiple values in the 2005-2009 period within this range. However, values this low have not been observed during the 2023-2025 period.

Data shown in Figure *7.10-26* from 2023 onwards represent *pH* measurements by the West Australian Biogeochemistry Centre (Greg Skrypek, UWA) using specialised rain collectors from Palmex Ltd. (Croatia). These have been co-located at four MRAMP AQMs (AQ01, AQ10, AQ14, AQ18). This figure also shows data from two other UWA rainfall monitoring sites established prior to MRAMP, including Rio Tinto's Aboriginal Training and Liaison (**ATAL**) offices (sampled by Dr Ken Mulvaney) and Rosemary Island (near TM02 - sampled by MRAMP for the last 3 years). Figure *7.10-26* also includes rain samples collected by Professor Jo McDonald in Dampier town during Tropical Cyclone Sean in January 2025. In addition, Figure *7.10-26* shows samples taken from the powered AQM air conditioner condensate drain during dry but humid conditions (AQ01, EX02, EX09). Notably these appear to be in the same *pH* range as rainfall measurements. This method appears to be a novel method of sampling wet deposition *pH* during dry conditions, which we cannot find previous literature for.

The rainfall *pH* from the four MRAMP AQMs collected in 2023 and 2024 were neutral or slightly alkaline. This is thought to be due to the contribution of salt(s) and/or dust/clay minerals. The rainfall *pH* values agree relatively well with the deposition sampler data.

Measurements taken during Tropical Cyclone Sean and condensate samples during dry conditions in 2025 show a slightly lower *pH* more consistent with expected average rainfall measurements. During the course of T.C. Sean, a time series of rainfall samples collected by Prof. Jo McDonald appear to show an initial *pH* of 7.0 asymptotes towards *pH* 5.6, which is the global background average for 'pure' rain/water that has fully equilibrated with atmospheric CO_2. Some caution should be used in interpreting these results however as they were opportunistically sampled using

non-standard collection devices.

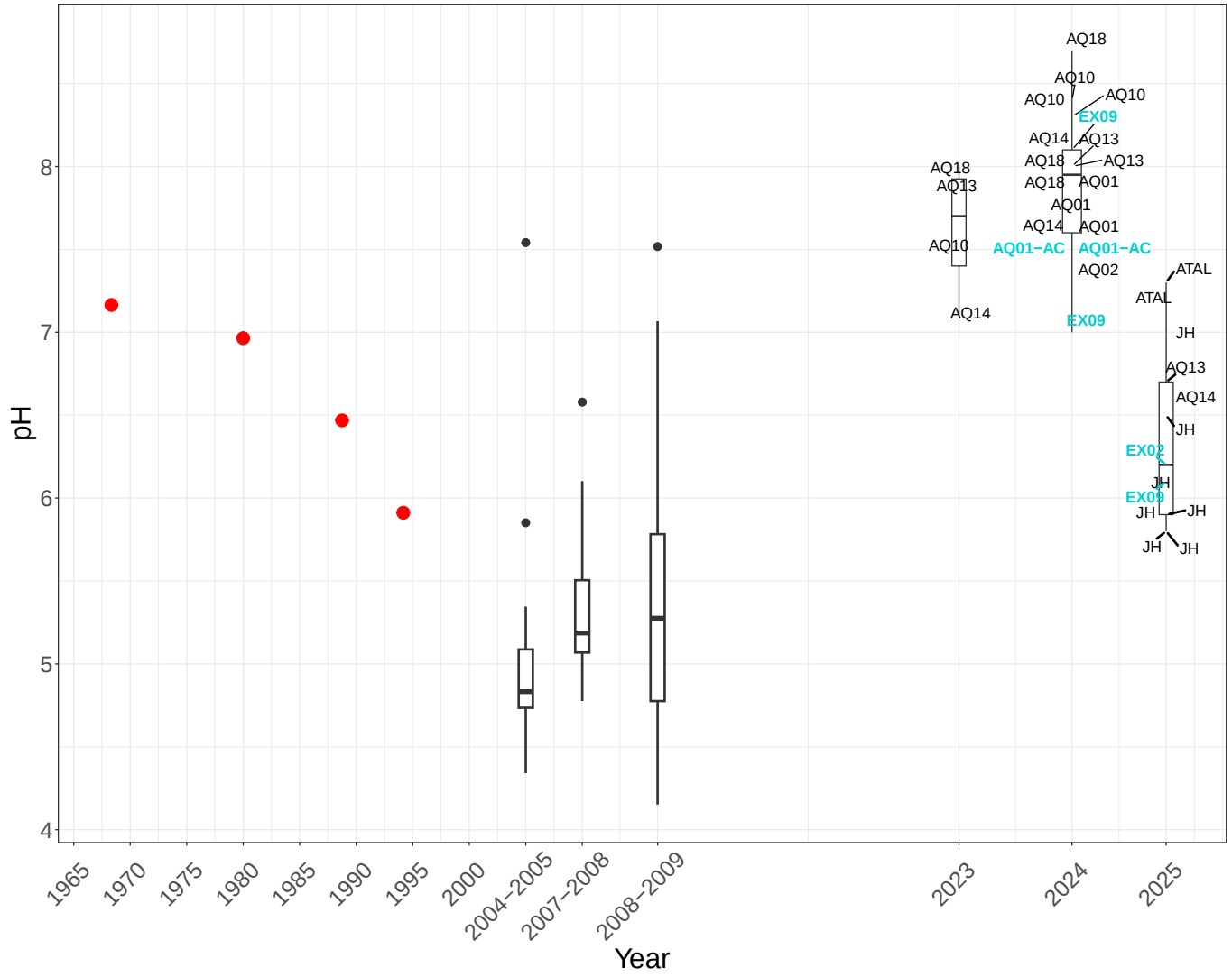

Figure 7.10-26: Historical and MRAMP measurements of rainfall pH plotted against the year of observation. The red dots are digitised from Bednarik (2007). 2004-2005, 2007-2008, and 2008-2009 data are from CSIRO monitoring studies report 2010. 2023 onwards are samples collected by MRAMP and analysed by Greg Skrypek, UWA. AQ01-AC denotes an air conditioner condensate sample during dry conditions. JH denotes samples collected by Professor Jo McDonald in Dampier during Tropical Cyclone Sean in January 2025.

Given both the deposition sampler and rainfall *pH* data, the historic acidic rain reported by CSIRO from 2005-2009 does not appear to be currently occurring. It is unfortunate that a more extensive rainfall *pH* record for the region does not appear to be available. Globally, rainfall *pH* is generally 5.0-6.0 in what are considered relatively unpolluted regions, with an average of 5.6 as stated above. Values below this can be considered acid rain, however definitions vary. Most sources would consider the onset of acid rain to occur at a *pH* range of 4.4-5.0. Rainfall *pH* above 7 is usually considered to be due to salt/sea spray or alkaline dust/clay minerals as discussed above. It is possible that rainfall was more acidic in the past when NO_2 and SO_2 levels in the airshed were

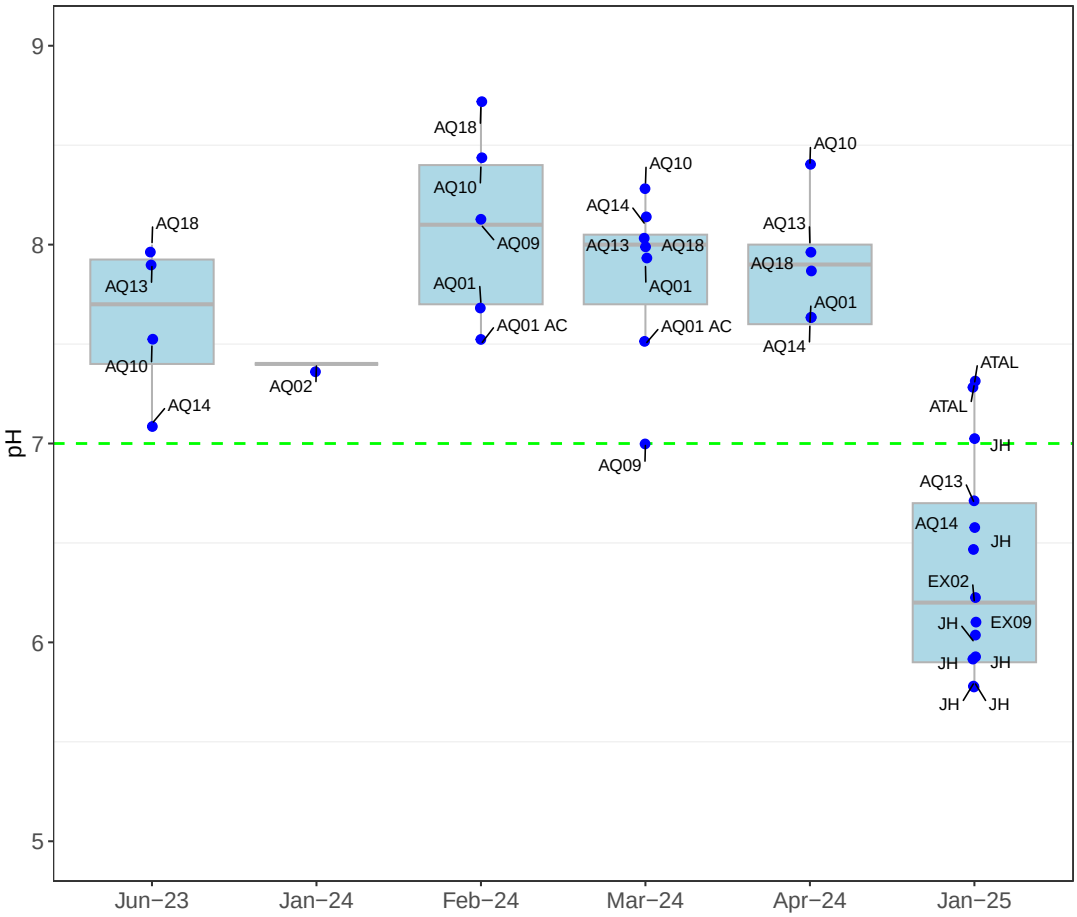

Figure 7.10-27: Rainfall pH measured during MRAMP studies plotted against month of observation. The green dashed line represents the neutral pH value.

higher, e.g., when additional sources such as higher sulfur fuels were combusted. The CSIRO 2006 data appears to show compelling evidence of some degree of acidic rainfall occurring as recently as 2009.

It is worth noting the former Dampier power station was still operating until 2010, and legislated fuel sulfur levels were higher (Curtin University, 2024a). Additionally, the fertiliser plant was reported to have commenced operation in 2006 and contains a seawater cooling tower as part of the plant, resulting in an inland source of salt aerosol.

This page is intentionally blank.

7.11 Total (flask) deposition sample

7.11.1 Background

Total deposition flasks were deployed to all sites and co-located with the 3-bucket deposition samplers. The lower right of Figure *5.3-2* shows the total deposition flask. These are composed of a 150 mm glass funnel in a 4 L reagent bottle, and are always open to the atmosphere. These are samplers as described in AS/NZS 3580.10.1, and they were deployed to allow comparison of the 3-bucket deposition sampler to a more established method for deposition sampling.

Due to the logistics associated with sample changeover, particularly the island sites, there have been some departures from the Australian Standard:

- Samples are recovered on site rather than collecting the whole flask and replacing it.
- Only soluble species are considered.
- Biocide additives are not used.

Recovery of deposition samples is performed using 250 mL of de-ionised (**DI**) water. In cases where rain water is present in the flask the volume is first measured. If less than 250 mL, it is made up to volume using DI water. If there is more than 250 mL of rainfall, then a 250 mL sample is taken. In all cases, water is used to wash anything deposited in the funnel into the flask, and the flask is gently shaken to ensure all the sample is recovered.

All recovered samples are returned to the laboratory at Curtin University for processing before being sent to the ChemCentre for analysis. Samples are analysed for the same suite of species as used for the 3-bucket sampler.

On a few occasions, samplers became damaged in the field. This damage has been in the form of broken glass funnels, especially after strong winds. These are replaced as needed. In the event of complete breakage of the funnel, this would mean the inability to collect deposition samples at the site until replacement.

Similar to Section 7.10 on the 3-bucket deposition sampler, this section displays boxplots, scatterplots and spatial smoothing of *pH* and chemical species concentrations provided by ChemCentre. Section 8.2 shows a comparison between the total deposition flask and the 3-bucket deposition sampler data.

7.11.2 Exploratory analysis of *pH* total (flask) deposition sampler data

Figure *7.11-1* shows boxplots of *pH* values for total deposition samples collected between September 2023 and March 2025, categorised by the date of sample collection. The median *pH* ranges from 6.3 to 7.5. There was a sudden drop in *pH* observed in March 2024. After March 2024, there was also a drop in *pH*, with February 2025 having the lowest median *pH* over the sampling period.

Figure *7.11-2* shows boxplots of the same *pH* data (September 2023 to March 2025), instead broken down by site. AQ18 shows by far the highest median *pH* of $\sim$8.5. This may be due to the site's very different geology compared to the Dampier archipelago. AQ17 has the next highest median *pH* values of about 7.5. Other sites have a median *pH* between 6.7 and 7.5. The lowest median *pH* values were at AQ05 and AQ07 with values around 6.7.

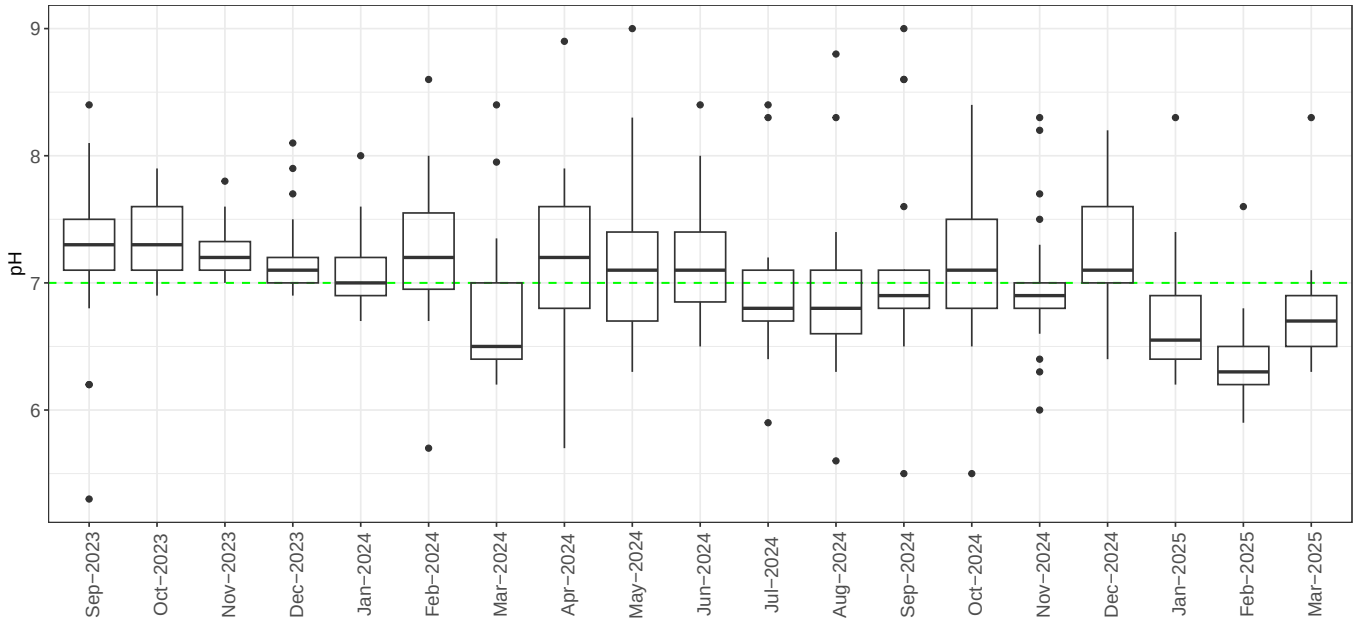

Figure 7.11-1: Boxplots of pH for the total (flask) deposition samples by sampling period. The green dashed line represents the neutral pH value.

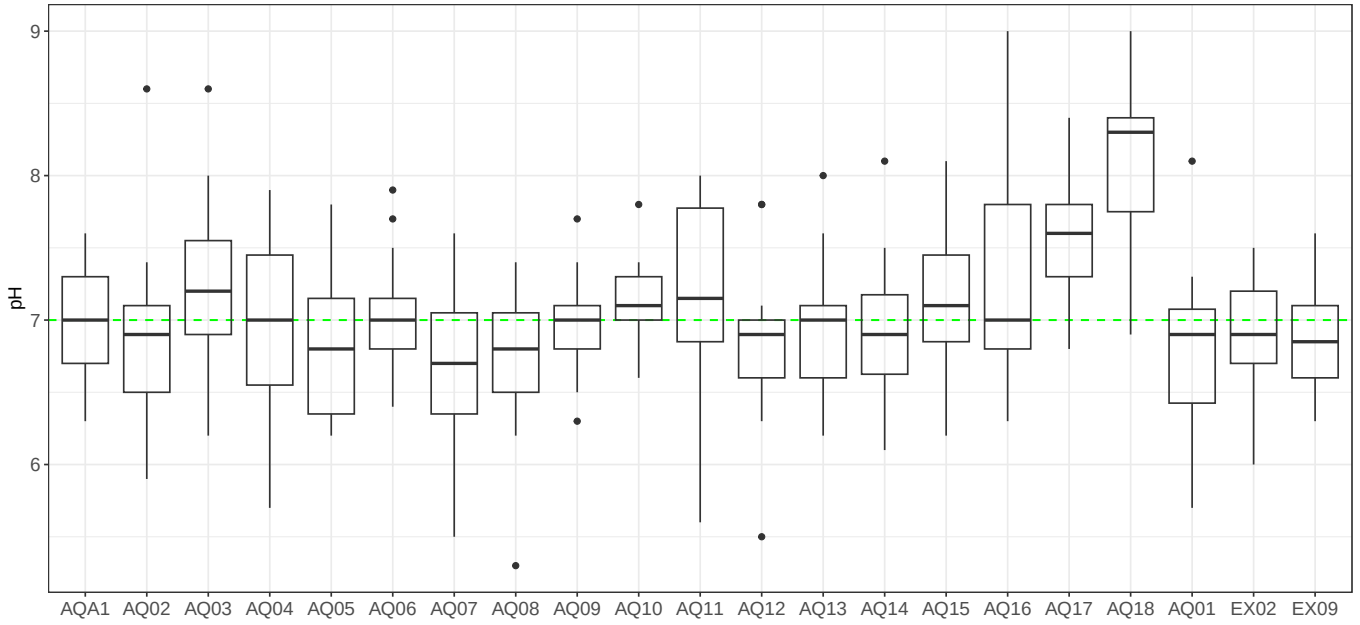

Figure 7.11-2: Boxplots of pH for the total (flask) deposition samples by sampling site. The green dashed line represents the neutral pH value.

The following comparisons have been made between pH measured from total deposition samplers and pH measured on the rock surface during field campaigns:

- Total deposition samples showed a median *pH* of approximately 7.3 in October–November 2023, which is slightly higher than the *pH* measured on the rock surfaces during campaign 6 (October–November 2023).
- The median *pH* of total deposition samples was 7.2 and 6.5 in February and March 2024, respectively, which is approximately the same as the *pH* measured on the rock surfaces during campaign 7 (February–March 2024).
- In June–July 2024, total deposition samples had a median *pH* of approximately 7, which is slightly higher than the median pH measured on rock surfaces during campaign 8 (June–July 2024).
- In October–November 2024, the median *pH* of the total deposition samples was about 7, which is noticeably higher than the *pH* of rock surfaces measured during campaign 9 (October–November 2024).
- In February and March 2025, the median *pH* of the total deposition samples was 6.3 and 6.7, respectively, which is noticeably higher than the *pH* of rock surfaces measured during campaign 10.

7.11.3 Exploratory analysis of chemical species concentrations from the total (flask) deposition sampler data

Similar to the 3-bucket (Section 7.10.4), chemical analysis of the total (flask) deposition samples also provided assayed concentrations of Ca^{2+}, K^{+}, Mg^{2+}, Cl^{-}, Na^{+}, $SO_4{}^{2-}$, $NH_4{}^{+}$, $NO_3{}^{-}$, P and $NO_2{}^{-}$. The concentration of $NO_2{}^{-}$ was below the detection limit and is not considered further in this analysis.

The concentration values provided by ChemCentre are given in mg/L for the chemical species. In the following analysis, these concentrations have been converted from the total deposition samplers to the deposition rates expressed in mg/m^2/day.

Figures *7.11-3* and *7.11-4* show boxplots of the calculated deposition rates of Ca^{2+}, K^{+}, and Mg^{2+} broken down by sampling date and by location, respectively.

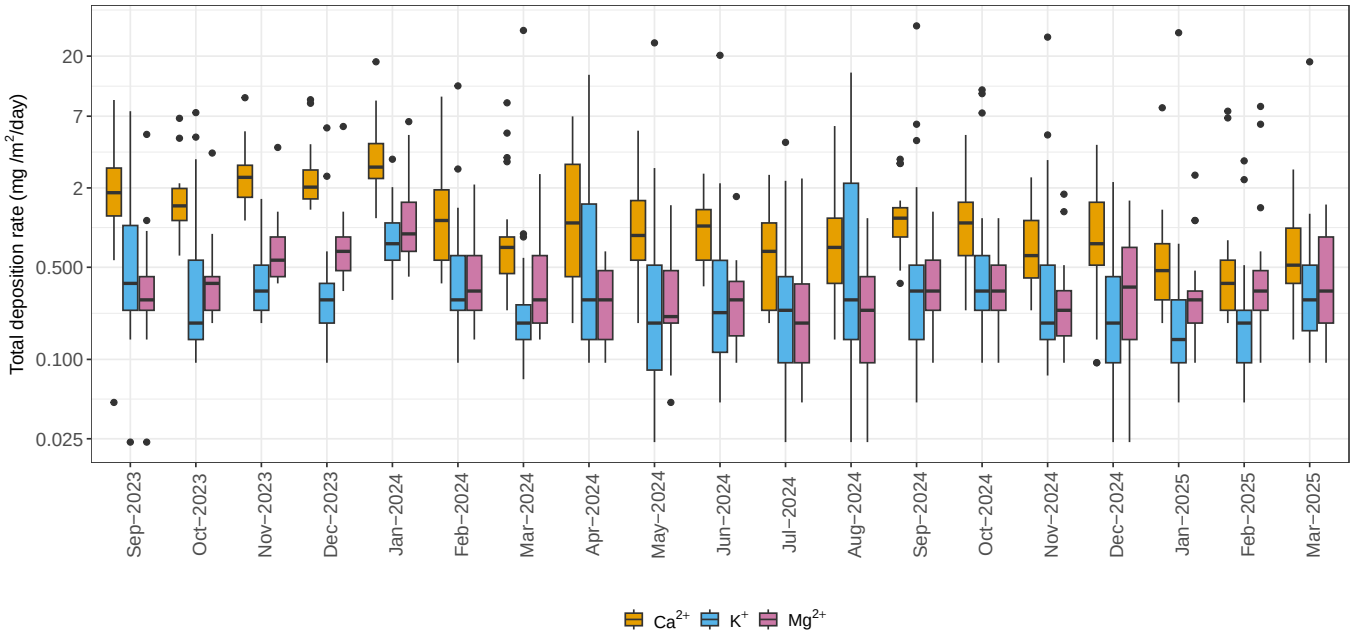

Figure 7.11-3: Boxplots of Ca^{2+}, K^{+}, and Mg^{2+} deposition rates for the total deposition samples by sampling period. Note logarithmic scale.

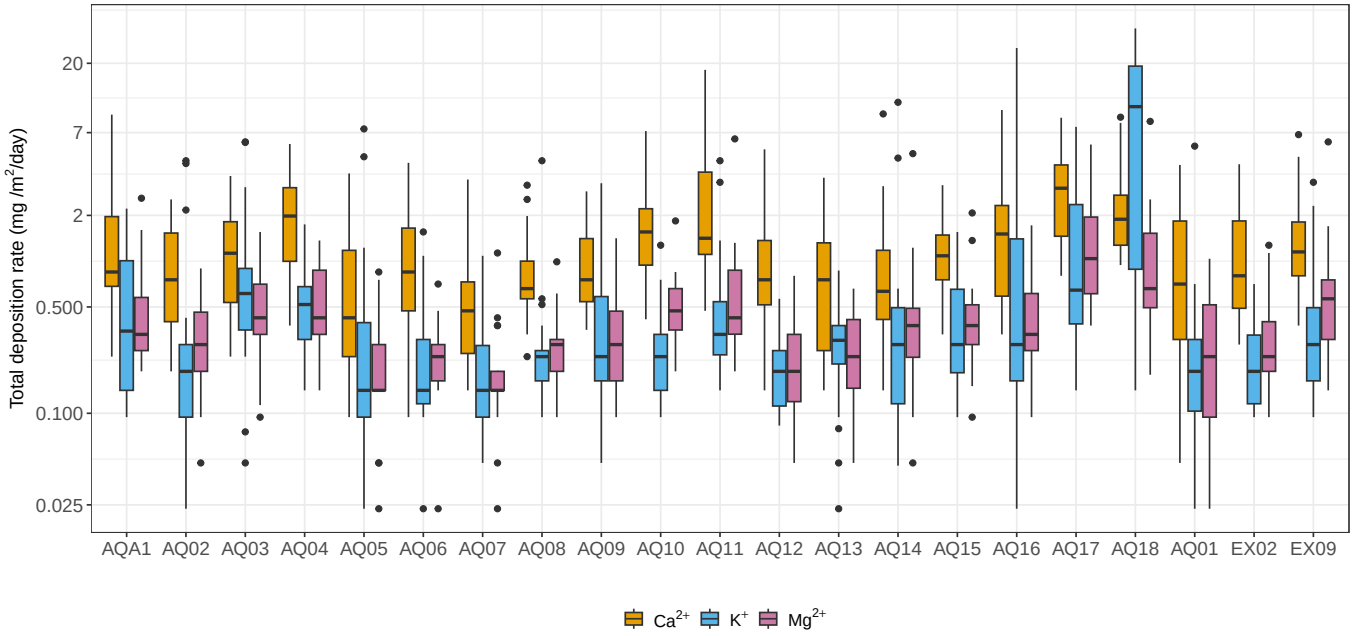

Figure 7.11-4: Boxplots of Ca^{2+}, K^{+}, and Mg^{2+} deposition rates for the total deposition samples by site. Note logarithmic scale.

Ca^{2+}, K^{+} and Mg^{2+} are all likely to arise mainly from geogenic sources and to be indicators of dust and clay mineral deposition, although other sources such as anthropogenic combustion or

bushfires remain possible. The ratio of these three species appears to be roughly constant, with some variation between sites. In this, Ca^{2+} concentrations are consistently higher than K^+ and Mg^{2+}, while K^+ and Mg^{2+} show a slight variation between sites.

Further data analysis will be undertaken. A possible explanation for systematic differences between sites is a composition/size relationship due to differences in dust transport distances. This may need investigation.

Figures *7.11-5* and *7.11-6* show boxplots of Cl^-, Na^+, and SO_4^{2-} deposition rates by sampling date and site, respectively. In contrast to the previous species, these three species may originate from numerous sources, such as geogenic dust, sea salt/sea spray (including anthropogenically generated NaCl from cooling towers), and, in the case of sulfates and SO_4^{2-}, may arise from combustion or biomass sources. Again, the ratios at each location appear consistent. In this, Na^+ concentrations are consistently higher than Cl^- and SO_4^{2-}, while SO_4^{2-} concentrations are consistently lower than Na^+ and Cl^-.

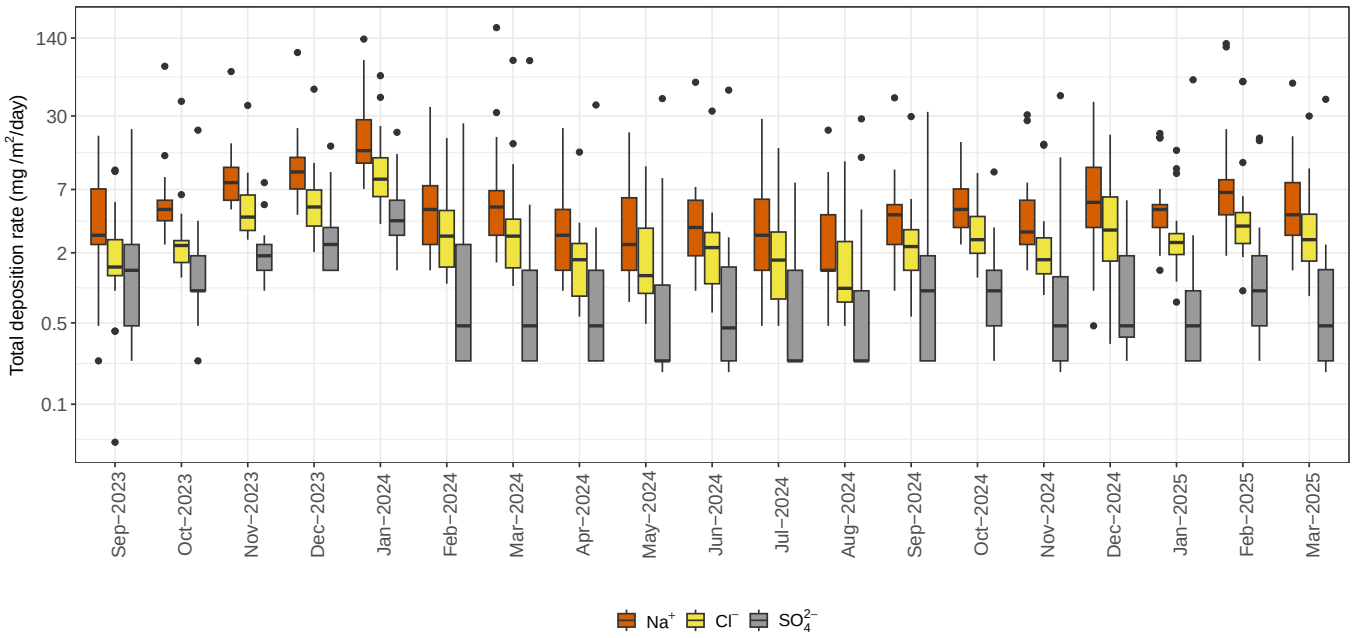

Figure 7.11-5: Boxplots of Na^+,Cl^-, and SO_4^{2-} deposition rates for the total deposition samples by sampling period. Note logarithmic scale.

Boxplots of NH_4^+, NO_3^-, and P deposition rates for each sampling date and location are shown in Figures *7.11-7* and *7.11-8*. These species may also arise from a range of natural, anthropogenic, marine, and terrestrial sources. In this, NH_4^+ concentrations appear to be consistently higher than NO_3^- and P. Other relationships are more variable, possibly due to lower levels, and require further investigation.

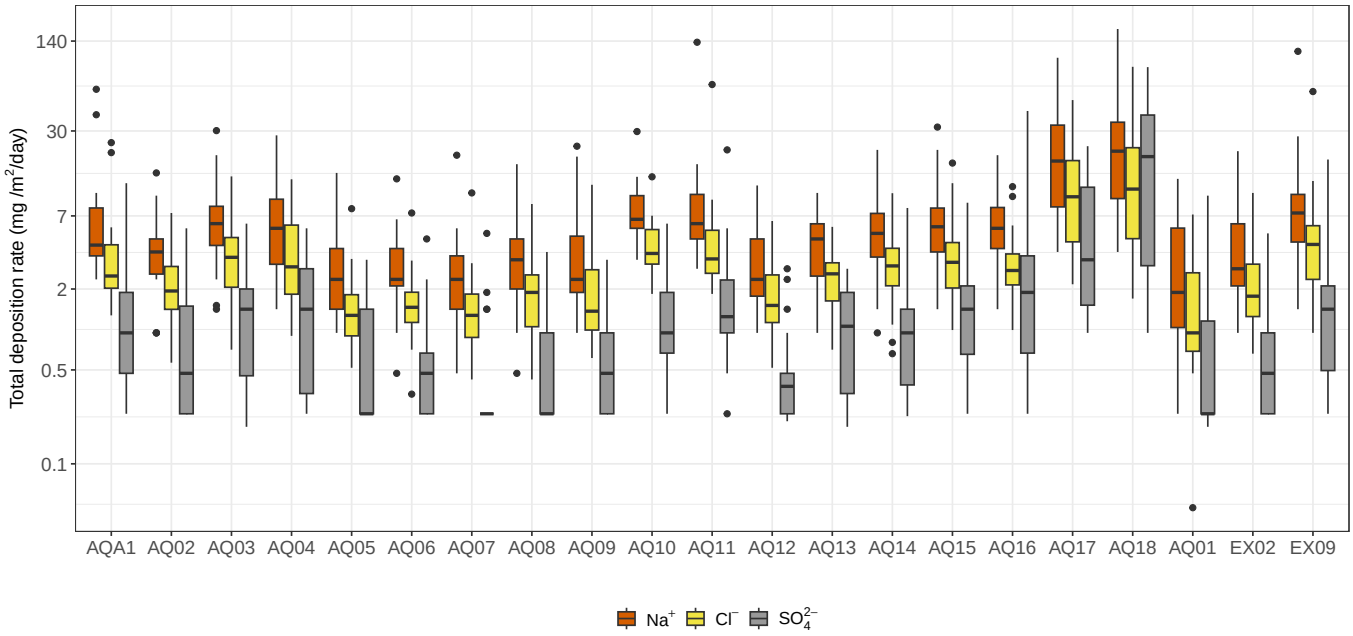

Figure 7.11-6: Boxplots of Na^+, Cl^-, and SO_4^{2-} deposition rates for the total deposition samples by site. Note logarithmic scale.

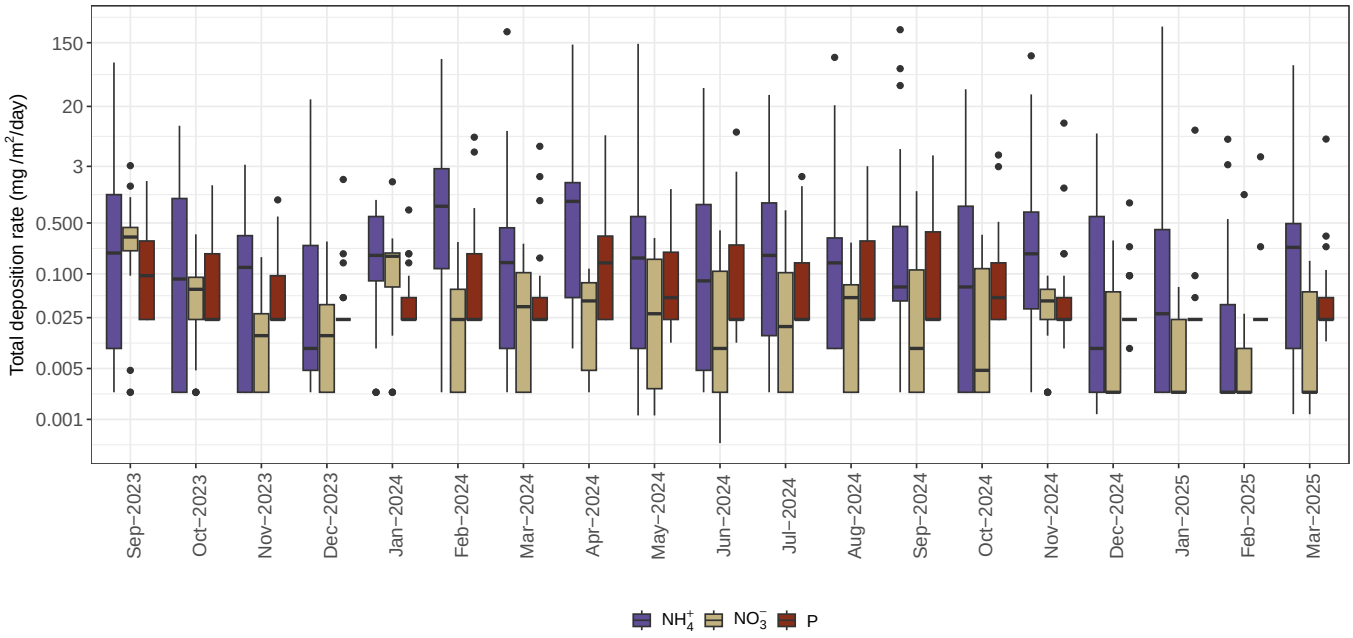

Figure 7.11-7: Boxplots of NH_4^+, NO_3^-, and P deposition rates for the total deposition samples by sampling period. Note logarithmic scale.

Figure *7.11-9* shows the average *pH* and total deposition rates of chemical species at each AQM site, and Figure *7.11-10* shows the median *pH* and total deposition rates of chemical species at

each AQM site. In each plot panel, sites are ordered by increasing value of the deposition rate, separately for each chemical species. It can be seen that AQ18 has the highest *pH* in both cases, whereas AQ17 or AQ18 has the highest mean values for many chemical species, largely due to a small number of high measurements (extreme outliers). Overall, however, some clear trends are appearing across the sites, which require more comprehensive investigation in conjunction with other datasets.

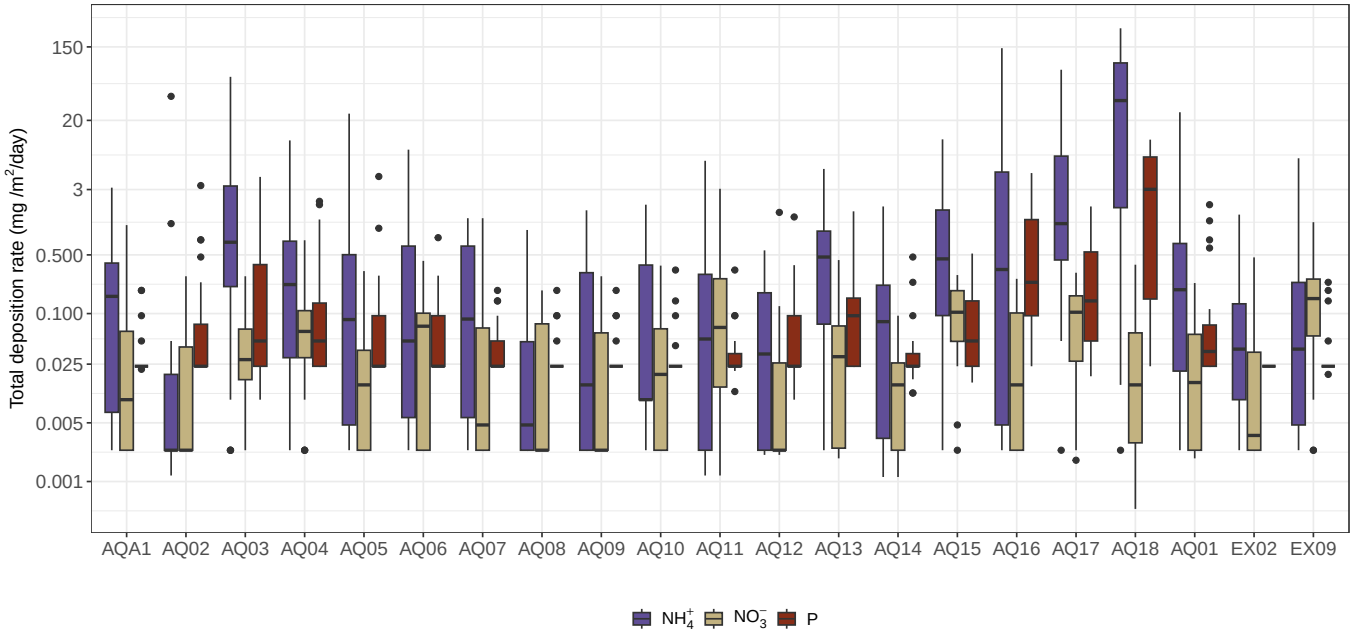

Figure 7.11-8: Boxplots of NH_4^+, NO_3^-, and P deposition rates for the total deposition samples by site. Note logarithmic scale.

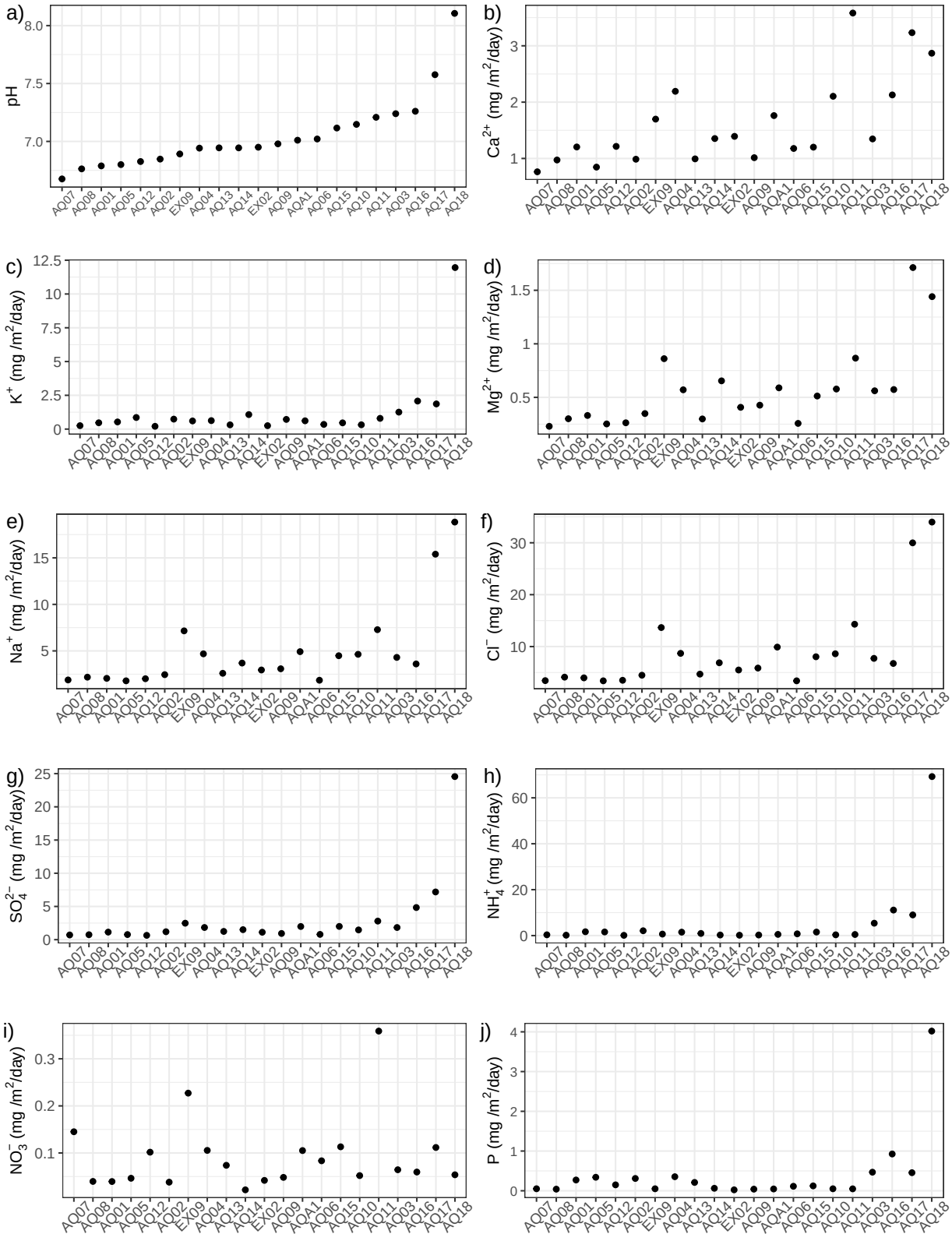

Figure 7.11-9: Average pH and total deposition rates by AQM. Data represent approximately 19 months of observation (September 2023 to March 2025).

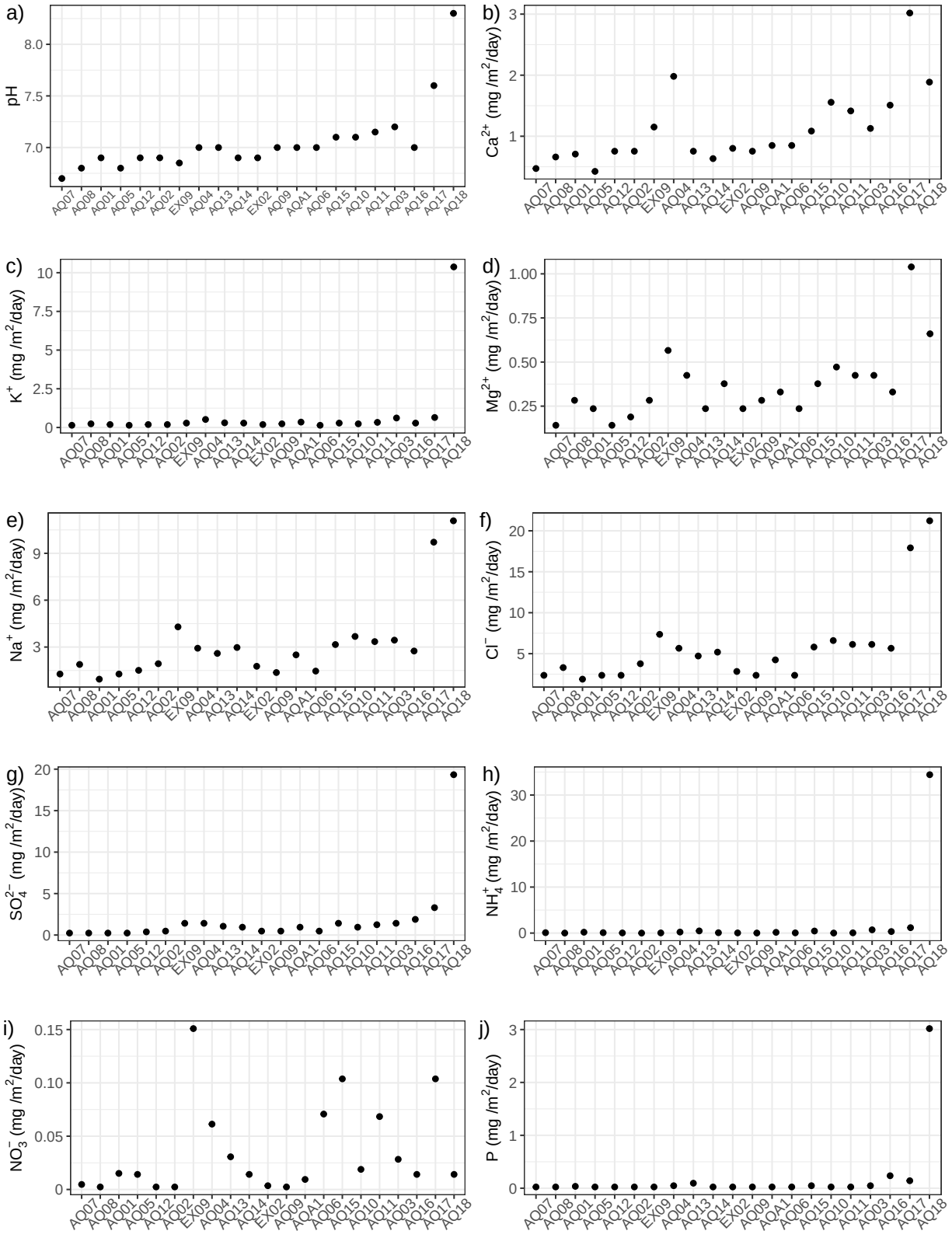

Figure 7.11-10: Median pH and total deposition rates by AQM. Data represent approximately 19 months of observation (September 2023 to March 2025).

7.11.4 Analysis of co-located AQM sites

Section 7.10.3 of the Monitoring Studies Report 2024 (Curtin University, 2024c) details the co-located air quality monitors (AQ07 and AQ08) used to assess variability over small spatial scales. Similar to Section 7.10, this section presents similar analyses for the total (flask) deposition data from September 2023 to March 2025 for AQ07 and AQ08.

Figure *7.11-11* shows boxplots of *pH* from all AQMs, AQ07 and AQ08. These boxplots show a similar trend for the *pH* at AQ07 and AQ08, although AQ07 has a lower median than AQ08.

Figure *7.11-12* shows boxplots of total deposition rates for different chemical species at AQ07 and AQ08.

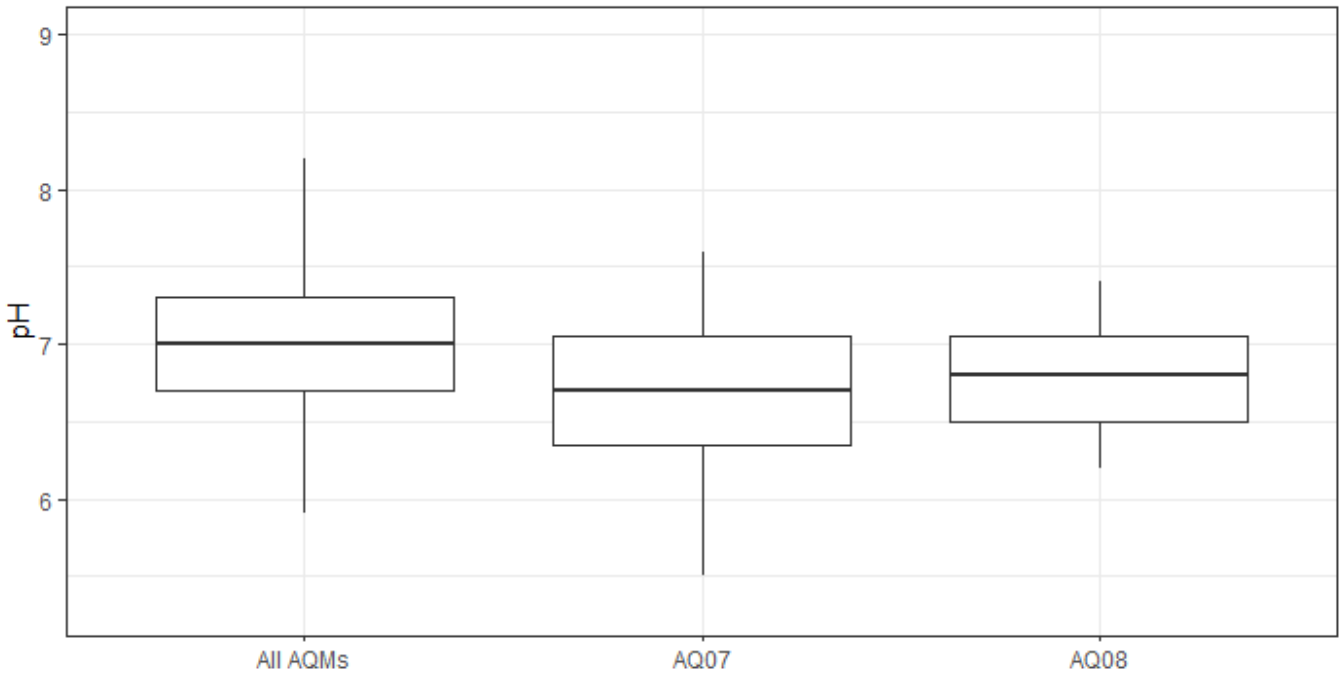

Figure 7.11-11: Boxplots of pH for total deposition samples from all AQMs, co-located AQ07 and AQ08 from September 2023 to March 2025.

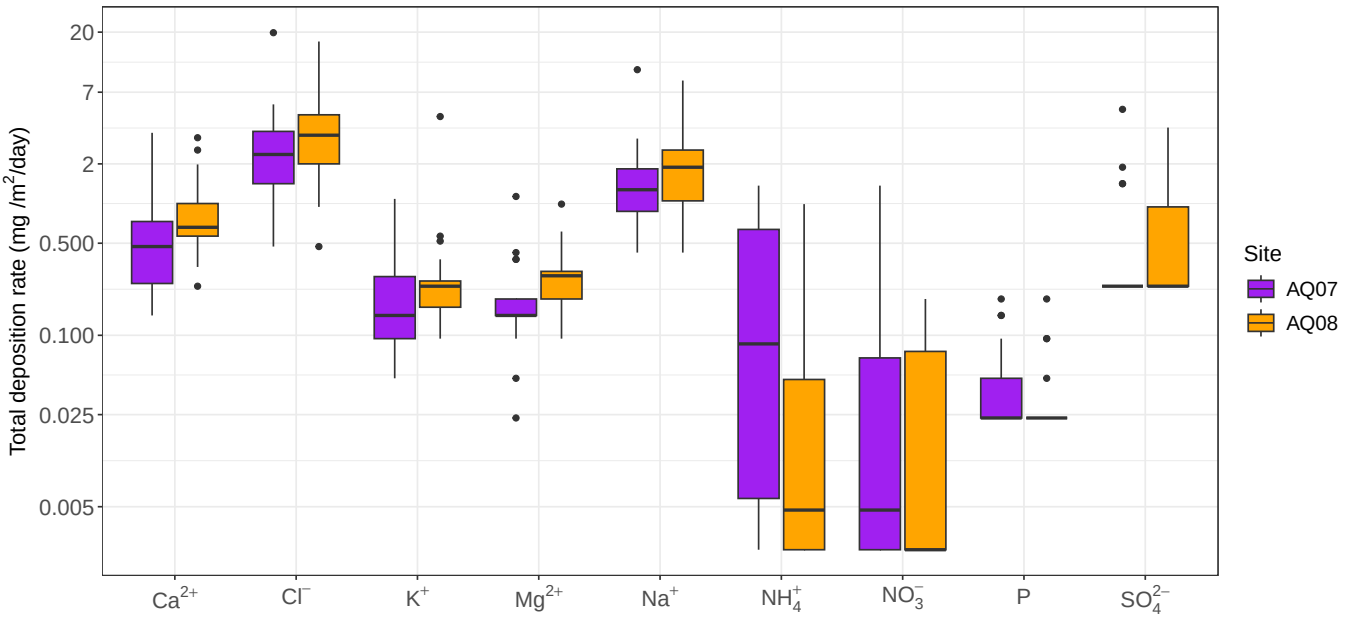

Figure 7.11-12: Boxplots of total (flask) deposition rates of chemical species from total deposition samples of co-located AQ07 and AQ08 sites; September 2023 to March 2025. Note logarithmic scale.

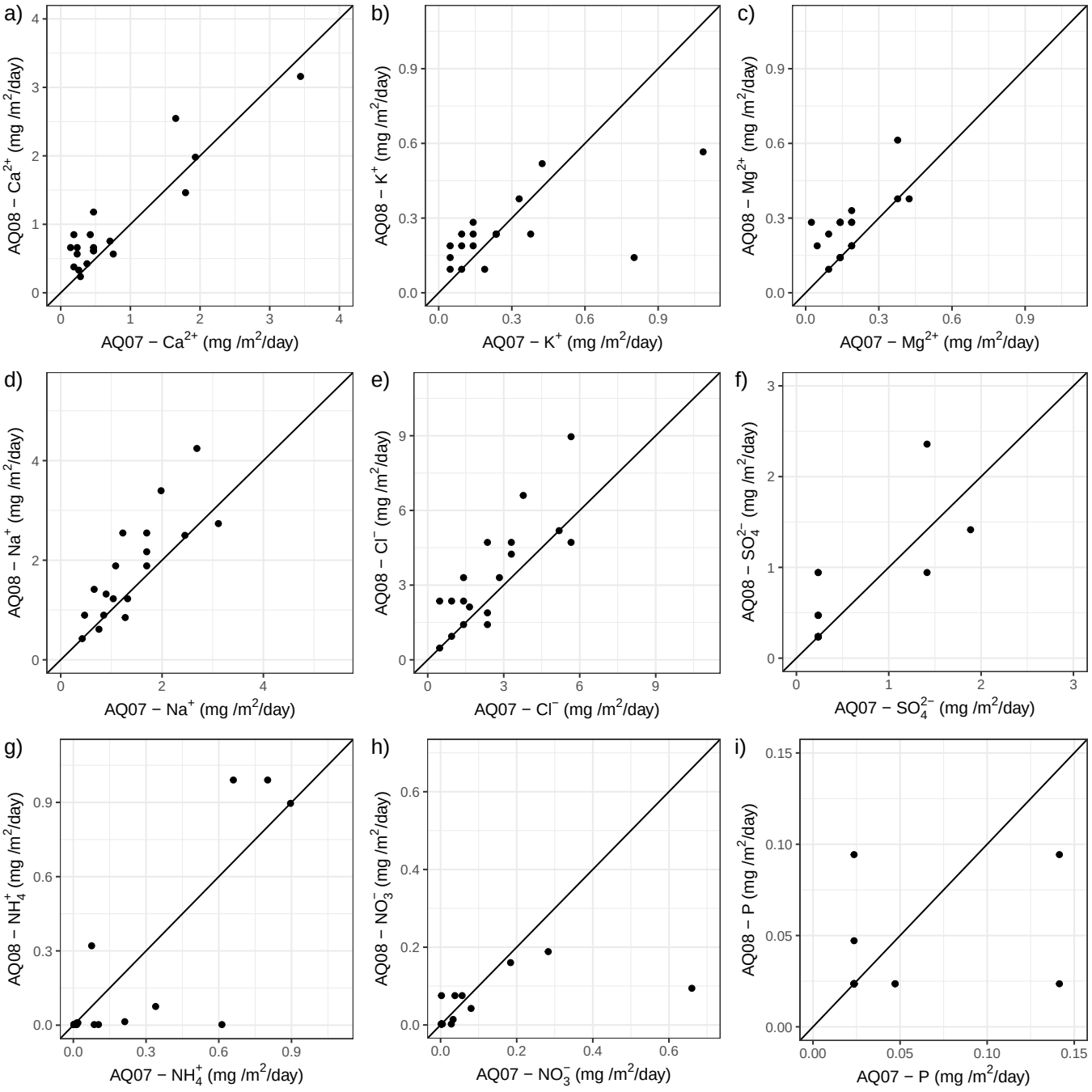

Figure 7.11-13: Scatterplots of the AQ07 vs AQ08 total (flask) deposition rates for each chemical species, September 2023 to March 2025. The black line (y = x) indicates the same deposition rate at both monitoring stations.

Figure *7.11-13* shows scatterplots of the total deposition rates observed at AQ07 and AQ08, separately for each chemical species. Observations at the two sites generally agree well, except for NH_4^+, SO_4^{2-}, and P. Similar results were obtained with dry deposition samples as well (Figure *7.10-14*).

Similar to Section 7.10.5, statistical tests were applied to compare the distributions of the total (flask) deposition rates at the two sites. The p-values from the Wilcoxon rank sum test are reported in the Table *7.11-1* and suggest that there is no evidence for a systematic discrepancy between the two sites (that is, no significant difference in distributions). Additionally, a strong positive relationship exists between samples at AQ07 and AQ08, except for K^+ and P, which show a moderate relationship. This relationship is quite similar to what was observed with the bucket samples (see Table *7.10-1*).

Table 7.11-1: p-values of the Wilcoxon rank-sum test (p-value), and Spearman correlation coefficient between samples at AQ07 and AQ08.

Sample	Number of observations (AQ07 and AQ08)	Wilcoxon Rank-Sum Test	Spearman correlation coefficient
Ca^{2+}	19	0.055	0.585
Cl^-	19	0.318	0.819
K^+	19	0.221	0.338
Mg^{2+}	19	0.042	0.658
Na^+	19	0.273	0.838
NH_4^+	19	0.085	0.661
NO_3^-	19	0.534	0.654
P	19	0.474	0.253
SO_4^{2-}	19	0.214	0.747

Figure *7.11-14* shows a multiple time series plot of total (flask) deposition rates against collection date, between September 2023 to March 2025. The overall impression is that colours cluster together, indicating that differences between AQ07 and AQ08 are generally much smaller than the variability in deposition rates over time.

- Na^+ and Cl^- deposition rates increase from September 2023 to January 2024, drop in February 2024, and then slowly rise again from April to March 2025.
- Mg^{2+} and Ca^{2+} deposition rates also increase from September 2023 to January 2024.
- K^+ and NH_4^+ deposition rates show considerable variability between September 2023 and March 2025.
- SO_4^{2-} deposition rates increase from September 2023 to January 2024, but remain largely unchanged afterward.
- NO_3^- levels are very low and often below the detection limit.
- P does not show notable variation over time compared to the scale of variability observed in other species.

Overall, a similar pattern was observed in the dry deposition samples (Figure *7.10-15*) over the same period, with only slight variations. That is, the above results indicate that the measurement

process is consistent and reliable.

7.11.5 Spatial smoothing of total (flask) deposition sampler data

Similar to Section 7.10.6, Nadaraya-Watson spatial smoothing was applied to the total (flask) deposition *pH* and the chemical species concentrations.

Figure *7.11-15* shows the results of Nadaraya-Watson spatial smoothing of the total deposition sample *pH* for each collection month. Other than October 2024, all other *pH* smoothed values are between 6.5 and 7.5, and there is relatively little spatial variation.

Figures *7.11-16* to *7.11-24* show the Nadaraya-Watson spatial smoothed surfaces for total deposition rates for each of the species Ca^{2+}, Mg^{2+}, K^{+}, Na^{+}, Cl^{-}, SO_4^{2-}, NH_4^{+}, NO_3^{-}, and P

- In January 2024, the Dampier and Burrup regions had the highest total deposition rates of Ca^{2+}, Mg^{2+}, K^{+}, Na^{+}, Cl^{-}, and SO_4^{2-}.
- Gidley Island had high Ca^{2+} total deposition rates during September to February 2024 and October 2024. Collier Rocks and the northern tip of Dolphin Island had high Ca^{2+} in February–March 2024 and January–February 2025. Enderby Island had high Ca^{2+} in January, March and April 2024. In May 2024, Ca^{2+} was high on Rosemary, Malus, West and East Lewis Islands.
- Gidley Island had high Mg^{2+} total deposition rates from September 2023 to February 2024, August 2024, October–December 2024, and March 2025. Collier Rocks and the northern tip of Dolphin Island had high Mg^{2+} in February–March 2024, May 2024, July 2024, September 2024, November 2024 and January–March 2025. Enderby Island had high Mg^{2+} in January 2024.
- K^{+} total deposition rates were high on Gidley Island from September 2023 to February 2024, and July–August 2024. Collier Rocks and the northern tip of Dolphin Island had high K^{+} from February 2024 to March 2025. K^{+} total deposition rates were also high on West Intercourse Island for June, August and September 2024. Enderby Island had high K^{+} in March 2025.
- Na^{+} total deposition rates were high on Gidley Island from September 2023 to February 2024, August 2024, October–December 2024 and March 2025. Collier Rocks and the northern tip of Dolphin Island had high Na^{+} February–November 2024, and January–March 2025. Na^{+} total deposition rates were also high on Enderby Island for November 2023 to January 2024 and October 2024. West Intercourse Island had high Na^{+} in January 2024.
- Cl^{-} total deposition rates were high on Gidley Island from September 2023 to February 2024, August 2024, November–December 2024 and March 2025. Collier Rocks and the northern tip of Dolphin Island had high Cl^{-} in March–July 2024, September 2024, November 2024, and January–March 2025. Cl^{-} total deposition rates were also high on Enderby Island for November 2023 to January 2024. West Intercourse Island had high Cl^{-} in January 2024.
- SO_4^{2-} total deposition rates were high on Gidley Island from September 2023 to February 2024, July–August 2024, and October–November 2024. Collier Rocks and the northern tip of Dolphin Island had high SO_4^{2-} in February 2024 to March 2025. High SO_4^{2-} also occurred on Enderby and West Intercourse Islands in January 2024.
- NH_4^{+} total deposition rates were below detection limit (**BDL**) for one or more months across most locations. NH_4^{+} was high on Gidley Island from September–October 2023, February-March 2024, May 2024, July–September 2024. Collier Rocks and the northern tip of Dolphin Island

had high NH_4^+ in February 2024 to March 2025. NH_4^+ was high on Enderby Island in January and March 2025.

- NO_3^- total deposition rates also had BDLs for some months. In September 2023, NO_3^- was high throughout the whole study region, except for Gidley Island. NO_3^- was high on Gidley Island in October 2023 to February 2024, and May–June 2024. NO_3^- was also high in parts of the Burrup region in May–October 2024, December 2024 and February–March 2025.
- P total deposition rates were high on Gidley Island from September–October 2023, February 2024, and May–September 2024. Collier Rocks and the northern tip of Dolphin Island had high values in February 2024 to March 2025. P was high on Rosemary, Malus, West and East Lewis Islands in September 2023, February 2024, April 2024 and September 2024. In March 2025, P was high on Enderby Island.

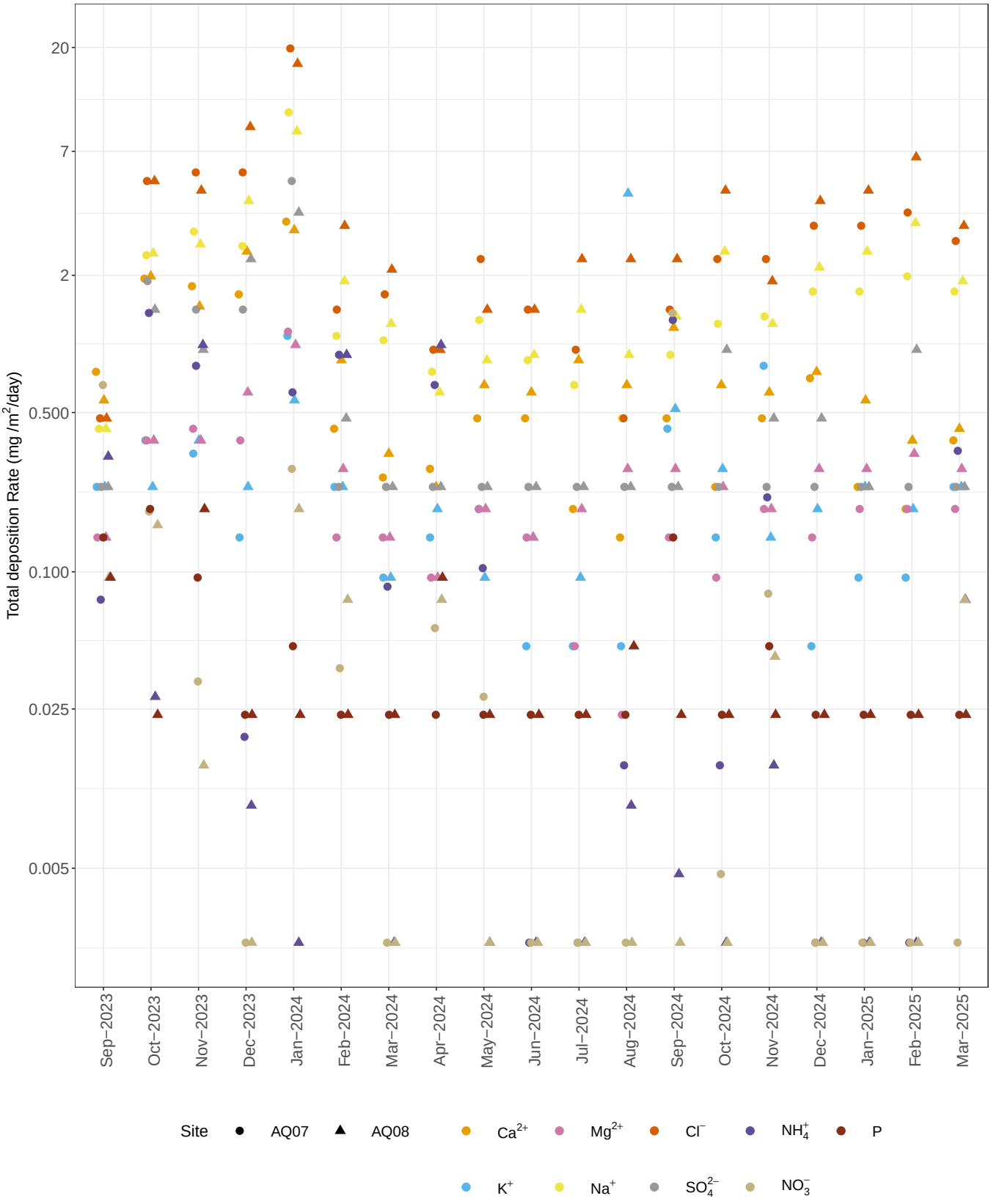

Figure 7.11-14: Time series plots of deposition rates of chemical species, from total deposition samples at co-located AQ07 (circles) and AQ08 (triangles) sites, against collection date. Note logarithmic scale. Points were jittered to avoid overlap.

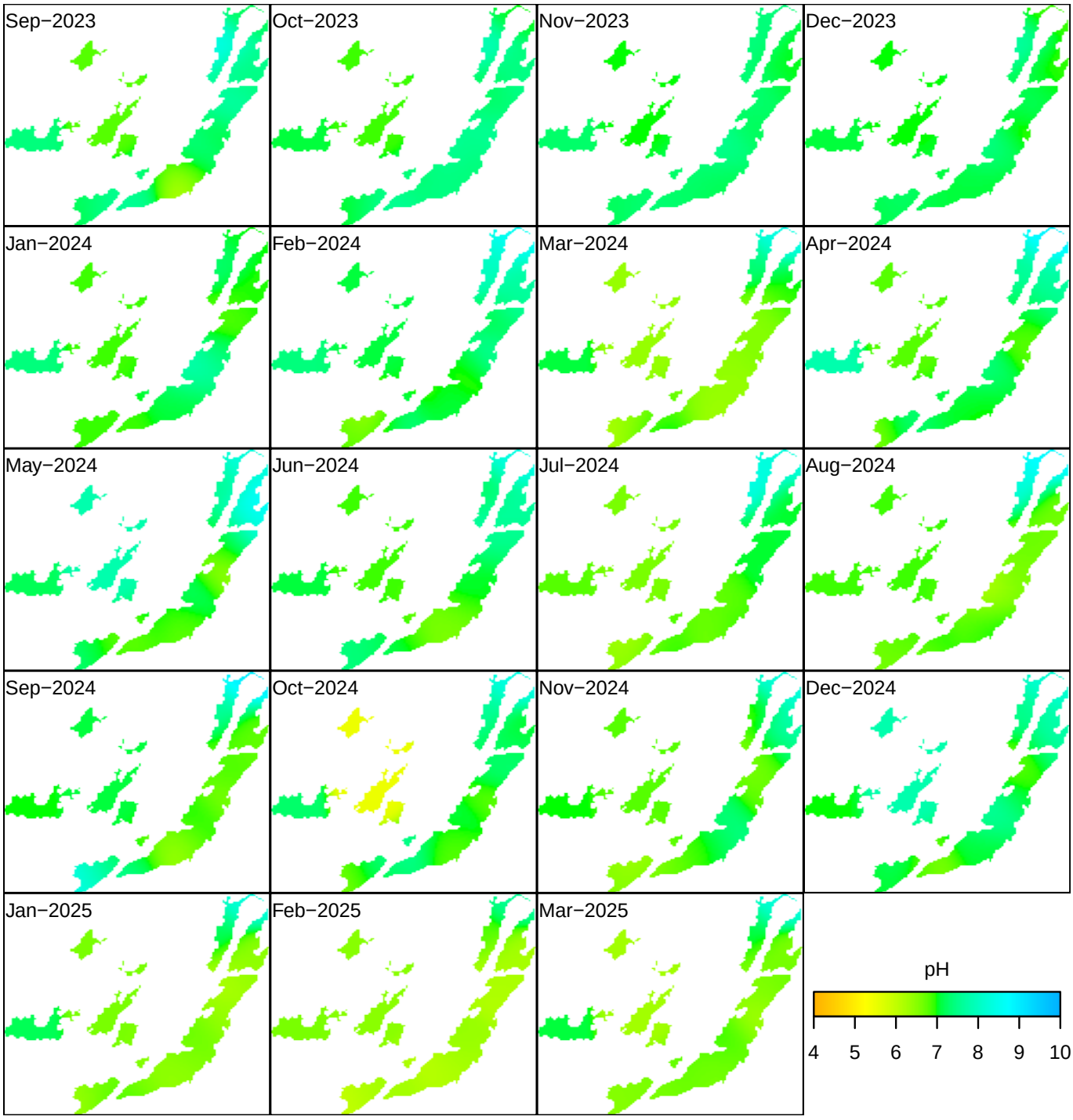

Figure 7.11-15: Spatially smoothed average pH for the total deposition samples by sampling period.

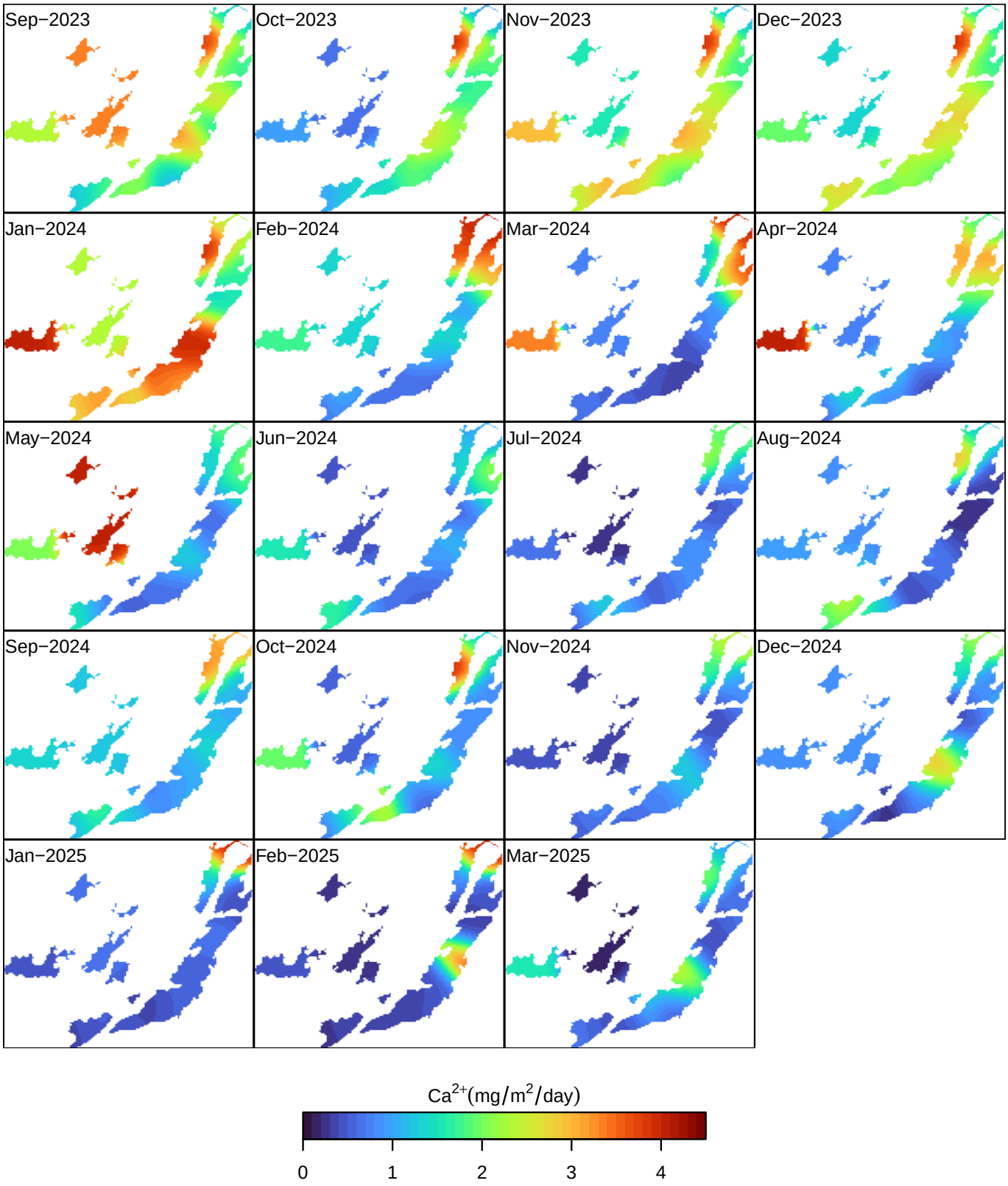

Figure 7.11-16: Spatially smoothed average Ca^{2+} deposition rate for the total deposition samples by sampling period.

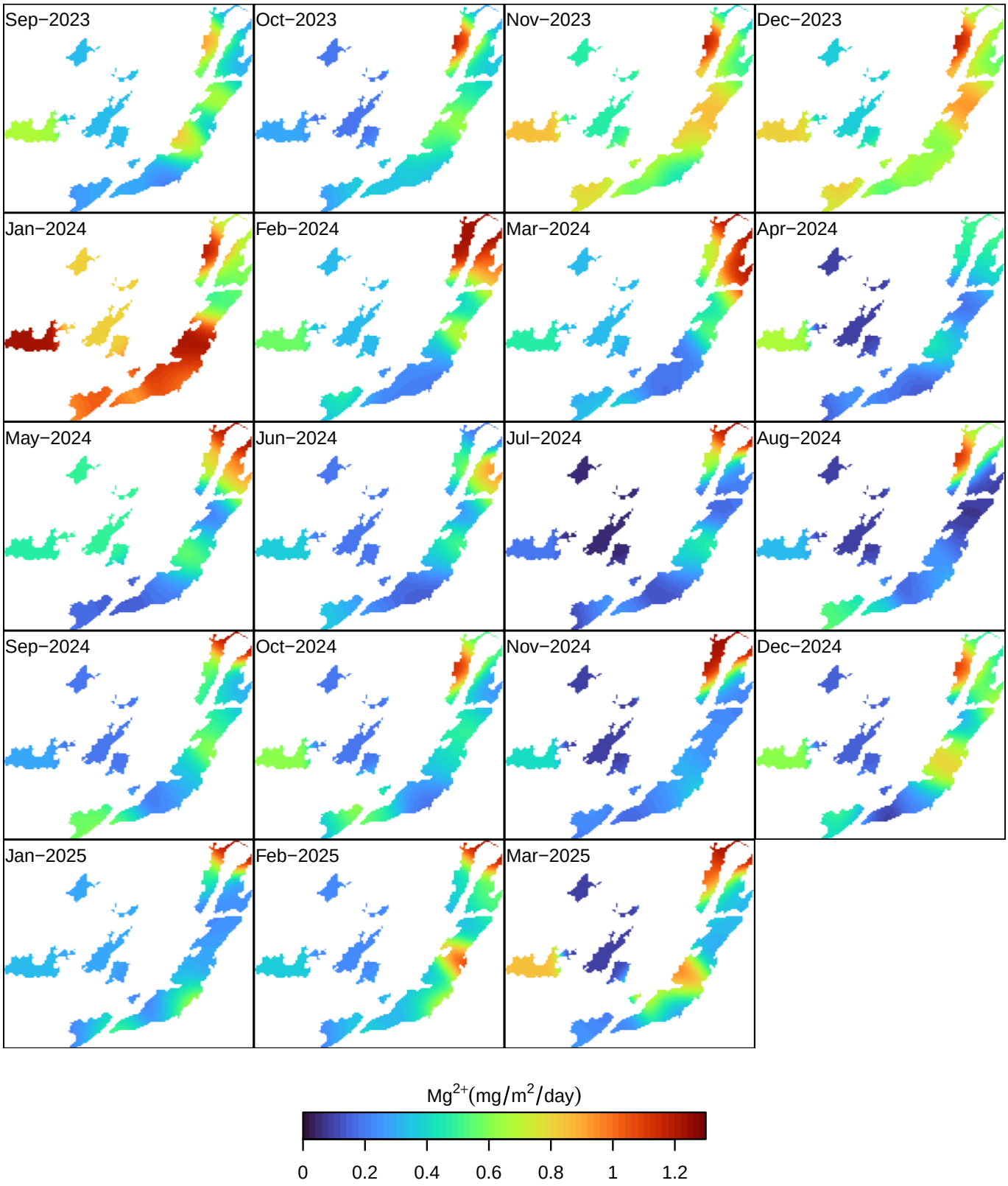

Figure 7.11-17: Spatially smoothed average Mg^{2+} deposition rate for the total deposition samples by sampling period.

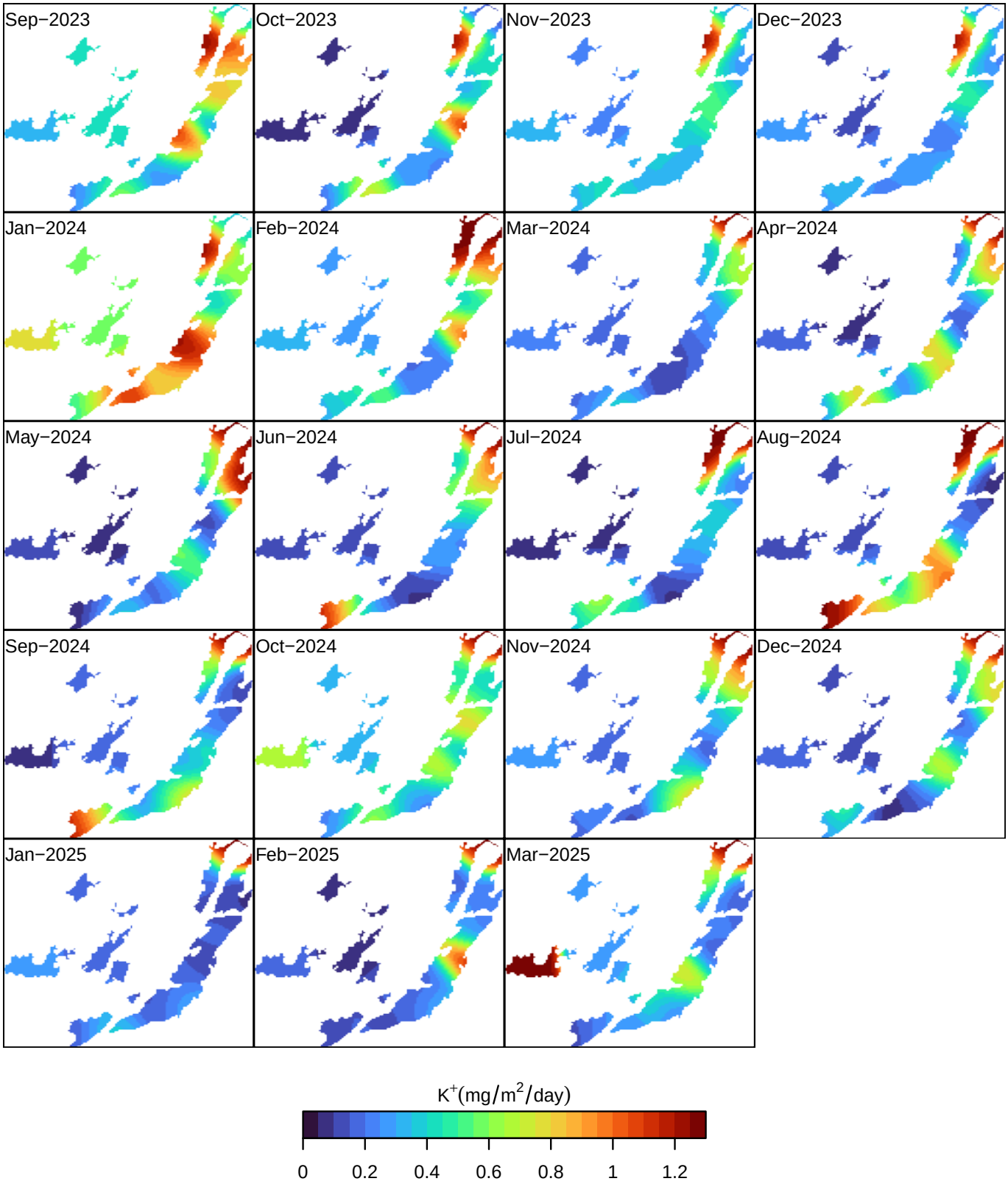

Figure 7.11-18: Spatially smoothed average K^+ deposition rate for the total deposition samples by sampling period.

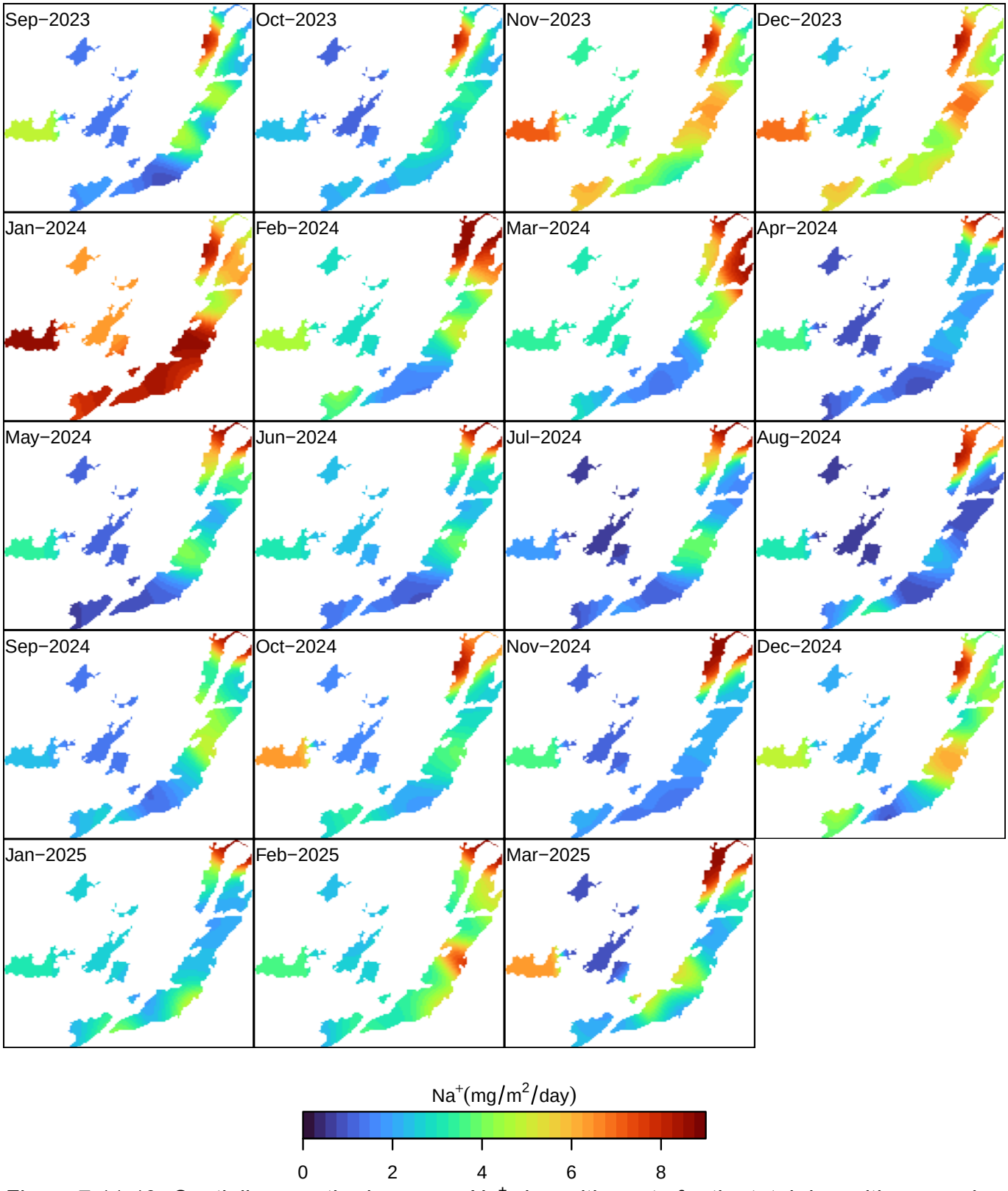

Figure 7.11-19: Spatially smoothed average Na^+ deposition rate for the total deposition samples by sampling period.

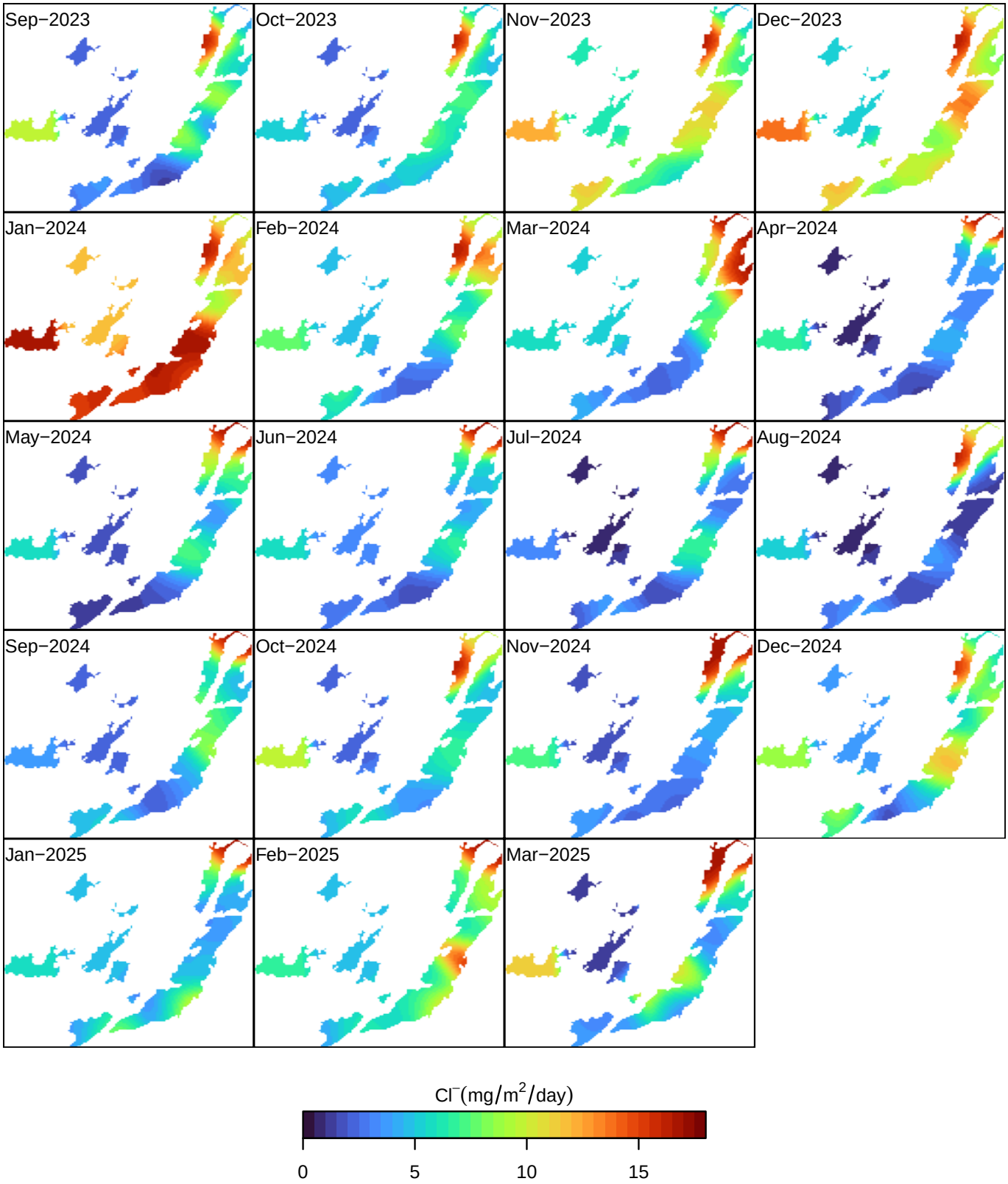

Figure 7.11-20: Spatially smoothed average Cl^- deposition rate for the total deposition samples by sampling period.

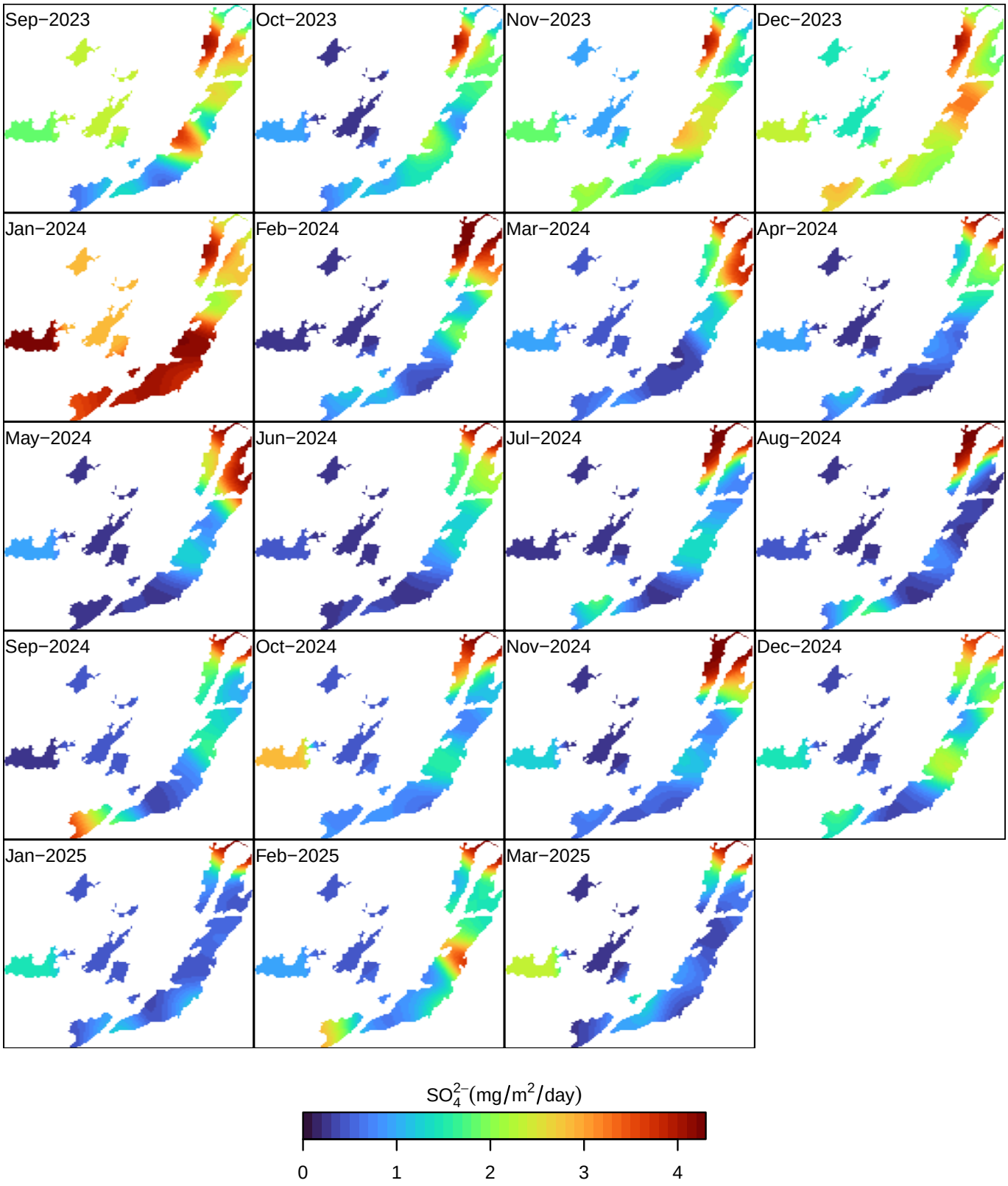

Figure 7.11-21: Spatially smoothed average SO_4^{2-} deposition rate for the total deposition samples by sampling period.

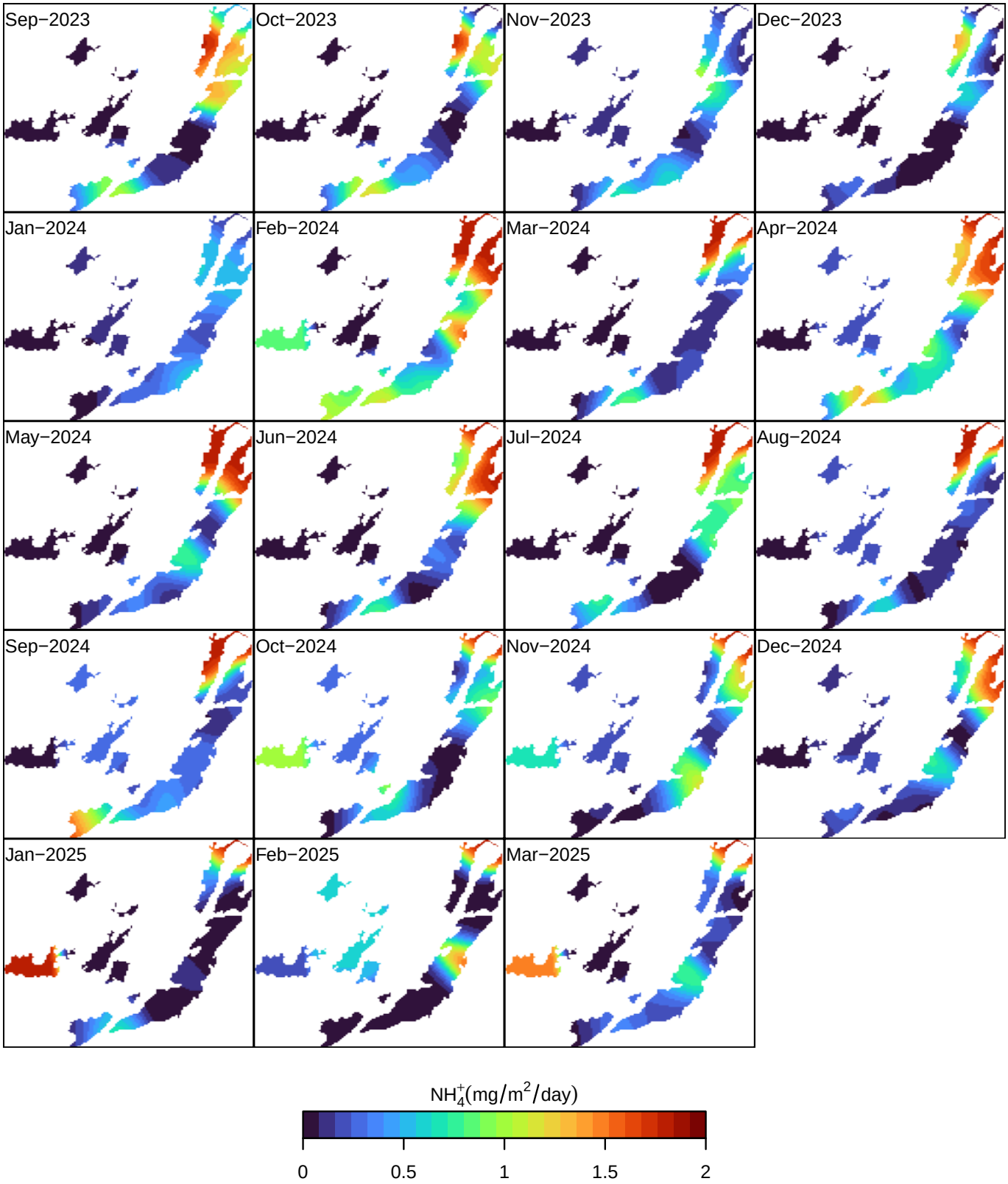

Figure 7.11-22: Spatially smoothed average NH_4^+ deposition rate for the total deposition samples by sampling period.

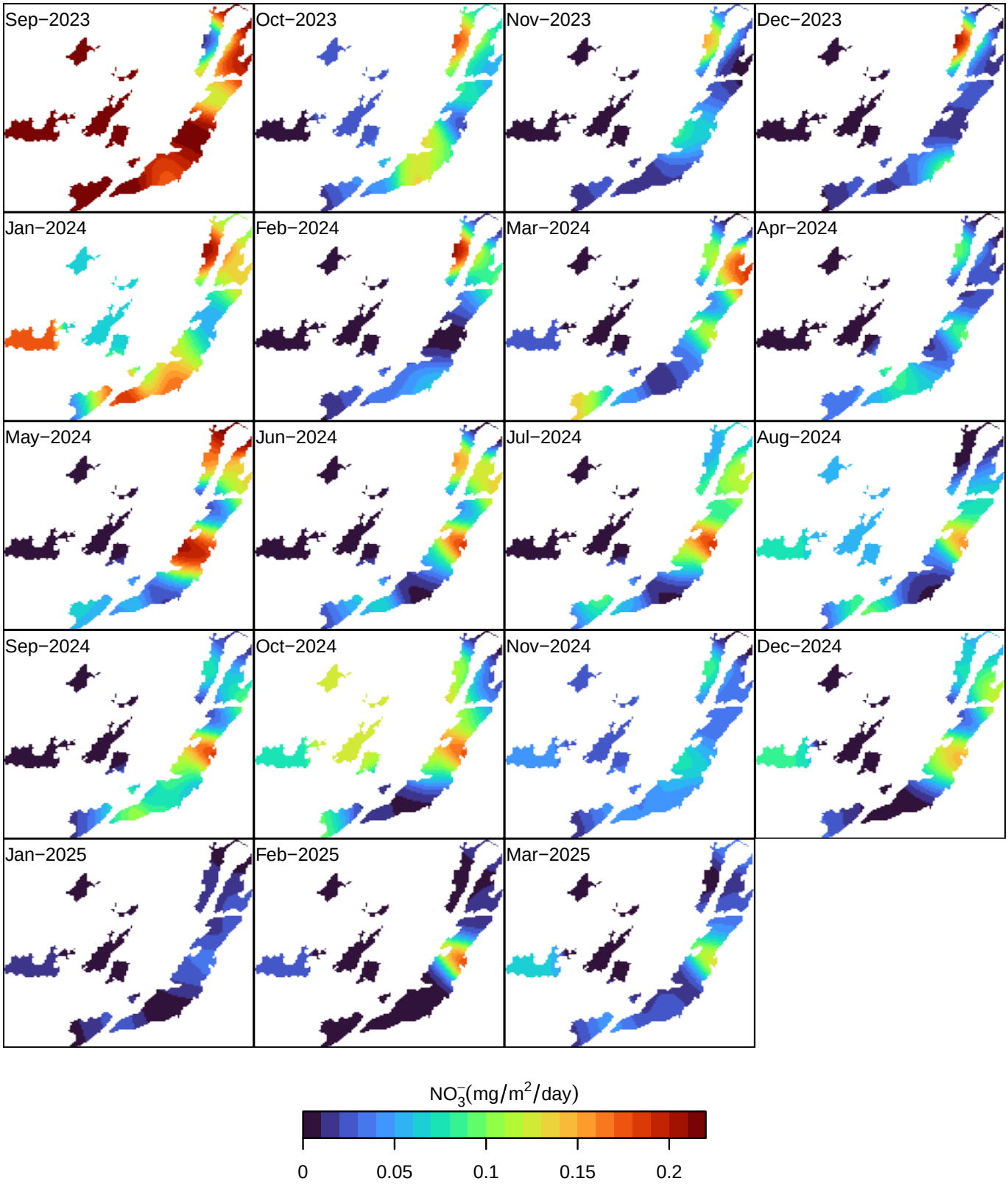

Figure 7.11-23: Spatially smoothed average NO_3^- deposition rate for the total deposition samples by sampling period.

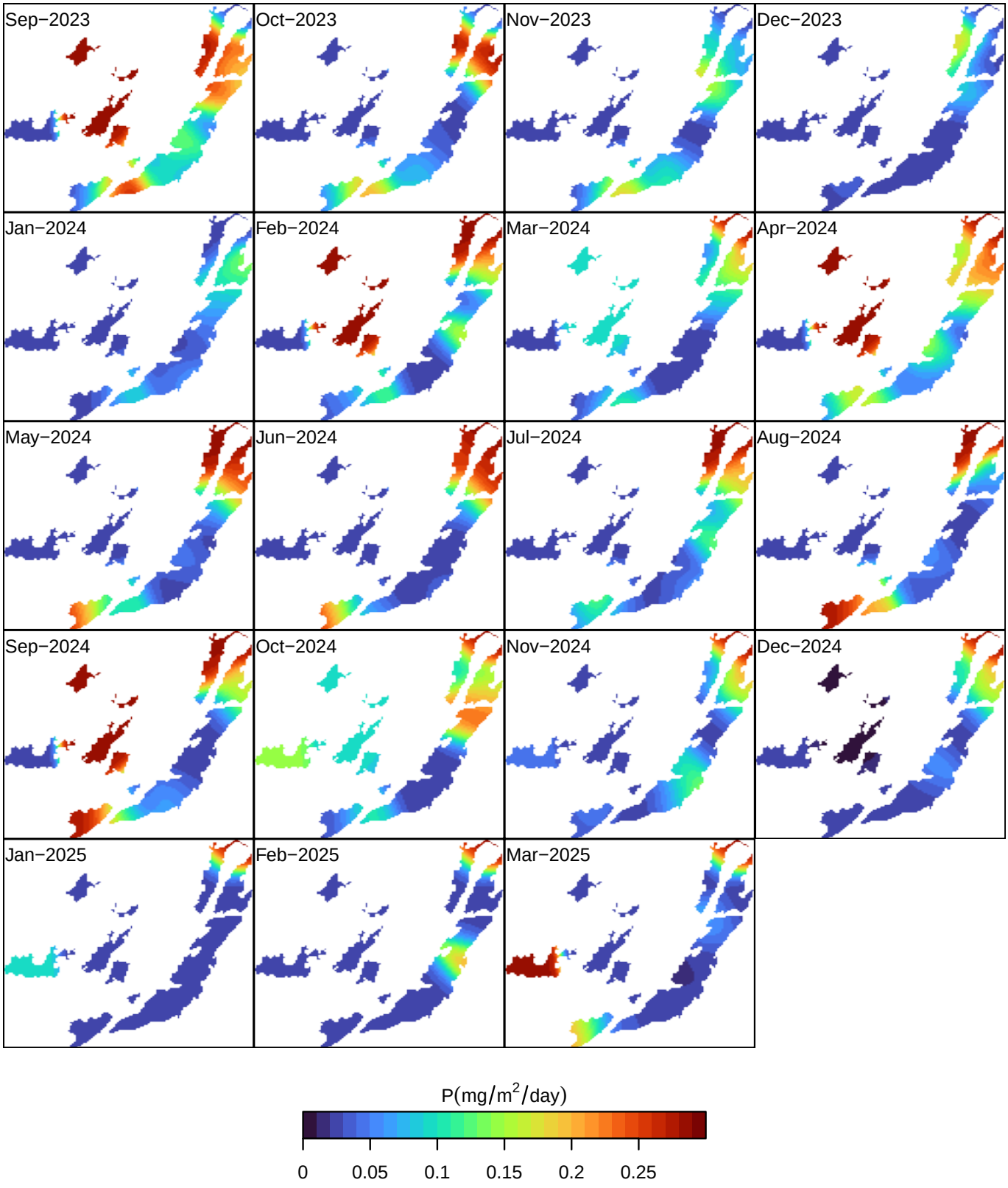

Figure 7.11-24: Spatially smoothed average P deposition rate for the total deposition samples by sampling period.

7.12 Passive samplers

7.12.1 Introduction

Air quality across Murujuga is measured by MRAMP using

- IVL passive diffusion samplers (discussed in this section),
- mains-powered real-time monitors (discussed in Section 7.13), and
- 'low power' real-time monitors (discussed in Section 7.14).

Passive samplers and low powered real-time monitors are deployed at all air quality monitoring sites across Murujuga, while the mains-powered real-time monitors are installed at only four locations (for further details see Section 5). For details on the IVL passive diffusion samplers see Monitoring Studies Report 2024 (Curtin University, 2024c).

This section concerns the data from the passive samplers:

- Subsection 7.12.1.1 notes changes to the monitoring network which have occurred since the Monitoring Studies Report 2024.
- Subsection 7.12.1.2 explains how Indigenous and non-Indigenous seasons will be used in the analysis of seasonal variation in the data.
- Subsection 7.12.2 presents the results of exploratory analysis of the passive sampler data.
- Subsection 7.12.3 presents analysis of correlations between the different gas species.
- Subsection 7.12.4 gives estimates of the 'intrinsic' variability in the results from the passive sampler technique, calculated by comparing results from duplicate samplers.
- Subsection 7.12.5 gives estimates of the variability between passive sampler results obtained at two stations a very short distance apart.
- Subsection 7.12.6 gives an exploratory analysis of spatial patterns of gas concentration.

7.12.1.1 Changes made this year

In the third year of studies, it was decided to deploy additional passive samplers at EX04, an existing industry AQM belonging to Yara Australia at the southern end of Hearson's Cove, and at two new temporary sites designated TM01 (at Hearsons Cove) and TM02 (on Rosemary Island). The passive samplers deployed at EX04 and TM01 are for NO_2 and NH_3 only, while the passive samplers at TM02 are for NO_2 and SO_2 only. Section 5 explains why only these passive samplers were deployed. Temperature measurements (required for the IVL assay procedure) are not available at these three sites. Instead, the monthly average temperature at the two nearest AQM sites is used in each case.

A decision was made to discontinue the use of the VOC samplers after just over a year of continuous monitoring. This was based on the relatively large proportion of results that were returned as BDL. The available VOC results are nevertheless reported here.

7.12.1.2 Seasons

To understand variation in the data over the calendar year, it can be useful to aggregate IVL sampler data by season. Two different seasonal groupings are considered in this report: the meteorological seasons for temperature latitudes in the southern hemisphere, henceforth called 'meteorological seasons'; and the seasons used by the Ngarda–Ngarli peoples Indigenous to Murujuga, henceforth called the 'Murujuga seasons'. The meteorological seasons are spring (September, October, and November), summer (December, January, and February), autumn (March, April, and May), winter (June, July, and August). The Murujuga seasons cover two key periods *Muthu* (in the Yindjibarndi and Ngarluma languages) (the cold time) and *Garrbarn* (Yindjibarndi) / *Garrwarn* (Ngarluma) (the hot time). The Murujuga seasons roughly correspond to the months of September to March for Garrbarn and April to October for Muthu. For further details see *meteorological seasons* and *Murujuga seasons* in Glossary Table *1.4-3* and DBCA 2021. For simplicity in plots and tables, the term *Garrbarn* is used for the hot season in this section.

In the majority of subsections, only the Murujuga seasons are presented. In these cases, Figures using meteorological seasons are presented in Appendix *D*.5.

7.12.2 Exploratory data analysis of passive sampler values

This report applies the exploratory data analysis techniques that were used in the Monitoring Studies Report 2024 (Curtin University, 2024c) to passive sampler data received from the IVL laboratory before the end of January 2025. The number of months of data available varied between gases and stations: data in this report was collected for field exposure periods from November 2022 to December 2024.

7.12.2.1 Summary statistics

Figures *7.12-1* and *7.12-2* show histograms of the passive sampler data, overlaid with kernel estimates of probability density. Histograms are normalised (scaled to have area equal to one) for comparison with density estimates. For further details see *histogram* and *density* in Glossary Table *1.4-3*. These figures were produced using all the available data for each analyte, pooled across all AQM stations and all months between November 2022 and December 2024.

The histograms give a general indication of the spread of values of the monthly average 'pollutant' gas species concentrations that are observed at Murujuga. They reflect all sources of variability that affect the passive samplers, including differences between locations, seasonal effects, weather variability, and other factors. Histograms in this section show density on the vertical scale: this is an estimation of the probability density or relatively likelihood that gas concentrations in a particular range will occur. This estimate is based on the frequency of observations with gas concentrations in that range. These plots also show probability density functions which are estimated from the data and plotted as a solid line over each histogram. The estimated probability function gives the relative likelihood of any gas concentration occurring and is represented by a continuous curve. Due to the highly skewed distributions observed for some variables, a logarithmic scale is used on the horizontal axis for the histograms of SO_2 and HNO_3 in panels (d)–(e) of Figure *7.12-1*, and n-octane, ethylbenzene, m-p-xylene, and o-xylene in panels (c)–(f) of Figure *7.12-2*.

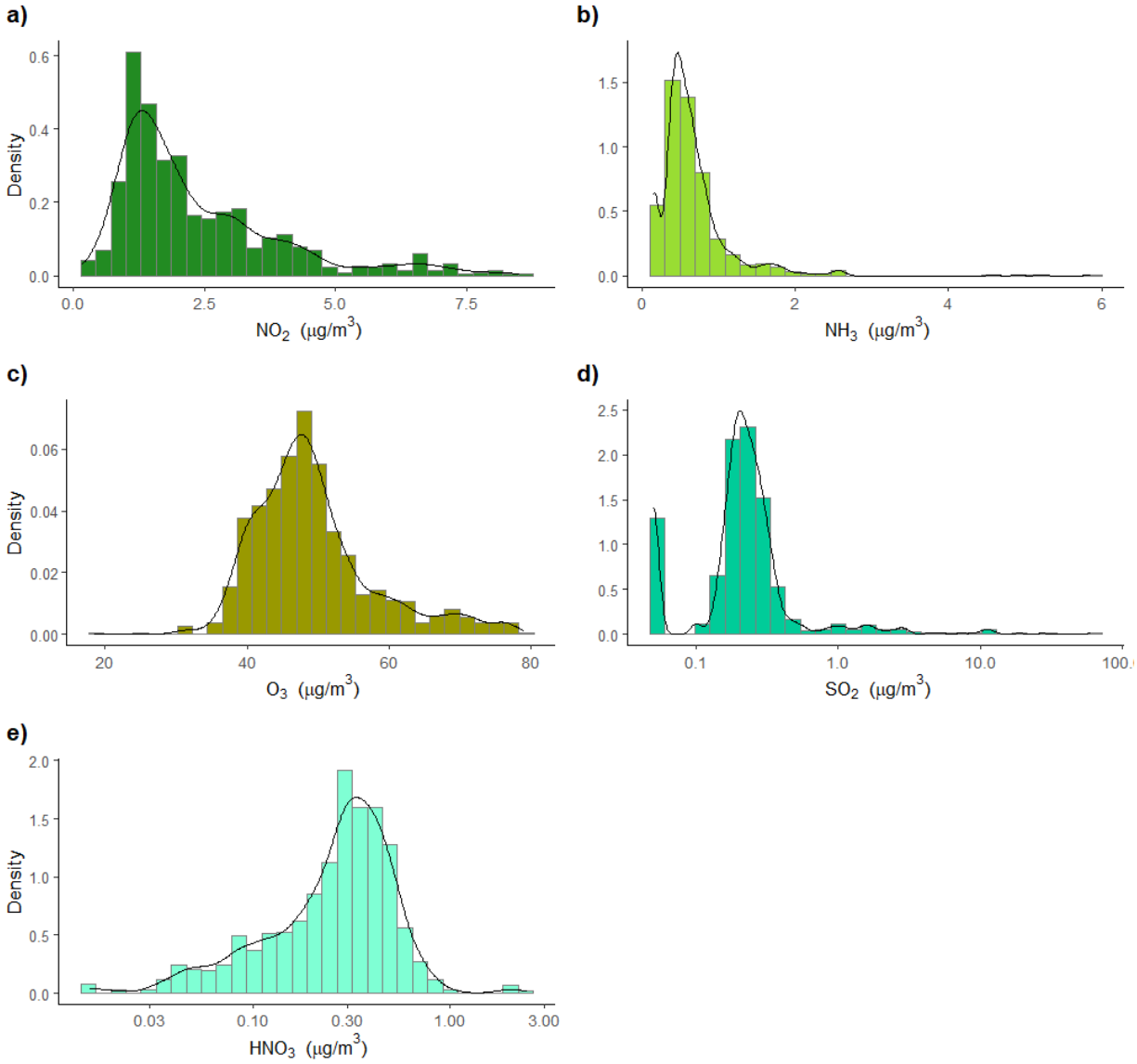

Figure 7.12-1: Histograms (colour bars) and density estimates (black curves) of IVL sampler gas concentration measurements from all stations and all months. Each panel displays one gas species: (a) NO_2, (b) NH_3, (c) O_3, (d) SO_2, and (e) HNO_3. Panels (d) and (e) use a logarithmic scale on the horizontal axis.

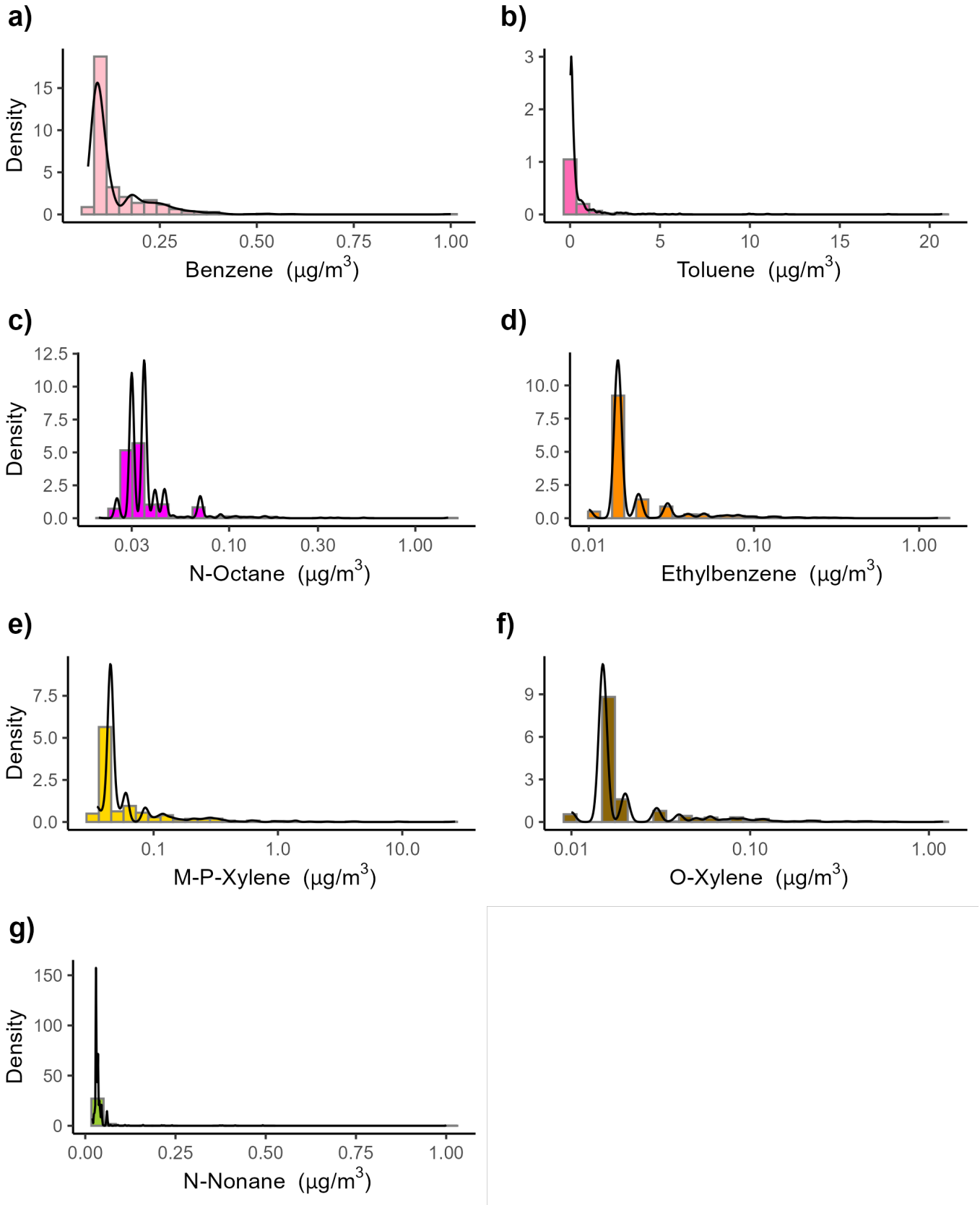

Figure 7.12-2: Histograms and density estimates of IVL sampler VOC concentration measurements for (a) benzene, (b) toluene, (c) n-octane, (d) ethylbenzene, (e) m-p-xylene, (f) o-xylene, and (g) n-nonane. Panels (c) – (f) use a logarithmic scale on horizontal axis.

Table *7.12-1* reports the overall summary statistics for the same data. Again, these were computed from all available data for each analyte, pooled across all AQM stations and all months. The columns in the table show the sample mean, sample variance, sample standard deviation, and the ratio of the standard deviation to the mean for each analyte.

Table 7.12-1: Overall summary statistics for passive sampler data. Mean, variance, standard deviation (SD), and ratio of standard deviation to mean, for assayed concentration of each analyte in $\mu g/m^3$, using data from all AQM stations and sampling months.

Gas	Mean	Variance	SD	SD/Mean
NO_2	2.399	2.442	1.563	0.652
NH_3	0.674	0.329	0.574	0.851
O_3	50.187	68.685	8.288	0.165
SO_2	0.466	5.214	2.283	4.902
HNO_3	0.314	0.040	0.200	0.635
Benzene	0.133	0.007	0.083	0.626
Toluene	0.489	2.077	1.441	2.950
Octane	0.043	0.003	0.059	1.362
Ethylbenzene	0.027	0.003	0.054	1.996
m-p xylene	0.143	0.930	0.965	6.757
o-xylene	0.033	0.004	0.066	2.037
n-nonane	0.041	0.002	0.049	1.208

The overall mean concentrations indicate the approximate levels of potential chronic exposure to these gases and compounds in the Murujuga region. The overall estimates of variance and standard deviation are more difficult to interpret, since they include the effects of any systematic differences between locations, seasonal variation, weather variability, and other sources of variation.

The standard deviation for SO_2 is 4.9 times the mean. For the other gases (NO_2, NH_3, O_3, HNO_3), the standard–deviation–to–mean ratio was less than one. Only one VOC, benzene, shows a standard-deviation-to-mean ratio of less than one. Two others, octane and n-nonane, show a ratio relatively close to one. The remaining VOCs all have standard-deviation-to-mean ratios greater than one, with m-p xylene showing a ratio of 6.8, reflecting the wide range of observations.

7.12.2.2 Gas concentrations at different monitoring sites

Figure *7.12-3* shows the individual monthly estimates of atmospheric gas concentration from the IVL passive gas samplers, plotted against the air quality station identifier. Data points are coloured according to the Murujuga seasons. Observations are assigned the calendar month that covered the majority of the exposure period, and then assigned to a Murujuga season based on that month. Appendix Figure *D.5-1* shows similar plots with observations coloured by meteorological seasons based on the month with the majority of exposure.

The ordering of the air quality stations on the horizontal axis is the same in each panel of Figure *7.12-3* and Appendix Figure *D.5-1*: stations are ordered by increasing value of the station's

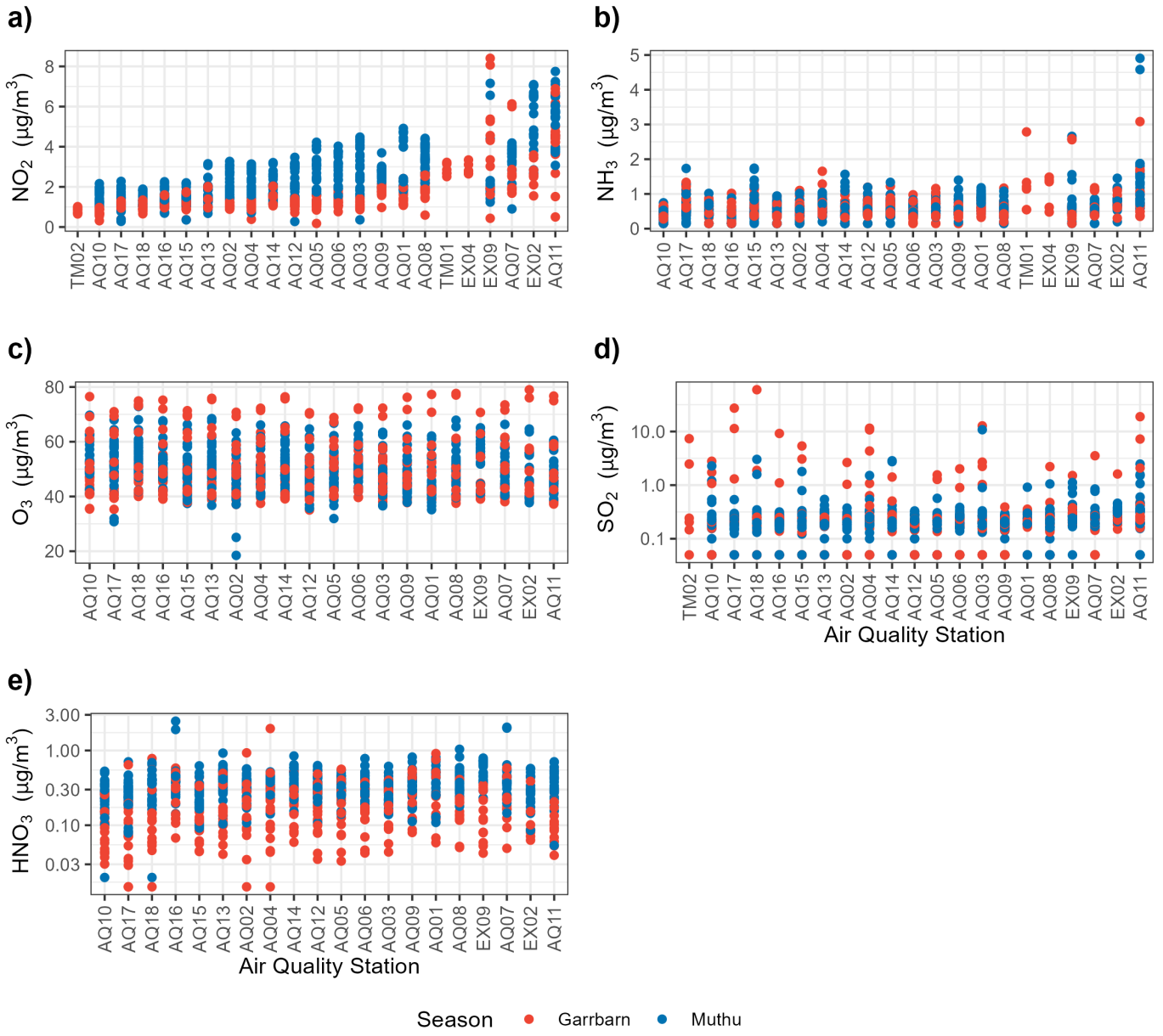

Figure 7.12-3: Plots of individual IVL sampler gas concentration estimates against air quality station identifier, coloured by Murujuga season. Separate gases are shown for each panel: (a) NO_2, (b) NH_3, (c) O_3, (d) SO_2, and (e) HNO_3. Panels (d) and (e) use logarithmic scale on the vertical axis.

overall average concentration of NO_2. This facilitates comparison between different panels in both figures.

Panel (a) of both Figure *7.12-3* and Appendix Figure *D.5-1* show individual estimated monthly concentrations of NO_2 over the air quality station. These panels indicate substantial systematic differences between the NO_2 levels at different stations. One possible explanation is a spatial gradient in exposure to NO_2 related to distance from the industrial areas. NO_2 concentrations are lowest at stations AQ18 and AQ17 (which are sited on the northern most islands), and are

highest at AQ11 and AQA1 (which are sited close to Dampier port) along with AQ07 and EX09 (which are relatively close to Dampier). The spatial pattern of NO_2 readings is considered further in Section 7.12.6. The substantial systematic differences in NO_2 values also justify the decision to rank the monitoring sites by increasing NO_2 rather than some other criterion.

Figure *7.12-3* (a) suggests that a distinct seasonal pattern related to the Murujuga seasons can be observed for NO_2 concentrations. Gas concentrations are generally higher in Muthu (cold time) compared to Garrbarn (hot time). Appendix Figure *D.5-1*(a) suggests a similar seasonal pattern in NO_2 concentration, with higher readings for winter months overall, lower readings for summer months, and intermediate values in autumn. Only a few measurements are available for spring, due to difficulties with a batch of NO_2 samplers. This is consistent with the pattern noted in the Monitoring Studies Report 2024 (Curtin University, 2024c). Ongoing monitoring and statistical analysis is required in order to confirm these apparent seasonal patterns.

Ammonia (NH_3) concentrations are shown in Figure *7.12-3*(b) and Appendix Figure *D.5-1*(b). There is a slight suggestion of a relationship where NH_3 increases with increasing NO_2. There is little evidence of a seasonal pattern in either Figure *7.12-3*(b) or Appendix Figure *D.5-5*(b). The four highest levels were all recorded at AQA1, with observations made during both summer (December 2024) and winter (July 2023), while the subsequent two highest levels are recorded at AQ11 during winter (July 2023). For NO_2, the highest readings are all recorded during Muthu (winter months plus data from April, May and September) suggesting the pattern of these gases is not seasonally aligned.

Note that the interpretation of panels (b)–(e) in Figures *7.12-3* and Appendix Figure *D.5-1* is different from the interpretation of panels (a). Any apparent “trend” in panels (b)–(e) would suggest a relationship in which the concentration of one gas increases with increasing NO_2. However, the shape of panel (a) is simply a representation of the distribution of values of NO_2 concentration.

Ozone (O_3) concentrations shown in Figure *7.12-3*(c) and Appendix Figure *D.5-1*(c) exhibit relatively small differences between stations relative to variability of observations for individual stations. O_3 gas concentration tends to be higher in sites AQ17 and AQ18, which are the sites located furthest north from Dampier port. A possible explanation is the dispersion of the gases and VOCs involved in O_3 production.

Sulfur dioxide (SO_2) concentrations shown in Figure *7.12-3*(d) and Appendix Figure *D.5-1* (d) exhibit the widest range of values and the most skewed distribution, hence a logarithmic scale is used to display these data. Most values range between 0.1 and 1 $\mu g/m^3$. There are a number of much higher readings, particularly in the Murujuga season of Garrbarn (September to March). Some of the highest readings were obtained from AQ18, AQ17 and AQ16, well to the north of the port. However, there are also high readings from AQ11 (in the port), AQ03 and AQ04, well to the west of Dampier port, and the new temporary station TM02 situated both north and west of the port on Rosemary Island. The SO_2 data also include numerous observations that are below detection limit (BDL); these are visible at the bottom of the plot. These BDLs have been recorded across all seasons.

Nitric acid (HNO_3) concentrations shown in Figure *7.12-3*(e) and Appendix Figure *D.5-1* (e) exhibit variation over two orders of magnitude, so again a logarithmic scale has been used to show these data. Measurements are highest for AQ07, AQ04, and AQ16 with high readings occurring in spring

(Muthu) for AQ16 and AQ07 but in summer (Garrbarn) for AQ04. The sites with the lowest HNO_3 values are AQ10, AQ15, AQ17 and AQ18. All these stations are either to the west or north of the port. There is also a seasonal pattern, with measurements usually higher for Muthu (autumn, winter and spring) and then lowest for Garrbarn (summer) samples.

It should be noted that the air quality values above are analysed with respect to spatial and seasonal trends. Changing levels of industrial activity (e.g., altered production/shipping rates, shutdown/maintenance), and other activities may also produce what appear to be seasonal trends in emissions. Apart from historic Ramboll 2022 models for 2014 and our own estimation of DPS and associated emissions from 1966-2010, data to study emissions in relation to industrial activity is not currently available, so has not been pursued in this report. (It should be noted that MRAMP scope is intended to establish safe levels of air quality to protect the rock art, leaving source apportionment and any required emissions reductions as a task for regulatory bodies).

7.12.2.3 Temporal variation in gas concentration

Figure *7.12-6* shows, in separate panels for each gas species, boxplots of gas concentration for each month of observation. Gas measurements are assigned to the calendar month which covered the majority of the exposure period. Each individual box is constructed from all the available data for the month in question, observed at any station. Plot panels are coloured according to the gas species.

Figure *7.12-4* shows boxplots of gas concentration from the IVL passive gas samplers pooled over all AQM stations and plotted against the Murujuga season, with separate panels for each gas species. Plots are coloured by season as either red (Garrbarn, hot) or blue (Muthu, cold). Appendix Figure *D.5-3* shows boxplots of the same data coloured by meteorological season.

Figure *7.12-5* shows histograms of the data coloured by Murujuga season, in separate panels for each gas species. The histograms are overlaid with kernel density estimates for each gas and each Murujuga season. The vertical axes show the estimated probability density. Appendix Figure *D.5-4* shows histograms of the same data by meteorological season.

Figure *7.12-6*(a) shows NO_2 monthly changes in measured gas concentrations. There is a clear pattern of lower measurements in the months of November to March, which increase in the months of April to October. A slight peak in median concentration (shown by the centre line across each boxplot) is apparent in July. There are a number of outliers (points beyond the boxplot whiskers) that may reflect differences in location or sampling period. Figure *7.12-4*(a) shows seasonal changes in gas concentrations for Murujuga seasons. NO_2 concentrations are lower in Garrbarn and higher in Muthu. The change is distinct with little overlap between the boxes representing the interquartile range of gas concentration values. Figure *7.12-5*(a) shows the distribution of NO_2 concentration by Murujuga season. The distributions for both seasons are unimodal with a right skew. NO_2 concentrations peak at a lower concentration in Garrbarn (approximately 1.25 $\mu g/m^3$) than in Muthu (approximately 1.25 $\mu g/m^3$). The Muthu NO_2 distribution also has a wider spread than the Garrbarn NO_2 distribution.

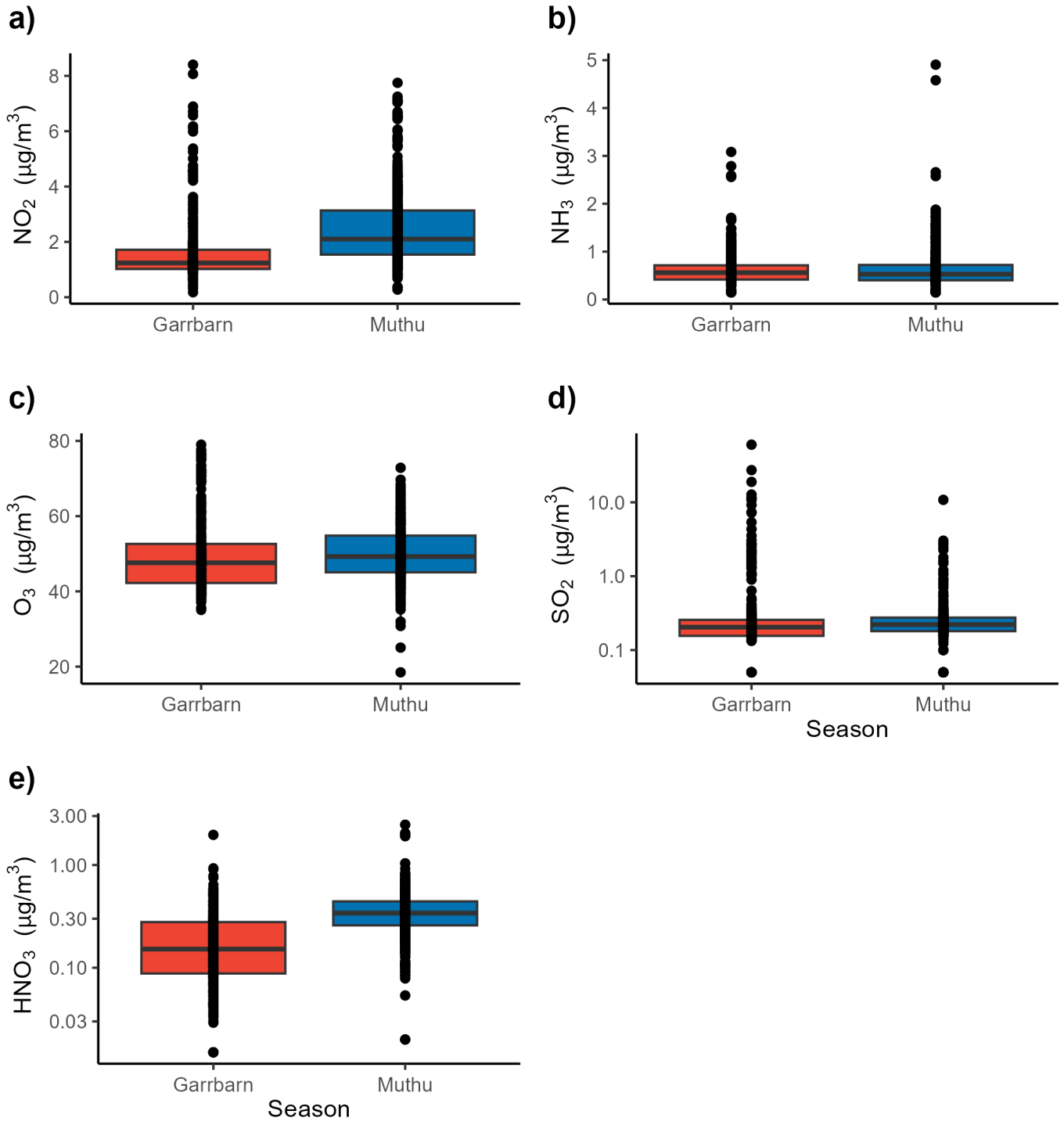

Figure 7.12-4: Boxplots of IVL sampler gas concentration observations for each gas species by Murujuga season across all stations. Separate gases are shown for each panel: (a) NO_2, (b) NH_3, (c) O_3, (d) SO_2 and (e) HNO_3. Panels (d) and (e) use logarithmic scale on the vertical axis.

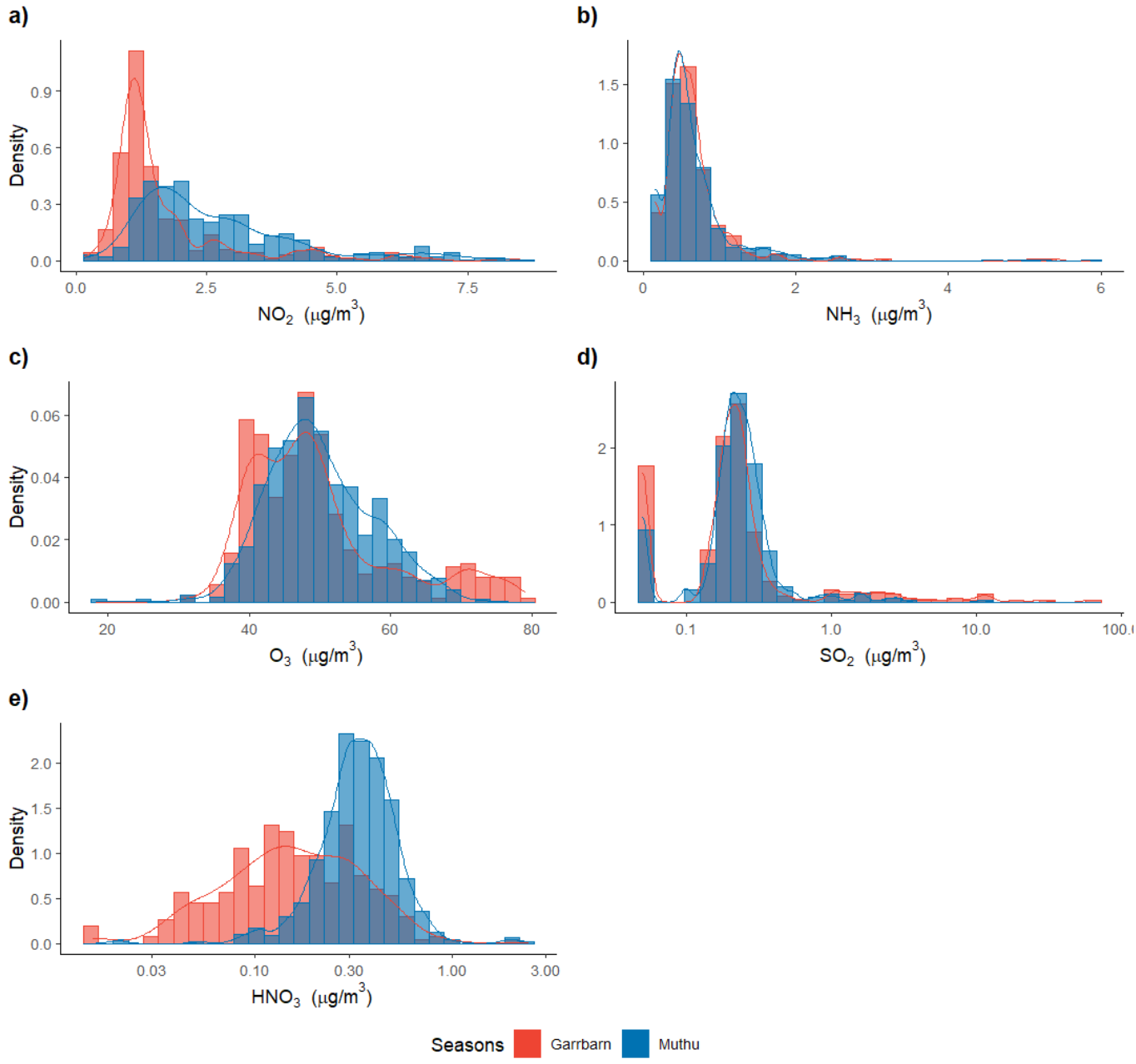

Figure 7.12-5: Histograms of IVL sampler gas concentration observations for each gas species by Murujuga season across all stations. Separate gases are shown for each panel: (a) NO_2, (b) NH_3, (c) O_3, (d) SO_2, and (e) HNO_3. Panels (d) and (e) use logarithmic scale on the horizontal axis.

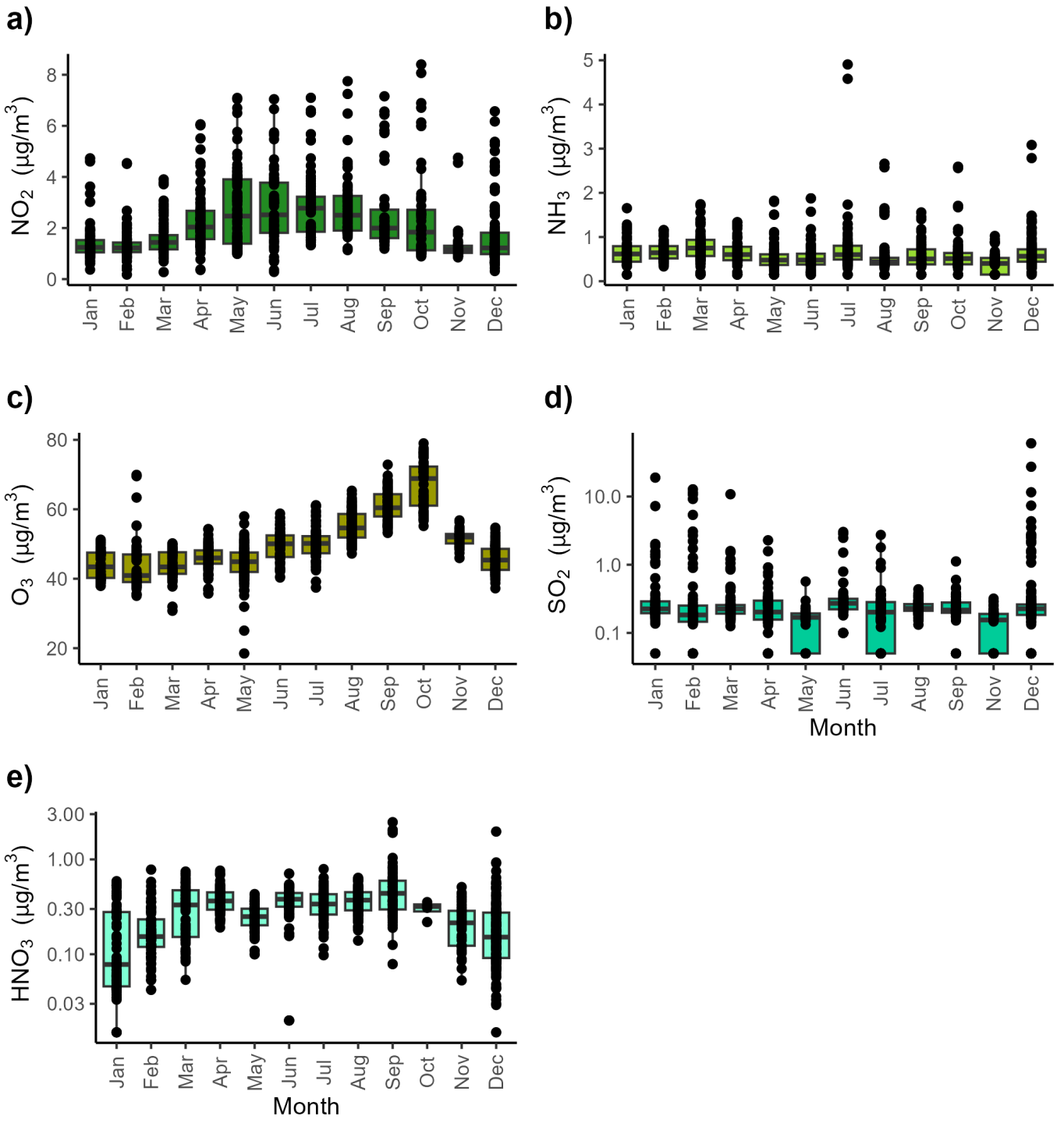

Figure 7.12-6: Boxplots of IVL sampler gas concentration observations for each month of observation: (a) NO_2, (b) NH_3, (c) O_3, (d) SO_2 and (e) HNO_3. Panels (d) and (e) use logarithmic scale on the vertical axis.

NH_3 concentrations in Figure *7.12-6*(b) show little monthly change. There may be slightly lower concentrations in May, August, and November, but no regular pattern is discernible. Figure *7.12-4*(b) shows there is also no discernible difference in gas concentrations for Murujuga seasons. Figure *7.12-5*(b) shows NH_3 concentration distributions by Murujuga season. The NH_3 distributions for both seasons is non-symmetric and bimodal with a strong right skew. For both distributions, there is a small first peak close to zero, followed by a much larger peak at 0.5-0.75 $\mu g/m^3$. The peak NH_3 concentration is at a slightly higher level in Garrbarn than in Muthu. Similarly, Appendix Figure *D.5-4*(b) shows little seasonal change in gas concentrations.

O_3 concentrations in Figure *7.12-6*(c) appear to be fairly similar for months from December to May. O_3 concentrations increase each month from June to October, with the highest concentrations measured in October. Concentrations drop in November and December. Figure *7.12-4*(c) does not show any major change in O_3 concentration between the Murujuga seasons. This is also reflected in the overlapping distributions for each Murujuga season shown by Figure *7.12-5*(c), even though the distribution for Muthu is unimodal and roughly symmetric, while the season for Garrbarn is bimodal with a right skew. O_3 concentration changes occur close to the change in the Murujuga seasons and hence are not shown by these seasons. However, Appendix Figure *D.5-4*(c) shows O_3 concentration distributions are distinct for each season: the summer and autumn distributions overlap, but the summer distribution appears bimodal while autumn has a single peak. Winter and spring are also unimodal, with the peaks occurring at higher concentrations of O_3 for successive seasons from autumn to spring. The spring distribution also has a wider spread than the other season's distributions.

SO_2 concentrations in Figure *7.12-6*(d) show little monthly change. There may be slightly lower concentrations in May, August, and November, similar to NH_3, but no regular pattern is discernible. Figure *7.12-4*(d) shows there is also no discernible difference in SO_2 gas concentrations for Murujuga seasons. Figure *7.12-5*(b) shows SO_2 concentration distributions by Murujuga season. Distributions are very similar for Garrbarn and Muthu: both are bimodal with strong right skew resulting in the use of a logarithmic scale for the horizontal axis. Both seasons show an initial peak at lower concentrations, followed by a single main peak with a right skew. Similar distributions are seen for the meteorological seasons in Appendix Figure *D.5-4*(d).

HNO_3 concentrations in Figure *7.12-6*(e) shows monthly changes that are discernible in the changing median. The median concentration increases each month from January to April, then stays at similar concentrations for June to October, before decreasing again for November to December. Figure *7.12-4*(e) shows HNO_3 concentration levels also change across Murujuga seasons, with higher concentrations in Muthu than Garrbarn. Figure *7.12-5*(e) shows the HNO_3 distributions for Muthu and Garrbarn. Muthu has a unimodal distribution with the peak occurring close to 0.5 $\mu g/m^3$. Garrbarn has a skewed bimodal distribution with an initial higher peak close to 0.1 $\mu g/m^3$ and a possibly smaller second peak close to 0.3 $\mu g/m^3$. This may reflect in part the changing gas concentrations close to the start and end of Garrbarn. Appendix Figure *D.5-4*(d) shows that HNO_3 concentration is lowest during summer and higher during autumn, winter and spring.

7.12.2.4 Volatile compound species and spatial locations

Figure *7.12-7* shows plots of the IVL passive sampler estimates of the concentration of each volatile organic compound, plotted against the air quality monitoring station identifier, with each point coloured by the Murujuga seasons Garrbarn (hot) and Muthu (cold). Appendix Figure *D.5-2* shows similar scatterplots but with each point coloured by meteorological seasons.

Overall, the VOC measurements include a high proportion of BDL observations. The detection limit varies according to the gas and the observation period. For some statistical analysis and graphics, BDL observations are assigned the value $(\text{Detection Limit})/2$. This can lead to bias in some calculations, but can provide valuable insight during exploratory analysis.

Toluene concentration, Figure *7.12-7*(b), shows a very high number of BDL observations, similar to the Monitoring Studies Report 2024 (Curtin University, 2024c). The above-detection- limit readings vary widely, without a consistent pattern being evident. The highest readings occur in both Murujuga seasons, Garrbarn (December and January) and Muthu (July and August). The two highest readings were measured at station AQ16, but most recordings at this station were BDLs.

N-octane concentration data, Figure *7.12-7*(c), consists mostly of BDL observations. Note that there is a wide range in detection limits for different months, as detection limits depend on the temperature at each site across the measurement period. Only twelve stations have measurements above the detection limit. Most of these measurements are at AQ11, which has detectable levels for most months. However the highest readings were measured at AQ10 (April) and AQ08 (December).

Ethylbenzene concentration data, Figure *7.12-7*(d), include readings above the detection limit for a wide range of months. Typically, ethylbenzene concentrations were higher during Muthu (cold) than Garrbarn season. There is variation between stations across the measurements, with the highest readings at AQ02, AQ10, AQ16, and EX02.

M-p-xylene, Figure *7.12-7*(e), in this case, using the Murujuga seasons provides a clearer pattern where concentrations are generally higher during Muthu (cold) than Garrbarn (hot) season. There is variation between stations across the Muthu measurements, with the highest readings at AQ16 and AQ10, and usually further away from the port, with the exception of AQA1. All stations recorded multiple BDLs as their lowest readings.

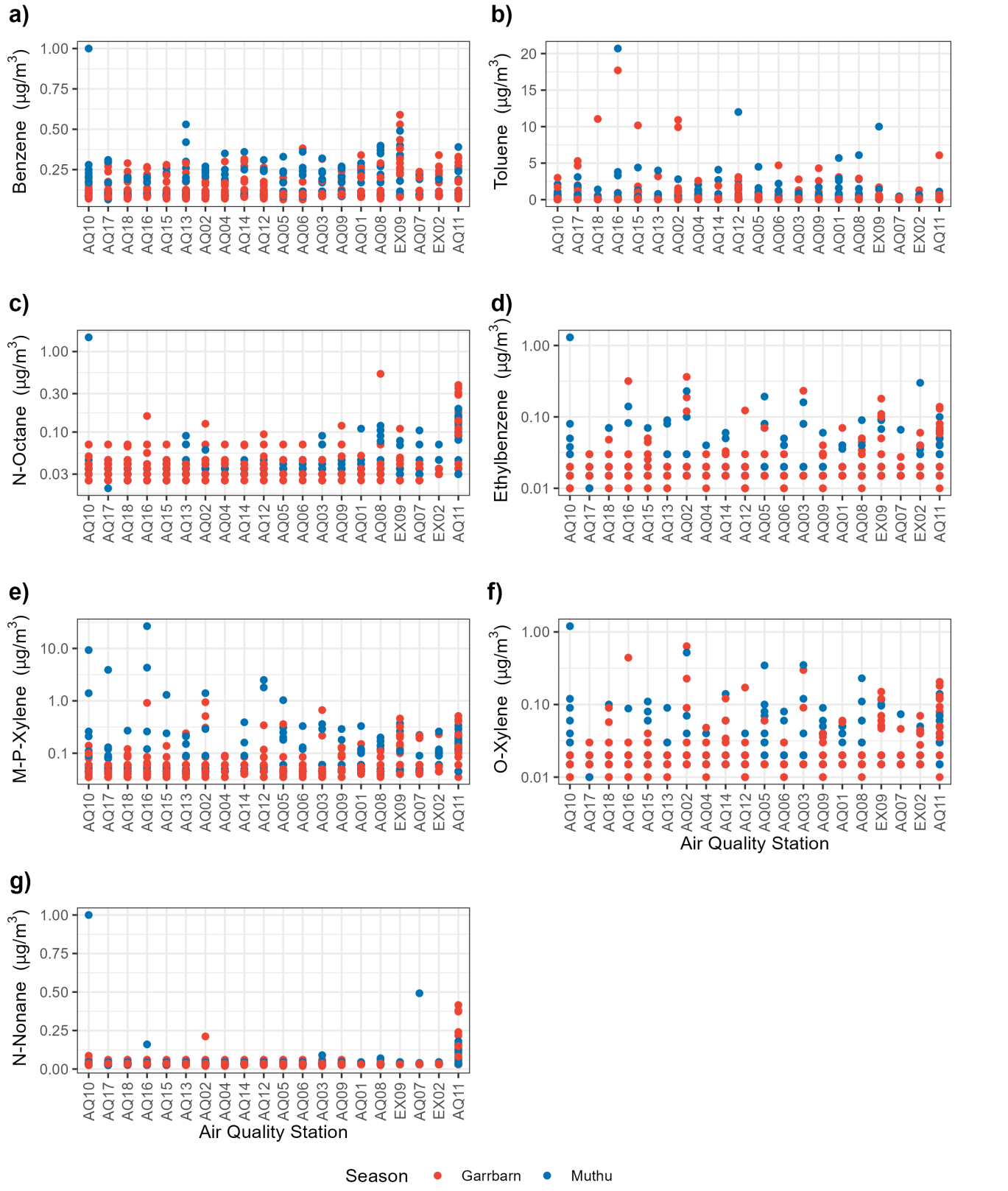

Figure 7.12-7: Plots of IVL sampler VOC measurements against air quality station for each VOC species, coloured by Murujuga season. AQM stations are ordered by increasing average NO_2 concentration. Panels: (a) benzene, (b) toluene, (c) n-octane, (d) ethylbenzene, (e) m-p-xylene, (f) o-xylene, and (g) n-nonane. Panels (c) — (f) use logarithmic scale on the vertical axis.

7.12.2.5 Volatile compound species and temporal variations

Figure *7.12-8* shows boxplots of VOC concentrations for each month, with a separate panel for each VOC species. Whilst, Figure *7.12-9* presents boxplots of VOC concentration across the two Murujuga seasons. Appendix Figure *D.5-5* shows boxplots of the same data categorised by meteorological seasons. Histograms of the VOC data categorised by meteorological seasons are shown in Appendix Figure *D.5-6* and categorised by Murujuga seasons in Appendix Figure *D.5-7*.

Benzene concentrations in Figure *7.12-8* (a) show a relatively flat distribution of VOC concentrations across most months. There is no easily discernable pattern, though there may be a slight increase in concentrations observed in October. Figure *7.12-9*(a) shows there is a small discernible difference in VOC concentrations for Murujuga seasons: the IQR for Garrbarn appears wider than for Muthu, though the ranges do overlap.

Toluene concentrations in Figure *7.12-8* (b) show some variation in VOC concentrations across the months: there is a decrease in median VOC concentrations from December to February, a relatively flat range in median values from February to May, followed by higher medians in June and July, which then declines in August. There is a period of relatively flat median values for the remaining months. Figure *7.12-9*(b) shows there no discernible difference in VOC concentrations for Murujuga seasons: median values are very similar and the IQRs are also very similar.

N – octane concentrations in Figure *7.12-8* (c) show some variation in VOC concentrations across the months. There is no easily discernable pattern, however the highest median concentration and largest IQR both occur in November. Figure *7.12-9*(c) shows that the IQR for Garrbarn is slightly wider than for Muthu, but they overlap.

The following VOCs - ethylbenzene, m-p-xylene, o-xylene, and n-nonane - follow a similar pattern to n-octane. Figure *7.12-8* panels (d) to (g) show some minor differences between the months for each VOC but no clear pattern apart from some increase in width of the IQR. The boxplots in Figure *7.12-9* show similar distributions with narrow IQR and similar median values between the two Murujuga seasons.

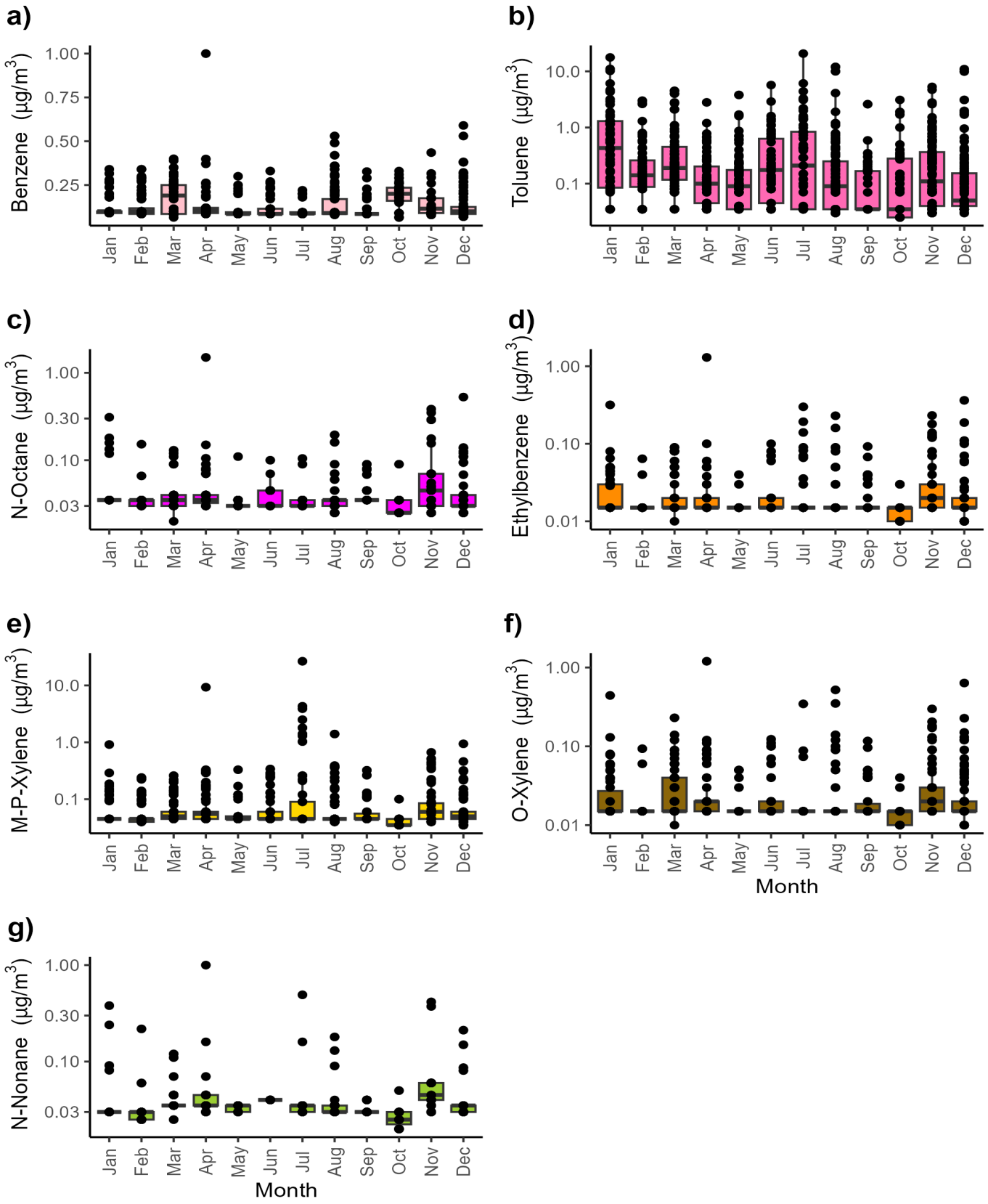

Figure 7.12-8: Boxplots of VOC IVL sampler gas concentration estimates for each month across all stations. Separate gases are shown for each panel: (a) benzene, (b) toluene, (c) n-octane, (d) ethylbenzene, (e) m-p-xylene, (f) o-xylene, and (g) n-nonane. Panels (c) — (f) use logarithmic scale on the vertical axis.

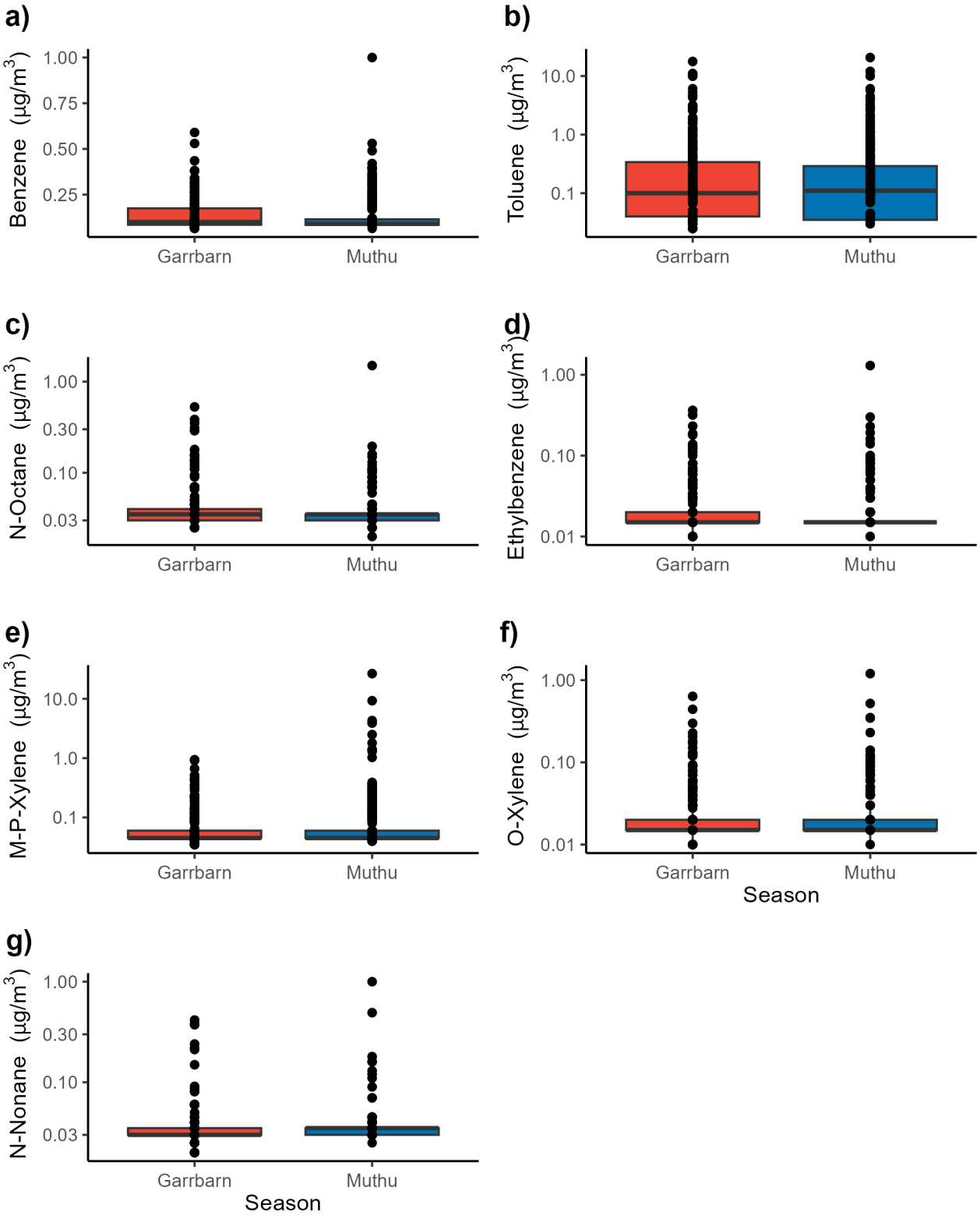

Figure 7.12-9: Boxplots of IVL sampler measurements for each VOC species by Murujuga season across all stations. Panels: (a) benzene, (b) toluene, (c) n-octane, (d) ethylbenzene, (e) m-p-xylene, (f) o-xylene, and (g) n-nonane. Panels (c) — (g) use logarithmic scale on the vertical axis.

7.12.3 Correlations between gases

Similar to Section 7.11.3 in the Monitoring Studies Report 2024 (Curtin University, 2024c), this section will investigate whether the different gas species exhibit similar patterns in concentration, both across space (gradients across the Murujuga region) and over time (seasonal patterns).

Table *7.12-2* presents the Spearman rank correlations between different gas species for spatial data averaged over all sampling periods. These correlations suggest moderate positive associations between NO_2 versus NH_3 and moderate negative associations between NO_2 versus O_3. There is also a moderate negative correlation between NH_3 and O_3. The associations between NO_2 versus HNO_3 and HNO_3 versus O_3 which were reported as significant in the previous report, are not significant with the larger amount of data available in this report.

Table 7.12-2: Spearman rank correlations between gases for spatial data. For each spatial measurement location, the average gas value was determined across all sampling periods for each gas from all available IVL passive sampler assay results. Each table entry shows the correlation between gases for these average spatial values. Statistically significant correlations are shown in bold type and annotated with one, two or three asterisks representing statistical significance at the 0.05, 0.01, and 0.001 level respectively.

	NO_2	**NH_3**	**HNO_3**	**O_3**	**SO_2**
NO_2		**0.643****	0.352	**-0.543***	-0.222
NH_3	**0.643****		-0.104	**-0.473***	0.219
HNO_3	0.352	-0.104		0.125	-0.321
O_3	**-0.543***	**-0.473***	0.125		0.314
SO_2	-0.222	0.219	-0.321	0.314	

Table *7.12-3* shows the Spearman rank correlations for the spatial-temporal (monthly) data. In this analysis, many of the gases are significantly correlated, but the correlation estimates are generally small (less than 0.5). More correlations may be significant here as the data are averaged over a smaller time period. These results may reflect the temporal component in the gas distributions. NO_2 has weak but significant positive correlations with NH_3 and HNO_3 at significance level 0.001. There is also a correlation between NO_2 and SO_2 which is significant at level 0.05, but which is particularly weak at less than 0.2. NH_3 has weak but significant positive correlations with NO_2 and SO_2. It also has a significant negative correlation with O_3, which is very weak. HNO_3 has weak but significant positive correlations with NO_2, O_3, and SO_2. O_3 has weak but significant positive correlations with HNO_3 and SO_2 as well as a very weak negative correlation with NH_3.

The correlations in the spatial-temporal data (Table *7.12-3*) include the effect of seasonal patterns and other variability over time, whereas correlations in Table *7.12-2* are more directly reflective of spatial gradients of gas concentration. The stronger correlations found in the annual average data suggest that spatial location is an influential factor in predicting gas concentration. The weaker correlations found in the spatial-temporal (monthly) data have several possible causes, including the small number of observations from which the monthly data are calculated and the higher variability of this data.

The above analyses do not attempt to explicitly take into account the temporal or spatial effects. An

Table 7.12-3: Spearman rank correlations between gas species for spatial temporal data. For each spatial measurement location and each month, the average gas measure was determined. Gas measures were assigned to the month in which the majority of the sampling period took place. Each table entry shows the correlation between gases for these average spatial monthly values. Values marked with one, two or three asterisks indicate results that are statistically significant at the levels 0.05, 0.01, and 0.001 respectively.

	NO_2	NH_3	HNO_3	O_3	SO_2
NO_2		**0.211*****	**0.363*****	0.056	**0.118***
NH_3	**0.211****		0.090	**-0.131****	**0.265*****
HNO_3	**0.363*****	0.090		**0.479*****	0.268***
O_3	0.056	**-0.131****	**0.479*****		**0.219*****
SO_2	**0.118***	**0.265*****	**0.268*****	**0.219*****	

RDA analysis was also undertaken and is reported in Appendix *D*.5.3. This analysis showed that explicitly allowing for time of year or location predictor variables does impact correlations between gas variables. The RDA analysis that included time of year explained 44% of total variation, whilst the RDA with location only explained 12.6% of the total variation. Different predictor variables, e.g. distance and bearing to port, and accounting for non-linear relations could improve the underlying model and will be explored in the final year report.

7.12.4 Residual variability

As stated in Section 7.11.4 of the Monitoring Studies Report 2024 (Curtin University, 2024c), the passive sampler tubes are deployed in duplicate pairs: two identical sampler tubes for each analyte are deployed within the same housing at each AQM for each month. Following on from Monitoring Studies Report 2024, summary statistics were calculated from the duplicate samples to help understand the intrinsic variability of the measurement technique.

Table *7.12-4* reports the gas species and VOCs summary statistics for the duplicate pairs of observations for sampling periods for 2023 and 2024. The second column is the mean of means, obtained by calculating the mean of each duplicate pair at each site and sampling period, and then taking the mean across all sites and periods. The third column is the residual variance, which is calculated as the mean of the variance at each location for each sampling period. The residual variance provides estimates of the intrinsic variability of the measurement technique and is the primary goal of this analysis. The fourth column is the residual standard deviation (**SD**), which is calculated as the mean of the standard deviation for each location and sampling period. The fifth column is the residual SD divided by the overall mean. This value describes the size of the remaining variability in the data relative to the average measurement. The last column is the proportion of residual variability, which is the residual variance divided by the total variance. This value indicates the proportion of the overall variability that is due to residual (within-site and within-period) variation.

The NO_2 residual (within-site / within-period) variance is about 8% of the mean concentration, this indicates highly consistent NO_2 measurements at that scale. Whereas, SO_2 has a very high residual variability (5.87), i.e. the residual variation is almost six times the mean concentration.

This indicates that the within-site and within-period variation dominates relative to its average concentration.

Table 7.12-4: Summary statistics for duplicate measurements from passive samplers for sampling periods for 2023 and 2024. For each analyte (gas species and VOCs) is the overall mean (mean of means), estimate of residual variance, estimate of residual standard deviation (SD), residual standard deviation divided by the overall mean, and proportion of residual variability. Mean measures are in $\mu g/m^3$.

Gas	Mean of Means	Residual Variance	Residual SD	Residual SD/Mean	Residual/Total Variance
NO_2	2.29	0.08	0.14	0.06	3.1%
NH_3	0.66	0.03	0.09	0.14	9.3%
O_3	49.90	2.96	1.29	0.03	4.1%
SO_2	0.50	5.87	0.42	0.74	95%
HNO_3	0.31	0.01	0.06	0.19	26%
Benzene	0.13	0.00	0.02	0.18	48%
Toluene	0.36	0.76	0.27	0.73	35%
Octane	0.04	0.00	0.01	0.14	80%
Ethylbenzene	0.03	0.00	0.01	0.29	84%
m-p xylene	0.14	0.78	0.08	0.58	79%
o-xylene	0.03	0.00	0.01	0.36	70%
n-nonane	0.04	0.00	0.01	0.14	79%

Figure *7.12-10* helps understand the variance-mean relationship further by showing the individual estimates S^2 of variance plotted against the corresponding individual estimates $\overline{X}$ of the mean. There is no evidence that the variance depends on the mean for all gas species (NO_2, NH_3, O_3 and HNO_3), suggesting that the foregoing analysis was appropriate.

For NH_3, there is a group of points with low mean concentrations but high paired variances, forming an approximately linear pattern. This arises because, for each of these points, one of the paired measurements is BDL.

For SO_2, the top two panels of Figure *7.12-11* are scatterplots of residual variance estimates against paired means, with both variables shown on a logarithmic scale. Colours represent months in the top left plot, and AQM stations in the top right plot. Residual variance estimates are plotted against calendar month in the bottom left panel, and against AQM station identifier in the bottom right panel. The top row strongly suggests an increasing relationship between variance and mean.

For SO_2, similar to NH_3, there is a group points with low mean concentrations but high paired variances. These points occur because one of the paired values for each point is BDL. The SO_2 points that have a large paired mean (logarithmic mean around 1.0 or greater) occur if there is a very large difference between the duplicate measurements.

Further diagnostic plots of residual variance estimates versus station and month for individual gases are given in Appendix *D*.5.4: Figures *D.5-10* to *D.5-13*.

For the VOCs, Figures *7.12-12* and *7.12-13* show similar diagnostic plots of the individual estimates

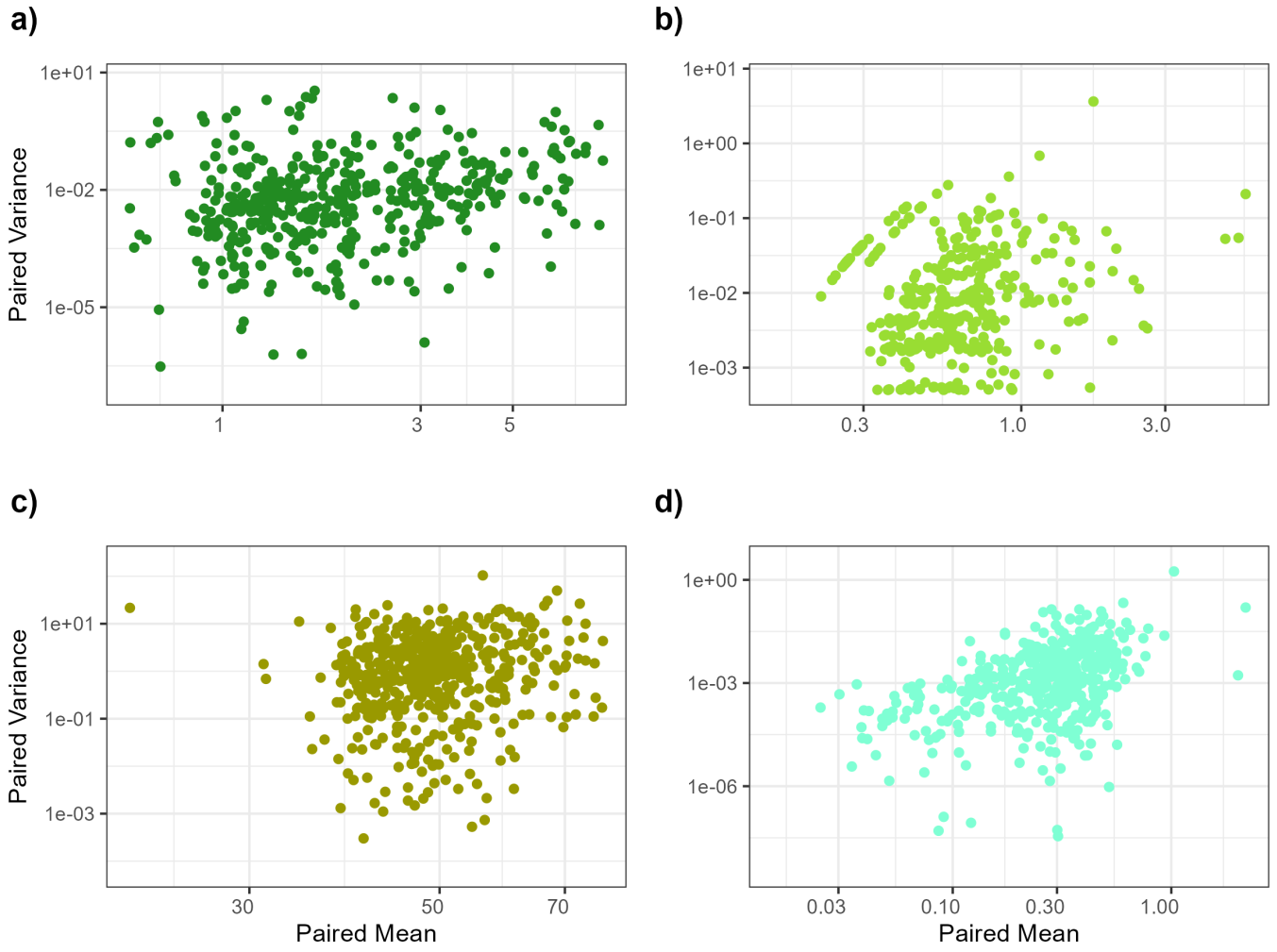

Figure 7.12-10: Diagnostic plots for the variance-mean relationship. Scatterplots of individual estimates of variance (S^2, "paired variance") versus individual estimates of mean value ($\overline{X}$, "paired mean") calculated from duplicate pairs of passive sampler measurements for each gas species: (a) NO_2, (b) NH_3, (c) O_3, and (d) HNO_3. Plots show paired measurements for measurements over 2023 and 2024. All axes use logarithmic scale.

of residual variance against individual estimates of the mean. Logarithmic axis scales have been used throughout.

All VOCs suggest an increasing relation between variance and mean (Figures *7.12-12* and *7.12-13*). There are numerous caveats, including the small sample size, the wide range of reported values, the high frequency of BDL observations, and the fact that all VOC species are assayed from the same sampler tube. Similar to NH_3 and SO_2, for some of the points, one of the paired measurements is BDL.

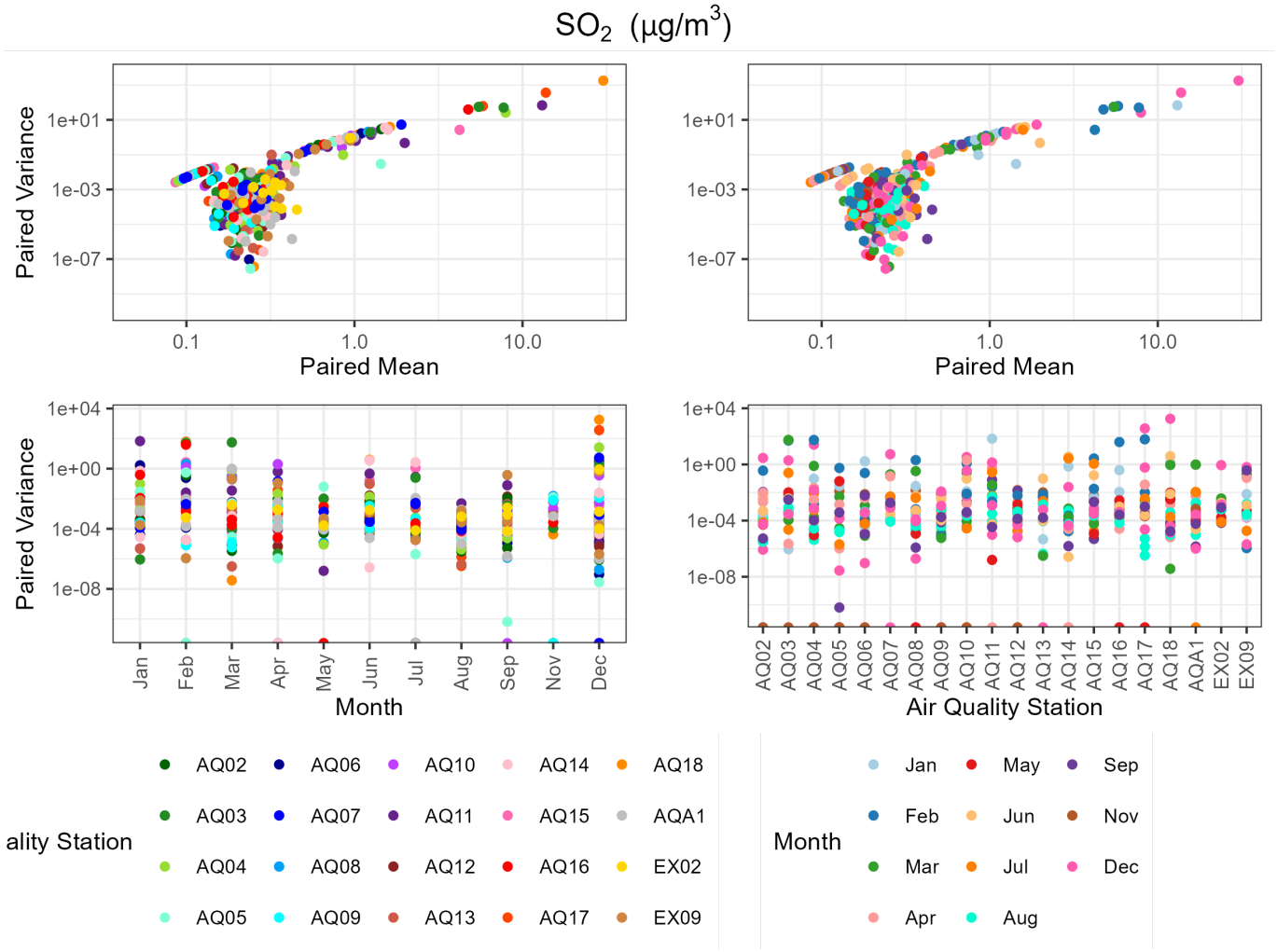

Figure 7.12-11: Diagnostic plots for the variance-mean relationship for SO_2 data. Top row shows a scatterplot of individual estimates of variance (S^2, "paired variance") versus individual estimates of mean value ($\overline{X}$, "paired mean") calculated from duplicate pairs of passive sampler measurements for SO_2. Left scatterplot is coloured according to calendar month; right scatterplot is coloured according to air quality station. Logarithmic scale is used for both variables. Bottom row shows individual estimates of variance plotted against calendar month (left) and against air quality station (right). Plots show paired measurements collected over 2023 and 2024. The legend on the bottom left hand side show the stations by colour while the legend on the bottom right hand side show the months by colour. The axis labels `1e-03` and `1e+01` (for example) are computer notation for 10^{-3} and 10^{1} respectively, that is, 0.001 and 10 respectively.

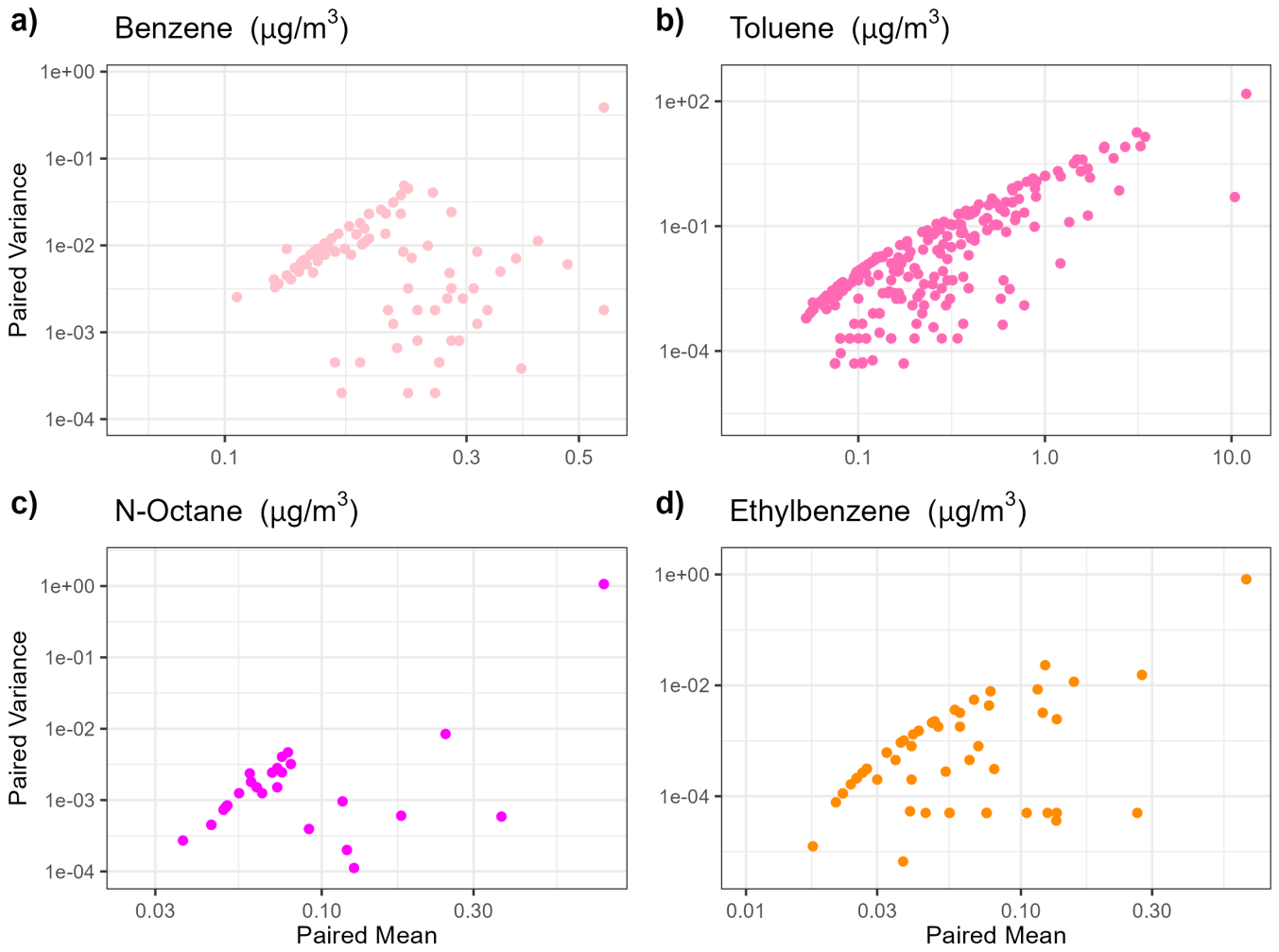

Figure 7.12-12: Scatter plots of pairwise variance by pairwise mean for VOC species (a) benzene, (b) toluene, (c) n-octane, and (d) ethylbenzene. Plots show paired measurements for sample data collected over 2023 and 2024. Both axes use logarithmic scale.

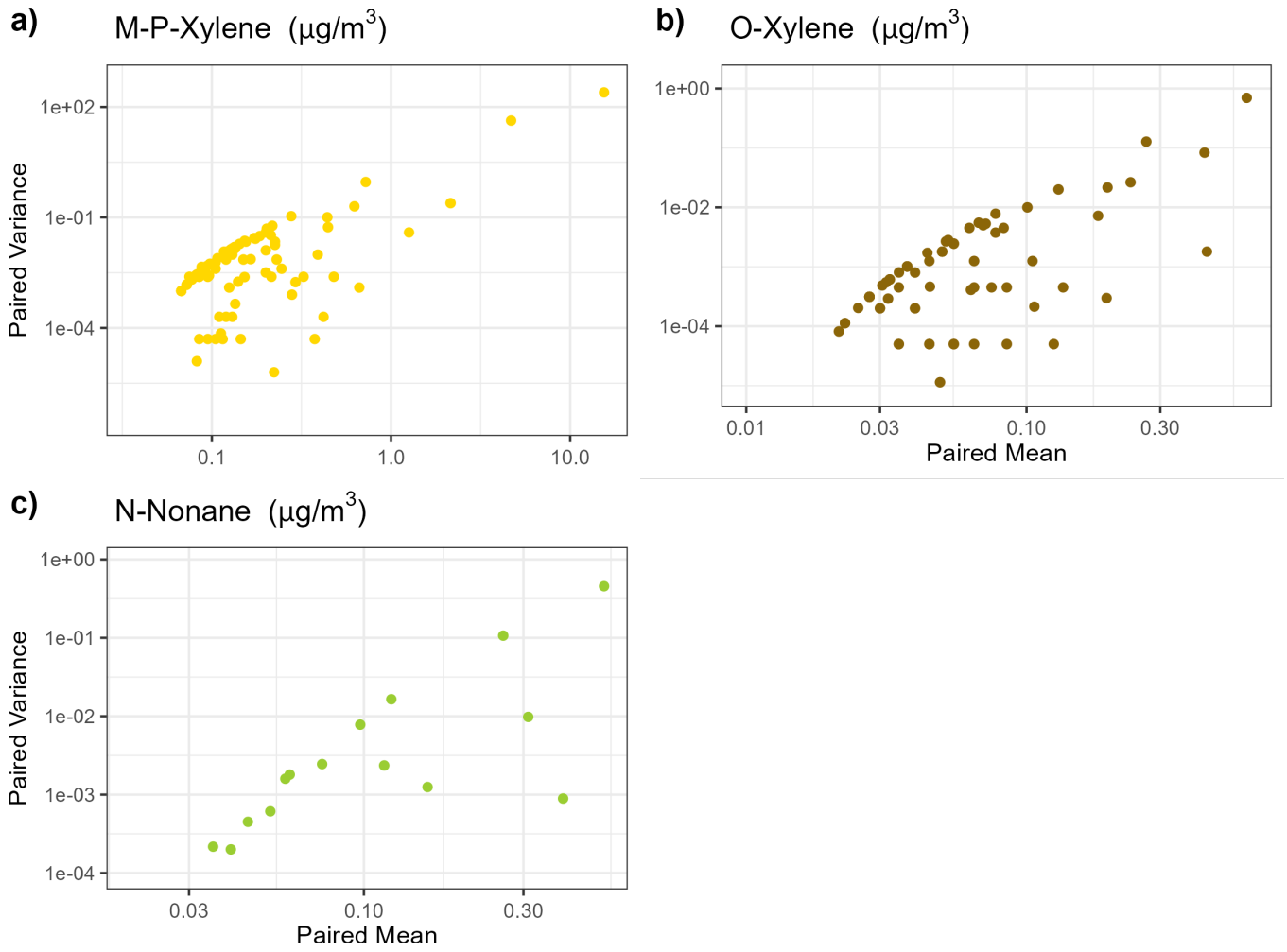

Figure 7.12-13: Scatter plots of residual variance versus mean for VOCs species (a) m-p-xylene, (b) o-xylene, and (c) n-nonane. Plots show paired measurements for sample data collected over 2023 and 2024. Both axes use logarithmic scale.

7.12.5 Short scale variability

An important consideration in statistical analysis of spatial data is the magnitude of short-scale variability. Section 7.11.5 of the Monitoring Studies Report 2024 (Curtin University, 2024c) explains that air quality monitoring stations AQ07 and AQ08, which are approximately 25 metres apart, are used to examine the short-scale variability. At the time of preparation of this report, IVL assay reports for gas and VOC species were available for the sampling months from June 2023 up to and including December 2024. This section provides an initial graphical comparison of gas observations from the two sites, followed by an update of the exploratory analysis determining the magnitude of short scale variability. Finally there is an analysis to determine if gas observations differ significantly between stations, firstly without considering temporal effects for all gas and VOC species. Then for gas species where a second order analysis is possible, the results of a two-way ANOVA by station and season are presented.

Graphical comparison of gas observations by station

Figure *7.12-14* shows the boxplots for the gas species, with the IQR for each station overlapping for all gas species. Median values for the two stations are also close for most gases. For NH_3, the median value for AQ07 is noticeably higher than AQ08: this may be due to the outlier values recorded at AQ07. Histograms of gas concentration data by station, see Appendix Figure *D.5-14*, show distributions consistent with the boxplot findings.

Figure *7.12-15* shows boxplots of gas species for the combined AQ07 and AQ08, other stations excluding AQ07 and AQ08, and all stations. The median of NO_2 is noticeably higher at AQ07 and AQ08 compared to the other stations. The median of HNO_3 is slightly higher at AQ07 and AQ08 compared to the other stations and SO_2 is also very slightly higher however difficult to see due to the logarithmic scale. The remaining two gas species (NH_3, O_3) concentrations are equivalent or lower at AQ07 and AQ08 compared to the other stations. AQ07 and AQ08 show a lower range of measurements for many species, compared to other stations.

Figure *7.12-16* shows the scatterplots of gas concentrations for station AQ07 versus AQ08. The plots show positive, generally linear relationships. Most points lie close to the 1:1 line indicating equal gas concentrations between the two stations, with some outliers observed for SO_2 and HNO_3.

Appendix Figure *D.5-16* shows boxplots of the gases categorised by meteorological season and Appendix Figure *D.5-17* shows boxplots categorised by Murujuga season for data pooled across AQ07 and AQ08. NO_2 and O_3 have noticeable seasonal changes at combined AQ07 and AQ08, which are similar to seasonal patterns across all stations.

Figure *7.12-17* shows boxplots for each VOC species. A large number of outliers are shown for all species except toluene (b) and n-nonane (g). The IQRs however, were quite narrow for many gases: this is due in part to the outliers. There are noticeable differences between stations AQ07 and AQ08 for benzene (a) and toulene (b): in both cases the IQR is wider for AQ08. Histograms of VOC concentration data by station, see Appendix Figure*D.5-15*, show highly right-skewed distributions consistent with the boxplot findings.

Figure *7.12-18* shows the scatterplots of VOC concentrations for station AQ07 versus AQ08. The plots show positive, generally linear relationships though some outliers are present. For instance toluene (b), shows most data clustered at low values with just a few higher points. Other plots, e.g.

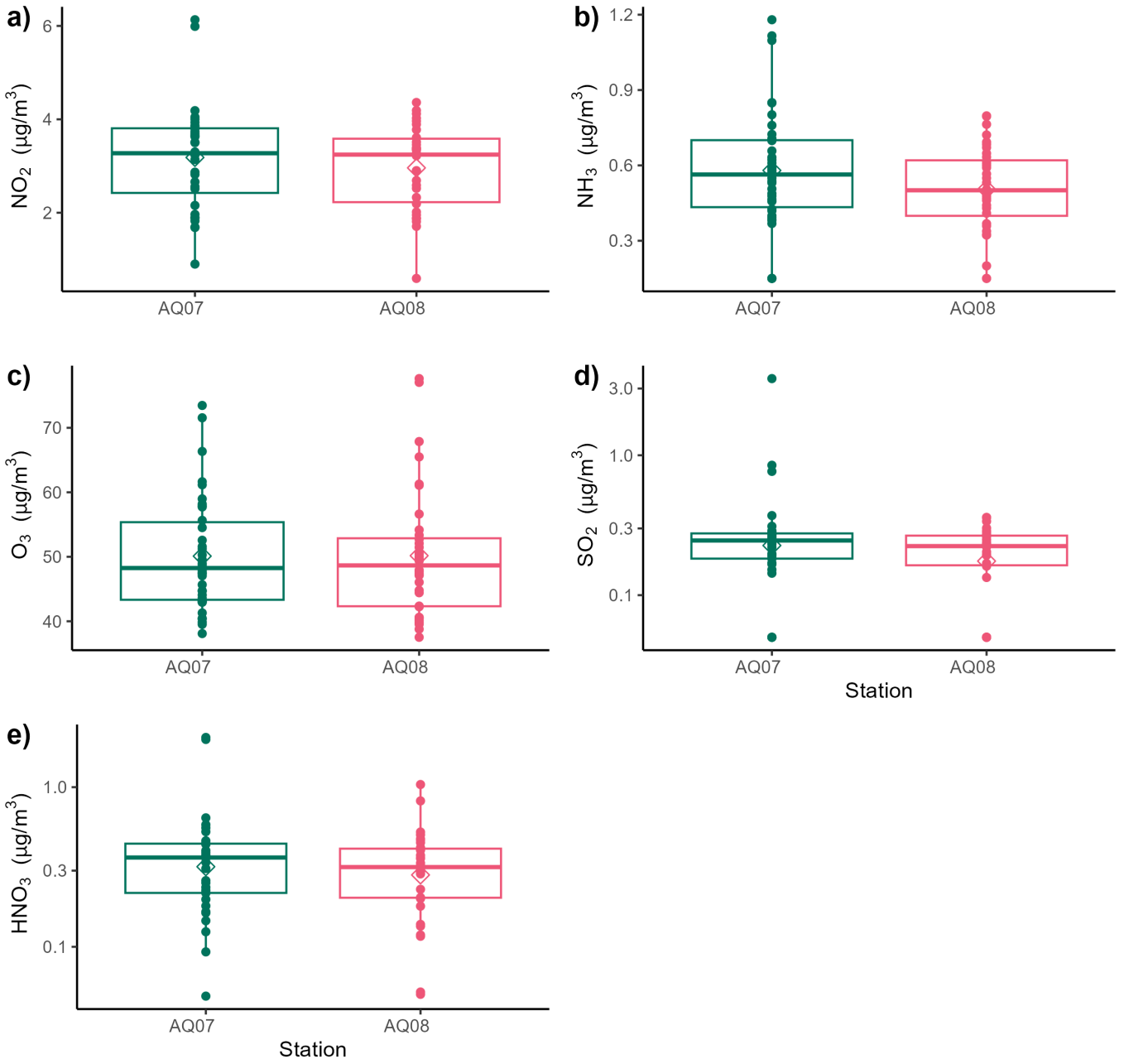

Figure 7.12-14: Boxplots of passive sampler gas concentration measurements for stations AQ07 and AQ08 for gas species (a) NO_2, (b) NH_3, (c) O_3, (d) SO_2 and (e) HNO_3. For each species, only data for which corresponding observations are available for both AQ07 and AQ08 have been used. The mean value is diamond shape. Panels (d) and (e) use logarithmic scale on the vertical axis.

N-nonane (c) show a strong linear relationship with most points close to the line showing an equal relation for gas concentrations between the stations.

Appendix Figure *D.5-18* shows boxplots of the VOCs categorised by meteorological season and Appendix Figure *D.5-19* shows boxplots categorised by Murujuga season for data pooled across AQ07 and AQ08. There were some seasonal differences in VOCs at combined AQ07 and AQ08.

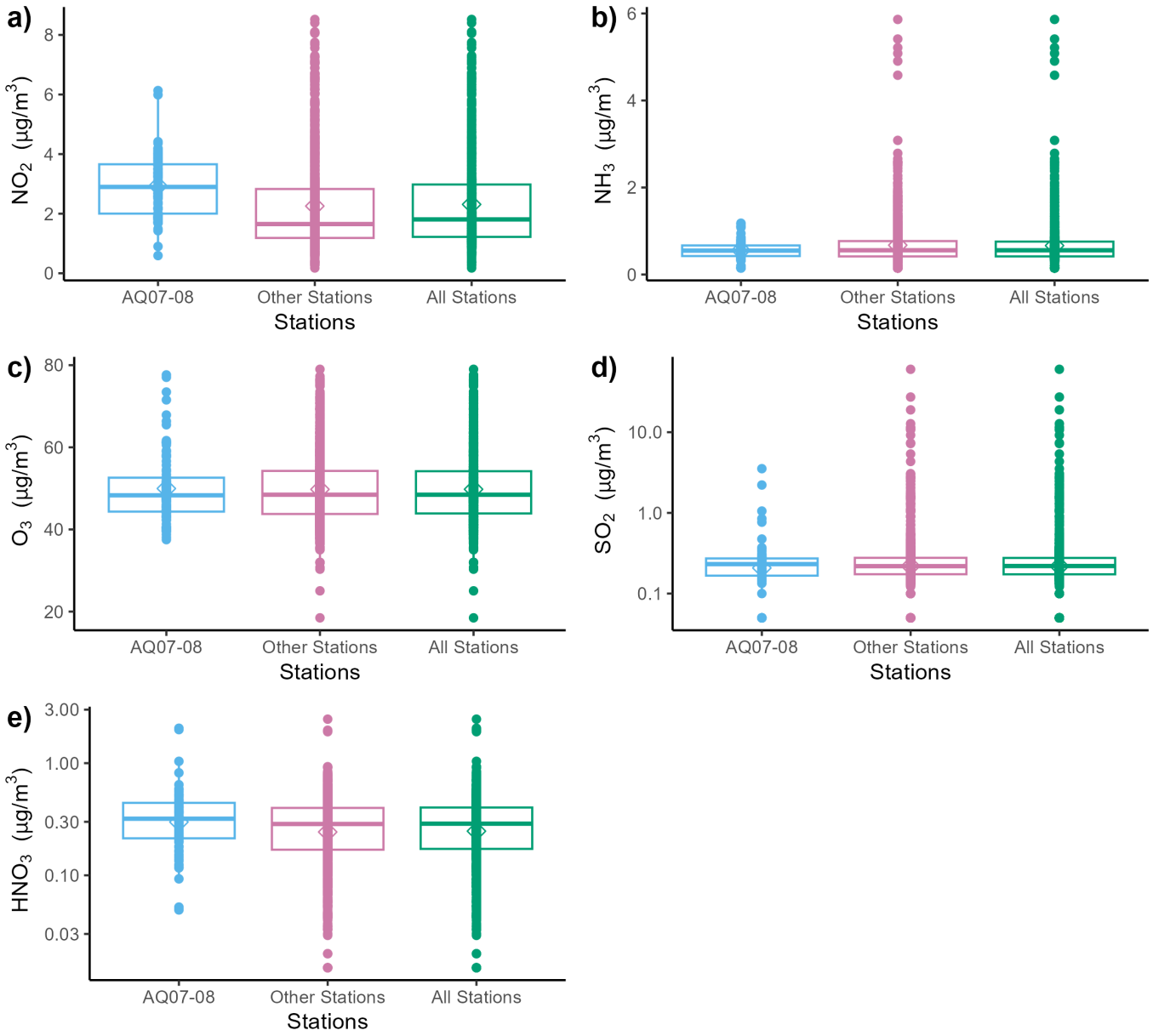

Figure 7.12-15: Boxplots IVL passive sampler for the combined AQ07 and AQ08, other stations (all stations except for AQ07 and AQ08) and all stations for (a) NO_2, (b) NH_3, (c) O_3, (d) SO_2 and (e) HNO_3. Panels (d) and (e) use logarithmic scale on the vertical axis.

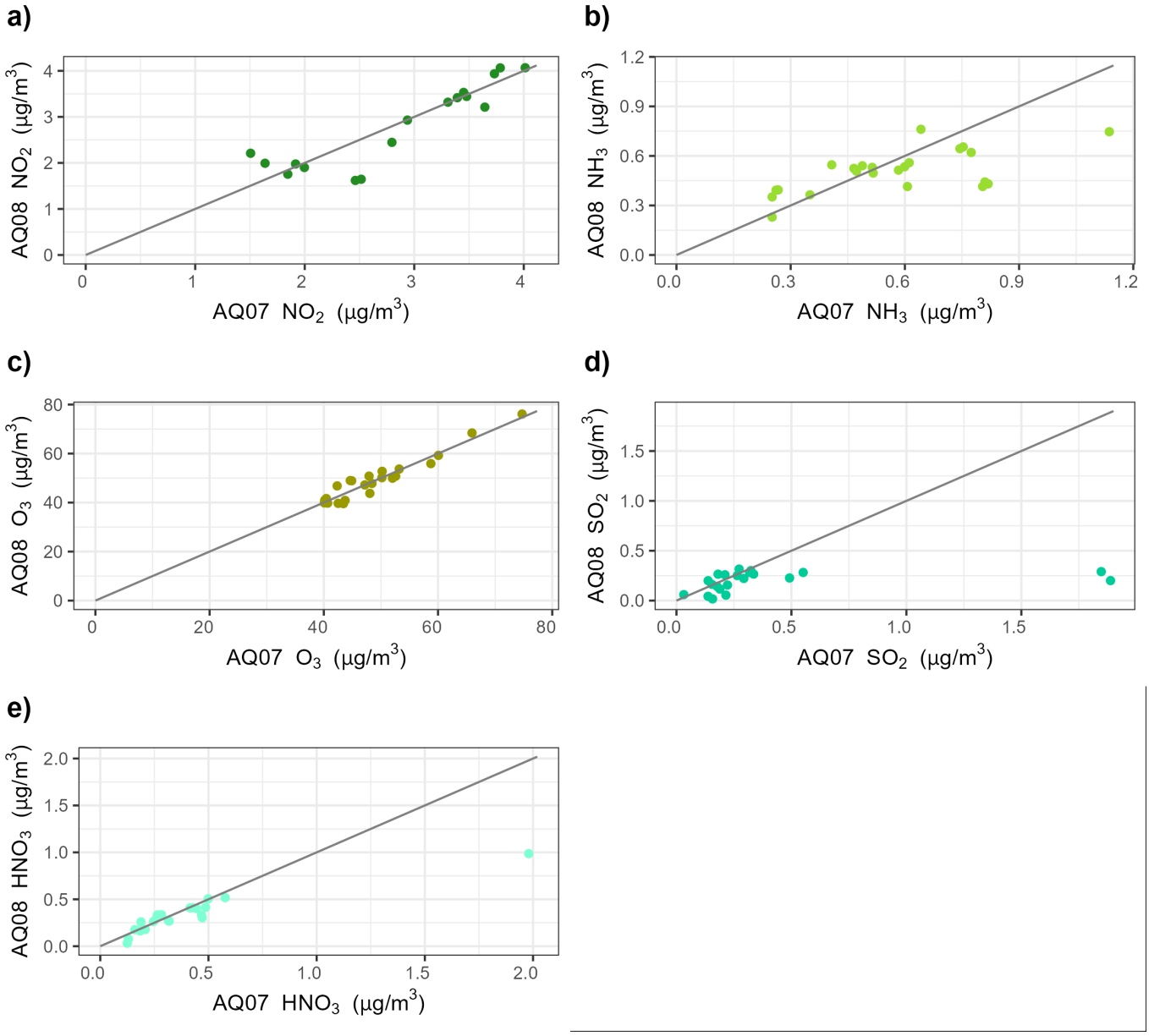

Figure 7.12-16: Scatterplots of passive sampler gas concentration measurements for station AQ07 versus station AQ08 for gas species: (a) NO_2, (b) NH_3, (c) O_3, (d) SO_2 and (e) HNO_3. For each species, only data for which corresponding observations are available for both AQ07 and AQ08 have been used. The 1:1 line corresponds to equal relation between AQ07 and AQ08. A small amount of jitter has been used in these plots so that all points can be seen.

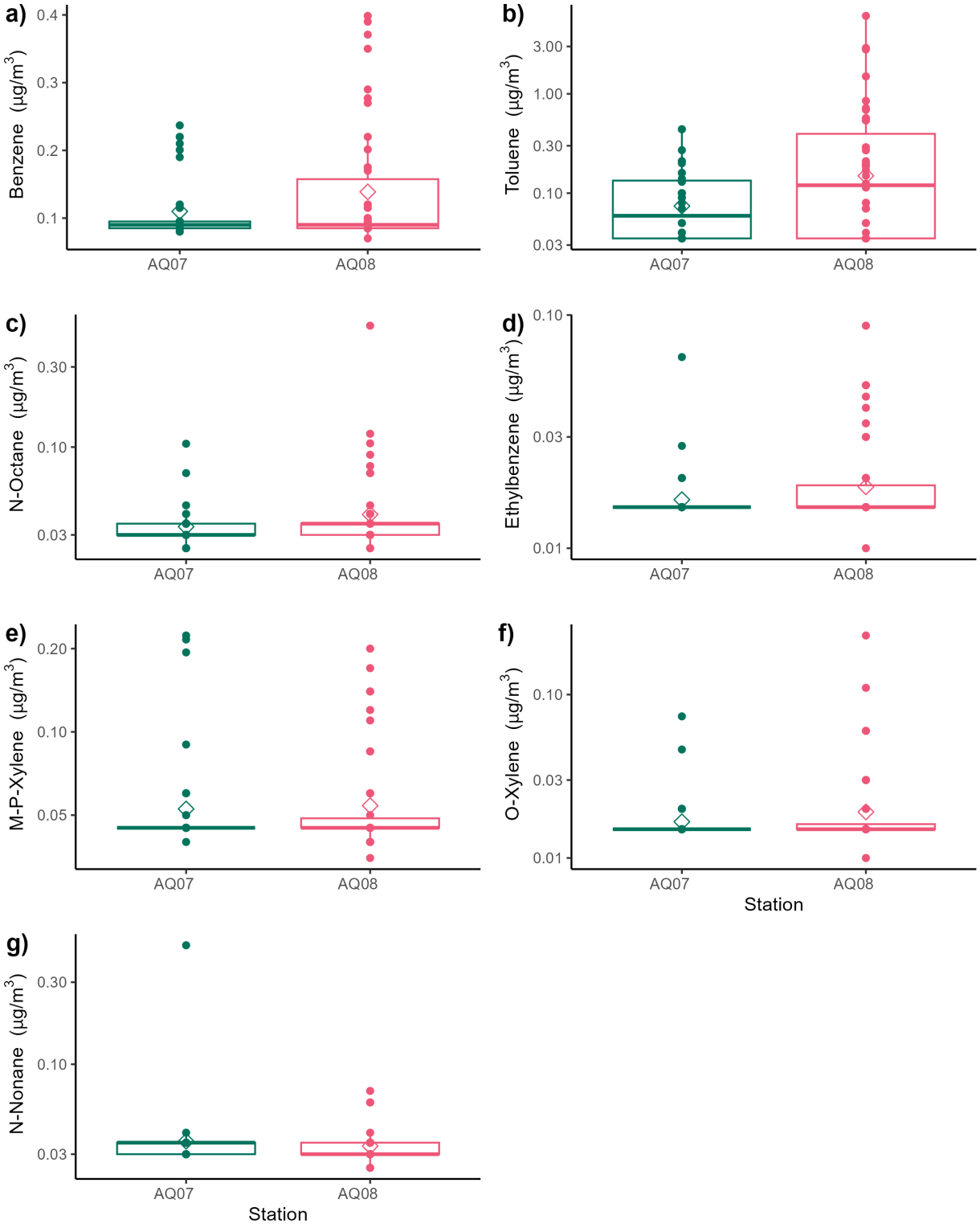

Figure 7.12-17: Boxplots of passive sampler gas concentration measurements for stations AQ07 and AQ08 for VOC species: (a) benzene, (b) toluene, (c) n-octane, (d) ethylbenzene, (e) m-p-xylene, (f) o-xylene, and (g) n-nonane. For each species, only data for which corresponding observations are available for both AQ07 and AQ08 have been used. The mean value is diamond shape. Panels (b) to (g) (inclusive) use logarithmic scale on the vertical axis.

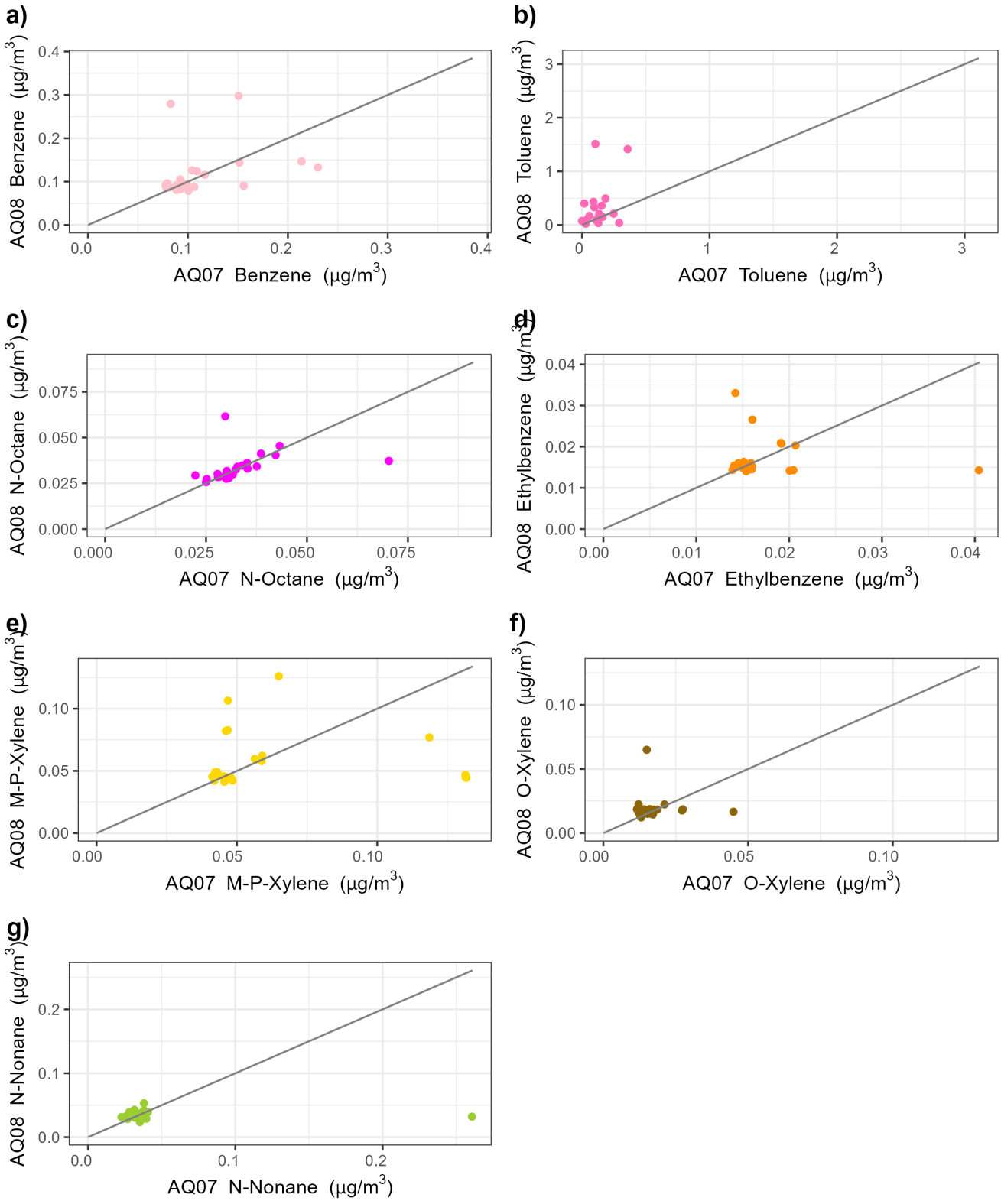

Figure 7.12-18: Scatterplots of passive sampler gas concentration measurements for station AQ07 versus station AQ08 for gas species (a) benzene, (b) toluene, (c) n-octane, (d) ethylbenzene, (e) m-p-xylene, (f) o-xylene, and (g) n-nonane. For each VOC, only data for which corresponding observations are available for both AQ07 and AQ08 have been used. The 1:1 line corresponds to equal relation between AQ07 and AQ08. A small amount of jitter has been used in these plots so that all points can be seen.

Short scale variance estimates

One objective of the exploratory analysis is to determine the magnitude of short-range variability. The Monitoring Studies Report 2024 (Curtin University, 2024c) compared estimates of overall variance in measurements and estimates of difference in measurements between the stations as explained below. This analysis is repeated using the extended dataset now available.

Table *7.12-5* shows the estimate of $\sigma^2 + \tau^2$, which is calculated as the average of the values $(\overline{X} - \overline{Y})^2$ over all months where data are available for both stations. The number n of months for which data were available is indicated. The estimate of τ^2 is then obtained by subtracting the estimate of σ^2 given in Table *7.12-4*. Negative estimates of τ^2 did occur in some cases in the Monitoring Studies Report 2024, but using the larger dataset now available, all estimates of τ^2 are non-negative.

Table 7.12-5: Calculation of raw estimates of the short-range mean square difference τ^2 between true values of gas concentrations at the sites AQ07 and AQ08. Columns give the number n of months for which paired data were available, the estimate of $\sigma^2 + \tau^2$, and the resulting estimate of τ^2 plus the ratio.

Gas	n	$\sigma^2 + \tau^2$	τ^2	$\tau^2/(\sigma^2 + \tau^2)$
NO_2	13	1.039	0.080	0.077
NH_3	16	0.422	0.026	0.063
O_3	16	68.243	4.265	0.063
SO_2	14	0.856	0.061	0.071
HNO_3	14	1.241	0.089	0.071
Benzene	16	0.113	0.007	0.062
Toluene	16	13.075	0.817	0.062
Octane	16	0.004	< 0.0001	0.063
Ethylbenzene	16	0.001	< 0.0001	0.063
m-*p* xylene	16	0.019	0.001	0.063
o-xylene	15	0.016	0.001	0.067
n-nonane	14	0.054	0.004	0.071

Determining difference between stations

One-way Analysis of Variance was conducted to identify if there were any differences between the two co-located AQMs. For further details see *ANOVA* in Glossary Table *1.4-3*.

For some sampling periods, data was only available for one station, this results in an unbalanced dataset. Therefore, a matched dataset was created for each gas species, in which samples were included only if data were available for both stations.

Both ANOVA and Kruskal-Wallis tests were applied to the matched data, with the monitoring station (AQ07 and AQ08) as the only factor. For a number of gas species and VOCs, the ANOVA normality assumptions were not met. Applying transforms, such as the logarithm, did not resolve this issue. Therefore, only Kruskal-Wallis results are presented here for each gas species and VOC.

Table *7.12-6* shows the Kruskal-Wallis test results for each gas species and VOCs Appendix Table *D.5-1*

shows all of the ANOVA and Kruskal-Wallis results). This table shows that there was no significant difference between the two stations for any gas species or VOC at a significance level of 0.05, except for Toluene.

Table 7.12-6: Results for the Kruskal-Wallis analysis of gas concentration by sites (AQ07 and AQ08) for matched data only. The column "total observations" gives the number of observations for a gas species across both sites, while the column "used observations" gives the number of observations in the matched dataset across the two sites. The column Kruskal-Wallis p-value shows the strength of supporting evidence for differences between gas concentration measurements using the Kruskal-Wallis test. p-values of less than 0.05 indicate there is evidence of significant difference in values between the two stations, these values are in bold.

Gas	Total Observations	Used Observations	Kruskal-Wallis p-value
NO_2	80	62	0.622
NH_3	92	74	0.218
O_3	92	74	0.922
SO_2	81	65	0.318
HNO_3	84	66	0.644
Benzene	86	69	0.478
Toluene	82	67	**0.029**
n-octane	86	69	0.374
Ethylbenzene	86	69	0.374
m-*p* xylene	86	69	0.754
o-xylene	78	61	0.254
n-nonane	70	55	0.916

Determining difference between stations including a seasonal factor

A problem with the previous analysis is that it only considers the variation between the two stations and does not take into account other factors that could affect gas measurements. One factor that may affect gas observations is the different months or seasons in which data were collected. This can be addressed by using a two way ANOVA test.

One issue with two way ANOVA is that non-parametric alternatives, such as the Kruskal-Wallis test are not available if the assumptions of constant variance and normal distribution of the residuals are not met. Data were analysed for both the matched data and the entire dataset. However, the ANOVA assumptions were not met for the VOC species, despite trying different transformations. Hence the results of the two way analyses for the VOCs are not presented in the main body of the report. An alternative technique called PERMANOVA which is a non-parametric test that can be applied to multivariate data. This approach may be considered for the final report.

For the Monitoring Studies Report 2024 (Curtin University, 2024c), very few observations were available for the short scale analysis. With data available to December 2024, there are now between 80 to 92 observations available per species across the two stations. For matched datasets, there are 55 to 74 observations across both stations depending on the gas species. However, the number of combinations of stations and months is relatively large compared to the number of observations

available. Hence it was decided to analyse the data in relation to seasons. Analysis was carried out for both Murujuga and meteorological seasons.

These analyses were conducted on matched datasets using both raw (untransformed) data and rank-transformed data (values converted to their order, from smallest to largest). Results are presented only shown for tests in which the residuals met the assumptions of normality and constant variance.

Two way ANOVA by station and meteorological seasons

Table *D.5-3* shows the results of the two-way ANOVA analysis for the gases species using meteorological seasons and stations as factors. None of the gas species showed a significant interaction between meteorological seasons and station. None of the gases species showed a significant difference between stations. However, NO_2 and O_3 had a significant difference between meteorological seasons.

A full set of results for gases is provided in Appendix Table *D.5-3*. Appendix Table *D.5-4* provides the results of the two-way analysis for VOCs. Appendix *D*.5.5.7 provides plots of gas concentrations by station and season, which align with the ANOVA results.

Table 7.12-7: Results of two-way ANOVA analysis of gas concentrations by sites (AQ07 and AQ08) and meteorological seasons for matched and ranked data only. The column "total observations" gives the number of observations for a gas species across both sites, while the column "used observations" gives the number of observations in the matched dataset across the two sites. The last three columns shows the p-value for station, meteorological seasons and the interaction between station and season. p-values less than 0.05 indicate a significant difference in values, these values are in bold.

Gas	Total Obs.	Used Obs.	Station p-value	Season p-value	Station $\times$ Season p-value
NO_2	80	62	0.495	**< 0.0001**	0.416
NH_3	92	74	0.198	0.062	0.897
O_3	92	74	0.986	**< 0.0001**	0.926
SO_2	81	65	0.311	0.327	0.680

Two way ANOVA by station and Murujuga season

Appendix Table *D.5-2* shows the results of the two-way ANOVA analysis for the gas species using Murujuga seasons and stations as factors. Results are only shown for those tests where the ANOVA assumptions were met.

None of the gas species showed a significant interaction between Murujuga seasons and station. None of the gases species showed a significant difference between stations. However, NO_2 and HNO_3 had a significant difference between Murujuga seasons.

Interestingly, the two-way ANOVA test of HNO_3 met the underlying normality assumptions when using the Murujuga seasons but not the meteorological seasons. Other gases (SO_2, O_3) met the normality assumptions for meteorological seasons but not for Murujuga seasons.

A full set of results for gases and VOCs is contained in Appendix Table*D.5-3* and *D.5-4*. Appendix *D*.5.5.4 also provides plots of gas concentrations by station and Murujuga season, which align with the ANOVA test results.

Table 7.12-8: Results of two-way ANOVA analysis of gas concentrations by sites (AQ07 and AQ08) and Murujuga seasons for matched and ranked data only. The column "total observations" gives the number of observations for a gas species across both sites, while the column "used observations" gives the number of observations in the matched dataset across the two sites. The last three columns shows the p-value for station, Murujuga seasons and the interaction between station and season. p-values less than 0.05 indicate a significant difference in values, these values are in bold.

Gas	Total Obs.	Used Obs.	Station p-value	Season p-value	Station × Season p-value
NO_2	80	62	0.576	**< 0.0001**	0.176
NH_3	92	74	0.21	0.595	0.739
HNO_3	84	66	0.613	**< 0.0001**	0.355

Conclusions on short scale variability

The initial one-way analysis using the Kruskal–Wallis test provides insight into differences between stations when seasonal effects are not considered. Only one VOC species (toluene), and no gas species, showed a significant difference between the two stations.

The results indicate that there is no significant interaction between seasons (meteorological and Murujuga) and station. Also there is no significant difference in gas concentrations between the two stations separated by a short distance (25 m), once seasonal differences are taken into account. Using either meteorological or Indigenous seasons, valid test results were obtained for all gas species. However, valid ANOVA results could not be obtained for the VOCs. For just NO_2, there is a significant difference between meteorological and Murujuga seasons. O_3 there is a significant difference between meteorological seasons. HNO_3 there is a significant difference between Murujuga seasons.

7.12.6 Spatial patterns of gas concentration

This section shows estimates of spatial gas distributions derived from the passive sampling measurements from the monitoring stations. In the Monitoring Studies Report 2024 (Curtin University, 2024c), data was available for at most 12 months, depending on the gas species. Now data are available for at least two years providing a better understanding of temporal-spatial changes in the gas distributions. This sections repeats the Nadaraya-Watson technique spatial smoothing described in the Monitoring Studies Report 2024 (Curtin University, 2024c) and introduces a new consensus rank and standard deviation approach to understand similarities and differences between sampling periods.

For exploratory purposes, the passive sampler data were spatially smoothed to produce colour images of the spatially-varying average gas concentration. Spatial smoothing estimates values across a geographic area from a set of observations and produces images showing the spatial

variations of a measure. Smoothing was performed using the Nadaraya-Watson technique described in the Monitoring Studies Report 2024 (Curtin University, 2024c) and demonstrated in Section 7.4. The smoothed value at each pixel is a weighted average of the passive sampler observations at different AQMs, where the weights depend on the distance from the query pixel to the AQM location. Similarly to the Monitoring Studies Report 2024 (Curtin University, 2024c), the concentration values can vary by several orders of magnitude, a nonlinear colour map has been used in these figures, in order to preserve important detail. Spatially smooth images were produced for passive sampler data from November 2022 to December 2024 which had been aggregated by month or seasonal (Murujuga and meteorological) data. In this section, the spatially smoothed estimates by meteorological seasons are presented. These images show the emergence of spatial patterns, which need to be verified over future measurements. Further spatial plots are included in Appendix Figures *D.5-24* to *D.5-28*. These spatial smooth images for each month of 2024, for each gas, show the variation in both gas measurements and spatial estimates between the sampling periods.

A new method has been employed to assess (dis)agreement between spatial estimates across different time periods. A common approach for measuring agreement—used, for example, in education and ecology—involves experts ranking observations or outcomes, with consensus assessed using the mean of the ranks and disagreement quantified using measures such as the variance or standard deviation.

A similar approach can be applied to images. To compare images, each pixel is ranked according to its intensity. In this analysis, the rank is defined as the proportion of pixels with intensity less than that of a given pixel, which is equivalent to applying the empirical cumulative distribution function (**ECDF**) to pixel intensities. For a set of ranked images, consensus is quantified as the pixel-wise mean rank across images, while disagreement is measured as the pixel-wise standard deviation.

Note that, in this work, ranking is applied to the smooth surface generated by the Nadaraya–Watson estimator, rather than to a saved image of the smooth, to avoid distortions introduced by non-linear image scaling.

In the analysis below, the overall consensus rank and overall rank standard deviation across all sampling periods are shown. Consensus rank by season is shown in Appendix *D*.5.6 for each gas species. The consensus rank images show where high or low ranks are generally found, while the rank standard deviation images show which areas have the least and most change. Further ranked spatial images are shown in Appendix *D*.5.6. Appendix Figures *D.5-29* to *D.5-33* show the seasonal ranked images for each gas. Seasonal rank patterns may differ from the averaged patterns shown in the main body of the report.

Figures *7.12-19*, *7.12-21*, *7.12-23*, *7.12-25*, and *7.12-27* show the spatially smoothed passive sampler estimates of gas concentration for each gas species from all observations acquired between November 2022 to December 2024 and aggregated by meteorological season. For each figure, the different panels (associated with different meteorological seasons) are depicted using a common colour map, shown at the right of each panel. This assists the reader in visualising seasonal variation.

Figure *7.12-19* displays the spatially smoothed average concentration of NO_2 by meteorological seasons. This image suggests that NO_2 concentrations are consistently higher close to the

Dampier port area. This question can be assessed using the concordance technique described in the Monitoring Studies Report 2024 (Curtin University, 2024c). Panel (a) of Figure *7.12-20* shows the consensus rank image. Values close to one are seen in the area near the Dampier port. These values indicate that, at any given time, this area consistently experienced the highest levels of NO_2 concentration across the Murujuga region. Values close to zero are seen in the far west and north of the Murujuga region, and indicate that these localities consistently experienced the lowest levels of NO_2. Panel (b) of Figure *7.12-20* shows the disagreement (standard deviation of ranks) image. Low disagreement values indicate that the spatial pattern of relative concentrations is quite consistent over different months. For NO_2, the lowest levels of variation correspond to the highest rank levels close to the Dampier port area.

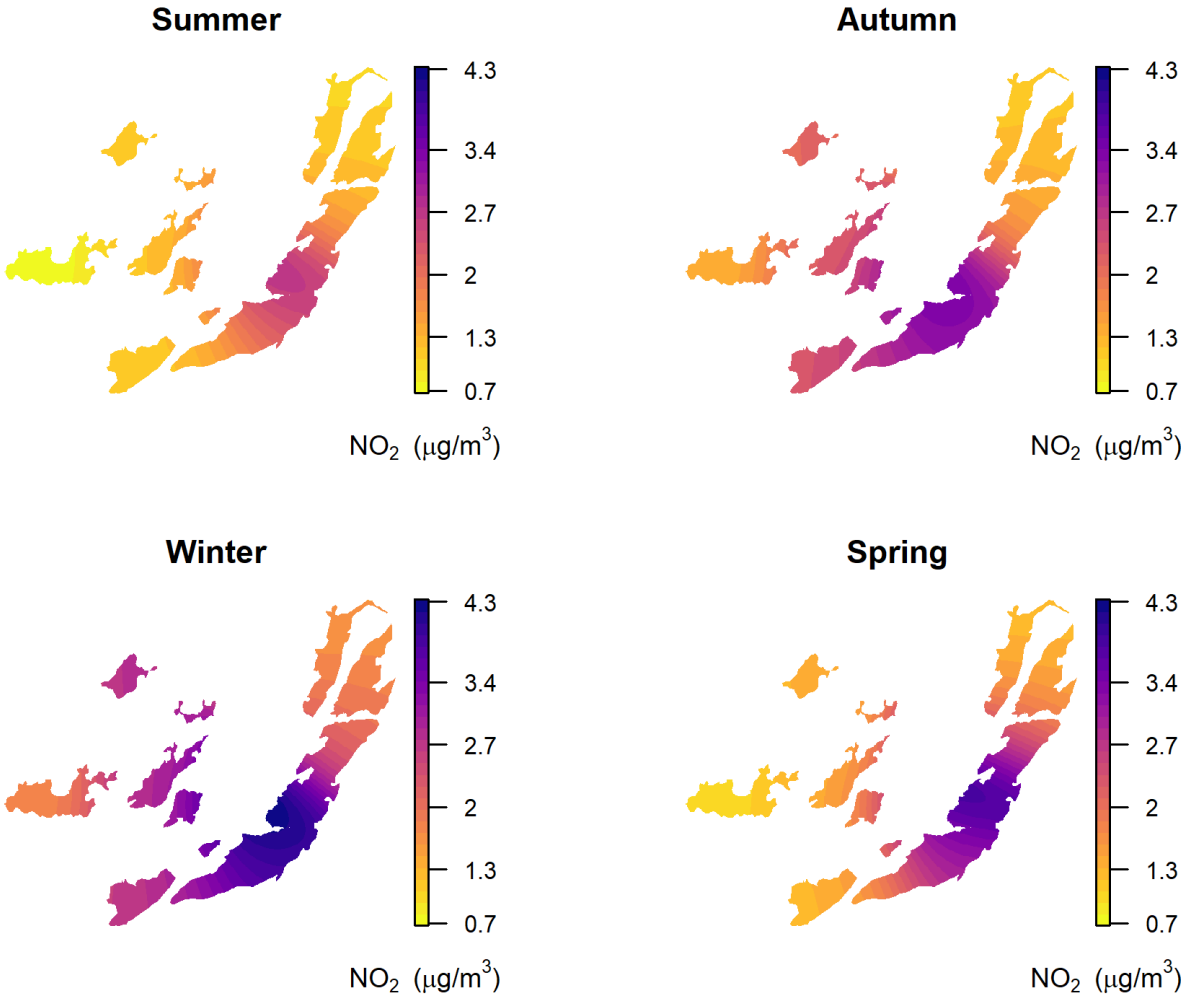

Figure 7.12-19: Spatially smoothed average concentration of NO_2 by meteorological seasons aggregated across all passive sampler data. Common colour map based on percentiles.

Figure *7.12-21* shows the spatially smoothed average concentration of NH_3 for each season. NH_3 concentrations vary between seasons: there is a more even distribution across the Murujuga area in summer compared to winter. In winter, NH_3 concentrations are highest close to the Dampier port

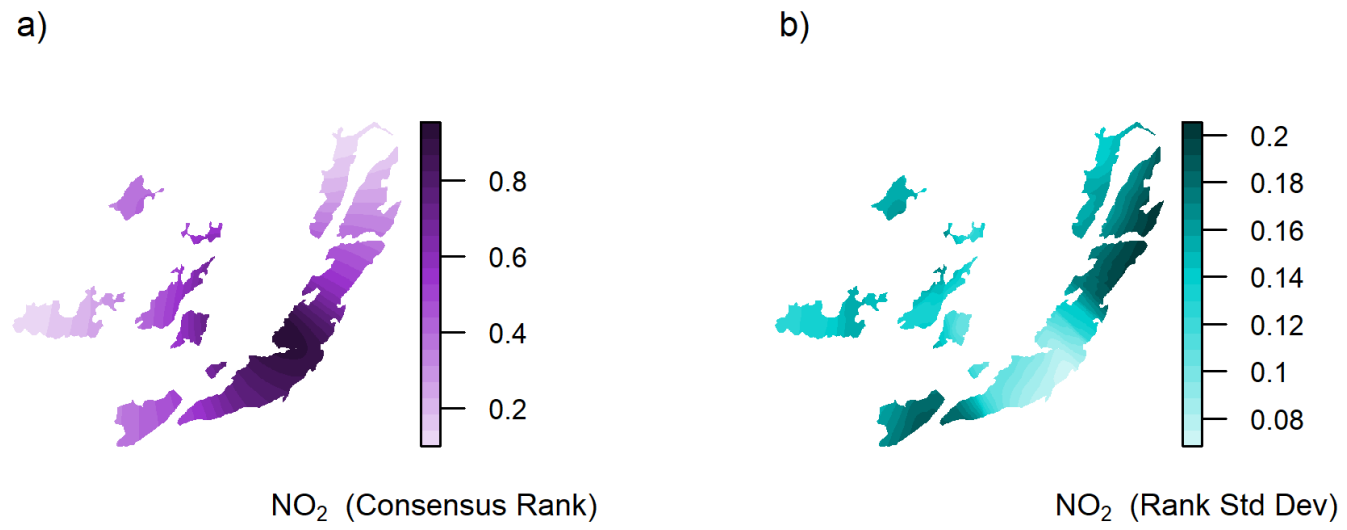

Figure 7.12-20: Assessment of concordance between spatial patterns of NO_2 concentration across all sampler periods, estimated from spatially smoothed passive sampler data. (a) consensus ranks; (b) disagreement (standard deviation).

area. Autumn and spring seem to be transition months, with higher concentrations just discernible near the port area.

Panel (a) of Figure *7.12-22* shows the consensus rank image for NH_3. This image shows that overall concentrations of NH_3 are highest closest to the Dampier port, a pattern that is very distinct for the consensus ranks. This pattern is not so distinct for each season, as shown in Figure *7.12-21*. There is also a similarity between the overall spatial patterns for NH_3 and NO_2, which may account for the correlation shown in Table *7.12-3*.

Figure *7.12-23* shows spatially smoothed average O_3 concentrations by season. O_3 concentrations are generally low in summer and autumn, then increase in winter, and reach their highest levels in spring. O_3 levels are lower closer to the Dampier port area and higher in the northern part of Murujuga. This pattern contrasts with the pattern seen for NO_2 (Figure *7.12-19*) and NH_3 (Figure *7.12-21*) Figure *7.12-24* presents the consensus ranks, which support this conclusion.

Figure *7.12-25* shows spatially smoothed average SO_2 concentrations by season. SO_2 concentrations are generally highest in summer, particularly in the northern part of the Murujuga area. The other three seasons show much lower SO_2 concentrations. Despite using a colour map based on the Probability Integral Transformation (Curtin University, 2024c), the high levels of gas concentration recorded in summer make it hard to discern spatial patterns of SO_2 in other seasons. Seasonal patterns may be more discernible using the ranked seasonal data, as shown in Appendix *D*.5.6.

Figure *7.12-26*(a) shows the consensus ranks for SO_2. The overall pattern shows relatively high levels of SO_2 generally occur close to the Dampier port area. Figure *7.12-26*(b) shows the variance in the ranked data, which shows that there may be higher variance of relative SO_2 levels in the north and west of the Murujuga area, and moderate variance close to the port area.

Figure *7.12-27* shows spatially smoothed average HNO_3 concentrations by season. HNO_3 concentrations are generally highest in spring and lowest in summer. Autumn and winter seasons

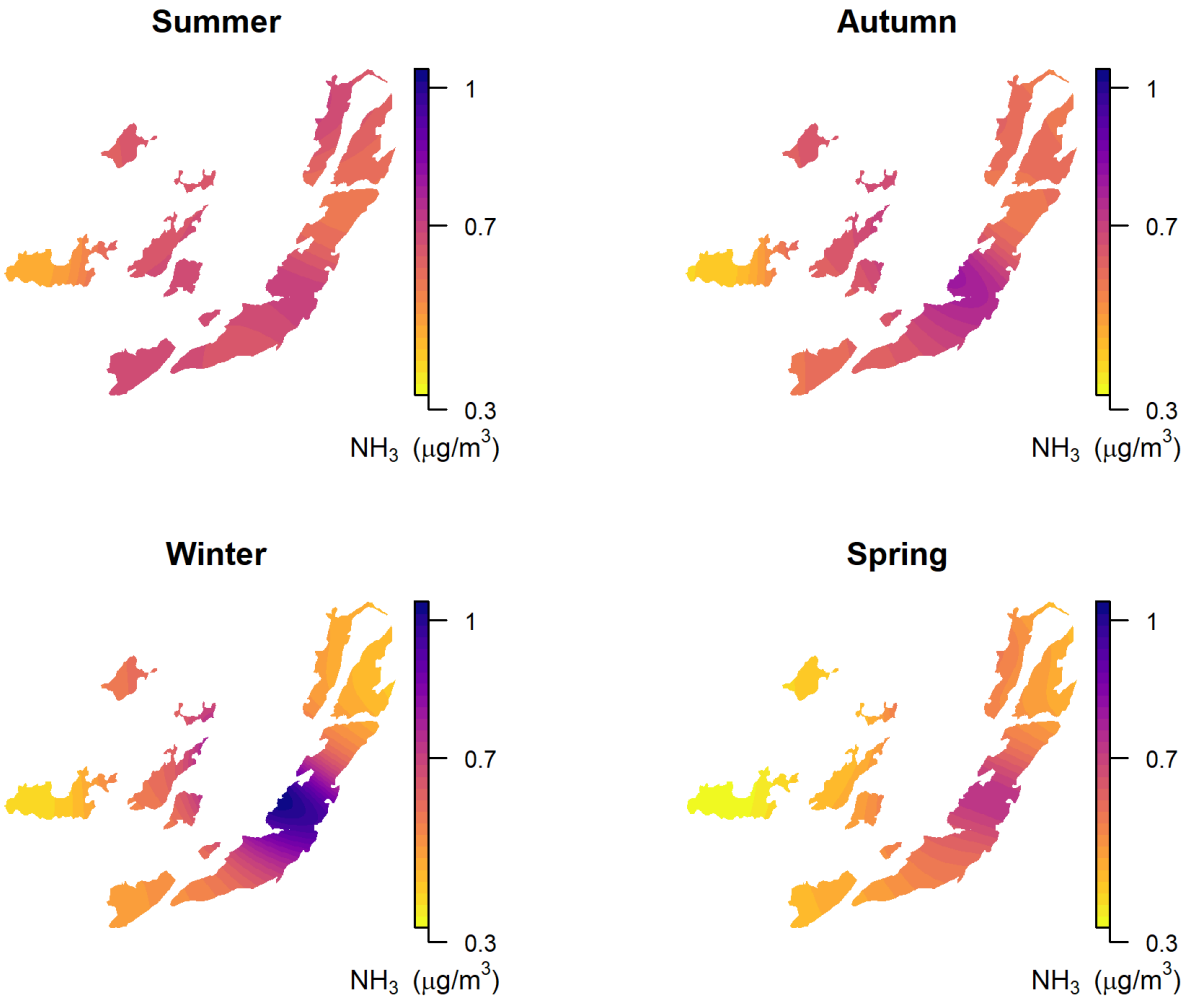

Figure 7.12-21: Spatially smoothed average concentration of NH_3 by meteorological season. Common colour map based on percentiles.

show a transitional levels in between the highest and lowest levels. The range in gas levels between seasons makes it hard to discern spatial patterns HNO_3. Seasonal patterns may be more discernible using the ranked seasonal data, as shown in Appendix *D*.5.6.

Figure *7.12-28*(a) shows the consensus ranks for HNO_3. The overall pattern also shows relatively higher levels of HNO_3 generally occur close to the Dampier port area, similar to NO_2 and NH_3 - though the relatively high concensus ranks for HNO_3 extended further north along the Burrup peninsula. Figure *7.12-28*(b) shows the variance in the ranked data: here variance is generally low around the central areas of Murujuga.

Using the rank consensus and rank standard deviation approach, it is possible to determine which areas have relatively high or low estimated gas concentrations across all current gas observations. We can see that there is a similar pattern with gas concentrations relatively high in the central Burrup Pennisula for four gases: NO_2, NH_3, SO_2 and HNO_3. These rank patterns emerge despite clear difference between spatial gas distribution patterns for individual months and even across

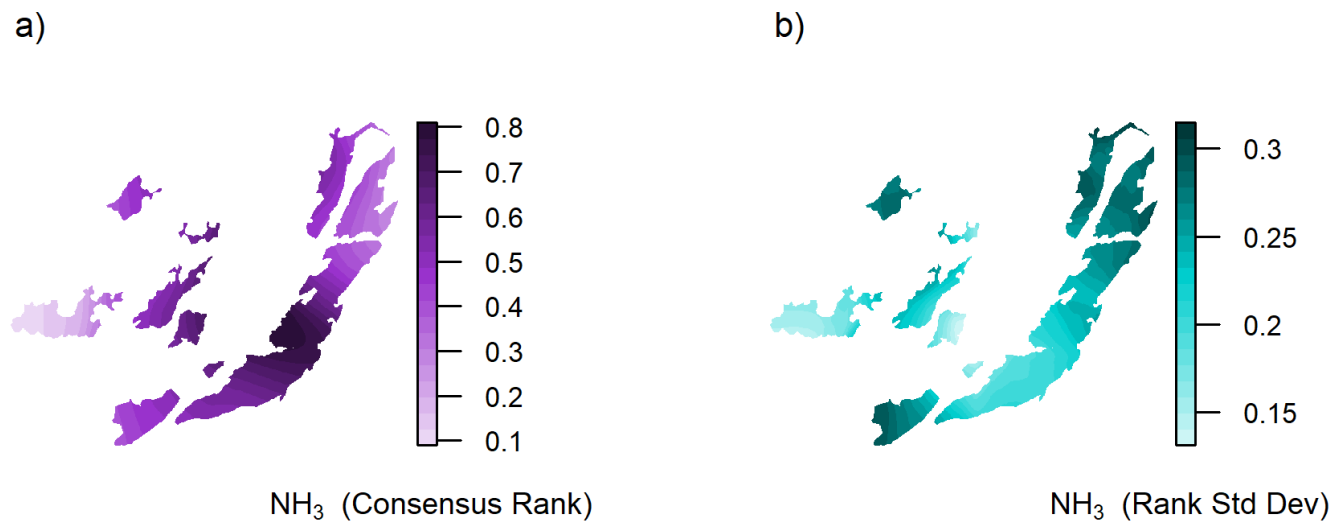

Figure 7.12-22: Assessment of concordance between spatial patterns of NH_3 concentration across all sampler periods, estimated from spatially smoothed passive sampler data. (a) consensus ranks; (b) disagreement (standard deviation).

seasons. The rank standard deviation show where there is the most change in overall gas patterns. For NO_2, NH_3, and HNO_3, the centre areas show the least change in rank while the areas to the north and south show the most change. This correlates to seasonal changes where gas measures increase further from the emission sources at particular times of the year. SO_2 shows the most change in the central area and then at the extremities, with areas in between showing less change. This corresponds to the large changes seen in SO_2 across the year, with potential emission from shipping lanes impacting the gas distribution at times. Finally, O_3 has a very different consensus distribution to the other gases, with the highest concentrations away from the initial emission sources but with only small differences seen across periods for the central and northern parts of Murujuga.

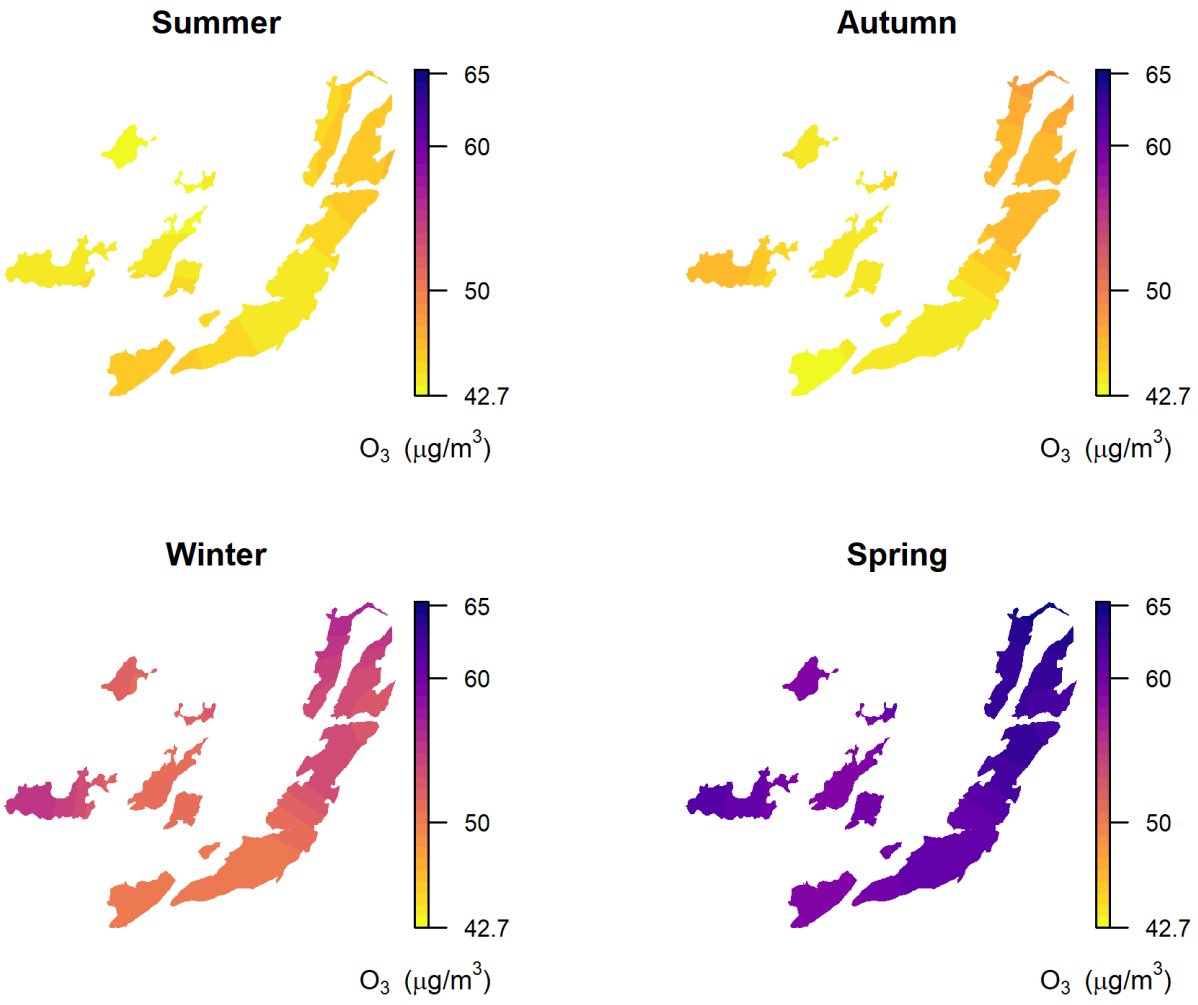

Figure 7.12-23: Spatially smoothed average concentration of O_3 by meteorological season. Common colour map based on percentiles.

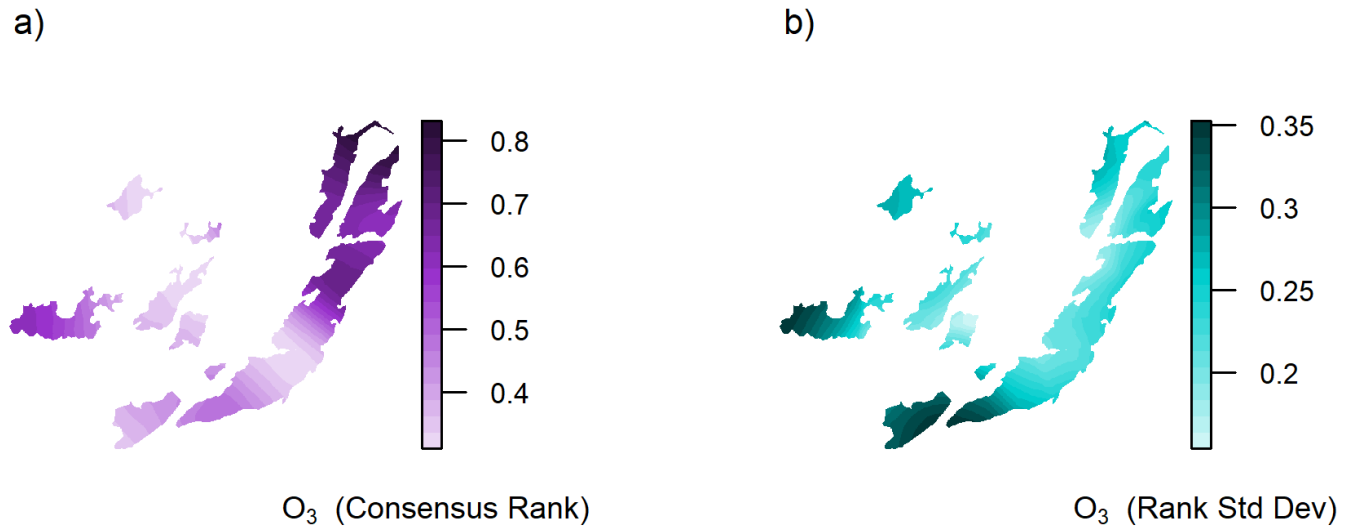

Figure 7.12-24: Assessment of concordance between spatial patterns of O_3 concentration across all sampler periods, estimated from spatially smoothed passive sampler data. (a) consensus ranks; (b) disagreement (standard deviation).

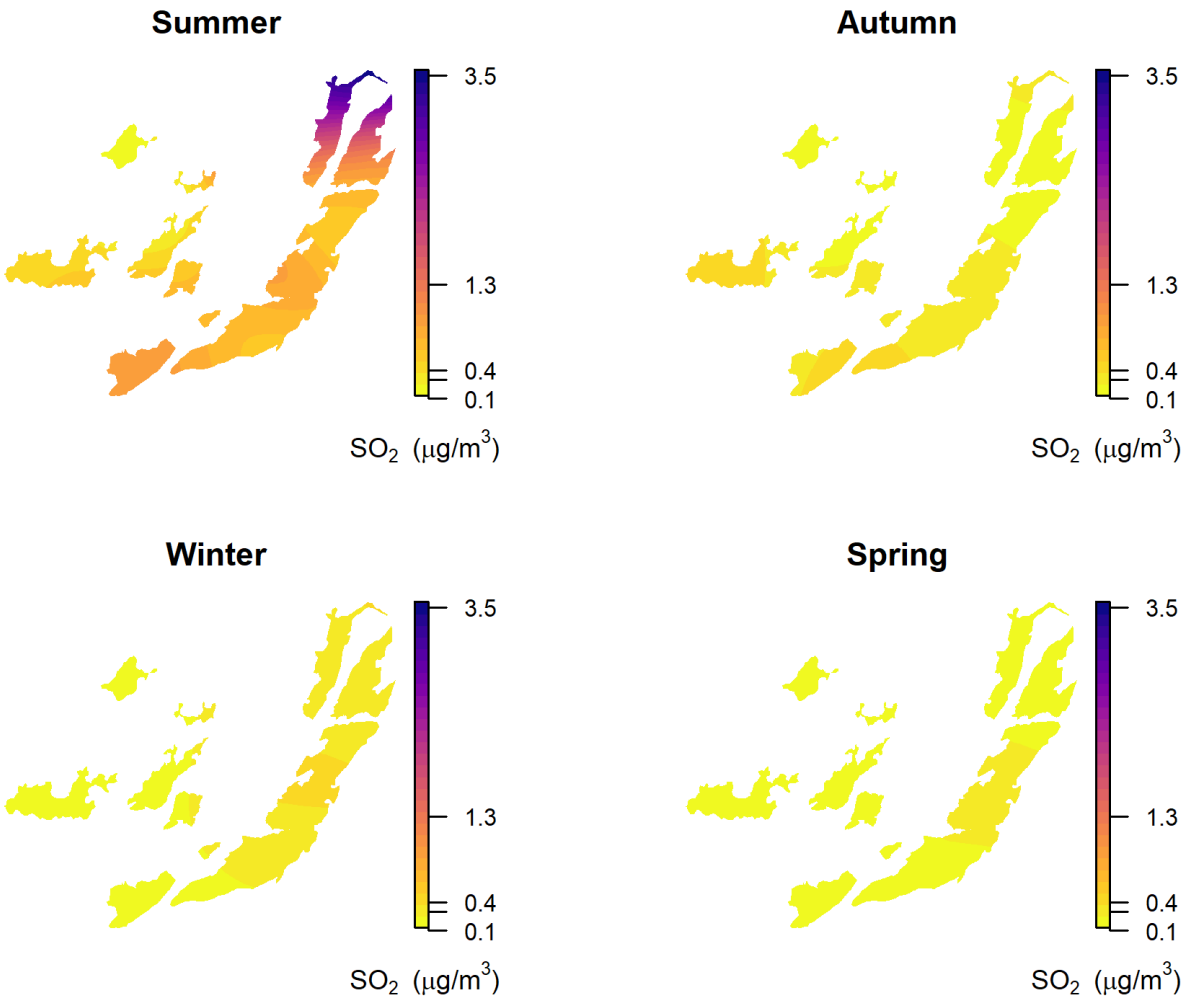

Figure 7.12-25: Spatially smoothed average concentration of SO_2 by meteorological season. Common colour map based on percentiles.

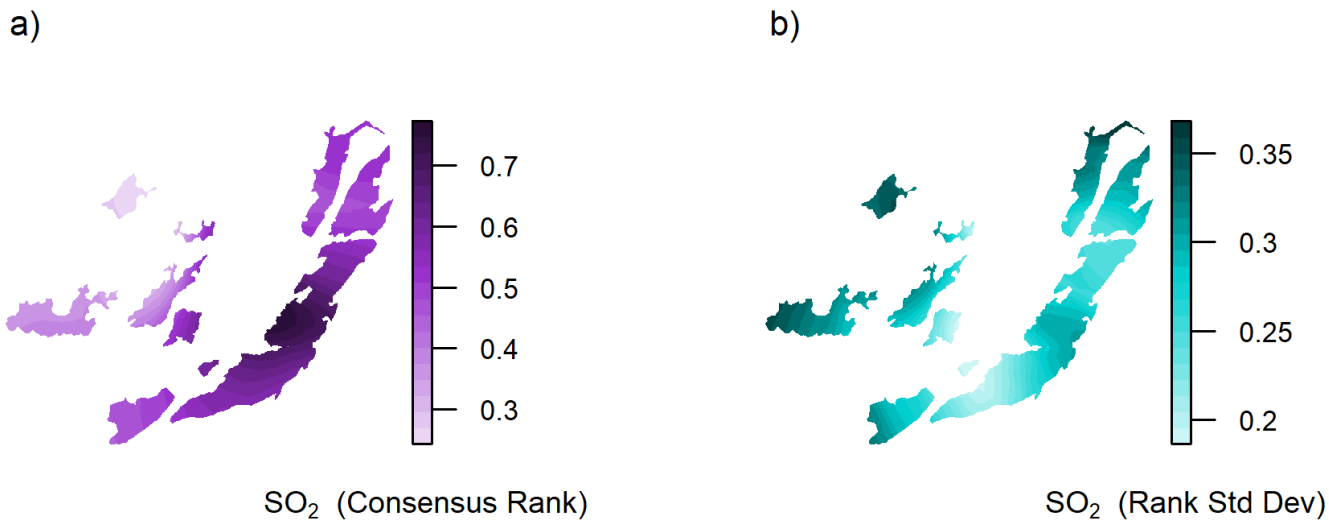

Figure 7.12-26: Assessment of concordance between spatial patterns of SO_2 concentration across all sampler periods, estimated from spatially smoothed passive sampler data. (a) consensus ranks; (b) disagreement (standard deviation).

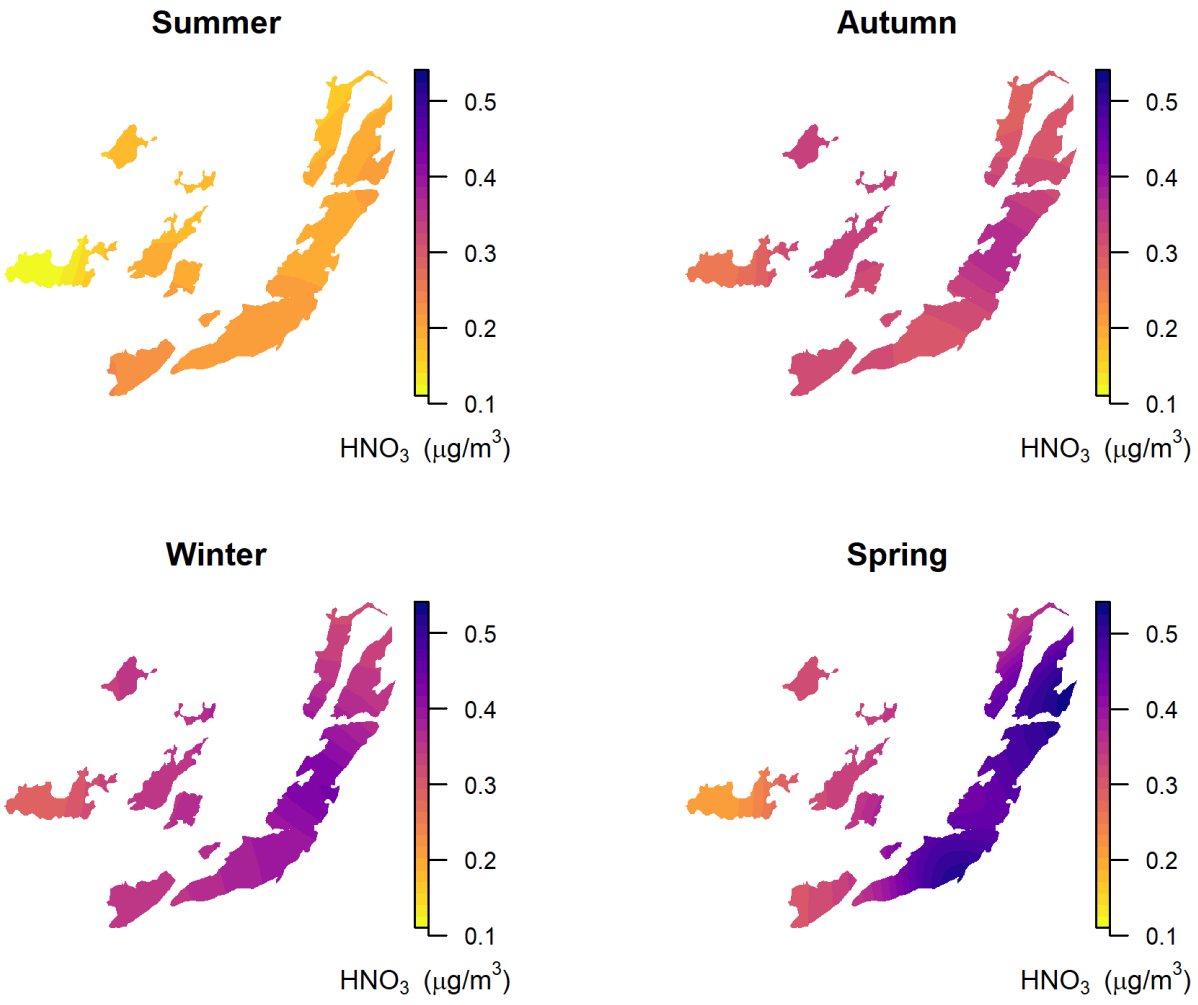

Figure 7.12-27: Spatially smoothed average concentration of HNO_3 by meteorological season. Common colour map based on percentiles.

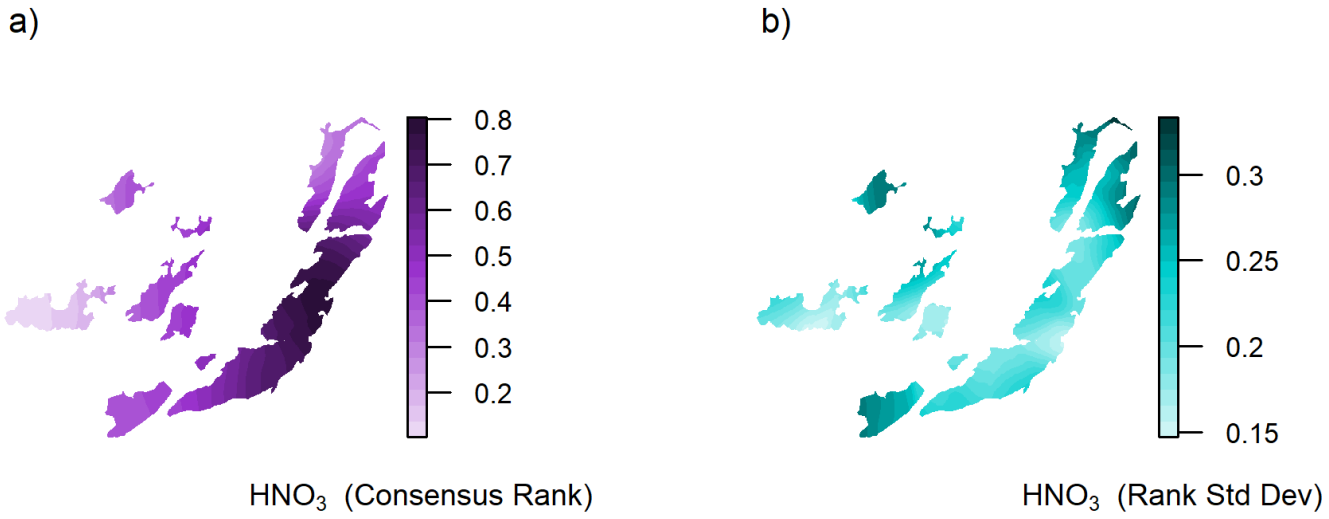

Figure 7.12-28: Assessment of concordance between spatial patterns of HNO_3 concentration in over all sampling periods, estimated from spatially smoothed passive sampler data. (a) consensus ranks; (b) disagreement (standard deviation).

This page is intentionally blank.

7.13 Real-time powered sites

Section 7.12 of the Monitoring Studies Report 2024 (Curtin University, 2024c) details the real time monitoring sites. Below provides further background information.

Three of the air quality monitoring stations operated by MRAMP include instruments for real time monitoring of selected gas species and particulates. These instruments require mains electrical power and operate best in a temperature-controlled environment. Each of our powered sites house the real time monitoring equipment in a customised, air-conditioned shipping container.

Data from a similar monitoring station operated by other users is also available, with results for the same suite of gas species and particulates available (though using equipment from a different vendor).

Data from each of the three powered sites operated by MRAMP researchers is live-streamed from the AQM's computer to our data store. As the suite of instruments is continuously logging, the volume of data produced is quite high. Many of the instruments allow multiple data channels to be logged. To limit the volume of data, we limit the transfer to the measurement results of the species/substances in question, as well as information viewed as critical for remote monitoring and diagnostics of system health (e.g., instrument sample flow rates, converter temperatures, system alerts). This allows early detection of any factors which may impact the reliability of results, as well as early identification of any need for unplanned maintenance or repairs.

Data from the fourth powered site (operated by ACOEM) is received monthly and added to our data store. This is received in the form of a validated report, with five minute averaged, hourly averaged, and daily averaged data for all species/substances. At the time of writing this report, the latest data received was for February 2025.

7.13.1 Gaseous species

The gas analysers deployed at each powered AQM, have been running continually over the current study year, with the exception of instruments requiring maintenance or repair. Any gaps in the data for particular instruments are noted below:

- A fault with the T100 (SO_2 analyser) at AQ01 resulted in the instrument reporting unrealistically high concentrations; this was removed from service and returned to the vendor for repair. At the time of writing, this instrument was still with the vendor, with no firm timeline for repair.
- Failure of a thermal converter at AQ01 requiring return to the vendor for repairs. This is expected to be returned and redeployed by June 2025. This fault appeared to impact ammonia measurement only.
- Water / humidity issues in the instruments NO, NH_3, SO_2, and O_3 at EX07 resulted in data from December 2024 being unavailable, with multiple instruments needing repair. At the time of writing, these were still offline.
- Issues with the thermal converter at EX09, which will require vendor repair. This does not appear to affect the measurement of NO or NO_2.
- Lamp voltage on the O_3 instrument at EX09 drifted outside of range, requiring manual adjustment.
- There were some power surges or power failures at the sites that caused the logging software

on the AQM computer to stop executing. This resulted in data not being uploaded to data storage, and the software needing to be restarted on the PC once power was restored. After such events, the data must be manually recovered from the individual instruments.

Table *7.13-1* presents the percentage of time which the powered instrument was offline due to inoperability or repair at each of the powered AQM sites. For most instruments, the percentage of days the instrument was not measuring was relatively low (less than 30%). However, at AQ01 NH_3 and SO_2 instruments were down or under repair 47.20% and 57.98% of days respectively. AQ01 is a background site that is not within the Murujuga boundary, so the preference was to move instruments from AQ01 to either EX02 or EX09 if extended downtime due to offsite repair was expected.

Table 7.13-1: Percentage of valid data (i.e. excluding time each powered instrument was inoperable or removed for repair at each of the powered AQM sites).

Gas Species/particulates	Instrument	AQ01	EX02	EX07	EX09
NO_2	T201	80.80	68.53	76.30	66.59
NO	T201	80.80	68.53	76.30	66.59
NH_3	T201	52.80	72.53	76.30	66.59
SO_2	T100	42.02	84.80	73.76	90.19
O_3	T400	81.87	85.33	66.26	89.15
$PM_{2.5}$, PM_{10}, TSP	Palas Fidas 200	86.56	15.67	87.54	76.95

Negative values of concentration were occasionally recorded. As these are not realistic, these are excluded for this analysis. In the event where there are concerns about data validity (e.g., substantial drift between calibrations, data collected immediately after a power outage, data logged after reinstallation of an instrument but prior to on-site calibration, data collected when instruments were reporting important alerts), affected data have been excluded.

Data for gas species are plotted in the figures below, with values from all four powered sites displayed, where available. Concentrations are reported in parts per billion (by volume) (ppb).

As illustrated in Figure *7.13-1*, SO_2 is consistently present at all sites at low concentrations, typically around the $\sim$1.5 - 2 ppb range. There are occasional higher readings, which may be related to activities near each site, with levels of up to 10 ppb recorded. The highest concentrations were recorded at EX02; the closest site to the port. The absence of an SO_2 peak at the corresponding times at the other sites would also support the suggestion that shipping may be the source, with the emissions being diluted by the time they reach other sites, or being transported away from other sites by wind. This of course would require consideration of the wind direction at the time, with relationships between concentration and wind direction still needing further exploration.

The Teledyne T201 instrument reports NO, NO_2, NOx, NH_3 and total nitrogen (TNX). A thermal converter that was with the vendor for repair was returned in mid-2024, allowing the recommissioning of the instruments at EX09. This resulted in no data for nitrogen species being recorded for the first part of 2024 at EX09. The T201 at EX09 was however one of the first instruments brought online, so some data are available for NO and NO_2 for late December 2023 to early January 2024.

This corresponds to the last time a calibration was performed prior to the thermal converter fault being detected.

The Teledyne T201 instrument reports NO, NO_2, NOx, NH_3 and total nitrogen (TNX). The T201 at EX09 was one of the first instruments brought online, so some data are available for NO and NO_2 for late December 2023 to early January 2024. However, the thermal converter for the EX09 T201 instrument was sent to the vendor for repair in mid January and returned in mid-2024, allowing the instruments at EX09 to be recommissioned. This resulted in no data for nitrogen species being recorded for the first part of 2024 at EX09. This report presents nitrogen species data from EX09 for late December 2023 to early January 2024, and from early June 2024 to mid February 2025.

Issues with the T201 instruments and their response to ammonia calibration gas were subsequently identified at AQ01 and recently at EX09. These faults appear to impact the measurement of NH_3 and not NO and NO_2 but will impact the determination of TNX. In order to keep measuring NO and NO_2, it was decided that only one site at a time would be taken offline for repair. The instruments from AQ01 are now ready for reinstallation. These will replace the instruments at EX09, which will then be sent to the vendor for repair. This will mean a gap in the data for nitrogen species at EX09 will be present in the next report, and a larger gap in the data for ammonia.

Data for NO is shown in Figure *7.13-2*. The plots show a number of peaks, rising well above typical levels observed at each site. The peaks do not appear to exhibit a regular periodic pattern. Indeed, these time series do not even appear to be statistically stationary over time. While there is insufficient data available to assess consistency between the time series from the different sites, there does appear to be more regular peaks at EX07, possibly due to the proximity of this site to the gas plants. The data available for EX09, shows consistently lower NO concentrations than the other sites, which may be due to the consistent wind around what is effectively an elevated site.

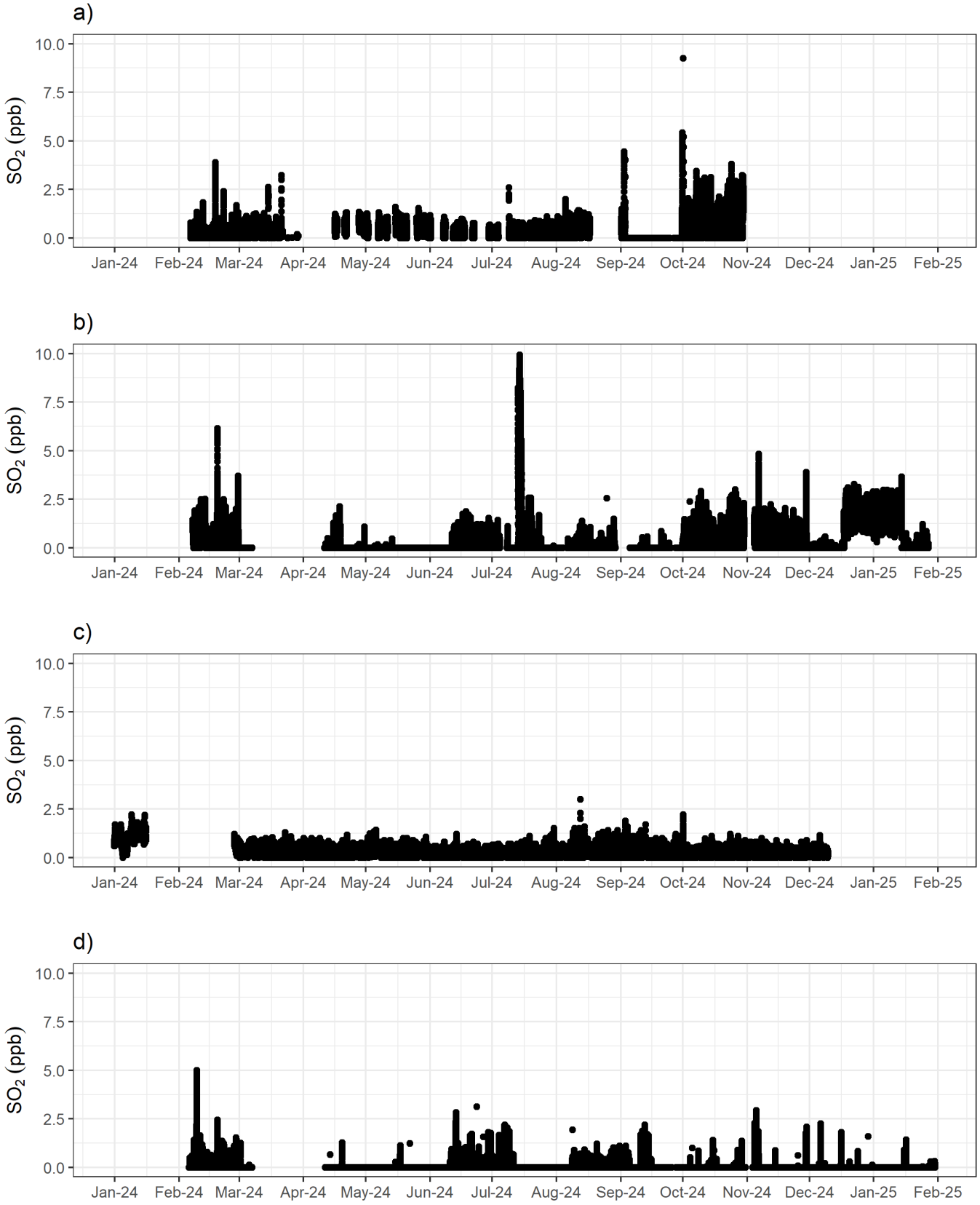

Figure 7.13-1: Time series plots for SO_2 concentration to date, for sites (a) AQ01, (b) EX02, (c) EX07 and (d) EX09. Gaps in the data correspond to times where the instruments were offline, or where the data have been excluded due to concerns about the validity.

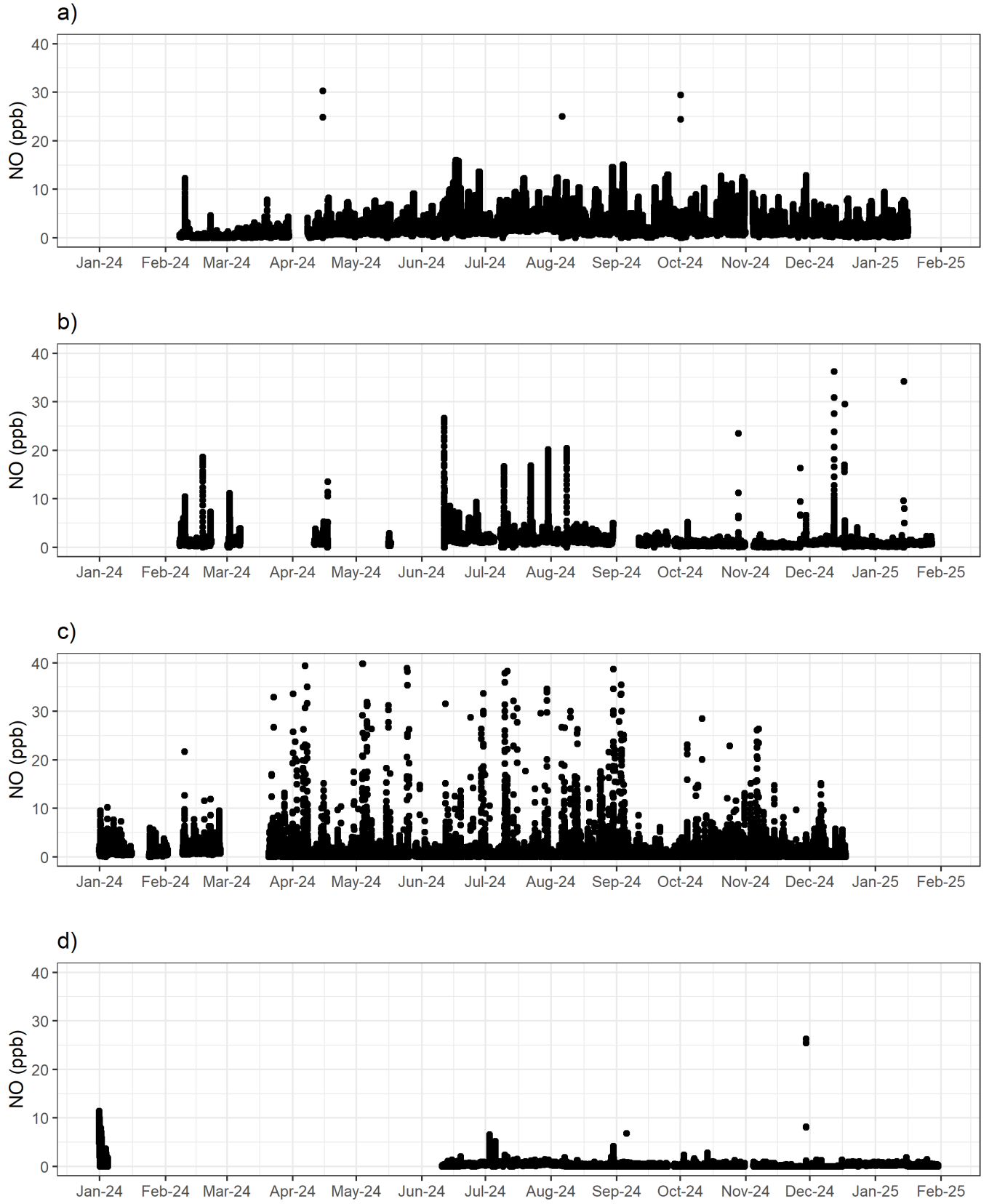

Figure 7.13-2: Time series plots for NO to date, where (a) AQ01, (b) EX02, (c) EX07 and (d) EX09. Gaps in the data correspond to times where the instruments were offline, or where the data have been excluded due to concerns about the validity.

The NO levels at AQ01 appear more consistent than at the other sites, which may be related to its proximity to the power plant. We would expect steadier more consistent emissions from a power plant than the flare towers at the gas plants (not accounting for other potential sources, e.g., bush fires). This does not however consider any chemical processes which may be occurring in the atmosphere.

As there will be an equilibrium NO and NO_2, which is dependent on both UV and temperature, some caution is required in consideration of NO and NO_2 levels. NO can be converted to NO_2 via reaction with O_3 and this process can be quite rapid, which may suggest that the irregularity of the time series for NO is attributable to combustion processes taking place around the AQM sites.

However, the data for NOx also needs to be considered in relation to weather conditions, specifically wind direction as the Ramboll modelling (Ramboll Australia, 2022) has shown that there can be long-range transport of gaseous species within the region, particularly in the direction of prevailing winds. When considering the conversion of NO to NO_2 in the atmosphere, we also need to consider the O_3 concentration, as well as the equilibrium between NO and NO_2 under the existing atmospheric conditions. In the absence of daylight and varying temperatures this equilibrium does shift, but given the near continuous emissions of NO, NO_2, and O_3, this may be difficult to isolate.

To further explore the relationship between NO and NO_2, we determined the ratio of mean NO to mean NO_2 and mean NO_2 to mean NOx, which are shown in Table *7.13-2*. These are provided with the distance from each site to the gas plant (closest of either the main Pluto or Karratha Gas Plant flare towers), an established source of NO and NO_2. There appears to be a general trend between the NO/NO_2 ratio and distance from the gas plant, where the amount of NO_2 relative to NO is higher closer to the gas plant. This suggests firstly that there is direct generation of NO_2 coming from combustion (e.g., flare towers). Secondly, this observation would be consistent with the rapid conversion of NO to NO_2 via reaction with O_3, which is formed in the atmosphere from reactions between NO_2, VOCs, and UV light. The decrease in NO_2 relative to NO as we get further from the gas plant is likely a result of further reactions between NO and O_3 being limited by atmospheric mixing and potentially a dilution of O_3 concentration, with increasing distance from sources of precursor emissions. The atmospheric transport of NO and NO_2 further distances would also allow time for the reactions producing NO_2 and the reactions producing NO to equilibrate, with the reaction between NO_2 and sunlight to produce NO becoming more apparent. This conclusion is supported by the comparison of NO_2/NOx ratios with distances from the gas plant also. Here we see the highest proportion of NO_2 at EX07 (the closest site to the gas plant). This then decreases with distance with a lower value at EX09 and then an again lower value at EX02. The value at AQ01 is comparable to EX02, though at over twice the distance from the gas plant. The proximity of AQ01 to the powerplant, however, is acknowledged, which would contribute to measured NO_2 and NOx levels.

In order to further explore NO, NO_2, and O_3 levels a week of data from November 2024 was selected. The data for NO are shown in Figure *7.13-3*. Here we also distinguish between daytime and nighttime measurements, so we can consider the impact of UV radiation (sunlight) and temperature on the relationship between NO and NO_2 concentrations.

Table 7.13-2: Mean NO/NO_2 and NO_2/NOx for each powered AQM site and distance to the LNG (km). Where LNG is defined as the closest of either the main Pluto or Karratha Gas Plant flare towers.

Site	Mean NO/NO_2	Mean NO_2/NOx	Distance to LNG (km)
AQ01	1.37	0.42	17.5
EX02	1.02	0.41	7.5
EX07	0.40	0.71	0.95
EX09	0.5	0.51	5.75

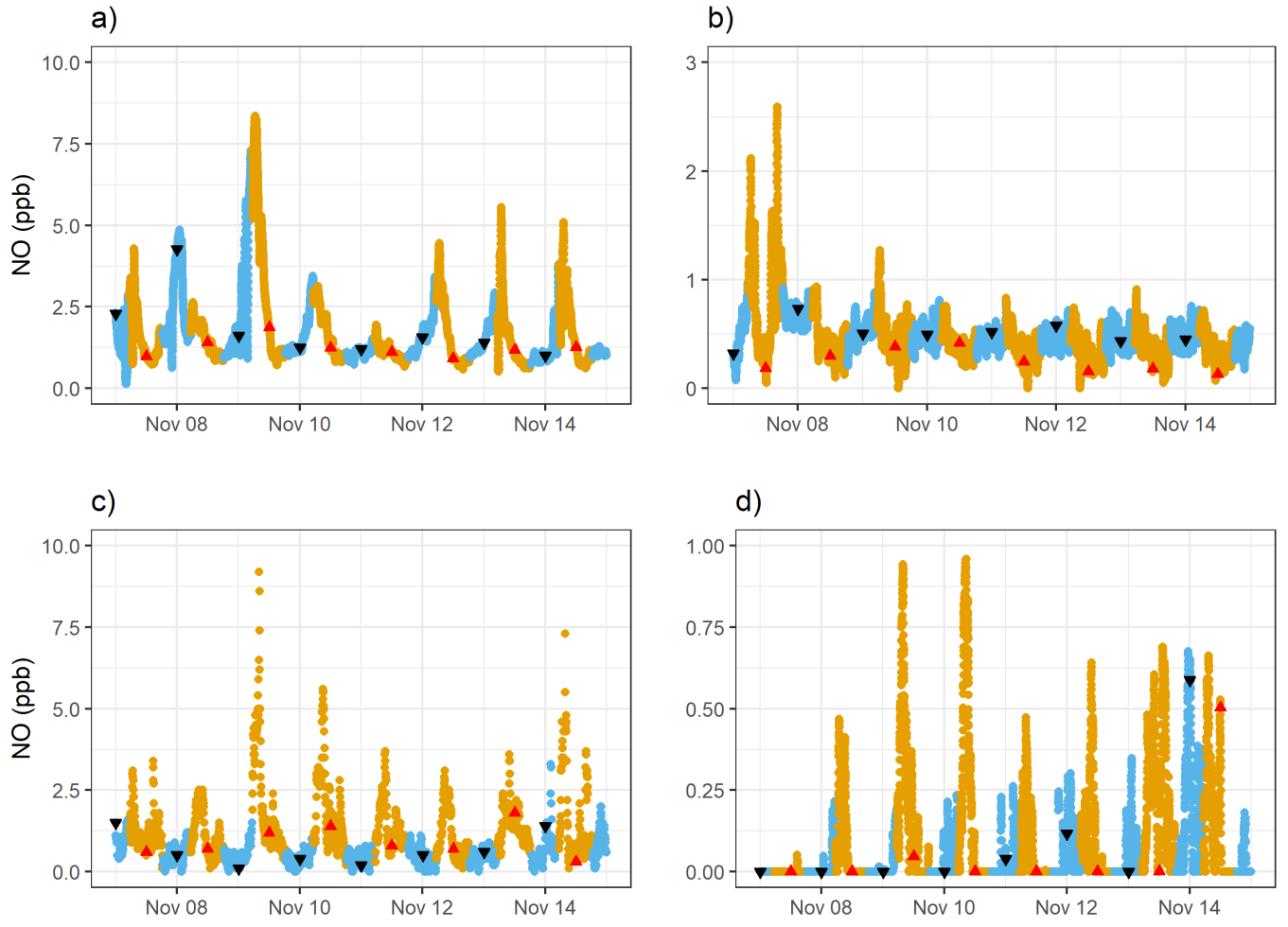

Figure 7.13-3: Time series plots for NO over one week in November 2024, where (a) AQ01, (b) EX02, (c) EX07 and (d) EX09. The data shown in blue corresponds to nighttime (defined as sunset to sunrise) measurements, and data shown in orange correspond to daytime (defined as sunrise to sunset). The red up-pointing triangles are midday, and black down-pointing triangles are midnight. Data have been excluded where the validity is in question.

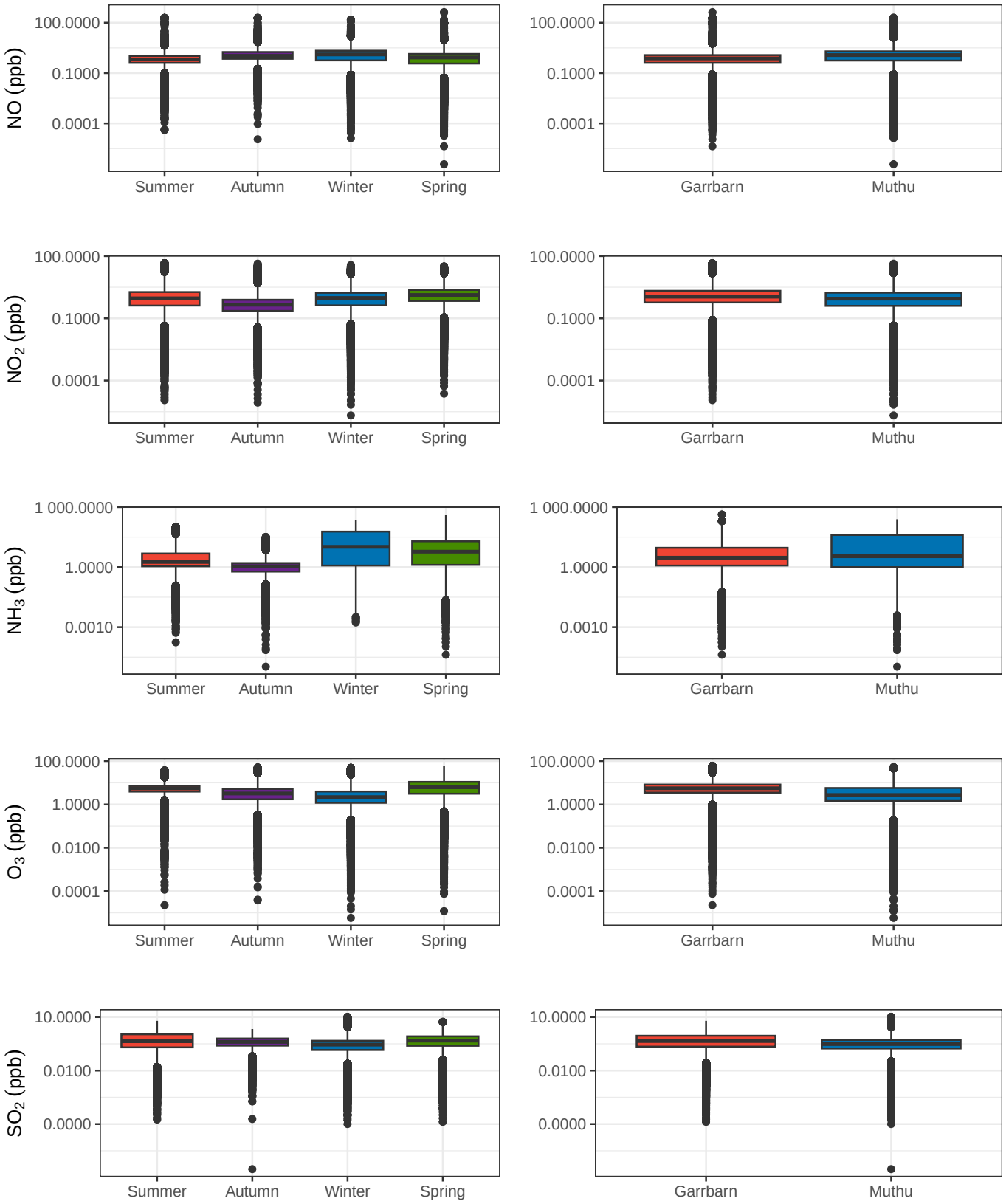

Figure 7.13-4: Boxplot of NO, NO_2, NH_3, O_3 and SO_2 for the four powered sites (AQ01, EX02, EX07, EX09) combined according to the meteorological and Murujuga seasons Garrbarn (hot) and Muthu (cold). Note the vertical axis is logarithmic scale for all panels.

Firstly consider NO concentrations. There appear to be regular daily peaks at all sites, though this is less pronounced at EX02, which given its distance from both the gas plant and power plant suggests that some dilution occurs in atmosphere. The exceptions here are the two pronounced peaks early in the week, which may be more related to port activity than other sources. These two peaks at EX02 are also present in the plot for NO_2 shown in Figure *7.13-6*, suggesting they likely originate from the same source. The results for NO_2 across all sites show a similar pattern of daily peaks to the plots for NO, however, with the higher peaks for NO_2 typically occurring at night.

The data for this selected week in November 2024 has also been plotted in terms of the NO/NO_2 ratio, and is shown in Figure *7.13-10*. These show daily variation in the ratios, though not always clear daily peaks. The values at AQ01, show clearer daily peaks than at the other sites. Here we generally see an increase in the NO/NO_2 ratio through the night, with a decrease the following day. This indicates higher nighttime levels of NO in relation to NO_2, with this reversing during the day, where the NO_2 levels are higher in relation to NO. This relationship appears to exist at other sites, but is less clear, particularly at EX02.

Figure *7.13-11* shows the NO_2/NOx ratios for the same selected week in November 2024. This figure shows that the variation in levels of NO_2 relative to total NOx from day to night over a week. For AQ01, there is a general drop in NO_2 to NOx ratio overnight, with an increase in NO_2/NOx during the day, with levels tending to peak in the early afternoon to late evening. A similar trend is seen at EX02, where NO_2/NOx are at their lowest in the early hours of the morning and gradually increase through the morning and into the early afternoon. However, for EX09, the NO_2/NOx are highest during the night, with a decrease during the day.

EX07, however, presents a slightly different trend, with higher levels of NO_2 relative to NOx reported at the hours around midnight, with a drop in the ratio commencing around first light and continuing until around midday, with the values then decreasing later in the afternoon. The changes in NO_2/NOx would then likely correspond with increasing temperature and UV levels through the morning, with a subsequent decrease in the late afternoon as temperature and UV levels decrease.

Some caution is needed in interpreting these ratios as there are ongoing variable emissions contributing to these values, and the transport of species, particularly to sites, further away from sources, will be heavily dependent on wind direction.

When considering the NO/NO_2, or NO/NOx ratios, we must also consider ozone levels. These are shown for the same selected week in Figure *7.13-9*. The plots for AQ01, EX07, and EX09 all show evidence of a daily trend with O_3 levels increasing during the day and then decreasing overnight. However, the maximum levels reached do vary between sites, with levels at EX07 consistently being the highest over the week, and the levels at AQ01 the lowest.

The pattern of O_3 concentrations is different at EX02, with generally higher levels observed at night. While this may appear unusual, it suggests that O_3 formed elsewhere during daylight hours is being transported to EX02. An examination of prevailing wind direction over this week may support this conclusion.

NO_2 data are shown in Figure *7.13-5*. The observed values for NO_2 are typically lower at AQ01 and EX02 than at EX07, potentially due to the proximity of EX07 to the gas plant. Values at AQ01 appear to be more consistent than at the other sites, as observed for the measurement of NO and likely for the same reasons. The levels at EX09 are generally lower, with noticeable peaks in

January and October 2024.

Available results for ammonia are shown in Figure *7.13-7*. These time series show all data from all sites, when the instruments were operational. There have been issues with the reliability of the thermal converters associated with the T201 units, as noted previously. There appears to always be some NH_3 present at all sites, with levels typically around the 10 ppb mark, though with some significant peaks. Notably, the early July 2024 peak was recorded at all sites, with the concentration being as high as 100 ppb. The highest concentrations of NH_3 have been reported at EX02, which is the closest location to Dampier Port. Elevated levels of NH_3 were noted at EX02 from August to October 2024, before dropping off. These levels however, remained generally higher in the period after October 2024, than the levels in July 2024. Some elevated levels of NH_3 were also noted in the August to September 2024 period at AQ01, though these were less pronounced.

Ozone data are shown in Figure *7.13-8*. While O_3 appears to be consistently present (when the instruments are measuring) there appears to be some variability between monitoring stations. O_3 levels appear to be more consistent at EX07, with more variation in levels at the other sites (AQ01, EX02 and EX09). Levels at all sites, however, appear to fall within the range of expected background concentrations for the region.

Given the formation and destruction of ozone in the presence of UV radiation, as well as its formation and titration by NOx in atmosphere, analysis of ozone measurements can present a challenge. In addition to the presence of species that lead to ozone formation, high daytime levels of UV radiation, there's also the possibility of long-range transport of O_3.

Ozone levels at EX07 are generally higher than at other sites (though comparable to EX09 for the August to October 2024 period). This site is closest to emissions sources of species that allow atmospheric ozone formation, which may offer a potential explanation, though this does not yet consider long-range transport or the influence of temperature and UV.

The O_3 measurements at EX02 appear generally lower than at other sites, with peaks generally not exceeding 30 ppb. This site is farther from possible emissions sources of NOx and VOCs, (e.g., the gas plants or power plant), which may suggest that the potential for formation of O_3 is reduced. The proximity of EX02 to the port however, may require further consideration. The peaks at EX02 may therefore be related to wind direction, with peaks occurring when there is a combination of winds from the port and shipping activity, or winds from the gas plant. The above considerations however, do not consider any impacts of long-range transport. Additional analysis is required to determine what may be considered 'typical' or 'baseline' levels, which may help identify the main ozone chemistry that is occurring in the atmosphere, at the monitoring sites.

The levels of O_3 at EX09 appear higher between August and November 2024 (and comparable to those at EX07), than for the other times of the year. This occurred at a time of the year with higher solar radiation and therefore enhanced OH photolysis of O_3, as would be expected. This further indicates that long-range transport of ozone cannot be ignored. Given that this location is higher than the other monitoring stations and the consistent winds noted, there may be a relationship between O_3 and wind direction. Some further analysis of gas species concentration, and weather parameters is provided in Section 8.5.

Murujuga observes two season: Garrbarn (Yindjibarndi) / Garrwarn (Ngarluma) (the hot time, wet season) and Muthu (cold time)

To explore any potential seasonal variation, the results for all gaseous species measured using the powered instruments were averaged across all sites and plotted according to season. These are shown in boxplots in Figure *7.13-4*. Here we consider NO, NO_2, NH_3, O_3, and SO_2 for both meteorological seasons (i.e., summer, autumn, winter, and spring) and Murujuga seasons - Garrbarn (the hot time, wet season) and Muthu (cold time) (for further details see Murujuga seasons in the Glossary Table *1.4-3* and Department of Biodiversity, Conservation and Attractions (DBCA) (2021)).

There appears to be minimal seasonal variation over the year. Given the gaps in NH_3 data (as shown in Figure *7.13-7*) for some sites the boxplots are heavily dependent on data from EX02 and EX07, which may account for the broader interquartile range in spring and winter (on the left) and in Muthu (shown on the right) in Figure *7.13-4*. Given the nature of the sources in the study area (i.e., the gas plant(s), port, and power station), we would expect there to be near continuous emissions, which may explain the apparent lack of seasonal variability.

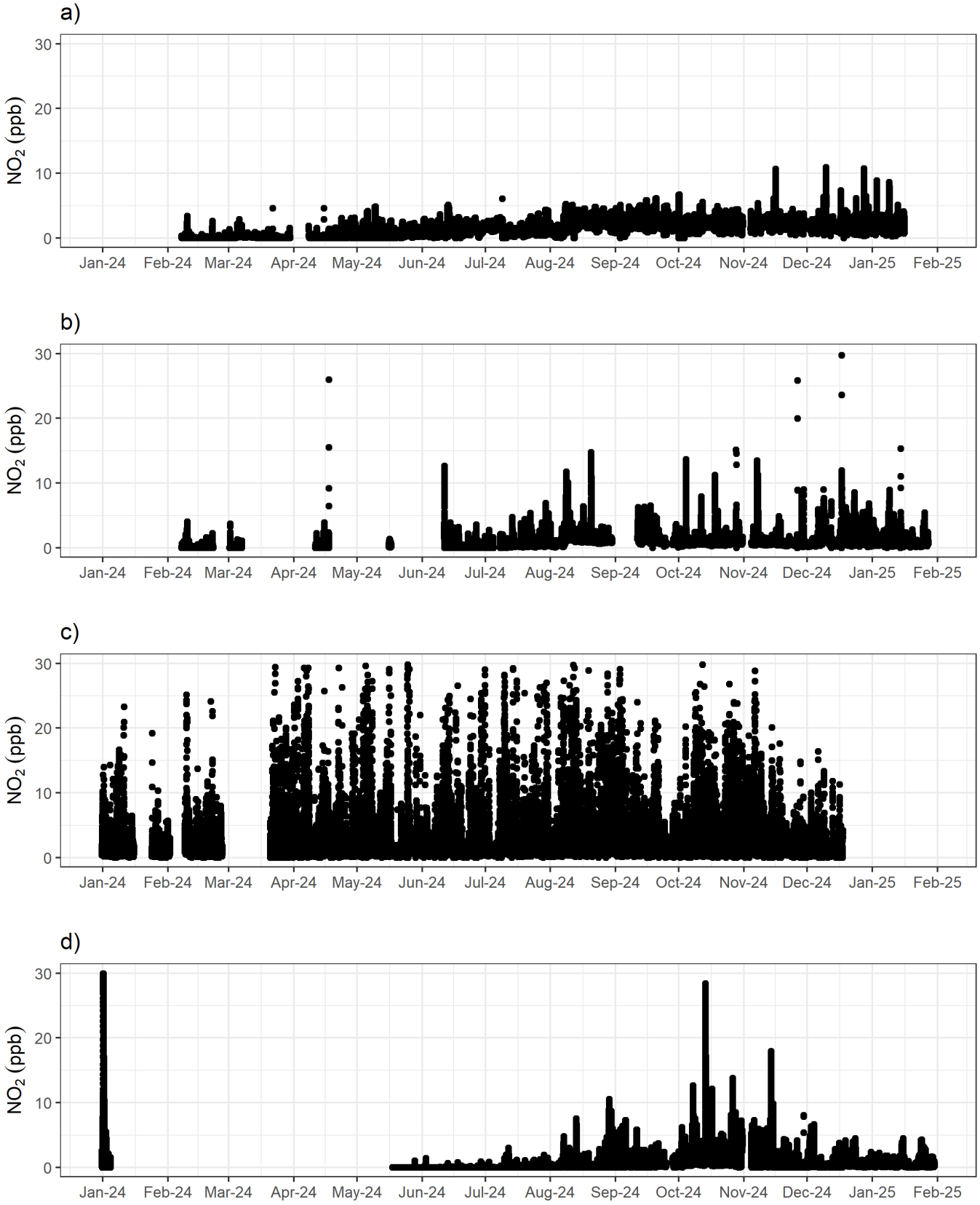

Figure 7.13-5: Time series data for NO_2, where (a) AQ01, (b) EX02, (c) EX07 and (d) EX09. Gaps in the data correspond to times where the instruments were offline, or where the data have been excluded due to concerns about the validity.

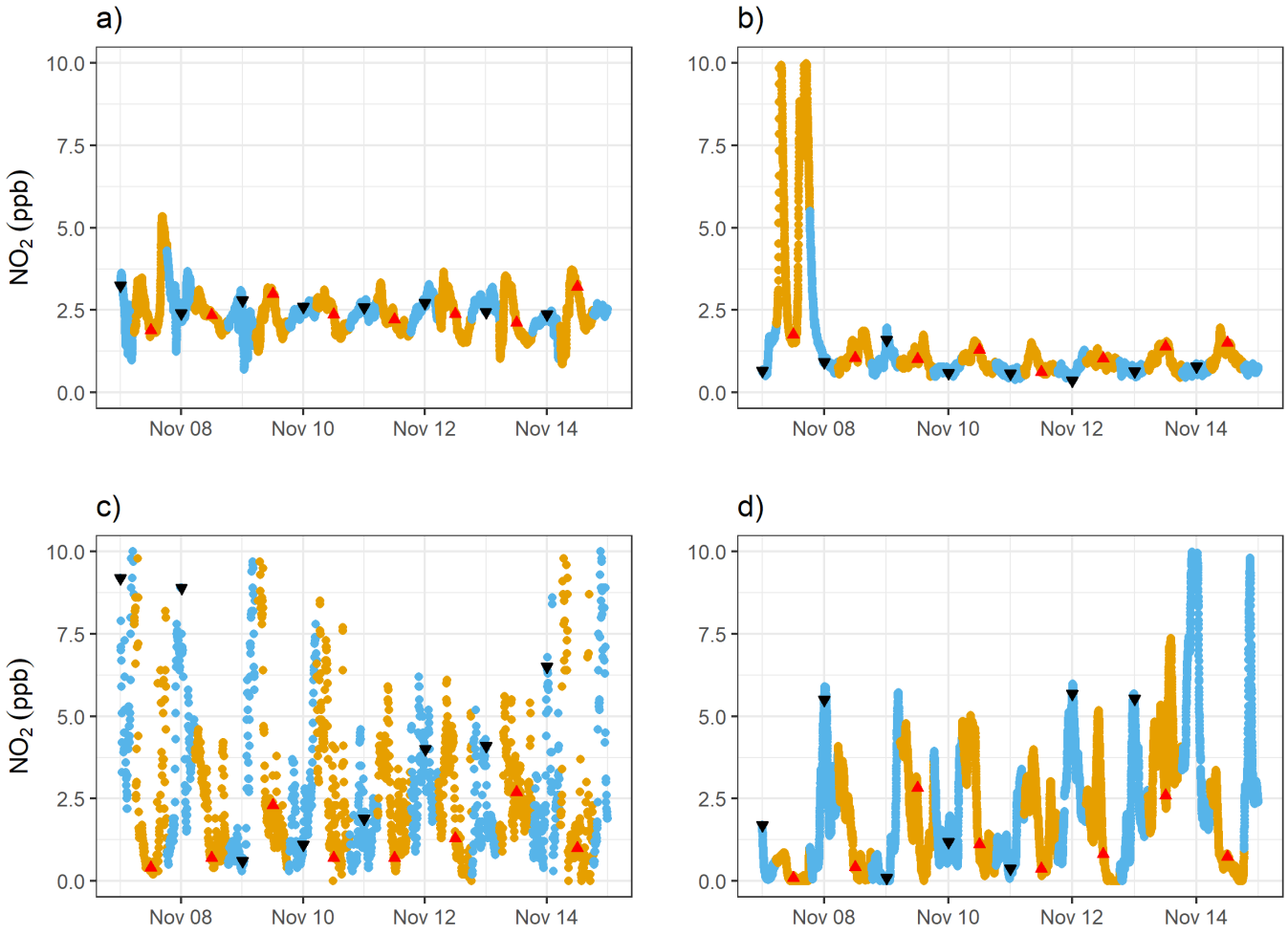

Figure 7.13-6: Time series plots for NO_2 over one week in November 2024, where (a) AQ01, (b) EX02, (c) EX07 and (d) EX09. The data shown in blue corresponds to nighttime (defined as sunset to sunrise) measurements, and data shown in orange correspond to daytime (defined as sunrise to sunset). The red up-pointing triangles are midday, and black down-pointing triangles are midnight. Data have been excluded where the validity is in question.

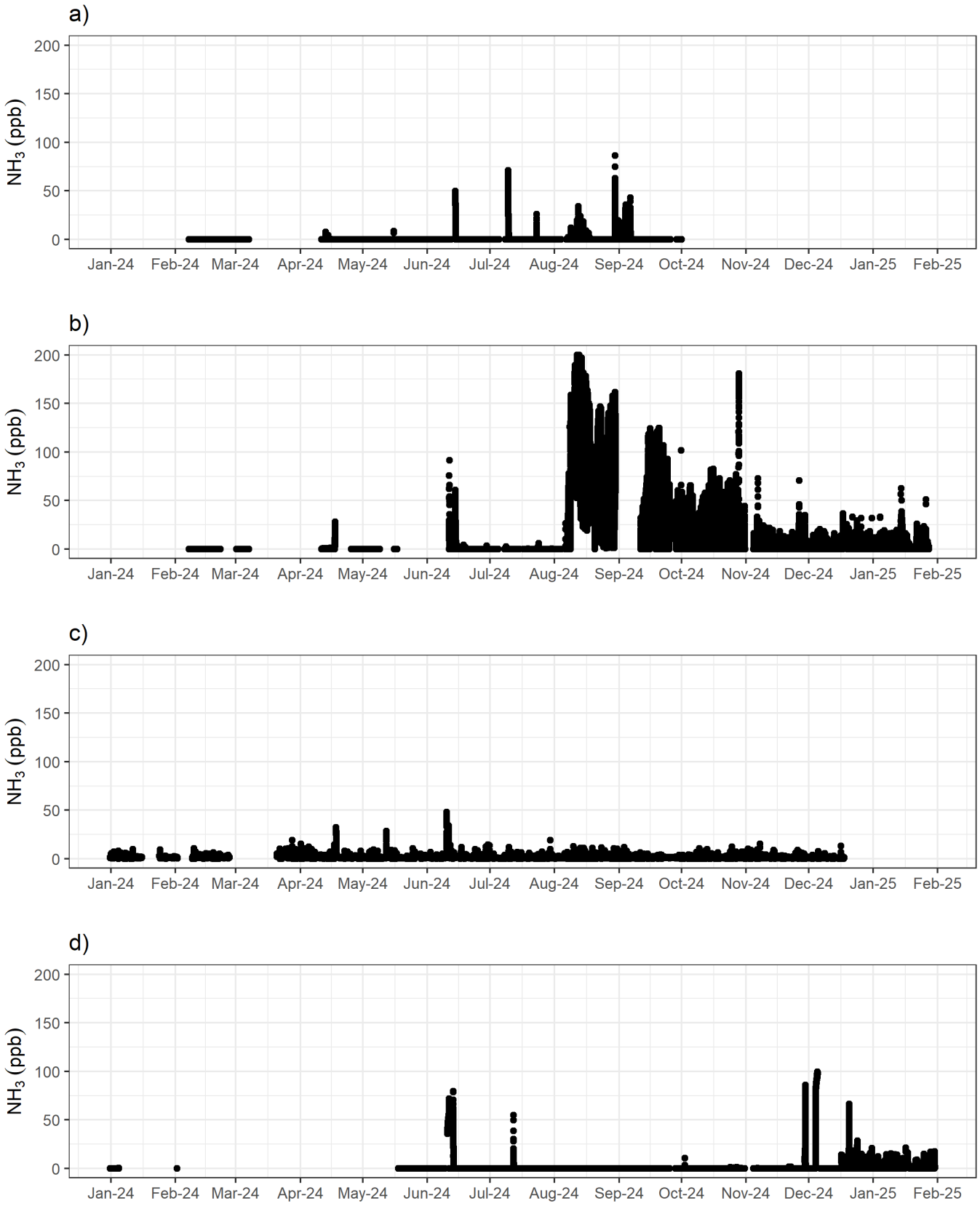

Figure 7.13-7: Time series data for NH_3 for (a) AQ01, (b) EX02 (c) EX07 and (d) EX09. Gaps in the data correspond to times where the instruments were offline, or where the data have been excluded due to concerns about the validity.

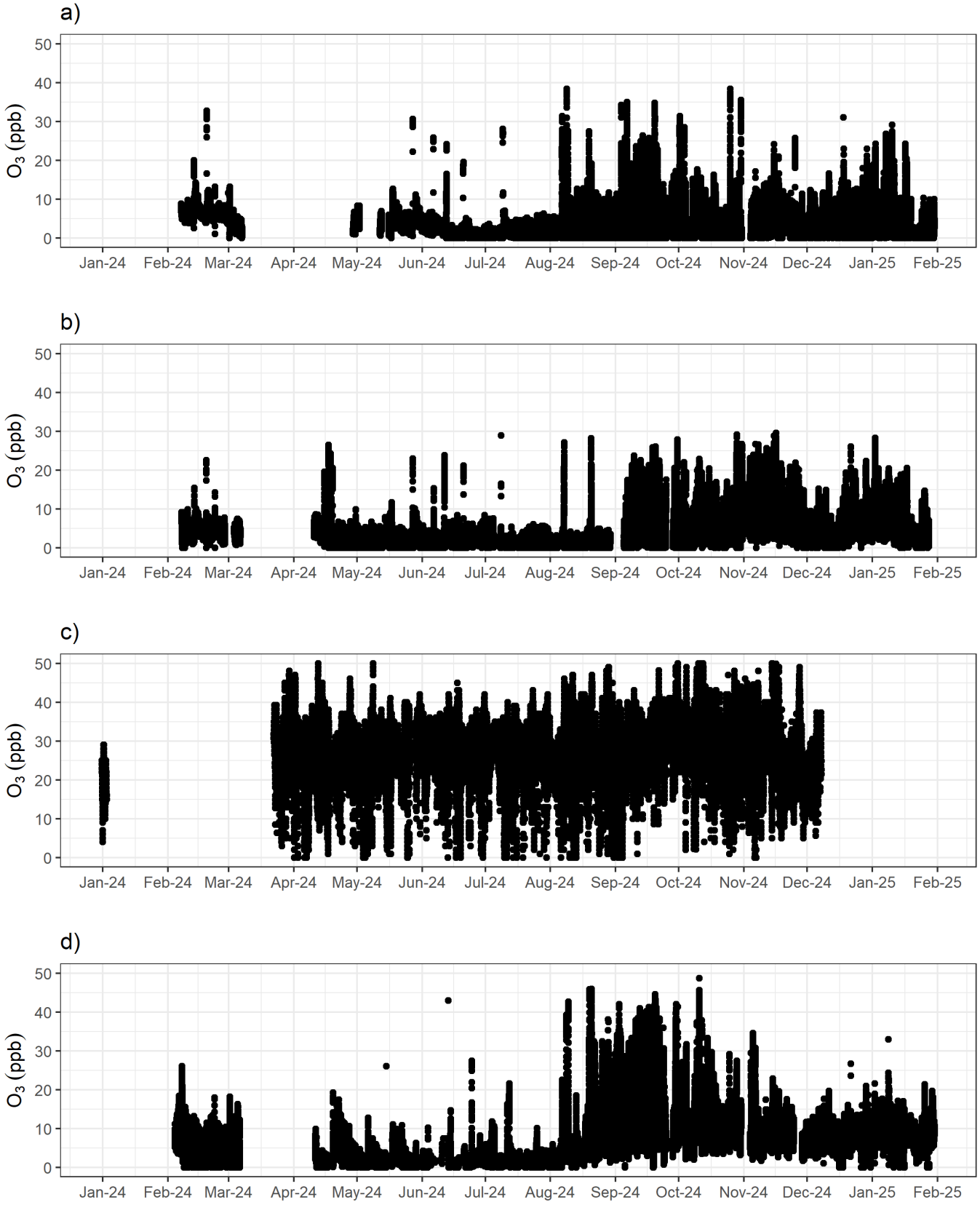

Figure 7.13-8: Time series plots for O_3 at (a) AQ01, (b) EX02, (c) EX07 and (d) EX09. Gaps in the data correspond to times where the instruments were offline, or where data have been excluded due to concerns about validity.

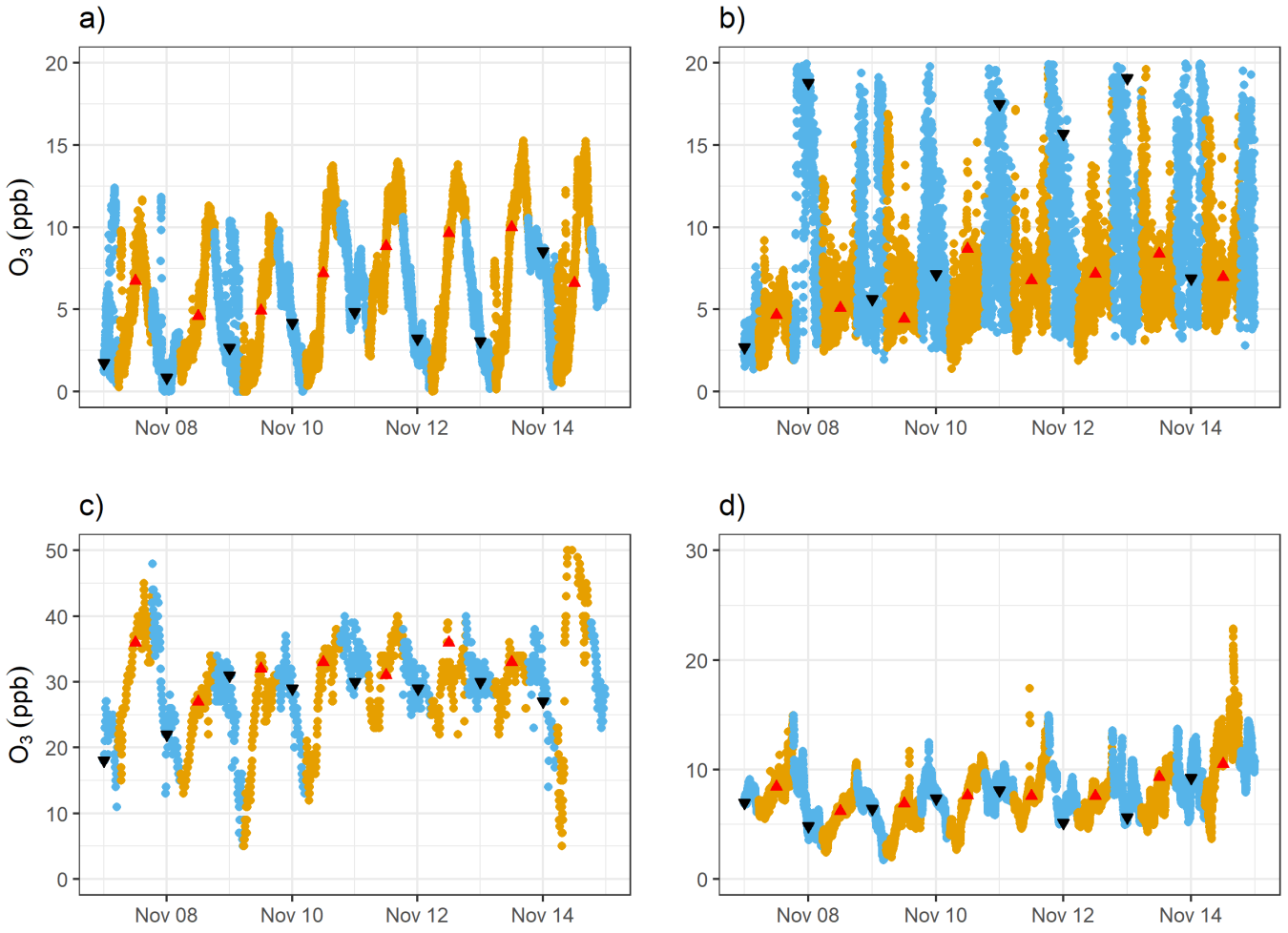

Figure 7.13-9: Time series plots for O_3 over one week in November 2024, where (a) AQ01, (b) EX02, (c) EX07, and (d) EX09. The data shown in blue corresponds to nighttime (defined as sunset to sunrise) measurements, and data shown in orange corresponds to daytime (defined as sunrise to sunset). The red up-pointing triangles are midday, and black down-pointing triangles are midnight. Data have been excluded where the validity is in question.

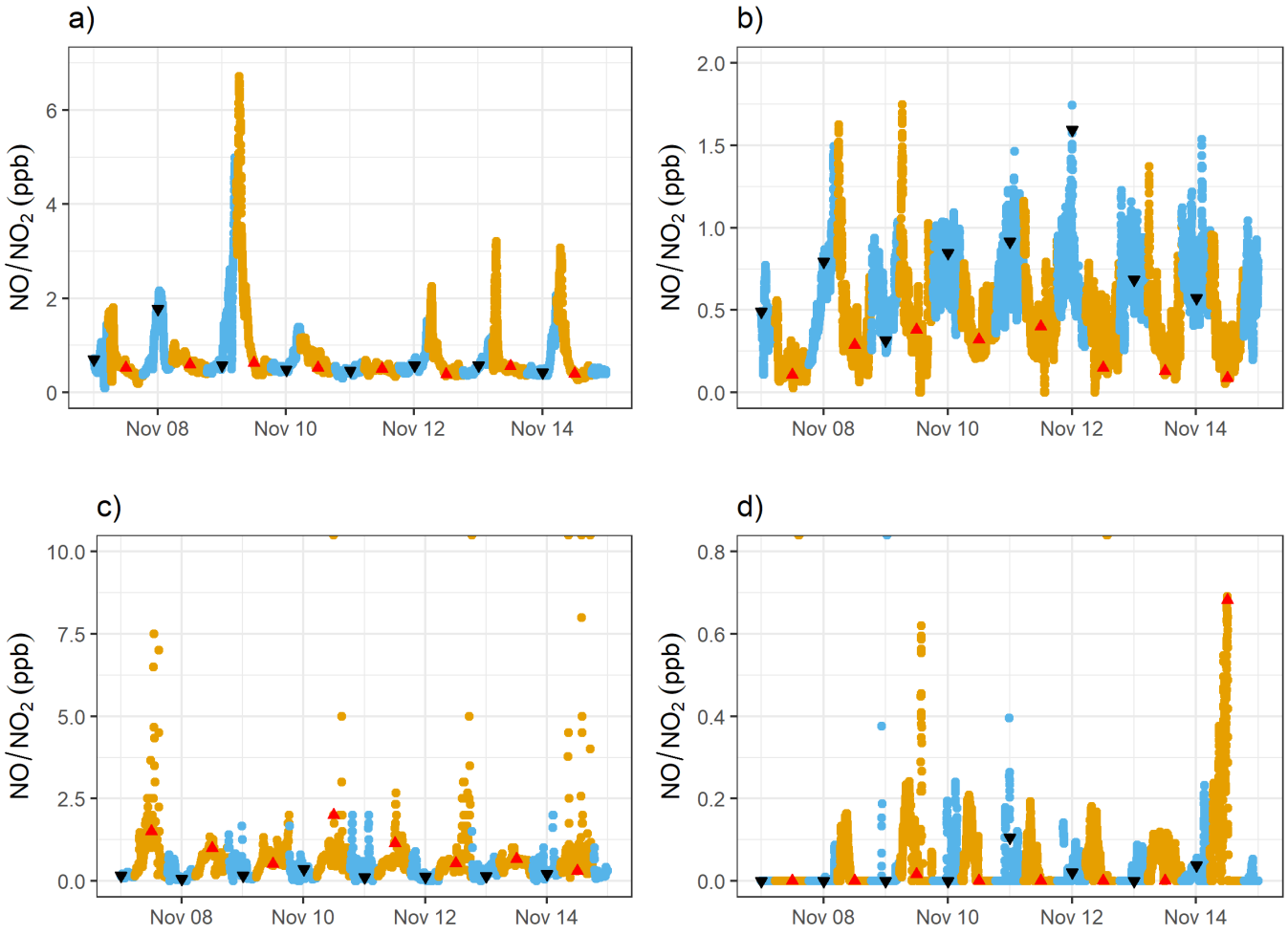

Figure 7.13-10: Time series plots for NO/NO_2 over one week in November 2024, where (a) AQ01, (b) EX02, (c) EX07, and (d) EX09. The data shown in blue corresponds to nighttime (defined as sunset to sunrise) measurements, and data shown in orange corresponds to daytime (defined as sunrise to sunset). The red up-pointing triangles are midday, and black down-pointing triangles are midnight. Data have been excluded where the validity is in question.

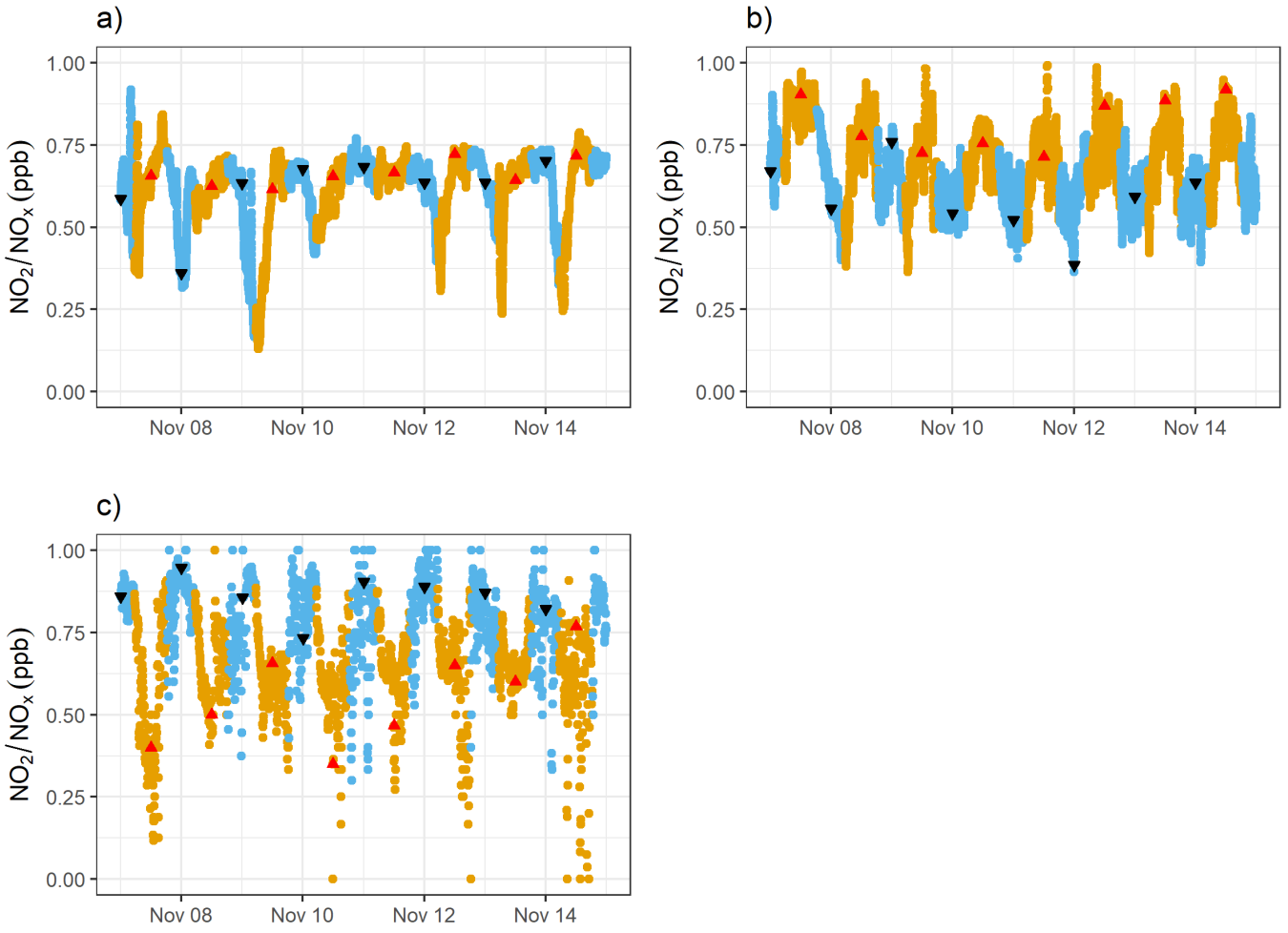

Figure 7.13-11: Time series plots for NO_2/NOx over one week in November 2024, where (a) AQ01, (b) EX02, (c) EX07, and (d) EX09. The data shown in blue corresponds to nighttime (defined as sunset to sunrise) measurements, and data shown in orange corresponds to daytime (defined as sunrise to sunset). The red up-pointing triangles are midday and black down-pointing triangles are midnight. Data have been excluded where the validity is in question.

7.13.2 Particulates

Palas Fidas 200 instruments are deployed at the four powered AQMs. These count particles across a range of size fractions, with time series plots for $PM_{2.5}$ and PM_{10} shown below (Figure *7.13-12* and *7.13-14*). These were brought online as they were installed and following an initial calibration check. Some challenges were encountered after initial installation, due to the humidity in the environment, but these have now been addressed. Particle data for AQ01, EX02, and EX09 is unavailable for some periods owing to equipment failure. The systems at AQ01, EX02, and EX09 have all suffered the same malfunction at different times, due to a corrupted internal data storage drive. The instruments have now been repaired and returned to service, but have continued to suffer downtime due to the challenging environment. Current status of instruments;

- Unit at AQ01 has had the power and hard drive replaced, and was brought back online in August 2024.
- Unit at EX02 has had the power supply and hard drive replaced, and was brought back online in August 2024. It subsequently experienced similar issues requiring further repair, ultimately being returned to site in February 2025.
- The instrument at EX07 became stuck in calibration mode after maintenance, resulting in no data being recorded for May 2024.
- The unit at EX09 has had the power supply and hard drive replaced, and was returned to service in August 2024.

Table *7.13-1* presents the percentage of days on which the Palas Fidas 200 was offline or under repair at each of the powered AQM sites. At all powered sites, except for EX02, this instrument was measuring valid data the majority of the time.

PM_{10} data are shown in Figure *7.13-14*. These show a similar trend to the data for $PM_{2.5}$ only with higher mass concentrations (as would be expected). A similar pattern is shown in Figure *7.13-16* for total suspended particulates (TSP), again with higher mass concentrations.

It does however, appear that a relatively large proportion of the dust at Murujuga falls into the $PM_{2.5}$ and PM_{10} size fractions, with less larger particles. Given the naturally dusty environment, consistent winds and extended dry periods there is the potential for a large amount of this to be natural dust; however visible dust clouds are regularly observed in the port area and along the rail lines. Given the issue with the operation of the instruments and missing data, it is not yet possible to meaningfully compare dust levels at the four sites, other than to acknowledge that dust levels were consistently high around EX02 and EX07 in January 2024.

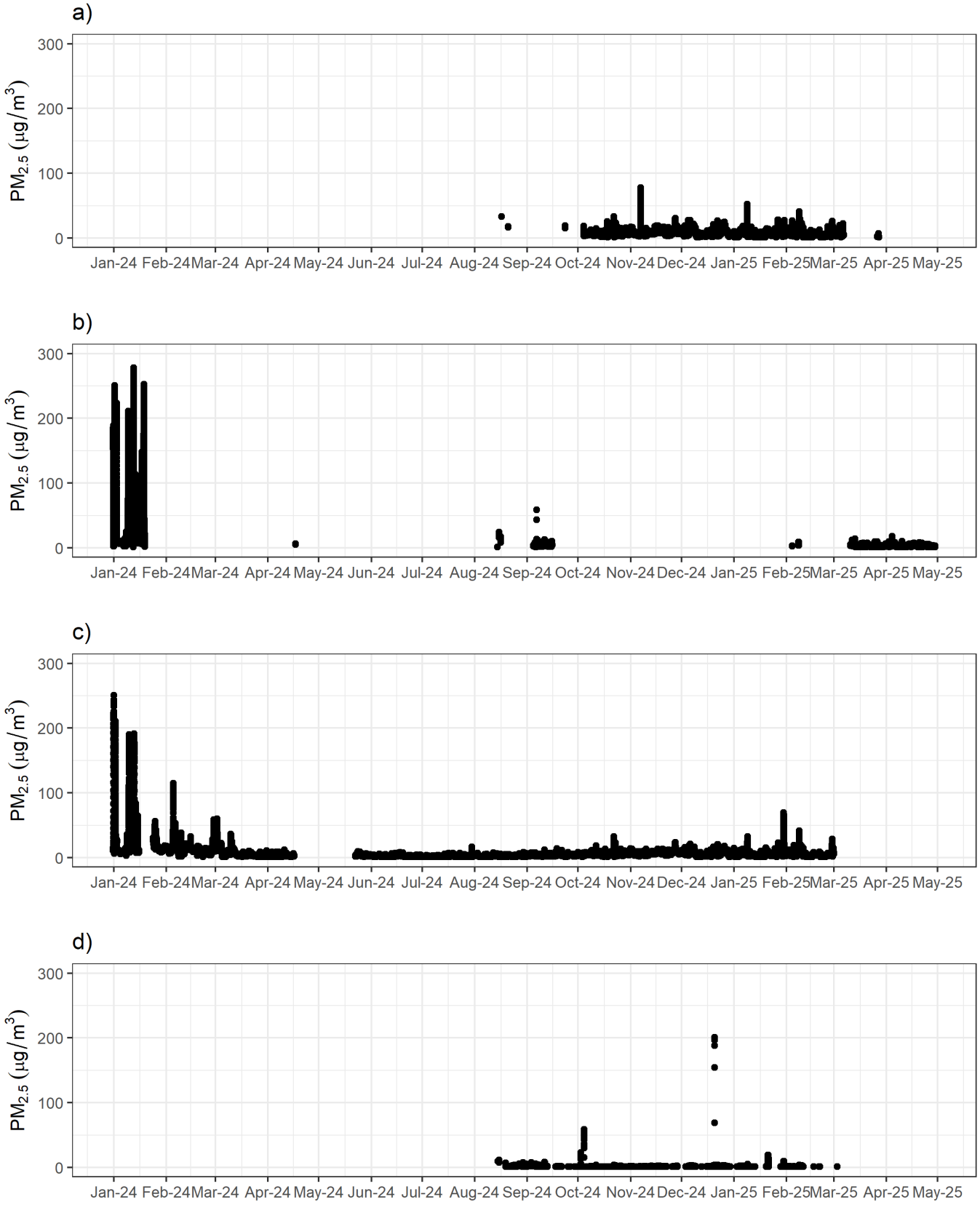

Figure 7.13-12: Time series plots for $PM_{2.5}$ at (a) AQ01, (b) EX02, (c) EX07 and (d) EX09. Gaps in the data correspond to times where the instruments were offline, or where the data have been excluded due to concerns about the validity.

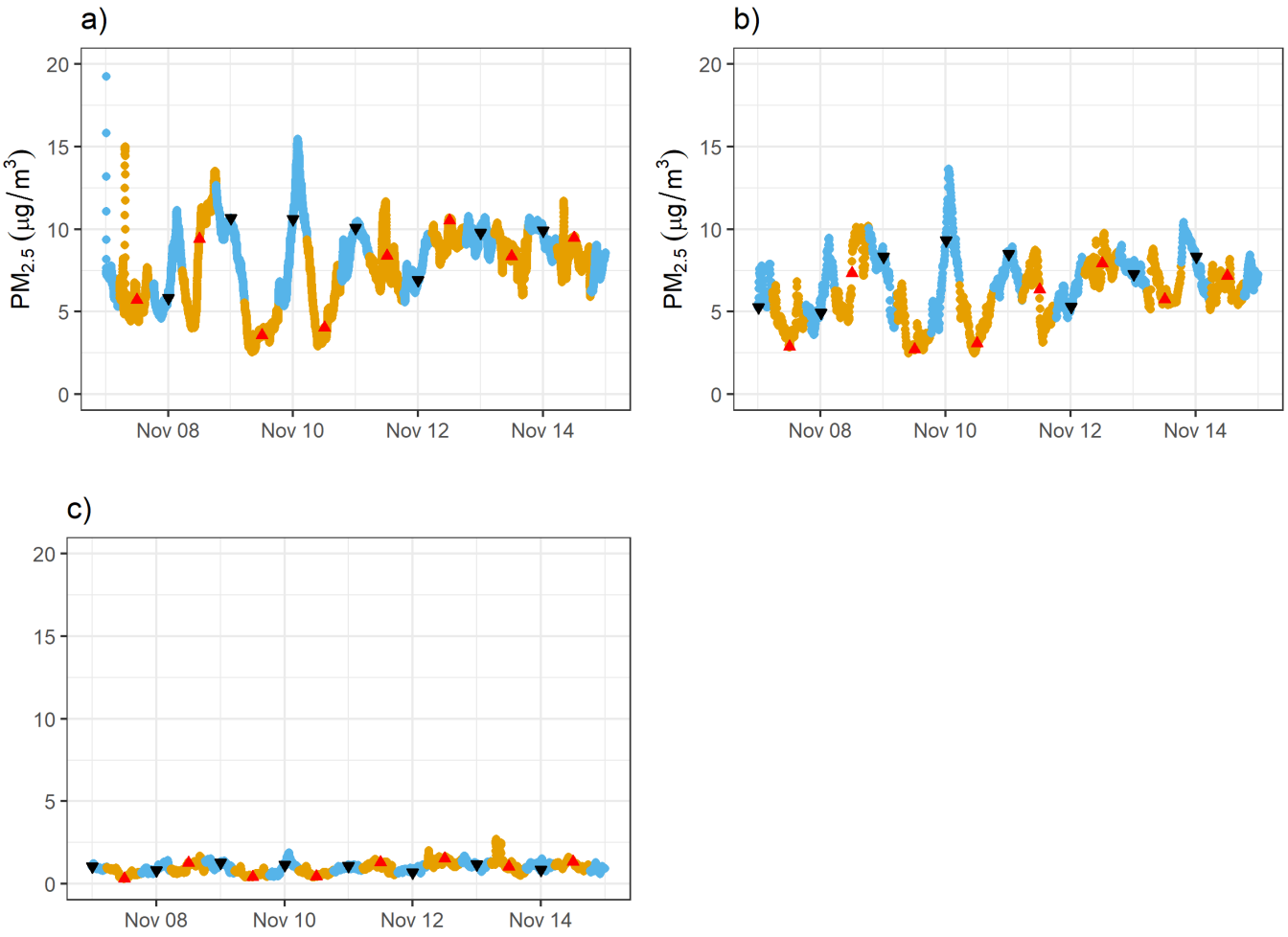

Figure 7.13-13: Time series plots for $PM_{2.5}$ over one week in November 2024, where (a) AQ01, (b) EX07, and (c) EX09. The data shown in blue corresponds to nighttime measurements, and data shown in orange corresponds to daytime. Data have been excluded where the validity is in question. Note EX02 had no data available in November 2024.

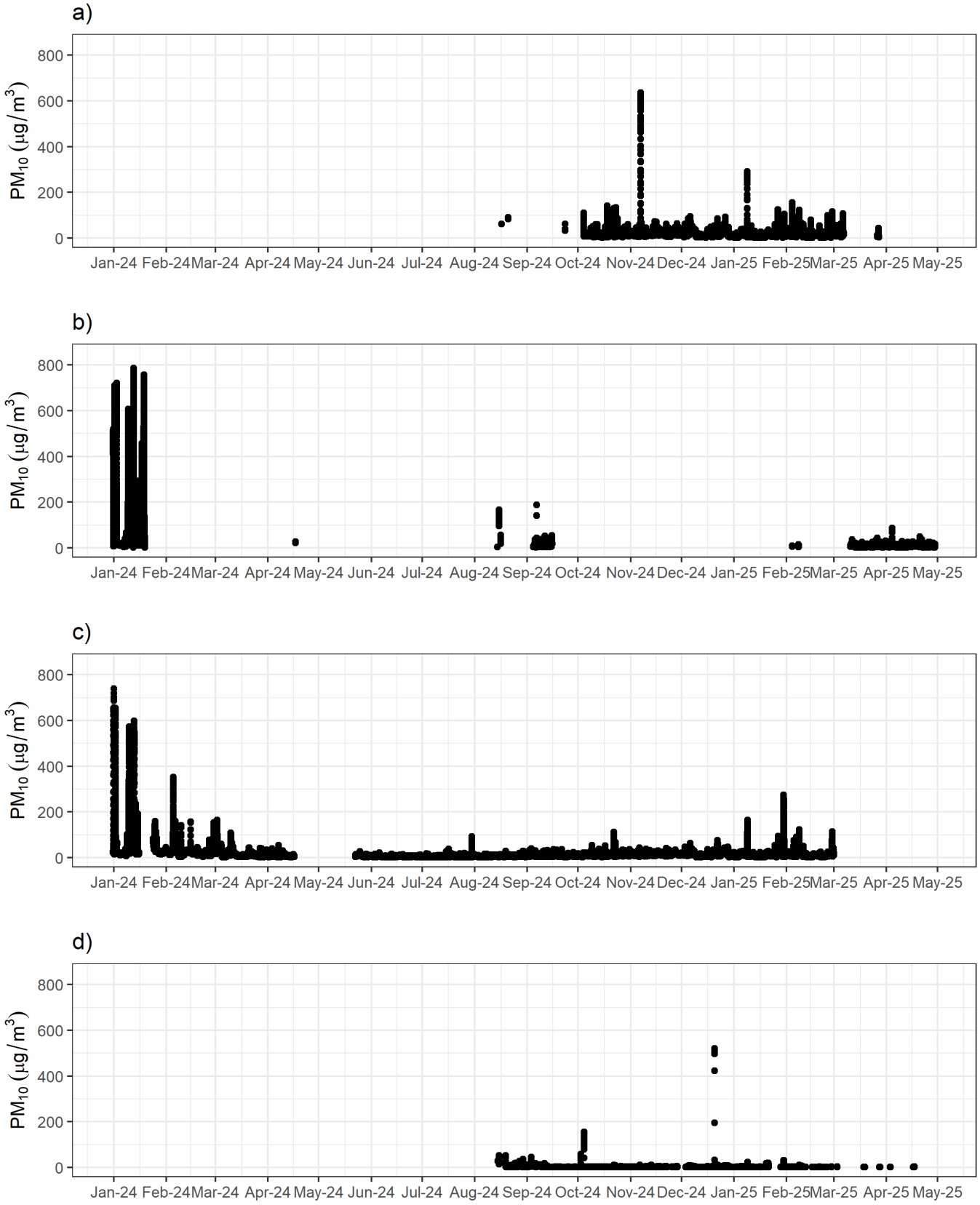

Figure 7.13-14: Time series plot for PM_{10} at (a) AQ01, (b) EX02, (c) EX07 and (d) EX09. Gaps in the data correspond to times where the instruments were offline, or where the data have been excluded due to concerns about the validity.

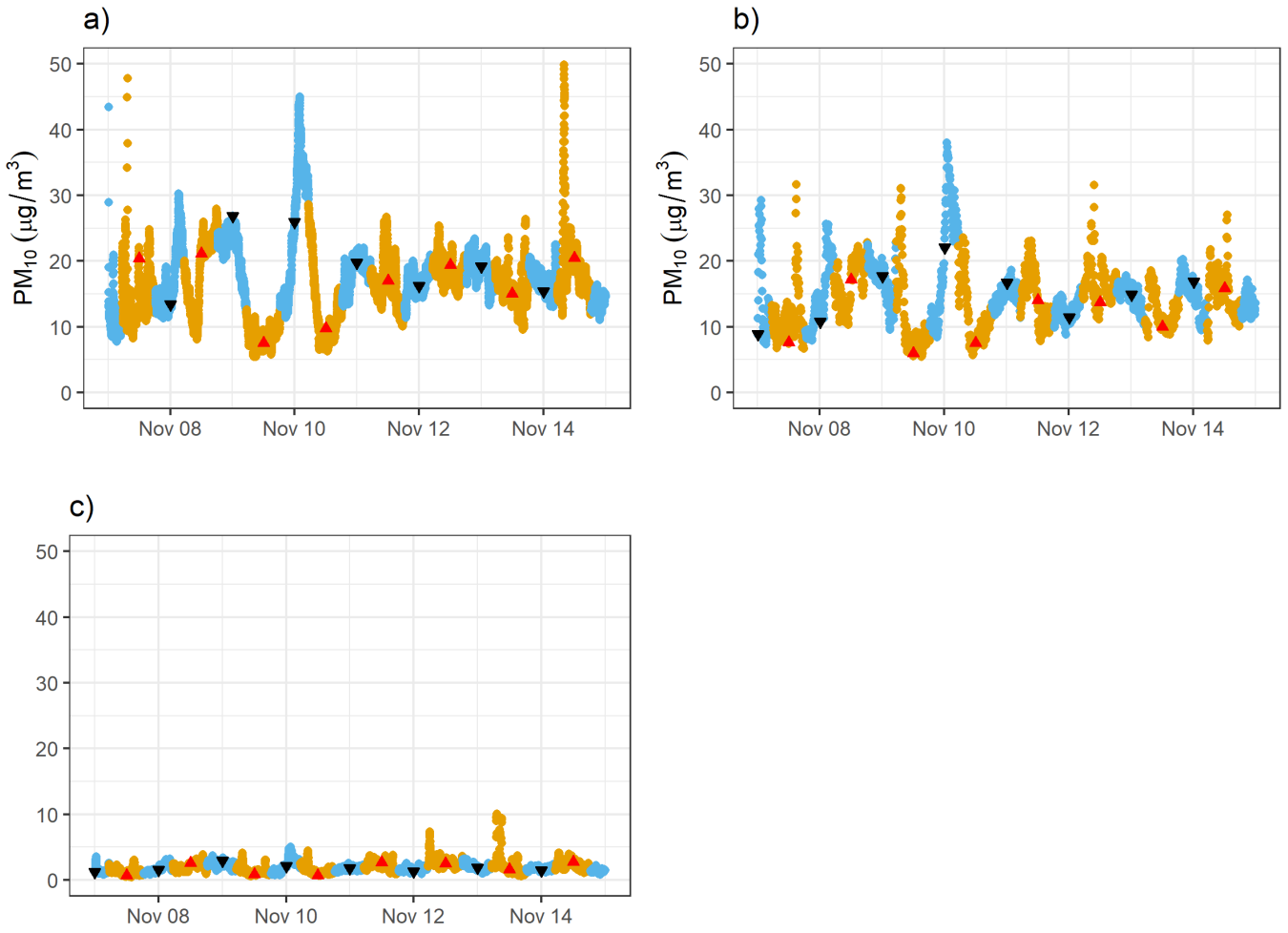

Figure 7.13-15: Time series plots for PM_{10} over one week in November 2024, where (a) AQ01, (b) EX07, and (c) EX09. The data shown in blue corresponds to nighttime measurements, and data shown in orange corresponds to daytime. Data have been excluded where the validity is in question. Note EX02 had no data available in November 2024.

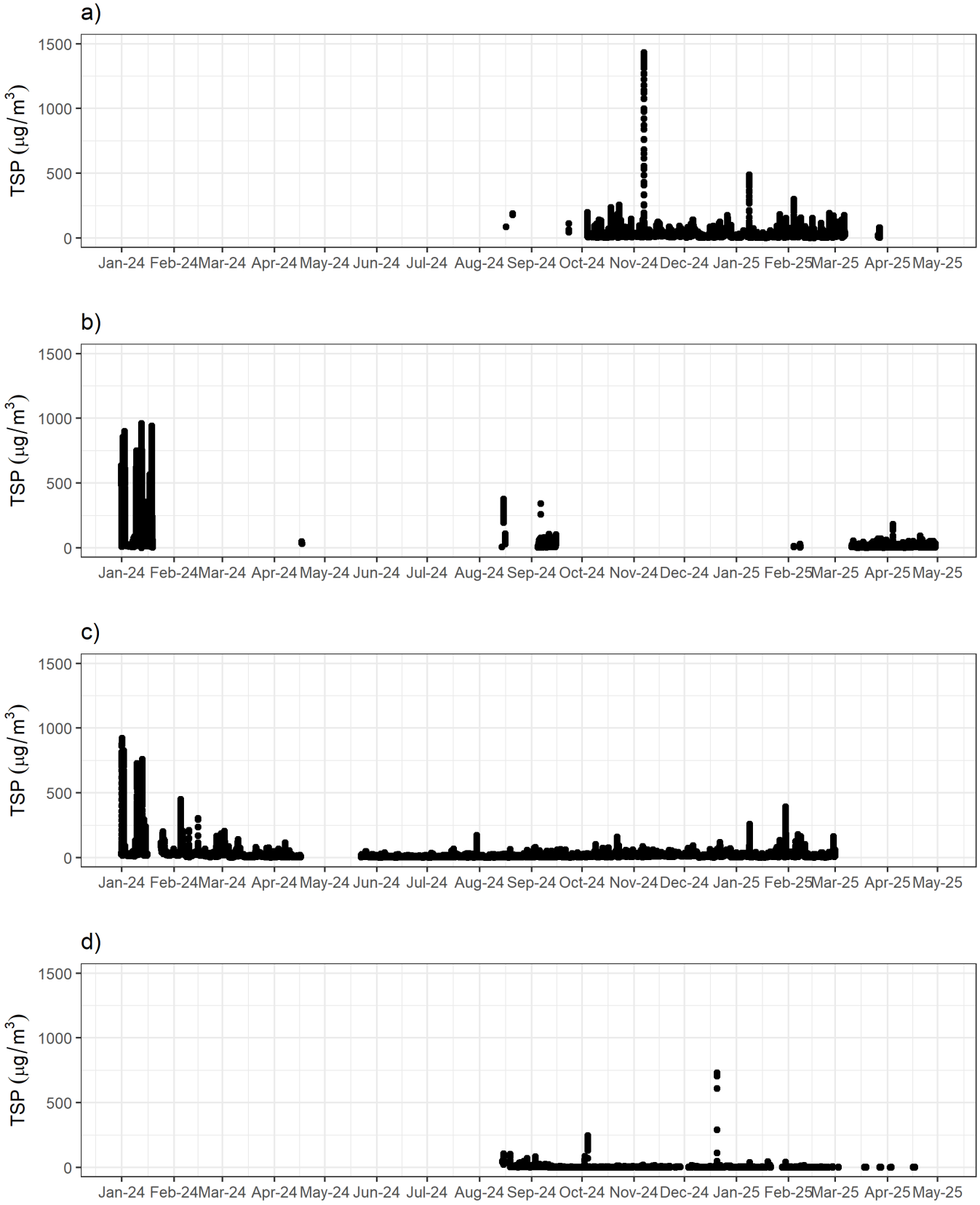

Figure 7.13-16: Time series plot of total suspended particulates (TSP) at (a) AQ01, (b) EX02, (c) EX07, and (d) EX09. Gaps in the data correspond to times where the instruments were offline, or where the data have been excluded due to concerns about the validity.

7.13.3 Other instruments

7.13.3.1 Aethalometer - black/brown carbon analyser

The aethalometer deployed at EX09 experienced a significant fault due to water ingress into the system in March 2025. The instrument was repaired and redeployed in 2024. However, despite the inclusion of an inlet dryer on the sampling line, the instrument once again sustained significant water damage and is currently under vendor inspection. There are therefore no additional data to that presented in Monitoring Studies Report 2024 (Curtin University, 2024c).

7.13.3.2 Picarro - methane, ethane, carbon dioxide spectrometer

The location of EX09 makes it well-suited for broader air quality monitoring. The height of the site relative to the surroundings and the consistently strong winds potentially allow us to detect the long-term transport of certain species. For this reason, this particular powered site was chosen for the installation of additional instrumentation to allow exploration of a wider range of chemical species, and potentially allow some source apportionment. This was the site chosen to deploy the isotopic methane analyser (Picarro G2210-i). This instrument was commissioned in December 2023 at the Mt Wongama site. Data has been collected for most of the monitoring period, except for short periods when the instrument has been offline.

Figure *7.13-17* shows the CO_2 levels for the site, starting from January 2024 onwards. The data typically sit around the 400 ppm level, in line with global averages, with a number of periodic peaks (several per month) approaching or exceeding 500 ppm. In some cases these reach concentrations above 2,000 ppm. These may correspond to flaring events at the gas plant(s), other combustion processes (e.g., bush fires), or emissions from ammonia production facilities. Given that the levels of CO_2 reach these higher levels from time to time, the impacts on the environment need to be considered. This could include atmospheric processes involving CO_2 (such as acidification), as well as the impact of CO_2 on the microbiome. This is consistent with the levels and patterns of CO_2 emissions measured in the prior sampling year.

Figure *7.13-19* shows the methane levels for the site. The methane levels are typically around or above the global background methane concentration of 1.9 ppm (Skeie et al., 2023). There are a number of peaks observed with the methane concentration at times exceeding 3 ppm. This may be explained by the proximity of the monitoring station to the gas plant, so further analysis and consideration of the carbon isotopes in the methane is required. Higher levels of methane may mean more potential for secondary organic aerosol formation, but this requires further investigation.

Ethane results have also been obtained over the same monitoring period and are shown in Figure *7.13-20*. These are typically low (under 10 ppb), with only a few days reaching concentrations over 20 ppb. The ethane levels are typically less variable than the methane levels, day to day. To explore methane and ethane levels further these are plotted together as an ethane:methane ratio in Figure *7.13-21*. The ratios show a high degree of variation over a single day (note the logarithmic scale on the y-axis) but a fairly consistent range of values day to day. The exception here is in late February 2025, where there is a notable peak. This also corresponds to the highest measured concentrations of ethane and methane. These again, are most likely explained by the proximity to the gas plant.

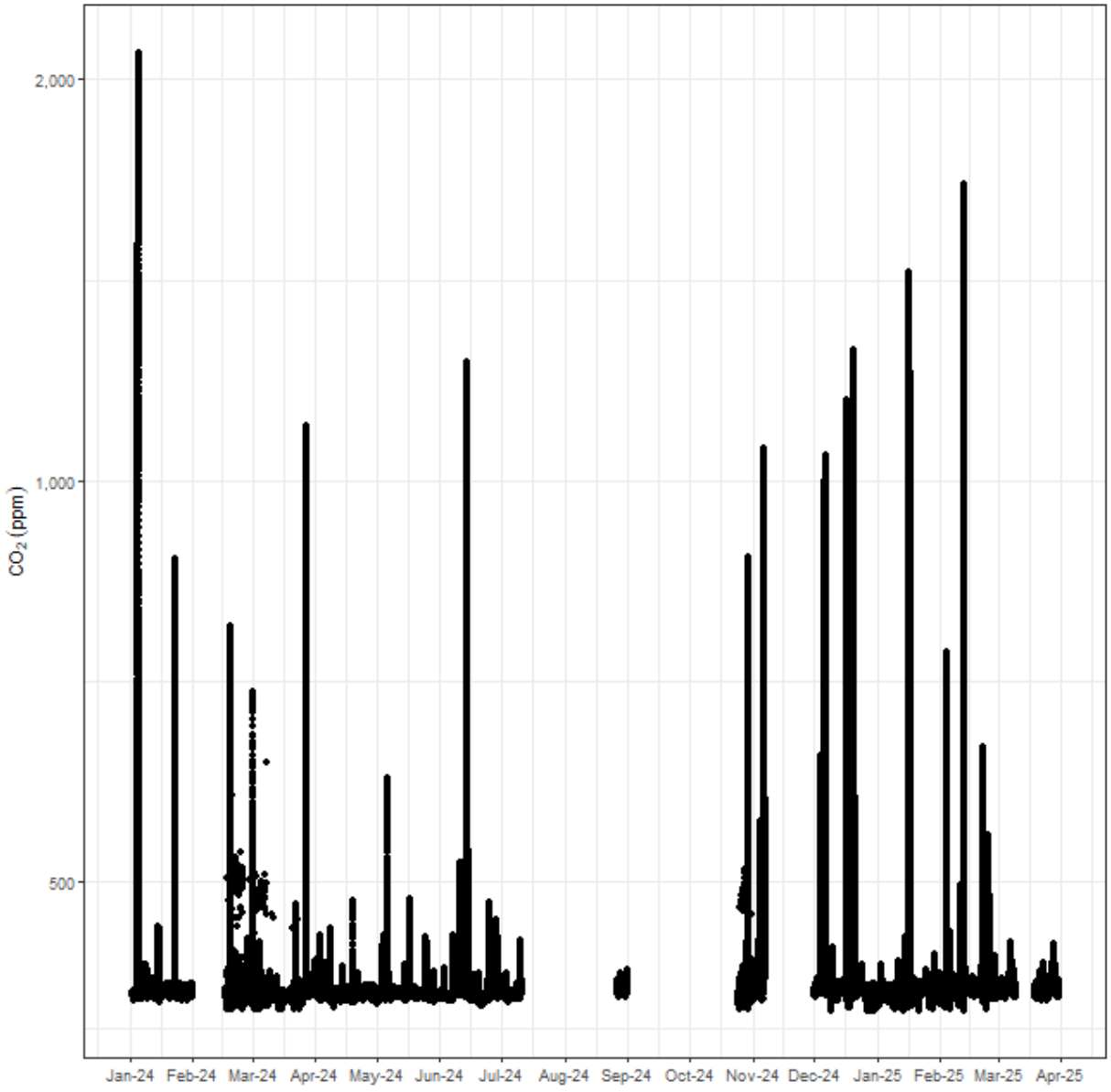

Figure 7.13-17: Time series plot of CO_2 from the Picarro instrument at EX09. Gaps in the data correspond to times where the instrument was offline, or where data have been excluded due to concerns about validity.

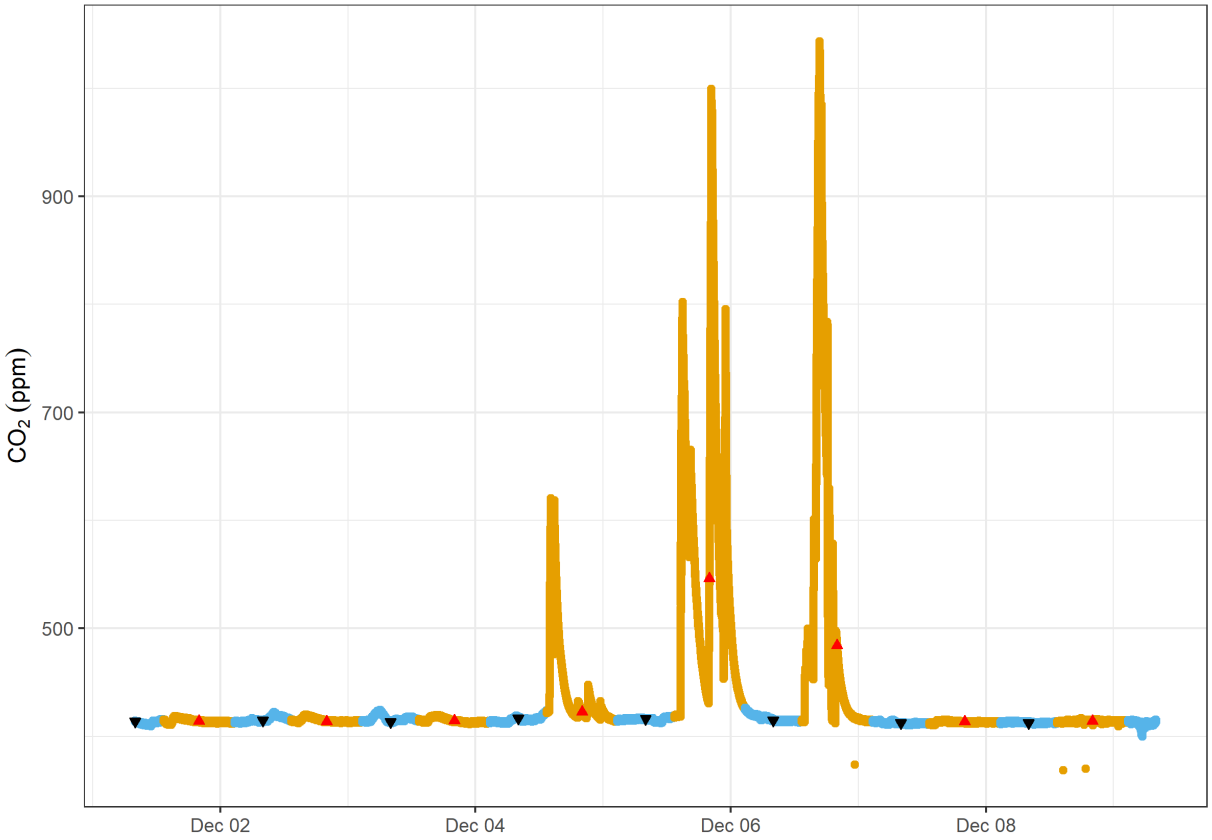

Figure 7.13-18: Time series plot of CO_2 from the Picarro instrument at EX09 over a week in December 2024. The data shown in blue corresponds to nighttime (defined as sunset to sunrise) measurements, and the data shown in orange corresponds to daytime (defined as sunrise to sunset). The red up-pointing triangles are midday, and black down-pointing triangles are midnight. Note that there was no data available for 11 to 14 November 2024, the period used for visualisation of daily peaks for other real time instruments.

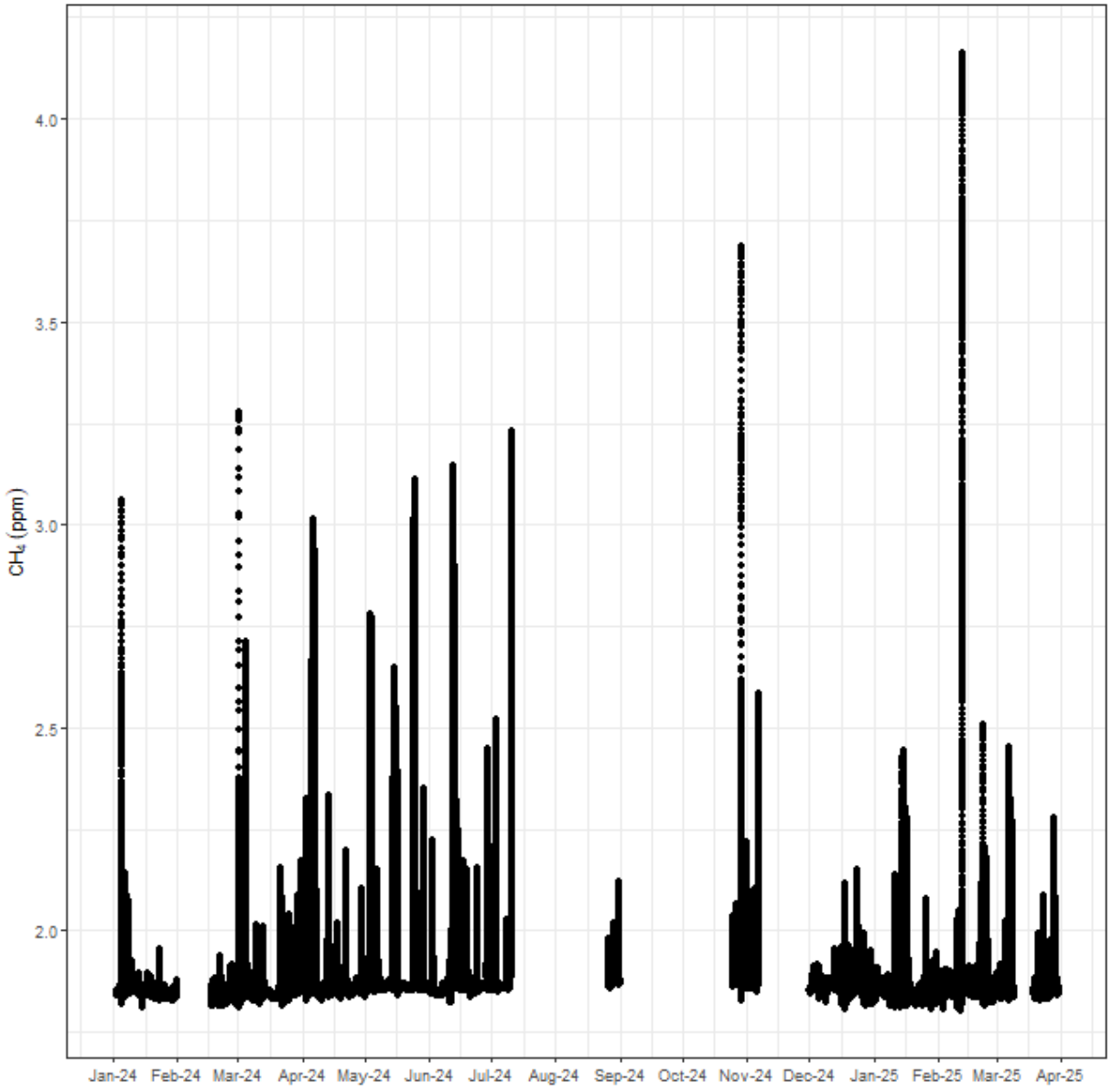

Figure 7.13-19: Time series plot of CH_4 from the Picarro instrument at EX09. Gaps in the data correspond to times where the instrument was offline, or where data have been excluded due to concerns about validity.

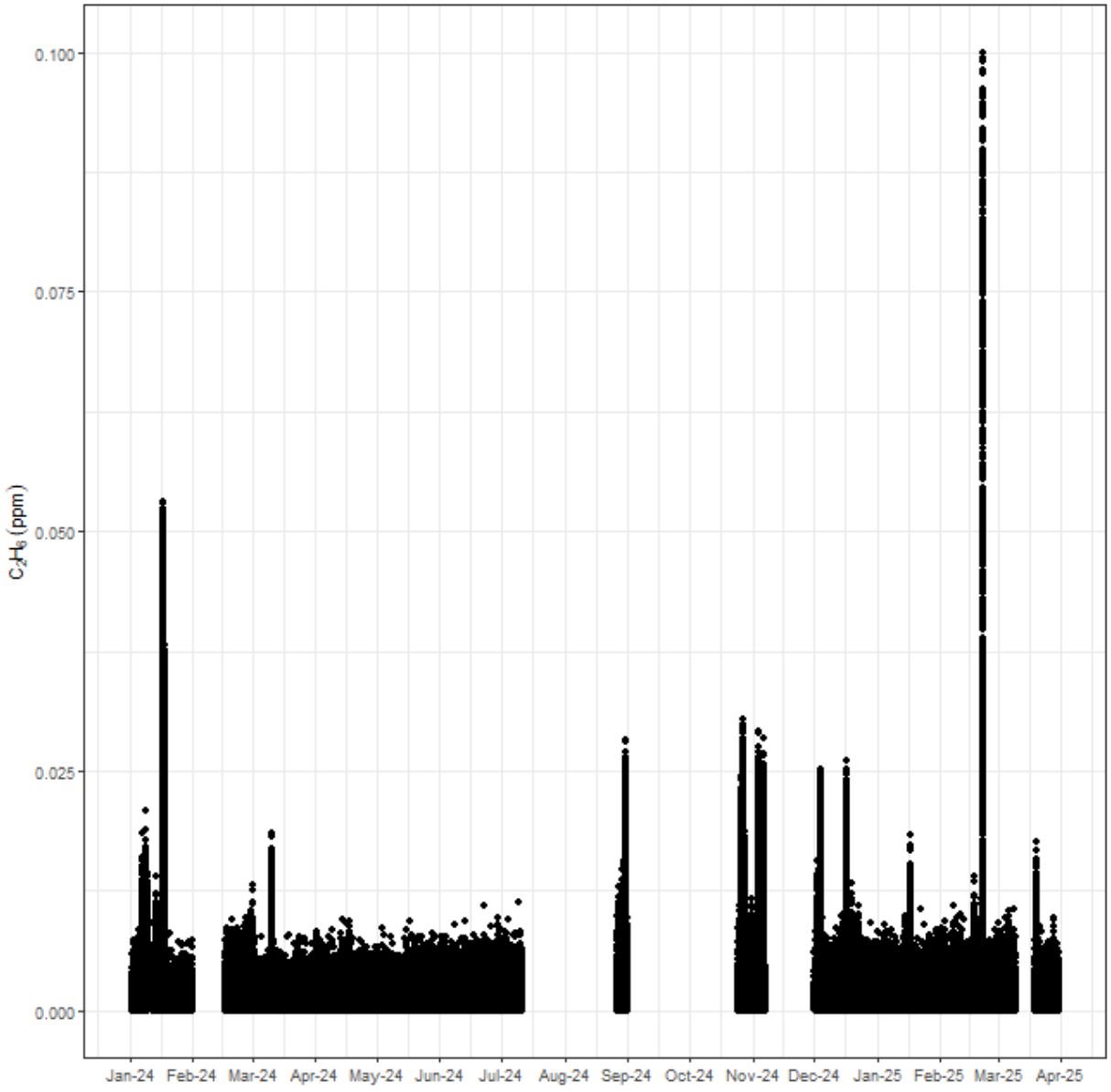

Figure 7.13-20: Time series plot of C_2H_6 from the Picarro instrument at EX09. Gaps in the data correspond to times where the instrument was offline, or where data have been excluded due to concerns about validity.

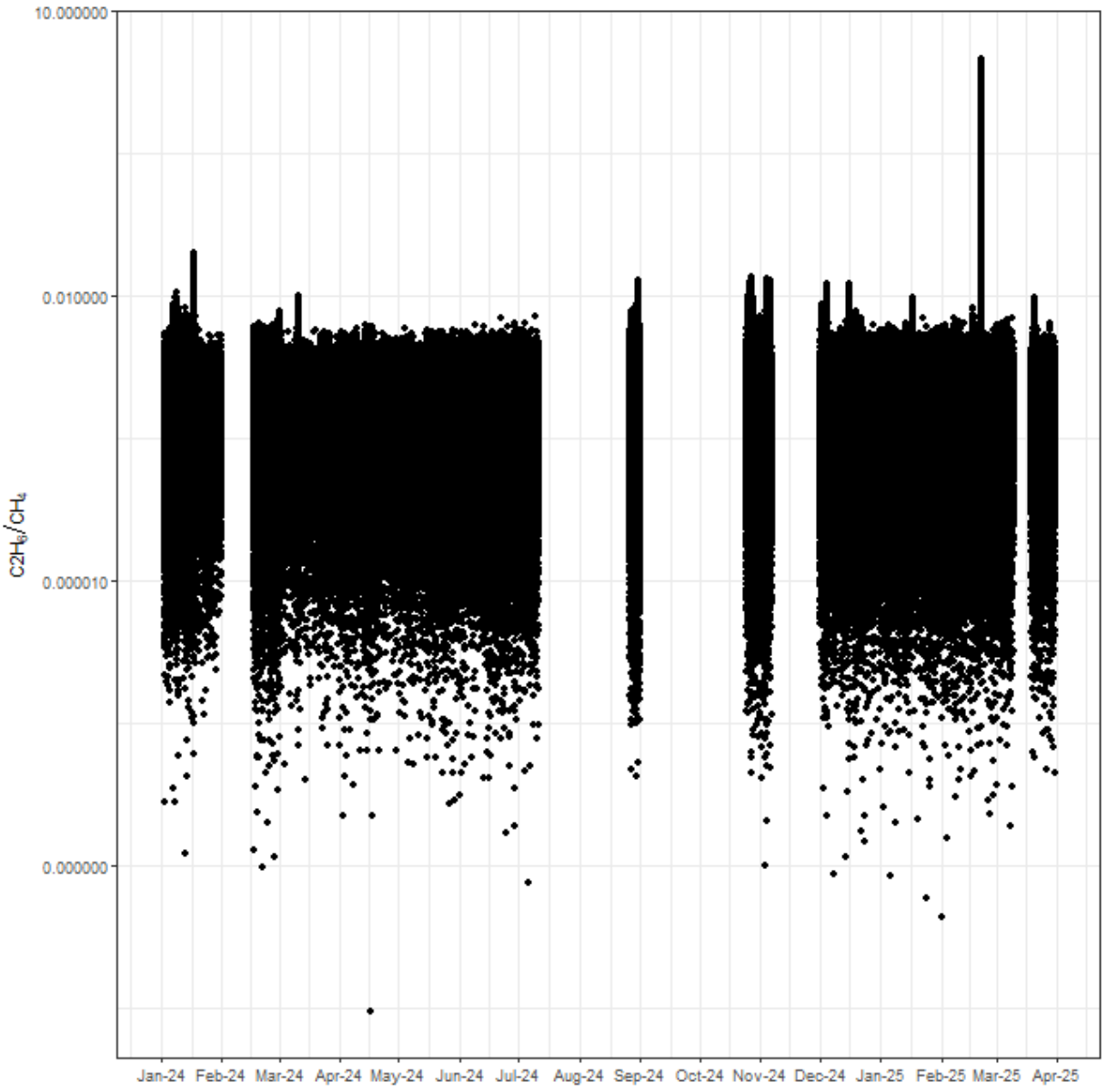

Figure 7.13-21: Time series plot of the ratio between C_2H_6 and CH_4 from the Picarro data. Gaps in the data correspond to times where the instrument was offline, or where data have been excluded due to concerns about validity.

7.13.3.3 MAxDOAS - remote/column measurements of nitrogen dioxide and formaldehyde

The Multi AXis Differential Optical Absorption Spectrometer (**MAxDOAS**) operates in a similar manner to satellite remote sensing, except that it is able to measure horizontally, vertically, and angles in between. It has an effective measurement path length of 15 to 25 km, depending on atmospheric conditions. It is only able to measure during daylight conditions. Data can be extracted and processed to obtain approximate concentrations of NO_2, SO_2, and selected other species such as formaldehyde (CH_2Oor HCHO), however in molecules per unit area (cm^2) rather than a volumetric concentration. Given the useful results from this instrument in the Monitoring Studies Report 2024 (Curtin University, 2024c), a second MAxDOAS, (2D) was purchased and installed at EX09 and the initial MAxDOAS (Compact) was relocated to EX02. The 2D model permits rotation in a horizontal plane to allow multiple measurement angles without repositioning. The MAxDOAS 2D is currently sited at EX09 (Mt Wongama) and is oriented such that an angle of 0° represents due west (W), 90° represents a vertical (V) orientation, and 180° represents due east (E). Angles in between 0 and 89° represent different azimuth angles in a westerly direction and angles between 91 and 180° represent azimuth angles in an easterly direction. Unfortunately the MAxDOAS Compact developed an internal fault during recommissioning at EX02 and is currently with the manufacturer for repair, therefore no data are available from EX02 for this report.

Figures *7.13-22* to *7.13-24* provide a comparison between gas concentrations near ground level (at 1, 10 and 30 ° elevation angles respectively). Values are shown for West (W), Vertical (V) and East(E) directions, for NO_2 and CH_2O. It can be seen that NO_2 exhibits strong vertical distribution characteristics (higher near ground level) as well as temporal variation. CH_2O however, is much more uniform both vertically and temporally.

Figures *7.13-25* and *7.13-26* provide a time series of gas concentrations near ground level (at 5 and 30 ° elevation angles respectively). Values are shown for West (W), Vertical (V) and East(E) directions, for NO_2 and CH_2O. It can be seen that both NO_2 and CH_2O levels are higher at the greater elevation angle.

Figures *7.13-27* to *7.13-29* provide daily time series of NO_2. Values are shown for West (W), Vertical (V) and East(E) directions. Near-surface, vertical and raw profiles are shown. Pronounced diurnal profiles of NO_2 can be observed on many of the days, which are most likely due to the formation of NO_2 from locally emitted NO. Most combustion processes primarily emit NO, most of which will later react to form NO_2 in the environment. These diurnal profiles become less pronounced for vertical column data, which supports this hypothesis. Figure *7.13-29* shows the same data for CH_2O. In this case, there are pronounced peaks near ground level near sunrise and sunset, which do not appear in vertical column data. Again, these data suggest formation of new CH_2O from local CH_4 emissions.

Figures *7.13-31* and *7.13-32* provide a scatterplot of NO_2 flux measured using the MAxDOAS against NO_2 measured using the reference real-time monitor (T201) at EX09. Figures show MAxDOAS near surface concentration and vertical column density respectively. As the MAxDOAS is a spatially integrated measure over several kilometres and the T201 is a point source measurement, these two measures do not show perfect agreement, however a weak correlation does appear to exist.

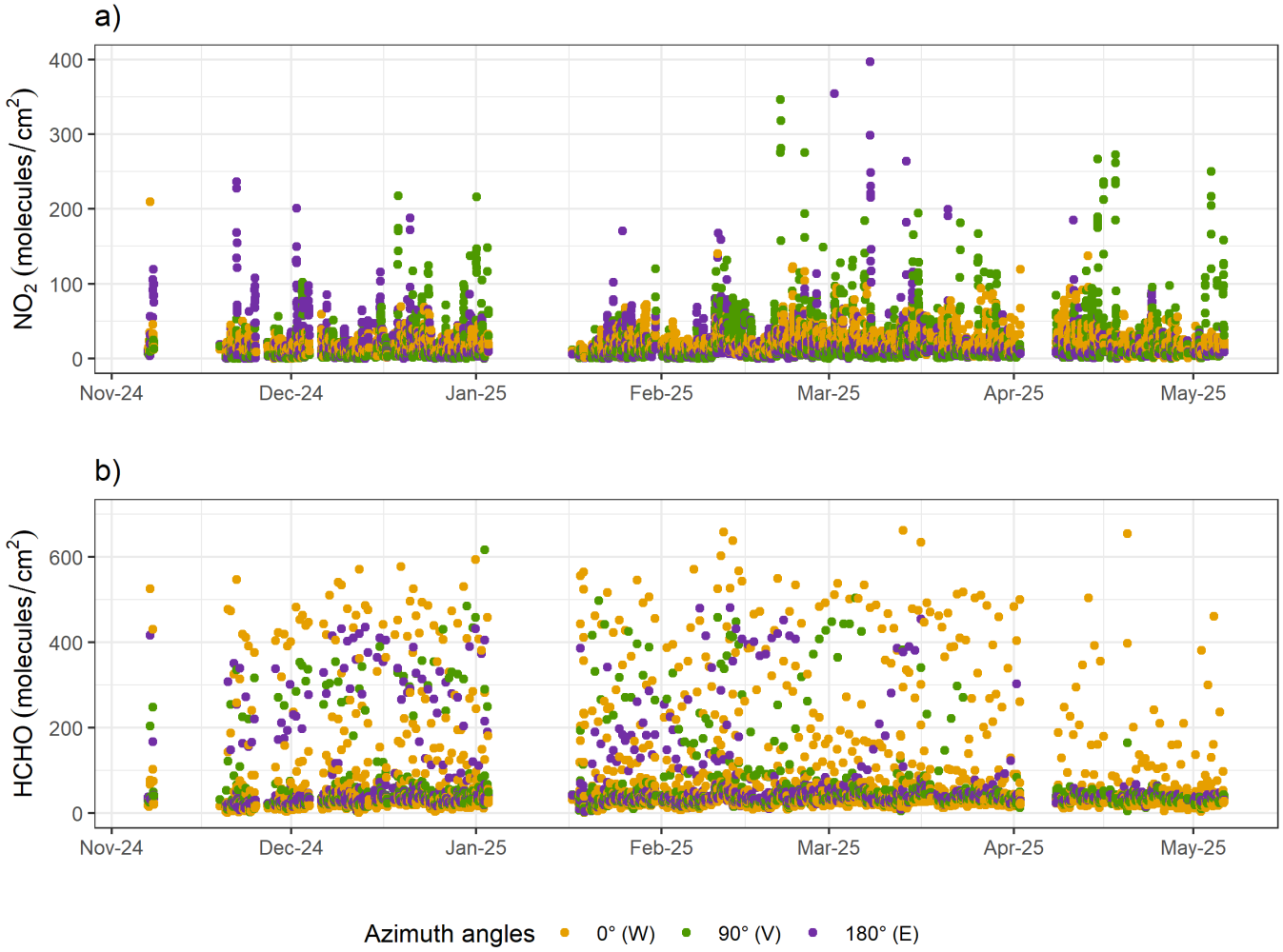

Figure 7.13-22: Time series plots for NO_2 and CH_2O from MAxDOAS at 1° elevation, raw data product from spectral fitting, trace gas concentration integrated over the atmospheric light path. Note that the NO_2 and CH_2O have been divided by 10^{15} (one hundred quadrillion) to simplify the tick marks on the y-axis.

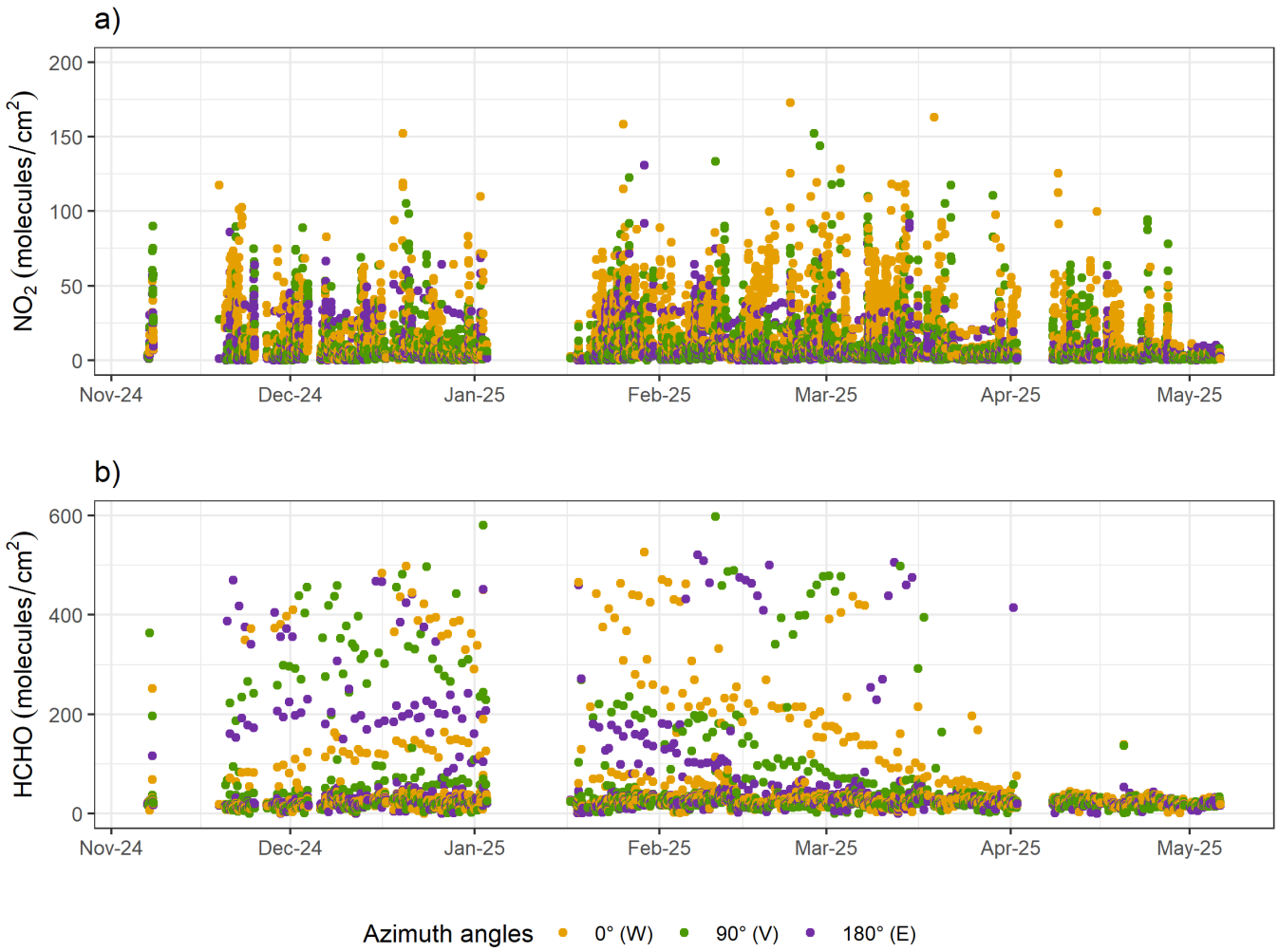

Figure 7.13-23: Time series plots for NO_2 and CH_2O from MAxDOAS at 10° elevation, raw data product from spectral fitting, trace gas concentration integrated over the atmospheric light path. Note that the NO_2 and CH_2O have been divided by 10^{15} (one hundred quadrillion) to simplify the tick marks on the y-axis.

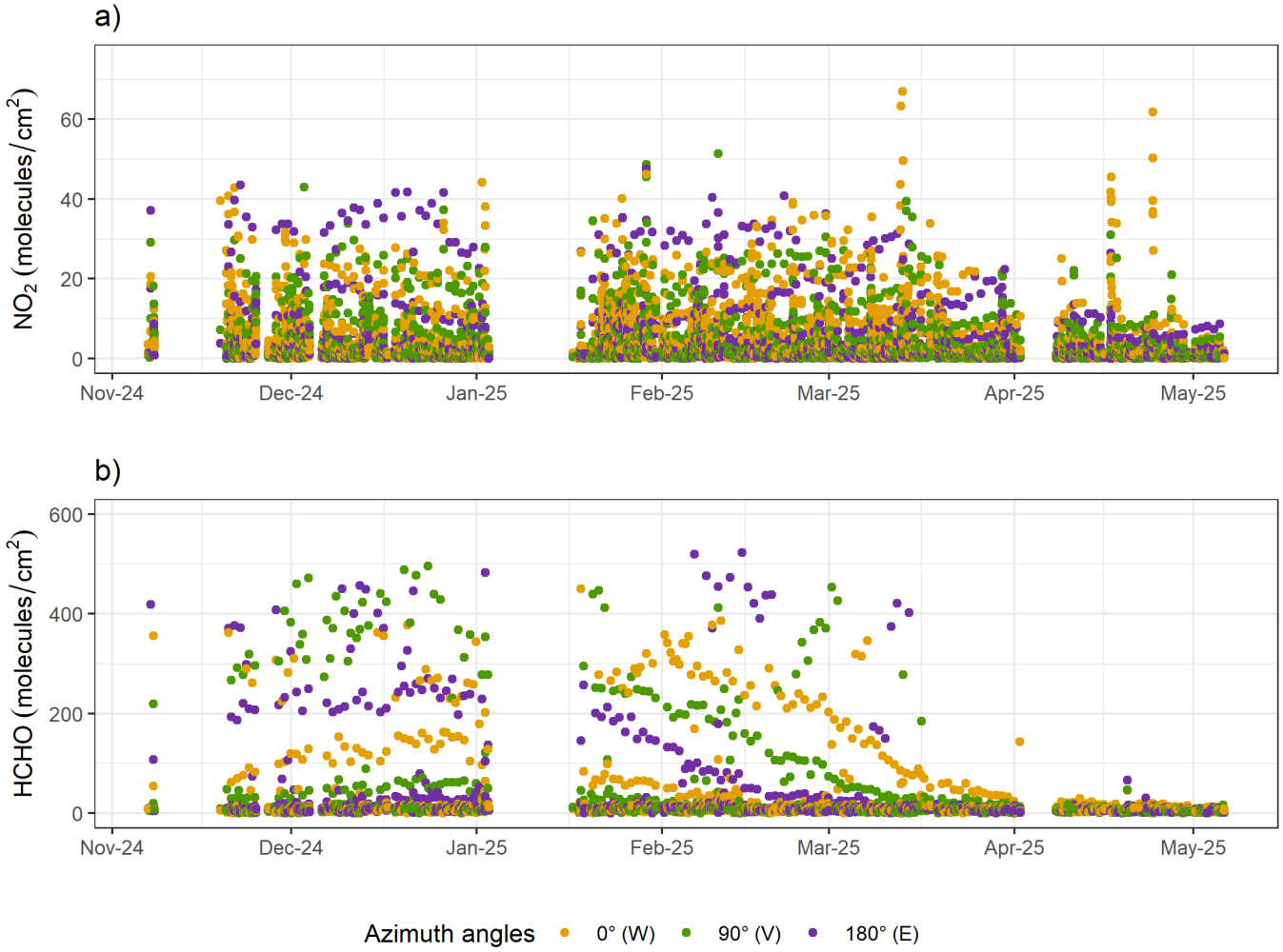

Figure 7.13-24: Time series plots for NO_2 and CH_2O from MAxDOAS at 30° elevation, raw data product from spectral fitting, trace gas concentration integrated over the atmospheric light path. Note that the NO_2 and CH_2O have been divided by 10^{15} (one hundred quadrillion) to simplify the tick marks on the y-axis.

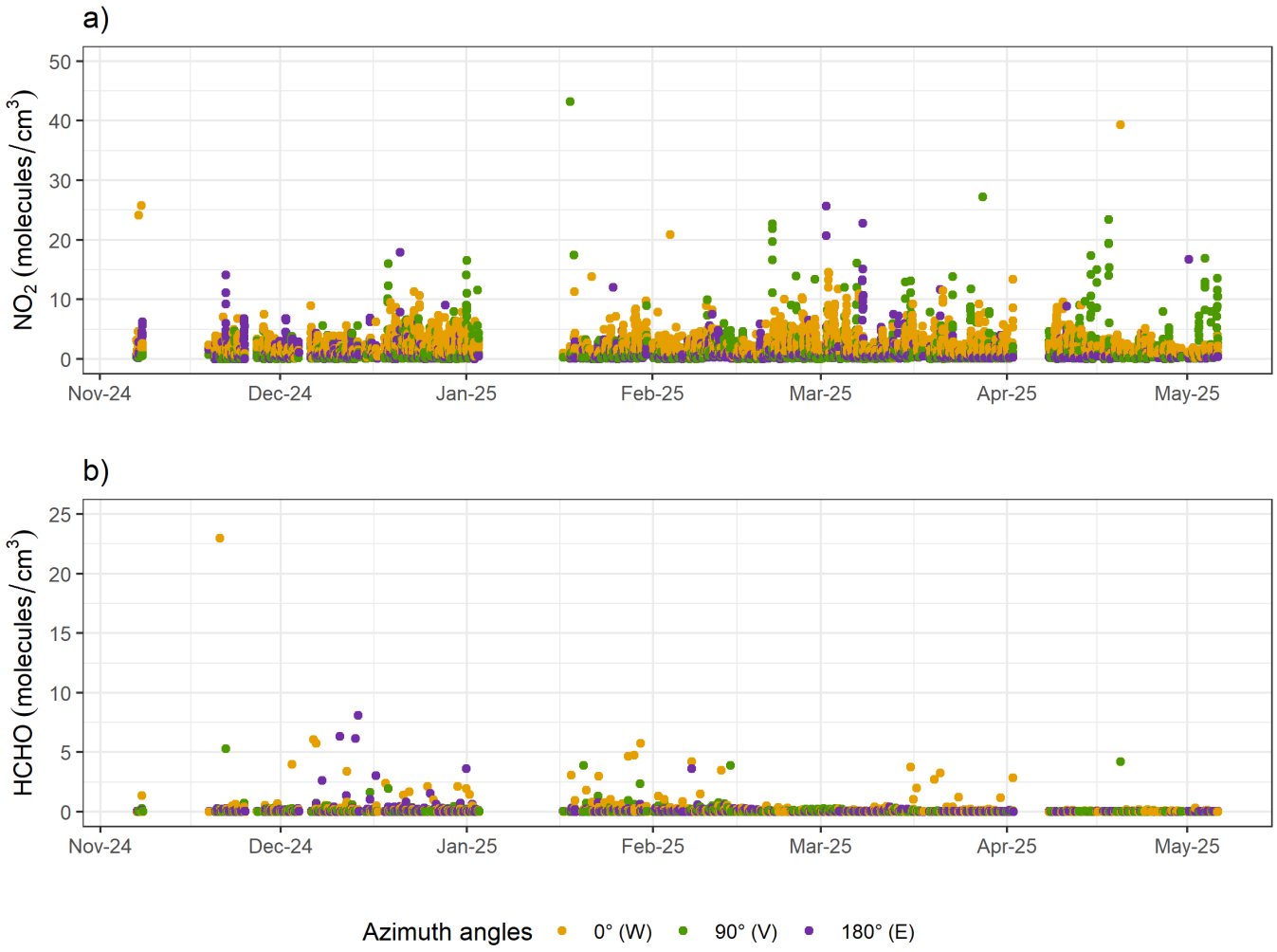

Figure 7.13-25: Time series plots for NO_2 and CH_2O from MAxDOAS at 5° elevation, near surface concentrations estimated from the raw data. Note that the NO_2 and CH_2O have been divided by 10^{10} (one hundred quadrillion) to simplify the tick marks on the y-axis.

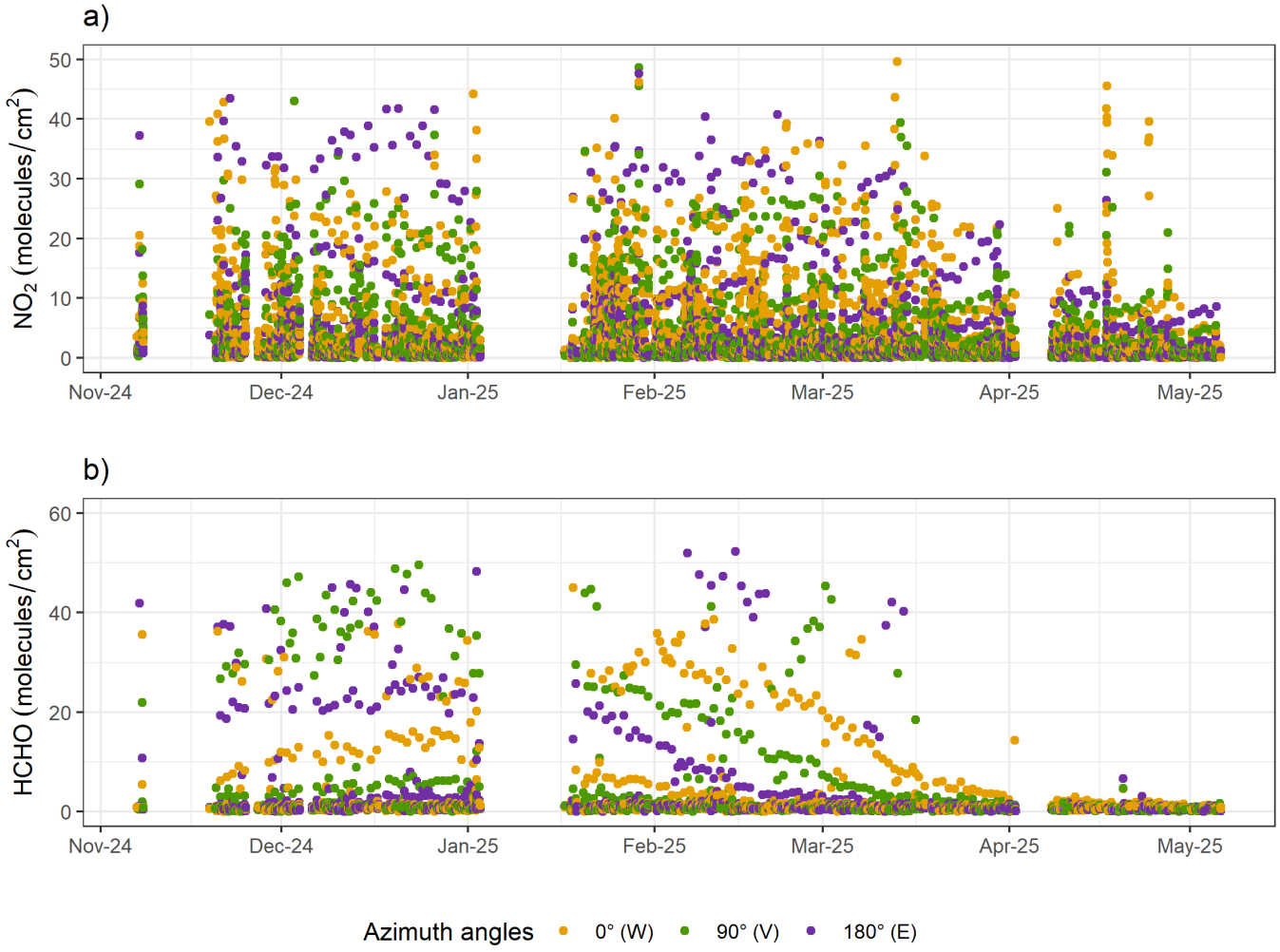

Figure 7.13-26: Time series plots for NO_2 and CH_2O from MAxDOAS at 30° elevation, vertical column density estimate for the trace gas. Note that the NO_2 and CH_2O have been divided by 10^{15} (one hundred quadrillion) to simplify the tick marks on the y-axis.

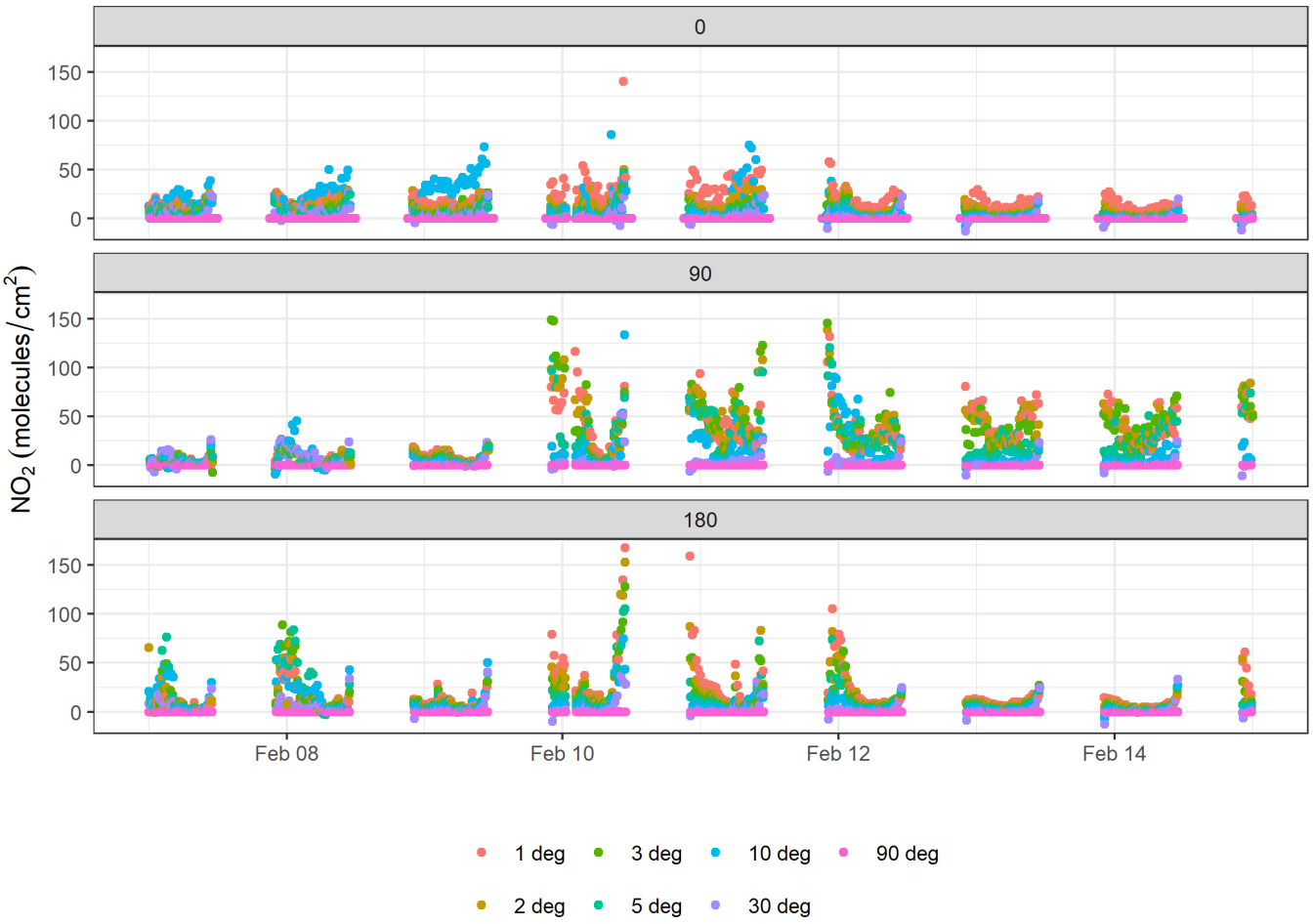

Figure 7.13-27: NO_2 from MAxDOAS for first two weeks in February 2025 at 0° (W), 180° (E) and 90° (N), points are coloured by elevation angle. NO_2 is the raw data product from spectral fitting, trace gas concentration integrated over the atmospheric light path.Note that the NO_2 has been divided by 10^{15} (one hundred quadrillion) to simplify the tick marks on the y-axis.

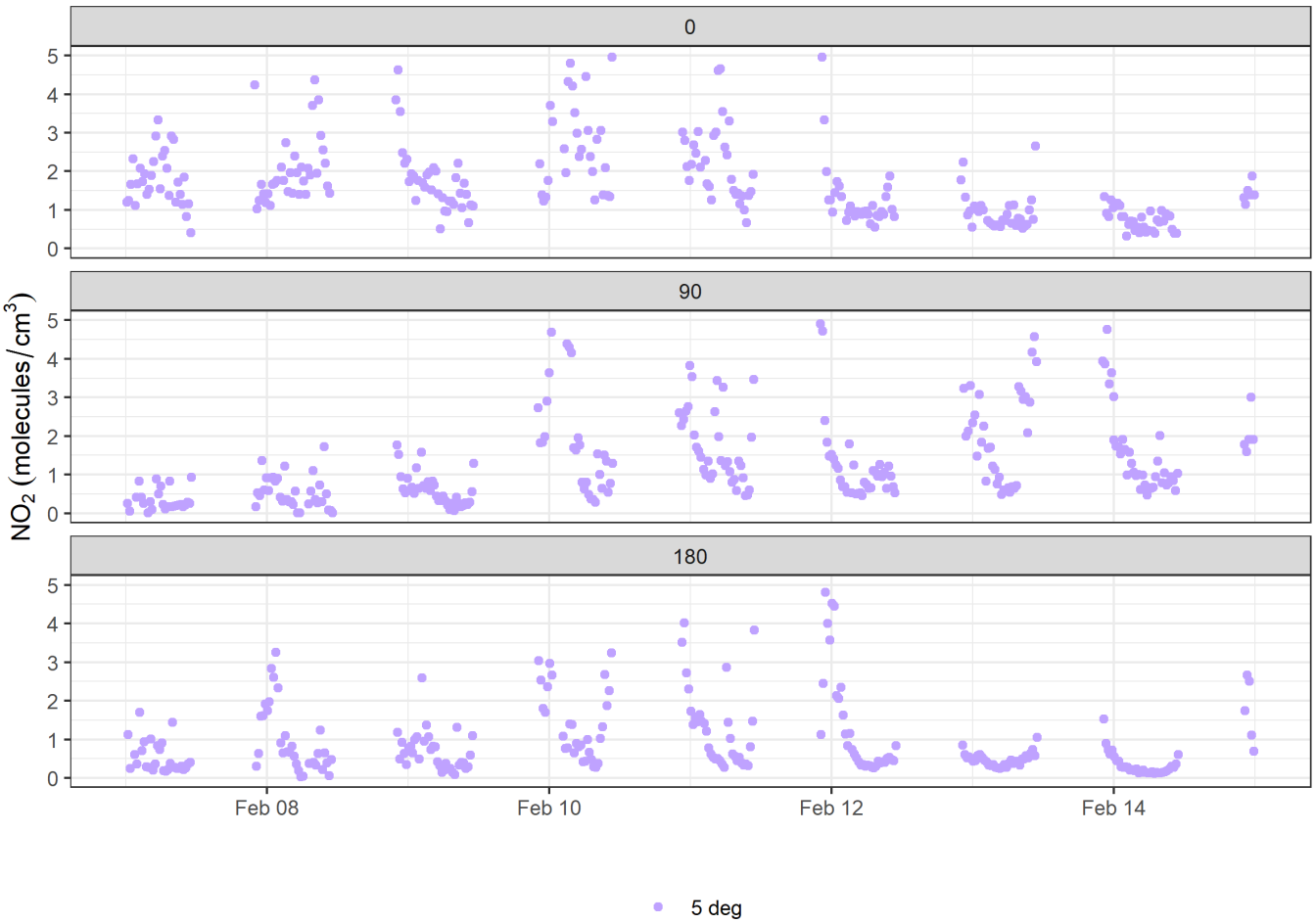

Figure 7.13-28: NO_2 from MAxDOAS for first two weeks in February 2025 at 0° (W), 90° (N) and 180° (E). NO_2 is the near surface concentration estimated from raw data. Note that the NO_2 has been divided by 10^{10} (one hundred quadrillion) to simplify the tick marks on the y-axis.

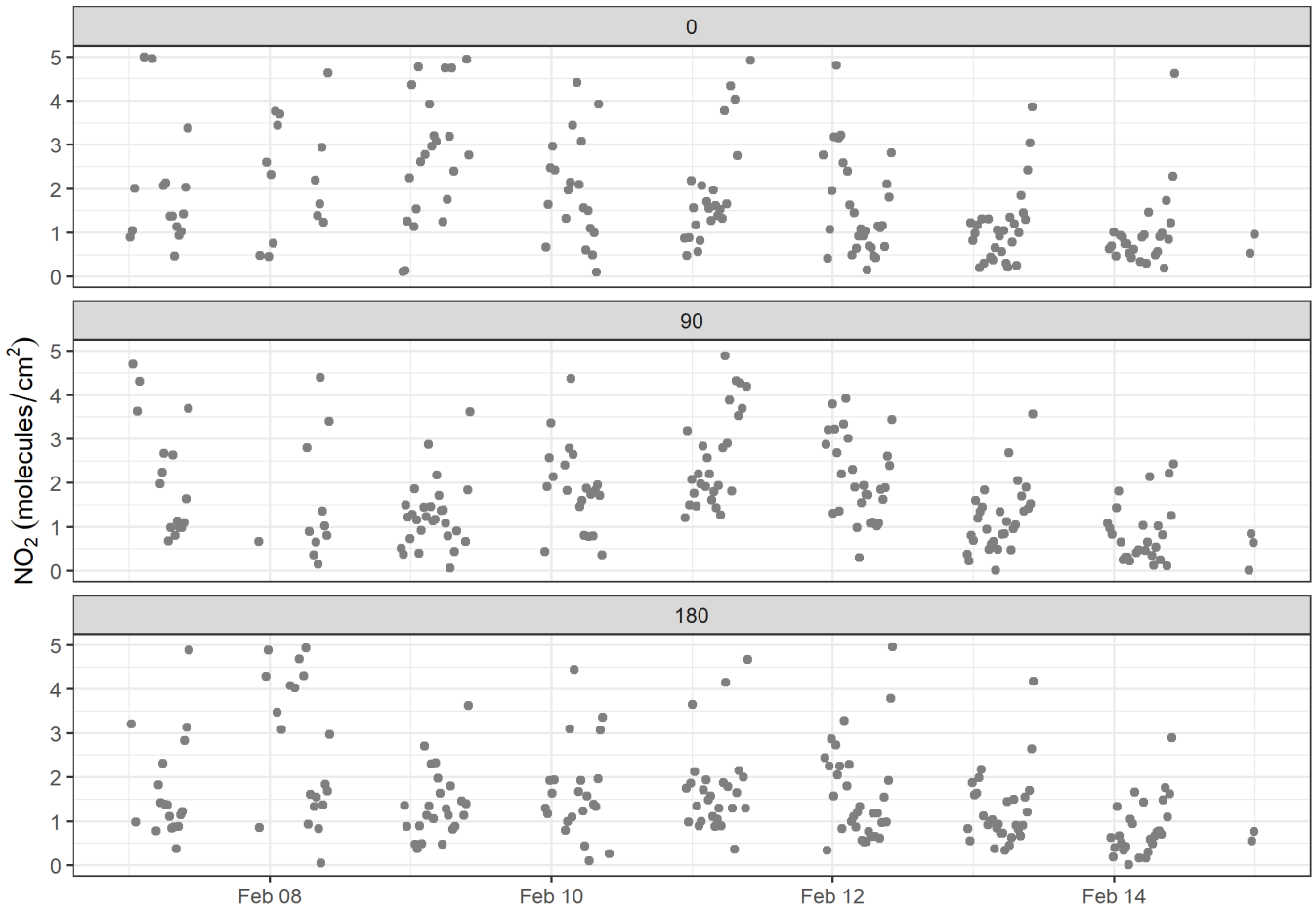

Figure 7.13-29: NO_2 from MAxDOAS for first two weeks in February 2025 at 0° (W), 90° (N) and 180° (E). NO_2 is vertical column density estimate for the trace gas. Note that the NO_2 has been divided by 10^{15} (one hundred quadrillion) to simplify the tick marks on the y-axis.

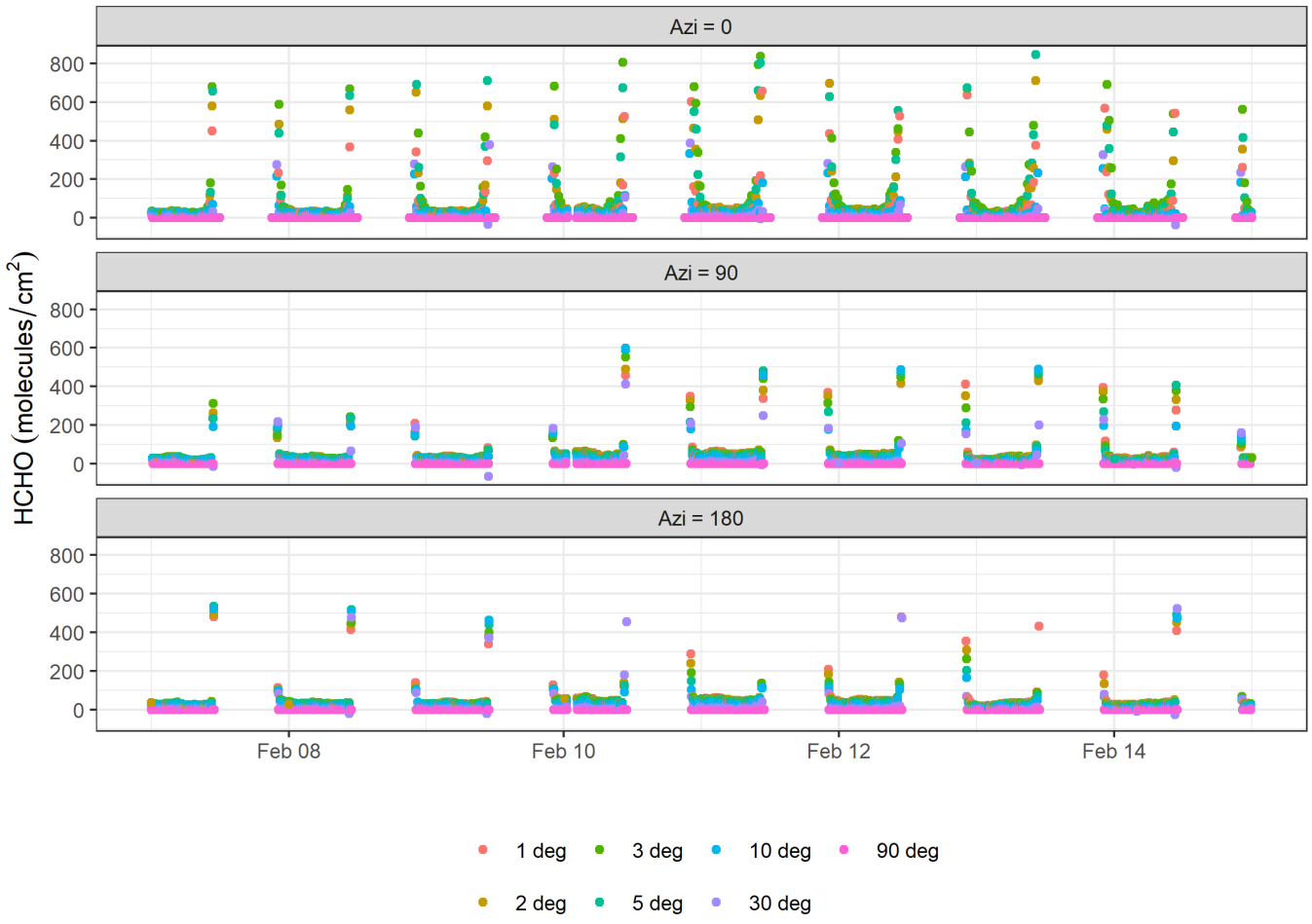

Figure 7.13-30: CH_2O from MAxDOAS for first two weeks in February 2025 at 0° (W), 90° (N) and 180° (E), raw data product from spectral fitting. Note that the CH_2O has been divided by 10^{15} (one hundred quadrillion) to simplify the tick marks on the y-axis.

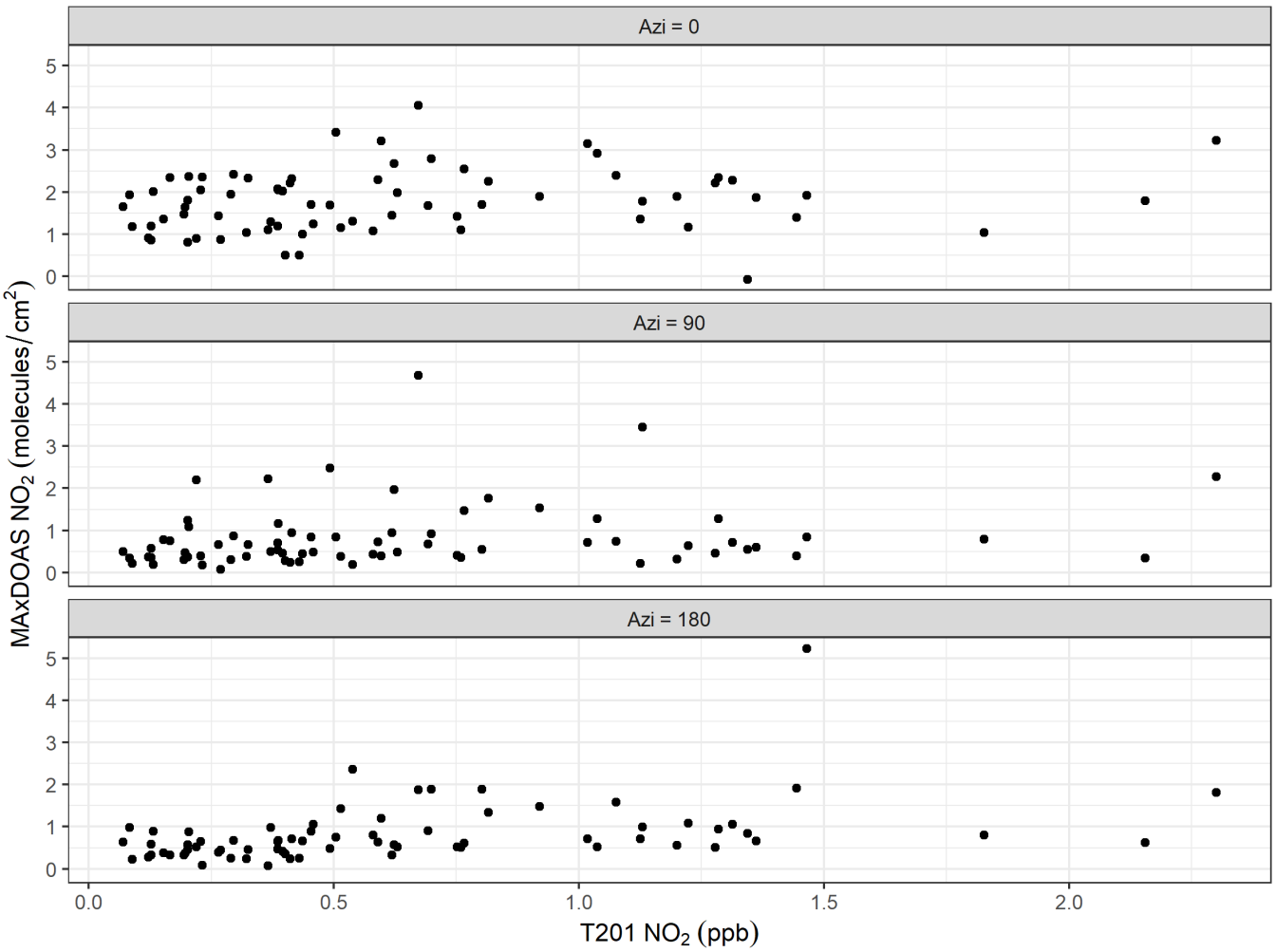

Figure 7.13-31: Scatterplot of NO_2 from T201 and MAxDOAS instruments. NO_2 from the MAxDOAS is the near surface concentrations estimated from the raw data. Note that the NO_2 from the MAxDOAS has been divided by 10^{15} (one hundred quadrillion) to simplify the tick marks on the y-axis.

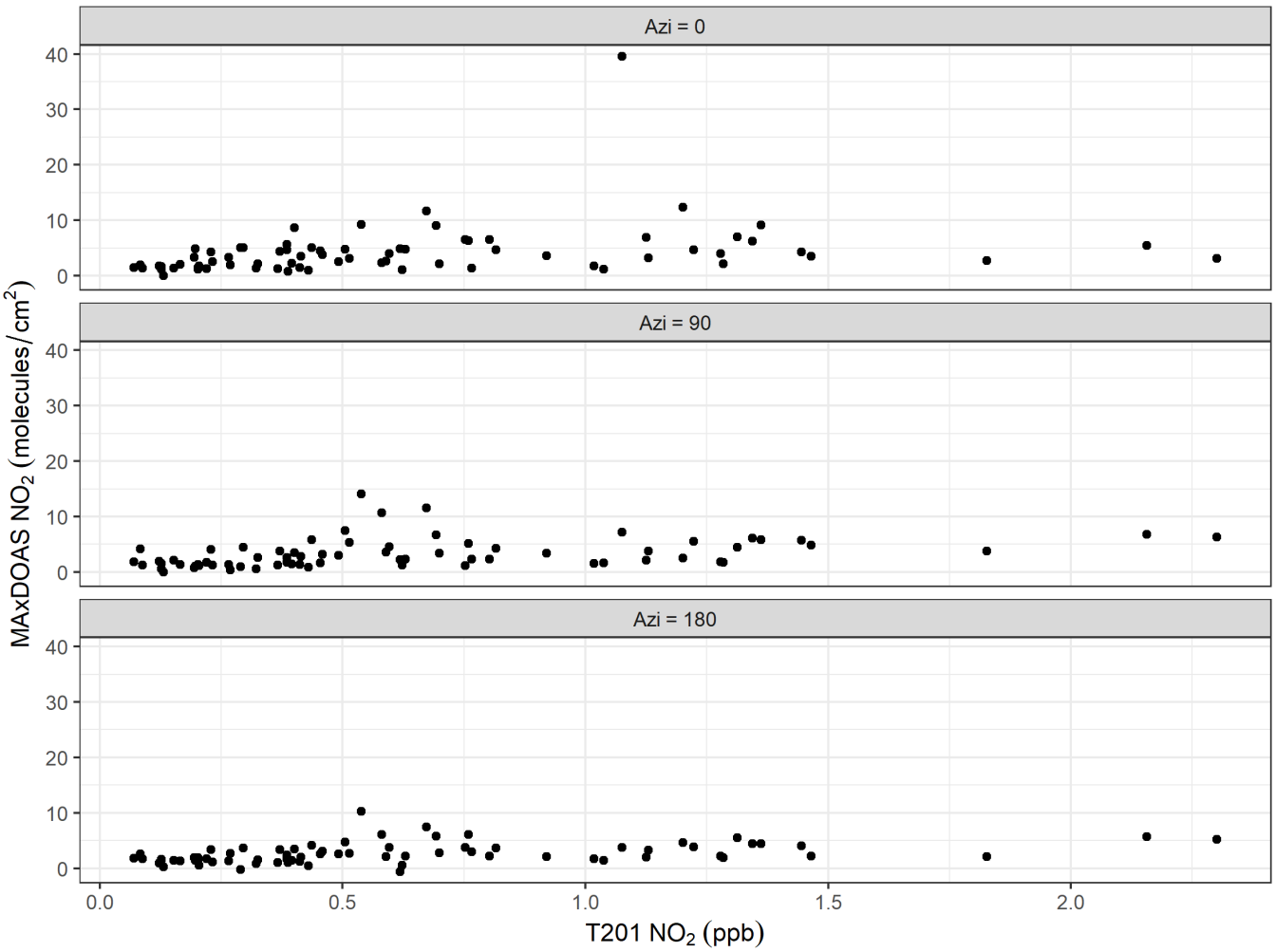

Figure 7.13-32: Scatterplot of NO_2 from T201 and MAxDOAS instruments. NO_2 from the MAxDOAS is the vertical column density estimate for the trace gas. Note that the NO_2 from the MAxDOAS has been divided by 10^{15} (one hundred quadrillion) to simplify the tick marks on the y-axis.

7.13.3.4 Radon

High resolution radon detectors such as the instrument installed at EX09 are typically used to inform the history of the air and air pollution being measured. Put simply, air that has travelled over land has higher levels of radon, sourced from decay of radium in the earth, whereas oceans do not emit any appreciably quantity of radon typically. This permits a greater understanding of air flow, meteorology and source apportionment relative of other pollutants relative to Rn concentration. As a simple example, shipping emissions and long range ocean transport of air pollutants would be associated with lower Rn compared to terrestrial or local land based sources.

It was for the above reason that the Radon detector was specified for the Murujuga AQM network.

Radon has a half-life of 3.82 days, so all radon in the air will be sufficiently depleted in the order of weeks. However, at Murujuga, if natural gas is extracted and combusted locally in a sufficiently short time, then radon will be emitted along with the usual hydrocarbons and other gas species. A preliminary analysis of radon with respect to wind direction appears to show that radon levels are highest when the wind is blowing across the gas plants to EX09, suggesting this is indeed the case.

So in this case it appears that Rn emissions from natural gas combustion may be a useful source apportionment tool for sufficiently ”fresh” gas combustion, rather an indirect association with terrestrial Rn and emissions coming from a south-easterly direction (main land concentration relative to EX09). Section 8 presents analysis and discusses this further.

A more thorough analysis will be provided in the final study report.

Figure *7.13-33* shows an example time series of diurnal radon measurements.

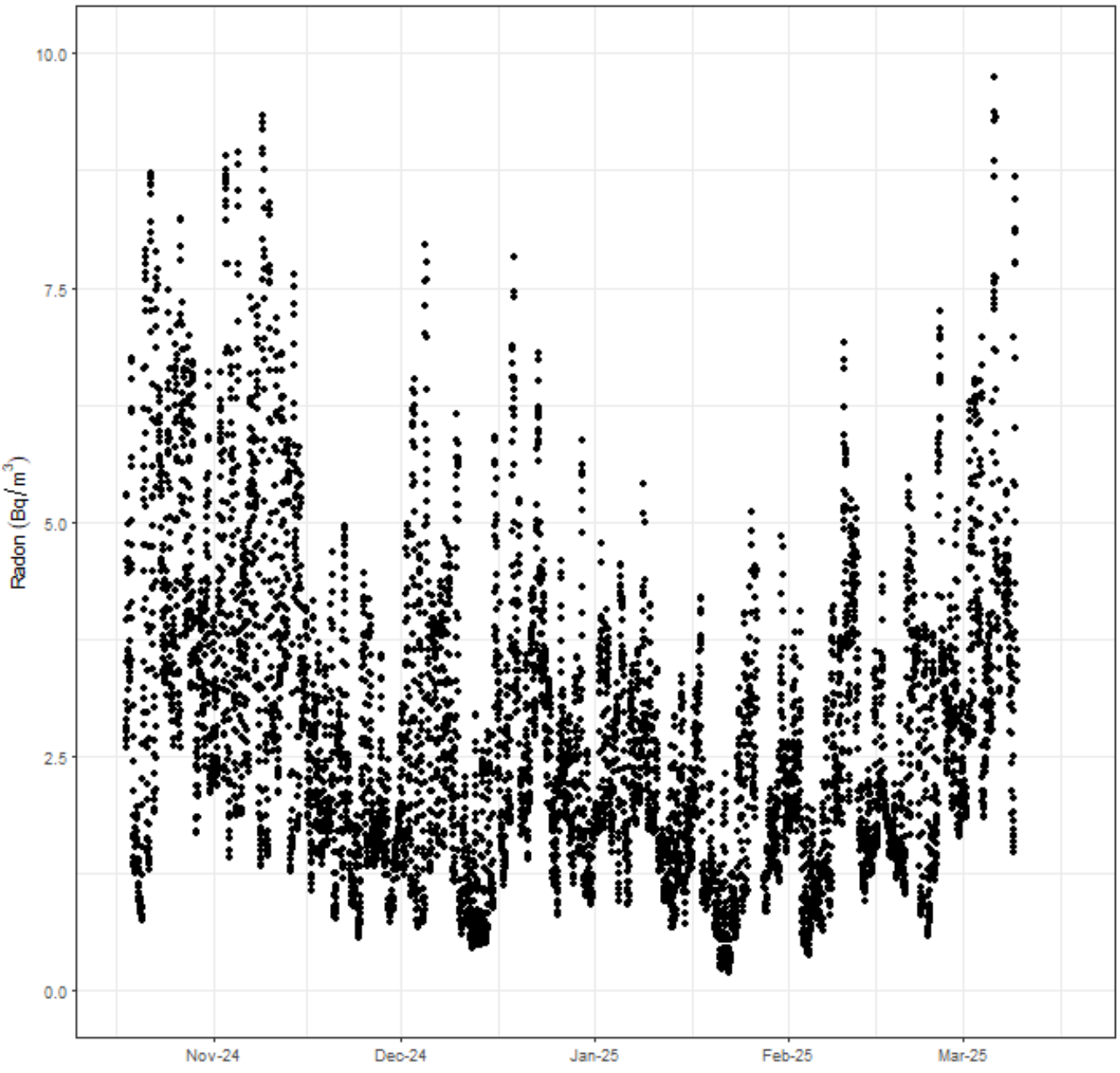

Figure 7.13-33: Time series plot of radon at EX09.

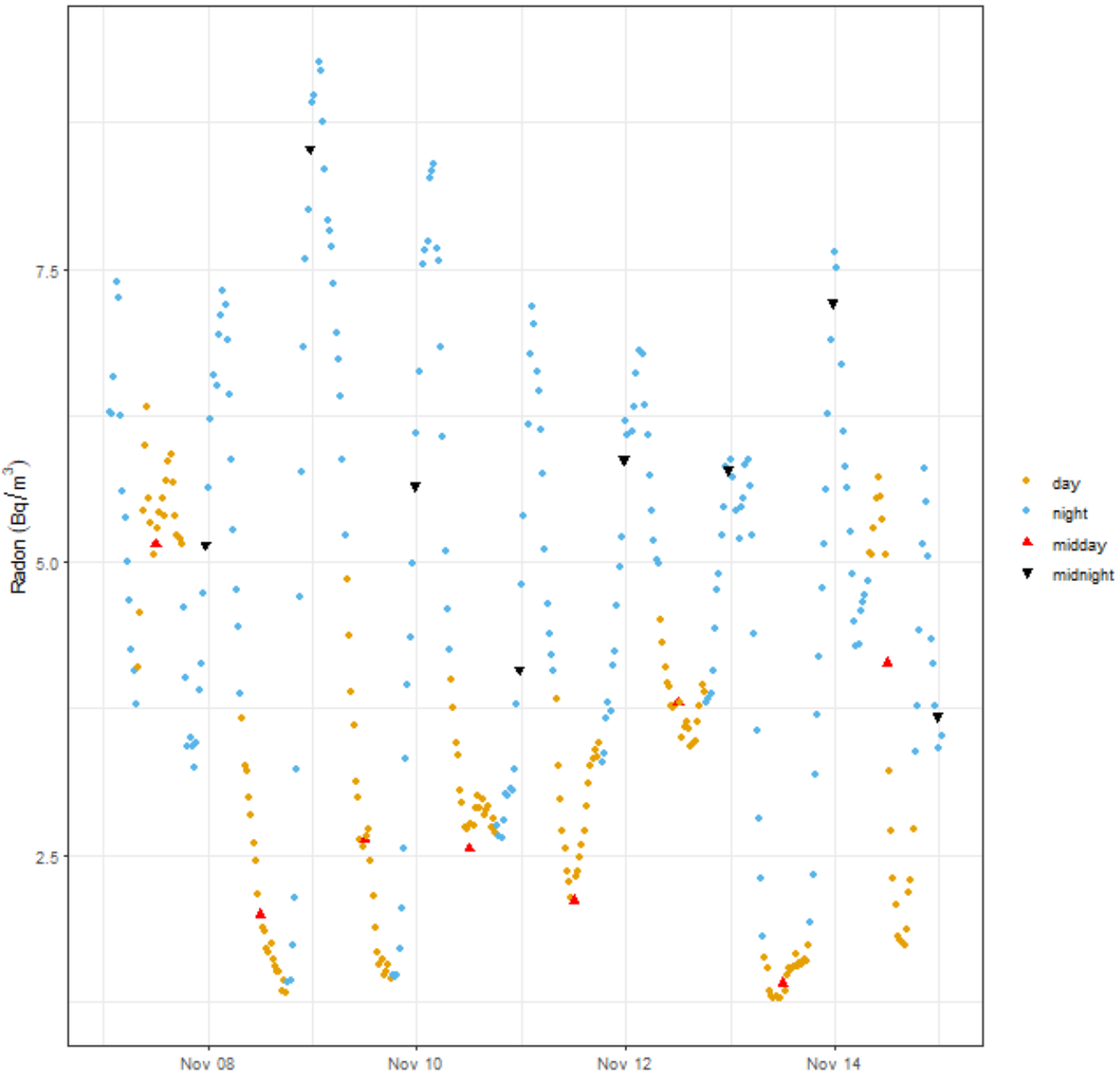

Figure 7.13-34: Time series plot of radon at EX09 over one week in November 2024. Daytime is defined as 8 am to 6 pm, associated with convective atmospheric mixing rather than daylight hours, and nighttime is the rest of each day.

This page is intentionally blank.

7.14 Low powered sensors

Each of the 21 AQMs deployed are fitted with a set of 'low powered' sensors for measurement of CO_2, NO, NO_2, NH_3, $PM_{2.5}$ and PM_{10}. While it is acknowledged that these do not measure to the same level of accuracy as the real time instruments in the powered AQMs, they may provide additional information on trends which cannot be captured via the passive samplers. The low powered sensors operate on the same measurement principle as many of the 'reference grade' powered instruments, however the latter operate in a temperature and humidity controlled environment with regular calibration. The sensors are typically supplied with a hard coded conversion from a voltage or a unit of concentration, e.g. ppm, count per unit volume or mass concentration. At the commencement of the MRAMP project it was decided to deploy the sensors without any further calibration (at least initially) since 3 systems would be co-located with the reference grade instruments. Data presented here is therefore "raw" data.

The ability to deploy the low powered sensors at each passive site provides additional temporal data that would otherwise not be available. Furthermore, the co-location of these with the real time instruments at the powered AQM sites provides a means of comparison and calibration. For further details see Section 5.

Low-powered sensor data are available for all sites, when there is uninterrupted power. From time to time, there have been power losses at the passive sites, owing to issues with the battery, solar chargers or fuses, meaning that low powered sensor data could not be captured. The low powered sensors (particularly the electrochemical sensors) have a short life-time with replacement needed approximately every two years, or when deterioration in performance is detected. Deteriorating performance of these sensors may affect analysis results. Some low powered sensors (e.g. NH_3) experience a hysteresis curve after power cycling, and require 30-60 minutes to return to an expected or previously measured value.

The data displayed in the following sections considers the concentrations obtained from the low powered sensors, applying only the manufacturer specified conversion from voltage to concentration. In many cases this is at least an order of magnitude different to actual levels and it is acknowledged that a more rigorous calibration procedure is likely required for these sensors, which can hopefully be retrospectively applied to existing datasets. While concentrations in the figures below are nominally provided in ppm, these values should not be used for any compliance monitoring purposes, or in isolation. Therefore, the results here are interpreted purely in terms of the trends and relative change in values, which would suggest that the sensors are functioning as intended, and responding to varying levels of chemical species in the field. Readings from these sensors are considered in relation to both ambient temperature and humidity, and the results of the low powered sensors at the powered sites are compared to the results of the co-located real time instruments in Section 8.4.

7.14.1 NO

Data from the low powered sensors for NO from January 2024 to February 2025 are shown in Figure *7.14-1*. Six selected sites are considered, three sites are co-located with the three powered sites (to allow for comparison to the powered instruments) and three sites spanning the range of monitoring stations from north to south (AQ18, AQ11 and AQ04). These show that NO is consistently present at these sites throughout the year and suggest that there may be some

variation in levels throughout the year.

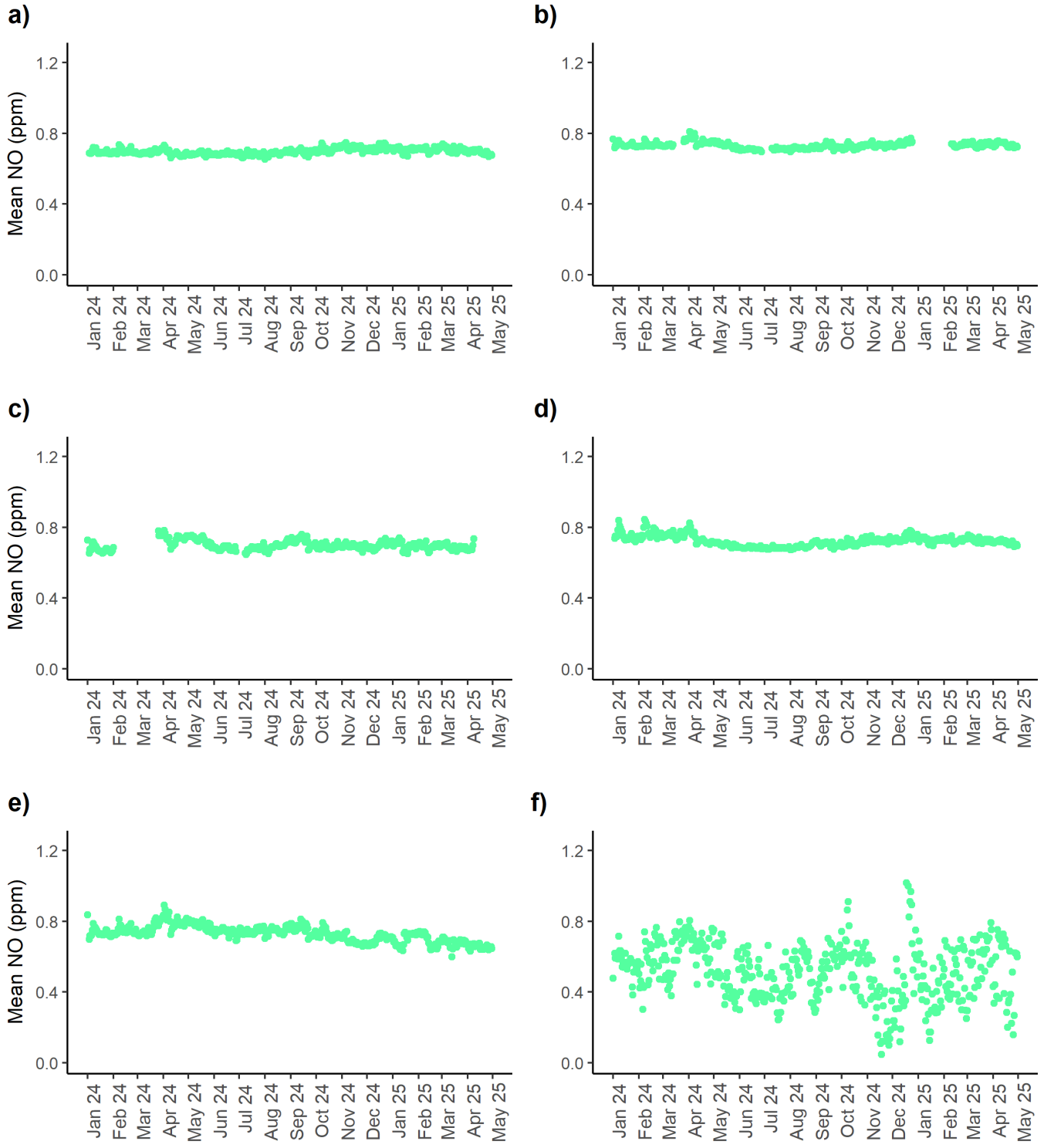

Figure 7.14-1: Time series plots for NO measurements from low powered sensors from January 2024 to February 2025 (inclusive), at locations (a) AQ01, (b) EX02, and (c) EX09, (d) AQ04, (e) AQ11, (f) AQ18. Where each point is the daily mean of NO.

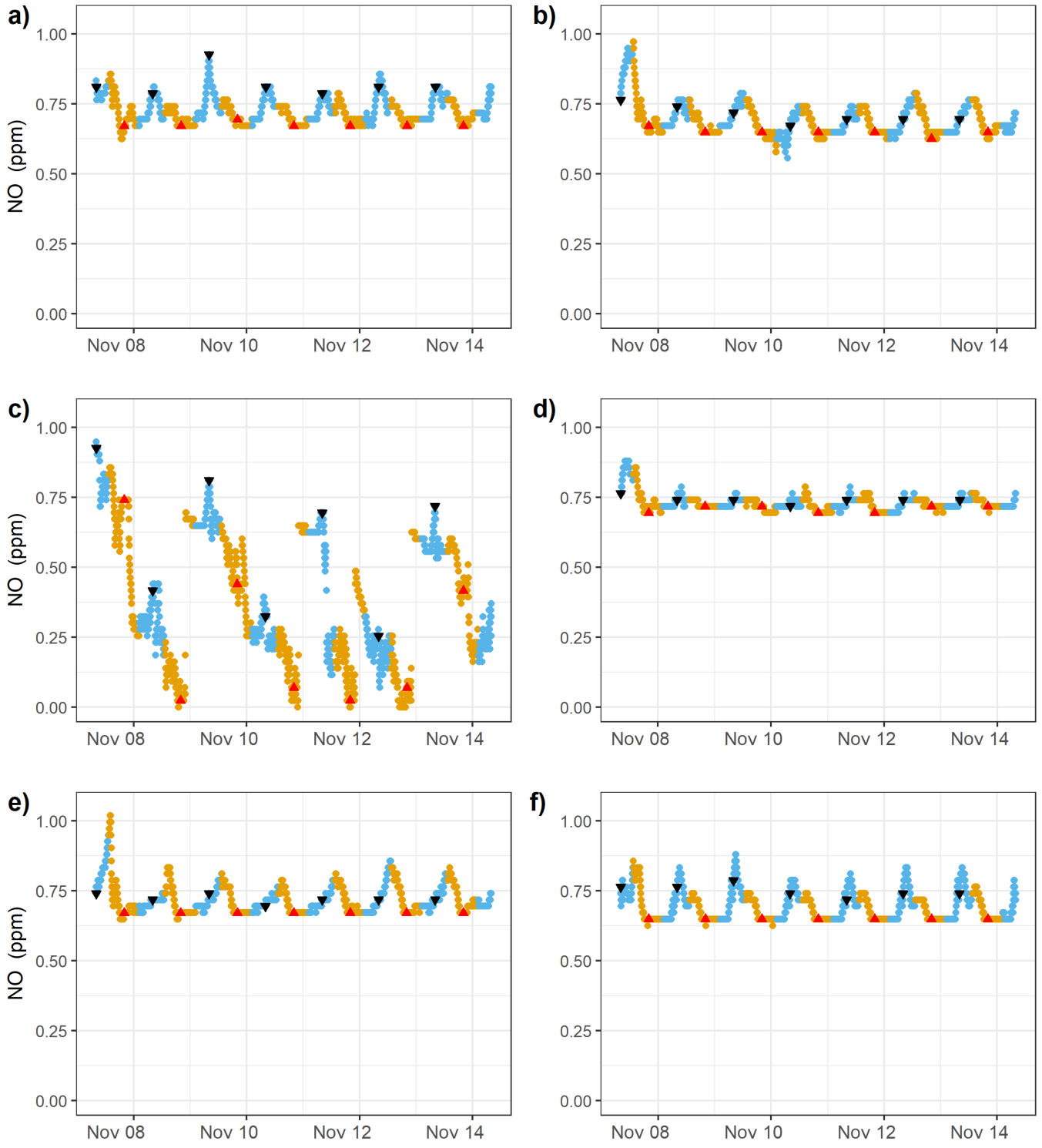

Figure 7.14-2: Time series plots for NO measurements from low powered sensors over one week in November 2024, at locations (a) AQ01, (b) EX02, and (c) EX09, (d) AQ04, (e) AQ11, (f) AQ18. The data shown in blue corresponds to nighttime (defined as sunset to sunrise) measurements, and data shown in orange correspond to daytime (defined as sunrise to sunset). The red up-pointing triangles are midday and black down-pointing triangles are midnight.

Similar to the real time powered instruments, low powered data was further examined by looking at a single selected week in. For consistency, the same week in November 2024, as previously used in Section 7.13.1, was selected. These results are shown in Figure *7.14-2*, for the same sites presented in Figure *7.14-1*. The data shown indicate a variation in levels of NO throughout the day, with levels tending to decrease in the morning hours and reaching a minimum around midday, before increasing again in the afternoon. This pattern is relatively consistent across all sites, with the exception of EX09 (Figure *7.14-2*(c)) where there is a general decline in levels over approximately two days, before a sharp increase during the nighttime and then a repeat of the pattern.

7.14.2 NO_2

Data from the low powered sensors for NO_2 from January 2024 to February 2025 are shown in Figure *7.14-3*. Figure *7.14-3* shows data for the same six sites selected for NO. For the three powered sites (Figure *7.14-3*(a) - (c)) and AQ04 (Figure *7.14-3*(d)) there appears to be minimal variation in NO_2 levels over time. For AQ11, there is slightly more variation over the year between May 2024 and May 2025, with an apparent decrease in levels. NO_2 levels at AQ18 appear less consistent, with noticeable variation over the measurement period.

To explore any variation over a shorter time period, the same week in November 2024 was again selected. These results are shown in Figure *7.14-4*. These generally show slight day-to-night fluctuations with lower nighttime levels.

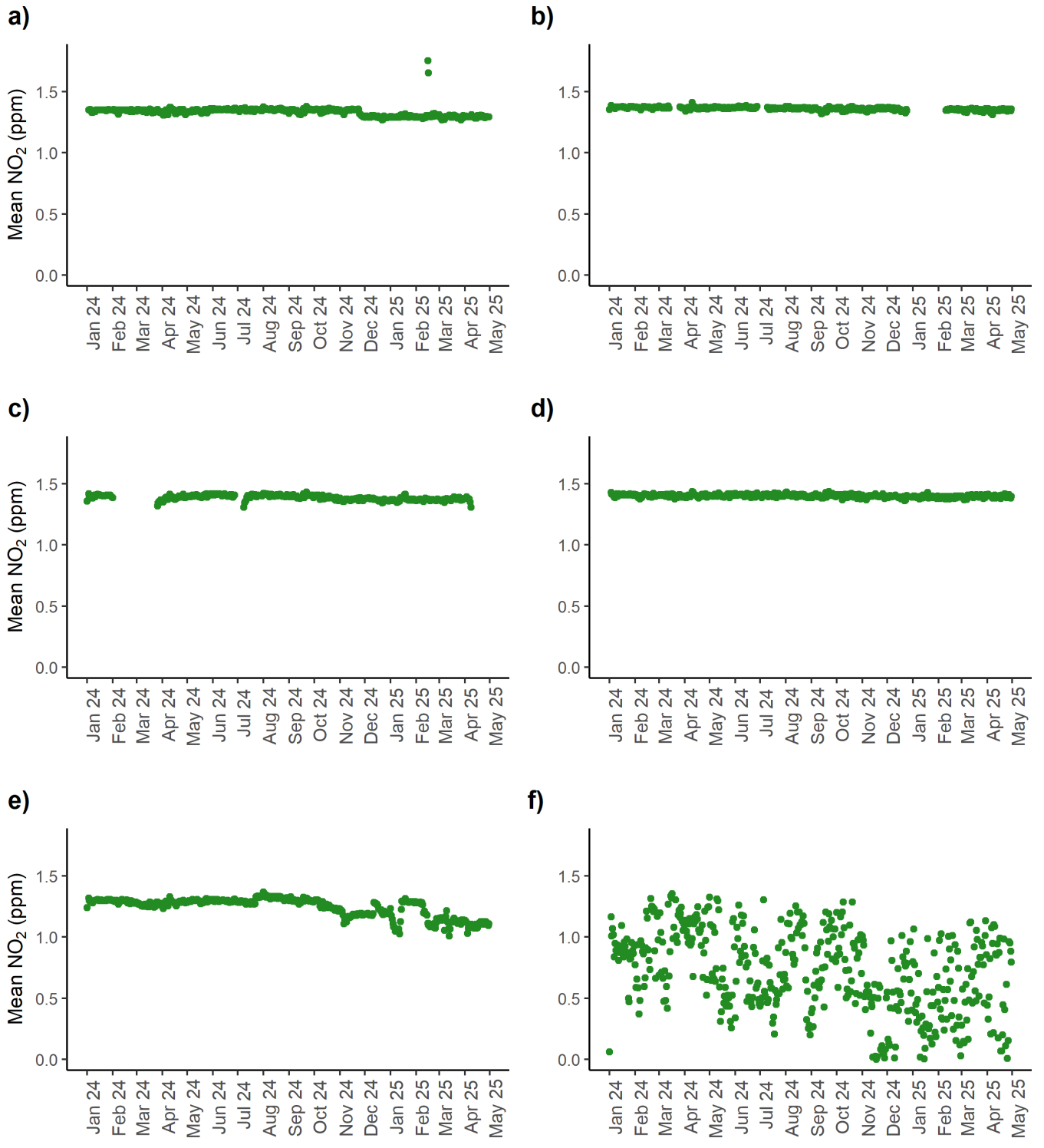

Figure 7.14-3: Time series plots for NO_2 measurements from low powered sensors from January 2024 to April 2025 (inclusive), at locations (a) AQ01, (b) EX02, and (c) EX09, (d) AQ04, (e) AQ11, (f) AQ18. Where each point is the daily mean of NO_2.

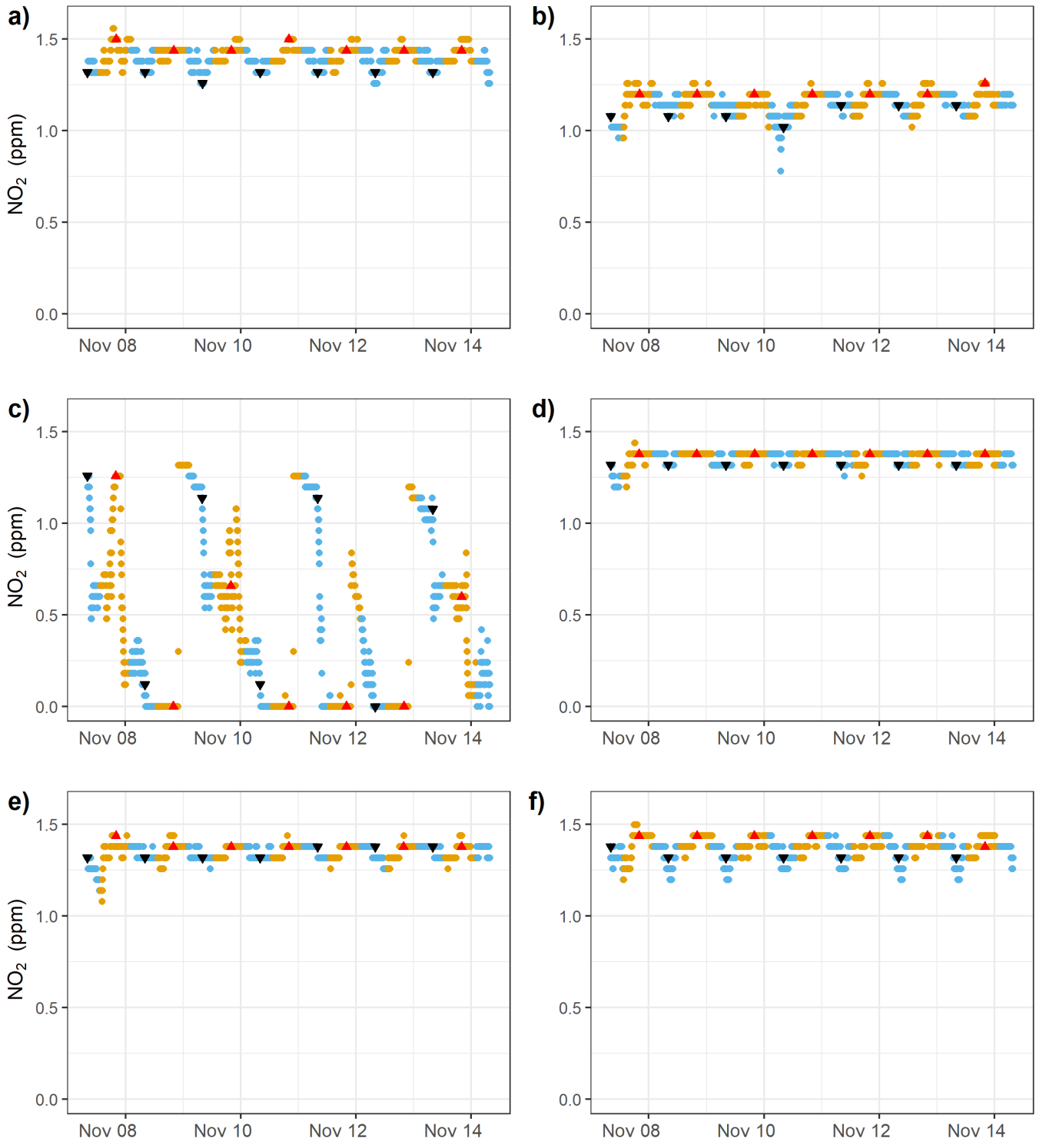

Figure 7.14-4: Time series plots for NO_2 measurements from low powered sensors over one week in November 2024, at locations (a) AQ01, (b) EX02, and (c) EX09. The data shown in blue corresponds to nighttime (defined as sunset to sunrise) measurements, and data shown in orange correspond to daytime (defined as sunrise to sunset). The red up-pointing triangles are midday and black down-pointing triangles are midnight. Data have been excluded where the validity is in question.

7.14.3 NH_3

Data from the low powered sensors for NH_3 from January 2024 to February 2025 are shown in Appendix D-6 . These figures show data for the same six sites selected for NO and NO_2. However, these figures show that the NH_3 measurements are degrading with the observed values tending to flatten out to a small range of low values. It was confirmed that the gas sensors have reached end of life and need replacing. The relevant plots have been placed in Appendix D-6-1. The measurements shown may not be reliable.

7.14.4 CO_2

Data from the low powered sensors for CO_2 from January 2024 to February 2025 are shown in Figure *7.14-5*. A calibration correction (dividing by 14.09) was applied to all CO_2 (See Section 8.4.2). Figure *7.14-5* shows data for the same six sites selected for NO, NO_2, and NH_3. The measurements fall around a similar mean value for all sites, but measurements can occasionally be considerably higher, which would not be considered unusual given the possible range of combustion-related events that occur in the region, and the irregular nature of some of these (e.g., bushfires, flaring events). These sensors have not been yet been calibrated beyond the manufacturer supplied calibration. The following section applies a preliminary calculation. Temperature and humidity related drift may be possible, as with the other sensors.

As before, the day-to-day sensor responses are shown more clearly by considering the same selected week in November 2024. Figure *7.14-6* shows evidence of a daily cycle in CO_2 levels, with the lowest levels occurring around midnight, followed by a steady increase through the morning with a daily peak occurring before midday, or sometimes mid-morning. This appears to be consistent across the six selected sites. The results show evidence of a second peak in the early afternoon at the start of the week. This may be evidence of an additional or unusual combustion event. This appears to impact the CO_2 levels across the six chosen sites.

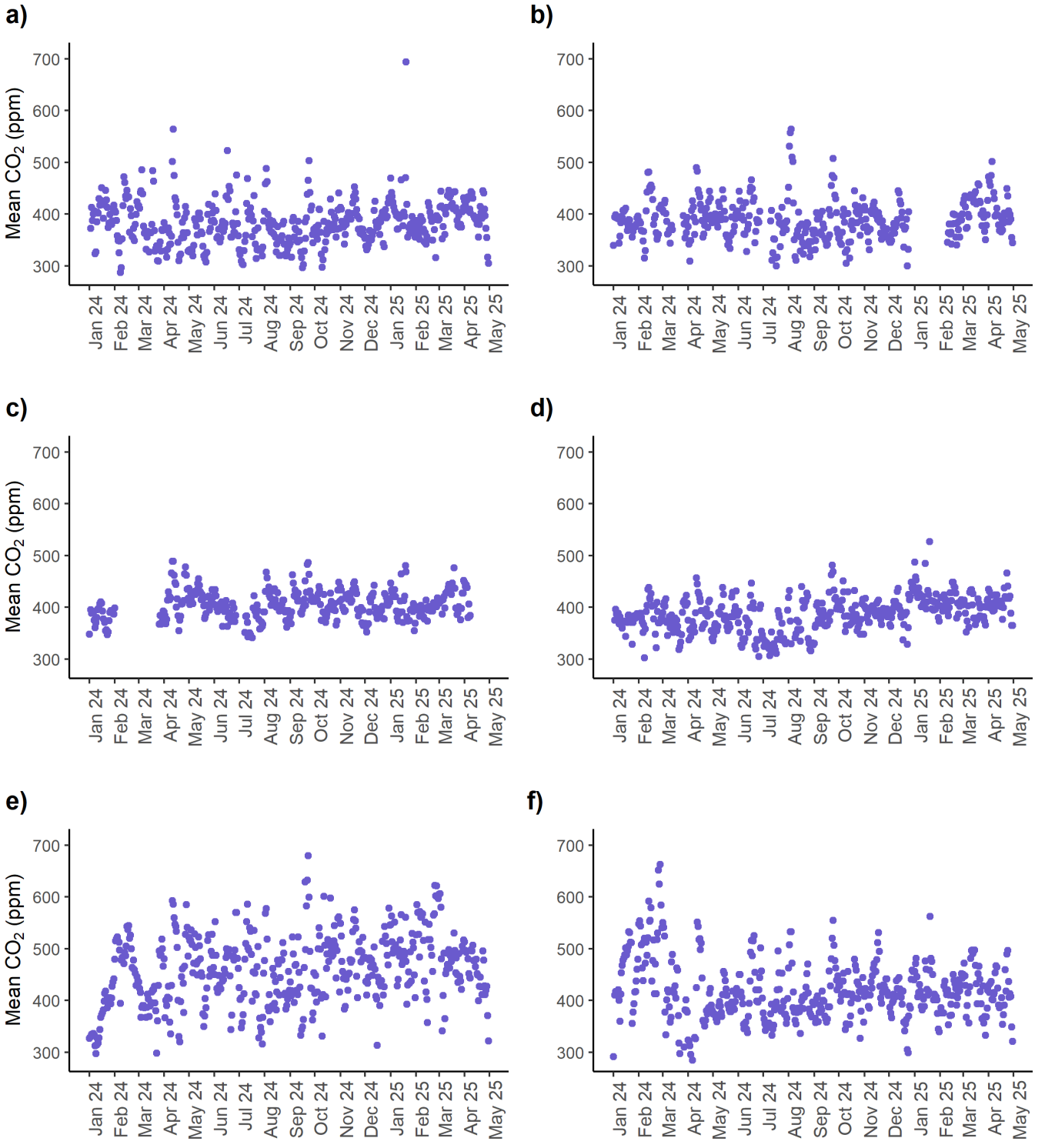

Figure 7.14-5: Time series plots for CO_2 measurements from low powered sensors from January 2024 to February 2025 (inclusive), at locations (a) AQ01, (b) EX02, (c) EX09, (d) AQ04, (e) AQ11, and (f) AQ18. Where each point is the daily mean of CO_2.

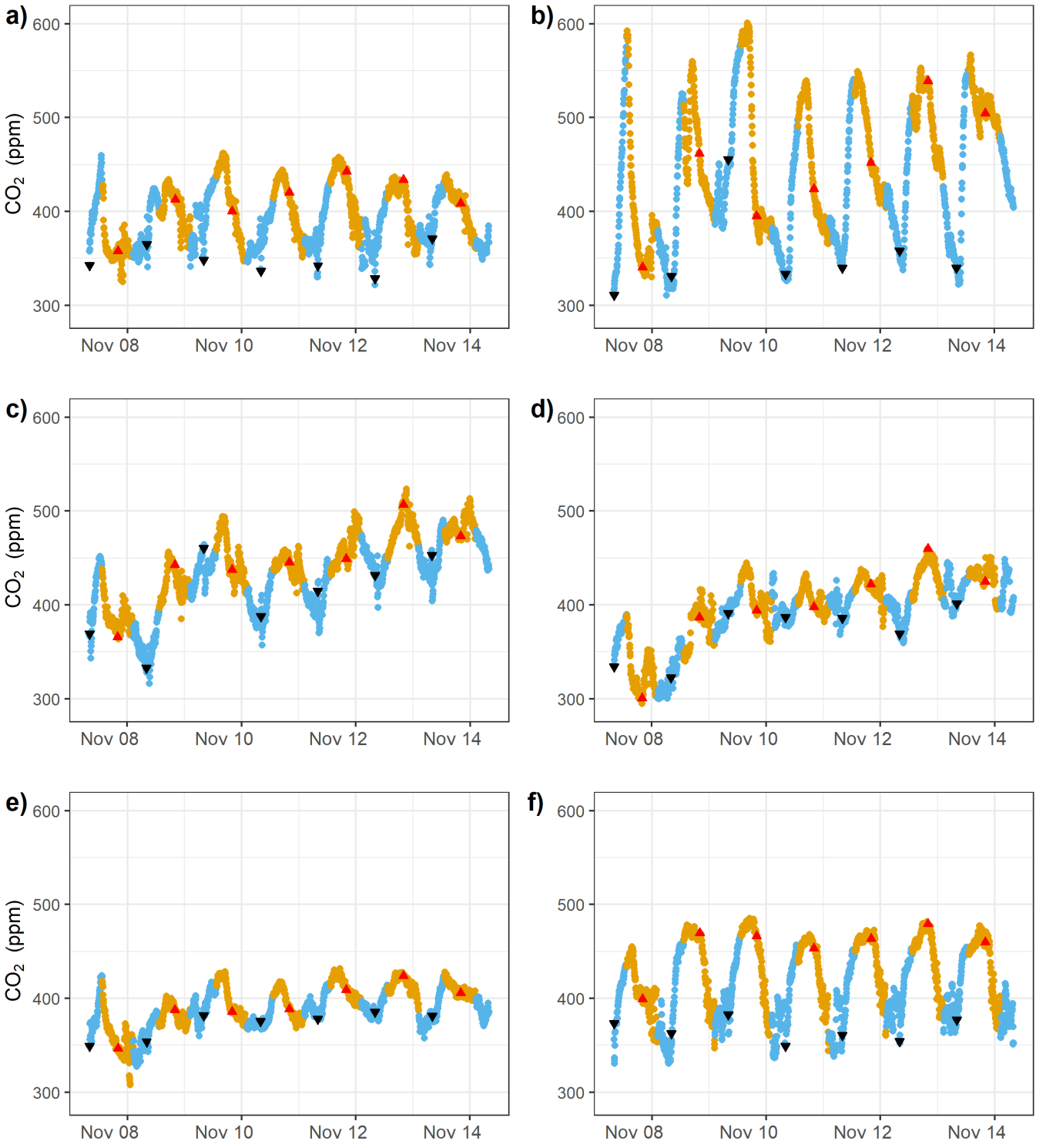

Figure 7.14-6: Time series plots for CO_2 measurements from low powered sensors over one week in November 2024, at locations (a) AQ01, (b) EX02, (c) EX09, (d) AQ04, (e) AQ11, and (f) AQ18. The data shown in blue corresponds to nighttime (defined as sunset to sunrise) measurements, and data shown in orange correspond to daytime (defined as sunrise to sunset). The red up-pointing triangles are midday and black down-pointing triangles are midnight.

7.14.5 Particulates

The low powered PM sensors utilise The same six sites used above are also considered in relation to the results for particulate ($PM_{2.5}$ and PM_{10}) measurements from the low powered sensors. While these sensors are claimed to be able to report other size fractions (e.g., PM0.3, PM0.5, PM1, and PM5), this analysis is limited to the most typically used fractions for environmental dust monitoring. The low powered PM sensors work on an optical, scattered light principle. Therefore the primary measurement is count based, which then must assume a density and shape factor to obtain a mass concentration as output. The sensor technical manual variously states that the output is given in $\mu g/m^3$, however other sections report the output is in particle count per 100 ml air sampled. Either way, the sensors clearly require additional calibration or unit conversion. Data presented here does not have any additional density correction or calibration imposed and is labelled with a placeholder unit of $-/cm3$.

The results for $PM_{2.5}$ are shown in Figure *7.14-7* for the period between January 2024 and May 2025. As with the results shown previously from the real time powered FIDAS instrument, these results show evidence of what could reasonably be described as a dusty environment. This is especially the case in early 2024, where the dust levels appear to be the highest across the six chosen sites (and across the north-to-south span of the monitoring sites). Of particular interest is EX09 (Figure *7.14-7*(c)), where the dust levels appear to be higher than at the other sites. Given that EX09 is the highest site and experiences considerable winds (and regular changes in wind direction), the possibility of both the transport of dust by air currents and the recirculation (and even the resuspension) of dust in the air over the monitoring sites should be considered.

The results also show a decrease in dust levels through the middle of the year, before there is an increase toward the end of the year, which may suggest that there is some seasonal variation or pattern in dust levels. This could be related seasonal wind patterns that affect the wind direction and average wind speed. Dust levels may also be affected by rainfall: extended wet periods may effectively remove dust from the air, with dust levels increasing once the rain stops and the ground has dried. Rainfall in the Murujuga area can be erratic, with large rainfall due to events such as tropical cyclones. This may explain the higher dust levels recorded in January 2024 compared to January 2025 when a tropical cyclone led to higher rainfall in that month.

Figure *7.14-8* shows the diurnal cycles more clearly, which often show peaks in the afternoon and evening, corresponding to typically higher winds during these times increasing local dust generation from natural and anthropogenic sources. While some $PM_{2.5}$ may be from combustion sources and is typically assumed to be the case for global particulate matter (especially in urban areas), our analysis of Pilbara dusts and ores show they tend to have a non-trivial fine ($PM_{2.5}$) fraction.

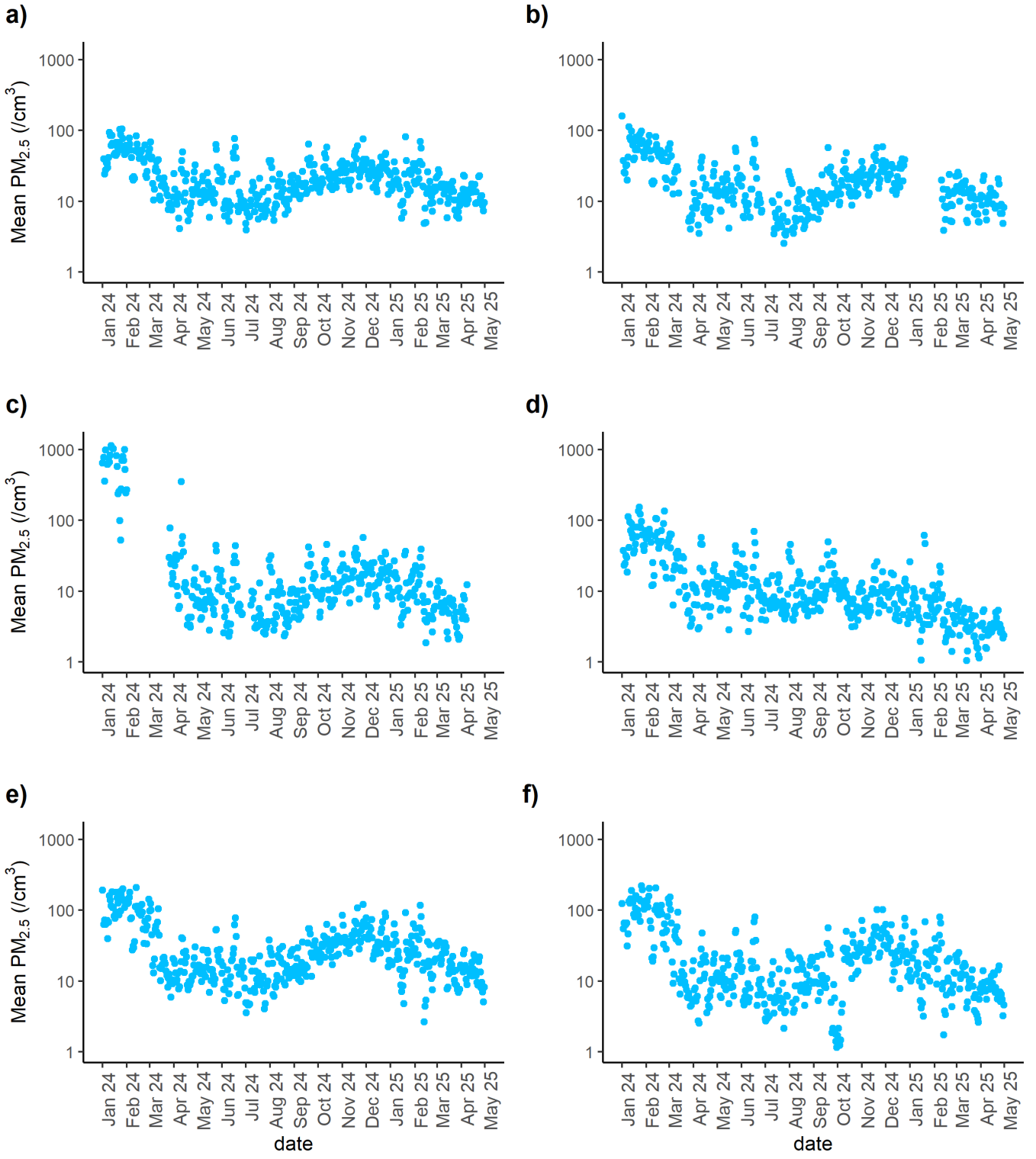

Figure 7.14-7: Time series plots for $PM_{2.5}$ measurements from low powered sensors from January 2024 to April 2025 (inclusive), at locations (a) AQ01, (b) EX02, and (c) EX09, (d) AQ04, (e) AQ11, and (f) AQ18. Each point is the daily mean of $PM_{2.5}$.

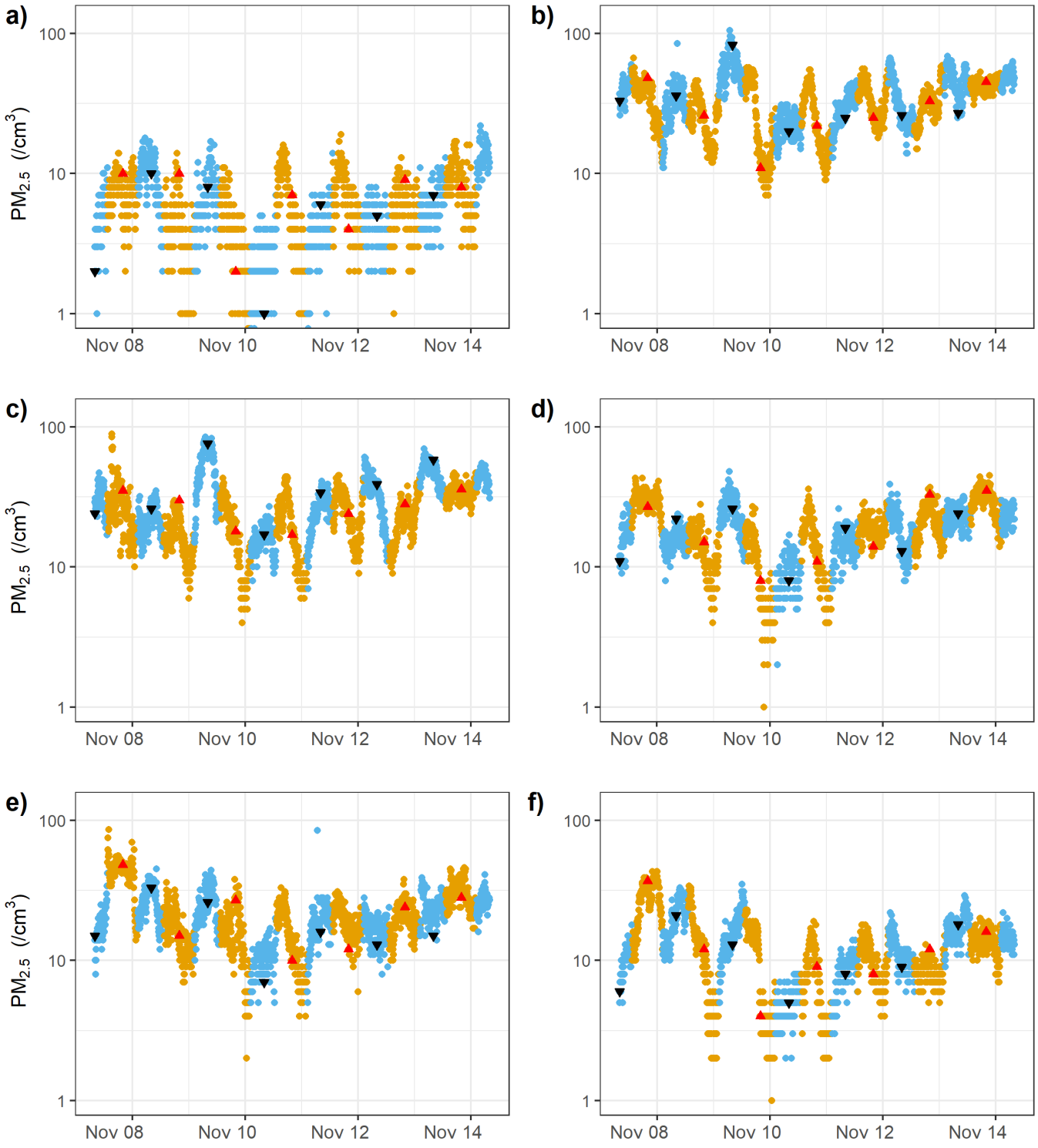

Figure 7.14-8: Time series plots for $PM_{2.5}$ measurements from low powered sensors over one week in November 2024, at locations (a) AQ01, (b) EX02, (c) EX09, (d) AQ04, (e) AQ11, and (f) AQ18. The data shown in blue corresponds to nighttime (defined as sunset to sunrise) measurements, and data shown in orange correspond to daytime (defined as sunrise to sunset). The red up-pointing triangles are midday, and black down-pointing triangles are midnight.

The results for PM_{10} are shown in Figure *7.14-9* for the period between January 2024 and May 2025. The trends appear broadly similar to those observed for $PM_{2.5}$, though with higher concentrations recorded (as would be expected). EX09 also shows higher concentrations in January 2024 than recorded at other sites (note the y-axis scale in Figure *7.14-9*). Again given the relationship between PM_{10} and $PM_{2.5}$ this is not unexpected, and the discussion around $PM_{2.5}$ levels could be applied equally here.

Figure *7.14-10* shows the diurnal cycles more clearly. As with $PM_{2.5}$ peaks in the afternoon and are typical, suggesting the same source of the bulk of the mass of $PM_{2.5}$ and PM_{10}.

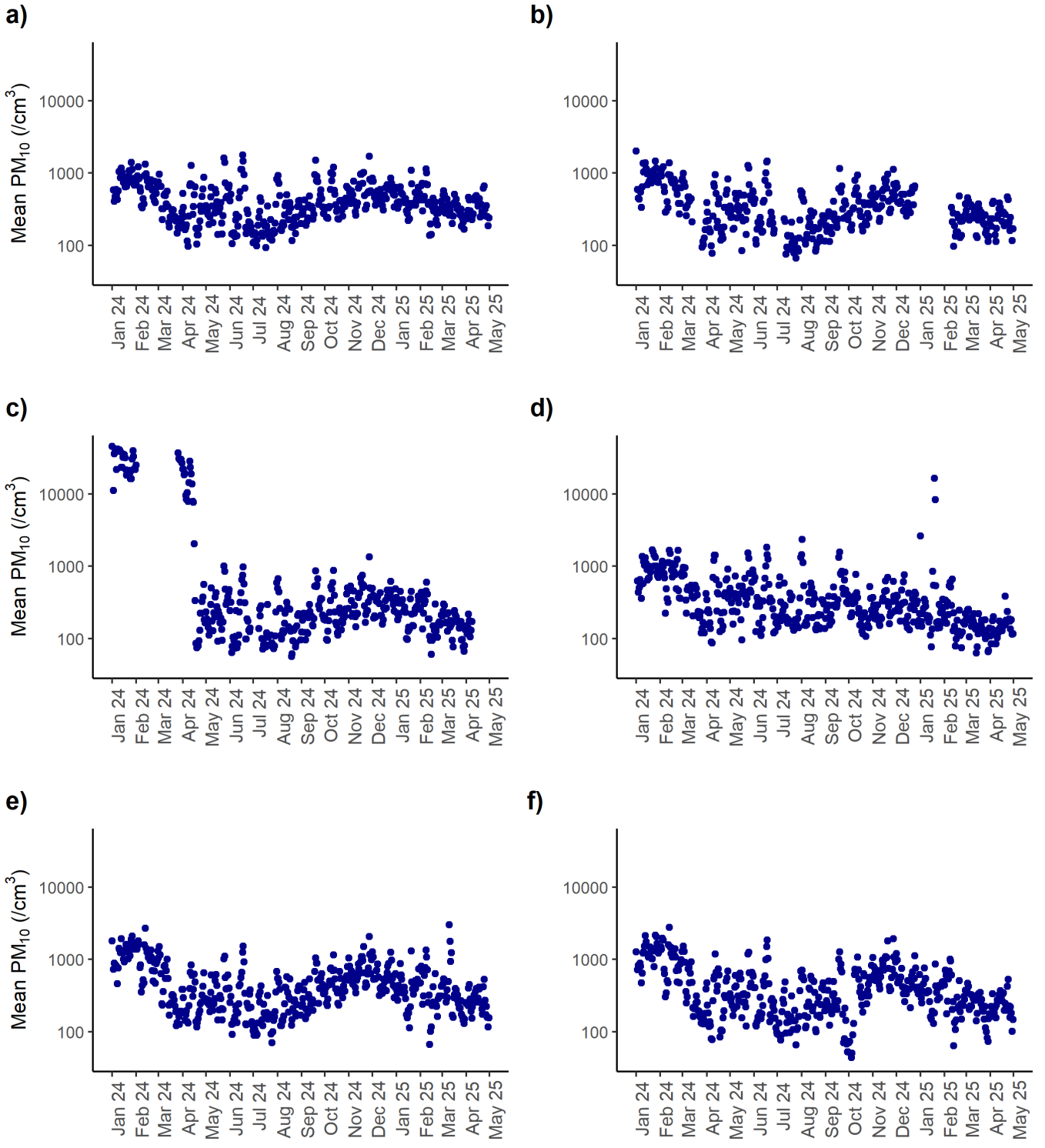

Figure 7.14-9: Time series plots for PM_{10} measurements from low powered sensors from January 2024 to April 2025 (inclusive), at locations (a) AQ01, (b) EX02, and (c) EX09, (d) AQ04, (e) AQ11, and (f) AQ18. Each point is the daily mean of PM_{10}

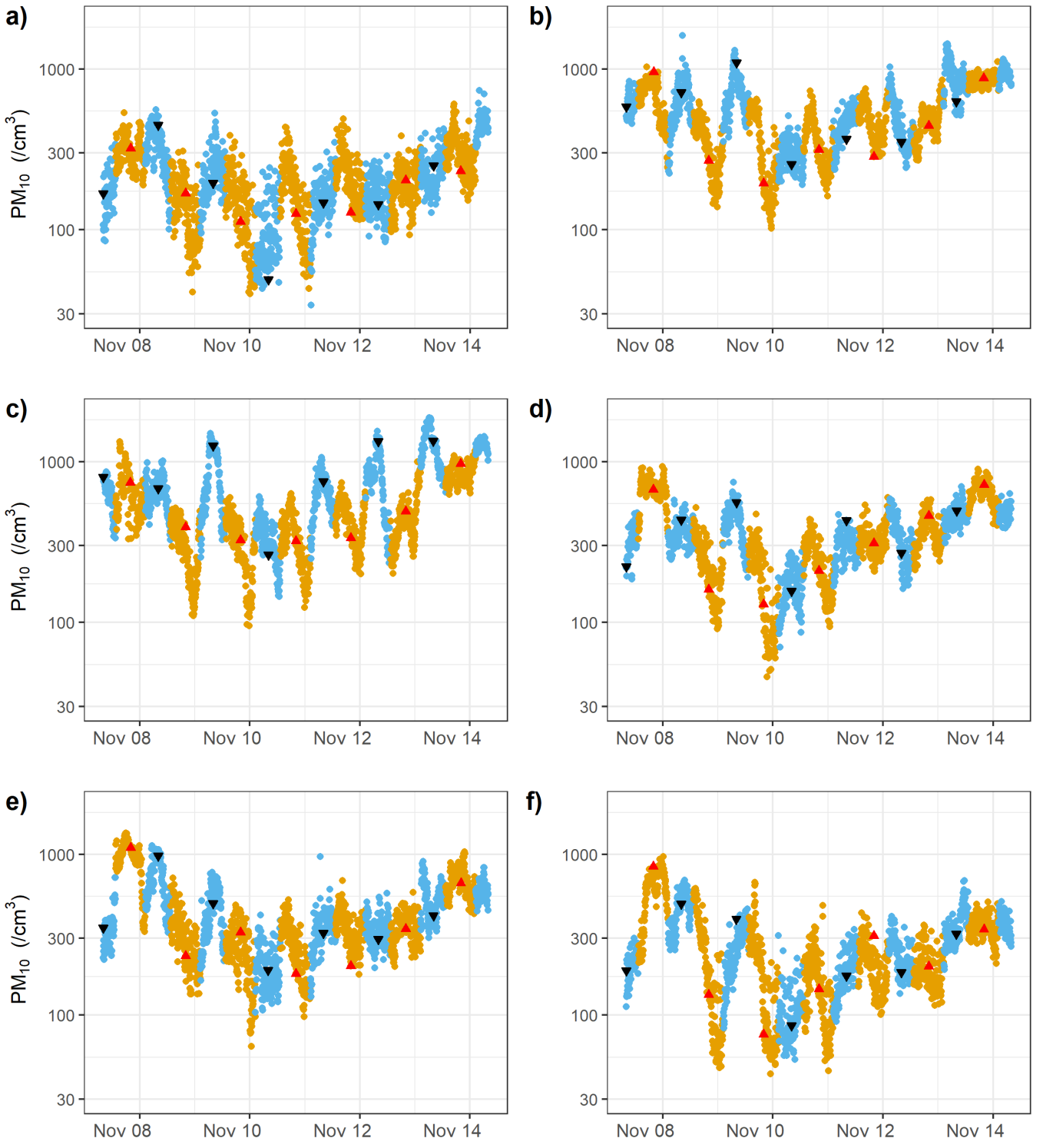

Figure 7.14-10: Time series plots for PM_{10} measurements from low powered sensors over one week in November 2024, at locations (a) AQ01, (b) EX02, (c) EX09, (d) AQ04, (e) AQ11, and (f) AQ18. The data shown in blue corresponds to nighttime (defined as sunset to sunrise) measurements, and data shown in orange correspond to daytime (defined as sunrise to sunset). The red up-pointing triangles are midday and black down-pointing triangles are midnight. Data have been excluded where the validity is in question.

7.14.6 Summary measures of gas species

Figure *7.14-11* shows mean gas concentrations by sampling period for all stations in relation to the local Murujuga seasons.

NO_2 in Figure *7.14-11* (a), and NO (b) both show remarkably similar low powered sensor readings across the stations and across seasons. No seasonal pattern is evident for the low powered sensors.

NH_3 in Figure *7.14-11* (c) shows a wide range of gas concentration measurements across stations, but no clear spatial trend or seasonal pattern is evident.

CO_2 in Figure *7.14-11* (d) shows a distinct gradient across the stations, with concentrations highest at AQ16, AQ13, EX02, and AQA1. These sensors give a reasonable spread of measured CO_2 concentrations at the stations, but there is no clear seasonal pattern.

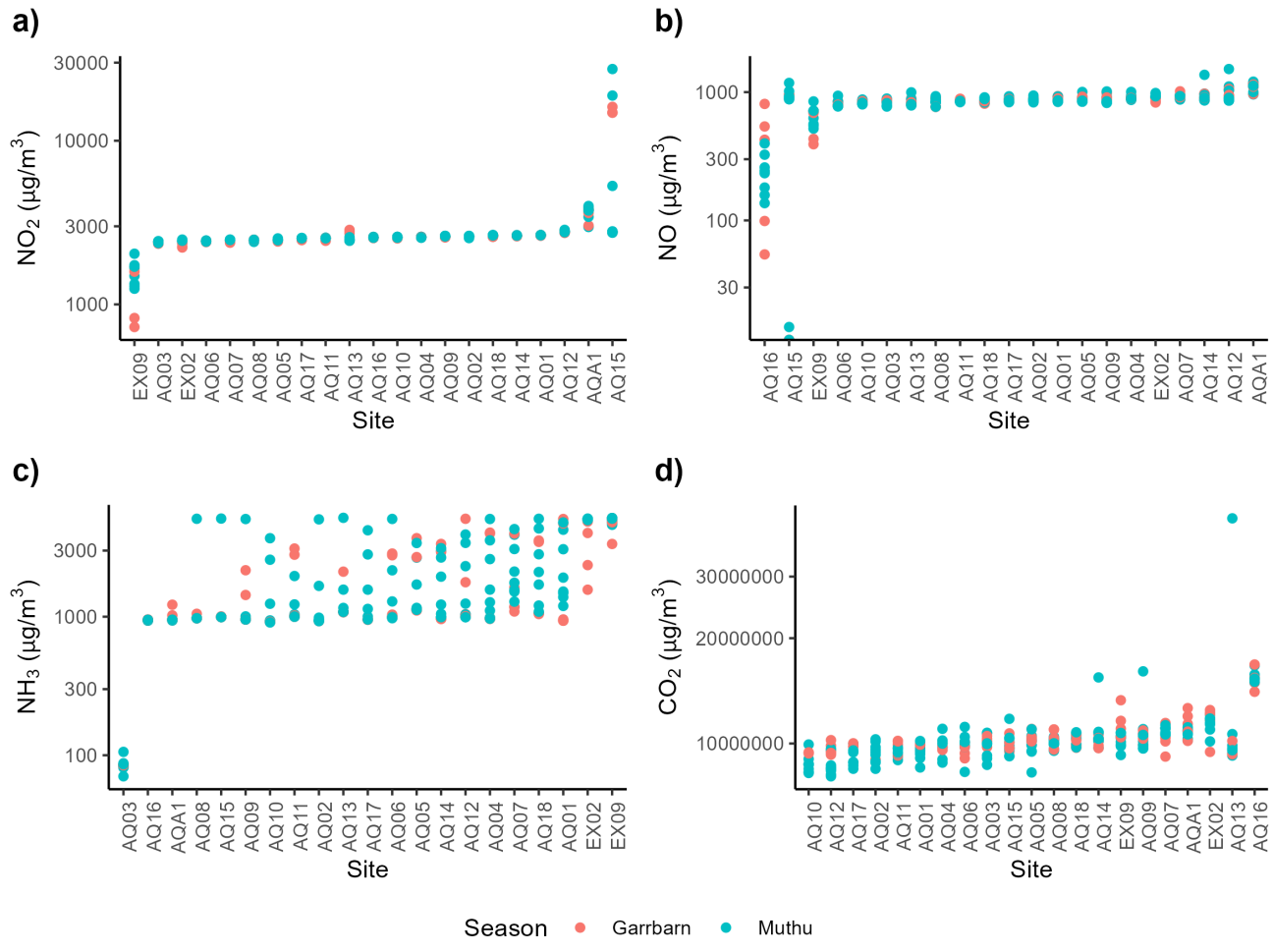

Figure 7.14-11: Scatterplots for mean gas concentration measurements from low powered sensors across all low powered sites and indicating Murujuga season for (a) NO_2, (b) NO, (c) NH_3, and (d) CO_2. Stations are ordered separately for each gas from highest to lowest: this allows us see how individual gases vary across sites. Means are across passive sampling periods in 2024 to allow comparison to passive sampling measures.

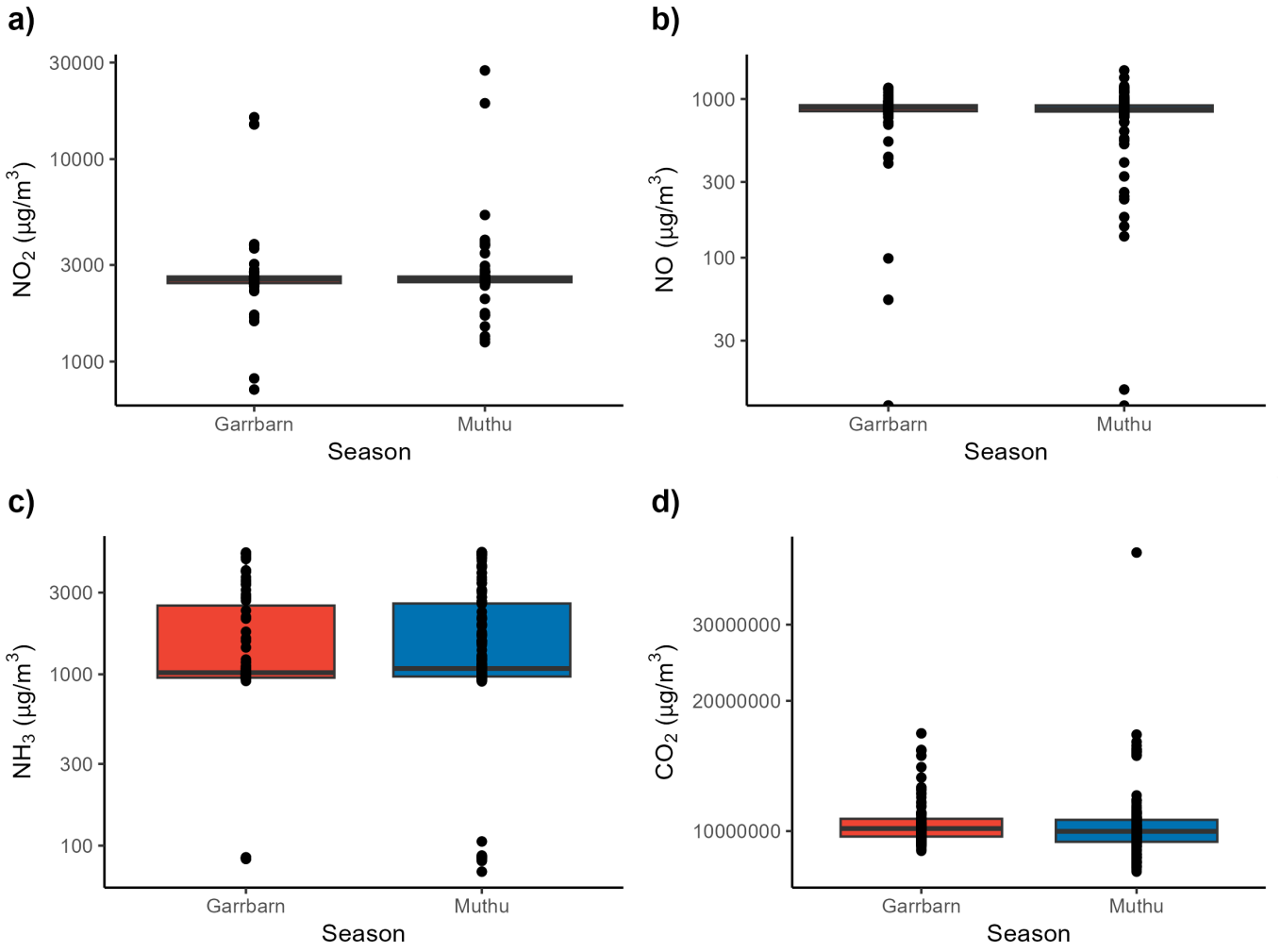

Figure 7.14-12: Boxplots of gas concentration measurements from low powered sensors across all sites by Murujuga season for (a) NO_2, (b) NO, (c) NH_3, and (d) CO_2. Means are across passive sampling periods in 2024 to allow comparison to passive sampling measures.

Figure *7.14-12* shows boxplots of gas concentrations by Murujuga seasons, indicating minimal variation in low powered sensor measurements across the two Murujuga seasons.

7.14.7 Summary measures of particulates

Figure *7.14-13* shows mean $PM_{2.5}$ and PM_{10} levels for each sampling period in relation to the local Murujuga seasons for each station. The seasonal pattern is very distinct with $PM_{2.5}$ levels highest in Garrbarn and lowest in Muthu.

Figure *7.14-14* shows boxplots of overall $PM_{2.5}$ and PM_{10} average concentrations by Murujuga seasons, indicating minimal variation in low powered sensor measurements across the two Murujuga seasons.

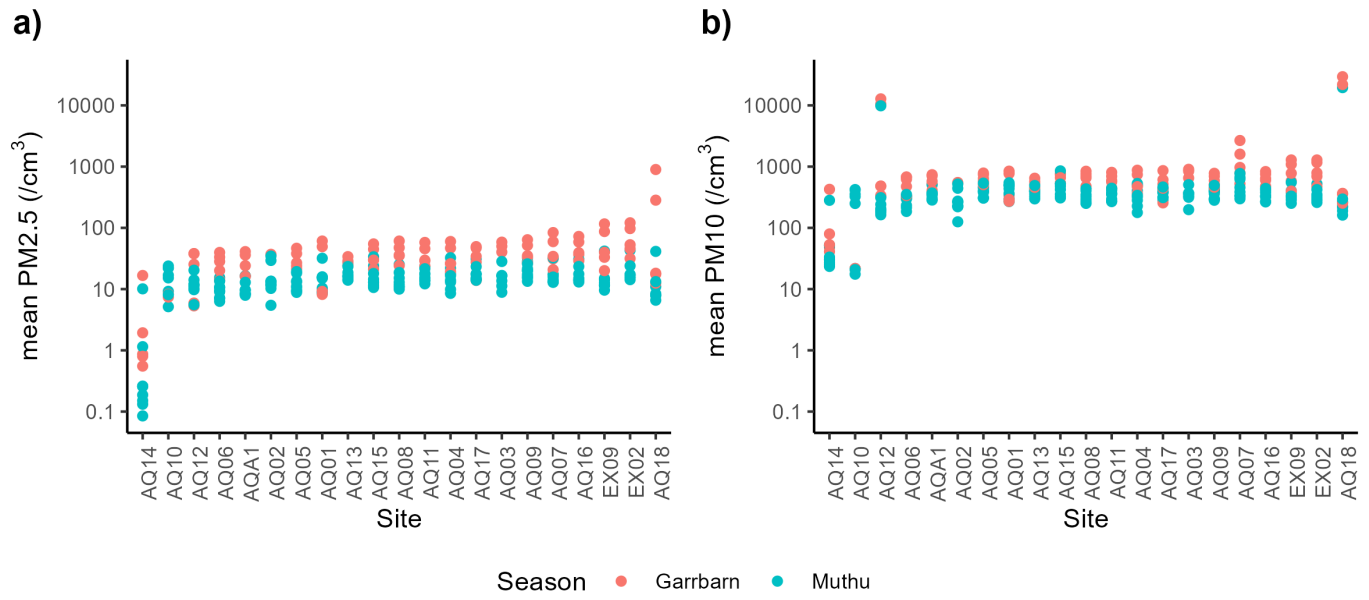

Figure 7.14-13: Scatterplots for mean particulate matter measurements from low powered sensors across all low powered sites and indicating Murujuga season for $PM_{2.5}$ and PM_{PM10}. Means are across passive sampling periods in 2024 to allow comparison to passive sampling measures.

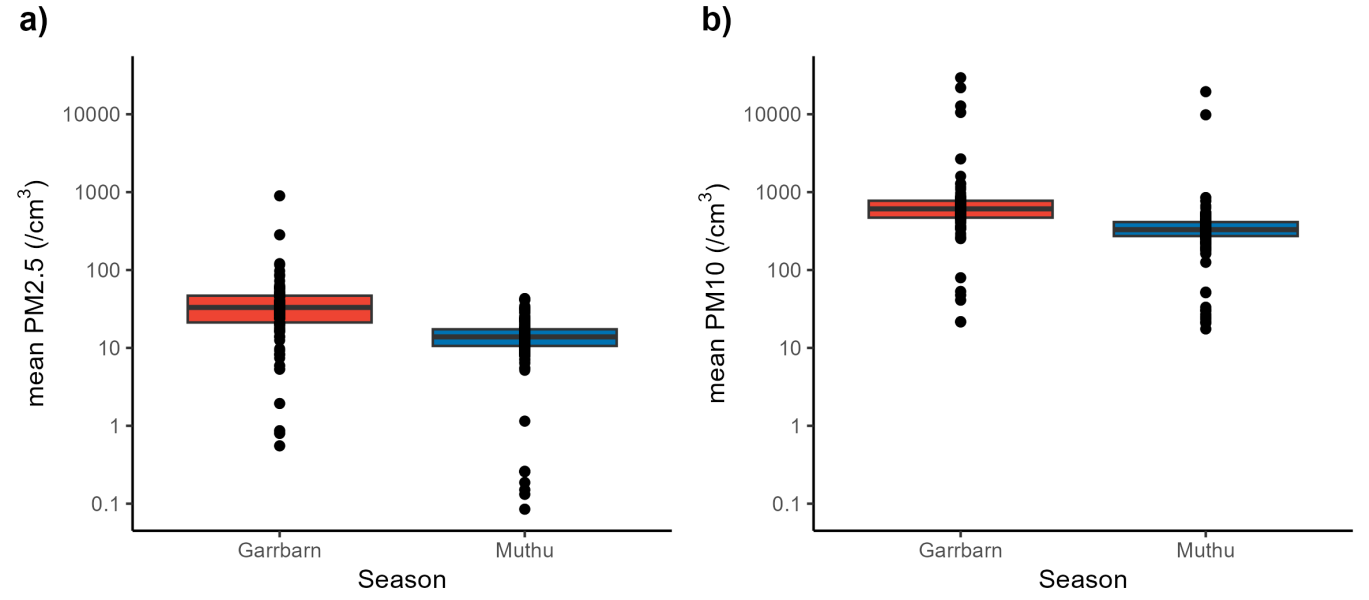

Figure 7.14-14: Boxplots of mean particulate matter measurements from low powered sensors across all sites by Murujuga season for $PM_{2.5}$. Means are across passive sampling periods in 2024 to allow comparison to passive sampling measures.

7.15 Weather: AQM and BoM stations

This section summarises the weather data (temperature, relative humidity and rainfall) from the MRAMP air quality monitoring (AQM) stations and closest Bureau of Meteorology (**BoM**) weather stations.

Table *7.15-1* displays the weather-data summaries for campaigns 5 to 10 (during the period July 2023 - March 2025) from the AQM weather stations (See Section 5 for further details of the AQM network across all of the Murujuga region). AQM stations were progressively installed, however all were online prior to campaign 5.

Campaigns 5 (July 2023) and 8 (July 2024) had the lowest temperature, that is, their minimum, mean, and maximum temperatures were the lowest compared to the other campaigns 6, 7, 9, and 10. Campaigns 7 (February - March 2024) and 10 (February - March 2025) were during summer, and they had the highest minimum and mean temperatures. The maximum temperature was 38°C or higher in almost all six campaigns 5 to 10.

For all campaigns, there was a wide range in relative humidity. Campaign 10 had one site (AQ06) with relative humidity over 100%, which occurs when the air is supersaturated.

Only during campaigns 7, 8, and 10 was rainfall recorded. In campaigns 7 and 10, all AQM stations received rainfall, however during campaign 8 only one station (AQ10) received rainfall.

Table 7.15-1: Summary of weather data for campaigns 5 to 10 (dates in brackets) from the AQM weather stations. Columns show the minimum, mean, and maximum over all AQM weather stations, for daily temperature (temp.; °C), daily relative humidity (RM; %), and daily total rainfall (mm).

Campaign no. (Dates)	Min temp. (°C)	Mean temp. (°C)	Max temp. (°C)	Min RH (%)	Mean RH (%)	Max RH (%)	Min total rain (mm)	Mean total rain (mm)	Max total rain (mm)
5 (03 - 21 Jul 2023)	11.92	20.60	30.86	16.17	50.54	91.07	0	0	0
6 (23 Oct -17 Nov 2023)	20.10	28.49	41.45	8.6	59.27	93.32	0	0	0
7 (26 Feb - 21 Mar 2024)	24.13	29.65	38.31	27.49	74.87	96.84	15.16	55.14	126.37
8 (01 - 26 Jul 2024)	12.16	21.66	31.67	15.59	56.56	97.03	0	0.01	0.24
9 (14 Oct - 07 Nov 2024)	19.26	28.82	42.78	9.58	58.04	95.04	0	0	0
10 (24 Feb - 21 Mar 2025)	23.94	32.22	43.14	16.82	66.94	142.26	2.37	16.96	35.38

BoM weather data for campaigns 1 to 10 were extracted from SILO API (https://www.longpaddock.qld.gov.au/silo/), in which these data were derived from BoM station observations. There are three BoM weather stations near Murujuga, namely:

- Dampier Port (http://www.bom.gov.au/climate/averages/tables/cw_004097.shtml),
- Dampier Salt (http://www.bom.gov.au/climate/averages/tables/cw_005061.shtml),
- Karratha Aero (http://www.bom.gov.au/climate/averages/tables/cw_004083.shtml).

Data for all three weather stations were extracted in `R` using the `weatherOz` package (Pires et al., 2024, 2025).

Table *7.15-2* shows the summary of BoM weather data for campaigns 1 to 10, summarised over Dampier Port (DP), Dampier Salt (DS) and Karratha Aero (KA).

The temperatures recorded at the AQM stations (Table *7.15-1*) and BoM stations (Table *7.15-2*) were similar for campaigns 5 to 10. However, the maximum temperatures recorded over Dampier Port, Dampier Salt, and Karratha Aero were slightly higher than those recorded at the AQM stations. There was a wider range in relative humidity recorded at the AQM stations compared to that at the BoM stations, with the minimum relative humidity lower and the maximum relative humidity higher at the AQM stations. During campaigns 7 and 10, there was a wider range in total rainfall recorded at the AQM stations compared to the BoM stations. During campaign 8, no rainfall was recorded at the BoM stations, but the maximum rainfall over all AQM stations was 0.24 mm, from one of the AQM sites.

Figure *7.15-1* shows the daily temperature (minimum and maximum) and daily relative humidity (minimum and maximum) during campaigns 7, 8 and 9 for AQM and BoM stations. These three campaigns were selected to show the seasonal differences in temperature and relative humidity over one year (2024).

For most days during campaigns 7, 8, 9, the minimum temperature was similar between AQM and BoM stations, particularly for campaign 9 (Figure *7.15-1*). The maximum temperature was typically similar during campaign 8; and during campaigns 7 and 9, the maximum temperature was typically higher at the BoM stations.

During these three campaigns, there was a wide range in daily relative humidity for the AQM stations and a much smaller range for the BoM stations (Figure *7.15-1*). To investigate the daily relative humidity further at the AQM stations, Figure *7.15-2* shows the relative humidity for AQ06 over the first week of campaign 10. Note that all other AQMs have a similar pattern with different maximum and minimum relative humidity. This figure shows that the relative humidity was lowest during the day (orange) and, at about midday (red up-pointing triangle), it started increasing; with the relative humidity being the highest around midnight (black down-pointing triangle).

Figure *7.15-3* shows the daily rainfall during campaigns 7 and 10 for AQM and BoM stations. Only these two campaigns are shown, since they received rainfall greater than 10 mm and rainfall data was recorded from both AQM and BoM stations. For some days, rainfall can vary between zero to almost 30 mm across the AQM and BoM stations. Thus, this figure demonstrates spatial variability in rainfall across Murujuga and the surrounding areas.

Table 7.15-2: Summary of BoM weather data for campaigns 1 to 10 (dates in brackets) at Dampier Port (DP), Dampier Salt (DS), and Karratha Aero (KA). Columns show the minimum and maximum temperature (temp.; °C) over all three stations, minimum and maximum relative humidity (RH; %) over all three stations, and total rainfall (mm) at each of Dampier Port (DP), Dampier Salt (DS), and Karratha Aero (KA).

Campaign no. (dates)	Min temp. (°C)	Max temp. (°C)	Min RH (%)	Max RH (%)	DP Total rain (mm)	DS Total rain (mm)	KA Total rain (mm)
1 (08 Mar - 08 Apr 2022)	24.7	42.9	26.9	66.8	3.2	1.5	2.2
2 (20 Jun - 29 Jul 2022)	7.9	29.9	31.5	60.2	0	0	0
3 (10 Oct - 04 Nov 2022)	14.4	35.8	17.8	46.6	0	0	0
4 (27 Feb - 24 Mar 2023)	23.5	42.4	37.7	69.2	13.4	26.2	7.6
5 (03 - 21 Jul 2023)	9.3	31.0	38.4	47.7	0	0	0
6 (23 Oct -17 Nov 2023)	20.7	41.2	24.1	64.5	0	0	0
7 (26 Feb - 21 Mar 2024)	24.9	40.2	55.4	68.8	46.8	34.2	63.2
8 (01 - 26 Jul 2024)	9.9	32.2	27.2	63.3	0	0	0
9 (14 Oct - 07 Nov 2024)	18.7	42.5	22.4	61.6	0	0	0
10 (24 Feb - 21 Mar 2025)	25	43.7	34.4	60.9	20.3	15.2	22.4

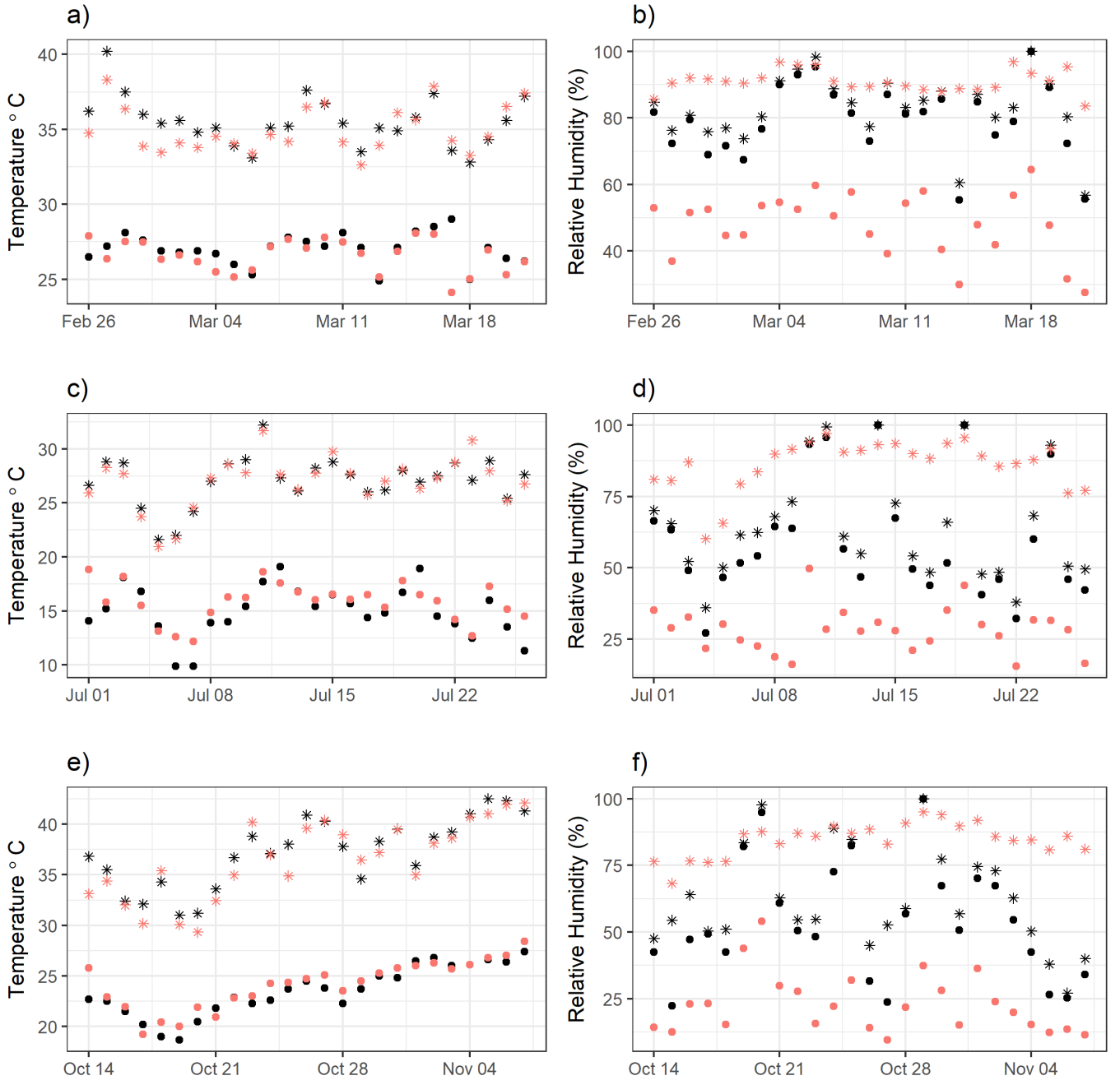

Figure 7.15-1: The daily temperature (first column) and daily relative humidity (second column) during campaigns 7 (26 February - 21 March 2024), 8 (01 July - 26 July 2024), and 9 (14 October - 07 November 2024) recorded at the AQM (red) and BoM (black) stations. The dots are the minimum daily values and the stars are the maximum daily values.

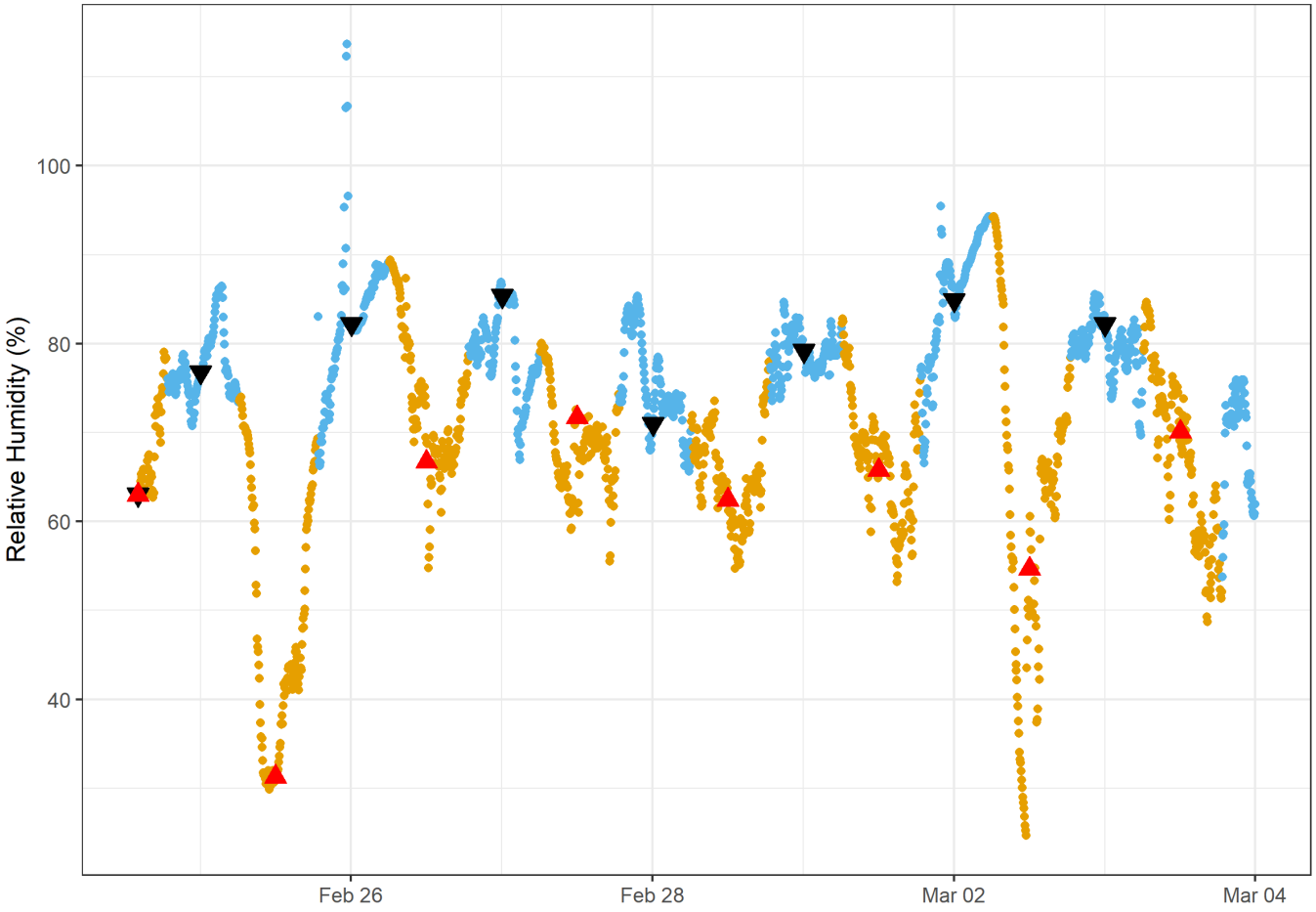

Figure 7.15-2: Time series plot for relative humidity over the first week of campaign 10. The data shown in blue correspond to the nighttime (defined as sunset to sunrise) measurements, and data shown in orange correspond to the daytime (defined as sunrise to sunset). The red up-pointing triangles are midday and black down-pointing triangles are midnight.

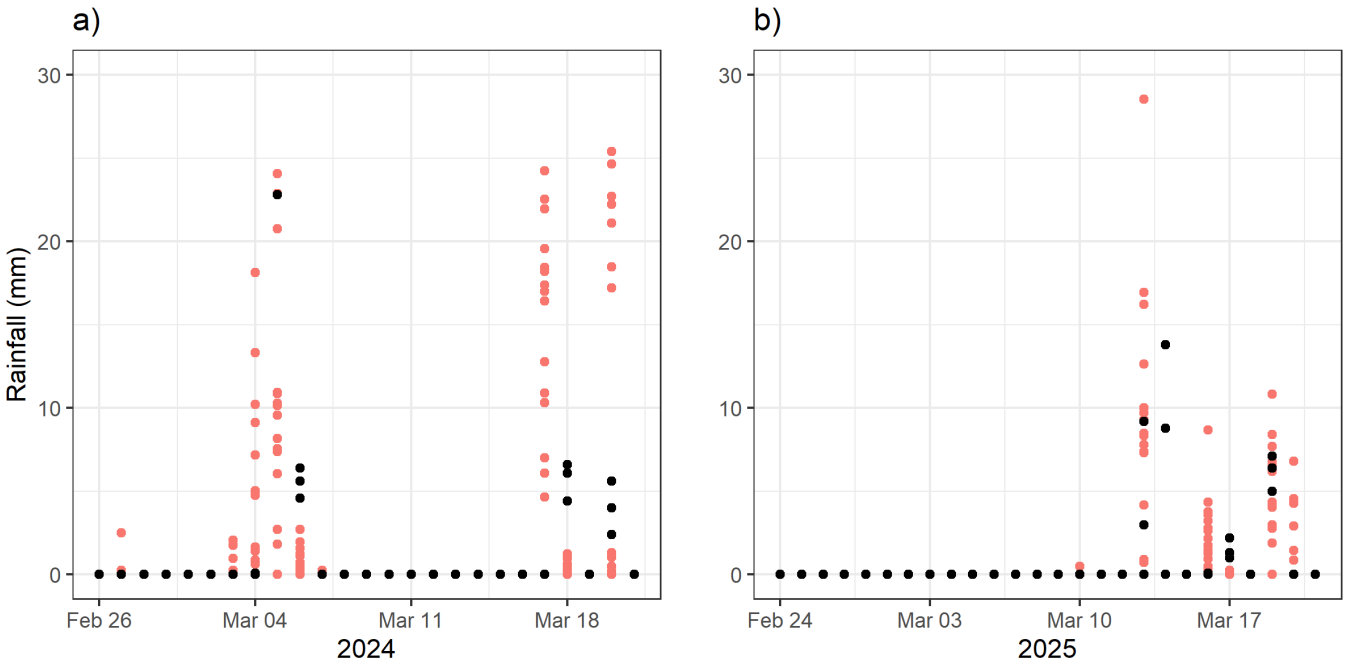

Figure 7.15-3: Rainfall during campaigns 7 and 10 recorded at the AQM (red) and BoM (black) stations. There is one red dot for each AQM station and one black dot for each BoM station.

7.16 Key findings from statistical analysis

This section summarises the key findings from the statistical analysis of data from each individual component study, as reported above.

Relationships between the variables measured in different component studies are investigated in Section 8 and summarised in Section 8.6.

7.16.1 Chamber studies

The analysis of the data from chamber experiments, reported in Section 7.1 suggested that the dose-response relationship between the amount of exposure to pollutant gases ('dose') and chemical changes in the rock ('response') was not monotonically increasing — that is, it suggested paradoxically that increasing the amount of exposure did not cause an increase in chemical changes to the rock.

On closer examination, the statistical team found several potential problems with the experimental procedure. Firstly, each individual unit of sample rock was typically re-used in different experiments. This suggests that the observations are not independent and that 'crossover effects' should be considered. Secondly, chamber experiments were not conducted in increasing order of exposure. In order to determine a reasonable range of exposure levels, it was common to start an experimental sequence by exposing the rocks to the maximum possible dose, then the minimum possible dose, and then a sequence of doses between these two limits. This suggests that the order of exposure is important. Initial diagnostic plots suggest that the response from a rock unit progressively decreases with each successive exposure.

The statistical team has made changes to the experimental design of these studies, in particular to ensure that each individual rock unit is used only once. The new experiments are currently under way, and results presented here should be viewed with caution.

Another perspective is provided by Henry's law, which relates to the solubility and reactivity of weak gas mixtures. According to Henry's law, SO_2 is approximately 110 times more potent in chemical weathering than NO_2, while NH_3 is approximately 5,000 times more potent. Consequently, SO_2 has historically been the major contributor to acid rain on a global scale.

Future EQC will develop a combined weathering index, which will account for varying concentrations and species of air pollutants.

7.16.2 Field measurement of colour

During campaigns 8 to 10, a total of 12 rock art panels were measured using the JAZ instrument and 119 were measured using the HDX instrument. The interactive app, developed to identify errors in the colour measurements of a rock art panel continues to be used during each field campaign (Monitoring Studies Report 2024 (Curtin University, 2024c)).

In this report, all analyses of field colour data were restricted to four sites, (AQ03_GPH, AQ04_GPH, AQ11_GPH and EX06_GPH), measured by both instruments during campaigns 7–10. The final MRAMP monitoring studies report will include analysis of all sites.

There was no temporal change in rock surface colour over the three-year study period (campaigns 1 to 10) for AQ03_GPH, AQ04_GPH, AQ11_GPH and EX06_GPH using the JAZ instrument.

The JAZ instrument was found to be more variable than the HDX instrument. This is most likely explained by the HDX taking only about 5 seconds to record all 100 replicates, whereas the JAZ measurements take several minutes. During this longer measurement time, the JAZ instrument is more likely to have been moved slightly, which could result in greater variation in the recorded colour measurements.

For campaigns 7 to 10, there was no difference in trends between the two instruments. Thus the spectral rock surface colour measurements are similar between JAZ and HDX instruments.

In conclusion, the HDX is reproducible and suitable instrument for the long-term monitoring of rock surface colour. However, given the HDX operational problems during the summer (Garrbarn) months, it is recommended that future colour monitoring should only be conducted in the cooler months (Muthu).

7.16.3 Industry data

Section 7.3 compares the data from the Woodside IVL and Radiello passive samplers. NO_2 measurements from both IVL and Radiello passive sampler are strongly correlated and NH_3 measurements are moderately correlated between the two passive samplers, indicating that this data can be used in an advanced analysis together with the MRAMP IVL data. However SO_2 and HNO_3 measurements show no correlation between the two passive samplers, potentially due to detection limit differences (to be investigated further).

7.16.4 Inorganic geochemistry — *pH*, *Eh*, Cl^-

Similar to the Monitoring Studies Report 2024 (Curtin University, 2024c), there continues to be striking differences in *pH* between different campaigns. Rainfall appears to have a substantial effect on *pH* over short periods, while differences due to spatial location and rock type appear to be far smaller.

Similar comments apply to the measures of chloride ion Cl^- concentration.

Oxidation–reduction potential (*ORP*) measurements continue to exhibit relatively small differences between all ten campaigns compared to the residual variability. No systematic differences could be seen between rock types, or between spatial locations.

7.16.5 Inorganic chemistry — pXRF

This report confirms that the pXRF instrument remains a useful tool for assessing rock surface elemental composition, showing broadly consistent results that support its internal reliability.

As for the Monitoring Studies Report 2024 (Curtin University, 2024c), the ratio of silica (SiO_2) to titanium (Ti) was calculated from the pXRF readings for all rocks classified as belonging to a specific type, such as granophyre. The ratios had a highly skew distribution. There was no visual evidence of a spatial trend in the ratio of silica to titanium in granophyre. Similar conclusions were reached for other elemental ratios.

7.16.6 Inorganic geochemistry — porosity

One of the main findings of the Monitoring Studies Report 2024 (Curtin University, 2024c) was that there is statistically significant evidence that the porosity of granophyre surfaces is higher in a region close to industry than it is in other parts of Murujuga. It was provisionally concluded that the most likely explanation is that chronic exposure to industrial output has caused the shallow layers of the rock surface to become more porous.

In order to verify this finding, additional sample rocks were collected and analysed for the current report. The additional data broadly confirms the findings of the Monitoring Studies Report 2024.

Due to a coding error in preparing the Monitoring Studies Report 2024, the region of statistically significant evidence of elevated porosity (coloured orange in the figures) was computed incorrectly in Figure 7.6-9 of the report. The effect of the coding error was that the threshold for statistical significance was set to a much stronger standard of evidence (probability less than 0.5% rather than the usual standard of probability less than 5%). The orange coloured region was consequently smaller than it should have been. The figure is corrected in Figure *7.6-8* of this report.

When the additional data collected this year are added, the analysis of the combined dataset on rock porosity broadly agrees with the (corrected) analysis of the data from Monitoring Studies Report 2024 (Curtin University, 2024c). The overall conclusion is that:

1. there is very strong statistically significant evidence ($p <= 0.001$) that an area of Murujuga has elevated porosity;
2. the best estimate of the area of elevated porosity is the area coloured orange in Figure *7.6-10* on page 219 above, which is an area of 80 km^2, centred on King Bay and ranging from Dampier town and Rio Tinto's 2-Mile Rail Maintenance Yard in the south to Withnell Bay and Cowrie Cove in the north.

7.16.7 Inorganic geochemistry – permeameter

The permeameter instrument is a non-destructive method of measuring porosity. It has been deployed to measure the permeability ("air permeability") of the rock art panels in campaigns 7 to 10. Overall, granite showed the highest median permeability in campaigns 7 and 8, basalt consistently had the lowest median permeability, and gabbro recorded the highest median permeability in campaign 10. Other rock types showed similar and moderately variable permeability.

Visual analysis indicated the spatial trend of permeameter measurements was consistent between campaigns, and the pattern of spatial variation in permeability appears broadly similar to that observed for the porosity data.

7.16.8 Microbiome

Analytical results are not yet available for the microbiome samples were collected in the third study year. These samples included surface swabs from the AQM rock cubes, and both surface swabs and Dremel swabs from a small set of new sample rocks collected from a railway cutting near Dampier. Results will be formally analysed and presented in the final study report.

7.16.9 Deposition sampler data

Analysis of data from the 3 bucket deposition sampler apparatus (Section 7.10) was confined to the "dry" bucket which is exposed to the atmosphere for the vast majority of the time.

The *pH* values exhibited appreciable differences between different dates, with particularly low *pH* values appearing to coincide with periods where low quantities of dust were deposited. There were some systematic differences between *pH* values at different sites.

Calculated deposition rates of Ca^{2+}, K^{+}, Mg^{2+}, Cl^{-}, Na^{+}, $SO_4{}^{2-}$, $NH_4{}^{+}$, $NO_3{}^{-}$ and P did not appear to exhibit large seasonal variation nor systematic differences between sites.

The rainfall *pH* values are neutral or slightly alkaline, which is thought to be due to the contribution of salt(s) and/or dust (clay minerals).

Given both the deposition sampler and rainfall *pH* data, there is no evidence of acid rain over the MRAMP measurement period to date. CSIRO 2006 provided evidence of acid rain in 2005, however MRAMP measurements are consistently higher *pH*. A small number of measurements from the dry deposition bucket sampler have been found to be acidic. However, these may be influenced by deposition of rust or guano in the sampler and similarly acidic *pH* has not been measured in co-located AS/NZS 3580.10.1 total deposition flasks.

Results obtained from the co-located sites (AQ07 and AQ08) indicate good agreement between the two.

7.16.10 Total (flask) deposition sample

The total deposition flasks (Australian Standard) were co-located with the 3-bucket deposition samplers.

pH measured from the 3-bucket deposition samplers largely lies between 5.5 and 7, whereas the total deposition sample *pH* was slightly higher, ranging from 6.5 to 7.5.

Similar to the 3-bucket deposition samplers, the calculated deposition rates of Ca^{2+}, K^{+}, Mg^{2+}, Cl^{-}, Na^{+}, $SO_4{}^{2-}$, $NH_4{}^{+}$, $NO_3{}^{-}$ and P from the total (flask) deposition samplers did not appear to exhibit large seasonal variation nor systematic differences between sites.

Results obtained from the co-located sites (AQ07 and AQ08) indicate good agreement between the two.

7.16.11 Organic geochemistry

Section 7.9 showed ratios of organic geochemical compound to aid comparison between sites.

Organic geochemical ratios reveal limited clustering near industrial areas. Only a few high values, such as BAB/n-C_{17} in dolerite and gymnosperm biomarkers (n-C_{17} and n-C_{18}) in granophyre, are found near industry. MP/P ratios show several elevated values near industrial sites, but MPI-1 values are broadly distributed without clustering. BAB/n-C_{18} shows its highest value far from industry, and fluoranthene/(fluoranthene + pyrene) ratios are symmetrically distributed, lacking any spatial pattern. Overall, most ratios near industrial areas are low, with few exceptions.

These findings suggest that while some organic geochemical ratios may be influenced by proximity to industrial areas, visually, no consistent spatial clustering is observed. Therefore, only selected ratios, particularly MP/P and certain gymnosperm biomarker values may be useful indicators for potential organic rock art degradation processes.

7.16.12 Passive samplers

Passive sampler tubes are exposed in the field for approximately 4 weeks then retrieved for chemical analysis, providing estimates of the average atmospheric concentration of various gases over the relevant sample periods. Sample periods are mapped to the month in which most of the exposure duration falls. Analysis of the passive sampler data was reported in Section 7.12.

Gases associated with industrial output show strong seasonal changes in concentration. Some gases, particularly NO_2, also show consistent spatial patterns. NO_2 concentration is clearly higher close to the Dampier port area. NH_3 shows a similar pattern but other gases show different patterns.

The study design specified that passive samplers should be placed at the AQ sites in duplicate for each gas of interest. This allowed validation of the passive sampler data, and estimation of the intrinsic variability of the technique, and thereby estimation of the underlying natural variation in gas concentration. Analysis of these duplicate observations indicated that the intrinsic variability of the technique is generally acceptable. SO_2 is the exception for the gases, and continues to show much higher relative differences across the IVL samplers.

The study design also specified that two monitoring sites (AQ07 and AQ08) should be placed close together. This allows an estimation of the short-scale spatial variability in gas concentration to be made. These stations also aid in validating the overall design of the monitoring installations. Analysis of passive sampler data between these two co-located sites indicated good agreement for NO_2, SO_2, NH_3, O_3 and HNO_3. There is also seasonal variation in NO_2, O_3 and HNO_3.

VOC monitoring data are available up to December 2024. These measurements continue to show quite low levels with many observations classified as below detection limit. Analysis of the duplicate VOC samplers across sites also showed high relative differences between these samplers for a number of VOC species.

This report also introduces a consensus rank and rank standard deviation approach, which highlights spatial patterns of relatively low to high gas concentrations across all sampling periods. This approach can therefore be used to compare spatial similarities and differences between gas species.

A similar spatial pattern is observed for four gases (NO_2, NH_3, SO_2 and HNO_3, with relatively high concentrations in the central Burrup Peninsula, close to the Dampier port and industrial area. NO_2, NH_3, HNO_3 also show similar patterns of spatial variability, with the most consistent concentrations in the centre of the Burrup Peninsula and the greatest variability at the extremities. In contrast, SO_2 exhibits a different pattern, with greater variability in the central Burrup Peninsula and in the western and northern parts of Murujuga.

7.16.13 Real-time powered sites

As stated in the Monitoring Studies Report 2024 (Curtin University, 2024c), the real-time air quality monitoring systems provide data on the atmospheric concentrations of important gases at the three powered site locations every five minutes. Data from a fourth real-time monitoring station are also provided to Curtin University retrospectively every month.

SO_2 is consistently present at all sites at low concentrations, typically around the $\sim$ 1.5 - 2 ppb range.

Throughout 2024, NO showed a number of peaks, some peaks rising well above the typical levels observed at each site. NO and NO_2 have regular daily peaks at all sites, with higher peaks for NO_2 typically occurring at night.

O_3 appears to be consistently present (when the instruments are measuring) and there appears to be some variability between monitoring stations. Levels at all sites, however, appear to fall within the range of expected background concentrations for the region.

The dust levels ($PM_{2.5}$, PM_{10}, and TSP) are high across all sites, with some peaks reaching 'extremely poor' air quality based on DWER criteria. While much of this dust is likely natural due to the region's environment, visible dust from human activities is also observed, and smaller particles make up a large proportion of the dust.

Due to its elevated location and strong winds, EX09 was chosen for additional instrumentation including an isotopic methane analyser to monitor a wider range of chemical species. Results show periodic peaks in CO_2 and methane likely linked to local industrial activities, with generally stable ethane levels, except for notable peaks in late February 2025, suggesting emissions from nearby gas plants.

High-resolution radon measurements at EX09 indicate that radon levels are highest when winds blow from the gas plants, suggesting local emissions from natural gas extraction and combustion. This supports the use of radon as an indicator of air mass origin and potential industrial contributions, with detailed analysis to be presented in the final report.

7.16.14 Low powered sensors

Section 7.14 summarises the 'low power' sensors used to measure CO_2, NO, NO_2, NH_3, $PM_{2.5}$ and PM_{10} at passive/solar AQMs.

There were some variations in CO_2, NO, NO_2 and $PM_{2.5}$ levels throughout the year. There were also daily variations in the CO_2, NO, NO_2 and $PM_{2.5}$. Typically, NO minimum levels are around midday, whereas NO_2 and CO_2 have their lowest levels around midnight. Given that the low powered sensors were used in an 'as is' form and are known to degrade over time, a certain degree of caution is needed in terms of interpreting the results. We are therefore reluctant to draw any firm conclusions on these measurements alone.

7.16.15 Weather: AQM and BoM stations

Section 7.15 summarises the weather-data (temperature, relative humidity and rainfall) from the MRAMP AQMs and Bureau of Meteorology (BoM) stations for campaigns 1 to 10.

The temperatures recorded at the AQM stations and BoM stations were similar for campaigns 5 to 10. However, the maximum temperatures recorded at the BoM stations were slightly higher than those at the AQM stations.

There was a wider range in relative humidity recorded at the AQM stations compared to that at the BoM stations. During campaign 8, no rainfall was recorded at the BoM stations, while one AQM station recorded 0.24 mm. These results indicate spatial variability in rainfall across Murujuga and the surrounding areas.

This page is intentionally blank.

8 Associations between variables

This section presents our statistical investigation of relationships or associations between variables recorded in the different component studies. Some of the analysis provides a cross-check on the validity of the techniques. Other analysis provides new findings on relationships between processes occurring at Murujuga. Key findings of this section are summarised in Section 8.6.

The plan of the section is as follows:

- Section 8.1 compares the 3-bucket deposition samplers with the passive samplers.
- Section 8.2 compares the 3-bucket deposition samplers with the total deposition samplers.
- Section 8.3 compares the IVL passive samplers with satellite observations.
- Section 8.4 compares the low-powered versus real-time powered instruments.
- Section 8.6 summarises key findings.

8.1 Deposition versus passive samplers

8.1.1 Background

The 3-bucket deposition samplers (Section 7.10) collect material deposited from environmental air into the “dry” bucket unless mist or rainfall is occurring. The passive samplers (Section 7.12) are continuously exposed to environmental air. Both the passive samplers and 3-bucket sampler buckets are collected (exchanged) periodically, but the sampled material is assayed for different sets of chemical species and particle populations. For validation and calibration, it is important to compare the two kinds of observations, although they are not strictly equivalent measurements. That is, the analysis presented here should be viewed as qualitative only.

Section 8.1.2 of the Monitoring Studies Report 2024 (Curtin University, 2024c) used “skeleton 2D boxplots” to compare:

- passive sampler SO_2 and dry deposition SO_4^{2-} data;
- passive sampler NH_3 and dry deposition NH_4^{+} data;
- passive sampler NO_2 and dry deposition NO_3^{-} data.

The skeleton 2D boxplots have a central dot, which is the median, that is the median of passive sample concentration estimates is plotted against the median of deposition concentrations. It also has line segments representing the inter-quantile ranges. When interpreting these skeleton 2D boxplots, it needs to be understood that the medians and inter-quantile ranges for each site were computed from all the available data for the site in question, collected at different calendar dates. Seasonal variation was not explicitly taken into account. The sample median for each site can be interpreted as an estimate of the overall annual median value at that site.

Last year’s report (Curtin University, 2024c) also used Spearman rank correlation coefficients between the median of dry deposition vs passive samplers.

This section contains updated skeleton 2D boxplots and Spearman rank correlation coefficient analyses. The previous study report (Curtin University, 2024c) presented data from early May 2023

to early December 2023. This current report now includes data from early May 2023 to January 2025.

Table *8.1-1* shows the Spearman rank correlation coefficients between the median of "dry" deposition vs passive samplers.

Figure *8.1-1* displays the skeleton 2D boxplots of dry deposition sample SO_4^{2-} and passive sample SO_2. Similar to the previous study report (Curtin University, 2024c) this figure suggests a moderate positive association between passive sample SO_2 and dry deposition sample SO_4^{2-}, however, the correlation is not statistically significant.

Figure *8.1-2* suggests that passive sample NO_2 and dry deposition sample NO_3^- are strongly positively associated. Last year's report (Curtin University, 2024c) reported a strong positive relationship between these variables, and it was statistically significant. This report also shows a strong positive relationship, with a Spearman correlation coefficient of 0.630 (Table *8.1-1*), and is statistically significant.

Figure *8.1-3* suggests only weak evidence of an association between passive sample NH_3 and dry deposition sample NH_4^+. Last year's report (Curtin University, 2024c) reported a weak relationship between passive NH_3 and dry deposition NH_4^+. Table *8.1-1* shows that there is a negative association between passive sample NH_3 and dry deposition sample NH_4^+, however this association is not statistically significant.

Table 8.1-1: Spearman rank correlation coefficients between corresponding measurements from the "dry" deposition samplers and passive samplers. Statistically significant correlations are shown in bold type, and annotated with one asterisk for $p < 0.05$, two asterisks for $p < 0.01$, and three asterisks for $p < 0.001$.

"dry" deposition	passive sampler	Spearman
SO_4^{2-}	SO_2	0.324
NO_3^-	NO_2	**0.631****
NH_4^+	NH_3	-0.156

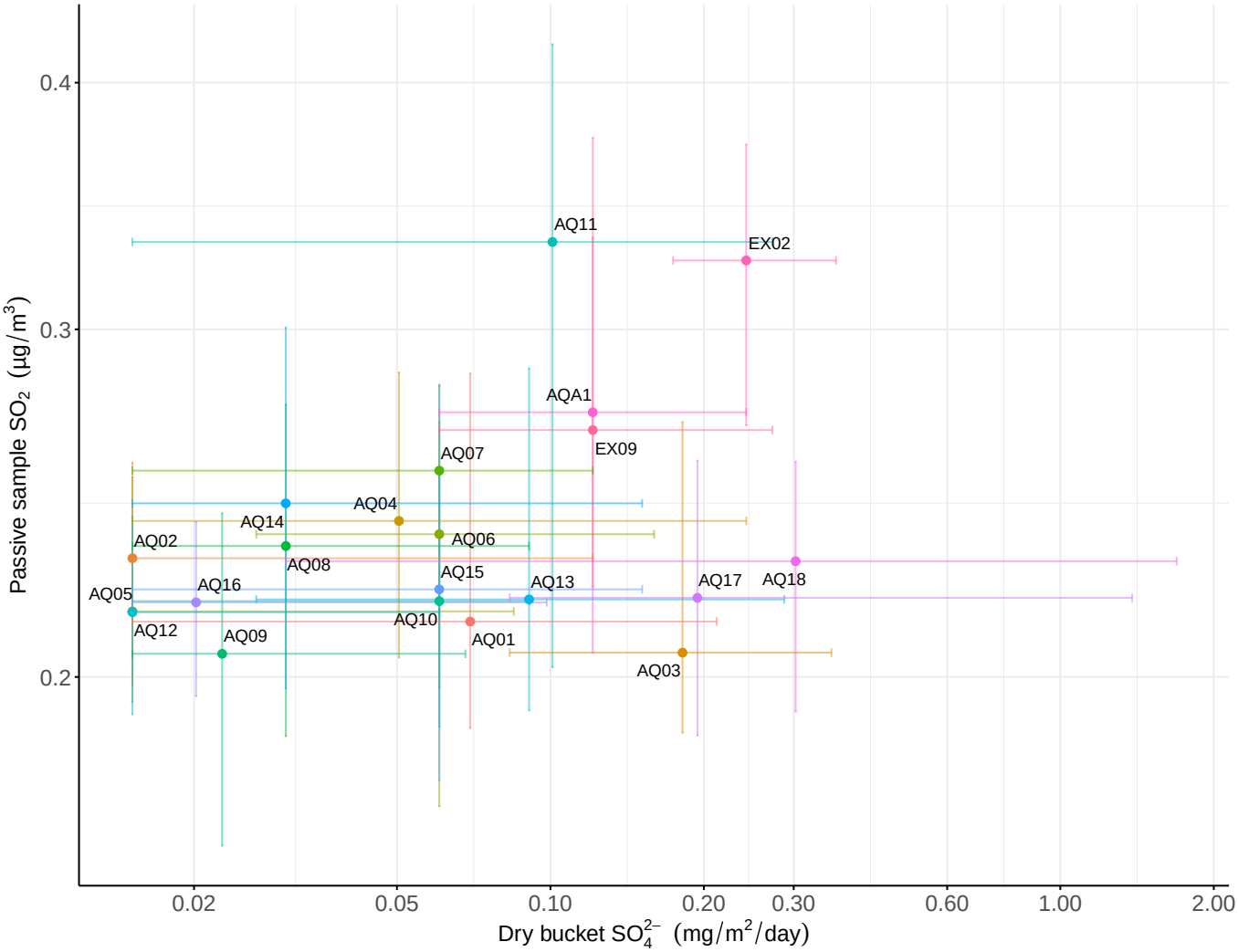

Figure 8.1-1: Simplified 2D boxplots of dry bucket SO_4^{2-} and passive sampler SO_2 from each AQ and EX site. The points are the median SO_4^{2-} and the median SO_2, and the horizontal and vertical lines are the inter-quartile ranges. Note the logarithmic scale in both axes. Data between May 2023 and January 2025.

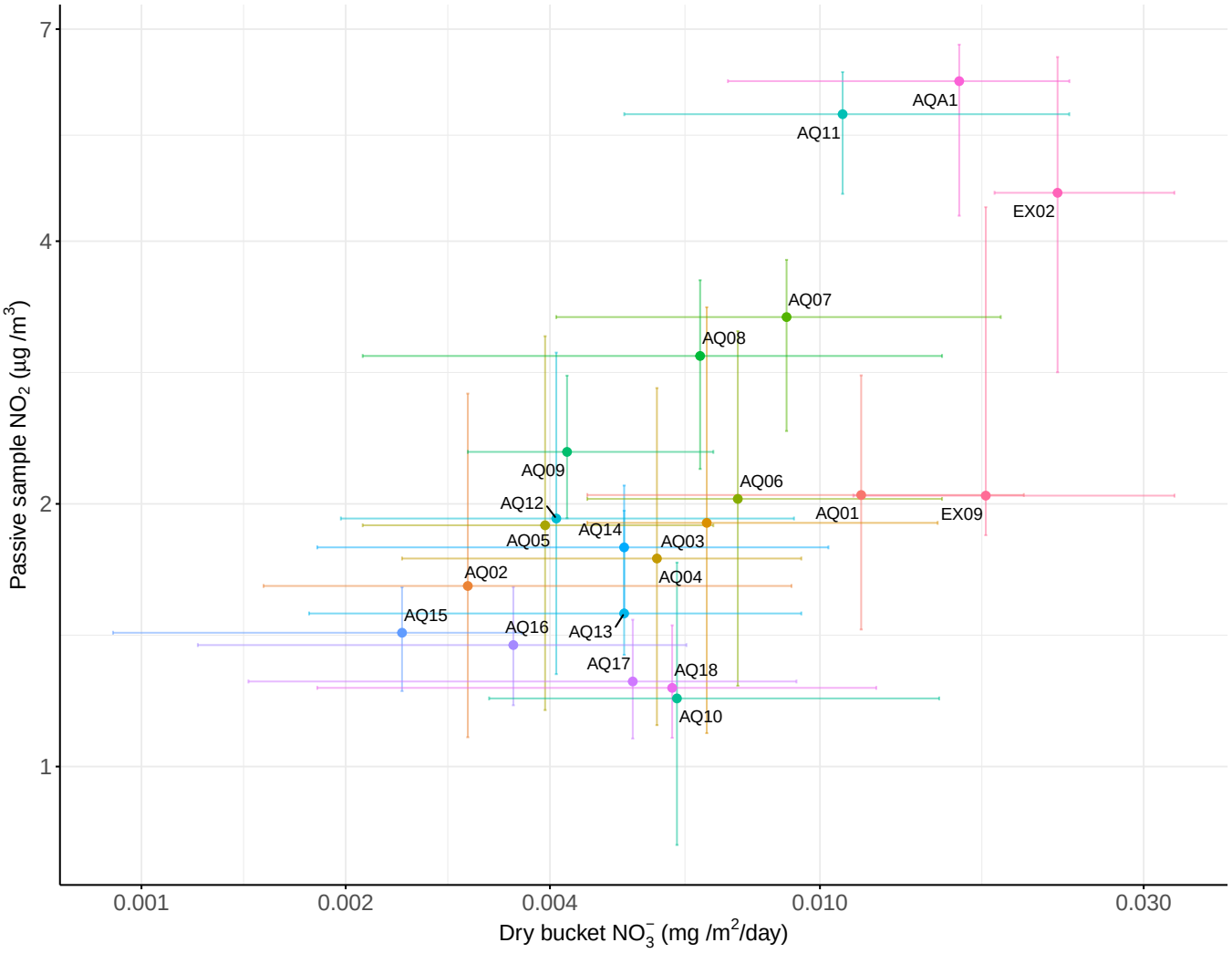

Figure 8.1-2: Simplified 2D boxplots of dry bucket NO_3^- and passive sampler NO_2 from each AQ and EX site. The points are the median NO_3^- and the median NO_2, and the horizontal and vertical lines are the inter-quartile ranges. Note the logarithmic scale in both axes. Data between May 2023 and January 2025.

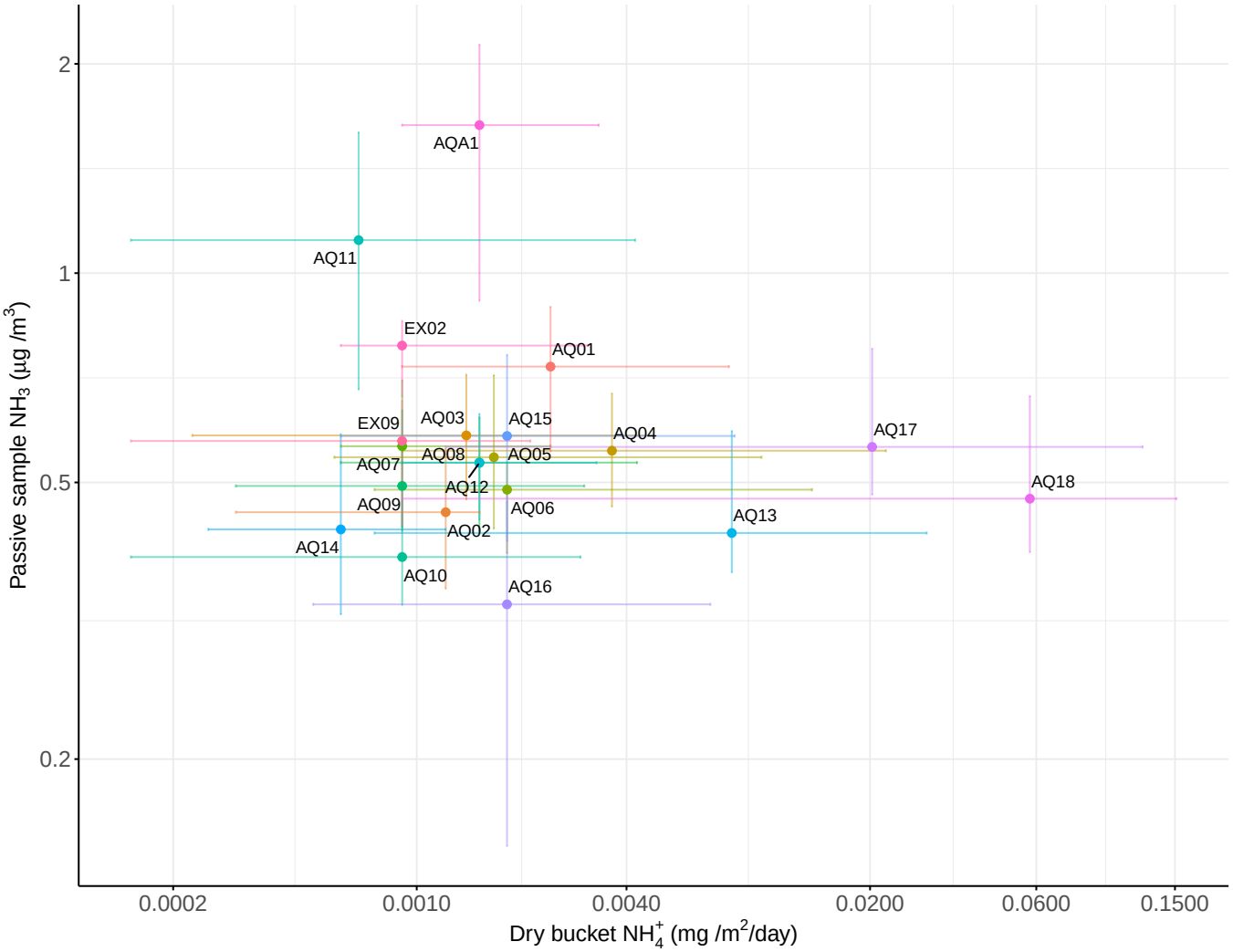

Figure 8.1-3: Simplified 2D boxplot of dry bucket NH_4^+ and passive sampler NH_3 from each AQ and EX site. The points are the median NH_4^+ and the median NH_3, and the horizontal and vertical lines are the inter-quartile ranges. Note the logarithmic scale in both axes. Data between May 2023 and January 2025.

In the final report, further statistical analysis and modelling will be conducted, explicitly incorporating seasonal effects and providing more accurate confidence intervals for annual average values and seasonal trends, enabling a more thorough examination of the relationships between variables.

8.2 Bucket deposition versus total flask deposition

Section 7.10 describes the 3-bucket deposition sampler and Section 7.11 describes the total flask deposition sampler. For both samplers, the ChemCentre provides concentrations of Ca^{2+}, K^{+}, Mg^{2+}, Cl^{-}, Na^{+}, SO_4^{2-}, NH_4^{+}, NO_3^{-}, P, and NO_2^{-}.

Figure *8.2-1* shows scatterplots of total flask deposition versus 3-bucket deposition for all chemical species concentrations. Concentrations of Ca^{2+}, Cl^{-}, K^{+}, Mg^{2+}, and Na^{+} show a slight positive association between the two samplers, indicating that both methods collect similar concentrations. However, NH_4^{+}, NO_3^{-}, P, and SO_4^{2-} do not show a clear relationship, as many values are below the detection limit for one or both samplers.

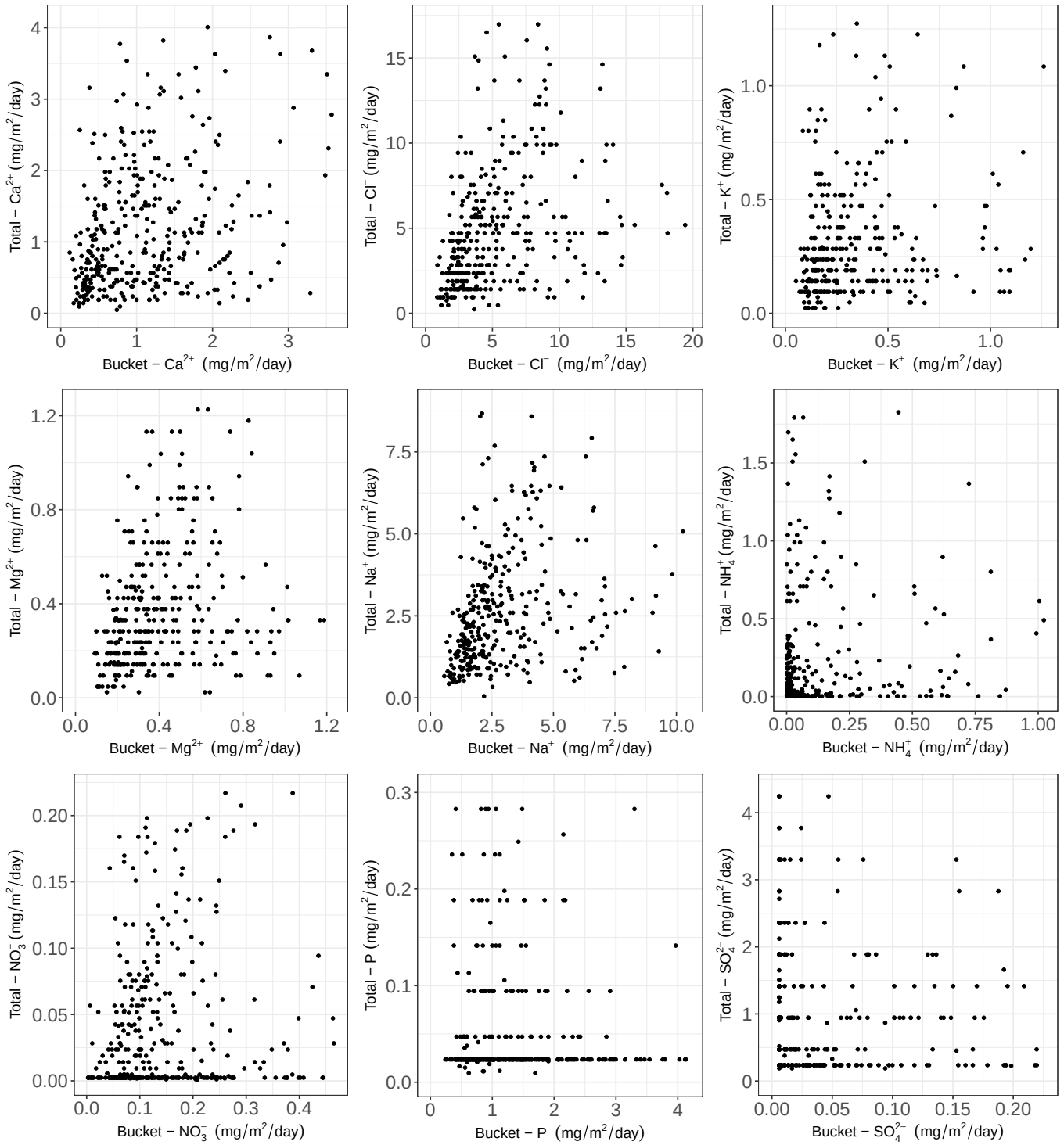

Figure 8.2-1: Scatterplots of 3-bucket deposition sampler (dry, wet, mist) and total flask deposition data. Combined data from September 2023 and March 2025.

8.3 Validation against satellite observations

Satellite observations and satellite-based predictive forecast data were retrieved from the Copernicus Atmospheric Monitoring Service (CAMS, https://atmosphere.copernicus.eu/) for the same chemical species as monitored by IVL passive samplers. It should be noted that CAMS models are not validated for the southern hemisphere, so a good agreement was not expected.

The CAMS global reanalysis (ECMWF Atmospheric Composition Reanalysis 4) monthly dataset is a globally complete and consistent atmospheric composition product produced by the CAMS using ECMWF's fourth-generation reanalysis system (Inness et al., 2019). It combines a physical and chemical atmospheric model with observations from around the world through data assimilation to produce regular monthly mean fields of many atmospheric variables, including trace gases, aerosols, meteorological and chemical species, on a $0.75° \times 0.75°$ global grid from 2003 to 2024. The dataset spans surface, pressure, and model levels, with updates released about twice a year.

For the IVL data, observations were assigned to the calendar month that covered the majority of the exposure period. As stated in Section 7.12.2, this report presents IVL data from November 2022 to December 2024. Therefore, surface level monthly means of NO_2, SO_2, HNO_3 and O_3 were extracted from CAMS for the same geographic location as each AQM across Murujuga in 2023 and 2024. To match the AQM locations with the grid points in the CAMS dataset, Euclidean distance (Raynor, 2025) was used to find the closest CAMS grid point to each AQM location. The Euclidean distance is the straight□line distance between two points in space and is commonly used to identify the nearest neighbour in spatial analyses when points are compared based on coordinates. For NO_2, SO_2, HNO_3 and O_3 data from CAMS were in kg kg^{-1} units. So that the CAMS data could be compared with the IVL data, the CAMS data were converted into ppb.

Figure *8.3-1* shows comparative boxplots of all IVL data for 2023 and 2024 compared to equivalent boxplots of data extracted from CAMS. The agreement between the two is excellent given the disparate data sources. The only notable exception is NO_2 where the IVL value lies between the CAMS NO_2 and NOx values, suggesting some possible issues with apportionment or partitioning of data between these two related species. Correlations between individual stations with satellite data was not as good, which was not unexpected.

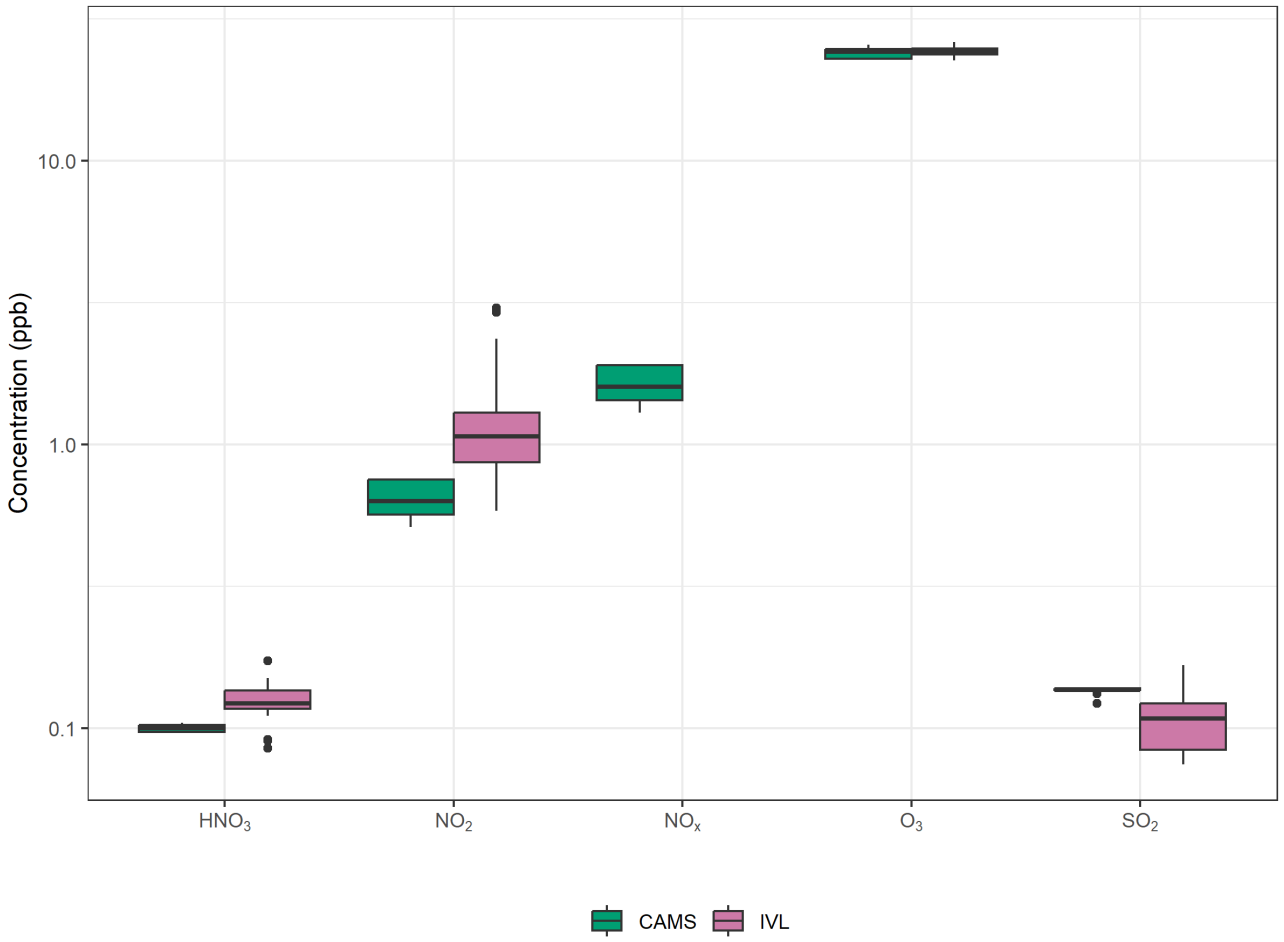

Figure 8.3-1: Boxplots comparing IVL passive samplers with satellite observations (generated using Copernicus Atmosphere Monitoring Service (CAMS)). Note the vertical axis is logarithmic scale.

8.4 Low-power versus real-time powered instruments

8.4.1 Background

Section 7.13 presents data from the real-time air quality monitoring stations and Section 7.14 shows data from the low-power sensors. For the purposes of comparing low power sensors and real time instruments, only the powered sites (AQ01, EX02, and EX09) where both systems were deployed are presented. This section compares the CO_2, NO, NO_2, $PM_{2.5}$ and PM_{10} concentrations from both instruments. Section 7.14.3 showed that the NH_3 low-power sensor had reached its life-time limit and that performance started degrading in early 2024; therefore, it is not presented in this section. The real-time instruments can potentially be used to calibrate the low-powered sensors.

As discussed in Section 7.14, the results for the low-power sensors are determined using the manufacturer provided calibration equations to convert sensor voltage to a concentration. It is known that the electrochemical sensors used for NO, NO_2 and NH_3 are sensitive to temperature and humidity changes so any additional or field calibration of such sensors should include these as variables. Therefore this section will also show temperature and humidity versus NO and NO_2.

8.4.2 Gaseous species

Figure *8.4-1* compares the low-power and real-time powered sensors for NO and NO_2 at AQ01, EX02 and EX09. The data presented in these scatterplots are over one week in November, the same week as presented in figures in Section 7.13 and 7.14. Each dot point is an hourly mean for both the low-power and real-time powered instrument.

This plots show there is some variation in the scale of the readings between the low-power and real-time instruments, with the results from the low-power sensors showing considerably higher concentrations.

Section 7.13.3.2 describes the real time Picarro (isotopic methane analyser) instrument that measures CO_2 levels. This reference instrument is only located at EX09. Thus, Figure *8.4-2* compares the low-power and powered sensors for CO_2 only at EX09. The data presented in these scatterplots are over one week in December, the same week as presented in Figure *7.13-18* in Section 7.13 and 7.14. Each dot point is an hourly mean for both the low-powered and real-time powered instrument. The overall CO_2 mean for the powered sensors in the selected week was 432.34. Applying a calibration correction (dividing by 14.09) to the low cost data matches the overall mean of the two datasets, however the low cost sensor peaks and reference (Picarro) powered peaks do not show a reasonable correlation.

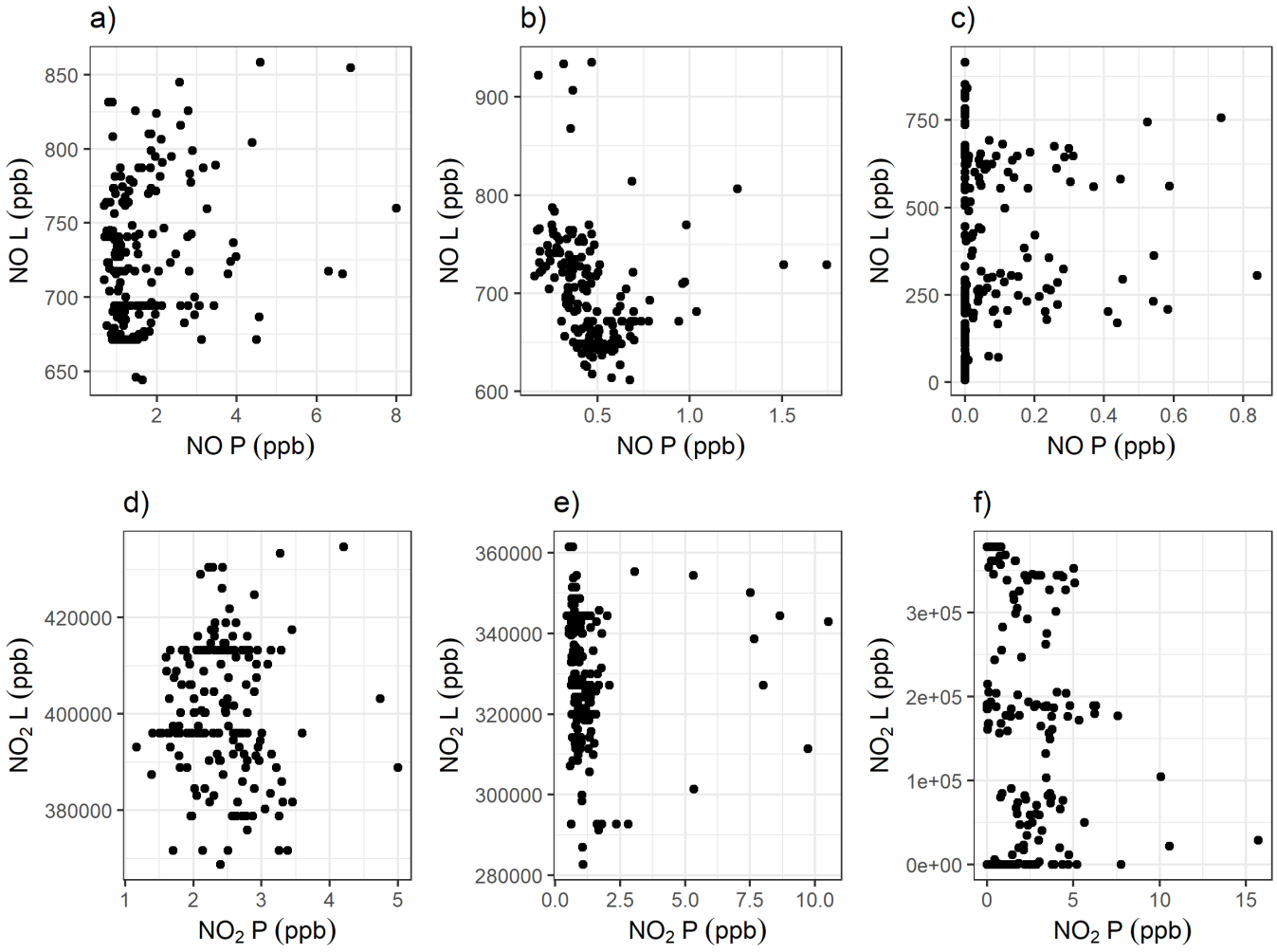

Figure 8.4-1: Scatterplots of low power ("L") versus powered ("P") sensors for NO (first row) and NO_2 (second row) at AQ01 (first column), EX02 (second column) and EX09 (third column) over one week in November 2024. Data have been excluded where the validity is in question.

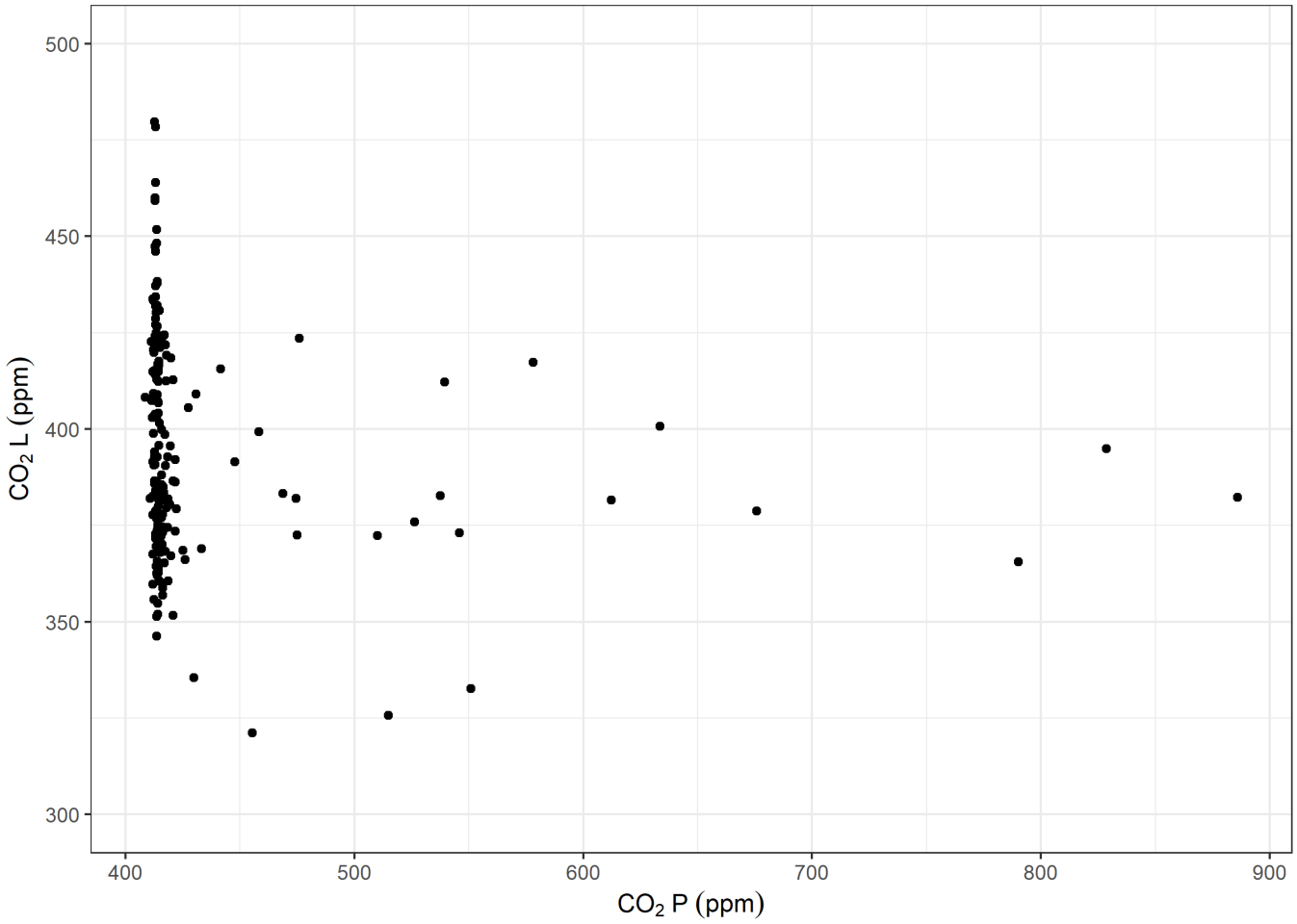

Figure 8.4-2: Scatterplots of low-power ("L") versus powered ("P") sensors for CO_2 at EX09 over one week in December 2024. Data have been excluded where the validity is in question.

8.4.3 Particulates

As with the gas species discussed above, the particulate readings from the low power sensors can be compared to the instrumentation at the powered sites. It should be noted that, given some of the issues with the FIDAS units (see Section 7.13.2), only data from AQ01 and EX09 are considered here.

The low power sensors used count particles across a number of size fractions. As stated in 7.14, the exact output unit for the particle sensors is unclear from the technical manuals. The device works on a similar principle to the FIDAS reference instrument, in that both are both primarily light scattering devices, however the FIDAS operates under controlled temperature and humidity with a high resolution (256 channel) particle count/size classifier and a robust gravimetric calculation to convert to mass concentration. The low cost sensor has 5 channels and a micro axial-flow fan to control airflow through the device. This section compares FIDAS and low-power sensor data and applies a rudimentary calibration by adjusting the mean of the low cost data to the mean of the FIDAS data.

Concentration data for particulates are shown in Figure *8.4-3*, which compares the low-power sensor and real-time powered FIDAS measurements for $PM_{2.5}$ and PM_{10} at AQ01 and EX09 for one week in November 2024.

It can be observed that some correlation exists in the data, which is weakly significant for AQ01 but not significant for EX09. The exact calibration values are not given here, as, since they only represent one week's worth of data, they are of limited value. The calibration applied to the data was $\sim$ 30 times higher for EX09. Notably however, the calibration was consistent across $PM_{2.5}$ and PM_{10} for the same sensor, with PM_{10} requiring a multiplier 1.3-1.6 times higher in both cases. This is inconsistent with literature data that these sensors consistently under-read PM_{10} compared to reference instruments. This was believed to be most likely due to system losses due to higher particle mass and poor airflow. While light scattering efficiency decreases with increasing particle size, this is more than compensated for by the greater particle cross sectional area, meaning that reference grade light scattering instruments generally perform better as particle size increases. However if the performance in the Murujuga climate is different to elsewhere the sensors have been deployed, it may be due to the impact of temperature or humidity.

Overall, it is apparent that sensor-specific calibrations for Murujuga environmental conditions and dust properties appear to be required to obtain even approximately accurate data from these low powered sensors.

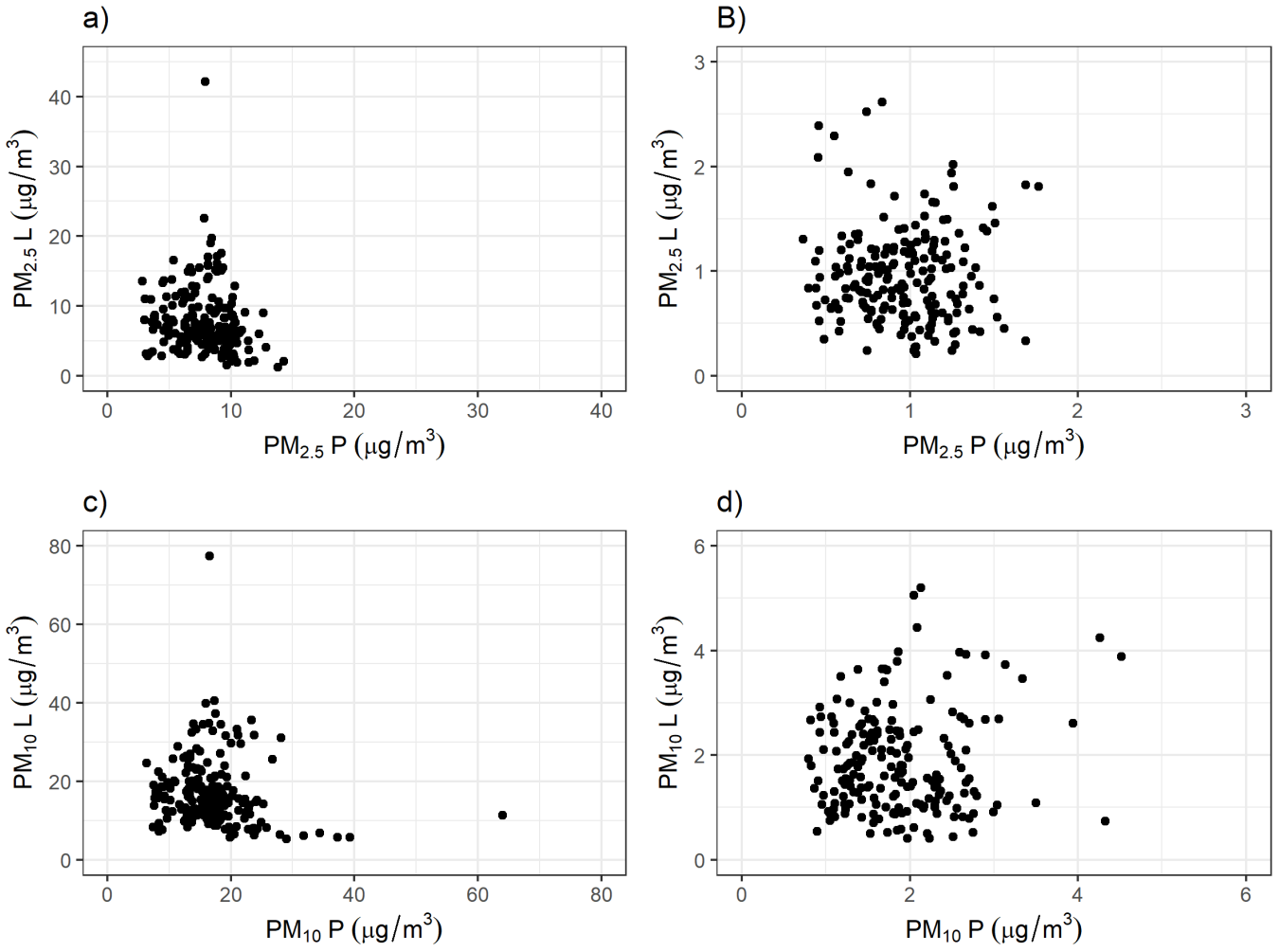

Figure 8.4-3: Scatterplots of low power ("L") versus powered ("P") sensors for $PM_{2.5}$ (first row) at AQ01 (first column) and EX09 (second column) over one week in November 2024. Data have been excluded where the validity is in question.

8.4.4 Comparison of temperature versus gaseous species.

As previously noted, there is a known impact of temperature on the results obtained from the low power electrochemical sensors used in this study. To explore any potential relationships between measured concentrations and on-site temperature, the measured concentration and temperature data from a selected week in November 2024 are considered. The results for NO and NO_2 are shown in Figure *8.4-4*.

There appears to be a linear relationship between NO concentration and temperature, which is most evident for EX02 in Figure *8.4-4*(b). Although the relationship between NO and temperature for AQ01 and EX09 is more scattered, it would still support a reasonable straight line fit. It should be noted that this does not consider the daily variations observed for NO, which may also be due to variable emissions rates, atmospheric chemistry processes, and transport.

Figure *8.4-4* (d), (e), (f) shows that the relationship between NO_2 and temperature is less clear.

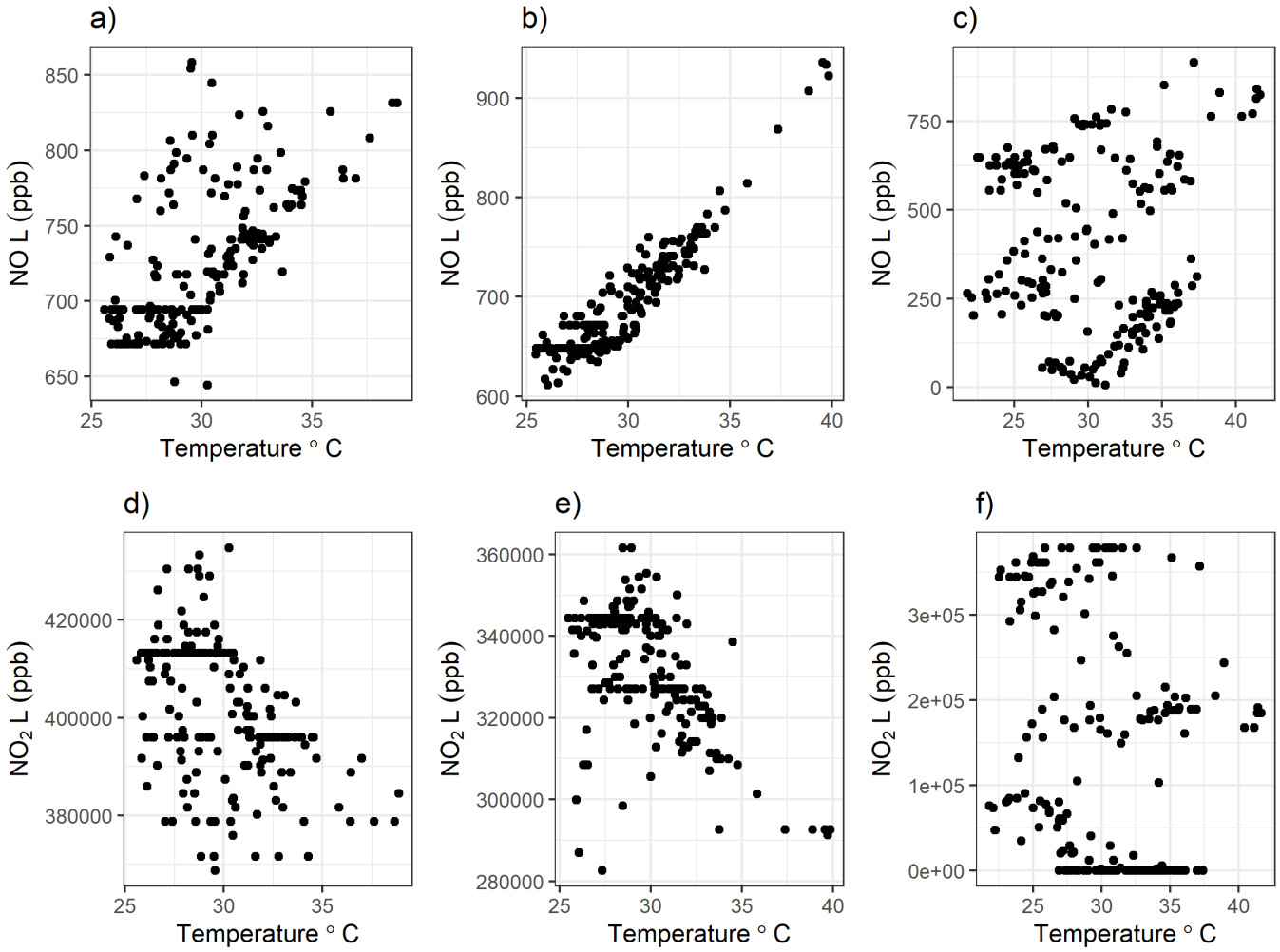

Figure 8.4-4: Scatterplots of low power ("L") versus temperature (°C) for NO (first row) and NO_2 (second row) at AQ01 (first column), EX02 (second column) and EX09 (third column) over one week in November 2024. Data have been excluded where the validity is in question.

However, a negative linear trend may exist for AQ01 and EX02.

It is suggested that, given the apparent relationship observed between temperature and concentration (while acknowledging other factors), any calibration or correction applied to the low power sensors should contain a term related to ambient temperature. In the final report, statistical analysis of the low power sensor calibration will be presented.

8.4.5 Comparison of humidity versus gaseous species

As noted, there is a known impact of humidity on the results obtained from the low power electrochemical sensors used in this study. To explore any potential relationships that exist between measured concentrations and on-site humidity, the measured concentration and humidity over a selected week in November 2024 are considered. The results for NO and NO_2 are shown in Figure *8.4-5*.

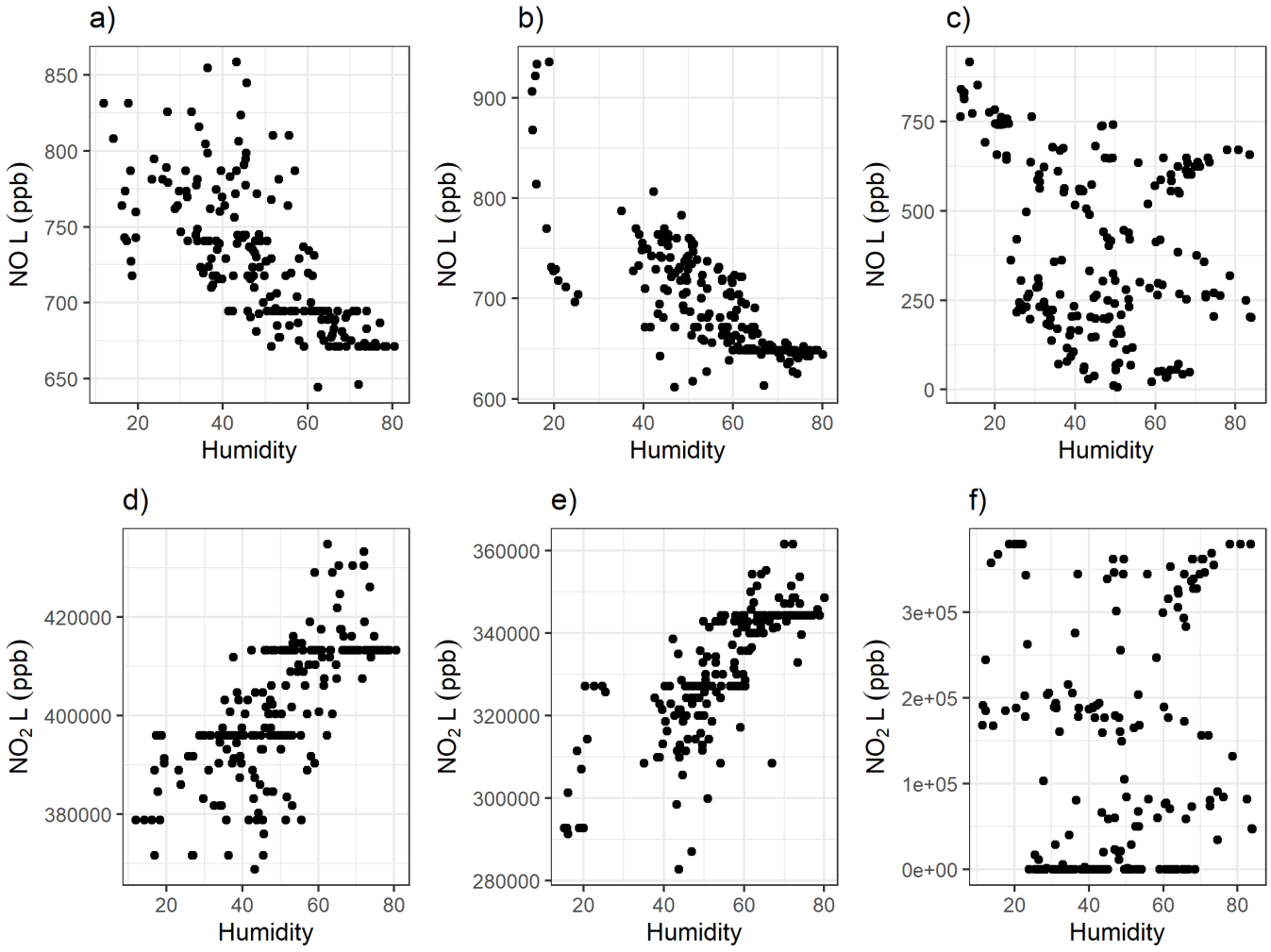

Figure 8.4-5: Scatterplots of low power ("L") versus relative humidity for NO (first row) and NO_2 (second row) at AQ01 (first column), EX02 (second column) and EX09 (third column) over one week in November 2024. Data have been excluded where the validity is in question.

For both AQ01 and EXO2 there is evidence of a negative linear trend between NO concentration and humidity. This is less apparent for EX09, though the range of NO concentrations is considerably broader. For NO_2 concentrations there appears to be a linear relationship between concentration and humidity, which is most apparent at AQ01 and EX02. Once again this is less clear at EX09, where there does not appear to be any identifiable relationship between concentration and humidity. It should also be noted that many of the readings at EX09 are below minimum detection concentration for the sensors, so could simply be electronic noise.

Nevertheless there appears to be a relationship between concentration and humidity in the field, so any applied calibration of the sensors as deployed for this study should consider humidity.

8.5 Exploration of relationships between datasets

Given the noted variation between the measured levels, either between sites or day-to-day, the consistent winds, and known interactions between certain chemical species in the atmosphere, a series of redundancy analyses (RDA) were performed to identify potential relationships between what are believed to be key parameters. For further details on RDAs see section 7.5.2 of the Monitoring Studies Report 2024 (Curtin University, 2024c).

The first RDA considers NO, NO_2, O_3, SO_2, NH_3, radon, $PM_{2.5}$, PM_{10} and wind direction. Where the gas species concentrations are from the real-time instruments presented in Section 7.13. For the purpose of this analysis, wind directions are grouped in bands corresponding to different points on a compass (e.g., N, NNE, NE, ENE, E, and so on), such that there are 16 different wind direction descriptors. All values have also been summarised into daily means.

The results of this analysis are shown in Figure *8.5-1*. NO and NH_3 are positively correlated with each other thus suggesting they vary together. Also NO and NH_3 are associated with wind directions ESE and SSE. NO_2 and SO_2 are associated with WNW winds. $PM_{2.5}$, PM_{10}, O_3 and radon cluster together thus suggesting they co-vary; plus are associated with winds from the S to SSW. Possibly the most interesting result of this RDA is the relationship between Radon and wind direction. As mentioned, the Radon instrument is only located at EX09 on Mt Wongama. Typically, it would be expected that Radon levels would be highest when the wind is coming from the main land mass (ESE) and lowest when the wind is coming from the ocean. However it appears that Radon levels are highest when the wind is coming from the direction of the gas plants. This would tend to suggest that locally combusted gas has had insufficient time for the Radon to decay before it is combusted/emitted. Radon has a half life of 3.8 days. An implication of this finding is the potential to use Radon as a means of source apportionment of gas plant emissions vs other emissions, since for other sources the fuel would likely have been stored long enough for the Radon to decay.

The second RDA considers the same gas species as the first, but in relation to temperature and humidity. Results also include data from the low-powered sensors. The results of this analysis are shown in Figure *8.5-2*. The following gas species are clustered together: NO_2 from both low-powered and powered sensors, low-powered NH_3, powered $PM_{2.5}$ and PM_{10} and powered SO_2. This indicates that all of these variables co-vary, suggesting they may share similar emission sources or be influenced by similar environmental conditions. The arrows for NO_2 from both low-powered and powered sensors overlap, indicating that the low-powered sensors are measuring NO_2 concentrations similar to those recorded by the powered sensors. The powered $PM_{2.5}$ is negatively correlated with low-powered $PM_{2.5}$ sensors, suggesting that the two sensor types respond differently to particulate matter or are influenced by differing local conditions. Temperature is positively correlated with O_3, which is understandable as UV radiation plays a key role in o_3 formation and can be expected to correlate with temperature. Furthermore, volatile organic compounds (VOCs) are required (along with NO_2 to form ozone. A major source of these would be biogenic VOSc (bVOCs) from the local vegetation (e.g. oils from eucalyptus and spinifex, among others) and could be expected to be emitted at rates corresponding with temperature. Humidity is negatively correlated with NH_3 and NO from both low-powered and powered sensors. Many species, particularly SO_2, NH_3 and NO_2 are known to react readily with water. There is also likely an inverse correlation between humidity and wind speed, with wind being a major driver for dust

(PM) emission from both natural and industrial sources.

In the final report, further statistical analysis and modelling will be undertaken to the compare low-powered and powered sensors, including calibration of the low-powered sensors.

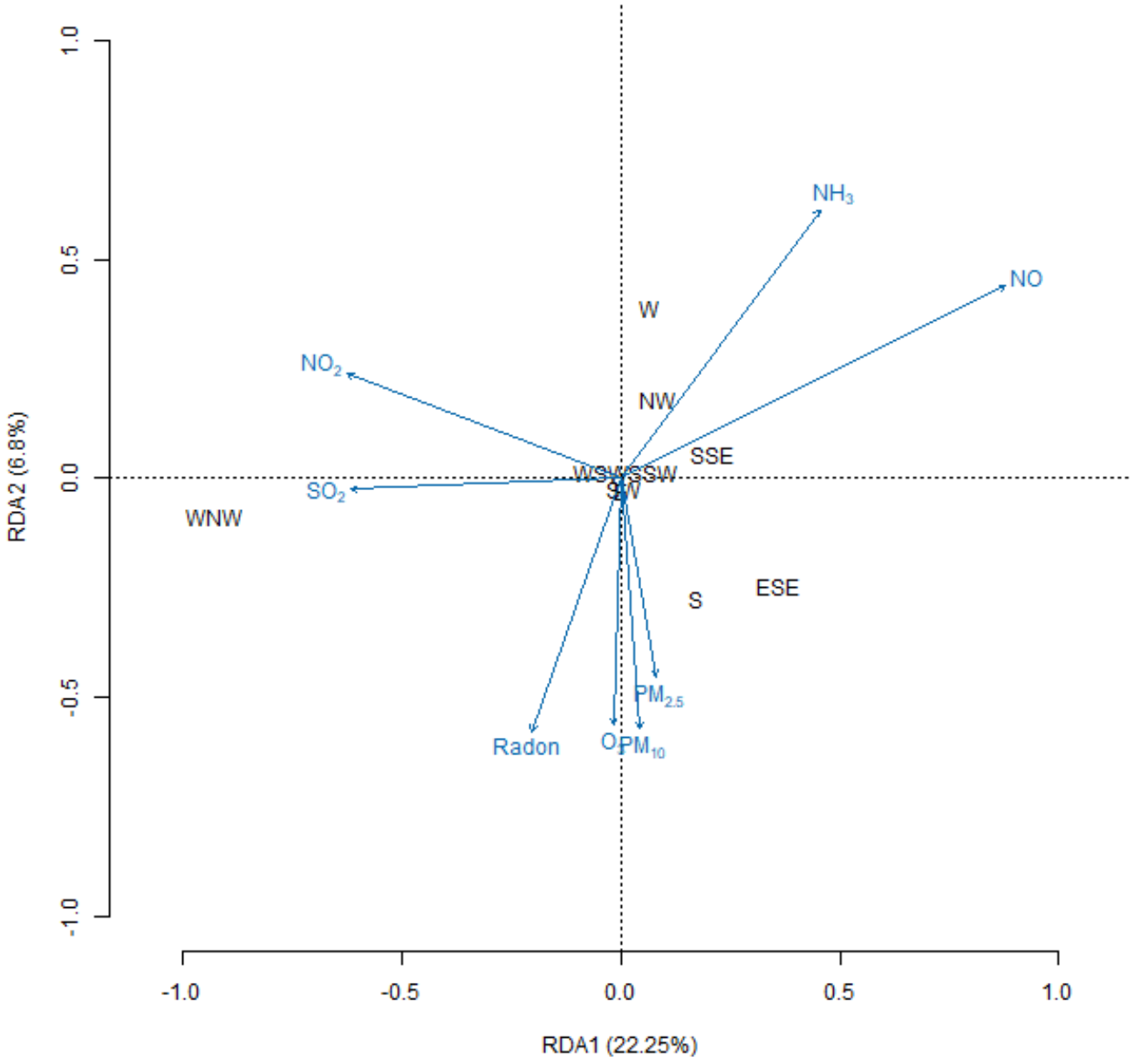

Figure 8.5-1: RDA of instruments T100, T201, T400, Radon and wind direction. Where the data has been summarised into daily means

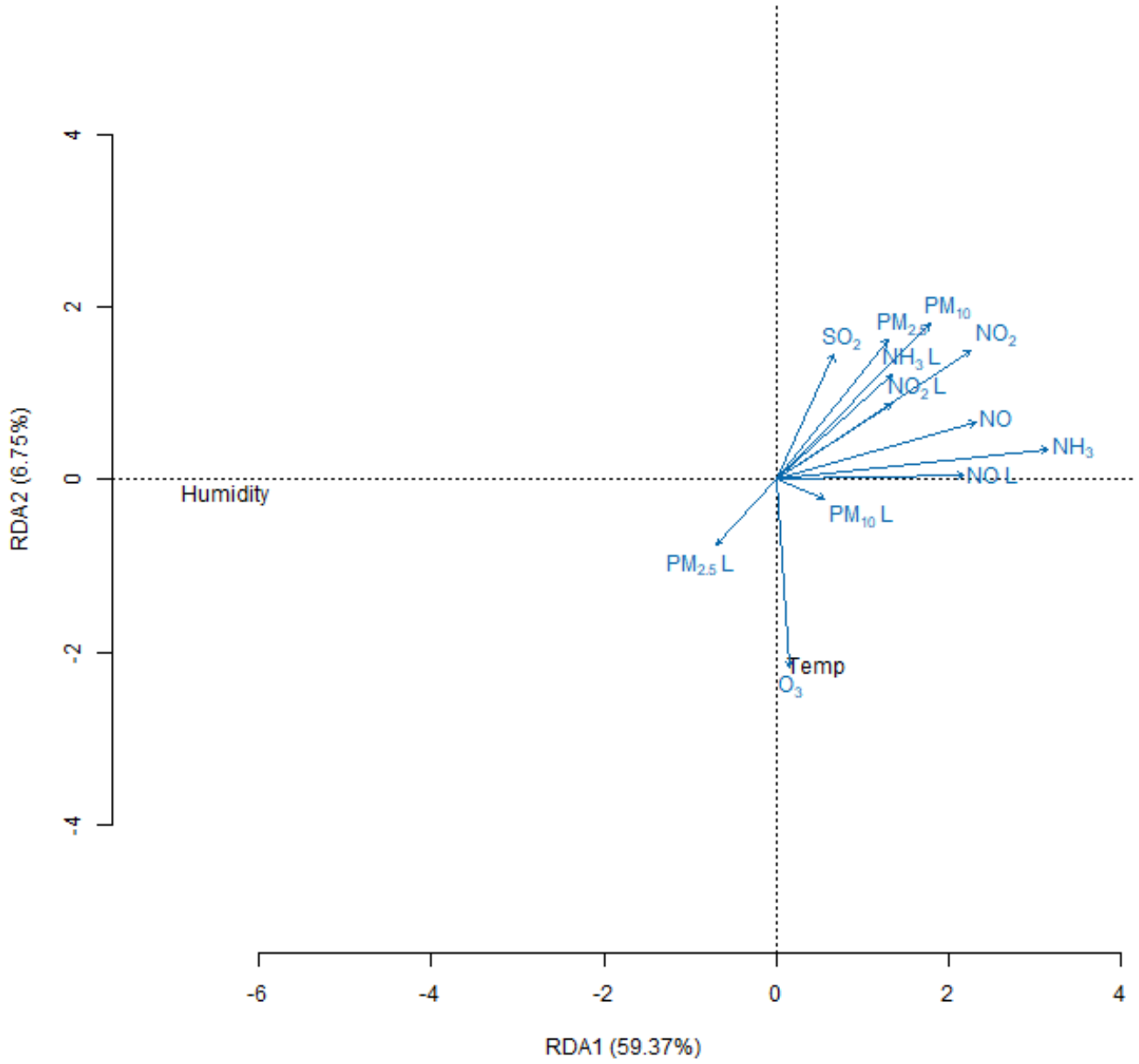

Figure 8.5-2: RDA of low cost, powered, temperature, relative humidity, wind direction. Where the data has been summarised into daily means.

8.6 Key findings from statistical comparative analysis

8.6.1 Deposition samplers vs passive samplers

The results in this section show a positive correlation between airborne NO_2 concentrations and NO_3^- as expected, showing that NO_2 is likely the dominant source of deposited NO_3^-.

SO_2 and SO_4^{2-} show a moderate positive correlation.

There is a negative correlation between NH_3 and NH_4^+ and this association is not statistically significant.

A detailed analysis of these observations combined with weather and other air quality data will be undertaken in the final report.

8.6.2 Bucket deposition versus total flask deposition

This section compared chemical species concentrations collected from 3-bucket deposition and total flask deposition samplers. Concentrations of Ca^{2+}, Cl^-, K^+, Mg^{2+}, and Na^+ show a slight positive association between the two samplers, suggesting that both methods measure similar levels

In contrast, NH_4^+, NO_3^-, P, and SO_4^{2-} show no clear relationship, likely because many values are below the detection limit for one or both samplers.

8.6.3 Validation against satellite observations

Ground-level air quality data for 2023 and 2024 were compared between AQM measurements and CAMS data for the same locations. Agreement was excellent overall, with the only notable difference being NO_2, where X values fell between CAMS NO_2 and NOx, suggesting potential issues with species apportionment.

In this section, satellite observations and predictive forecast data were compared with the IVL passive samplers for the same locations. Agreement was excellent overall, with the only notable difference being NO_2, where IVL values fell between CAMS NO_2 and NOx, suggesting potential issues with species apportionment.

8.6.4 Low power versus real time powered instruments

The majority of the low-power sensors show a very strong response to temperature and/or humidity, typically stronger than their response to powered sensors. This has also been reported in the literature by others who have used the same sensors. However, for stable conditions, NO and NO_2 sensors at minimum show a good agreement with reference instruments, therefore the prospects are good to develop a suitable calibration if necessary. This will be explored further in the final report.

8.6.5 Exploration of relationships between datasets

This section shows initial analysis exploring relationships between chemical species, particulates, radon, temperature, humidity and wind direction.

The first RDA, using daily means of nine air quality variables and grouped wind directions, found distinct relationships between species and wind sectors. NO and NH_3 covaried and were linked to ESE–SSE winds, NO_2 and SO_2 to WNW winds, and $PM_{2.5}$, PM_{10}, O_3, and radon to S–SSW winds. Notably, radon peaked with winds from nearby gas plants, suggesting insufficient decay before combustion and potential for source apportionment.

The second RDA related the same species (including low powered sensor data) to temperature and humidity. Results showed overlapping NO_2 from both sensor types, positive temperature and O_3 correlation likely driven by photochemistry and bVOC emissions, and negative humidity–NH_3/NO associations, possibly from aqueous reactions and reduced dust emissions.

9 General summary

9.1 Summary

This report has focused on extending and verifying the findings and relationships provided in the Monitoring Studies Report 2024 (Curtin University, 2024c). Given the massive body of data collected to-date, this approach is more appropriate than attempting analysis and synthesis of new datasets likely to be less critical for answering the key research questions.

Three fieldwork campaigns were undertaken during the third year of this study, between April 2024 and March 2025 inclusive, with ten campaigns completed to date. The third year of fieldwork comprised 18 weeks' duration in total. Fieldwork involved monitoring 54 rock art panels across the five rock types found in the study area. All fieldwork on Murujuga, including rock sample collection, is approved by the Murujuga Aboriginal Corporation (**MAC**) Elders. To date, over 186,200 spectral/colour measurements of rock art condition have been recorded, along with over 5,500 surface electrochemical measurements (*pH*, *Eh*, Cl^-). Surface elemental measurements using x-ray fluorescence (pXRF) were discontinued this year as the previous analysis found the measure not to be useful for monitoring change over time.

The 64 rock samples and additional microbial samples collected in 2022 and further 26 sample rocks collected in 2024 have been subject to ongoing analysis of their microstructure, organic chemistry, inorganic geochemistry, and surface microbial communities, the bulk of which is now well advanced. Further results of geological/geochemical analyses are presented in this report. However, much of the organic geochemistry, microbial and air quality studies are still ongoing, as is more extensive statistical data analyses and syntheses.

Air quality

The Murujuga air quality monitoring network of 18 solar/passive air quality and weather monitoring stations and four mains-powered monitoring stations continues to operate as planned. A further 12 months of monitoring data from all operational air quality monitoring instruments has been analysed for this report. The concentrations and spatial patterns of air quality data are broadly consistent between the year two and year three datasets.

Air quality remains good, on average, and is well within relevant health guideline limits and the (lower) interim EQC Guideline concentrations for: ammonia (NH_3), sulfur dioxide (SO_2), and nitrogen dioxide (NO_2) that were established following the second year of studies. Exploratory results are provided from the Murujuga AQM network data across all locations:

- NH_3, was detected consistently highest at AQA1 and AQ11 sites, which are located in the King Bay area between the fertiliser plant(s) and the Port of Dampier export terminal.
- SO_2 levels were highest at AQ11 (which overlooks the King Bay port facilities and is close to Port of Dampier), and on the outer islands (e.g., AQ18), depending on prevailing winds. SO_2 level appears to be determined by shipping activities, however some may be the result of gas combustion or flaring. SO_2 is highly reactive so levels are likely to reduce faster than other species post emission.
- NO_2 and nitric acid (HNO_3, a secondary air pollutant) are highest in the region spanning Dampier (EX02), Mt Wongama (EX09) and Katrin's Hill (AQ07/08), which overlooks the airport.

- Ozone (O_3), has less spatial variability, due to the time scales and organic species required for formation. The peak ozone concentration in 2023 was at EX09 and at AQ18 in 2024 .

As discussed in the Monitoring Studies Report 2024 (Curtin University, 2024c), moderate levels of formaldehyde (CH_2O) have also been measured, which is an intermediate product in the decomposition of methane (CH_4). CH_2O is a weak but non-trivial contributor to O_3 formation when combined with NO_2. There is no suggestion at this stage that organic air pollutant species are significantly affecting rock art, however, sufficiently high concentrations of CH_2O or O_3 at ground level could be expected to impact the microbiome or accelerate reaction rates or oxidation processes.

Moderate levels of black carbon (soot) have also been recorded. Again, this requires further investigation due to suggestions it may contribute to rock surface delamination (Dorn, 2020). Some black carbon is due to natural sources such as bushfires, however the majority appears to be anthropogenic (e.g. from sources such as gas flares, shipping and land transport).

Real-time AQM data reveal significant spikes in CH_4 and CO_2. These spikes are short-term, however, and there is no expectation that these greenhouse gases are impacting the microbiome. Measured peaks in (non-greenhouse) air pollutant gas species are within human health guidelines. However further investigation is needed (via the microbiome chamber studies) to confirm if they can impact the rock/microbiome complex. While not a primary focus of this project, radon measurements appear a useful means of apportioning emissions from the gas plants, as other hydrocarbon fuels would be expected to be sufficiently aged to no longer contain appreciable radon.

***pH* and rainfall measurements**

Measurements of *pH* from inert surfaces such as the deposition samplers and rainfall samplers clearly show that wet and dry deposition over the past three years continues to be neutral or slightly alkaline, on average. *pH* measurements undertaken on fresh rock cubes installed in AQMs were found to be close to neutral and differentiated by rock type. Average rainfall *pH* is 7.4 across all data and deposition sampler dry *pH* is 6.7. These results contrast to previous measurements in 2005 by CSIRO 2006, which show a median rainfall pH of 4.8 and an average of 5.

Murujuga is near the centre of the ’D’ cyclone region (spanning Carnarvon-Pardoo) which receives the most severe cyclones on the Australian mainland. In early 2025 it experienced the Category 1 Tropical Cyclone Sean, which caused an all time record of 274 mm rainfall over 24 hours in the Karratha Aero (Bureau of Meteorology) station and 303 mm at two MRAMP stations. This event led to a lower rainfall *pH* of 5.6-7, which is closer to global average values.

pH measurement on ‘live’ or patinated rock surfaces tend to be slightly acidic. These data are more complex to interpret. However, the lower *pH* appears to be primarily due to microbial activity. Measurements from the surface of bushfire-exposed rocks in year two showed a clear alkaline signal, which reverted to baseline over 9-12 months post exposure. Another important consideration in rock *pH* measurement is the contribution of clay minerals (e.g., dust), which are expected to be alkaline, as well as sea spray (which may range from acidic to slightly alkaline). Additional data collected appears to confirm previous observations of microbial responses to rainfall or dust deposition, which may result in the production of organic acids by the microbiome.

Porosity and patina formation

The porosity of the weathered rind (subsurface layer) of granophyre rock was higher in a region centered around King Bay, extending to south of Dampier town, north to encompass the industrial precincts and lower elsewhere. As all natural causes have at this stage been ruled out, this pattern appears to represent historic anthropogenic impact, most likely from historic (higher) emission levels and associated ground level air quality of chemical species. An error in the significance analysis in the Monitoring Studies Report 2024 (Curtin University, 2024c) has been found, which has resulted in an apparent increase in the region of statistically significant porosity. It should be noted that this does not represent an increase since the year two data, rather it was a computational error in the level of statistical significance data was tested to. The spatial porosity pattern determined from the original rock samples collected in 2022 and a second validation set collected in 2024 present comparable results when analysed using appropriate statistical techniques developed for the project.

Chamber accelerated weathering studies and Interim EQC

The chamber studies have demonstrated a mechanism by which exposure to air pollution can increase rock porosity, which can theoretically occur without rainfall. This mechanism has been confirmed chemically through analysis of leachate, and physically through high resolution imaging of minerals before and after exposure. Interim EQC were developed following the second year of studies for NH_3, NO_2 and SO_2. The latter two chemical species were given as a linked EQC as results were from combustion experiments producing both species, as well as a range of carbon compounds.

In order to differentiate individual responses, geochemical weathering studies switched to single gas exposures, and microbial culture exposures commenced. Some possible issues with sample rock reuse and experiment sequencing were identified and additional experiments have been undertaken to address this. Most importantly, the experiments have found no response to NO_2, apart from a likely response at the highest possible dose obtainable under the revised/improved experimental protocol. Other weathering literature has suggested this is due to Henry's law, which relates to the solubility and reactivity of weak gas mixtures. Henry's law suggests that SO_2 is approximately 110 times more important to weathering than NO_2 and NH_3 approximately 5,000 times more important. For this reason, SO_2 has always been the major contributor to acid rain globally. In agreement with this theory, a clear dose-response relationship has been found for SO_2 using both the original and revised experimental protocol. It is expected that a combined weathering index can be developed for future EQC, which will account for varying concentrations and species of air pollutants.

Microbiome chamber studies are progressing on schedule, however, are not yet at a stage where they can contribute to EQC development. Preliminary results appear to agree with the relative importance of NO_2 vs SO_2 found in the abiotic experiments, however some groups or genera may respond differently to others, which adds complexity.

Field rock art spectrometry and photogrammetry

Spectral imaging of rock art is now producing high quality results after considerable work to optimise the method, with initial analysis and error detection taking place in the field in real time. Novel software with a graphical user interface has been developed for this purpose, which integrates with the (current) HDX instrument, to validate measurements at the time of data collection. A

sufficient body of comparable measurements have now been obtained to permit temporal analysis to identify any trends. The JAZ instrument is more variable than the HDX instrument. The four sites examined to-date do not show a changing trend of rock(art) surface colour over the three years of measurements undertaken to-date. Similar analysis for all sites will be presented in the following report, along with an ongoing rock art condition monitoring plan. In the interim, monitoring will continue once per year in the cooler (mid-year) months.

Additionally, a simplified photogrammetry approach has been developed and validated. This complementary approach is reliably able to detect changes in rock art panels at the sub-millimetre scale.

9.2 Conclusion

The monitoring data contained in this report is broadly consistent with the findings presented in the Monitoring Studies Report 2024 (Curtin University, 2024c) following the second year of studies. The additional year of research and analysis presented in this report, however, clarifies some key aspects of results and relationships observed in the Monitoring Studies Report 2024 (Curtin University, 2024c).

The porosity findings have been reconfirmed using a second subset of data, which produced a significant porosity area when the Monitoring Studies Report 2024 (Curtin University, 2024c) plot is corrected to a true 95% confidence value. Some minor/random errors in sample preparation for porosity analysis were also detected, however were determined not to influence results.

The overall air quality remains below the Interim EQC Guideline levels established following the second year of studies last year. Rainfall and wet deposition are not acidic during the study period. A small number of dry deposition values do fall within the acidic range (in the AQM dry bucket samples) but not in corresponding AQM total deposition flasks. This finding requires further investigation to confirm if it is a real phenomenon or an outlier due to the deposition of rust or guano in the samplers. The small number of acidic samples are equally spread between sites near and distant from industrial sites, however a number are at AQA1, located at the MAC offices and near the bulk of industry and AQ08, near the airport.

The importance of NO_2 to rock surface weathering would appear to less than suggested in the Monitoring Studies Report 2024 (Curtin University, 2024c) and associated Interim EQC. Given literature data and the single gas chamber studies findings, this will be accounted for in the revised Interim EQC following the current report.

The CSIRO 2005-2009 acidic rain measurements (Bednarik, 2007; Department of Environment and Conservation, Western Australia, 2010) add further support to a hypothesis that historic emissions (particularly SO_2) were the most likely contributor to abiotic weathering leading to increased porosity found in the rock samples. However the possibility of pollutant-microbiome interactions leading to organic acid induced weathering is also being explored.

The techniques developed as part of this project are robust and effective at monitoring changes in the rock art over time, well before they can be detected by the naked human eye. Combined with the atmospheric and deposition monitoring, the data generated in this report appears sufficient to give early notice if any changes in the airshed occur that may revert to previous conditions of

concern for damaging rock surfaces.

Further combined analysis will be presented in the final report, including microbiome interactions.

This page is intentionally blank.

References

Aho, K. and Weaver, T. (2006). Measuring water relations and pH of cryptogram rock-surface environments. *The Bryologist*, 109(3):348–357.

Baddeley, A. and Jensen, E. V. (2005). *Stereology for Statisticians*. Chapman and Hall/CRC, Boca Raton.

Bakhshi, M., Zare, R., and Jafary, H. (2022). Toxicocladosporium crousianum and t. eucalyptorum, two new foliar fungi associated with eucalyptus trees. 21(9):77.

Bednarik, R. G. (2007). The science of Dampier rock art–Part 1. *Rock Art Research*, 24(2):209–246.

Benjamini, Y. and Hochberg, Y. (1995). Controlling the false discovery rate: a practical and powerful approach to multiple testing. *Journal of the Royal Statistical Society B*, 57:289–300.

Bezerra, J. D. P., Sandoval-Denis, M., Paiva, L. M., Silva, G. A., Groenewald, J. Z., Souza-Motta, C. M., and Crous, P. W. (2017). New endophytic toxicocladosporium species from cacti in brazil, and description of neocladosporium gen. nov. 8:77–97. Place: London Publisher: BioMed Central.

Biswas, C. and Johri, B. M. (2014). *The gymnosperms*. Springer Berlin, Heidelberg.

Black, J. L., Box, I., and Diffey, S. (2017). Inadequacies of research used to monitor change to rock art and regulate industry on Murujuga (Burrup Peninsula), Australia. *Rock Art Research*, 34(2):130–148.

Bolen, J. (2014). Modern air pollution control for iron ore induration. *Minerals and Metallurgical Processing*, 31(2):103–114.

Booth, A. M., Sutton, P. A., Lewis, C. A., Lewis, A. C., Scarlett, A., Chau, W., Widdows, J., and Rowland, S. J. (2007). Unresolved complex mixtures of aromatic hydrocarbons: Thousands of overlooked persistent, bioaccumulative, and toxic contaminants in mussels. *Environmental Science & Technology*, 41(2):457–464.

Boreham, C., Crick, I., and Powell, T. (1988). Alternative calibration of the methylphenanthrene index against vitrinite reflectance: Application to maturity measurements on oils and sediments. *Organic Geochemistry*, 12(3):289–294.

Bracewell, J. M. and Robertson, G. W. (1984). Quantitative comparison of nitrogen containing pyrolytic products and aminoacids composition of soil humic acids. *Journal of Analytical and Applied Pyrolysis*, 6:19–29.

Broomandi, P., Jahanbakhshi, A., Fathian, A., Darynova, Z., Janatian, N., Nikfal, A., Kim, J. R., and Karaca, F. (2022). Impacts of ambient air pollution on UNESCO world cultural heritage sites in Eastern Asia: Dose-response calculations for material corrosions. *Urban Climate*, 46:101275.

Buck, R., Rondinini, A., Covington, F., Baucke, C., Brett, M., Camoes, M., Milton, T., Mussini, R., Naumann, K., Pratt, R., Spitzer, R., and Wilson, G. (2002). Measurement of pH. Definition, standards, and procedures. *Pure and Applied Chemistry*, 74:2169–2200.

Bush, R. T. and McInerney, F. A. (2013). Leaf wax n-alkane distributions in and across modern plants: Implications for paleoecology and chemotaxonomy. *Geochimica et Cosmochimica Acta*, 117:161–179.

Callahan, B. J., Mcmurdie, P. J., Rosen, M. J., Han, A. W., Johnson, A. J. A., and Holmes, S. P. (2016). DADA2: High-resolution sample inference from illumina amplicon data. 13(7):581–583. Place: New York Publisher: Nature Publishing Group.

Che, Y.-H., Wang, J.-F., Ding, W.-P., Xiao, Z.-H., Shi, X.-F., Wu, J.-M., Wang, F.-Z., and Zhang, S. (2024). New diketopiperazine alkaloids from the haima cold seep-derived fungus toxicocladosporium sp. CYH-18. 60:96–100.

Chiavari, G. and Galletti, G. C. (1992). Pyrolysis-gas chromatography/mass spectrometry of amino acids. *Journal of Analytical and Applied Pyrolysis*, 24(2):123–137.

Chikaraishi, Y. (2014). $^{13}C/^{12}C$ Signatures in Plants and Algae. In Falkowski, P. G. and Freeman, K. H., editors, *Treatise on Geochemistry*, volume 12, chapter 8, pages 95–123. Elsevier, Oxford, 2 edition.

Collister, J. W., Rieley, G., Stern, B., Eglinton, G., and Fry, B. (1994). Compound-specific $\delta^{13}c$ analyses of leaf lipids from plants with differing carbon dioxide metabolisms. *Organic Geochemistry*, 21:619–627.

Costa, M. S., Rego, A., Ramos, V., Afonso, T. B., Freitas, S., Preto, M., Lopes, V., Vasconcelos, V., Magalhaes, C., and Leao, P. N. (2016). The conifer biomarkers dehydroabietic and abietic acids are widespread in cyanobacteria. *Scientific Reports*, 6(1):23436.

Cronan, J. E. and Thomas, J. (2009). Bacterial fatty acid synthesis and its relationships with polyketide synthetic pathways. *Methods in Enzymology*, 459:395–433.

Crous, P., Braun, U., Schubert, K., and Groenewald, J. (2007). Delimiting cladosporium from morphologically similar genera. 58:33–56.

Cruywagen, E. M., Crous, P. W., Roux, J., Slippers, B., and Wingfield, M. J. (2015). Fungi associated with black mould on baobab trees in southern africa. 108(1):85–95. Place: Dordrecht Publisher: Springer Nature B.V.

Curtin University (2022). *Murujuga Rock Art Monitoring Program: Monitoring Studies Data Collection and Analysis Plan*. Report prepared by Curtin University for the Murujuga Aboriginal Corporation and Department of Water and Environmental Regulation, Government of Western Australia (COPP21065-PLN-G-102_0). Government of Western Australia. https://www.wa.gov.au/government/publications/murujuga-rock-art-monitoring-program-monitoring-studies-data-collection-and-analysis-plan.

Curtin University (2023). *Murujuga Rock Art Monitoring Program: Monitoring Studies Report 2023*. Report prepared by Curtin University for the Murujuga Aboriginal Corporation and Department of Water and Environmental Regulation, Government of Western Australia (COPP-21065-REP-G-101). Government of Western Australia. https://www.wa.gov.au/government/publications/murujuga-rock-art-monitoring-program-monitoring-studies-report-2023.

Curtin University (2024a). *Murujuga Rock Art Monitoring Program: Interim Environmental Quality Criteria*. Report prepared by Curtin University for the Murujuga Aboriginal Corporation and the Department of Water and Environmental Regulation, Government of Western Australia.

Curtin University (2024b). *Murujuga Rock Art Monitoring Program: Monitoring Studies Data Collection and Analysis Amendment Plan*. Report prepared by Curtin University for the Murujuga Aboriginal Corporation and Department of Water and Environmental Regulation, Government of Western Australia (COPP21065-PLN-G-105 (Rev 3)). Government of Western Australia.

Curtin University (2024c). *Murujuga Rock Art Monitoring Program: Monitoring Studies Report 2024*. Final Report prepared by Curtin University for the Department of Water and Environmental Regulation and the Murujuga Aboriginal Corporation (COPP21065-REP-G-105). Government of Western Australia.

Curtin University (2025a). *Murujuga Rock Art Monitoring Program: Interim Environmental Quality Criteria*. Report prepared by Curtin University for the Murujuga Aboriginal Corporation and the Department of Water and Environmental Regulation, Government of Western Australia.

Curtin University (2025b). *Murujuga Rock Art Monitoring Program: Monitoring Studies Report 2026*. Draft Report prepared by Curtin University for the Department of Water and Environmental Regulation and the Murujuga Aboriginal Corporation (COPP21065-REP-G-105). Government of Western Australia.

Department of Biodiversity, Conservation and Attractions (DBCA) (2021). *Murujuga National Park Visitor Guide*. https://exploreparks.dbca.wa.gov.au/sites/default/files/2021-10/murujuga-national-park-visitor-guide.pdf. Accessed: 2025-07-02.

Department of Environment and Conservation, Western Australia (2006). *Burrup Peninsula Air Pollution Study: Final Report*. Report Submitted to WA DOIR Rock Art Committee.

Department of Environment and Conservation, Western Australia (2010). *Burrup Peninsula Air Pollution Study: Final Report*. Report Submitted to WA DOIR Rock Art Committee.

Department of Water and Environmental Regulation (DWER) (2019). *Murujuga Rock Art Strategy: A monitoring, analysis and decision-making framework to protect Aboriginal rock art located on Murujuga (the Dampier Archipelago and Burrup Peninsula)*. Government of Western Australia. https://www.wa.gov.au/government/publications/murujuga-rock-art-strategy.

Department of Water and Environmental Regulation (DWER) (2021). *Murujuga Rock Art Monitoring Program: Conceptual Model* [Fact sheet]. Government of Western Australia. https://www.wa.gov.au/government/publications/murujuga-rock-art-monitoring-conceptual-model.

Diefendorf, A. F. and Freimuth, E. J. (2017). Extracting the most from terrestrial plant-derived n-alkyl lipids and their carbon isotopes from the sedimentary record: A review. *Organic Geochemistry*, 103:1–21.

Dorn, R. I. (2020). Anthropogenic interactions with rock varnish. *Biogeochemical cycles: ecological drivers and environmental impact*, pages 267–283.

Dorn, R. I. (2024). Rock varnish revisited. *Progress in Physical Geography: Earth and Environment*, 48(3):389–419.

Drever, J. and Clow, D. (1995). Weathering rates in catchments. *Reviews in mineralogy*, 31:463–484.

Environmental Protection Authority (2016). *Technical Guidance: Protecting the Quality of Western Australia's Marine Envrionment.* https://www.epa.wa.gov.au/sites/default/files/Policies_and_Guidance/TechnicalGuidance_ProtectingTheQualityOfWAMarineEnvironment-131216_0.pdf.

Environmental Protection Authority (2017). *Environmental quality criteria reference document for Cockburn Sound*. A supporting document to the State Environmental (Cockburn Sound) Policy 2015. https://www.epa.wa.gov.au/sites/default/files/Policies_and_Guidance/EQCRefDocforCockburnSoundFeb2017-2.pdf.

Exxon Mobil (2025). Product data sheet, commercial jet fuel, australia. https://www.exxonmobil.com/en/aviation/products-and-services/products/exxonmobil-jet-a-1. Accessed: 2025-08-08.

Fotedar, R., Sandoval-Denis, M., Kolecka, A., Zeyara, A., Al Malki, A., Al Shammari, H., Al Marri, M., Kaul, R., and Boekhout, T. (2019). Toxicocladosporium aquimarinum sp. nov. and toxicocladosporium qatarense sp. nov., isolated from marine waters of the arabian gulf surrounding qatar. 69(10):2992–3000. Publisher: Microbiology Society Type: Journal Article.

Greenshields, C. (2022). *OpenFOAM v10 User Guide*. The OpenFOAM Foundation, London, UK.

Grice, K., Audino, M., Boreham, C. J., Alexander, R., and Kagi, R. I. (2001). Distributions and stable carbon isotopic compositions of biomarkers in torbanites from different palaeogeographical locations. *Organic Geochemistry*, 32(10):1195–1210.

Grice, K., Backhouse, J., Alexander, R., Marshall, N., and Logan, G. A. (2005). Correlating terrestrial signatures from biomarker distributions, $\delta^{13}c$, and palynology in fluvio-deltaic deposits from nw australia (triassic–jurassic). *Organic Geochemistry*, 36(10):1347–1358.

Grice, K. and Brocks, J. J. (2011). Biomarkers (organic, compound-specific isotopes). In Reitner, J. and Thiel, V., editors, *Encyclopedia of Geobiology*, pages 167–182. Springer, Dordrecht, The Netherlands.

Gull, M. and Pasek, M. A. (2021). The role of glycerol and its derivatives in the biochemistry of living organisms, and their prebiotic origin and significance in the evolution of life. *Catalysts*, 11(1):86.

Gutiérrez-Flores, L. M., Mauricio-Gutiérrez, A., Carcaño-Montiel, M. G., Portillo-Manzano, E., Gómez-Velázquez, L., Sánchez-Alonso, P., and López-Reyes, L. (2020). Fungi associated with sick trees of pinus patula in tetela de ocampo, puebla, mexico. 53(13):591–611. Publisher: Taylor & Francis.

Haman, C., Dauchy, X., Rosin, C., and Munoz, J.-F. (2015). Occurrence, fate and behavior of parabens in aquatic environments: A review. *Water Research*, 68:1–1.

Hamersley News (1974). Scrubber installed as part of upgrade. *Hamersley News*, 11 April 1974, p.5. Available online at: https://trove.nla.gov.au/newspaper/article/214545833. Last accessed 13/05/2025.

Hashimoto, K., Oda, H., Saito, Y., Akimoto, M., Nojiri, T., and Kawakami, Y. (2021). Isolation of simplicillium sympodiophorum and toxicocladosporium irritans from the blowout air of household air conditioners. 26(2):105–111.

Hatcher, P. G. and Clifford, D. J. (1994). Flash pyrolysis and in situ methylation of humic acids from soil. *Organic Geochemistry*, 21:1081–1092.

Hatcher, P. G., III, H. E. L., Kotra, R. K., and Verheyen, T. V. (1988). Pyrolysis g.c.—m.s. of a series of degraded woods and coalified logs that increase in rank from peat to subbituminous coal. *Fuel*, 67:1069–1075.

He, M., Qin, C.-X., Wang, X., and Ding, N.-Z. (2020). Plant unsaturated fatty acids: Biosynthesis and regulation. *Frontiers in Plant Science*, 11:390.

Hites, R. A. and Raff, J. D. (2012). *Elements of Environmental Chemistry*. Wiley, New Jersey.

Holman, A. I., Poropat, S. F., Greenwood, P. F., Bhandari, R., Tripp, M., Hopper, P., Schimmelmann, A., Brosnan, L., Rickard, W. D. A., Wolkenstein, K., and Grice, K. (2024). Significance of lignin and fungal markers in the devonian (407 ma) rhynie chert. *Geobiology*, 22:e12616.

Hu, B., Zhang, Z., Xie, W.-l., Liu, J., Li, Y., Zhang, W.-M., Fu, H., and Lu, Q. (2022). Advances on the fast pyrolysis of biomass for the selective preparation of phenolic compounds. *Fuel Processing Technology*, 237:107465.

Huang, H., Li, Z., Wen, Z., Han, D., and Pan, R. (2019). Biodegradation influence on alkylphenanthrenes in oils from bongor basin, sw chad. *Scientific Reports*, 9(1):12960.

Inness, A., Ades, M., Agustí-Panareda, A., Barré, J., Benedictow, A., Blechschmidt, A.-M., Dominguez, J. J., Engelen, R., Eskes, H., Flemming, J., Huijnen, V., Jones, L., Kipling, Z., Massart, S., Parrington, M., Peuch, V.-H., Razinger, M., Remy, S., Schulz, M., and Suttie, M. (2019). The CAMS Reanalysis of Atmospheric Composition (EAC4). *Atmospheric Chemistry and Physics*, 19:3515–3556. CAMS global reanalysis (EAC4) dataset.

Jaklitsch, W. M., Fournier, J., Dai, D. Q., Hyde, K. D., and Voglmayr, H. (2015). Valsaria and the valsariales. 73(1):159–202. Place: Dordrecht Publisher: Springer Nature B.V.

Kaneda, T. (1991). Iso- and anteiso-fatty acids in bacteria: biosynthesis, function, and taxonomic significance. *Microbiological Reviews*, 55(2):288–302.

Khadem, S. and Marles, R. J. (2010). Monocyclic phenolic acids; hydroxy- and polyhydroxybenzoic acids: Occurrence and recent bioactivity studies. *Molecules*, 15(11):7985–8005.

Kingston, A. M., Myers, G. R., Latham, S. J., Recur, B., Li, H., and Sheppard, A. P. (2018). Space-filling x-ray source trajectories for efficient scanning in large-angle cone-beam computed tomography. *IEEE Transactions on Computational Imaging*, 4(3):447–458.

Latham, S. J., Kingston, A. M., Recur, B., Myers, G. R., Delgado-Friedrichs, O., and Sheppard, A. P. (2018). Reprojection alignment for trajectory perturbation estimation in microtomography. *IEEE Transactions on Computational Imaging*, 4(2):271–283.

Legendre, P. and Gallagher, E. D. (2001). Ecologically meaningful transformations for ordination of species data. *Oecologia*, 129:271–280.

Leng, L., Yang, L., Chen, J., Leng, S., Li, H., Li, H., Yuan, X., Zhou, W., and Huang, H. (2020). A review on pyrolysis of protein-rich biomass: Nitrogen transformation. *Bioresource Technology*, 315:123801.

Lockhart, R., Berwick, L. J., Greenwood, P., Grice, K., Kraal, P., and Bush, R. (2013). Analytical pyrolysis for determining the molecular composition of contemporary monosulfidic black ooze. *Journal of Analytical and Applied Pyrolysis*, 104:640–652.

Los, D. A. and Mironov, K. S. (2015). Modes of fatty acid desaturation in cyanobacteria: An update. *Life*, 5:554–567.

Luo, Z., Wang, S., Liao, Y., and Cen, K. (2004). Mechanism study of cellulose rapid pyrolysis. *Industrial & Engineering Chemistry Research*, 43:5605–5610.

MacLeod, I. D. (2005). Effects of moisture, micronutrient supplies and microbiological activity on the surface ph of rocks in the burrup peninsula. In *Preprints for ICOM-CC Triennial Meeting, Den Haag, The Netherlands*, volume 2, pages 386–93.

Malmström, M. E., Destouni, G., Banwart, S. A., and Strömberg, B. H. (2000). Resolving the scale-dependence of mineral weathering rates. *Environmental science & technology*, 34(7):1375–1378.

Marynowski, L. and Simoneit, B. R. T. (2022). Saccharides in atmospheric particulate and sedimentary organic matter: Status overview and future perspectives. *Chemosphere*, 288(1):132376.

Meng, B. (1992). Moisture-transport-relevant characterization of pore structure. *Proceedings of the 7th International Congress on Deterioation and Conservation of Stone*, page 387–396.

Michałowicz, J. (2014). Bisphenol a – sources, toxicity and biotransformation. *Environmental Toxicology and Pharmacology*, 37(2):738–758.

Montero-Lobato, Z., Fuentes, J. L., Garbayo, I., Ascaso, C., Wierzchos, J., Vega, J. M., and Vílchez, C. (2020). Identification, biochemical composition and phycobiliproteins production of *Chroococcidiopsis* sp. from arid environment. *Process Biochemistry*, 97:112–120.

Neumann, J. T. (2025). *Experimental weathering of Aboriginal rock art from the Murujuga Peninsula, Western Australia: Do emissions from the local industry have an impact on the rock art weathering rate?* Phd thesis, University of Bonn, North Rhine-Westphalia, Germany.

Neumann, J. T., Black, J. L., Hœrlé, S., Smith, B. W., Watkins, R., Lagos, M., Ziegler, A., and Geisler, T. (2022). Artificial weathering of rock types bearing petroglyphs from Murujuga, Western Australia. *Heritage Science*, 10(1):77.

Niu, C., Hou, D., Cheng, X., Han, X., and Li, Y. (2022). Origin and environmental implications of dibenzothiophenes in the huanghekou east sag and the laizhouwan northeast sag, bohai bay basin. *Marine and Petroleum Geology*, 142:105739.

Nordstrom, D. and Wilde, F. (2005). Chapter A6. Section 6.5. Reduction-Oxidation Potential (Electrode Method) (Version 1.2). *U.S. Geological Survey Techniques of Water-Resources Investigations*, 09:1–22.

Paiva, D. S., Fernandes, L., Trovão, J., Mesquita, N., Tiago, I., and Portugal, A. (2022). Uncovering the fungal diversity colonizing limestone walls of a forgotten monument in the central region of portugal by high-throughput sequencing and culture-based methods. 12(20):10650. Place: Basel Publisher: MDPI AG.

Pancost, R. D. and Pagani, M. (2006). Controls on the carbon isotopic compositions of lipids in marine environments. In Volkman, J. K., editor, *Marine Organic Matter: Biomarkers, Isotopes and DNA*, pages 209–249. Springer Berlin Heidelberg.

Phillips, J. B. and Beens, J. (1999). Comprehensive two-dimensional gas chromatography: a hyphenated method with strong coupling between the two dimensions. *Journal of chromatography A*, 856(1-2):331–347.

Picó, Y. and Barceló, D. (2020). Pyrolysis gas chromatography-mass spectrometry in environmental analysis: Focus on organic matter and microplastics. *TrAC Trends in Analytical Chemistry*, 130:115964.

Pires, R., Hepworth, A., O'Leary, R., Carroll, J., Goldie, J., Marchiori, D., Melloy, P., Padgham, M., Parsonage, H., and Sparks, A. H. (2024). weatheroz: An API Client for Australian Weather and Climate Data Resources in R. *Journal of Open Source Software*, 9(98):6717.

Pires, R., Hepworth, A., O'Leary, R., Carroll, J., Goldie, J., Marchiori, D., Melloy, P., Padgham, M., Parsonage, H., and Sparks, A. H. (2025). *weatherOz: An API Client for Australian Weather and Climate Data Resources in R*. R package version 2.0.1.

Pouwels, A. D., Tom, A., Eijkel, G. B., and Boon, J. J. (1987). Characterisation of beech wood and its holocellulose and xylan fractions by pyrolysis-gas chromatography-mass spectrometry. *Journal of Analytical and Applied Pyrolysis*, 11:417–436.

Ramboll Australia (2022). *Study of the cumulative impacts of air emissions in the Murujuga airshed*. Final Report prepared by Ramboll for the Department of Water and Environmental Regulation. Government of Western Australia (18000883-14 Rev B).

Raynor, W. (2025). *Euclidean Distance*. Taylor & Francis. Definition and properties of Euclidean distance.

Saiz-Jimenez, C. (1995). The origin of alkylbenzenes and thiophenes in pyrolysates of geochemical samples. *Organic Geochemistry*, 23(1):81–85.

Sarchami, T., Batta, N., and Berruti, F. (2021). Production and separation of acetic acid from pyrolysis oil of lignocellulosic biomass: a review. *Biofuels, Bioproducts and Biorefining*, 15:1912–1937.

Scarlett, A., Rowland, S. J., Galloway, T. S., Lewis, A. C., and Booth, A. M. (2008). Chronic sublethal effects associated with branched alkylbenzenes bioaccumulated by mussels. *Environmental Toxicology and Chemistry*, 27(3):561–567.

Schirmer, A., Rude, M. A., Li, X., Popova, E., and Del Cardayre, S. B. (2010). Microbial biosynthesis of alkanes. *Science*, 329(5991):559–562.

Singh, S., Elumalai, S. P., and Pal, A. K. (2016). Rain pH estimation based on the particulate matter pollutants and wet deposition study. *Science of The Total Environment*, 563-564:293–301.

Skeie, R. B., Hodnebrog, O., and Myhre, G. (2023). Trends in atmospheric methane concentrations since 1990 were driven and modified by anthropogenic emissions. *Communications Earth and Environment*, 4:317.

Spezzano, P. (2021). Mapping the susceptibility of UNESCO World Cultural Heritage sites in Europe to ambient (outdoor) air pollution. *Science of the Total Environment*, 754:142345.

Sterflinger, K. (2010). Fungi: Their role in deterioration of cultural heritage. 24(1):47–55.

Tsuge, S. and Matsubara, H. (1985). High-resolution pyrolysis-gas chromatography of proteins and related materials. *Journal of Analytical and Applied Pyrolysis*, 8:49–64.

US Environmental Protection Agency (1997). *Emission Factor Documentation for AP-42 Section 11.23, Taconite Ore Processing*.

van Der Kaaden, A., Haverkamp, J., Boon, J. J., and De Leeuw, J. W. (1983). Analytical pyrolysis of carbohydrates: I. chemical interpretation of matrix influences on pyrolysis-mass spectra of amylose using pyrolysis-gas chromatography-mass spectrometry. *Journal of Analytical and Applied Pyrolysis*, 5:199–220.

Vancampenhout, K., Wouters, K., Vos, B. D., Buurman, P., Swennen, R., and Deckers, J. (2009). Differences in chemical composition of soil organic matter in natural ecosystems from different climatic regions – a pyrolysis–gc/ms study. *Soil Biology and Biochemistry*, 41(3):568–579.

Vitzthum von Eckstaedt, C. D., Grice, K., Ioppolo-Armanios, M., Kelly, D., and Gibberd, M. (2012). Compound specific carbon and hydrogen stable isotope analyses of volatile organic compounds in various emissions of combustion processes. *Chemosphere*, 89:1407–1413.

Volkman, J. K. (2005). Sterols and other triterpenoids: source specificity and evolution of biosynthetic pathways. *Organic Geochemistry*, 36:139–159.

Volkman, J. K., Barrett, S. M., Blackburn, S. I., Mansour, M. P., Sikes, E. L., and Gelin, F. (1998). Microalgal biomarkers: A review of recent research developments. *Organic Geochemistry*, 29(5–7):1163–1179.

Wang, Y., Wang, F., Zhou, Y., Liu, F., Zeng, Q., Liu, C., Chen, X., Xu, X., Liu, Y., and Yang, C. (2023). Trunk rot of juglans regia caused by myrmaecium fulvopruinatum in china. 107(9):2843. Publisher: Scientific Societies.

Wang, Y., Zhang, H., Liu, X., Liu, X., and Song, W. (2021). Fungal communities in the biofilms colonizing the basalt sculptures of the leizhou stone dogs and assessment of a conservation measure. 9(1):36.

Wang, Z., Fingas, M., Shu, Y., Sigouin, L., Landriault, M., Lambert, P., Turpin, R., Campagna, P., and Mullin, J. (1999). Quantitative characterization of pahs in burn residue and soot samples and differentiation of pyrogenic pahs from petrogenic pahs- the 1994 mobile burn study. *Environmental science & technology*, 33(18):3100–3109.

White, D. M., Garland, D. S., Beyer, L., and Yoshikawa, K. (2004). Pyrolysis-gc/ms fingerprinting of environmental samples. *Journal of Analytical and Applied Pyrolysis*, 71(1):107–118.

Xue, L.-L., Chen, H.-H., and Jiang, J.-G. (2017). Implications of glycerol metabolism for lipid production. *Progress in Lipid Research*, 68:12–25.

Zhang, J. T. (2013). *Analysis of Variance for Functional Data*. Chapman and Hall/ CRC, 1 edition.

Zhang, W., Hu, W., Zhu, Q., Niu, M., An, N., Feng, Y., Kawamura, K., and Fu, P. (2024). Hydroxy fatty acids in the surface earth system. *Science of The Total Environment*, 906:167358.

Zhou, Q., Gu, J., Wang, J., Girolamo, A. D., Yang, S., and Zhang, L. (2023). High production of furfural by flash pyrolysis of c6 sugars and lignocellulose by pd-pdo/$znso_4$ catalyst. *Nature Communications*, 14:1563.

A Organic geochemistry – additional tables and figures

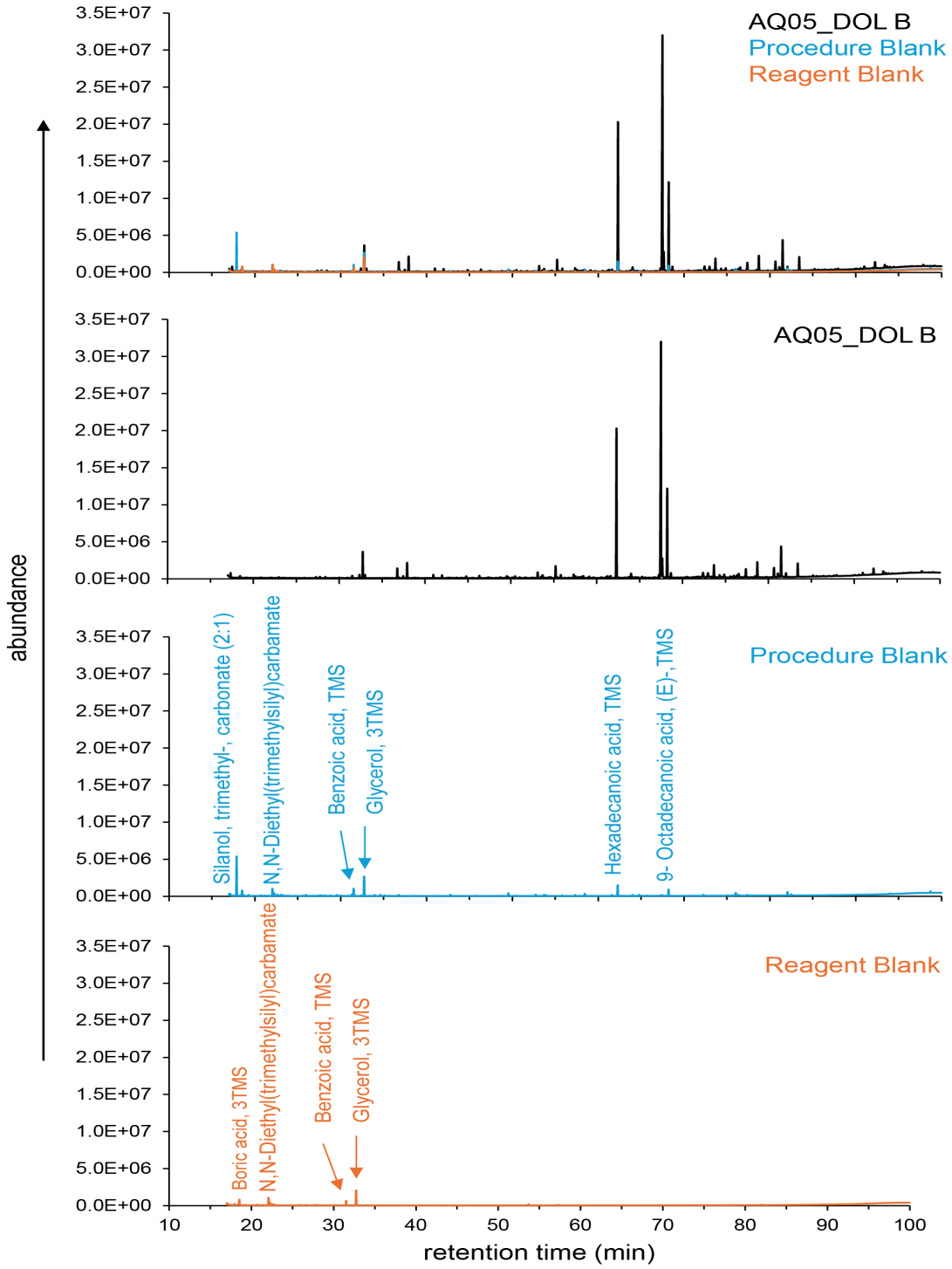

Figure A-1: GC-MS total ion chromatograms. a) overlaid chromatograms of rock surface sample AQ05_DOL B, procedure blank and reagent blank, b) AQ05_DOL B, c) procedure blank, d) reagent blank. Observed ions ranged from 50 to m/z 550.

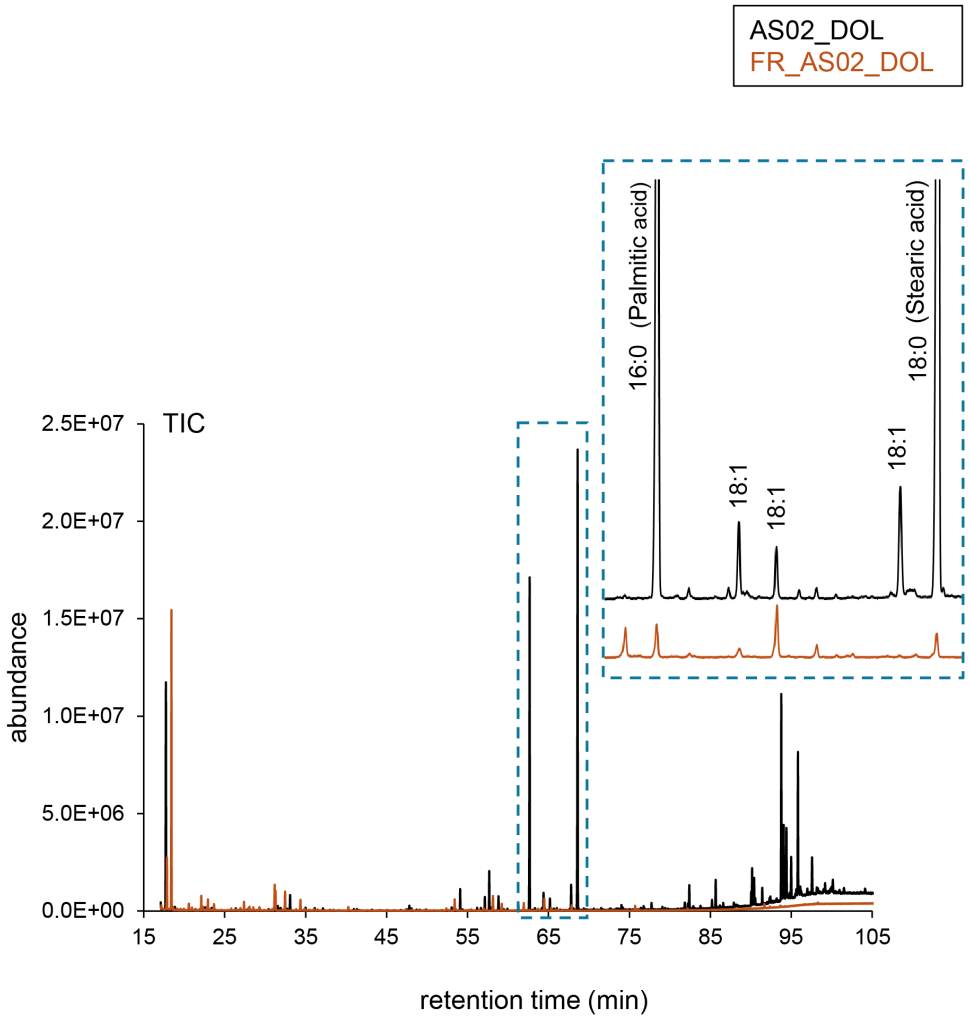

Figure A-2: GC-MS total ion chromatogram (TIC) of the derivatised polar fraction from rock surface sample AS02_DOL and corresponding fresh rock sample FR_AS02_DOL. The shift in the retention time between the samples is due to time difference in the time of analysis. Retention time has been adjusted in the magnified section. Observed ion ranged from m/z 50 to m/z 550.

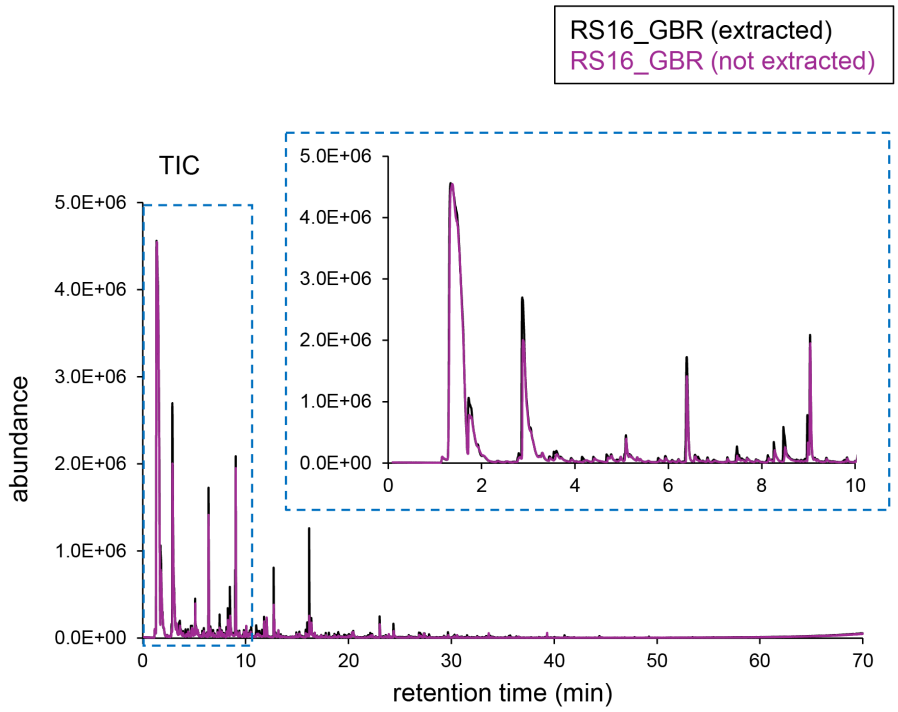

Figure A-3: Flash Pyrolysis GC-MS total ion chromatogram (TIC) of rock surface sample RS16_GBR extracted and not extracted for comparison. Observed ions ranged from 50 to m/z 550.

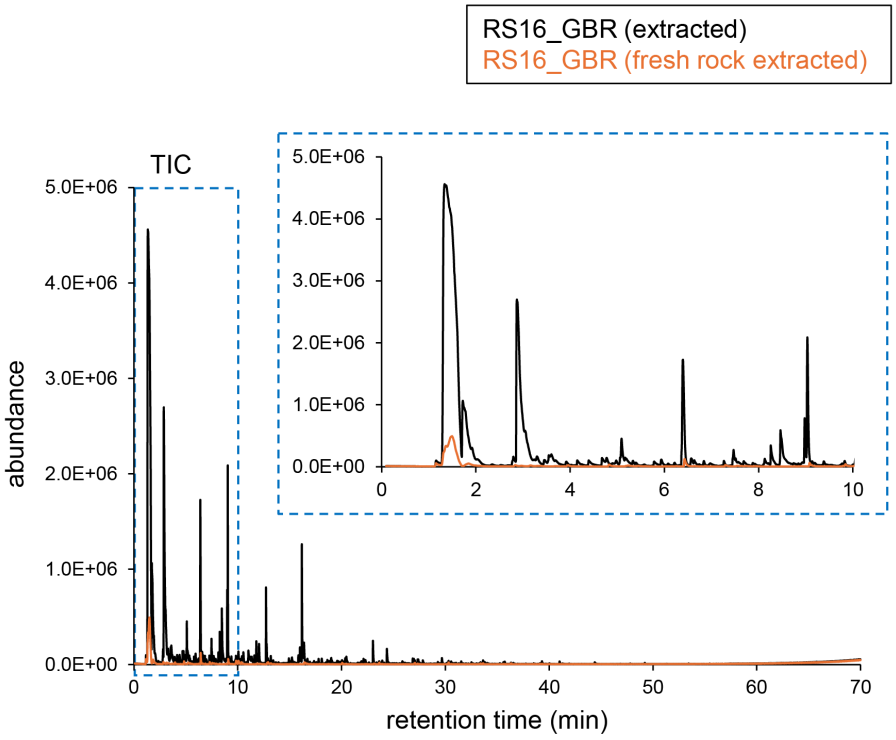

Figure A-4: Flash Pyrolysis GC-MS total ion chromatogram (TIC) of rock surface sample RS16_GBR extracted and fresh rock sample extracted for comparison. Observed ions ranged from 50 to m/z 550.

Table A-1: Compound-specific carbon isotope ratio $^{13}C/^{12}C$ ($\delta^{13}C$) for specific n-alkanes on the rock surface. Carbon isotope data are reported relative to the Pee Dee Belemnite (PDB) standard.

Sample ID	n-C_{15} (‰)	SD	n-C_{17} (‰)	SD	n-C_{27} (‰)	SD	n-C_{29} (‰)	SD	n-C_{31} (‰)	SD	n-C_{33} (‰)	SD
AQ03_ GBR	-26.1	0.1	-27.1	0.2			-22.9	0.3	-24.0	0.3	-25.8	0.1
AQ03_ GPH	-27.8	0.2	-28.1	0.2								
AQ05_ DOL A			-26.8	0.2	-25.6	0.0	-22.2	0.1	-22.1	0.3	-24.4	0.1
AQ05_ DOL B	-25.6	0.1	-26.8	0.1	-26.1	0.2	-23.7	0.3	-24.2	0.5	-25.2	0.3
AQ05_ GPH	-25.8	0.1	-24.7	0.3	-27.3	0.2	-24.1	0.1	-22.9	0.3	-25.5	0.6
AQ07_ GRT	-27.0	0.2	-26.9	0.2			-21.3	0.2	-22.6	0.2	-23.8	0.4
AQ09_ GBR			-22.1	0.0								
AQ10_ GPH			-25.6	0.2								
AQ13_ GPH	-26.0	0.3	-25.7	0.5								
AQ15_ GBR			-28.0	0.1								
AQ16_ GBR	-24.9	0.1	-23.5	0.1								
AS01_ DOL			-29.1	0.1	-29.2	0.2						
AS02_ GRT			-27.4	0.2								
EX02_ GPH	-26.5	0.1	-26.1	0.2	-28.5	2.3						
EX04_ GBR	-25.0	0.1	-25.0	0.1								
EX07_ GPH					-25.2	0.4	-21.6	0.2	-21.6	0.2	-24.8	0.1
EX08_ GPH	-27.7	0.2										

Sample ID	n-C_{15} (‰)	SD	n-C_{17} (‰)	SD	n-C_{27} (‰)	SD	n-C_{29} (‰)	SD	n-C_{31} (‰)	SD	n-C_{33} (‰)	SD
EX09_ GBR B	-25.4	0.2	-25.2	0.2								
EX09_ GPH			-25.6	0.1	-25.7	0.4	-22.8	0.8	-23.5	0.1	-25.2	0.6
RS01_ GPH	-26.1	0.1	-26.9	0.3	-25.6	0.2	-24.4	0.1	-24.4	0.1	-25.4	0.1
RS02_ GBR			-29.4	0.2			-21.4	0.1	-22.6	0.1		
RS03_ GPH	-25.9	0.2	-28.1	0.1	-23.5	0.3	-23.2	0.1	-24.9	0.3	-25.1	0.5
RS03_ GRT	-26.8	0.2	-27.7	0.3			-20.7	0.1	-23.9	0.3	-26.1	0.2
RS04_ GBR	-25.8	0.1	-25.5	0.2								
RS04_ GPH	-25.7	0.0	-24.1	0.2								
RS05_ GPH #1	-27.5	0.2	-27.5	0.2			-22.7	0.0	-23.9	0.1	-24.2	0.2
RS05_ GPH #2			-25.9	0.1								
RS06_ GPH	-26.7	0.1	-26.3	0.0					-31.5	0.5	-31.4	0.2
RS08_ BAS	-27.3	0.1	-26.4	0.1	-24.6	0.2			-25.4	1.0	-25.6	0.3
RS08_ DOL											-24.1	0.2
RS09_ DOL S#191	-26.4	0.4	-25.3	0.2	-26.7	0.2			-24.5	0.8	-23.8	0.2
RS10_ GBR	-28.9	0.11	-29.2	0.02								
RS11_ GPH							-18.3	0.1	-22.4	0.1	-24.8	0.4
RS12_ BAS			-23.4	0.1					-23.9	0.5	-23.2	0.2
RS13_ GBR			-25.5	0.2								

Sample ID	n-C_{15} (‰)	SD	n-C_{17} (‰)	SD	n-C_{27} (‰)	SD	n-C_{29} (‰)	SD	n-C_{31} (‰)	SD	n-C_{33} (‰)	SD
RS14_ GPH	-26.4	0.1	-25.9	0.2								
RS16_ GBR A&B	-27.0	0.1	-29.0	0.1	-32.6	0.1	-33.6	0.1	-32.3	0.1	-26.7	0.0
RS18_ GPH					-26.1	0.2	-26.5	0.4	-26.4	0.3	-26.9	0.5

This page is intentionally blank.

B Photogrammetry

B-1 Introduction

Rock surface changes at Murujuga can be monitored in a number of ways. Previous research focused on colour change as a reasonable indicator (Ramanaidou and Lau, 2015). In the MRAMP studies, surface colour was also used but numerous other indicators were added, including electrochemistry, microbiome and permeability (Curtin University, 2022, 2025). CSIRO researchers also trialled techniques for measuring morphological change using stereometric imaging (Ramanaidou and Lau, 2015, pp. 27–28).

Appendix B describes and evaluates a proposed technique for photogrammetry of the Murujuga rock surfaces. Photogrammetry involves collecting multiple images of the same rock surface viewed from different angles, and combining the images to obtain a three-dimensional view. This approach would make it possible to monitor changes in the texture of the rock surface, such as spalling. By incorporating colour information it would also be possible to detect colour changes, such as discolouration of the patina over time.

Section B.1 provides some background about the motivation behind the proposed approach, giving examples of physical changes observed in rock surfaces during the first three years of this study. Section B.2 describes the proposed photogrammetry technique. Section B.3 compares the performance of the proposed smartphone method with the more traditional method using a DSLR camera, for the purpose of generating a three-dimensional surface relief. Section B.4 describes how colour measurement can be performed as part of the photogrammetry technique.

B-2 Surface alterations observed from spectroscopy registration images

The main motivation for adopting a site-wide photogrammetric technique at lower resolution than the optimised DSLR technique is several observations of change seen in the low-quality images used to record the spectrometer probe location at each target for every campaign.

To provide a record of probe placement for the 540 targets, each target surface is imaged twice for every campaign. This is primarily to be able to verify that the sensed area is the same for each set of spectra and that if there is significant spectral shift, poor probe alignment can be ruled out.

Photogrammetric data generated during the first campaign (March 2022) has not been referenced in this study, because the camera used at that time had a different geometry with respect to the light source and image sensor, which resulted in poor comparative imaging. All images generated since July 2022 have used the Oppo smartphone (CPH2195) with no changes to the probe orientation or the light exclusion box on which the camera is mounted (Figure B-2-1). Two images are taken at two zoom settings to provide confirmation of accurate probe placement each campaign. The images are taken expressly for probe placement verification and are not ideal for surface comparison analysis. They are poorly lit for surface study and can be slightly out of focus. The photographic record reflects what is up to 5-20 minutes of surface examination, which gives a far clearer view of the surface. For each campaign the probe aligner will report on whether there is any visible

Figure B-2-1: The spectrometry setup with phone camera mounted over the target area. Two images are taken at two zoom settings to provide confirmation of accurate probe placement each campaign

Figure B-2-2: A band of dark spots below the probe in July 2022 (left) have disappeared by March 2025.

change to the surface. This has arisen because on some occasions the exact alignment features in the surface appear missing or obscured. This may be in the form of bird faeces as it is gradually washed down the surface, but in some notable instances there has been some combination of micro-spalling, loss of dark patination, and an increase in dark patination.

Surface alteration has been an important observation to make, not just as a measure of gross alteration, as discussed here, but as a record of any chromatic change, no matter how transitory, that will affect the spectral data. There are several instances where obvious bird faeces has intruded onto the target. In one case, during campaign 10 (March 2025), a termite mound was found built over one rock, affecting several other targets. Manifest alterations such as these will produce dramatic colour change, whereas an adjacent dropping or mud deposit will have visually indistinct appearance but significant spectral response. It is expected that if these changes have occurred over the MRAMP field studies timespan of July 2022 to July 2025, there will be significant ongoing change. Moving forward, a macro-photogrammetry approach using a smartphone is the best means of studying each of the rock surfaces. No samples would need to be excluded from ongoing studies if this approach is used. The images in Figure B-2-2 and Figure B-2-3 indicates change to the surface. The images in Figure B-2-2 show a loss of dark material and the image pair in Figure B-2-3 show what appears to be an increase in the darker surface.

It cannot be said what the losses and gains consist of. At first impression the darker material in the Figure B-2-2 pair appears to be patina, and it is hard to image any sort of ephemeral deposit of this dark colour and fine dimensions. Other targets show more definite patina alteration.

The darkening of Figure B-2-3 is a very real alteration, with darkening in the recessed features on the left but not those on the right, highlighted by the blue arrows. There is also one instance of a white fleck appearing, marked with a yellow arrow, which may well be the common fluctuation of bird faeces seen in several samples. A complete record of surface alteration will be presented after campaign 11 (July 2025).

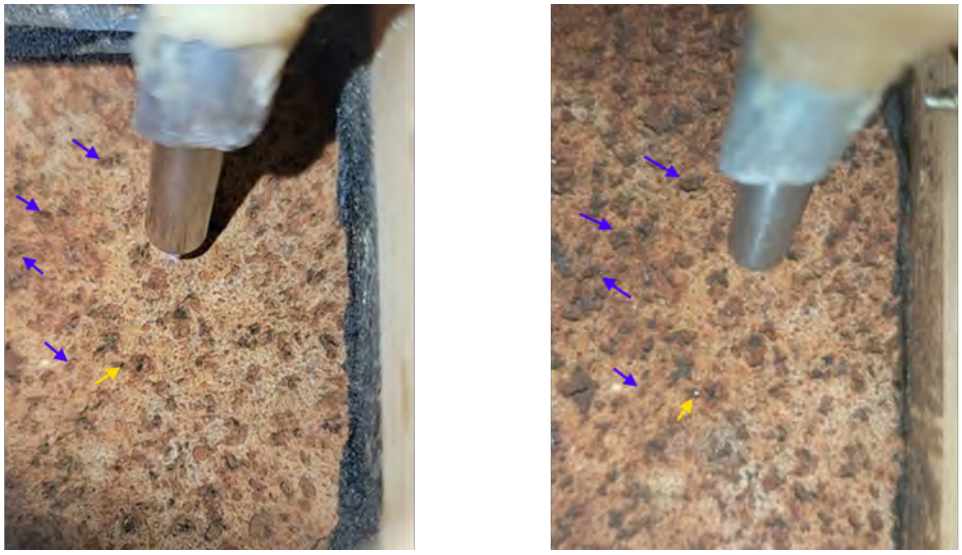

Figure B-2-3: Various pits in the surface appear lighter in campaign 2 (July 2022, left image) as compared to their darker appearance by campaign 10 (March 2025, right image) denote by the blue arrows. The yellow denote a change from dark to light

B-3 Photogrammetry methodology

B-3-1 Introduction

This section is a revised version from Appendix H in the Monitoring Studies Report 2024 (Curtin University, 2025).

The term micro-photogrammetry refers to image acquisition through a microscope objective mounted to a 35 mm DSLR camera. It can be argued that the imaging is macroscopic, given that the field of view is approximately 16 x 12 mm. The technique allows for closer imaging, subject to the limitations of the optical configuration, constrained by the objective employed and the resolving power of the digital camera. CSIRO researchers recognised the value of morphological monitoring in 2015 (Ramanaidou and Lau, 2015), although the technique was only applied for one year. The approach is noted for taking stereoscopic images only and capturing the whole surface at a distance of either 1.800 m or 3.000 m. It is doubtful that such broad imaging will enable fine-detailed analysis at that scale. The imaging configuration chosen was a Nikon D200 (10.2 Mp) camera with an AF Micro Nikkor 60 mm 1:2.8 D lens. The use of the term “Micro” is simply label from the manufacture denoting a mid-range macro lens. At macro settings a 60 mm lens gives a similar field of view as a 100 mm or longer lens, with the focal increasing from 60 mm to 100 mm, making the latter preferable for imaging a rock surface. At 60 mm and greater the image will be more or less free from lens distortion.

To summarise the CSIRO approach (Ramanaidou and Lau, 2015), a 10.2 Mp sensor at 1.800 m from the subject will provide an image 800 x 530 mm with a pixel density of 5 pixels per linear millimetre.

TThe configuration adopted for the MRAMP studies has been in two formats:

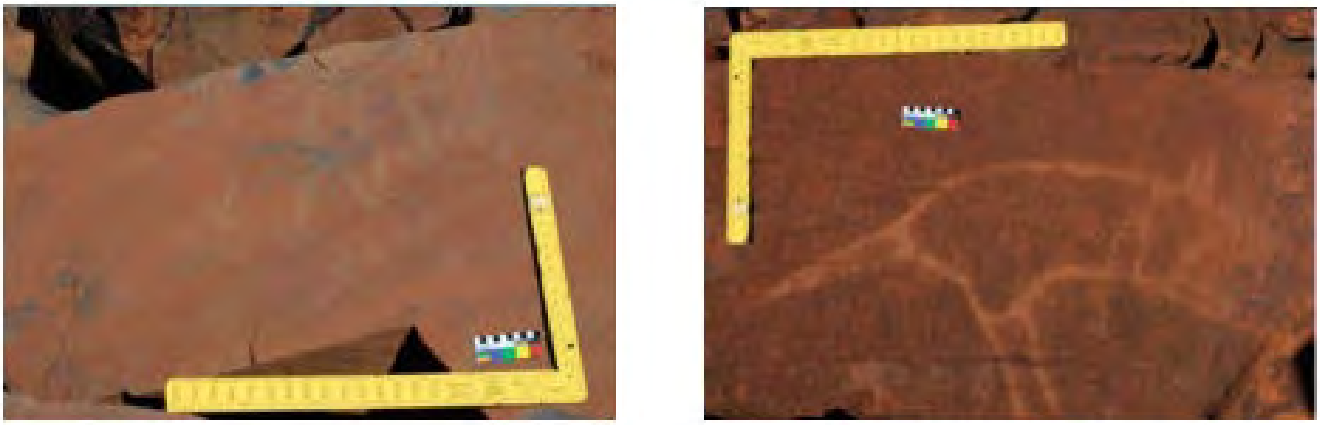

Figure B-3-1: Two sites in the current research EX06_GPH and EX04_GBR that have been studied by CSIRO in 2015. The imaging scale is apparent.

- The first is using a 24 Mp camera with a 4x Zeiss Planachromat (microscopic) objective attached.
- The second relies on imaging through a smartphone at 200 Mp using a magnifier app.

For the first method, the microscope objective provides a flat field of view of 16 x 12 mm with a pixel density of 377 pixels per linear millimetre. Through a scanning methodology, focus stacking and photogrammetric processing described below, a particle of less than 30 microns (0.03 mm) can be discretely resolved. This compares to a sand grain that will be in the order of 0.2-1.0 mm in diameter and hence alterations at crystal dimensions can be observed, not just grain loss but deformation of a surface without loss. Other benefits of the applied system over a stereoscopic imaging process include the greater ability to resolve depth due to the multiple views of a particular point in the surface. In the described stereoscopic imaging, each point is imaged twice. In the currently applied photogrammetric system each point is imaged at least 4 times.

The second and less precise method employed takes a series of handheld images, ensuring that offsets are developed through imprecise camera angles. This method does not produce the same precision and resolution of the first method. It does however replicate the results in a more time efficient method and is more easily deployable in the field as it mitigates some of the adverse conditions that prove the limiting factor with the first method.

Both systems take perpendicular images, although the current system can image at any offset to perpendicular desired.

B-3-2 DLSR field capture method

B-3-2.1 Imaging options

One of the considerations was establishing an image frame size that provides the desired level of detail at a time efficient rate and then to assess various optical systems that can achieve adequate resolution and general image quality at that size. A nominal 100 x 100 mm area was considered sufficient to be able to observe morphological change, reflecting overall change across a rock

surface. Sufficient detail in the final 3D model was considered to be at least sub-100 micron. In this case being able to recognize a surface detail, such as a particle, discontinuity, or coloured surface, would be possible even if the magnification level did not provide perfectly sharp details. Given that some of the techniques would be stereoscopic, that is with the sensor always perpendicular to the surface, there will always be a degree of resolution loss in more vertically inclined surfaces. Capturing these more vertical surfaces would require that the imaging has a suitable depth of focus. Image dimensions required to resolve sub-100 µm details were determined to be no greater than 20 mm on the longest side of the frame.

The several available imaging systems (Table B-3-1) were evaluated for imaging at close range for the project. Examples of such systems are shown in Figure B-3-2.

Table B-3-1: Optical options at close range. Examples are shown in Figure B-3-2

Instrument	Image width	Comment
Olympus SZ40 zoom	17 mm	Too bulky to carry into the field, especially given that only the monocular camera tube was required.
DSLR with 100 mm macro lens	22 mm	Good depth of focus and depth of field. Bulkier than other options.
DSLR with microscope objective mounted in purpose made mount	16 mm @ 4x 12 mm @ 5x 3 mm @ 10x	Desired frame size achieved with 4x Zeiss objective. 5x too close for current needs, with very low focal length and depth of focus.
51 Mp digital camera with zoom lens attachment	5 mm @ max zoom	Zoom capability and large depth of focus make this ideal, except that it requires a computer for image capture. Connection to an Android phone possible.

Creating three-dimensional (3D) images under a microscope is not a new concept, although most previous efforts have relied on moving the object in a mechanical stage rather than scanning the microscope across a static surface. In the researcher's own laboratory, with seven microscopes and various macro-imaging options the preferred technique for small objects has been a stereo microscope with a DSLR mounted to the phototube. It is noted that a phototube is monocular and hence for field operation the emphasis has been on developing a relatively portable system and methodology that could be operated at any of the 54 study sites.

The 51 Mp digital camera with dedicated zoom lens provided the greatest flexibility, capable of providing sharp images 5 mm wide, at the greatest zoom factor, with a focal distance of 40 mm. Focal distance is significant for this technique as the surface must be artificially illuminated. 40 mm is slightly less than ideal to ensure even dispersion of light from a ring light. The imager can be run from an Android phone with only additional power required to run the 5V ring light. A 5V battery will provide sufficient power to run both the ring light and maintain charge in the phone via a wireless charging pad, as the USB port is required to power and operate the imager. The 51 Mp digital camera is the lightest and most compact system, weighing 365 g.

Of the DSLR systems, the weight difference is between a microscope objective (option 3) and a much bulkier macro lens (option 2). The 4x Zeiss objective has a focal distance of 80 mm and the macro lens, 90 mm. These were better focal lengths, but 40 mm on the digital camera could be made to work, given that the ring light can be raised a further 40 mm without casting a shadow on the image plane.

a) *b)*

c) *d)*

Figure B-3-2: Examples of the options listed in Table B-3-1. (a) Option 1 - Olympus SZ40 with a camera mounting option; (b) Option 2 - Canon EOS7D with a 100mm F/2.8L EF Macro Lens; (c) DSLR fitted with a 4x microscope objective lens and adaptor mount. The actual system used (with light ring) can be seen in Figure B-3-3; (d) Option 4 - a 51Mp microscope camera fitted with zoom lens and control from a computer or external device.

Based on image quality and the operational considerations, it was decided to proceed with the microscope objective system (option 3). One important consideration here has been weight. While a 4x Zeiss objective has been chosen there is very little weight added to the kit with one or two additional objectives added for greater flexibility.

B-3-2.2 Scanning options

Regardless of the imaging system, at the magnification required, no system could be expected to:

- Cover the entire frame in one image, so a scanning method of multiple images needs to the used and the images combined into one frame through post-processing
- Maintain adequate focus across all images and across the surface variations, so multiple images need to be stacked to generate a single sharp image.

A manual scanning system was considered unworkable at the frame sizes being imaged, given that a 100 mm linear scan with a 16 mm frame width achieving a 65% overlap for photogrammetric processing, would require 12 frames horizontally by 17 vertically. To resolve a 100 x 100 mm surface three-dimensionally it is necessary to ensure that the perimeter has also been imaged stereoscopically, therefore the actual scan area would need to be at least 120 x 120 mm. 204 images would be required to image the entire surface and every one of them must be in focus and with the overlap maintained.

The Zeiss 4x objective and the 51 Mp digital camera provided similar 4 mm depth of focus, which in a scanning context has to be maintained not just within the individual frame, but across the entire 100 x 100 mm study surface. It was anticipated that any chosen surface would have depths of at least 4 mm and that the elevations across the surface may also vary by 4-6 mm. Having determined that no imaging system could maintain a perfectly focused image across the study surface the focus stacking method was considered an essential step in achieving a perfectly resolved image.

Considering the depth of focus on the Zeiss 4x objective, the Z axis (vertical) was programmed to take 20 images at 1 mm intervals. The excess frame count allowed not only for the depth at any one location, where a point at any elevation should be in focus in four frames, but also any variation in vertical profile across the study area.

It was also established that the motors were directionally anisotropic and required programming in both directions and for the precise inclination of the rock surface. AQ11, for example has a dip of 15° and a strike of 7°. This is shown in Figure B-3-4. Figure B-3-5 highlights an extreme case at EX08, where the scanning system needs to be mounted vertically. Hence maintaining uniform frame spacing required specific programming. Despite the very precise control attainable there was always some drift throughout the 4,000 image process, effecting the overlap and stacking.

The best means of achieving this would be to automate the imaging by way of a scanning system or robotic arm. A scanning frame was chosen as it was readily within the mechanical and electronics capabilities of the researcher. The Curtin University team have since confirmed that a robotic arm would be an unworkable option.

Figure B-3-3: Camera configuration with objective partially obscured by ring light attached to the objective mount. When activated, the ring light LED array provides a uniformly lit scene, removing all shadows created by the surface morphology.

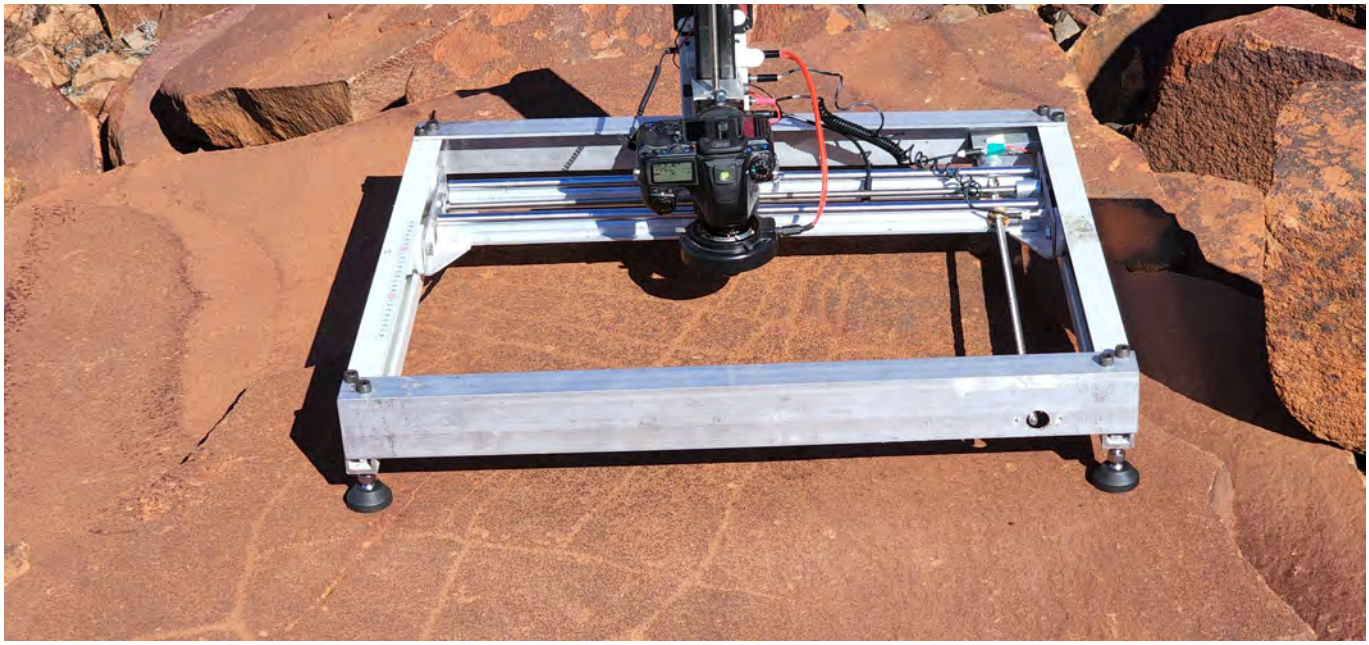

Figure B-3-4: Imaging system mounted onto scanning frame and set on engraved surface at AQ11.

Figure B-3-5: Scanning frame mounted vertically at EX08. This orientation required considerable reprogramming to achieve uniform movements in the three motors.

B-3-2.3 DSLR field procedure

Three sites were proposed in the MSDCA Plan (Curtin University, 2022) to demonstrate the value of morphological measurement as an adjunct to colour change, pH and gas permeability. Challenges of establishing the technique on site have led to just one site being imaged. This has provided very good resolution images, albeit without having achieved the objective of a full 100 x 100 mm study area being fully and consistently modelled in 3D across all sites.

The system adopted relies on a Zeiss 4x magnification objective attached to a 24 Mp DSLR, which is in turn mounted to a programmable scanning frame as described (Figure B-3-4). The 4x Zeiss objective was selected following consideration of workable image size and focal distance from the surface. The image dimensions of 16 x 12 mm is an optimal balance between focal distance, depth of focus, and image alignment in downstream processing. To create a 3D image an ideal 60-65% overlap between adjacent images becomes increasingly difficult to maintain with higher magnification. Focal distance of the Zeiss is approximately 80 mm, ensuring that a 5 V ring light can uniformly illuminate the scene, essential for removing shadows.

Objectives of greater magnification, even a 5x lens, prove too magnified and various other 4x objectives gave very short focal distances. When mounted to the camera the objective becomes the front lens with no other glassware between it and the imaging sensor. The DSLR was chosen after trials with a stereo microscope proved too bulky and various digital imaging systems provided less resolution than the camera at greater expense. Field portability and affordability become significant in choosing the imaging system and in this case the only additional expenditure, assuming a DSLR is already available, is the objective and its camera mount.

The imaging system in Figure B-3-4 is attached to a scanning frame (Figure B-3-5) whose movement is controlled by an Arduino control board driving Adafruit motor controllers that allow the camera to scan vertically and in the two planar axes. The Arduino is programmed to control the increments in each of the three axes, which inevitably requires adjustment for the outward and return journeys for each motor controlling the due to the directionally anisotropic nature of the movement. Naturally the vertical movement falls more readily than it rises, but this appears also to be the case for the two lateral motors. Slight out-of-horizontal mounting of the frame requires further programming to ensure uniform increments in each plane.

The mounting frame sits on rubber feet to ensure no impact on the surface. The feet are placed away from any engraved channels and can be further cushioned over sensitive surfaces. One limitation, although in some respects an advantage, of the microscope objective is that the camera cannot self-focus. The advantage of non-focusing is that the objective captures exactly at the focal plane without attempting to guess what the scene is. The Zeiss objective has a depth of focus of four millimetres. Twenty frames are captured in the perpendicular axis at 1 mm increments, meaning that any point is in focus for four frames. A location with a 3 mm depth will have seven useable images out of the twenty captured.

It has proven difficult to maintain smooth movements at the operating magnification, however this is not a disadvantage but rather provides slightly offset capture angles for the four in-focus images, aiding the three-dimensional interpretation of the surface in the photogrammetric processing. These movements are also within the aligning capabilities of the focus stacking software described in Section B-3-4. Once a perpendicular run has been completed, the first of the lateral movements

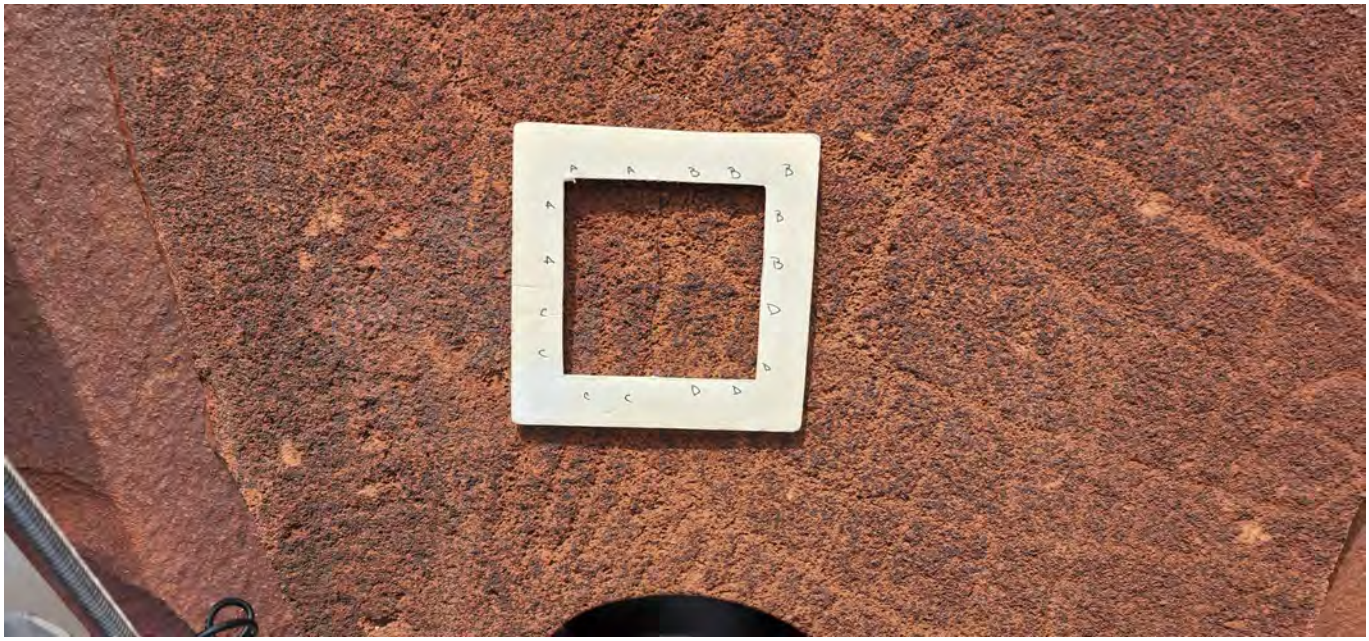

Figure B-3-6: The area to be scanned is defined by a 100 x 100 mm template that can be accurately realigned in subsequent scans.

advances the camera 60% of the frame width before commencing to capture twenty more images in the reverse direction.

The scanned area is nominally 100 x 100 mm, although this is over-run by 20% to ensure a processed image of those dimensions. The target area is first registered with a general location shot for realignment in subsequent scans. A section of 4 mm square tube is inserted into the scene to provide scale.

Due to the stop-start image gathering at 12 mm advances, the process is time consuming, taking over two hours to complete the 120 x 120 mm scan area. Automation ensures that this time is not wasted, and the system is powered to complete a full run, although the camera battery needs to be changed at least once, which can be done without pausing the process. The ring light and scanning motors are all run from a multi voltage battery that remains above 50% at conclusion.

B-3-3 Data capture with mobile phone

B-3-3.1 Sensor options

As previously highlighted, the microscope objective scanning method described in the previous section has proven more complex and intensive when used in the field than anticipated due to the harsh conditions leading to equipment irregularities. It has also been realized that the initial proposal of three sites does not provide a representative sample of the 54 study surfaces and is thus not compliant with the spatial statistical integrity required. To partially overcome this, a second more time efficient method has been adopted. This method does not provide the resolution and hence the analytical strength of the scanning frame approach. It does however allow for the 3D imaging of all 54 study surfaces at a resolution that allows for identification of broad scale change.

The method lies somewhere between the 30 µm resolution of the scanning frame and the very broad imaging advocated by CSIRO in 2015.

Cameras in smartphones have advanced to a point where they rival DSLR cameras for image gathering. Their main failing is the inherently excessive image manipulation they provide at default settings. These enhancements are almost exclusively tonal adjustments and thus do not compromise the resolution of the image in any way. If colour is not a factor, then the quality of the image comes down to sensor size and the number of pixels that gather the image.

Smartphone sensors are smaller than DSLRs overall, however they make up for this in pixel density, with the cameras used in this project having up to 200 Mp capabilities in the Samsung phones and 48 Mp in the Oppo. The Oppo produces an image using all pixels whereas the Samsung processes a cluster of nine pixels in the sensor into one pixel in the image.

For higher resolution for macro observations, the smartphone runs a magnifier app “Magnifying Glass and Flashlight” (https://play.google.com/store/apps/details?id=com.rvappstudios.magnifyingglass&hl=en_AU). Although other apps are available that will serve the purpose, provided they can keep the LED illuminated and can be operated using the triggering app (described in the capturing section). That has the critical features of permanent light source combined with variable and readily controllable magnification. The app has been compared to the imaging options on a Samsung Galaxy 24 Ultra, providing either 12 Mp, 50 Mp or 200 Mp image resolution. The native camera app cannot focus quite as closely and thus cannot achieve the sharpness required. Table B-3-2 provides a comparison based on a pixel count for the closest range for a suitably sharp image. Table B-3-2 demonstrates that the magnifier app approach provides an effective pixel density slightly better than a 50 Mp image from the primary camera of a 200 Mp Galaxy sensor.

Table B-3-2: Pixel count for four smartphone imaging options.

Imaging method	**Pixel grid per linear mm**	**Total pixels per mm^2**
Galaxy 24ultra 12 Mp	42 pixels / mm	1,764
Galaxy 24 ultra 50 Mp	90 pixels /mm	8,100
Galaxy 24 ultra 200 Mp	180 pixels /mm	32,400
Magnifier app	100 pixels /mm	10,000

The magnifier app, as used to register targets in the spectroscopy program, is zoomed to a set degree based on field needs. In conjunction with a 105 mm monopod the magnifier app zoomed to 2x and 3x produces an image measuring approximately 70 x 52 mm and 53 x 35 mm respectively. The magnifier app activates the camera LED, providing the same shadow free scene as the ring light on the scanning frame configuration. Figure B-3-7 shows the imaging of graph paper at 2x and 3x magnification to demonstrate there is very little linear distortion at either zoom range. Both images have been straightened along their central vertical axis only, for the sake of being able to apply the red rectangle true to this central orientation. The red rectangle has been drawn around the perimeter to assess whether the edges of either image distort.

In this approach it is not necessary to focus stack, as the camera is self-focusing and can capture the full depth of the subject in perfect focus from top to bottom. This has been described as a negative above but in this technique the camera is approximately 100 mm above the surface and

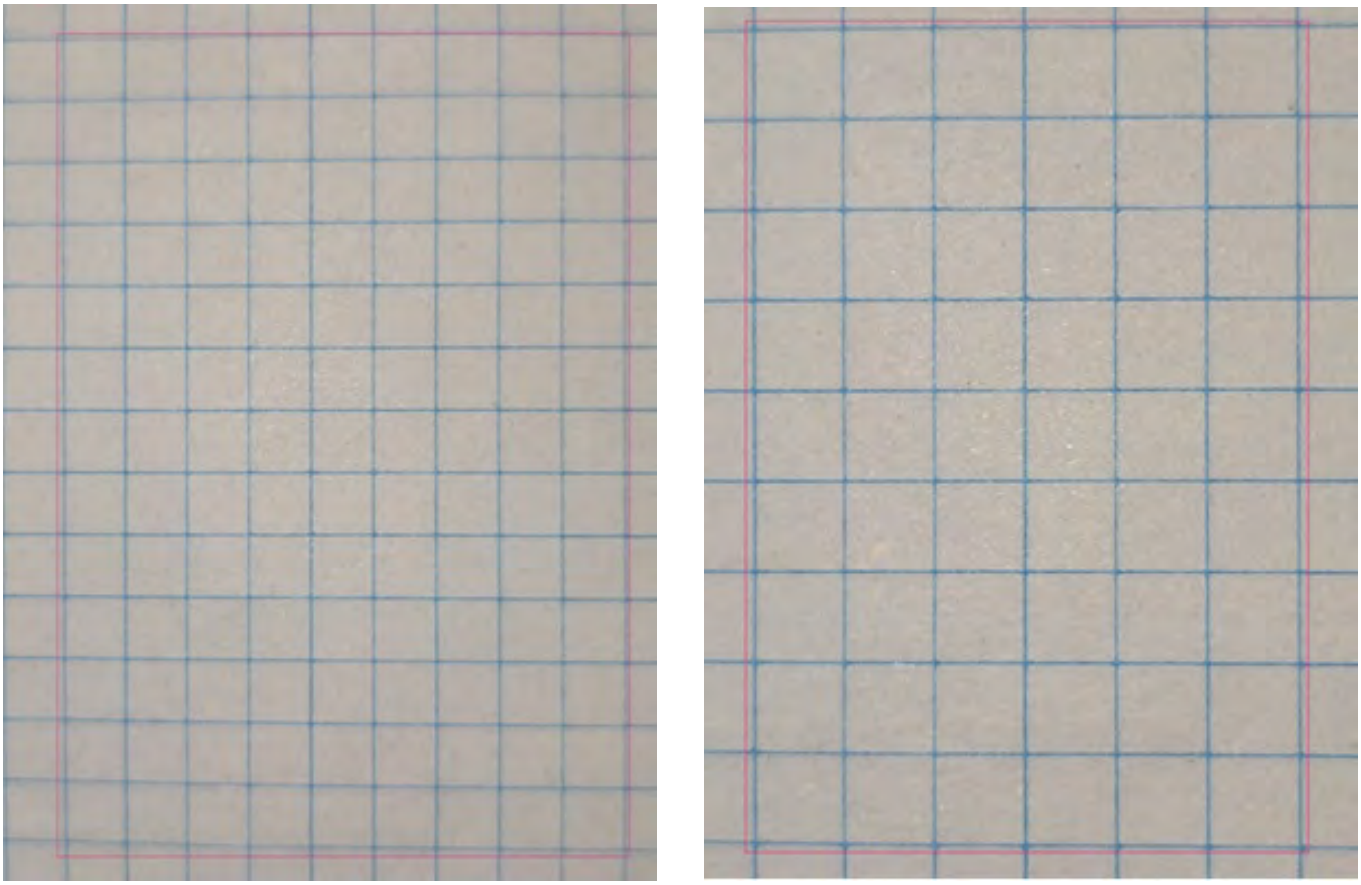

a) *b)*

Figure B-3-7: Graph paper imaged with the Magnifier app at a) 2x and b) 3x. While there is a little non-linearity in both images, due to imperfect perpendicular imaging, the two images are distortion free.

the focal depth sufficiently great enough for the depth profile of the Murujuga surfaces in a single image.

B-3-3.2 Capture method for macroscopic resolution

The similar approach has been adopted at a macroscopic scale over a target area of 120 x 120 mm to produce a resolved 3D image of 100 x 100 mm to that of the DSLR scanning frame. Instead of a scanning frame, a systematic manual approach and monopod is used to get a consistence distance and overlap between the images over the target area. The reduction from the template target area to the final frame size is necessary to trim margins where the camera positions do not provide sufficient coverage to resolve a fully 3D model.

Early trials aimed to replicate the image dimensions of the scanning frame method. This required a high-quality macro attachment to a Samsung Galaxy phone camera, together with a dimmable ring light and a 105 mm leg to ensure constant distance from the surface. Using the magnifier app to control the lighting and magnification, the camera is triggered at prescribed intervals using an app, OP Auto Clicker, allowing the photographer to concentrate on camera position and coverage

without having to operate the screen buttons. OP Auto Clicker has been chosen as it allows for multiple button presses at timed intervals. Five button presses are used for the macro imaging; two to focus the screen and three to capture and store the image.

A full scan takes seven minutes however a second run at 90° provides better photogrammetric resolution. The freehand nature of the imaging provides a more random orientation that aids in model production. The double run not only provides better imaging geometry but ensures there are no holes in the coverage.

The two runs take 15 minutes to complete on-site and with a further 15 minutes of processing to achieve both the 3D model and the consequent rectified two-dimensional (2D) image. Typically, sixty images are gathered and provide a very detailed perpendicular view of the surface. Where the model degrades in quality is on the sides of deep features where the perpendicular imaging has not been able to capture sufficient detail on the vertical walls of the feature. Given the purpose of this approach, to observe surface change, there is no alteration that is unique to the walls of a feature that would not manifest in the surface view.

The smartphone imaging technique was introduced in campaign 7 (March 2024) as part of the standard documentation of each of the 54 study surfaces. Of the twenty or more surfaces imaged in March 2024, none had holes in the final 3D model, a problem that has limited the progress of the scanning frame approach. However, completing a whole scan in campaign 10 wet season conditions proved far too stressful. While the resultant images were excellent, equal to those from the DSLR, alignment using free-form positioning (manual scanning) proved far too difficult. This approach is currently being fitted to a robotic arm to match the scanning capabilities of the DSLR system. The still significant drawback is the time it takes to acquire a full set of images. Twenty-one study surfaces were imaged with this technique in campaign 10, and it is anticipated than all 54 will be completed by the end of the MRAMP studies.

The aims of imaging at this scale are to observe macro alterations. These have already been observed under the spectroscopic re-registration imaging process (as discussed later). The spectroscopic survey gathers 540 pairs of macro images each campaign. In at least twelve of these registration images substantial alterations have been observed. Apart from the obvious bird faeces deposition other features have been added or removed. Several of these are dark patina forms that were thought to be permanent. Such changes have substantial implications for spectroscopy but also add to the inventory of alteration, hence the expansion of this macro imaging.

B-3-3.3 Capture method for site documentation

In addition to the macro-level recording, another of the documentation requirements has been to provide an image of the overall engraved study surface, primarily to study gross alterations such as spalling. To do this a photogrammetric approach has been adopted, imaging the surface at normal scale, typically in the order of 0.500-1.200 m wide images. Multiple images are taken at various orientations to cover the entire surface ensuring that sufficient overlap between the images (65% or better). These images are then processed to form a photogrammetric model.

The reason behind this is that it is often difficult to gain a perpendicular aspect to capture a perfectly rectified image that is shadow free and that can capture all of a curved surface. In this case, the images have been captured using a Samsung smartphone at either 1x magnification at 108 Mp or

3x magnification at 10 Mp. The 1x magnification is the obvious choice for sharpest detail regardless of the dimensions of the scene. OP Auto Clicker is also used as it allows the photographer to focus on the capture without looking at the screen, and more importantly, has a trigger aligned to the position of the camera button whether in portrait of landscape orientation. Capture time, for even the largest site, is under five minutes and processing time around 15 minutes to generate a 3D image.

By imaging as if for photogrammetric modelling, all parts of the surface are captured. The resulting model and rectified images can be extracted later. During the photogrammetric model construction, it is possible to choose which parts of the overlapping are employed in the creation. This allows the production of a shadow free detailed image of the engraved surface. More detail of this is explained in the processing section.

B-3-4 Processing

B-3-4.1 DLSR stacking

Using the DSLR method, a successful run will capture over 4,000 images are gathered from 204 horizontal locations, of which less than 35% are useable. Each of these 204 locations generate sets of twenty images. These sets need to be processed through a focus stacking program to combine the focused parts of the set of images in order produce a single sharp image. These can then be used in the photogrammetry process to from a model of the surface.

Without tabulating the strengths of the various systems trialled, several focus stacking apps were tested, together with some existing add-ons to Adobe Photoshop and Corel Paintshop Pro. Of the 6-8 programs evaluated, Helicon Focus 8 (Helicon Focus - Helicon Soft) provided superior quality final images at a minimal once off cost of approximately US$ 40. The program is intuitive and fast, and the results far sharper than all others at the selected settings. The preferred settings are:

- Method B (depth map)
- Radius = 8
- Smoothing = 4.

All fully out-of-focus images can be manually discarded prior to submitting the useable set to Helicon Focus.

This program has proven better suited to the current project than several others commonly employed. It is possible to automate the 20-image sets and process them or select the in-focus images only. Processing is completed in less than five seconds with the final images being compiled from all the in-focus parts of the primary set. Figure B-3-8 shows an example the results from the image stacking process, comparing the combined sharpen image created from the image stack using the Helicon Focus application.

It should be noted that the photogrammetric software used to combine the 204 locations (Metashape) requires EXIF data to process images in order to get the camera properties. These have been stripped from the focus stacked images as they no longer apply. By selecting an arbitrary 35 mm focal distance, Metashape can still processes the focus stacked images without issues into a combined model.

a)

b)

Figure B-3-8: a) A focus stacked image from AQ11, b) compared to the most in-focus image from the primary set. Note how the left third of the primary image is now in focus on the stacked image. Image width 16 mm.

B-3-4.2 3D model creation

In all acquisition systems discussed the final 3D model is developed with Agisoft Metashape (Agisoft Metashape: Agisoft Metashape) This program comes in Professional and Standard versions with the latter sufficient for the current project. The professional version allows for mensuration, among

other tools, however this can equally be achieved by on-processing through additional software, required for the analysis of the model regardless of which Metashape version is used.

Photomodeller has also been trialled in previous studies, and despite having a slight edge in processing it has a very steep learning curve and is time-consuming to use. It also has an expensive maintenance program making it unsuited to occasional use, such as the ongoing needs at Murujuga. Curtin University have not recommended an alternative that will meet the project needs better than Metashape in terms of costing, ease of use and settings, and the output required in terms of 3D model, Ortho mosaics, and reporting.

B-3-4.2.1 DSLR processing

For the DSLR method a folder of 275 stacked images (processed using focus stacking software) are processed using Metashape and stitched together based on feature matching in the overlapping areas. Because of the comparatively low number of images compared to larger scale jobs, optimal settings can be used to generate the highest resolution and quality possible. As mentioned, the stacked images have no exit information, so it is processed as a '35mm' camera. The parameters are solved based on this, and the final product is then scaled based on the reference frame or objects in the scene using CloudCompare (CloudCompare - Downloads).

An example of the detail resolved using the DSLR method is provided in Figure B-3-8. This is not the complete model, a task that has yet to completely scan the entire surface due to environmental and equipment limitations. The result is still useable for further analysis. Figures B-3-8, B-3-9, and B-3-10 illustrate the level of visual detail achievable using the scanning DSLR method.

The final analysis is conducted through various measuring systems including Cloud Compare (CloudCompare - Downloads) and conventional CAD software. Cloud Compare can compare two versions of the same model at different epochs and to reveal morphological changes in a heat map of difference. A comparison of the models will be presented over the course of this project. The heat map highlights area of alteration that can then be relocated either in the model or the primary images used to construct it.

CAD software can accept 3D models, albeit in less realistic appearance than the Metashape generated model. CAD provides several useful mensuration tools that can be used on a profile of the model. This is achieved by slicing the model through a given axis, much like a depth profile on a geological map. And example of this is the presented in Figure B-3-11. This profile can then be submitted to CAD where both linear and volume measurements can be applied. Cloud Compare also provide linear mensuration and both it and CAD are used to determine change. The advantage of using primarily Cloud Compare is that it is an open-source function that has many of the analytical tools and simple surface tools required for this analysis, such as the ability to scale objects, matching between surfaces and calculating distances, the ability to take sections, and the ability to create rectified images from the 3D model. The software is seeing an increasing inclusion of functionality relating to geological mapping,

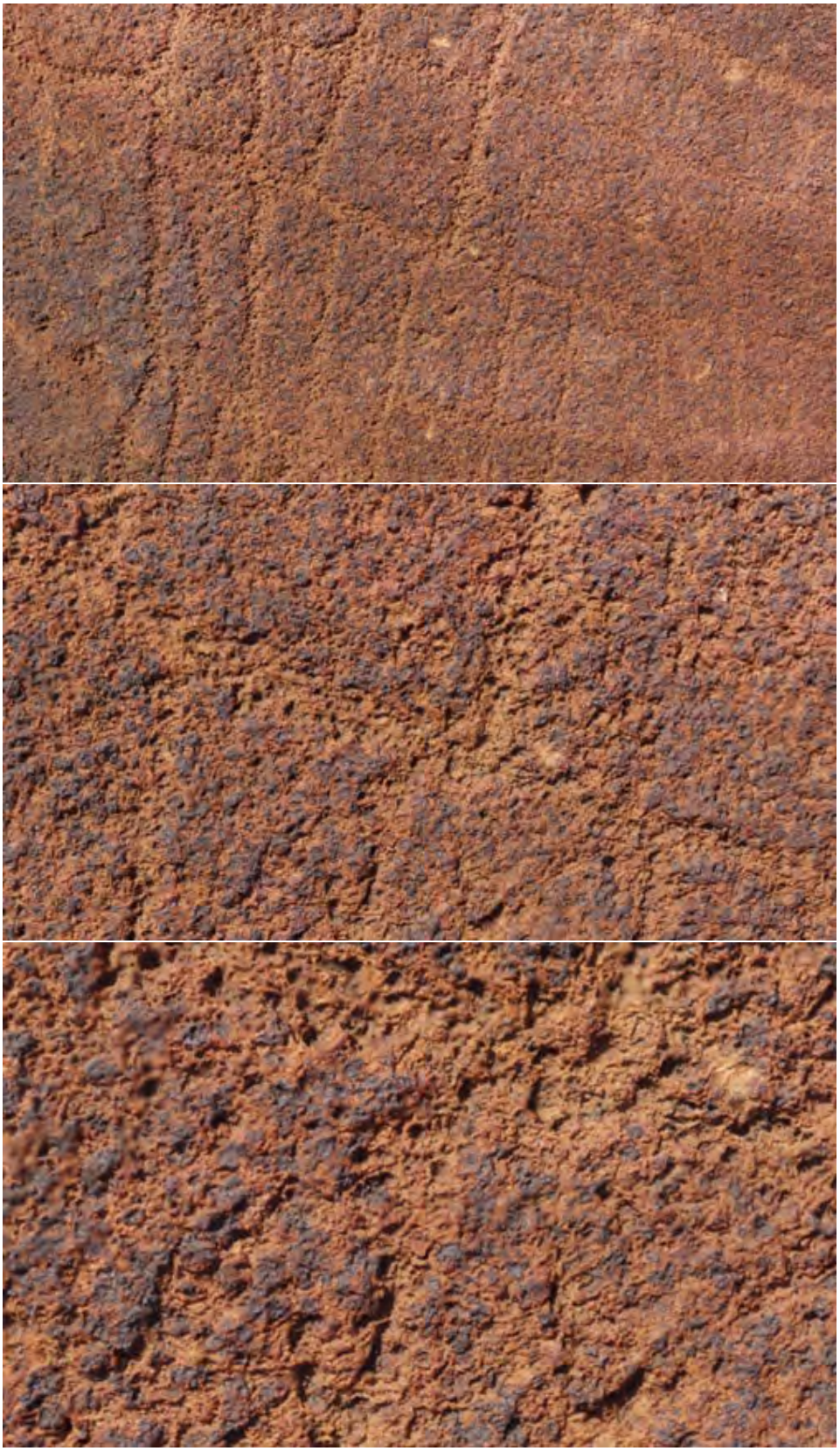

Figure B-3-9: A range of screen shots from the photogrammetric model.

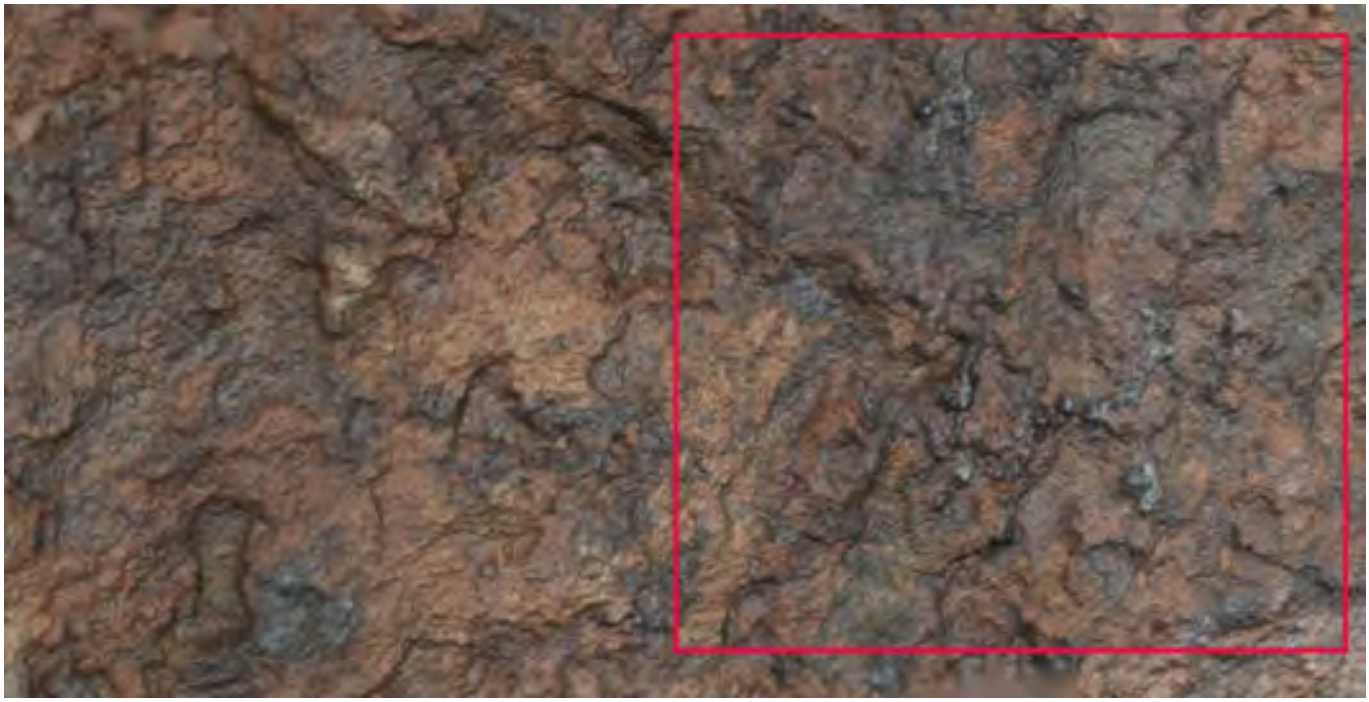

Figure B-3-10: Detail of the surface with a 4x4 mm reference grid.

Figure B-3-11: This ribbon cross-section through the surface in Figure B-3-8. This view illustrates one way a detailed study of the surface profile can be made through appropriate mensuration software.

B-3-4.2.2 Smartphone processing

The smartphone images (approximately 60 primary images) are processed in the same way as the DSLR stacked images (minus the need for applying the focus stacking method), and again because of the number of images the optimal settings can be applied.

The smartphone imaging method does not attempt to provide the same level of detail as the DSLR method, despite being able to capture suitably sharp images of the same frame size. The main purpose of the smartphone approach is to provide a detailed view of one part of the engraved surface to act as a reference for observing visual alteration. The imaging configuration is the same as that used to re-image the surface during spectroscopy, in that case to confirm that the probe has been positioned precisely in the same location on each occasion.

It has been noted that in at least 10 of the 540 spectroscopy reference images some form of alteration has occurred. This can be the sudden inclusion of bird faeces or its gradual dissipation over twelve months or more surprising alterations such as the increase or loss of patination features that had been considered permanent re-alignment reference features. The fact that some of the surfaces have undergone change at a very rapid rate, with substantial implications for the spectroscopic study, has prompted this more resolved approach to developing a reference area for ongoing study.

Coupled with this is the need to ensure that any technique that provide evidence of change must do so across the entire study suite to allow for statistically valid interpretation. Acknowledging this need does not however preclude the value of a single observation of a mechanism hitherto not documented. For example, given the potential for sodium sulphate formation to be increased with increased sulphur in the atmosphere, it is reasonable to expect that spalling of the rock surface will increase. Apart from the manifestly visible large scale spalling present on many rocks, it is also possible that micro-spalling may increase. Observations of this type of spalling will not necessarily be apparent in normal viewing conditions or at the imaging scale employed by CSIRO in 2015.

It is a quick method that takes 15 minutes to complete on-site and with a further 15 minutes of processing to achieve both the 3D model and the consequent rectified two-dimensional (2D) image. An example of the rectified image is presented in Figure B-3-12. Figure B-3-12 is a low-resolution representation of the image produced, which is most useful when studied in its 3D form. Nevertheless the 2D image provides a reasonable level of detail, as seen in Figure B-3-13 and B-3-14.

The application of this method provides a better understanding of morphological stability and a broader observational analysis of chromatic change in loss and gain to coloured features that lack form. Chromatic change determined from digital images is possible but far less precise than the current spectroscopic techniques. It is noteworthy that one of the critiques of previous work relied on the use of hardcopy reproductions from which they determined colour values. This is not a satisfactory means of assessing colour as the lighting conditions under which the primary image was recorded has not been included in the image, in the form of a colour standard. Added to this is the unreliability of the printing process to render colours consistently. Thus, any use of printed images, images without colour reference, or images that have been duplicated cannot be used for scientific purposes.

JPEG images are equally unreliable for colour comparison as the compression algorithm, relies

Figure B-3-12: An engraved rock showing gross spalling along the left side of the block. The engraved section on the right is also spalling but at a macro-scale that appears as lightening of the surface. It is this macro-spall area that is best studied with the macro-imaging technique. The area marked at right would make the ideal study area, having a deep groove that would reveal rounding and various surfaces, including engraved channels.

Figure B-3-13: The rectified image of the reference area at AQ02.

Figure B-3-14: Detail of Figure B-3-12. Width of image 20 mm.

Figure B-3-15: Section view of the 3D model showing the well-developed contours achieved using the smartphone, capturing 60 images in 15 minutes.

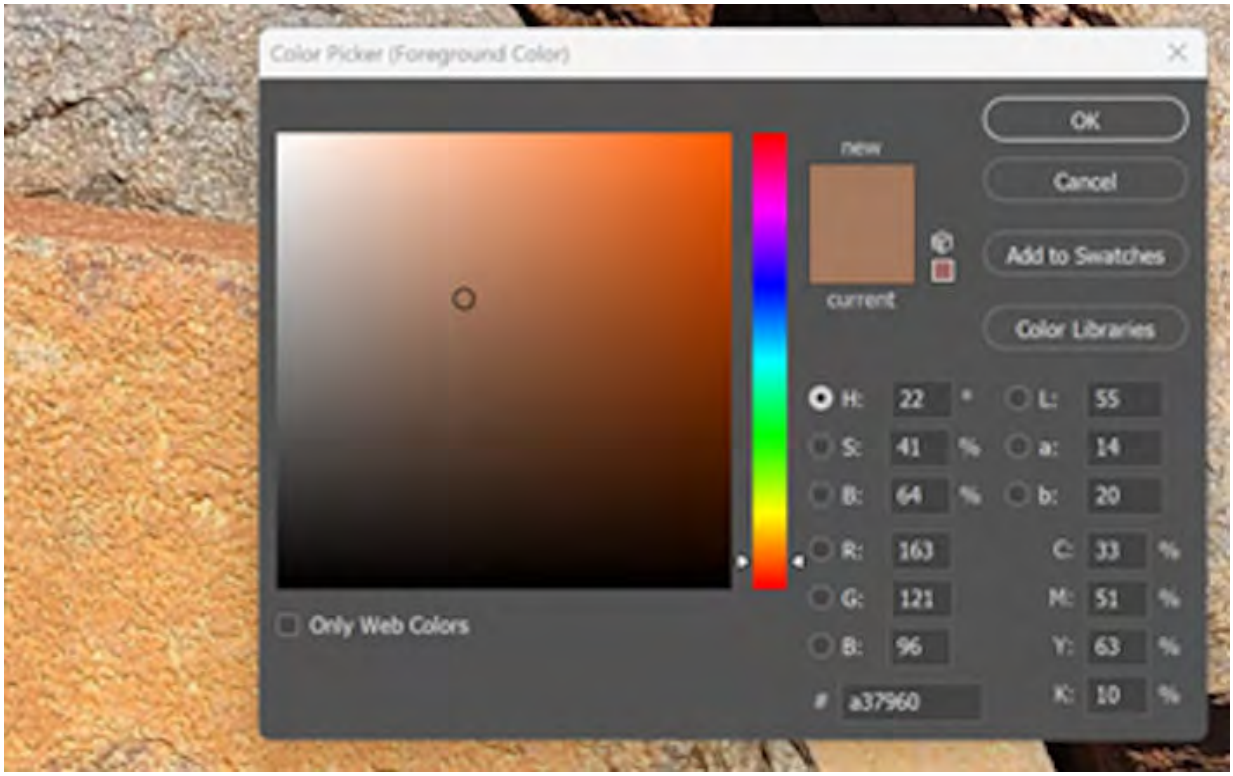

*Figure B-3-16: Screenshot of the Photoshop Color Picker tool with various measurement systems including L*a*b*.*

entirely on reducing the full gamut of colour available to the imaging device to fewer colours that more or less accurately render the image true to colour at a substantially reduced file size. The implication for making colour judgements is that the compression will not always convert a pixel in TIFF or RAW format to the same JPG value every time.

The imaging presented here is not intended to be used for colour measurement. It is acquired under more or less uniform lighting conditions using the camera's light, but sunlight still contributes substantially. No colour scale has been used at this point as the resultant images have not been intended for colour analysis. A scale is included, and this could easily be substituted with a standard colour scale, assuming that future scales are printed with the same inks and remain true to colour over time. CIELab colours can then be measured using the eyedropper tool in Photoshop, clicking in the colour swatch and reading the $L \times a \times b$ values from the screen (Figure B-3-16).

This method is strengthened by taking readings in the standard colour card and defining a colour as the difference between the target and each of the four reference colours. While this system can be applied to any photograph of reliable colour integrity it is time consuming and falls far short of the accuracy of a spectrometer.

For these reasons, the field of imaging has focused on rectified images and low-level 3D models that can provide a reasonably high degree of information about surface alterations at minimal expense in terms of field time.

B-3-4.3 3D model analysis and rectified images

The imaging techniques have not advanced in time to allow for any meaningful analysis. This will come in future years during the monitoring phase. Two forms of analysis are available to the 3D images. One is the use of Cloud Compare. As mentioned, it is a visualisation tool offering one very strong tool for analysis of 3D models, and is used to scale the models from the Metashape processing. It also allows for the spatial alignment of two models of the same object or surface. In this case, any of the study surfaces using either the DSLR or smartphone imaging approaches. Several of the models developed from the March 2024 campaign will be compared to those from the March 2025 campaign to assess whether any morphological changes have developed since the introduction of the technique.

The other method used the production of rectified images. All 54 study surfaces have been imaged since project commencement using the broad scale recording for documentation of the sites (i.e the boarder-scale documentation at the metre level, as oppose the methods used for macro scale change detection). This has emerged to allow for the long-term study of delamination and other gross surface alterations. One of the challenges of imaging the rocks is that most are in partial shadow for much of the day and attempting a perfectly perpendicular camera angle casts further shadows. With some surfaces extending to more than three metres and others curved such that the entire engraved surfaces cannot be captured in one image. The most appropriate imaging system is one of multiple images stitched together to form a single high-definition image. This is particularly beneficial where shadows being cast by the operator are unavoidable, as the Metashape processing itself will remove shadows that do not occur in the same position in two images. There is thus an incentive for the photographer to stay on the move and capture the surface quickly. The 3D model from Metasahpe is saved in OBJ format and imported into Cloud Compare. It can then be oriented to any planar view and saved as a 2D rectified image using the Raster tool.

Two adjacent sites are presented here to illustrate the benefits of the 3D approach. AQ09_GBR (presented in Figure B-3-17) is a large, rounded block with engravings around the north-eastern surface, beyond the imaging range of a single photograph. Two images could be taken; however the 3D model exported to Cloud Compare allows for the composition of a perfectly perpendicular distortion-free view of any point on the surface without having to position the camera each time. This advantage can be applied to any site where a perfectly composed image of any part of the surface can be constructed at any time off-site. A side benefit of this approach, imaging for photogrammetric construction, is that the photographer is consciously imaging every part of the surface from every angle, resulting in a comprehensive catalogue of images. Instead of one or two images typically taken as routine documentation, this approach provides a folder of 60+ images covering all parts of the engraved surface and beyond.

Another strong feature of the 3D-2D pathway is that the background can be removed so that just the engraved block can be focussed on. While this doesn’t provide any greater detail it certainly makes the surface less busy. The detail in Figure B-3-17 is not exceptional, but it has been achieved from imaging that focussed on the general rock form. Better close-up images can be achieved however the rock can be viewed in its entirety at this detail. The aim of these images has been to observe gross surface changes and the resolution certainly provides for that.

AQ09_GPH is a 4 x 3 m inclined slab that cannot be imaged in its entirety at a suitably perpendicular angle. At most times of day, the photographer’s shadow dominates the scene. What is remarkable

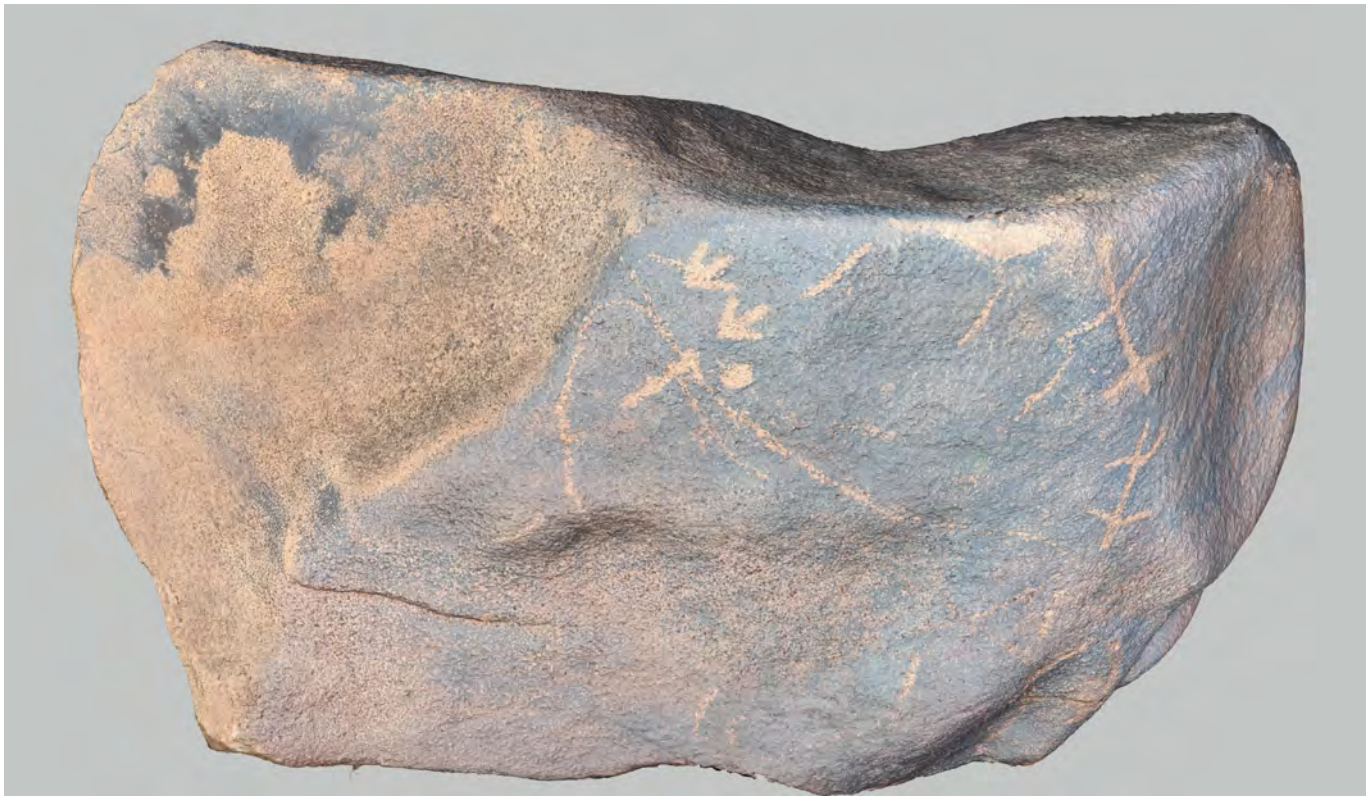

Figure B-3-17: AQ09: image oriented post-processing to provide the best view of the engravings. The background has been removed in Metashape.

Figure B-3-18: Detail of the image above zoomed up to just before pixelation. This is not an extraordinary level of detail but has been achieved through 60+ general shots of the rock.

about Figure B-3-18 is that it has been constructed from a series of photographs, almost all of which have compromising shadows. Figure B-3-18 offers an almost shadow free view not physically attainable on site. The other benefit of the multi-image construction is that the resultant image is of a higher contrast than achievable with a single shot, such as that of Figure B-3-19 which shows a rectified reconstructed image, compared to Figure B-3-20 that contains only a single captured image.

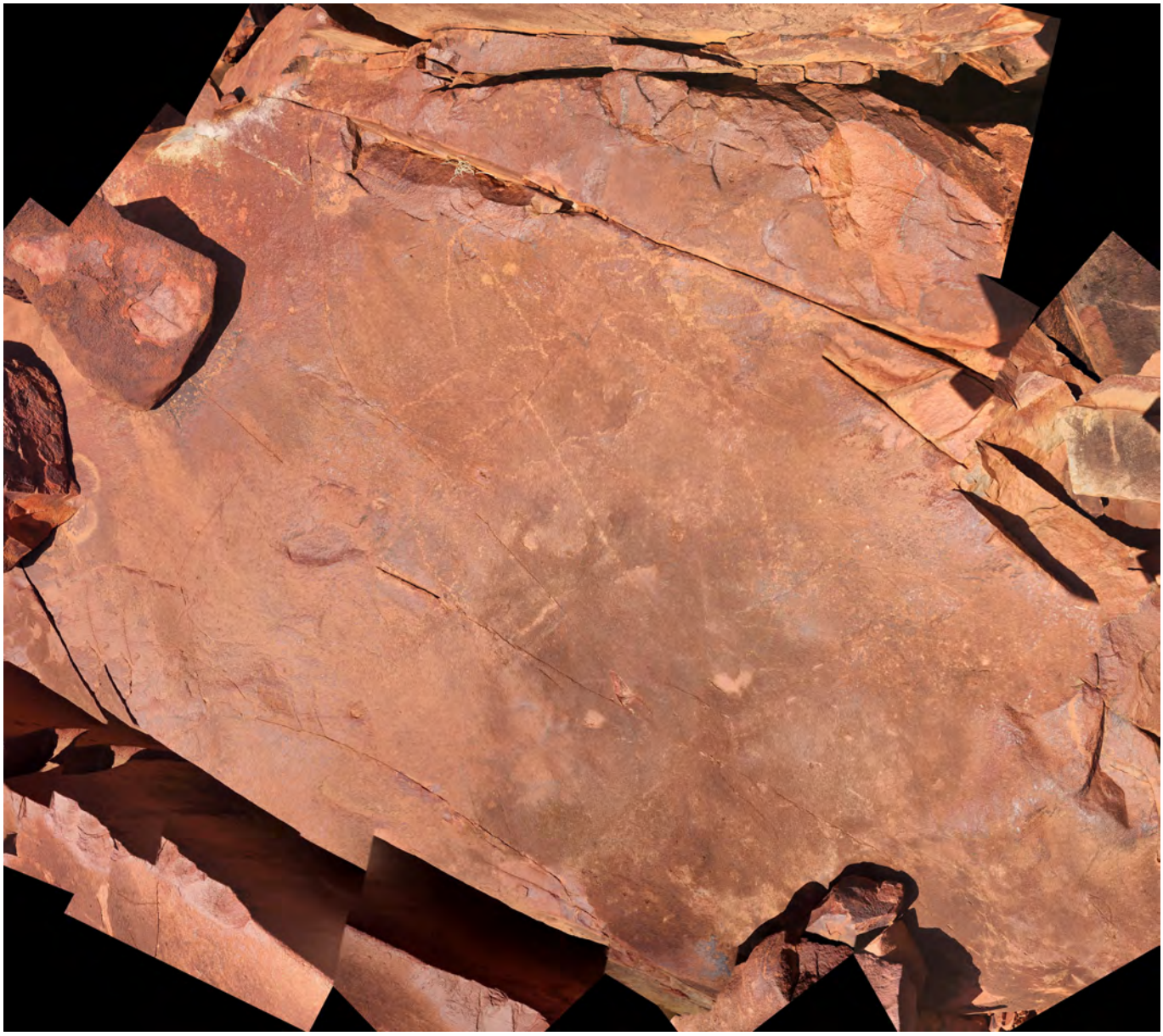

Figure B-3-19: AQ09_GPH constructed from 60+ images and processed through Metashape and Cloud Compare to arrive at a shadow free perpendicular view. On close inspection some shadows do remain as slightly darker areas.

Figure B-3-20: A single shot view of AQ09_GPH shows strong shadows and very low contrast in the engraving.

B-4 Comparison between DSLR and phone rock capturing

B-4-1 Introduction

This section reports a comparison between the proposed methodology for capturing and monitoring the surface topology of a rock for recording and measurement, and more traditional photogrammetric approach using a DSLR. In laboratory conditions, a sample rock was sampled using both methods. For the DSLR, the data was captured using orbits. For the phone it was captured in a grid manner with four different captured image sets over two days. The data was compared geometrically in the 3D domain to examine the differences in topography between the methods. In addition, the differences between to the different capture image sets were examined in 3D domain (to detect geometric differences) and the spectral domain (to detect differences in the surface response).

B-4-2 Data capture

B-4-2.1 DSLR image capture

As a baseline for comparison, the rock surface was captured with a Nikon D750 full frame camera with a 70 mm zoom lens. The zoom and focus were setup and fixed so that the rock could be observed in the full frame and the settings were left unchanged for all following photos. The capture was done with the following considerations:

- Zoom and focus fixed after first image
- Small aperture (F20) to increase the depth of field
- Low ISO and long exposure time so no flash was needed
- Diffuse and consistent lighting to remove effects caused sharp shadows
- Tripod and turntable used to ensure no moment during capture and no shadowing from the setup over the rock
- Images taken with several orbits, varying the distance and angle of the camera to the surface, and rotating the camera on its side between orbits

This was done to ensure good images, a good spread of images around the rock, and diversifying the geometry of the final photogrammetry reconstruction to try and eliminate any correlation between parameters. A frame was used to help define the scale of the final reconstructed surface.

B-4-2.2 Mobile phone image capture

For the data capture using a mobile phone camera, four different sets of images were taken of the same rock and target as captured by the DSLR camera. Sets 0, 1 and 2 were taken with slight physical alterations made to the surface between the captures. Set 3 was taken on the following day with no alterations to the rock surface made. Each capture was done in the same manner. In this case the focus was set in the first image and fixed. The subsequent images were then taken in a grid pattern with a:

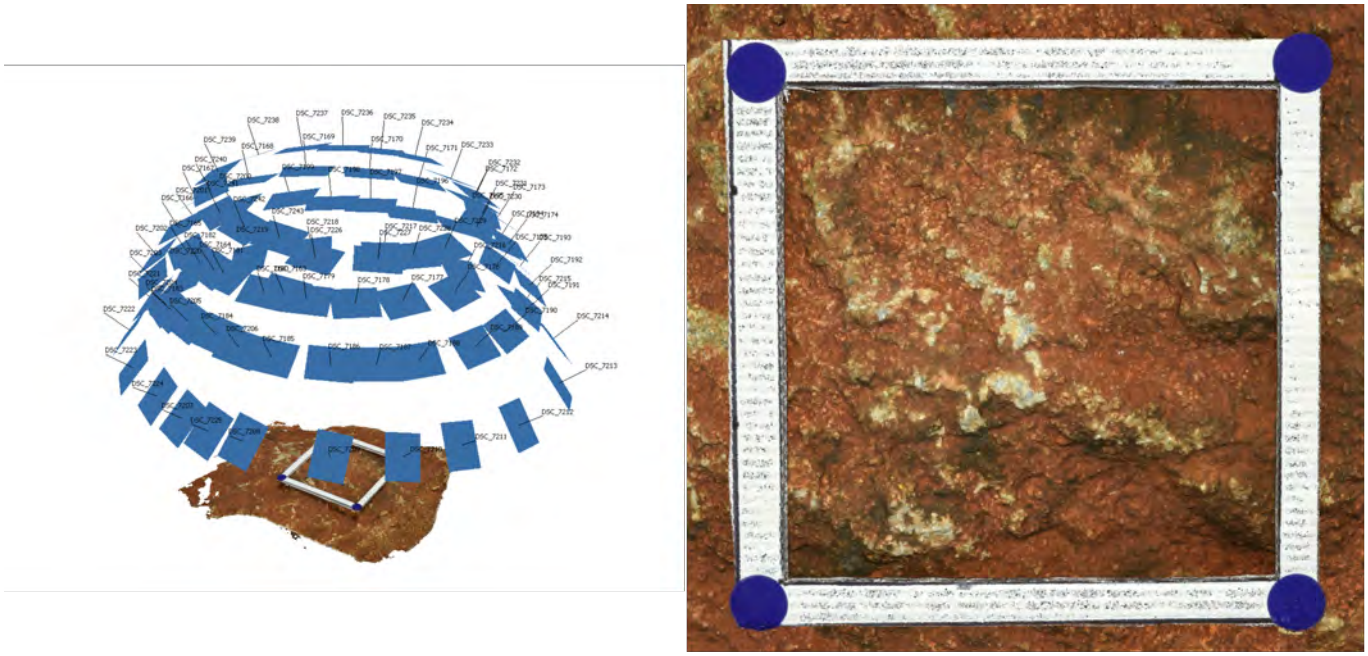

(a) (b)

Figure B-4-1: DSLR capture of the sample rock surface. (a) shows the locations of the images taken around the targeted rock surface, and (b) shows a reconstructed surface of the targeted area

- A constant distance to the surface was ensured by use of a short monopod.
- Consistent overlap between images was kept as the phone was moved.
- A second grid of images was captured for each set, by rotating the camera 90^{o} between grids.
- The camera was left on for each image to ensure no shadowing on the surface and consistent lighting.

An example of the image location is relation to the rock surface is shown in Figure B-4-2. As can be seen, due to the variations of the topography of the rock surface and the two grids captured, there is some variation in terms of the depth of the phone location (but this is dependent on the surface). More details on the exact capture methodology can be found in Appendix H in Monitoring Studies Report 2024 (Curtin University, 2025).

B-4-3 Processing of images and alignment

B-4-3.1 Processing of DSLR

The processing of the DSLR took place using Agisoft Metashape, the same software used in the generation of the existing surface models. This was done using a (in-situ) self-calibration from automatically extracted tie points. The parameters were calibrated in the pixel coordinate system and included:

- Focal length (F)
- Principle Point Offset (Cx and Cy)
- Radial Distortions (K1, K2, and K3)

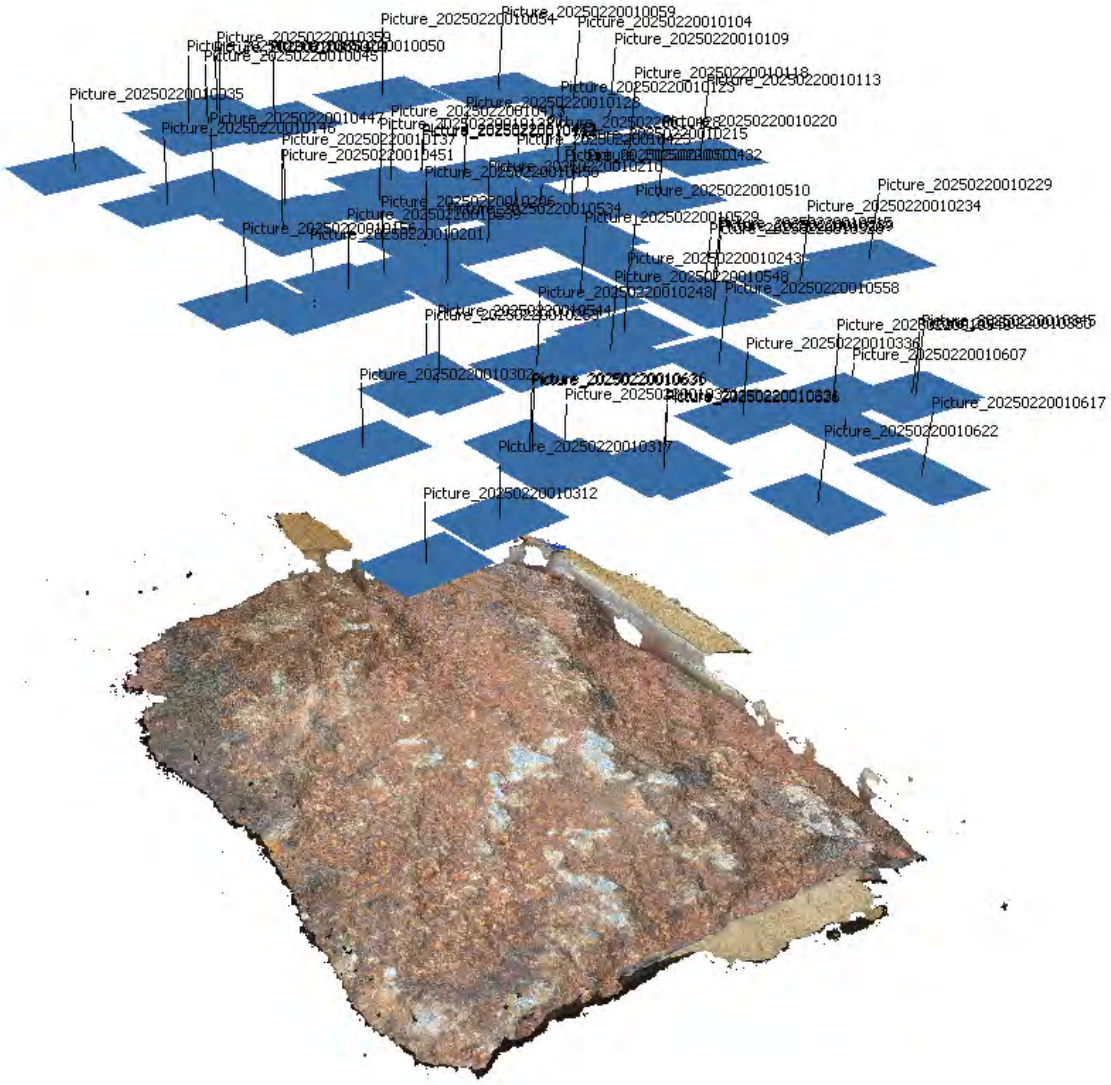

Figure B-4-2: Image acquisition pattern for the phone camera in relation to the reconstructed surface. This specific pattern was for Set 0.

- Tangential Distortions (P1 and P2)

Ideally these would have been pre-calibrated on a test field, but it was decided to do it in-situ to replicate field conditions and depth of fields to the rock surface. The capture geometry (image location was selected to ensure a good calibration result; however, there are some values that are correlated. These could be improved by angling the centre of the image away from the centre of the rock in some of the images captured to improve geometric diversity.

Table B-4-1: Calibration results from the Nikon DSLR.

			Correlations							
	Value	**Error**	**F**	**Cx**	**Cy**	**K1**	**K2**	**K3**	**P1**	**P2**
F (mm)	59.973	1.26E-06	1	0.15	-0.6	-0.1	0.13	-0.1	0.13	-0.5
Cx (mm)	-0.3464	1.32E-06		1	-0.2	0.04	-0	0.04	0.96	-0.2
Cy (mm)	0.0075	1.85E-06			1	-0.1	0.04	-0	-0.2	0.95
K1	.0702	0.00022				1	-1	0.88	0.02	-0.2
K2	-0.5959	0.0044					1	-1	-0	0.05
K3	4.0633	0.026						1	0.04	-0
P1	-0.0002	8.70E-06							1	-0.2
P2	0.0006	1.30E-05								1

Overall, the results produced had the following characteristics, presenting in Table B-4-1

Table B-4-2: Summary from Nikon D750 DSLR processing results.

Number of images	81
Tie points (Key points)	22995 (33015)
Average images per tie point	10.6376
Reprojection error in pixels RMS (max)	0.8961 (20.4888)

A dense point cloud reconstruction was then performed creating a surface representation. This point cloud was then scaled using the targets (and surrounding square) to get a surface in millimetres (see Figure B-4-1(b)). This surface was used to compare those created from the phone image processing.

B-4-4 Processing phone camera images

Agisoft Metashape was used to process the four image sets from the phone camera. The same settings were used as for the Nikon DSLR, including the calculation of the calibration, and the same parameters in the pixel coordinate system. In theory, if the same capture was completed under the same conditions, the calibration parameters should be the same, but a unique set of calibration parameters were calculated for each set. The results are summarised in Table B-4-3 and Table B-4-4.

Table B-4-3: Summary from phone processing results for the four datasets captured

Dataset	**Set 0**	**Set 1**	**Set 2**	**Set 3**
Number of images	61	60	73	90
Tie points (key points)	68428 (81252)	69875 (78512)	71119 (83474)	66515 (73608)
Average images per tie point	3.1532	3.44579	3.77890	5.30705
Reprojection error in pixels RMS (max)	1.2850 (27.5603)	0.94272 (19.2961)	0.98356 (25.4499)	1.03608 (20.0198)

Table B-4-4: Summary of the camera calibration parameters of the phone images for the four different datasets.

Parameters	**Set 0**		**Set 1**		**Set 2**	
	Value	Error	Value	Error	Value	Error
F	7708.76	6.8	7588.03	5.1	7328.34	4.9
Cx	-2.8837	0.43	0.5379	0.33	-5.3262	0.28
Cy	-9.9532	0.44	8.5909	0.34	-0.9647	0.28
K1	0.4270	0.0015	0.3061	0.0011	0.2703	0.0009
K2	-5.8421	0.03	-4.2092	0.019	-3.4932	0.015
K3	24.628	0.2	15.8169	0.12	11.8089	0.084
P1	-1.9E-05	2.7E-05	1.2E-04	1.9E-05	-1.6E-04	1.4E-05
P2	-0.0008	2.5E-05	0.0004	1.8E-05	0.0009	1.4E-05

Parameters	**Set 3**	
	Value	Error
F	7247.69	2.1
Cx	-3.0616	0.26
Cy	7.6739	0.25
K1	0.2524	0.0006
K2	-3.2054	9.5E-03
K3	10.4096	5.6E-02
P1	2.8E-04	1.4E-05
P2	0.0011	1.3E-05

It should be noted that RMS reprojection error is close to 1 pixel, which is expected for a good reprojection. The overlap is lower that the DSLR using orbits to capture the images which could lead to some loss of strength in the geometry (often some higher or oblique shots covering the entire area are used in drone capturing to increase the overlap and strength). What is if more interest is that the values for the focal length (and some of the other calibrated parameters) are quite different. This is unexpected if it is the same capture repeated four times, the values should be comparable. This does indicate some variability between the different captures that could lead to differences in the surface reconstructions but may also be a function of higher correlations

between the calibrated parameters. After the photogrammetric adjustment, a dense point cloud reconstruction was then performed for each of the sets of processed images. These were used in the comparison to the DSLR reconstruction, and to each other.

B-4-5 Surface reconstruction alignment

For the comparison, Cloud Compare (version 2.12.1) was used as a readily available software, that is open sourced and commonly used in the processing of different types of the datasets. As the point cloud reconstruction for both the DSLR and the four datasets from the phone were all carried out in the pixel dimension, the first step was to scale and then align them to each other. To do this, first the distance between the dots in the frame (see Figure B-4-1(b)) was used to scale the DSLR reconstruction from pixels into millimetres. In addition, a plane was fitted to the data to roughly alight the vertical (z direction) to the surface normal of the region, and to rotate them point cloud to align the frame roughly to the x and y directions. Next the four sets of images from the phone were scaled and aligned to the DSLR reconstruction, so it could be used as a 'reference surface'. This was achieved in two stages.

- The first stage was to manually select nine points in common between the DSLR reconstruction, and each of the phone image reconstructions. Figure 3 shows the approximate locations of the points selected and these were chosen based on easily identifiable features in both image sets, a good generally spread across the surfaces to be aligned, and to be selectable to within a millimetre. These points were then used to provide an initial transform the phone reconstruction to coincide with the DSLR reconstruction through solving the scale, rotation, and translation.
- The next stage involves using the built-in Iterative Closest Point (**ICP**) function in Cloudcompare. This worked by solving the transformation parameters to minimise the distances between all the points between the two surfaces. This allowed for a finer and more precise alignment between the surface reconstruction.

Once this alignment was complete, a comparison between the surfaces could now take place.

B-4-6 Comparison results

B-4-6.1 Comparison to DSLR reference surface

The first assessment was to compare the surface of the four sets of phone images to the DSLR reconstruction. This was done by fitting a local mesh to the DSLR point cloud to create a reference surface. Then each image set was compared to the reference surface by calculating the distance of each point in reconstruction to the reference surface in the normal direction. If the methods are comparable, they should have minimal deviations representing they are the same surface. The results in from the comparison are shown in Figure B-4-4 (for image Set 0 and 1) and Figure B-4-5 (for image Set 2 and 3). The differences shown in millimetres and we can that for the first dataset of the phone (Set 0), there is a large bowing effect between the DSLR surface reconstruction and phone image reconstruction. A similar effect is also present in Set 1. Set 2 show a similar effect (all be it much reduced), while Set 3 seems to show an agreement between the surface re-construction. If we go back to Table B-4-3 and Table B-4-4, we can possible see some of the cause of this effect. In Table B-4-4, we can see that the focal length is decreasing from Set 0 to Set 3. What this means is that it is possible that from the image sets, it was not possible to accurately calibrate this value.

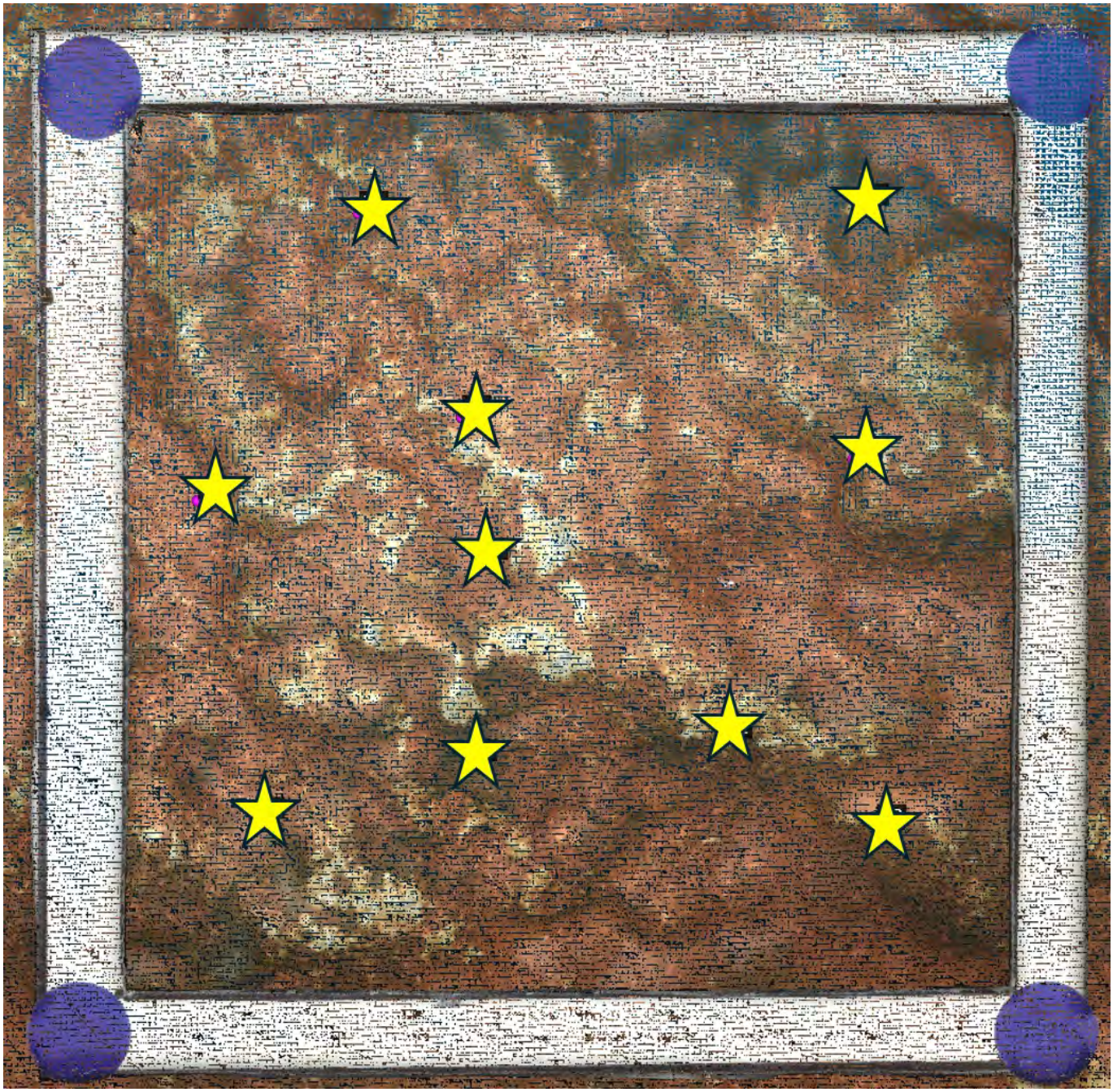

Figure B-4-3: Approximate locations of the nine manual points used to align the DSLR reconstruction to teach of the reconstructions from the phone.

The higher value in Set 0 (compared to Set 3) is most likely causing the re-construction to bend (as well as some differences in the radial lens parameters between the sets). Indeed, as we see the decreasing focal length from Set 0 to Set 3, we also see the decrease in the bending effect in the difference between the DSLR, meaning that the focal length calculated in Set 3 is more likely the correct value. In Table B-4-3 we can also see a potential cause for this variation in the camera parameters. As we go from Set 0 to Set 3, we see an:

- Increase in the number of images captured
- Increase in the number of overlapping images generating tie-points

Looking at Figure B-4-6, we can also see the overlap of the images increasing from Set 0 to Set 3. This may indicate that with the increase overlap, the geometry of the adjustment and reconstruction is increasing and so the calculated calibration parameters are being determined more accurately. Based on this, to reduce this bending effect we could potential:

- Increase the number of images and overlap
- Include some higher or oblique shots covering the entire area
- Determine the calibration parameters and hold them fixed

Note that while it can not be said that the DSLR is the ground truth dataset, it does highlight that the captures in this case do not producing the same results for each image set, as also seen in the changing calibration parameters.

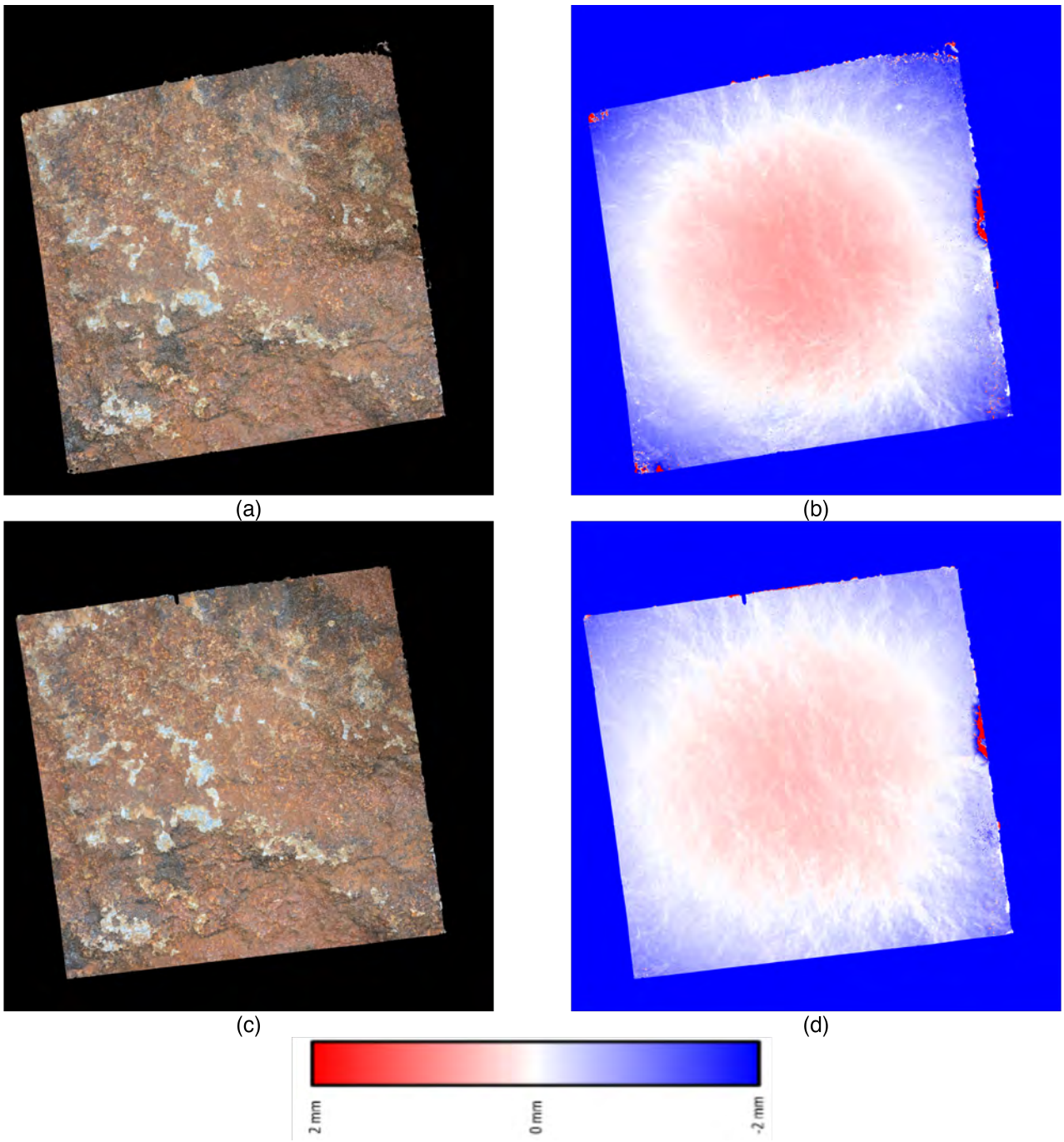

Figure B-4-4: Ortho image and differences compared to the surface generated by DSLR processing. (a) and (b) represents the reconstructed ortho image and surface difference of Set 0 to the DSLR surface reconstruction. (c) and (d) represents the reconstructed ortho image and surface difference of Set 1 to the DSLR surface reconstruction. Differences are in mm.

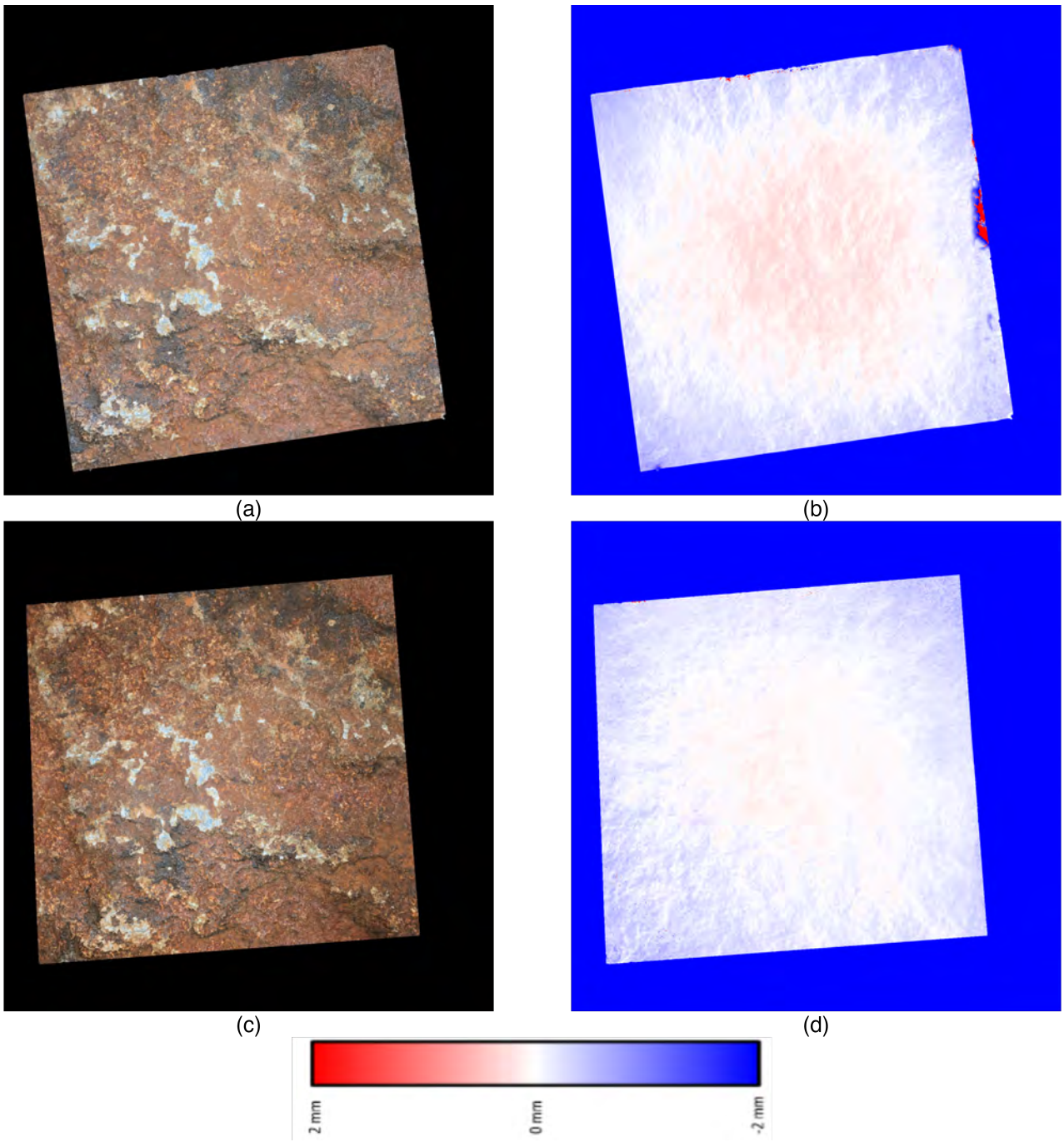

Figure B-4-5: Ortho image and differences compared to the surface generated by DSLR processing. (a) and (b) represents the reconstructed ortho image and surface difference of Set 2 to the DSLR surface reconstruction. (c) and (d) represents the reconstructed ortho image and surface difference of Set 3 to the DSLR surface reconstruction. Differences are in mm.

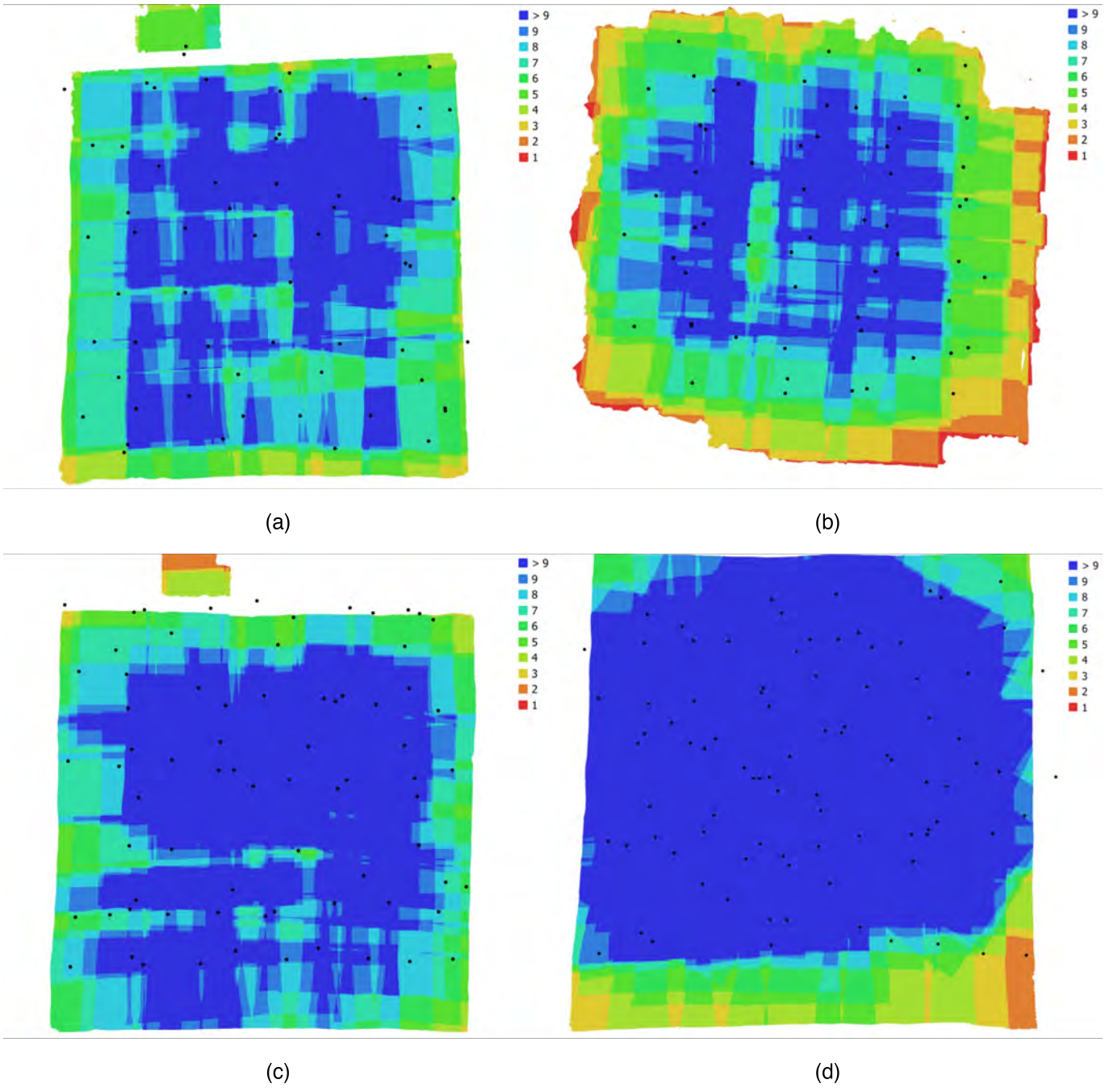

Figure B-4-6: Overlap for the phone images. (a), (b), (c) and (d) corresponds to image sets 0, 1, 2 and 3 respectively.

B-4-6.2 Comparison between the image sets

The primary purpose of these image set comparisons is to find changes in the surfaces between captures. The consecutive captures were therefore compared to each other to determine the differences between Sets 0 and 1, Sets 1 and 2, and Sets 2 and 3. While the results in the images show deviations between the DSLR reference reconstruction and each other, most of these errors appear to be in the long wavelength. The differences we are trying to identify are smaller, and more in the short wavelength. To remove long wavelength differences, a 2^{nd} order polynomial was fitted to the difference values between the surfaces (to model the effect) and these values were remove from the initial difference calculations to leave behind the short wavelength differences. Figure B-4-7 shows the results of this comparison. In Figure B-4-7 (a), (c) and (e) we see the raw difference still being affected by the bending error. In Figure B-4-7 (b), (d) and (f) we see the differences that remain after the polynomial correction has been applied to remove this effect. Because of this we can more clearly see the smaller topographical differences.

B-4-6.3 Comparison between the orthoimages

While some of the difference can be observed by changes in the surface distances, others may be too small to see in relation to the noise or inaccuracies in the surface reconstruction. To try and define the changes that are too small to be detect by surface topography changes, the ortho images can be examined. To do this an ortho image is created for each of the phone image sets (as seen in Figure B-4-4 (a) and (c), and Figure B-4-5 (a) and (c)). These RGB values can then be compared to check for changes. The RGB values are often sensitive to changes in lighting conditions and camera settings (ISO, shutter speed, and aperture for example). So the images should be colour corrected using a calibration target either in the software (which Metashape is capable of doing) or in post processing, directly to the ortho image. This was not done in this case, however, the RGB colour space was converted to the HSV space instead. The hue, saturation, and intensity could then be compared independently to remove some of the correlation in changes that can be observed in the RGB space. The results of the comparison are shown in Figure B-4-8. We can see the difference between the intensity values in Figure B-4-8 (a), (c) and (e) for the difference between image Sets 0 and 1, Sets 1 and 2, and Sets 2 and 3 respectively. In this case it is shown as a percentage change with zero denoting no change, 1 going from black to white, and -1 going from white to black. This does show some difference between the sets, but it also shows that there are some slight misalignment errors that still exist between the orthoimages generated from each step. To combat this, the different Sets were aligned to each other using feature points and an image transformation. Feature points were calculated using a SURF function in Matlab for each orthoimage and then matched between the consecutive datasets. From the matched features, a projective transformation was used to transform the image onto the precious capture and to more closely align them. Once this was done, the difference between the intensity values were once again calculated. The results of this process can be seen in Figure B-4-8 (a), (c) and (e) for the corrected for the difference between image Sets 0 and 1, Sets 1 and 2, and Sets 2 and 3 respectively. In this case white denotes a change of more than 50%, and black denotes a change of 0% or less. We can still see some areas (dark grey) that show some difference, but the white spots seen highlight the changes that can be seen due to a change in surface colour (specifically a change in colour intensity.

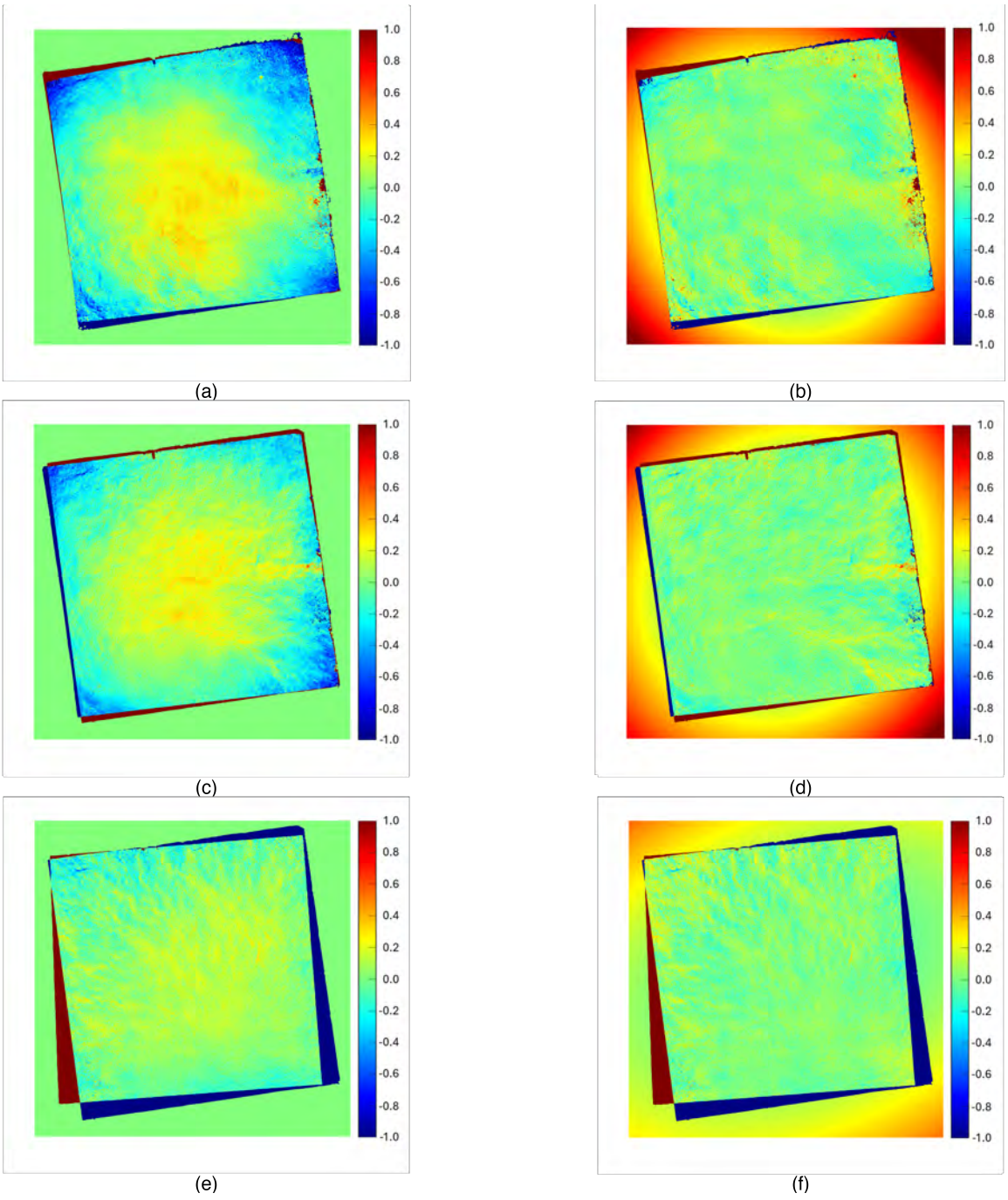

Figure B-4-7: The differences between the reconstruction from the different sets of images from the phone. (a), (c) and (e) represents the differences between the raw surfaces values of the DEM between sets 0 and 1, sets 1 and 2, and sets 2 and 3 respectively. (b), (d) and (f) represent the differences between the correct surfaces values of the DEM between sets 0 and 1, sets 1 and 2, and sets 2 and 3 respectively. Differences are in mm.

B-4-7 Discussion

This comparison shows that under control conditions, it is possible to perform a surface reconstruction with a phone camera that is comparable to traditional photogrammetric reconstruction performed with a DSLR camera. However, care must be taken in the capture to ensure that the calibration parameters are adequately calculated, and the final reconstruction does not suffer from any distortions. That said, there are additional steps that can be taken to enable comparison between different image captures. This includes correcting for these distortions for detecting differences in the 3D domain, as well as projecting and aligning the orthoimage in the spectral (RGB and HSV) domain. This does demonstrate the ability to detect some changes over time with the captured data if care and appropriate techniques are used.

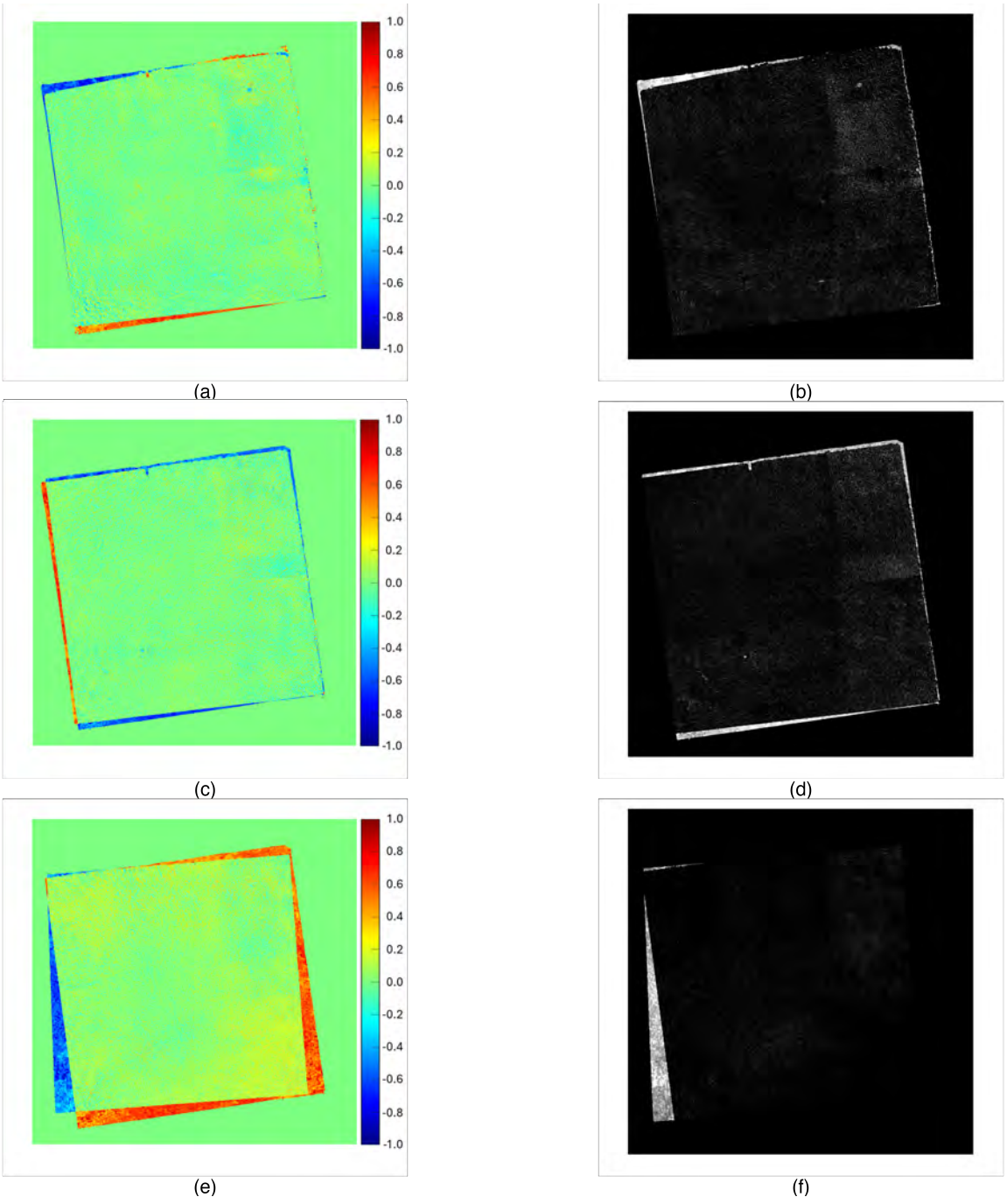

Figure B-4-8: Differences between the grayscale values of the orthoimages generated from the image sets 0, 1, 2 and 3 from the phone. (a), (c) and (e) are the differences (in percentages) from the orthoimages. (b), (d) and (f) are the differences after a further 2D alignment was performed with black denoting no change and white denoting a large change (of approximately 50% or more).

B-5 Condition survey database

The project proposal included the observational study of up to 2,000 engravings, to give an overview of the general condition of the group. This was anticipated prior to the project starting and without knowing what logistical parameters would be available. With two dedicated MAC Rangers assigned it is not possible to undertake general survey work beyond the commitments of spectrometry and other surface measurements at the 54 rocks under study.

To meet the objective and to allow for a broader understanding of conditions the survey has been confined to imaging with interpretation of conditions from the images. While face to face condition assessment provides far more vital information, there is enough in the images to build a reasonable picture of Murujuga. To date around 1,500 engravings have been imaged with geotagged location details, and a GIS mapping system partially developed to interpret conditions spatially and to show the representativeness of the rocks observed.

The imaging has been carried out without consideration for cultural meaning and it is expected that many of the images may need to have viewing or access restrictions imposed. This issue has already been discussed with the MAC Heritage Research Manager who will receive the completed archive and advise on on cultural protocols in consultation with the Circle of Elders. All images and data will be retained.

Conditions that will emerge from the study will only be fully understood when the survey is almost completed however will include.

- Extent of delamination
- Granular erosion in terms of engraving faintness.
- Extent and distribution of bird excreta
- Biological growth
- Vandalism*
- Erosion pattern by rock type, based on GIS geological map overlay.

* It is important to note that although vandalism may be detected and reported to MAC and appropriate authorities, vandalism is not within the scope of impact that the MRAMP study is designed to detect or prevent.

B-5-1 Colour measurement using the macro-photogrammetric system

B-5-2 Introduction

Photospectrometry, through the use of precision spectrometers such as the Ocean HDX, used for the past two years to monitor changes in surface spectral reflectance, is the most reliable method for measuring surface colour change. One important differentiating feature of the spectrometers employed, including the JAZ, has been the ability to measure reflectance well beyond the visible in both the UV and NIR regions. The term reflectance is preferred to colour, to emphasize the fact that these spectrometers measure beyond the waveband for human colour perception (380-780 nm). There are significant reflectance characteristics of some minerals present at Murujuga that appear outside the human visual perception waveband.

Spectroscopy has proven to be a time-intensive procedure, given that surface change may be happening at a rate not readily captured in the time frame of the current project. Furthermore in pursuit of achievable morphological and surface appearance change the macro-photogrammetric approach has proven to be a useful and manageable tool, for its easy adoption, low cost, and time efficiency in the field. The incorporation of an internal reflectance calibration tile opens the possibility of also taking reliable colour measurements. The terminology has deliberately moved from reflectance to colour, to indicate that the technique described here is limited to the waveband corresponding to human colour perception.

By adding a calibration tile to the macro-photogrammetry template it is possible to reliably measure colour using the CIELab colour space model. This study assesses whether this approach is feasibly integrated onto the photogrammetric imaging or whether it is better achieved with colour measurement specific imaging.

B-5-3 Internal reference options and standardisation

The use of controlled imaging to derive CIE Lab values was developed by the author (not in isolation) as a means of establishing colour comparison prior to adopting spectrometric approaches over twenty years ago. It has been revived for this project as a beneficial adjunct to the photogrammetric recording using digital cameras. The problem with imaging any surface with a camera, be it digital, or analogue with its plethora of film types, is how to recreate the exact colorimetric setup from one epoch to another. Sunlight, for example varies significantly both in intensity and colour temperature. Flash photography introduces a slightly better control however it too is subject to variation in angle and distance to the surface. The surface itself may be glossy, which may vary over time, and this specular reflectance can vastly alter the pixel-by-pixel colour information.

Film cameras are of limited use due to the colour degradation inherent in the processed film stock, hence the only viable means of achieving repeatable colour is through the use of digital sensors. If digital imaging is considered the most reliable it then suffers from evolutionary improvements and the fact that each camera and each app will record and process an image differently.

The most common image format across all digital technologies is jpeg, a compressed file format that relies heavily on rationalizing the colour values found in a given image. While the camera may shoot in 24-bit colour (16.7M hues) or higher, the jpeg compression algorithm seeks out a reduced

palette by averaging four pixels into one, among other compression techniques. This emphasizes the need for high pixel count sensors, such as the currently employed Samsung Galaxy S24 and S25, featuring 200Mp image sensors. While shooting in uncompressed formats, such as TIFF and RAW would avoid any pixel averaging reductions, not all apps offer this option. The preferred app for the macro-photogrammetry technique described here is limited to jpeg output only.

The issue of gloss arises in two ways. Initial trials using the UWA rock art colour card produced burnt out glossy patches in the image. This could be avoided by angling the camera however the primary image gathering is for photogrammetry, with the aim to be able to measure the colour of any part of the 100x100 mm imaged surface. The surface itself may be glossy, given the single point illumination provided by the phone's in-built flash. This hasn't been identified as an issue, however the contribution of specular reflection to the final image is not something that can be gauged by eye looking at an image.

Two approaches have been adopted to avoid specular reflectance errors. The first is to include a matte barium sulphate calibration tile into the reference template, and the second is to add a pair of polarising filters. A small piece of polarising film covers the flash, and a rotating polar is placed over the lens. Before imaging, the camera is pointed at a very reflective surface; a vehicle windscreen or sunglasses are ideal field-available surfaces, and the polar rotated until reflections are reduced to the optimal non-reflective state. If the surface is very matte there is no need to use the polarisation system.

The polarised set-up is also ideal for the photogrammetric imaging itself, as the software cannot make sense of reflection and may interpret it as a surface ridge or peak when in fact it is a lower facet perpendicular to the camera and thus more reflective.

B-5-4 System requirements

Adaptation of the macro-photogrammetry procedure to allow for moderately reliable colour measurement requires the addition of an internal calibration reference fixed to the location template, and the use of the colour picking tools in Adobe Photoshop that measure image pixels in CIELab co-ordinates. It is important to ensure that the internal reference is non-reflective under the lighting conditions of the camera system required and that it can be maintained in a clean state.

B-5-5 Calibration reference

Calibration is an essential preliminary for spectroscopic measurement and is facilitated with an industry standard Spectralon tablet of known reflectance characteristics. Spectralon in its various forms is manufactured from barium sulphate with various binding agents. Figure B-5-1 shows the reflectance spectrum of the Spectralon supplied with the Ocean Optics JAZ spectrometer compared to an acrylic bound barium sulphate test billet. Barium sulphate production is an industrial process that will not always be consistent, however the Spectralon tablet is based on barium sulphate as well. Any differences will be through the influence of manufacturing of the pigment, the binding medium, and possibly the substrate, given that Barium sulphate is a moderately transparent mineral.

The spectra have been converted to CIELab trinomial colour space co-ordinates as follows. It is notable that the L^* values is greater than 100, which is the definition of pure white, when paired

with 0,0 in the a,b axes.

- Spectralon $L^*a^*b^*$ (112.6, 6.7, 12.9)
- Barytes $L^*a^*b^*$ (104.4, 5.9, 3.4)

The L^* value, or light intensity, can be explained as a slight difference in geometry. Whereas the a^* and b^* values show the chosen barium sulphate to be truer to a white standard, where zero is the optimal value for a true white (100,0,0).

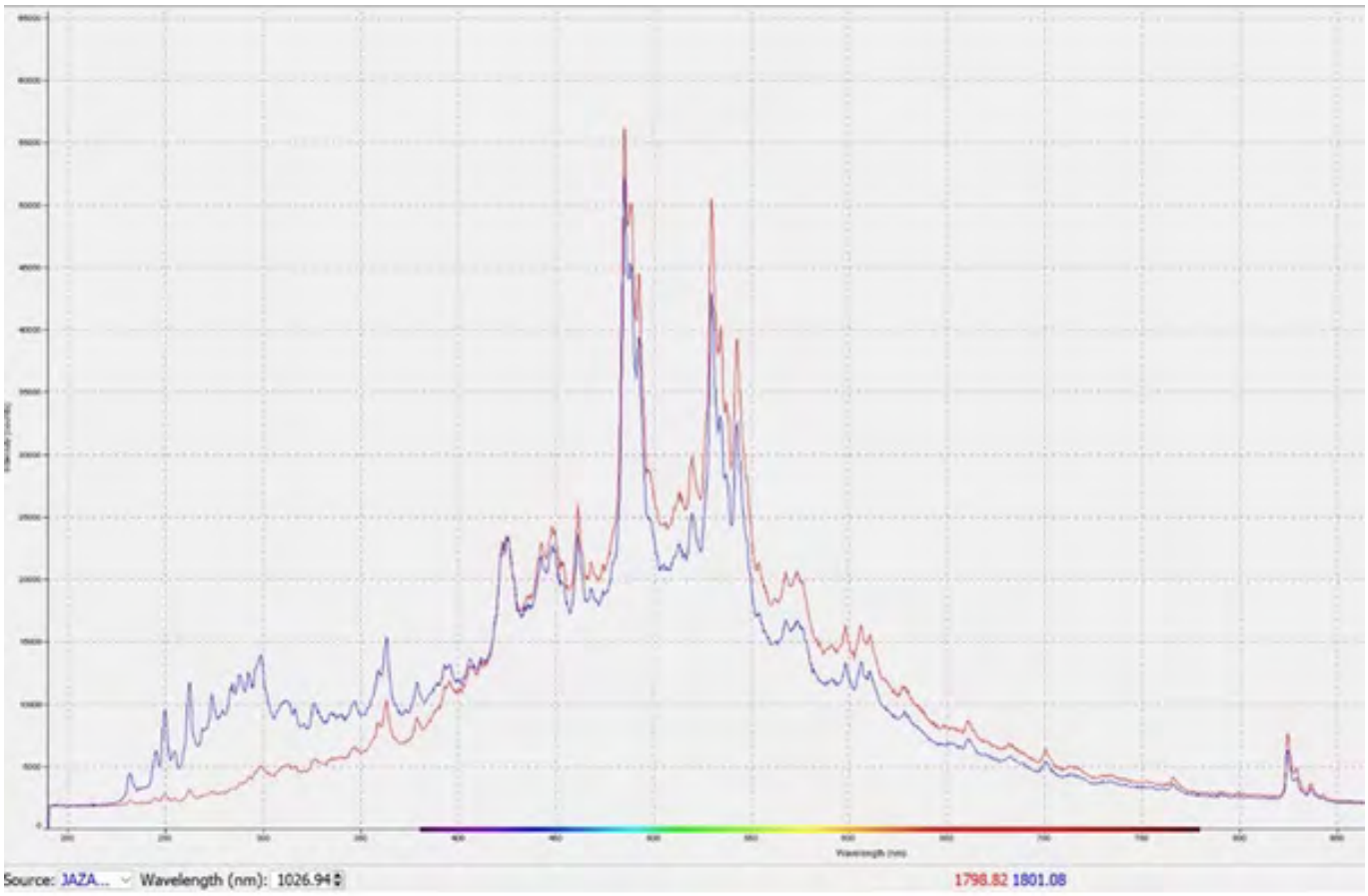

Figure B-5-1: Plot of xenon reflectance curves for the JAZ Spectralon calibration tile (red) and a test billet of barium sulphate bound in acrylic emulsion to produce a matte surface (blue). The barium sulphate is more reflective at wavelengths below 410 nm and less reflective above 470 nm. A scale bar for visual perception is included along the X axis to show that the high reflectance in the UV is generally at lower wavelengths than human colour perception.

Regardless of differences, as highlighted above and in Figures B-5-1 and B-5-2, the use of a commercial barium sulphate applied as a thick paste to the reference template, will provide a reliable reference for internal calibrate.

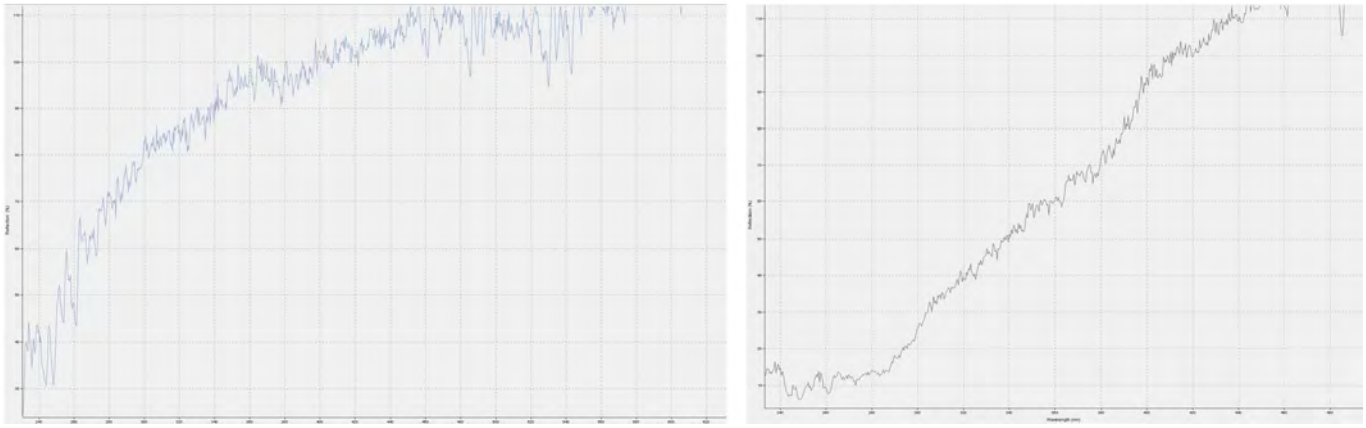

Figure B-5-2: Comparison of daylight adjusted reflectance. The Barium sulphate curve at left has more intense reflectance in the shorter wavelengths than the Spectralon at right.

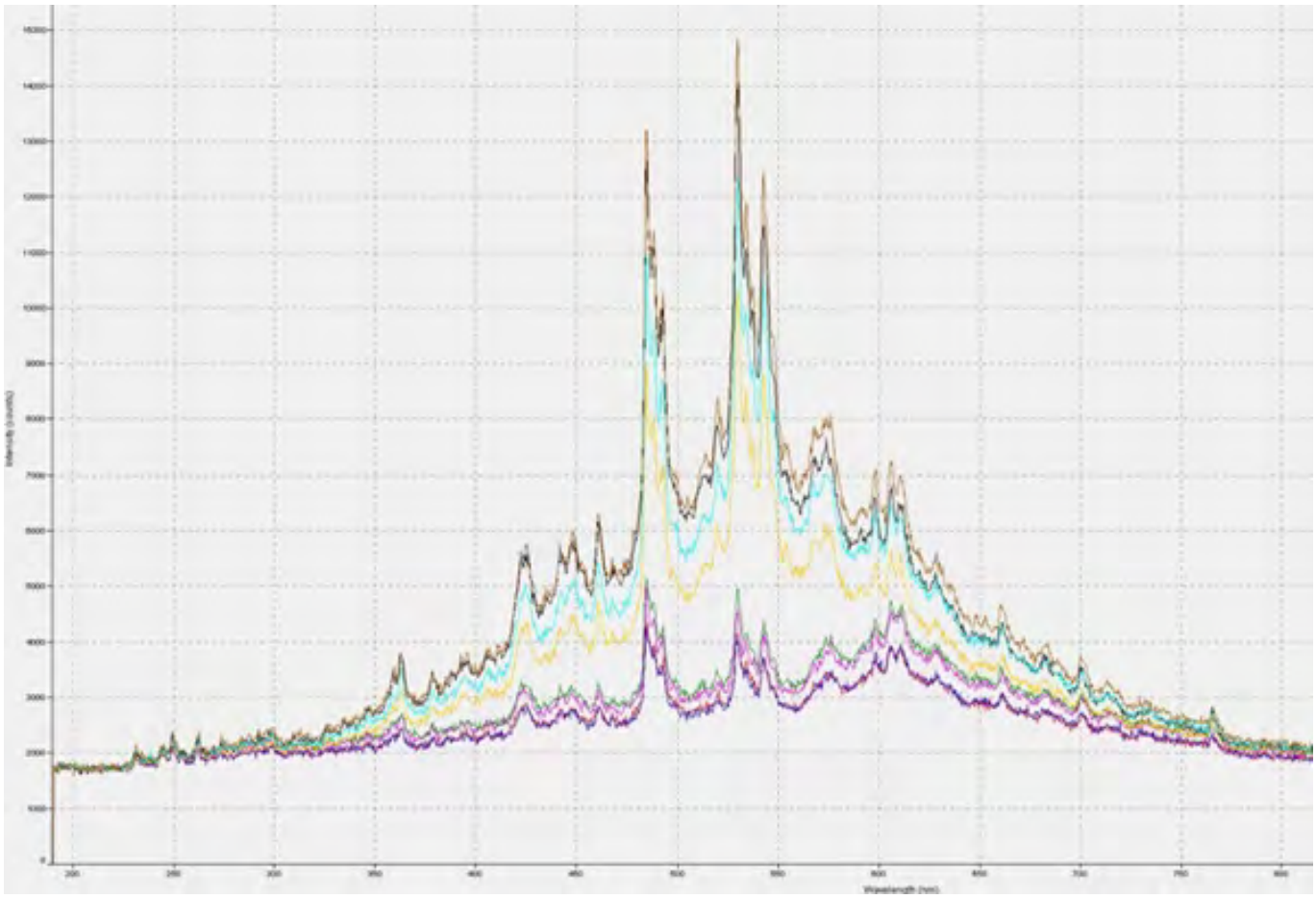

Figure B-5-3: Reference tile with Spectralon and Barytes calibration. The upper traces are two Barytes (black, yellow) and two Spectralon calibrated spectra. The lower cluster are the same spectra for the red area of the tile.

B-5-6 Imaging device

The preferred imaging method is that adopted for the macro-photogrammetry described above. There is no need to alter the acquisition method or equipment for colour measurement, other than to ensure a fresh, clean barium sulphate calibration is included in the location template. The following studies compare 12 Mp compression to 50 Mp compression achieved from the 200 Mp Galaxy 24 ultra sensor, and these with the image quality gained from the magnifier app. It has been noted in Table 1 that the Galaxy 24 ultra using the magnifier app produces a pixel density of 10,000 pixels/mm^2, 20% denser than the 50 Mp image from the primary camera. This density is a combination of the sensing resolution and the closer imaging distance to the rock surface. The aim of this technique is to be able, retrospectively, if necessary, to measure any point in the model and record suitably accurate colour data for timeline comparison, from which a reasonable metric for colour change can be determined. It is not an alternative to the precision of photospectrometry, but does provide a sufficient indicator of change that may then trigger a more refined study with a spectrometer. The main benefit of the technique is in establishing the interval for colour change measurement, not to definitively state colour change has occurred.

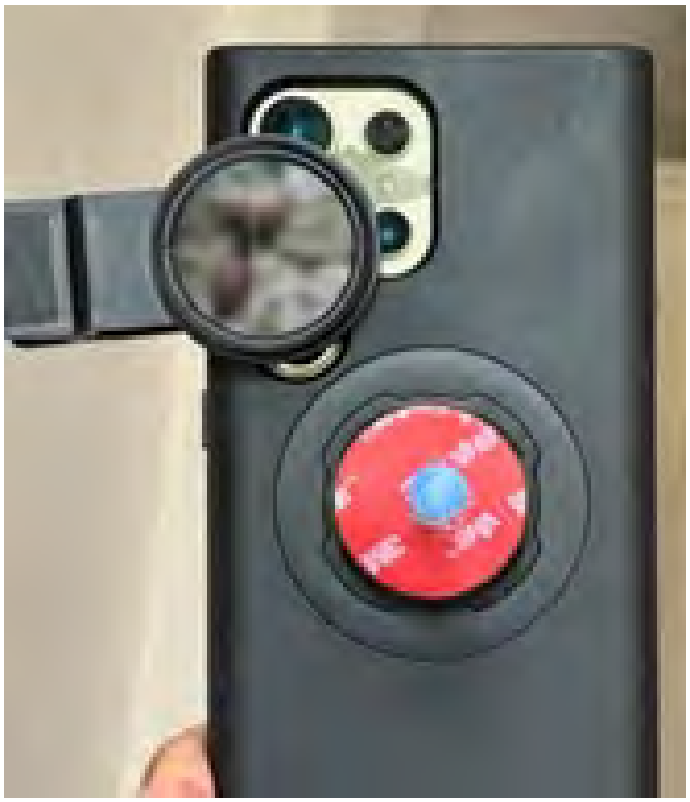

Figure B-5-4: Galaxy 24 Ultra with polarizing film fitted over the LED, rotating polar over the relevant imaging lens, and with the central monopod in place.

Images have been recorded for colour measurement using the following configurations.

- Galaxy 24 ultra, 12 Mp and 50 Mp, Daylight in shade (no dappled tree shade)
- Galaxy 24 ultra, 12 Mp and 50 Mp, Artificial LED light at 3,000K[1]
- Galaxy 24 ultra, 12 Mp and 50 Mp, Artificial LED light at 4,000K[1]

- Galaxy 24 ultra, 12 Mp and 50 Mp, Artificial LED light at 6,500K[1]
- Galaxy Ultra, Magnifier App non-polarised 2x magnification
- Galaxy Ultra, Magnifier App non-polarised 3x magnification
- Galaxy Ultra, Magnifier App Crossed polars[2] 2x magnification
- Galaxy Ultra, Magnifier App Crossed polars[2] 3x magnification

Note 1: The three LED colour temperatures were generated from the same pair of variable light sources. The colour temperatures are those quoted by the manufacturer, but do not correspond with measurements taken. This does not affect the relevance or value of this part of the study.

Note 2: The crossed polars configuration follows that used in petrographic microscopy, whereby a piece of polyester polarizing film, in this case, is placed over the LED and a glass polariser over the camera lens. The camera polariser, or analyser in microscopy parlance, is then rotated to produce a reflection free view of a highly reflective surface, such as a vehicle windshield that has a highly oriented tension structure. Following this the polar orientation is confirmed and adjusted on the rock surface itself.

Figure B-5-5: The same surface imaged without polars at left and with crossed polars at right. Significant gloss evident on the left has been eliminated in the right-hand image. Rock gloss levels vary across the 54 study sites; however, some are glossier than this test tile. Note that the colour appearance has also been altered. While the red appears darker, the yellow is distinctly more reddish in the polarised image at right. The white reference is also altered.

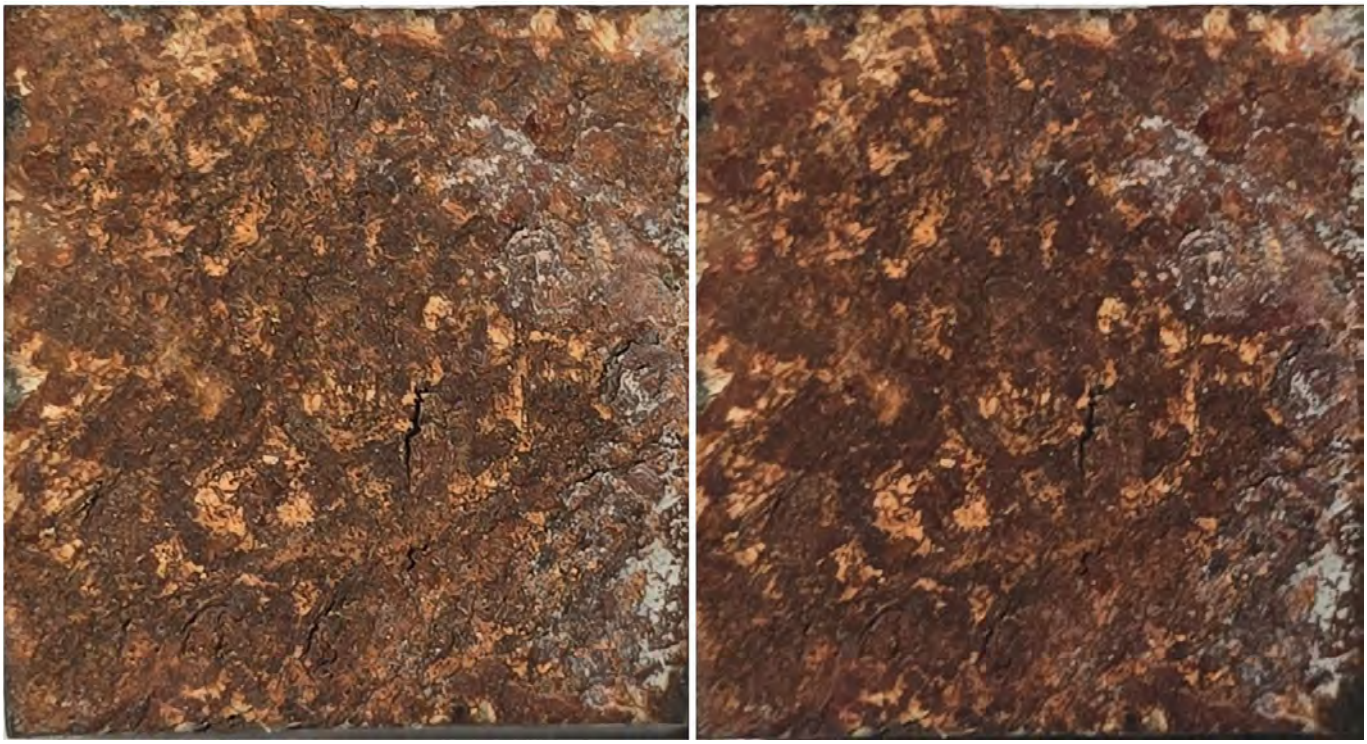

Figure B-5-6: A typical granophyre surface imaged without polars at left and with crossed polars at right. On this surface there is no noticeable gloss suppression, however on close examination of the images on screen there is a loss of sharpness in the polarized image.

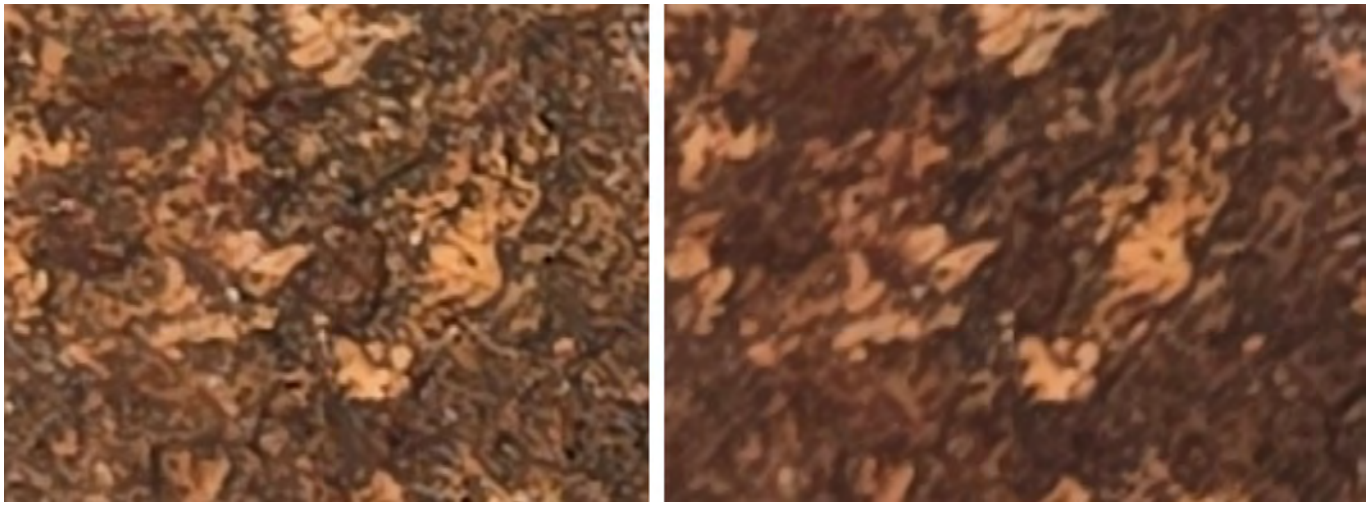

Figure B-5-7: Enlarged detail of the two images above, showing the loss of sharpness in the polarized image at right.

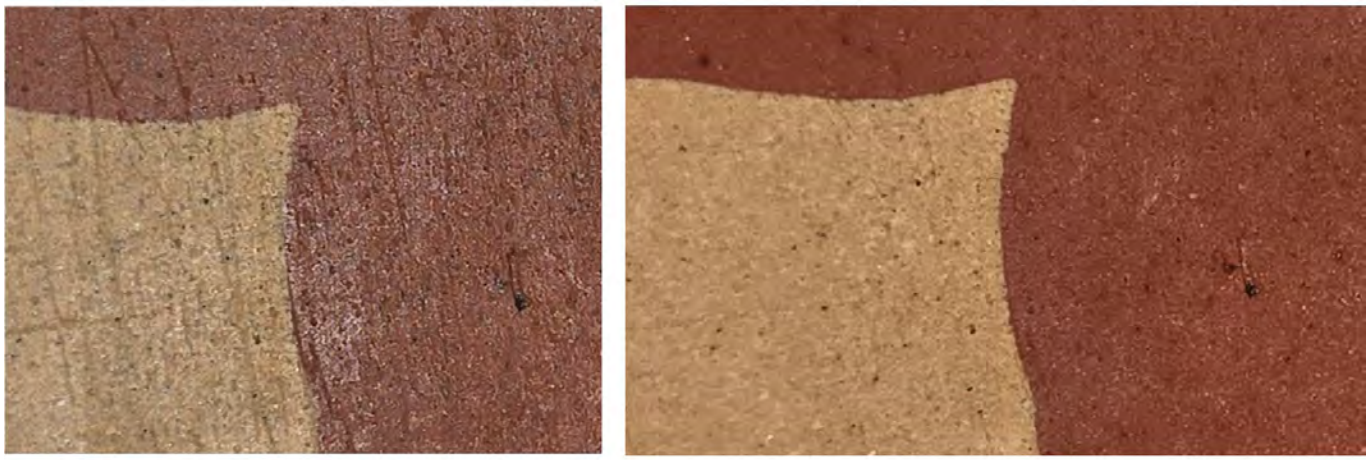

Figure B-5-8: Magnified comparison between the non-polarised image at left and polarised image at right. Polarisation has removed the gloss but at the expense of detail clarity. The loss of detail is less significant for colour measurement than the influence of gloss.

Figure B-5-9: The test configuration for imaging the test tile. In this case, the variable colour temperature lamps are in place. In this demonstration, one is set at 3,000K and the other 6,500K, as evidenced by the two different wall colours behind the tile. This tile has been selected for its comparable gloss but stronger colour contrast, rather than having direct relevance to the Murujuga engravings.

Figure B-5-10 shows an over-zoomed comparison between the Galaxy 24 Ultra at left with the same magnifier app imaging through the Oppo used for Spectrometry probe registration. While both images are poorly resolved due to the zoom factor it can be seen that much of the detail in the red region is barely recognizable with the Oppo image. This lack of resolution is equally applied at the lower zoom factor employed to place the reference targets in the white, yellow and red regions for CIELab measurement in Adobe Photoshop, as seen in Figure B-5-11. The ability for either imaging system to reproduce colour is assessed in following sections.

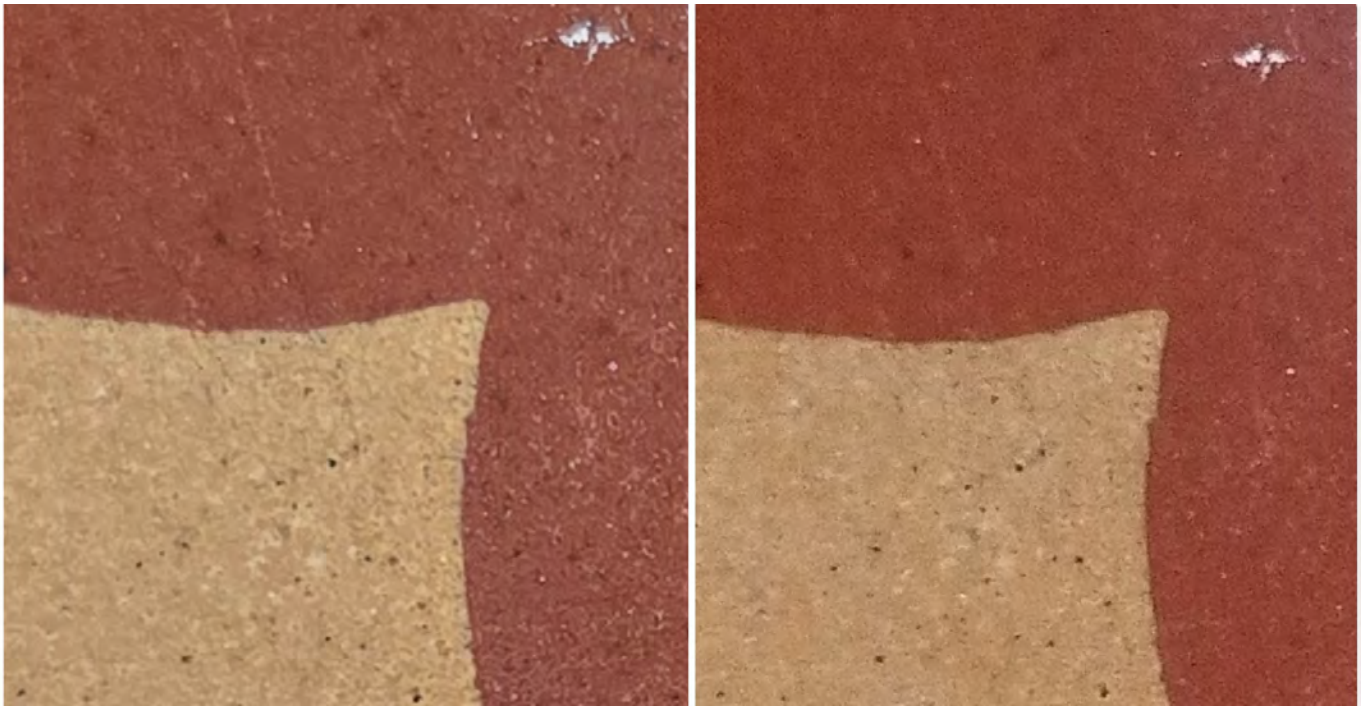

Figure B-5-10: Over-zoomed images of the same tile using the same magnifier app. At left, the 200 Mp Galaxy 24 Ultra (left) has far better resolved details than the 48 Mp Oppo sensor. The zoom factor portrayed is not that used for CIELab colour measurement, however, it was found that the reference points for each of the three targets were far harder to align with the loss of detail from the Oppo system.

B-5-7 Colour measurement

Adobe Photoshop, uniquely among commercial image editing software, offers the ability to measure a section of an image in CIELab colour space units. Conversion software allows for other programs to be used where the RGB values can be converted to Lab. There are several on-line converters, but the author prefers the windows app Munsell Conversion for its suite of colour measurement and conversion tools (http://WallkillColor.com). Photoshop is the preferred program for its immediacy in providing Lab values directly.

Lab values in Photoshop are found through the following sequence with the relevant image open.

- Select the eyedropper tool from the sidebar

- Select the sample size from the eyedropper menu near the top left of the screen. Here 11 x 11 pixel averaging has been selected. The choice of sample area should be determined from the primary image and its chosen target character. Figure B-5-5 demonstrates the need for this.

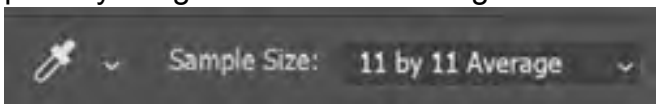

- Select the target to be measured with a left mouse click

- Click on the colour swatch
- This will bring up several colour measuring systems, including $L^*a^*b^*$, top right column

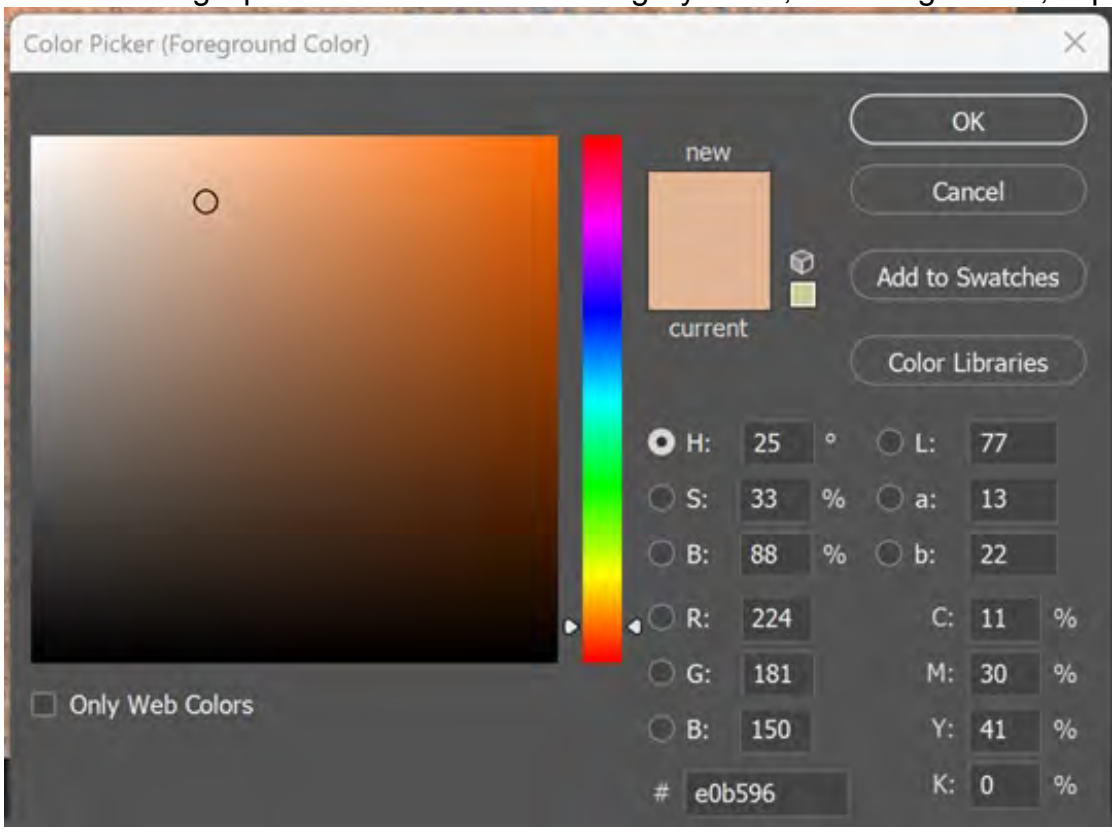

When selecting the location in the image to be measured, the first step is to place a reference zone onto the image, as seen in the left-hand image of Figure B-5-7. This has been created by embedding the letter O at a suitable scale, cognisant of the need to select 5 x 5 pixels within the unaffected internal pixels, as illustrated in the central image of Figure B-5-7. It is recommended that a mouse with spontaneous precision adjustment be used, such as the Logitech MX series with a

dedicated button for fine movement, in addition to general scrolling settings. This fine control allows for placing the Photoshop eyedropper more precisely in the centre of the reference zone, without accessing the settings. The target area is sampled 5 times, with each set of $L^*a^*b^*$ values averaged in a pre-formatted spreadsheet. The pre-formatted spreadsheet facilitates critical calculations, such as the correction factors that ensure that readings from different epochs are normalised to the same white reference values. The measurement process has been timed to take 12 minutes from opening the image file in Photoshop, registering targets, and completing the spreadsheet data for five repeats on three targets.

White reference normalisation is achieved by adjusting all imaged white references to the ideal 100,0,0. The white reference values in the Magnifier images vary but are typically lower than the ideal 100,0,0 co-ordinates for pure white. In Table B-5-1, the white reference is 88, -3, -8 for the polarizer free Magnifier image, which are normalized to the ideal by adding 12,3,8 to the recorded values. These same adjustment values are then applied to the measured target values taken from the rock surface.

Table B-5-1: Showing typical values, in this case derived from the Magnifier image at 2x zoom without polars. The yellow box shows the adjustment factors to normalise the white reference to ideal with the bold red figures under the yellow target and red target reflecting that adjustment.

White reference				**Yellow target**				**Red target**			
L	a	b		L	a	b		L	a	b	
88	-3	-8		63	5	20		63	26	41	
88	-3	-8		64	6	20		60	26	42	
88	-3	-8		65	6	20		63	25	41	
89	-3	-8		63	6	20		58	27	41	
88	-3	-8		87	6	43		63	26	42	
88.2	-3	-8	**Averaged**	68.4	5.8	24.6	**Averaged**	61.4	26	41.4	**Averaged**
11.8	3	8	**Adjust**	80.2	8.8	32.6	**Corrected**	73.2	29	49.4	**Corrected**

Figure B-5-11: The tile imaged with the Magnifier zoomed 2x with no polars, at left. Above are the screen colours generated by Munsell Conversion using the corrected Lab co-ordinates of table 2. There is a clear discrepancy indicating that this configuration is not satisfactory at generating accurate colour.

B-5-8 Spectral image processing

The following series of images and CIELab measurements address various validations for how well a digital camera can reliably measure colour.

Table B-5-2: CIELab values of the various imaging techniques compared to the JAZ spectrometer results for both the Spectralon calibration tile and a barytes calibration tile. The 4^{th} column gives colour difference values (ΔE) between the barytes calibration tile, the Spectralon, and each of the imaging techniques.

	L^*	a^*	b^*	**ΔE barytes**
Red sample				
JAZ Barytes Red	44.7	29.3	20.6	
JAZ Spectralon Red	48.1	30.7	21.3	3.72
Daylight shade	42	25.6	26.4	7.36
Galaxy 24U 12 Mp 3,000 K	61.4	26	41.4	26.85
Galaxy 24U 12 Mp 4,000 K	62.2	30.4	33	21.45
Galaxy 24U 12 Mp 6,500 K	58.6	26	25.8	15.17
Galaxy 24U Magnifier 2x no polars	73.2	29	49.4	40.49
Galaxy 24U Magnifier 3x no polars	57.4	17.8	15.4	17.87
Galaxy 24U Magnifier 2x crossed polars	47.8	27	26.8	7.27
Galaxy 24U Magnifier 3x crossed polars	48.4	26	23.6	5.75
Yellow sample				
JAZ Barytes Yellow	66	16.4	26	
JAZ Spectralon Yellow	70.6	17.9	28	5.19
Daylight shade	76.8	14	34.2	13.78
Galaxy 24U 12 Mp 3,000 K	86.6	5.8	42.4	28.39
Galaxy 24U 12 Mp 4,000 K	85.8	7.8	36.2	23.88
Galaxy 24U 12 Mp 6,500 K	84.8	5	27	22
Galaxy 24U Magnifier 2x no polars	75.4	8.8	28	12.24
Galaxy 24U Magnifier 3x no polars	73.4	8.2	23.2	11.38
Galaxy 24U Magnifier 2x crossed polars	77	12	33	13.76
Galaxy 24U Magnifier 3x crossed polars	77.4	13	31	12.91

Figure B-5-12: Visual comparison of the Spectrometer CIELab values and the four Magnifier app values for the red (top row) and yellow. (bottom row) (np = no polars, xp = crossed polars.)

The visual comparison in Figure B-5-13 shows the discrepancies between spectrometer generated CIELab values and those of each of the four Galaxy 24 U with Magnifier app values.

Table B-5-2 and Figure B-5-13 indicate that none of the imaging techniques are able to render the surface hues anywhere close to that determined by the JAZ Spectrometer, using either the Spectralon calibration reference or the purpose made barytes calibration reference. That, however, is not the aim of this approach. What is more important is that the preferred imaging technique can provide repeatable results and reliably plot a change from condition A to condition B. It is also worth determining whether the results are reliable between imaging devices, in the inevitable event that the same camera will not be carried to the site year after year. This is where the correction values play their greatest role, in that, regardless of variations in LED intensity and angle relative to the imaging lens, together with processing variables, the relationship between the embedded calibration reference and the surface should remain constant.

Figure B-5-12 illustrates the different geometry between a Galaxy 24U and the Oppo that has been the imaging device for repositioning the probe in the Spectroscopy program. The Galaxy has the LED slightly above the lens used by the Magnifier app whereas for the Oppo the LED is well below the relevant lens. This difference in geometry was made apparent when the Oppo replaced a Galaxy 22 as the repositioning camera in the spectroscopy program, rendering the rugose surface quite differently due to cast shadows and reflections. The geometry affects the manner in which the image is rendered, potentially resulting in chromatic differences.

B-5-9 Single shot colour-controlled image

To improve the colour reliability a second option has been evaluated, whereby a single image is recorded with a barytes reference tile placed directly adjacent to the target to be measured. The reference tile is mounted into a soft neoprene holder, to avoid surface impact. The holder slides onto the foot of the monopod and can be swung into vision once the monopod is placed onto the

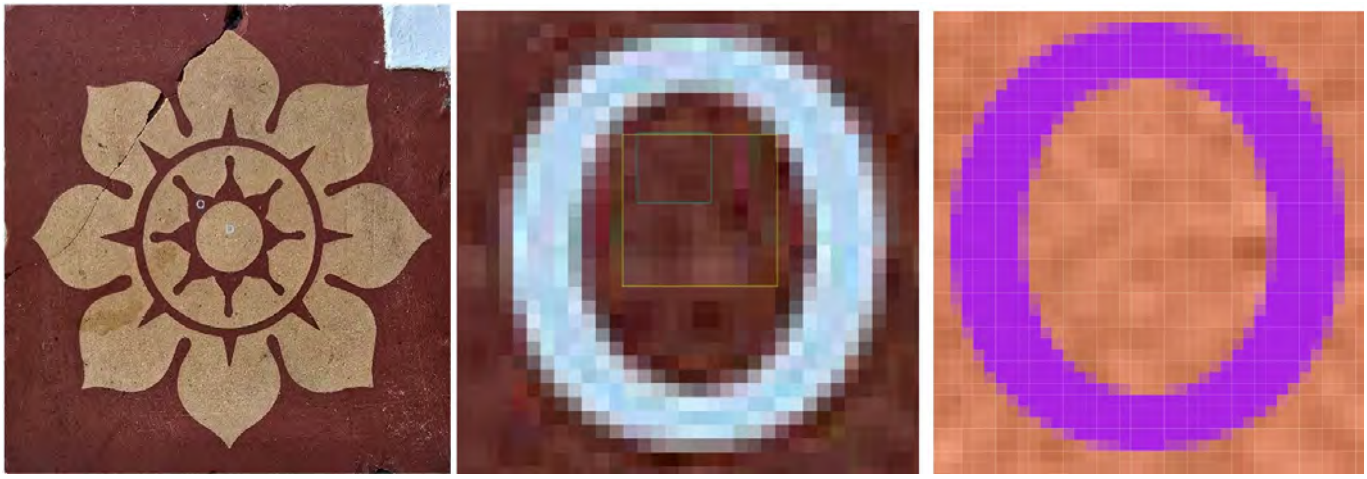

Figure B-5-13: Test tile at left imaged at 12 Mp in shaded daylight, with barium sulphate calibration reference set in top right corner. Two sampling references have been drawn onto the surface to indicate colour sampling zones. Five readings are taken within each sampling zone. A zoomed target at the centre shows the variation in pixel hues from the shaded daylight sample. A 5 x 5 sample area has been outlined in green, and an 11 x 11 sample area in yellow. At right, a more uniform pixelation from the 4,000 K LED sample is evident, supporting the need for uniform artificial lighting rather than any form of sunlight.

surface. Figure B-5-15 shows the reference tablet embedded into its holder and the holder in position on the surface. Because the reference tablet moves with the camera it can always be positioned immediately adjacent to the target to be measured. Despite being 8-10 mm above the rock surface the image is sharp for both. Given the more precise colour control achieved with this technique it is worth the extra effort to take an additional image at the end of the photogrammetric survey. It appears that having the reference tablet at the edge of the image is less reliable than having it in close proximity. All imaging protocols for the macro-photogrammetry are followed, including keeping the surface shaded to avoid chromatic distortion from sunlight. Targets are selected from within the photogrammetric template so there is no need to establish a separate location system. It is best to mark up the photogrammetric location image with lines to indicate more precisely where the colorimetric targets are located within the template. There is no limit on how many targets can be measured calorimetrically and they should include a representative sample of at least two targets, one lighter and one darker. Staying within the photogrammetric template is a convenience but there is no reason to not go to other surfaces where colour is of greater interest. The only additional steps are the need to establish a template reference for the new location. Processing the images is the same as previously described.

For this evaluation, a rocky surface has been chosen that emulates more closely the typical surface contrasts at Murujuga. Two targets have been chosen, one lighter and one darker, but both quite heterogenous compared to the tile used in previous studies.

The surface was imaged five times at ten-minute intervals, with the reference tablet positioned to be adjacent to the target. A tighter relationship would have been possible, and the tablet normally positioned for each target separately. In this case the two targets were chosen around the tablet. The camera was completely removed and repositioned for each of the five repeat images.

Figure B-5-14: Comparison of LED to imaging lens geometry between the Samsung Galaxy 24 Ultra with a 200 Mp sensor (left) and the Oppo CPH2195 with 48 Mp sensor. There is no image compression with the Oppo.

The two targets and the tablet were measured using the Photoshop Colour Picker, with five repeats and the result averaged. The targets were normalised with a correction factor that would bring the barytes tablet to (100, 0, 0) in the $L^*a^*b^*$ colour space, from the averaged values in the image of (83.9, -1.6, 2.4).

The two targets in each image were read five times, averaged, and normalised by the compensation factor of 16.1, 1.6, -2.4. A colour difference was calculated between all five images whereby the median value was used as ΔE=0.

The following Table B-5-3 shows the very tight control achieved. It is worth remembering that the CSIRO instruments were not capable of better colour resolution. In fact the BYK calibration date returned a ΔE = 16, the KM ΔE = 9, and the FieldSpecPro ΔE = 2. The JAZ by contrast recorded a ΔE = 0.5.

Figure B-5-15: A barytes reference tablet is mounted to the monopod foot to make direct contact with the rock surface. The reference tablet is readily replaced, and several replacement tablets are carried.

Table B-5-3: ΔE colour difference values for the five repeat images.

	ΔE ave-x		
	Reference	**Lighter**	**Darker**
Image 1	1.17	0.72	1.96
Image 2	0.57	1.52	1.47
Image 3	0.73	1.88	1.83
Image 4	0.73	1.88	1.89
Image 5	0.99	1.75	2.09

From this data, it can be stated that imaging with a Samsung Galaxy 24 Ultra in full shade, using a monopod with a calibration tablet attached and shooting with the nominated Magnifier app, is capable of measuring colour with sufficient precision to act as a reliable tool for tracking colour change.

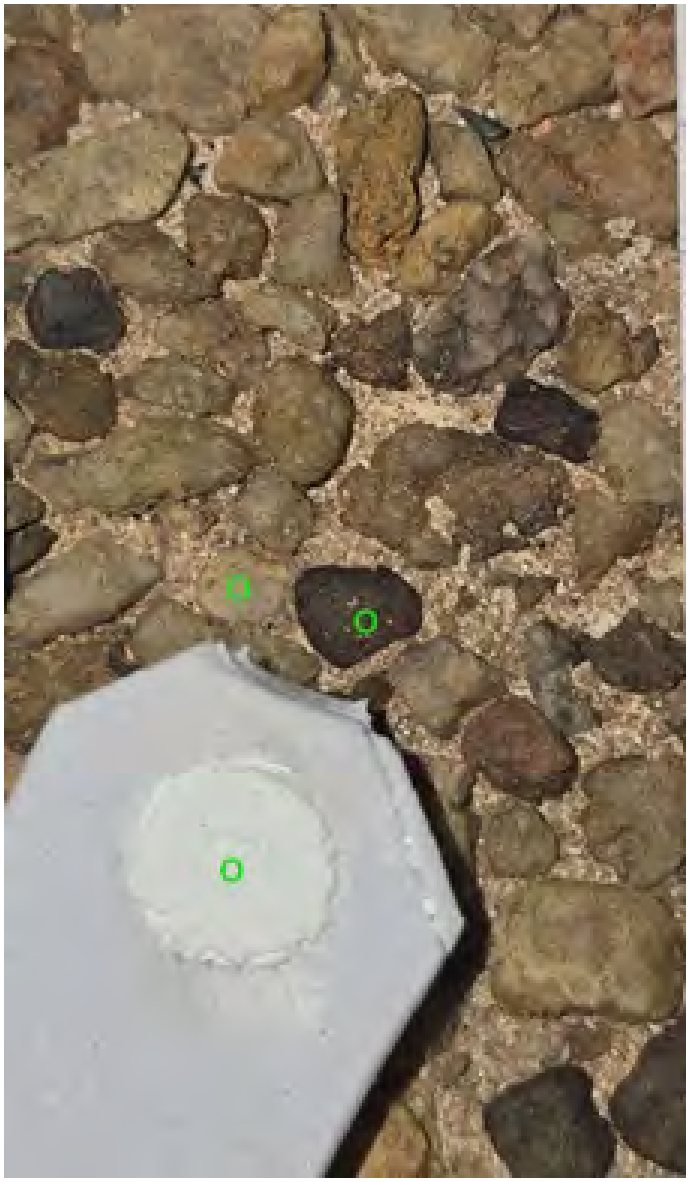

Figure B-5-16: The surrogate rough surface with the location of the three targets in place on the image.

B-5-10 Conclusion

The use of a Samsung Galaxy 24 Ultra, and later versions, has been trialled against alternative techniques to study the rock surface in three dimensions. The technique described here, using a smartphone imager on a monopod, can achieve the desired outcome, which has primarily been to develop a fully restituted and uniformly illuminated two-dimensional image of a control surface. The 2D image is achieved by extraction from a 3D photogrammetric model, which itself can be used for comparative studies.

Further, after establishing that the same imaging process cannot produce reliable colorimetric values an alternative using the same imaging configuration, with the addition of a white reference tablet can produce reliable colour measurements with an error below the $\Delta E > 2$, considered to be the increment for perceived colour difference. This reliability factor is better than two of the instruments deployed in previous studies at Murujuga and equal to the best of the three instruments used in that period. By using the described method an effective colour monitoring can be achieved through the use of rapid imaging techniques.

Imaging of the control surface for photogrammetric processing takes 15 minutes, whereas the colour measurement imaging can be achieved in the same time frame. Altogether, including setup, the system can gather all necessary data at the site in approximately 45 minutes.

Processing of the data requires less than an hour for the 3D model and 2D extraction, and a further hour for colorimetric processing. Downstream analysis of morphological alteration will add another hour using Cloud Compare software.

The key requirement is to gather the images in both series. Development of the model and processing for morphological and colorimetric change is only required when a query is generated. This may be as infrequently as once every five years, once the preliminary analysis over the first 3–5 years shows no substantial alteration.

Appendix C References

Curtin University (2022). *Murujuga Rock Art Monitoring Program: Monitoring Studies Data Collection and Analysis Plan*. Report prepared by Curtin University for the Murujuga Aboriginal Corporation and Department of Water and Environmental Regulation, Government of Western Australia (COPP21065-PLN-G-102_0). Government of Western Australia. https://www.wa.gov.au/government/publications/murujuga-rock-art-monitoring-program-monitoring-studies-data-collection-and-analysis-plan.

Curtin University (2025). *Murujuga Rock Art Monitoring Program: Monitoring Studies Report 2025*. Final Report prepared by Curtin University for the Department of Water and Environmental Regulation and the Murujuga Aboriginal Corporation (COPP21065-REP-G-105). Government of Western Australia.

Ramanaidou, E. and Lau, D. (2015). Heritage monitoring of 6 sites within 2km of the Yara Pilbara Nitrates Pty Ltd plant site (Western Australia).

C Amended estimation of major historic emissions (Dampier power station) to account for historic Iron Pellet Plant

Monitoring Studies Report 2024 (Curtin University, 2024c) presented an estimate of the historical emission rates of pollutants (NOx and SO_2) in the power plant complex operating in the Dampier peninsula in 1966 to 2010. The plants were operated predominantly using heavy fuel oil prior to 1986, before switching to natural gas-based operations. Estimates of the emission rates were obtained based on two models: the “100% utilisation” model, which assumed full utilisation of all available power infrastructure in the area, and the “Growth” model, which assumed a steady increase in electricity consumption within the Dampier region. The outcomes of these analyses show substantial historical emission rates compared to current emission models (Ramboll Australia, 2022), predominantly due to the use of heavy fuel oil in the years prior to 1986. The average NOx emission rate out of the power plant complex was estimated to be in the range of 23-53% of the total NOx emission rates estimated by the 2014 Ramboll model (the two percentage values were obtained based on the Growth and 100% utilisation models, respectively), or 36-82% of the industry emission rate according to the 2014 Ramboll model. On the other hand, the SO_2 emission rates were found to be 5-8% of the total SO_2 emission rate of the 2014 Ramboll model. Relative to current levels of industrial activities (a significant proportion of the SO_2 emission in the 2014 Ramboll model is due to shipping activities), the mean SO_2 emission rates were found to be approximately 95-148% of current levels of SO_2 industrial emissions.

The estimation of major historic industrial emissions in the region has recently been updated to include the contribution of an indurating/pelletisation plant (‘iron pellet plant’) operating in 1966-1980 at Parker Point, close to the old Dampier power station (Hamersley News, 1974). The plant was noted to have emitted significant amounts of sulfur, due to the absence of a scrubber, which was only fitted in 1974. The timeline of the iron pellet plant relative to the power plant complex is shown in Figure *C*.1-1

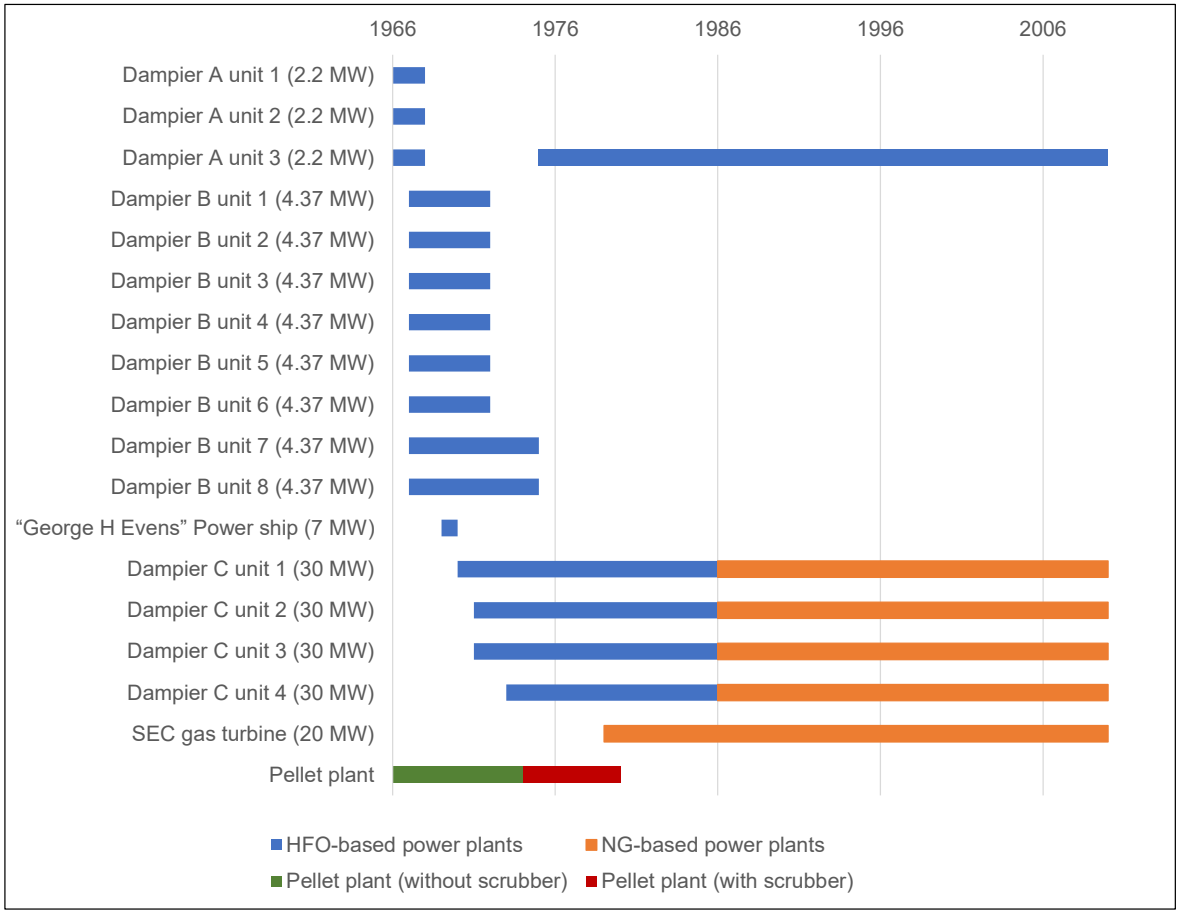

Figure C.1-1: Timeline of the Dampier power plant complex, categorised according to fuel type, including the Parker Point iron pellet plant.

The SO_2 and NO_x emission rates out of the iron pellet plant from 1966-1974 (without scrubbers) were estimated based on data published by the EPA on the typical emission rates of US induration furnaces (US Environmental Protection Agency, 1997) and Bolen's review of air pollution control technologies (Bolen, 2014). SO_2 emissions are known to vary significantly depending on the fuel used for the plant, ranging from 0.1 kg/tonne of pellet using natural gas to 1.1 kg/tonne pellet using coal. An estimate of 1.1 kg SO_2/tonne of pellet was adopted based on the historical use of heavy fuel oil in the region, with a typical iron pellet production rate of 3 MTPa. Thus, the SO_2 emission rate was estimated to be 3300 tonne/year. On the other hand, the NO_x emission rate was estimated to be 600 g/tonne of pellet, equivalent to 1800 tonne/year. The emission rates of these pollutants were assumed to be negligible post 1974, when the iron pellet plant was fitted with scrubbers.

Figures *C*.1-2 and *C*.1-3 show estimates of NO_x and SO_2 emission rates of the iron pellet plant in comparison to those of the Dampier power plant. As can be seen, while the NO_x emissions due

to the iron pellet plant do not appear to be significant compared to those due to the power plant, considerable alterations in the emission estimates of SO_2 are expected with the inclusion of the iron pellet plant in the model.

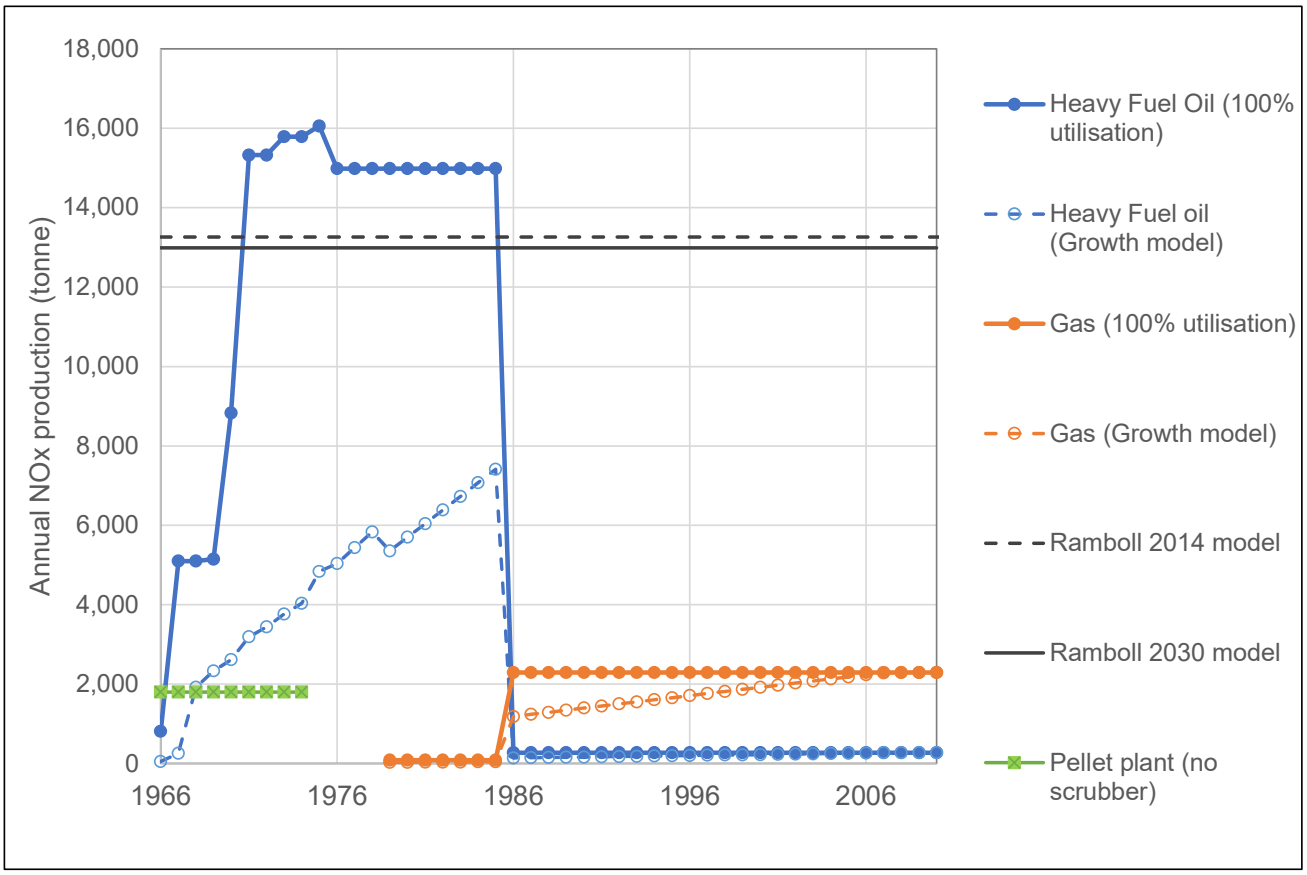

Figure C.1-2: Estimated annual emission rates of NOx out of the Dampier power plant site, including the iron pellet plant.

Figures *C*.1-4 and *C*.1-5 show the updated average and maximum NOx and SO_2 emission values over the 44-year period, respectively. The average NOx emission rate due to the combined effect of the power and iron pellet plants was found to be in the range of 26-56% of the total emission rate as estimated via the Ramboll 2014 model (the lower and higher estimates were calculated based on the Growth and 100% utilisation of the power plants, respectively). Compared to industrial NOx emission rates, the mean NOx emission rates of the combined power and iron pellet plants were found to range around 40-86%. On the other hand, the average SO_2 emission rate was found to be in the range of 15-18% of the total 2014 Ramboll emission values, representing an increase in average emission rate of 660 tonnes/year over the 44-year period compared to previous results Curtin University (2024c). This amounts to approximately 282-336% of the SO_2 emission rate from industrial activities as modelled in the 2014 Ramboll model.

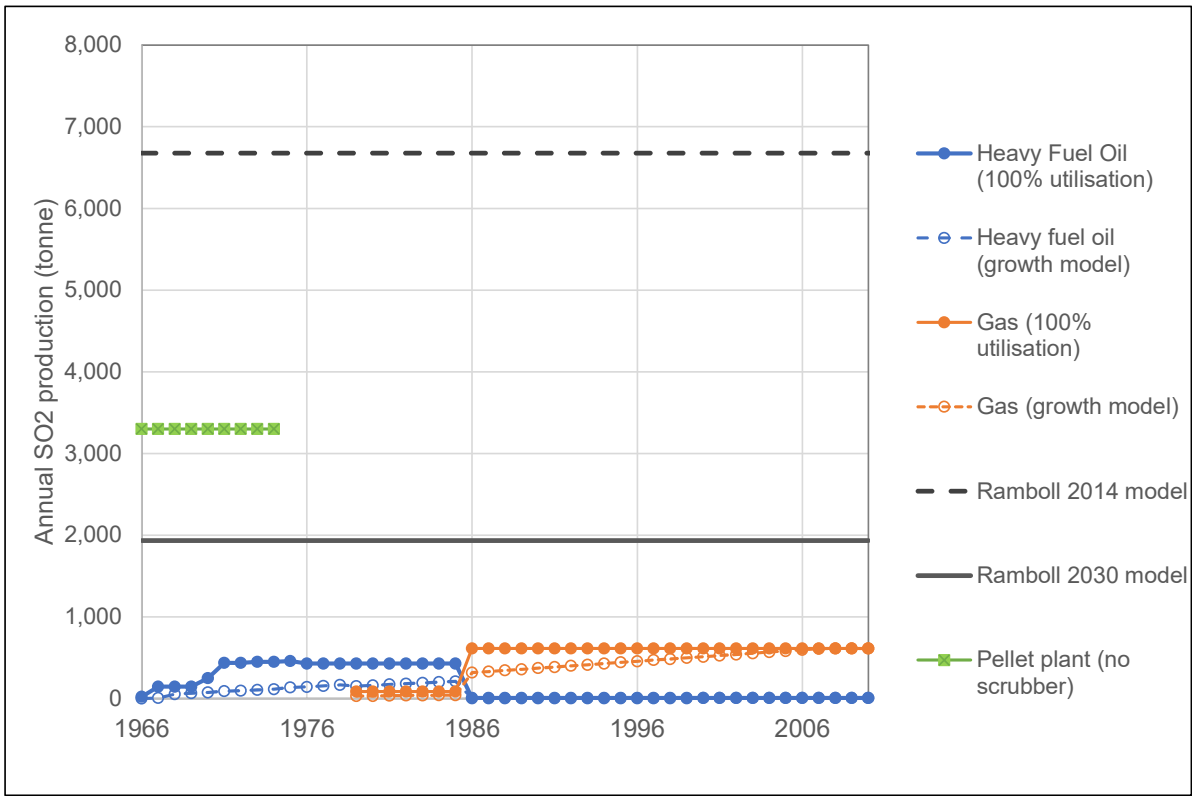

Figure C.1-3: Estimated annual emission rates of SO_2 out of the Dampier power plant site, including the iron pellet plant.

Current data suggest that the indurating / pelletisation plant operating at Parker Point contributed significantly to the emission rates of SO_2 within the region, particularly prior to the installation of gas scrubbers in 1974. As such, its inclusion within the emission model is highly pertinent to gather a further understanding on the historical emission of pollutants within the region.

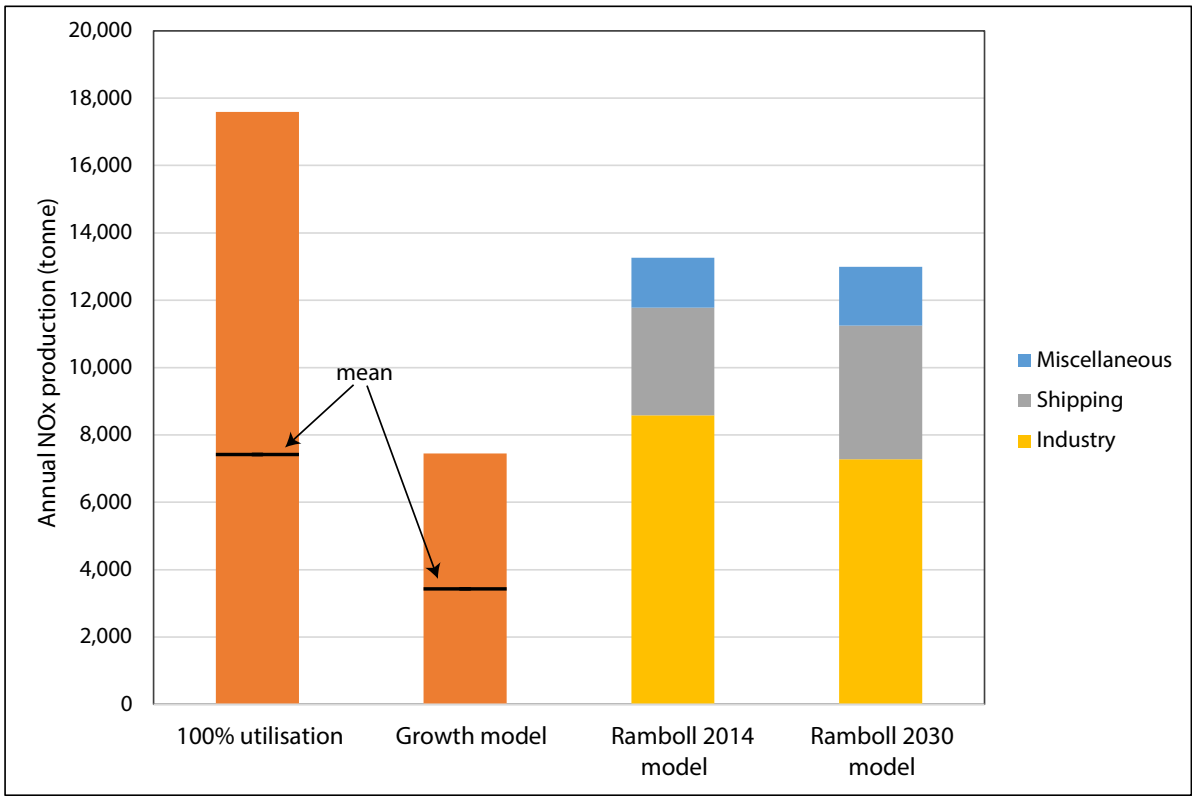

Figure C.1-4: maximum values of the NOx emission rate using the 100% utilisation and growth models (mean values are indicated by black horizontal lines), compared against the Ramboll 2014 and 2030 models.

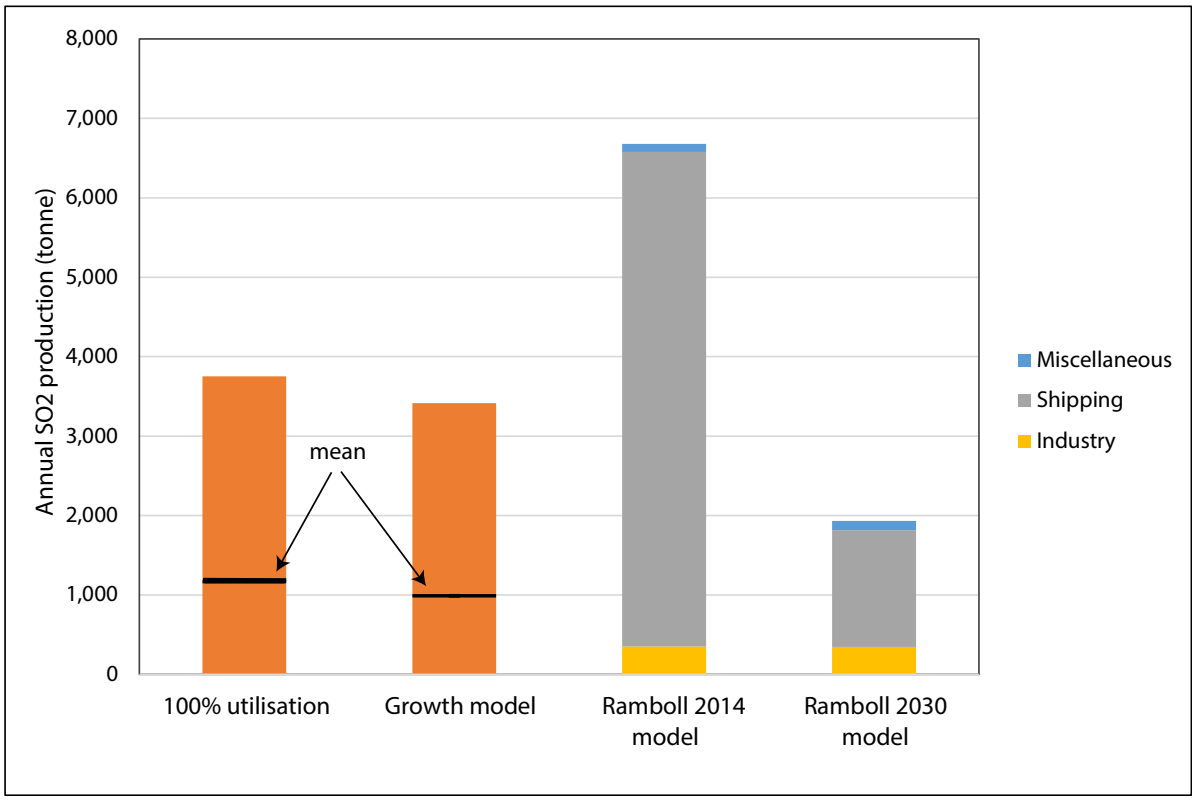

Figure C.1-5: maximum values of the SO_2 emission rate using the 100% utilisation and growth models (mean values are indicated by black horizontal lines), compared against the Ramboll 2014 and 2030 models.

D Statistical analysis: additional results

D.1 Introduction

This Appendix reports further analysis of the data, including diagnostic checks on the validity of the data, diagnostics for assessing the appropriateness of the statistical methodology used, and re-analysis of the data using different choices of methodology:

- Section *D*.2 gives further details of various anomalies detected in the colorimetry data, and comparison of trends between campaigns 1 to 10 for JAZ instrument. Additionally, provides comparison of trends between campaigns 1 to 10 for JAZ instrument.
- Section *D*.3 gives further analysis of the industry gas measurements in Section 7.3.
- Section *D*.4 gives further analysis of the organic geochemistry data in Section 7.9.
- Section *D*.6 gives further analysis of the low powered data in Section 7.14.

D.2 Field colour

D.2.1 Faulty field colour data

In Section G.3 of Monitoring Studies Report 2024 (Curtin University, 2024c) describes the JAZ and HDX faults identified. Below describes briefly three more faults:

1. % reflectance was not-a-number (`NaN`). This occurs when S-D is negative and R-D is positive, the instrument returns NaN value.
2. Battery problem, which results in two % reflectance curves
3. High peak in % reflectance before 400 nm, e.g., AQ03-2 campaign 7 and AQ04 campaign 10. This problem is due to reference count being too low before 400 nm.

D.2.2 Comparison of trends between campaigns 1 to 10 for JAZ instrument

For each of the four sites, a one-way functional ANOVA was performed to compare the trends (mean reflectance curves) between campaigns for the JAZ instrument. For all sites, there were no statistically significant differences between campaigns (Appendix Table *D.2-1*).

Table D.2-1: Comparison of mean trends (mean reflectance curves) between two campaigns. Bold p-values indicate statistically significant at the 0.05 level.

Site	Campaign	Adjusted p-values
AQ_03-2	2 vs 3	NA
AQ_03-2	2 vs 4	0.328
AQ_03-2	3 vs 4	NA
AQ_03-2	2 vs 5	0.643
AQ_03-2	3 vs 5	NA

Site	Campaign	Adjusted p-values
AQ_03-2	4 vs 5	0.328
AQ_03-2	2 vs 6	0.694
AQ_03-2	3 vs 6	NA
AQ_03-2	4 vs 6	0.328
AQ_03-2	5 vs 6	0.643
AQ_03-2	2 vs 7	0.439
AQ_03-2	3 vs 7	NA
AQ_03-2	4 vs 7	0.294
AQ_03-2	5 vs 7	0.328
AQ_03-2	6 vs 7	0.297
AQ_03-2	2 vs 9	0.449
AQ_03-2	3 vs 9	NA
AQ_03-2	4 vs 9	0.294
AQ_03-2	5 vs 9	0.544
AQ_03-2	6 vs 9	0.558
AQ_03-2	7 vs 9	0.294
AQ_03-2	2 vs 10	0.705
AQ_03-2	3 vs 10	NA
AQ_03-2	4 vs 10	0.297
AQ_03-2	5 vs 10	0.643
AQ_03-2	6 vs 10	0.746
AQ_03-2	7 vs 10	0.294
AQ_03-2	9 vs 10	0.520
AQ_04	2 vs 4	0.765
AQ_04	2 vs 5	0.643
AQ_04	4 vs 5	0.665
AQ_04	2 vs 6	0.732
AQ_04	4 vs 6	0.643
AQ_04	5 vs 6	0.558
AQ_04	2 vs 7	0.558
AQ_04	4 vs 7	0.392
AQ_04	5 vs 7	0.294
AQ_04	6 vs 7	0.694

Site	Campaign	Adjusted p-values
AQ_04	2 vs 8	0.732
AQ_04	4 vs 8	0.756
AQ_04	5 vs 8	0.618
AQ_04	6 vs 8	0.643
AQ_04	7 vs 8	0.441
AQ_04	2 vs 10	0.719
AQ_04	4 vs 10	0.643
AQ_04	5 vs 10	0.607
AQ_04	6 vs 10	0.813
AQ_04	7 vs 10	0.865
AQ_04	8 vs 10	0.643
AQ_11	1 vs 3	NA
AQ_11	1 vs 4	NA
AQ_11	3 vs 4	0.294
AQ_11	1 vs 5	NA
AQ_11	3 vs 5	0.598
AQ_11	4 vs 5	0.688
AQ_11	1 vs 6	NA
AQ_11	3 vs 6	0.790
AQ_11	4 vs 6	0.558
AQ_11	5 vs 6	0.690
AQ_11	1 vs 9	NA
AQ_11	3 vs 9	0.643
AQ_11	4 vs 9	0.328
AQ_11	5 vs 9	0.617
AQ_11	vs 6 vs 9	0.804
AQ_11	1 vs 10	NA
AQ_11	3 vs 10	0.618
AQ_11	4 vs 10	0.328
AQ_11	5 vs 10	0.607
AQ_11	6 vs 10	0.526
AQ_11	9 vs 10	0.617
EX_06	2 vs 3	0.641

Site	Campaign	Adjusted p-values
EX_06	2 vs 4	0.607
EX_06	3 vs 4	0.676
EX_06	2 vs 6	0.607
EX_06	3 vs 6	0.643
EX_06	4 vs 6	0.558
EX_06	2 vs 7	0.328
EX_06	3 vs 7	0.328
EX_06	4 vs 7	0.294
EX_06	6 vs 7	0.617
EX_06	2 vs 9	0.765
EX_06	3 vs 9	0.765
EX_06	4 vs 9	0.607
EX_06	6 vs 9	0.607
EX_06	7 vs 9	0.328
EX_06	2 vs 10	0.520
EX_06	3 vs 10	0.618
EX_06	4 vs 10	0.617
EX_06	6 vs 10	0.643
EX_06	7 vs 10	0.328
EX_06	9 vs 10	0.520

D.3 Industry gas measurements: further results and diagnostics

Figure *D.3-1* shows the histograms of gas concentrations measured by the two sampler instruments from all observations collected across all Woodside stations from September 2021 to December 2022. The plots also show probability density functions, see *density* in Glossary Table *1.4-3*, estimated from the measurements.

- NO_2 concentrations in Figure *D.3-1*(a), the distribution curves largely overlap, though the peak concentration is slightly higher for IVL than Radiello.
- NH_3 concentrations in Figure *D.3-1*(b) the distribution curves largely overlap, though the peak concentration is slightly lower for IVL than Radiello.
- SO_2 concentrations in Figure *D.3-1*(c), and HNO_3 concentrations in Figure *D.3-1*(d) the IVL curves tend to peak at higher concentrations for IVL than Radiello. These differences may be due to the innate random variability of measures or to more systematic differences between these instruments.

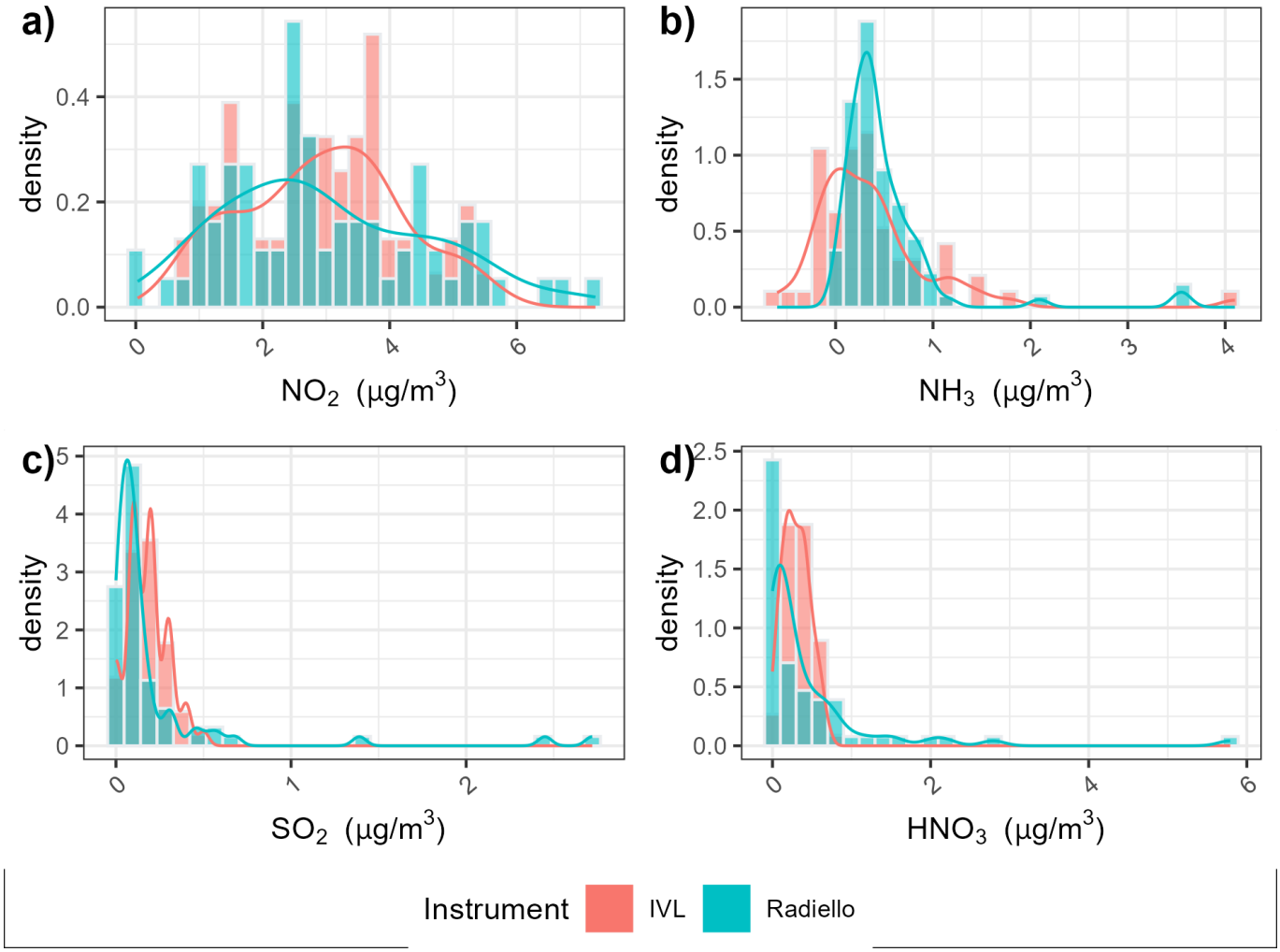

Figure D.3-1: Histograms (colour bars) and density estimates (black curves) of IVL and Radiello sampler gas concentration measurements from all Woodside stations from September 2021 to November 2022. Each panel shows histogram for one gas species: (a) NO_2, (b) NH_3, (c) SO_2, and (d) HNO_3.

D.4 Organic geochemistry

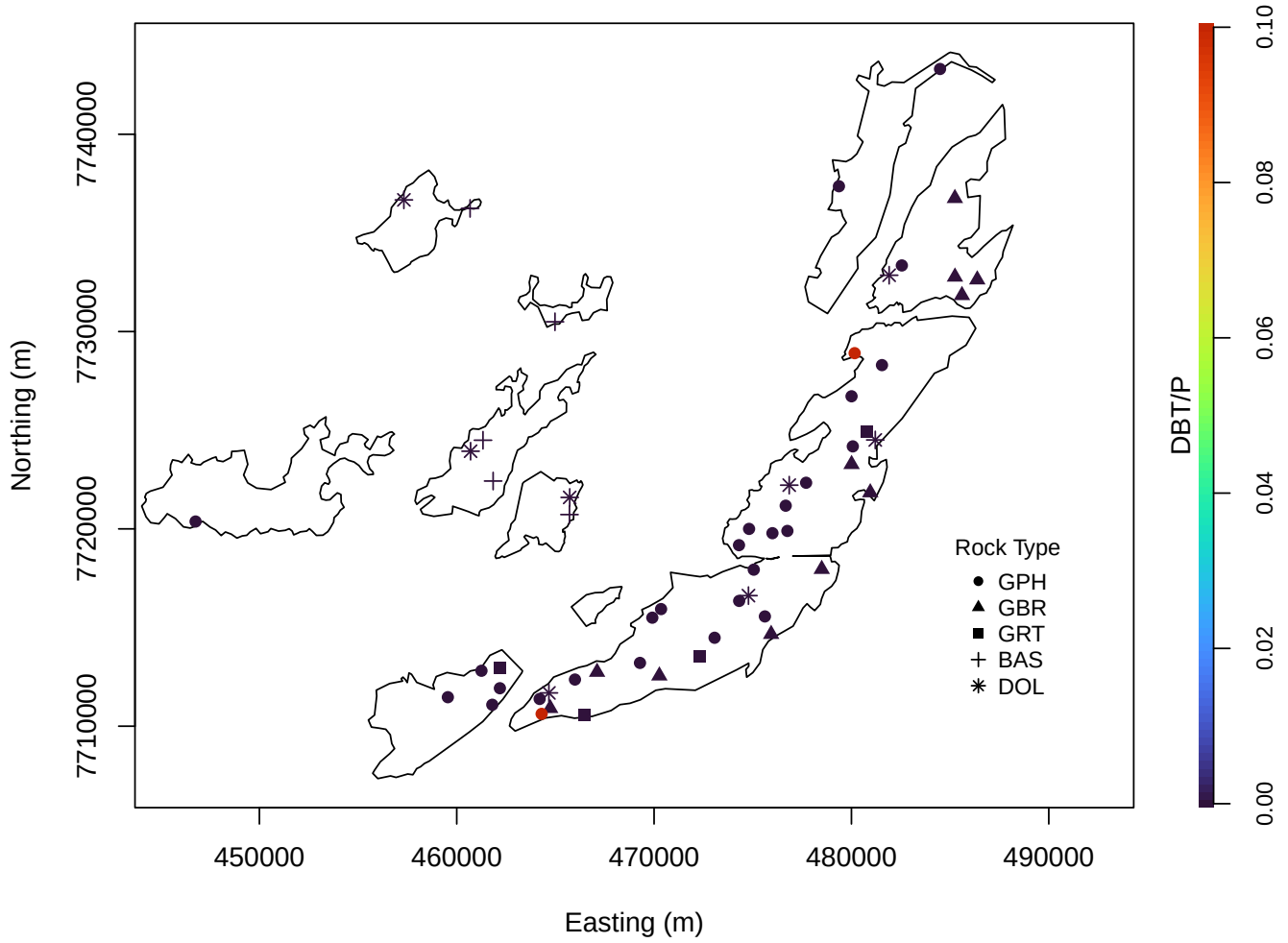

Figure D.4-1: Spatial plot of Dibenzothiophene/phenanthrene (DBT/P).

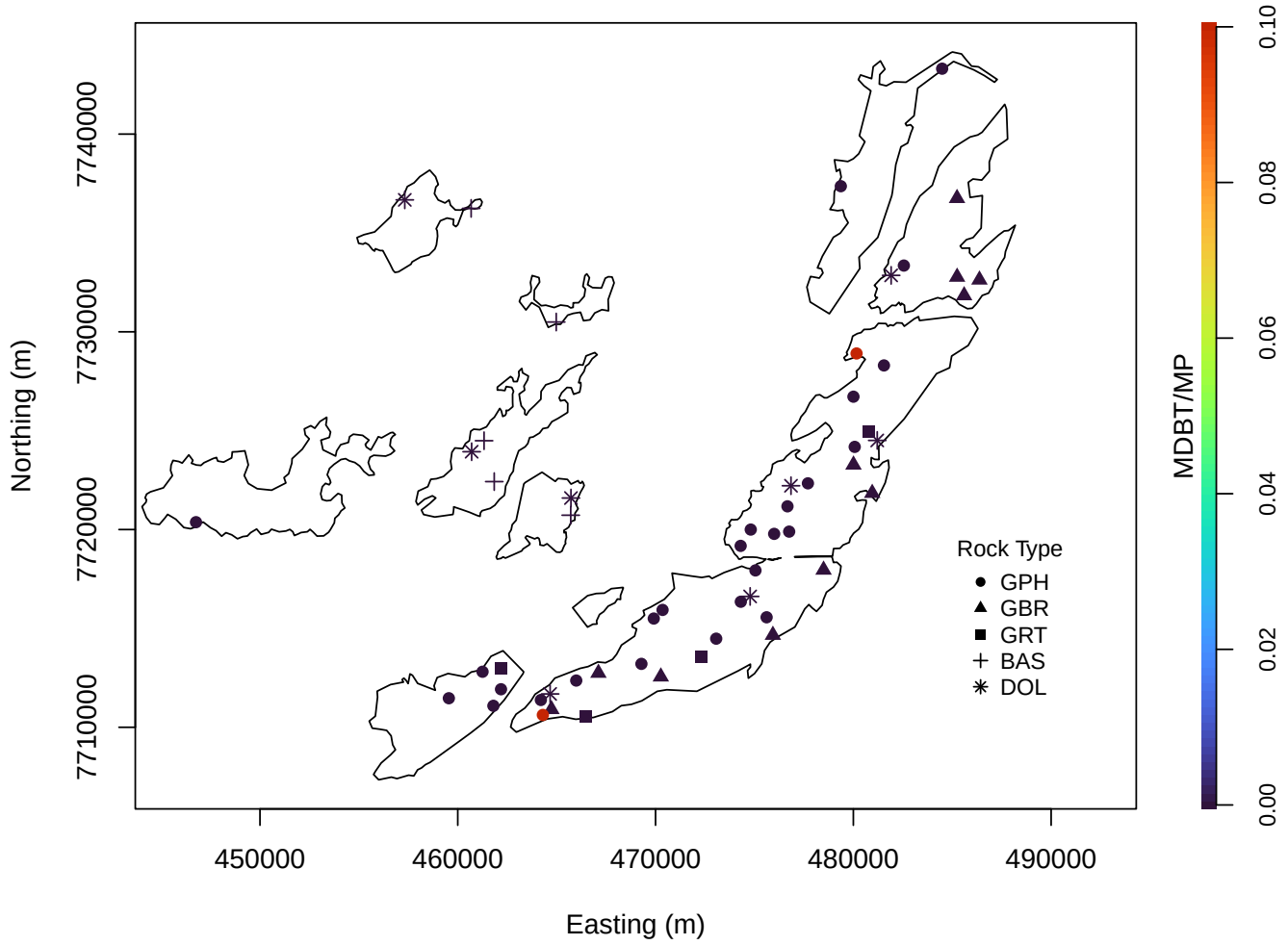

Figure D.4-2: Spatial plot of methyldibenzothiophene/methylphenanthrene (MDBT/MP).

D.5 IVL Passive sampler: further results and diagnostics

D.5.1 Exploratory analysis

D.5.1.1 Gases species

Figure *D.5-1* shows the individual monthly estimates of atmospheric gas concentration from each IVL passive gas species samplers plotted against the air quality monitoring (AQM) station, coloured by meteorological season. AQM stations are ordered by the overall average concentration of NO_2 for all plots. Observations are assigned to the calendar month that covered the majority of the exposure period, and then classified by meteorological season based on that month.

NO_2 concentrations, Figure *D.5-1*(a), show a seasonal pattern with the highest gas concentration measurements in winter.

O_3 concentrations, Figure *D.5-1*(c), suggest a distinct seasonal pattern with consistently high measurements for spring, lower measurements for summer and autumn, and winter measurements in-between. This seasonal pattern is strongly associated with spring and hence is not visible in the plots labelled according to the Murujuga seasons.

SO_2 concentrations, Figure *D.5-1*(d), suggests gas concentration are higher in summer for many stations.

HNO_3 concentrations, Figure *D.5-1*(e), suggests gas concentration are lowest in summer.

D.5.1.2 VOC

Figure *D.5-2* shows plots of the IVL passive sampler estimates of the concentration of each volatile organic compound (VOC), plotted against the air quality monitoring station identifier, coloured by meteorological seasons. AQM stations are ordered by the overall average concentration of NO_2 and data points are coloured by meteorological season for all plots.

Seasonal patterns are not clear from these plots.

M-P-Xylene concentration in Figure *D.5-2*(e), is generally higher in winter, though there are some high values from other season; while N-Octane concentrations, Figure *D.5-2*(c), are slightly higher in spring.

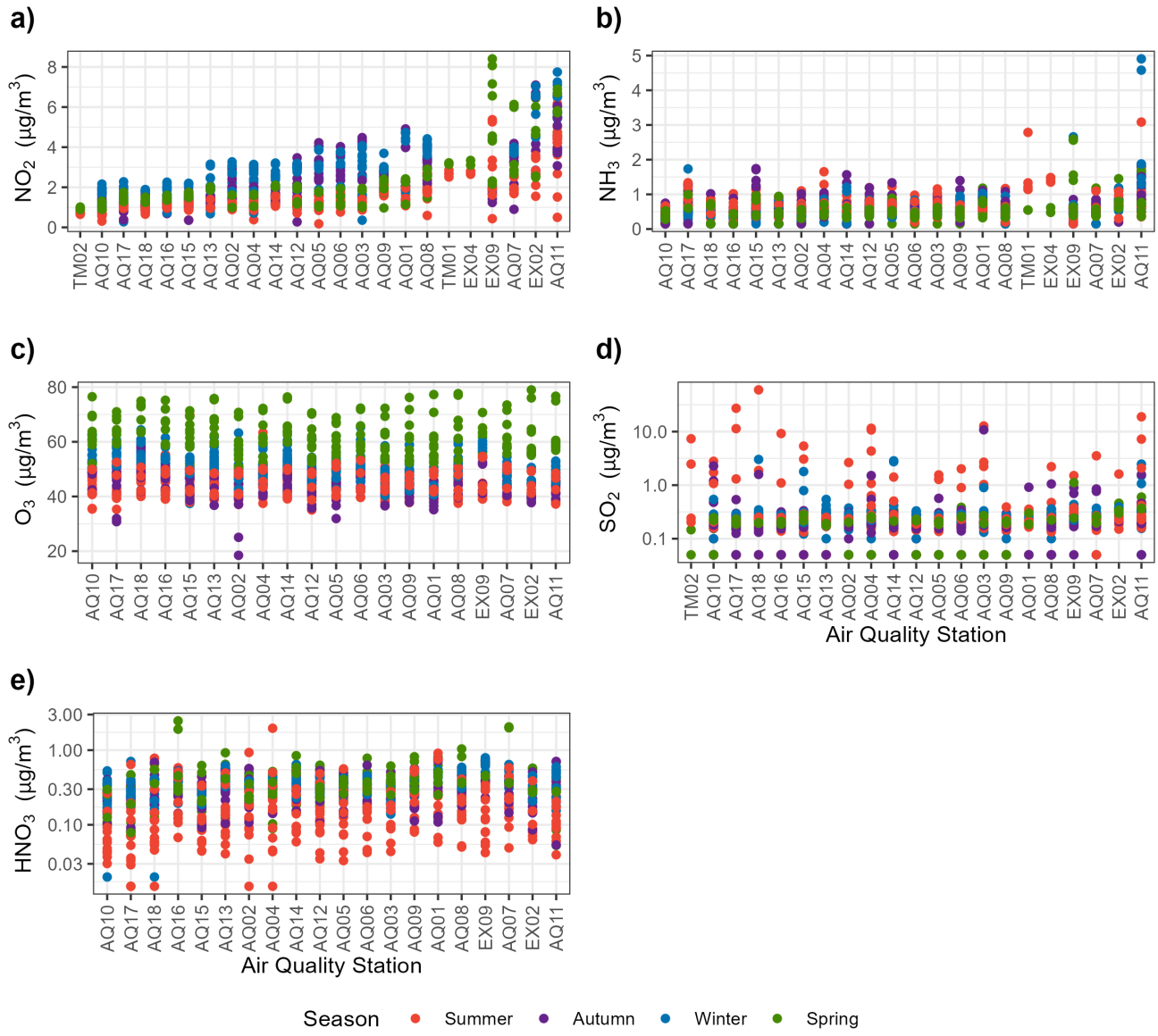

Figure D.5-1: Plots of individual IVL sampler VOC concentration estimates against air quality station identifier, labelled by meteorological season (colour) and month (shape). Each panel shows results for one gas species: (a) NO_2, (b) NH_3, (c) O_3, (d) SO_2, and (e) HNO_3. Panels (d) and (e) use logarithmic scale on the vertical axis.

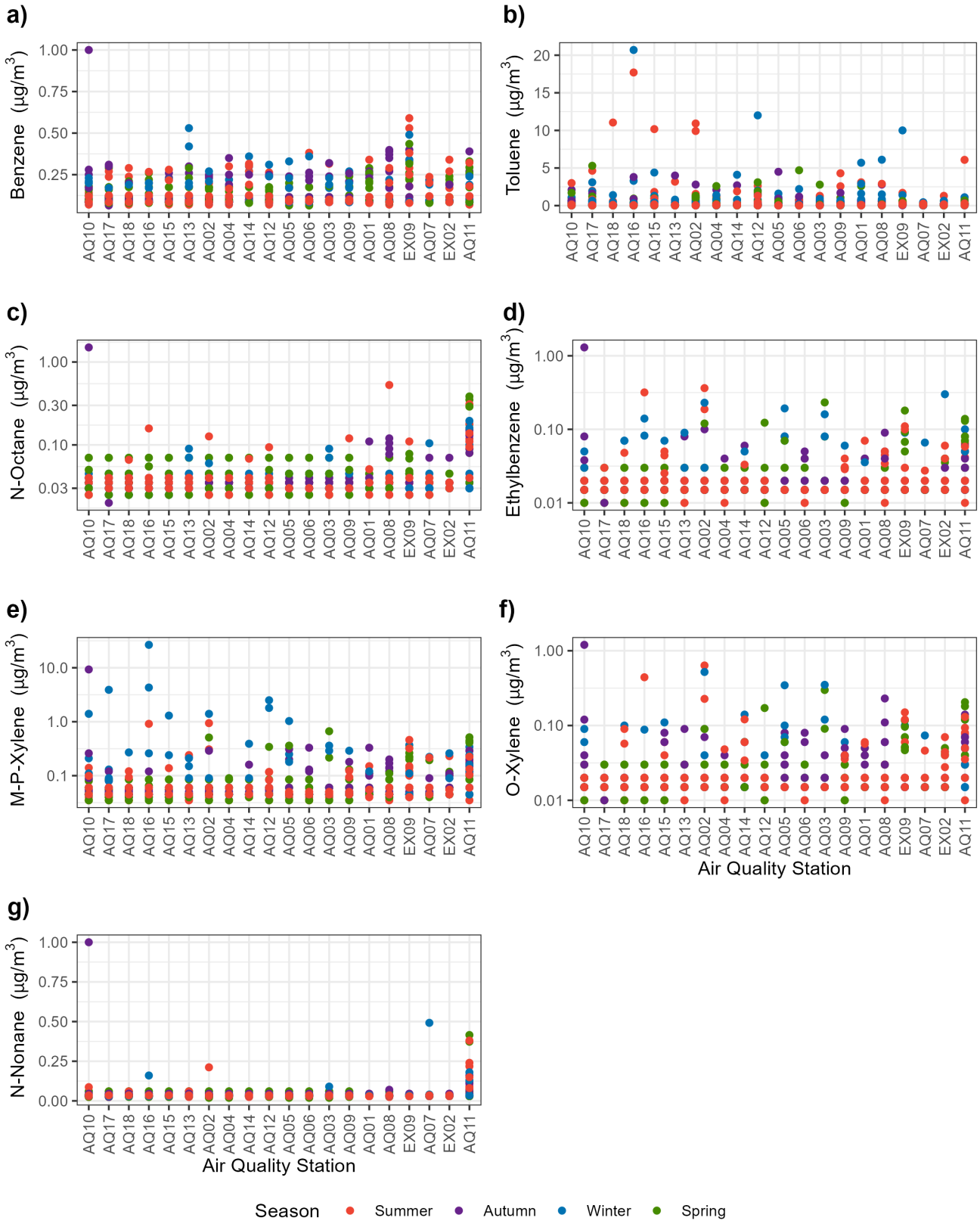

Figure D.5-2: Scatterplots of IVL sampler gas concentration estimates against air quality station identifier, coloured by meteorological season (colour). Separate gases are shown for each panel: (a) benzene, (b) toluene, (c) n-octane, (d) ethylbenzene, (e) m-p-xylene, (f) o-xylene, and (g) n-nonane. Panels (c) — (f) use logarithmic scale on vertical axis.

D.5.2 Temporal analysis

D.5.2.1 Gases species

Figure *D.5-3* shows boxplots of the passive sampler gas data, aggregated by meteorological season.

Figure *D.5-4* shows histograms of the gas concentration data grouped by the four meteorological seasons for each gas species. The seasonal histograms overlay each other and are also overlaid by kernel density estimates for each gas and season. Histograms are coloured according to season.

NO_2 concentrations in Figure *D.5-3*(a) are lowest in summer, increasing through to winter and starting to decline again in spring. The NO_2 histograms in Figure *D.5-4*(a) show a right skew for each season. Spring, summer, and autumn are unimodal with the peak occurring at similar NO_2 concentrations (1.25 to 1.5 $\mu g/m^3$). The spread of concentrations is wider for spring and autumn. NO_2 appears to have a skewed, bimodal distribution over winter. An initial peak occurs at approximately 1.75 $\mu g/m^3$, with the second, smaller peak occurring at approximately 3 $\mu g/m^3$. This winter distribution has a wide spread of NO_2 concentrations.

NH_3 concentrations in Figure *D.5-3*(b), and SO_2 concentrations in Figure *D.5-3*(d), shows little seasonal change in. Figure *D.5-4*(b) shows that gas concentration by season for NH_3 largely overlap. Figure *D.5-4*(d) show that gas concentration by season for SO_2 also overlap. Due to the strong, right skew in the data, the horizontal axis uses a log scale. All seasonal distributions appear to be bimodal with an initial density peak at a concentration of approximately 0.05 $\mu g/m^3$, which may be due to BDL observations. The second density peak for each seasonal distribution occurs at concentrations of approximately 0.5 $\mu g/m^3$.

Figure *D.5-3*(c) shows O_3 concentrations also vary with meteorological seasons: gas levels are low during summer and autumn, then increase during winter and reach high levels in spring. Figure *D.5-4*(c) show the same pattern of O_3 concentrations with season.

HNO_3 concentrations in Figure *D.5-3*(e) shows that HNO_3 concentrations are lower during the summer months, before increasing to a consistently high level most of autumn, winter, and spring. Winter may have a slightly higher median concentration. Figure *D.5-4*(e) shows the HNO_3 concentration distribution changes with meteorological seasons. There is a strong right-hand skew, so a log scale is used on the horizontal axis. Each distribution is unimodal. In summer, HNO_3 has a lower density peak but much wider spread than the other seasons. In spring and autumn, HNO_3 concentrations peaks at around (0.3 $\mu g/m^3$) while winter concentrations peak at a higher level.

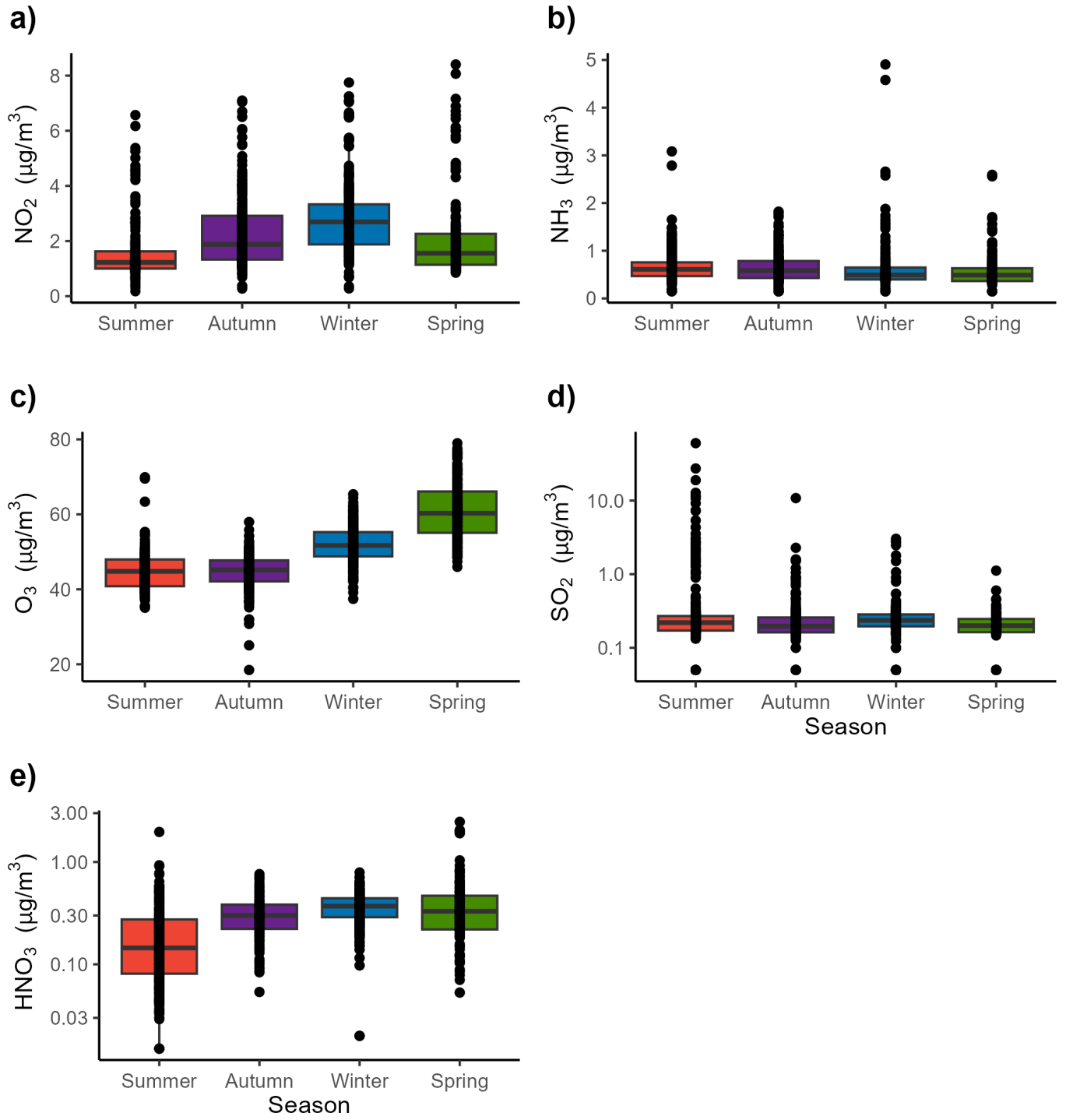

Figure D.5-3: Boxplots of IVL sampler gas concentration observations for each gas species by meteorological season across all stations. Separate gases are shown for each panel: (a) NO_2, (b) NH_3, (c) O_3, (d) SO_2, and (e) HNO_3. Panels (d) and (e) use logarithmic scale on the vertical axis.

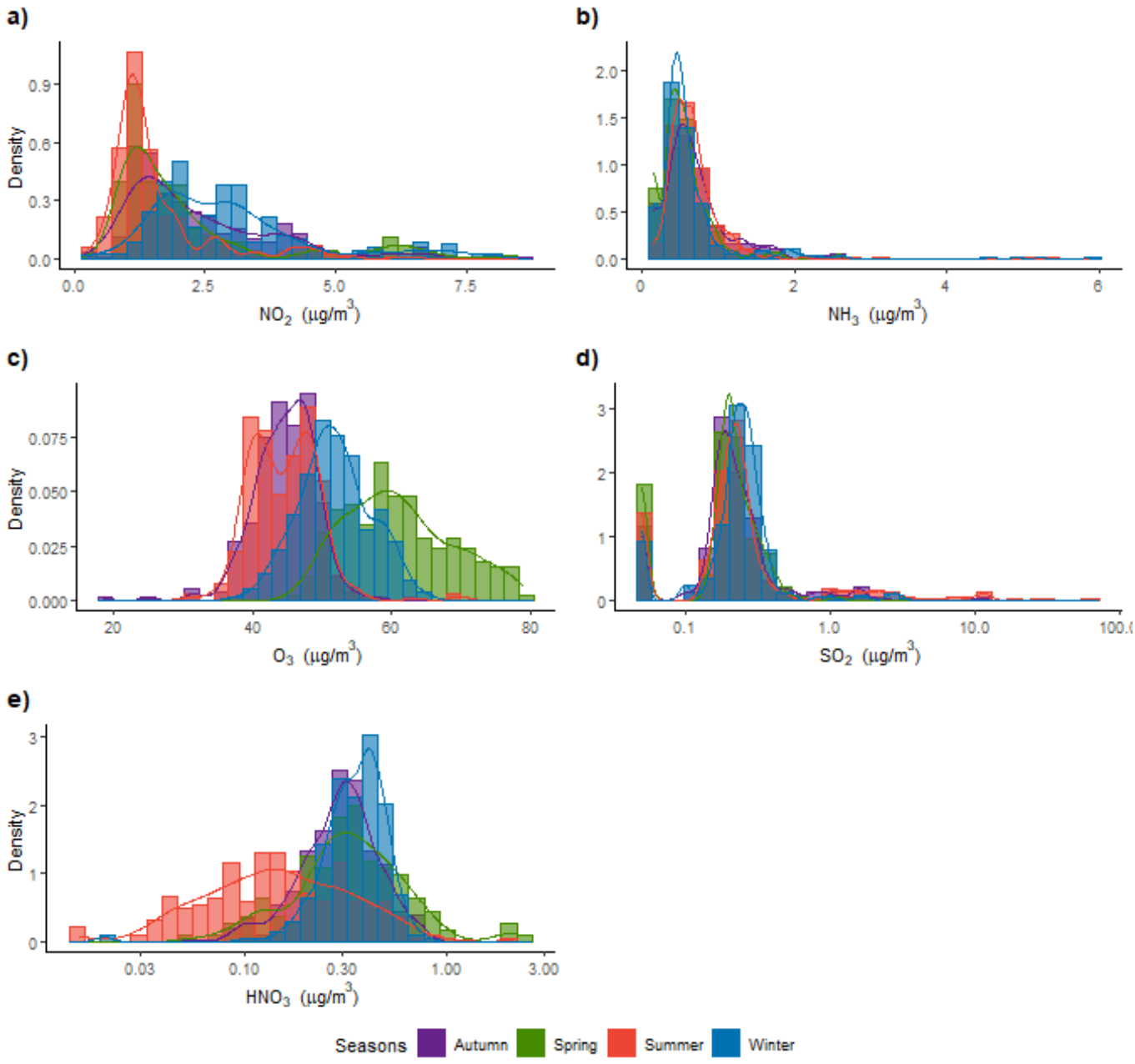

Figure D.5-4: Histograms of IVL sampler gas concentration observations for each Gas species by meteorological season across all stations. Separate gases are shown for each panel: (a) NO_2, (b) NH_3, (c) O_3, (d) SO_2, and (e) HNO_3. Panels (d) and (e) use logarithmic scale on the horizontal axis.

D.5.2.2 VOCs

Figure *D.5-5* shows boxplots of the passive sampler VOC data by meteorological season. Figure *D.5-6* shows histograms of the VOC data grouped by the four meteorological seasons for each gas species; while Figure *D.5-7* shows histograms of the gas concentration data grouped by the two Murujuga seasons.

Benzene concentration in Figure *D.5-4* shows little seasonal change, with benzene concentrations ranges overlapping between seasons. Figure *D.5-5*(a) shows benzene concentration distributions for all seasons are non-symmetric, with a peak occurrence at low levels, possibly reflecting a large number of BDLs, and with a long right-hand skew. Distributions for all seasons except spring are unimodal, while the spring distribution seems bimodal. Figure *D.5-7*(a) shows Benzene concentration distributions by Murujuga season. As for the meteorological seasons, both seasons have a non-symmetric distributions with a peak at low concentrations and a long right hand tail. However, for Garrbarn, there is a wider range and number of benzen observations, resulting in a lower peak.

Toluene concentrations in Figure *D.5-5*(b), shows only minor seasonal changes. The median values increase slightly from summer to winter and then decline noticeably in spring. Figure *D.5-4*(b) shows histogram of Toluene concentrations for all seasons are non-symmetric. While the histograms show a peak in for the low concentrations, possibly due to BDLs, the probability distribution curve is much flatter which a relatively low initial peak and a slow decline and heavy right hand skew. Some seasons, including spring and autumn may have bimodal distributions. Figure *D.5-7*(b) shows Toluene concentration distributions by Murujuga season. As for the meteorological seasons, both seasons have a non-symmetric distributions with a low peak at low concentrations, a gradual decline and a long right hand tail.

N-Octane concentrations in Figure *D.5-5*(c) shows little difference between seasons. Inter-quartile range (IQR), the range between the 25th and 75th percentile, widest in spring and narrowest in summer and winter. Figure *D.5-4*(c) shows shows N-Octane concentrations for each season have a number of distinct peaks. The two highest peaks for winter and summer coincide. All distributions show a long right-hand skew. In Figure *D.5-7*(c) both Murujuga seasons have a non-symmetric distributions with a low peak at low concentrations, and a number of small discrete peaks, a gradual decline and a long right hand tail. This is similar to the meteorological seasons.

Histograms of the remaining VOCs for both meteorological seasons in Figure *D.5-4*(d) to (g), and Murujuga seasons in Figure *D.5-7*(d) to (g), have major peak at low concentrations for each VOC followed by a long right-hand tail which may have a number of distinct smaller peaks. Generally, the major peaks coincide for each season for each VOC, except for N Nonane where spring has a peak at a lower concentration than autumn while summer and winter have a bimodal distribution with peaks at similar concentrations as shown in Figure *D.5-4* (g). The boxplots in Figure *D.5-5*(d) to (g) show a wider interquartile range for spring than for the other seasons for each VOC.

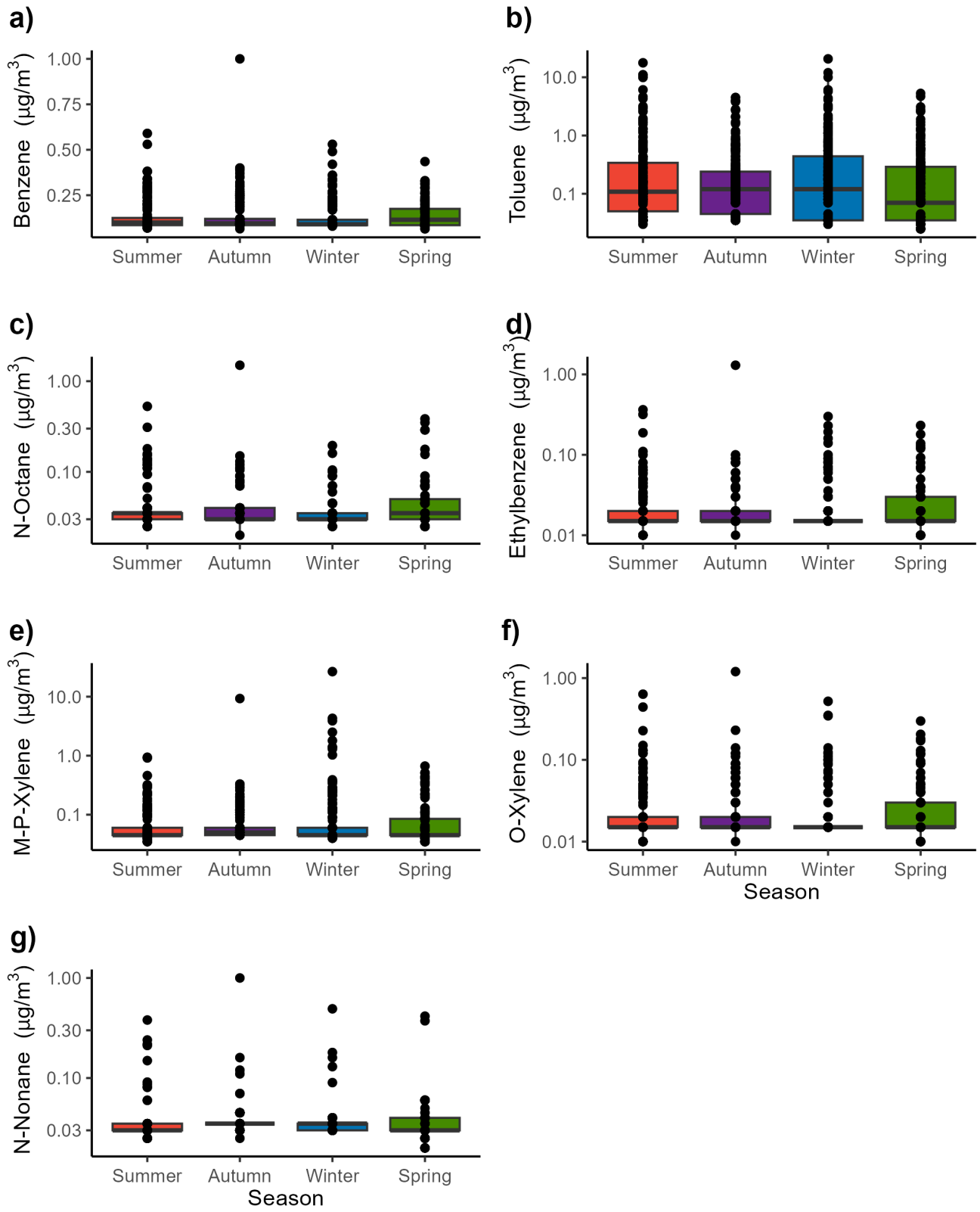

Figure D.5-5: Boxplots of IVL sampler VOC measurements for each VOC species by meteorological season across all stations. Panels: (a) benzene, (b) toluene, (c) n-octane, (d) ethylbenzene, (e) m-p-xylene, (f) o-xylene, and (g) n-nonane. Panels (c) – (g) use logarithmic scale on vertical axis.

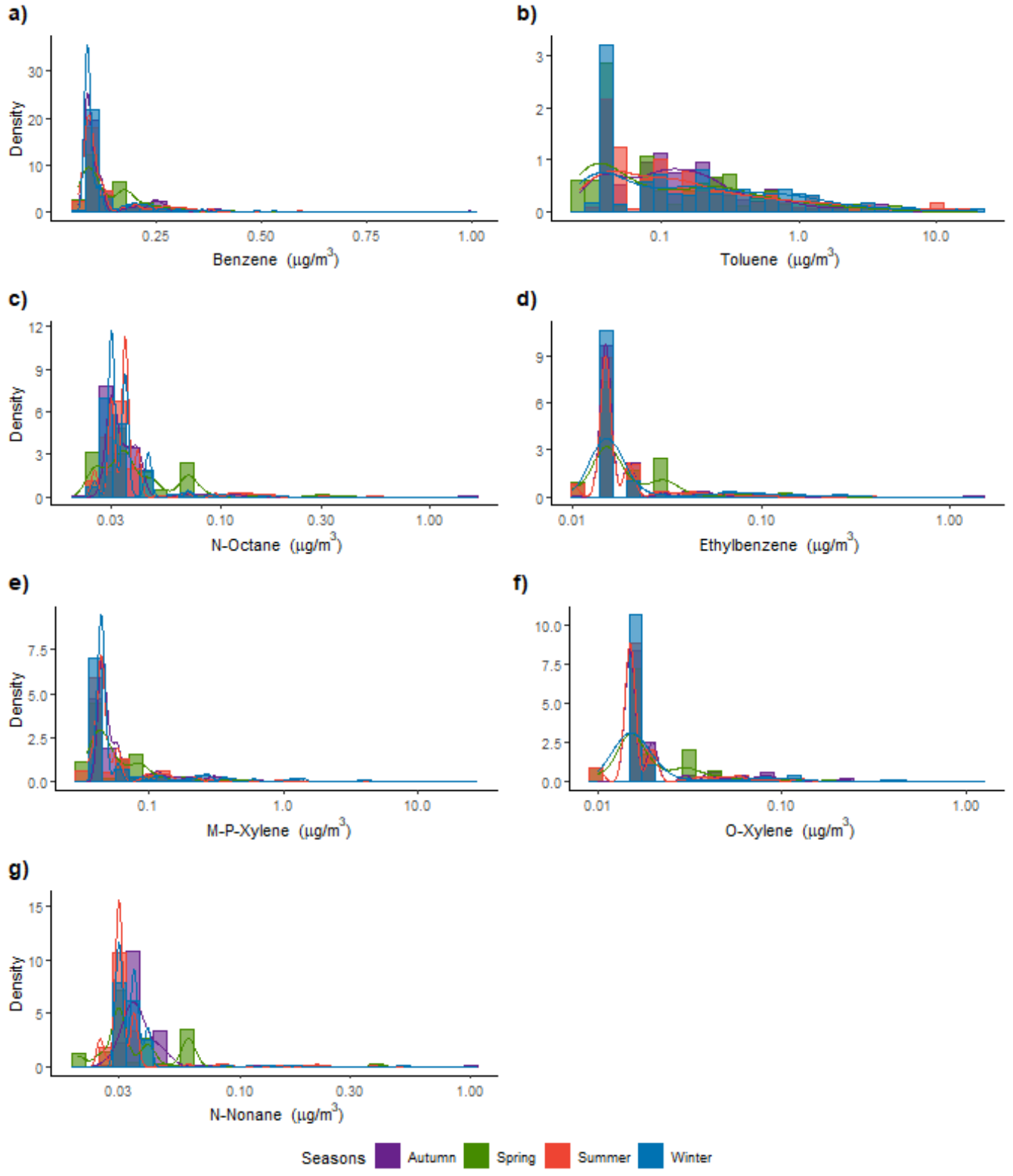

Figure D.5-6: Histograms of IVL sampler VOC measurements for each VOC species by meteorological season across all stations. Panels: (a) benzene, (b) toluene, (c) n-octane, (d) ethylbenzene, (e) m-p-xylene, (f) o-xylene, and (g) n-nonane. Panels (c) – (g) use logarithmic scale on horizontal axis.

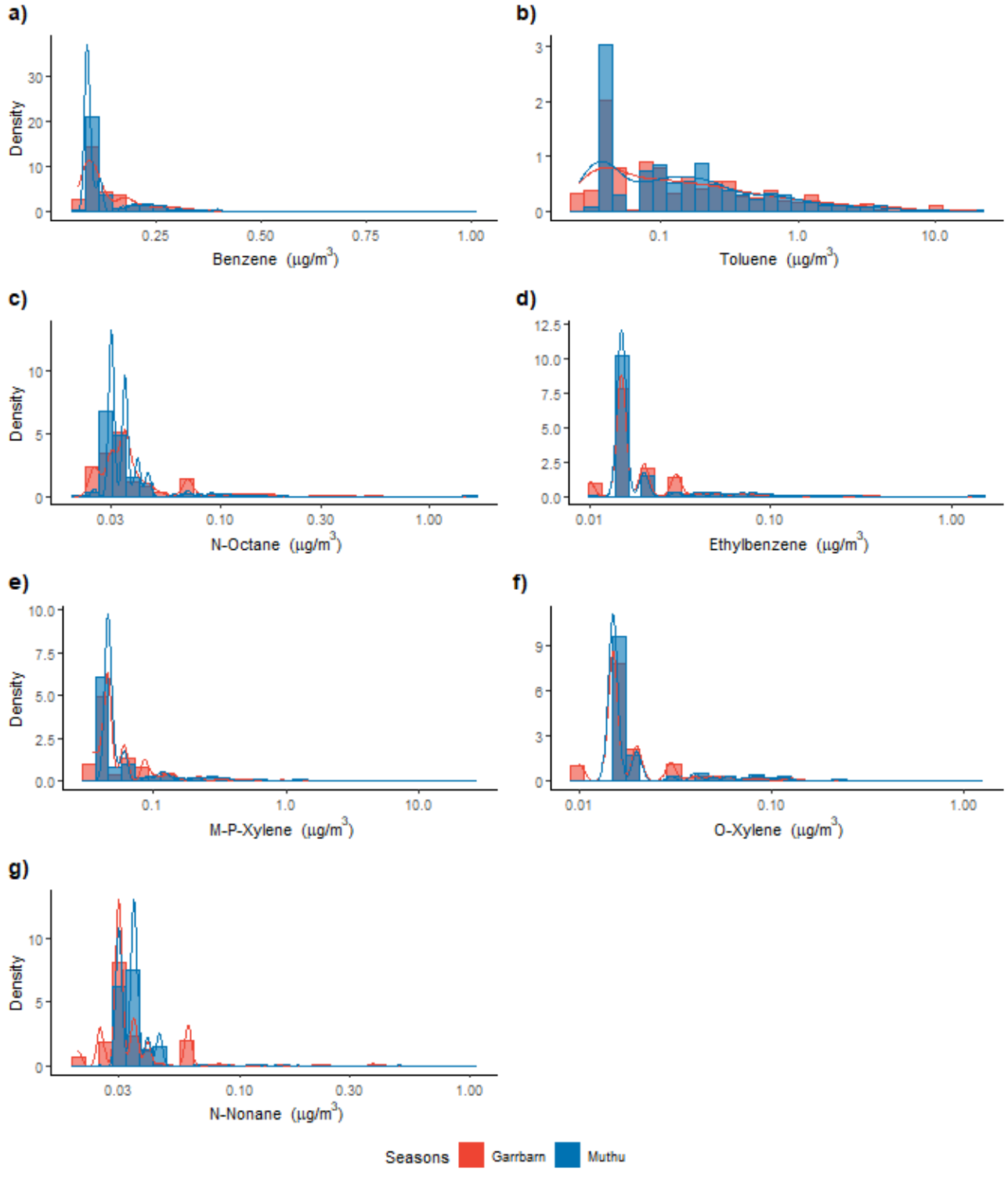

Figure D.5-7: Histograms of IVL sampler VOC measurements for each VOC species by Murujuga season across all stations. Panels: (a) benzene, (b) toluene, (c) n-octane, (d) ethylbenzene, (e) m-p-xylene, (f) o-xylene, and (g) n-nonane. Panels (c) — (g) use logarithmic scale on the horizontal axis.

D.5.3 Correlations between gases

Correlations reported in Monitoring Studies Report 2025 (Curtin University, 2025b) Section 7.12.3. show associations between gases but did not explicitly account for variables such as time of year or site location. As in the Monitoring Studies Report 2024 (Curtin University, 2024c), RDA was used to examine the relationship between IVL gas measurements and site-specific information, including time of year, site location and elevation. RDA was conducted in `R` using the function `rda` in the `vegan` package. IVL gas measurements were normalised using the `Hellinger` normalisation (Legendre and Gallagher, 2001).

Time of year was based on the month of each IVL sample, encoded as an integer from one to 12. In order to identify seasonal effects, the months of the year were treated as a circular variable with sine and cosine terms:

$$\text{Month sin} = \sin(\frac{2\pi(\text{month})}{12})$$

$$\text{Month cos} = \cos(\frac{2\pi(\text{month})}{12})$$

The RDA analysis was also applied treating months or meteorological seasons as categorical variables. The results consistent with treating months as circular variable, but the latter returned the strongest results correlation results.

The site location was defined by northing, easting, and elevation was measured in metres above sea level for each AQM. These variables were standardised using the `range` method to a value between zero and one, using the function `decostand` in the `vegan` package in `R`.

Figure *D.5-8* shows the RDA biplot displaying the relationship between the IVL gas measurements and time of year (month sin and cos). The first two principal components of this RDA explain 44.2% of the total variation.

NO_2 is positively correlated with HNO_3, with only a small angle between them. Both these gases are negatively correlated with SO_2, with approximately 180 degrees between them. NH_3 and O_3 are also negatively correlated. NH_3 and O_3 are both approximately 90 degrees from NO_2, HNO_3, and O_3, which indicates there is no correlation between these two groups of gases. NH_3 is positively correlated with ‘month sin’, which is highest in Autumn and lowest in Spring. SO_2 is positively correlated with ‘month cos’, which is highest in summer and lowest in winter.

Figure *D.5-9* shows the RDA biplot displaying the relationship between the IVL gas measurements and location (northing and easting). The first two principal components of this RDA explains 12.6% of the total variation. The northing and east effect is small relative to the month effect. Combining location and monthly factors does not result in higher levels of explanation of variation by the first two principal components.

In Figure *D.5-9*, NO_2 and NH_3 are positively correlated with each other. This contrasts with the seasonal relationship whereNO_2 and NH_3 are relatively independent, the difference may relate to emissions from closely related sites. This relation is also consistent with the strong correlation between NO_2 and NH_3 shown by the spatial correlation in Monitoring Studies Report 2025 (Curtin University, 2025b), Section 7.12.3. SO_2 and HNO_3 also show positive correlations when taking location into account: this may relate to the more even spread of these gases across the area as shown in the spatial plots Monitoring Studies Report 2025 (Curtin University, 2025b), Section 7.12.6.

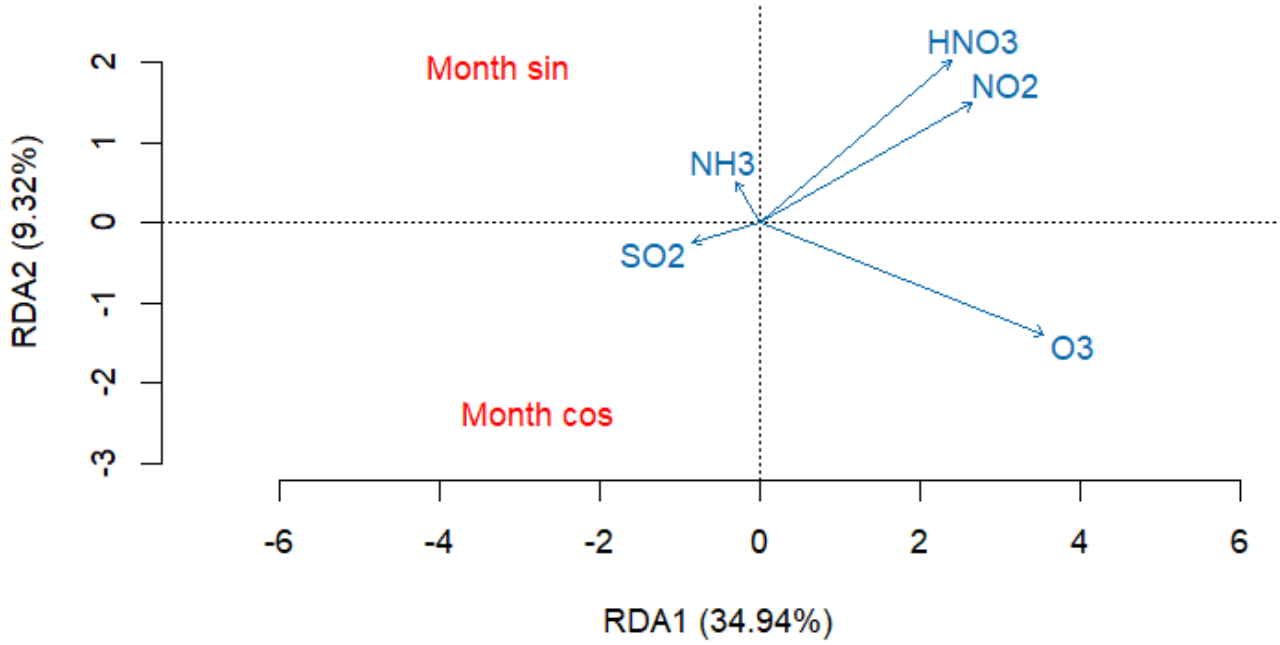

Figure D.5-8: RDA biplot showing the relationship between gas measurements (NO_2, NH_3,O_3, SO_2, and HNO_3) and time of year (month sin and month cos).

These gases however have very different seasonal changes, resulting in a negative correlation in the previous Figure *D.5-8*. NO_2 and NH_3 are negatively correlated with northing: this is the strongest of the location factors. HNO_3, O_3, and SO_2 are positively correlated with easting, but these are all relatively weak associations.

This analysis shows that time of year and location effect the correlations between the gases. Correlations differ depending on which variable is taken into account, but the strongest response is using the time of year as a circular variable (month sine and cos). The RDA correlations do not always correspond to the Spearmans correlations in reported in Monitoring Studies Report 2025 (Curtin University, 2025b) Section 7.12.3: this may be due to missing predictor variables or more complicated relationships than those considered in an RDA analysis. Differences could also be due to Spearman's correlations relating to ranked rather than normalised observations. Future analysis could use distance and bearing to port as a alternative variables to location. More complex modelling could also be attempted in the data fusion models being developed for the final report.

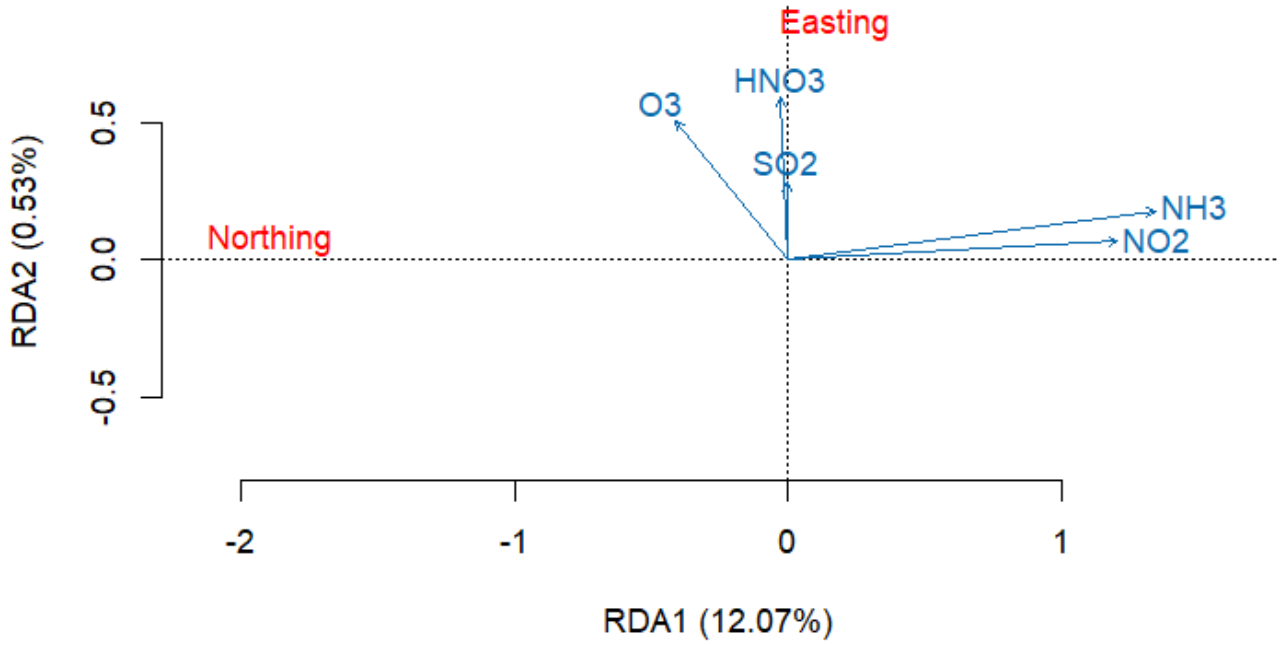

Figure D.5-9: RDA biplot showing the relationship between gas measurements (NO_2, NH_3, O_3, SO_2 and HNO_3) and Northing and Easting.

D.5.4 Residual variability

Figures *D.5-10* to *D.5-13* residual variance estimates against paired means for four gas species: NO_2, NH_3, O_3, and HNO_3. The plots also show residual variance estimates plotted against calendar months and against air quality monitoring stations. These plots can show trends or patterns in the variance.

There are no discernible trends in residual variance estimates versus either the months or the air quality monitoring stations for any of the gases. The residual variance estimates for NO_2 in Figure *D.5-10*, NH_3 in Figure *D.5-11*, and O_3 in Figure *D.5-12*, show no trend in relation to the mean values. These plots suggest that variance is constant for these gases. The residual variance estimates for HNO_3 in Figure *D.5-13*, may show a slight increasing trend against the paired means.

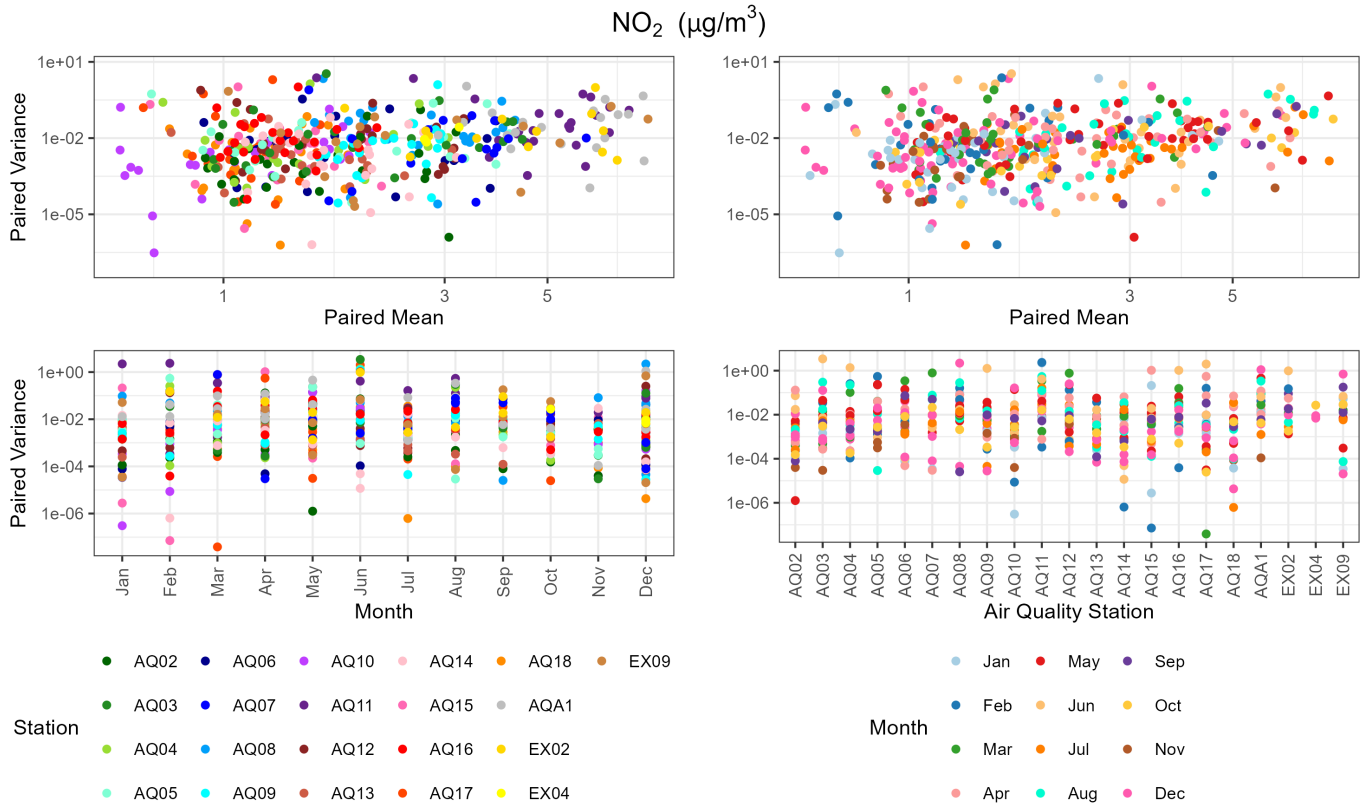

Figure D.5-10: Diagnostic plots for the variance-mean relationship for NO_2 data. Top row shows a scatterplot of individual estimates of variance (S^2, "paired variance") versus individual estimates of mean value ($\overline{X}$, "paired mean") calculated from duplicate pairs of passive sampler measurements for NO_2. Left scatterplot is coloured according to calendar month; right scatterplot is coloured according to air quality station. Logarithmic scale is used for both variables. Bottom row shows individual estimates of variance plotted against calendar month (left) and against air quality station (right). Plots show paired measurements collected over 2023 and 2024. The legend on the bottom left hand side show the stations by colour while the legend on the bottom right hand side show the months by colour. The axis labels `1e-03` and `1e+01` (for example) are computer notation for 10^{-3} and 10^{1} respectively, that is, 0.001 and 10 respectively.

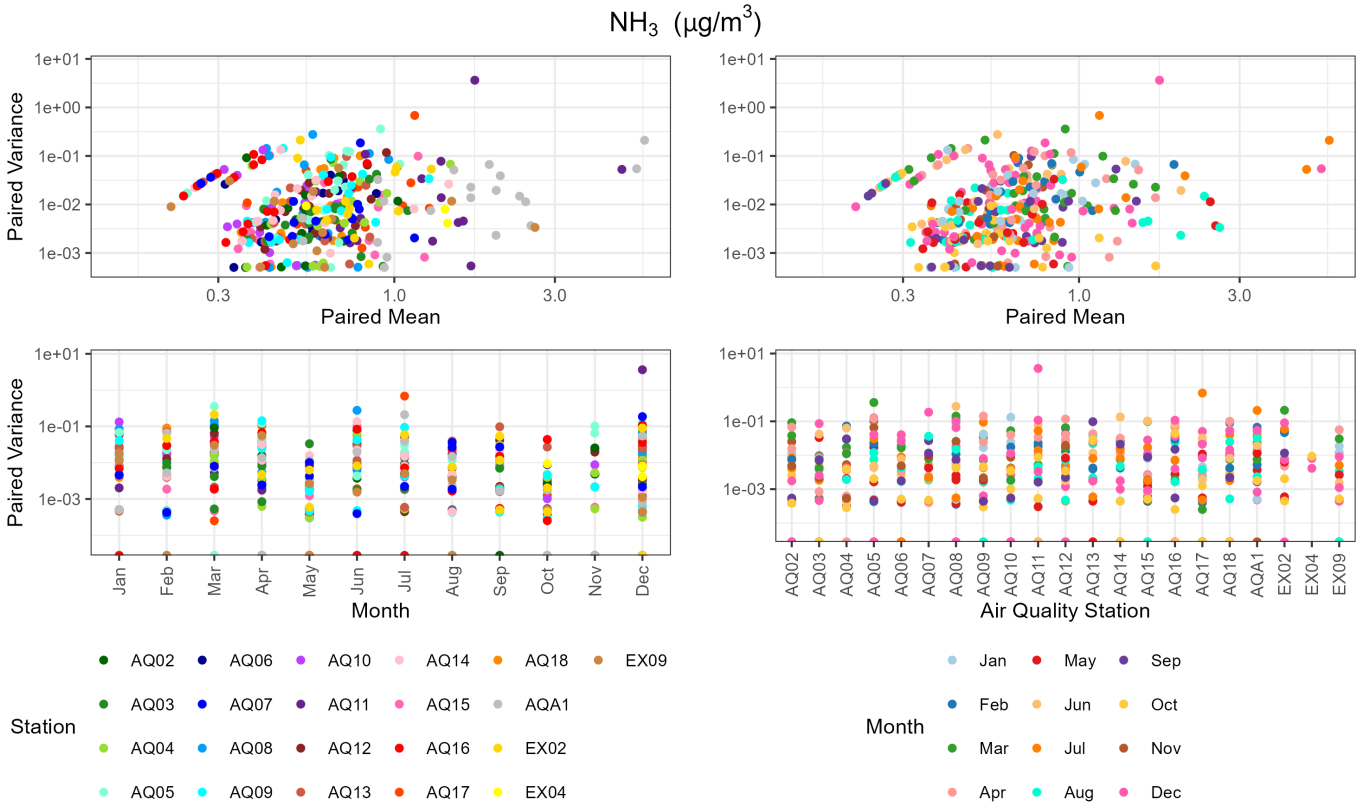

Figure D.5-11: Diagnostic plots for the variance-mean relationship for NH_3 data. Top row shows a scatterplot of individual estimates of variance (S^2, "paired variance") versus individual estimates of mean value ($\overline{X}$, "paired mean") calculated from duplicate pairs of passive sampler measurements for NH_3. Left scatterplot is coloured according to calendar month; right scatterplot is coloured according to air quality station. Logarithmic scale is used for both variables. Bottom row shows individual estimates of variance plotted against calendar month (left) and against air quality station (right). Plots show paired measurements collected over 2023 and 2024. The legend on the bottom left hand side show the stations by colour while the legend on the bottom right hand side show the months by colour. The axis labels `1e-03` and `1e+01` (for example) are computer notation for 10^{-3} and 10^{1} respectively, that is, 0.001 and 10 respectively.

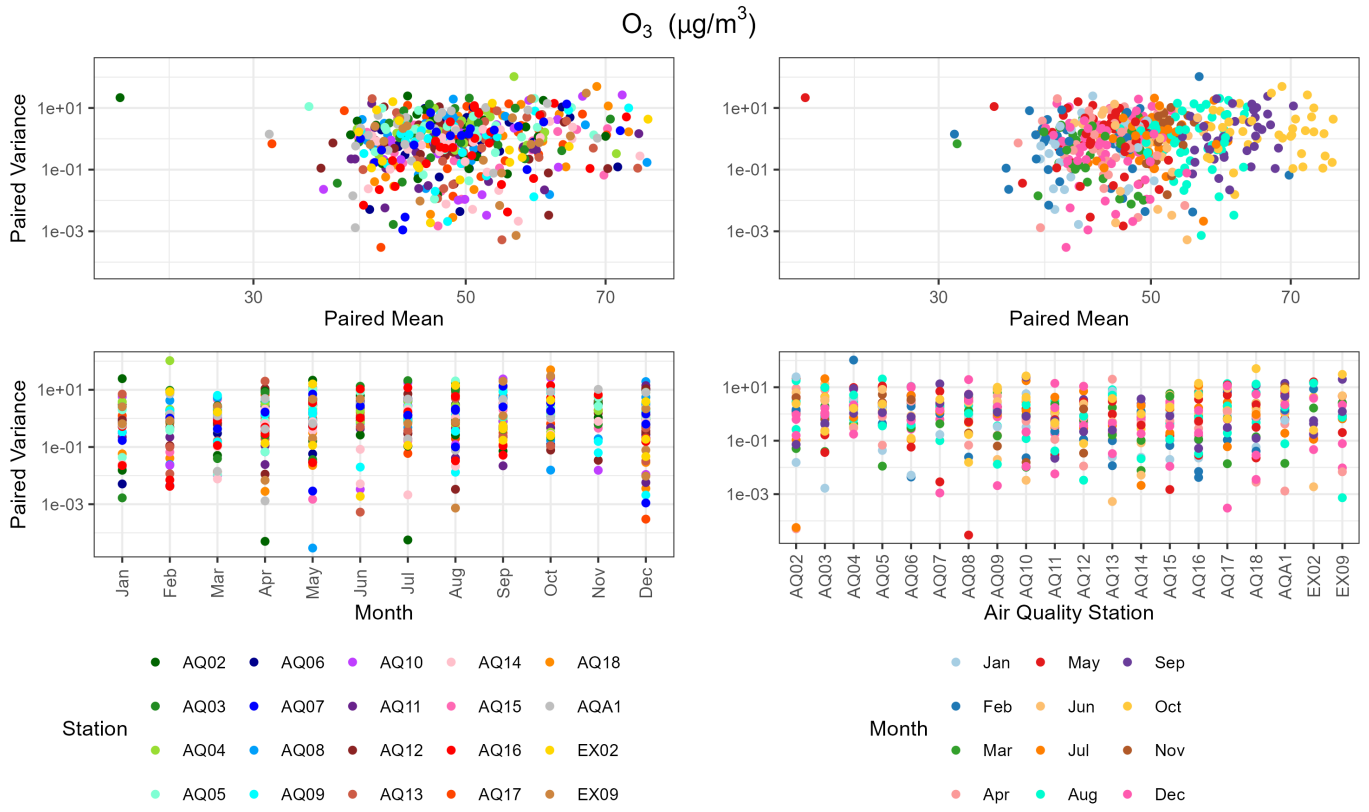

Figure D.5-12: Diagnostic plots for the variance-mean relationship for O_3 data. Top row shows a scatterplot of individual estimates of variance (S^2, "paired variance") versus individual estimates of mean value ($\overline{X}$, "paired mean") calculated from duplicate pairs of passive sampler measurements for O_3. Left scatterplot is coloured according to calendar month; right scatterplot is coloured according to air quality station. Logarithmic scale is used for both variables. Bottom row shows individual estimates of variance plotted against calendar month (left) and against air quality station (right). Plots show paired measurements collected over 2023 and 2024. The legend on the bottom left hand side show the stations by colour while the legend on the bottom right hand side show the months by colour. The vertical axis labels `1e-03` and `1e+01` (for example) are computer notation for 10^{-3} and 10^{1} respectively, that is, 0.001 and 10 respectively.

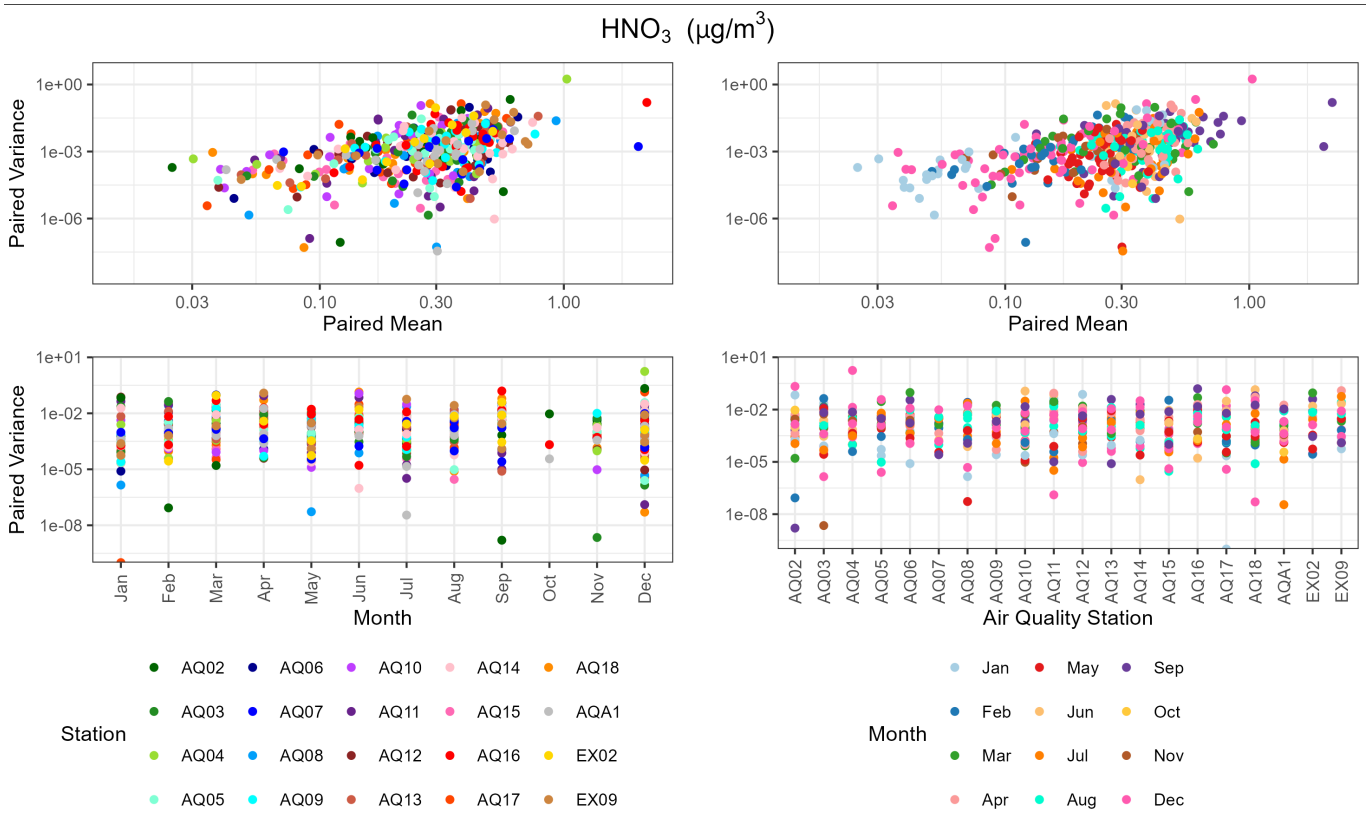

Figure D.5-13: Diagnostic plots for the variance-mean relationship for HNO_3 data. Top row shows a scatterplot of individual estimates of variance (S^2, "paired variance") versus individual estimates of mean value ($\overline{X}$, "paired mean") calculated from duplicate pairs of passive sampler measurements for HNO_3. Left scatterplot is coloured according to calendar month; right scatterplot is coloured according to air quality station. Logarithmic scale is used for both variables. Bottom row shows individual estimates of variance plotted against calendar month (left) and against air quality station (right). Plots show paired measurements collected over 2023 and 2024. The legend on the bottom left hand side show the stations by colour while the legend on the bottom right hand side show the months by colour. The vertical axis labels `1e-03` and `1e+01` (for example) are computer notation for 10^{-3} and 10^{1} respectively, that is, 0.001 and 10 respectively.

D.5.5 Short scale comparison further analysis

D.5.5.1 Short scale variability by station

Figure *D.5-14* shows histograms and probability density estimates for the passive sampler gas concentration measurements at each of the two neighbouring sites, AQ07 and AQ08. Each panel represents the data for a particular gas species.

For NO_2 in Figure *D.5-14* (a) the AQ07 probability density function peaks at higher gas concentration than AQ08.

For NO_2 and O_3 shown in panels Figure *D.5-14* (a) and (c) respectively, there are large overlaps between the histograms of gas concentration recorded at the two stations.

For NH_3, SO_2, and HNO_3 shown in panels Figure *D.5-14*(b), (d), and (e) respectively, the gas concentration distributions for the two stations are quite similar.

For O_3, the AQ08 probability density function has a more defined mode (probability density peak) at a slightly higher gas concentration than for AQ07 (Figure *D.5-14* (c). Further analysis is required to determine if there are any significant differences and to assess the effect of monthly and seasonal variations.

Figure *D.5-15* shows the distribution of the VOC species. These distributions tend to follow a similar pattern with a probability density function peak at low VOC concentrations which reflects the high number of BDLs. The distributions show strong right wing skew, even using the log scale for the horizontal axes. The distributions are generally similar between the two stations. M-P Xylene concentrations vary from this pattern with a bimodal distribution where the two peaks coincide at similar VOC concentrations for both stations.

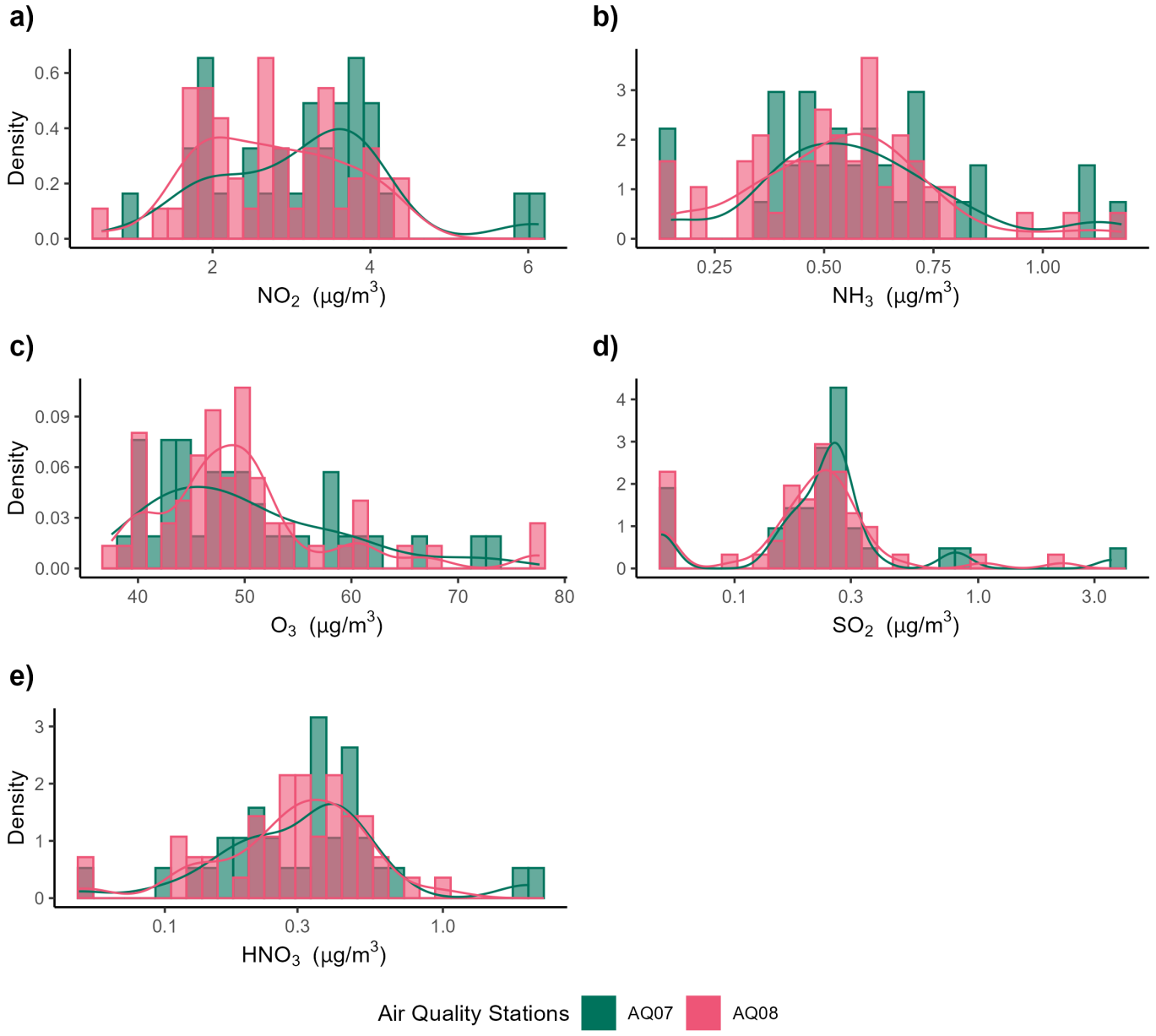

Figure D.5-14: Histograms (coloured bars) and probability density estimates (coloured curves) of passive sampler gas concentration measurements for stations AQ07 and AQ08 for gas species (a) NO_2, (b) NH_3, (c) O_3, (d) SO_2, and (e) HNO_3. Panels (d) and (e) use logarithmic scale on the horizontal axis.

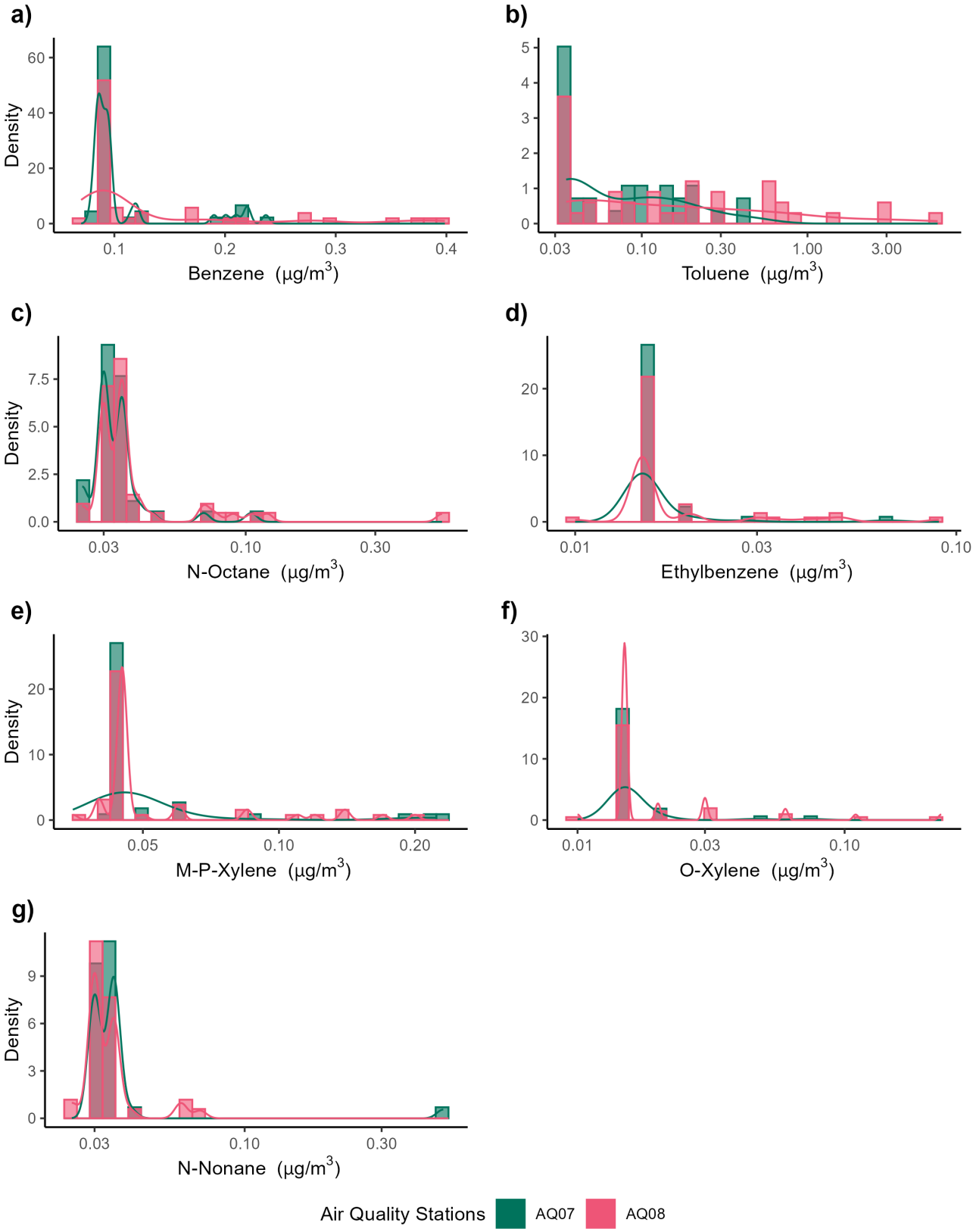

Figure D.5-15: Histograms and density estimates of passive sampler VOC concentration measurements for stations AQ07 and AQ08 for VOC species (a) benzene, (b) toluene, (c) n-octane, (d) ethylbenzene, (e) m-p-xylene, (f) o-xylene, and (g) n-nonane. Panels (b) to (g) (inclusive) use logarithmic scale on the horizontal axis.

D.5.5.2 One-way ANOVA analysis by station

Table *D.5-1* shows the ANOVA results for each gas and VOC species. It also shows if the constant variance and normal conditions are met. If they are not, an alternative test is applied: the Welch One way Test if variance is not constant and the Kruskal-Wallis Test if data is not normal. These tests are applied to both the complete set of data (all) and matched data, where an observation for a species at one station is only included if for the same sample period there is a corresponding observation at the other station.

Table *D.5-1* shows that the ANOVA test did not find significant differences for any gas or VOC species at a significance level of 0.05, except for Toluene. However, the Toluene data did not exhibit constant variance. Applying a Welch One way test showed a significant result for analysis across all data, but not for the matched data. The complete dataset includes data for sampling periods for AQ07 for which there are no data for AQ08 and vice versa. The unmatched data could impact this result. Testing suggested that all other gas and VOC species had constant variance between the groups.

Testing for normality of residuals of the ANOVA test showed that only NO_2 and NH_3 had normal residuals, though the latter result is only for the complete dataset. Hence the ANOVA test provides no evidence of significant difference between stations for NO_2 (complete or matched data) or for NH_3 (complete data only). Applying the Kruskal-Wallis test to other gas and VOC species confirms that most species show no evidence of significant difference at 0.05 significance level. Toluene is again an exception for both complete and matched datasets. This suggests that there may, in fact, be a significant difference between these species.

Table D.5-1: Results of ANOVA analysis of gas concentrations by sites (AQ07 and AQ08). The column total observations gives the number of observations for a gas species across both sites, while the column used observations gives the number observations used by a specific analysis across the two sites. The column ANOVA p-value:station shows the strength of supporting evidence for differences between gas concentration measurements. For a significance level of 0.05, p-values less than 0.05 indicate there is evidence of a significant difference in values. The constant variance and normal distribution columns indicate if key assumptions about the data for the ANOVA analysis are met or not. The Levine-Walsh test is an alternative test to ANOVA that does not assume constant variance; while the Kruskal-Wallis test is an alternative test to ANOVA that does not assume a specific distribution of the data. As before, p-values of less than 0.05 indicate there is evidence of significant difference in values between stations, these values are in bold.

Gas	Data	Total Observation	Used Observation	ANOVA p-value	Constant Variance	Welch One-way p-value	Normal Distribution	Kruskal-Wallis p-value
NO_2	all, raw	80	80	0.071	yes	NA	yes	0.135
NO_2	match, raw	80	62	0.404	yes	NA	yes	0.622
NH_3	all, raw	92	92	0.423	yes	NA	no	0.513
NH_3	match, raw	92	74	0.123	yes	NA	yes	0.218
O_3	all, raw	92	92	0.896	yes	NA	no	0.918
O_3	match, raw	92	74	0.976	yes	NA	no	0.922
SO_2	all, raw	81	81	0.420	yes	NA	no	0.366
SO_2	match, raw	81	65	0.177	yes	NA	no	0.318
HNO_3	all, raw	84	84	0.209	yes	NA	no	0.668
HNO_3	match, raw	84	66	0.324	yes	NA	no	0.644
Benzene	all, raw	86	86	0.075	yes	NA	no	0.473
Benzene	match, raw	86	69	0.085	yes	NA	no	0.478
Toluene	all, raw	82	82	**0.037**	no	**0.025**	no	**0.039**
Toluene	match, raw	82	67	**0.039**	no	0.069	no	**0.029**
n-octane	all, raw	86	86	0.180	yes	NA	no	0.073
n-octane	match, raw	86	69	0.321	yes	NA	no	0.374
Ethylbenzene	all, raw	86	86	0.142	yes	NA	no	0.156
Ethylbenzene	match, raw	86	69	0.689	yes	NA	no	0.374
m-*p* xylene	all, raw	86	86	0.944	yes	NA	no	0.805
m-*p* xylene	match, raw	86	69	0.934	yes	NA	no	0.754
o-xylene	all, raw	78	78	0.238	yes	NA	no	0.332
o-xylene	match, raw	78	61	0.207	yes	NA	no	0.254
n-nonane	match, raw	70	55	0.460	yes	NA	no	0.916

D.5.5.3 Short scale variability by seasons

Figure *D.5-16* shows how gas concentrations vary across meteorological seasons for the two stations combined.

NO_2 concentrations in Figure *D.5-16*(a), and O_3 concentrations in Figure *D.5-16*(c), have noticeable seasonal changes similar to the seasonal patterns across all stations shown in Figure *D.5-3*.

NH_3 concentrations in Figure *D.5-16*(b) display clear seasonal pattern that is not apparent across all stations in Figure *D.5-3*(b), with the lowest gas concentrations in spring and the highest NH_3 concentrations in autumn.

Figure *D.5-16*(d) shows minor seasonal variation in SO_2 concentrations similar to Figure *D.5-3*(d).

HNO_3 in Figure *D.5-16*(e) shows a clearer seasonal pattern than in Figure *D.5-3*(e), with low concentrations in summer and high concentrations in winter. Median values increase from summer until winter and then drop slightly in spring, although there is a wide variation of values during that season.

Figure *D.5-17* shows how gas concentrations vary across local Murujuga seasons for the two stations combined.

NO_2 in Figure *D.5-17*(a) and HNO_3 in Figure *D.5-17*(e) show strong seasonal changes similar to the seasonal patterns shown across all stations as shown in Section 7.3 for the local Murujuga seasons. The other gases show only minor seasonal variations, which is similar to the results across all stations for the local Murujuga seasons.

Figure *D.5-18* shows how VOC concentrations vary across meteorological seasons for the two stations combined. Most VOCs show only small variations in median values across these seasons. The exception is Toluene, Figure *D.5-18*(b), where the median values are lowest in spring, and then higher at a similar level for summer, autumn and winter. Some VOCs have different ranges of gas values between seasons. For example, Benzene in Figure *D.5-18*(a) has a wide IQR in summer and autumn. Also N-Octane and M-P-Xylene in Figure *D.5-18*(d) and (e) respectively, have a wide IQR in autumn.

Figure *D.5-19* shows how VOC concentrations vary across Murujuga seasons for the two stations combined. There is little variation in median VOC concentration levels between the Murujuga season for any of the VOCs. The boxplots indicate large numbers of upper outliers which indicates strong skew for the VOC concentrations.

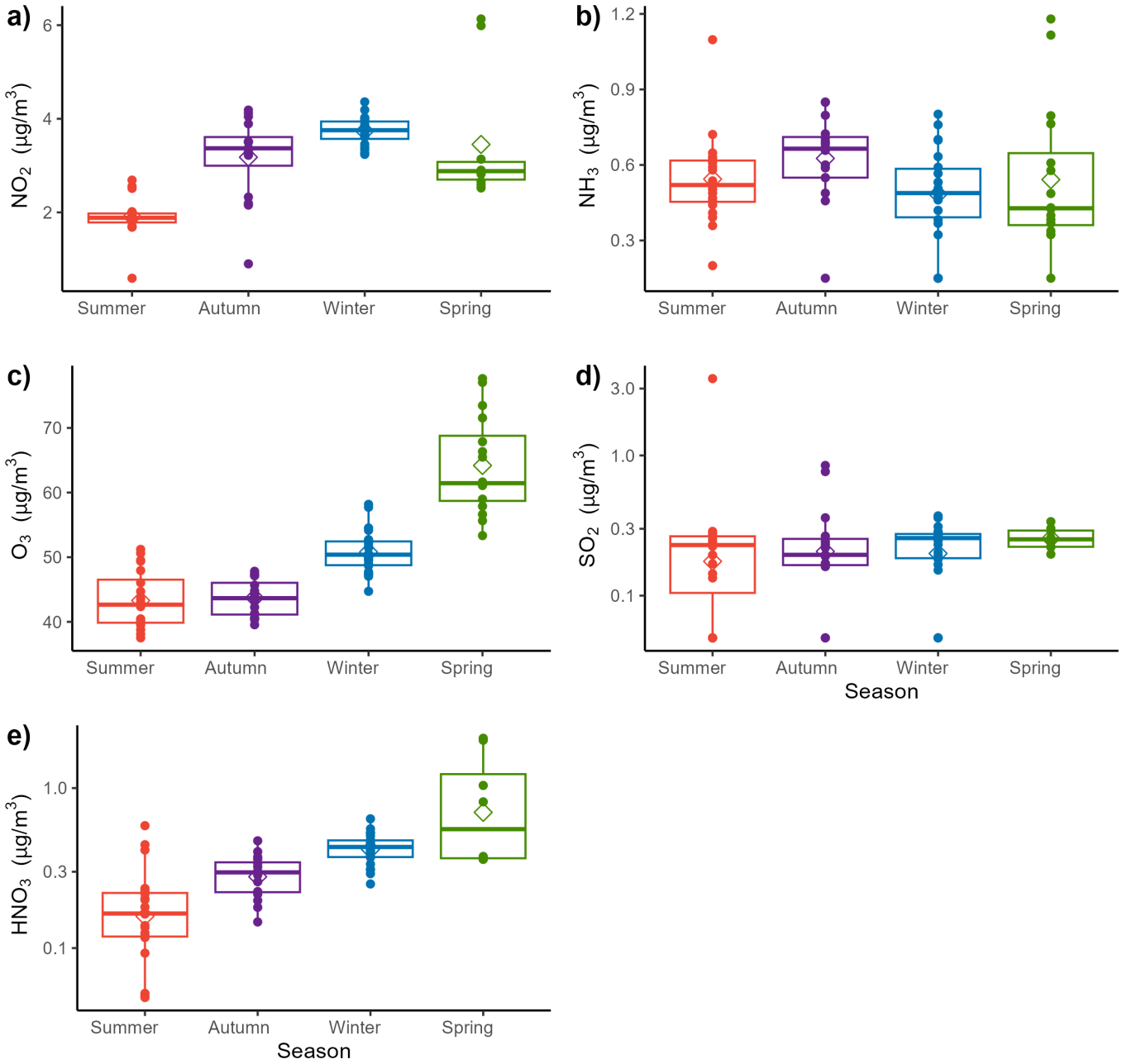

Figure D.5-16: Boxplots of passive sampler gas concentration measurements by meteorological season across both stations AQ07 and AQ08 for gas species (a) NO_2, (b) NH_3, (c) O_3, (d) SO_2 and (e) HNO_3. Panels (d) and (e) use logarithmic scale on vertical axis.

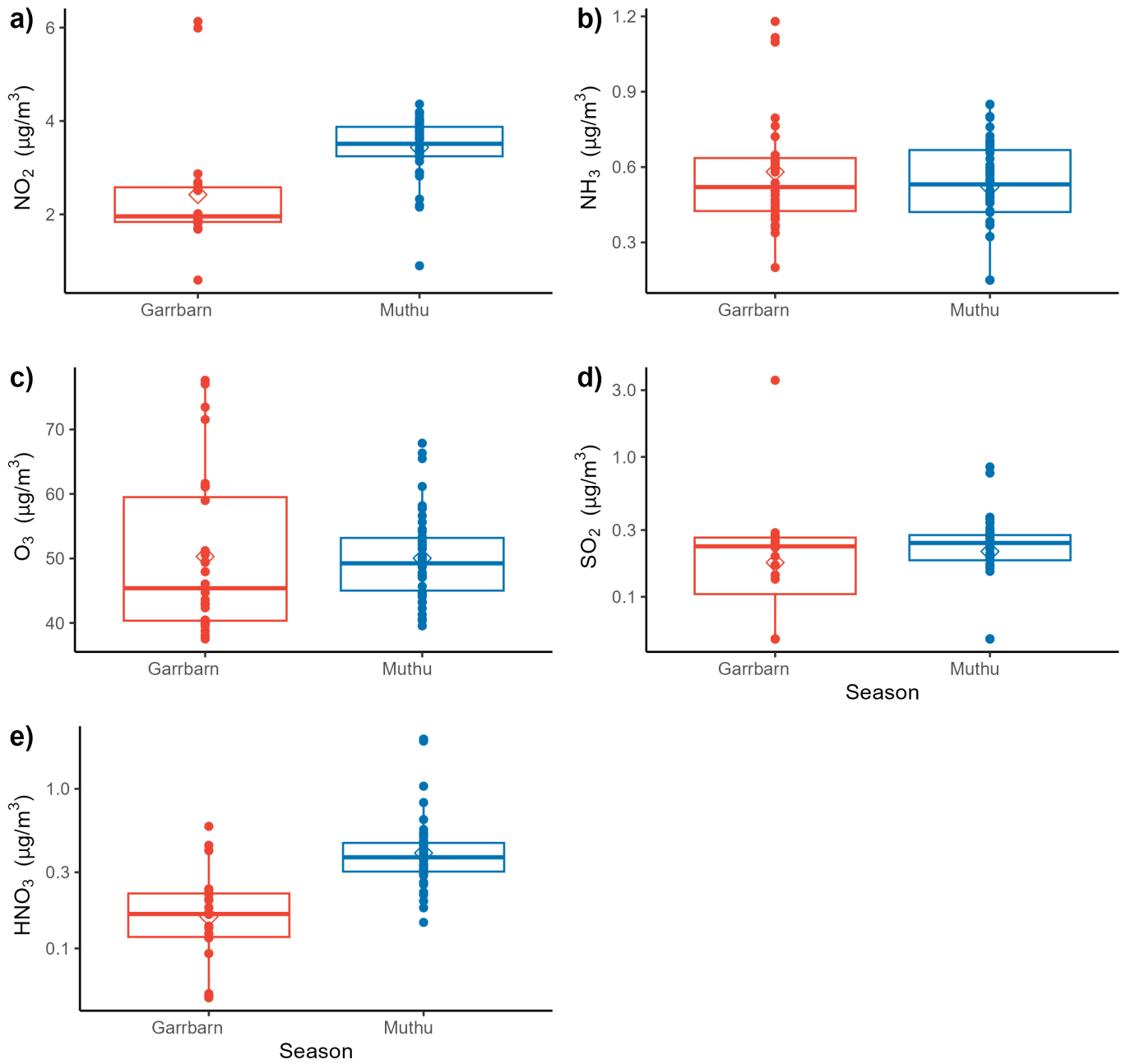

Figure D.5-17: Boxplots of passive sampler gas concentration measurements by Murujuga season across both stations AQ07 and AQ08 for gas species (a) NO_2, (b) NH_3, (c) O_3, (d) SO_2 and (e) HNO_3. Panels (d) and (e) use logarithmic scale on vertical axis.

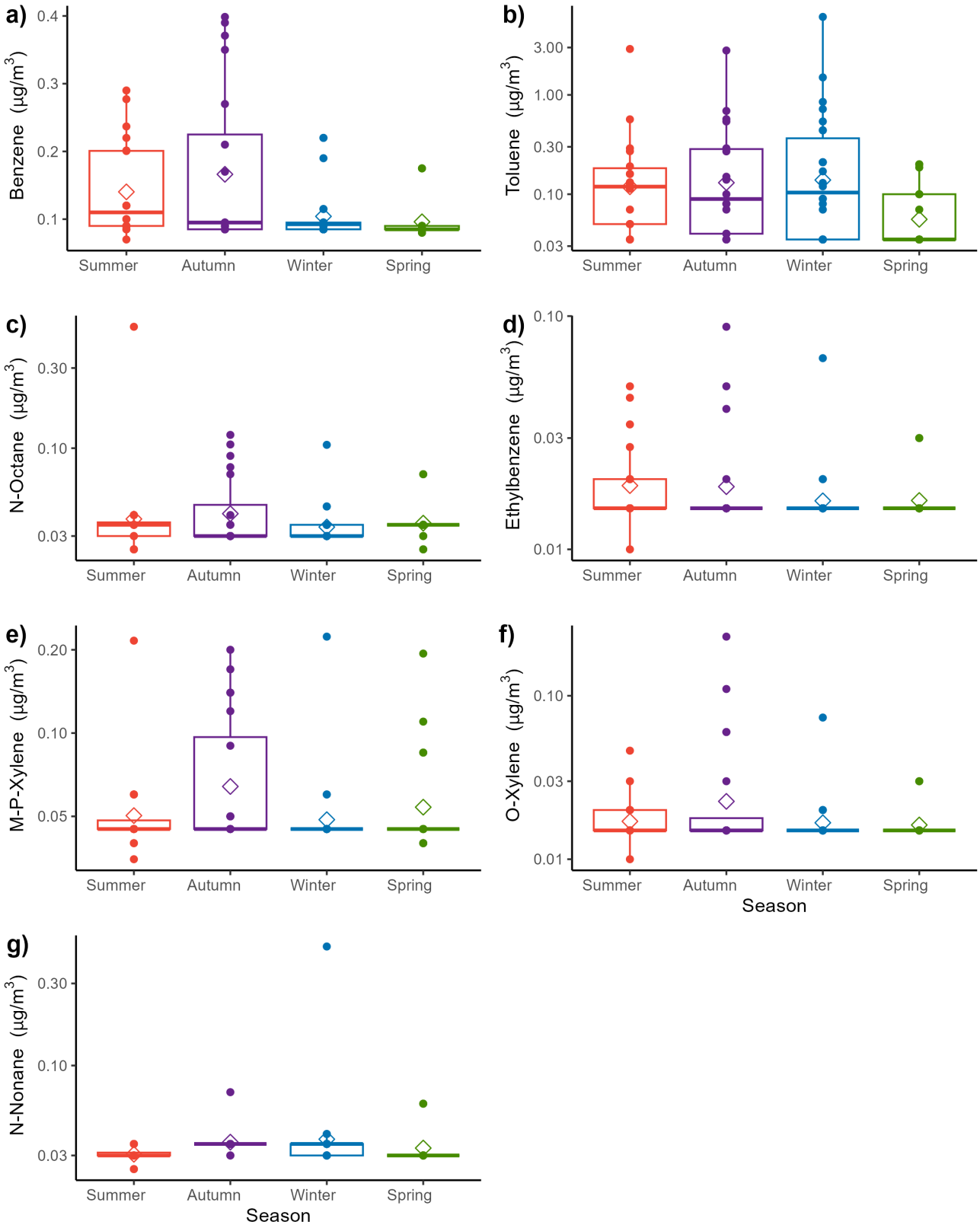

Figure D.5-18: Boxplots of passive sampler gas concentration measurements by meteorological season across both stations AQ07 and AQ08 for VOC species: (a) benzene, (b) toluene, (c) n-octane, (d) ethylbenzene, (e) m-p-xylene, (f) o-xylene, and (g) n-nonane. Panels (b) to (g) (inclusive) use logarithmic scale on vertical axis.

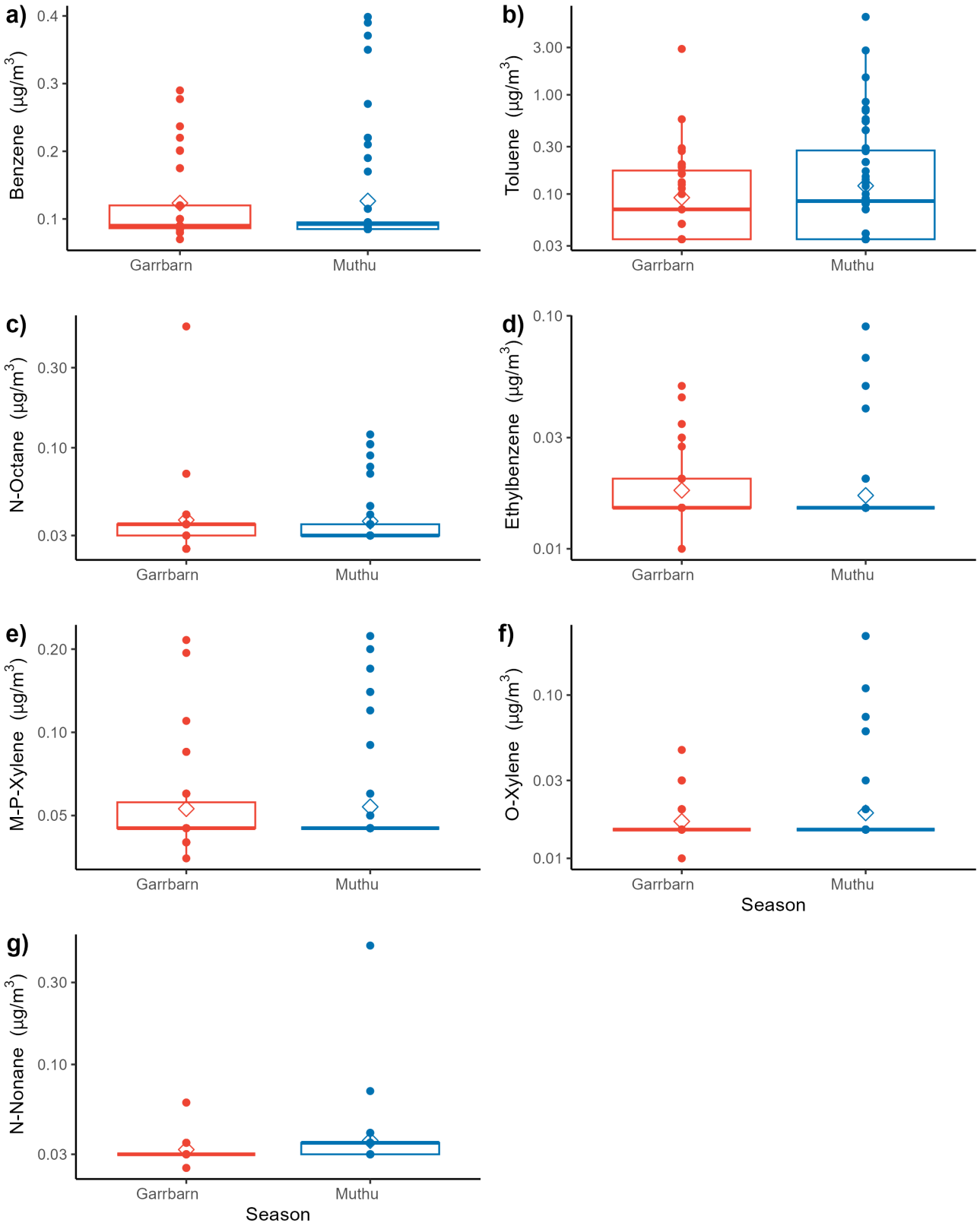

Figure D.5-19: Boxplots of passive sampler gas concentration measurements by Murujuga season across both stations AQ07 and AQ08 for VOC species: (a) benzene, (b) toluene, (c) n-octane, (d) ethylbenzene, (e) m-p-xylene, (f) o-xylene, and (g) n-nonane. Panels (b) to (g) (inclusive) use logarithmic scale on vertical axis.

D.5.5.4 Two way analysis by station and indigenous season

Table *D.5-2* shows the results of the ANOVA investigation of gas concentrations by station and Murujuga season for matched datasets. Data may be either raw (no transformation applied) or rank transformed, which is indicated by the data column. The next two columns show the total number of observations available and the number used in the analysis. The next three columns show the p-value from the ANOVA testing: the first p-value relates to the stations; the second relates to the Murujuga seasons; and the third relates to the combination of station and Murujuga season. The final two columns report on tests relating to two assumptions of ANOVA testing, constant variance and normality of residuals. Constant variance is tested using the Levene test, while normality is tested using the Shapiro-Wilk test. A value of yes means the condition has been met (i.e, there is no evidence that the variance is different or that the residuals are not normal for the 0.05 significance level). If the two conditions are not met, we cannot rely on the results of the ANOVA test.

Table D.5-2: ANOVA results for gas concentrations by sites (AQ07 and AQ08) and Murujuga seasons. The column total observations gives the number of observations for a gas species across both sites, while the column used observations gives the number of observations used by a specific analysis across the two sites. The three columns starting p-value show the strength of supporting evidence for differences in observations for a given factor, where p-values less than 0.05 indicate a significant difference in values, these values are in bold. The three factors are station, season, and station for each season. The final two columns indicate if two key assumptions about the data for the ANOVA analysis are met or not.

Gas	Data	Total Obs.	Used Obs.	p-value Station	p-value Season	p-value Station: Season	Constant Variance	Normal Distribution
NO_2	match	80	62	0.337	0.000	0.069	yes	no
NO_2	match, rank	80	62	0.576	**< 0.0001**	0.176	yes	yes
NH_3	match	92	74	0.122	0.211	0.353	yes	yes
NH_3	match, rank	92	74	0.21	0.595	0.739	yes	no
O_3	match	92	74	0.976	0.905	0.789	yes	no
O_3	match, rank	92	74	0.992	0.235	0.883	yes	no
SO_2	match	81	65	0.178	0.378	0.288	yes	no
SO_2	match, rank	81	65	0.308	0.225	0.675	yes	no
HNO_3	match	84	66	0.297	0.003	0.879	yes	no
HNO_3	match, rank	84	66	0.613	**< 0.0001**	0.355	yes	yes

D.5.5.5 Plots of short scale variability for Indigenous season versus station

Figure *D.5-20* shows boxplots for gas species by Murujuga season and station for the matched datasets.

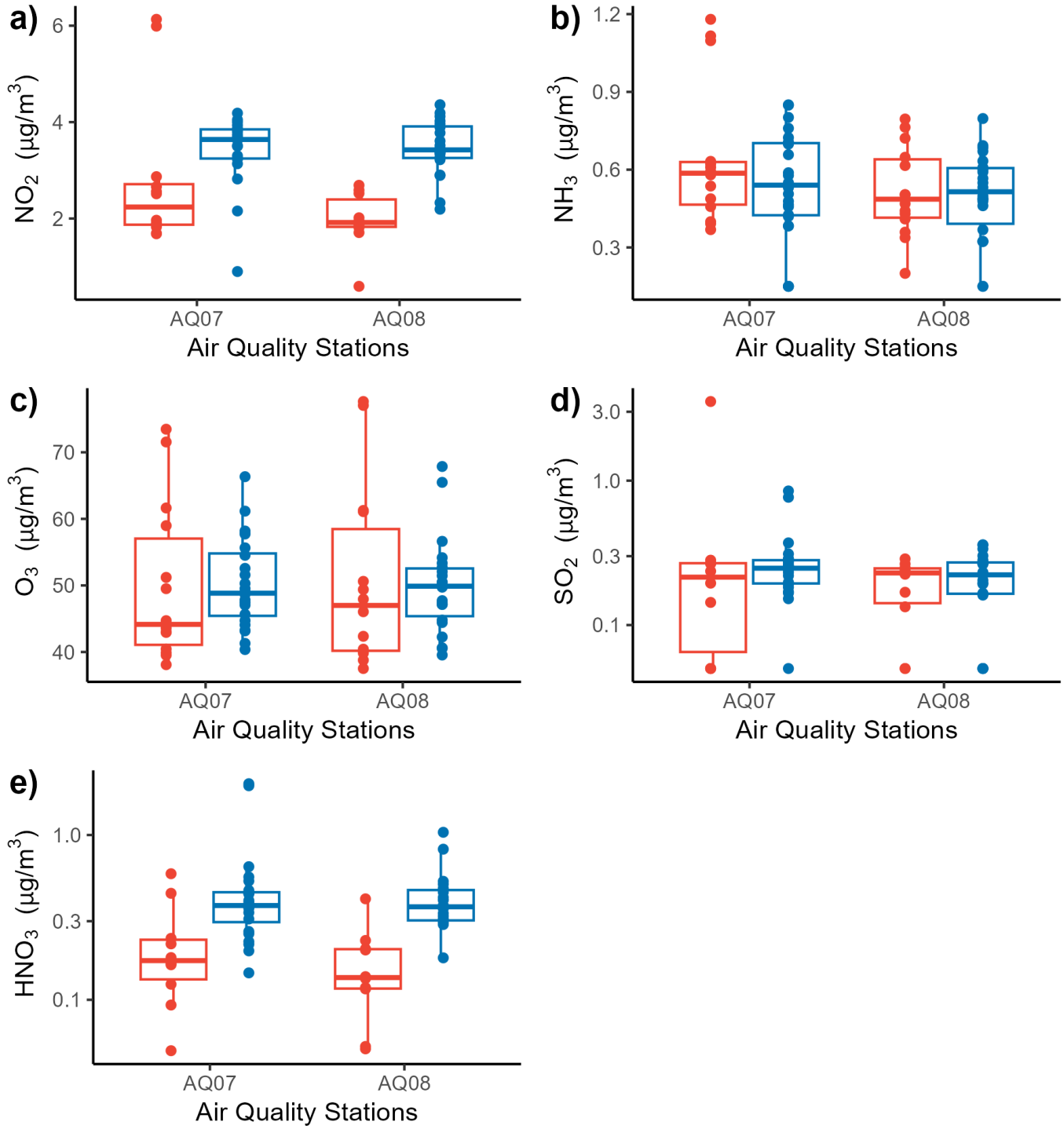

Figure D.5-20: Boxplots of passive sampler gas concentration measurements by station and Murujuga seasons for gas species (a) NO_2, (b) NH_3, (c) O_3, (d) SO_2, and (e) HNO_3. Boxplots for Garrbarn (hot) are in red and boxplots for Muthu (cold) are in blue. Logarithmic scale is used on the vertical axes for SO (d) and HNO_3 (e).

NO_2 concentrations in Figure *D.5-20* (a) show distinct seasonal differences for both stations, with no overlap between the interquartile ranges shown by the boxplots for each season. The IQR for

the same season for the different stations overlap. This suggests there is seasonal variation in gas concentrations, but there are not large differences in the gas concentrations between stations.

NH_3 concentrations in Figure *D.5-20* (b) show little seasonal differences for either station: the IQRs overlap between the two seasons for both stations. The IQRs also overlap between stations. This suggest there is little seasonal or short range variation in gas concentration.

O_3 concentrations in Figure *D.5-20* (c) also shows little seasonal differences for either station: the IQRs shown by the boxplots overlap between the two seasons for both stations. The IQRs also overlaps between stations. This suggests there is little seasonal or short range variation in gas concentration. However Appendix D-4, Figure D-4-20 shows the boxplots by meteorological season, these boxplots suggest there may be some seasonal variation discernible between the meteorological season gas distributions - in particular between spring, winter and summer.

SO_2 concentrations in Figure *D.5-20* (b) show only minor seasonal differences for either station: the IQRs overlap between the two seasons for both stations. The IQRs also overlap between stations. The Garrbarn distribution for AQ07 has a much wider IQR, but the median values are very similar for the two seasons. Median values are also similar between the two stations. This suggests there is little seasonal or short range variation in concentration.

HNO_3 concentrations in Figure *D.5-20* (a) show distinct seasonal differences for both stations, with no overlap between the IQR for each season. The IQR for the same season between the same station overlap. This suggests there is seasonal variation in gas concentration, but there are not large differences in the gas concentrations between stations.

Figure *D.5-21* shows the boxplots for VOC species by Murujuga season and station for the matched dataset. Logarithmic scale is used on the vertical axes for all plots.

Benzene concentrations in Figure *D.5-21* (a) show only minor seasonal differences for either station: the interquartile ranges largely overlap between the two seasons for both stations. The interquartile range also overlaps between stations. However, the Muthu distribution for AQ07 has a narrower and slightly lower interquartile range than the Garrbarn distribution, although the median values are very similar for the two seasons. Median values are also similar between the two stations. This suggests there is little seasonal or short range variation in benzene concentration.

Toluene concentrations in Figure *D.5-21* (b) show some seasonal differences for both stations: the interquartile range largely overlaps between the two seasons for both stations, however for AQ08, the Muthu interquartile range is much wider than the Garrbarn interquartile range. There are also noticeable differences between the median values between seasons for each station and also between the same season for different stations. This suggests there is may be some seasonal and short range variations in toluene concentration.

N – octane concentrations in Figure *D.5-21* (c) show some seasonal differences for both stations: for AQ08 the Garrbarn interquartile range is much narrower than the interquartile range for Muthu; and for AQ07 the interquartile range for Garrbarn is wider than for Muthu. There are also noticeable differences between median values between seasons for each station but the medians are similar for each season between the two stations. This suggests there may be some seasonal variation but little short range variations in n-octane concentration.

Ethylbenzene concentrations in Figure *D.5-21* (d) show some minor seasonal differences for AQ08

where the interquartile range for Garrbarn is wider than for Muthu. However, the median values are very similar across seasons and stations.

O – xyline concentrations in Figure *D.5-21* (f) follow a very similar pattern to ethylbenzene concentrations. This suggests there is little seasonal or short range variation in the concentrations of ethylbenzene and o-xylene.

M – *p* xylene concentrations in Figure *D.5-21* (e), have a similar pattern, except that the widest interquartile range is observed for Garrbarn at AQ07. As for the previous VOCs, there is no difference in median values across stations or seasons, which suggests again that there is little seasonal or short range variation.

N – nonane concentrations in Figure *D.5-21* (g) show some minor seasonal differences for both stations: the interquartile ranges are slightly wider during Muthu for both AQ07 and AQ08. Further, the median values for Muthu are slightly higher than for Garrbarn. The median values are similar for each season for the two stations. This suggests there may be some seasonal variation in n-nonane concentration but no discernible variations between the stations.

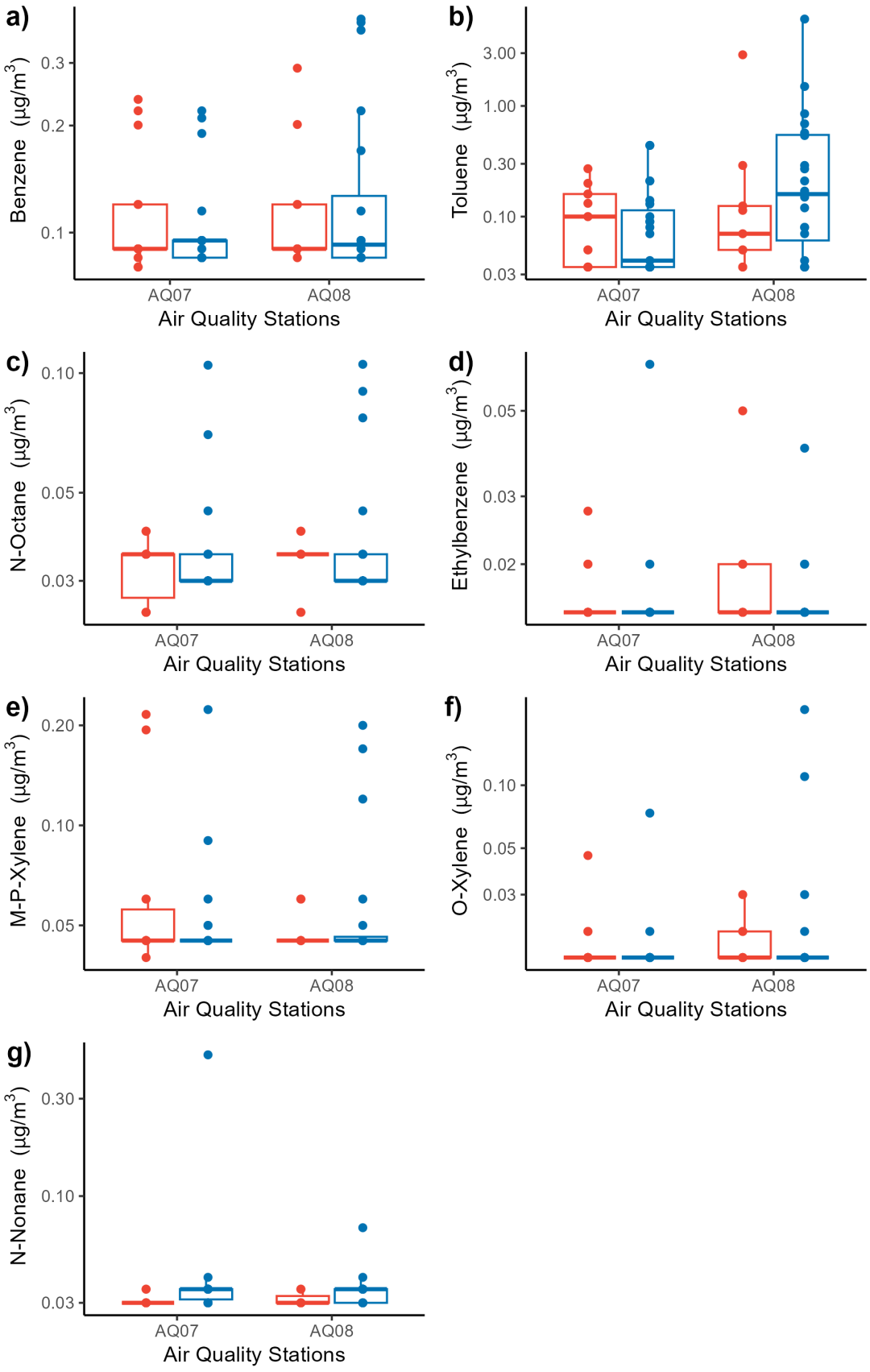

Figure D.5-21: Boxplots of passive sampler gas concentration measurements by station and Murujuga season for VOC species (a) benzene, (b) toluene, (c) n-octane, (d) ethylbenzene, (e) m-p-xylene, (f) o-xylene, and (g) n-nonane.

D.5.5.6 Two way analysis by station and meteorological season

Table *D.5-3* shows the results of the two-way ANOVA analysis for the gases. None of the gases indicate variability in concentrations between stations. These tests are conducted on matched data (i.e. only data when the sampling periods for both stations coincide used) for either raw (untransformed) data or rank transformed data. NO_2, O_3, and HNO_3 indicate variability between the seasons. None of the gases indicate variability in concentrations for season-stations combinations. Not all these tests meet the assumptions of constant variance and normality. However, analysis of the matched-ranked data for NO_2, NH_3, O_3, and SO_2 satisfy both these assumptions, and the results of these tests may be considered valid. The matched (non-ranked or raw) NH_3 data also satisfies the two requirements. HNO_3 data does not meet the assumptions for either matched-ranked or matched data; hence the results for this gas can only be considered suggestive.

Table D.5-3: Results of ANOVA analysis of gas concentrations by sites (AQ07 and AQ08) and meteorological seasons. The column total observations gives the number of observations for a gas species across both sites, while the column used observations gives the number of observations used by a specific analysis across the two sites. The three columns starting ANOVA p-value shows the strength of supporting evidence for differences in observations for a given factor, where p-values less than 0.05 indicate a significant difference in values. The three factors are station, season, and station for each season. The final two columns indicate if two key assumptions about the data for the ANOVA analysis are met or not.

Gas	Data	Total Observation	Used Observation	Anova p-value Station	Anova p-value Season	Anova p-value Station: Season	Constant Variance	Normal Distribution
NO_2	match	80	62	0.246	0.000	0.147	Yes	No
NO_2	match, rank	80	62	0.495	0.000	0.416	Yes	Yes
NH_3	match	92	74	0.127	0.221	0.954	Yes	Yes
NH_3	match, rank	92	74	0.198	0.062	0.897	Yes	Yes
O_3	match	92	74	0.953	0.000	0.890	No	Yes
O_3	match, rank	92	74	0.986	0.000	0.926	Yes	Yes
SO_2	match	81	65	0.190	0.825	0.668	Yes	No
SO_2	match, rank	81	65	0.311	0.327	0.680	Yes	Yes
HNO_3	match	84	66	0.187	0.000	0.057	No	No
HNO_3	match, rank	84	66	0.569	0.000	0.572	Yes	No

Table *D.5-4* shows the results of the two way ANOVA analysis for the VOCs. These tests are conducted on matched data for raw and rank transformed data. Generally, these results don't indicate significant differences for gas concentrations between stations with the exception of Toluene. A number of VOCs indicate seasonal variations including Benzene, Toluene, EthylBenzene and N Octane. However, the assumption of normality of the residuals is not met for either matched or matched-ranked data. Hence the test cannot be considered valid: results are suggestive only.

Table D.5-4: Results of ANOVA analysis of VOC concentrations by sites (AQ07 and AQ08) and meteorological seasons. The column total observations gives the number of observations for a gas species across both sites, while the column used observations gives the number of observations used by a specific analysis across the two sites. The three columns starting ANOVA p-value shows the strength of supporting evidence for differences in observations for a given factor, where p-values less than 0.05 indicate a significant difference in values. The three factors are station, season, and station for each season. The final two columns indicate if two key assumptions about the data for the ANOVA analysis are met or not.

VOC	Data	Total Observation	Used Observation	Anova p-value Station	Anova p-value Season	Anova p-value Station: Season	Constant Variance	Normal Distribution
Benzene	match	86	69	0.062	0.026	0.052	No	No
Benzene	match, rank	86	69	0.413	0.007	0.281	Yes	No
Toluene	match	82	67	0.041	0.469	0.471	Yes	No
Toluene	match, rank	82	67	0.016	0.049	0.115	Yes	No
Octane	match	86	69	0.309	0.230	0.185	Yes	No
Octane	match, rank	86	69	0.379	0.549	0.669	Yes	No
EBenz	match	86	69	0.693	0.578	0.519	Yes	No
EBenz	match, rank	86	69	0.357	0.041	0.629	Yes	No
MP Xylene	match	86	69	0.933	0.587	0.172	Yes	No
MP Xylene	match, rank	86	69	0.747	0.059	0.741	Yes	No
O Xylene	match	78	61	0.192	0.295	0.107	Yes	No
O Xylene	match, rank	78	61	0.244	0.129	0.255	Yes	No
Nonane	match	70	55	0.476	0.709	0.816	Yes	No
Nonane	match, rank	70	55	0.901	0.000	0.915	Yes	No

D.5.5.7 Plots of short scale variability for meteorological season versus station

Figure *D.5-22* shows how gases are distributed across meteorological seasons for the two stations.

NO_2 concentrations in Figure *D.5-22*(a) have a seasonal pattern that is similar for both stations. Gas concentrations are low in summer and increase to high values in winter and spring. The median gas concentration decreases in spring from the high winter level, though there may be outliers resulting in a large range in concentrations for AQ07.

O_3 concentrations in Figure *D.5-22*(c) have a distinct seasonal pattern that is similar for both stations. Gas concentrations are low in summer and autumn, and high in spring.

SO_2 concentrations in Figure *D.5-22*(d) and NH_3 concentrations in Figure *D.5-22*(c) show little variation between seasons.

HNO_3 concentrations in Figure *D.5-22*(e) shows a distinct seasonal pattern that is similar for both stations. HNO_3 concentrations are low in summer and high in spring, with levels increasing throughout the intervening seasons.

Figure *D.5-23* shows how gases are distributed across meteorological seasons for the two stations. Most VOCs, see Figure *D.5-23* (c) to (g) inclusive, show little seasonal variability in median values. Though the interquartile ranges may indicate some differences in range, the medians tend to be similar for each season and the absolute differences in concentration are quite small. Benzene, Figure *D.5-23*(a) has high concentrations in summer for AQ07, but concentrations for AQ08 are high in summer and autumn and low in winter and spring. This may indicate some variability in measurements between the stations. Toluene, Figure *D.5-23*(b) shows lower concentrations in spring than in the other three months.

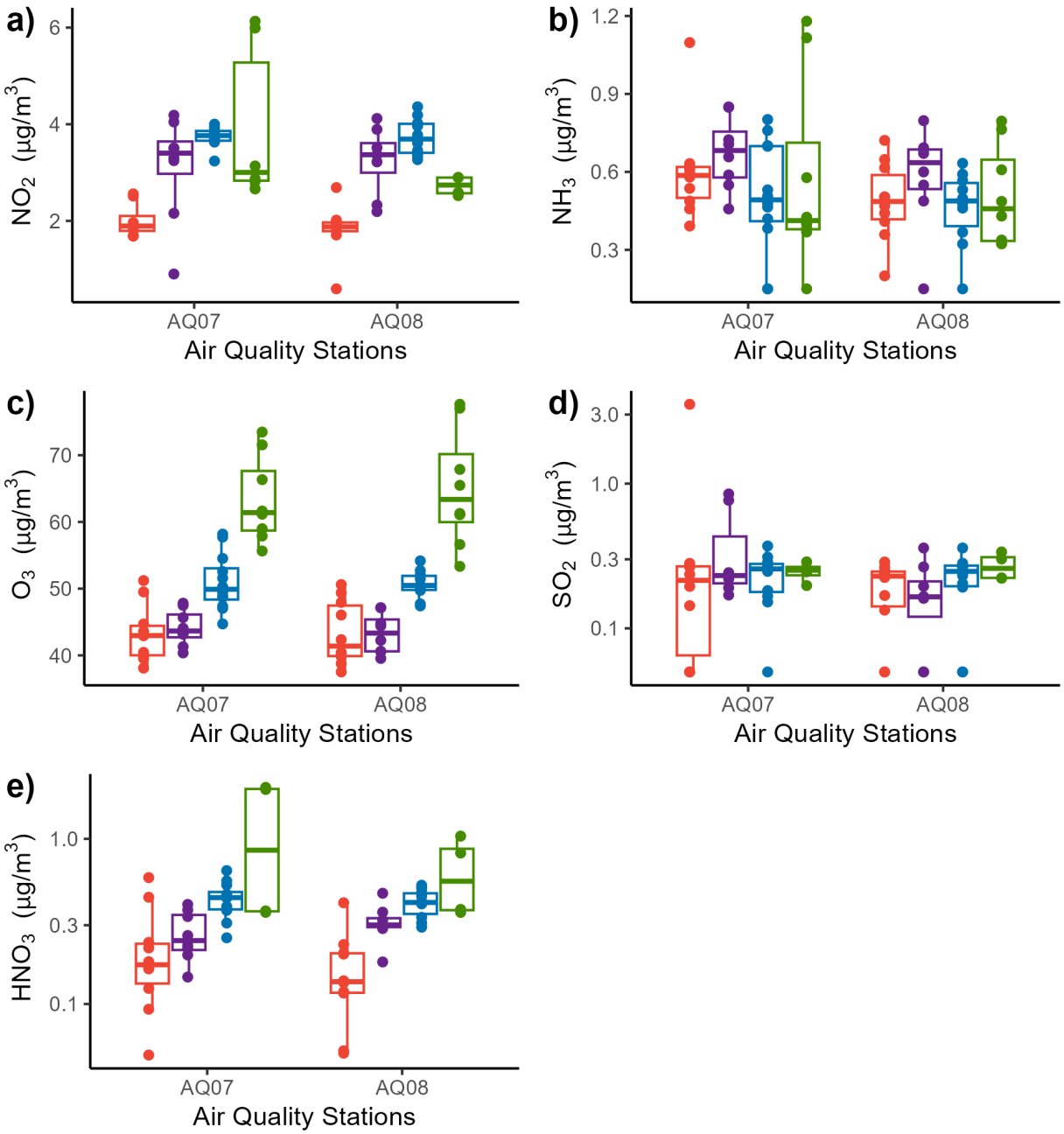

Figure D.5-22: Boxplots of passive sampler gas concentration measurements by station and meteorological season for gases species (a) NO_2, (b) NH_3, (c) O_3, (d) SO_2 and (e) HNO_3. Panels (d) and (e) use logarithmic scale on horizontal axis.

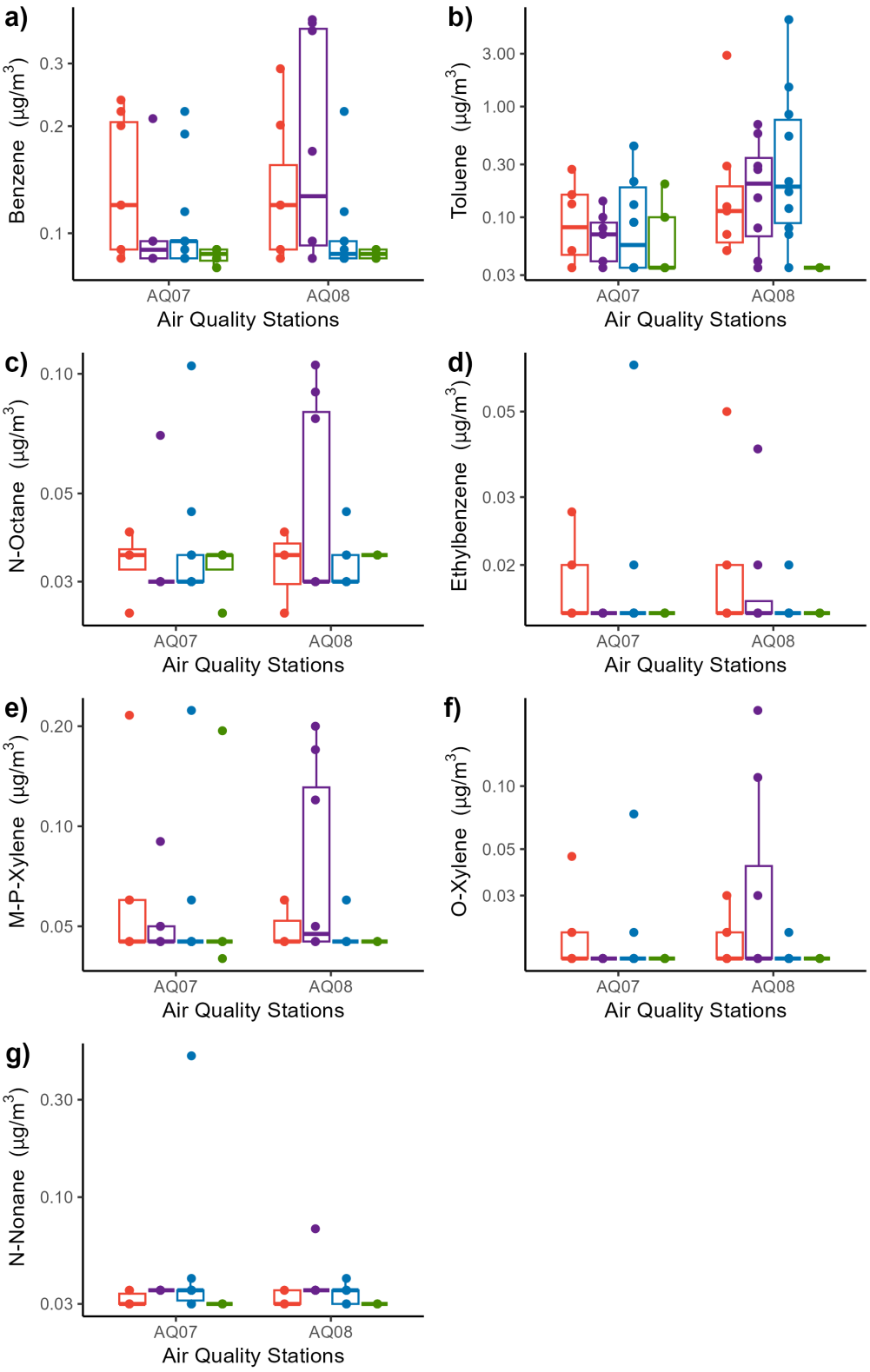

Figure D.5-23: Boxplots of passive sampler gas concentration measurements by station and meteorological season for VOC species (a) benzene, (b) toluene, (c) n-octane, (d) ethylbenzene, (e) m-p-xylene, (f) o-xylene, and (g) n-nonane. All panels use logarithmic scale on vertical axis.

D.5.6 Spatial Analysis

Figures *D.5-24* to *D.5-28* show the spatial smooths generated from aggregated data from the passive sampler IVL observations. Passive sampler data is assigned a calendar month based on the month in which the majority of days of the sampling period falls. These plots show monthly aggregated gas concentrations for 2024 only: data from previous years is not included. These plots provide a snap shot of gas concentrations for specific time period and variations from overall seasonal patterns. For instance in Figures *D.5-25* shows an unusual decrease in NH_3 concentrations in August 2024, while neighbouring sampling periods show higher concentrations.

Figures *D.5-29* and *D.5-33* show the spatial smooths generated from ranked gas concentration data for passive sampler data aggregated by meteorological season. Passive sample data is drawn from all available sampler observations from November 2022 to December 2024. These plots indicate patterns of relatively high concentrations to relatively concentrations of each gas by season. Using ranked data, which is ranked from 0 to 1 for each season overcomes issues with large changes in absolute gas values that may obscure relative changes in spatial plots of absolute gas concentration values.

NO_2 in Figure *D.5-29* shows a consistent pattern for ranked data with the highest ranks lying close to the Dampier port area in the centre of the Burrup peninsula.

NH_3 in Figure *D.5-30* shows a similar pattern of ranked data, with high ranks usually grouped close to the Dampier port area, but with some high ranks also present in outlying areas that differ with season.

O_3 in Figure *D.5-31* shows a consistent pattern of ranked data, low to medium ranks generally falling to the centre or south of the Burrup peninsula and high ranks in the northern Murujuga area. Some high ranks also present on western or southern islands depending on the season.

SO_2 in Figure *D.5-32* shows a variable pattern across seasons. For winter and spring, concentrations tend to be highest round the Dampier port area, or just north of that area. In summer the highest ranks are concentrated in the Northern part of the Murujuga area while in autumn the highest ranks tend to be concentrated in the south-western islands.

HNO_3 in Figure *D.5-33* also shows a variable pattern across seasons. In winter and autumn the concentrations tend to be highest round the Dampier port area, while in spring the port area has more moderate ranks, while higher ranks are found south or north of this area. In summer the highest ranks are concentrated in the southern part of the Murujuga area.

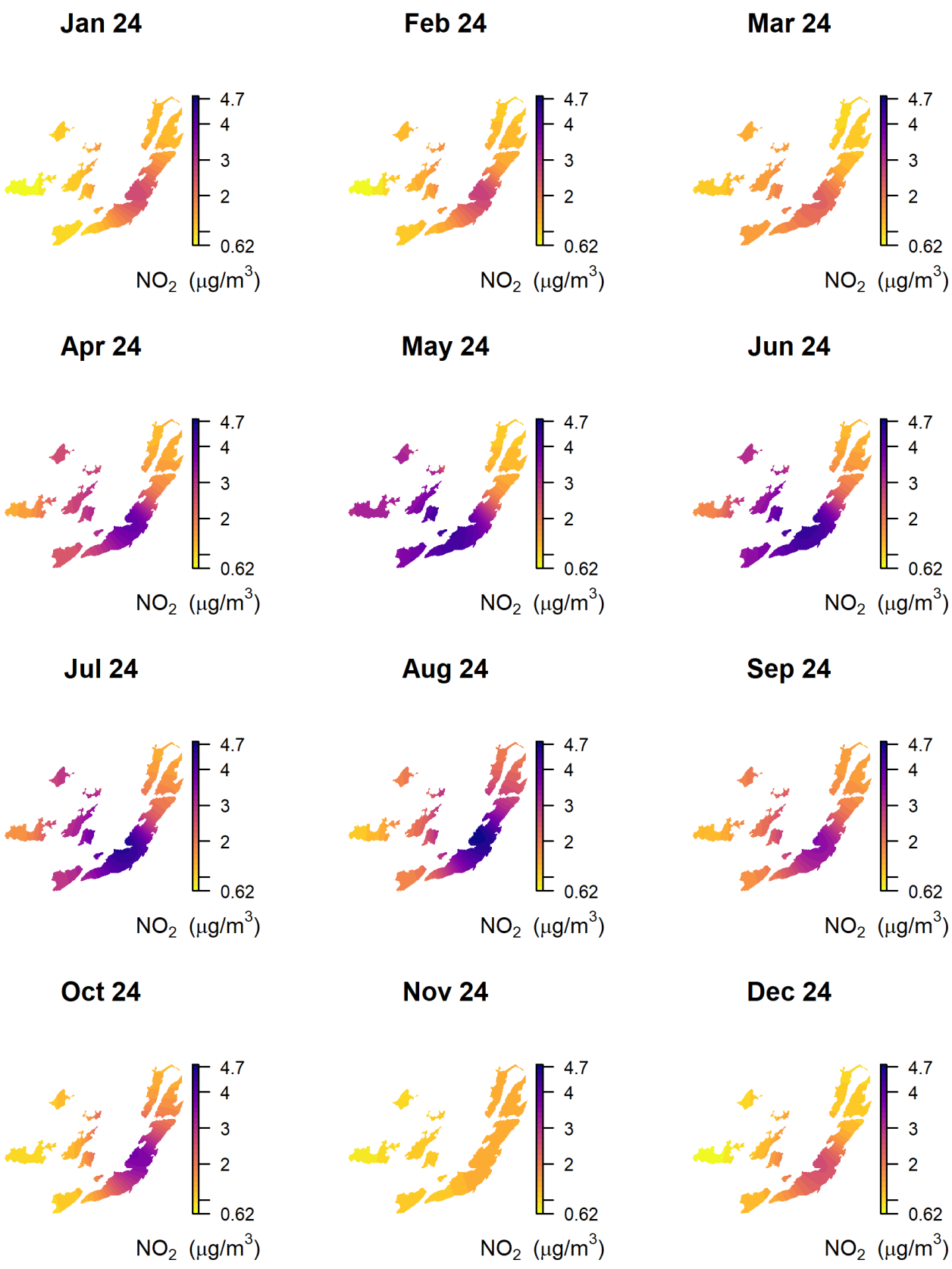

Figure D.5-24: Spatially smoothed monthly average concentration of NO_2 by majority month for 2024. Common colour map based on percentiles.

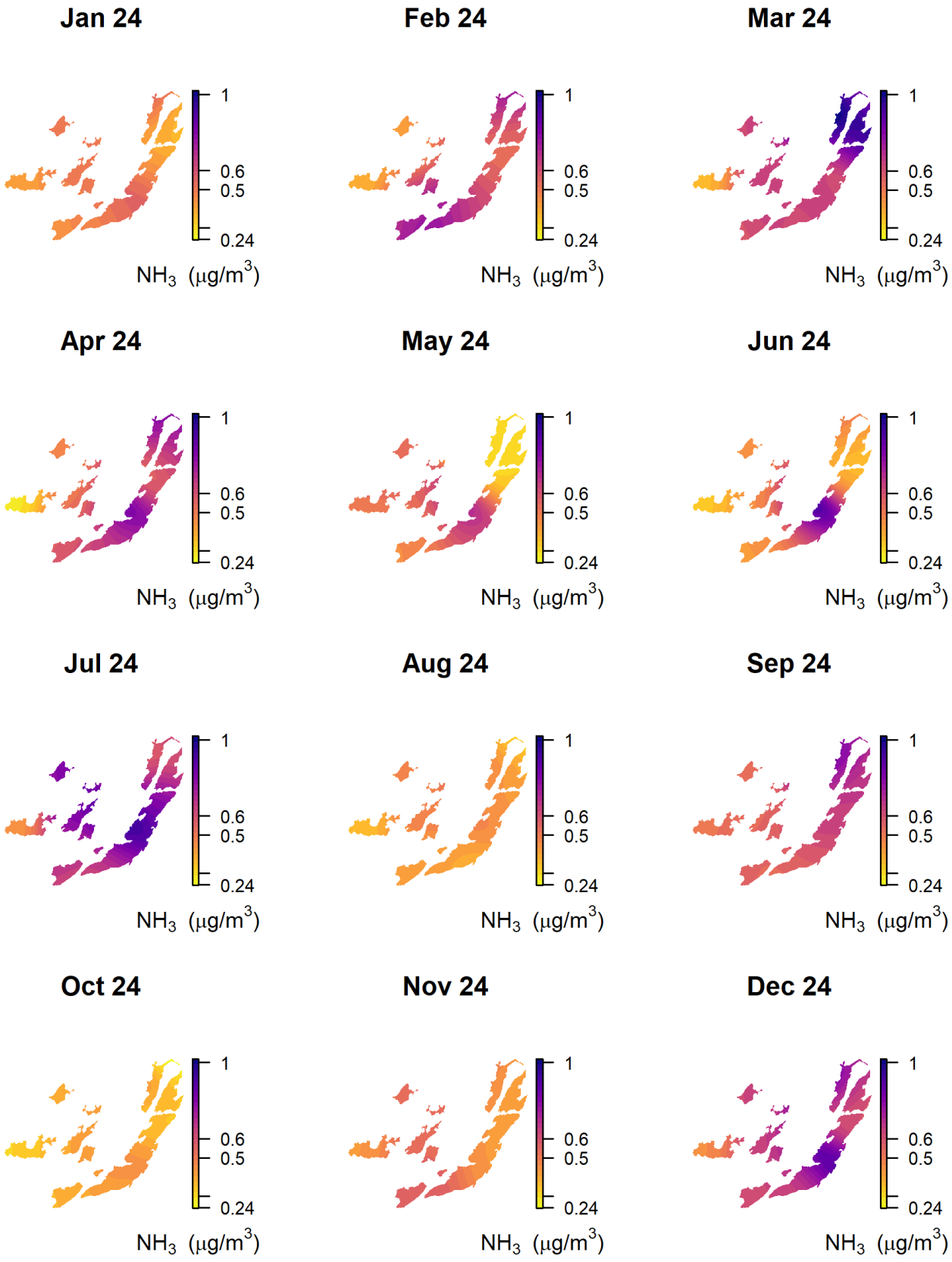

Figure D.5-25: Spatially smoothed monthly average concentration of NH_3 by majority month for 2024. Common colour map based on percentiles.

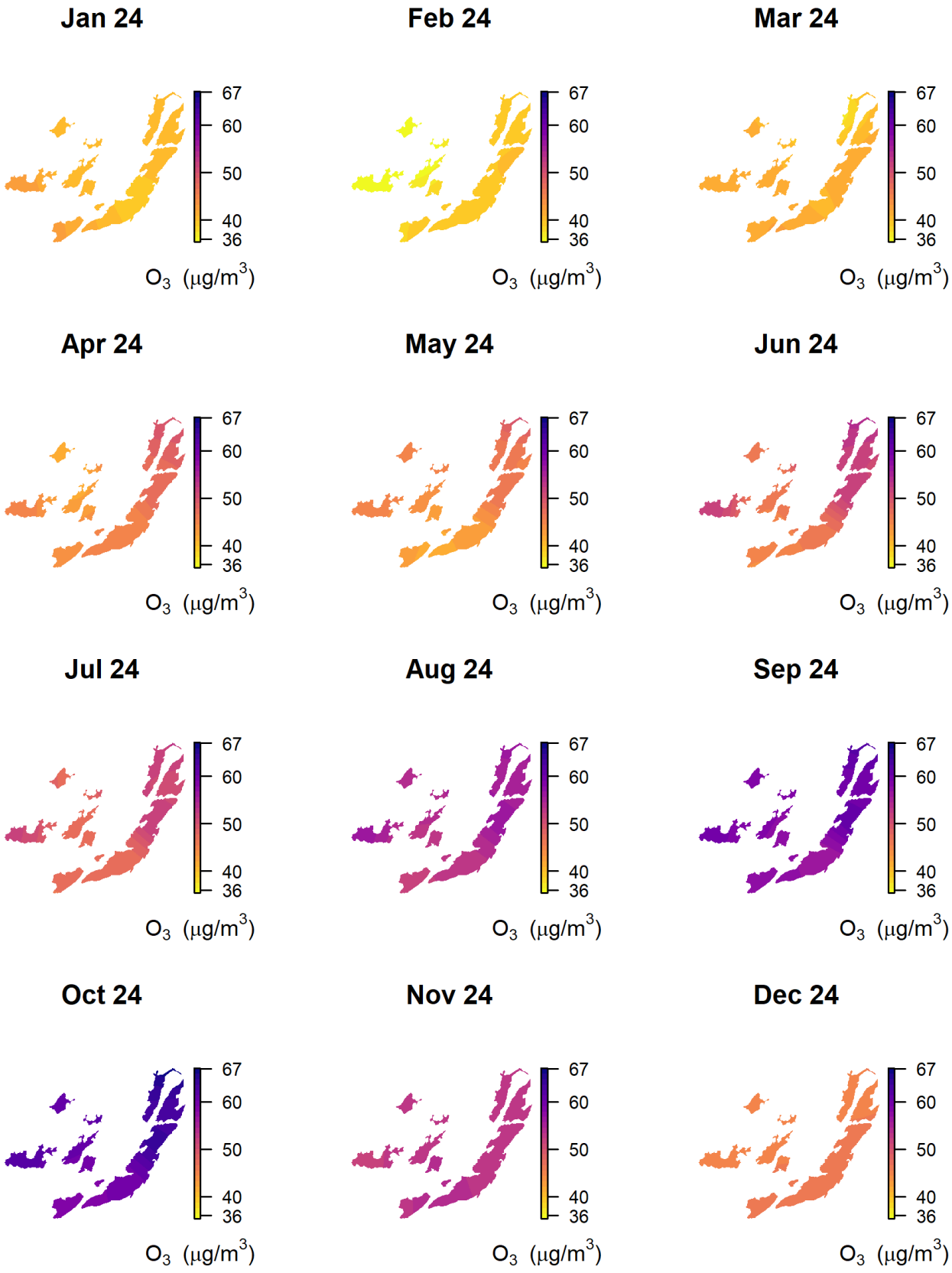

Figure D.5-26: Spatially smoothed monthly average concentration of O_3 by majority month for 2024. Common colour map based on percentiles.

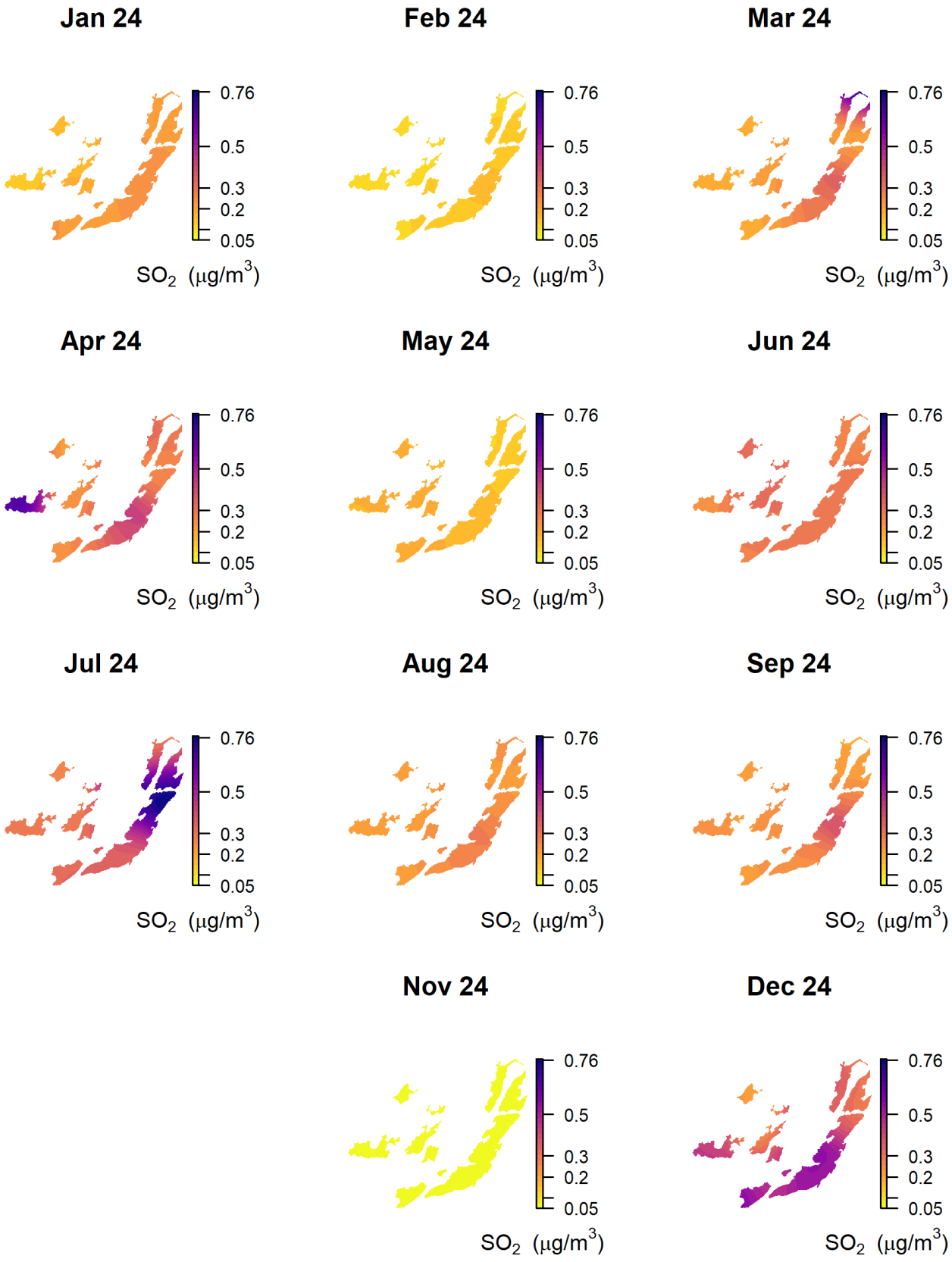

Figure D.5-27: Spatially smoothed monthly average concentration of SO_2 by majority month for 2024. Common colour map based on percentiles.

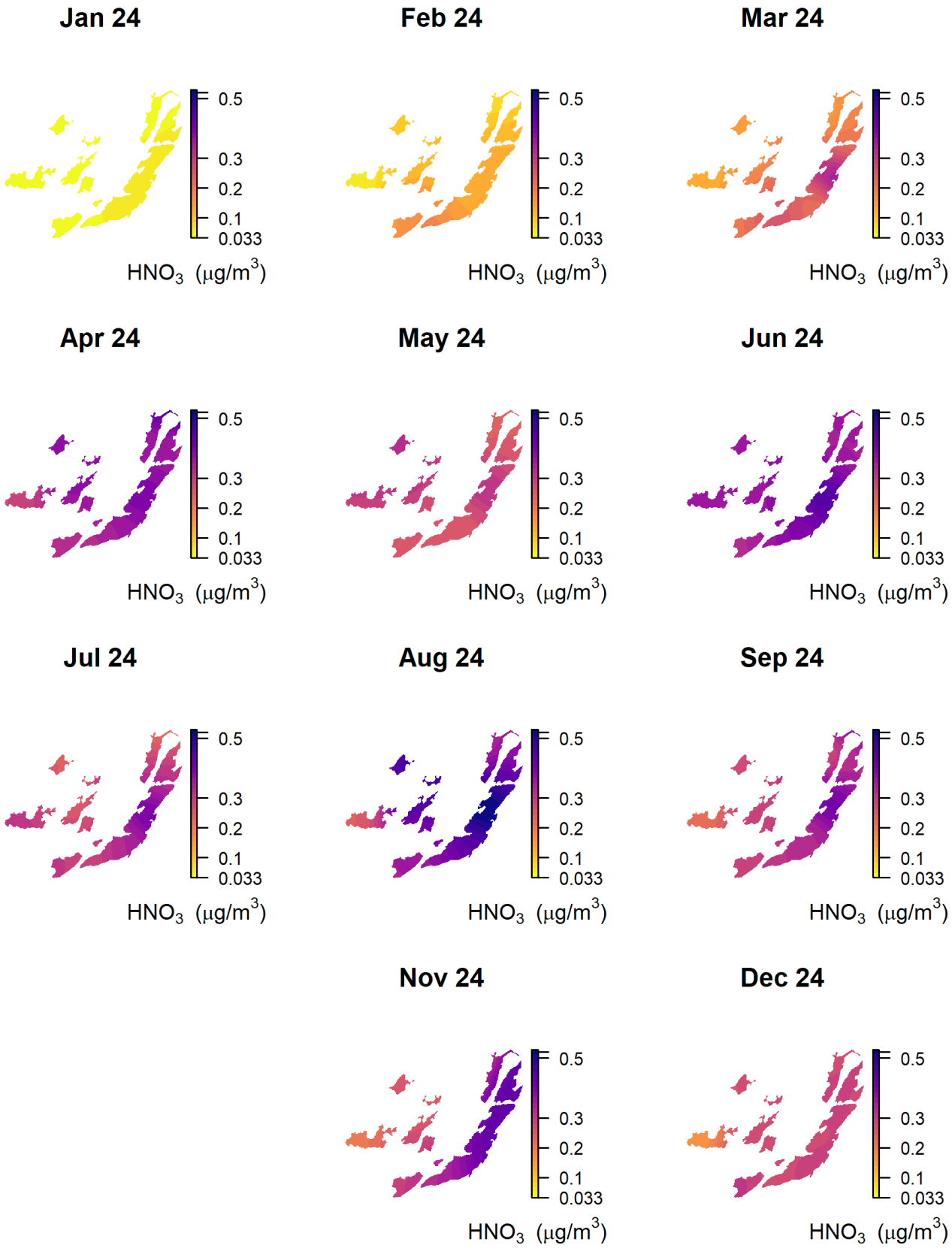

Figure D.5-28: Spatially smoothed monthly average concentration of HNO_3 by majority month for 2024. Common colour map based on percentiles.

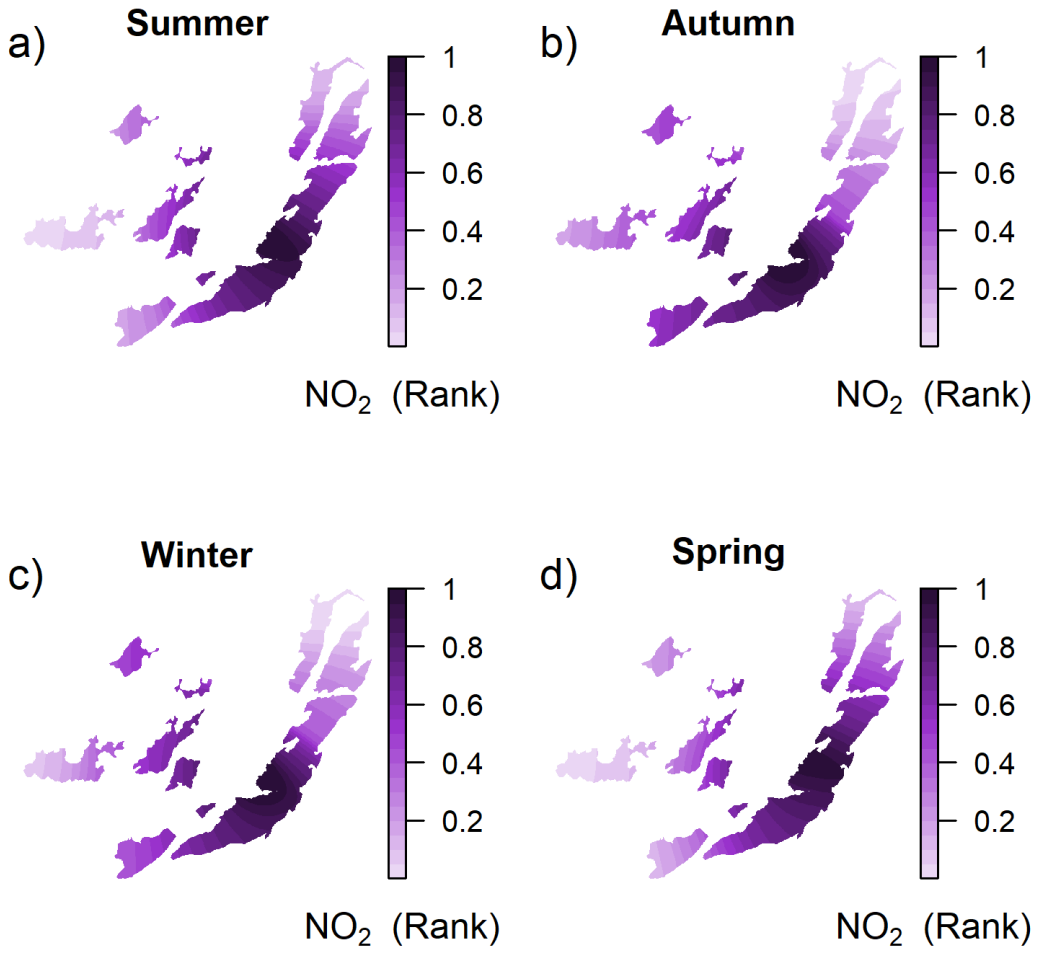

Figure D.5-29: Assessment of concordance between spatial patterns of NO_2 concentration in different seasons, estimated from spatially smoothed passive sampler data.

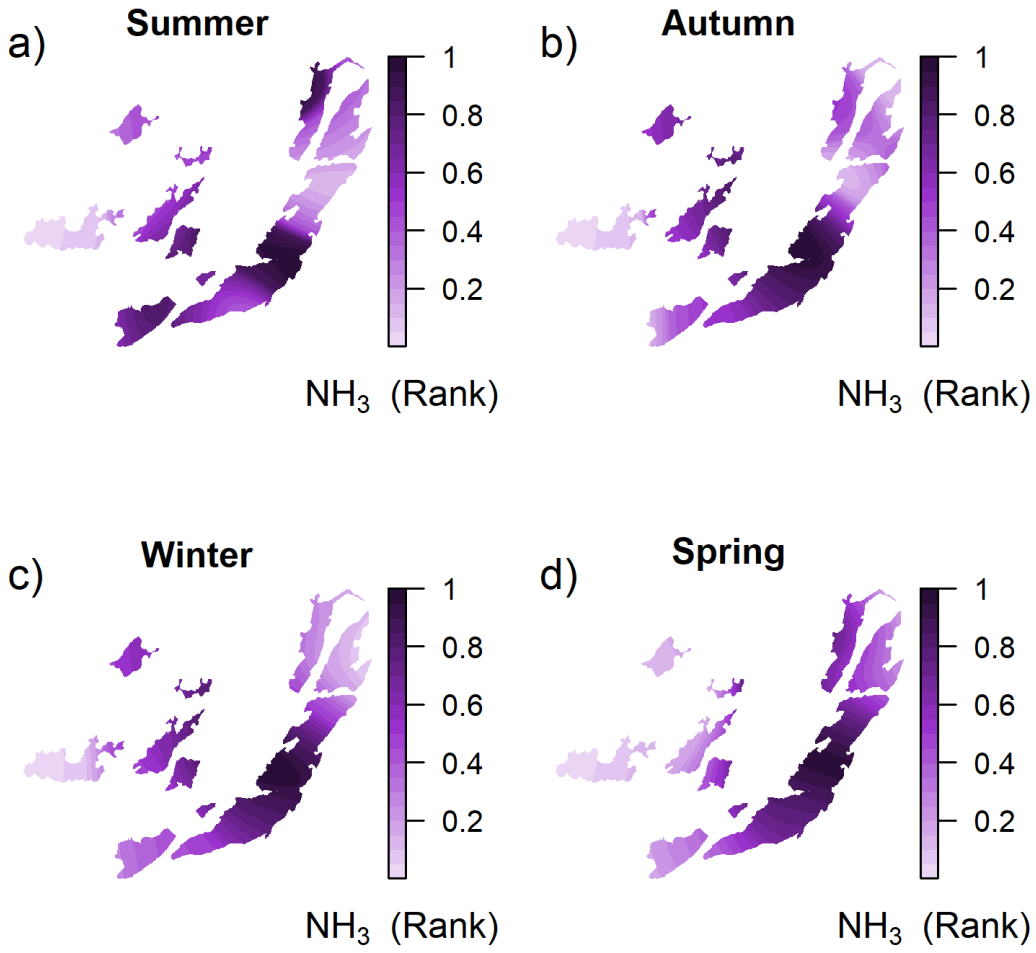

Figure D.5-30: Assessment of concordance between spatial patterns of NH_3 concentration in different seasons, estimated from spatially smoothed passive sampler data.

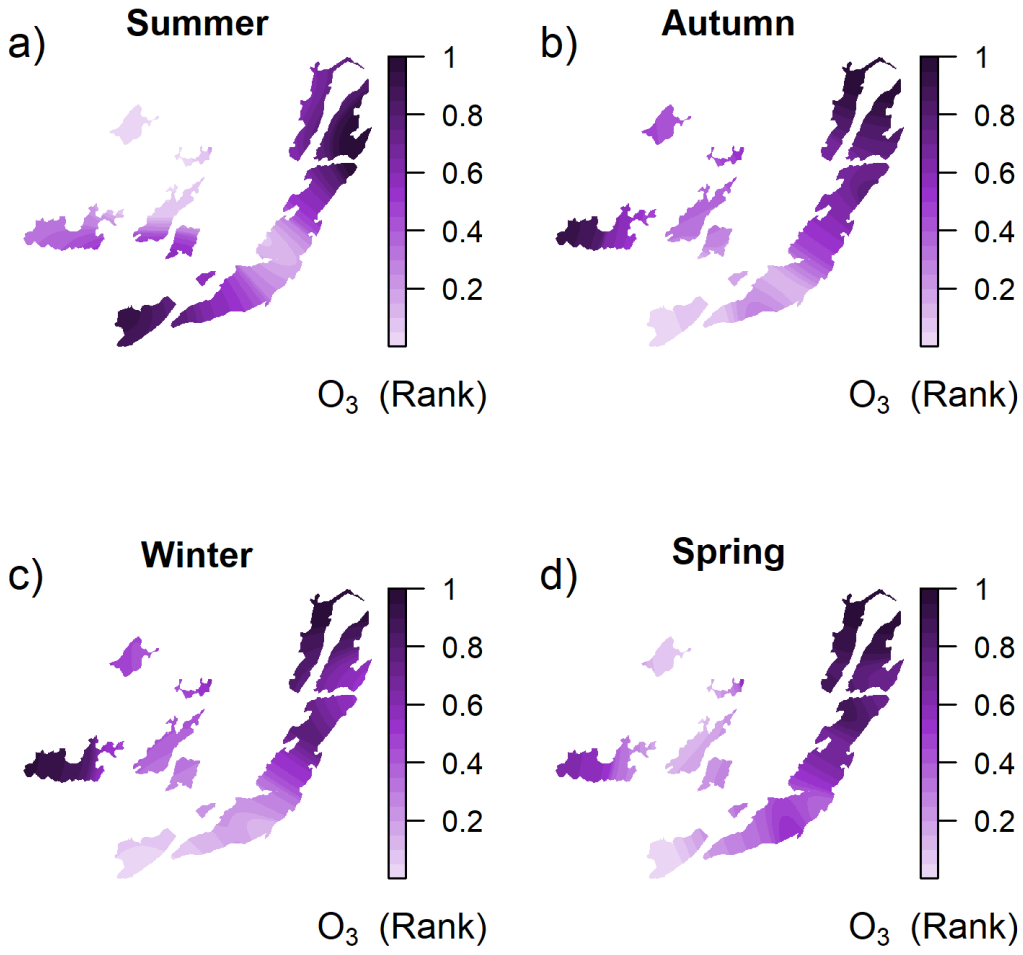

Figure D.5-31: Assessment of concordance between spatial patterns of O_3 concentration in different seasons, estimated from spatially smoothed passive sampler data.

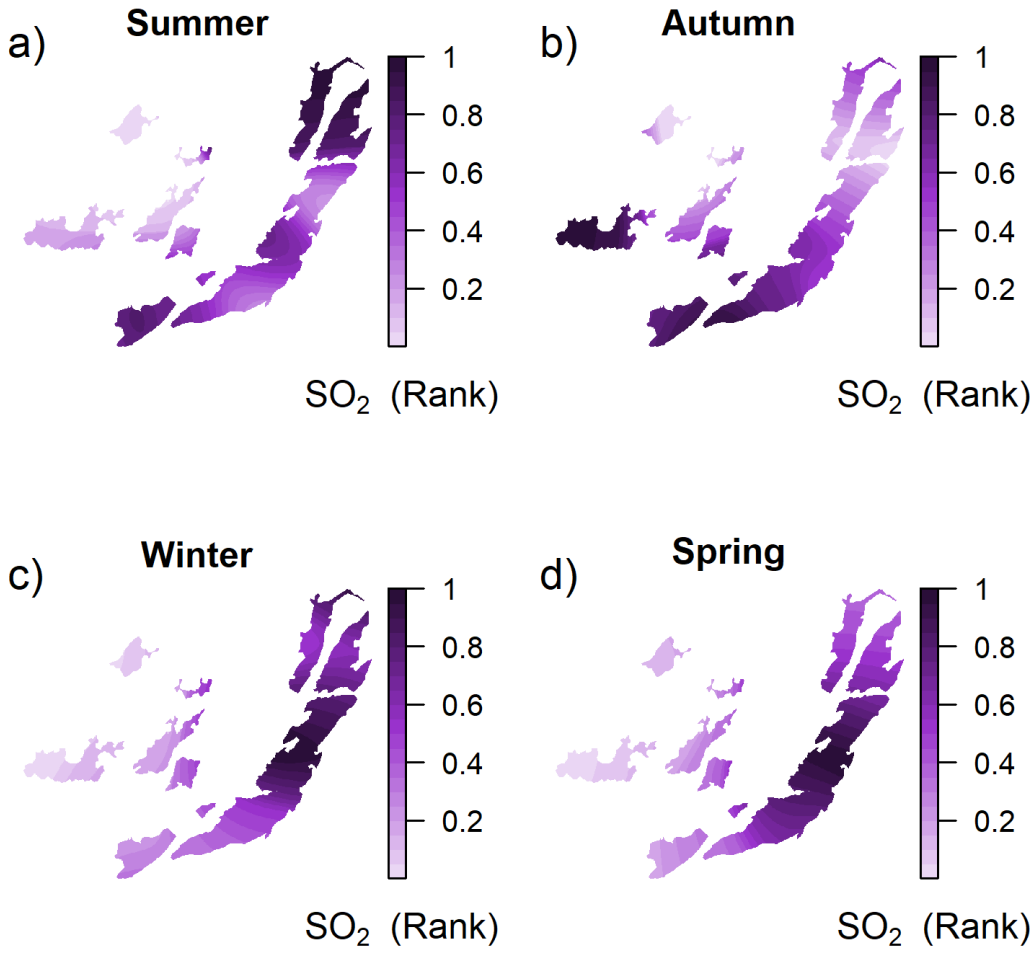

Figure D.5-32: Assessment of concordance between spatial patterns of SO_2 concentration in different seasons, estimated from spatially smoothed passive sampler data.

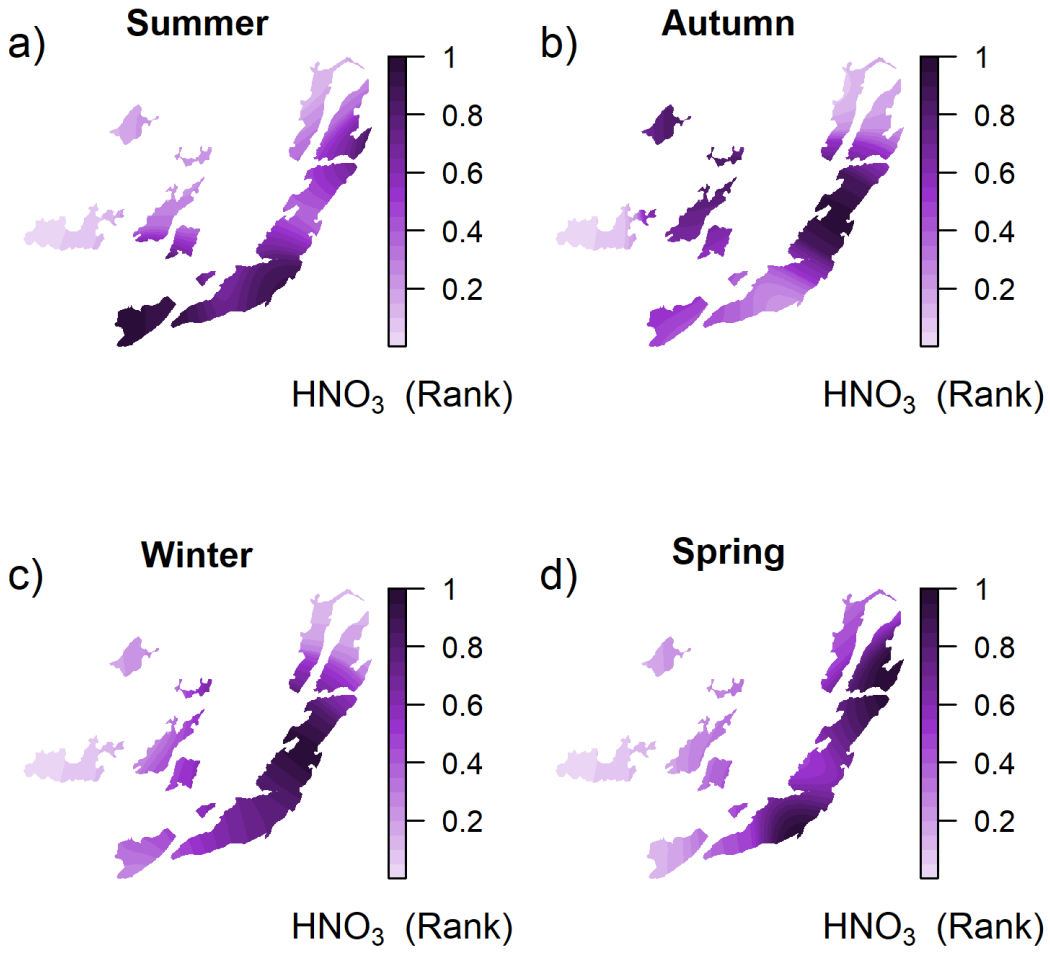

Figure D.5-33: Assessment of concordance between spatial patterns of HNO_3 concentration in different seasons, estimated from spatially smoothed passive sampler data.

D.6 Low powered sensors

D.6.1 NH_3 long term and week plots

Data from the low powered sensors for NH_3 from January 2024 to February 2025 are shown in Figure *D.6-1*. Figure *D.6-1* shows data for the same six sites selected for NO and NO_2.The levels at the three powered sites (AQ01, EX02 and EX09, see Figure *D.6-1*(a)-(c)) appear to begin high, with some variability, before decreasing in the early half of 2024, before remaining fairly constant until May 2025. A similar pattern is observed at AQ04 (Figure *D.6-1*(d)). The NH_3 levels at AQ11 (Figure *D.6-1*(e)) appear fairly constant from January to October 2024, with a similar maximum value to the other sites, before dropping off to a lower level, similar to that of the other sites in early 2025. NH_3 levels at AQ18 (Figure *D.6-1*(f)) show a similar initial pattern to gas concentrations at AQ11. However, after a drop in levels in January 2025, the levels increase back to the previous (higher) level.

The maximum operating range of the NH_3 sensors used is 100 ppm, which suggests that the sensors are not at their maximum voltage in Figure *D.6-1*. The sudden fall in NH_3 levels shown in Figure *D.6-1* are not seasonal and occur at different dates for different sensors. This likely indicates that the NH_3 low powered sensors have reached the end of their usable life and will be replaced. This effect is common with many electrochemical sensors.

The day-to-day sensor responses are shown more clearly by considering the same selected week in November 2024 as previously used for NO and NO_2. These measurements are shown in Figure *D.6-2*. The results for EX02 (Figure *D.6-2*(b)) show signs of daily fluctuations in NH_3 levels, which appear to be consistent (in trend only) with those observed using the real time powered T201 instrument. Notably, this is the only site in the chosen week where NH_3 levels span the range of concentrations shown in Figure *D.6-1*. The other sites showed less variation over the week, which suggests that the levels were fairly consistent, or that changes were smaller than the sensitivity of the sensors. The magnitude of some of these measurements fall within the error range of the sensors, hence these observations must be used with caution.

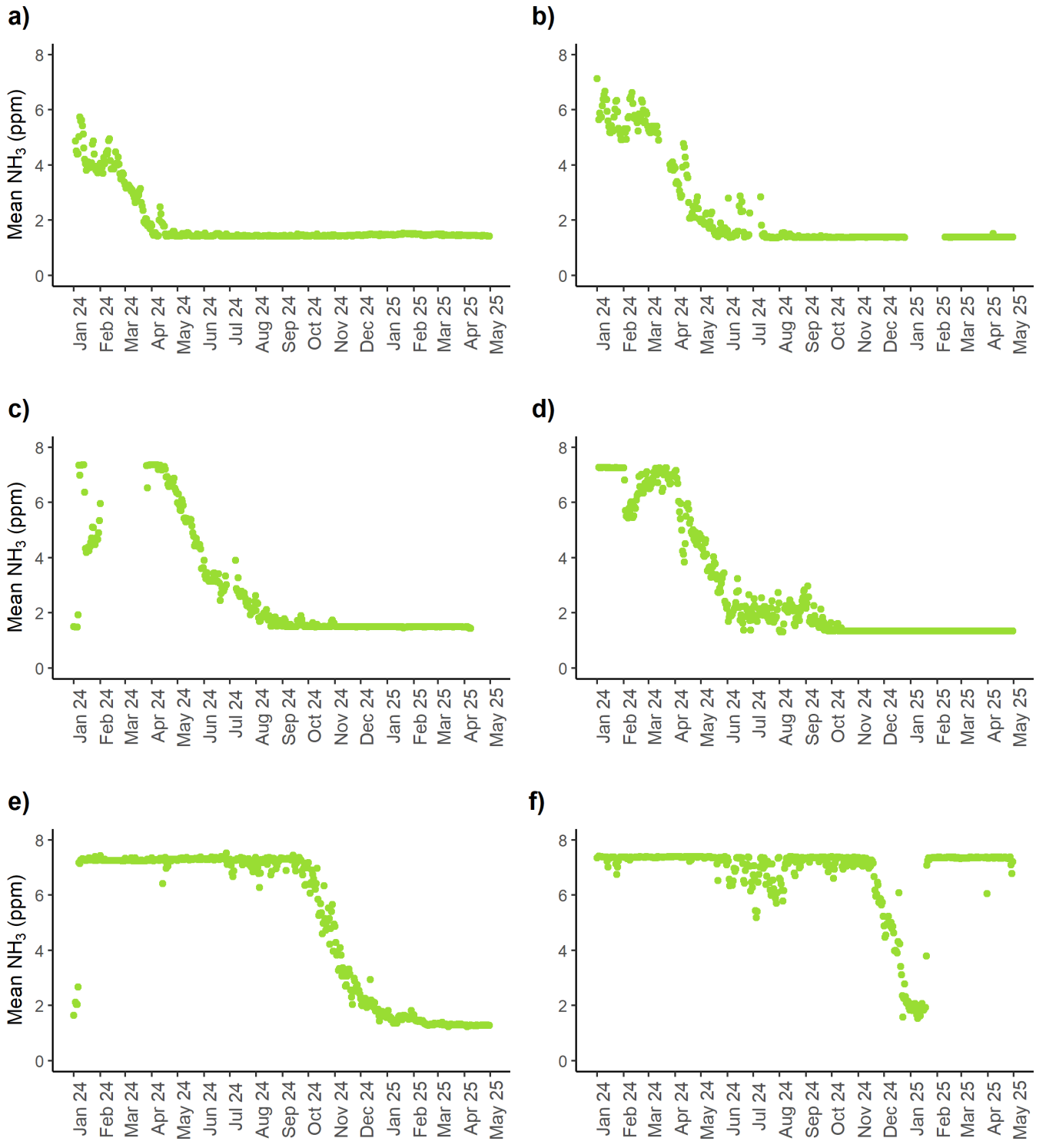

Figure D.6-1: Time series plots for NH_3 measurements from low powered sensors from January 2024 to February 2025 (inclusive), at locations (a) AQ01, (b) EX02, (c) EX09, (d) AQ04, (e) AQ11, and (f) AQ18. Where each point is the daily mean of NH_3.

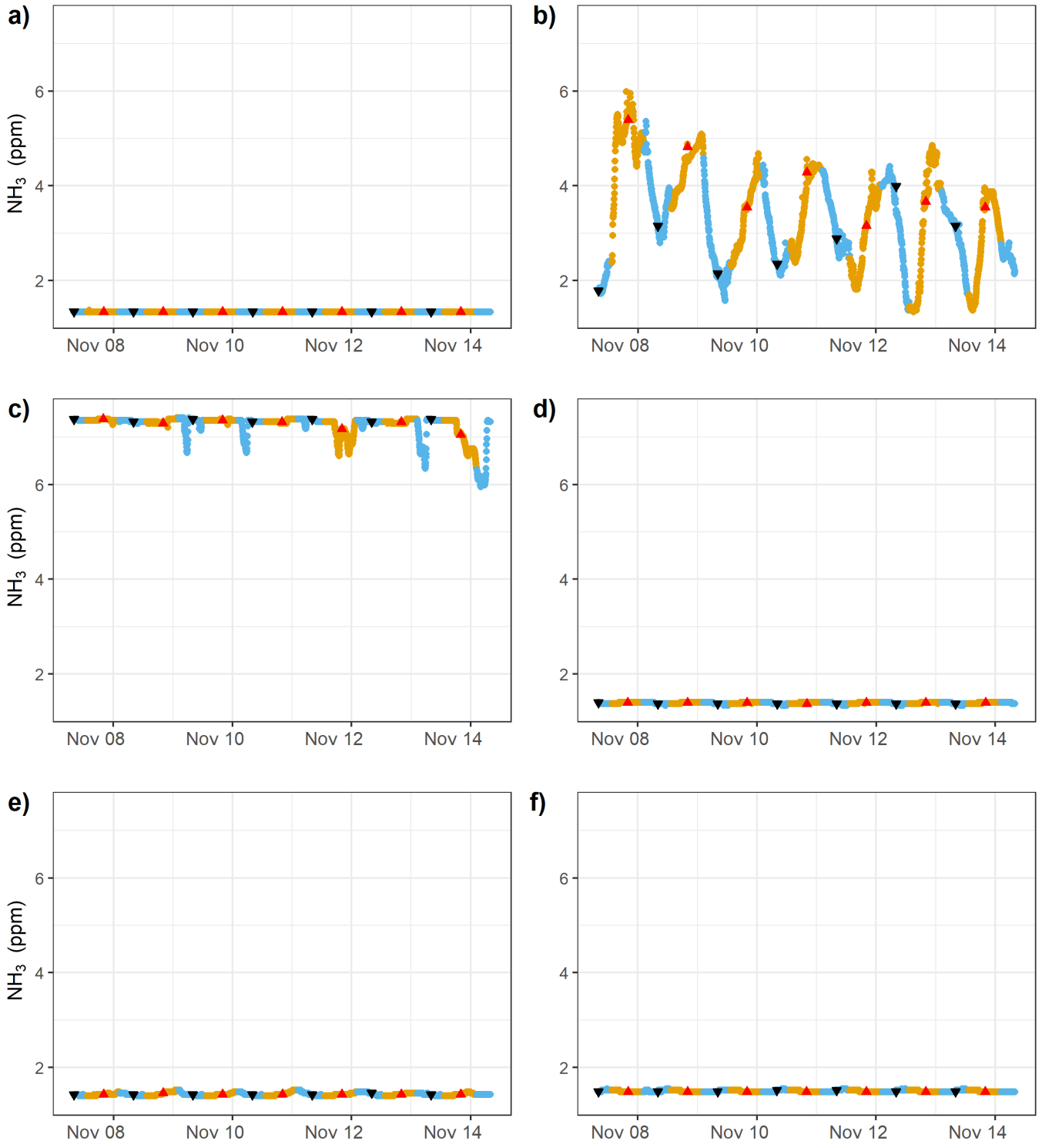

Figure D.6-2: Time series plots for NH_3 measurements from low powered sensors over one week in November 2024, at locations (a) AQ01, (b) EX02, (c) EX09, (d) AQ04, (e) AQ11, and (f) AQ18. The data shown in blue corresponds to nighttime (defined as sunset to sunrise) measurements, and data shown in orange correspond to daytime (defined as sunrise to sunset). The red up-pointing triangles are midday and black down-pointing triangles are midnight.

D.6.2 Further low powered gas and particulate matter summaries

D.6.2.1 Gas summaries

Figure *D.6-3* shows the monthly pattern across all stations for each gas species.

For NO_2 Figure *D.6-3* (a), median values are very similar for all months, but there are more upper outliers for months from August to December.

Figure *D.6-3* (b) shows a similar pattern for NO_2 with very similar medians for each month.

Figure *D.6-3* (c) show a significant decrease in NH_3 measurements across all stations with the highest levels in January to May. However, this may be an artefact caused by a decrease in function of these sensors. (This plot only shows data for 2024, the previous time line, see Figure 7.14-5, shows the new low levels persist into 2025.)

Figure *D.6-3* (d) shows the CO_2 concentrations are much higher than those recorded other gases.

Figure *D.6-4* shows scatterplots of the gas concentrations for each the stations, where stations are ordered by NO_2 concentrations.

The highest concentrations of NO_2 recorded by the low powered sensors are at AQ15, with the lowest concentrations at EX09, see Figure *D.6-4* (a). However, overall the mean gas concentration levels recorded by the low powered sensors are very similar with little deviation across season. Measurements are so closely grouped it is hard to distinguish the different seasons.

A similar pattern is shown for NO, see Figure *D.6-4* (b), with exception of some much lower values required for AQ16.

Figure *D.6-4* (c), shows NH_3 has a a much wider range in values. However this may be due to the failure of the sensors during 2024.

Figure *D.6-4* (d) shows CO_2 values vary across site, though not in the same order as the NO_2 orderings. The highest CO_2 readings are mainly recorded at AQ16.

Figure *D.6-5* shows little difference in low powered sensor gas concentrations distributions by meteorological seasons.

NO_2 in Figure *D.6-5* (a) and NO in Figure *D.6-5* (b) both have very narrow boxes indicate the range of values between the 25% t0 75% percentile is limited across all stations.

NH_3 in Figure *D.6-5* (c) show a much greater range of values, but it not clear if some of this is due to failures in these sensors during the year.

CO_2 in Figure *D.6-5* (d) show some minor variations between seasons, with slightly lower CO_2 concentrations in winter.

Figure *D.6-6* shows the histograms of gas concentrations for each Murujuga season.

For both NO_2 in Figure *D.6-6*(a), and NO in Figure *D.6-6*(b) for Garrbarn and Muthu strongly overlap. In these figures only the Muthu distribution season is visible, but this means the Garrban distribution is very similar. The NO_2 distribution has a number of very high outliers, while the NO distribution has a number of quite low outliers.

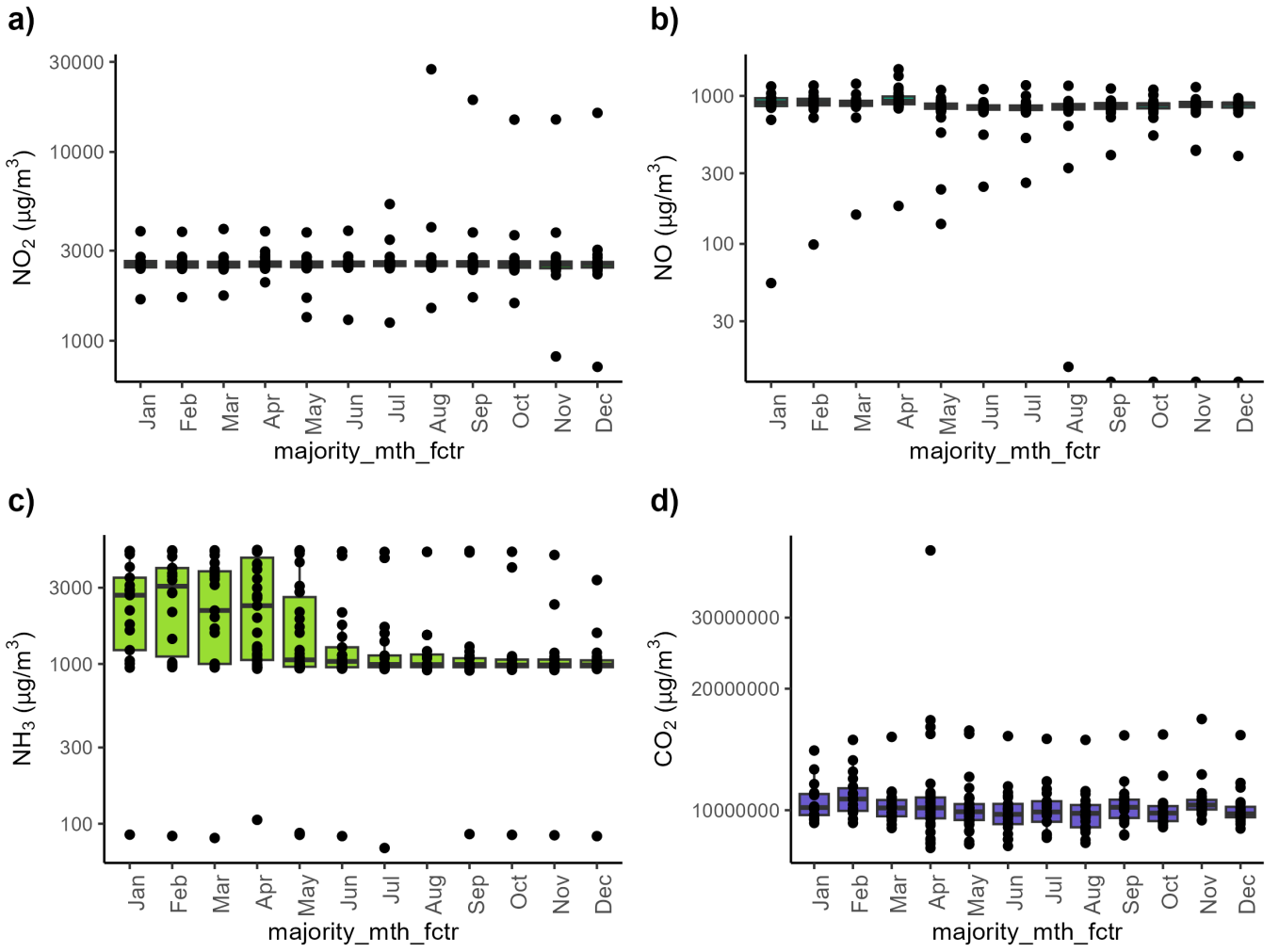

Figure D.6-3: Boxplots of mean gas concentration measurements from low powered sensors by month for all low powered sites for (a) NO, (b) NO_2, (c) NH_3, and (d) CO_2. Means are across passive sampling periods in 2024 to allow comparison to passive sampling measures. Boxplot colours indicate the particulate matter type: NO is sea green, NO_2 is forest (or dark) green, NH_3 is medium green, and CO_2 is slate blue. A log scale is used for the vertical axis.

NH_3 in Figure *D.6-6*(c) also shows a strong overlap between the two Murujuga seasons. Here only the Muthu distribution can be seen, thus it can be assumed that Garrbarn distribution is very similar.

CO_2 in Figure *D.6-6*(d) again shows a strong overlap between the two Murujuga seasons.

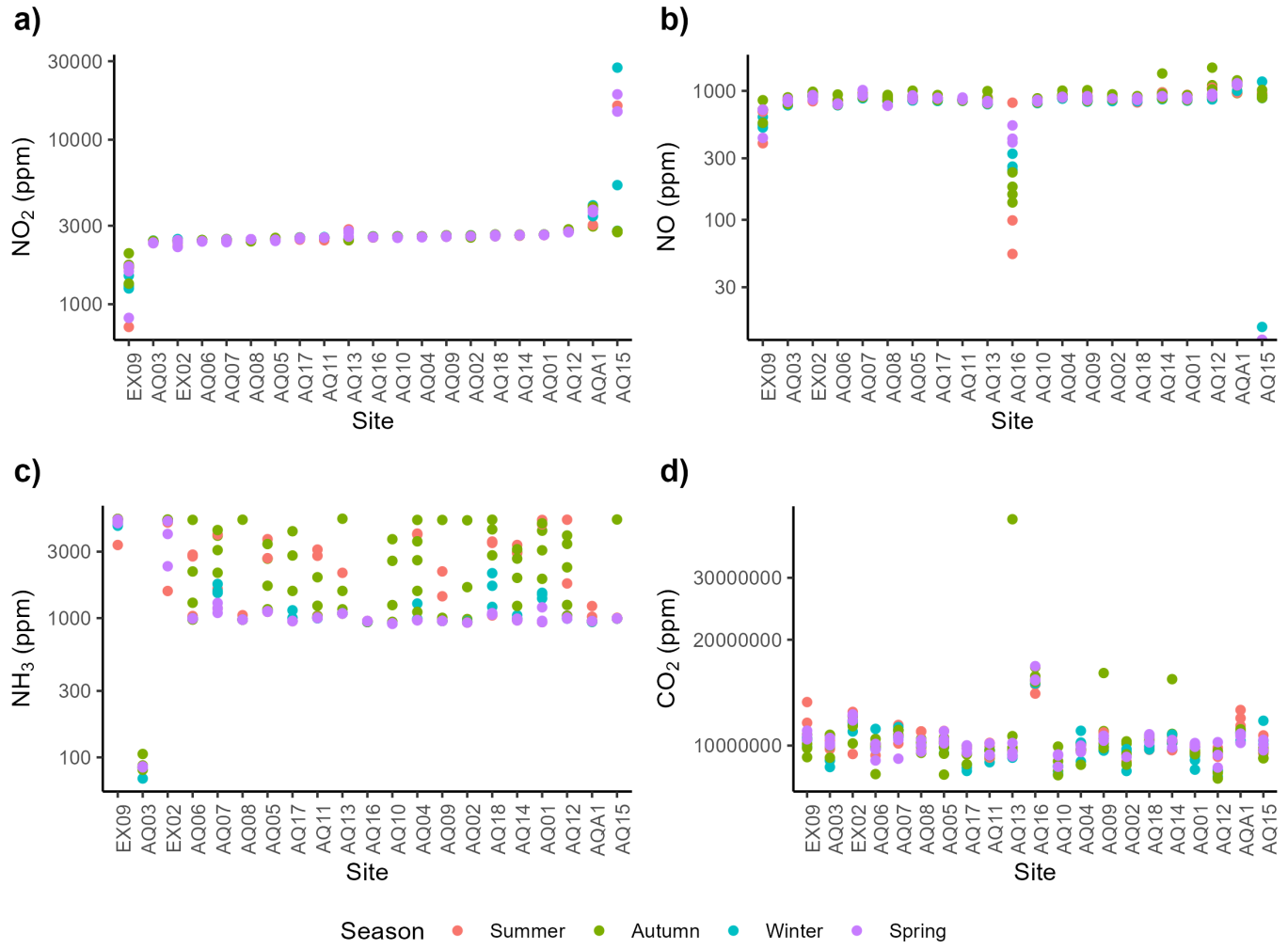

Figure D.6-4: Scatterplots for mean gas concentration measurements from low powered sensors across all low powered sites and indicating meteorological season for (a) NO_2, (b) NO, (c) NH_3, and (d) CO_2. Means are across passive sampling periods in 2024 to allow comparison to passive sampling measures. Seasons are shown by colour where red points indicate summer, purple points indicate autumn, blue points indicate winter, and green points indicate spring. The stations for all plots are ordered by NO_2 levels from highest to lowest: this allows us to compare gas concentrations to NO_2. The vertical axis uses a log scale in all plots.

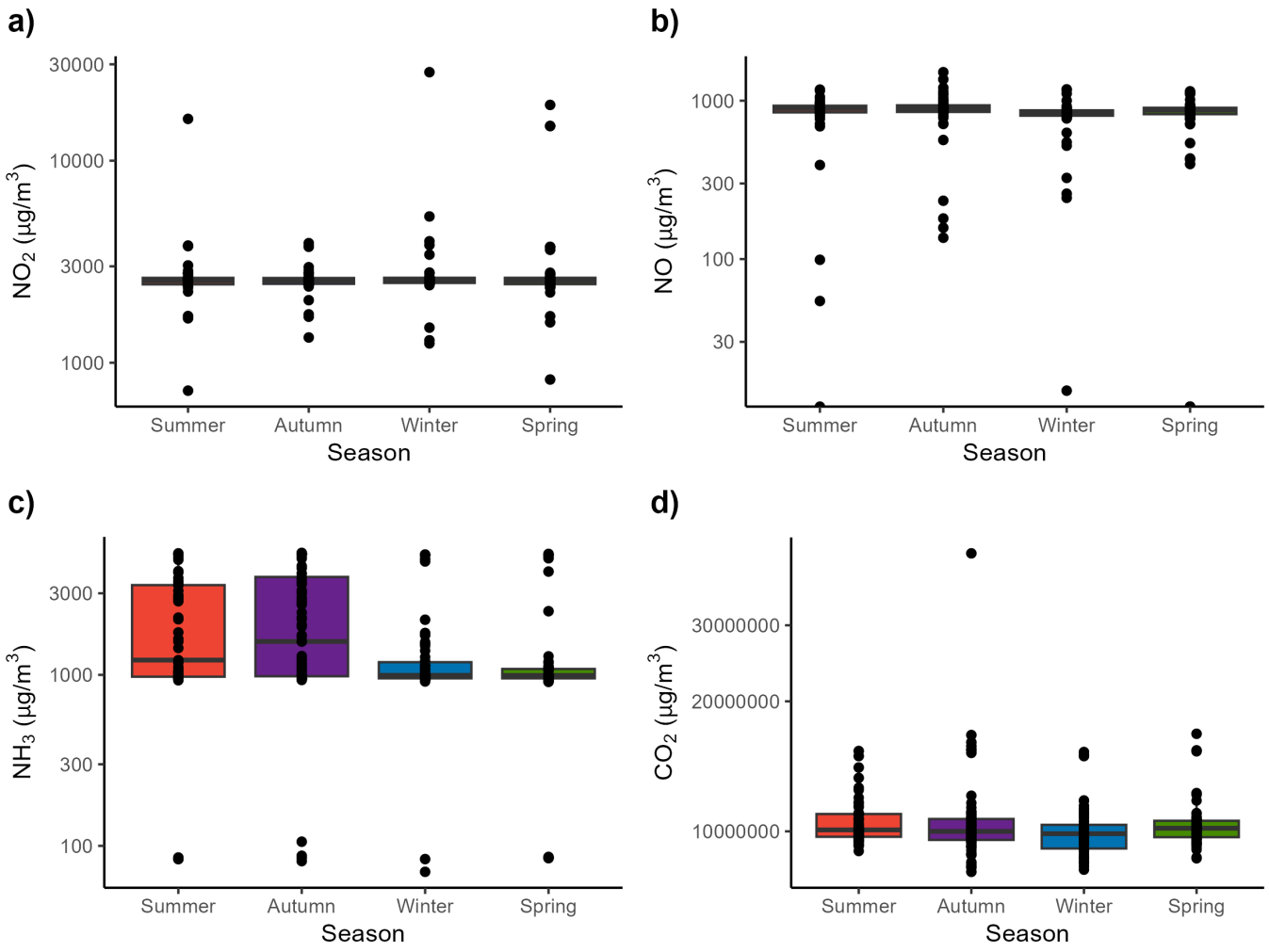

Figure D.6-5: Boxplots of gas concentration measurements from low powered sensors across all low powered sites by meteorological season for (a) NO_2, (b) NO, (c) NH_3, and (d) CO_2. Means are across passive sampling periods in 2024 to allow comparison to passive sampling measures. Seasons are shown by colour where red points indicate summer, purple points indicate autumn, blue points indicate winter, and green points indicate spring.

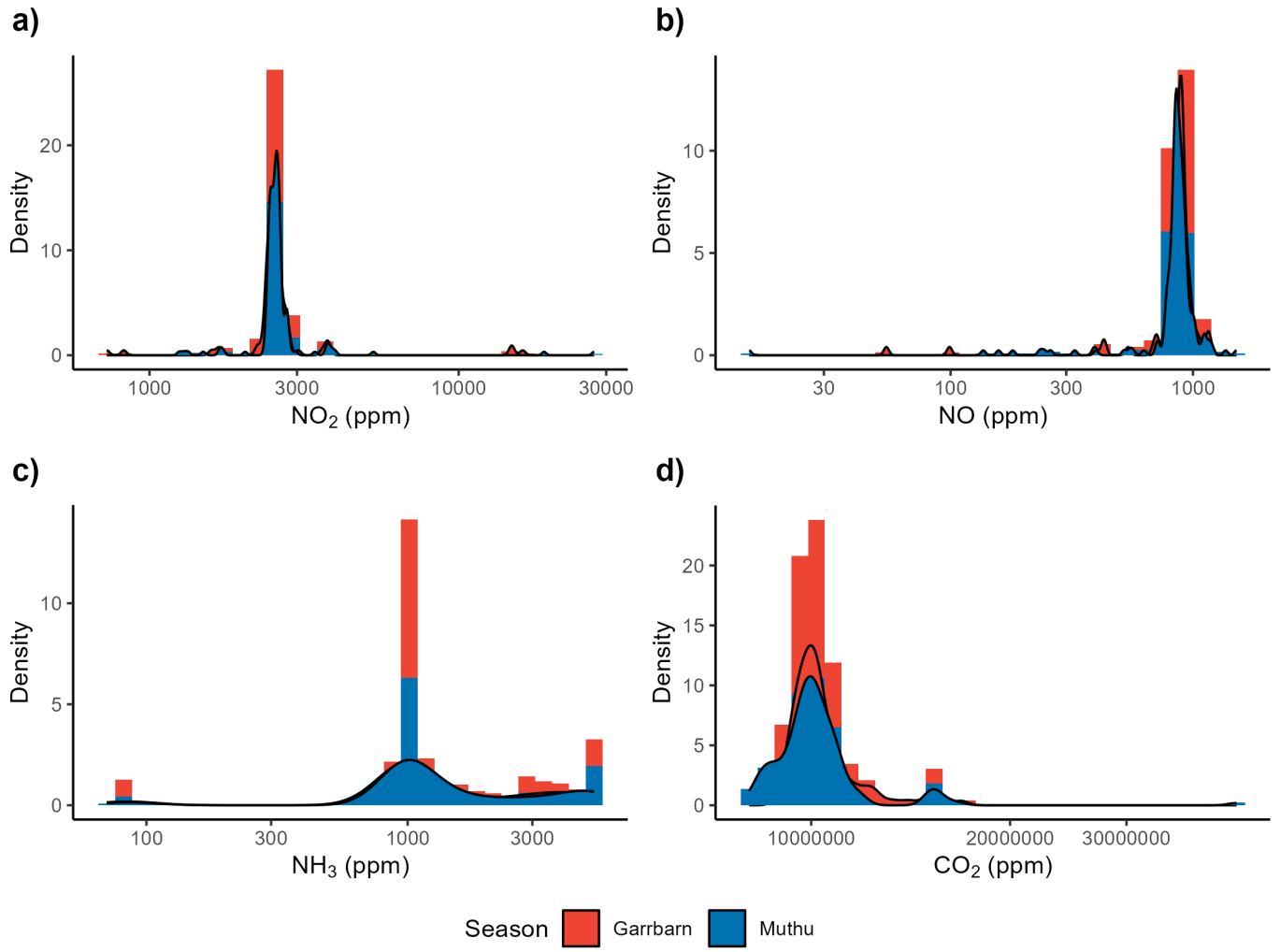

Figure D.6-6: Histograms of gas concentration measurements from low-power sensors across all low-power sites by Murujuga season for (a) NO_2, (b) NO, (c) NH_3, and (d) CO_2. Means are across passive sampling periods in 2024 to allow comparison to passive sampling measures. Seasons are shown by colour where red points indicate Garrbarn (hot) and blue points indicate Muthu (cold) season. The horizontal axis uses a logarithmic scale.

Plot (a) shows the scale in exponential notation, where e indicates the first value is multiplied by exponential of 10, the numbers following e show the power of the exponential. For example $1e+02$ is $1 \times 10^2 = 1 \times 100 = 100$, while $1e-02$ is $1 \times 10^{-2} = 1 \times 0.01 = 0.01$

D.6.2.2 Particulate matter (PM) summaries

Figure *D.6-7* shows the monthly pattern across all stations for $PM_{2.5}$ and PM_{10}.

For $PM_{2.5}$ in Figure *D.6-7* (a) the median values are very similar for the months April to August, with higher median in September and October. Median levels increase from October to a peak in January, and then decrease again until April.

Figure *D.6-7* (b) shows a similar pattern for PM_{10}. Here levels from April to August are lower than those from September to March.

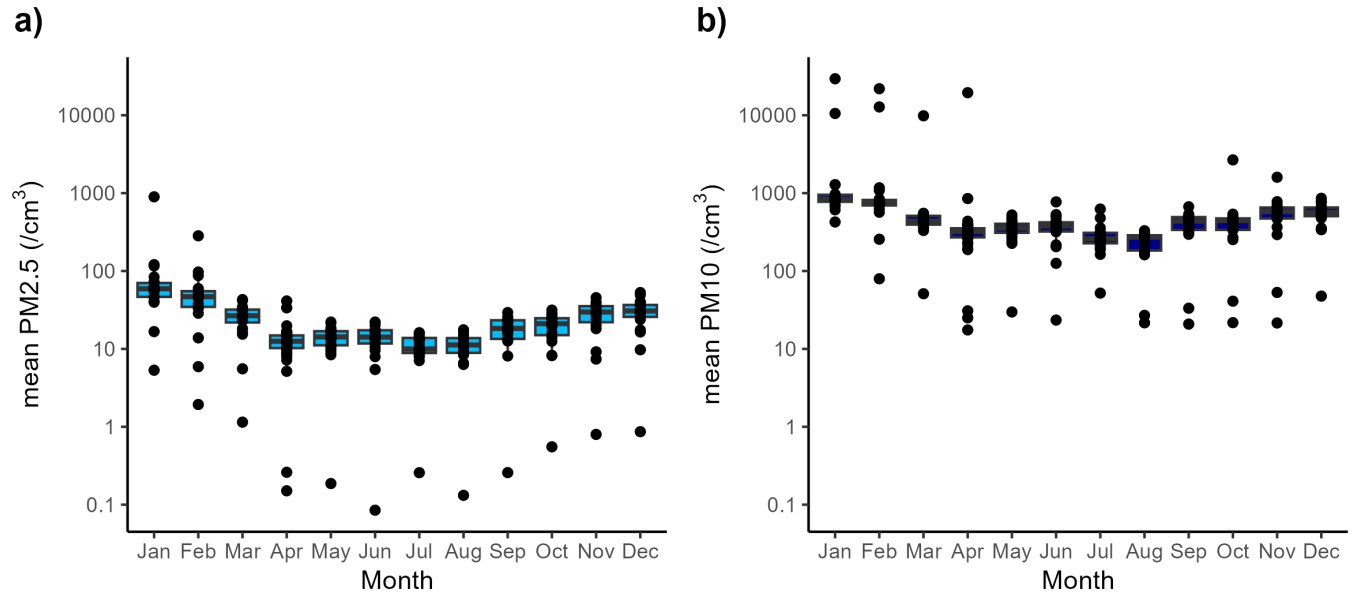

Figure D.6-7: Boxplots of mean particulate matter measurements from low powered sensors by month for all low powered sites for (a) $PM_{2.5}$ and (b) PM_{10}. Means are across passive sampling periods in 2024 to allow comparison to passive sampling measures. Boxplot colours indicate the particulate matter type: light blue is $PM_{2.5}$ and dark blue is PM_{10}. A log scale is used for the vertical axis.

Figure *D.6-8* shows scatterplots of $PM_{2.5}$ and PM_{10} for each the stations. The highest levels for both are recorded at AQ18, in the north of Murujuga. These high levels are possibly the result of exposure to the sea. This figure also shows that levels of $PM_{2.5}$ are highest during the summer months, while many of the lowest levels are recorded in winter (Figure *D.6-8* (a). Spring and autumn levels tend to fall in between summer and winter levels. A similar pattern is shown for PM_{10} by Figure *D.6-8* (b).

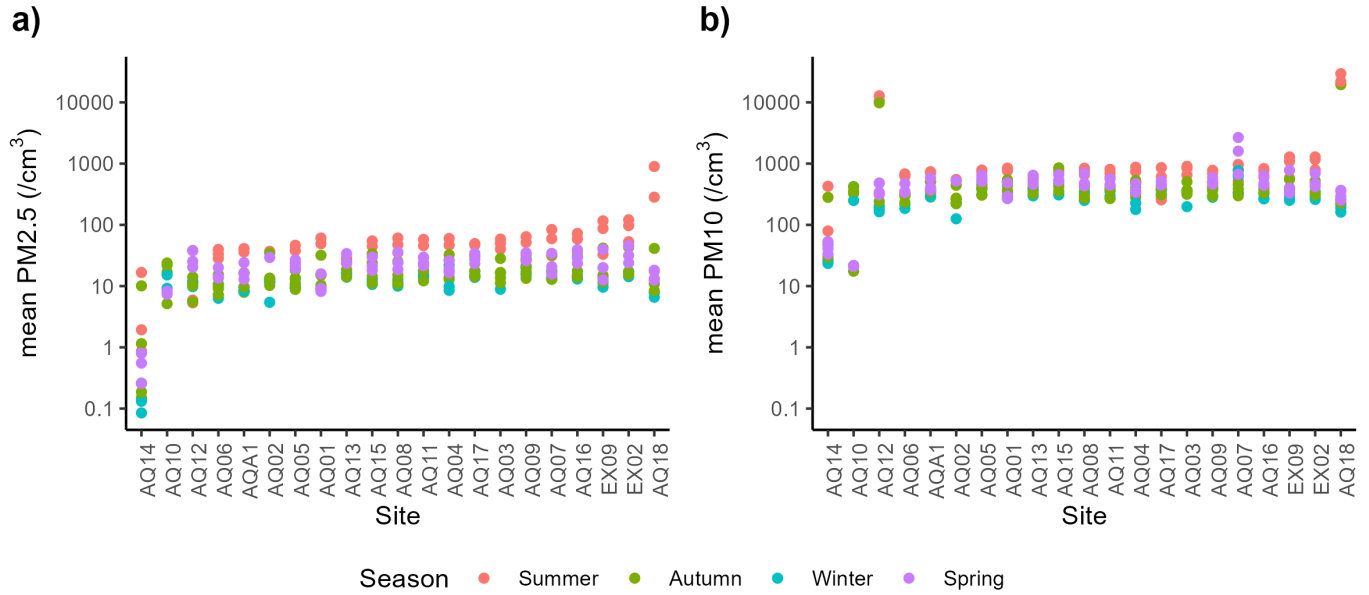

Figure D.6-8: Scatterplots for mean particulate matter measurements from low powered sensors across all low powered sites and indicating meteorological season for (a) $PM_{2.5}$ and (b) PM_{10}. Means are across passive sampling periods in 2024 to allow comparison to passive sampling measures. Seasons are shown by colour where red points indicate summer, purple points indicate autumn, blue points indicate winter, and green points indicate spring. The stations for both plots are ordered by $PM_{2.5}$ levels from highest to lowest.

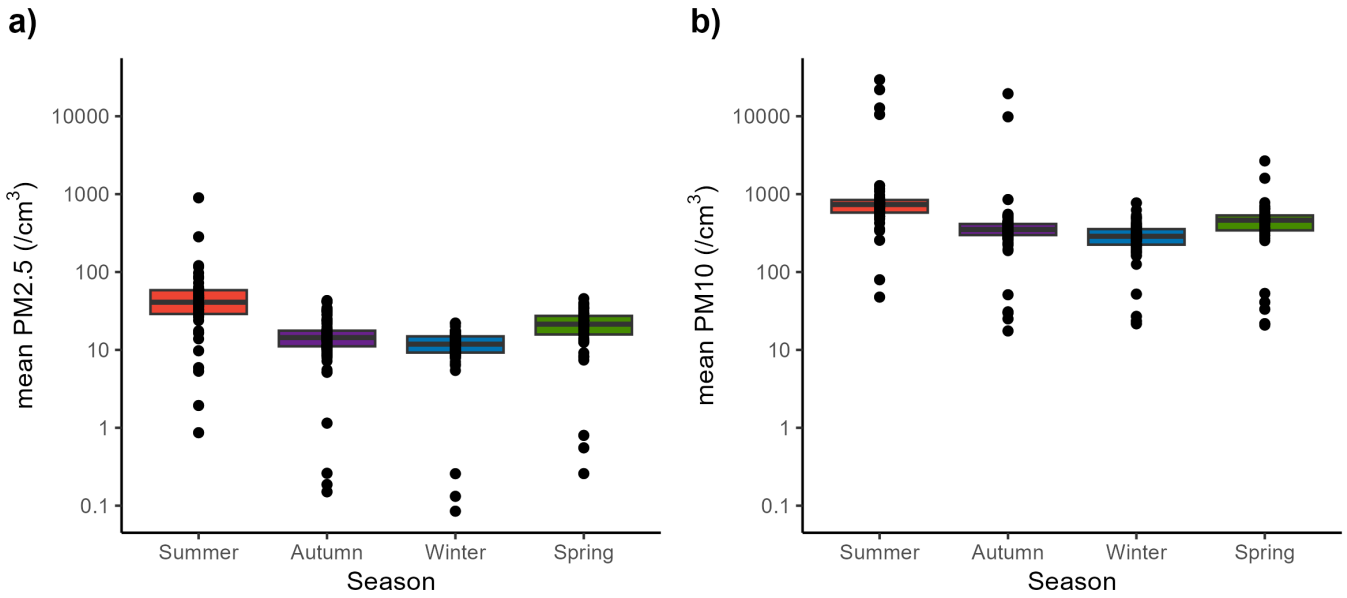

Figure D.6-9: Boxplots of particulate matter measurements from low powered sensors across all low powered sites by meteorological season for (a) $PM_{2.5}$ and (b) PM_{10}. (Means are across passive sampling periods in 2024 to allow comparison to passive sampling measures. Seasons are shown by colour where red points indicate summer, purple points indicate autumn, blue points indicate winter, and green points indicate spring. The stations for both plots are ordered by $PM_{2.5}$ levels from highest to lowest.

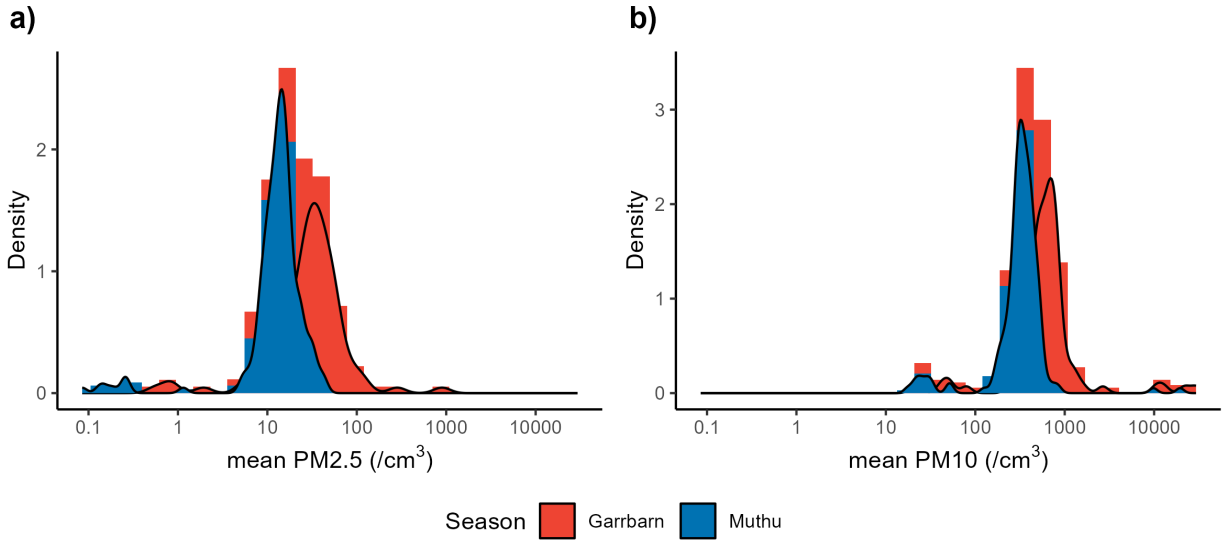

Figure D.6-10: Histograms of mean particulate matter measurements from low-power sensors across all sites by Murujuga season for (a) $PM_{2.5}$ and (b) PM_{10}. Means are across passive sampling periods in 2024 to allow comparison to passive sampling measures. Seasons are shown by colour where red points indicate Garrbarn (hot) and blue points indicate Muthu (cold) season. The horizontal axis uses a log scale. Plot (a) uses exponential notation, where e indicates "times ten to the power of". The numbers after e is the exponent. For example 1e+02 is $1 \times 10^{2}=1 \times 100=100$, while 1e-02 is $1 \times 10^{-2}=1 \times 0.01=0.01$

Figure *D.6-10* shows the histograms of $PM_{2.5}$ (a) and PM_{10} (b) for each Murujuga season. Using the log scale, these distributions are a similar shape and nearly symmetric. However, the mean (peak) value for each season is different: the peak levels are higher for Garrbarn (hot time) than Muthu (cold time).